CELLULAR NEUROPHYSIOLOGY EDITORS' PICK 2021

EDITED BY: Enrico Cherubini and Arianna Maffei
PUBLISHED IN: Frontiers in Cellular Neuroscience



frontiers Research Topics



frontiers

Frontiers eBook Copyright Statement

The copyright in the text of individual articles in this eBook is the property of their respective authors or their respective institutions or funders. The copyright in graphics and images within each article may be subject to copyright of other parties. In both cases this is subject to a license granted to Frontiers.

The compilation of articles constituting this eBook is the property of Frontiers.

Each article within this eBook, and the eBook itself, are published under the most recent version of the Creative Commons CC-BY licence. The version current at the date of publication of this eBook is CC-BY 4.0. If the CC-BY licence is updated, the licence granted by Frontiers is automatically updated to the new version.

When exercising any right under the CC-BY licence, Frontiers must be attributed as the original publisher of the article or eBook, as applicable.

Authors have the responsibility of ensuring that any graphics or other materials which are the property of others may be included in the CC-BY licence, but this should be checked before relying on the CC-BY licence to reproduce those materials. Any copyright notices relating to those materials must be complied with.

Copyright and source acknowledgement notices may not be removed and must be displayed in any copy, derivative work or partial copy which includes the elements in question.

All copyright, and all rights therein, are protected by national and international copyright laws. The above represents a summary only. For further information please read Frontiers' Conditions for Website Use and Copyright Statement, and the applicable CC-BY licence.

ISSN 1664-8714
ISBN 978-2-88966-957-8
DOI 10.3389/978-2-88966-957-8

About Frontiers

Frontiers is more than just an open-access publisher of scholarly articles: it is a pioneering approach to the world of academia, radically improving the way scholarly research is managed. The grand vision of Frontiers is a world where all people have an equal opportunity to seek, share and generate knowledge. Frontiers provides immediate and permanent online open access to all its publications, but this alone is not enough to realize our grand goals.

Frontiers Journal Series

The Frontiers Journal Series is a multi-tier and interdisciplinary set of open-access, online journals, promising a paradigm shift from the current review, selection and dissemination processes in academic publishing. All Frontiers journals are driven by researchers for researchers; therefore, they constitute a service to the scholarly community. At the same time, the Frontiers Journal Series operates on a revolutionary invention, the tiered publishing system, initially addressing specific communities of scholars, and gradually climbing up to broader public understanding, thus serving the interests of the lay society, too.

Dedication to Quality

Each Frontiers article is a landmark of the highest quality, thanks to genuinely collaborative interactions between authors and review editors, who include some of the world's best academicians. Research must be certified by peers before entering a stream of knowledge that may eventually reach the public - and shape society; therefore, Frontiers only applies the most rigorous and unbiased reviews.
Frontiers revolutionizes research publishing by freely delivering the most outstanding research, evaluated with no bias from both the academic and social point of view. By applying the most advanced information technologies, Frontiers is catapulting scholarly publishing into a new generation.

What are Frontiers Research Topics?

Frontiers Research Topics are very popular trademarks of the Frontiers Journals Series: they are collections of at least ten articles, all centered on a particular subject. With their unique mix of varied contributions from Original Research to Review Articles, Frontiers Research Topics unify the most influential researchers, the latest key findings and historical advances in a hot research area! Find out more on how to host your own Frontiers Research Topic or contribute to one as an author by contacting the Frontiers Editorial Office: frontiersin.org/about/contact

CELLULAR NEUROPHYSIOLOGY EDITORS' PICK 2021

Topic Editors:
Enrico Cherubini, European Brain Research Institute, Italy
Arianna Maffei, Stony Brook University, United States

Citation: Cherubini, E., Maffei, A., eds. (2021). Cellular Neurophysiology Editors' Pick 2021. Lausanne: Frontiers Media SA. doi: 10.3389/978-2-88966-957-8

Table of Contents

05 ***Group II Metabotropic Glutamate Receptors Mediate Presynaptic Inhibition of Excitatory Transmission in Pyramidal Neurons of the Human Cerebral Cortex***
Marco Bocchio, Istvan P. Lukacs, Richard Stacey, Puneet Plaha, Vasileios Apostolopoulos, Laurent Livermore, Arjune Sen, Olaf Ansorge, Martin J. Gillies, Peter Somogyi and Marco Capogna

20 ***Sirtuin 1 and Autophagy Attenuate Cisplatin-Induced Hair Cell Death in the Mouse Cochlea and Zebrafish Lateral Line***
Jiaqi Pang, Hao Xiong, Ting Zhan, Gui Cheng, Haiying Jia, Yongyi Ye, Zhongwu Su, Hongyu Chen, Hanqing Lin, Lan Lai, Yongkang Ou, Yaodong Xu, Suijun Chen, Qiuhong Huang, Maojin Liang, Yuexin Cai, Xueyuan Zhang, Xiaoding Xu, Yiqing Zheng and Haidi Yang

31 ***Amyloid β Oligomers Increase ER-Mitochondria $Ca2^+$ Cross Talk in Young Hippocampal Neurons and Exacerbate Aging-Induced Intracellular $Ca2^+$ Remodeling***
Maria Calvo-Rodriguez, Elena Hernando-Perez, Lucia Nuñez and Carlos Villalobos

49 ***Cellular Differences in the Cochlea of CBA and B6 Mice May Underlie Their Difference in Susceptibility to Hearing Loss***
Huihui Liu, Gen Li, Jiawen Lu, Yun-Ge Gao, Lei Song, Geng-Lin Li and Hao Wu

59 ***The Fine Tuning of Drp1-Dependent Mitochondrial Remodeling and Autophagy Controls Neuronal Differentiation***
Chiara Vantaggiato, Marianna Castelli, Matteo Giovarelli, Genny Orso, Maria Teresa Bassi, Emilio Clementi and Clara De Palma

79 ***Organs to Cells and Cells to Organoids: The Evolution of* in vitro *Central Nervous System Modelling***
Dario Pacitti, Riccardo Privolizzi and Bridget E. Bax

101 ***Cortical Pain Processing in the Rat Anterior Cingulate Cortex and Primary Somatosensory Cortex***
Zhengdong Xiao, Erik Martinez, Prathamesh M. Kulkarni, Qiaosheng Zhang, Qianning Hou, David Rosenberg, Robert Talay, Leor Shalot, Haocheng Zhou, Jing Wang and Zhe Sage Chen

115 ***Diazepam Accelerates $GABA_AR$ Synaptic Exchange and Alters Intracellular Trafficking***
Joshua M. Lorenz-Guertin, Matthew J. Bambino, Sabyasachi Das, Susan T. Weintraub and Tija C. Jacob

135 ***Human Mesenchymal Stem Cells Prevent Neurological Complications of Radiotherapy***
Bernat Soria, Alejandro Martin-Montalvo, Yolanda Aguilera, Nuria Mellado-Damas, Javier López-Beas, Isabel Herrera-Herrera, Escarlata López, Juan A. Barcia, Manuel Alvarez-Dolado, Abdelkrim Hmadcha and Vivian Capilla-González

149 ***Human Dorsal Root Ganglia***
Rainer Viktor Haberberger, Christine Barry, Nicholas Dominguez and Dusan Matusica

166 **PARK2** ***Mutation Causes Metabolic Disturbances and Impaired Survival of Human iPSC-Derived Neurons***
Helle Bogetofte, Pia Jensen, Matias Ryding, Sissel I. Schmidt, Justyna Okarmus, Louise Ritter, Christina S. Worm, Michaela C. Hohnholt, Carla Azevedo, Laurent Roybon, Lasse K. Bak, Helle Waagepetersen, Brent J. Ryan, Richard Wade-Martins, Martin R. Larsen and Morten Meyer

180 ***Mitochondria are Dynamically Transferring Between Human Neural Cells and Alexander Disease-Associated GFAP Mutations Impair the Astrocytic Transfer***
Longfei Gao, Zhen Zhang, Jing Lu and Gang Pei

196 ***Lack of Neuronal Glycogen Impairs Memory Formation and Learning-Dependent Synaptic Plasticity in Mice***
Jordi Duran, Agnès Gruart, Olga Varea, Iliana López-Soldado, José M. Delgado-García and Joan J. Guinovart

207 ***A Kinetic Map of the Homomeric Voltage-Gated Potassium Channel (Kv) Family***
Rajnish Ranjan, Emmanuelle Logette, Michela Marani, Mirjia Herzog, Valérie Tâche, Enrico Scantamburlo, Valérie Buchillier and Henry Markram

232 ***High-Fat Diet Induces Neuroinflammation and Mitochondrial Impairment in Mice Cerebral Cortex and Synaptic Fraction***
Gina Cavaliere, Giovanna Trinchese, Eduardo Penna, Fabiano Cimmino, Claudio Pirozzi, Adriano Lama, Chiara Annunziata, Angela Catapano, Giuseppina Mattace Raso, Rosaria Meli, Marcellino Monda, Giovanni Messina, Christian Zammit, Marianna Crispino and Maria Pina Mollica

245 **Bi-Directional Communication Between Neurons and Astrocytes Modulates Spinal Motor Circuits**
Matthew J. Broadhead and Gareth B. Miles

259 ***Advantages of Acute Brain Slices Prepared at Physiological Temperature in the Characterization of Synaptic Functions***
Kohgaku Eguchi, Philipp Velicky, Elena Hollergschwandtner, Makoto Itakura, Yugo Fukazawa, Johann Georg Danzl and Ryuichi Shigemoto

276 ***Glucagon-Like Peptide-1 Secreting L-Cells Coupled to Sensory Nerves Translate Microbial Signals to the Host Rat Nervous System***
Maria M. Buckley, Rebecca O'Brien, Eilish Brosnan, R. Paul Ross, Catherine Stanton, Julliette M. Buckley and Dervla O'Malley

289 ***Modeling a Nociceptive Neuro-Immune Synapse Activated by ATP and 5-HT in Meninges: Novel Clues on Transduction of Chemical Signals Into Persistent or Rhythmic Neuronal Firing***
Alina Suleimanova, Max Talanov, Oleg Gafurov, Fail' Gafarov, Ksenia Koroleva, Anaïs Virenque, Francesco M. Noe, Nikita Mikhailov, Andrea Nistri and Rashid Giniatullin

frontiers in Cellular Neuroscience

ORIGINAL RESEARCH
published: 08 January 2019
doi: 10.3389/fncel.2018.00508

Group II Metabotropic Glutamate Receptors Mediate Presynaptic Inhibition of Excitatory Transmission in Pyramidal Neurons of the Human Cerebral Cortex

Marco Bocchio[1†], Istvan P. Lukacs[1], Richard Stacey[2], Puneet Plaha[2], Vasileios Apostolopoulos[2], Laurent Livermore[2], Arjune Sen[3,4], Olaf Ansorge[4], Martin J. Gillies[4], Peter Somogyi[1] and Marco Capogna[5,6]**

[1] Department of Pharmacology, University of Oxford, Oxford, United Kingdom, [2] Department of Neurosurgery, John Radcliffe Hospital, Oxford University Hospitals NHS Foundation Trust, Oxford, United Kingdom, [3] Oxford Epilepsy Research Group, NIHR Biomedical Research Centre, Oxford, United Kingdom, [4] Nuffield Department of Clinical Neurosciences, Medical Sciences Division, University of Oxford, Oxford, United Kingdom, [5] Department of Biomedicine, Aarhus University, Aarhus, Denmark, [6] The Danish Research Institute of Translational Neuroscience, Nordic EMBL Partnership for Molecular Medicine – Department of Biomedicine, Aarhus University, Aarhus, Denmark

OPEN ACCESS

Edited by:
Enrico Cherubini,
Scuola Internazionale Superiore di Studi Avanzati (SISSA), Italy

Reviewed by:
Annalisa Scimemi,
University at Albany, United States
Huib Mansvelder,
VU University Amsterdam, Netherlands

***Correspondence:**
Peter Somogyi
peter.somogyi@pharm.ox.ac.uk
Marco Capogna
marco.capogna@biomed.au.dk

†Present address:
Marco Bocchio,
INMED, INSERM U1249, Marseille, France

Received: 29 October 2018
Accepted: 07 December 2018
Published: 08 January 2019

Citation:
Bocchio M, Lukacs IP, Stacey R, Plaha P, Apostolopoulos V, Livermore L, Sen A, Ansorge O, Gillies MJ, Somogyi P and Capogna M (2019) Group II Metabotropic Glutamate Receptors Mediate Presynaptic Inhibition of Excitatory Transmission in Pyramidal Neurons of the Human Cerebral Cortex. Front. Cell. Neurosci. 12:508. doi: 10.3389/fncel.2018.00508

Group II metabotropic glutamate receptor (mGluR) ligands are potential novel drugs for neurological and psychiatric disorders, but little is known about the effects of these compounds at synapses of the human cerebral cortex. Investigating the effects of neuropsychiatric drugs in human brain tissue with preserved synaptic circuits might accelerate the development of more potent and selective pharmacological treatments. We have studied the effects of group II mGluR activation on excitatory synaptic transmission recorded from pyramidal neurons of cortical layers 2–3 in acute slices derived from surgically removed cortical tissue of people with epilepsy or tumors. The application of a selective group II mGluR agonist, LY354740 (0.1–1 μM) inhibited the amplitude and frequency of action potential-dependent spontaneous excitatory postsynaptic currents (sEPSCs). This effect was prevented by the application of a group II/III mGluR antagonist, CPPG (0.1 mM). Furthermore, LY354740 inhibited the frequency, but not the amplitude, of action potential-independent miniature EPSCs (mEPSCs) recorded in pyramidal neurons. Finally, LY354740 did slightly reduce cells' input resistance without altering the holding current of the neurons recorded in voltage clamp at −90 mV. Our results suggest that group II mGluRs are mainly auto-receptors that inhibit the release of glutamate onto pyramidal neurons in layers 2–3 in the human cerebral cortex, thereby regulating network excitability. We have demonstrated the effect of a group II mGluR ligand at human cortical synapses, revealing mechanisms by which these drugs could exert pro-cognitive effects and treat human neuropsychiatric disorders.

Keywords: presynaptic receptor, glutamatergic, EPSC, cognitive enhancer, transmitter release, epilepsy, mGluR, human cortex

INTRODUCTION

Pre- and postsynaptic metabotropic glutamate receptors (mGluRs) are activated by L-glutamate, the major excitatory transmitter in the mammalian central nervous system (CNS). These receptors regulate neuronal excitability and synaptic plasticity and mediate the actions of neuroactive drugs (Anwyl, 1999; Cartmell and Schoepp, 2002; Niswender and Conn, 2010). Eight subtypes of mGluRs have been identified and these are classified into three groups (mGluRs I, II, and III) according to their amino acid sequence similarities, agonist selectivity, and interactions with transduction mechanisms (Conn and Pin, 1997). Group II receptors (mGlu2 and mGlu3) are intriguing due to their peri- and extra-synaptic location outside the synaptic junction (Shigemoto et al., 1997; Corti et al., 2002), predicting receptor activation in an activity-dependent manner when glutamate spills over from the release site (Scanziani et al., 1997). This process may be of interest not only under physiological but also under pathological conditions (Molinari et al., 2012). Group II mGluRs are often coupled to the cyclic AMP cascade (Conn and Pin, 1997) and are potently activated by a series of compounds developed by several pharmaceutical companies and particularly by Eli Lilly and Company, for example (1)-2-aminobicyclo[3.1.0] hexane-2,6-dicarboxylic acid (LY354740) (Schoepp et al., 1999).

Work performed in rodents shows that the activation of group II mGluRs have pre- and post-synaptic effects, consistent with receptor locations (Anwyl, 1999; Cartmell and Schoepp, 2002; Niswender and Conn, 2010). For example, presynaptic group II mGluRs, expressed by the perforant pathway from the entorhinal cortex depress excitatory synaptic responses recorded from hippocampal CA1 pyramidal cells or interneurons of stratum lacunosum moleculare (Kew et al., 2001; Capogna, 2004; Price et al., 2005). Conversely, activation of postsynaptic mGlu3 expressed by hippocampal CA3 pyramidal neurons enhances excitability by inhibiting a K^+ conductance and by activating a calcium-sensitive cationic conductance (Ster et al., 2011). Moreover, mGlu3R activation enhances mGlu5R-mediated somatic Ca^{2+} mobilization in pyramidal cells of the mouse prefrontal cortex (Di Menna et al., 2018).

Furthermore, pharmacological or genetic manipulation of mGlu2 gate synaptic plasticity, for instance at hippocampal mossy fiber to CA3 pyramidal cell synapses (Yokoi et al., 1996). Thus, the cellular mechanisms by which group II mGluRs regulate network function are heterogeneous. Additional complexity is given by the fact that group II mGluRs are expressed on axons that target specific cell types but not others (Kintscher et al., 2012).

Group II mGluRs can be down-regulated during development (Doherty et al., 2004), indicating that these receptors could be critical for network maturation as well as for neurodevelopmental disorders. Conversely, group II mGluRs are up-regulated following epileptic seizures (Doherty and Dingledine, 2001). These observations suggest that these receptors could play a role in various brain disorders. Indeed, group II mGluRs are currently investigated as potential drug targets for treating neurological and psychiatric disorders. Several agonists have been developed with the aim of improving cognitive dysfunction in schizophrenia, Alzheimer's disease and anxiety disorders (Caraci et al., 2018; Ferraguti, 2018; Stansley and Conn, 2018). For example, agonists of group II mGluRs show anxiolytic activity in a wide range of animal models of anxiety disorder (Swanson et al., 2005) and improve cognition (Stansley and Conn, 2018). Experimentally, LY354740 rescues deficits in stereotypy, locomotion, spatial working memory and cortical glutamate efflux induced by pharmacological blockade of NMDA receptors in rodents (Moghaddam and Adams, 1998). Furthermore, several mGlu2 positive allosteric modulators (PAMs) have shown efficacy in preclinical animal models of schizophrenia (Spooren et al., 2000; Galici, 2005) (see review: Maksymetz et al., 2017).

Behavioral effects of mGluR activation in humans provide translational validity of the results obtained in animal models. For example, group II mGluR agonists attenuate NMDA receptor activation-induced deficits in working memory in human subjects (Krystal et al., 2005). However, clinical trials using group II mGluR agonists or PAMs in psychiatric patients have not led to the introduction of novel clinical treatments (see reviews: Maksymetz et al., 2017; Ferraguti, 2018). Reasons for translational failure are complex, including species differences, lack of appropriate animal models, insufficient dosing and limited bioavailability of the drugs tested (Jucker, 2010). As for many other receptor systems, there is a gap between the vast amounts of information available on the actions of group II mGluRs in rodent versus human CNS. The aim of the present study is to help closing this gap and to elucidate the action of the potent and selective group II mGluR agonist LY354740 on pyramidal neurons recorded from acute slices derived from surgically removed human cortical tissue.

MATERIALS AND METHODS

Ethics Statement and Patients

Surgical specimens were obtained from the temporal neocortex of drug resistant temporal lobe epilepsy (TLE) (patients A–E, **Table 1A**, five females) and from the temporal and frontal neocortex of low grade glioma oncological patients with brain tumors (patients F–H, **Table 1B**, one female, two males) operated at the John Radcliffe Hospital, Oxford, United Kingdom. All studied tissues were necessarily removed during the surgical procedure and were surplus to diagnostic requirements. Ethics approval was sought and obtained from Research Ethics Committees, National Health Service, Health Research Authority, United Kingdom (NRES Committee South Central – Oxford C: reference 15/SC/0639; NRES Committee East of England – Cambridgeshire and Hertfordshire: reference 14/EE/1098). Fully informed written consent was obtained from each patient who participated.

Slice Preparation

A small piece of cortical tissue (size $< 1\ cm^3$) including all layers and some white matter was isolated using a scalpel, removed and immediately immersed in cutting artificial cerebrospinal fluid (ACSF) saturated with carbogen (95% O_2/5% CO_2), at ∼4°C. The

solution containing the block of tissue was continuously bubbled with carbogen. Transportation from the operating theater to the laboratory lasted 15–60 min. The block of tissue was placed in a petri dish containing ice-cold cutting ACSF bubbled with carbogen. In some cases, the block of tissue was divided into smaller pieces before transportation. Next, the block of tissue was glued on a platform of a vibratome (Microm HM 650 V, Thermo Fisher Scientific) and cut into slices at a setting of 325 μm thickness in cutting ACSF at 4°C. The block of tissue was oriented in a way to slice perpendicular to the pia and parallel to the apical dendrites of the pyramidal cells. The cutting ACSF contained the following compounds (in mM): 65 sucrose, 85 NaCl, 25 $NaHCO_3$, 2.5 KCl, 1.25 NaH_2PO_4, 0.5 $CaCl_2$, 7 $MgCl_2$, 10 glucose (pH 7.3, ∼300 mOsm/L). Slices were incubated in cutting ACSF at 36°C. After ∼10 min, the cutting ACSF was replaced with recording ACSF at 36°C using a peristaltic pump (Gilson) operated at ∼5 mL/min. The recording ACSF contained the following compounds (in mM): 126 NaCl, 2.5 KCl, 1.2 NaH_2PO_4, 26 $NaHCO_3$, 2 $CaCl_2$, 2 $MgCl_2$, 10 glucose, (pH 7.3, ∼300 mOsm/L). Slices were heated at 36°C for 30 min, after which they were stored at room temperature and continuously bubbled with carbogen.

Electrophysiological Recordings

Slices were submerged in a recording chamber and stabilized with a plastic string harp. The chamber was continuously perfused with oxygenated recording ACSF at a rate of 10 mL/min by a peristaltic pump (Gilson) at a temperature of 33 ± 1°C. Neurons were visualized using a differential interference contrast (DIC) microscope (Olympus BX51WI) using a LUMPlanFL 60× water objective (Olympus) and equipped with a camera (Zyla, ANDOR) connected to a desktop computer. Glass electrodes (4–6 MΩ) were prepared from borosilicate glass capillaries (1.2 mm; GC120F, Harvard Apparatus) using a DMZ Universal puller (Zeitz-Instrument). Electrodes were filled with an intracellular solution composed of the following (in mM): 126 K-gluconate, 4 KCl, 4 ATP-Mg, 0.3 GTP-Na_2, 10 Na_2-phosphocreatine, 10 HEPES, and 0.05% biocytin, with osmolarity of 270–280 mOsmol/L without biocytin, at pH 7.3 adjusted with KOH. Somatic whole-cell patch-clamp recordings were performed from visualized neurons in cortical layers 2–3. Electrophysiological signals were amplified using an EPC10 triple patch clamp amplifier (HEKA Electronik), digitized at 20 kHz for recordings in voltage-clamp mode and at 5 kHz for recordings in current-clamp mode, and acquired using Patchmaster software (HEKA Electronik). All reported voltage values were compensated for a calculated 16 mV liquid junction potential between the ACSF and the recording pipette. Spontaneous or miniature excitatory postsynaptic currents (sEPSCs or mEPSCs) were recorded in continuous voltage clamp with a holding potential of −90 mV (corresponding to the calculated Cl^- reversal potential). The mEPSCs were recorded after the addition of 1 μM tetrodotoxin (TTX) to the recording ACSF. Uncompensated series resistance was monitored using a 20 ms-long −10 mV voltage step applied at the beginning of every sweep (i.e., every minute). The sEPSCs or mEPSCs were recorded continuously for up to ∼30 min. After 3–4 min of baseline recording 0.1–1 μM LY354740 was perfused

TABLE 1(A) | Clinical data of temporal lobe epilepsy cases.

Patient		Surgery details			Seizure pathology			Histological findings at site of pathology	
Code	Age*	Sample origin site **	Anesthesia	No. of cells	Age at onset	Seizure frequency pre-op	Semiology	Cortical dysplasia	Sclerosis/other histological alterations
A	56–60	Right inferior temporal gyrus	Dexamethasone, flucloxacillin, metaraminol, paracetamol, propofol, remifentanil	2	54	Clusters every 2 weeks	Complex and simple partial seizures, no secondary generalization	Inconclusive	Sclerosis **** – right hippocampus
B	26–30	Left middle temporal gyrus	Flucloxacillin, gentamicin, metaraminol, propofol, remifentanil, vecuronium	5	21	1–3 focal seizures per day	Complex partial seizures, occasional secondary generalization	No dysplasia	Diffuse gliosis – left temporal neocortex; ILAE type 1 sclerosis – left hippocampus
C	30–35	Left middle temporal gyrus	Ceftriaxone, dexamethasone, gentamicin, remifentanil, paracetamol, propofol, vecuronium	2	14	Once every 2–3 weeks	Partial seizures, no secondary generalization	Focal cortical dysplasia	Gliosis – left temporal lobe; sclerosis **** – left hippocampus
D	36–40	Left inferior temporal gyrus	Flucloxacillin, gentamicin, metaraminol, propofol, remifentanil, vecuronium	7	7	Daily	Complex partial seizures, occasional secondary generalization	No dysplasia	ILAE type 2 sclerosis – left hippocampus
E	26–30	Right inferior temporal gyrus	Atracurium, co-amoxiclav, dexamethasone, gentamicin, paracetamol, propofol, remifentanil	2	14	Once per week	Complex partial seizures, occasional generalized tonic–clonic seizures	No dysplasia	ILAE type 1 sclerosis – right hippocampus

(Continued)

TABLE 1(A) | Continued

Patient	Medication at time of surgery (dose/day, in mg) – duration			Medication history (dose/day, in mg) - duration			Other relevant pathology
Code	**Anti-convulsive medication**	**Psychiatric medication**	**Other medication *****	**Anticonvulsive medication**	**Psychiatric medication**	**Other medication *****	**Medical history**
A	Phenytoin (500) – 1 year; clobazam (20) – 1 year	Prochlorperazine (15) – 1 year	Betahistine (24) – 1 year; propranolol (30) – 1 year	Carbamazepine (200) – 2 days; levetiracetam (250) – 5 months; pregabalin (25) – 1 month; valproate (1000) – 1 year	Amitriptyline (10) – 9 months	Bendroflumethiazide (2.5) – 9 months	Parieto-occipital meningioma, secondary focal seizures – resected 2005; brainstem cavernoma, telangiectasia, hemorrhage – right pons; brainstem syndrome; temporal choroid plexus meningioma/papilloma – resected 2014
B	Lamotrigine (200) – 3 years; clobazam (20) – 1.5 years; topiramate (250) – 3 years	None – n.a.	None – n.a.	Valproate (500) – 2 weeks; carbamazepine (800) – 3 years; lacosamide (200) – 3 months; levetiracetam (750) – 1 month	None – n.a.	None – n.a.	Depression; migraine
C	Levetiracetam (2000) – 2.5 years; perampanel (8) – 1.5 years	Citalopram (10) – 2.5 years	Cyclosporin (200) – 2.5 years; methotrexate (12.5/week) – 2.5 years; folic acid (5) – 2.5 years; omeprazole (20) – 2.5 years	Eslicarbazepine (1000) – 2.5 years; clobazam (10) – 4 months; phenytoin (500) – 3 years; carbamazepine (1600) – 3 years; lamotrigine (200) – 3 years; pregabalin (600) – 3 years; lacosamide (200) – 3 years; zonisamide (400) – 2 years; topiramate (25) – 1 year; gabapentin (2700) – 3 years	None – n.a.	None – n.a.	Left temporal lobe epilepsy – left temporal lobectomy 2007; benign paroxysmal positional vertigo; psoriasis; depression
D	Tegretol retard (1600) – 22 years; topiramate (100) – 2.5 years; clobazam (10) – 5 years; sertraline (200) – 5 years	None – n.a.	Cetirizine (10) – not known	Valproate (1000) – 4 years; lamotrigine (200) – 4 years; levetiracetam (1500) – 4 years; phenobarbitone (not known) – in childhood	None – n.a.	None – n.a.	Depression
E	Lamotrigine (50) – 8 years; levetiracetam (6000) – 6 years; sertraline (150) – 2 years	None – n.a.	Ovranette (150/30) – 10 years; folic acid (5) – not known	Valproate (500) – 2 years	None – n.a.	None – n.a.	Irritable bowel syndrome; anxiety; asthma

**Patient in this age range; **sample origin site is from the same hemisphere as the pathology; ***no steroids; ****ILAE type not determined; ILAE, International League Against Epilepsy.*

TABLE 1(B) | Clinical data of glioma cases.

Patient		Surgery details			Tumor pathology and medication***					
Code	**Age***	**Sample origin site**	**Anesthesia**	**No of cells**	**Diagnosis**	**WHO grade**	**Type**	**Site of tumor pathology**	**Cortical infiltration**	**Increased intracranial pressure/oedema**
F	50–55	Right inferior temporal gyrus	Flucloxacillin, gentamicin, metaraminol, propofol, remifentanil, vecuronium	4	Diffuse astrocytoma, not otherwise specified	II	Wild-type	Right temporal lobe	No	No/no
G	20–25	Left inferior frontal gyrus	Flucloxacillin, gentamicin, metaraminol, propofol, remifentanil, vecuronium	3	Oligodendroglioma	II	IDH1-H132R mutated	Left frontal lobe	No	No/yes
H	20–25	Right inferior temporal gyrus	Flucloxacillin, gentamicin, mannitol, metaraminol, propofol, remifentanil, vecuronium	5	Anaplastic astrocytoma	III	IDH1-H132R mutated	Right temporal lobe	Yes	Yes*****/no

(Continued)

TABLE 1(B) | Continued

Patient	Seizure pathology and medication (dose/day, in mg) – duration			Other relevant pathology and medication**** (dose/day, in mg) – duration		
Code	**Seizures**	**Onset**	**Anticonvulsive medication**	**Steroid medication**	**Other medication**	**Medical history**
F	Partial seizures	1970	Carbamazepine** (200) – 47 years; phenytoin (not known) – 31 years; levetiracetam** (1500) – 16 years	Dexamethasone** (16) – once before surgery	None – n.a.	Posterior fossa astrocytoma – resected 1970; radiotherapy; traumatic brain injury 1990; left temporal meningioma – resected 2016
G	Partial seizure	Two seizures on 29/10/2017	Levetiracetam** (1000) – 2.5 months	Dexamethasone** (8) – 2.5 months	Omeprazole (20) – not known	None
H	None	n.a.	Levetiracetam** (500) – 1.5 months	Dexamethasone** (16) – 1.5 months	Lansoprazole (20) – not known	None

**Patient in this age range; **present at time of surgery; ***no previous oncological treatment; ****no psychiatric medication; *****local increase in pressure, no evidence of generalized increase in intracranial pressure; WHO, World Health Organization; IDH1, isocitrate dehydrogenase 1; diagnosis based on the 2016 WHO classification of CNS tumors.*

into the recording chamber for 5 min. The drug was subsequently washed out for 10–20 min.

Signal Analysis and Inclusion Criteria

Analysis of synaptic currents and intrinsic membrane responses was performed using Igor Pro (WaveMetrics). PatchMaster files were loaded into Igor Pro with Patcher's Power Tools (Max-Planck-Institute, Department of Membrane Biophysics). The input resistance (R_{in}) was calculated from the slope of steady-state voltage responses to a series of 8–10 subthreshold current injections lasting 400 ms. Spike threshold, half-width and fast after-hyperpolarization (AHP_{fast}, in mV) were determined from the first spike in response to a juxtathreshold positive current injection. The spike half-width was defined as the duration at half-amplitude measured between the threshold potential and the peak of the action potential. The membrane time constant τ was estimated from the monoexponential curve fitting of voltage responses to a −30 pA hyperpolarizing pulse. The membrane capacitance was calculated as the ratio between membrane τ and R_{in}. The rheobase (in pA) was determined as a 50 ms current injection, able to generate a spike in 50% of the cases in 10 trials. The instantaneous firing rate (in Hz) was defined as the number of action potentials evoked during a 1 s-long depolarizing current pulse of twice the amplitude of the rheobase current. The adaptation index (range, 0–1) was defined as the ratio between the first and last inter-spike intervals (ISIs; in ms) elicited by the same current pulse used to measure the instantaneous firing rate. The resting membrane potential was estimated by averaging a 20 s current-clamp trace recorded at a 0 pA holding current. Changes in R_{in} evoked by LY354740 application were assessed in voltage clamp mode by applying regular hyperpolarizing voltage steps (−10 mV). For these experiments, R_{in} was calculated as follows:

$$R_{in} = R_{tot} - R_s$$

where R_{tot} is the total resistance and R_s is the series resistance. R_s was calculated as follows:

$$R_s = \frac{V}{I_P}$$

where V is the amplitude of the voltage step and I_p is the amplitude of the peak of the capacitive current transient. R_{tot} was calculated as follows:

$$R_{tot} = \frac{V}{I_s}$$

where I_s is the amplitude of the steady state current.

The following criteria were determined in order to accept or reject event files: (1) recorded neurons were able to generate at least one spike upon current injection in current clamp mode at the beginning of the recording; (2) the holding current to clamp the cell at −90 mV was <−100 pA; (3) the series resistance was <30 MΩ and did not change more than 20% during the recording. Spontaneous synaptic events were detected using TaroTools toolbox for Igor Pro[1]. The threshold for event detection was set between −5 and −7 pA depending on the signal-to-noise ratio of the recording. Events with 20–80% rise-time longer than 3 ms and half-width shorter than 1 ms were removed. Subsequently, all events were visually inspected for the entire recording period in order to confirm the reliability of the automatic detection. Events were rejected if they did not display typical fast EPSC kinetic (i.e., ratio between decay time and 20–80% rise-time <3). Statistical analysis was performed using Prism software (GraphPad, San Diego, CA, United States), and the tests used are specified throughout the results. Unless indicated otherwise, values presented in the text and in the figures represent the median and the interquartile range (IQR). All data sets were tested for statistically significant outliers using the Rout test (Q = 1%).

[1]https://sites.google.com/site/tarotoolsregister

Visualization of Recorded Cells

After recording, slices were immersed in a fixative containing 4% paraformaldehyde, 15% v/v picric acid dissolved in 0.1 M phosphate buffer (PB) pH 7.2–7.4, overnight at 4°C. Slices were then thoroughly washed in 0.1M PB until all fixative was removed from the tissue and were either embedded in 20% gelatin and re-sectioned into 60 μm thickness on a vibratome (VT 1000S, Leica) or were processed further without re-sectioning. After permeabilization with Tris Buffered Saline (TBS), containing 0.3% w/v Triton (Tx) (Sigma), the recorded cells were visualized with overnight incubation in Alexa-488-conjugated streptavidin (Invitrogen, Thermo Fisher Scientific), diluted 1:1000 in the same buffer. Sections were then washed with TBS-Tx three times for 10 min and were mounted in Vectashield (Vector Laboratories) on glass slides for microscopic examination. Visualized neurons were examined using an epifluorescent microscope (Leitz DMRB, Leica) equipped with a camera (ORCA-ER, Hamamatsu) and connected to a desktop computer, using a 480/40 excitation and a 527/30 emission filter, corresponding to the fluorophore used. All visualized cells were confirmed to be pyramidal neurons based on the distribution of dendrites and axon and the presence of dendritic spines. Images of Z-stacks of some of the labeled neurons were made using a laser-scanning microscope (LSM 710, Zeiss) with a Plan-Apochromat 20x/0.8 objective (Zeiss).

Chemicals and Drugs

Salts used in the preparation of the internal recording solution and ACSF were obtained from either BDH or Sigma-Aldrich. LY354740 (1)-2-aminobicyclo[3.1.0] hexane-2,6-dicarboxylic acid, CPPG (*RS*)-α-cyclopropyl-4-phosphonophenylglycine and tetrodotoxin (TTX) were purchased from Tocris Bioscience, LY354740 was stored as frozen aliquots of 10 mM in DMSO. CPPG was stored as frozen aliquots of 100 mM in 1 M NaOH. TTX was stored as frozen aliquots of 1 μM in 10 mM sodium citrate buffer, pH 4.8.

RESULTS

Identity and Spiking Patterns of the Recorded Neurons

Neurons were recorded under visual control (n = 30; n = 8 patients: five TLE, three tumor) and I/V protocols were

performed in whole cell current clamp mode to assess the spiking patterns of the recorded cells in response to depolarizing rectangular current pulses. All neurons included in this study displayed membrane responses, action potential kinetics and discharge patterns consistent with features commonly observed in human cortical pyramidal neurons in layers 2–3 (Molnár et al., 2008) (**Table 2** and **Figure 1**). A subset of slices (16 out 30 from six patients, patient IDs: A–D and G, H) were histologically processed to visualize the biocytin-filled neurons. In 15/16 processed slices, the recorded neuron could be identified as pyramidal cells on the basis of spiny dendrites and axonal distribution, consistent with the electrophysiological properties (**Figure 1**). In one slice the recorded neuron was not recovered.

Pharmacological Activation of Group II mGluRs Depresses Excitatory Synaptic Transmission in Human Cortical Pyramidal Cells

Based on the evidence of group II mGluR modulation of glutamatergic transmission and pyramidal cell excitability in the rodent brain (Anwyl, 1999), we tested the effect of these receptors in human cortical pyramidal cells. We recorded sEPSCs from pyramidal cells in voltage clamp mode at −90 mV. The median frequency of sEPSCs was 2.4 Hz (IQR: 1.4–8.2 Hz), whereas the median amplitude was 13.2 (IQR: 8–15.6 pA; n = 10 from five patients).

Application of the selective group II mGluR agonist LY354740 (0.1 μM, n = 2; or 1 μM, n = 6) significantly depressed the frequency and the amplitude of sEPSCs (p = 0.003, Kruskal–Wallis test, pooled n = 8, **Figure 2**). Specifically, LY354740 reduced sEPSC frequency by 35% (median; IQR: 32–61%; n = 8) from baseline ($p < 0.01$) and sEPSC amplitude by 12% (median; IQR: 7–21%; n = 8) from baseline ($p < 0.01$, Dunn's *post hoc* test). The depression of sEPSCs partially persisted after 10–20 min post-LY354740 recovery period and could not be fully washed out (baseline vs. washout $p < 0.05$; LY354740 vs. washout $p > 0.05$, LY354740 n = 8, washout n = 6, Dunn's *post hoc* test).

We sought to verify that the inhibition of sEPSCs observed upon application of LY354740 was indeed due to group II mGluRs, and not due to other factors, for example spontaneous sEPSC rundown in the slice. To this end, we pre-incubated slices for ∼10 min with the group II/III mGluR antagonist, CPPG (0.1 mM) prior to the additional application of LY354740 (1 μM). Under these conditions, LY354740 did not trigger significant depression of the frequency (change from baseline: median +9%, IQR: −1 to +22%, p = 0.312, Wilcoxon test, n = 6) or amplitude (change from baseline: median +3%, IQR: −10 to

TABLE 2 | Electrophysiological parameters of human cortical pyramidal cells and experimental protocols related to patient and cell codes.

Parameter/experiment	Median	IQR	Cell #	Patient/cell codes
$V_{m\ rest}$ (mV)	−91.6	−89.3 – −93	n = 10	A1, B4–B6, C7, D8–D12
R_{in} (MΩ)	160.3	123 – 195.5	n = 11	A1, B4–B6, C7, D8–D13
Membrane tau (ms)	22.6	19.2 – 28	n = 11	A1, B4–B6, C7, D8–D13
Capacitance (pF)	145.7	137.9 – 188	n = 11	A1, B4–B6, C7, D8–D13
Rheobase current (pA)	85	39 – 154	n = 11	A1, B4–B6, C7, D8–D13
Spike threshold (mV)	−55.8	−48.5 – −61.3	n = 11	A1, B4–B6, C7, D8–D13
Spike amplitude (mV)	90.4	87.6 – 91.9	n = 11	A1, B4–B6, C7, D8–D13
Spike half-width (ms)	1.1	1 – 1.2	n = 11	A1, B4–B6, C7, D8–D13
AHP_{fast} (mV)	12.7	7.2 – 14.5	n = 11	A1, B4–B6, C7, D8–D13
Sag ratio (−100 pA)	0.882	0.864 – 0.904	n = 9	A1, B5, C7, D8–D13
Rebound amplitude (−100 pA; mV)	1.9	1.3 – 3.5	n = 9	A1, B5, C7, D8–D13
Instantaneous firing rate (Hz)	14	12 – 17.5	n = 11	A1, B4–B6, C7, D8–D13
Adaptation index	0.233	0.189 – 0.322	n = 11	A1, B4–B6, C7, D8–D13
sEPSC frequency (Hz)	2.4	1.4 – 8.2	n = 10	A1, B2–B4, C8, D9, D12, E16–E18
sEPSC amplitude (pA)	13.2	8 – 15.6	n = 10	A1, B2–B4, C8, D9, D12, E16–E18
mEPSC frequency (Hz)	1.7	1.6 – 3.3	n = 9	D13, D14, E15, F19–F21, G23–G25
mEPSC amplitude (pA)	8.6	8.1 – 10.2	n = 9	D13, D14, E15, F19–F21, G23–G25
LY354740 (1 μM) tested on sEPSCs	–	–	n = 6	A1, B2–B4, C8, E16
LY354740 (0.1 μM) tested on sEPSCs	–	–	n = 2	D9, D12
CPPG (0.1 mM) + LY354740 (1 μM) tested on sEPSCs	–	–	n = 6	F22, H26–H30
LY354740 (1 μM) tested on mEPSCs	–	–	n = 6	F19–F21, G23–G25
LY354740 (0.1 μM) tested on mEPSCs	–	–	n = 3	D13, D14, E15
LY354740 (1 μM) tested on holding current	–	–	n = 11	A1, B4, C8, E16, E17, F19–F21, G23–G25
LY354740 (0.1 μM) tested on R_{in}	–	–	n = 5	D9, D12, D13, D14, E15
LY354740 (1 μM) tested on R_{in}	–	–	n = 6	F19, F20, F21, G23, G24, G25
CPPG (0.1 mM) + LY354740 (1 μM) tested on R_{in}	–	–	n = 6	F22, H26, H27, H28, H29, H30

$V_{m\ rest}$, resting membrane potential; R_{in}, input resistance; AHP_{fast}, fast afterhyperpolarization; sEPSCs, spontaneous excitatory postsynaptic currents; mEPSCs, miniature excitatory postsynaptic currents; IQR, inter-quartile range.

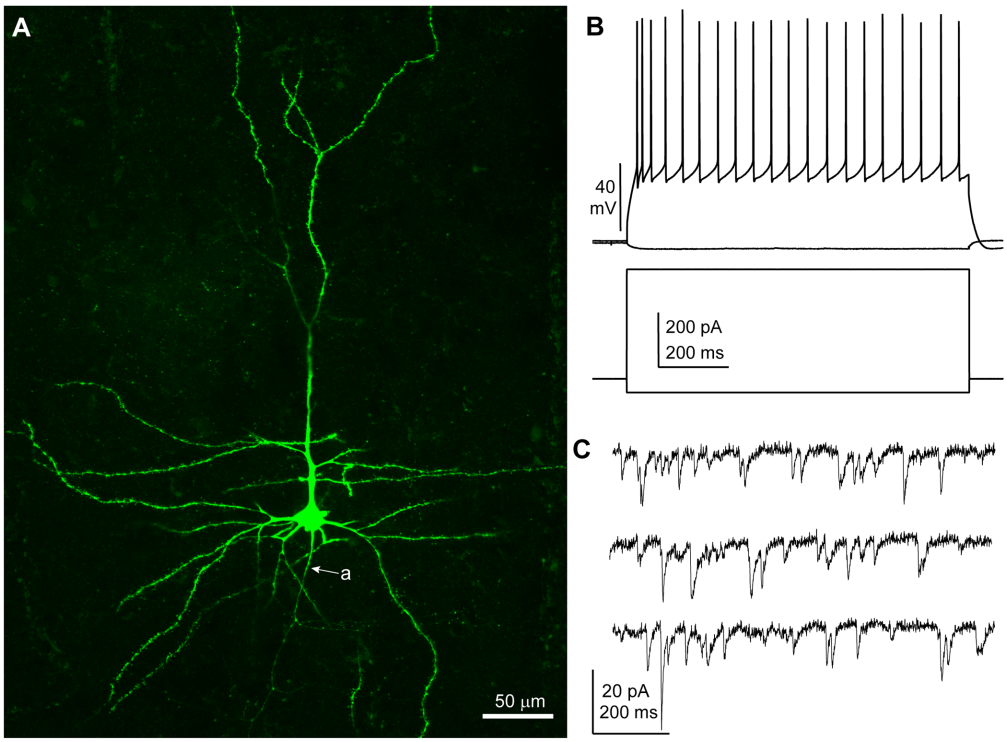


FIGURE 1 | Features of a human cortical pyramidal cell. **(A)** Confocal microscopic image of a biocytin-filled human cortical pyramidal cell in layer 3 (patient/cell code: H26) showing spiny dendrites, a prominent apical dendrite and axon (a) descending toward the white matter; maximum intensity projection of a z-stack of ∼24 μm thickness; 1.8 μm optical slice thickness; interval 0.9 μm; 25 slices). **(B)** Voltage responses of the cell shown in **(A)** recorded in current clamp mode to hyperpolarizing (–50 pA) and depolarizing (+400 pA) current steps (holding potential: –80 mV). **(C)** Representative traces of spontaneous EPSCs recorded in voltage clamp mode at –90 mV; traces are low-pass filtered at 1 kHz and notch filtered at 50 Hz (width: 0.05 Hz). **(A–C)** Same cell.

+12%, $p > 0.999$, Wilcoxon test, $n = 6$) of sEPSCs (**Figure 3**). The frequency and amplitude of sEPSCs in control and in the presence of CPPG were not significantly different (frequency in control: median 2.4 Hz, IQR: 1.4–8.2 Hz, $n = 10$; frequency with CPPG: median 4 Hz, IQR: 1.7–6.5 Hz, $n = 6$, $p = 0.865$, Mann–Whitney test; amplitude in control: median 13.2 pA, IQR: 8–15.6 pA, $n = 10$; amplitude with CPPG: median 10.5, IQR: 9.1–11.7 pA, $n = 6$, $p = 0.534$, Mann–Whitney test), suggesting poor or no endogenous activation of group II mGluRs by glutamate under our experimental conditions.

Group II mGluRs Depress Excitatory Synaptic Transmission Mainly via a Presynaptic Effect

In pyramidal cells of the rodent hippocampus (Ster et al., 2011) and primate prefrontal cortex (Jin et al., 2017), the activation of group II mGluRs change postsynaptic conductances. The observed depression of sEPSCs in our experiments may be due to: (1) presynaptic inhibition of glutamate release; (2) a hyperpolarization of other pyramidal cells innervating the recorded pyramidal cell; (3) a purely postsynaptic effects on the recorded cells (e.g., changes of AMPA receptor conductance), or a combination of the above. To discriminate between these scenarios, we tested in voltage clamp mode whether LY354740 application altered the holding current and the R_{in} of the recorded pyramidal cells (**Figure 4**). We did not observe a change in the holding current upon the application of LY354740 (1 μM) in neurons at −90 mV (change from baseline: median 2.6 pA, IQR −0.5 to 10.4 pA, $p = 0.175$, Wilcoxon test, $n = 11$, **Figures 4A,B**), suggesting that, at least at this membrane potential, pyramidal cells are not hyperpolarized by this drug. Nonetheless, LY354740 application (0.1 μM, $n = 5$; or 1 μM, $n = 6$) triggered a small but significant reduction of R_{in} (median change −5%, IQR: 3–10%, $p = 0.04$, Kruskal–Wallis test, pooled $n = 11$; baseline vs. LY354740 $p < 0.05$, LY354740 vs. washout $p > 0.05$, baseline vs. washout $p > 0.05$, Dunn's *post hoc* test). This effect was absent when CPPG (0.1 mM) was applied prior to the additional application of LY354740 (1 μM; $p = 0.7$, Wilcoxon test, $n = 6$). The reduction of R_{in} from baseline triggered by LY354740 was significantly smaller in the presence of CPPG ($p = 0.03$, Mann–Whitney test), suggesting that this effect was mediated by activation of group II mGluRs. Thus, group II mGluRs appear to trigger small changes in membrane conductance in pyramidal cells.

Next, in order to further discriminate between presynaptic and postsynaptic effects, we tested the drug on spontaneous mEPSCs recorded from pyramidal cells. In the presence of 1 μM TTX to block action potentials, mEPSC frequency had a median value of 1.7 Hz (IQR: 1.6–3.3 Hz) and mEPSC amplitude had a median

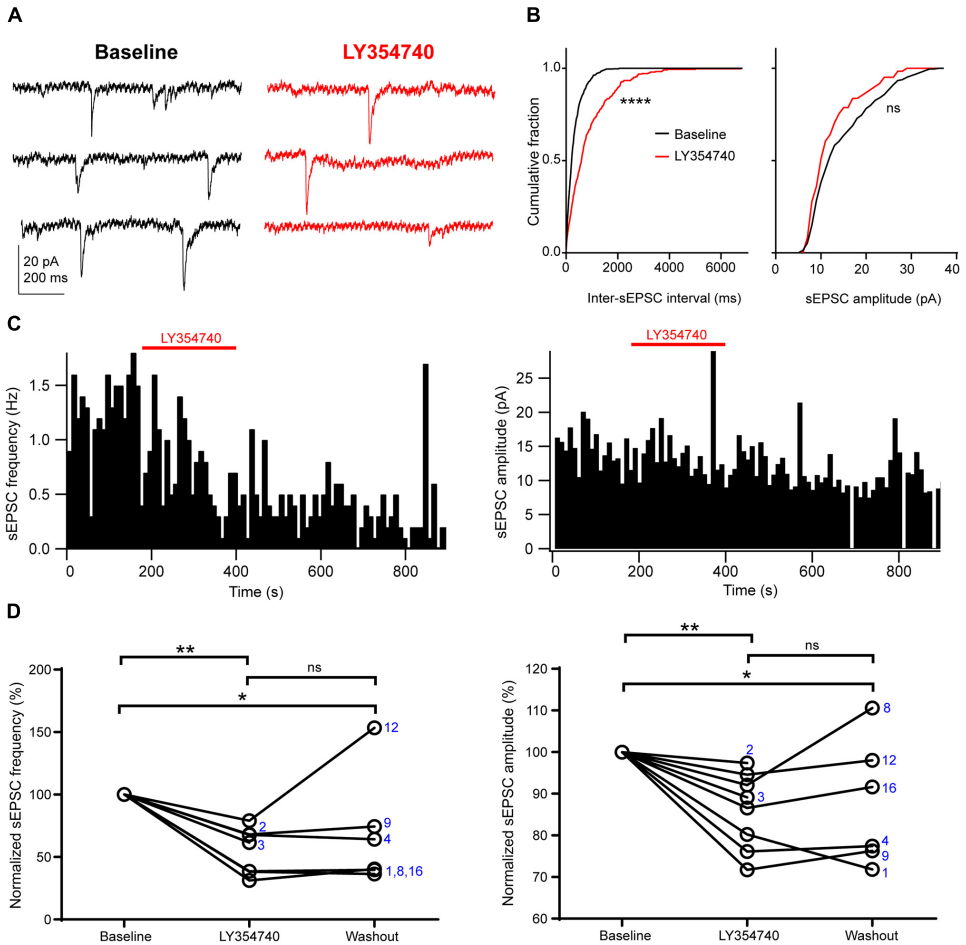


FIGURE 2 | Activation of group II mGluRs depresses excitatory synaptic transmission in human cortical pyramidal cells. **(A)** Representative traces in voltage clamp mode (–90 mV) during baseline and application of the group II mGluR agonist LY354740 (0.1 μM) to a pyramidal cell. **(B)** Cumulative probability distributions of the inter-sEPSC intervals and sEPSC amplitudes for the cell shown in **(A)**. LY354740 significantly reduces sEPSC frequency (left, $p = 0.0001$, Kolmogorov–Smirnov test), and non-significantly decreases sEPSC amplitude (right, $p = 0.056$, Kolmogorov–Smirnov test). **(C)** Event time histograms (bin size: 10 ms, cell in **A,B**) showing the effect of LY354740 application on sEPSC frequency (left) and amplitude (right). **(D)** Baseline normalized effects of LY354740 (0.1 or 1 μM) on individual cells (see **Table 2**) show significant reduction of sEPSC frequency (left, $p = 0.003$ Kruskal–Wallis test; baseline vs. LY354740 $p < 0.01$, baseline vs. washout $p < 0.05$, LY354740 vs. washout $p > 0.05$, Dunn's *post hoc* test, $n = 8$) and sEPSC amplitude (right, $p = 0.003$ Kruskal–Wallis test; baseline vs. LY354740 $p < 0.01$, baseline vs. washout $p < 0.05$, LY354740 vs. washout $p > 0.05$, Dunn's *post hoc* test, $n = 8$). In some cells, washout could not be analyzed due to changes in series resistance (>20% baseline). Numbers denote codes of individual cells (see **Table 2**). *$p < 0.05$, **$p < 0.01$, ****$p < 0.0001$.

value of 8.6 pA (IQR: 8.1–10.2 pA, $n = 9$). Application of 0.1 μM ($n = 3$ cells) or 1 μM LY354740 ($n = 6$) caused a significant reduction in the frequency of mEPSCs (change from baseline: median −50%, IQR: −29 to −67%, $p = 0.019$ Kruskal–Wallis test; baseline vs. LY354740 $p < 0.05$, Dunn's *post hoc* test, $n = 9$ cells pooled, **Figure 5**). In contrast, mEPSC amplitude was not significantly altered by LY354740 (change from baseline: median −2%, IQR −4 to +2%, $p = 0.239$ Kruskal–Wallis test; $n = 9$, **Figure 5**). Taken together, these results suggest that activation of group II mGluRs leads to presynaptic and postsynaptic effects in pyramidal cells. However, the lack of changes in holding current (at least at −90 mV) and the modest changes in R_{in} suggest that the depression of excitatory transmission is predominantly caused by inhibition of glutamate release from glutamatergic terminals innervating pyramidal cells.

DISCUSSION

We have demonstrated that activation of group II mGluRs inhibits spontaneous excitatory transmission impinging onto pyramidal neurons in layers 2–3 of the human cerebral cortex. The group II mGluR agonist LY354740 depressed the frequency and amplitude of action potential-dependent sEPSCs but did not alter the holding current of pyramidal cell, although it slightly reduced the cells' input resistance. It also reduced the frequency but not the amplitude of action potential-independent mEPSCs. Overall, these findings suggest that group II mGluRs act predominantly via a presynaptic effect on glutamate release, rather than via hyperpolarization of layers 2–3 pyramidal cells or postsynaptic effects on ionotropic glutamate receptor conductance. However, we cannot exclude that activation of

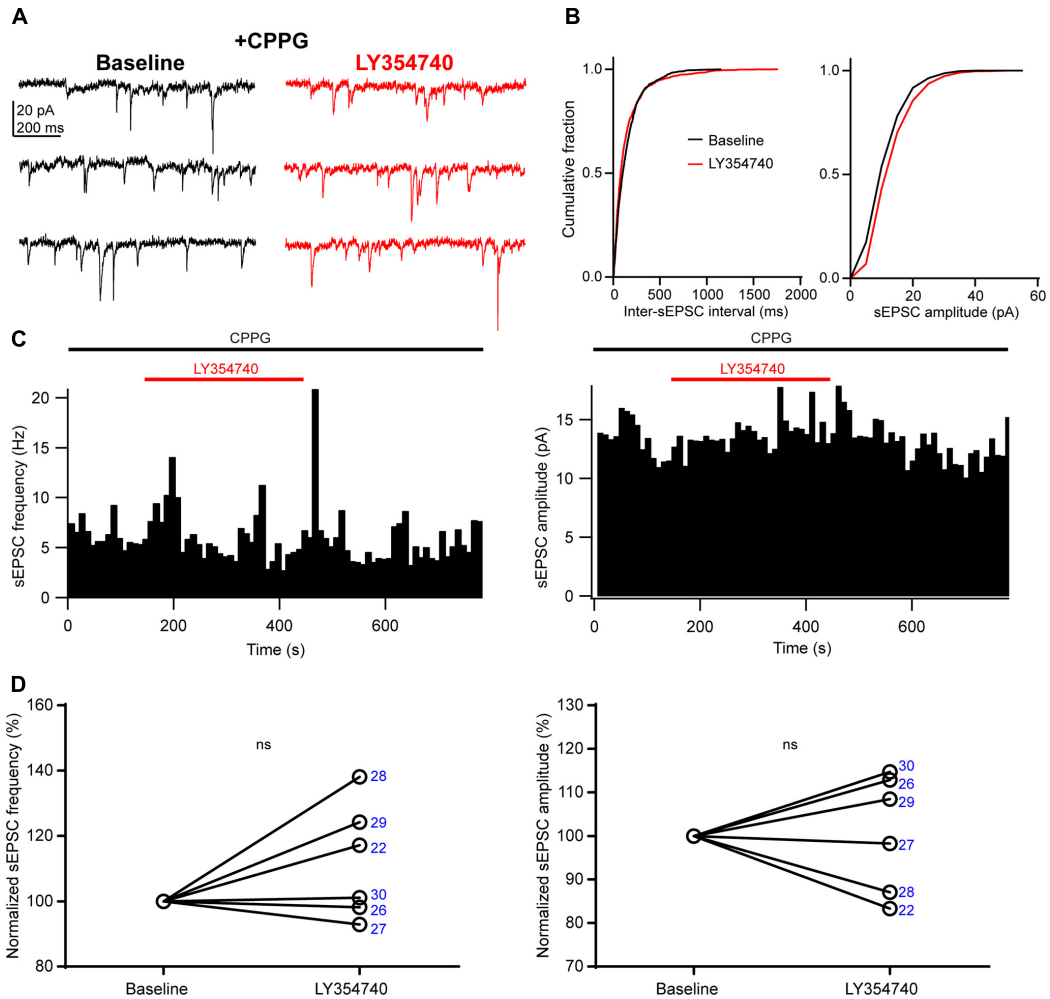


FIGURE 3 | An antagonist of group II/III mGluRs prevents depression of excitatory synaptic transmission by LY354740. **(A)** Representative traces in voltage clamp mode (–90 mV) during baseline and application of LY354740 (1 μM) in the presence of the group II/III mGluR antagonist CPPG (0.1 mM) in a neuron. **(B)** Cumulative probability distributions of the inter-sEPSC intervals and sEPSC amplitudes for the cell shown in **(A)**. LY354740 does not reduce sEPSC frequency ($p = 0.967$, Kolmogorov–Smirnov test) or amplitude ($p = 0.999$, Kolmogorov–Smirnov test). **(C)** Event time histograms (bin size: 10 ms, cell in **A,B**) showing the effect of LY354740 application on sEPSC frequency (left) and amplitude (right) in presence of CPPG. **(D)**, on average, LY354740 (1 μM) does not significantly change sEPSC frequency (left, $p = 0.312$ Wilcoxon test, $n = 6$) or sEPSC amplitude ($p > 0.999$ Wilcoxon test, $n = 6$). Numbers denote codes of individual cells (see **Table 2**).

postsynaptic group II mGluRs in pyramidal cells can lead to network effects. Increases in membrane conductance could lead to membrane hyperpolarization when the cell's membrane potential is more depolarized and/or to a reduction of the cell's excitability. If large numbers of pyramidal neurons express group II mGluRs in the human cortex, even a small hyperpolarization or reduction in excitability could alter network dynamics. Our results confirm the negative 'autoreceptor' role of this receptor observed in rodent neocortex (e.g., Libri et al., 1997) and hippocampus (e.g., Capogna, 2004). Although group II mGluRs on glutamatergic terminals are activated by glutamate, the source of this transmitter may be either the same terminal that is being suppressed or nearby terminals. In fact, the receptors are widely distributed along the axons and the non-junctional bouton membrane, and glutamate release sites are densely distributed in the neuropil. Therefore, the term 'autoreceptor' describes the chemical nature of the terminal and the receptor, and not necessarily a terminal-autonomous regulatory mechanism.

Preclinical studies have demonstrated that group II mGluR agonists exhibit antipsychotic-like properties in animal models of schizophrenia (Stansley and Conn, 2018). However, when these compounds were tested in clinical trials on schizophrenic patients, results were not encouraging (Muguruza et al., 2016). This may be due to patient selection or previous exposure to atypical antipsychotics (Muguruza et al., 2016; Maksymetz et al., 2017). Nonetheless, it is important to acknowledge that rodent animal models do not fully capture the complexities of psychiatric disorders and often show poor predictive power for drug efficacy (Nestler and Hyman, 2010).

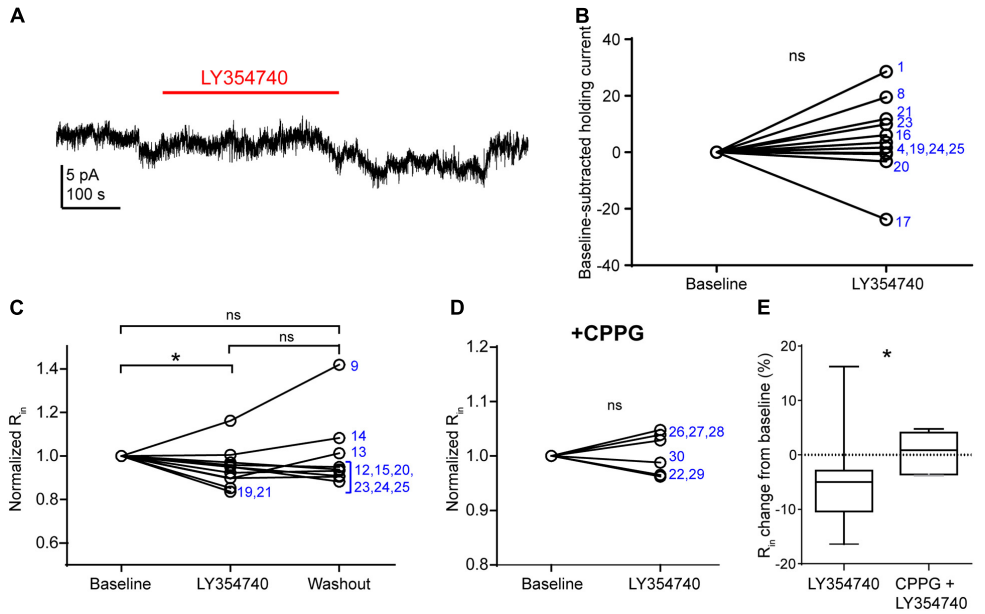


FIGURE 4 | Activation of group II mGluRs does not lead to detectable inward currents in human cortical pyramidal cells. **(A)** Representative trace in voltage clamp mode (–90 mV) during baseline and application of LY354740 (1 μM). The trace was processed with a low pass filter (5 Hz stop band), a notch filter (50 Hz) and boxcar averaging (window of 50 data points; original sampling rate: 20 kHz) to remove synaptic events and isolate the holding current. **(B)** LY354740 (1 μM) does not significantly affect the holding current ($p = 0.175$, Wilcoxon test, $n = 11$). Numbers denote codes of individual cells (see **Table 2**). **(C)** Baseline normalized effects of LY354740 (0.1 or 1 μM) on individual cells (see **Table 2**) show significant reduction of R_{in} (median change –5%, IQR: 3–10%, $p = 0.04$ Kruskal–Wallis test; baseline vs. LY354740 $p < 0.05$, baseline vs. washout $p > 0.05$, LY354740 vs. washout $p > 0.05$, Dunn's *post hoc* test, $n = 11$). **(D)** On average, LY354740 (1 μM) does not significantly impact pyramidal cells' R_{in} when CPPG (0.1 mM) is pre-applied ($p = 0.7$, Wilcoxon test, $n = 6$). **(E)** Boxplot showing significantly bigger reduction of R_{in} between application of LY354740 only and LY354740 with CPPG ($p = 0.03$, Mann–Whitney test). In some cells, washout could not be analyzed due to changes in series resistance (>20% baseline). Numbers denote codes of individual cells (see **Table 2**). $^*p < 0.05$.

Unraveling the cellular effects of group II mGluRs in human cortex could facilitate the identification of causes underlying the poor efficacy of current drugs and help design new, more effective pharmacological treatments. We have tested the effect of a ligand of broad interest for drug development, an agonist for type II mGluRs, on synaptic events recorded from human cortical neurons. Our results demonstrate that this ligand, tested previously in rodents, is effective in inhibiting EPSCs recorded in human pyramidal cells. Future studies using human cortical slices may also help to design novel antipsychotic drugs by shedding light on the physiological effects of PAMs of group II mGluRs (e.g., LY487379 or AZD8529), designed to improve cognition deficits with fewer side effects than more traditional drugs (Singewald et al., 2015).

Our data show that LY354740 inhibited the frequency and amplitude of action potential-dependent sEPSCs as well as the frequency, but not amplitude, of action potential-independent mEPSCs. The latter effect by a drug is usually interpreted as inhibition of spontaneous vesicle fusion and transmitter release (Scanziani et al., 1992). However, LY354740 also appears to trigger postsynaptic effects, as indicated by the small but significant effect of LY354740 on cells' input resistance. Future studies could confirm the effect of group II mGluRs on neurotransmitter release by examining calcium-dependent release evoked by electrical stimulation of a set of presynaptic fibers. Calcium-dependent and independent neurotransmitter release have been often assumed to share similar mechanisms (Scanziani et al., 1992), although more recent data suggest that the pool of vesicles underlying spontaneous transmitter release can be different from that involved in evoked release (Sara et al., 2005).

In the present study, we could test only a small number of neurons due to limited availability of human cortical tissue. Therefore, we have not explored the subcellular or molecular mechanisms leading to presynaptic depression of glutamatergic transmission. In rodent hippocampus, these receptors are found at pre-terminal axons and on the boutons at some distance from release sites (Shigemoto et al., 1997; Corti et al., 2002), but whether similar localization also occurs in the human cerebral cortex is not known. Based on rodent data, group II mGluR activation could act downstream on N- and P/Q type Ca^{2+} channels, presynaptic K^+ channels, intrinsic release machinery proteins or could be activated by retrograde release of endogenous transmitters from the postsynaptic cells (Niswender and Conn, 2010). Furthermore, our data cannot rule out a contribution of group II mGluRs expressed by pyramidal cells' dendritic membrane, perhaps at some distance from the soma. Finally, mGlu3 is expressed in human astrocytes where it enhances the uptake of glutamate from the synapse by increasing the expression of glial glutamate transporters (Aronica et al., 2003), and this mechanism could contribute to the inhibition of glutamatergic synaptic events observed in our experiments.

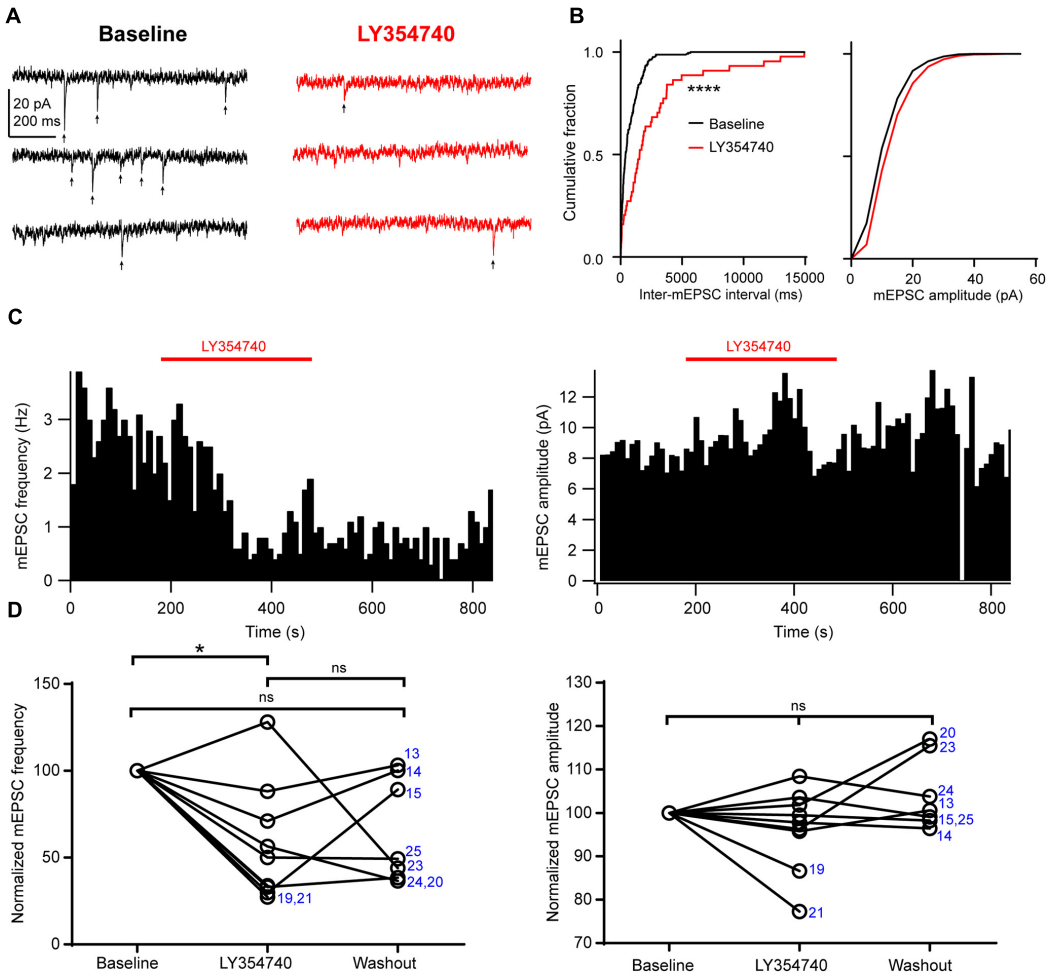


FIGURE 5 | Activation of group II mGluRs depresses excitatory synaptic transmission via a presynaptic effect. **(A)** Representative traces in voltage clamp mode (–90 mV) from a neuron during baseline and application of the group II mGluR agonist LY354740 (1 μM) in the presence of 1 μM tetrodotoxin; mEPSCs are marked with arrows. **(B)** Cumulative probability distributions of the inter-mEPSC intervals and mEPSC amplitudes for the cell shown in **(A)**. LY354740 significantly reduces mEPSC frequency (left, $p < 0.0001$, Kolmogorov–Smirnov test) but not mEPSC amplitude (right, $p = 0.999$, Kolmogorov–Smirnov test). **(C)** Event time histograms (bin size: 10 ms, cell in **A,B**) showing the effect of LY354740 application on mEPSC frequency (left) and amplitude (right). **(D)** Baseline normalized effect of (0.1 μM, $n = 3$ cells, or 1 μM, $n = 6$ cells) on individual cells. LY354740 significantly reduces mEPSC frequency (left, $p = 0.019$ Kruskal–Wallis test; baseline vs. LY354740 $p < 0.05$, baseline vs. washout $p > 0.05$, LY354740 vs. washout $p > 0.05$, Dunn's *post hoc* test, $n = 9$) but not mEPSC amplitude (right, $p = 0.239$ Kruskal–Wallis test; $n = 9$). In some cells, washout could not be analyzed due to change in series resistance (>20% baseline). Numbers denote codes of individual cells (see **Table 2**). *$p < 0.05$, ****$p < 0.0001$.

We have only investigated the activation of group II mGluRs by an exogenous ligand. However, it is unclear whether endogenous ligands (likely glutamate) could also modulate neurotransmission. The frequency and amplitude of sEPSCs detected in the presence of the mGluR II/III antagonist CPPG were similar to control conditions, suggesting undetectable levels of group II mGluR activation by endogenous glutamate in acute slices. Future studies should investigate activity-dependent activation of group II mGluRs, as demonstrated in rodents hippocampus (Kew et al., 2001, 2002; Capogna, 2004), which may also be relevant to mechanisms of synaptic plasticity (Tzounopoulos et al., 1998). In the human cortex, group I mGluRs trigger long-term depression of excitatory transmission impinging on fast-spiking GABAergic interneurons (Szegedi et al., 2016), but it is not yet known whether group II mGluRs can mediate analogous effects.

It is yet to be determined whether group II mGluRs depress transmission at all glutamatergic synapses on pyramidal cells or at specific pathways. Spontaneous synaptic events recorded from pyramidal neurons could be mainly due to glutamate released either from thalamus and/or from cortical inputs (Pasquale and Sherman, 2012). Future experiments using selective stimulation of anatomically identified fibers could determine what input(s) physiologically activate group II mGluRs in the human cerebral cortex.

Whether group II mGluR activation leads to depression of most glutamatergic synapses or to suppression of specific pathways, a marked reduction of excitatory transmission in layers

2–3 pyramidal cells is likely to trigger dramatic network effects. Intriguingly, altered activity of cortical neuronal ensembles has been reported in two mouse models of schizophrenia (Hamm et al., 2017), a finding that suggests that group II mGluRs – despite unsuccessful clinical trials to date – could still represent a promising target for this disorder.

It is likely that activation of group II mGluRs causes changes in neurotransmission that are not restricted to glutamatergic synapses onto pyramidal cells. First, these receptors might be located on glutamatergic axons innervating at least some GABAergic interneurons, similar to the modulation of excitability of fast-spiking GABAergic neurons of human cortex by group I mGluRs (Szegedi et al., 2017). Group II mGluRs might be expressed in a cell-type dependent manner, comparable to the expression of mGluR7 (Shigemoto et al., 1996), or other presynaptic metabotropic receptors, e.g., the cannabinoid 1 receptor (Ludanyi et al., 2008). Second, group II mGluRs might also modulate GABAergic transmission (Hayashi et al., 1993; Ohishi et al., 1994). It will be interesting to investigate whether similar mechanisms occur in the human cortex.

Which group II mGluRs were activated in the present experiments? LY354740 is a potent and selective agonist (up to 1 μM) at mGlu2 and mGlu3 receptors with an EC50 of about 10–50 nM in the rat cortex, hippocampus and striatum, and 10 or 30 nM in cells expressing recombinant mGlu2 or mGlu3, respectively (Schoepp et al., 1999). The concentrations used in this study, therefore, were several fold higher than the EC50, in order to ensure activation of mGluRs throughout the entire depth of the slice. Although the concentrations used in this study still predict selectivity over groups I and III mGluRs (EC50: 300 μM and 100 μM, respectively), we did not discriminate between mGlu2 and mGlu3 activation (e.g., Johnson et al., 2013). Thus, future investigations could attempt to discriminate between mGlu2 and mGlu3, also because understanding the different roles of these two receptors could help to design more selective drugs.

The action of group II mGluRs is regulated by development, network events and epileptic-like events in rodents (Doherty et al., 2004). Future studies using tissue closer to pathological focus could test whether pathological processes can cause functional upregulation of receptors.

It is important to acknowledge that the use of tissue from human cerebral cortex of patients subjected to neurosurgery has some methodological limitations. One of these is that the tissue may have some pathological features that remain undetected. We have used cortical tissue from people with epilepsy refractory to medications or from low grade glioma tumor patients (except one patient that was grade III). We have performed the experiments only on cortical tissue that was located outside the focal epileptic region. Accordingly, we have not observed any epileptic-like signal in the human cortical slices used for our study, such as rhythmic spike bursts in current clamp or rhythmic sEPSC bursts in voltage clamp. In the samples obtained from the periphery of diffuse gliomas as assessed by magnetic resonance imaging, variability may be caused by the degree of glial infiltration. Another possible limitation is the variability due to heterogeneity of cortical areas of provenance, different age and sex of the patients, their individual clinical and pharmacological history. Despite this variability, we observed basal functional parameters that were rather homogeneous across samples and patients and consistency in the effects mediated by group II mGluRs. In addition, cortical tissue removed from remote brain tumor sites has been used as control, non-epileptic tissue in a study investigating cellular activities in human epileptic tissue (Jiang et al., 2012).

CONCLUSION

In conclusion, the present study suggests that the activation of group II mGluRs mainly leads to inhibition of glutamate release at synapses on layers 2–3 pyramidal neurons of human cerebral cortex via presynaptic 'autoreceptors.' We have established an experimental framework to test the neurophysiological effects of ligands that are relevant to neuropsychiatric conditions in acute slices of human neocortex. Clarifying the mechanisms of action by these ligands has the potential to shed light on their actions in the human brain and bolster the design of more potent and selective drugs.

AUTHOR CONTRIBUTIONS

RS, PP, and VA performed neurosurgery. LL, AS, OA, and MHG helped with human tissue collection and regulated procedures. MB, IL, PS, and MC performed the experiments and analyses, and wrote the manuscript with comments from all the authors.

FUNDING

This work was supported by an ERC grant (ERC-2015-AdG 694988), the Oxford NIHR Biomedical Research Centre, and by the Medical Research Council (MC_UU_12024/4 and MR/R011567/1 to PS).

ACKNOWLEDGMENTS

We acknowledge the Oxford Brain Bank, supported by the Medical Research Council (MRC), Brains for Dementia Research (BDR) (Alzheimer Society and Alzheimer Research, United Kingdom), Autistica, United Kingdom, and the NIHR Oxford Biomedical Research Centre. MHG is a Clinical Lecturer funded by the NIHR Academy (National Institute for Health Research Trainee Coordinating Centre) ref CL-2013-13-001. The views expressed are those of the author(s) and not necessarily those of the NHS, the NIHR or the Department of Health. We are grateful to Dr. Karri Lamsa for pilot experiments and stimulating discussions that led to this project, Ms. Kristina Wagner, Mr. Michael Howarth, and Ms. Kathryn Newton for excellent technical assistance and to Dr. Jozsef Somogyi for help with microscopy.

REFERENCES

Anwyl, R. (1999). Metabotropic glutamate receptors: electrophysiological properties and role in plasticity. *Brain Res. Rev.* 29, 83–120. doi: 10.1016/S0165-0173(98)00050-2

Aronica, E., Gorter, J. A., Ijlst-Keizers, H., Rozemuller, A. J., Yankaya, B., Leenstra, S., et al. (2003). Expression and functional role of mGluR3 and mGluR5 in human astrocytes and glioma cells: opposite regulation of glutamate transporter proteins. *Eur. J. Neurosci.* 17, 2106–2118. doi: 10.1046/j.1460-9568.2003.02657.x

Capogna, M. (2004). Distinct properties of presynaptic group II and III metabotropic glutamate receptor-mediated inhibition of perforant pathway CA1 EPSCs. *Eur. J. Neurosci.* 19, 2847–2858. doi: 10.1111/j.1460-9568.2004.03378.x

Caraci, F., Nicoletti, F., and Copani, A. (2018). Metabotropic glutamate receptors: the potential for therapeutic applications in Alzheimer ' s disease. *Curr. Opin. Pharmacol.* 38, 1–7. doi: 10.1016/j.coph.2017.12.001

Cartmell, J., and Schoepp, D. D. (2002). Regulation of neurotransmitter release bymetabotropic glutamate receptors. *J. Neurochem.* 75, 889–907. doi: 10.1046/j.1471-4159.2000.0750889.x

Conn, P. J., and Pin, J. (1997). Pharmacology and functions of metabotropic glutamate receptors. *Annu. Rev. Pharmacol. Toxicol.* 37, 205–237. doi: 10.1146/annurev.pharmtox.37.1.205

Corti, C., Aldegheri, L., Somogyi, P., and Ferraguti, F. (2002). Distribution and synaptic localisation of the metabotropic glutamate receptor 4 (mGluR4) in the rodent CNS. *Neuroscience* 110, 403–420. doi: 10.1016/S0306-4522(01)00591-7

Di Menna, L., Joffe, M. E., Iacovelli, L., Orlando, R., Lindsley, C. W., Mairesse, J., et al. (2018). Functional partnership between mGlu3 and mGlu5 metabotropic glutamate receptors in the central nervous system. *Neuropharmacology* 128, 301–313. doi: 10.1016/j.neuropharm.2017.10.026

Doherty, J., and Dingledine, R. (2001). Reduced excitatory drive onto interneurons in the dentate gyrus after status epilepticus. *J. Neurosci.* 21, 2048–2057. doi: 10.1523/JNEUROSCI.21-06-02048.2001

Doherty, J. J., Alagarsamy, S., Bough, K. J., Conn, P. J., Dingledine, R., and Mott, D. D. (2004). Metabotropic glutamate receptors modulate feedback inhibition in a developmentally regulated manner in rat dentate gyrus. *J. Physiol.* 2, 395–401. doi: 10.1113/jphysiol.2004.074930

Ferraguti, F. (2018). Metabotropic glutamate receptors as targets for novel anxiolytics. *Curr. Opin. Pharmacol.* 38, 37–42. doi: 10.1016/j.coph.2018.02.004

Galici, R. (2005). A selective allosteric potentiator of metabotropic glutamate (mGlu) 2 receptors has effects similar to an orthosteric mGlu2/3 receptor agonist in mouse models predictive of antipsychotic activity. *J. Pharmacol. Exp. Ther.* 315, 1181–1187. doi: 10.1124/jpet.105.091074

Hamm, J. P., Peterka, D. S., Gogos, J. A., and Yuste, R. (2017). Altered cortical ensembles in mouse models of schizophrenia. *Neuron* 94, 153–167. doi: 10.1016/j.neuron.2017.03.019

Hayashi, Y., Momiyama, A., Takahashi, T., Ohishi, H., Ogawa-Meguro, R., Shigemoto, R., et al. (1993). Role of a metabotropic glutamate receptor in synaptic modulation in the accessory olfactory bulb. *Nature* 366, 687–690. doi: 10.1038/366687a0

Jiang, M., Zhu, J., Liu, Y., Yang, M., Tian, C., Jiang, S., et al. (2012). Enhancement of asynchronous release from fast-spiking interneuron in human and rat epileptic neocortex. *PLoS Biol.* 10:e1001324. doi: 10.1371/journal.pbio.1001324

Jin, L. E., Wang, M., Yang, S. T., Yang, Y., Galvin, V. C., Lightbourne, T. C., et al. (2017). MGluR2/3 mechanisms in primate dorsolateral prefrontal cortex: evidence for both presynaptic and postsynaptic actions. *Mol. Psychiatry* 22, 1615–1625. doi: 10.1038/mp.2016.129

Johnson, P. L., Fitz, S. D., Engleman, E. A., Svensson, K. A., Schkeryantz, J. M., and Shekhar, A. (2013). Group II metabotropic glutamate receptor type 2 allosteric potentiators prevent sodium lactate-induced panic-like response in panic-vulnerable rats. *J. Psychopharmacol.* 27, 152–161. doi: 10.1177/0269881112454230

Jucker, M. (2010). The benefits and limitations of animal models for translational research in neurodegenerative diseases. *Nat. Med.* 16, 1210–1214. doi: 10.1038/nm.2224

Kew, J. N. C., Ducarre, J., Pflimlin, M., Mutel, V., and Kemp, J. A. (2001). Activity-dependent presynaptic autoinhibition by group II metabotropic glutamate receptors at the perforant path inputs to the dentate gyrus and CA1. *Neuropharmacology* 40, 20–27. doi: 10.1016/S0028-3908(00)00118-0

Kew, J. N. C., Pflimlin, M. C., Kemp, J. A., and Mutel, V. (2002). Differential regulation of synaptic transmission by mGlu2 and mGlu3 at the perforant path inputs to the dentate gyrus and CA1 revealed in mGlu2 -/- mice. *Neuropharmacology* 43, 215–221. doi: 10.1016/S0028-3908(02)00084-9

Kintscher, M., Breustedt, J., Miceli, S., Schmitz, D., and Wozny, C. (2012). Group II metabotropic glutamate receptors depress synaptic transmission onto subicular burst firing neurons. *PLoS One* 7:e45039. doi: 10.1371/journal.pone.0045039

Krystal, J. H., Abi-Saab, W., Perry, E., D'Souza, D. C., Liu, N., Gueorguieva, R., et al. (2005). Preliminary evidence of attenuation of the disruptive effects of the NMDA glutamate receptor antagonist, ketamine, on working memory by pretreatment with the group II metabotropic glutamate receptor agonist, LY354740, in healthy human subjects. *Psychopharmacology* 179, 303–309. doi: 10.1007/s00213-004-1982-8

Libri, V., Constanti, A., Zibetti, M., and Postlethwaite, M. (1997). Metabotropic glutamate receptor subtypes mediating slow inward tail current (I(ADP)) induction and inhibition of synaptic transmission in olfactory cortical neurones. *Br. J. Pharmacol.* 120, 1083–1095. doi: 10.1038/sj.bjp.0701021

Ludanyi, A., Eross, L., Czirjak, S., Vajda, J., Halasz, P., Watanabe, M., et al. (2008). Downregulation of the CB1 cannabinoid receptor and related molecular elements of the endocannabinoid system in epileptic human hippocampus. *J. Neurosci.* 28, 2976–2990. doi: 10.1523/JNEUROSCI.4465-07.2008

Maksymetz, J., Moran, S. P., and Conn, P. J. (2017). Targeting metabotropic glutamate receptors for novel treatments of schizophrenia. *Mol. Brain* 10, 1–19. doi: 10.1186/s13041-017-0293-z

Moghaddam, B., and Adams, B. W. (1998). Reversal of phencyclidine effects by a group II metabotropic glutamate receptor agonist in rats. *Science* 281, 1349–1352. doi: 10.1126/science.281.5381.1349

Molinari, F., Cattani, A. A., Mdzomba, J. B., and Anikstejn, L. (2012). Glutamate transporters control metabotropic glutamate receptors activation to prevent the genesis of paroxysmal burst in the developing hippocampus. *Neuroscience* 207, 25–36. doi: 10.1016/j.neuroscience.2012.01.036

Molnár, G., Oláh, S., Komlósi, G., Füle, M., Szabadics, J., Varga, C., et al. (2008). Complex events initiated by individual spikes in the human cerebral cortex. *PLoS Biol.* 6:e222. doi: 10.1371/journal.pbio.0060222

Muguruza, C., Meana, J. J., and Callado, L. F. (2016). Group II Metabotropic glutamate receptors as targets for novel antipsychotic drugs. *Front. Pharmacol.* 7:130. doi: 10.3389/fphar.2016.00130

Nestler, E. J., and Hyman, S. E. (2010). Animal models of neuropsychiatric disorders. *Nat. Neurosci.* 13, 1161–1169. doi: 10.1038/nn.2647

Niswender, C. M., and Conn, P. J. (2010). Metabotropic glutamate receptors: physiology, pharmacology, and disease. *Annu. Rev. Pharmacol. Toxicol.* 50, 295–322. doi: 10.1146/annurev.pharmtox.011008.145533

Ohishi, H., Ogawa-Meguro, R., Shigemoto, R., Kaneko, T., Nakanishi, S., and Mizuno, N. (1994). Immunohistochemical localization of metabotropic glutamate receptors, mGluR2 and mGluR3, in rat cerebellar cortex. *Neuron* 13, 55–66. doi: 10.1016/0896-6273(94)90459-6

Pasquale, R. D., and Sherman, S. M. (2012). Modulatory effects of metabotropic glutamate receptors on local cortical circuits. *J. Neurosci.* 32, 7364–7372. doi: 10.1523/JNEUROSCI.0090-12.2012

Price, C. J., Karayannis, T., and Capogna, M. (2005). Group II and III mGluRs-mediated presynaptic inhibition of EPSCs recorded from hippocampal interneurons of CA1 stratum *lacunosum* moleculare. *Neuropharmacology* 49, 45–56. doi: 10.1016/j.neuropharm.2005.05.009

Sara, Y., Virmani, T., Deák, F., Liu, X., and Kavalali, E. T. (2005). An isolated pool of vesicles recycles at rest and drives spontaneous neurotransmission. *Neuron* 45, 563–573. doi: 10.1016/j.neuron.2004.12.056

Scanziani, M., Capogna, M., Gähwiler, B. H., and Thompson, S. M. (1992). Presynaptic inhibition of miniature excitatory synaptic currents by baclofen and adenosine in the hippocampus. *Neuron* 9, 919–927. doi: 10.1016/0896-6273(92)90244-8

Scanziani, M., Salin, P. A., Vogt, K. E., Malenka, R. C., and Nicoll, R. A. (1997). Use-dependent increases in glutamate concentration activate presynaptic metabotropic glutamate receptors. *Nature* 385, 630–634. doi: 10.1038/385630a0

Schoepp, D. D., Jane, D. E., and Monn, J. A. (1999). Pharmacological agents acting at subtypes of metabotropic glutamate receptors. *Neuropharmacology* 38, 1431–1476. doi: 10.1016/S0028-3908(99)00092-1

Shigemoto, R., Kinoshita, A., Wada, E., Nomura, S., Ohishi, H., Takada, M., et al. (1997). Differential presynaptic localization of metabotropic glutamate receptor subtypes in the rat. *Hippocampus* 17, 7503–7522. doi: 10.1523/JNEUROSCI.17-19-07503.1997

Shigemoto, R., Kulik, A., Roberts, J. D. B., Ohishi, H., Nusser, Z., Kaneko, T., et al. (1996). Target-cell-specific concentration of a metabotropic glutamate receptor in the presynaptic active zone. *Nature* 381, 523–525. doi: 10.1038/381523a0

Singewald, N., Schmuckermair, C., Whittle, N., Holmes, A., and Ressler, K. J. (2015). Pharmacology of cognitive enhancers for exposure-based therapy of fear, anxiety and trauma-related disorders. *Pharmacol. Ther.* 149, 150–190. doi: 10.1016/j.pharmthera.2014.12.004

Spooren, W. P., Gasparini, F., van, der Putten H, Koller, M., Nakanishi, S., and Kuhn, R. (2000). Lack of effect of LY314582 (a group 2 metabotropic glutamate receptor agonist) on phencyclidine-induced locomotor activity in metabotropic glutamate receptor 2 knockout mice. *Eur. J. Pharmacol.* 397, R1–R2. doi: 10.1016/S0014-2999(00)00269-7

Stansley, B. J., and Conn, P. J. (2018). The therapeutic potential of metabotropic glutamate receptor modulation for schizophrenia. *Curr. Opin. Pharmacol.* 38, 31–36. doi: 10.1016/j.coph.2018.02.003

Ster, J., Mateos, J. M., Grewe, B. F., Coiret, G., Corti, C., Corsi, M., et al. (2011). Enhancement of CA3 hippocampal network activity by activation of group II metabotropic glutamate receptors. *Proc. Natl. Acad. Sci.* 1, 8–12. doi: 10.1073/pnas.1100548108

Swanson, C. J., Bures, M., Johnson, M. P., Linden, A. M., Monn, J. A., and Schoepp, D. D. (2005). Metabotropic glutamate receptors as novel targets for anxiety and stress disorders. *Nat. Rev. Drug Discov.* 4, 131–144. doi: 10.1038/nrd1630

Szegedi, V., Molnár, G., Paizs, M., Csakvari, E., Barzó, P., Tamás, G., et al. (2017). High-precision fast-spiking basket cell discharges during complex events in the human neocortex. *eNeuro* 4:ENEURO.0260-17.2017. doi: 10.1523/ENEURO.0260-17.2017

Szegedi, V., Paizs, M., Csakvari, E., Molnar, G., Barzo, P., Tamas, G., et al. (2016). Plasticity in single axon glutamatergic connection to GABAergic interneurons regulates complex events in the human neocortex. *PLoS Biol.* 14:e2000237. doi: 10.1371/journal.pbio.2000237

Tzounopoulos, T., Janz, R., Su, T. C., Nicoll, R. A., and Malenka, R. C. (1998). A Role for cAMP in long-term depression at hippocampal mossy fiber synapses. *Neuron* 21, 837–845. doi: 10.1016/S0896-6273(00)80599-1

Yokoi, M., Kobayashi, K., Manabe, T., Takahashi, T., Sakaguchi, I., Katsuura, G., et al. (1996). Impairment of hippocampal mossy fiber LTD in mice lacking mGluR2. *Science* 273, 645–647. doi: 10.1126/science.273.5275.645

Conflict of Interest Statement: The authors declare that the research was conducted in the absence of any commercial or financial relationships that could be construed as a potential conflict of interest.

Copyright © 2019 Bocchio, Lukacs, Stacey, Plaha, Apostolopoulos, Livermore, Sen, Ansorge, Gillies, Somogyi and Capogna. This is an open-access article distributed under the terms of the Creative Commons Attribution License (CC BY). The use, distribution or reproduction in other forums is permitted, provided the original author(s) and the copyright owner(s) are credited and that the original publication in this journal is cited, in accordance with accepted academic practice. No use, distribution or reproduction is permitted which does not comply with these terms.

frontiers in Cellular Neuroscience

ORIGINAL RESEARCH
published: 14 January 2019
doi: 10.3389/fncel.2018.00515

Sirtuin 1 and Autophagy Attenuate Cisplatin-Induced Hair Cell Death in the Mouse Cochlea and Zebrafish Lateral Line

Jiaqi Pang[1,2,3†], Hao Xiong[1,2†], Ting Zhan[1,3†], Gui Cheng[4], Haiying Jia[4], Yongyi Ye[5], Zhongwu Su[1,2,3], Hongyu Chen[2], Hanqing Lin[1,2,3], Lan Lai[1,2,3], Yongkang Ou[1,2], Yaodong Xu[1,2], Suijun Chen[1,2], Qiuhong Huang[1,2], Maojin Liang[1,2], Yuexin Cai[1,2], Xueyuan Zhang[1,2], Xiaoding Xu[3,6], Yiqing Zheng[1,2] and Haidi Yang[1,2]**

[1]Department of Otolaryngology, Sun Yat-sen Memorial Hospital, Sun Yat-sen University, Guangzhou, China, [2]Department of Hearing and Speech Science, Xinhua College, Sun Yat-Sen University, Guangzhou, China, [3]Guangdong Provincial Key Laboratory of Malignant Tumor Epigenetics and Gene Regulation, Medical Research Center, Sun Yat-sen Memorial Hospital, Sun Yat-sen University, Guangzhou, China, [4]Department of Otolaryngology, The First Affiliated Hospital of Jinan University, Guangzhou, China, [5]School of Public Health, Sun Yat-sen University, Guangzhou, China, [6]RNA Biomedical Institute, Sun Yat-sen Memorial Hospital, Sun Yat-sen University, Guangzhou, China

OPEN ACCESS

Edited by:
Davide Cervia, Università degli Studi della Tuscia, Italy

Reviewed by:
Soledad Levano, Universität Basel, Switzerland
Federico Kalinec, University of California, Los Angeles, United States

***Correspondence:**
Yiqing Zheng
zhengyiq@mail.sysu.edu.cn
Haidi Yang
yanghd@mail.sysu.edu.cn

†These authors have contributed equally to this work

Received: 13 September 2018
Accepted: 12 December 2018
Published: 14 January 2019

Citation:
Pang J, Xiong H, Zhan T, Cheng G, Jia H, Ye Y, Su Z, Chen H, Lin H, Lai L, Ou Y, Xu Y, Chen S, Huang Q, Liang M, Cai Y, Zhang X, Xu X, Zheng Y and Yang H (2019) Sirtuin 1 and Autophagy Attenuate Cisplatin-Induced Hair Cell Death in the Mouse Cochlea and Zebrafish Lateral Line. Front. Cell. Neurosci. 12:515. doi: 10.3389/fncel.2018.00515

Cisplatin-induced ototoxicity is one of the major adverse effects in cisplatin chemotherapy, and hearing protective approaches are unavailable in clinical practice. Recent work unveiled a critical role of autophagy in cell survival in various types of hearing loss. Since the excessive activation of autophagy can contribute to apoptotic cell death, whether the activation of autophagy increases or decreases the rate of cell death in CDDP ototoxicity is still being debated. In this study, we showed that CDDP induced activation of autophagy in the auditory cell HEI-OC1 at the early stage. We then used rapamycin, an autophagy activator, to increase the autophagy activity, and found that the cell death significantly decreased after CDDP injury. In contrast, treatment with the autophagy inhibitor 3-methyladenine (3-MA) significantly increased cell death. In accordance with *in vitro* results, rapamycin alleviated CDDP-induced death of hair cells in zebrafish lateral line and cochlear hair cells in mice. Notably, we found that CDDP-induced increase of Sirtuin 1 (SIRT1) in the HEI-OC1 cells modulated the autophagy function. The specific SIRT1 activator SRT1720 could successfully protect against CDDP-induced cell loss in HEI-OC1 cells, zebrafish lateral line, and mice cochlea. These findings suggest that SIRT1 and autophagy activation can be suggested as potential therapeutic strategies for the treatment of CDDP-induced ototoxicity.

Keywords: SIRT1, autophagy, cisplatin, cell death, ototoxicity

INTRODUCTION

Since the discovery of its anticancer properties in the 1960's, Cisplatin [*cis*-diammine dichloroplatinum (II); CDDP] has been widely used as the most potent chemotherapeutic drug for a variety of solid tumors, such as those found in testicular, ovarian, breast, head and neck, lung, and many other types of cancers (Wang and Lippard, 2005; Cepeda et al., 2007).

Despite decades of research, effective approaches against CDDP-induced side effects including ototoxicity, nephrotoxicity, and neurotoxicity remain unavailable (Rybak et al., 2007; Florea and Büsselberg, 2011; Kim et al., 2018). The ototoxicity induced by CDDP limits its utility and therapeutic profile in both children and adult patients (Rybak et al., 2007; Langer et al., 2013). Therefore, finding effective medications that have a therapeutic effect on existing CDDP-induced ototoxicity remains an unmet medical need.

CDDP ototoxicity is manifested as bilateral, irreversible sensorineural hearing loss (Fang and Xiao, 2014). The ototoxicity is common, in particular among children (Li et al., 2004). The organ of Corti, the spiral ganglions, and the stria vascularis are profoundly damaged in CDDP injury (Gabaizadeh et al., 1997; Tsukasaki et al., 2000; Cardinaal et al., 2004). It's noteworthy that the severe hair cell loss is primarily found in CDDP exposure (Wang et al., 2003; van Ruijven et al., 2005). Although CDDP accumulation is consistently high in the stria vascularis (Breglio et al., 2017), the sensory cells in the cochlea, including outer hair cells (OHCs) and inner hair cells (IHCs), are more susceptible to CDDP-induced damage (Borse et al., 2017).

Autophagy is known to be a general cellular response to starvation or stress that degrades cytoplasmic waste or aggregation depending on lysosome pathway (Klionsky et al., 2016). In addition to the maintenance of cellular homeostasis, autophagy also plays important roles in development, physiology, and pathogenesis of a variety of diseases (Mizushima et al., 2008; Janda et al., 2012; Ohsumi, 2014; He et al., 2017; Pang et al., 2017; Song et al., 2017). In various types of hearing loss, autophagy has been proven to be a protective factor for the survival of hair cells (He et al., 2017; Pang et al., 2017). However, it is also implicated in cell death processes (Shen and Codogno, 2011). In CDDP ototoxicity, it is still not well established as to whether autophagy plays a protective or destructive role (Fang and Xiao, 2014; Youn et al., 2015; Li et al., 2018; Yin et al., 2018). Furthermore, understanding how autophagy is regulated during CDDP ototoxicity also remains elusive. In view of these findings and questions, we investigated the effects of autophagy in CDDP-induced cytotoxicity. To confirm our results, several models have been employed, including the auditory cell line HEI-OC1 (Kalinec et al., 2016), the lateral line hair cell of zebrafish (Jiang et al., 2014), and the C57BL/6 mice.

Sirtuin 1 (SIRT1), the most conserved member among a family of NAD^+-dependent protein deacetylases, has been proven to have protective effects in various common neurodegenerative disorders (Herskovits and Guarente, 2014). In our previous study, we also demonstrated that decreased SIRT1 level was correlated with age-related hair cell loss and hearing loss in C57BL/6 mice (Xiong et al., 2014, 2015), although the detailed mechanism remains elusive. Interestingly, the effect of SIRT1 in the modulation of autophagy has been proven by the fact that SIRT1 could directly deacetylating multiple autophagy-related proteins, including ATG5, ATG7 and ATG8 (Lee et al., 2008). Therefore, in the present study we aimed to explore SIRT1's modulation of autophagy during CDDP ototoxicity.

MATERIALS AND METHODS

Cell Culture

Since the HEI-OC1 cell line displays a variety of markers for sensory hair cells, including math1, myosin7a and prestin, it becomes a common cell line used for the elucidation of hair cell pathology. HEI-OC1 cells (kindly provided by F. Kalinec at the House Ear Institute, Los Angeles, CA, USA) were cultured in high-glucose Dulbecco's Modified Eagle's Medium (DMEM; Gibco BRL, Grand Island, NY, USA), supplemented with 10% fetal bovine serum (FBS; Gibco BRL, Grand Island, NY, USA) at 33°C and 10% CO_2 in a humidified atmosphere without antibiotics. For *in vitro* cisplatin (CDDP) toxicity test, HEI-OC1 cells were exposed to CDDP at indicated concentrations for indicated hours for cell viability analysis. HEI-OC1 cells were pretreated with different agents for 24 h and then exposed to CDDP at 20 μM for 24 h.

Materials

Cisplatin (CDDP, Selleck, S1166, Huston, TX, USA), Rapamycin (RA, Selleck, S1039, TX, USA), 3-Methyladenine (3-MA, S2767, Selleck, Huston, TX, USA), SRT1720 (SRT1720, S1129, Selleck, Huston, TX, USA). Chloroquine (CQ, C6628, Sigma-Aldrich, MO, USA), LC3-II/LC3B (#3868, Cell Signaling Technology, Boston, MA, USA), SIRT1 (#9475, Cell Signaling Technology, Boston, MA, USA), p62 (#5114, Cell Signaling Technology, Boston, MA, USA), β-actin (#4970, Cell Signaling Technology, Boston, MA, USA), p53 (#2524, Cell Signaling Technology, Boston, MA, USA), Acetyl-p53 (#2525, Cell Signaling Technology, Boston, MA, USA), Western Antibody Dilution Buffer (RM00016, ABclonal, Cambridge, UK).

Protein Extraction and Western Blot

Images of HEI-OC1 cells treated with different reagents were captured by optical microscope. Then, the total proteins of treated cells or tissues were extracted by RIPA lysis buffer (Thermo, 89901, USA), in which proteinase inhibitor (1:100, Selleck, TX, USA) was added. After the concentration measurements by BCA assay kit (Beyotime Biotechnology, Shanghai, China), equal amounts of protein were denatured and then separated by 12% SDS-PAGE electrophoresis, followed by transfer to polyvinylidene fluoride membranes (PVDF, Millipore, Darmstadt, Germany). The membranes were blocked in 5% non-fat milk for 1 h at room temperature. After washing with TBS containing 0.05% tween 20 (TBST) three times, the membranes were incubated with related primary antibodies (1:1,000) in TBST with 5% BSA overnight. Then, they were incubated with secondary antibodies (1:5,000–1:10,000) for 1 h after three washes with TBST. Finally, the protein signals were detected by use of the ECL kit (Millipore, WBKLS0010, Darmstadt, Germany) and analyzed by ImageJ software.

Cell Viability Assay

Cells were seeded at the density of 2,000 cells/well in a 96-well plate and allowed to attach overnight for 16 h. After treatment with or without SRT1720 (0.5 μM) or RA (0.5 μM) for 24 h,

they were exposed to CDDP (20 μM) with or without 3-MA (5 mM) for another 24 h. Next, 10 μl CCK-8 reagent (Beyotime Biotechnology, Shanghai, China) was added to each well and reacted for 2 h. Absorbance at 450 nm was detected through the Multiskan MK3 microplate reader (Labsystems, USA) for cell viability.

Transfection of Cells With Fluorescent LC3

The lentivirus containing the green fluorescent protein (GFP)-LC3 fusion gene was purchased from Hanbio (Shanghai, China). The HEI-OC1 cells were transfected with lentivirus-mediated GFP-LC3 to generate GFP-LC3-expressing cells. HEI-OC1 cells were seeded into six-well dishes ($1*10^5$ cells per well) and infected with the recombinant lentivirus following the manufacturer's instructions (a MOI of 100). After 48 h, cells were selected by culture in the presence of puromycin for 2 weeks. Cells were treated with SRT1720 (0.5 μM) or CQ (10 μM) with or without CDDP (20 μM) injury. Observation of autophagosome formation was determined after fluorescent staining by evaluating the number of GFP puncta (puncta/cell was counted).

Assessment of Apoptosis by Flow Cytometry

Cell apoptosis was also measured by a FITC Annexin V Apoptosis Detection Kit (BD, Franklin Lakes, NJ, USA). Briefly, cells were harvested and washed twice by cold PBS solution, and resuspended with 100 μl 1× binding buffer softly. Ten microliter Annexin V and 5 μl propidium iodide (PI) were added to each group and incubated in dark room for 15 min. Approximately 10,000 cells of each group were measured by a FACS Calibur system (BD Biosciences, Franklin Lakes, NJ, USA).

Zebrafish Breeding

Zebrafish embryos of the ET4 transgenic wildtype hair cells that are specifically labeled produced adult fish and maintained at a density of 50 embryos per 100 mm Petri dish in 28.5°C embryo medium (15.0 mM NaCl, 0.5 mM KCl, 1.0 mM $CaCl_2$, 1.0 mM $MgSO_4$, 0.14 mM KH_2PO_4, 0.06 mM Na_2HPO_4, and 0.5 mM $NaHCO_3$).

Lateral Line Hair Cell Counting in Zebrafish

Five days post-fertilization (dpf) zebrafish larvae were used for experiments. The experiment was set as eight groups, including control group (DMSO), CDDP group, RA group, CDDP with RA pre-treatment for 1 h, CDDP with RA group, SRT1720 group, CDDP with SRT1720 pre-treatment for 1 h and CDDP with SRT1720 group. The concentration of CDDP was 600 μM, RA 10 μM and SRT1720 5 μM. By using a 12-hole plate, with eight larvae per hole, each group set up two holes. After the CDDP exposure for 12 h and 24 h, 6 zebrafish larvae of each group were selected to fix at 4°C in 4% paraformaldehyde (PFA) for 0.5 h, flushed with PBST, then mounted in glycerin on 25 × 60 mm Non-slip off coverslips. We then determined the counts of three hair cell aggregations of lateral line hair cells in each zebrafish using a confocal microscope (Carl Zeiss, Germany) and calculated the average count of lateral line hair cells.

Animals

Forty-eight C57BL/6 mice at the age of 7 weeks were obtained from Laboratory Animal Center, Sun Yat-sen University. After a hearing test to exclude hearing abnormal mice, the rest of them were randomly divided into six groups, a "Control" group (DMSO intraperitoneal injection), a "CDDP" group (16 mg/kg, intraperitoneal injection), two drug groups (rapamycin, 7.5 mg/kg, intraperitoneal injection; SRT1720, 100 mg/kg, intragastric administration) and two "CDDP+drug" groups. Auditory brainstem response (ABR) were tested 72 h after CDDP administration. Animal care and experimental treatment were carried out in accordance with the recommendations of Constitution of Animal Ethical and Welfare Committee (AEWC). The protocol was approved by the Animal Research Committee at Sun Yat-sen University.

Auditory Brainstem Response

ABR measurements were performed when mice were anesthetized with intraperitoneal injection (100 mg/kg ketamine and 10 mg/kg xylazine mixture). Three needle electrodes were inserted sub-dermally at the vertex (active), under the left ear (reference), and the back (ground). The acoustic signals were generated, and the responses were processed with Tucker-Davis Technologies (TDT System III, Alachua, FL, USA) hardware and software. Ten-millisecond (ms) tone bursts with a 1 ms rise or fall time were presented at 4, 8, 16 and 32 kHz at a rate of 21.1/s. The average response to different sound intensity at 4 kHz, 8 kHz, 16 kHz and 32 kHz was collected and processed by TDT by attenuating the sound intensity 5 dB intervals from 100 dB to 0 dB. The hearing threshold was defined as the lowest stimulation dB level at which a positive wave in the evoked response trace was evident (Pang et al., 2016).

Animal Drug Administration

Cisplatin (CDDP, Selleck, S1166, Huston, TX, USA) was dissolved in DMSO and intraperitoneally injected (16 mg/kg). Rapamycin (RA, Selleck, S1039, TX, USA) was dissolved in DMSO, and intragastric administration (7.5 mg/kg) was performed three times 24 h before and after CDDP exposure, and 1 h before CDDP exposure. SRT1720 (Selleck, S1129, Huston, TX, USA) was dissolved in normal saline (NS; 5 mg/ml) and intragastric administration (100 mg/kg) was performed three times, 12 h and 1 h before CDDP exposure and immediately after CDDP exposure.

Tissue Preparation

After ABR recordings, the deeply anesthetized mice were decapitated, and the cochleae were taken out under microscope to fix in 4% PFA overnight at 4°C on the shakers. The cochleae were decalcified in 4% sodium ethylenediaminetetraacetic acid for 48 h, and then the osseous labyrinth, stria vascularis, spiral ligament, Reissner's and tectorial membrane were carefully cut away under the microscopy, and the remaining basal membrane were subjected to immunofluorescent staining.

Hair Cells Counting

Cochlear sections were incubated in 3% Triton X-100 for 45 min at room temperature on the shaker, washed with PBS three times and blocked with blocking solution (10% goat serum in PBS) for 1 h. Specimens were counterstained with 4',6-diamidino-2-phenylindole (DAPI; 10 mg/ml, Sigma-Aldrich, MO, USA) for 10 min. The tissues were mounted on glass slides in 50% glycerol. Cochlear samples were observed and imaged with an Olympus BX63 microscope. Hair cells were counted from the apex to the base along the entire length of the cochlear epithelium. The percentage of hair cell loss in each 0.5 mm length of epithelium was plotted vs. cochlear length as a cytocochleogram.

Statistical Analysis

All values were shown as mean ± SEM. and analyzed by one-way analysis of variance (ANOVA) with Fisher *post hoc* test or independent *t*-test. Values of $p < 0.05$ were considered statistically significant.

RESULTS

SIRT1 and Autophagy Increase in CDDP Induced Cell Death in HEI-OC1 Cells

CDDP-induced cytotoxicity was measured by monitoring cell viability and using annexin V and PI staining in the auditory cell line HEI-OC1. In our experiments, HEI-OC1 cells started to have a decreased survival rate when exposed to 20 μM CDDP at 24 h, and this aggravated at 36 h and 48 h (**Figure 1A**). Then we exposed the cells to various CDDP concentrations for 24 h. Dose-dependent HEI-OC1 cell death increased by 47.0 ± 10.1% at 20 μM with a 50% of maximal effect (EC50) being ∼20 μM (**Figure 1B**). In agreement with these findings, FACS analysis showed that CDDP induced apoptosis (**Figures 1C,D**). In the mRNA levels, CDDP only increased LC3B expression (**Supplementary Information 1 Figure S1**), but not p62. As an autophagosome marker, LC3-II increased, while the autophagic degeneration marker p62 decreased. Interestingly, CDDP significantly increased SIRT1, accompanied with autophagy (**Figures 1E,F**).

Rapamycin Promotes HEI-OC1 Cell Survival After CDDP-Induced Damage

Rapamycin (RA), a well-known mTOR inhibitor, has been widely reported to induce autophagy both *in vivo* and *in vitro* (Tanemura et al., 2012). The cell death attenuated when co-treated with RA compared with the single CDDP exposure. Around 20%–30% of total cells did not experience death (**Figure 2A**). CDDP exposure caused more detached cells, while RA attenuated the ototoxicity (**Figure 2B**). Although the mRNA levels of LC3B and p62 did not change in RA treatment with or without CDDP (**Supplementary Information 1 Figure S1**), in the protein levels, LC3-I to LC3-II conversion further increased in RA treatment, while p62 protein decreased even in CDDP exposure (**Figures 2C,D**). These findings revealed that autophagy activated by RA could attenuate CDDP mediated ototoxicity.

SIRT1 Activates Autophagy and Promotes HEI-OC1 Cells Survival After CDDP-Induced Damage

SRT1720, a new synthetic small molecule, has been confirmed as the selective activator of SIRT1 (Yao et al., 2012; Sun et al., 2018). Previous biochemical studies have shown that the affinity of SIRT1 to SRT1720 is approximately 1,000 times as strong as that with another SIRT1 activator resveratrol. To examine the activation from SRT1720, the protein expression of p53,

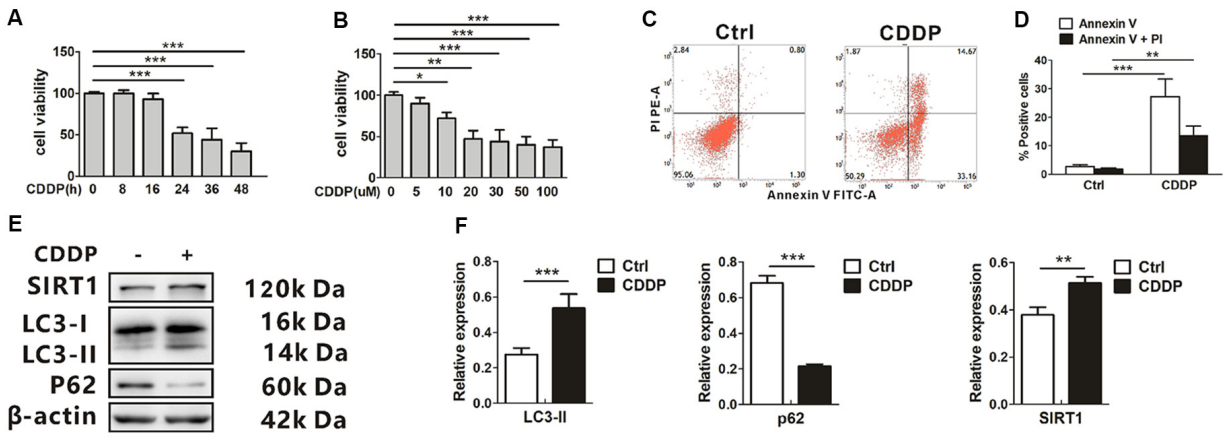


FIGURE 1 | CDDP induces cell death and increases both sirtuin 1 (SIRT1) and autophagy in HEI-OC1 cells. **(A)** The CCK8 assay was performed to examine cell viability of HEI-OC1 cells in CDDP (20 μM) exposure from 0 h to 48 h ($n = 3$ individual experiments). **(B)** The CCK8 assay was performed to examine cell viability of HEI-OC1 cells in CDDP exposure from 0 μM to 100 μM for 24 h ($n = 3$ individual experiments). **(C,D)** Apoptosis measured by annexin V and propidium iodide (PI) staining for HEI-OC1 cells in CDDP (20 μM) exposure for 24 h ($n = 3$ individual experiments) and its analysis. **(E,F)** Western blots and densitometry analysis for SIRT1 and autophagy marker LC3-II and p62 in CDDP (20 μM) exposure for 24 h ($n = 3$ individual experiments). Data represent the mean ± SEM. $^*p < 0.05$, $^{**}p < 0.01$, $^{***}p < 0.001$. CDDP, cisplatin.

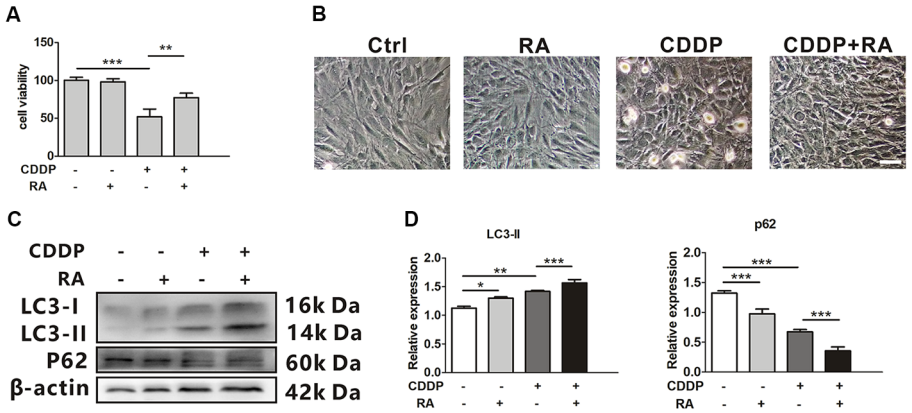


FIGURE 2 | Rapamycin promotes HEI-OC1 cell survival after cisplatin-induced damage. **(A)** The CCK8 assay was performed to examine cell viability of HEI-OC1 cells following CDDP (20 μM) exposure for 24 h with or without RA (0.5 μM; $n = 3$ individual experiments). **(B)** The image of HEI-OC1 cells following CDDP (20 μM) exposure for 24 h with or without RA (0.5 μM; $n = 3$ individual experiments). **(C,D)** Western blots and densitometry analysis for autophagy marker LC3-II and p62 in CDDP (20 μM) exposure for 24 h with or without RA (0.5 μM; $n = 3$). Data represent the mean ± SEM. $^{*}p < 0.05$, $^{**}p < 0.01$, $^{***}p < 0.001$. CDDP, cisplatin; RA, rapamycin.

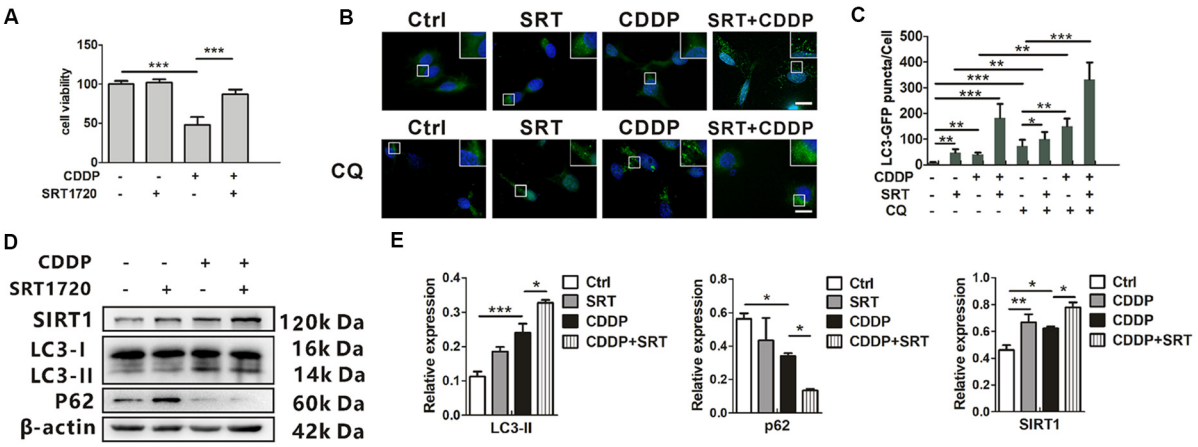


FIGURE 3 | SIRT1 activates autophagy and promotes HEI-OC1 cell survival after cisplatin-induced damage. **(A)** The CCK8 assay was performed to examine cell viability of HEI-OC1 cells following CDDP (20 μM) exposure for 24 h with or without SRT1720 pre-treatment for 24 h (0.5 μM; $n = 3$ individual experiments). **(B,C)** The fluorescence image of green fluorescent protein (GFP)-LC3 HEI-OC1 cells after CDDP (20 μM) exposure with or without SRT1720 (0.5 μM) and CQ (10 μM). Scale bar, 10 μm. Quantity analysis of green puncta was detected in five cells/experiment ($n = 3$ individual experiments). **(D,E)** Western blots and densitometry analysis for SIRT1 and autophagy marker LC3-II and p62 in CDDP (20 μM) exposure for 24 h with or without SRT1720 pre-treatment for 24 h (0.5 μM; $n = 3$ individual experiments). Data represent the mean ± SEM. $^{*}p < 0.05$, $^{**}p < 0.01$, $^{***}p < 0.001$. CDDP, cisplatin; SRT, SRT1720.

and ac-p53 as a deacetylated target of SIRT1, were measured by western blotting. The ratios of acetylated p53 to total p53 attenuated in HEI-OC1 cells (**Supplementary Information 1 Figure S2**). Then, we found that SRT1720 could reduce cell death in CDDP exposure. Around 40% of total cells were prevented from experiencing cell death (**Figure 3A**). In the mRNA levels, LC3B and p62 mRNA had no significant difference in SRT1720 treatment with or without CDDP exposure (**Supplementary Information 1 Figure S1**). To robustly demonstrate the modulation that SIRT1 activates autophagy, GFP-LC3 HEI-OC1 cells were employed to describe the modulation with autophagic degradation blocker chloroquine (CQ). CDDP or SRT1720 treatment could increase the formation of LC3, and blocker CQ captured even more. Then, the green puncta were the highest in SRT1720 treatment with CDDP exposure (**Figures 3B,C**). Meanwhile, SRT1720 could also further increasing LC3-II in CDDP exposure in western blot. In contrast, p62 expression decreased in CDDP exposure and further decreased with SRT1720 treatment (**Figures 3D,E**). These results suggest that although HEI-OC1 cells might increase SIRT1 to activate autophagy against CDDP damage that may not be enough for cells to pull through. Therefore, we find that the external activation of autophagy and SIRT1 prevent cells from death.

SIRT1 Reduces CDDP Induced Ototoxicity Through Autophagy in HEI-OC1 Cells

To confirm whether SIRT1 reduced CDDP induced ototoxicity through autophagy, we employed the phosphatidylinositol-3-kinase inhibitor (3-MA), the most widely used autophagy inhibitor (Seglen and Gordon, 1982), to suppress autophagy. As expected, autophagy inhibition accelerated CDDP-induced cell death. Moreover, we found that the prevention of autophagy diminished the SIRT1 activation-mediated HEI-OC1 survival in the CDDP exposure (**Figure 4**). These results imply that the effects of SIRT1 in cell survival protection were nearly abolished in the autophagic inhibition by 3-MA. Collectively, SIRT1 reduced CDDP mediated ototoxicity via the induction of autophagy.

Autophagy Activation Promotes the Lateral Line Hair Cell Survival After CDDP-Induced Damage in Zebrafish

The lateral line of zebrafish can sense water motion and initiate the appropriate behavioral response for capturing prey and avoiding predators. The lateral line hair cells are located in the skin and easy to observe. Both lateral line and ear hair cells are the sensory hair cells, and they develop and differentiate by similar developmental mechanisms. Mutations in genes disrupting hair cell function in the zebrafish lateral line and vestibular system also cause deafness in humans (Nicolson, 2005). Since both the lateral line and ear hair cells share the similar genetic background, and the lateral line accessibility makes it easier in experimental manipulation and visualization, the zebrafish recently has been recognized as an excellent model for discovering and functionally characterizing genes crucial for hair cell pathology (Behra et al., 2009; Brignull et al., 2009; Liang et al., 2012; Rubel et al., 2013; Jiang et al., 2014). The analysis of hair cell survival allowed us to draw comparisons between CDDP exposure with or without RA at 12 h and 24 h (**Figure 5A**). At 12 h after CDDP treatment, more than half of hair cells were eliminated. As expected, nearly half of hair cells remained in the pre-treat or with RA or SRT1720 in CDDP exposure. Although at 24 h after CDDP exposure, nearly all hair cells were eliminated, while pre-treatment with RA or SRT1720 significantly attenuated cisplatin-induced hair cell loss (**Figures 5A–C**).

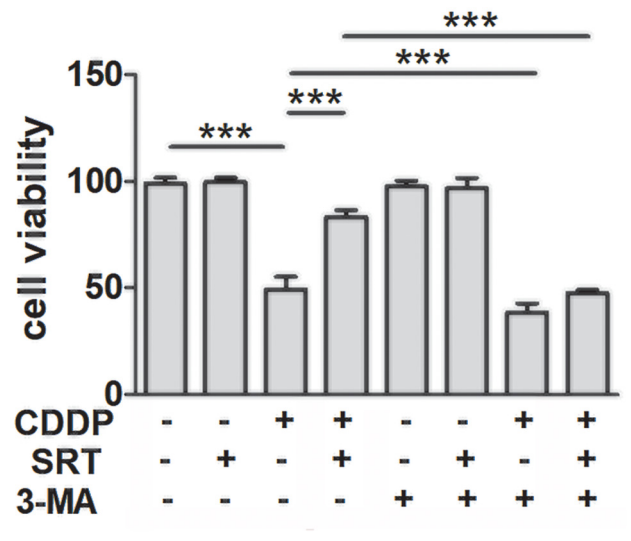


FIGURE 4 | SIRT1 protects against cisplatin-induced cell death via autophagy in HEI-OC1 cells. The CCK8 assay was performed to examine cell viability of HEI-OC1 cells in CDDP (20 μM) exposure for 24 h combined with 3-MA (5 mM) treatment with or without SRT1720 pre-treatment for 24 h (0.5 μM; $n = 4$ individual experiments). Data represent the mean ± SEM. ***$p < 0.001$. CDDP, cisplatin; SRT, SRT1720; 3-Methyladenine, 3-MA.

Autophagy Activation Promotes Hair Cell Survival After CDDP-Induced Damage in C57BL/6 Mice

To demonstrate the major role that the activation of autophagy plays in CDDP-mediated hearing loss, we examined the effect of RA on CDDP-induced hearing loss. C57BL/6 mice at 7 weeks old developed a significant ABR threshold shift after CDDP exposure at various frequencies (26.0 ± 6.5 dB at 4 kHz, 26.3 ± 2.5 dB at 8 kHz, 23.0 ± 5.7 dB at 16 kHz and 20.0 ± 7.1 dB at 32 kHz). To supplement with RA at 20 mg/kg 24 h before and after CDDP exposure, plus 1 h before CDDP exposure, we used intraperitoneal injection. RA significantly reduced CDDP-mediated auditory threshold shifts at various frequencies (10.0 ± 5.0 dB at 4 kHz, 5.0 ± 0.0 dB at 8 kHz, 3.3 ± 2.9 dB at 16 kHz and 8.8 ± 2.5 dB at 32 kHz; **Figure 6A**). Additionally, RA significantly decreased OHC loss in CDDP exposure (**Figures 6B,C**). Taken together, these results support that RA strengthened OHCs' survival in CDDP ototoxicity in both zebrafish and mice. Moreover, RA attenuated CDDP-mediated hearing loss in C57BL/6 mice.

SIRT1 Activation Attenuates CDDP-Induced Hair Cell Loss and Hearing Loss in C57BL/6 Mice

As proven before, SIRT1 also raised HEI-OC1 cells survival via autophagy in CDDP exposure. To demonstrate whether the activation of SIRT1 attenuates CDDP-mediated hearing loss in mice, we examined the effect of SRT1720 on CDDP-induced hearing loss. In agreement with the experiment before, CDDP developed a severe hearing loss at various frequencies (36.0 ± 11.4 dB at 4 kHz, 30.0 ± 8.9 dB at 8 kHz, 32.1 ± 11.5 dB at 16 kHz and 28.3 ± 4.0 dB at 32 kHz; **Figure 7A**). To supplement with SRT1720 at 100 mg/kg 12 h before and after, plus 1 h before CDDP exposure, we used gavage. SRT1720 significantly reduced CDDP-mediated auditory threshold shifts at various frequencies (8.8 ± 4.8 dB at 4 kHz, 5 ± 5 dB at 8 kHz, 5.5 ± 3.7 dB at 16 kHz and 5 ± 5 dB at 32 kHz; **Figure 7A**). Additionally, SRT1720 significantly decreased OHC loss in CDDP exposure (**Figures 7B,C**). Collectively, SRT1720 strengthens OHC survival to attenuate CDDP induced hearing loss in C57BL/6 mice.

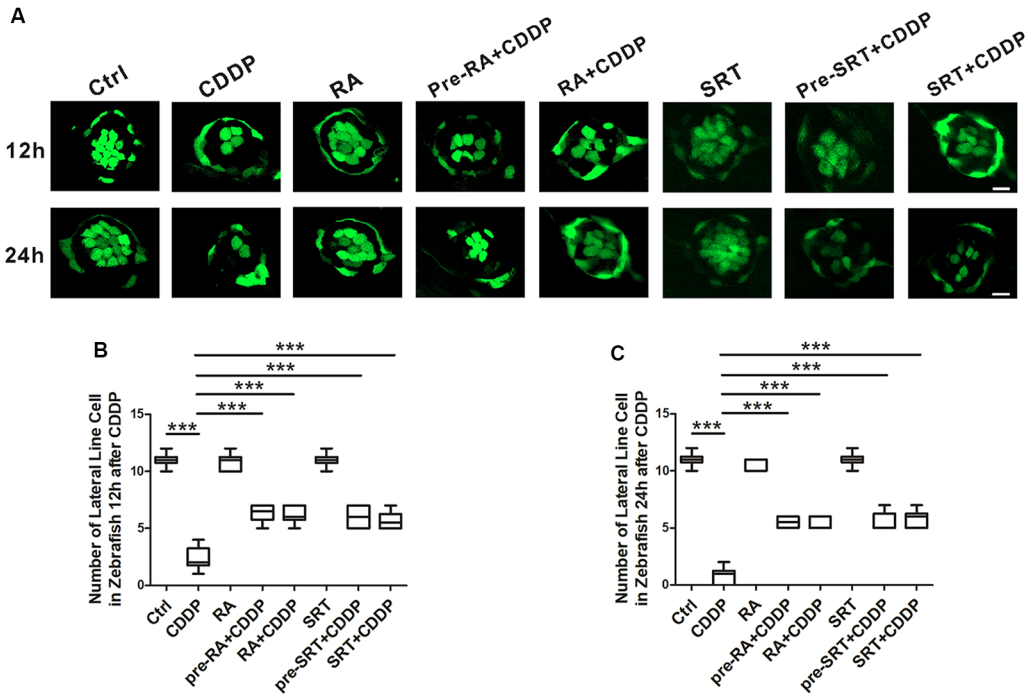


FIGURE 5 | Autophagy activation promotes hair cell survival after cisplatin-induced damage in zebrafish lateral line. **(A)** Hair cell counts obtained from CDDP exposure for 12 or 24 h with or without RA or SRT1720 treatment (n = 6 zebrafish larvae). Scale bar, 10 μm. **(B)** The hair cells were counted at 12 h after CDDP exposure. **(C)** The hair cells were counted 24 h after CDDP exposure. Data represent the mean ± SEM. ***$p < 0.001$. Control, zebrafish larvae cultured in the same dose DMSO as the CDDP and RA group; RA, zebrafish larvae cultured in RA; CDDP, zebrafish larvae cultured in CDDP; pre-RA+CDDP, zebrafish larvae cultured in RA for 1 h followed by exposure to CDDP; RA + CDDP, zebrafish larvae cultured in CDDP and RA. SRT1720, zebrafish larvae cultured in SRT1720; pre-SRT1720+CDDP, zebrafish larvae cultured in SRT1720 for 1 h followed by exposure to CDDP; SRT1720 + CDDP, zebrafish larvae cultured in CDDP and SRT1720. CDDP, cisplatin; RA, rapamycin; SRT, SRT1720.

DISCUSSION

Although the relationship between autophagy and cell death has been extensively investigated in the past decade, whether the activation of autophagy induces the cell death or survival in diseases is still controversial. Autophagy is known to be a general cellular process to strengthen cell ability to survive under starvation or stress conditions (Klionsky et al., 2016). However, excessive activation of autophagy leads to autophagic cell death (Yu et al., 2004; Ryter et al., 2014), such as cardiac myocyte death during ischemia/reperfusion (Liu et al., 2016). In contrast, the activation of autophagy also plays a positive role during various pathological and physiological states (Rubinsztein et al., 2015; Deng et al., 2017; Song et al., 2017), including aminoglycoside-induced and age-related hearing loss (He et al., 2017; Pang et al., 2017). Recent work has shown that the role of activation of autophagy in CDDP ototoxicity is still being debated. Autophagy, more specifically mitophagy, alleviated CDDP-induced ototoxicity (Fang and Xiao, 2014; Yang et al., 2018). In addition, the increase of the key autophagy protein Beclin-1 was observed in the model of attenuating ototoxicity induced by CDDP (Fang and Xiao, 2014; Yang et al., 2018). These results suggest that autophagy is important in preventing CDDP-induced ototoxicity. In contrast, autophagy was significantly increased after exposure to CDDP for 48 h along with cell death (Youn et al., 2015). At that moment, the autophagy inhibitor can help to decrease CDDP-induced cell apoptosis (Li et al., 2018). However, the significant apoptosis starts at 24 h, the same as our current work, and the excessive activation of autophagy occurred 48 h after CDDP exposure, which made it difficult to account for the apoptosis. Perhaps the excessive activation of autophagy along with cell death was only part of the progress at the later stage. To thoroughly determine the role of activation of autophagy at the early stage of CDDP-induced injury, when we could intervene, we employed three different models, an auditory cell line of HEI-OC1 cells, the lateral line hair cells of zebrafish, and C57BL/6 mice. We found that the induction of autophagy was markedly increased when the CDDP-induced cell death started in HEI-OC1 cells. Then, enhancing or blocking autophagy with autophagy activators or inhibitors could help us to understand the role of autophagy in CDDP ototoxicity. With the activator of autophagy rapamycin, the CDDP induced cell death was alleviated in HEI-OC1 cells, which agrees with the results in the lateral line hair cells of zebrafish. Meanwhile, the inhibitor of autophagy 3-MA promoted CDDP-induced HEI-OC1 cells death. Following CDDP exposure, the mice developed severe hearing loss, which is consistent with the results of other

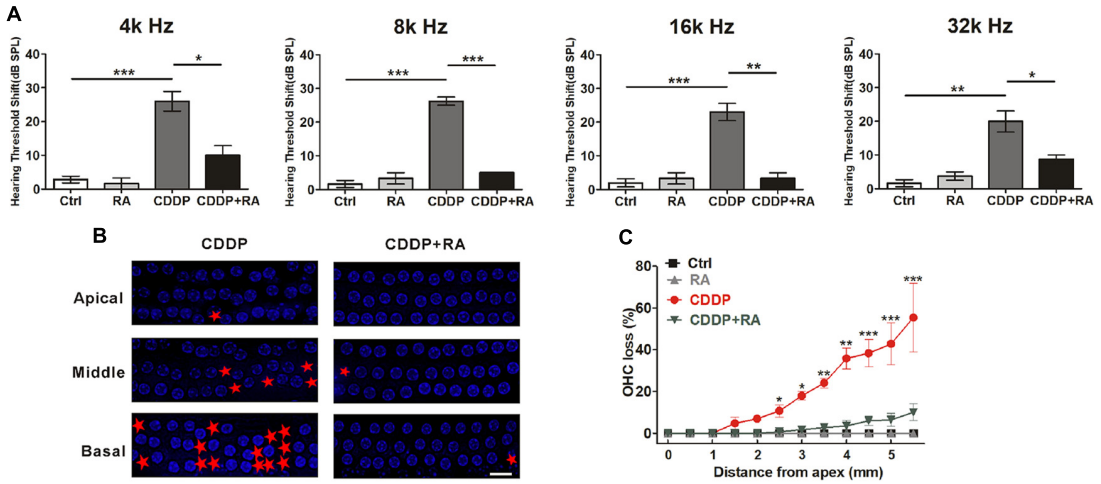


FIGURE 6 | Autophagy activation attenuates cisplatin-induced hair cell loss and hearing loss in C57BL/6 mice. **(A)** Auditory brainstem response (ABR) thresholds decreased with RA (7.5 mg/kg, intraperitoneal injection pre-24 h, pre-1 h, post-24 h) treatment mice in CDDP (16 mg/kg, intraperitoneal injection) exposure compared with the CDDP groups at 4, 8, 16 and 32 kHz (n = 6 mice). **(B,C)** Surface preparations were stained with 4′,6-diamidino-2-phenylindole (DAPI). Hair cell counts obtained for the CDDP and CDDP+RA group (n = the right cochlea of six mice). Scale bar, 10 μm. Data represent the mean ± SEM. $^{*}p < 0.05$, $^{**}p < 0.01$, $^{***}p < 0.001$. Control, mice were intraperitoneally injected with the same dose DMSO as the CDDP group; RA, mice were intraperitoneally injected with rapamycin three times; CDDP, mice were intraperitoneally injected with CDDP; CDDP+RA, mice were intraperitoneally injected with CDDP once and rapamycin three times. CDDP, cisplatin; RA, rapamycin; Apical, the apical turn; Middle, the middle turn; Basal, the basal turn; Red asterisks, lost hair cells.

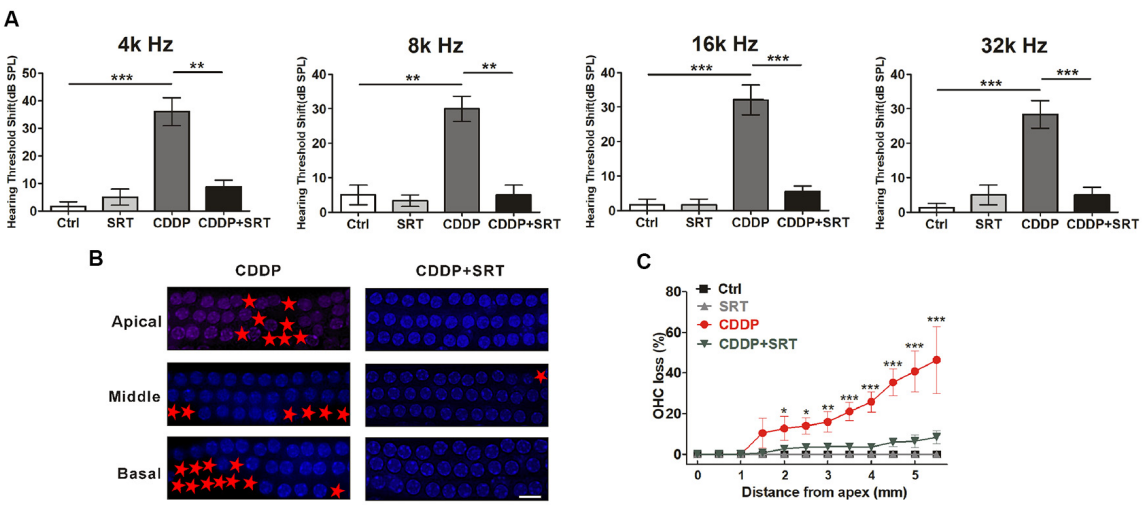


FIGURE 7 | SIRT1 activation attenuates cisplatin-induced hair cell loss and hearing loss in C57BL/6 mice. **(A)** ABR thresholds decreased with SRT1720 (100 mg/kg, intragastric administration pre-12 h, pre-1 h, post-12 h) treatment mice following CDDP (16 mg/kg, intraperitoneal injection) exposure compared with the CDDP group at 4, 8, 16 and 32 kHz (n = 6 mice). **(B,C)** Surface preparations were stained with DAPI. Hair cell counts obtained from the CDDP and CDDP+SRT1720 group (n = the right cochlea of six mice). Scale bar, 10 μm. Data represent the mean ± SEM. $^{*}p < 0.05$, $^{**}p < 0.01$, $^{***}p < 0.001$. Control, mice intraperitoneally injected with the same dose DMSO as the CDDP group; SRT1720, mice gavage SRT1720 three times; CDDP, mice intraperitoneally injected with CDDP; CDDP + SRT1720, mice intraperitoneal injected with CDDP once and gavage SRT1720 three times. CDDP, cisplatin; SRT, SRT1720; Apical, the apical turn; Middle, the middle turn; Basal, the basal turn; Red asterisks, lost hair cells.

studies observing a 35 dB–55 dB threshold shift at 4, 8, 16 and 32 kHz (Kim et al., 2014; Benkafadar et al., 2017; Breglio et al., 2017). However, our ABR results showed no difference between different frequencies, while one study indicated higher levels of severity at the highest frequencies (Breglio et al., 2017). Furthermore, the activator of autophagy rapamycin alleviated the CDDP-maintained hair cell death in C57BL/6 mice and attenuated hearing shift. These findings suggest that autophagy plays a protective role against CDDP injury as the way to rescue itself until the point where the damage breaks through its limit.

It has been postulated that the generation of excessive ROS is considered to be one of the major causes of CDDP-induced ototoxicity, in particular the sensory cells of the organ of Corti (Kopke et al., 1997; Dehne et al., 2001; Korver et al., 2002; Hyppolito et al., 2006; Hill et al., 2008). Antioxidants showed good promise against CDDP-induced hearing loss (Borse et al., 2017). On the basis of what has been reported so far, autophagy could suppress ROS accumulation in cells by the p62 delivery pathway (Wang et al., 2018) and its specific mitophagy pathway (Kim et al., 2007). To promote cell survival, induced autophagy decreases ROS concentration and reduces the oxidative damage to biomolecules and organelles (Filomeni et al., 2015; Van Erp et al., 2017). Additionally, in neomycin or gentamicin ototoxicity, autophagy mediates its protective effects by reducing levels of ROS (He et al., 2017). Although the experimental conditions differ between reports in different tissue and our study, our data in HEI-OC1 cells, the lateral line hair cells of zebrafish and the cochlea hair cells in mice are consistent with these studies regarding the activation of autophagy against cytotoxicity, especially CDDP-induced ototoxicity.

Since autophagy activation is an important contributor to alleviate CDDP-induced ototoxicity, the underlying modulator-induced autophagy is not fully understood. SIRT1, the well-studied NAD^+-dependent deacetylase, has been proven to have protective effects in various common neurodegenerative disorders (Herskovits and Guarente, 2014). Besides, SIRT1 can extend lifespan in lower organisms (Finkel et al., 2009; Burnett et al., 2011). According to recent studies, in addition to the FoxO-mediated mechanisms (Hariharan et al., 2010; Kume et al., 2010), SIRT1 could also directly deacetylate autophagy proteins, including ATG5, ATG7 and ATG8, to induce autophagy (Lee et al., 2008). Therefore, SIRT1 is one of the modulators of autophagy. In our previous study, we found that the hearing loss is associated with the expression of SIRT1 in the hair cells of C57BL/6 mice (Xiong et al., 2014). SIRT1 plays a protective role to prevent hair cell death in age-related hearing loss (Xiong et al., 2015). As expected, the levels of SIRT1 significantly increased in the hair cell after CDDP exposure, which was accompanied by autophagic induction in the current work. We speculated that SIRT1 might function upstream of autophagy and protect cells against hair cell toxicity and cell death during the early stage of CDDP-induced injury since the hair cells are eager to survive. By enhancing SIRT1 activity with its specific activator SRT1720, the autophagic cavity further improved. Moreover, the CDDP-induced cell death was alleviated in HEI-OC1 cells, in the lateral line hair cells of zebrafish and in cochlear hair cells of C57BL/6 mice. Nevertheless, the protective effect on cell survival was almost diminished by the autophagy inhibitor. These results reveal that the mechanism of increasing SIRT1 to activate autophagy is the way hair cells attenuate CDDP-induced cell death. To our knowledge, this is the first study that describes the modulation between SIRT1 and autophagy in CDDP exposure in hearing.

Apart from the induction of autophagy, rapamycin can modulate other cellular processes (Martin et al., 2017). We have performed immunoblot experiments to detect autophagy via the combined analysis of LC3-II and p62 levels. Rapamycin's ability to alleviate CDDP-induced ototoxicity is at least partly due to its effect on autophagy. For further study, a specific autophagy modulator needs to be employed. In the previous studies, rapamycin and SRT1720 were applied to animals by systemic administration. However, considering that these agents might inhibit CDDP's chemotherapeutic efficacy (Lawenda et al., 2008), local application should be considered as the way to intervene in the SIRT1/autophagy activation.

In conclusion, this study shows that CDDP injury activates SIRT1 and autophagy in HEI-OC1 cells. We report for the first time that there is a protective way for the sensory hair cells to rescue themselves by raising SIRT1 and autophagy at the early stage of CDDP injury. Both SIRT1 and autophagy play important roles in hair cell survival after CDDP exposure in HEI-OC1 cells, the lateral line hair cells of zebrafish, and in C57BL/6 mice. Our results suggest that SIRT1 modulates autophagy in CDDP ototoxicity, and provide new insights into the interplay between autophagy and CDDP-induced cell death. On the basis of the present results, we can suggest potential therapeutic strategies for overcoming the CDDP-induced ototoxicity through SIRT1 and autophagy activation.

AUTHOR CONTRIBUTIONS

JP conceived and designed the study, interpreted and analyzed the data, and wrote the manuscript. HX conceived and designed the study, interpreted and analyzed the data, and approved the final manuscript. TZ designed and performed the experiment, interpreted and analyzed the data, and wrote the manuscript. YZ and HY conceived and designed the study, interpreted and analyzed the data, and wrote the manuscript. GC, YY, and HC performed the experiment. HJ, ZS, HL, LL, YX, SC, QH, ML, XZ, XX, YO, and YC conceived and designed the study, interpreted and analyzed the data.

FUNDING

This work was supported by the Project funded by China Postdoctoral Science Foundation (2018M640863), the National Natural Science Foundation of China (81771018, 81570935, 81570916 and 81873699), the Guangdong Natural Science Foundation (2015A030313084 and 2017A030313585) and Yixian Research Launch Project (YXQH201807). The Guangzhou Science and Technology Foundation (2014Y2-00511).

ACKNOWLEDGMENTS

We thank LetPub (www.letpub.com) for its linguistic assistance during the preparation of this manuscript.

SUPPLEMENTARY MATERIAL

The Supplementary Material for this article can be found online at: https://www.frontiersin.org/articles/10.3389/fncel.2018.00515/full#supplementary-material

REFERENCES

Behra, M., Bradsher, J., Sougrat, R., Gallardo, V., Allende, M. L., and Burgess, S. M. (2009). Phoenix is required for mechanosensory hair cell regeneration in the zebrafish lateral line. *PLoS Genet.* 5:e1000455. doi: 10.1371/journal.pgen.1000455

Benkafadar, N., Menardo, J., Bourien, J., Nouvian, R., François, F., Decaudin, D., et al. (2017). Reversible p53 inhibition prevents cisplatin ototoxicity without blocking chemotherapeutic efficacy. *EMBO Mol. Med.* 9, 7–26. doi: 10.15252/emmm.201606230

Borse, V., Al, A. R., Sheehan, K., Sheth, S., Kaur, T., Mukherjea, D., et al. (2017). Epigallocatechin-3-gallate, a prototypic chemopreventative agent for protection against cisplatin-based ototoxicity. *Cell Death Dis.* 8:e2921. doi: 10.1038/cddis.2017.314

Breglio, A. M., Rusheen, A. E., Shide, E. D., Fernandez, K. A., Spielbauer, K. K., McLachlin, K. M., et al. (2017). Cisplatin is retained in the cochlea indefinitely following chemotherapy. *Nat. Commun.* 8:1654. doi: 10.1038/s41467-017-01837-1

Brignull, H. R., Raible, D. W., and Stone, J. S. (2009). Feathers and fins: non-mammalian models for hair cell regeneration. *Brain Res.* 1277, 12–23. doi: 10.1016/j.brainres.2009.02.028

Burnett, C., Valentini, S., Cabreiro, F., Goss, M., Somogyvari, M., Piper, M. D., et al. (2011). Absence of effects of Sir2 overexpression on lifespan in C. elegans and *Drosophila*. *Nature* 477, 482–485. doi: 10.1038/nature10296

Cardinaal, R. M., De Groot, J. C., Huizing, E. H., Smoorenburg, G. F., and Veldman, J. E. (2004). Ultrastructural changes in the albino guinea pig cochlea at different survival times following cessation of 8-day cisplatin administration. *Acta Otolaryngol.* 124, 144–154. doi: 10.1080/00016480310015164

Cepeda, V., Fuertes, M. A., Castilla, J., Alonso, C., Quevedo, C., and Perez, J. M. (2007). Biochemical mechanisms of cisplatin cytotoxicity. *Anticancer Agents Med. Chem.* 7, 3–18. doi: 10.2174/187152007779314044

Dehne, N., Lautermann, J., Petrat, F., Rauen, U., and de Groot, H. (2001). Cisplatin ototoxicity: involvement of iron and enhanced formation of superoxide anion radicals. *Toxicol. Appl. Pharmacol.* 174, 27–34. doi: 10.1006/taap.2001.9171

Deng, Z., Purtell, K., Lachance, V., Wold, M. S., Chen, S., and Yue, Z. (2017). Autophagy receptors and neurodegenerative diseases. *Trends Cell Biol.* 27, 491–504. doi: 10.1016/j.tcb.2017.01.001

Fang, B., and Xiao, H. (2014). Rapamycin alleviates cisplatin-induced ototoxicity *in vivo*. *Biochem. Biophys. Res. Commun.* 448, 443–447. doi: 10.1016/j.bbrc.2014.04.123

Finkel, T., Deng, C. X., and Mostoslavsky, R. (2009). Recent progress in the biology and physiology of sirtuins. *Nature* 460, 587–591. doi: 10.1038/nature08197

Filomeni, G., De Zio, D., and Cecconi, F. (2015). Oxidative stress and autophagy: the clash between damage and metabolic needs. *Cell Death Differ.* 22, 377–388. doi: 10.1038/cdd.2014.150

Florea, A. M., and Büsselberg, D. (2011). Cisplatin as an anti-tumor drug: cellular mechanisms of activity, drug resistance and induced side effects. *Cancers* 3, 1351–1371. doi: 10.3390/cancers3011351

Gabaizadeh, R., Staecker, H., Liu, W., Kopke, R., Malgrange, B., Lefebvre, P. P., et al. (1997). Protection of both auditory hair cells and auditory neurons from cisplatin induced damage. *Acta Otolaryngol.* 117, 232–238. doi: 10.3109/00016489709117778

Hariharan, N., Maejima, Y., Nakae, J., Paik, J., Depinho, R. A., and Sadoshima, J. (2010). Deacetylation of FoxO by Sirt1 plays an essential role in mediating starvation-induced autophagy in cardiac myocytes. *Circ. Res.* 107, 1470–1482. doi: 10.1161/CIRCRESAHA.110.227371

He, Z., Guo, L., Shu, Y., Fang, Q., Zhou, H., Liu, Y., et al. (2017). Autophagy protects auditory hair cells against neomycin-induced damage. *Autophagy* 13, 1884–1904. doi: 10.1080/15548627.2017.1359449

Herskovits, A. Z., and Guarente, L. (2014). SIRT1 in neurodevelopment and brain senescence. *Neuron* 81, 471–483. doi: 10.1016/j.neuron.2014.01.028

Hill, G. W., Morest, D. K., and Parham, K. (2008). Cisplatin-induced ototoxicity: effect of intratympanic dexamethasone injections. *Otol. Neurotol.* 29, 1005–1011. doi: 10.1097/MAO.0b013e31818599d5

Hyppolito, M. A., de Oliveira, J. A., and Rossato, M. (2006). Cisplatin ototoxicity and otoprotection with sodium salicylate. *Eur. Arch. Otorhinolaryngol.* 263, 798–803. doi: 10.1007/s00405-006-0070-6

Janda, E., Isidoro, C., Carresi, C., and Mollace, V. (2012). Defective autophagy in Parkinson's disease: role of oxidative stress. *Mol. Neurobiol.* 46, 639–661. doi: 10.1007/s12035-012-8318-1

Jiang, L., Romero-Carvajal, A., Haug, J. S., Seidel, C. W., and Piotrowski, T. (2014). Gene-expression analysis of hair cell regeneration in the zebrafish lateral line. *Proc. Natl. Acad. Sci. U S A* 111, E1383–E1392. doi: 10.1073/pnas.1402898111

Kalinec, G., Thein, P., Park, C., and Kalinec, F. (2016). HEI-OC1 cells as a model for investigating drug cytotoxicity. *Hear. Res.* 335, 105–117. doi: 10.1016/j.heares.2016.02.019

Kim, K. H., Lee, B., Kim, Y. R., Kim, M. A., Ryu, N., Jung, D. J., et al. (2018). Evaluating protective and therapeutic effects of α-lipoic acid on cisplatin-induced ototoxicity. *Cell Death Dis.* 9:827. doi: 10.1038/s41419-018-0888-z

Kim, H. J., Oh, G. S., Shen, A., Lee, S. B., Choe, S. K., Kwon, K. B., et al. (2014). Augmentation of NAD^+ by NQO1 attenuates cisplatin-mediated hearing impairment. *Cell Death Dis.* 5:e1292. doi: 10.1038/cddis.2014.255

Kim, I., Rodriguez-Enriquez, S., and Lemasters, J. J. (2007). Selective degradation of mitochondria by mitophagy. *Arch. Biochem. Biophys.* 462, 245–253. doi: 10.1016/j.abb.2007.03.034

Klionsky, D., Abdelmohsen, K., Abe, A., Abedin, M., Abeliovich, H., Acevedo Arozena, A., et al. (2016). Guidelines for the use and interpretation of assays for monitoring autophagy (3rd edition). *Autophagy* 12, 1–222. doi: 10.1080/15548627.2015.1100356

Kopke, R. D., Liu, W., Gabaizadeh, R., Jacono, A., Feghali, J., Spray, D., et al. (1997). Use of organotypic cultures of Corti's organ to study the protective effects of antioxidant molecules on cisplatin-induced damage of auditory hair cells. *Am. J. Otol.* 18, 559–571.

Korver, K. D., Rybak, L. P., Whitworth, C., and Campbell, K. M. (2002). Round window application of D-methionine provides complete cisplatin otoprotection. *Otolaryngol. Head Neck Surg.* 126, 683–689. doi: 10.1067/mhn.2002.125299

Kume, S., Uzu, T., Horiike, K., Chin-Kanasaki, M., Isshiki, K., Araki, S., et al. (2010). Calorie restriction enhances cell adaptation to hypoxia through Sirt1-dependent mitochondrial autophagy in mouse aged kidney. *J. Clin. Invest.* 120, 1043–1055. doi: 10.1172/JCI41376

Langer, T., Am, Z. A., Radtke, S., Meitert, J., and Zolk, O. (2013). Understanding platinum-induced ototoxicity. *Trends Pharmacol. Sci.* 34, 458–469. doi: 10.1016/j.tips.2013.05.006

Lawenda, B. D., Kelly, K. M., Ladas, E. J., Sagar, S. M., Vickers, A., and Blumberg, J. B. (2008). Should supplemental antioxidant administration be avoided during chemotherapy and radiation therapy? *J. Natl. Cancer Inst.* 100, 773–783. doi: 10.1093/jnci/djn148

Lee, I. H., Cao, L., Mostoslavsky, R., Lombard, D. B., Liu, J., Bruns, N. E., et al. (2008). A role for the NAD-dependent deacetylase Sirt1 in the regulation of autophagy. *Proc. Natl. Acad. Sci. U S A* 105, 3374–3379. doi: 10.1073/pnas.0712145105

Li, H., Song, Y., He, Z., Chen, X., Wu, X., Li, X., et al. (2018). Meclofenamic acid reduces reactive oxygen species accumulation and apoptosis, inhibits excessive autophagy and protects hair cell-like HEI-OC1 cells from cisplatin-induced damage. *Front. Cell. Neurosci.* 12:139. doi: 10.3389/fncel.2018.00139

Li, Y., Womer, R. B., and Silber, J. H. (2004). Predicting cisplatin ototoxicity in children: the influence of age and the cumulative dose. *Eur. J. Cancer* 40, 2445–2451. doi: 10.1016/j.ejca.2003.08.009

Liang, J., Wang, D., Renaud, G., Wolfsberg, T. G., Wilson, A. F., and Burgess, S. M. (2012). The stat3/socs3a pathway is a key regulator of hair cell regeneration in zebrafish. [corrected]. *J. Neurosci.* 32, 10662–10673. doi: 10.1523/JNEUROSCI.5785-10.2012

Liu, X., Zhang, C., Zhang, C., Li, J., Guo, W., Yan, D., et al. (2016). Heat shock protein 70 inhibits cardiomyocyte necroptosis through repressing autophagy in myocardial ischemia/reperfusion injury. *In Vitro Cell. Dev. Biol. Anim.* 52, 690–698. doi: 10.1007/s11626-016-0039-8

Martin, A. R., Pollack, R. A., Capoferri, A., Ambinder, R. F., Durand, C. M., and Siliciano, R. F. (2017). Rapamycin-mediated mTOR inhibition uncouples HIV-1 latency reversal from cytokine-associated toxicity. *J. Clin. Invest.* 127, 651–656. doi: 10.1172/JCI89552

Mizushima, N., Levine, B., Cuervo, A. M., and Klionsky, D. J. (2008). Autophagy fights disease through cellular self-digestion. *Nature* 451, 1069–1075. doi: 10.1038/nature06639

Nicolson, T. (2005). The genetics of hearing and balance in zebrafish. *Annu. Rev. Genet.* 39, 9–22. doi: 10.1146/annurev.genet.39.073003.105049

Ohsumi, Y. (2014). Historical landmarks of autophagy research. *Cell Res.* 24, 9–23. doi: 10.1038/cr.2013.169

Pang, J., Xiong, H., Lin, P., Lai, L., Yang, H., Liu, Y., et al. (2017). Activation of miR-34a impairs autophagic flux and promotes cochlear cell death via repressing ATG9A: implications for age-related hearing loss. *Cell Death Dis.* 8:e3079. doi: 10.1038/cddis.2017.462

Pang, J., Xiong, H., Yang, H., Ou, Y., Xu, Y., Huang, Q., et al. (2016). Circulating miR-34a levels correlate with age-related hearing loss in mice and humans. *Exp. Gerontol.* 76, 58–67. doi: 10.1016/j.exger.2016.01.009

Rubel, E. W., Furrer, S. A., and Stone, J. S. (2013). A brief history of hair cell regeneration research and speculations on the future. *Hear. Res.* 297, 42–51. doi: 10.1016/j.heares.2012.12.014

Rubinsztein, D. C., Bento, C. F., and Deretic, V. (2015). Therapeutic targeting of autophagy in neurodegenerative and infectious diseases. *J. Exp. Med.* 212, 979–990. doi: 10.1084/jem.20150956

Rybak, L. P., Whitworth, C. A., Mukherjea, D., and Ramkumar, V. (2007). Mechanisms of cisplatin-induced ototoxicity and prevention. *Hear. Res.* 226, 157–167. doi: 10.1016/j.heares.2006.09.015

Ryter, S. W., Mizumura, K., and Choi, A. M. (2014). The impact of autophagy on cell death modalities. *Int. J. Cell Biol.* 2014:502676. doi: 10.1155/2014/502676

Seglen, P. O., and Gordon, P. B. (1982). 3-Methyladenine: specific inhibitor of autophagic/lysosomal protein degradation in isolated rat hepatocytes. *Proc. Natl. Acad. Sci. U S A* 79, 1889–1892. doi: 10.1073/pnas.79.6.1889

Shen, H. M., and Codogno, P. (2011). Autophagic cell death: loch ness monster or endangered species? *Autophagy* 7, 457–465. doi: 10.4161/auto.7.5.14226

Song, L., Zhou, F., Cheng, L., Hu, M., He, Y., Zhang, B., et al. (2017). MicroRNA-34a suppresses autophagy in alveolar type II epithelial cells in acute lung injury by inhibiting FoxO3 expression. *Inflammation* 40, 927–936. doi: 10.1007/s10753-017-0537-1

Sun, J., He, X., Zhu, Y., Ding, Z., Dong, H., Feng, Y., et al. (2018). SIRT1 activation disrupts maintenance of myelodysplastic syndrome stem and progenitor cells by restoring TET2 function. *Cell Stem Cell* 23, 355.e9–369.e9. doi: 10.1016/j.stem.2018.07.018

Tanemura, M., Ohmura, Y., Deguchi, T., Machida, T., Tsukamoto, R., Wada, H., et al. (2012). Rapamycin causes upregulation of autophagy and impairs islets function both *in vitro* and *in vivo*. *Am. J. Transplant.* 12, 102–114. doi: 10.1111/j.1600-6143.2011.03771.x

Tsukasaki, N., Whitworth, C. A., and Rybak, L. P. (2000). Acute changes in cochlear potentials due to cisplatin. *Hear. Res.* 149, 189–198. doi: 10.1016/s0378-5955(00)00182-9

Van Erp, A. C., Hoeksma, D., Rebolledo, R. A., Ottens, P. J., Jochmans, I., Monbaliu, D., et al. (2017). The crosstalk between ROS and autophagy in the field of transplantation medicine. *Oxid. Med. Cell. Longev.* 2017:7120962. doi: 10.1155/2017/7120962

van Ruijven, M. W., de Groot, J. C., Klis, S. F., and Smoorenburg, G. F. (2005). The cochlear targets of cisplatin: an electrophysiological and morphological time-sequence study. *Hear. Res.* 205, 241–248. doi: 10.1016/j.heares.2005.03.023

Wang, D., and Lippard, S. J. (2005). Cellular processing of platinum anticancer drugs. *Nat. Rev. Drug Discov.* 4, 307–320. doi: 10.1038/nrd1691

Wang, J., Lloyd, F. R., Fetoni, A., Guitton, M. J., Pujol, R., and Puel, J. L. (2003). Local application of sodium thiosulfate prevents cisplatin-induced hearing loss in the guinea pig. *Neuropharmacology* 45, 380–393. doi: 10.1016/s0028-3908(03)00194-1

Wang, Y., Mandal, A. K., Son, Y. O., Pratheeshkumar, P., Wise, J., Wang, L., et al. (2018). Roles of ROS, Nrf2, and autophagy in cadmium-carcinogenesis and its prevention by sulforaphane. *Toxicol. Appl. Pharmacol.* 353, 23–30. doi: 10.1016/j.taap.2018.06.003

Xiong, H., Dai, M., Ou, Y., Pang, J., Yang, H., Huang, Q., et al. (2014). SIRT1 expression in the cochlea and auditory cortex of a mouse model of age-related hearing loss. *Exp. Gerontol.* 51, 8–14. doi: 10.1016/j.exger.2013.12.006

Xiong, H., Pang, J., Yang, H., Dai, M., Liu, Y., Ou, Y., et al. (2015). Activation of miR-34a/SIRT1/p53 signaling contributes to cochlear hair cell apoptosis: implications for age-related hearing loss. *Neurobiol. Aging* 36, 1692–1701. doi: 10.1016/j.neurobiolaging.2014.12.034

Yang, Q., Sun, G., Yin, H., Li, H., Cao, Z., Wang, J., et al. (2018). PINK1 protects auditory hair cells and spiral ganglion neurons from cisplatin-induced ototoxicity via inducing autophagy and inhibiting JNK signaling pathway. *Free Radic. Biol. Med.* 120, 342–355. doi: 10.1016/j.freeradbiomed.2018.02.025

Yao, H., Chung, S., Hwang, J. W., Rajendrasozhan, S., Sundar, I. K., Dean, D. A., et al. (2012). SIRT1 protects against emphysema via FOXO3-mediated reduction of premature senescence in mice. *J. Clin. Invest.* 122, 2032–2045. doi: 10.1172/JCI60132

Yin, H., Yang, Q., Cao, Z., Li, H., Yu, Z., Zhang, G., et al. (2018). Activation of NLRX1-mediated autophagy accelerates the ototoxic potential of cisplatin in auditory cells. *Toxicol. Appl. Pharmacol.* 343, 16–28. doi: 10.1016/j.taap.2018.02.007

Youn, C. K., Kim, J., Park, J. H., Do, N. Y., and Cho, S. I. (2015). Role of autophagy in cisplatin-induced ototoxicity. *Int. J. Pediatr. Otorhinolaryngol.* 79, 1814–1819. doi: 10.1016/j.ijporl.2015.08.012

Yu, L., Alva, A., Su, H., Dutt, P., Freundt, E., Welsh, S., et al. (2004). Regulation of an ATG7-beclin 1 program of autophagic cell death by caspase-8. *Science* 304, 1500–1502. doi: 10.1126/science.1096645

Conflict of Interest Statement: The authors declare that the research was conducted in the absence of any commercial or financial relationships that could be construed as a potential conflict of interest.

Copyright © 2019 Pang, Xiong, Zhan, Cheng, Jia, Ye, Su, Chen, Lin, Lai, Ou, Xu, Chen, Huang, Liang, Cai, Zhang, Xu, Zheng and Yang. This is an open-access article distributed under the terms of the Creative Commons Attribution License (CC BY). The use, distribution or reproduction in other forums is permitted, provided the original author(s) and the copyright owner(s) are credited and that the original publication in this journal is cited, in accordance with accepted academic practice. No use, distribution or reproduction is permitted which does not comply with these terms.

frontiers in Cellular Neuroscience

ORIGINAL RESEARCH
published: 08 February 2019
doi: 10.3389/fncel.2019.00022

Amyloid β Oligomers Increase ER-Mitochondria Ca^{2+} Cross Talk in Young Hippocampal Neurons and Exacerbate Aging-Induced Intracellular Ca^{2+} Remodeling

Maria Calvo-Rodriguez[1]†, Elena Hernando-Perez[1], Lucia Nuñez[1,2] and Carlos Villalobos[1]*

[1]*Instituto de Biología y Genética Molecular (IBGM), Consejo Superior de Investigaciones Científicas (CSIC) and Universidad de Valladolid, Valladolid, Spain,* [2]*Departamento de Bioquímica y Biología Molecular y Fisiología, Universidad de Valladolid, Valladolid, Spain*

OPEN ACCESS

Edited by:
Francesco Moccia, University of Pavia, Italy

Reviewed by:
Cesar Cardenas, Universidad Mayor, Chile
Cláudia Pereira, Universidade de Coimbra, Portugal

****Correspondence:***
Maria Calvo-Rodriguez
mcalvorodriguez@mgh.harvard.edu

†Present address:
Maria Calvo-Rodriguez, Alzheimer Research Unit, Department of Neurology, Massachusetts General Hospital and Harvard Medical School, Charlestown, MA, United States

Received: *20 August 2018*
Accepted: *17 January 2019*
Published: *08 February 2019*

Citation:
Calvo-Rodriguez M, Hernando-Perez E, Nuñez L and Villalobos C (2019) Amyloid β Oligomers Increase ER-Mitochondria Ca^{2+} Cross Talk in Young Hippocampal Neurons and Exacerbate Aging-Induced Intracellular Ca^{2+} Remodeling. Front. Cell. Neurosci. 13:22. doi: 10.3389/fncel.2019.00022

Alzheimer's disease (AD) is the most common neurodegenerative disorder and strongly associated to aging. AD has been related to excess of neurotoxic oligomers of amyloid β peptide (Aβo), loss of intracellular Ca^{2+} homeostasis and mitochondrial damage. However, the intimate mechanisms underlying the pathology remain obscure. We have reported recently that long-term cultures of rat hippocampal neurons resembling aging neurons are prone to damage induced by Aβ oligomers (Aβo) while short-term cultured cells resembling young neurons are not. In addition, we have also shown that aging neurons display critical changes in intracellular Ca^{2+} homeostasis including increased Ca^{2+} store content and Ca^{2+} transfer from the endoplasmic reticulum (ER) to mitochondria. Aging also promotes the partial loss of store-operated Ca^{2+} entry (SOCE), a Ca^{2+} entry pathway involved in memory storage. Here, we have addressed whether Aβo treatment influences differentially intracellular Ca^{2+} homeostasis in young and aged neurons. We found that Aβo exacerbate the remodeling of intracellular Ca^{2+} induced by aging. Specifically, Aβo exacerbate the loss of SOCE observed in aged neurons. Aβo also exacerbate the increased resting cytosolic Ca^{2+} concentration, Ca^{2+} store content and Ca^{2+} release as well as increased expression of the mitochondrial Ca^{2+} uniporter (MCU) observed in aging neurons. In contrast, Aβo elicit none of these effects in young neurons. Surprisingly, we found that Aβo increased the Ca^{2+} transfer from ER to mitochondria in young neurons without having detrimental effects. Consistently, Aβo increased also colocalization of ER and mitochondria in both young and aged neurons. However, in aged neurons, Aβo suppressed Ca^{2+} transfer from ER to mitochondria, decreased mitochondrial potential, enhanced reactive oxygen species (ROS) generation and promoted apoptosis. These results suggest that modulation of ER—mitochondria coupling in hippocampal neurons may be a novel physiological role of Aβo. However, excess of Aβo in the face of the remodeling of intracellular Ca^{2+} homeostasis associated to aging may lead to loss of ER—mitochondrial coupling and AD.

Keywords: calcium, Alzheimer's disease, aging, endoplasmic reticulum, mitochondria, store-operated calcium entry, hippocampal neurons

INTRODUCTION

Alzheimer's disease (AD) is the most common form of dementia, accounting for 60%–80% of all dementia cases. Despite of all the efforts, the mechanisms underlying the pathology are still unknown. The two main hallmarks of AD are extracellular plaques composed of amyloid β (Aβ) peptide and intracellular neurofibrillary tangles composed of hyperphosphorylated and misfolded tau. Most AD cases are sporadic (late-onset AD) and affect elderly people, but some cases (around 5%) are inherited in an autosomal dominant fashion, caused by mutations in the genes that encode presenilin1 (PS1), PS2 and amyloid precursor protein (APP; early-onset AD or familial AD). One of the most accepted hypothesis of AD is the "amyloid cascade hypothesis," which postulates that the deposition of the Aβ is a central event to the pathology of AD (Hardy and Selkoe, 2002). This hypothesis considers that the pathology of AD is caused by an abnormal processing of the protein Aβ, occasioned by a reduction in its clearance or by an increase in its production. Most AD cases are sporadic, being aging the most important risk factor for the disease. During aging and, particularly, in neurodegenerative diseases, the systems that regulate intracellular Ca^{2+} homeostasis are affected, leading to synaptic dysfunction, plasticity detriment and neuronal degeneration. Consequently, a wide amount of studies has shown that the disturbance of Ca^{2+} homeostasis is associated with the neurotoxicity that occurs in AD (Mattson, 2007; Bezprozvanny, 2009; Berridge, 2010). The "Ca^{2+} hypothesis of AD" (Khachaturian, 1989) postulates that the activation of the amyloidogenic pathway induces a remodeling of the neuronal Ca^{2+} signaling, disturbing the normal Ca^{2+} homeostasis and therefore, the mechanisms responsible for learning and memory. In addition, oxidative stress, alterations in mitochondrial energetic metabolism and protein aggregation, such as Aβ in AD, affect negatively the intracellular Ca^{2+} homeostasis. Recent studies have also shown that impaired function of intracellular organelles such as the endoplasmic reticulum (ER) and mitochondria plays an important role in the regulation of Ca^{2+} during aging and AD (Toescu and Verkhratsky, 2003). In this manner, PSs, located in the membrane of the ER, have been associated to familial AD. They are integral membrane proteins that form the catalytic core of the γ-secretase complex that cleaves APP. Mutations in PSs increase the production of $A\beta_{1-42}$ form or reduce the production of $A\beta_{1-40}$ (Borchelt et al., 1996; Lemere et al., 1996). In addition, PSs are believed to form low conductivity channels, being involved in the formation of the *leak* channels of the ER, releasing Ca^{2+} in a passive manner from the ER to the cytoplasm (Tu et al., 2006). Mutations in PSs result in an increased release of Ca^{2+} from the ER (Nelson et al., 2007), probably due to a loss of function of the leak channel. The other key player of intracellular Ca^{2+} homeostasis, mitochondria, are dynamic organelles that generate ATP and contribute to many cellular functions. They play a main role in apoptotic signaling, lipid synthesis and buffering of intracellular Ca^{2+}. Many reports have also proposed mitochondrial dysfunction in AD. In this manner, dysfunction of mitochondrial bioenergetics (Atamna and Frey, 2007; Yao et al., 2009), increased fission and decreased fusion (Wang et al., 2009; Santos et al., 2010), morphological changes (Hirai et al., 2001; DuBoff et al., 2013; Xie et al., 2013) and redistribution of mitochondria (Kopeikina et al., 2011) have been extensively reported.

ER and mitochondria are connected through the mitochondria-associated ER membranes (MAMs). They play a central role in the processes that occur between ER and mitochondria, such as communication between the two organelles, which includes Ca^{2+} transport. When the Ca^{2+} from the ER is released to the cytoplasm, part of this Ca^{2+} is taken up by mitochondria, acting as a buffer of Ca^{2+} (Szabadkai et al., 2003). If normal flux is affected, the amount of Ca^{2+} taken up by mitochondria could be increased. If there is mitochondrial Ca^{2+} overload, the mitochondrial permeability transition pore (PTPm) will open, mitochondrial membrane potential will collapse and proapoptotic factors such as cytochrome c will be released, activating the caspase pathway and triggering apoptosis. In addition, an excessive Ca^{2+} increase will enhance the production of reactive oxygen species (ROS), that will also contribute to the opening of the PTPm (Berridge, 2010).

Alteration of the correct MAM function has been previously shown in AD (Müller et al., 2018). In this manner, increased connectivity ER-mitochondria was found in human fibroblasts from patients with familiar AD mutations as well as in fibroblasts from patients with sporadic AD (Area-Gomez et al., 2012; Area-Gomez and Schon, 2017). Our group has also previously reported that Aβ oligomers (Aβo), unlike the fibrils, promote the entry of Ca^{2+} into the cell, causing mitochondrial Ca^{2+} overload and cell death by apoptosis (Sanz-Blasco et al., 2008; Calvo-Rodríguez et al., 2016a). Also, exposure of primary hippocampal neurons to conditioned media containing Aβo increased the contact points ER-mitochondria. In addition, these media also increased ER-mitochondria Ca^{2+} transfer in neuroblastoma cells (Hedskog et al., 2013). However, the effects of oligomers in the context of aging has not been addressed. Moreover, this study has never been performed in primary neurons.

We have previously described an intraorganellar Ca^{2+} remodeling with aging, involving ER-mitochondria cross-talk and loss of store-operated Ca^{2+} entry (SOCE) in rat hippocampal neurons (Calvo-Rodríguez et al., 2016b). Most studies on mechanisms underlying the pathology of AD use transgenic animal models that develop the pathology at early ages (i.e., around 6 months of age), cells from AD patients that are therefore already diagnosed, or cell lines exposed to Aβ peptides. In consequence, the alterations in the intraorganellar Ca^{2+} remodeling in AD in the context of aging have not been described, and the full spectrum of mechanisms through which Ca^{2+} homeostasis is altered in AD in aging is still missing. Based on this, we decided to study whether the soluble oligomers of the most toxic peptide involved in AD, $A\beta_{1-42}$ (Aβo), are able to alter: (1) resting levels of cytosolic free Ca^{2+} concentration ($[Ca^{2+}]_{cyt}$); (2) SOCE; (3) the content and release of Ca^{2+} from the internal stores, as well as; (4) the

Ca^{2+} transfer from ER-to mitochondria; (5) the interaction ER-mitochondria; and (6) the expression of the mitochondrial Ca^{2+} uniporter (MCU) and inositol trisphosphate receptors (IP_3Rs) in young and aged hippocampal neurons. In order to model aging, we have employed an *in vitro* culture of hippocampal rat neurons maintained for several days *in vitro* (DIV).

Primary rat hippocampal neurons in long-term culture have been previously used as a model of aging by our group and others (Porter et al., 1997; Brewer et al., 2007; Calvo-Rodríguez et al., 2016b, 2017). Importantly, some of the changes that occur in aging are mimicked by this *in vitro* model of aging, such as accumulation of ROS, lipofuscin granules, heterochromatic foci, activation of the Jun N-terminal protein kinase (pJNK) and p53/p21 pathways and changes in NMDA receptor expression (Sodero et al., 2011; Calvo et al., 2015a). By using fluorescence Ca^{2+} imaging of fura-2 loaded cells, we have evaluated the change in the Ca^{2+} content in the ER, SOCE, the Ca^{2+} depletion from ER induced by different physiological agonists and the coupling ER-mitochondria, in young (4–8 DIV, short-term) and aged (15–21 DIV, long term) hippocampal neurons cultured *in vitro* and exposed to Aβo as a model of AD and *in vitro* aging.

MATERIALS AND METHODS

Animals and Reagents

Wistar rat pups (newborn P0–1) were obtained from the Valladolid University animal facility. All animals were handled according to the ethical standard of Valladolid University under protocols approved by the animal housing facility and in accordance with the European Convention 123/Council of Europe and Directive 86/609/EEC. Fura-2/AM and Rhod-5N are from Invitrogen (Barcelona, Spain). Fetal bovine serum (FBS) is from Lonza (Barcelona, Spain). Horse serum, neurobasal medium, HBSS medium, B27, L-glutamine and gentamycin are from Gibco (Barcelona, Spain). Papain solution is from Worthington (Lakewood, NJ, USA). The poly-D-lysine and annexin V are from BD (Madrid, Spain). DNase I and antibody against the MCU are from Sigma (Madrid, Spain). IP_3R1 and IP_3R2 primary antibodies are from Santa Cruz Biotechnology (Dallas, TX, USA). IP_3R3 primary antibody is from BD Transduction Laboratories (Madrid, Spain). ER tracker, mitotracker, tetramethylrhodamine, methyl ester (TMRM) and CM-H2DCFDA are from ThermoFisher Scientific. $A\beta_{1-42}$ peptide is from Bachem AG (Bubenforf, Switzerland). Other reagents and chemicals were obtained either from Sigma or Merck.

Primary Hippocampal Neuron Culture

Hippocampal neurons were prepared from Wistar rat pups under sterile conditions as reported by Brewer et al. (1993) with further modifications by Pérez-Otaño et al. (2006). Briefly, newborn rat pups were decapitated and, after brain removal, meninges were discarded and hippocampi were separated from cortex. Hippocampal tissue was cut in small pieces, transferred to papain solution (20 u./ml) and incubated at 37°C for 30 min. After 15 min, DNase I (50 μl/ml) was added. Tissue pieces were washed with Neurobasal medium and cell suspension was obtained using a fire-polished pipette in Neurobasal medium supplemented with 10% FBS. Cells were centrifuged at 160 *g* for 5 min and pellet was suspended in Neurobasal medium. Hippocampal cells were plated onto poly-D-lysine-coated, 12 mm diameter glass coverslips at 30×10^3 cells/dish (plating density, 169 cells/mm^2), and grown in Neurobasal media supplemented with L-glutamine (2 mM), gentamicin (1 μg/ml), 2% B27 and 10% FBS, maintained in a humidified 37°C incubator with 5% CO_2 without further media exchange. Cells were cultured for 4–8 DIV for young cultures, and 15–21 DIV for aged cultures. Other details have been reported in detail elsewhere (Calvo et al., 2015a; Calvo-Rodríguez et al., 2015).

$A\beta_{1-42}$ Oligomers Preparation

$A\beta_{1-42}$ oligomers (Aβo) were prepared as previously reported by a new procedure (Caballero et al., 2016). Briefly, $A\beta_{1-42}$ peptide was initially solved at 1 mM concentration in iced cold hexafluoroisopropanol (HFIP), and separated into aliquots in sterile microcentrifuge tubes. The solution was then incubated for 2 h at room temperature (RT) to allow monomerization of the peptide. HFIP was removed under vacuum in a speed vacuum (800 *g* × 10 min at RT), and the peptide film was stored desiccated at −20°C. For aggregation, the peptide was first suspended in dry DMSO at 5 mM concentration. For complete suspension of the peptide, it was subjected to ultrasounds for 10 min, aliquoted in propylene non-siliconized tubes, and stored at −20°C until use. MEM (Gibco) medium supplemented with 0.5 mg/ml Fe^{2+}, 0.5 mg/ml Cu^{2+} and 0.5 mg/ml Zn^{2+} was added to bring the peptide to a concentration of 80 μM. Finally, it was incubated at 37°C for 24 h. For experiments, $A\beta_{1-42}$ was solved in the culturing media to 1 μM final concentration. Composition of these oligomers has been characterized previously (Caballero et al., 2016; Calvo-Rodríguez et al., 2016b).

Effects of Aβo on Apoptosis in Young and Aged Neurons

For apoptosis, hippocampal neurons were exposed to either vehicle or Aβo 1 μM for 24 h. Cells were then washed with phosphate buffered saline (PBS) and apoptosis was evaluated using annexin V (1:20, 10 min) in annexin binding buffer 1× (in mM) NaCl, 140; CaCl2, 2.5; Hepes, 10 (pH 7.4) and assessed by fluorescence microscopy using a Nikon Eclipse TS100 microscope (objective 40×).

Fluorescence Imaging of Cytosolic Free Ca^{2+} Concentration

Hippocampal cells were cultured for 4–8 DIV (short-term) or 15–21 DIV (long-term) and exposed to either vehicle (supplemented MEM) or 1 μM Aβo for 24 h before the experiment. The day of the experiment, hippocampal cells were washed in standard external medium (SEM) containing (in mM) NaCl 145, KCl 5, $CaCl_2$ 1, $MgCl_2$ 1, glucose 10 and Hepes/NaOH 10 (pH 7.4). Then cells were incubated in the

same medium containing fura-2 (4 μM) for 60 min at RT in the dark. Then coverslips were placed on the perfusion chamber of a Zeiss Axiovert 100 TV, perfused continuously with the same pre-warmed medium at 37°C and epi-illuminated alternately at 340 and 380 nm using a filter wheel. Light emitted at 520 nm was recorded every 1–5 s with a Hamamatsu ER camera (Hamamatsu Photonics France). Pixel by pixel ratios of consecutive frames were captured and cytosolic Ca^{2+} concentration ($[Ca^{2+}]_{cyt}$) values from regions of interest (ROIs) corresponding to individual neurons were averaged and expressed as the ratio of fluorescence emission following excitation at 340 and 380 nm as reported in detail previously (Sanz-Blasco et al., 2008; Calvo et al., 2015b). For estimation of Ca^{2+} increase, responses (calculated as area under curve, A.U.C.) were averaged from responsive neurons (selected by their morphology different from glial cells in the brightfield). Fraction was calculated by dividing responsive cells for the total cell number in the field, considering responsive cells the ones showing a change in the slope of the Ca^{2+} recording after application of the stimulus.

For measurements of SOCE, fura-2-loaded cells were treated with the sarcoplasmic and ER Ca^{2+} ATPase (SERCA) pump blocker thapsigargin (1 μM) for 15 min in the same SEM devoid of extracellular Ca^{2+} before imaging as reported elsewhere (Calvo-Rodríguez et al., 2016b). Then cells were subjected to fluorescence imaging and stimulated with 5 mM Ca^{2+} to monitor the SOCE-dependent rise in $[Ca^{2+}]_{cyt}$. Recordings were made in the presence of TTX to prevent activation of voltage-gated Ca^{2+} channels by connected neurons.

For estimation of Ca^{2+} store content, the rise in $[Ca^{2+}]_{cyt}$ induced by low concentrations of the Ca^{2+} ionophore ionomycin (400 nM) added in the absence of extracellular Ca^{2+} was monitored as reported previously (Villalobos and García-Sancho, 1995).

Fluorescence Imaging of Mitochondrial Free Ca^{2+} Concentration

Hippocampal cells cultured for 4–8 DIV (short-term) or 15–21 DIV (long-term) were exposed to either vehicle or 1 μM Aβo for 24 h before the experiment. The day of the experiment, hippocampal cells were washed in SEM and incubated in the same medium containing Rhod-5N AM (1 μM) for 30 min at RT in the dark and washed in SEM for additional 30 min. Then coverslips were placed on the perfusion chamber of a Zeiss Axiovert 100 TV, perfused continuously with the same pre-warmed medium at 37°C and epi-illuminated in the red channel (551 nm). Light emitted at 576 nm was recorded every 5 s with a Hamamatsu ER camera (Hamamatsu Photonics France). Pixel by pixel ratios of consecutive frames were captured and mitochondrial Ca^{2+} concentration ($[Ca^{2+}]_{mit}$) values from ROIs corresponding to individual neurons were averaged and expressed as normalized fluorescence emission (F/F_0). For estimation of Ca^{2+} increase, responses (calculated as amplitude of the peak) were averaged from responsive neurons (selected by their morphology different from glial cells in the brightfield). Fraction was calculated by dividing responsive cells for the total cell number in the field, considering responsive cells the ones showing a change in the slope of the Ca^{2+} recording after application of the stimulus.

Immunofluorescence of the Mitochondrial Calcium Uniporter (MCU) and IP_3 Receptors

Hippocampal cells at different culture periods and exposed to either vehicle or 1 μM Aβo for 24 h were washed with phosphate buffered saline (PBS), fixed with p-formaldehyde 4% and incubated with antibodies against MCU (1:200) and IP_3 receptors IP_3R1 (1:50), IP_3R2 (1:50) and IP_3R3 (1:50) at 4°C overnight. Immunopositive cells were revealed using Alexafluor 488-tagged antibodies (1:300). Optical density was measured in selected ROIs corresponding to individual neurons using ImageJ software. Further details have been reported elsewhere (Calvo-Rodríguez et al., 2016b).

ER-Mitochondria Colocalization

Cells in every condition were stained for 10 min with 200 nM MitoTracker green and ERTracker red and imaged directly using a confocal microscope. High resolution images of cells were recorded by using a Leica TCS SP5 confocal microscope (Leica Microsystems, Mannheim, Germany). The Mitotracker and ER-tracker were excited with 488 and 543 laser lines, respectively, and emission was acquired with a charged CCD camera. The images were analyzed in LAS AF Lite software (Leica Microsystems, Mannheim, Germany). Background was subtracted from all images. Colocalization analysis for the two markers was performed on Z-stacks acquired with steps of 0.8 μm. For colocalization analysis, green and red channel images were acquired independently. Analysis were carried out on single-plane images using ImageJ plug-ins. Manders2 and Pearson's coefficients were calculated applying the ImageJ Colocalization analysis plug-in.

Mitochondrial Membrane Potential

For mitochondrial membrane potential measurements, hippocampal neurons were exposed to either vehicle or Aβo 1 μM for 24 h. Then, cells were washed in SEM and loaded with the mitochondrial potential probe (TMRM, 10 nM) for 30 min at RT in the dark. Then coverslips containing cells were placed on a Zeiss Axiovert 100 TV inverted microscope and subjected to fluorescence imaging. Fluorescence images were captured with the rhodamine filter set with a Hamamatsu ER-Orca fluorescence camera as reported previously (Calvo-Rodríguez et al., 2016b).

Generation of Reactive Oxygen Species (ROS)

For ROS generation measurements, hippocampal neurons were exposed to either vehicle or Aβo 1 μM for 24 h. Then, cells were washed in SEM and loaded with the ROS probe 5-(and-6)-chloromethyl-2′,7′-dichlorodihydrofluorescein diacetate (CM-H2DCFDA 2 μM) for 40 min at RT in the dark. Then coverslips containing cells were placed on a Zeiss Axiovert 100 TV inverted

microscope and subjected to fluorescence imaging. Fluorescence images were captured with the FITC filter set with a Hamamatsu ER-Orca fluorescence camera.

Statistics

Changes in fluorescence ratio are expressed as area under the curve (AUC) and maximum increase in ratio (Δratio). Calculation of AUC and Δratios were performed using Origin Lab 7.0. Data are presented as mean ± SEM. When only two means were compared, Student's *t*-test was used. For more than two groups, statistical significance of the data was assessed by one-way or multifactorial analysis of variance (ANOVA), depending on the number of factors considered. Differences were considered significant at $p < 0.05$, where 0.05 is the signification level.

RESULTS

Aβ Oligomers Induce Apoptosis Only in Aged Neurons

We tested the effects of $A\beta_{1-42}$ oligomers (Aβo) on the rate of apoptosis in rat hippocampal neurons cultured for 4–8 DIV representing young neurons, or in neurons cultured for 15–21 DIV that represent many characteristics of aged neurons as reported previously (Calvo-Rodríguez et al., 2016a). Short-term (4–8 DIV) and long-term (15–21 DIV) cultured hippocampal neurons were exposed for 24 h to 1 μM Aβo or to vehicle (supplemented MEM, see "Materials and Methods" section). This latter condition was taken as control group.

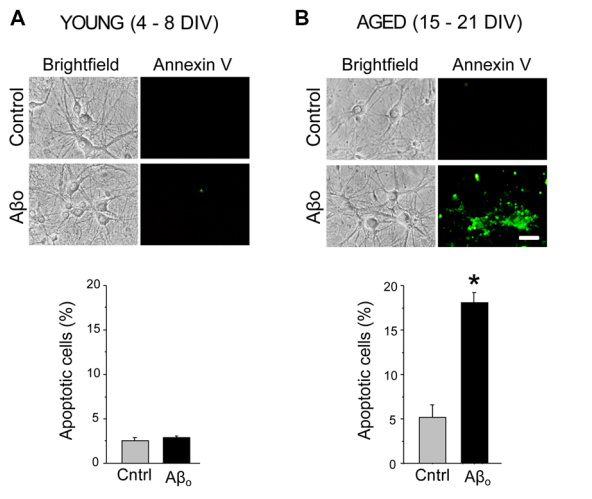


FIGURE 1 | Amyloid β peptide oligomers (Aβo) induce apoptosis only in aged neurons. Short-term (young) and long-term (aged) hippocampal cultures were exposed for 24 h Aβo (1 μM) or vehicle. Then, the relative abundance (percent, %) of apoptotic neurons was assessed by incubation with annexin V. Pictures show representative bright field cultures of short-term **(A)** and long-term cultures **(B)** of rat hippocampal neurons. Bars represent mean ± standard external medium (SEM) percentage of apoptotic cells per condition. $n = 339$ and 330 cells from three independent experiments for young neurons **(A)** and 452 and 417 cells from four independent experiments, respectively for aged neurons **(B)**. $^*p < 0.05$ compared to control group.

Figure 1 shows that, in resting conditions, only less than 3% of the young neurons display apoptosis. Aβo do not increase the rate of apoptosis in these cultured cells. About 5% of aged neurons display apoptosis in basal conditions. In contrast, Aβo increase the percent of apoptotic cells by nearly four-fold. These results confirm our previous results reported elsewhere (Caballero et al., 2016; Calvo-Rodríguez et al., 2016a) and indicate that Aβo toxicity depends on the time in culture of rat hippocampal neurons.

In our hands, cultured rat hippocampal cells display a mix of neurons and glial cells and their relative abundance changes with aging in culture mostly because glial cells proliferate while neuron cells do not. The fraction of neurons amounts 60% at 5 DIV, decreases to 23% at 14 DIV and decreases further to only 15% at 20 DIV. Therefore, for monitoring of effects of Aβo in neurons, it is convenient to carry out measurements at the single cell level in identified neurons. Fortunately, hippocampal neurons can be easily identified and distinguished from astrocytes or glial cells according to morphometric characteristics for the expert eye. Next, we addressed whether treatment of rat hippocampal neurons with Aβo promote differential changes in intracellular Ca^{2+} homeostasis in young and aged neurons.

Aβ Oligomers Increase Resting $[Ca^{2+}]_{cyt}$ and Synchronous Ca^{2+} Oscillations in Aged Neurons

We have tested the effects of chronic treatment of Aβo on resting $[Ca^{2+}]_{cyt}$, a parameter previously reported to vary as hippocampal neurons age in culture (Calvo et al., 2015a). Short-term (4–8 DIV) and long-term (15–21 DIV) cultured hippocampal neurons were exposed for 24 h to 1 μM Aβo or to vehicle (supplemented MEM). The effects of treatments were assessed by calcium imaging of fura-2 loaded neurons. Neurons were clearly distinguished from surrounding glial cells by their morphometric characteristics as previously reported (Calvo-Rodríguez et al., 2016b). **Figure 2** shows that short-term cultured, rat hippocampal neurons display spontaneous, synchronous $[Ca^{2+}]_{cyt}$ oscillations. Notice that the average recording runs in parallel to the recordings of individual cells, indicating that oscillations are synchronous. These synchronous oscillations reflect synchronous synaptic activity and the formation of neural networks *in vitro* (Nunez et al., 1996; Calvo-Rodríguez et al., 2016b). Long-term cultured rat hippocampal neurons exposed to Aβo (1 μM, 24 h) display increased $[Ca^{2+}]_{cyt}$ levels (resting level) when compared to the control neurons (**Figure 2C**). Moreover, treatment of long-term cultured hippocampal neurons with 1 μM Aβo for 24 h increases significantly the synchronous and spontaneous $[Ca^{2+}]_{cyt}$ oscillations compared to the control group measured as oscillations index (OI), a parameter representing both the frequency and amplitude of $[Ca^{2+}]$ oscillations (**Figure 2D**; Nunez et al., 1996). In contrast, exposure of short-term cultured neurons to 1 μM Aβo had a little or no effect on both parameters, resting $[Ca^{2+}]_{cyt}$ and OI. These results suggest that prolonged exposure of hippocampal neurons *in vitro* to Aβo increases the excitability of the neuronal circuit, at the

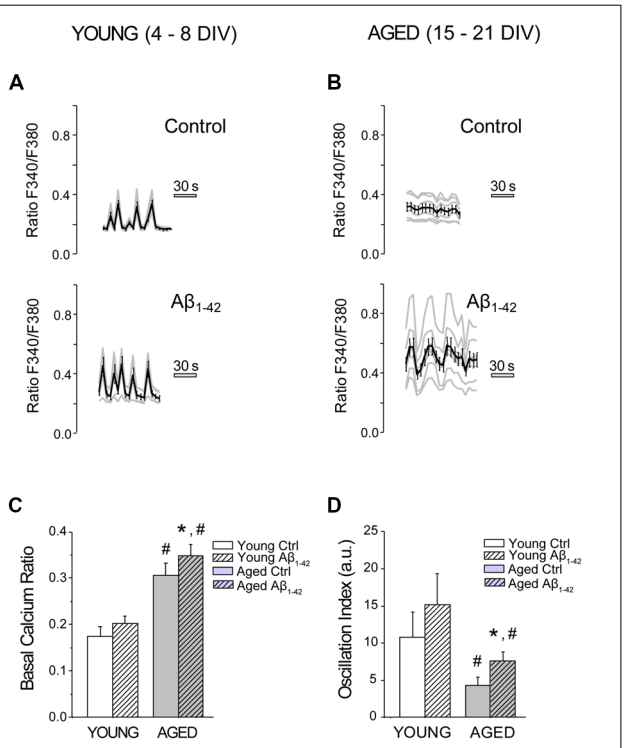


FIGURE 2 | The exposure of aged hippocampal neurons to Aβo increases basal Ca^{2+} and synchronous and spontaneous Ca^{2+} oscillations. Hippocampal neurons cultured for different days *in vitro* (DIV), were exposed to vehicle or Aβo (1 μM, 24 h), and $[Ca^{2+}]_{cyt}$ was monitored by fluorescence imaging using fura-2. **(A,B)** Traces show individual cells (gray lines) and mean ± SEM (black line) of the increase in $[Ca^{2+}]_{cyt}$ prior to any stimulus in young **(A)** and aged **(B)** cultured hippocampal neurons exposed to either Aβo (1 μM) or vehicle. **(C,D)** Bars represent mean ± SEM of basal Ca^{2+} (ratio F340/F380; **C**) and the oscillation index **(D)** for young and aged neurons, treated in absence (ctrl) of presence of the Aβo ($Aβ_{1–42}$, hatched bars). n = 113, 97, 131 and 169 neurons from four to six independent experiments, respectively. $^*p < 0.05$ compared to control group. $^\#p < 0.05$ compared to the young ones.

level of basal Ca^{2+} and spontaneous oscillations. This effect is statistically significant only in aged neurons and Aβo has no effect in this regard in young neurons.

Aβ Oligomers Dampen Further the Decreased Store Operated Ca^{2+} Entry (SOCE) in Aged Neurons

We have previously shown that SOCE, the Ca^{2+} entry pathway activated after depletion of intracellular Ca^{2+} stores, decreases with *in vitro* aging (Calvo-Rodríguez et al., 2016b). This process has been associated to a downregulation of stromal interaction molecule 1 (Stim1) and Orai1, molecular players involved in SOCE in most cell types. Here, we assessed the effect of Aβo on SOCE in our model of *in vitro* aging. Short-term and long-term cultured hippocampal neurons were exposed to either vehicle (Control) or Aβo (1 μM, 24 h), and SOCE was monitored by fluorescence imaging of $[Ca^{2+}]_{cyt}$. For this end, cultured neurons were loaded with fura-2 and treated with Tg (1 μM) for 15 min in medium devoid of extracellular

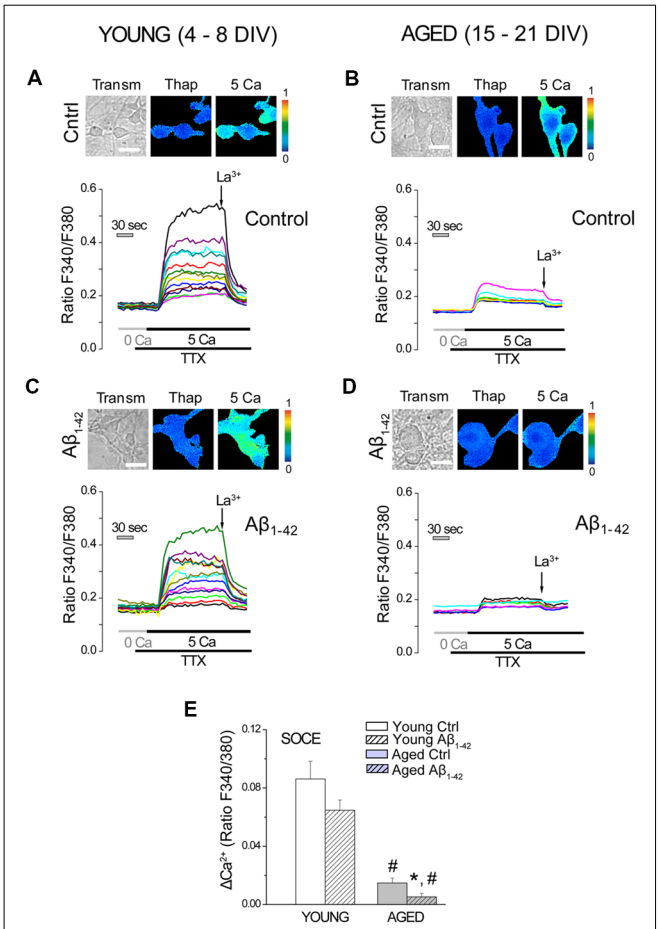


FIGURE 3 | Store operated Ca^{2+} entry (SOCE) decreases in long-term cultured hippocampal neurons exposed to Aβo. Short- and long-term cultured hippocampal neurons were either exposed to vehicle (ctrl) or Aβo (1 μM, 24 h), and SOCE was monitored by fluorescence imaging of Ca^{2+}. Neurons were incubated with fura-2 and treated with Tg (1 μM) for 15 min in medium devoid of Ca^{2+} (0 Ca). Subsequently, Ca^{2+} 5 mM in presence of TTX (500 nM) was added to elicit an increase in the $[Ca^{2+}]_{cyt}$. La^{3+} (100 μM) was added to block SOCE. **(A–D)** Pictures show typical fluorescence images of transmission (transm) and $[Ca^{2+}]_{cyt}$ coded in pseudocolor of thapsigargin (Thap) and after addition of 5 Ca. Pseudocolor scale is shown at right. Bars represent 10 μm. Traces are representative recordings of fluorescence ratios of individual short-term (young, 4–8, **A**,**C**) and long-term (aged, 15–21, **B,D**) cultured neurons. **(E)** Bars correspond to the averaged SOCE (mean ± SEM). n = 65, 84, 35 and 45 individual cells studied in three and three independent experiments, respectively. $^*p < 0.05$ compared to control group. $^\#p < 0.05$ compared to the young ones.

Ca^{2+} (0 Ca) in order to fully deplete the intracellular Ca^{2+} stores. Subsequently, medium containing Ca^{2+} 5 mM and TTX (500 nM) was added for 5 min to activate SOCE. TTX was added to block the electrical connectivity of cultured neurons. La^{3+} (100 μM) was added later to block this pathway. Pictures in **Figure 3** show typical bright field images (transm) and fluorescence images coded in pseudocolor representing $[Ca^{2+}]_{cyt}$ before (basal) and after addition of 5 mM Ca^{2+} (5 Ca). Representative recordings of fluorescence ratios of individual short-term (young, 4–8 DIV, **Figures 3A,C**) and long-term (aged, 15–21 DIV, **Figures 3B,D**) cultured neurons are also

shown. **Figure 3E** shows bars corresponding to the averaged SOCE calculated as ΔRatioF340/F380 (mean ± SEM). Data confirm our previous results showing that SOCE is reduced significantly in *in vitro* aged neurons relative to young neurons. In addition, they show that AβO decrease SOCE further but this effect is only statistically significant in aged neurons.

Aβ Oligomers Increases Further the Enhanced Ca^{2+} Store Content in Aged Neurons

We have reported previously that *in vitro* aging increases Ca^{2+} store content in rat hippocampal neurons (Calvo-Rodríguez et al., 2016b). Ca^{2+} store content was assessed after chronic exposure to Aβo in young and aged neurons. For this end, Ca^{2+} store content was tested using the Ca^{2+} ionophore ionomycin added in medium devoid of external Ca^{2+}. This procedure has been reported previously to estimate Ca^{2+} store content in living cells (Villalobos and García-Sancho, 1995; Calvo-Rodríguez et al., 2016b). Ca^{2+} store content was monitored by fluorescence imaging in short-term and long-term cultured hippocampal neurons, exposed to Aβo (1 μM, 24 h), and compared to the controls (exposed to the vehicle for dilution of Aβo, MEM). These experiments were always carried out in medium devoid of extracellular Ca^{2+} (0 Ca), in order to avoid the entry of Ca^{2+} from the external medium. The stimulation of hippocampal neurons with 400 nM ionomycin in Ca^{2+} free medium (0 Ca; **Figure 4**) increased $[Ca^{2+}]_{cyt}$ in all neurons studied (measured as AUC). Exposure of the short-term cultured cells to Aβo did not modify the increase in $[Ca^{2+}]_{cyt}$ induced by ionomycin (**Figures 4A,C**). However, in the long-term cultured cells, chronic exposure to Aβo for 24 h increased significantly the content of the stores, as shown by the enhanced increase in the $[Ca^{2+}]_{cyt}$ induced by ionomycin in 0 Ca medium (**Figures 4B,D**). These results suggest that the chronic treatment of cultured hippocampal neurons with Aβo increases further Ca^{2+} store content exclusively in the long-term cultured neurons, an effect that could be related to the increase in the basal Ca^{2+} levels that were appreciated in the aged neurons exposed to the Aβo, but that does not occur in the young cultured ones.

Aβ Oligomers Increase Further the Enhanced Release of Ca^{2+} Induced by Acetylcholine in Aged Neurons

In order to understand the functional consequences of the increase in the levels of Ca^{2+} in the intracellular stores, we then analyzed the release of Ca^{2+} from the ER that is mobilized by different agonists. The release of Ca^{2+} mediated by the IP_3 receptor was first evaluated using the neurotransmitter acetylcholine (ACh). In order to cancel the contribution of the entry of Ca^{2+} and just focus on the release from the stores, all the experiments were carried out in the absence of free Ca^{2+} in the extracellular medium (0 Ca). Application of ACh to cultured hippocampal neurons in 0 Ca produced an increase in the $[Ca^{2+}]_{cyt}$, as described previously (Calvo-Rodríguez et al., 2016b). **Figure 5** shows representative recordings in short-term and long-term cultured hippocampal neurons exposed to either Aβo (1 μM, 24 h) or vehicle, and subjected to fluorescence Ca^{2+} imaging. It can be observed that the chronic treatment with Aβo does not affect the increase in the $[Ca^{2+}]_{cyt}$ induced by ACh in short-term cultured hippocampal neurons (**Figures 5A,C**). In contrast, chronic exposure of long-term cultured hippocampal neurons to Aβo promoted a larger $[Ca^{2+}]_{cyt}$ response to ACh

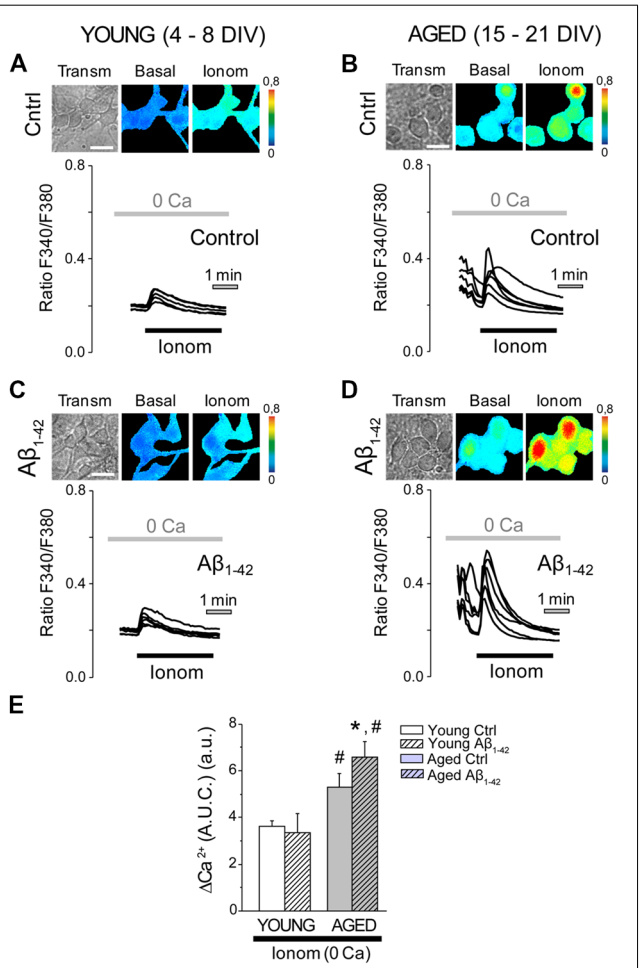


FIGURE 4 | The exposure of aged hippocampal neurons to Aβo increases Ca^{2+} store content. Hippocampal neurons exposed to either Aβo (1 μM) or vehicle and loaded with fura-2 were stimulated with ionomycin (400 nm) in external medium devoid of Ca^{2+} (0 Ca) and subjected to fluorescence imaging to estimate the content of Ca^{2+} deposits. **(A–D)** Pictures show transmission (transm) and pseudocolor images of fluorescence ratios in basal conditions (basal) and after ionomycin (Ionom) stimulation in short-term (**A,C**, Young 4–8 DIV) and long-term (**B,D**, Aged 15–21 DIV) cultured hippocampal neurons not exposed (**A,B**, control) or exposed (**C,D**, $Aβ_{1–42}$) to Aβo (1 μM, 24 h). Pseudocolor bars are shown at right. Bar represent 10 μm. Traces are representative recordings of the Ca^{2+} release induced by ionomycin (400 nM) in medium devoid of Ca^{2+} (0 Ca) in individual neurons subjected to fluorescence imaging. **(E)** Bars represent the average (mean ± SEM) in the increase of $[Ca^{2+}]_{cyt}$ in response to ionomycin (measured as area under the curve, AUC) in short-term (young) and long-term (aged) hippocampal neurons exposed to either Aβo (1 μM, 24 h) or vehicle. n = 55, 42, 81 and 114 individual cells from three to six independent cultures, respectively. $^{*}p < 0.05$ compared to control group. $^{\#}p < 0.05$ compared to the young ones.

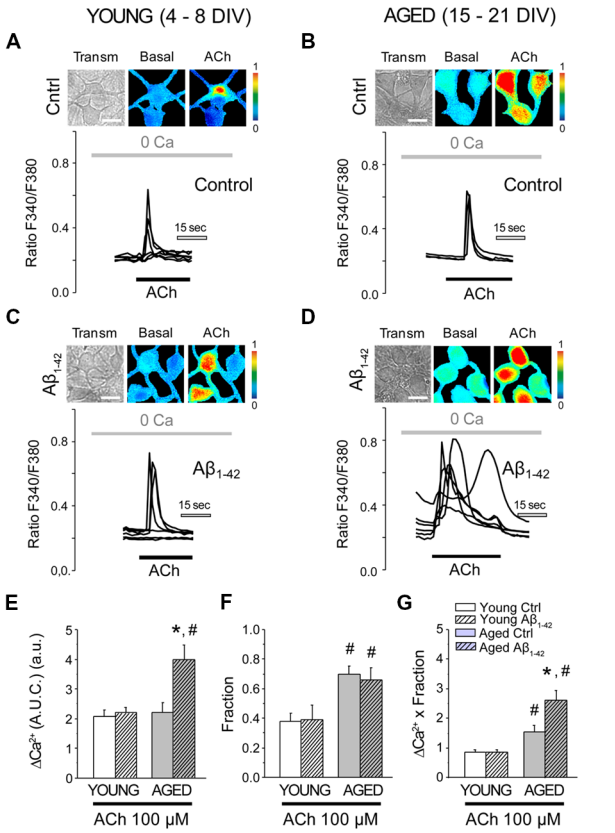


FIGURE 5 | The exposure of aged hippocampal neurons to Aβo increases Ca^{2+} responses to acetylcholine (ACh) in rat hippocampal neurons. Hippocampal neurons incubated with vehicle or Aβo (1 μM, 24 h) and loaded with fura-2 were subjected to fluorescence imaging for monitoring the Ca^{2+} released by ACh in short-term and long-term cultured neurons. Cells were stimulated with ACh in Ca^{2+} free medium. **(A–D)** Pictures show transmission images (transm) and pseudocolor images of fluorescence ratios taken before (Basal) and after ACh stimulation. Pseudocolor scale is shown at right. Bars correspond to 10 μm. Traces represent significant fluorescence recordings in single neurons of the Ca^{2+} release induced by ACh (100 μM) in young and aged cultures not exposed (**A,B**, control) or exposed (**C,D**, $A\beta_{1-42}$) to Aβo (1 μM, 24 h). **(E–G)** Bars represent the summary results for 102, 94, 39 and 59 cells from four independent cultures, respectively (mean ± SEM, AUC) of responsive cells **(E)**, the fraction of responsive cells **(F)**, and the product of both parameters **(G)**. $^{*}p < 0.05$ compared to control group. $^{\#}p < 0.05$ compared to the young ones.

when compared to control cells (**Figures 5B,D**). **Figures 5E–G** show the quantification of the response. Bars represent the mean value of the $[Ca^{2+}]_{cyt}$ increase, represented as AUC (AUC ± SEM) of the Ca^{2+} response (**Figure 5E**). The fraction of cells that presented an increase in the $[Ca^{2+}]_{cyt}$ is also showed (**Figure 5F**). It can be observed that the fraction of cells that responded to the stimulation with ACh is higher in long-term cultured hippocampal neurons. In order to compare the response between young and aged neurons, a measure of global release of Ca^{2+} involving both parameters (Ca^{2+} released and fraction of responding cells) was calculated. For this end we multiplied the AUC of the cells that showed an increase in the $[Ca^{2+}]_{cyt}$ by the fraction of cells that responded to the stimulus. **Figure 5G** shows the global difference in Ca^{2+} release from the stores among the four populations. Notice that whereas aging increases the fraction of neurons responsive to ACh, treatment with Aβo enhances instead the release of Ca^{2+} in each individual cell. Thus, aging increases the fraction of neurons responsive to ACh and Aβo enhances the rise in Ca^{2+} elicited by ACh in aged neurons. No effect was observed in young neurons.

Aβ Oligomers Increase Further the Enhanced Release of Ca^{2+} Induced by Caffeine in Aged Neurons

Next, we assessed the effects of Aβo on Ca^{2+} release induced by activation of ryanodine receptors (RyRs) in short-term and long-term cultured neurons. Caffeine (Caff; 20 mM) was employed as an agonist of the RyRs. Caffeine is an agonist of the RyRs, which are sensitive to Ca^{2+}-induced Ca^{2+} released (CICR) processes. In this case, nominally free Ca^{2+} (without adding EGTA) was used as external cellular medium to be able to activate CICR, while minimizing the effect of Ca^{2+} entry from the extracellular medium into the cytosol. To avoid high osmotic variation following the application of 20 mM Caff, 20 mM glucose was added to the extracellular medium prior to its addition, subsequently replaced by 20 mM Caff (Calvo-Rodríguez et al., 2016b). When hippocampal neurons were stimulated by caffeine in nominally free Ca^{2+}, a rapid and transient increase in the $[Ca^{2+}]_{cyt}$ could be observed (**Figure 6**). The bars shown in **Figure 6E** represent the mean ± SEM value of the increase in $[Ca^{2+}]_{cyt}$ (quantified as AUC). ER Ca^{2+} mobilized by caffeine was similar in the young neurons (exposed or not exposed to 1 μM Aβo for 24 h) and in the non-exposed cultured-aged neurons. However, in cultured-aged neurons previously exposed to Aβo (1 μM, 24 h), the increase in $[Ca^{2+}]_{cyt}$ was significantly higher than in the control group. **Figure 6G** shows the global increase (AUC Ca^{2+} increase × fraction) produced by stimulation with caffeine under these conditions. Therefore, Ca^{2+} release induced by both IP_3 receptor and RyR agonists is further enhanced by Aβo treatment in aged neurons but not in young neurons.

Aβ Oligomers Enhance ER-Mitochondria Cross Talking in Young Neurons but They Promote Opposite Effects in Aged Neurons

Next, we tested the effects of Aβo on ER-mitochondria cross-talk, i.e., Ca^{2+} transfer from ER to mitochondria. For this end, we measured the increase in mitochondrial $[Ca^{2+}]$ ($[Ca^{2+}]_{mit}$) induced by Ca^{2+} release elicited by ACh in medium devoid of Ca^{2+} (0 Ca), in the same manner as for **Figure 5**. Short-term and long-term cultured hippocampal neurons were incubated either with vehicle (Control) or Aβo (1 μM, 24 h). Then cells were washed and preincubated with the mitochondrial Ca^{2+} probe Rhod-5N, a fluorescent calcium probe that targets mitochondria (de la Fuente et al., 2012), and subjected to fluorescence imaging in single neurons. Neurons treated with either vehicle (control) or Aβo were perfused with the agonist ACh in medium devoid of Ca^{2+} (0 Ca) to induce the release of Ca^{2+} from the ER.

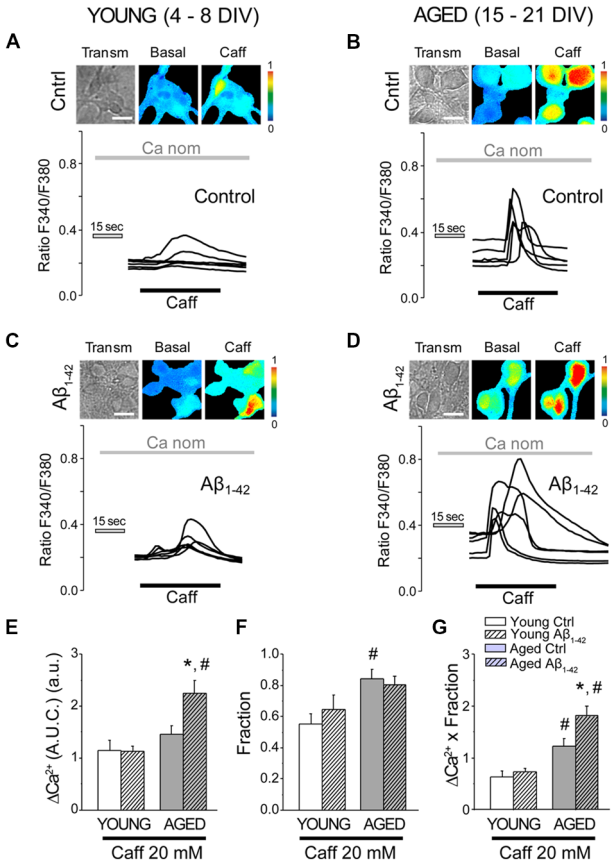


FIGURE 6 | The exposure of aged hippocampal neurons to Aβo increases Ca^{2+} responses to caffeine in rat hippocampal neurons. Short-term (young, 4–8 DIV) and long-term (aged, 15–21 DIV) cultured hippocampal neurons were either exposed to vehicle or Aβo (1 μM, 24 h) and loaded with fura-2 and subjected to fluorescence imaging. Pictures show representative images of transmission (transm) and pseudocolor coded of basal and the maximum response of Ca^{2+} to caffeine in young **(A,C)** and aged cells **(B,D)**. Pseudocolor scale is shown at right. Bars correspond to 10 μm. Traces represent single-cell recordings of young and aged cells non-exposed (ctrl) or exposed ($Aβ_{1–42}$) to Aβo (1 μM, 24 h) of the Ca^{2+} response induced by caffeine 20 mM in medium nominal Ca^{2+}. **(E–G)** Bars represent mean ± SEM of the response of $[Ca^{2+}]_{cyt}$ to caffeine (expressed as AUC) of 56, 78, 94 and 105 cells from three to five independent cultures, respectively **(E)**. Panel **(F)** shows the fraction of cells that responded. Panel **(G)** represents the overall result of the multiplication of both factors. $^{*}p < 0.05$ compared to control group. $^{\#}p < 0.05$ compared to the young ones.

Figure 7 shows bright field and Rhod-5N fluorescence images in basal conditions and after stimulation with ACh (100 μM) in short-term (4–8 DIV) and long-term (15–21 DIV) cultured hippocampal neurons. Representative recordings of $[Ca^{2+}]_{mit}$ obtained in single cells before and after stimulation with ACh are also shown. Bars represent the quantification of the rises in $[Ca^{2+}]_{mit}$ induced by ACh in 0 Ca (left), the fraction of responsive cells (middle) and the global response by taking into account both factors (right). As shown previously using mitochondria-targeted aequorin (Calvo-Rodríguez et al., 2016b), the rise in $[Ca^{2+}]_{mit}$ induced by ACh is larger in aged neurons than in young neurons. Therefore, these results confirm our previous results and validate monitoring of $[Ca^{2+}]_{mit}$ with Rhod-5N. The larger rise in $[Ca^{2+}]_{mit}$ in aged neurons is due to both the increase in mitochondrial Ca^{2+} uptake in every cell (left panel) and the fraction of responsive cells (middle panel) corresponding to a large global ER-mitochondria cross talk in aged neurons relative to young neurons (right panel; **Figure 7C**). Interestingly, Aβo increased the rise in $[Ca^{2+}]_{mit}$ induced by ACh in young neurons (left panel) and this effect was not due to changes in the fraction of responsive cells (middle panel). Therefore, Aβo increase ER-cross talk in young neurons (right panel, **Figure 7C**). It is noteworthy that this effect cannot be due to increased ER Ca^{2+} content (**Figure 4E**) and is the only effect induced by Aβo that we have observed in young neurons.

It is also remarkable that the effects of Aβo on the rise in $[Ca^{2+}]_{mit}$ induced by ACh in young and aged neurons are opposite. Aβo increases Ca^{2+} transfer from ER to mitochondria in young neurons and decreases it in aged neurons. In fact, Aβo nearly abolishes the rise in $[Ca^{2+}]_{mit}$ induced by ACh in aged neurons and this effect is due to decreases in both the amount of Ca^{2+} transferred per neuron and the fraction of neurons responsive to ACh. Taken together, these results show that Aβo significantly increases ER-mitochondria cross-talk in young neurons, but they rather abolish it in aged neurons.

Aβ Oligomers Enhance Further the Increased Expression of the Mitochondrial Ca^{2+} Uniporter in Aged Neurons

Ca^{2+} enters the mitochondria through the MCU, located into the inner mitochondrial membrane (Baughman et al., 2011; De Stefani et al., 2011). To address the opposite effects of Aβo on mitochondrial Ca^{2+} uptake in young and aged neurons, we also tested the effects of Aβo on MCU expression. Short-term and long-term cultured neurons were incubated either with vehicle (ctrl) or Aβo (1 μM, 24 h). Then, immunostaining against MCU was evaluated by immunofluorescence. **Figure 8** shows representative images of the fluorescence detection of MCU in short-term (young) and long-term (aged) cultured hippocampal neurons and the quantitative analysis of fluorescence intensity (optical density, arbitrary units) of the MCU. As reported previously (Calvo-Rodríguez et al., 2016b), we found that optical density of MCU immunofluorescence is enhanced in aged neurons relative to young neurons, thus confirming our previous results. In addition, we found that Aβo significantly increased the expression of MCU in the long-term cultured hippocampal neurons but not in young neurons. These results indicate that the opposite effects of Aβo on ER-mitochondria cross talking in young and aged neurons are not due to changes in expression of MCU.

Aging Increases Expression of IP_3 Receptors in Rat Hippocampal Neurons

Ca^{2+} release from intracellular stores takes place after activation of IP_3 receptors at the ER. In addition, IP_3 receptors are an ER component of the MAMs (Hedskog et al., 2013). Therefore, these receptors are critical to the coupling between ER and

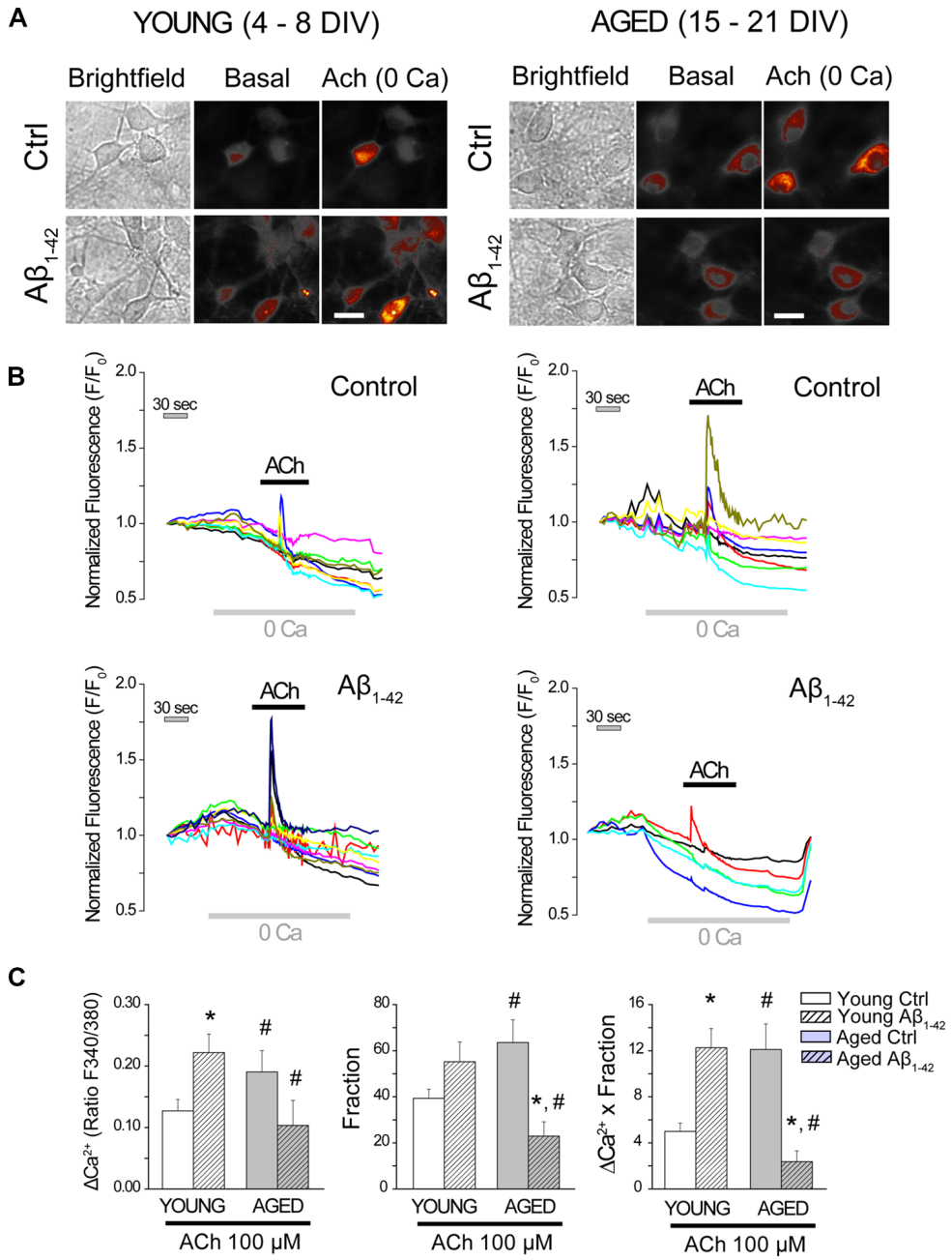


FIGURE 7 | The exposure of hippocampal neurons to Aβo affects the cross-talk endoplasmic reticulum (ER)–mitochondria. Hippocampal neurons cultured for 4–8 (young) and 15–21 (aged) DIV were incubated with Rhod-5N (1 μM) and subjected to fluorescence imaging to measure $[Ca^{2+}]_{mit}$ in single cell. Cells exposed to either vehicle (control) or Aβo (1 μM, 24 h) were stimulated with the agonist ACh in medium devoid of Ca^{2+} (0 Ca). **(A)** Pictures show typical fluorescence images of transmission (transm) and Rhod-5N fluorescence in basal conditions of after stimulation with ACh (100 μM) in medium 0 Ca of short and long-term cultured hippocampal neurons. The bars represent 10 μm. **(B)** Traces represent characteristic response of $[Ca^{2+}]_{mit}$ in single cells by stimulating with ACh (100 μM) in medium 0 Ca. **(C)** Bars represent mean ± SEM of the increase in $[Ca^{2+}]_{mit}$ induced by ACh in 0 Ca, the fraction of response and the global response by taking into account both factors. The global response to ACh is significantly higher in the young neurons exposed to Aβo (1 μM, 24 h) and significantly smaller in the exposed aged ones. n = 44, 66, 29 and 31 individual cells studied in three and three independent experiments, respectively. $^{*}p < 0.05$ compared to control group. $^{\#}p < 0.05$ compared to the young ones.

mitochondria. Moreover, IP_3 receptors have been involved in the enhanced cytosolic $[Ca^{2+}]$ induced by oligomers in AD (Ferreiro et al., 2004; Demuro and Parker, 2013). Accordingly, we tested whether expression of the three IP_3 receptor isoforms (IP_3R1, IP_3R2 and IP_3R3) changes during *in vitro* aging. **Figure 9A** shows representative immunofluorescence images

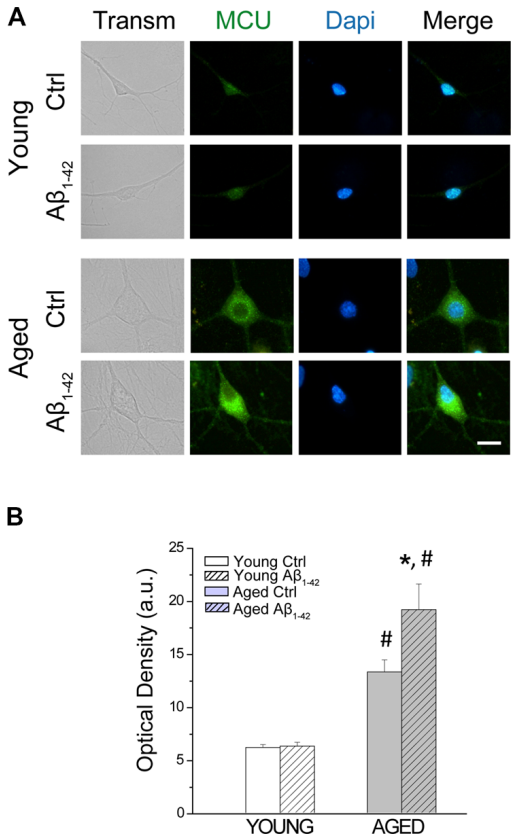


FIGURE 8 | The exposure of aged hippocampal neurons to Aβo increases the expression of the mitochondrial Ca^{2+} uniporter (MCU). Immunostaining against MCU was assessed in hippocampal neurons incubated either with vehicle (ctrl) or Aβo (1 μM, 24 h). **(A)** Representative images of the fluorescence detection of MCU in short-term (young) and long-term (aged) cultured hippocampal neurons. Bar represents 10 μm and applies to all images. **(B)** Quantitative analysis of fluorescence intensity (optical density, arbitrary units) of the MCU. Bars represent average ± SEM. n = 112, 81, 90 and 59 cells respectively from three independent cultures. $^{*}p < 0.05$ compared to control group. $^{\#}p < 0.05$ compared to the young ones.

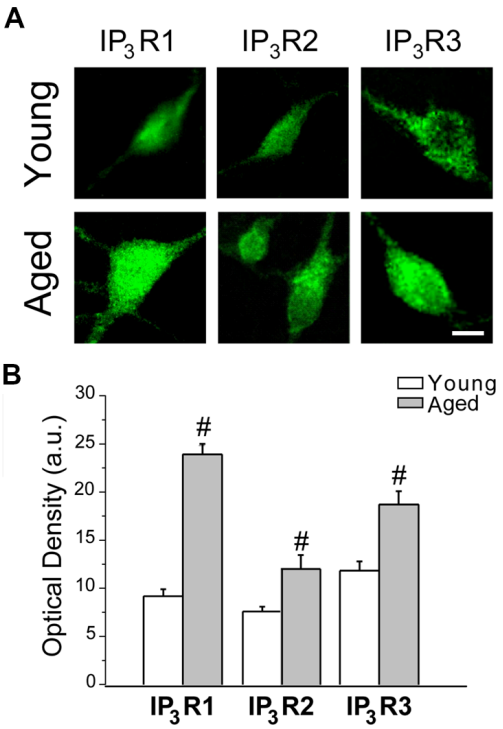


FIGURE 9 | IP_3 receptor expression increases in aged rat hippocampal neurons. Immunostaining against IP_3R1, IP_3R2 and IP_3R3 was assessed in short-term and long-term cultured hippocampal neurons representing young and aged neurons. **(A)** Representative images of the fluorescence detection of the three isoforms in short-term (young) and long-term (aged) cultured hippocampal neurons. Bar represents 10 μm and applies to all images. **(B)** Quantitative analysis of fluorescence intensity (optical density, arbitrary units) of the three IP_3R isoforms. Bars represent average ± SEM. n = 34, 15, 39, 4, 29 and 14 cells, respectively from three independent cultures. $^{\#}p < 0.05$ aged vs. young neurons.

of all three IP_3 receptor isoforms obtained in short-term (young) and long-term (aged) cultured hippocampal neurons. **Figure 9B** shows the quantitative analysis of fluorescence intensity (optical density, arbitrary units) corresponding to expression of all three IP_3R isoforms in young and aged neurons. Results show that optical density of all three IP_3R isoforms is significantly increased in aged neurons relative to young neurons. These results indicate that changes in expression of IP_3 receptors may contribute to enhanced response to Aβo in aged neurons and enhanced ER-mitochondria cross talking in aging.

Aging and Aβ Oligomers Increase ER-Mitochondrial Colocalization in Rat Hippocampal Neurons

We investigated ER-mitochondria colocalization using confocal fluorescence imaging of young and aged rat hippocampal neurons loaded with both MitoTracker green and ER-Tracker red. **Figure 10A** shows representative confocal images of signals in the green and the red channels of hippocampal neurons treated with vehicle or Aβo 1 μM for 24 h. For colocalization analysis of ER and mitochondria, we computed the Manders2 and Pearson coefficients. **Figure 10B** shows Manders2 and Pearson coefficients of colocalization of ER and mitochondria. Results show that colocalization coefficients increase significantly in long-term cultured neurons corresponding to aged neurons relative to short-term cultured neurons representing young neurons. In addition, coefficients are further enhanced in neurons treated with Aβo. These results indicate that both aging and Aβo enhance ER-mitochondria colocalization.

The above results may contribute to explain how Aβo increase Ca^{2+} transfer from ER to mitochondria in young neurons (**Figure 7**). However, they cannot explain why this transfer is rather impaired in aged neurons treated with Aβo. To address this issue, we investigated next the effects of aging and Aβo on mitochondrial membrane potential and ROS generation in rat hippocampal neurons.

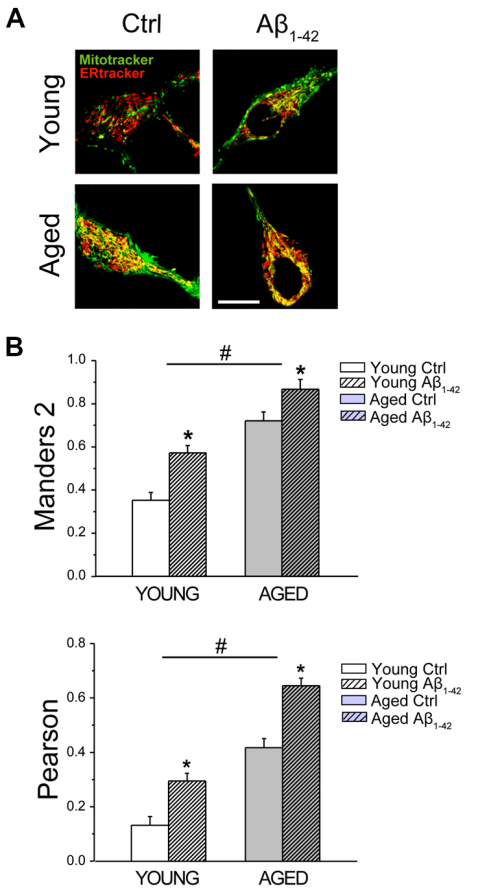


FIGURE 10 | Aging and Aβo increase ER–mitochondria colocalization in rat hippocampal neurons. Short-term (young) and long-term (aged) hippocampal cultures were exposed for 24 h to Aβo (1 μM) or vehicle. Then, cells were incubated with mito-tracker green and ER-tracker red and mitochondrial—ER colocalization was assessed by confocal fluorescence imaging. **(A)** Pictures show representative confocal fluorescence images of short-term (young) and long-term (aged) cultures of rat hippocampal neurons treated with vehicle (Ctrl) or $A\beta_{1-42}$ oligomers. Bar represents 10 μm and applies to all images. **(B)** Bars represent Manders2 and Pearson colocalization coefficients (mean ± SEM) obtained in ROIs corresponding to identified young and aged neurons treated with vehicle (Cntrl) or $A\beta_{1-42}$. Data corresponds to three experiments. $^{*}p < 0.05$ vs. control group. $^{\#}p < 0.05$ vs. young neurons.

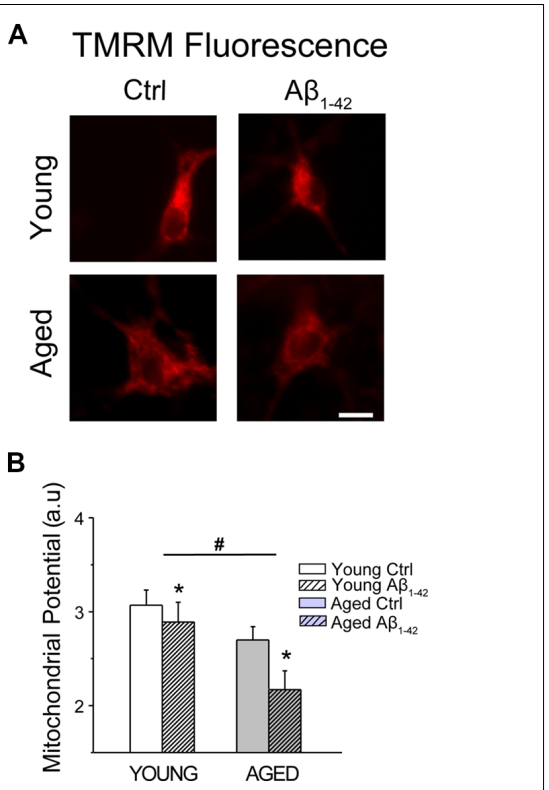


FIGURE 11 | Aging and Aβo decrease mitochondrial membrane potential in rat hippocampal neurons. Short-term (young) and long-term (aged) hippocampal cultures were exposed for 24 h to Aβo (1 μM) or vehicle. Then, cells were incubated with TMRM and mitochondrial membrane potential was assessed by fluorescence imaging. **(A)** Pictures show representative fluorescence images of short-term (young) and long-term (aged) cultures of rat hippocampal treated with vehicle (Ctrl) or $A\beta_{1-42}$ oligomers. Scale bar represents 10 μm and applies to all images. **(B)** Bars represent mean ± SEM values of TMRM fluorescence intensity in selected ROIs corresponding to identified young and aged neurons treated with vehicle (Cntrl) or Aβo. Data correspond to three independent experiments. $^{*}p < 0.05$ vs. control group. $^{\#}p < 0.05$ vs. young neurons.

Aging and Aβ Oligomers Decrease Mitochondrial Membrane Potential in Rat Hippocampal Neurons

We have shown previously that *in vitro* aging is associated to a loss of mitochondrial membrane potential in rat hippocampal neurons (Calvo-Rodríguez et al., 2016b). Here, we tested whether Aβo influence also mitochondrial membrane potential. For this end, short-term and long-term cultures of rat hippocampal neurons corresponding to young and aged neurons, respectively, were treated with vehicle or Aβo (1 μM, 24 h). Then, cells were loaded with the mitochondrial potential probe TMRM and subjected to fluorescence imaging. **Figure 11A** shows representative TMRM fluorescence images of young and aged neurons treated with vehicle or Aβo. Bars in **Figure 11B** show average (mean ± SEM) optical density values of ROIs corresponding to hippocampal neurons. Results confirm that mitochondrial membrane potential decreases in aged neurons relative to young ones. In addition, the results show that Aβo decrease it further in young and aged neurons. The effect of Aβo on mitochondrial membrane potential is relatively larger in aged neurons than in young ones. The loss of mitochondrial membrane potential favors PTPm, a process that is also enhanced by ROS generation. Accordingly, we investigated next the generation of ROS in young and aged neurons either treated or not with Aβo.

Aβ Oligomers Increase ROS Generation in Aged Rat Hippocampal Neurons

We tested whether aging and Aβo influence also ROS generation in rat hippocampal neurons. For this end, short-term and long-term cultures of rat hippocampal neurons representing young and aged neurons, respectively, were treated with vehicle

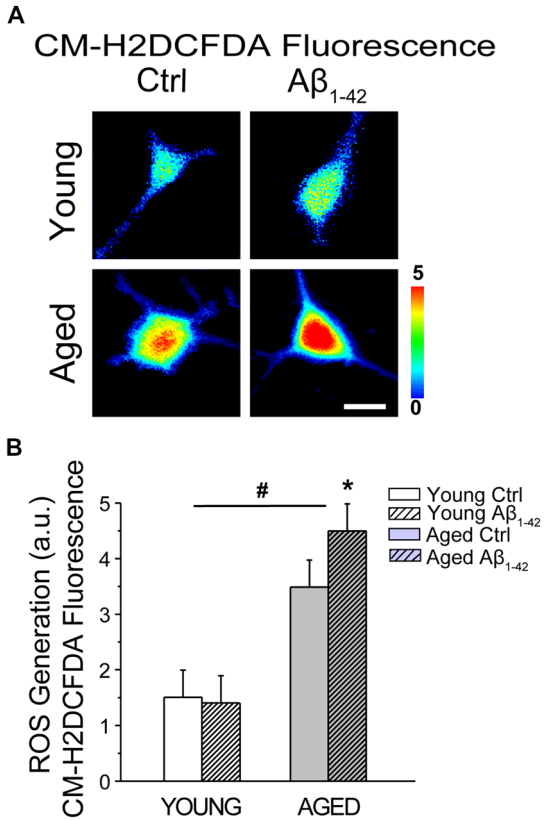


FIGURE 12 | Aging and Aβo enhance reactive oxygen species (ROS) generation in rat hippocampal neurons. Short-term (young) and long-term (aged) hippocampal cultures were exposed for 24 h to Aβo (1 μM) or vehicle. Then, cells were incubated with CM-H2DCFDA and ROS generation was assessed by fluorescence imaging. **(A)** Pictures show representative CM-H2DCFDA fluorescence images coded in pseudocolor of short-term (young) and long-term (aged) cultures of rat hippocampal treated with vehicle (Ctrl) or $A\beta_{1-42}$ oligomers. Scale bar represents 10 μm and applies to all images. **(B)** Bars represent mean ± SEM values of CM-H2DCFDA fluorescence intensity in selected regions of interest (ROIs) corresponding to identified young and aged neurons treated with vehicle (Control) or Aβo. Data corresponds to three experiments. $^{*}p < 0.05$ vs. control group. $^{\#}p < 0.05$ vs. young neurons.

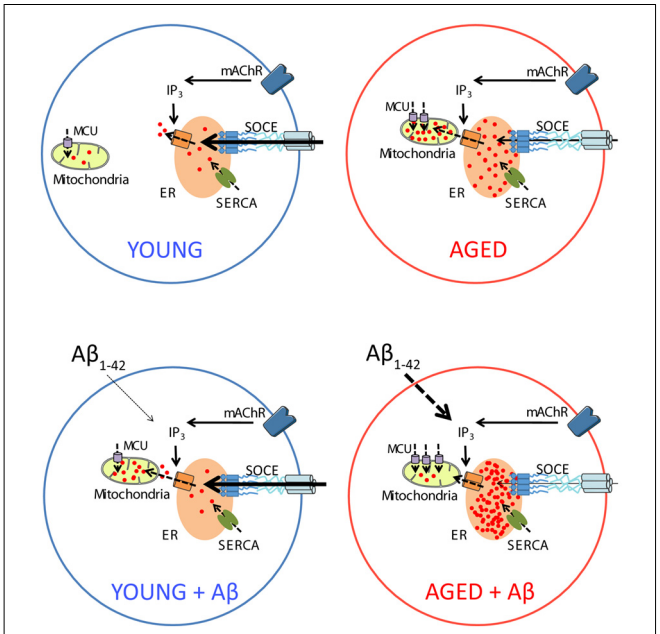


FIGURE 13 | Schematic representing the effects of Aβo on intracellular Ca^{2+} homeostasis in young and aged neurons *in vitro*. In young neurons (top left), activation of metabotropic ACh receptors induce IP_3 synthesis and release of Ca^{2+} from intracellular stores in the ER. Depletion of Ca^{2+} stores activate SOCE that rise intracellular Ca^{2+} to refill Ca^{2+} stores after activation of the sarcoplasmic and ER Ca^{2+} ATPase (SERCA). Ca^{2+} release is also taken by mitochondria through the MCU for activation of mitochondrial metabolism. Treatment with Aβo increases Ca^{2+} transfer from ER to mitochondria in young neurons without altering any other parameter or promoting apoptosis (bottom left). Aging increases Ca^{2+} store content at the ER, MCU expression and Ca^{2+} transfer from ER to mitochondria but decreases SOCE (top right). Treatment of aged neurons with Aβo exacerbates the increases in Ca^{2+} store content and MCU expression as well as SOCE loss. However, in contrast to young neurons, treatment with Aβo decreases Ca^{2+} transfer from ER to mitochondria in aged neurons and promotes apoptosis (bottom right).

or Aβo (1 μM, 24 h). Then cells were loaded with the ROS probe CM-H2DCFDA and subjected to fluorescence imaging. **Figure 12A** shows representative fluorescence images of young and aged neurons treated with vehicle or Aβo. Bars in **Figure 12B** show average (mean ± SEM) optical density values for ROIs corresponding to hippocampal neurons. The results show that aging increases significantly CM-H2DCFDA fluorescence consistently with enhanced ROS generation in aged neurons relative to young ones. In addition, we found that Aβo increase ROS generation further in aged neurons, having no effect in the young ones. These results are consistent with detrimental effects of Aβo in aged neurons but not in young ones.

Accordingly, the present results show that Aβo enhance ER-mitochondrial coupling in short-term cultured hippocampal neurons corresponding to young neurons but this is not associated to a detrimental effect. In contrast, in long-term cultured hippocampal neurons, corresponding to aged neurons, Aβo also increases ER-mitochondrial colocalization, but this effect is associated to loss of ER-mitochondrial coupling and detrimental effect (**Figure 13**).

DISCUSSION

Signaling by Ca^{2+} plays a fundamental role in learning and memory processes, and participates in survival and neuronal death. Intracellular Ca^{2+} dyshomeostasis has been extensively related to many neurodegenerative diseases, including AD (LaFerla, 2002; Bezprozvanny and Mattson, 2008). Ca^{2+} pathology in AD involves altered Ca^{2+} influx processes as well as Ca^{2+} release from the internal stores and impaired Ca^{2+} buffering capacity. Furthermore, sustained up-regulation of Ca^{2+} levels could both initiate and accelerate the features of AD, including plaque deposition and synaptic loss (Stutzmann, 2007), although if Ca^{2+} dysregulation is a cause or a consequence of AD is still under debate.

Here, we show that chronic exposure to Aβo exacerbates largely the remodeling of subcellular Ca^{2+} associated to *in vitro*

aging in cultured hippocampal neurons. First, we show that Aβo increase further basal $[Ca^{2+}]_{cyt}$ and spontaneous and synchronous $[Ca^{2+}]_{cyt}$ oscillations. These results are consistent with previous reports *in vivo* showing that brains of AD patients exhibit increased $[Ca^{2+}]_{cyt}$ levels (Murray et al., 1992). Moreover, recent *in vivo* studies using intravital Ca^{2+} imaging of APP/PS1 transgenic mouse, a mouse model of familial AD, show that basal $[Ca^{2+}]_{cyt}$ levels are elevated significantly in approximately 35% of neurites located in areas in close proximity to amyloid plaques (Kuchibhotla et al., 2008). A possible explanation for the increase in the basal $[Ca^{2+}]_{cyt}$ levels is the ability of the Aβo to generate ROS, disturbing the function of the membrane ATPases and, thus leading to an increase in the resting $[Ca^{2+}]_{cyt}$ level (Mark et al., 1995). Previous studies have shown that the increase in the basal $[Ca^{2+}]_{cyt}$ relates to the increase in neuronal excitability and, therefore, with circuit connectivity (Catterall and Few, 2008). Therefore, it could be also speculated that chronic treatment with Aβo increases the excitability of the circuit, as shown by our own *in vitro* experiments, and previously by other groups that use *in vivo* imaging in AD mouse models (Busche et al., 2008, 2012; Šišková et al., 2014). Interestingly, the risk of epileptic activity is particularly high in AD patients with early-onset dementia and during early stages of the disease, which a much higher incidence of crises compared to the reference population of the same age (Amatniek et al., 2006).

SOCE, also called capacitative Ca^{2+} entry, is a Ca^{2+} influx pathway activated after the release of Ca^{2+} from the ER in order to replenish intracellular stores that subserves many different cell and physiological functions in a large variety of cell types (Parekh and Putney, 2005). In neurons, SOCE is involved in synaptic processes as well as neuronal excitability (Moccia et al., 2015). In addition, it has been described to be extensively altered in neurodegenerative disorders (Secondo et al., 2018). The components that participate in SOCE are also dysregulated in neurodegenerative disorders. We have previously shown that SOCE decreases with *in vitro* aging, and this effect is at least partially due to downregulation of Stim1 and Orai1 (Calvo-Rodríguez et al., 2016b). Here, we show that exposure of cultured hippocampal neurons to Aβo has a further detrimental effect on SOCE in the aged neurons without having significant effects in young neurons. Previous work by Tong et al. (2016) using cultured hippocampal neurons expressing mutant PS1 proposed that mutations in PS1 enhance the activity of γ-secretase, thus increasing the cleavage of Stim1 and therefore reducing the activation of Orai1, and SOCE. These effects disrupted dendritic spines arguing that PS1 mutations could contribute to memory loss through SOCE dysregulation. Consistently, treatment of AD mouse models with the SOCE positive modulator NSN21778 stimulates SOCE in the spines and rescues hippocampal long-term potentiation impairment (Zhang et al., 2016). In addition, inasmuch as SOCE contributes to ER Ca^{2+} refilling, it could be reasoned that SOCE downregulation in the aged neurons, and in aged neurons exposed to Aβo, is a compensatory effect to the enhanced filling state of intracellular stores in aging and Aβo treated neurons. In any case, SOCE is strongly downregulated in aged neurons and this process is further exacerbated by Aβo exposure. Interestingly, this effect of Aβo is only statistically significant in aging neurons suggesting that a permissive mechanism associated to aging is involved in the mechanism linking Aβo to SOCE downregulation.

PSs are integral proteins located in the ER membrane that may form low conductivity channels in the ER, known as *leak* channels. These channels may release Ca^{2+} in a passive and constant manner from the ER into the cytoplasm (Tu et al., 2006). Work on transgenic mice has shown that mutations in these proteins, as it occurs in familial AD, result in loss of function of the leak channel activity, causing an increase in the Ca^{2+} level on the intracellular stores (Nelson et al., 2007). We have previously shown that Ca^{2+} store content is significantly increased in aged hippocampal neurons (Calvo-Rodríguez et al., 2016b). Our present data confirm these previous results. In addition, our results show that the chronic treatment of hippocampal neurons *in vitro* with the toxic species of AD, Aβo, increases Ca^{2+} store content further, thus proving that chronic exposure to Aβo causes a similar effect than mutations in PS. These results are supported by previous experiments in PC12 cells exposed to chronic treatment (24 h) with $Aβ_{1–42}$, where an excess release of Ca^{2+} from intracellular stores was shown after stimulation with thapsigargin in free calcium media (Pannaccione et al., 2012). This effect is only observed in long-term cultured hippocampal neurons exposed to Aβo, proving the resistance of the short-term cultured ones to the effects of Aβo. Interestingly, a similar tendency has recently been shown by Lerdkrai et al. (2018). These authors found significant differences in the filling state of the intracellular Ca^{2+} stores in AD compared with WT mice *in vivo*, mainly in hyperactive AD cells. In accordance with this line, the chronic exposure of cultured hippocampal neurons to the Aβo notably increases the peak of $[Ca^{2+}]_{cyt}$ induced by both ACh and Caff. This is again pointing to an increased concentration of Ca^{2+} in the ER after exposure to Aβo. Consistently, previous studies in fibroblast from AD patients (Gibson et al., 1996) or in cells carrying the mutated human PS1 (Stutzmann, 2007), showed an abnormal Ca^{2+} release through IP_3Rs. In addition, aberrant Ca^{2+} increases mediated by IP_3 in fibroblasts of asymptomatic members of families with AD have also been described (Etcheberrigaray et al., 1998). Other studies have also implicated the RyRs as responsible for this increased release of intracellular Ca^{2+} in animals carrying the PS1 mutation (Chan et al., 2000). Also, $Aβ_{1–42}$ peptides could be responsible for an increase of the isoform RyR3 in transgenic mouse models of AD (Supnet et al., 2006), influencing the amount of Ca^{2+} that is released from the stores when they are activated. Therefore, Ca^{2+} store content is increased in aged neurons and this process is further enhanced by Aβo. Again, Aβo do not influence Ca^{2+} store content in young neurons.

Mitochondria play also an important role in intracellular Ca^{2+} homeostasis by shaping neuronal Ca^{2+} signaling. Mitochondria and ER are structurally and functionally connected in contact points enriched in MAMs (Csordás and Hajnóczky, 2009; Hayashi et al., 2009). MAMs play different roles in cholesterol ester synthesis, phospholipid transport and

Ca^{2+} transfer from ER to mitochondria. It has been previously shown that MAM function is altered in the pathology of AD. Area-Gomez et al. (2012) showed a few years ago that there is an enhanced ER-mitochondria connectivity in AD patients of sporadic and familial AD. Consistently, we reported recently that *in vitro* aging is associated to enhanced Ca^{2+} transfer from ER to mitochondria in rat hippocampal neurons (Calvo-Rodríguez et al., 2016b). This view was supported by two findings. First, the increased rise in mitochondrial $[Ca^{2+}]$ induced by ACh in Ca^{2+} free medium in aged neurons compared to young neurons. Second, the increased rise in $[Ca^{2+}]_{cyt}$ induced by ACh in the presence of the mitochondrial uncoupler FCCP in aged neurons compared to young neurons (Calvo-Rodríguez et al., 2016b). Our present results confirm these previous findings that were carried out using aequorin targeted to mitochondria using an alternative probe for mitochondrial Ca^{2+}, Rhod-5N.

Interestingly, we show now that Aβo enhance Ca^{2+} transfer from mitochondria to ER in young neurons. This view is supported by the finding that Aβo enhance the rise in $[Ca^{2+}]_{mit}$ elicited by Ca^{2+} release induced by ACh without increasing either the resting levels of $[Ca^{2+}]_{cyt}$, the Ca^{2+} store content or the fraction of cells responsive to ACh. This effect is also independent of changes in the expression of MCU, the calcium channel involved in mitochondrial Ca^{2+} uptake. Thus, the most likely explanation for our results is that Aβo oligomers reinforce the relative position and/or coupling between ER and mitochondria. Consistently with this view, it has been shown that Aβ peptide increases inositol-1,4,5-triphosphate receptor and voltage-dependent anion channel protein expression and elevates the number of ER-mitochondria contact points and mitochondrial calcium concentrations in cultured hippocampal neurons (Hedskog et al., 2013). Unfortunately, the time in culture of these neurons was not reported. In these lines, we show here that expression of all three IP_3 receptor isoforms, including IP_3R1, IP_3R2, and IP_3R3, is increased in aged neurons, which may enhance ER-mitochondrial coupling in aging. In addition, confocal imaging of living neurons and colocalization analysis indicated increased ER-mitochondria colocalization in aged neurons relative to young neurons. Moreover, colocalization was intensified by Aβo in both young and aged neurons. The effects of Aβo on ER—mitochondria coupling in young neurons are not necessarily detrimental since they may favor increased Ca^{2+} transfer between ER and mitochondria to support increased energy demands and Aβo do not induce apoptosis in young neurons, suggesting a physiological role for Aβo in the modulation of ER—mitochondria coupling.

Surprisingly, and in striking contrast with the results in young neurons, exposure of aged neurons to Aβo decreased rather than increased the rise in $[Ca^{2+}]_{mit}$ induced by ACh. These results cannot be explained by lack of ACh receptors as $[Ca^{2+}]_{cyt}$ responses to ACh are indeed enhanced in aged neurons treated with Aβo. They cannot be explained either by depletion of Ca^{2+} stores since Ca^{2+} stores are actually enhanced in aged neurons treated with Aβo. Finally, lack of Ca^{2+} transfer from ER to mitochondria in aged neurons treated with Aβo cannot be attributed either to MCU downregulation as MCU expression is actually enhanced in aged neurons treated with Aβo. These results suggest that, contrary to our expectations, Aβo nearly abolish ER—mitochondria cross talk in aged neurons and this effect, together with exacerbated remodeling of intracellular Ca^{2+} induced by aging, is highly detrimental as Aβo induces apoptosis to a large fraction of aged neurons.

It is well established that an adequate flux of Ca^{2+} transfer from ER to mitochondria is required to maintain the Krebs cycle (Cárdenas et al., 2010). Thus, loss of Ca^{2+} transfer from ER to mitochondria in aged neurons treated with Aβo may compromise OXPHOS activity leading to mitochondrial damage and collapse of the mitochondrial potential. However, excess of Ca^{2+} transfer associated to enhanced Ca^{2+} store content may lead to mitochondrial Ca^{2+} overload.

Several studies by others have proposed that mitochondrial dysfunction is an early event the pathology of AD. Yao et al. (2009) described mitochondrial bioenergetics deficits before plaque deposition in females in a mouse model of AD. By using Thy-1 APP mice, an AD model that deposits plaques at 6 months of age, Hauptmann et al. (2009) showed mitochondrial dysfunction associated with higher levels of ROS, including mitochondrial membrane potential decrease and reduced ATP levels as soon as 3 months of age, when extracellular deposits are not present. In AD patients, low glucose metabolism at baseline and decline of glucose metabolism is used for monitoring changes in cognition and functionality in AD and mild cognitive impairment (MCI; Landau et al., 2011; Shokouhi et al., 2013). Also, oxidative stress, solidly related to mitochondrial dysfunction, has been proposed before plaque deposition in AD mouse models (Praticò et al., 2001; Rönnbäck et al., 2016) and before clinical symptoms in AD patients (Mosconi et al., 2008). Consistently with previous results (Calvo-Rodríguez et al., 2016b), we show here that *in vitro* aging is associated to a partial loss of mitochondrial membrane potential and this loss is further decreased by Aβo in both young and aged neurons. The effect is mild in young neurons. However, aged neurons treated with Aβo display a quite large loss of mitochondrial membrane potential, thus reducing rather dramatically the driving force for mitochondrial Ca^{2+} uptake. In addition, we also found that aged neurons show increased ROS generation compared with young neurons. Moreover, Aβo increase further ROS generation in aged neurons having no effect in young neurons. Accordingly, loss of mitochondrial membrane potential and enhanced ROS generation induced by Aβo in aged neurons may constrain Ca^{2+} transfer from ER to mitochondria.

In summary, we show that Aβo modulate differentially ER–mitochondria cross talk in young and aged neurons. In young neurons, Aβo increase ER–mitochondria coupling without having a detrimental effect. In contrast, in aged neurons, although Aβo increase also ER-mitochondria colocalization, the loss of mitochondrial membrane potential and enhanced ROS generation impairs Ca^{2+} transfer from ER to mitochondria despite Ca^{2+} stores are overloaded and the expression of

molecular players involved in Ca^{2+} transfer increases, thus leading to mitochondrial damage and apoptosis. It has been reported that MAM-associated proteins are up-regulated in AD brain and APP Swe/Lon mouse models (Hedskog et al., 2013), and this effect is mirrored by nanomolar concentrations of Aβ-peptide. Changes in MAM associated proteins in AD could be a rescue response to dysfunctional ER-mitochondria coupling. However, in the face of increased Ca^{2+} store content associated to age and/or AD-related mutations, the further rise in ER-mitochondria coupling likely induced by Aβo may somehow collapse the own coupling leading to neuron damage. Further research is required to address this critical question. In addition, all the above results have been obtained in identified neurons in an *in vitro* model of neuronal aging. As stated above, the fraction of glial cells in hippocampal cultures increases with *in vitro* aging. Whether glial cell may contribute to Ca^{2+} remodeling in aged neurons treated with Aβo remains to be established.

Taken together, our data show that intraorganellar Ca^{2+} remodeling is a hallmark of the aging that is exacerbated in the presence of Aβo. Aging decreases SOCE required for spine stability and increases Ca^{2+} store content and MCU and IP_3 receptors expression that favors Ca^{2+} transfer from ER to mitochondria. Most of these effects are exacerbated by Aβo but only in aged neurons. In contrast, in young neurons Aβo increase ER-mitochondrial colocalization and Ca^{2+} transfer from ER to mitochondria without having effects on ROS generation or apoptosis and only a minor decrease in mitochondrial membrane potential, probably related to increased use of this potential for ATP synthesis. However, the effect of Aβo may become highly detrimental in the aged neuron and the mechanism for this switch may play a fundamental role in AD and warrants further consideration.

AUTHOR CONTRIBUTIONS

MC-R, LN and CV designed the study and wrote the manuscript. MC-R and EH-P performed research and analyzed data.

FUNDING

This work was supported by grants BFU2012-37146 and BFU2015-70131R from Ministry of Economy and Competitivity (Spain) and grants VA145U13, BIO/VA33/13 and VA294P18 from Regional Government of Castilla y León (Spain). MC-R was supported by a pre-doctoral fellowship from Regional Government of Castilla y León (Spain) and the European Social Fund.

ACKNOWLEDGMENTS

We thank Enrique Pérez-Riesgo for help with statistical analysis and Cristina Sánchez-Vicente for help with colocalization analysis.

REFERENCES

Amatniek, J. C., Hauser, W. A., DelCastillo-Castaneda, C., Jacobs, D. M., Marder, K., Bell, K., et al. (2006). Incidence and predictors of seizures in patients with Alzheimer's disease. *Epilepsia* 47, 867–872. doi: 10.1111/j.1528-1167.2006.00554.x

Area-Gomez, E., Del Carmen Lara Castillo, M., Tambini, M. D., Guardia-Laguarta, C., de Groof, A. J., Madra, M., et al. (2012). Upregulated function of mitochondria-associated ER membranes in Alzheimer disease. *EMBO J.* 31, 4106–4123. doi: 10.1038/emboj.2012.202

Area-Gomez, E., and Schon, E. A. (2017). On the pathogenesis of Alzheimer's disease: the MAM hypothesis. *FASEB J.* 31, 864–867. doi: 10.1096/fj.201601309

Atamna, H., and Frey, W. H. II. (2007). Mechanisms of mitochondrial dysfunction and energy deficiency in Alzheimer's disease. *Mitochondrion* 7, 297–310. doi: 10.1016/j.mito.2007.06.001

Baughman, J. M., Perocchi, F., Girgis, H. S., Plovanich, M., Belcher-Timme, C. A., Sancak, Y., et al. (2011). Integrative genomics identifies MCU as an essential component of the mitochondrial calcium uniporter. *Nature* 476, 341–345. doi: 10.1038/nature10234

Berridge, M. J. (2010). Calcium hypothesis of Alzheimer's disease. *Pflugers Arch.* 459, 441–449. doi: 10.1007/s00424-009-0736-1

Bezprozvanny, I. (2009). Calcium signaling and neurodegenerative diseases. *Trends Mol. Med.* 15, 89–100. doi: 10.1016/j.molmed.2009.01.001

Bezprozvanny, I., and Mattson, M. P. (2008). Neuronal calcium mishandling and the pathogenesis of Alzheimer's disease. *Trends Neurosci.* 31, 454–463. doi: 10.1016/j.tins.2008.06.005

Borchelt, D. R., Thinakaran, G., Eckman, C. B., Lee, M. K., Davenport, F., Ratovitsky, T., et al. (1996). Familial Alzheimer's disease-linked presenilin 1 variants elevate Aβ1–42/1–40 ratio *in vitro* and *in vivo*. *Neuron* 17, 1005–1013. doi: 10.1016/s0896-6273(00)80230-5

Brewer, G. J., Torricelli, J. R., Evege, E. K., and Price, P. J. (1993). Optimized survival of hippocampal neurons in B27-supplemented Neurobasal, a new serum-free medium combination. *J. Neurosci. Res.* 35, 567–576. doi: 10.1002/jnr.490350513

Brewer, L. D., Thibault, O., Staton, J., Thibault, V., Rogers, J. T., Garcia-Ramos, G., et al. (2007). Increased vulnerability of hippocampal neurons with age in culture: temporal association with increases in NMDA receptor current, NR2A subunit expression and recruitment of L-type calcium channels. *Brain Res.* 1151, 20–31. doi: 10.1016/j.brainres.2007.03.020

Busche, M. A., Chen, X., Henning, H. A., Reichwald, J., Staufenbiel, M., Sakmann, B., et al. (2012). Critical role of soluble amyloid-β for early hippocampal hyperactivity in a mouse model of Alzheimer's disease. *Proc. Natl. Acad. Sci. U S A* 109, 8740–8745. doi: 10.1073/pnas.1206171109

Busche, M. A., Eichhoff, G., Adelsberger, H., Abramowski, D., Wiederhold, K. H., Haass, C., et al. (2008). Clusters of hyperactive neurons near amyloid plaques in a mouse model of Alzheimer's disease. *Science* 321, 1686–1689. doi: 10.1126/science.1162844

Caballero, E., Calvo-Rodríguez, M., Gonzalo-Ruiz, A., Villalobos, C., and Núñez, L. (2016). A new procedure for amyloid β oligomers preparation enables the unambiguous testing of their effects on cytosolic and mitochondrial Ca^{2+} entry and cell death in primary neurons. *Neurosci. Lett.* 612, 66–73. doi: 10.1016/j.neulet.2015.11.041

Calvo, M., Sanz-Blasco, S., Caballero, E., Villalobos, C., and Núñez, L. (2015a). Susceptibility to excitotoxicity in aged hippocampal cultures and neuroprotection by non-steroidal anti-inflammatory drugs: role of mitochondrial calcium. *J. Neurochem.* 132, 403–417. doi: 10.1111/jnc.13004

Calvo, M., Villalobos, C., and Núñez, L. (2015b). Calcium imaging in neuron cell death. *Methods Mol. Biol.* 1254, 73–85. doi: 10.1007/978-1-4939-2152-2_6

Calvo-Rodríguez, M., de la Fuente, C., García-Durillo, M., García-Rodríguez, C., Villalobos, C., and Núñez, L. (2017). Aging and amyloid β oligomers enhance TLR4 expression, LPS-induced Ca^{2+} responses, and neuron cell death in cultured rat hippocampal neurons. *J. Neuroinflammation* 14:24. doi: 10.1186/s12974-017-0802-0

Calvo-Rodríguez, M., García-Durillo, M., Villalobos, C., and Núñez, L. (2016a). Aging enables Ca^{2+} overload and apoptosis induced by amyloid-β oligomers in rat hippocampal neurons: neuroprotection by non-steroidal anti-inflammatory

drugs and R-flurbiprofen in aging neurons. *J. Alzheimers Dis.* 54, 207–221. doi: 10.3233/jad-151189

Calvo-Rodríguez, M., García-Durillo, M., Villalobos, C., and Núñez, L. (2016b). *In vitro* aging promotes endoplasmic reticulum (ER)-mitochondria Ca^{2+} cross talk and loss of store-operated Ca^{2+} entry (SOCE) in rat hippocampal neurons. *Biochim. Biophys. Acta* 1863, 2637–2649. doi: 10.1016/j.bbamcr.2016.08.001

Calvo-Rodríguez, M., Villalobos, C., and Nuñez, L. (2015). Fluorescence and bioluminescence imaging of subcellular Ca^{2+} in aged hippocampal neurons. *J. Vis. Exp.* 106:e53330. doi: 10.3791/53330

Cárdenas, C., Miller, R. A., Smith, I., Bui, T., Molgó, J., Müller, M., et al. (2010). Essential regulation of cell bioenergetics by constitutive InsP3 receptor Ca^{2+} transfer to mitochondria. *Cell* 142, 270–283. doi: 10.1016/j.cell.2010.06.007

Catterall, W. A., and Few, A. P. (2008). Calcium channel regulation and presynaptic plasticity. *Neuron* 59, 882–901. doi: 10.1016/j.neuron.2008.09.005

Chan, S. L., Mayne, M., Holden, C. P., Geiger, J. D., and Mattson, M. P. (2000). Presenilin-1 mutations increase levels of ryanodine receptors and calcium release in PC12 cells and cortical neurons. *J. Biol. Chem.* 275, 18195–18200. doi: 10.1074/jbc.m000040200

Csordás, G., and Hajnóczky, G. (2009). SR/ER-mitochondrial local communication: calcium and ROS. *Biochim. Biophys. Acta* 1787, 1352–1362. doi: 10.1016/j.bbabio.2009.06.004

de la Fuente, S., Fonteriz, R. I., Montero, M., and Alvarez, J. (2012). Dynamics of mitochondrial [Ca^{2+}] measured with the low-Ca^{2+}-affinity dye rhod-5N. *Cell Calcium* 51, 65–71. doi: 10.1016/j.ceca.2011.10.007

De Stefani, D., Raffaello, A., Teardo, E., Szabò, I., and Rizzuto, R. (2011). A forty-kilodalton protein of the inner membrane is the mitochondrial calcium uniporter. *Nature* 476, 336–340. doi: 10.1038/nature10230

Demuro, A., and Parker, I. (2013). Cytotoxicity of intracellular aβ42 amyloid oligomers involves Ca^{2+} release from the endoplasmic reticulum by stimulated production of inositol trisphosphate. *J. Neurosci.* 33, 3824–3833. doi: 10.1523/JNEUROSCI.4367-12.2013

DuBoff, B., Feany, M., and Götz, J. (2013). Why size matters—balancing mitochondrial dynamics in Alzheimer's disease. *Trends Neurosci.* 36, 325–335. doi: 10.1016/j.tins.2013.03.002

Etcheberrigaray, R., Hirashima, N., Nee, L., Prince, J., Govoni, S., Racchi, M., et al. (1998). Calcium responses in fibroblasts from asymptomatic members of Alzheimer's disease families. *Neurobiol. Dis.* 5, 37–45. doi: 10.1006/nbdi.1998.0176

Ferreiro, E., Oliveira, C. R., and Pereira, C. (2004). Involvement of endoplasmic reticulum Ca^{2+} release through ryanodine and inositol 1,4,5-triphosphate receptors in the neurotoxic effects induced by the amyloid-β peptide. *J. Neurosci. Res.* 76, 872–880. doi: 10.1002/jnr.20135

Gibson, G. E., Zhang, H., Toral-Barza, L., Szolosi, S., and Tofel-Grehl, B. (1996). Calcium stores in cultured fibroblasts and their changes with Alzheimer's disease. *Biochim. Biophys. Acta* 1316, 71–77. doi: 10.1016/0925-4439(96)00002-6

Hardy, J., and Selkoe, D. J. (2002). The amyloid hypothesis of Alzheimer's disease: progress and problems on the road to therapeutics. *Science* 297, 353–356. doi: 10.1126/science.1072994

Hauptmann, S., Scherping, I., Dröse, S., Brandt, U., Schulz, K. L., Jendrach, M., et al. (2009). Mitochondrial dysfunction: an early event in Alzheimer pathology accumulates with age in AD transgenic mice. *Neurobiol. Aging* 30, 1574–1586. doi: 10.1016/j.neurobiolaging.2007.12.005

Hayashi, T., Rizzuto, R., Hajnoczky, G., and Su, T. P. (2009). MAM: more than just a housekeeper. *Trends Cell Biol.* 19, 81–88. doi: 10.1016/j.tcb.2008.12.002

Hedskog, L., Pinho, C. M., Filadi, R., Rönnbäck, A., Hertwig, L., Wiehager, B., et al. (2013). Modulation of the endoplasmic reticulum-mitochondria interface in Alzheimer's disease and related models. *Proc. Natl. Acad. Sci. U S A* 110, 7916–7921. doi: 10.1073/pnas.1300677110

Hirai, K., Aliev, G., Nunomura, A., Fujioka, H., Russell, R. L., Atwood, C. S., et al. (2001). Mitochondrial abnormalities in Alzheimer's disease. *J. Neurosci.* 21, 3017–3023. doi: 10.1523/JNEUROSCI.21-09-03017.2001

Khachaturian, Z. S. (1989). The role of calcium regulation in brain aging: reexamination of a hypothesis. *Aging* 1, 17–34. doi: 10.1007/bf03323872

Kopeikina, K. J., Carlson, G. A., Pitstick, R., Ludvigson, A. E., Peters, A., Luebke, J. I., et al. (2011). Tau accumulation causes mitochondrial distribution deficits in neurons in a mouse model of tauopathy and in human Alzheimer's disease brain. *Am. J. Pathol.* 179, 2071–2082. doi: 10.1016/j.ajpath.2011.07.004

Kuchibhotla, K. V., Goldman, S. T., Lattarulo, C. R., Wu, H. Y., Hyman, B. T., and Bacskai, B. J. (2008). Aβ plaques lead to aberrant regulation of calcium homeostasis *in vivo* resulting in structural and functional disruption of neuronal networks. *Neuron* 59, 214–225. doi: 10.1016/j.neuron.2008.06.008

LaFerla, F. M. (2002). Calcium dyshomeostasis and intracellular signalling in Alzheimer's disease. *Nat. Rev. Neurosci.* 3, 862–872. doi: 10.1038/nrn960

Landau, S. M., Harvey, D., Madison, C. M., Koeppe, R. A., Reiman, E. M., Foster, N. L., et al. (2011). Associations between cognitive, functional, and FDG-PET measures of decline in AD and MCI. *Neurobiol. Aging* 32, 1207–1218. doi: 10.1016/j.neurobiolaging.2009.07.002

Lemere, C. A., Lopera, F., Kosik, K. S., Lendon, C. L., Ossa, J., Saido, T. C., et al. (1996). The E280A presenilin 1 Alzheimer mutation produces increased A β 42 deposition and severe cerebellar pathology. *Nat. Med.* 2, 1146–1150. doi: 10.1038/nm1096-1146

Lerdkrai, C., Asavapanumas, N., Brawek, B., Kovalchuk, Y., Mojtahedi, N., Olmedillas Del Moral, M., et al. (2018). Intracellular Ca^{2+} stores control *in vivo* neuronal hyperactivity in a mouse model of Alzheimer's disease. *Proc. Natl. Acad. Sci. U S A* 115, E1279–E1288. doi: 10.1073/pnas.1714409115

Mark, R. J., Hensley, K., Butterfield, D. A., and Mattson, M. P. (1995). Amyloid β-peptide impairs ion-motive ATPase activities: evidence for a role in loss of neuronal Ca^{2+} homeostasis and cell death. *J. Neurosci.* 15, 6239–6249. doi: 10.1523/JNEUROSCI.15-09-06239.1995

Mattson, M. P. (2007). Calcium and neurodegeneration. *Aging Cell* 6, 337–350. doi: 10.1111/j.1474-9726.2007.00275.x

Moccia, F., Zuccolo, E., Soda, T., Tanzi, F., Guerra, G., Mapelli, L., et al. (2015). Stim and Orai proteins in neuronal Ca^{2+} signaling and excitability. *Front. Cell. Neurosci.* 9:153. doi: 10.3389/fncel.2015.00153

Mosconi, L., Pupi, A., and De Leon, M. J. (2008). Brain glucose hypometabolism and oxidative stress in preclinical Alzheimer's disease. *Ann. N Y Acad. Sci.* 1147, 180–195. doi: 10.1196/annals.1427.007

Müller, M., Ahumada-Castro, U., Sanhueza, M., Gonzalez-Billault, C., Court, F. A., and Cárdenas, C. (2018). Mitochondria and calcium regulation as basis of neurodegeneration associated with aging. *Front. Neurosci.* 12:470. doi: 10.3389/fnins.2018.00470

Murray, F. E., Landsberg, J. P., Williams, R. J., Esiri, M. M., and Watt, F. (1992). Elemental analysis of neurofibrillary tangles in Alzheimer's disease using proton-induced X-ray analysis. *Ciba Found. Symp.* 169, 201–210; discussion 210–216. doi: 10.1002/9780470514306.ch12

Nelson, O., Tu, H., Lei, T., Bentahir, M., de Strooper, B., and Bezprozvanny, I. (2007). Familial Alzheimer disease-linked mutations specifically disrupt Ca^{2+} leak function of presenilin 1. *J. Clin. Invest.* 117, 1230–1239. doi: 10.1172/jci30447

Nunez, L., Sanchez, A., Fonteriz, R. I., and Garcia-Sancho, J. (1996). Mechanisms for synchronous calcium oscillations in cultured rat cerebellar neurons. *Eur. J. Neurosci.* 8, 192–201. doi: 10.1111/j.1460-9568.1996.tb01180.x

Pannaccione, A., Secondo, A., Molinaro, P., D'Avanzo, C., Cantile, M., Esposito, A., et al. (2012). A new concept: $A\beta_{1-42}$ generates a hyperfunctional proteolytic NCX3 fragment that delays caspase-12 activation and neuronal death. *J. Neurosci.* 32, 10609–10617. doi: 10.1523/JNEUROSCI.6429-11.2012

Parekh, A. B., and Putney, J. W. Jr. (2005). Store-operated calcium channels. *Physiol. Rev.* 85, 757–810. doi: 10.1152/physrev.00057.2003

Pérez-Otaño, I., Luján, R., Tavalin, S. J., Plomann, M., Modregger, J., Liu, X. B., et al. (2006). Endocytosis and synaptic removal of NR3A-containing NMDA receptors by PACSIN1/syndapin1. *Nat. Neurosci.* 9, 611–621. doi: 10.1038/nn1680

Porter, N. M., Thibault, O., Thibault, V., Chen, K. C., and Landfield, P. W. (1997). Calcium channel density and hippocampal cell death with age in long-term culture. *J. Neurosci.* 17, 5629–5639. doi: 10.1523/JNEUROSCI.17-14-05629.1997

Praticò, D., Uryu, K., Leight, S., Trojanoswki, J. Q., and Lee, V. M. (2001). Increased lipid peroxidation precedes amyloid plaque formation in an animal model of Alzheimer amyloidosis. *J. Neurosci.* 21, 4183–4187. doi: 10.1523/JNEUROSCI.21-12-04183.2001

Rönnbäck, A., Pavlov, P. F., Mansory, M., Gonze, P., Marlière, N., Winblad, B., et al. (2016). Mitochondrial dysfunction in a transgenic mouse model expressing human amyloid precursor protein (APP) with the Arctic mutation. *J. Neurochem.* 136, 497–502. doi: 10.1111/jnc.13410

Santos, R. X., Correia, S. C., Wang, X., Perry, G., Smith, M. A., Moreira, P. I., et al. (2010). A synergistic dysfunction of mitochondrial fission/fusion dynamics and mitophagy in Alzheimer's disease. *J. Alzheimers Dis.* 20, S401–S412. doi: 10.3233/jad-2010-100666

Sanz-Blasco, S., Valero, R. A., Rodríguez-Crespo, I., Villalobos, C., and Núñez, L. (2008). Mitochondrial Ca^{2+} overload underlies Aβ oligomers neurotoxicity providing an unexpected mechanism of neuroprotection by NSAIDs. *PLoS One* 3:e2718. doi: 10.1371/journal.pone.0002718

Secondo, A., Bagetta, G., and Amantea, D. (2018). On the role of store-operated calcium entry in acute and chronic neurodegenerative diseases. *Front. Mol. Neurosci.* 11:87. doi: 10.3389/fnmol.2018.00087

Shokouhi, S., Claassen, D., Kang, H., Ding, Z., Rogers, B., Mishra, A., et al. (2013). Longitudinal progression of cognitive decline correlates with changes in the spatial pattern of brain 18F-FDG PET. *J. Nucl. Med.* 54, 1564–1569. doi: 10.2967/jnumed.112.116137

Šišková, Z., Justus, D., Kaneko, H., Friedrichs, D., Henneberg, N., Beutel, T., et al. (2014). Dendritic structural degeneration is functionally linked to cellular hyperexcitability in a mouse model of Alzheimer's disease. *Neuron* 84, 1023–1033. doi: 10.1016/j.neuron.2014.10.024

Sodero, A. O., Weissmann, C., Ledesma, M. D., and Dotti, C. G. (2011). Cellular stress from excitatory neurotransmission contributes to cholesterol loss in hippocampal neurons aging *in vitro*. *Neurobiol. Aging* 32, 1043–1053. doi: 10.1016/j.neurobiolaging.2010.06.001

Stutzmann, G. E. (2007). The pathogenesis of Alzheimers disease is it a lifelong "calciumopathy"? *Neuroscientist* 13, 546–559. doi: 10.1177/1073858407299730

Supnet, C., Grant, J., Kong, H., Westaway, D., and Mayne, M. (2006). Amyloid-β-(1–42) increases ryanodine receptor-3 expression and function in neurons of TgCRND8 mice. *J. Biol. Chem.* 281, 38440–38447. doi: 10.1074/jbc.m606736200

Szabadkai, G., Simoni, A. M., and Rizzuto, R. (2003). Mitochondrial Ca^{2+} uptake requires sustained Ca^{2+} release from the endoplasmic reticulum. *J. Biol. Chem.* 278, 15153–15161. doi: 10.1074/jbc.m300180200

Toescu, E. C., and Verkhratsky, A. (2003). Neuronal ageing from an intraneuronal perspective: roles of endoplasmic reticulum and mitochondria. *Cell Calcium* 34, 311–323. doi: 10.1016/s0143-4160(03)00142-8

Tong, B. C., Lee, C. S., Cheng, W. H., Lai, K. O., Foskett, J. K., and Cheung, K. H. (2016). Familial Alzheimer's disease-associated presenilin 1 mutants promote γ-secretase cleavage of STIM1 to impair store-operated Ca^{2+} entry. *Sci. Signal.* 9:ra89. doi: 10.1126/scisignal.aaf1371

Tu, H., Nelson, O., Bezprozvanny, A., Wang, Z., Lee, S. F., Hao, Y. H., et al. (2006). Presenilins form ER Ca^{2+} leak channels, a function disrupted by familial Alzheimer's disease-linked mutations. *Cell* 126, 981–993. doi: 10.1016/j.cell.2006.06.059

Villalobos, C., and García-Sancho, J. (1995). Capacitative Ca^{2+} entry contributes to the Ca^{2+} influx induced by thyrotropin-releasing hormone (TRH) in GH3 pituitary cells. *Pflugers Arch.* 430, 923–935. doi: 10.1007/bf01837406

Wang, X., Su, B., Lee, H. G., Li, X., Perry, G., Smith, M. A., et al. (2009). Impaired balance of mitochondrial fission and fusion in Alzheimer's disease. *J. Neurosci.* 29, 9090–9103. doi: 10.1523/JNEUROSCI.1357-09.2009

Xie, H., Guan, J., Borrelli, L. A., Xu, J., Serrano-Pozo, A., and Bacskai, B. J. (2013). Mitochondrial alterations near amyloid plaques in an Alzheimer's disease mouse model. *J. Neurosci.* 33, 17042–17051. doi: 10.1523/JNEUROSCI.1836-13.2013

Yao, J., Irwin, R. W., Zhao, L., Nilsen, J., Hamilton, R. T., and Brinton, R. D. (2009). Mitochondrial bioenergetic deficit precedes Alzheimer's pathology in female mouse model of Alzheimer's disease. *Proc. Natl. Acad. Sci. U S A* 106, 14670–14675. doi: 10.1073/pnas.0903563106

Zhang, H., Sun, S., Wu, L., Pchitskaya, E., Zakharova, O., Fon Tacer, K., et al. (2016). Store-operated calcium channel complex in postsynaptic spines: a new therapeutic target for Alzheimer's disease treatment. *J. Neurosci.* 36, 11837–11850. doi: 10.1523/JNEUROSCI.1188-16.2016

Conflict of Interest Statement: The authors declare that the research was conducted in the absence of any commercial or financial relationships that could be construed as a potential conflict of interest.

Copyright © 2019 Calvo-Rodriguez, Hernando-Perez, Nuñez and Villalobos. This is an open-access article distributed under the terms of the Creative Commons Attribution License (CC BY). The use, distribution or reproduction in other forums is permitted, provided the original author(s) and the copyright owner(s) are credited and that the original publication in this journal is cited, in accordance with accepted academic practice. No use, distribution or reproduction is permitted which does not comply with these terms.

frontiers in Cellular Neuroscience

ORIGINAL RESEARCH
published: 27 February 2019
doi: 10.3389/fncel.2019.00060

Cellular Differences in the Cochlea of CBA and B6 Mice May Underlie Their Difference in Susceptibility to Hearing Loss

Huihui Liu[1,2,3], *Gen Li*[1,2,3], *Jiawen Lu*[1,2,3], *Yun-Ge Gao*[1,2,3], *Lei Song*[1,2,3], *Geng-Lin Li*[1,2,3]* and *Hao Wu*[1,2,3]*

[1] Department of Otolaryngology-Head and Neck Surgery, Shanghai Ninth People's Hospital, Shanghai Jiao Tong University School of Medicine, Shanghai, China, [2] Ear Institute, Shanghai Jiao Tong University School of Medicine, Shanghai, China, [3] Shanghai Key Laboratory of Translational Medicine on Ear and Nose Diseases, Shanghai, China

Hearing is an extremely delicate sense that is particularly vulnerable to insults from environment, including drugs and noise. Unsurprisingly, mice of different genetic backgrounds show different susceptibility to hearing loss. In particular, CBA/CaJ (CBA) mice maintain relatively stable hearing over age while C57BL/6J (B6) mice show a steady decline of hearing, making them a popular model for early onset hearing loss. To reveal possible underlying mechanisms, we examined cellular differences in the cochlea of these two mouse strains. Although the ABR threshold and Wave I latency are comparable between them, B6 mice have a smaller Wave I amplitude. This difference is probably due to fewer spiral ganglion neurons found in B6 mice, as the number of ribbon synapses per inner hair cell (IHC) is comparable between the two mouse strains. Next, we compared the outer hair cell (OHC) function and we found OHCs from B6 mice are larger in size but the prestin density is similar among them, consistent with the finding that they share similar hearing thresholds. Lastly, we examined the IHC function and we found IHCs from B6 mice have a larger Ca^{2+} current, release more synaptic vesicles and recycle synaptic vesicles more quickly. Taken together, our results suggest that excessive exocytosis from IHCs in B6 mice may raise the probability of glutamate toxicity in ribbon synapses, which could accumulate over time and eventually lead to early onset hearing loss.

Keywords: hearing loss, hair cell, spiral ganglion neuron, ribbon synapse, calcium current, exocytosis

OPEN ACCESS

Edited by:
Peter S. Steyger, Oregon Health and Science University, United States

Reviewed by:
Hongzhe Li, VA Loma Linda Healthcare System, United States
Kevin Ohlemiller, Washington University in St. Louis, United States

***Correspondence:**
Geng-Lin Li
genglin@sh9hospital.org
Hao Wu
wuhaoent@sh9hospital.org

Received: *16 October 2018*
Accepted: *06 February 2019*
Published: *27 February 2019*

Citation:
Liu H, Li G, Lu J, Gao Y-G, Song L, Li G-L and Wu H (2019) Cellular Differences in the Cochlea of CBA and B6 Mice May Underlie Their Difference in Susceptibility to Hearing Loss. Front. Cell. Neurosci. 13:60. doi: 10.3389/fncel.2019.00060

INTRODUCTION

The dysfunction and/or loss of sensorineural cells in cochlea often result in hearing impairment, which is a major social and health problem worldwide (Fujimoto et al., 2017). Sensorineural hearing loss involves in mixed pathology including loss of hair cells and/or spiral ganglion neurons (SGNs), atrophy of stria vascularis, decline of endolymphatic potential and cochlear anatomical alterations (Schuknecht and Gacek, 1993). Hair cells, including inner hair cells (IHCs) and outer hair cells (OHCs) in cochlea, play an essential role in converting sound vibrations into neural signals. SGNs are the first order of spike-generating neurons in the auditory pathway, and they connect hair cells to neurons in cochlear nuclei in the brainstem. However, both of them are prone to be damaged by multiple and complex underlying etiologies, such as aging, acoustic exposure, ototoxic drugs, genetic disorders, etc. (Mammano and Bortolozzi, 2018). Exploring possible mechanisms of

sensorineural cell dysfunction will expand our understanding of neural and molecular basis of this sensory deficit.

Animal models for studying hearing loss have been utilized over half a century and mice are now the widely used species for hearing research (Ohlemiller, 2006). Among them, CBA/CaJ (CBA) and C57BL/6J (B6) mice are two of the most useful animal models for investigating hearing loss. B6 mice are highly susceptible to acoustic overstimulation while CBA mice are fairly resistant to noise trauma (Davis et al., 2001). Previous studies had found that B6 mice have a rapid hearing loss, reaching severe levels by about 1 year of age. In contrast, CBA mice have excellent cochlear sensitivity and a slow progressive hearing loss over age, so that they maintain sensitive hearing well into old ages (Jimenez et al., 1999). B6 mice carry a *cadherin23* (*Cdh23*) mutation, also known as *Ahl* (Noben-Trauth et al., 2003). *Cdh23* encodes cadherin 23, which is critically important for hair cell development. Specifically, cadherin 23 is required for proper maintenance of hair cell structures such as stereociliary tip links (Siemens et al., 2004; Kazmierczak et al., 2007), kinocilial and transient lateral links (Lagziel et al., 2005; Michel et al., 2005). Mutations in *Cdh23* cause kinocilium displacement and splayed stereocilia during early hair cell differentiation (Di Palma et al., 2001). Another locus, *Ahl3*, has been shown to cause hearing loss and is also identified in B6 (Nemoto et al., 2004). Besides gene expression differences between the two mouse strains, significant morphological differences in the cochlea are also found at the age of 6 months, including efferent nerve endings under OHCs and SGNs (Park et al., 2010, 2011).

However, structural and functional differences in early ages could affect the development and progress of hearing loss and there has been a lack of side-by-side comparison of cellular functions in the cochlea of these two mouse strains, especially before hearing loss starts. To fill this knowledge gap, we used juvenile animals with normal hearing to explore cellular differences in the cochlea of these two mouse strains, aiming to identify candidate mechanisms of early onset hearing loss.

MATERIALS AND METHODS

Auditory Brainstem Responses (ABRs)

Male CBA/CaJ (CBA) and C57BL/6J (B6) mice of 4 weeks old (SIPPR-BK Laboratory Animal Ltd., Shanghai, China) were used throughout this study. All animal handling was complied with the Guide for the Care and Use of Laboratory Animals (8th edition), published by the National Institutes of Health (NIH, USA) and approved by the University Committee of Laboratory Animals of Shanghai Jiao Tong University.

For ABR recording, animals were anesthetized with chloral hydrate (480 mg/Kg i.p.) and the body temperature was maintained near 37°C with a heating blanket. ABRs were recorded via three sub dermal needle electrodes, placed at the vertex of skull, the mastoid area of test ear and the shoulder of opposite side. Short tone pips of 3 ms that consist 1 ms rise and fall cosine ramp were delivered at 20 Hz rate through a computer-generated acoustic stimulation system (Tucker-Davis Technologies). For each frequency and each sound pressure level (SPL), 400 responses were collected and averaged in BioSigRZ (Tucker-Davis Technologies). All ABR recordings were conducted by the same experimenter. Hearing thresholds were defined as the lowest SPL that can evoke appropriate ABR responses, in 5 dB steps descending from 90 dB SPL (Song et al., 2006). The amplitude and latency of ABR Wave I was measured manually offline.

Whole-Cell Patch-Clamp Recording

Patch-clamp recordings were performed in IHCs and OHCs in the apical turn of basilar membrane through an EPC10/2 amplifier (HEKA Electronics, Lambrecht Pfalz, Germany), driven by Patchmaster (HEKA Electronics). Recording pipettes were pulled from borosilicate glass capillaries (World Precision Instruments) and coated with dental wax. The pipettes had a typical resistance of about 6 MΩ when filled with pipette solution containing (in mM) 135 Cs-methane sulfonate, 10 CsCl, 10 HEPES, 10 TEA-Cl, 1 EGTA, 3 Mg-ATP, and 0.5 Na-GTP (290 mOsm, pH 7.20). Extracellular solution contained (in mM) 110 NaCl, 2.8 KCl, 25 TEA-Cl, 5 $CaCl_2$, 1 $MgCl_2$, 2 Na-pyruvate, 5.6 D-glucose, and 10 HEPES (300 mOsm, pH 7.40). All patch-clamp experiments were carried out at room temperature and the liquid junction potential was corrected offline.

Conductance-voltage relationships were calculated from Ca^{2+} current responses to ramp stimulation from −90 mV to +50 mV and fitted to the Boltzmann equation:

$$G(V) = \frac{G_{max}}{1 + e^{\frac{V_{half} - V}{k_{slope}}}}$$

where V is the command membrane potential, G_{max} is the maximum conductance, V_{half} is the half-activation voltage, k_{slope} is the slope factor that defines steepness of voltage dependence in current activation.

For IHCs, whole-cell membrane capacitance measurements were performed with the lock-in feature and "Sine + DC" method in Patchmaster (HEKA). Briefly, sine waves of 1 kHz and 70 mV (peak-to-peak) were superposed on the holding potential, and the resulting current responses were used to determine whole-cell capacitance (C_m). The net increase of C_m before and after stimulation (ΔC_m) was used to assess exocytosis from IHCs.

For OHCs, whole-cell capacitance was measured with an Axon 200B amplifier (Molecular Devices, Sunnyvale, CA) and a two-sine voltage command (10 to 20 mV, with a primary frequency of 390.6 Hz and harmonic of 781.2 Hz), superimposed on to a voltage ramp (Santos-Sacchi and Song, 2014). The extracellular solution contained (in mM) 100 NaCl, 20 TEA-Cl, 20 CsCl, 2 $CoCl_2$, 1 $MgCl_2$, 1 $CaCl_2$, and 10 HEPES (300 mOsm, pH 7.40). The pipette solution contained (in mM) 140 CsCl, 2 $MgCl_2$, 10 HEPES, and 10 EGTA (300 mOsm, pH 7.20). Two-state Boltzmann function was used to fit linear and non-linear capacitance data:

$$C_m(V) = Q_{max} \times \frac{ze}{kT} \times \frac{b}{(1+b)^2} + C_{lin}; b = e^{\frac{-ze(V - V_{half})}{kT}}$$

Where, Q_{max} is the maximum non-linear charge moved, V_{half} is the half-maximum voltage, z is the valence, and C_{lin} is the linear membrane capacitance, i.e., the resting membrane capacitance.

Whole-Mount Cochlear Staining

Cochleae were acutely dissected after animals were anesthetized deeply and sacrificed. For fluorescence staining, the apical turn of basilar membranes was excised and fixed with 4% paraformaldehyde (PFA) for 2 h, permeabilized with 5% Triton X-100 for 30 min, and blocked in 5% BSA for 60 min. The tissue was then incubated overnight at 4°C with two primary antibodies, mouse anti-CtBP2 (BD Biosciences, catalog # 612044, 1:200 dilution) and mouse anti-GluR2 (Millipore, catalog # MAB397, 1:100 dilution). Next day, after three washes in PBS, the tissue was incubated with two secondary antibodies, Alexa Fluor 568-conjugated goat anti-mouse IgG1 (Invitrogen, catalog # A-21124, 1:200 dilution) and Alexa Fluor 647-conjugated IgG2 (Invitrogen, catalog # A-21241, 1:200 dilution). Fluorescence images were acquired on a Zeiss confocal microscope (LSM 510 META).

For histological staining, cochleae were fixed in 4% PFA overnight at 4°C, decalcified in PBS with 10% EDTA for 7 days at 4°C and dehydrated in 30% sucrose. Cochleae were then embedded in OCT, frozen at −20°C, and sectioned parallel to the modiolus at 5 µm per section (ThermoFisherScientific Inc., Waltham, MA). The slides were dried, washed with PBS for three times, blocked in 0.1% Triton X-100 with 5% BSA in PBS for 1 h at room temperature and incubated overnight at 4°C with the primary antibody mouse anti-TUJ1 (Covance, catalog # MMS-435P, 1:500 dilution). HRP-conjugated rat anti-mouseIgG2a secondary antibody (Invitrogen, catalog#04-6220, 1:500 dilution) was used to visualize the primary antibodies and the slides were stained with DAB. Images were captured with a digital camera, and the density of spiral ganglion neurons (SGNs) was calculated for the apical, medial and basal turn of cochleae, by dividing the number of SGNs with the area surveyed.

Data Analysis and Statistical Tests

Data were analyzed in Igor Pro (WaveMetrics, USA) with home-made macros and statistical tests were performed in Prism (GraphPad, USA) with built-in functions. Depending on the nature of data set, statistical significance was assessed with unpaired Student's *t*-test, Mann-Whitney test or two-way ANOVA followed by Bonferroni *post-hoc* test. Data are presented as Mean ± SD in text and as Mean ± SEM in figures, and the level of significance was set to $p < 0.05$. In figures, N.S. means $p > 0.05$, *means $p < 0.05$, ** means $p < 0.01$, and *** means $p < 0.001$.

RESULTS

Hearing Performance

To examine differences of hearing performance between CBA and B6 mice, we presented short tone burst to animals under anesthesia and recorded auditory brainstem responses (ABRs). This is a non-invasive way to assess hearing performance, and the first wave, i.e., Wave I, represents summated activity of

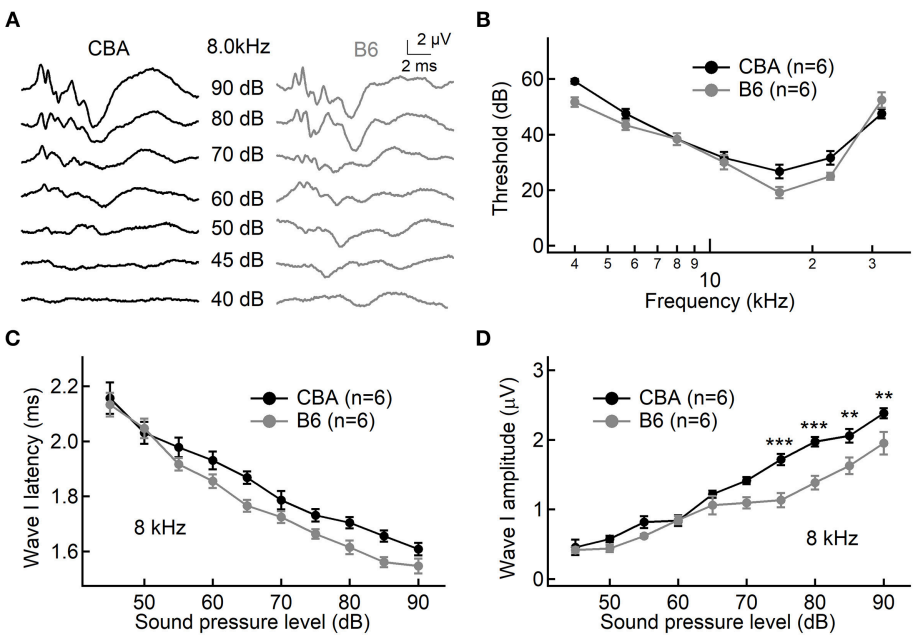


FIGURE 1 | Hearing performance of juvenile CBA and B6 mice. **(A)** Representative auditory brainstem responses (ABRs) recorded from two mice, one from each strain. **(B,C)** Across all frequencies tested, no significant differences were found in either the ABR threshold **(B)** or ABR Wave I latency **(C)** between the two mouse strains. **(D)** As the sound pressure level (SPL) went beyond 70 dB, the ABR Wave I amplitude from B6 mice became significantly smaller than that of CBA mice. For both mouse strains, pure tone pips of 8 kHz with an increasing SPL were presented to induce ABRs. For all figures, data are depicted as Mean ± SEM, ** means $p < 0.01$, and *** means $p < 0.001$.

responding auditory afferent fibers (**Figure 1A**). Consistent with previous studies (Frisina et al., 2007; Ohlemiller et al., 2016; Hickox et al., 2017), we found no significant difference between the two mouse strains in either the ABR threshold or Wave I latency ($n = 6$ for both mouse strains, two-way ANOVA, $p > 0.05$, **Figures 1B,C**).

Next, we examined ABR Wave I amplitude at 8 kHz, a frequency located in the apical turn. We chose to focus on the apical turn for this entire study because this is the only region in adult cochlea where hearing epithelium can be excised with sufficient tissue integrity for patch-clamp analysis on inner hair cells (IHCs), an approach we would like to take for later experiments. Although there is no significant difference for low sound pressure levels (SPLs, 45–70 dB), Wave I amplitude is significantly smaller for B6 mice at high SPLs starting from 75 dB (1.72 ± 0.20 vs. 1.13 ± 0.25 μV, $n = 6$ for both mouse strains, two-way ANOVA, $p < 0.001$). This difference in the Wave I amplitude for louder sounds is not unique to the apical turn, as we observed similar difference for both medial and basal turn (16 and 32 kHz, data not shown).

Inner Hair Cell (IHC) Function

To examine functional differences in IHCs between the two mouse strains, we conducted whole-cell patch-clamp recording in IHCs from the apical turn. We first applied ramp stimulation and recorded the Ca^{2+} current (I_{Ca}, **Figure 2A**). We found that the peak amplitude of I_{Ca} is significantly larger in IHCs from B6 mice (-128 ± 12.3 vs. -212 ± 37.0 pA, $n = 17$ and 12 cells; Mann-Whitney *U*-test, $p < 0.001$; **Figure 2C**). As expected, we found no significant different in the Ca^{2+} reversal potential between the two mouse strains (26.4 ± 2.57 vs. 28.5 ± 3.58 mV, $n = 17$ and 12; unpaired Student's *t*-test, $p > 0.05$; **Figure 2F**). Next, we converted I_{Ca} to conductance point-by-point and fitted conductance-voltage relationship to the Boltzmann function (**Figure 2B**), yielding the half-activation voltage (V_{half}) and the slope of activation (k_{slope}). We found that I_{Ca} in B6 mice has a more negative V_{half} (-19.7 ± 3.17 vs. -23.9 ± 2.95 mV, $n = 17$ and 12; unpaired Student's *t*-test, $p < 0.01$; **Figure 2D**) and a steeper activation slope (6.77 ± 0.28 vs. 6.07 ± 0.44 mV, $n = 17$ and 12; unpaired Student's *t*-test, $p < 0.001$; **Figure 2E**), suggesting that Ca^{2+} channels in B6 IHCs could bring more Ca^{2+} influx into the cell at physiological conditions.

To assess exocytosis in IHCs, we applied step stimulation and conducted whole-cell capacitance measurement (Neher and Marty, 1982) to determine membrane area increase (ΔC_m, **Figure 3A**). We varied stimulation duration from 10 to 500 ms, and we found more Ca^{2+} influx (Q_{Ca}) in IHCs from B6 mice (see **Table 1** and **Figure 3B**), consistent with the aforementioned finding that I_{Ca} in B6IHCs has a larger peak amplitude. Additionally, we found IHCs from B6 mice released more synaptic vesicles for both short and long stimulation (see **Table 1** and **Figure 3C**), suggesting that they have a large readily releasable pool of synaptic vesicles and that they replenish synaptic vesicles more efficiently. Although they release more

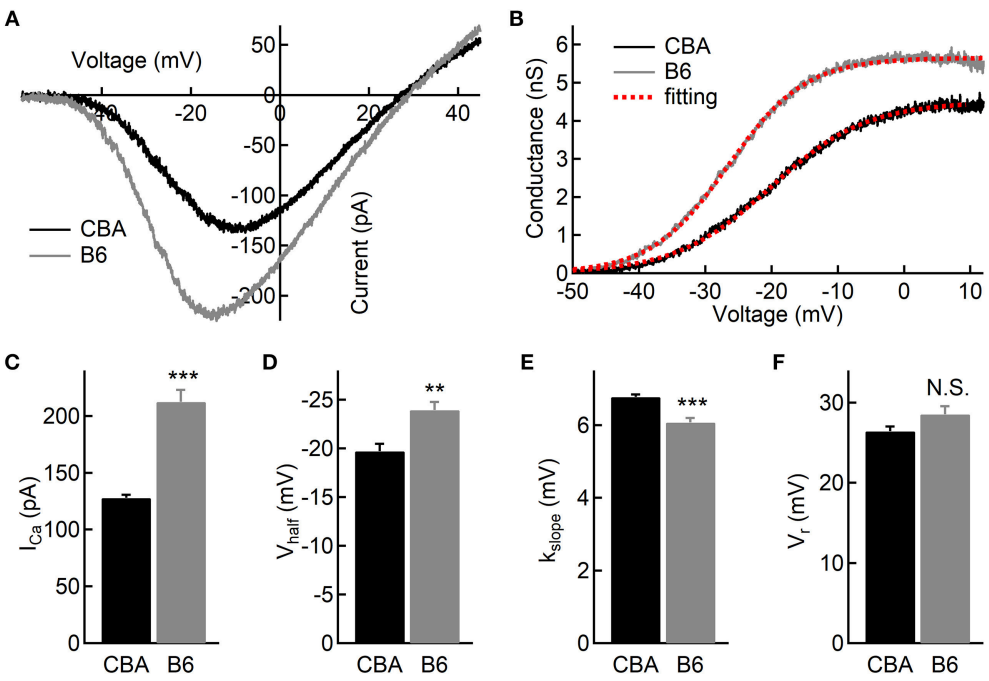


FIGURE 2 | Ca^{2+} current in inner hair cells (IHCs) of CBA and B6 mice. **(A)** Representative Ca^{2+} currents recorded from two IHCs, one from each mouse strain, induced by a voltage ramp from −90 to +50 mV under voltage-clamp. **(B)** Based on the Ca^{2+} current shown in **(A)**, the conductance was calculated point-by-point and plotted against the membrane potential applied. The dashed lines in red depict Boltzmann fitting. **(C–E)** The Ca^{2+} current in IHCs from B6 mice has a larger peak amplitude (I_{Ca}, **C**), a more negative half-activation voltage (V_{half}, **D**) and a steeper voltage dependency (k_{slope}, **E**). **(F)** No statistical significance was found in the reversal potential of the Ca^{2+} current (V_r) between the two mouse strains. N.S. means $p > 0.05$, ** means $p < 0.01$ and *** means $p < 0.001$.

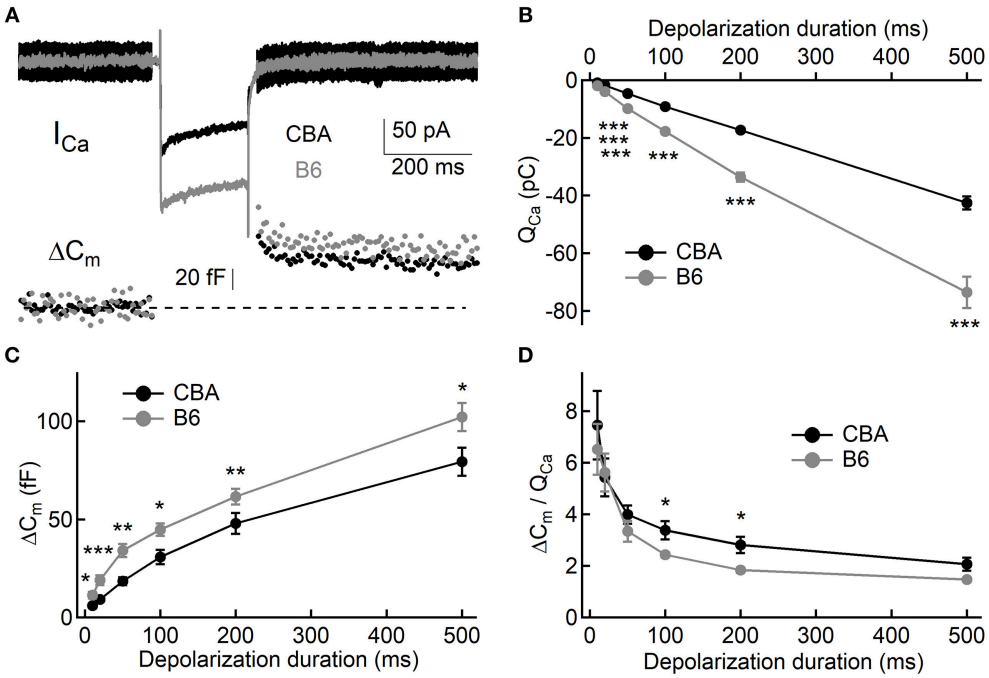


FIGURE 3 | Exocytosis from IHCs. **(A)** Representative Ca^{2+} currents and whole-cell capacitance measurements in two IHCs, one from each mouse strain. Small sine waves were superposed on the holding potential before and after a step depolarization. The step depolarization induced a Ca^{2+} current (I_{Ca}) and triggered exocytosis, which can be quantified with capacitance increase (ΔC_m). **(B,C)** Both Ca^{2+} influx (Q_{Ca}, **B**) and exocytosis (ΔC_m, **C**) are significantly larger in IHCs from B6 mice. **(D)** Ca^{2+} efficiency in triggering exocytosis, i.e., the ratio of $\Delta C_m/Q_{Ca}$, is significantly lower in IHCs from B6 mice. * means $p < 0.05$, ** means $p < 0.01$ and *** means $p < 0.001$.

synaptic vesicles, the Ca^{2+} efficiency of triggering exocytosis, assessed with the ratio of $\Delta C_m/Q_{Ca}$, is less efficient for stimulation of both 100 and 200 ms (**Table 1** and **Figure 3D**). To directly examine synaptic vesicle replenishment, we applied double-pulse stimulation with different intervals and built recovery curves of exocytosis for IHCs from both mouse strains (**Figure 4**). We found that indeed exocytosis recovered quicker for IHCs from B6 mice. For an interval of 50 ms, ΔC_m in CBA mice recovered to 0.35 ± 0.16 ($n = 14$) while ΔC_m in B6 mice recovered to 0.55 ± 0.13 ($n = 13$, unpaired Student's *t*-test, $p < 0.01$). Similar result was observed for an interval of 100 ms (0.49 ± 0.20 vs. 0.70 ± 0.22, $n = 15$ and 12, unpaired Student's *t*-test, $p < 0.05$), reinforcing the idea that synaptic vesicle replenishment is more efficient in IHCs of B6 mice.

Outer Hair Cell (OHC) Function

While the vast majority of auditory signals is conveyed to auditory afferent fibers through IHCs, OHCs play a crucial role in amplifying sound-evoked vibrations and thus their impact on dictating hearing performance cannot be overstated. To assess the OHC function, we performed whole-cell patch-clamp recording and measured whole-cell membrane capacitance with two-sine protocol (Santos-Sacchi and Song, 2014). As previously demonstrated by one of our co-authors, we observed non-linear capacitance in OHCs from both mouse strains, which is directly related to their ability to amplify mechanical vibrations (**Figure 5A**). We then fitted capacitance-voltage relationship to the first derivative of the Boltzmann function, and we found that OHCs from B6 mice have more non-linear capacitance (Q_{max}, 0.72 ± 0.05 vs. 0.86 ± 0.02 pC, for CBA and B6 mice, respectively, $n = 7$ and 5; unpaired Student's *i*-test, $p < 0.001$, **Figure 5B**) and more linear capacitance (C_{lin}, 5.97 ± 0.68 vs. 7.69 ± 0.66 fF, $n = 7$ and 5; unpaired Student's *t*-test, $p < 0.01$, **Figure 5C**). However, when we calculated the ratio of Q_{max}/C_{lin}, we found no significant difference between the two mouse strains (0.12 ± 0.02 vs. 0.11 ± 0.01, $n = 7$ and 5; unpaired Student's *t*-test, $p > 0.05$, **Figure 5D**). Given that the specific membrane capacitance is relatively constant for different cell types (Gentet et al., 2000), C_{lin} is expected to be proportional to the total cell surface area, so that it can be taken as a measurement of cell size. Therefore, our results suggest that although OHCs from B6 mice are larger in size, the prestin density is similar between the two mouse strains. Finally, we observed that activating non-linear capacitance in OHCs from B6 mice required a more depolarized membrane potential (−48.5 ± 4.62 vs. −61.6 ± 3.78 mV, $n = 7$ and 5; unpaired Student's *t*-test, $p < 0.001$, **Figure 5E**), which may have a negative impact on their amplifying capability.

Counting Ribbon Synapses and Spiral Ganglion Cells

It is puzzling that IHCs inB6 mice release more glutamate and thus function more efficiently in activating auditory afferent fibers, yet ABR Wave I amplitude in these mice is smaller

TABLE 1 | Summary of ΔC_m, Q_{Ca}, and $\Delta C_m/Q_{Ca}$ in IHCs.

		10 ms	20 ms	50 ms	100 ms	200 ms	500 ms
ΔC_m	CBA (fF)	6.03 ± 2.06 (n = 11)	9.20 ± 3.95 (n = 17)	18.5 ± 7.75 (n = 15)	30.8 ± 12.7 (n = 12)	43.6 ± 11.4 (n = 11)	79.4 ± 21.3 (n = 9)
	B6 (fF)	13.2 ± 7.44 (n = 10)	22.0 ± 9.80 (n = 11)	32.4 ± 8.86 (n = 17)	43.7 ± 9.43 (n = 10)	61.3 ± 12.4 (n = 7)	107.2 ± 22.5 (n = 8)
P-value		Mann-Whitney tests (p = 0.015)	Unpaired student's t-test (p = 0.0004)	Unpaired student's t-test (p = 0.0013)	Unpaired student's t-test (p = 0.015)	Unpaired student's t-test (p = 0.007)	Unpaired student's t-test (p = 0.02)
Q_{Ca}	CBA (pC)	−0.91 ± 0.21 (n = 11)	−1.81 ± 0.36 (n = 17)	−4.65 ± 0.83 (n = 15)	−9.14 ± 1.55 (n = 12)	−17.3 ± 2.62 (n = 11)	−42.6 ± 6.95 (n = 9)
	B6 (pC)	−1.96 ± 0.38 (n = 10)	−3.97 ± 0.86 (n = 11)	−9.84 ± 1.23 (n = 17)	17.7 ± 2.70 (n = 10)	−33.6 ± 4.08 (n = 7)	−73.5 ± 15.3 (n = 8)
P-value		Unpaired student's t-test (p < 0.0001)	Unpaired student's t-test (p < 0.0001)	Unpaired student's t-test (p < 0.0001)	Unpaired student's t-test (p < 0.0001)	Unpaired student's t-test (p < 0.0001)	Unpaired student's t-test (p < 0.0001)
$\Delta C_m/Q_{Ca}$	CBA (fF/pC)	7.46 ± 4.39 (n = 11)	5.43 ± 3.04 (n = 17)	3.99 ± 1.36 (n = 15)	3.38 ± 1.22 (n = 12)	2.58 ± 0.81 (n = 11)	1.95 ± 0.76 (n = 9)
	B6 (fF/pC)	6.51 ± 3.13 (n = 10)	5.62 ± 2.41 (n = 11)	3.34 ± 1.08 (n = 17)	2.43 ± 0.33 (n = 10)	1.83 ± 0.28 (n = 7)	1.47 ± 0.18 (n = 8)
P-value		Unpaired student's t-test (p = 0.58)	Unpaired student's t-test (p = 0.86)	Unpaired student's t-test (p = 0.94)	Unpaired student's t-test (p = 0.03)	Mann-Whitney tests (p = 0.046)	Mann-Whitney tests (p = 0.16)

*Summary of ΔC_m, Q_{Ca}, and $\Delta C_m/Q_{Ca}$ from patch-clamp recordings in IHCs (**Figures 3B,C**). Data are presented mean ± SD; n = number of IHCs; statistical tests and p-values are presented for each dataset.*

(**Figure 1D**). To account for this discrepancy, we first wondered that if this is due to a smaller number of spiral ganglion cells (SGNs) contacting each IHC inB6 mice. We thus performed fluorescence staining on whole-mount organs of Corti of both mouse strains. We used two primary antibodies directed against Ribeye, a major structural component of synaptic ribbons (Schmitz et al., 2000), and post-synaptic AMPA receptor subunit 2 (GluR2). We defined each punctum of double staining as a ribbon synapse and we found no significant difference in the number of ribbon synapses per IHC between the two mouse strains (14.5 ± 1.79 vs. 14.9 ± 2.01, for CBA and B6 mice, respectively, $n = 22$ and 28; unpaired Student's t-test, $p > 0.05$; **Figure 6**), consistent with previous studies (Wang and Ren, 2012; Ohlemiller et al., 2016; Hickox et al., 2017; Cui et al., 2018). This result suggests the smaller ABR Wave I amplitude in B6 mice is not due to a smaller number of SGNs contacting each IHC.

Given that B6 mice have significantly larger OHCs (**Figure 5C**), we next wondered if they have fewer OHCs and IHCs, and therefore likely fewer SGNs. To count SGNs, we stained cochleae with TUJ1 (**Figure 7**) and examined cell bodies of SGNs found in cochlear modiolus. For quantitative comparison, we calculated the SGN density as the number of SGNs per 10,000 μm^2 (Leake et al., 2011). In the apical turn, there are indeed fewer SGNs in B6 mouse cochlea (50.2 ± 8.92 vs. 40.9 ± 5.62, for CBA and B6 mice, respectively; $n = 9$ and 12, unpaired Student's t-test, $p < 0.01$, **Figure 7**). Similar results were observed for both medial (49.7 ± 6.68 vs. 43.2 ± 4.52, unpaired Student's t-test, $p < 0.05$) and basal turn (39.2 ± 5.52 vs. 30.5 ± 5.11, unpaired Student's t-test, $p < 0.01$). While we cannot rule out other possibilities, the smaller number of SGNs in B6 mice is likely to contribute to the smaller ABR Wave I amplitude in these animals.

DISCUSSION

Hearing loss is a complex disorder that can be attributed to many genetic and environmental factors, all of which are constantly interacting to shape the hearing performance. As two illustrating examples, CBA and B6 mice have been used extensively to explore mechanisms underlying hearing loss for many years (Li and Hultcrantz, 1994; Spongr et al., 1997; Brewton et al., 2016). B6 mouse strain is a long-lived strain and the most widely used mouse model for studying aging and age-associated diseases. Previous studies have shown that B6 mice carry a specific mutation in *Cdh23*, whose protein product binds with protocadherin 15 and forms tip links between adjacent stereocilia (Ohlemiller, 2006), and mutations in *Cdh23* lead to disorganized hair bundles (Noben-Trauth et al., 2003). Furthermore, it has been shown that hair cells with *Cdh23* mutations are more vulnerable to oxidative stress and more prone to apoptosis (Someya et al., 2009). In this present study, we sought to examine cellular differences in the cochlea of the two mouse strains in their juvenile stage, during which the hearing performance is comparable. We believe that these cellular differences are useful in interpreting current findings *in vivo*, especially those concerning early onset hearing loss and aging of hearing.

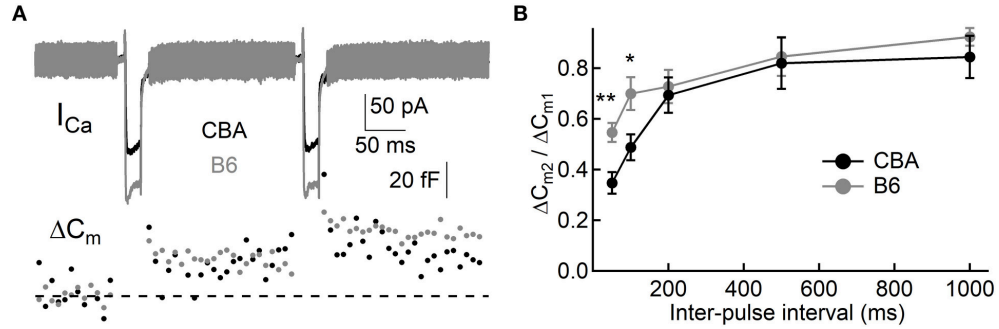


FIGURE 4 | Synaptic vesicle replenishment in IHCs. **(A)** Representative current responses of two IHCs to double pulse stimulation, one from each mouse strain. Both pulses (20 ms) induced notable I_{Ca} and ΔC_m, and the ratio of $\Delta C_{m2}/\Delta C_{m1}$ can be calculated and used to quantify synaptic vesicle replenishment. **(B)** Synaptic vesicle replenishment was significantly faster in IHCs from B6 mice. * means $p < 0.05$ and ** means $p < 0.01$.

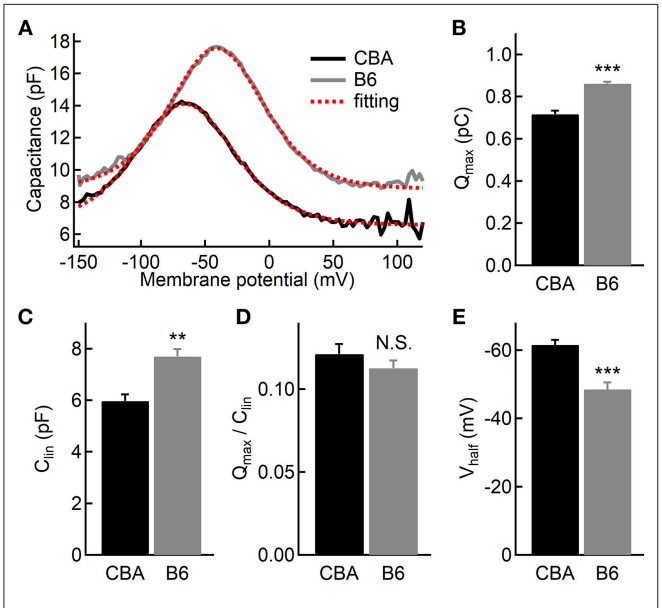


FIGURE 5 | Electromotility of outer hair cells (OHCs). **(A)** Capacitance recordings from two OHCs in response to a voltage ramp. The dashed lines in red depict two-state Boltzmann fitting (see the Materials and Methods). **(B–D)** Both non-linear **(B)** and linear **(C)** capacitances are significantly larger in OHCs from B6 mice, but the ratio of the two parameters is comparable **(D)** between the two mouse strains. **(E)** OHCs from B6 mice had a more positive half-activation voltage (V_{half}). N.S. means $p > 0.05$, ** means $p < 0.01$ and *** means $p < 0.001$.

Hearing relies on faithful transmission of auditory signals from IHCs to SGNs across ribbon synapses in between (Wichmann and Moser, 2015). Voltage-gated Ca^{2+} channels lie beneath synaptic ribbons, and they are activated according to the graded membrane potential in IHCs and modulate exocytosis of synaptic vesicles. We found that Ca^{2+} current in IHCs from B6 mice has a larger peak amplitude and steeper voltage dependence and activates at a more negative membrane potential, all of which may function synergistically to bring substantially more Ca^{2+} influx into the cell under physiological conditions. This excessive load of Ca^{2+} into IHCs is likely to cause excessive exocytosis and glutamate toxicity, which has been directly linked to hearing loss. In addition, the excessive load of Ca^{2+} for a prolonged period of time could cause damages in IHCs by making them more prone to Ca^{2+}-induced cytotoxicity (Verkhratsky and Toescu, 1998).

In response to Ca^{2+} influx, IHCs release glutamate-containing synaptic vesicles through exocytosis at their ribbon synapses. Previous studies have established that exocytosis from hair cells displays an initial quick phase, representing release of synaptic vesicles from the readily releasable pool (RRP), and a sustained release that could last for seconds, owing to the quick and efficient replenishment of synaptic vesicles (Johnson et al., 2005). We found that IHCs from B6 mice release more synaptic vesicles for both short and long step stimulations, suggesting that IHCs from these mice not only have a larger RRP but also replenish synaptic vesicles more quickly. Indeed, when we applied double-pulse stimulation, we found that exocytosis from B6 IHCs recovers more quickly, which is probably due to the greater Ca^{2+} influx (Babai et al., 2010). Interestingly, we found that Ca^{2+} is less efficient in triggering synaptic vesicle releases in IHCs from B6 mice. Owing to the greater Ca^{2+} influx, IHCs in B6 mice manage to release significantly more synaptic vesicles. This excessive release of synaptic vesicles could cause glutamate toxicity, which accumulates over time and eventually causes early onset hearing loss found in this strain of mice. However, while we would like suggest thatB6 mice are more prone to glutamate toxicity, it has been well documented that these mice show resistance to hidden hearing loss, a condition caused, at least in part, by glutamate toxicity (Shi et al., 2015a,b). It is likely that early onset hearing loss and hidden hearing loss are mediated through overlapping yet distinct mechanisms, and the involvement of glutamate toxicity in either condition remained to be carefully examined.

It is perplexing that although IHCs in B6 mice release more glutamate but the ABR Wave I amplitude is not any larger in these animals. On the contrary, it is indistinguishable from that of CBA mice for low SPLs, and it is even smaller when SPL increases beyond 70 dB. The ABR wave I amplitude represents sound-evoked spikes of all responding SGNs, and there is a strong correlation between the number of ribbon synapses and

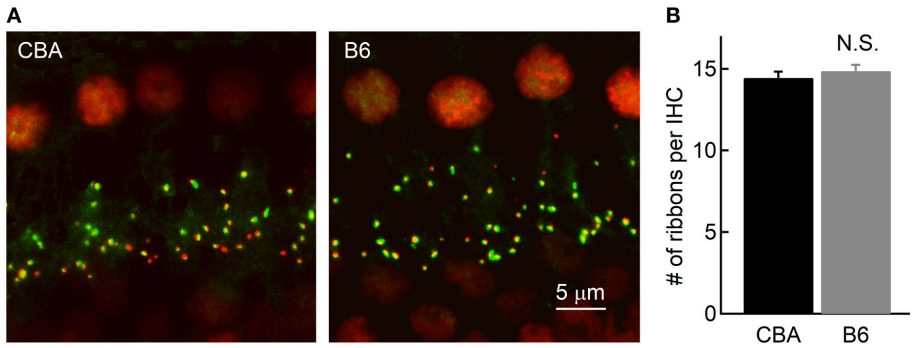


FIGURE 6 | Counting the number of ribbon synapses in IHCs. **(A)** Confocal images of whole-mount immunostaining of two cochleae in the apical turn, which were double stained for CtBP2 (red) and GluR2 (green). **(B)** Ribbon synapses were counted based on fluorescence puncta, as shown in **(A)**. Note that the cochleae of the two mouse strains have a similar number of ribbon synapses per IHC.

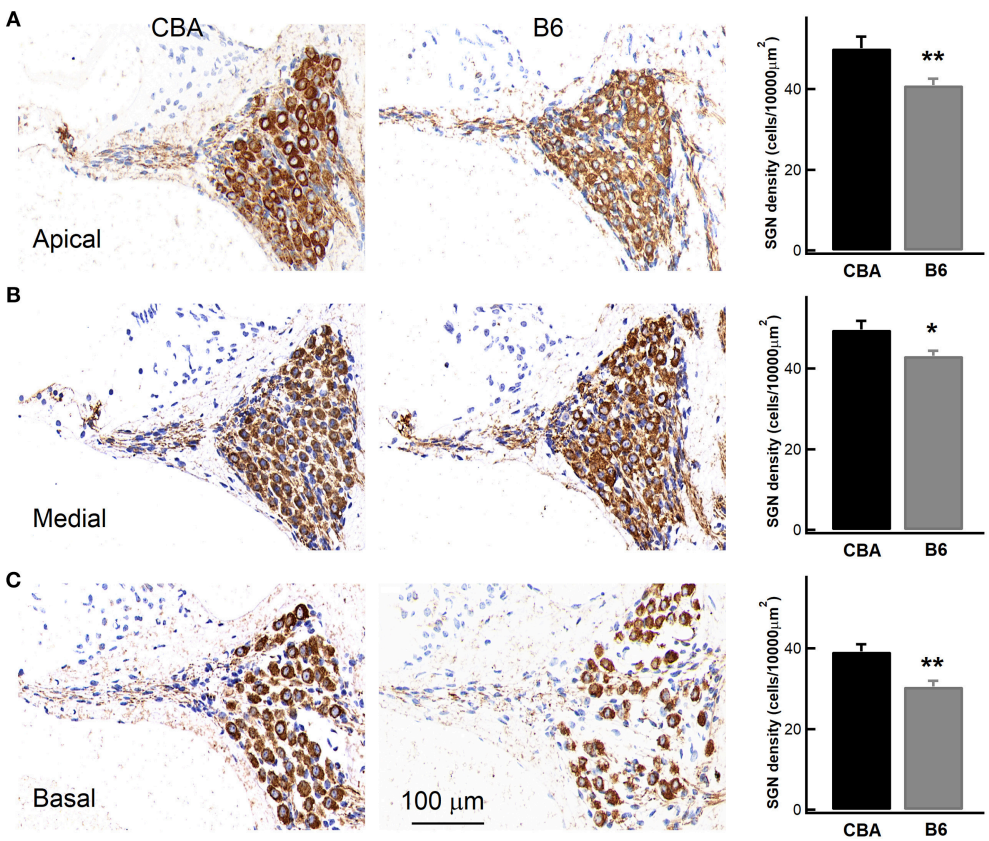


FIGURE 7 | Examining the density of spiral ganglion neurons (SGNs) in the cochlea. Left, staining of cochlear sections in the apical **(A)**, medial **(B),** and basal turn **(C)**. SGNs were stained with an antibody, which is depicted in brown. Right, SGN density, quantified as the number of SGNs per 10,000 μm^2, was pooled from multiple experiments, showing that the B6 cochleae have significantly lower SGN density for all the three turns. * means $p < 0.05$ and ** means $p < 0.01$.

the ABR Wave I amplitude (Altschuler et al., 2015). Therefore, we examined both the number of ribbon synapses per IHC and the total number of SGNs in the apical turn in both mouse strains, and we found that while the number of ribbon synapses per IHC is similar between the two mouse strains, B6 mice have significantly fewer SGNs, which could account for the smaller ABR Wave I amplitude found in these animals (Lenzi et al., 2002; Pangrsic et al., 2015). Furthermore, we also found B6 mice have fewer SGNs at the medial and basal turn, which could contribute to the smaller ABR Wave I amplitude for louder sounds because louder sounds at 8 kHz are likely to activate SGNs in the medial and basal turn (Taberner and Liberman, 2005) and B6 mice have fewer SGNs available to be recruited across all frequencies.

The cochlear outer hair cells (OHCs) have been shown to be capable of amplifying sound-evoked vibrations (Santos-Sacchi and Dilger, 1988), owing to dense expression of the motor protein prestin in their lateral membrane. Therefore, changesin the prestin density in OHCs could have a significant impact on hearing sensitivity, which could be an underlying mechanism for hearing loss (Hoben et al., 2017). We thus examined the OHC function in both mouse strains by measuring linear and non-linear capacitance. We found that the prestin density, i.e., the ratio between linear and non-linear capacitance, is similar between the two mouse strains, consistent with the aforementioned finding that the two strains share similar hearing thresholds across all frequencies tested.

In summary, we found IHCs in B6 mice are more prone to Ca^{2+} overload and release excessive glutamate onto auditory afferent fibers, both of which could accumulate over a prolonged time of period and lead to substantial hearing loss. These findings provide useful clues for understanding hearing impairment in general and aging of hearing in particular.

DATA AVAILABILITY

All datasets generated for this study are included in the manuscript and/or the supplementary files.

AUTHOR CONTRIBUTIONS

HW and G-LL designed and supervised the whole study. LS designed the experiments in outer hair cells and GL carried out the experiments. HL, JL, and Y-GG performed the rest of experiments and wrote the manuscript.

ACKNOWLEDGMENTS

This work was supported by two research grants from the National Natural Science Foundation of China to HW (81330023 and 81730028) and an institutional research grant from Shanghai Science and Technology Commission to Shanghai Key Laboratory of Translational Medicine on Ear and Nose Diseases (14DZ2260300).

REFERENCES

Altschuler, R. A., Dolan, D. F., Halsey, K., Kanicki, A., Deng, N., Martin, C., et al. (2015). Age-related changes in auditory nerve-inner hair cell connections, hair cell numbers, auditory brain stem response and gap detection in UM-HET4 mice. *Neuroscience* 292, 22–33. doi: 10.1016/j.neuroscience.2015.01.068

Babai, N., Bartoletti, T. M., and Thoreson, W. B. (2010). Calcium regulates vesicle replenishment at the cone ribbon synapse. *J. Neurosci.* 30, 15866–15877. doi: 10.1523/JNEUROSCI.2891-10.2010

Brewton, D. H., Kokash, J., Jimenez, O., Pena, E. R., and Razak, K. A. (2016). Age-related deterioration of perineuronal nets in the primary auditory cortex of mice. *Front. Aging Neurosci.* 8:270. doi: 10.3389/fnagi.2016.00270

Cui, W., Wang, H., Cheng, Y., Ma, X., Lei, Y., Ruan, X., et al. (2018). Longterm treatment with salicylate enables NMDA receptors and impairs AMPA receptors in C57BL/6J mice inner hair cell ribbon synapse. *Mol. Med. Rep*. 19, 51–58. doi: 10.3892/mmr.2018.9624

Davis, R. R., Newlander, J. K., Ling, X., Cortopassi, G. A., Krieg, E. F., and Erway, L. C. (2001). Genetic basis for susceptibility to noise-induced hearing loss in mice. *Hear. Res.* 155, 82–90. doi: 10.1016/S0378-5955(01)00250-7

Di Palma, F., Holme, R. H., Bryda, E. C., Belyantseva, I. A., Pellegrino, R., Kachar, B., et al. (2001). Mutations in Cdh23, encoding a new type of cadherin, cause stereocilia disorganization in waltzer, the mouse model for Usher syndrome type 1D. *Nat. Genet.* 27, 103–107. doi: 10.1038/83660

Frisina, R. D., Newman, S. R., and Zhu, X. (2007). Auditory efferent activation in CBA mice exceeds that of C57s for varying levels of noise. *J. Acoust. Soc. Am.* 121, El29–34. doi: 10.1121/1.2401226

Fujimoto, C., Iwasaki, S., Urata, S., Morishita, H., Sakamaki, Y., Fujioka, M., et al. (2017). Autophagy is essential for hearing in mice. *Cell Death Dis.* 8:e2780. doi: 10.1038/cddis.2017.194

Gentet, L. J., Stuart, G. J., and Clements, J. D. (2000). Direct measurement of specific membrane capacitance in neurons. *Biophys. J.* 79, 314–320. doi: 10.1016/S0006-3495(00)76293-X

Hickox, A. E., Larsen, E., Heinz, M. G., Shinobu, L., and Whitton, J. P. (2017). Translational issues in cochlear synaptopathy. *Hear. Res.* 349, 164–171. doi: 10.1016/j.heares.2016.12.010

Hoben, R., Easow, G., Pevzner, S., and Parker, M. A. (2017). Outer hair cell and auditory nerve function in speech recognition in quiet and in background noise. *Front. Neurosci.* 11:157. doi: 10.3389/fnins.2017.00157

Jimenez, A. M., Stagner, B. B., Martin, G. K., and Lonsbury-Martin, B. L. (1999). Age-related loss of distortion product otoacoustic emissions in four mouse strains. *Hear. Res.* 138, 91–105. doi: 10.1016/S0378-5955(99)00154-9

Johnson, S. L., Marcotti, W., and Kros, C. J. (2005). Increase in efficiency and reduction in Ca2+ dependence of exocytosis during development of mouse inner hair cells. *J. Physiol.* 563, 177–191. doi: 10.1113/jphysiol.2004.074740

Kazmierczak, P., Sakaguchi, H., Tokita, J., Wilson-Kubalek, E. M., Milligan, R. A., Muller, U., et al. (2007). Cadherin 23 and protocadherin 15 interact to form tip-link filaments in sensory hair cells. *Nature* 449, 87–91. doi: 10.1038/nature06091

Lagziel, A., Ahmed, Z. M., Schultz, J. M., Morell, R. J., Belyantseva, I. A., and Friedman, T. B. (2005). Spatiotemporal pattern and isoforms of cadherin 23 in wild type and waltzer mice during inner ear hair cell development. *Dev. Biol.* 280, 295–306. doi: 10.1016/j.ydbio.2005.01.015

Leake, P. A., Hradek, G. T., Hetherington, A. M., and Stakhovskaya, O. (2011). Brain-derived neurotrophic factor promotes cochlear spiral ganglion cell survival and function in deafened, developing cats. *J. Comp. Neurol.* 519, 1526–1545. doi: 10.1002/cne.22582

Lenzi, D., Crum, J., Ellisman, M. H., and Roberts, W. M. (2002). Depolarization redistributes synaptic membrane and creates a gradient of vesicles on the synaptic body at a ribbon synapse. *Neuron* 36, 649–659. doi: 10.1016/S0896-6273(02)01025-5

Li, H. S., and Hultcrantz, M. (1994). Age-related degeneration of the organ of Corti in two genotypes of mice. *ORL J. Otorhinolaryngol. Relat. Spec.* 56, 61–67. doi: 10.1159/000276611

Mammano, F., and Bortolozzi, M. (2018). Ca(2+) signaling, apoptosis and autophagy in the developing cochlea: milestones to hearing acquisition. *Cell Calcium* 70, 117–126. doi: 10.1016/j.ceca.2017.05.006

Michel, V., Goodyear, R. J., Weil, D., Marcotti, W., Perfettini, I., Wolfrum, U., et al. (2005). Cadherin 23 is a component of the transient lateral links in the developing hair bundles of cochlear sensory cells. *Dev. Biol.* 280, 281–294. doi: 10.1016/j.ydbio.2005.01.014

Neher, E., and Marty, A. (1982). Discrete changes of cell membrane capacitance observed under conditions of enhanced secretion in bovine adrenal chromaffin cells. *Proc. Natl. Acad. Sci. U.S.A.* 79, 6712–6716. doi: 10.1073/pnas.79.21.6712

Nemoto, M., Morita, Y., Mishima, Y., Takahashi, S., Nomura, T., Ushiki, T., et al. (2004). Ahl3, a third locus on mouse chromosome 17 affecting age-related hearing loss. *Biochem. Biophys. Res. Commun.* 324, 1283–1288. doi: 10.1016/j.bbrc.2004.09.186

Noben-Trauth, K., Zheng, Q. Y., and Johnson, K. R. (2003). Association of cadherin 23 with polygenic inheritance and genetic modification of sensorineural hearing loss. *Nat. Genet.* 35, 21–23. doi: 10.1038/ng1226

Ohlemiller, K. K. (2006). Contributions of mouse models to understanding of age- and noise-related hearing loss. *Brain Res.* 1091, 89–102. doi: 10.1016/j.brainres.2006.03.017

Ohlemiller, K. K., Jones, S. M., and Johnson, K. R. (2016). Application of mouse models to research in hearing and balance. *J. Assoc. Res. Otolaryngol.* 17, 493–523. doi: 10.1007/s10162-016-0589-1

Pangrsic, T., Gabrielaitis, M., Michanski, S., Schwaller, B., Wolf, F., Strenzke, N., et al. (2015). EF-hand protein Ca2+ buffers regulate Ca2+ influx and exocytosis in sensory hair cells. *Proc. Natl. Acad. Sci. U.S.A.* 112, E1028–1037. doi: 10.1073/pnas.1416424112

Park, S. N., Back, S. A., Choung, Y. H., Kim, H. L., Akil, O., Lustig, L. R., et al. (2011). Alpha-Synuclein deficiency and efferent nerve degeneration in the mouse cochlea: a possible cause of early-onset presbycusis. *Neurosci. Res.* 71, 303–310. doi: 10.1016/j.neures.2011.07.1835

Park, S. N., Back, S. A., Park, K. H., Kim, D. K., Park, S. Y., Oh, J. H., et al. (2010). Comparison of cochlear morphology and apoptosis in mouse models of presbycusis. *Clin. Exp. Otorhinolaryngol.* 3, 126–135. doi: 10.3342/ceo.2010.3.3.126

Santos-Sacchi, J., and Dilger, J. P. (1988). Whole cell currents and mechanical responses of isolated outer hair cells. *Hear. Res.* 35, 143–150. doi: 10.1016/0378-5955(88)90113-X

Santos-Sacchi, J., and Song, L. (2014). Chloride-driven electromechanical phase lags at acoustic frequencies are generated by SLC26a5, the outer hair cell motor protein. *Biophys. J.* 107, 126–133. doi: 10.1016/j.bpj.2014.05.018

Schmitz, F., Konigstorfer, A., and Sudhof, T. C. (2000). RIBEYE, a component of synaptic ribbons: a protein's journey through evolution provides insight into synaptic ribbon function. *Neuron* 28, 857–872. doi: 10.1016/S0896-6273(00)00159-8

Schuknecht, H. F., and Gacek, M. R. (1993). Cochlear pathology in presbycusis. *Ann. Otol. Rhinol. Laryngol.* 102, 1–16. doi: 10.1177/00034894931020S101

Shi, L., Guo, X., Shen, P., Liu, L., Tao, S., Li, X., et al. (2015b). Noise-induced damage to ribbon synapses without permanent threshold shifts in neonatal mice. *Neuroscience* 304, 368–377. doi: 10.1016/j.neuroscience.2015.07.066

Shi, L., Liu, K., Wang, H., Zhang, Y., Hong, Z., Wang, M., et al. (2015a). Noise induced reversible changes of cochlear ribbon synapses contribute to temporary hearing loss in mice. *Acta Otolaryngol.* 135, 1093–1102. doi: 10.3109/00016489.2015.1061699

Siemens, J., Lillo, C., Dumont, R. A., Reynolds, A., Williams, D. S., Gillespie, P. G., et al. (2004). Cadherin 23 is a component of the tip link in hair-cell stereocilia. *Nature* 428, 950–955. doi: 10.1038/nature02483

Someya, S., Xu, J., Kondo, K., Ding, D., Salvi, R. J., Yamasoba, T., et al. (2009). Age-related hearing loss in C57BL/6J mice is mediated by Bak-dependent mitochondrial apoptosis. *Proc. Natl. Acad. Sci. U.S.A.* 106, 19432–19437. doi: 10.1073/pnas.0908786106

Song, L., McGee, J., and Walsh, E. J. (2006). Frequency- and level-dependent changes in auditory brainstem responses (ABRS) in developing mice. *J. Acoust. Soc. Am.* 119, 2242–2257. doi: 10.1121/1.2180533

Spongr, V. P., Flood, D. G., Frisina, R. D., and Salvi, R. J. (1997). Quantitative measures of hair cell loss in CBA and C57BL/6 mice throughout their life spans. *J. Acoust. Soc. Am.* 101, 3546–3553. doi: 10.1121/1.418315

Taberner, A. M., and Liberman, M. C. (2005). Response properties of single auditory nerve fibers in the mouse. *J. Neurophysiol.* 93, 557–569. doi: 10.1152/jn.00574.2004

Verkhratsky, A., and Toescu, E. C. (1998). Calcium and neuronal ageing. *Trends Neurosci.* 21, 2–7. doi: 10.1016/S0166-2236(97)01156-9

Wang, Y., and Ren, C. (2012). Effects of repeated "benign" noise exposures in young CBA mice: shedding light on age-related hearing loss. *J. Assoc. Res. Otolaryngol.* 13, 505–515. doi: 10.1007/s10162-012-0329-0

Wichmann, C., and Moser, T. (2015). Relating structure and function of inner hair cell ribbon synapses. *Cell Tissue Res.* 361, 95–114. doi: 10.1007/s00441-014-2102-7

Conflict of Interest Statement: The authors declare that the research was conducted in the absence of any commercial or financial relationships that could be construed as a potential conflict of interest.

Copyright © 2019 Liu, Li, Lu, Gao, Song, Li and Wu. This is an open-access article distributed under the terms of the Creative Commons Attribution License (CC BY). The use, distribution or reproduction in other forums is permitted, provided the original author(s) and the copyright owner(s) are credited and that the original publication in this journal is cited, in accordance with accepted academic practice. No use, distribution or reproduction is permitted which does not comply with these terms.

frontiers in Cellular Neuroscience

ORIGINAL RESEARCH
published: 04 April 2019
doi: 10.3389/fncel.2019.00120

The Fine Tuning of Drp1-Dependent Mitochondrial Remodeling and Autophagy Controls Neuronal Differentiation

Chiara Vantaggiato[1], Marianna Castelli[1], Matteo Giovarelli[2], Genny Orso[3], Maria Teresa Bassi[1], Emilio Clementi[1,2] and Clara De Palma[4]*

[1]Scientific Institute, IRCCS E. Medea, Laboratory of Molecular Biology, Lecco, Italy, [2]Unit of Clinical Pharmacology, Department of Biomedical and Clinical Sciences "Luigi Sacco", "Luigi Sacco" University Hospital, Università di Milano, Milan, Italy, [3]Department of Pharmaceutical and Pharmacological Sciences, University of Padova, Milan, Italy, [4]Unit of Clinical Pharmacology, "Luigi Sacco" University Hospital, ASST Fatebenefratelli Sacco, Milan, Italy

Mitochondria play a critical role in neuronal function and neurodegenerative disorders, including Alzheimer's, Parkinson's and Huntington diseases and amyotrophic lateral sclerosis, that show mitochondrial dysfunctions associated with excessive fission and increased levels of the fission protein dynamin-related protein 1 (Drp1). Our data demonstrate that Drp1 regulates the transcriptional program induced by retinoic acid (RA), leading to neuronal differentiation. When Drp1 was overexpressed, mitochondria underwent remodeling but failed to elongate and this enhanced autophagy and apoptosis. When Drp1 was blocked during differentiation by overexpressing the dominant negative form or was silenced, mitochondria maintained the same elongated shape, without remodeling and this increased cell death. The enhanced apoptosis, observed with both fragmented or elongated mitochondria, was associated with increased induction of unfolded protein response (UPR) and ER-associated degradation (ERAD) processes that finally affect neuronal differentiation. These findings suggest that physiological fission and mitochondrial remodeling, associated with early autophagy induction are essential for neuronal differentiation. We thus reveal the importance of mitochondrial changes to generate viable neurons and highlight that, rather than multiple parallel events, mitochondrial changes, autophagy and apoptosis proceed in a stepwise fashion during neuronal differentiation affecting the nuclear transcriptional program.

Keywords: Drp1, neuronal differentiation, mitochondrial remodeling, autophagy, mitochondrial fission

OPEN ACCESS

Edited by:
Xin Qi,
Case Western Reserve University, United States

Reviewed by:
Amit U. Joshi,
Stanford University, United States
Ozgun Gokce,
Ludwig Maximilian University of Munich, Germany

****Correspondence:***
Chiara Vantaggiato
chiara.vantaggiato@lanostrafamiglia.it

Received: *14 September 2018*
Accepted: *11 March 2019*
Published: *04 April 2019*

Citation:
Vantaggiato C, Castelli M, Giovarelli M, Orso G, Bassi MT, Clementi E and De Palma C (2019) The Fine Tuning of Drp1-Dependent Mitochondrial Remodeling and Autophagy Controls Neuronal Differentiation. Front. Cell. Neurosci. 13:120. doi: 10.3389/fncel.2019.00120

Abbreviations: Drp1, dynamin-related protein 1; eIF2α, eukaryotic translation initiation factor 2 alpha; ERAD, ER-associated degradation; ESCs, embryonic stem cells; Fis1, fission 1; Mff, mitochondrial fission factor; Mfn1, mitofusins 1; Mfn2, mitofusins 2; MiD, mitochondrial dynamics proteins; mtCO1, mitochondrial Cytochrome C Oxidase I; mtDNA, mitochondrial DNA; Opa1, optic atrophy 1 protein; RA, retinoic acid; TMRM, tetramethylrhodamine methyl ester; UPR, unfolded protein response; VDAC, voltage-dependent anion channels.

INTRODUCTION

Mitochondrial dynamics and the balance between fusion and fission are key adaptative mechanisms to the metabolic needs of the cell (Gomes et al., 2011; Schrepfer and Scorrano, 2016). Recent evidence suggests that mitochondrial activity, shape and localization have an impact on nuclear programs and ultimately, cell fate. Therefore mitochondria are directly involved in differentiation and developmental processes (Kasahara and Scorrano, 2014). Mitochondria morphology, distribution and function are regulated by fusion and fission in response to the cellular environment and differentiation (Chang et al., 2006; Saxton and Hollenbeck, 2012). Three large GTPases are involved in mitochondrial fusion: Mitofusins 1 and 2 (Mfn1 and Mfn2), that mediate outer mitochondrial membrane fusion, and Optic atrophy 1 protein (Opa1), the mediator of inner-membrane fusion (Chan, 2012). Mitochondrial fission is coordinated by dynamin-related protein 1 (Drp1), mitochondrial adaptors, such as mitochondrial fission factor (Mff), the 49 and 51 kDa Mitochondrial Dynamics proteins (MiD49 and MiD51) and fission 1 (Fis1; Chan, 2012; Otera et al., 2013), and cytoplasmic elements. Among these, Drp1 is the major regulator of mitochondrial shape, distribution and maintenance (Reddy et al., 2011). Drp1 acts as a cytosolic receptor, linking fission and mitochondrial function to the cytoplasmic state of the cell. For instance changes in cytosolic Ca^{2+} levels activates the Ca^{2+}-dependent phosphatase calcineurin enhancing Drp1 dephosphorylation on Ser637 and its translocation to mitochondria (Cereghetti et al., 2008). Conversely, cyclic AMP activates protein kinase A (PKA), resulting in inhibitory phosphorylation of Ser637 that blocks Drp1 translocation and promotes mitochondrial elongation (Cribbs and Strack, 2007).

Fission and fusion imbalance is a pathogenic mechanism common to many processes such as apoptosis, autophagy, aging and neurodegeneration and is correlated to myopathies, obesity, diabetes, cancer and neurodegenerative diseases (Wallace, 2005; Liesa et al., 2009; Itoh et al., 2013). The brain consumes about 20% of the body's energy and considering its greatly metabolic activity, the delicate maintenance of mitochondrial function is essential for neurons (Chen and Chan, 2006; Kann and Kovács, 2007). As highly polarized cells, neurons require a suitable and appropriate distribution of mitochondria to provide energy fuel for neuronal activities, such as synaptic transmission, axonal and dendritic transport, and synaptic vesicle recycling (Li et al., 2004). This is allowed by mitochondrial fission and fusion that maintains cell bioenergetics and regulates mitochondria trafficking along the axons and at the synapses (Li et al., 2004, 2008; Chen and Chan, 2006). Mice lacking Drp1 die during embryogenesis and show neuronal development defects with depletion of mitochondria from neurites, reduced neurite outgrowth and impaired synapses formation (Ishihara et al., 2009; Wakabayashi et al., 2009; Kageyama et al., 2014). Drp1 and mitochondrial dynamics have also a role in the induction of pluripotent stem cells (iPSCs) from somatic cells (Xu et al., 2013; Wang et al., 2014; Prieto et al., 2016) and Drp1 depletion in mouse embryonic stem cells (ESCs) reduces the differentiation capacity to neurogenesis (Wang et al., 2014). Alterations in fission and fusion genes are associated with several neurodegenerative diseases: Mfn2 and Opa1 mutations are responsible for Charcot-Marie-Tooth (CMT) type 2A (Züchner et al., 2004) and dominant optic atrophy (DOA; Delettre et al., 2000) respectively, while Drp1 mutations have been associated with abnormal brain development (Waterham et al., 2007; Chang et al., 2010) and optic atrophy (Gerber et al., 2017).

Increased Drp1 expression and mitochondrial fragmentation are early and key events observed in a wide range of neurodegenerative disorders (Hu et al., 2017), including Alzheimer's (Cho et al., 2009; Manczak et al., 2011; Manczak and Reddy, 2012), Huntington's (Costa et al., 2010; Song et al., 2011; Shirendeb et al., 2012) and Parkinson's diseases (Wang et al., 2011). Abnormal interactions between Drp1 and amyloid beta, phosphorylated Tau and Huntingtin proteins have also been reported (Wang et al., 2011; Manczak and Reddy, 2012). Increasing evidence indicates that mitochondrial dynamics also influence complex signaling pathways, affecting gene expression and cell differentiation (Kasahara and Scorrano, 2014), and that Drp1 and mitochondrial fission also plays a role in these processes. Indeed, migrating adult neural stem cells require appropriate Drp1 activity to maintain an efficient ATP synthesis and to differentiate properly (Kim et al., 2015). Moreover, NGF-induced neuronal differentiation is accompanied by higher Drp1 phosphorylation levels, early-upregulation of Opa1 and later induction of Mfn2, accounting for constant remodeling of mitochondria to suit morphological and functional changes of post-mitotic neurons (Martorana et al., 2018).

So far, the majority of the data available on Drp1 concerns the effects of the inhibition of mitochondrial fission by Drp1 silencing; considering the association between neurological disorders and high Drp1 levels we focused our study on the effects of increased levels of Drp1 on neuronal differentiation of P19 cells, a suitable model for the study of mammalian neuronal cell pathophysiology (Bain et al., 1994; Vantaggiato et al., 2009, 2011). In the presence of retinoic acid (RA) P19 cells form aggregates and differentiate into neurons and glia in a chronological order similar to that of cell differentiation in the brain. For this cell line an accurate protocol of neuronal differentiation was established (Bain et al., 1994) and we previously characterized morphological and biochemical markers specific for the different stages of the process (Vantaggiato et al., 2009, 2011). By genetically modulating Drp1, we found that the process of neuronal differentiation can be modified by changes in Drp1 levels and function, such that it is severely impaired by both Drp1 overexpression and depletion or inactivation. Increased fission or excessive fusion of mitochondria share similarities in the impairment of neuronal differentiation, inducing a transcriptional reprogramming that affects the response to RA with increased unfolded protein response (UPR) and ER-associated degradation (ERAD) pathways. This study also reveals that mitochondrial changes, autophagy and apoptosis proceed in a stepwise fashion and are permissive events for a correct neuronal differentiation.

MATERIALS AND METHODS

Expression Constructs

pCMV6-MycDDK-Drp1wt and pCMV6-MycDDK-Drp1K38A vectors were purchased from OriGene Technologies, Inc., Rockville, MD, USA. The plasmids for RNA interference studies were purchased from SABiosciences Corporation (Frederick, MD, USA). A set of four different short-hairpin-RNAs (shRNAs) was tested (with neomycin selection or with the GFP reporter gene) and the most efficient one (shRNA1) was chosen. The shRNA specificity was determined by analysis of Drp1 expression levels in P19 cells transiently transfected with the shRNAs or with the scrambled control sequence by quantitative Real-Time PCR.

Generation of Stable Clones

For neuronal differentiation experiments, P19 cells were stably transfected with pcDNA3.1/CTGFP vector alone, pCMV6-MycDDK-Drp1wt, pCMV6-MycDDK-Drp1K38A or Drp1shRNA plasmids, all with neomycin selection gene. Stable transfectants were obtained after selection in 500 μg/ml G418 (Invitrogen, Carlsbad, CA, USA, Thermo Fisher Scientific, Waltham, MA, USA) and Drp1 levels were analyzed by SDS-PAGE and Western Blot. The expression levels of endogenous Drp1 in the shRNA-transfected clones were determined by quantitative Real-Time PCR. For each vector, three different clones with comparable Drp1 levels were used independently in the experiments with similar results. Results shown for each vector are an average of the three clones, whereas limited to immunofluorescence images, we always reported representative pictures taken from the same clone.

Cells Cultures and P19 Cells Neuronal Differentiation

The mouse embryo carcinoma P19 cells (Bain et al., 1994) were grown in Dulbecco's Modified Eagle's Medium (DMEM, Invitrogen, Carlsbad, CA, USA, Thermo Fisher Scientific, Waltham, MA, USA) supplemented with 10% Fetal bovine serum (FBS, Euroclone, Milano, Italy), 100 U/ml penicillin/streptomycin and 2 mM L-glutamine (Invitrogen, Carlsbad, CA, USA, Thermo Fisher Scientific, Waltham, MA, USA). P19 cells were differentiated into neurones and glial cells with 5 μM *all trans*-RA (Sigma-Aldrich, San Louis, MO, USA) for 4 days in bacteriological non-adhesive plates. Aggregates were then dissociated with trypsin, suspended in Neurobasal medium with N2 supplement (Invitrogen, Carlsbad, CA, USA, Thermo Fisher Scientific, Waltham, MA, USA) and 0.5 mM L-glutamine and plated onto 6-well plates coated with 100 μg/ml poly-L-lysine (Sigma-Aldrich, St. Louis, MO, USA), 1×10^6 cells/well. For immunofluorescence, analysis cells were seeded on poly-L-lysine coated coverslip. Cells were cultured for a total of 14 days. Duplicate samples for each day were used for RNA or protein extraction.

mRNA Levels Analysis

RNA was prepared using Trizol (Invitrogen, Carlsbad, CA, USA, Thermo Fisher Scientific, Waltham, MA, USA) and 1 μg/samples were reverse-transcribed into cDNA using the Superscript First Strand Synthesis System for RT-PCR kit (Invitrogen, Carlsbad, CA, USA, Thermo Fisher Scientific, Waltham, MA, USA) and random hexamers. The expression levels of Drp1, Mash1, Wnt1, Oct3/4, Sox2, Opa1, Mfn1, Mfn2, Fis1, MAP2, Tubulin beta III and Gap43 were analyzed by quantitative Real-Time PCR on an ABI PRISM® 7900HT Fast Real-Time PCR Systems (Applied Biosystems, Foster City, CA, USA) using specific gene expression assays. TATA box binding protein (Tbp) was used for normalization. The expression levels of GP78, HRD1, GRP78, GRP94, CHOP and GADD34 were analyzed by quantitative Real Time PCR on the same instrument using specific primers. 36B4 was used for normalization. Primers used were: GRP78 F: 5′-TGTGGTACCCACCAAGAAGTC-3′ and R: 5′-TTCAG CTGTCACTCGGAGAAT-3′; GRP94 F: 5′-CTCAGAAGACGC AGAAGACTCA-3′ and R: 5′-AAAACTTCACATTCCCTCT CCA-3′; CHOP F: 5′-ATATCTCATCCCCAGGAAACG-3′ and R: 5′-TCTTCCTTGCTCTTCCTCCTC-3′; GADD34 F: 5′-GAG GGACGCCCACAACTTC-3′ and R: 5′-TTACCAGAGACA GGGGTAGGT-3′; GP78 F: 5′-AGCCTGTTCGTGTGGGTTC-3′ and R: 5′-AAATCTGTCTTTGCAGAGCTGAA-3′; HRD1 F: 5′-CGTGTGGACTTTATGGAACGC-3′ and R: 5′-CGGGTC AGGATGCTGTGATAAG-3′; 36B4 F: 5′-AGATTCGGGATAT GCTGTTGG 3′ and R: 5′-AAAGCCTGGAAGAAGGAGG TC-3′. Undifferentiated P19 cells stably transfected with the vector alone were used as endogenous control. Data were analyzed using the delta-delta-Ct method.

Quantification of Mitochondrial DNA

Mitochondrial DNA (mtDNA) was quantified as described with slight modifications (Mouchiroud et al., 2013; De Palma et al., 2014). Total DNA was isolated from undifferentiated P19 cell clones using the QIAamp DNA mini kit (Sigma-Aldrich, St. Louis, MO, USA) according to the manufacturer's instructions. The mtDNA content was measured by Real Time PCR by using specific primers for the not-polymorphic mitochondrial gene (NADH dehydrogenase 1, ND1). The single-copy nuclear gene RNAse P was used for normalization. Primers used were: mtND1 F: 5′-CCTATCACCCTTGCCATCAT-3′ and R: 5′-GAG GCTGTTGCTTGTGTGAC-3′; RNAse P F: 5′-GAAGGCTCT GCGCGGACTCG-3′ and R: 5′-CGAGAGACCGGAATGGGGC CT-3′. Undifferentiated P19 cells stably transfected with the vector alone were used as endogenous control. Data were analyzed using the delta-delta-Ct method.

Mitochondria Isolation

For mitochondria isolation, undifferentiated and differentiated P19 cell clones were washed in PBS and suspended in ice-cold lysis buffer (0.3 M sucrose, 10 mM MES, 1 mM $MgSO_4$, 1 mM KCl supplemented with proteases inhibitor cocktail from Sigma-Aldrich, St. Louis, MO, USA). Cells were sonicated and centrifuged at 1,500 rpm for 5 min at 4°C to pellet nuclei and cellular debris. Supernatants containing the mitochondrial fraction were collected and centrifuged at 10,000 rpm for 10 min at 4°C. Pellets were suspended in lysis buffer, assayed and subjected to SDS-PAGE and Western Blot. Voltage-dependent anion channels (VDAC) and GAPDH were used as mitochondrial and cytosolic markers, respectively.

Immunoprecipitation

Cells were lysed in ice-cold lysis buffer (20 mM Tris-HCl pH 7.4, 150 mM NaCl, 0.1% Triton X-100, 10 mM $MgCl_2$, 0.4 mM PMSF and protease inhibitor cocktail), sonicated and centrifuged at 13,000 rpm for 10 min at 4°C. Supernatants were assayed and an equal amount of total proteins for each cell line was immunoprecipitated with GTP-agarose beads (Sigma-Aldrich, St. Louis, MO, USA), that specifically binds GTP-bound proteins. Samples were rotated for 1 h at 4°C, immune-complexes were then washed three times with lysis buffer, eluted in 5× sample buffer plus 1 mM DTT at 95°C for 5 min and subjected to SDS-PAGE and Western Blot.

SDS-PAGE and Western Blot

Cells were lysed in Tris-HCl 0.125 M pH 6.8 and 2.5% SDS, loaded on 10% or 12% polyacrylamide gel, blotted onto nitrocellulose membranes and probed with the indicated primary antibodies. Horseradish peroxidase-conjugated secondary antibodies were used and signals were detected using ECL (GE Healthcare, Chalfont St. Giles, UK).

Antibodies

Antibodies (Abs) against MAP1LC3B, ERK1/2, phospho-ERK1/2, Akt, phospho-Akt, Smad1, phospho-Ser206-Smad1, GSK3β, phospho-Ser9-GSK3β, active caspase 7, active caspase 9, phospho-eIF2α and eukaryotic translation initiation factor 2 alpha (eIF2α) were purchased from Cell Signaling Technology, Inc. Danvers, MA, USA. Anti-Gap43 and β-actin Abs were purchased from Santa Cruz Biotechnology, Inc. Heidelberg, Germany. Anti-mitochondrial Cytochrome C Oxidase I (mtCO1), VDAC1, Tubulin β-III, MAP2 and Aconitase1 (ACO1) Abs were purchased from Abcam, Cambridge, UK. Anti-DDK Ab was purchased from OriGene Technologies. Anti-OPA1 and Drp1 Abs were purchased from Becton, Dickinson and Company, Franklin Lakes, NJ, USA. Anti-p62 and BNIP3 Abs were purchased from Sigma Aldrich.

Confocal Immunofluorescence

Cells were fixed with 4% paraformaldehyde for 10 min and permeabilized with PBS containing 0.1% saponin and 1% bovine serum albumin for 30 min. Samples were then incubated for 2 h with primary Abs and revealed using the secondary Abs AlexaFluor-488, 546 and 647 (Invitrogen, Carlsbad, CA, USA, Thermo Fisher Scientific, Waltham, MA, USA). For the staining of autophagosomes, cells were transfected with the pCMVMAP1RFPLC3B vector (Addgene, Cambridge, MA, USA). For the staining of mitochondria, cells were transfected with the pDsRed2-Mito vector (Clontech Laboratories, Inc., CA, USA). Nuclei were counterstained with 4′,6′-diamidino-2-phenylindole (DAPI, Sigma-Aldrich, St. Louis, MO, USA). Images were acquired using a Leica TCS SP2 AOBS confocal laser scanning microscope with a 63× oil immersion lens at 1,024 × 1,024 pixels resolution, at the same laser attenuation.

Mitochondria Morphometric Analysis

To quantify mitochondria morphology, an ImageJ macro was used (Dagda et al., 2009). The red channel of cells transfected with pDsRed2-Mito vector was extracted to grayscale, thresholded to optimally resolve individual mitochondria and converted to a binary image. The macro traces mitochondrial outlines using "analyze particles" and quantifies mitochondrial size, interconnectivity and elongation for each mitochondrion. The mitochondrial size was a measure of the area. The mean area/perimeter ratio was used as an index of mitochondrial interconnectivity, while inverse circularity was used as a measure of mitochondrial elongation. Interconnectivity describes the network of the mitochondria and higher scores for interconnectivity indicate that mitochondria have more physical connections, while lower scores indicate more fragmented mitochondria. Elongation describes the shape of mitochondria and a value of 1 would be considered a perfect circle, while a higher value represents elongated mitochondria. For the analysis of mitochondrial branching, the binary image was converted to a skeleton that represents the features in the original image, by using "skeletonize." Finally, the length of each branch and the number of branches were determined by using the "analyze skeleton" plugin (Wiemerslage and Lee, 2016).

Mitochondrial Membrane Potential Analysis

Mitochondria were labeled using tetramethylrhodamine methyl ester (TMRM; ThermoFisher Scientific, Waltham, MA, USA). Cells were seeded in 30 mm culture dish in complete medium and incubated with 100 nM TMRM and 1 μg/ml DAPI for 30 min at 37°C (Vega-Naredo et al., 2014). Images were acquired without replacing the medium, with a Spinning disk Nikon confocal microscope, with a 20× air lens and a 516 × 516 resolution, at the same laser attenuation. Fluorescence intensity was measured using the ImageJ programme as the average pixel intensity within a box of defined size drawn on the cell body. TMRM fluorescence was also determined by using a Fluoroskan (Ascent FL, ThermoFisher Scientific, Waltham, MA, USA). Cells were trypsinized, counted and incubated with 100 nM TMRM for 30 min at 37°C. Fluorescence was measured by using TRITC filter, accordingly to the manufacturer's instruction. After background subtraction, the data were normalized on cell number.

Mitochondria Respiratory Rate

Mitochondria respiratory rates were measured into the O2K oxygraph chambers (Oroboros Instruments, Innsbruck, Austria) at 37°C in the respiration medium MiR06 (0.5 mM EGTA, 3 mM $MgCl_2$, 60 mM K-lactobionate, 20 mM taurine, 10 mM KH_2PO_4 20 mM Hepes, 110 mM sucrose and 1 g/l bovine serum albumin fatty acid-free, 280 U/ml catalase (pH 7.1)).

Drp1 clones were grown in standard conditions and 1×10^6 viable cells were transferred into oxygraph chambers. Oxygen consumption reached a steady state level indicating Basal respiration. The addition of oligomycin (0.5 μM) resulted in Leak respiration. Subsequently, the mitochondrial proton gradient was lost by stepwise titration (0.5 μM each step) of the uncoupler FCCP (Carbonyl cyanide-*4*-(trifluoromethoxy) phenylhydrazone) until the maximum respiration was achieved.

The addition of 0.5 μM rotenone and 2.5 μM antimycin A (AA) blocked mitochondrial respiration, showing residual oxygen consumption. The initial addition of pyruvate (10 mM) and malate (2 mM) was performed to test the integrity of the plasma membrane. Oxygen fluxes were corrected by subtracting residual oxygen consumption from each steady state.

Cell Death Analysis

Control, Drp1wt, Drp1K38A and Drp1shRNA P19 stable clones were induced to differentiate with RA and cell death was analyzed 24 h later using propidium iodide (PI) and DAPI (Hamada-Kanazawa et al., 2004). Cell aggregates were incubated with 3 μM PI (Sigma-Aldrich, St. Louis, MO, USA) and 1 μg/ml DAPI for 15 min at room temperature to stain respectively nuclei of dead and living cells and photographed using a Leica DMIRE2 microscope at 20× magnification and 1,024 × 1,024 pixels resolution. Apoptosis on d1 of neuronal differentiation was quantified by using a DeadEnd Fluorometric TUNEL system kit (Promega, Madison, WI, USA), accordingly with manufacturer's instructions. Briefly, on d1 aggregates were dissociated, counted, fixed in 1% paraformaldehyde for 20 min on ice and permeabilized with PBS containing 0.2% TRITON-X100 for 10 min. Cells were then incubated with the Terminal Deoxynucleotidyl Transferase enzyme at 37°C. Nuclei were counterstained with 1 μg/ml DAPI. TUNEL fluorescence was quantified by using a Fluoroskan with FITC filter. After background subtraction, the data were normalized on cell number.

Apoptosis was detected in the same cells treated with RA after aggregates dissociation on day 5 and 6 of neuronal differentiation using a Caspase 3 Colorimetric Activity Assay kit (Merck Millipore, Burlington, MA, USA), according to the manufacturer's instructions.

Statistical Analysis

One-way or two way ANOVA followed by Sidak's, Dunnett's or Tukey's multiple comparison test were performed using GraphPad Prism version 8.0.1 for Windows, GraphPad Software, San Diego, California USA[1]. Student's *t*-test for unpaired variables (two-tailed) was used for mitochondrial elongation, interconnectivity and branch length control data analysis of **Figure 1E**. Results are reported as individual data plus the mean and standard error of the mean (SEM). p values of less than 0.05 were considered significant. Double or triple symbols refer to statistical probabilities ($p < 0.01$ and <0.001, respectively), measured in the various experimental conditions as detailed in the legend of the figures.

RESULTS

Drp1 and Mitochondrial Remodeling Are Involved in Neuronal Differentiation

We first analyzed changes in Drp1 levels and mitochondrial morphology during neuronal differentiation. We incubated P19 cells with RA for 4 days in floating conditions to induce the formation of neurospheres and neural stem cells that differentiate into neurons after dissociation and plating in adherent conditions on d4 (**Figure 1A**). We found that Drp1 expression levels gradually increased in neural stem cells during RA treatment to rich 2.5–3-fold increase in differentiated neurons (d9-d10; **Figures 1B,C** and **Supplementary Figure S1**), suggesting that the regulation of Drp1 levels could be a key event during neuronal differentiation. Moreover, we found that P19 cells neuronal differentiation is characterized by changes in the expression levels of other fission and fusion genes (**Figure 1D**). Indeed, the expression of the fission gene Fis1 increased in neural stem cells with a peak between d2 and d4 to decrease thereafter. Opa1 decreased after RA addition and remained low or similar to basal for the whole differentiation process. Mfn2 levels increased during neuronal differentiation quadrupling its expression in the later stages (**Figure 1D**). Finally, Mfn1 had a bimodal expression pattern with a peak in the early phase of differentiation around d3 and later on d9.

To assess mitochondrial morphology, cells were transfected with pDsRed2-Mito vector and mitochondrial size, interconnectivity, elongation and branch length were quantified (**Figure 1E** and **Supplementary Figure S2**). We found that differentiated neurons on d6 presented filamentous mitochondria with increased interconnectivity, elongation and branch length compared with undifferentiated cells. Moreover, while undifferentiated cells presented a mixed population of fragmented and elongated mitochondria, differentiated neurons showed a decrease in the percentage of fragmented mitochondria and an increase in the elongated one (**Figure 1E**), confirming changes in mitochondrial morphology observed between undifferentiated P19 cells and neural stem cells on d4 (Vega-Naredo et al., 2014).

Different Expression of Drp1 Impacts on Mitochondrial Morphology and Functionality

We then studied how altered Drp1 levels and increased fragmentation could affect neuronal differentiation. To this purpose, we stably transfected P19 cells with wild-type Drp1 (Drp1wt), the dominant negative mutated form (Drp1K38A), a specific shRNA to silence the gene (Drp1 shRNA) or an empty vector as control. Three clones for each vector with comparable Drp1 expression levels were selected for the experiments. The selected Drp1-silenced clones showed a reduction of 80% in Drp1 expression levels (**Figures 2A,B**), while Drp1 was two-fold increase in Drp1wt and Drp1K38A selected clones (**Figure 2C** and **Supplementary Figure S3**).

Neuronal differentiation in control cells was accompanied by a progressive increase in Drp1 levels (**Figure 1B**); surprisingly this also occurred in Drp1wt and Drp1K38A clones (**Figure 2D**). By contrast, changes in Drp1 levels were not associated with changes in the expression of the other fission and fusion genes, Fis1, Mnf1, Mnf2 and Opa1, in both undifferentiated and differentiated cells (**Supplementary Figures S4A,B**), nor in Opa1 activity (**Supplementary Figures S4C,D**), excluding any compensatory activity.

[1] www.graphpad.com

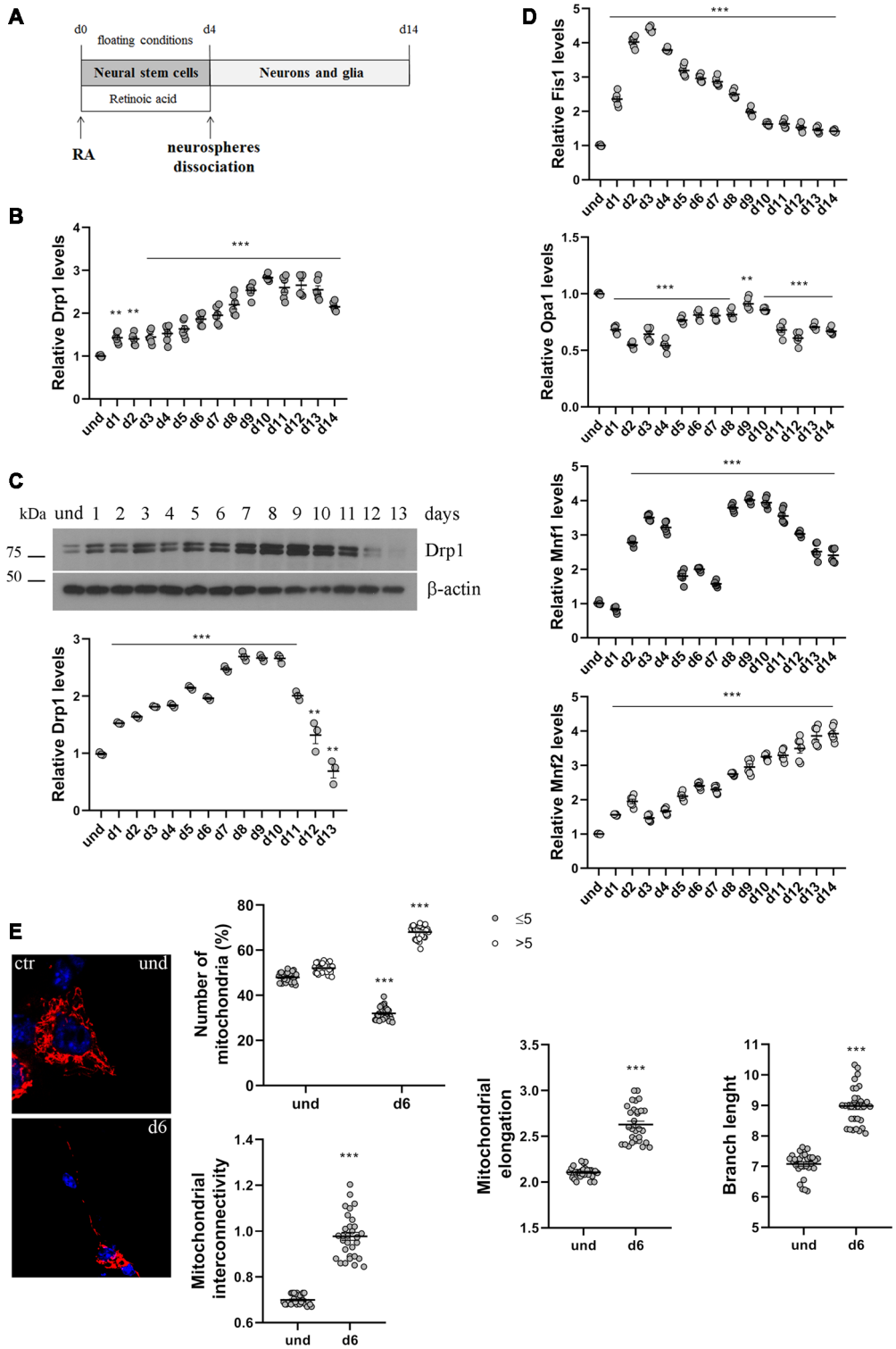


FIGURE 1 | P19 cells neuronal differentiation. **(A)** Schematic representation of P19 cells neuronal differentiation. Cells were incubated with retinoic acid (RA) for 4 days in floating conditions to induce the formation of neurospheres and the differentiation in neural stem cells. On d4 neurospheres were dissociated and plated in adherent conditions to differentiate in neurons and glia. **(B)** Analysis of Drp1 expression levels during neuronal differentiation. P19 cells were induced to differentiate with RA and RNA was extracted every day from d1 to d14 and used to analyze Drp1 expression levels by Real-Time PCR. Results are expressed as fold increase of undifferentiated control cells, used as endogenous control, as individual data plus the mean ± standard error of the mean (SEM) (one-way ANOVA followed by

(*Continued*)

FIGURE 1 | Continued
Dunnett's multiple comparison test, $n = 6$). **(C)** Analysis of Drp1 protein levels during neuronal differentiation. P19 cells were induced to differentiate with RA and total extracts were prepared every day, run on a 10% SDS-polyacrylamide gel and probed with anti Drp1 and actin Abs. Drp1 levels were quantified, normalized on actin levels and expressed as fold increase of undifferentiated cells. The graph shows individual data plus the mean ± SEM (one-way ANOVA followed by Dunnett's multiple comparison test, $n = 6$). Uncropped gels are in **Supplementary Figure S1**. **(D)** Analysis of fission and fusion genes expression levels during neuronal differentiation. RNA extracted every day of neuronal differentiation was used to analyze Opa1, Mfn1, Mfn2 and Fis1 expression levels by Real-Time PCR. Results are expressed as fold increase of undifferentiated control cells, used as endogenous control, as individual data plus the mean ± SEM (one-way ANOVA followed by Dunnett's multiple comparison test, $n = 6$). **(E)** Mitochondrial morphology in undifferentiated and differentiated P19 cells. Undifferentiated cells and neurons on d5 were transfected with the pDsRed2-Mito vector for the staining of mitochondria and fixed after 24 h. Nuclei were stained with DAPI. Image was acquired by confocal microscopy and morphometric analysis was performed with ImageJ. Red channels were converted into a black binary image and skeletonized (binary and skeleton images are in **Supplementary Figure S2**). Mitochondrial interconnectivity, elongation and branch length are showed in the graphs as individual data plus the mean ± SEM (unpaired *t*-test). Mitochondrial interconnectivity is a measure of physical connections and low scores indicate fragmented mitochondria; mitochondrial elongation describes the shape of mitochondria and a value of 1 would be considered a perfect circle, while higher value represents elongated mitochondria. The number of fragmented or elongated mitochondria, with an area lower or higher than 5 μm^2 respectively, was also determined and reported in the graph as individual data plus the mean ± SEM (two-way ANOVA followed by Sidak's multiple comparison test). Data were obtained from three independent experiments for a total of at least 30 cells for each sample. * vs und (***$p < 0.001$; **$p < 0.01$).

Next, we analyzed the effect of Drp1wt, Drp1K38A overexpression and gene silencing on mitochondrial morphology and functionality during neuronal differentiation. Drp1 mostly localizes into the cytoplasm and is recruited to mitochondria membrane to induce fission (Ingerman et al., 2005). We quantified the amount of Drp1 in the mitochondrial fraction in undifferentiated cells and we found that while in control cells 60% of Drp1 was localized in the mitochondria and the remaining 40% was in the cytosol, in Drp1wt and Drp1K38A overexpressing clones Drp1 showed almost a complete translocation on mitochondria (**Figure 2E** and **Supplementary Figure S5**). This mitochondrial recruitment correlated with an increase in Ser616 and a decrease in Ser637 phosphorylation levels in both clones compared with control (**Figure 2F**), a condition that induces Drp1 translocation (Otera et al., 2013). Moreover, we found that neuronal differentiation affected Drp1 translocation on mitochondria *per se*. Indeed, on d6 of neuronal differentiation control cells displayed a complete localization of Drp1 on mitochondria (**Figure 2G** and **Supplementary Figure S5**), while no differences were observed in Drp1-modified clones, showing a complete Drp1 translocation in both undifferentiated and differentiated conditions (**Figures 2E,G**).

We next assessed mitochondrial morphology by staining mitochondria with pDsRed2-Mito vector and quantifying mitochondrial size, interconnectivity, elongation, branch length and the number of fragmented and elongated mitochondria (**Figure 3A** and **Supplementary Figure S6A**). In undifferentiated conditions, Drp1wt overexpressing clones displayed mitochondrial fragmentation with a higher percentage of small round mitochondria (70%) compared with control (40%) and decreased elongation, interconnectivity and branch length (**Figure 3A**), in agreement with the increased translocation of Drp1 on mitochondria. Conversely, Drp1-silenced and Drp1K38A-expressing clones presented filamentous mitochondria, characterized by increased mitochondrial elongation, interconnectivity and branch length compared with control (**Figure 3A**). When we analyzed mitochondrial remodeling during neuronal differentiation we found that mitochondria in differentiated Drp1wt overexpressing clones (d6) presented unchanged elongation but increased interconnectivity and branch length, compared to undifferentiated conditions (d6 vs. und), however, these parameters were still significantly reduced compared to control (**Figure 3B** and **Supplementary Figure S6B**). This indicates that neuronal differentiation activates mitochondrial remodeling in Drp1wt clones, but fails to induce the correct and required elongation. Surprisingly, in Drp1K38A and Drp1-silenced clones mitochondria maintained the same shape in differentiated and undifferentiated conditions, without remodeling (**Figure 3B**, d6 vs. und).

Finally, we investigated mitochondria functionality with TMRM, a red fluorescent dye that is sequestered by active mitochondria, to assess mitochondrial membrane potential. All clones were incubated with TMRM and fluorescence intensity was captured in live cells by confocal microscopy (**Supplementary Figure S7**) and quantified by Fluoroskan (**Figure 3C**). Of note, all Drp1-modified clones presented a decrease in TMRM fluorescence compared with control, indicating low mitochondria membrane potential and likely poor functionality, regardless of morphology. To further assess whether the mitochondrial metabolism was impaired we measured oxygen consumption in undifferentiated clones (**Figure 3D**). In agreement with TMRM analysis, basal mitochondrial respiration was impaired in Drp1wt and Drp1K38A clones compared to control and all Drp1-modified clones were not able to sustain the increased workload driven by the addition of the protonophore FCCP. Consistently, spare respiratory capacity calculated by subtracting basal respiration from FCCP-induced respiration was reduced in all clones, indicating that the alterations of Drp1 levels/activity affect the capability of the respiratory chain to match an energetic request, as well as the maximal respiration achievable by the cells. These data confirm a mitochondrial bioenergetic defect regardless of mitochondrial morphology.

Different Expression of Drp1 Impacts on Mitophagy

Dysfunctional mitochondria are removed by mitophagy, allowing their selective degradation. To monitor the activation of mitophagy in our clones we evaluated the autophagosomal marker LC3 and SQSTM1/p62, a protein targeting poly-ubiquitinated proteins to autophagosomes for degradation. During autophagosome formation the cytosolic LC3-I isoform is converted into LC3-II and is incorporated

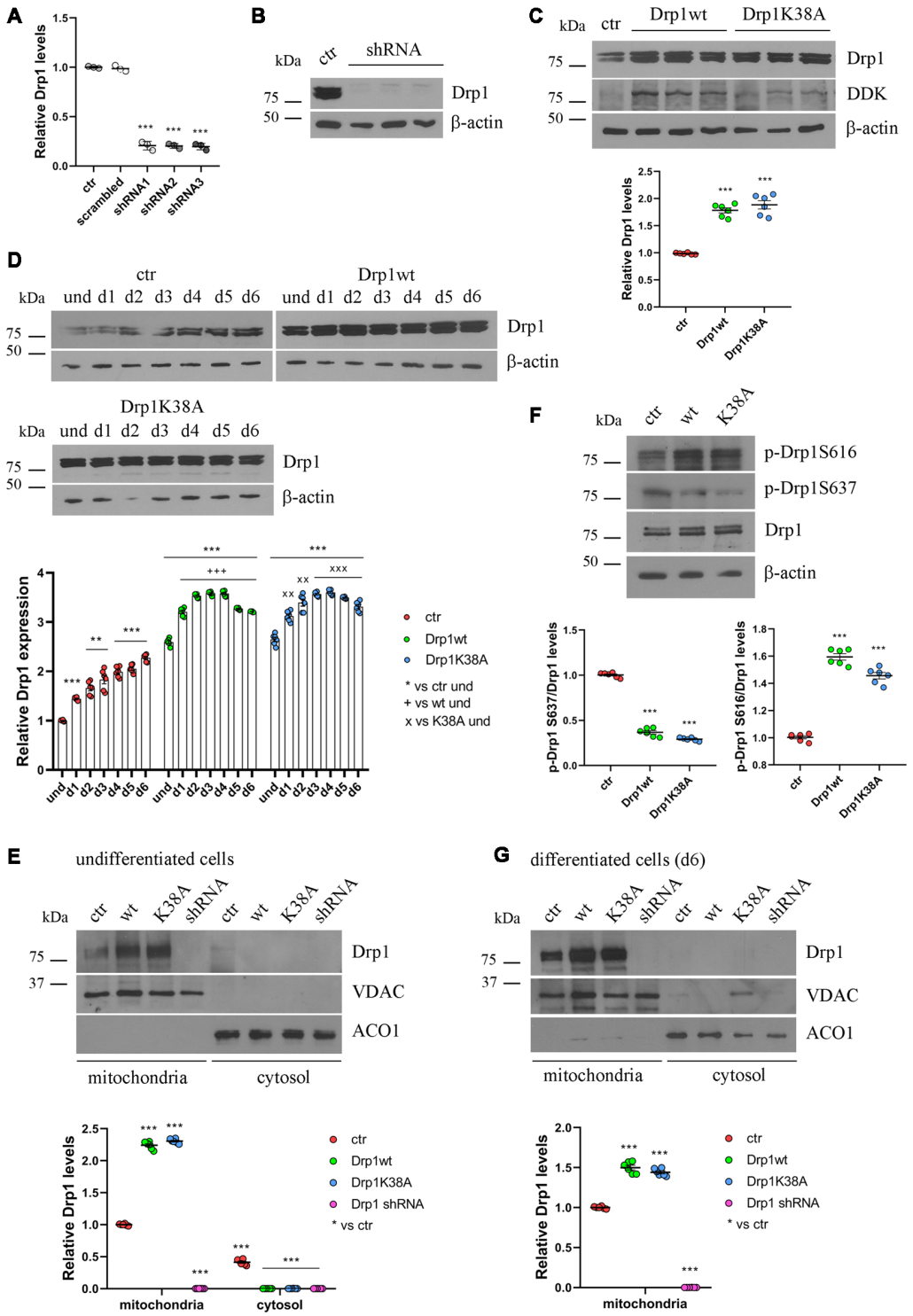


FIGURE 2 | Drp1 levels and localization in Drp1-modified clones. **(A)** Drp1 expression levels in Drp1 shRNA stable clones. RNA was extracted from P19 clones stably transfected with Drp1 shRNA. Drp1 expression levels were analyzed by Real Time PCR and compared with Drp1 levels in P19 transfected with the scrambled sequence. P19 cells stably transfected with the vector alone were used as endogenous control (ctr, set at 1). The graph shows the residual Drp1 expression in the three Drp1 shRNA clones used in the experiments. Results are expressed as individual data plus the mean ± SEM (one-way ANOVA followed by Dunnett's multiple comparison test, $n = 3$). * vs ctr (*** $p < 0.001$). **(B)** Drp1 protein levels in Drp1 shRNA stable clones. Total extracts prepared from the three Drp1 shRNA clones selected for the experiments were run on a 10% gel and probed with anti Drp1. Uncropped gels are in **Supplementary Figure S3**. **(C)** Drp1 protein levels in

(*Continued*)

FIGURE 2 | Continued
Drp1wt and Drp1K38A overexpressing clones. Total extracts prepared from the Drp1wt and Drp1K38A stable clones selected for the experiments, were run on 10% gel and probed with anti Drp1, DDK and actin Abs. Drp1 levels were quantified, normalized on actin levels and expressed as fold increase of control. The graph shows individual data plus the mean ± SEM (one-way ANOVA followed by Dunnett's multiple comparison test, $n = 6$). * vs ctr (***$p < 0.001$). Uncropped gels are in **Supplementary Figure S3**. **(D)** Drp1 expression levels increase during Drp1wt and Drp1K38A stable clones neuronal differentiation. Total extracts from undifferentiated Drp1wt, Drp1K38A and control clones and from d1 to d6 of neuronal differentiation, were run on a 10% SDS-polyacrylamide gel and probed with anti Drp1 and actin Abs. Drp1 levels were quantified, normalized on actin levels and expressed as fold increase of undifferentiated control levels. The graph shows individual data plus the mean ± SEM (two-way ANOVA followed by Tukey's multiple comparison test, $n = 6$). * vs ctr und (***$p < 0.001$, **$p < 0.01$); + vs Drp1wt und ($^{+++}p < 0.001$); × vs Drp1K38A und ($^{\times\times\times}p < 0.001$, $^{\times\times}p < 0.01$). Uncropped gels are in **Supplementary Figure S3**. **(E)** Localization of Drp1 on mitochondria in undifferentiated Drp1-modified clones. Mitochondrial and cytosolic extracts were prepared from undifferentiated Drp1wt, Drp1K38A, Drp1 shRNA and control clones, run on 10% SDS-polyacrylamide gels and probed with anti Drp1, VDAC and ACO1 Abs. VDAC and ACO1 were used as mitochondrial and cytosolic marker respectively. Drp1 levels were quantified, normalized on VDAC levels and expressed as fold increase of control. The graph shows individual data plus the mean ± SEM (two-way ANOVA followed by Tukey's multiple comparison test, $n = 6$). * vs ctr (***$p < 0.001$). Uncropped gels are in **Supplementary Figure S5**. **(F)** Drp1 phosphorylation levels in undifferentiated Drp1wt and Drp1K38A clones. Total extracts from Drp1wt, Drp1K38A and control clones were run on 10% SDS-polyacrylamide gels and probed with anti Drp1, phospho-Drp1 Ser616, phospho-Drp1 Ser637 and actin Abs. The phosphorylation level of Ser616 and Ser637 were quantified, normalized on total Drp1 levels and expressed as fold increase of control. The graph shows individual data plus the mean ± SEM (one-way ANOVA followed by Dunnett's multiple comparison test, $n = 6$). * vs ctr (***$p < 0.001$). Uncropped gels are in **Supplementary Figure S3**. **(G)** Localization of Drp1 on mitochondria in Drp1-modified clones-derived neurons. Mitochondrial and cytosolic extracts were prepared from Drp1wt, Drp1K38A, Drp1 shRNA and control clones on d6 of neuronal differentiation and processed as in **(E)**. Drp1 levels were normalized on VDAC levels and expressed as fold increase of control. The graph shows individual data plus the mean ± SEM (one-way ANOVA followed by Dunnett's multiple comparison test, $n = 6$). * vs ctr (***$p < 0.001$). Uncropped gels are in **Supplementary Figure S5**.

in the autophagosome membrane, thus LC3-II amount correlates with the number of autophagosomes (Kabeya et al., 2000). In undifferentiated Drp1-silenced and Drp1K38A clones, LC3-II and p62 levels were similar to control, while Drp1wt overexpressing clones showed increased LC3-II and reduced p62 levels, indicating increased autophagy (**Figure 4A** and **Supplementary Figure S8**). Consistently, the number of RFP-LC3 positive autophagosomes was enhanced in Drp1wt overexpressing clones compared with control (**Figure 4B**).

Moreover, BNIP3, a potent inducer of mitophagy (Lee et al., 2011), raised in Drp1wt overexpressing clones (**Figure 4A**) and the sequestration of mitochondria into lysosomes, measured by colocalization between the mitochondrial marker Mito-dsRed and the lysosomal marker Lamp1 (**Figure 4C**), was evident in these clones, clearly highlighting mitophagy activation. No differences were observed between control and Drp1 silenced clones, confirming previous data (Kageyama et al., 2014). In agreement with these findings, Drp1wt overexpressing clones showed a reduction in mtDNA content compared with control, Drp1-silenced and Drp1K38A clones (**Figure 4D**). Accordingly, the levels of two mitochondrial proteins, mtCO1 and VDAC, were lower in undifferentiated Drp1wt overexpressing cells, confirming the reduction of mitochondrial mass only in this clone (**Figure 4E**).

We then analyzed autophagy during neuronal differentiation. Autophagy plays a role in the first days of neuronal differentiation removing old material and providing recycled constituents for building up new structures (Guan et al., 2013). As expected, autophagy in control cells enhanced at d1 during neurogenesis and decreased during the time (**Figure 4F**). The pattern of autophagy induction was similar in all clones, but with the highest levels in Drp1wt overexpressing clones (**Figure 4F**), confirming that high Drp1 levels impact on both basal and stimulated autophagy, enhancing the process.

Physiological Levels of Drp1 Are Required for the Expression of Neurogenic Transcription Factors and the Downregulation of Pluripotency Genes, Preventing Apoptosis

All clones were induced to differentiate with RA and formed neurospheres similar in number and size, thus on d4 they were dissociated, plated and cultured for several days. We started our analysis from the first phases of neuronal differentiation corresponding to the expression of the RA-induced neurogenic transcription factors (Bain et al., 1994; Vantaggiato et al., 2011). We found that, while in control cells RA treatment induced the expression of Mash1, Wnt1 and N-cadherin (**Figure 5A**), their levels were significantly reduced in all Drp1-modified clones, indicating that any manipulation of Drp1 affected RA-induced transcription. Neuronal differentiation is also defined by the loosing of pluripotency through the downregulation of Oct3/4 and Sox2 genes (Li et al., 2013). While in control cells Oct3/4 expression levels were dramatically reduced by RA treatment starting from d1 to disappear on d2, accordingly with previous data (Bain et al., 1994; Yamada et al., 2013), in all Drp1-modified clones Oct3/4 levels were higher than control on d1 and residual levels were still present on d4 (**Figure 5B**). Sox2 is a neural stem cells marker and maintains neuronal progenitor identity (Graham et al., 2003), therefore its expression levels slightly increase on d1 of neuronal differentiation and slowly decrease during the next 4 days to reach the lowest levels in differentiated neurones (d5–d7; Yamada et al., 2013), as we observed in control cells (**Figure 5B**). By contrast, all Drp1-modified clones presented increased Sox2 levels on d1 of neuronal differentiation, that remained higher also on d5 and d6 (**Figure 5B**). On the contrary, no differences in Oct3/4 and Sox2 expression were observed among undifferentiated Drp1-modified and control clones (**Supplementary Figure S9**), indicating that Drp1 is not necessary for the maintenance of pluripotency in undifferentiated cells, but it is required for pluripotency genes downregulation during neuronal differentiation.

In parallel to its role in neuronal differentiation induction, RA, together with BMP4, is involved also in apoptosis, through

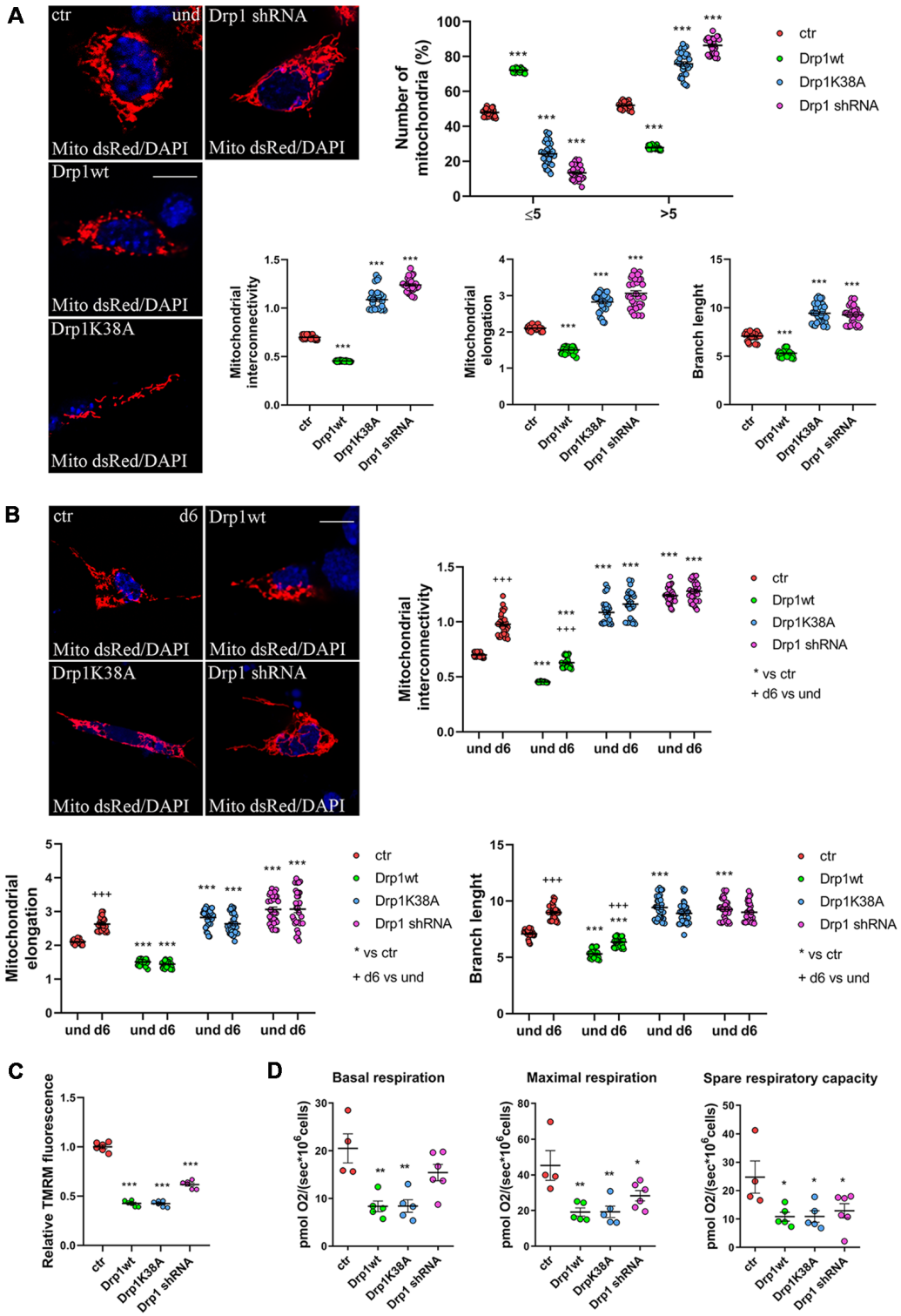


FIGURE 3 | Mitochondrial morphology. **(A)** Mitochondrial morphology in undifferentiated Drp1-modified clones. Drp1wt, Drp1K38A, Drp1 shRNA and control cells were transfected with the pDsRed2-Mito vector for the staining of mitochondria and fixed after 24 h. Nuclei were stained with DAPI. Images were acquired by confocal microscopy and morphometric analysis was performed with ImageJ. Red channels were converted into a black binary image and skeletonized (binary and skeleton images are in **Supplementary Figure S6A**). Mitochondrial interconnectivity, elongation and branch length are showed in the graphs as individual data plus the mean ± SEM (one-way ANOVA followed by Dunnett's multiple comparison test). The number of fragmented or elongated mitochondria, with an area

(*Continued*)

FIGURE 3 | Continued
lower or higher than 5 μm^2 respectively, was also determined and reported in the graph. Results are expressed as individual data plus the mean ± SEM (two-way ANOVA followed by Sidak's multiple comparison test). Data were obtained from three independent experiments for a total of at least 30 cells for each sample. Scale bar: 10 μm. * vs ctr (*** $p < 0.001$). **(B)** Mitochondrial morphology in differentiated neurons (d6). Drp1wt, Drp1K38A, Drp1 shRNA and control clones were induced to differentiate with RA, on d5 neurons were transfected with the pDsRed2-Mito vector and processed as described in **(A)**. Binary and skeleton images are in **Supplementary Figure S6B**. Mitochondrial interconnectivity, elongation and branch length are shown in the graphs. Results are expressed as individual data plus the mean ± SEM (two-way ANOVA followed by Sidak's multiple comparison test). * vs ctr (***$p < 0.001$); $^{+}$d6 vs und ($^{+++}p < 0.001$). Data were obtained from three independent experiments for a total of at least 30 cells for each sample. Scale bar: 10 μm. **(C)** Mitochondrial membrane potential. Undifferentiated cells were trypsinized, counted and incubated with 100 nM TMRM for 30 min at 37°C. Fluorescence was measured with a Fluoroskan by using a TRITC filter. After background subtraction, the data were normalized on cell number and reported as fold increase of control. Results are expressed as individual data plus the mean ± SEM (one-way ANOVA followed by Tukey's multiple comparison test, $n = 6$). * vs ctr (***$p < 0.001$). **(D)** Oxygen consumption measurement on intact undifferentiated clones. Basal and maximal respiratory capacity are reported while spare respiratory capacity was obtained by subtracting basal respiration from maximal respiration rates. Results show individual data plus the mean ± SEM (one-way ANOVA followed by Dunnett's multiple comparison test, $n = 4$–6). * vs ctr (**$p < 0.01$, *$p < 0.05$).

the induction of caspase 9 and caspase 3 (Miho et al., 1999). The fate between neuronal differentiation and cell death depends on a fine regulation of the pro-apoptotic RA/BMP4 signaling and the pro-survival FGF8 pathway (Massagué, 1998; Vantaggiato et al., 2011). We analyzed FGF8 levels and its activated pathways, i.e., PI3K/Akt and ERK1/2 MAPK (Wang et al., 2006; Vantaggiato et al., 2011), during neuronal differentiation and we found that FGF8 expression levels (**Figure 5C**) as well as Akt, ERK1/2 and GSK3β-Ser9 phosphorylation levels had the same trend in all clones compared to control (**Figure 5D**, **Supplementary Figures S10, S11**). Also, the ERK1/2-dependent inhibitory phosphorylation on Ser206 of Smad1, a BMP4-activated protein that induces the expression of BMP target genes (Pera et al., 2003), was similar in Drp1-modified and control clones, indicating a correct inhibition of the BMP4 pathway.

RA induces the upregulation of several ER stress-responsive genes and ER stress play a critical role in neuronal differentiation of mouse ESCs (Liu et al., 2012; Godin et al., 2016; Murao and Nishitoh, 2017). Several stimuli activate the UPR and the ERAD pathway and both are upregulated during RA-induced differentiation (Liu et al., 2012). We analyzed UPR and ERAD pathways during neuronal differentiation (**Figure 6**, **Supplementary Figures S12, S13**) and we found that all Drp1-modified clones presented increased phosphorylation of the UPR protein eIF2α (**Figure 6A** and **Supplementary Figure S12**) compared with control and increased expression of the eIF2α downstream genes Grp78 and Grp94, the pro-apoptotic gene CHOP and of the negative regulator GADD34 (**Supplementary Figure S13**). Moreover also the expression levels of Gp78 and HRD1 (**Figure 6B**), two regulators of ERAD, were increased in Drp1-modified clones compared with control, indicating that both UPR and ERAD pathways are activated by changes in Drp1 levels.

Since Drp1 can affect cells vitality during neuronal differentiation and RA can induce apoptosis through the activation of ER stress response (Godin et al., 2016; Murao and Nishitoh, 2017), we measured cell death in neural stem cells. We used PI and DAPI to stain dead and living cells respectively (Cummings and Schnellmann, 2004), 24 h after RA induction and we found that Drp1wt, Drp1K38A and Drp1 shRNA aggregates presented higher levels of dead, PI-positive cells compared with control (**Figure 6C**). Apoptosis was also assessed by using a DeadEnd Fluorometric TUNEL system (**Figure 6D**). On d1 of neuronal differentiation, we found induction of apoptosis in all Drp1-modified clones compared to control, with however higher levels in Drp1wt when compared to Drp1K38A and Drp1 shRNA clones. No differences were observed in undifferentiated clones (**Supplementary Figure S14**). As a consequence of increased apoptosis and cell death, no alive cells were present in any Drp1-modified clones in late phases of neuronal differentiation and only control cells differentiated for the whole 14 days period (**Figure 6E**). We then analyzed apoptosis in differentiated cells quantifying the levels of caspase 3 activity on d5 and d6. While control cells presented a small increase in caspase 3 activity compared with undifferentiated cells, caspase 3 activity was significantly increased in all Drp1-modified clones, with remarkable induction in Drp1wt overexpressing clones (**Figure 6F**). Consistently, the levels of the activated forms of caspase 9 and caspase 7 on d5 and d6 were increased in all Drp1-modified clones compared with control (**Supplementary Figure S15**).

These data indicate that any Drp1 manipulation inhibits neurogenesis favoring apoptosis, regardless of mitochondrial shape.

Physiological Levels of Drp1 Are Required for Final Neuronal Differentiation

Neuronal differentiation required both the induction of neurogenic transcription factors and the downregulation of pluripotent genes. Considering the increased levels of the pluripotent Oct3/4 and Sox2 genes and the decreased levels of the RA-induced genes Mash1, Wnt1 and N-cadherin we detected in all Drp1-modified clones, we assessed the formation of neurons. The expression levels of Tubulin β-III, Gap43 and MAP2, markers respectively of neurofilaments, growth cones and neurites, were significantly reduced in all Drp1-modified clones compared to control (**Figure 7A**), however with a more severe effect of Drp1wt overexpression. In agreement, while in control cells the 90% of differentiated cells were positive for neuronal markers and showed normal development of neuronal processes and extensive connections, as described (Bain et al., 1994), only a few cells in Drp1-modified clones were positive for Tubulin β-III, Gap43 and MAP2 (**Figure 7B**).

DISCUSSION

The importance of mitochondrial dynamics in neurons and brain physiology has become increasingly clear. Neurons

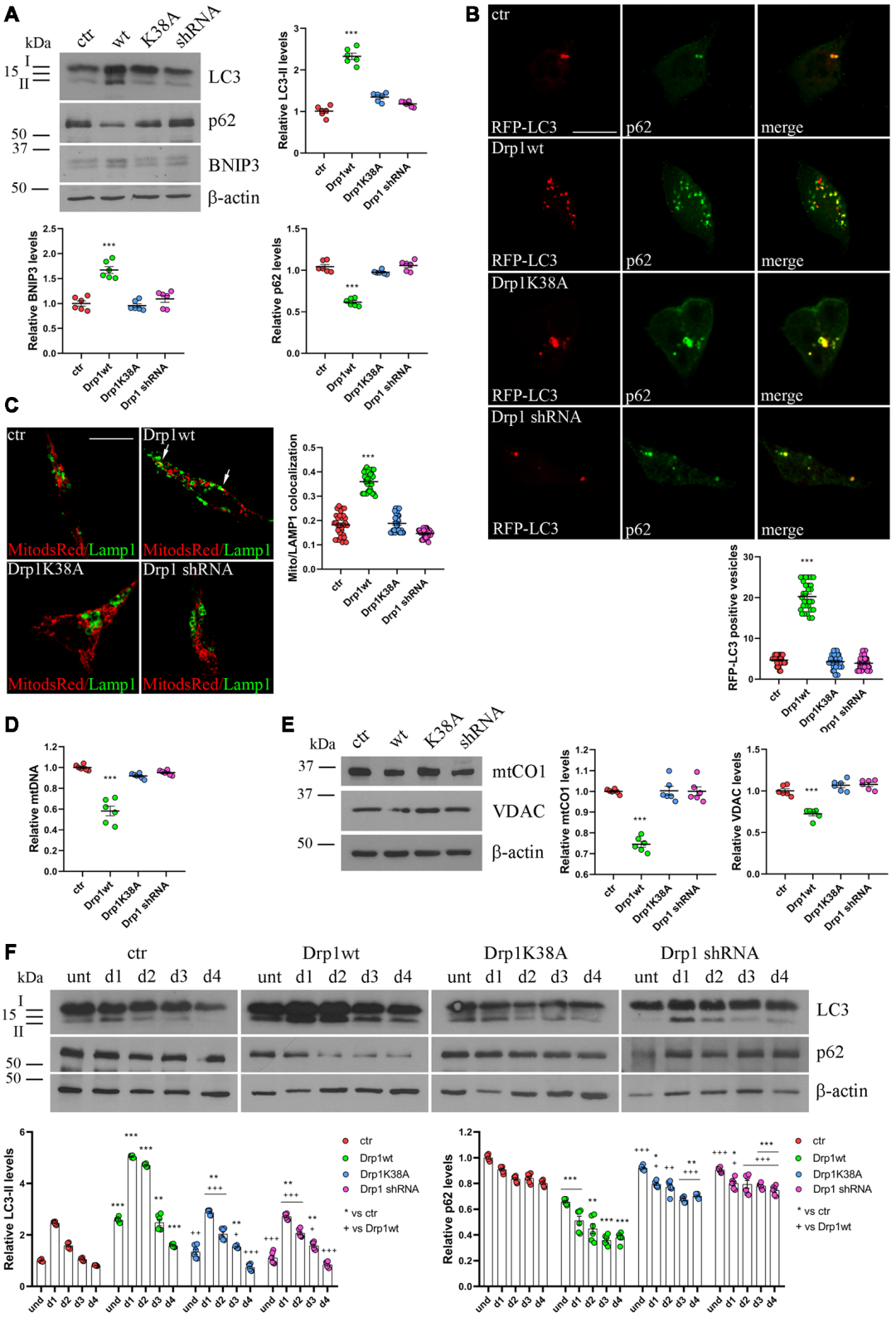


FIGURE 4 | Mitochondrial biogenesis and autophagy in Drp1-modified clones. **(A)** Autophagy is altered in clones overexpressing Drp1wt. Total extracts from Drp1wt, Drp1K38A, Drp1 shRNA and control cells were run onto 12% or 10% SDS-polyacrylamide gels and probed with anti MAP1LC3B, p62, BNIP3 and actin Abs. The two isoforms LC3-I and LC3-II are indicated. LC3-II, p62 and BNIP3 levels were quantified, normalized on actin levels and expressed as fold increase of

(*Continued*)

FIGURE 4 | Continued
control. The graphs show individual data plus the mean ± SEM (one-way ANOVA followed by Dunnett's multiple comparison test, $n = 6$). Uncropped gels are in **Supplementary Figure S8**. **(B)** Drp1wt, Drp1K38A, Drp1 shRNA and control cells were transfected with MAP1LC3B-RFP for the staining of autophagosomes (red), fixed 24 h later and immunostained with anti p62 (green) Ab. Yellow in the merge images indicates colocalization of p62 and RFP-LC3. Total RFP-LC3 positive vesicles number is shown in the graph as individual data plus the mean ± SEM (one-way ANOVA followed by Dunnett's multiple comparison test). Data were obtained from three independent experiments for a total of at least 30 cells for each sample. Scale bar: 10 μm. **(C)** Mitophagy is altered in clones overexpressing Drp1wt. Drp1wt, Drp1K38A, Drp1 shRNA and control clones were transfected with pDsRed2-Mito vector for the staining of mitochondria (red), fixed 24 h later and immunostained with anti Lamp1 (green). Yellow indicates co-localization. Pearson's correlation coefficients for Mito dsRed and Lamp1 colocalization were determined in at least 30 cells/staining and reported in the graph as individual data plus the mean ± SEM (one-way ANOVA followed by Dunnett's multiple comparison test). Scale bar: 10 μm. **(D)** Drp1wt overexpressing clones show reduced mitochondrial DNA (mtDNA). DNA was extracted from undifferentiated clones and used to quantify mtDNA by Real-Time PCR by using specific primers for NADH dehydrogenase 1 (ND1). RNAse P was used for normalization. Results are expressed as fold increase of control. Graph shows individual data plus the mean ± SEM (one-way ANOVA followed by Dunnett's multiple comparison test, $n = 6$). **(E)** Drp1wt overexpressing clones show reduced mitochondrial content. Total extracts were prepared from undifferentiated clones, run on 10% SDS-polyacrylamide gels and probed with anti mtCO1 and VDAC Abs. mtCO1 and VDAC levels were quantified and normalized on actin levels. Results are expressed as fold increase of control individual data plus the mean ± SEM (one-way ANOVA followed by Dunnett's multiple comparison test, $n = 6$). Uncropped gels are in **Supplementary Figure S8**. **(F)** Autophagy levels in neural stem cells aggregates. Drp1wt, Drp1K38A, Drp1 shRNA and control clones were induced to differentiate with RA and total protein extracts were prepared each day from d1 to d4, run onto 15% or 10% SDS-polyacrylamide gels and probed with anti MAP1LC3B, p62 and actin Abs. LC3-II and p62 levels were quantified, normalized on actin levels and expressed as fold increase of control. The graphs show individual data plus the mean ± SEM (two-way ANOVA followed by Tukey's multiple comparison test, $n = 6$). Lines indicate samples to whom symbols are referred. Uncropped gels are in **Supplementary Figure S8**. * vs ctr (***$p < 0.001$; **$p < 0.01$; *$p < 0.05$); $^{+}$vs Drp1wt ($^{+++}p < 0.001$; $^{++}p < 0.01$; $^{+}p < 0.05$).

require high levels of energy for survival and for their specialized functions. These highly polarized cells are particularly vulnerable to mitochondrial fission and fusion defects that lead to deficient cell bioenergetics and incorrect distribution of mitochondria along the axons and at the synapses. At these sites, high levels of ATP are required for transmission and for synapses organization (Li et al., 2004, 2008; Chen and Chan, 2006). While Drp1-dependent mitochondrial fission seems to be dispensable for the function of non-polarized cells, this function is required for extremely polarized cells such as neurons. Many studies dissected the physiological role of mitochondrial fission in neurons evaluating the effects of Drp1 deletion. Drp1 is required for the development of the mammalian nervous system (Waterham et al., 2007; Ishihara et al., 2009; Wakabayashi et al., 2009) and Drp1 deficiency results in depletion of mitochondria from developing neurites, reduced neurite outgrowth, impaired synapse formation (Ishihara et al., 2009) finally leading to neurodegeneration (Kageyama et al., 2012, 2014). Drp1 ablation alters neuronal functions also in adult neurons, affecting synaptic transmission and memory, however, compensatory circuits are sufficient to maintain overall neuronal morphology and viability (Oettinghaus et al., 2016). Moreover, Drp1 hyper-phosphorylation at Ser-637 induces abnormal mitochondrial elongation and is associated with hereditary spastic paraplegia (Lavie et al., 2017). The reduction in Drp1-mediated fission compromises mitochondrial health in spastic ataxia of Charlevoix Saguenay (Bradshaw et al., 2016). All these findings describe the effects of extensively fused mitochondrial structure. Conversely, a wide range of neurodegenerative disorders, such as Alzheimer's (Cho et al., 2009; Manczak et al., 2011; Manczak and Reddy, 2012), Huntington's (Costa et al., 2010; Song et al., 2011; Shirendeb et al., 2012) and Parkinson's diseases (Wang et al., 2011) are associated with increased Drp1 levels and mitochondrial fragmentation (Hu et al., 2017). The biological significance of the increased Drp1 levels in neuronal differentiation was not investigated. We, therefore, analyzed the effects of increased levels of Drp1 on P19 cell neuronal differentiation, comparing the phenotype of Drp1 overexpression to that of the well-known Drp1 deletion. We demonstrate here that P19 cell neuronal differentiation is associated with key changes in mitochondrial fission and fusion genes. In particular, Drp1 levels gradually increased during RA treatment to reach 2.5–3-fold increase in differentiated neurons, confirming the reported augment of Drp1 observed in the late stage of ESCs differentiation (Wang et al., 2014). This Drp1 expression pattern is paralleled by enhanced Mfn1/2 expression and both contribute to mitochondrial remodeling, with prevalently small and round mitochondria in undifferentiated cells that become elongated in differentiated neurons. These data are also in agreement with the metabolic shift observed in undifferentiated P19 cells that are essentially glycolytic, while differentiated neurons are more oxidative (Vega-Naredo et al., 2014). We genetically manipulated Drp1 generating P19 stable clones overexpressing Drp1wt, Drp1K38A or silencing the gene, and, differently from previous studies, we monitored neuronal differentiation. Neuronal differentiation is characterized by the induction of RA-dependent neurogenic transcription factors, and by the downregulation of pluripotency genes, such as Oct3/4 and Sox2. All Drp1-modified clones shared similarities in the response to RA showing lower levels of the RA-induced genes Mash1, Wnt1 and N-cadherin and failed to downregulate Oct3/4 and Sox2 expression, suggesting that mitochondrial changes can induce a transcriptional reprogram that negatively impacts on neuronal differentiation. Sox2 is expressed in multipotent neuronal stem cells and is downregulated during differentiation. Here, we found that Sox2 expression was not downregulated in Drp1-modified clones during induction of neuronal differentiation and was still high on d5–d7, inhibiting final neuronal differentiation. Consistently, we found that the concomitant reduction in the expression of neurogenic transcription factors and the increased levels of pluripotency genes in Drp1wt, Drp1K38A and Drp1-silenced clones, correlated with a defective differentiation with decreased expression of Tubulin β-III, MAP2 and Gap43 neuronal markers in mature neurons. Indeed,

FIGURE 6 | Continued
Uncropped gels are in **Supplementary Figure S12**. **(B)** Drp1wt, Drp1K38A, Drp1 shRNA and control clones were induced to differentiate with RA. RNA was extracted from d1 to d4 and used to analyze GP78 and HRD1 levels by Real-Time PCR. Undifferentiated P19 cells stably transfected with the vector alone were used as endogenous control. Results are expressed as fold increase of endogenous control and reported as individual data plus the mean ± SEM (two-way ANOVA followed by Tukey's multiple comparison test, $n = 8$). **(C)** Cell death levels in neural stem cells aggregates. Drp1wt, Drp1K38A, Drp1 shRNA and control P19 stable clones were induced to differentiate with RA and 24 h later aggregates were stained with DAPI and propidium iodide (PI) to detect living and dead cells respectively. Scale bar: 50 μm. **(D)** Morphology of differentiated cultures. Drp1wt, Drp1K38A, Drp1 shRNA and control clones were induced to differentiate with RA, on d4 were dissociated and photographed from d5 to d7. Scale bar: 50 μm. Shown are representative images. **(E)** Apoptosis levels in neural stem cells on d1 of neuronal differentiation. Drp1wt, Drp1K38A, Drp1 shRNA and control clones were induced to differentiate with RA. On d1 aggregates were dissociated and apoptosis was analyzed with TUNEL assay. TUNEL fluorescence intensity was quantified and expressed as fold increase of control. The graph shows individual data plus the mean ± SEM (one-way ANOVA followed by Tukey's multiple comparison test, $n = 6$). **(F)** Apoptosis levels in differentiated neurons. Drp1wt, Drp1K38A, Drp1 shRNA and control clones were induced to differentiate with RA, on d4 aggregates were dissociated, plated and tested for caspase 3 activity on d5 and d6. Results shown are individual data plus the mean ± SEM (two-way ANOVA followed by Tukey's multiple comparison test, $n = 6$). * vs ctr (***$p < 0.001$, **$p < 0.01$); $^{+}$ vs Drp1wt ($^{+++}p < 0.001$). Lines indicate sample to whom symbols are referred.

Sox2 is mutually exclusive with Tubulin β-III marker and its constitutive expression inhibits neuronal differentiation in CNS and results in the maintenance of progenitor characteristics (Graham et al., 2003).

Our data indicate that these defects occur in a mitochondrial-dependent manner. During neuronal differentiation, control clones undergo mitochondrial remodeling characterized by increased elongation, branch length and interconnectivity. Autophagy induction during the first phases of differentiation is likely to concur to this specific mitochondrial network organization and both events allow correct neurogenesis. This is common to other differentiation processes, such as myogenesis, in which Drp1-mediated fission appears to be crucial for mitophagy. Following the mitochondrial clearance stage, mitochondria are substituted and form a more organized network and this rebuilding phase does not occur until mitochondrial clearance takes place (Sin et al., 2016).

High Drp1 levels specifically increase mitochondrial fission with less organized and more fragmented mitochondria that are able to undergo remodeling during neuronal differentiation, increasing interconnectivity and branch length, but fails to elongate, thus definitely impairing neurogenesis. Consistently, autophagy and apoptosis are extremely enhanced, preventing differentiation. Both the Drp1K38A overexpression and Drp1 silencing enhance mitochondria elongation, interconnectivity and branch length in undifferentiated conditions, likely due to inhibition of fission and unopposed fusion, as supported by unchanged MFNs expression and identical Opa1 activity, similarly to other models (Kageyama et al., 2012, 2014). Also, Drp1K38A overexpression and Drp1 silencing prevent the required mitochondrial remodeling, leading to increased apoptosis and neuronal death.

Inhibition of mitochondrial respiration and increased ROS production affect gene expression resulting in the impairment of differentiation capability and the enhancement of stem cell pluripotency (Varum et al., 2009). Accordingly, inefficient oxidative metabolism increases ROS production and prevents P19 cells neuronal differentiation (Pashkovskaia et al., 2018). In line with this, our clones, regardless of their mitochondria shape, displayed reduced mitochondrial membrane potential and bioenergetic defects, leading to inefficient neuronal differentiation.

We demonstrate that neuronal differentiation is dramatically susceptible to abnormal mitochondrial fission and high Drp1 expression and not only to the complete absence of the protein, suggesting that physiological fission and mitochondrial remodeling, associated with early autophagy induction, are essential for neuronal differentiation. Any unbalance of mitochondrial remodeling affects autophagy, apoptosis or both, thereby impairing neuronal differentiation. Considering that neither the FGF8 activated pathways, i.e., ERK1/2 and Akt, nor BMP4 pathway, through Smad1 inhibition, are affected in Drp1-modified clones, we can conclude that increased apoptosis could derive from altered RA response, likely through hyperactivation of UPR and ERAD pathways. Indeed, while a progressive increase in UPR is required for normal neuronal differentiation, prolonged UPR activation can induce apoptosis and cell death (Godin et al., 2016; Murao and Nishitoh, 2017).

The link between mitochondrial fission and apoptosis is not surprising (Itoh et al., 2013) and also the knockdown and the dominant-negative interference of endogenous Drp1 have been demonstrated to cause cell death in cortical neurons (Uo et al., 2009; Bradshaw et al., 2016), indicating a high vulnerability of neurons to alterations in Drp1 levels and activity. Moreover, Drp1 has been reported to induce mitochondrial damage and apoptosis independently of its GTPase activity (Bras et al., 2007).

In summary, we found that neuronal differentiation is susceptible to changes in Drp1 levels and function, and it is severely impaired by both Drp1 overexpression and protein depletion or inactivation. This suggests the existence of a relationship between mitochondrial dynamics and neurodegeneration involving both fission induction and suppression. This appears to be of broad significance as strategies normalizing mitochondrial dynamics appear to be effective for a wide range of neurodegenerative diseases (Guo et al., 2013; Franco et al., 2016; Joshi et al., 2018).

Finally, our study provides novel information on the role of Drp1 in neuronal differentiation induction adding hints to the knowledge regarding the effects of Drp1 depletion in post-mitotic neurons. This study thus reveals the importance of mitochondrial changes at the onset of neuronal differentiation, sharing similarity with other stem cells and differentiation pathways, and highlights that, rather than multiple parallel events, mitochondrial changes, autophagy and apoptosis proceed

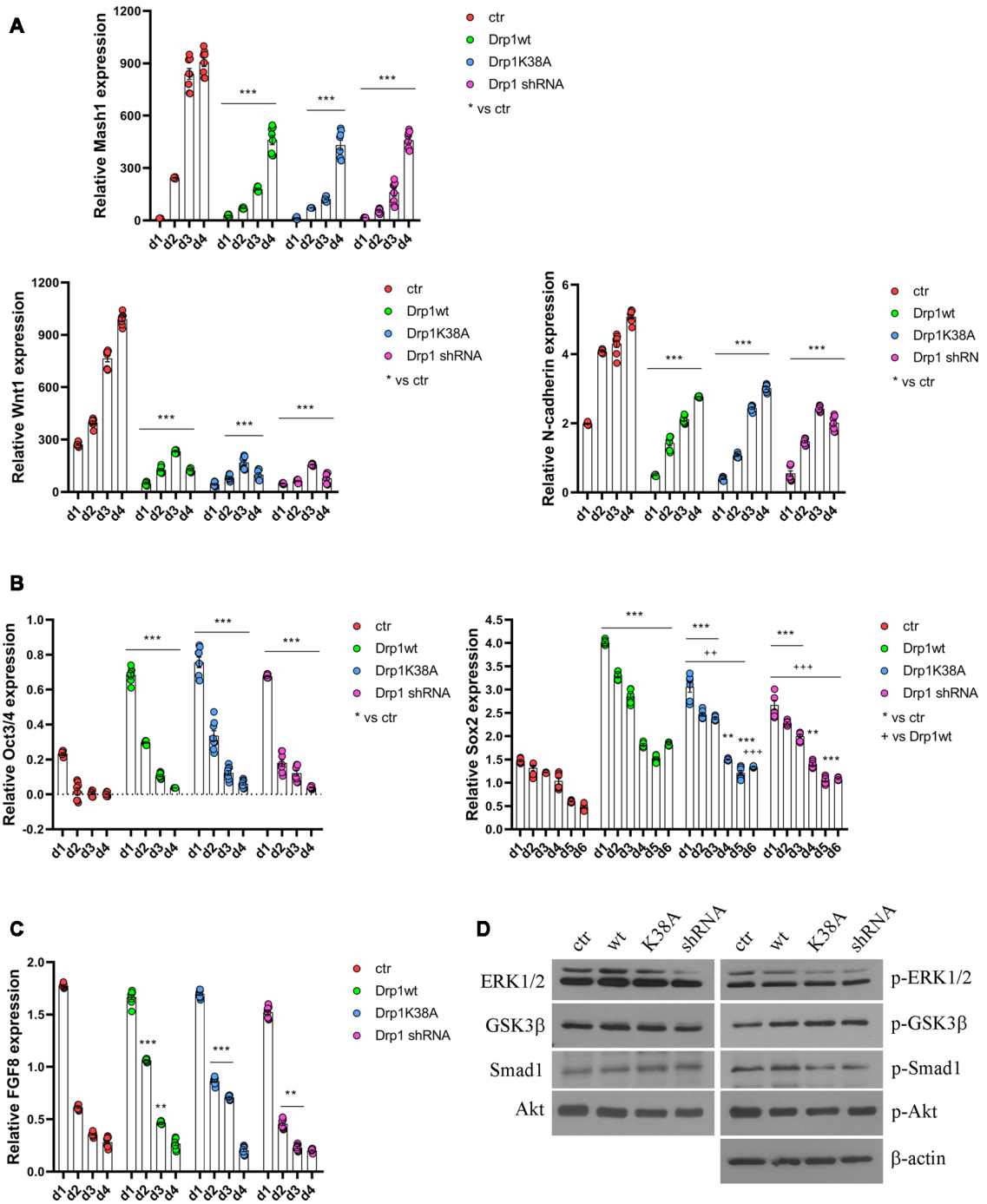


FIGURE 5 | Alterations in Drp1 levels and function affect neuronal differentiation induction. Drp1wt, Drp1K38A, Drp1 shRNA and control P19 stable clones were induced to differentiate with RA. RNA was extracted from d1 to d6 and used to analyze Mash1, Wnt1 and N-cadherin (d1–d4; **A**), Oct3/4 (d1–d4) and Sox2 (d1–d6) **(B)**, and FGF8 (d1–d4) expression levels **(C)** by Real-Time PCR. Undifferentiated P19 cells stably transfected with the vector alone were used as an endogenous control (set at 1). Results are expressed as fold increase of endogenous control and reported as individual data plus the mean ± SEM (two-way ANOVA followed by Tukey's multiple comparison test, $n = 8$). * vs ctr (***$p < 0.001$, **$p < 0.01$); $^{+}$ vs Drp1wt ($^{+++}p < 0.001$, $^{++}p < 0.01$). Lines indicate samples to whom asterisks are referred. **(D)** Total extracts were prepared from Drp1wt, Drp1K38A, Drp1 shRNA and control clones 24 h after RA addiction, run on a 10% SDS-PAGE gel and probed with anti phospho-Akt (p-Akt), Akt, phospho-Ser9-GSK3β (p-GSK3β), GSK3β, phospho-ERK1/2 (p-ERK), ERK1/2, phospho-Ser206-Smad1 (p-Smad1) and Smad1 Abs. Uncropped gels are in **Supplementary Figure S10**. Quantification is reported in **Supplementary Figure S11**.

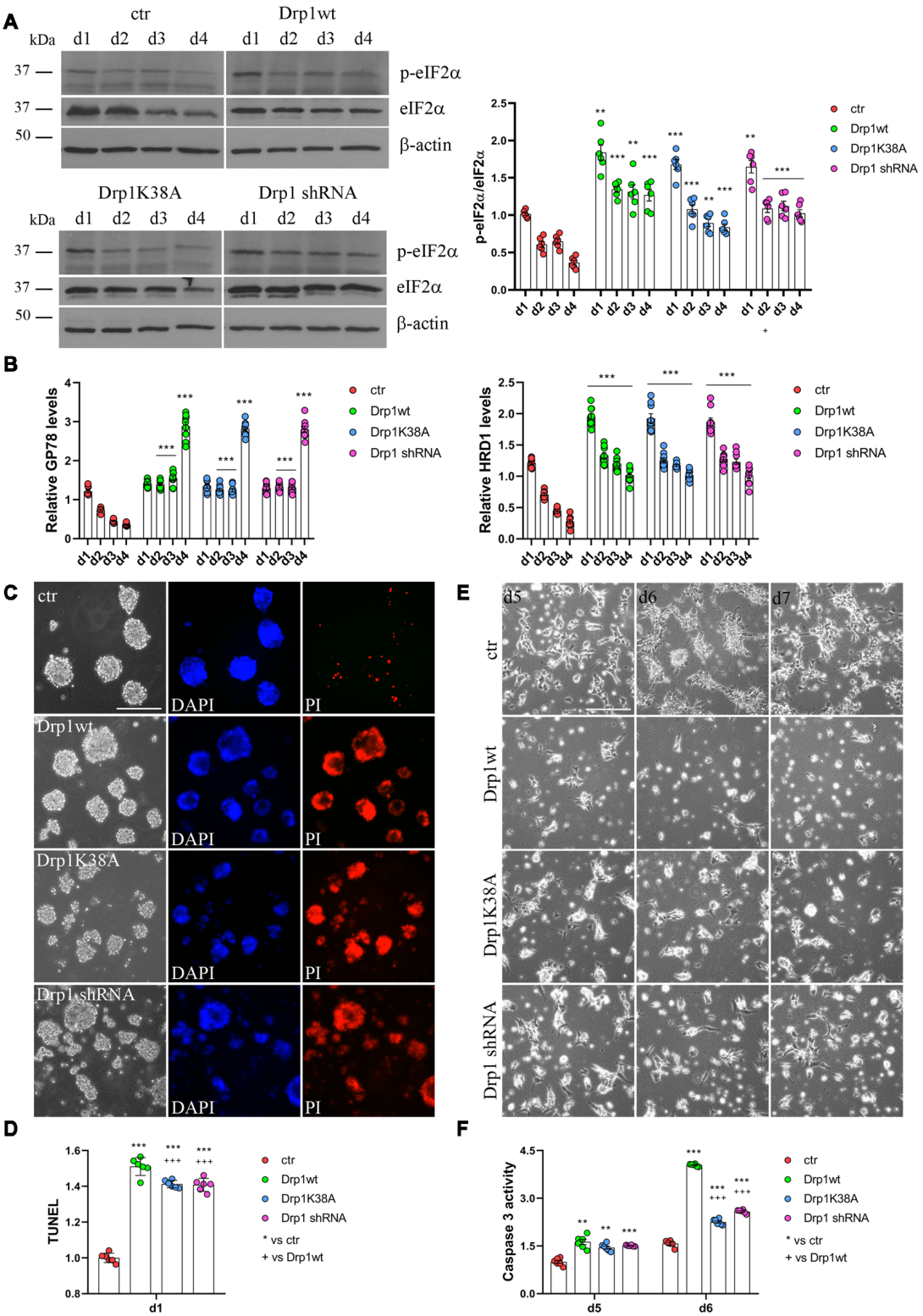


FIGURE 6 | Drp1 is necessary for survival. **(A)** Drp1wt, Drp1K38A, Drp1 shRNA and control clones were induced to differentiate with RA. Total protein extracts were prepared from d1 to d4, run on 10% SDS-PAGE gels and probed with anti phospho-eIF2α (p-eIF2α) and eIF2α Abs. p-eIF2α levels were quantified, normalized on eIF2α levels and expressed as fold increase of control as individual data plus the mean ± SEM (two-way ANOVA followed by Tukey's multiple comparison test, $n = 6$). (*Continued*)

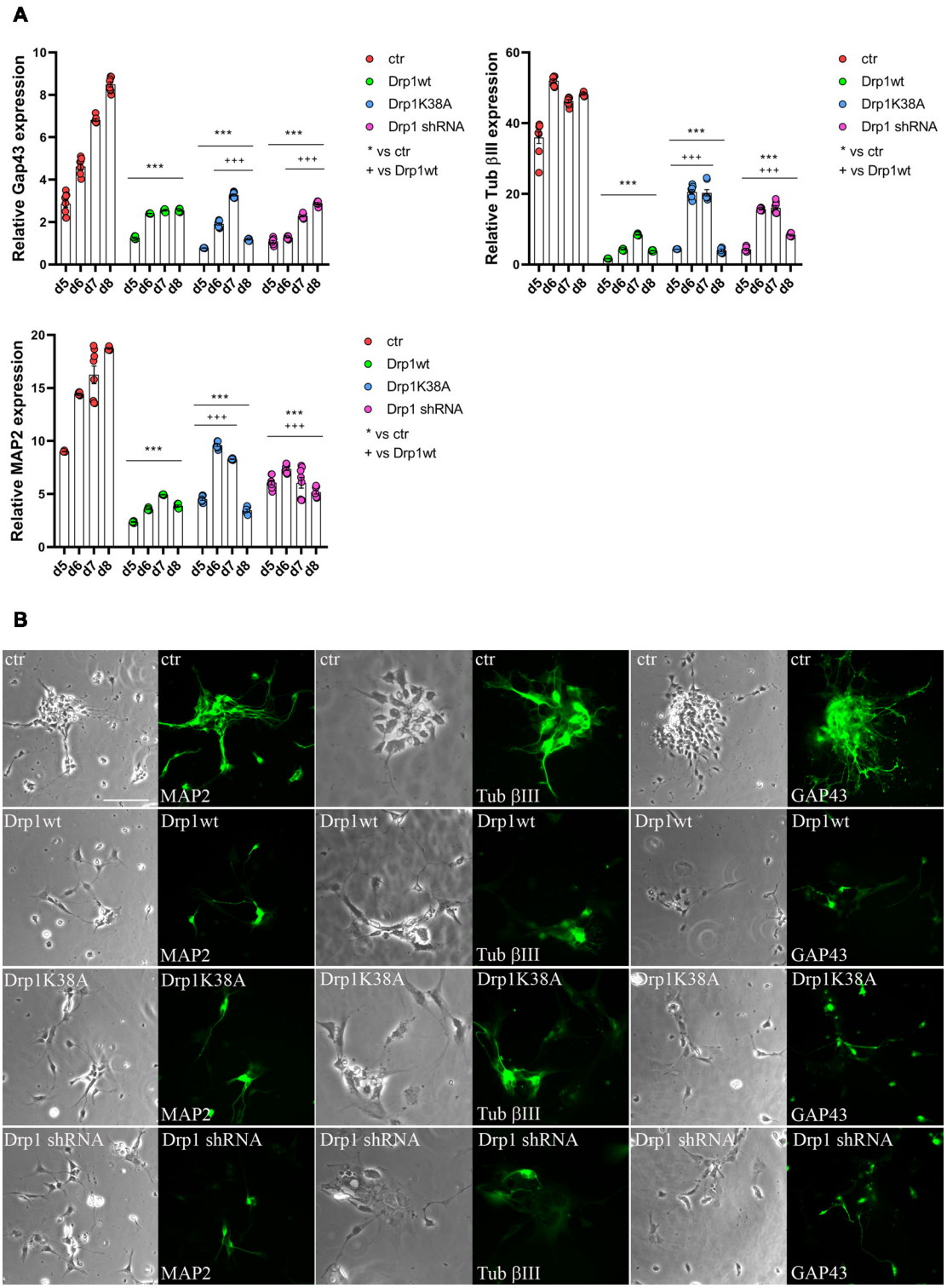


FIGURE 7 | Alterations in Drp1 levels and function affect final neuronal differentiation. **(A)** Drp1wt, Drp1K38A, Drp1 shRNA and control clones were induced to differentiate with RA. RNA was extracted every day from d5 to d8 and used to analyze Tubulin β-III, MAP2 and Gap43 expression levels by Real-Time PCR. Undifferentiated P19 cells stably transfected with the vector alone were used as endogenous control. Results are expressed as fold increase of endogenous control and reported as individual data plus the mean ± SEM (two-way ANOVA followed by Tukey's multiple comparison test, $n = 6$). * vs ctr (***$p < 0.001$); $^{+}$ vs Drp1wt ($^{+++}p < 0.001$). Lines indicate samples to whom symbols are referred. **(B)** Drp1wt, Drp1K38A, Drp1 shRNA and control clones were induced to differentiate with RA and on d6 neurons were fixed and stained with anti-Tubulin β-III, MAP2 and Gap43 Abs (green). Scale bar: 50 μm.

in a stepwise fashion during neuronal differentiation altering the nuclear transcriptional program.

AUTHOR CONTRIBUTIONS

CV analyzed, differentiated and undifferentiated Drp1 clones, performed neuronal differentiation, autophagy and cell death analysis, immunofluorescence, western-blot and statistical analysis, designed the experiments, interpreted the data and wrote the manuscript. MC prepared Drp1 stable clones, performed neuronal differentiation and analyzed gene expression levels. MG performed mitochondrial fractionation, mtDNA analysis and mitochondrial membrane potential quantification. GO performed immunofluorescence, confocal analysis and mitochondrial morphometric analysis. MB and EC interpreted the data, supervised the research and critically revised the manuscript. CDP designed the experiments, interpreted the data and wrote the manuscript.

FUNDING

This work was supported by the Italian Ministry of Health (Grants No. GR-2011-02350544 to CDP and CV, RC2018 and RC2019 to MB).

SUPPLEMENTARY MATERIAL

The Supplementary Material for this article can be found online at: https://www.frontiersin.org/articles/10.3389/fncel.2019.00120/full#supplementary-material

REFERENCES

Bain, G., Ray, W. J., Yao, M., and Gottlieb, D. I. (1994). From embryonal carcinoma cells to neurons: the P19 pathway. *Bioessays* 16, 343–348. doi: 10.1002/bies.950160509

Bradshaw, T. Y., Romano, L. E., Duncan, E. J., Nethisinghe, S., Abeti, R., Michael, G. J., et al. (2016). A reduction in Drp1-mediated fission compromises mitochondrial health in autosomal recessive spastic ataxia of Charlevoix Saguenay. *Hum. Mol. Genet.* 25, 3232–3244. doi: 10.1093/hmg/ddw173

Bras, M., Yuste, V. J., Roué, G., Barbier, S., Sancho, P., Virely, C., et al. (2007). Drp1 mediates caspase-independent type III cell death in normal and leukemic cells. *Mol. Cell. Biol.* 27, 7073–7088. doi: 10.1128/mcb.02116-06

Cereghetti, G. M., Stangherlin, A., Martins de Brito, O., Chang, C. R., Blackstone, C., Bernardi, P., et al. (2008). Dephosphorylation by calcineurin regulates translocation of Drp1 to mitochondria. *Proc. Natl. Acad. Sci. U S A* 105, 15803–15808. doi: 10.1073/pnas.0808249105

Chan, D. C. (2012). Fusion and fission: interlinked processes critical for mitochondrial health. *Annu. Rev. Genet.* 46, 265–287. doi: 10.1146/annurev-genet-110410-132529

Chang, D. T., Honick, A. S., and Reynolds, I. J. (2006). Mitochondrial trafficking to synapse in cultured primary cortical neurons. *J. Neurosci.* 26, 7035–7045. doi: 10.1523/JNEUROSCI.1012-06.2006

Chang, C. R., Manlandro, C. M., Arnoult, D., Stadler, J., Posey, A. E., Hill, R. B., et al. (2010). A lethal *de novo* mutation in the middle domain of the dynamin-related GTPase Drp1 impairs higher order assembly and mitochondrial division. *J. Biol. Chem.* 285, 32494–32503. doi: 10.1074/jbc.m110.142430

Chen, H., and Chan, D. C. (2006). Critical dependence of neurons on mitochondrial dynamics. *Curr. Opin. Cell. Biol.* 18, 453–459. doi: 10.1016/j.ceb.2006.06.004

Cho, D. H., Nakamura, T., Fang, J., Cieplak, P., Godzik, A., Gu, Z., et al. (2009). S-nitrosylation of Drp1 mediates β-amyloid-related mitochondrial fission and neuronal injury. *Science* 324, 102–105. doi: 10.1126/science.1171091

Costa, V., Giacomello, M., Hudec, R., Lopreiato, R., Ermak, G., Lim, D., et al. (2010). Mitochondrial fission and cristae disruption increase the response of cell models of Huntington's disease to apoptotic stimuli. *EMBO Mol. Med.* 2, 490–503. doi: 10.1002/emmm.201000102

Cribbs, J. T., and Strack, S. (2007). Reversible phosphorylation of Drp1 by cyclic AMP-dependent protein kinase and calcineurin regulates mitochondrial fission and cell death. *EMBO Rep.* 8, 939–944. doi: 10.1038/sj.embor.7401062

Cummings, B. S., and Schnellmann, R. G. (2004). Measurement of cell death in mammalian cells. *Curr. Protoc. Pharmacol.* Chapter 12:Unit 12.8. doi: 10.1002/0471141755.ph1208s25

Dagda, R. K., Cherra, S. J. III., Kulich, S. M., Tandon, A., Park, D., and Chu, C. T. (2009). Loss of PINK1 function promotes mitophagy through effects on oxidative stress and mitochondrial fission. *J. Biol. Chem.* 284, 13843–13855. doi: 10.1074/jbc.M808515200

De Palma, C., Morisi, F., Pambianco, S., Assi, E., Touvier, T., Russo, S., et al. (2014). Deficient nitric oxide signalling impairs skeletal muscle growth and performance: involvement of mitochondrial dysregulation. *Skelet. Muscle* 4:22. doi: 10.1186/s13395-014-0022-6

Delettre, C., Lenaers, G., Griffoin, J. M., Gigarel, N., Lorenzo, C., Belenguer, P., et al. (2000). Nuclear gene OPA1, encoding a mitochondrial dynamin-related protein, is mutated in dominant optic atrophy. *Nat. Genet.* 26, 207–210. doi: 10.1038/79936

Franco, A., Kitsis, R. N., Fleischer, J. A., Gavathiotis, E., Kornfeld, O. S., Gong, G., et al. (2016). Correcting mitochondrial fusion by manipulating mitofusin conformations. *Nature* 540, 74–79. doi: 10.1038/nature20156

Gerber, S., Charif, M., Chevrollier, A., Chaumette, T., Angebault, C., Kane, M. S., et al. (2017). Mutations in DNM1L, as in OPA1, result in dominant optic atrophy despite opposite effects on mitochondrial fusion and fission. *Brain* 140, 2586–2596. doi: 10.1093/brain/awx219

Godin, J. D., Creppe, C., Laguesse, S., and Nguyen, L. (2016). Emerging roles for the unfolded protein response in the developing nervous system. *Trends Neurosci.* 39, 394–404. doi: 10.1016/j.tins.2016.04.002

Gomes, L. C., Di Benedetto, G., and Scorrano, L. (2011). During autophagy mitochondria elongate, are spared from degradation and sustain cell viability. *Nat. Cell Biol.* 13, 589–598. doi: 10.1038/ncb2220

Graham, V., Khudyakov, J., Ellis, P., and Pevny, L. (2003). SOX2 functions to maintain neural progenitor identity. *Neuron* 39, 749–765. doi: 10.1016/s0896-6273(03)00497-5

Guan, J. L., Simon, A. K., Prescott, M., Menendez, J. A., Liu, F., Wang, F., et al. (2013). Autophagy in stem cells. *Autophagy* 6, 830–849. doi: 10.4161/auto.24132

Guo, X., Disatnik, M. H., Monbureau, M., Shamloo, M., Mochly-Rosen, D., and Qi, X. (2013). Inhibition of mitochondrial fragmentation diminishes Huntington's disease-associated neurodegeneration. *J. Clin. Invest.* 123, 5371–5388. doi: 10.1172/jci70911

Hamada-Kanazawa, M., Ishikawa, K., Ogawa, D., Kanai, M., Kawai, Y., Narahara, M., et al. (2004). Suppression of Sox6 in P19 cells leads to failure of neuronal differentiation by retinoic acid and induces retinoic acid-dependent apoptosis. *FEBS Lett.* 577, 60–66. doi: 10.1016/j.febslet.2004.09.063

Hu, C., Huang, Y., and Li, L. (2017). Drp1-dependent mitochondrial fission plays critical roles in physiological and pathological progresses in mammals. *Int. J. Mol. Sci.* 18:E144. doi: 10.3390/ijms18010144

Ingerman, E., Perkins, E. M., Marino, M., Mears, J. A., McCaffery, J. M., Hinshaw, J. E., et al. (2005). Dnm1 forms spirals that are structurally tailored to fit mitochondria. *J. Cell Biol.* 170, 1021–1027. doi: 10.1083/jcb.200506078

Ishihara, M., Nomura, A., Jofuku, H., Kato, S. O., Suzuki, K., Masuda, H., et al. (2009). Mitochondrial fission factor Drp1 is essential for embryonic development and synapse formation in mice. *Nat. Cell Biol.* 11, 958–966. doi: 10.1038/ncb1907

Itoh, K., Nakamura, K., Iijima, M., and Sesaki, H. (2013). Mitochondrial dynamics in neurodegeneration. *Trends Cell Biol.* 23, 64–71. doi: 10.1016/j.tcb.2012.10.006

Joshi, A. U., Saw, N. L., Vogel, H., Cunnigham, A. D., Shamloo, M., and Mochly-Rosen, D. (2018). Inhibition of Drp1/Fis1 interaction slows progression of amyotrophic lateral sclerosis. *EMBO Mol. Med.* 10:e8166. doi: 10.15252/emmm.201708166

Kabeya, Y., Mizushima, N., Ueno, T., Yamamoto, A., Kirisako, T., Noda, T., et al. (2000). LC3, a mammalian homologue of yeast Apg8p, is localized in autophagosome membranes after processing. *EMBO J.* 19, 5720–5728. doi: 10.1093/emboj/19.21.5720

Kageyama, Y., Hoshijima, M., Seo, K., Bedja, D., Sysa-Shah, P., Andrabi, S. A., et al. (2014). Parkin-independent mitophagy requires Drp1 and maintains the integrity of mammalian heart and brain. *EMBO J.* 33, 2798–2813. doi: 10.15252/embj.201488658

Kageyama, Y., Zhang, Z., Roda, R., Fukaya, M., Wakabayashi, J., Wakabayashi, N., et al. (2012). Mitochondrial division ensures the survival of postmitotic neurons by suppressing oxidative damage. *J. Cell Biol.* 197, 535–551. doi: 10.1083/jcb.201110034

Kann, O., and Kovács, R. (2007). Mitochondria and neuronal activity. *Am. J. Physiol. Cell Physiol.* 292, C641–C657. doi: 10.1152/ajpcell.00222.2006

Kasahara, A., and Scorrano, L. (2014). Mitochondria: from cell death executioners to regulators of cell differentiation. *Trends Cell Biol.* 24, 761–770. doi: 10.1016/j.tcb.2014.08.005

Kim, H. J., Shaker, M. R., Cho, B., Cho, H. M., Kim, H., Kim, J. Y., et al. (2015). Dynamin-related protein 1 controls the migration and neuronal differentiation of subventricular zone-derived neural progenitor cells. *Sci. Rep.* 5:15962. doi: 10.1038/srep15962

Lavie, J., Serrat, R., Bellance, N., Courtand, G., Dupuy, J. W., Tesson, C., et al. (2017). Mitochondrial morphology and cellular distribution are altered in SPG31 patients and are linked to Drp1 hyperphosphorylation. *Hum. Mol. Genet.* 26, 674–685. doi: 10.1093/hmg/ddw425

Lee, Y., Lee, H. Y., Hanna, R. A., and Gustafsson, Å. B. (2011). Mitochondrial autophagy by Bnip3 involves Drp1-mediated mitochondrial fission and recruitment of Parkin in cardiac myocytes. *Am. J. Physiol. Heart Circ. Physiol.* 301, H1924–H1931. doi: 10.1152/ajpheart.00368.2011

Li, H., Chen, Y., Jones, A. F., Sanger, R. H., Collis, L. P., Flannery, R., et al. (2008). Bcl-xL induces Drp1- dependent synapse formation in cultured hippocampal neurons. *Proc. Natl. Acad. Sci. U S A* 105, 2169–2174. doi: 10.1073/pnas.0711647105

Li, H., Fan, R., Sun, M., Jiang, T., and Gong, Y. (2013). Nspc1 regulates the key pluripotent Oct4- Nanog-Sox2 axis in P19 embryonal carcinoma cells via directly activating Oct4. *Biochem. Biophys. Res. Commun.* 440, 527–532. doi: 10.1016/j.bbrc.2013.09.095

Li, Z., Okamoto, K., Hayashi, Y., and Sheng, M. (2004). The importance of dendritic mitochondria in the morphogenesis and plasticity of spines and synapses. *Cell* 119, 873–887. doi: 10.1016/j.cell.2004.11.003

Liesa, M., Palacín, M., and Zorzano, A. (2009). Mitochondrial dynamics in mammalian health and disease. *Physiol. Rev.* 89, 799–845. doi: 10.1152/physrev.00030.2008

Liu, L., Liu, C., Zhong, Y., Apostolou, A., and Fang, S. (2012). ER stress response during the differentiation of H9 cells induced by retinoic acid. *Biochem. Biophys. Res. Commun.* 417, 738–743. doi: 10.1016/j.bbrc.2011.12.026

Manczak, M., Calkins, M. J., and Reddy, P. H. (2011). Impaired mitochondrial dynamics and abnormal interaction of amyloid β with mitochondrial protein Drp1 in neurons from patients with Alzheimer's disease: implications for neuronal damage. *Hum. Mol. Genet.* 20, 2495–2509. doi: 10.1093/hmg/ddr139

Manczak, M., and Reddy, P. H. (2012). Abnormal interaction between the mitochondrial fission protein Drp1 and hyperphosphorylated tau in Alzheimer's disease neurons: implications for mitochondrial dysfunction and neuronal damage. *Hum. Mol. Genet.* 21, 2538–2547. doi: 10.1093/hmg/dds072

Martorana, F., Gaglio, D., Bianco, M. R., Aprea, F., Virtuoso, A., Bonanomi, M., et al. (2018). Differentiation by nerve growth factor (NGF) involves mechanisms of crosstalk between energy homeostasis and mitochondrial remodeling. *Cell Death Dis.* 9:391. doi: 10.1038/s41419-018-0429-9

Massagué, J. (1998). TGF-β signal transduction. *Annu. Rev. Biochem.* 67, 753–791. doi: 10.1146/annurev.biochem.67.1.753

Miho, Y., Kouroku, Y., Fujita, E., Mukasa, T., Urase, K., Kasahara, T., et al. (1999). bFGF inhibits the activation of caspase-3 and apoptosis of P19 embryonal carcinoma cells during neuronal differentiation. *Cell Death Differ.* 6, 463–470. doi: 10.1038/sj.cdd.4400506

Mouchiroud, L., Houtkooper, R. H., Moullan, N., Katsyuba, E., Ryu, D., Canto, C., et al. (2013). The NAD^+/sirtuin pathway modulates longevity through activation of mitochondrial UPR and FOXO signaling. *Cell* 154, 430–441. doi: 10.1016/j.cell.2013.06.016

Murao, N., and Nishitoh, H. (2017). Role of the unfolded protein response in the development of central nervous system. *J. Biochem.* 162, 155–162. doi: 10.1093/jb/mvx047

Oettinghaus, B., Schulz, J. M., Restelli, L. M., Licci, M., Savoia, C., Schmidt, A., et al. (2016). Synaptic dysfunction, memory deficits and hippocampal atrophy due to ablation of mitochondrial fission in adult forebrain neurons. *Cell Death Differ.* 23, 18–28. doi: 10.1038/cdd.2015.39

Otera, H., Ishihara, N., and Mihara, K. (2013). New insights into the function and regulation of mitochondrial fission. *Biochim. Biophys. Acta* 1833, 1256–1268. doi: 10.1016/j.bbamcr.2013.02.002

Pashkovskaia, N., Gey, U., and Rödel, G. (2018). Mitochondrial ROS direct the differentiation of murine pluripotent P19 cells. *Stem Cell Res.* 30, 180–191. doi: 10.1016/j.scr.2018.06.007

Pera, E. M., Ikeda, A., Eivers, E., and De Robertis, E. M. (2003). Integration of IGF, FGF, and anti- BMP signals via Smad1 phosphorylation in neural induction. *Genes Dev.* 17, 3023–3028. doi: 10.1101/gad.1153603

Prieto, J., León, M., Ponsoda, X., Sendra, R., Bort, R., Ferrer-Lorente, R., et al. (2016). Early ERK1/2 activation promotes DRP1-dependent mitochondrial fission necessary for cell reprogramming. *Nat. Commun.* 7:11124. doi: 10.1038/ncomms11124

Reddy, P. H., Reddy, T. P., Manczak, M., Calkins, M. J., Shirendeb, U., and Mao, P. (2011). Dynamin-related protein 1 and mitochondrial fragmentation in neurodegenerative diseases. *Brain Res. Rev.* 67, 103–118. doi: 10.1016/j.brainresrev.2010.11.004

Saxton, W. M., and Hollenbeck, P. J. (2012). The axonal transport of mitochondria. *J. Cell Sci.* 125, 2095–2104. doi: 10.1242/jcs.053850

Schrepfer, E., and Scorrano, L. (2016). Mitofusins, from mitochondria to metabolism. *Mol. Cell* 61, 683–694. doi: 10.1016/j.molcel.2016.02.022

Shirendeb, U. P., Calkins, M. J., Manczak, M., Anekonda, V., Dufour, B., McBride, J. L., et al. (2012). Mutant Huntingtin's interaction with mitochondrial protein Drp1 impairs mitochondrial biogenesis and causes defective axonal transport and synaptic degeneration in Huntington's disease. *Hum. Mol. Genet.* 21, 406–420. doi: 10.1093/hmg/ddr475

Sin, J., Andres, A. M., Taylor, D. J., Weston, T., Hiraumi, Y., Stotland, A., et al. (2016). Mitophagy is required for mitochondrial biogenesis and myogenic differentiation of C2C12 myoblasts. *Autophagy.* 12, 369–380. doi: 10.1080/15548627.2015.1115172

Song, W., Chen, J., Petrilli, A., Liot, G., Klinglmayr, E., Zhou, Y., et al. (2011). Mutant huntingtin binds the mitochondrial fission GTPase dynamin-related protein-1 and increases its enzymatic activity. *Nat. Med.* 17, 377–382. doi: 10.1038/nm.2313

Uo, T., Dworzak, J., Kinoshita, C., Inman, D. M., Kinoshita, Y., Horner, P. J., et al. (2009). Drp1 levels constitutively regulate mitochondrial dynamics and cell survival in cortical neurons. *Exp. Neurol.* 218, 274–285. doi: 10.1016/j.expneurol.2009.05.010

Vantaggiato, C., Bondioni, S., Airoldi, G., Bozzato, A., Borsani, G., Rugarli, E. I., et al. (2011). Senataxin, defective in different neurodegenerative diseases modulates neurite growth through the fibroblast growth factor 8 signalling. *Brain* 134, 1808–1828. doi: 10.1093/brain/awr084

Vantaggiato, C., Redaelli, F., Falcone, S., Perrotta, C., Tonelli, A., Bondioni, S., et al. (2009). A novel CLN8 mutation in late-infantile-onset neuronal ceroid lipofuscinosis (LINCL) reveals aspects of CLN8 neurobiological function. *Hum. Mutat.* 30, 1104–1116. doi: 10.1002/humu.21012

Varum, S., Momcilović, O., Castro, C., Ben-Yehudah, A., Ramalho-Santos, J., and Navara, C. S. (2009). Enhancement of human embryonic stem cell pluripotency through inhibition of the mitochondrial respiratory chain. *Stem Cell Res.* 3, 142–156. doi: 10.1016/j.scr.2009.07.002

Vega-Naredo, I., Loureiro, R., Mesquita, K. A., Barbosa, I. A., Tavares, L. C., Branco, A. F., et al. (2014). Mitochondrial metabolism directs stemness and

differentiation in P19 embryonal carcinoma stem cells. *Cell Death Differ.* 21, 1560–1574. doi: 10.1038/cdd.2014.66

Wakabayashi, J., Zhang, Z., Wakabayashi, N., Tamura, Y., Fukaya, M., Kensler, T. W., et al. (2009). The dynamin- related GTPase Drp1 is required for embryonic and brain development in mice. *J. Cell Biol.* 186, 805–816. doi: 10.1083/jcb.200903065

Wallace, D. C. (2005). A mitochondrial paradigm of metabolic and degenerative diseases, aging and cancer: a dawn for evolutionary medicine. *Annu. Rev. Genet.* 39, 359–407. doi: 10.1146/annurev.genet.39.110304.095751

Wang, H., Song, P., Du, L., Tian, W., Yue, W., Liu, M., et al. (2011). Parkin ubiquitinates Drp1 for proteasome-dependent degradation: implication of dysregulated mitochondrial dynamics in Parkinson disease. *J. Biol. Chem.* 286, 11649–11658. doi: 10.1074/jbc.m110.144238

Wang, C., Xia, C., Bian, W., Liu, L., Lin, W., Chen, Y. G., et al. (2006). Cell aggregation-induced FGF8 elevation is essential for P19 cell neural differentiation. *Mol. Biol. Cell* 17, 3075–3084. doi: 10.1091/mbc.e05-11-1087

Wang, L., Ye, X., Zhao, Q., Zhou, Z., Dan, J., Zhu, Y., et al. (2014). Drp1 is dispensable for mitochondria biogenesis in induction to pluripotency but required for differentiation of embryonic stem cells. *Stem Cells Dev.* 23, 2422–2434. doi: 10.1089/scd.2014.0059

Waterham, H. R., Koster, J., van Roermund, C. W., Mooyer, P. A., Wanders, R. J., Leonard, J. V., et al. (2007). A lethal defect of mitochondrial and peroxisomal fission. *N. Engl. J. Med.* 356, 1736–1741. doi: 10.1056/nejmoa 064436

Wiemerslage, L., and Lee, D. (2016). Quantification of mitochondrial morphology in neurites of dopaminergic neurons using multiple parameters. *J. Neurosci. Methods* 262, 56–65. doi: 10.1016/j.jneumeth.2016.01.008

Xu, X., Duan, S., Yi, F., Ocampo, A., Liu, G. H., and Izpisua Belmonte, J. C. (2013). Mitochondrial regulation in pluripotent stem cells. *Cell Metab.* 18, 325–332. doi: 10.1016/j.cmet.2013.06.005

Yamada, T., Urano-Tashiro, Y., Tanaka, S., Akiyama, H., and Tashiro, F. (2013). Involvement of crosstalk between Oct4 and Meis1a in neural cell fate decision. *PLoS One* 8:e56997. doi: 10.1371/journal.pone.0056997

Züchner, S., Mersiyanova, I. V., Muglia, M., Bissar-Tadmouri, N., Rochelle, J., Dadali, E. L., et al. (2004). Mutations in the mitochondrial GTPase mitofusin 2 cause Charcot-Marie-Tooth neuropathy type 2A. *Nat. Genet.* 36, 449–451. doi: 10.1038/ng1341

Conflict of Interest Statement: The authors declare that the research was conducted in the absence of any commercial or financial relationships that could be construed as a potential conflict of interest.

Copyright © 2019 Vantaggiato, Castelli, Giovarelli, Orso, Bassi, Clementi and De Palma. This is an open-access article distributed under the terms of the Creative Commons Attribution License (CC BY). The use, distribution or reproduction in other forums is permitted, provided the original author(s) and the copyright owner(s) are credited and that the original publication in this journal is cited, in accordance with accepted academic practice. No use, distribution or reproduction is permitted which does not comply with these terms.

frontiers in Cellular Neuroscience

REVIEW
published: 09 April 2019
doi: 10.3389/fncel.2019.00129

Organs to Cells and Cells to Organoids: The Evolution of *in vitro* Central Nervous System Modelling

Dario Pacitti[1,2], *Riccardo Privolizzi*[3] *and Bridget E. Bax*[1]*

[1] *Molecular and Clinical Sciences Research Institute, St George's, University of London, London, United Kingdom,* [2] *College of Medicine and Health, St Luke's Campus, University of Exeter, Exeter, United Kingdom,* [3] *Gene Transfer Technology Group, Institute for Women's Health, University College London, London, United Kingdom*

With 100 billion neurons and 100 trillion synapses, the human brain is not just the most complex organ in the human body, but has also been described as "the most complex thing in the universe." The limited availability of human living brain tissue for the study of neurogenesis, neural processes and neurological disorders has resulted in more than a century-long strive from researchers worldwide to model the central nervous system (CNS) and dissect both its striking physiology and enigmatic pathophysiology. The invaluable knowledge gained with the use of animal models and *post mortem* human tissue remains limited to cross-species similarities and structural features, respectively. The advent of human induced pluripotent stem cell (hiPSC) and 3-D organoid technologies has revolutionised the approach to the study of human brain and CNS *in vitro*, presenting great potential for disease modelling and translational adoption in drug screening and regenerative medicine, also contributing beneficially to clinical research. We have surveyed more than 100 years of research in CNS modelling and provide in this review an historical excursus of its evolution, from early neural tissue explants and organotypic cultures, to 2-D patient-derived cell monolayers, to the latest development of 3-D cerebral organoids. We have generated a comprehensive summary of CNS modelling techniques and approaches, protocol refinements throughout the course of decades and developments in the study of specific neuropathologies. Current limitations and caveats such as clonal variation, developmental stage, validation of pluripotency and chromosomal stability, functional assessment, reproducibility, accuracy and scalability of these models are also discussed.

Keywords: CNS, hiPSC, human neurons, human glia, neurogenesis, neurological disorders, cerebral organoids, organotypic

OPEN ACCESS

Edited by:
Lavinia Alberi,
SICHH, Switzerland

Reviewed by:
Herb Lachman,
Albert Einstein College of Medicine, United States
Tiago G. Fernandes,
University of Lisbon, Portugal

***Correspondence:**
Bridget E. Bax
bebax@sgul.ac.uk

Received: *04 December 2018*
Accepted: *14 March 2019*
Published: *09 April 2019*

Citation:
Pacitti D, Privolizzi R and Bax BE (2019) Organs to Cells and Cells to Organoids: The Evolution of in vitro Central Nervous System Modelling. Front. Cell. Neurosci. 13:129. doi: 10.3389/fncel.2019.00129

INTRODUCTION

The study of neurogenesis (summarised in **Figure 1**), neural processes and neurological disorders is a very challenging science, as the brain is a uniquely complex organ and is largely inaccessible for experimental investigations in living humans, which is mostly limited to discarded post-surgical tissue samples or neuroimaging, transcranial magnetic stimulation and electroencephalography studies (Komssi and Kähkönen, 2006; Stan et al., 2006; Brammer, 2009; Eyal et al., 2016).

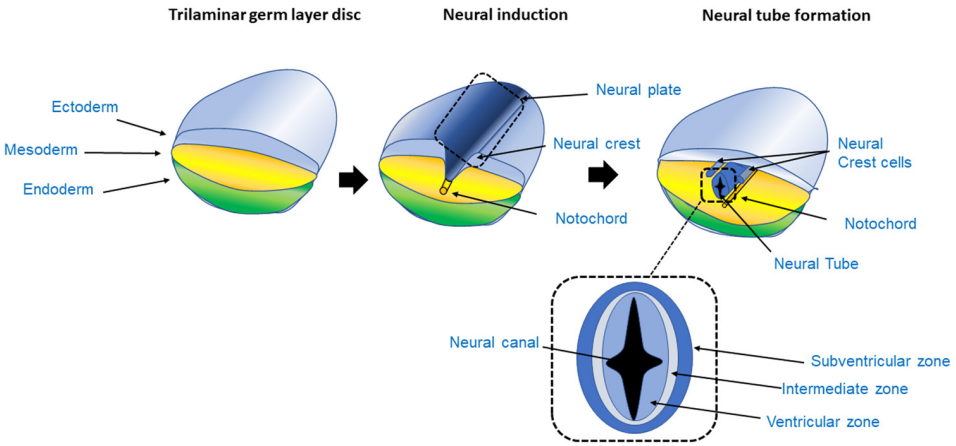


FIGURE 1 | Process of neurogenesis. The CNS originates from the ectoderm layer of the trilaminar germ disc. The process of neurogenesis begins with the formation of the neuroepithelium from the neuroectoderm, giving rise to the neural tube in a process called primary neurulation (Johns, 2014). The trilaminar germ layer disc is composed of the three germ layer tissues, the endoderm, mesoderm and ectoderm. The mesoderm gives rise to the notochord, a tubular mesodermal structure which on releasing trophic factors, triggers neural induction, whereby uncommitted or naïve ectoderm becomes committed to the neural lineage, and subsequently stimulates the formation of the neural tube in the overlying ectoderm (Dickinson et al., 1995). As the ectoderm acquires a neuroectoderm identity, it forms a fold, initially giving rise to the neural plate and subsequently forms the neural fold. The grooves at either side of the fold are called the neural crest. The crest then detaches from the margins of the neural fold giving rise to the peripheral nervous system. The neural plate continues to fold on itself giving rise to the hollow neural tube; the lumen of the neural tube is called neural canal. As the neural tube closes, it forms a fluid filled cavity that generates the ventricular zone, an area occupied by progenitor cells such as neuroblasts and glioblasts (Johns, 2014; Brodal, 2016; Kelava and Lancaster, 2016a). In the transverse section of the neural tube the VZ, intermediate zone and subventricular area can be seen. In the VZ mitosis takes place generating radial glia during neurogenesis.

While animal models have appreciably advanced the understanding of human brain development and neurodegenerative diseases, the inherent developmental, anatomical and physiological differences between the central nervous system (CNS) of animals and the human can add complexity to the interpretation of findings (Elston et al., 2001; DeFelipe et al., 2002; Roth and Dicke, 2005; Herculano-Houzel, 2009; Mohan et al., 2015). A detailed discussion of these models would go beyond the scope of this review and it has been reported elsewhere (Chesselet and Carmichael, 2012; Dawson et al., 2018). As such, the current understanding of human brain development has been limited to common features shared with other animal species (Kelava and Lancaster, 2016b). Although centuries of human *post mortem* tissue examinations have contributed to the fundaments of modern neuroscience, allowing the study of specific features of the human brain, these tissues cannot be implemented in functional studies (Filis et al., 2010; Kelava and Lancaster, 2016a). Consequently, researchers have strived to develop and optimise *in vitro* neural culture systems for advancing the understanding of the functioning of the CNS and the underlying pathogenesis of neurological diseases. Animal models, *ex vivo* and *post mortem* tissues have been utilised in other areas of brain research.

The seminal work of the pioneering "fathers" of neuroscience and Nobel laureates, Santiago Ramón y Cajal and Camillo Golgi provided the foundations for investigating the intricacies of the human nervous system's macro and micro anatomy (Ramón y Cajal, 1904; Golgi, 1906). In his published volumes, Santiago Ramón y Cajal artistically summarised his work describing the structure and organisation of the vertebrate nervous systems and discussed his theories including, amongst others, the "neuron doctrine," the law of dynamic, functional or axipetal polarisation of electrical activity in neurons and his ideas on neurogenesis, neural plasticity and neuronal regeneration/degeneration (Ramón y Cajal, 1894, 1904, 1909, 1913). Since then, neuroscientists have strived on the wealth of knowledge inherited from Cajal and Golgi, who immensely contributed to the evolution of modern neuroscience over these centuries.

In this review, we present an evolutionary overview of CNS modelling through an historical excursus (**Figure 2**), starting from the origins of neural cell cultures from tissue explants and organotypic cultures, to cell monolayers, aggregates and ultimately leading to the generation of complex three-dimensional (3-D) cultures such as cerebral organoids from patient-specific isolated cells, emphasising the growing excitement for the latter in the quest for the most representative human CNS model.

TISSUE EXPLANTS AND ORGANOTYPIC CULTURES

The first *in vitro* nervous system culture was established by Ross Harrison in 1907, where frog embryo grafts consisting of pieces of medullary tubes were cultured as hanging drops in lymph. Although Harrison was able to observe neurite extensions and maintained the culture for up to 4 weeks, it was not possible to generate permanent specimens with intact nerve fibres (Harrison, 1907, 1910). Decades later, the first culture of intact CNS from chick embryos was established, permitting the



FIGURE 2 | Evolution timeline of CNS modelling. The timeline illustrates the evolution from organ explants to the use of 2-D neural cell lines, and subsequently a shift toward pluripotent stem cell derived neural cultures leading to the development of CNS specific organoids. For each category of modelling a time excursus is presented chronologically over 100 years.

recapitulation of the developing brain architecture *in vitro*, by displaying the formation of early retinal tissue (Hoadley, 1924; Waddington and Cohen, 1936).

The original long term culture (up to 143 days) of human foetal brains was established in 1946 by Mary Jane Hogue by using the roller tube approach (Hogue, 1946, 1947). Costero and Pomerat (1951) successfully cultured neurons obtained from the cerebral and cerebellar cortex explants of adult human brains, for up to 5 weeks, using Maximow's flying-drop.

The first CNS organotypic culture was pioneered by Bousquet and Meunier (1962) using rat hypophysis. In 1966, Crain cultured explants from embryonic rat spinal cord and ganglia on collagen coated glass demonstrating that grafted neural tissue possessed organotypic differentiation and bioelectric properties for electrophysiological studies (Crain, 1966). Since then, brain slices of several cerebral areas have been established as organotypic cultures, including the hippocampus, substantia nigra, locus coeruleus, striatum and basal forebrain (LaVail and Wolf, 1973; Whetsell et al., 1981; Knopfel et al., 1989; Ostergaard et al., 1995; Robertson et al., 1997).

Although tissue explants and organotypic slice cultures more accurately recapitulate the cerebral cytoarchitecture, they are difficult to acquire and cell specific functional studies are subject to severe limitations (Kelava and Lancaster, 2016b). For instance, the handling of organotypic preparations remains quite challenging with respect to preserving the sterility, viability and the cytoarchitecture of the tissues (Walsh et al., 2005). Additionally, cell maturation in culture may differ within the explanted tissues, with some cell types displaying a mature phenotype while others remain immature, being dependent on the age of the subject at the time of tissue collection (Gähwiler, 1981).

2-D NEURAL CELL CULTURES

The improvement in the ability to maintain cell cultures for extended periods has enabled a range of isolated primary nerve cell cultures to be established, including hippocampal neurons derived from rat foetuses (Dotti et al., 1988), cortical, hippocampal, cerebellar and midbrain neurons from rat embryos (Brewer, 1995; Lingor et al., 1999), forebrain neurons of adult canaries (Goldman, 1990) and primary microglia from cerebral tissues of neonatal rats (Giulian and Baker, 1986). The generation of glial cell cultures, viable for several weeks, was also achieved as described in the seminal study by McCarthy and De Vellis; dissociated cerebral cortices of 1–2 days old rat pups brains were used to isolate primary astrocytes and oligodendrocytes that were devoid of any viable neuronal cell (McCarthy and de Vellis, 1980).

Culturing of primary neural cells, however, is hampered by a limited culture lifespan and the finite number of achievable passages with non-proliferating quiescent mature neurons (Gordon et al., 2013). To overcome this, the first neural stem cells (NSCs) were isolated from rat forebrains in

1989, establishing a self-renewing line of multipotent progenitors with the plasticity to generate progenies of the main neuronal phenotypes (Temple, 1989).

In 1992, Reynold and Weiss demonstrated the presence of NSCs in the adult CNS of murine brains through the isolation of nestin expressing cells from the striata and inducing their differentiation into neurons and astrocytes *in vitro*, thereby establishing appropriate culture conditions to demonstrate the functional attributes of these stem cells (Reynolds and Weiss, 1992). The availability of NSCs facilitated the culture of neuronal or glial cells, without the need for complex and laborious isolations of the latter cells from whole explants (Gordon et al., 2013).

In parallel, the development of immortalised cell lines eliminated the need for multiple acquisitions of tissue for neural cell culturing. The first immortalised neuronal line was derived from lymph nodes, infiltrated bone marrow and liver tissue of children with neuroblastoma cancer; these cells were cultured *in vitro* for up to 1 year and were capable of differentiating into tissues resembling mature ganglion cells (Goldstein et al., 1964). However due to the clinical heterogeneity of neuroblastoma, cultured cells were characterised by morphological variability, and thus efforts were made to develop more defined cell lines and improve the longevity of cultures (Biedler et al., 1973). This led to the generation of the SK-N-SH neuroblastoma cell line from metastatic bone tumour (Biedler et al., 1973), which was further subcloned to establish the widely used SH-SY5Y neuroblastoma line (Biedler et al., 1978).

To induce cells to display a more neuronal phenotype, the culture environment can be manipulated by the addition of growth factors and signalling molecules such as retinoids and dibutyryl cAMP (Kuff and Fewell, 1980; Kovalevich and Langford, 2013); this is exemplified by the experiment conducted by Pahlman et al. (1984), where neuroblastoma cells were exposed to retinoic acid to display a neuroblast-like phenotype expressing immature neuronal markers (Pahlman et al., 1984).

Other secondary immortalised cell lines developed for modelling neuronal cells include the mouse neuroblastoma Neuro-2a (LePage et al., 2005), PC12, a rat derived adrenal pheochromocytoma line (Greene and Tischler, 1976), the immortalised LUHMES cell line from human embryonic mesencephalic tissue and NT2 cells, a human neuronally committed teratoma derived line capable of differentiating into a mixed population of neuronal and glial cells under retinoic acid exposure (Pleasure and Lee, 1993; Coyle et al., 2011).

In neurobiology, the majority of primary neuronal tissue cultures is derived from animal sources, and as such, the techniques used to develop them suffered the same limitations of animal models, such as costs, ethical considerations, the obvious inter-species differences and the incorrect assumption that orthologous genes share similar functions in closely related living systems (Hartung, 2008; Gharib and Robinson-Rechavi, 2011; Ko and Frampton, 2016; Shipley et al., 2016). Moreover, the main concern with using immortalised cell lines for the study of neurobiology and for modelling neurological conditions, is that these cells contain genetic and metabolic abnormalities which may not represent a normal cell or those of human patients (Gordon et al., 2013; Carter and Shieh, 2015).

In 1999, Vescovi et al. established the first human multipotent NSCs derived from a 10.5-week embryonic diencephalon (Vescovi et al., 1999). The establishment of human NSCs opened exciting opportunities in neurobiology, since normal cells of human derivation, with self-renewing and long-term culturing capabilities, could be used for the generation of a multitude of functional neuronal and glial progenies for disease modelling and potential clinical applications (Carpenter et al., 1999; Jakel et al., 2004).

Although efforts for the successful long-term *in vitro* culturing of NSCs have been made (Sun et al., 2008), these cells were found to be incapable of accurately representing stem cells *in vivo*, due to their inability to recapitulate the entire range of neural lineages and hence brain development (Conti and Cattaneo, 2010; Kelava and Lancaster, 2016b).

More recently, multipotent neural cells were obtained by direct conversion of fibroblasts by the ectopic expression of *ASCL1*, *BRN2A* and *MYT1L* (Vierbuchen et al., 2010) or by the sole expression of *SOX2* (Ring et al., 2012). However, it is not clear to what extent the reprogrammed neural progenitors are capable of retaining epigenetic memory and the fidelity of the resemblance with neural progenitors is yet to be determined (Velasco et al., 2014).

HUMAN PLURIPOTENT STEM CELL-DERIVED NEURAL CULTURES

The advent of human embryonic stem cells (ESCs) in 1998 (Thomson et al., 1998) and then human induced pluripotent stem cells (iPSC) in 2007 (Takahashi et al., 2007), have provided exciting prospects in the field of neuroscience. The tremendous plasticity of these cells as an unlimited source of specific cell types, and their replicative capacity *in vitro*, rendered them the ideal candidate for neurodevelopmental studies. In particular, the possibility to generate neuronal cells directly from iPS cells derived from patients affected by a specific disorder provides an unprecedented opportunity to study the very phenotype of these diseases *in vitro*. **Figure 3**, summarises the different methods of derivation of iPSCs and the various characterisation criteria for qualifying as pluripotent cells.

The differentiation of ESCs *in vitro* reproduces with great fidelity the *in vivo* neuroectoderm formation (Wu et al., 2010), and indeed, neuronal cells were amongst the first lineages to be differentiated using PSC technology (Reubinoff et al., 2001; Zhang et al., 2001). This was first achieved using ESCs, by inducing their neuronal differentiation in spheroid-like aggregates of cells [called embryoid bodies (EBs)], cultured in serum-free conditions to selectively promote the growth of neural cells, which self-organised to form rosettes (Zhang et al., 2001). These rosettes generated structures reminiscent of neural tubes (Curchoe et al., 2012), organised as progenitor zones resembling the ventricular and subventricular zones (SVZs) with the presence of radial glia (Shi et al., 2012b; Edri et al., 2015).

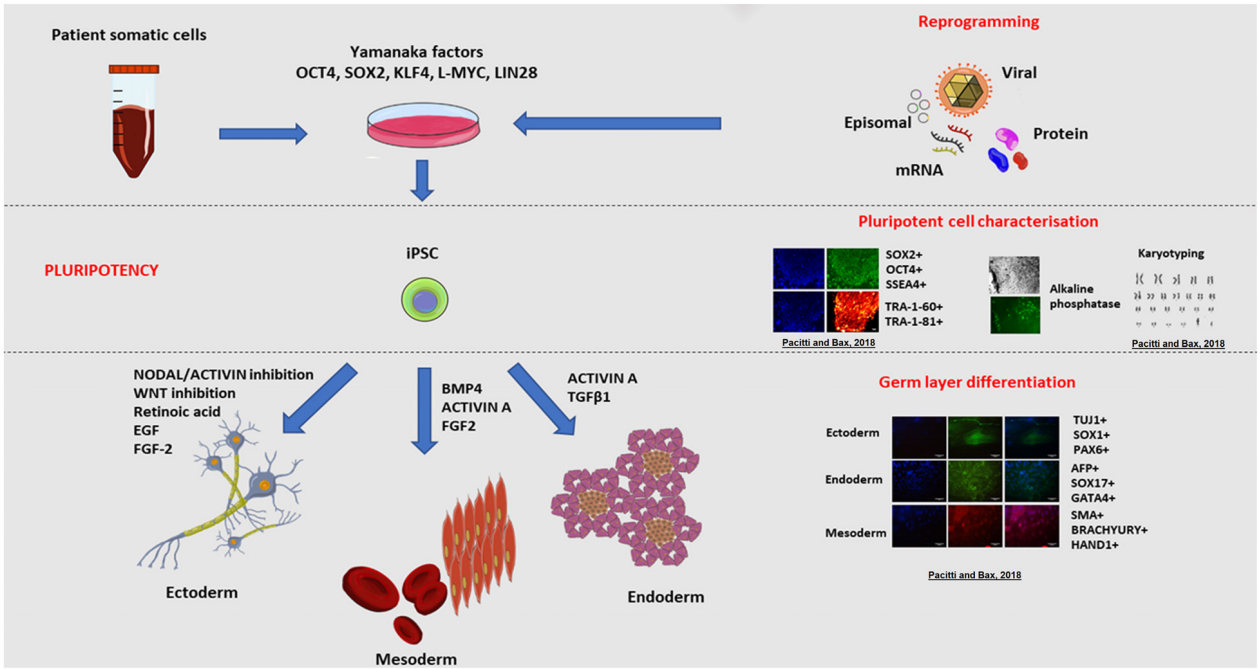


FIGURE 3 | Induced pluripotent stem cell (iPSC) derivation and characterisation. The ectopic overexpression of the transcription factors *OCT3/4*, *KLF4*, *SOX2*, *L-MYC*, *LIN28*, known to be expressed in ESCs, reverts mature somatic cells such as dermal fibroblasts and peripheral blood mononuclear cells (PBMC) to display a pluripotent embryonic-like phenotype (Takahashi et al., 2007; Okita et al., 2013). Transfection of cells with vectors expressing these transcription factors enables the epigenetic reprogramming of cells, through a series of stochastic events, to express endogenous OCT4 and NANOG, the characteristic transcription factors determining the pluripotency, self-renewal and proliferative capacity of cells (Lohle et al., 2012). In synergy, the ectopic overexpression of these genes triggers a sequence of epigenetic modifications leading to DNA demethylation and chromatin changes that eventually result in the acquisition of a pluripotent state in transfected cells (Jaenisch and Young, 2008). A multitude of vectors have been used to deliver the reprogramming factors and these approaches are broadly divided into non-viral and viral, and integration and non-integration methods. For instance, reprogramming could be achieved using viral vectors including retroviruses, lentiviruses and more recently Sendai non-integrating virus. Alternatively, non-viral methods include mRNA or protein delivery or transient expression achieved with episomal plasmids. Pluripotent stem cells are defined by the presence of specific markers including cell surface proteoglycans (TRA-1-60 and TRA-1-81) and glycosphingolipids (SSEA-3 and SSEA-4) and the expression of transcription factors OCT4 and SOX2 (Thomson et al., 1998; Tonge et al., 2011). The resulting pluripotent cells, have the same embryonic plasticity for differentiating into almost any tissue type of the three germ layers (endoderm, mesoderm and ectoderm) when stimulated by the appropriate signalling molecules and growth factors (Itskovitz-Eldor et al., 2000; Okita et al., 2013). Examples of cells derived from the germ layers include nervous and epidermal tissue from the ectoderm, haematopoietic and muscle cells from the mesoderm, and pancreatic cells from the endoderm. Copyright permission was obtained for the reproduction of images taken from Pacitti and Bax (2018).

Subsequent studies improved methodologies to differentiate ESCs to neural precursors in the complete absence of serum or growth factors (Ying et al., 2003). The combination of the embryoid body-derived rosette and the serum free media provided the foundation for the serum-free embryoid bodies culture, which in the presence of inductive signals, including Wnt and Nodal antagonists (Dkk1 and LeftyA, respectively) and Sonic hedgehog could generate forebrain (telencephalic) precursors on poly-D-lysine/laminin/fibronectin coated dishes (Watanabe et al., 2005) and could be further differentiated into cortical neurons (Gaspard et al., 2008).

However, because ESCs are of embryonic origin, they are subjected to considerable ethical and practical issues. The development of iPSCs has since introduced an advantageous tool for the study of neurodevelopment and neuropathology; the possibility of generating ESC-like cells from adult somatic cells, not only circumvents issues related to ethics and sample acquisition, but also provides the advantage of developing pluripotent lines directly from diseased patients, and hence the study of neurobiology and neurological disorders accounting for genetic variations within a more heterogeneous cohort of relevant genotypes/phenotypes (Avior et al., 2016). In fact, the same differentiation protocols can be applied to the generation of iPSCs for the provision of neural progenitors and specific neural lineages (Mariani et al., 2012).

Several different PSC differentiation methods were developed, although these are highly variable and unpredictable due to undefined factors such as the use of neural inducing stromal feeder cells, the heterogeneous nature of embryoid bodies and inefficient methods for the selective survival of neural cells (Schwartz et al., 2008; Denham and Dottori, 2011).

The development of neuralization protocols for PSCs has been one of the main areas of investigation in neuroscience and it is being achieved by the improved understanding of the underlying signalling pathways involved, leading to the development of more efficient methodologies such as dual SMAD inhibition (Chambers et al., 2009). The dual SMAD inhibition was accomplished by using Noggin and the small molecule

SB431542 to inhibit the NODAL/Activin, TGF-β and bone morphogenic protein (BMP) signalling, thereby inhibiting the differentiation into cells with a non-neural fate (Chambers et al., 2009; Pauklin and Vallier, 2015). The dual SMAD inhibition method obviated the need for stromal cells and embryoid body based techniques and permitted the efficient generation of a broad repertoire of PSC-derived neural progenitors within shorter differentiation times in adherent monolayer cultures (Chambers et al., 2009). The dual SMAD inhibition method was further improved by the addition of a glycogen synthase kinase 3 (GSK3) inhibitor to induce Wnt signalling activation, yielding progenitors which matched the gene expression profiles of developing foetal brains, and with a broad range of regional differentiation phenotypes, from rostro-caudal to midbrain and dorso-ventral patterning of neural progenitors (Kirkeby et al., 2012). In another experiment, dual SMAD inhibition was combined with retinoid signalling to enhance differentiation of PSCs to cortical neurons (Shi et al., 2012b).

Lineage priming of PSCs to the neural lineage has also been achieved by the forced expression of the single transcription factor Neurogenin-2 (or NeuroD1) which yielded the generation of mature neurons expressing glutamatergic receptors and forming spontaneous synaptic networks within 2 weeks from transfection (Zhang et al., 2013). Another study demonstrated that the forced synergistic expression of the transcription factors ASCL1 and DLX2 induced the differentiation of PSC to near pure GABAergic neurons (Yang et al., 2017).

Another common differentiation protocol uses retinoic acid treatment on embryoid bodies for promoting commitment to the neural lineage (Schuldiner et al., 2001). In participation with FGF and Wnt, retinoic acid is a potent caudalizing factor of the neuroectoderm and is a differentiation-inducing molecule essential for the development of the neural crest and the generation of cortical neurons (Villanueva et al., 2002; Diez del Corral and Storey, 2004; Siegenthaler et al., 2009). Retinoic acid has been demonstrated to inhibit neural proliferation and promote neurogenesis by inhibiting the expression of genes that negatively regulate neuronal differentiation (such as Notch and Geminin), while promoting the expression of proneural and neurogenic genes (Janesick et al., 2015). However, it is important to note that although retinoids play a fundamental regulatory role during neural tube formation, their function in neural development and axial patterning are strictly context, time and dose-dependent, and therefore it is crucial to include retinoids at an appropriate differentiation stage in cultures (Maden, 2002).

MONOLAYER CULTURES TO ORGANOIDS

With the improvement of differentiation methods, culturing techniques have also been refined to introduce structural complexities that better recapitulate the *in vivo* development and cytoarchitecture. Availability of this technology has led to a tremendous interest from researchers worldwide, particularly from the prospective of generating more representative models of the human phenotype, and as a means to "replace, reduce and refine" the use of animal models (Sneddon et al., 2017). The culture substrate is as essential to neural cell culture as the use of appropriate inducing factors. In the CNS, extra cellular matrixes (ECMs) are crucial for cell migration and differentiation, therefore *in vitro* substrates are fundamental for the preferred differentiation of NSCs and support of differentiated cells (Franco and Müller, 2011).

The best-described substrates used for the *in vitro* culture of neural cells (whether NSC or PSC-derived) are poly-L-ornithine, poly-L-lysine, fibronectin, collagen and laminin (Ge et al., 2015). All these substrates have been found to support neural differentiation to differing degrees (Ma et al., 2008). One study reports that poly-L-ornithine induces preferred differentiation of NSCs into neurons and oligodendrocytes, compared to poly-L-lysine and fibronectin (Ge et al., 2015). However, other studies suggested that laminin or laminin-rich substrates enhance differentiation of NSC to neurons (Hall et al., 2008; Ma et al., 2008).

Nevertheless, the ECM is a complex mixture of molecules (laminins, proteoglycans, collagens) and therefore specific combinations of substrates may be necessary to better reproduce the *in vivo* scenario (Ma et al., 2008; Franco and Müller, 2011). Hydrogel scaffolds such as Matrigel, which consist of a mixture of extracellular molecules including laminin, collagen IV, heparan sulphate proteoglycans and entactin (Kleinman and Martin, 2005) are often successfully employed for the culture and long-term support of neural cells (Ma et al., 2008; Lee et al., 2015). Matrigel is not only advantageous as a substrate for monolayer cultures, but due to its polymerizing nature, it can be utilised as a semi-solid scaffold matrix for 3-D cultures (Tibbitt and Anseth, 2009). However, even Matrigel is not immune from major limitations, being an animal-derived matrix characterised by batch variation and with an undefined composition that may produce a source of variability in experimental conditions (Hughes et al., 2010).

Traditional 2-dimensional (2-D) culturing has contributed immensely to the understanding of neuroscience but is substantially limited for recapitulating the *in vivo* complexities of the CNS. Advancement in cell culturing techniques for the generation of neural cell lines has greatly improved with the directed differentiation of iPSCs into monolayers of specific neural cell types (Pasca et al., 2014; Barral and Kurian, 2016; McKinney, 2017). A summary of various CNS neural tissues derived from the differentiation of iPSC is presented in **Table 1**.

However, these 2-D cultures are unlikely to recapitulate the intricate cytoarchitecture, the elaborate network of diverse neural cell types and the functional complexity of the *in vivo* CNS (Paşca, 2018). Cell differentiation and maturation is critically dependent on both intrinsic and extrinsic cues originating from the interactions with various neural cells and ECM molecules, and the cross-talk and dynamic interaction of neural cells is crucial for the recapitulation of a physiologically relevant system (Gomes et al., 2001; Rowitch and Kriegstein, 2010; Jiang and Nardelli, 2016).

Nevertheless, 2-D cultures have the advantage of a greater scalability, with less complex directed differentiation approaches

TABLE 1 | Summary of different CNS neural cells differentiated from iPSC.

Disease group	Disease modelled	Genetic/ chromosomal abnormality	iPSC-derived cells	Reprogramming method	Reference
Lysosomal storage disorders	Jansky–Bielschowsky disease	*CLN5*	CLN5 neurons	Sendai-virus transduction	Uusi-Rauva et al., 2017
	Batten disease	*CLN3, TPP1*	CLN3 neurons	Retrovirus transduction	Lojewski et al., 2014
	Pompe disease	*GAA*	Pompe neurons	Retrovirus transduction	Higuchi et al., 2014
	Niemann-Pick type C1	*NPC1*	NPC1 neurons, astrocytes	Retrovirus transduction, lentivirus transduction	Trilck et al., 2013 Efthymiou et al., 2015
Metabolic disorders	Lesch–Nyhan syndrome	*HPRT*	Neurons	Retrovirus transduction	Mastrangelo et al., 2012
	Gaucher's disease	*GBA1*	Dopaminergic neurons, neurons	Lentivirus transduction	Panicker et al., 2012 Tiscornia et al., 2013 Awad et al., 2015 Sun et al., 2015
	Metachromatic leukodystrophy	*ARSA*	Neural stem cells, astroglial progenitor cells	Retrovirus transduction	Doerr et al., 2015
	X-linked Adrenoleukodystrophy	*ABCD1*	Neurons, astrocytes, oligodendrocytes	Retrovirus transduction, lentivirus transduction	Jang et al., 2011 Baarine et al., 2015
Neurodegenerative disorders	Parkinson's disease (PD), idiopathic PD	*LRRK2, ?*	Midbrain dopaminergic neurons	Cre-recombinase excisable viruses, retrovirus transduction	Soldner et al., 2009 Nguyen et al., 2011 Sanchez-Danes et al., 2012 Fernandez-Santiago et al., 2015
	Amyotrophic lateral sclerosis (ALS)	*TDP-43, SOD1*	Spinal motor neurons, astrocytes	Retrovirus transduction, TALEN transfection, sendai-virus transduction, episomal transfection	Bilican et al., 2012 Egawa et al., 2012 Serio et al., 2013 Yang et al., 2013 Bhinge et al., 2017
Neurodevelopmental disorders	Rett syndrome	*TRPC6, MECP2*	Neural progenitor cells, glutamatergic neurons, astrocytes	Retrovirus transduction	Muotri et al., 2010 Marchetto et al., 2010 Ananiev et al., 2011 Kim et al., 2011 Williams et al., 2014 Djuric et al., 2015 Griesi-Oliveira et al., 2015 Tang et al., 2016
	Atypical Rett syndrome	*CDKL5*	Glutamatergic neurons, GABAergic neurons	Lentivirus transduction, retrovirus transduction	Amenduni et al., 2011 Ricciardi et al., 2012
	Timothy syndrome	*CACNA1C*	Neural progenitor cells, cortical glutamatergic neurons	Retrovirus transduction	Pasca et al., 2011 Tian et al., 2014
	Down Syndrome	Trisomy 21	Cortical glutamatergic neurons	Lentivirus transduction	Shi et al., 2012a
	Familial dysautonomia	*IKBKAP*	Neural crest precursors	Lentivirus transduction	Lee et al., 2009, 2012
	Fragile X Syndrome	*FMR1*	Neural progenitor cells, forebrain neurons, glial cells	Retrovirus transduction, episomal transfection	Urbach et al., 2010 Doers et al., 2014 Park et al., 2015 Halevy et al., 2015
	Cockayne syndrome	*ERCC6*	Neural progenitor cells	Sendai-virus transduction	Vessoni et al., 2016
	Angelman/Prader-Willi syndromes	*UBE3A*	Neurons, astrocytes	Retrovirus transduction	Chamberlain et al., 2010
	Phelan-McDermid syndrome	22q13 deletion	Forebrain neurons	Retrovirus transduction	Shcheglovitov et al., 2013
Neuropsychiatric diseases	Frontotemporal dementia (FTD)	*CHMP2B, C9ORF72*	Forebrain cortical neurons	Retrovirus transduction, episomal transfection	Almeida et al., 2013 Zhang et al., 2017
Epilepsy	Dravet syndrome	*SCN1A*	Dopaminergic, GABAergic, glutamatergic neurons, forebrain interneurons, glial cells	Retrovirus transduction	Higurashi et al., 2013 Jiao et al., 2013 Liu et al., 2013, 2016

(Continued)

TABLE 1 | Continued

Disease group	Disease modelled	Genetic/ chromosomal abnormality	iPSC-derived cells	Reprogramming method	Reference
	Early infantile epileptic encephalopathy	*STXBP1*	GABAergic, glutamatergic neurons	Episomal transfection	Yamashita et al., 2016
Neuromuscular disorders	Spinal muscular atrophy (SMA)	*SMN1*	Forebrain, sensory, motor neurons, astrocytes	Lentivirus transduction, retrovirus transduction, episomal transfection	Ebert et al., 2009 Chang et al., 2011 Sareen et al., 2012 Corti et al., 2012 McGivern et al., 2013 Schwab and Ebert, 2014 Yoshida et al., 2015 Boza-Moran et al., 2015 Ng et al., 2015 Nizzardo et al., 2015 Liu et al., 2015 Fuller et al., 2015 Xu et al., 2016 Patitucci and Ebert, 2016
Movement disorders	Huntington's disease	*HTT*	Medium spiny neurons	Lentivirus transduction	The Hd iPsc Consortium, 2012
	Hereditary spastic paraplegia	*SPG3A, SPG4, SPG11, ATL1, SPAST*	Cortical neural progenitor cells, forebrain, glutamatergic neurons	Lentivirus transduction, episomal transfection, retrovirus transduction	Denton et al., 2014 Havlicek et al., 2014 Zhu et al., 2014 Mishra et al., 2016
	Ataxia telangiectasia	*ATM*	Neural progenitor cells, GABAergic neurons	Lentivirus transduction	Nayler et al., 2012 Carlessi et al., 2014
	Friedrich's ataxia	*FXN*	Neural progenitor cells, neural crest cells, peripheral sensory neurons, glial cells	Retrovirus transduction, lentivirus transduction, transposon transfection	Liu et al., 2011 Eigentler et al., 2013 Hick et al., 2013 Bird et al., 2014

Neural cells characteristic of the CNS have been generated by directed differentiation of pluripotent stem cell derived lines, to recapitulate specific cell types or disease condition.

and facilitated imaging. However, 2-D cells also favour stronger interactions with the surfaces of the culturing vessel rather than cell–cell interactions or between cells and the ECM, altering their proliferation and differentiation capabilities (Paşca, 2018). Three dimensional models can overcome 2-D culturing limitations, allowing the dynamic interactions between cells and ECMs and the recreation of signalling, metabolites and oxygen gradients across the culture (Ko and Frampton, 2016).

A variety of 3-D culture methods have been developed, with one example in the form of tissue explant cultures, such as whole brain sections grown in culture dishes or microfluidic devices (Ullrich et al., 2011; Huang et al., 2012).

For instance, recently, an organotypic human Alzheimer disease model consisting of a 3-D triculture system of neurons, astrocytes and microglia co-cultured in a microfluidic system was engineered. Authors developed this 3-D culture system to model the neuroinflammation and neurodegeneration aspects of the disease, employing human iPSC-derived NSCs overexpressing mutant *APP* and *PSEN1* genes associated with familial Alzheimer's. This system successfully recapitulated the tauopathy, β-amyloid accumulation and microglia mediated neuroinflammation more efficiently than the 2-D models (Park et al., 2018).

However, these cultures are often problematic to maintain in the long-term and are generally derived from animal sources, and hence not representative of human development (Ko and Frampton, 2016). Self-organised aggregate cultures are an alternative 3-D *in vitro* culture approach, encompassing neural spheroids (Dingle et al., 2015). Further sophistication of culture methods has led to the modification of self-aggregating cultures for the generation of organ-like structures, termed organoids (Kelava and Lancaster, 2016b).

Central nervous system organoids can be divided in two categories based on their patterning approach, either being self-patterned or extrinsically patterned. Self-patterned organoids are organoids that are cultured without the addition of exogenous morphogens that favour specific brain regions, whereas extrinsically patterned organoids refer to the generation of brain specific regional identities via the addition of morphogens and neurotrophic factors such as FGF, Sonic Hedgehog, Nodal, Wnt and BMP (Clevers, 2016; Brawner et al., 2017). **Figure 4** illustrates the different brain regionals identities recapitulated in CNS organoids.

To illustrate this, the seminal study of Eiraku et al. (2008) demonstrated that serum-free embryoid bodies with quick reaggregation are capable of self-organising into stratified cortical

tissues in cultures, thus showing that ESCs spontaneously differentiate toward a neural state by default. This notion provided the fundaments to generate the first self-patterned CNS organoid, employing serum-free embryoid bodies to generate neuroepithelial cysts, which further self-organised into optic cup organoids, to present regions with retinal identities upon treatment with Nodal protein and culture on Matrigel basement membrane (Eiraku et al., 2011).

Extrinsic-patterning organoids can be exemplified by the generation of the first dorsal telencephalon organoid recapitulating a human cerebral cortex at 8–10-week gestation by Mariani et al. (2012), where serum-free embryoid bodies were treated with Wnt and TGF-β inhibitors and cultured on poly-L-ornithine, laminin and fibronectin for up to 70 days. Similarly, other adaptations of the method developed by Eiraku and colleagues led to the generation of neocortical forebrain organoids maintained on Matrigel for over 3 months (Kadoshima et al., 2013). Further modifications of protocols for the generation of organoids patterned with other brain specific regions and sub-regions have been developed to model the adenohypophysis (using hedgehog agonists) (Suga et al., 2011), hypothalamus (by Nodal/Activin/TGF-β, and BMP mediated inhibition) (Wataya et al., 2008), cerebellum (using the Nodal/Activin/TGF-β inhibition and the addition of FGF2 and FGF19) (Muguruma et al., 2015), midbrain (by using the dual SMAD inhibition and Wnt activation) (Jo et al., 2016) and hippocampal-choroid plexus (by treatment with BMP and Wnt) (Sakaguchi et al., 2015). Combining the strong neuralizing dual SMAD inhibition with the serum-free embryoid body approach also enabled the generation of cortical spheroids, which represented 3-D tissues containing neurons and astrocytes and mimicked cortical development stages up to the mid-foetal period (Pasca et al., 2015).

Lancaster and Knoblich (2014) introduced, for the first time, the concept of whole-brain organoid or cerebral organoids (**Figure 5**), representing different brain regions within the same 3-D platform. Cerebral organoids, are generated from PSC-derived serum-free embryoid bodies obtained by culturing in low concentrations of bFGF-2 and with ROCK inhibitors to promote cell survival (Lancaster and Knoblich, 2014). The serum-free embryoid bodies are subsequently induced to differentiate to the neuroectoderm within suspension cultures, establishing a radially organised neuroepithelium around the spheroid (Lancaster and Knoblich, 2014; Sutcliffe and Lancaster, 2017).

The resulting neurospheres are embedded into Matrigel hydrogel droplets, allowing the growth of continuous and orientated neuroepithelial buds and, the apicobasal expansion of the layer of neuroepithelial cells throughout the ECM basement scaffold. After the embedding, budding neuroepithelia generate fluid filled cavities reminiscent of ventricles. The neuroepithelium begins to migrate outwardly to generate the cortical layers consisting of Cajal-Retzius cells, deep and superficial cortical progenitors. On exposure to retinoic acid, cerebral organoids self-organise through self-patterning mechanisms to display sparse populations of neural progenitors including radial glia, which begin to expand forming cerebral structures (Lancaster and Knoblich, 2014). Retinoic acid is only added for terminal differentiation, as being a potent caudalizing factor it inhibits neurogenesis in the early stages of neuroepithelium formation (Petros et al., 2011).

The region in which radial glia originate, recapitulates the *in vivo* ventricular zone (VZ) and SVZ (Kelava and Lancaster, 2016a). Therefore, similar to *in vivo* neurogenesis, neural progenitors migrate to form the cortical plate, spontaneously giving rise to distinct brain regions reminiscent of the dorsal cortex, ventral forebrain, hindbrain, midbrain, retina, hippocampus and choroid plexus (Lancaster and Knoblich, 2014).

As cerebral organoids expand in culture, the neuronal population increases in number, resulting in the enlargement of tissues, reaching sizes of up to 4 mm in diameter (Sutcliffe and Lancaster, 2017). The whole development process requires 7–10 days for the generation of neurospheres, and more than 20 days before the appearance of the first mature neural population (Lancaster and Knoblich, 2014; Sutcliffe and Lancaster, 2017). After 1 month in culture the cerebral tissue begins to thicken, showing tissues of different regional identities, as evidenced by the expression of FOXG1 (forebrain), TTR (choroid plexus), FZD9 (hippocampus) and SOX2 (VZ radial glia) (Lancaster and Knoblich, 2014). Later studies have confirmed that cerebral organoids display with high fidelity the gene expression signatures of a foetal developing neocortex (Camp et al., 2015).

The increase in size introduces problems with regard to nutrient and oxygen diffusion through the central regions of tissue, causing necrosis (Lancaster and Knoblich, 2014). Therefore, the organoids are grown in spinning bioreactors to provide agitation and maximise oxygen and nutrient exchange (Kelava and Lancaster, 2016b). Within bioreactors, cerebral organoids are capable of displaying a longevity of up to 1 year, although it has been reported that growth becomes stationary after 5 months, with organoids shrinking in size in subsequent months due to neuronal loss and disappearance of progenitors (Lancaster and Knoblich, 2014).

MODELLING NEUROLOGICAL DISORDERS WITH CNS ORGANOIDS

Since the generation of the first brain organoids, unsurprisingly, there has been an exponential surge in publications employing this technology (**Figure 6**), due to their amenability for the study of neurodevelopment and neurological diseases, but also as a potential platform for the development of novel neurotherapeutics. When searching Pubmed using the terms "Cerebral organoid," "Brain organoid," "CNS organoid," and "Cortical organoid" the number of publications for the year 2013 were 4, compared to 52 and 77 for the years 2017 and 2018, respectively. Due to the significant expansion and importance of this technology, this section of the review will primarily focus on the applications and advancements in this field. Cerebral organoids are indeed a relatively new platform but are finding wider application as *in vitro* disease modelling tools, not only for many developmental disorders, but also for

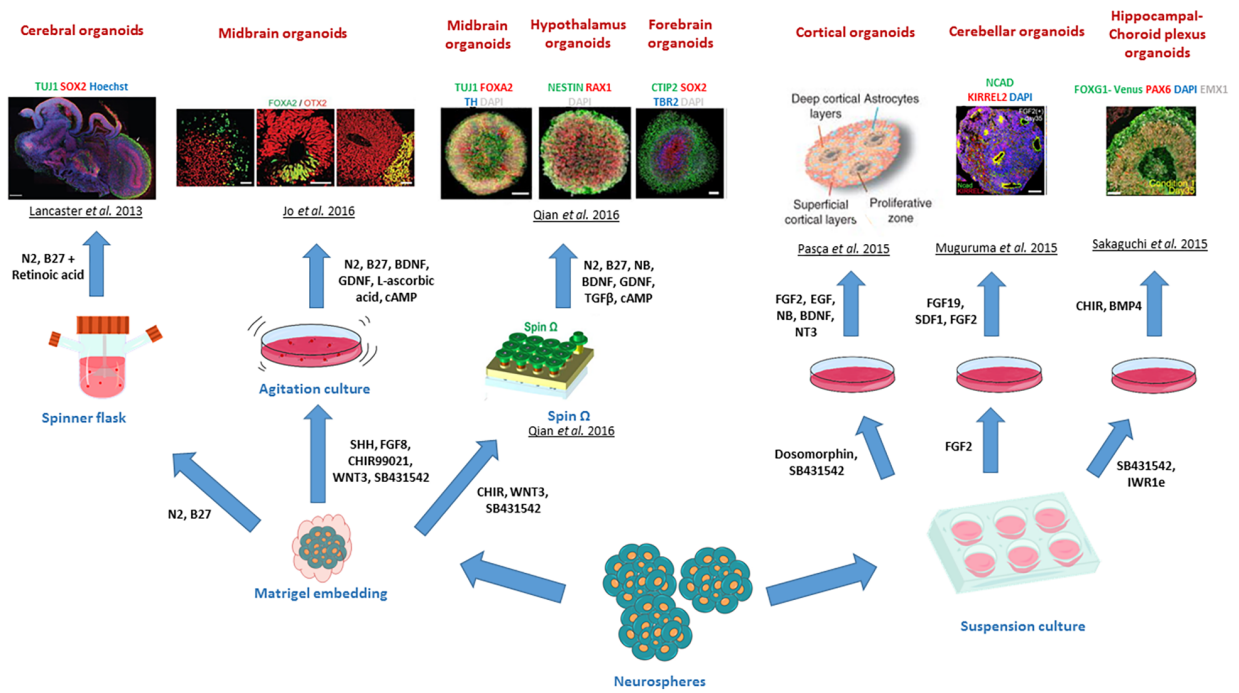


FIGURE 4 | Different brain regional identities recapitulated by CNS organoids. The diagram summarises the various patterning methods developed to generate region specific CNS organoids. Copyright permission was obtained for the reproduction of images taken from Lancaster et al. (2013); Muguruma et al. (2015), Pasca et al. (2015); Sakaguchi et al. (2015), Jo et al. (2016); Qian et al. (2016).

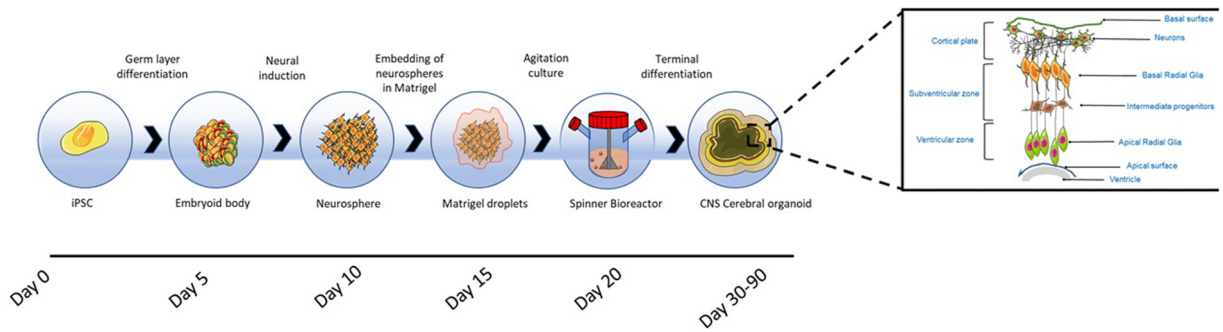


FIGURE 5 | Cerebral organoid formation. Cerebral organoids originate from pluripotent stem cell derived embryoid bodies cultured in low concentrations of bFGF-2 and with ROCK inhibitors to prevent anoikis. The embryoid bodies are differentiated toward neuroectoderm, resulting in the formation of neurospheres, which are embedded into Matrigel hydrogel droplets. After the embedding, budding neuroepithelia generate fluid filled cavities reminiscent of ventricles. The neuroepithelium begins to migrate outwardly to generate the cortical layers consisting of Cajal-Retzius cells, deep and superficial cortical progenitors. On exposure to retinoic acid, cerebral organoids self-organise through self-patterning mechanisms to display diverse populations of neural progenitors including radial glia, which expand forming cerebral structures (Lancaster and Knoblich, 2014). The region in which radial glia originate, recapitulates the *in vivo* VZ and SVZ (Kelava and Lancaster, 2016a). Prior to neurogenesis, radial glia are formed from the neuroepithelial cells and facilitate the migration of the neural and glial progenitors (Howard et al., 2008; Johns, 2014); these cells are characterised by the asymmetric self-renewal division leading to the generation of one neuron and one radial glia (Gotz and Huttner, 2005; Lancaster and Knoblich, 2012). Radial glia migrate, establishing the SVZ, where cells divide symmetrically forming intermediate progenitors (Haubensak et al., 2004; Miyata et al., 2004). Radial glia produce outer radial glia in the SVZ, which are self-renewing (Fietz et al., 2010; Hansen et al., 2010). Radial glia residing in the VZ divide at the apical surface adjacent to the ventricle. Intermediate progenitors and basal radial glia migrate basally to the SVZ. Neurons formed from radial glia, migrate radially from the ventricular and SVZ toward the basal region to establish the cortical plate (Johns, 2014; Kelava and Lancaster, 2016a). The neuronal migration depends on a layer of Cajal-Retzius cells and the outward migration is regulated by the protein reelin secreted by the latter cells (Frotscher, 1998). Within the intermediate zone of the cerebral hemispheres, neurons undergo apoptosis, and the region becomes the subcortical white matter (Johns, 2014).

psychiatric diseases and neurodegenerative conditions (Lancaster et al., 2013; Mariani et al., 2015; Garcez et al., 2016; Jo et al., 2016; Kelava and Lancaster, 2016a; Raja et al., 2016; Bershteyn et al., 2017; Birey et al., 2017; Iefremova et al., 2017). The advent of genome editing techniques such as CRISPR/Cas9 has changed the scene for tackling genetic disorders and opened

a new chapter for potential stem cell applications in the clinic (Waddington et al., 2016). In particular, organoids' versatility and adaptability to genome editing techniques or gene therapy approaches make them valuable candidates for the identification and testing of novel therapeutic approaches (Yin et al., 2016; Gonzalez-Cordero et al., 2018).

Microcephaly

Lancaster and colleagues generated organoids from a patient harbouring a *CDK5RAP2* mutation, and demonstrated that the organoids from the patient with microcephaly were smaller compared to a healthy control. This was explained by fewer proliferating progenitors and a premature differentiation in the disease tissues. The group also demonstrated that the phenotype could be rescued by inducing the expression of the wild-type gene (Lancaster et al., 2013).

Furthermore, cerebral organoids have aided the understanding of microcephaly associated with neuroinfection with the Zika virus. In the study of Garcez et al. (2016) human cortical organoids infected with Zika virus exhibited a 40% decrease in size compared to non-infected controls. An elegant study by Qian et al. (2016) introduced an innovation in culturing cerebral organoids through the use of miniaturised spinning bioreactors (the SpinΩ), and the authors determined that infection of organoids with Zika virus resulted in an increase in apoptosis with consequent reduction in cell proliferation and a marked thinning of the ventricular zone. Another study found that human iPSC-derived cerebral organoids infected with Zika virus had a decrease in PAX6 expressing progenitors in the proliferative zones and consequently a decrease in differentiated neurons leading to a disruption in the cortical plate formation (Cugola et al., 2016). Dang et al. (2016) found that Zika virus infection in organoids induced a significant upregulation of Toll-like receptor 3 gene, leading to apoptosis and dysregulation of neurogenesis.

Macrocephaly

Li et al. (2017) demonstrated the recapitulation of macrocephaly in cerebral organoids, by the genetic ablation of *PTEN* using CRISPR/Cas9. Edited organoids exhibited an activation in AKT signalling in neural progenitors regulating cortical maturation, resulting in a delay in neuronal differentiation, an increase in cellular proliferation or radial glia progenitors, and a significant increment in organoid sizes (Li et al., 2017).

Autistic Spectrum Disorder

Mariani and colleagues employed iPSCs derived from patients with idiopathic autism spectrum disorder to generate cerebral organoids; the patient tissues exhibited an overgrowth of neurites and synapses, in a similar fashion to that observed in post mortem brain investigations of individuals with autism. The same study observed an increased production of GABA-ergic inhibitory interneurons in patient organoids, while also identifying an upregulation of *FOXG1*, thus indicating a correlation between the two observations (Mariani et al., 2015). Using cerebral organoids combined with monolayer cultures, Mellios et al. (2017) characterised defects in neurogenesis associated with MeCP2 deficiency in Rett syndrome, which consisted primarily in expanded ventricular zones with enhanced PAX6+ ventricle-like structures. In this study, through the inhibition of miR-199, affected signalling pathways (PKB/AKT and ERG/MAPK) were rescued and the dysregulations in neural differentiation ameliorated (Mellios et al., 2017).

Miller-Dieker Syndrome

Miller-Dieker syndrome, a form of lissencephaly, was modelled using patient-derived iPSCs, enabling the identification of a stalled mitosis of outer radial glia, thus suggesting that dysfunctions in progenitor cell cycles could be a feature of cortical malformations in the disease (Bershteyn et al., 2017). Another study identified non-cell autonomous defects in Wnt signalling associated with Miller-Diekers syndrome (Iefremova et al., 2017).

Sandhoff Disease

Allende et al. (2018) developed cerebral organoids from iPSCs derived from an infant with Sandhoff disease and from isogenic controls corrected for the *HEXB* mutation by gene editing. The authors demonstrated that GM2 ganglioside only accumulated in the disease organoids and affected organoids displayed an increase in size and cellular proliferation compared to the isogenic control counterpart (Allende et al., 2018).

Schizophrenia

In their study examining the association of *DISC1* gene with schizophrenia, Ye et al. (2017) used human cortical organoids to demonstrate that DISC1/Ndel1 interactions regulate mitotic events in NSCs and that a delay in mitosis was observed in organoids derived from a patient with a *DISC1* mutation.

Modelling Prenatal and Perinatal Drug Exposure

Cerebral organoids have been used to investigate how the prenatal exposure to substances of abuse including illegal drugs, alcohol and tobacco affect neurogenesis. A study examining the exposure of cocaine, demonstrated that cytochrome P450 CYP3A5-mediated oxidative metabolism was responsible for the developmental abnormalities of the foetal neocortex, resulting in the inhibition of neuroepithelial progenitor proliferation, premature neuronal differentiation and a reduction in the cortical plate formation (Lee et al., 2017). Zhu et al. (2017a) investigated the effects of ethanol exposure in organoids to better understand alcohol-induced defects in neurogenesis in foetal alcohol syndrome, and where able to identify through a transcriptome analysis, gene expression alterations in the Hippo pathway and in other genes including *GSX2* and *RSPO2*. Another study using organoids-on-chip investigated the effect of nicotine on neural development, demonstrating a disruption in cortical development in exposed organoids (Wang et al., 2018). The use of organoids for studies on the effect of drug exposure on embryonic CNS development would not be limited to substances of abuse, but could also be used in the context of neurodevelopmental toxicity whereby toxicological profiles of compounds on teratogenicity or

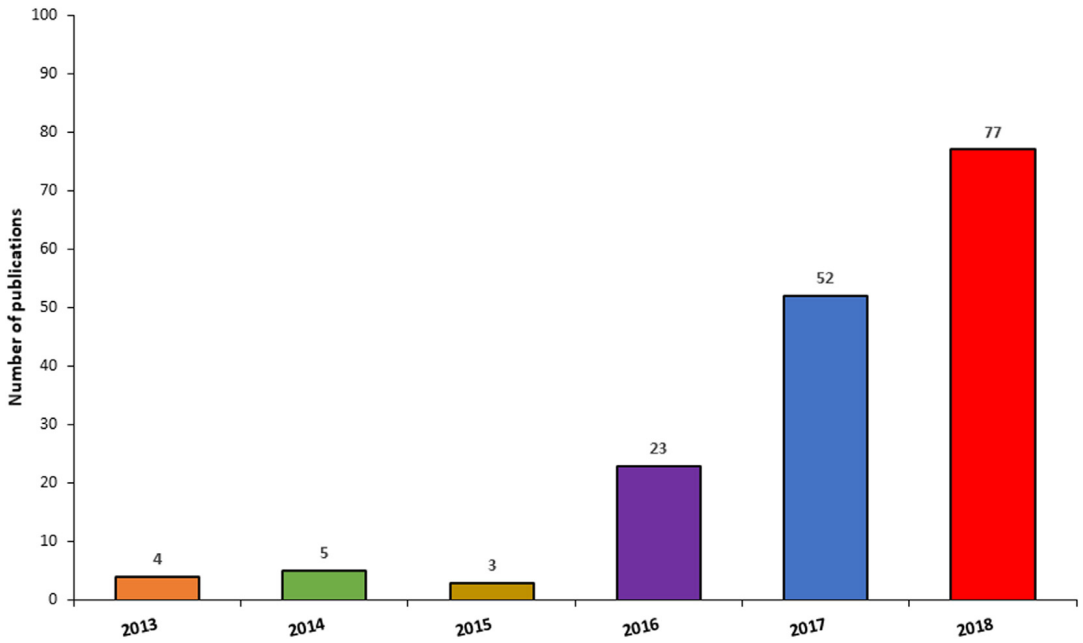


FIGURE 6 | Frequency of publications reporting the use of CNS organoids by year. The chart illustrates a surge in publications involving the use of CNS organoids, between 2014 and 2018.

neurotoxicity could also be assessed in the system, such as for the evaluation of the neural teratogenic effect of valproic acid or the effect of environmental chemicals (Schwartz et al., 2015; Miranda et al., 2018b; Wood et al., 2018).

Alzheimer's Disease

The limitations of cerebral organoids in recapitulating only early neurogenesis, hinders their application for studying late-onset neurodegenerative diseases such as Alzheimer's, Parkinson's and Huntington's (Kelava and Lancaster, 2016a). Nevertheless, Raja et al. (2016) developed cerebral organoids derived from patients with early onset familial Alzheimer's, and were able to recapitulate the disease phenotype through the demonstration of β-amyloid aggregation, hyperphosphorylated tau proteins and abnormal endosomes. The authors further demonstrated that β-amyloid and tau pathologies were significantly reduced when treating patient organoids with β and γ secretase inhibitors (Raja et al., 2016).

OTHER DEVELOPMENTS AND APPLICATIONS

More recently, research groups have sought to optimise and advance methods for the generation of more reproducible and morphologically complex organoids. For instance, Basuodan et al. (2018) have generated 3-D cultures with characteristics similar to cerebral organoids by transplanting iPSC-derived neurospheres embedded in ECM matrix, into brains of ischaemic mice (Basuodan et al., 2018).

Organoids also provide a powerful tool for the study of evolutionary developmental biology, and for comparing neurogenesis between species *in vitro* (Giandomenico and Lancaster, 2017). More recently, due to the advancement in gene editing technologies, such as CRISPR/Cas9, Neanderthal cerebral organoids were generated by introducing the Neanderthal gene *NOVA1* in human iPSCs. This study demonstrated that Neanderthal brain organoids resembled to a certain degree, organoids generated from patients with autism, indicating that these similarities may be linked to socialisation behaviours (Cohen, 2018).

Moreover, organoids have been used to study cellular migration, cross-talk and circuitry assembly by either generating region-specific organoids and fusing them, or by co-culturing cells from different lineages in a single organoid, and thus generating structures referred to as assembloids (Birey et al., 2017; Workman et al., 2017; Pham et al., 2018). By using this approach, forebrain assembloids derived from patients with Timothy syndrome, were shown to have defects in the migration of cortical interneurons, and these could be restored pharmacologically by modulating the mutated L-type calcium channel, thus contributing significantly to the understanding of epilepsy and autism associated with the syndrome (Birey et al., 2017).

The substantial versatility of organoid applications is demonstrated in the interesting experiment conducted by Mattei and colleagues, where cerebral organoids were employed to investigate how neurogenesis and neural development could be affected by microgravity. In projection of spaceflight advancements, the authors cultured human organoids in rotary cell culture system to demonstrate that microgravitational

changes influenced the expression of rostral-caudal patterning genes and cortical markers (Mattei et al., 2018).

Literature reports on the ability of organoids to recapitulate the composition of an adult CNS were elusive in the initial phases. Seminal studies on the comparison of cerebral organoids to foetal brains, initially suggested that the development of fully matured cerebral organoids could only parallel the early embryonic cerebral development observed at 8–10 weeks gestation (Mariani et al., 2012; Kelava and Lancaster, 2016a,b). However single cell sequencing experiments have revealed that organoids are capable of replicating late-mid foetal periods of a 19–24 weeks gestational brain (Pasca et al., 2015).

Given the ability of organoids to recapitulate developmental timing, much interest has also been directed at the types of CNS neural cell populations which compose organoids and their maturation stage, such as glial cells. A recent study conducted by Monzel et al. (2017) reported the presence of differentiated glial cells in midbrain organoids from as early as day 27 of development, with myelinating oligodendrocytes ensheathing neurites at day 61 (Monzel et al., 2017). Moreover, the same study demonstrated that after 61 days, mature astrocytes staining for S100β and AQP4 characterised mature midbrain organoids (Monzel et al., 2017). Additional studies have further demonstrated that cerebral organoids cultured for prolonged periods, ranging from months up to 1.5 years, displayed the presence of differentiated astrocytes and oligodendrocytes (Camp et al., 2015; Renner et al., 2017; Matsui et al., 2018). Furthermore, using culture times of over a year has been shown to yield organoids exhibiting a large proportion of mature glial cells and gene expression profiles comparable to those of post-natal brains (Renner et al., 2017; Sloan et al., 2017).

Our group has used cerebral organoids to model mitochondrial neurogastrointestinal encephalomyopathy (MNGIE), a rare metabolic disorder which manifests with leukoencephalopathy amongst other neurological and gastrointestinal symptoms (Pacitti, 2018; Pacitti and Bax, 2018). The ability of organoids to produce differentiated astrocytes and myelinating oligodendrocytes, and most importantly the recreation of a physiologically relevant cross-talk between cells has been a great asset for investigating the leukodystrophic manifestations of the disease and shed light on the poorly understood pathomolecular mechanisms of the CNS involvement in MNGIE (Pacitti, 2018; Pacitti and Bax, 2018).

In comparison to 2-D cultures, brain organoids represent a valuable tool for the study of glial cells as, for instance, when dealing with astrocytes, traditional monolayer cultures are inadequate since the morphological complexity and the vast heterogeneity cannot be appropriately modelled (Imura et al., 2006; Lange et al., 2012; Puschmann et al., 2013). Also, astrocytes cultured in 2-D preferentially interact with plastic surfaces rather than between cells and the ECM (Paşca, 2018). Most importantly, astrocytes in 2-D cultures tend to have an undesirably high baseline reactivity, possibly caused by serum components, although this can be minimised by using serum-free neurobasal formulations (Foo et al., 2011; Pekny and Pekna, 2014; Pasca et al., 2015). However, iPSC-derived astroglial cells in 2-D cultures require extensive timing to allow for maturation, and thus practicalities inherent to long term culturing of cell monolayers, for appropriate astrocyte maturation, represent a major challenge (Dezonne et al., 2017; Sloan et al., 2017). In addition to cell intrinsic properties, astrocyte maturation may require interactions with other neural cells types, which would not be represented in pure astrocyte cultures differentiated by pluripotent cells, unless specifically co-cultured after differentiation (Chandrasekaran et al., 2016).

Three dimensional cultures, like cerebral organoids, allow the recreation of a more physiological spatial environment that favours a representative organisation of astrocytes and their interactions with other neural cells and ECM components (Pasca et al., 2015; Liddelow and Barres, 2017). Compared to 2-D cultures, 3-D cultures have indeed demonstrated a better capacity for recapitulating astrocyte heterogeneity (Puschmann et al., 2013; Puschmann et al., 2014; Liddelow and Barres, 2017). Moreover, in 3-D cultures, basal reactivity of astrocytes is negligible, rendering them the ideal platform for the study of the heterogeneous spectrum of astrocyte subtypes and their activation (Puschmann et al., 2013; Pasca et al., 2015; Liddelow and Barres, 2017).

CURRENT CAVEATS AND ADVANCEMENT IN THE ORGANOID TECHNOLOGY

While cerebral organoids offer an advantageous culture system with diversified neural cells for modelling as closely as possible the intercellular interactions during organogenesis, the technology also suffers from some limitations, which are constantly being addressed with ongoing research efforts. One of the greatest limitations of the 3-D platform is the confounding batch variability (Di Lullo and Kriegstein, 2017; Paşca, 2018). Cell differentiation relies on spontaneous events that are characterised by a high degree of stochasticity as they lack developmental axes (Paşca, 2018). This results in regional identities that could differ in distribution, composition and densities between organoids, generating concerns regarding reproducibility, accuracy and scalability (Di Lullo and Kriegstein, 2017). The spontaneous self-patterning mechanisms on which cerebral organoids rely, results in the formation of several brain regional identities, when compared to brain region-specific organoids. As such, cerebral organoids are characterised by a great level of heterogeneity and complexity, which result in morphological variabilities between and within organoid batches, leading to inherent reproducibility issues (Lancaster et al., 2013; Kelava and Lancaster, 2016a). Referring to this elevated variability, Lancaster and colleagues suggested that if using organoids to detect phenotypes in the context of genetic disorders, defects must be robust enough to be noticeable (Lancaster and Knoblich, 2014; Kelava and Lancaster, 2016b; Giandomenico and Lancaster, 2017). In fact, organoid variability could have severe implications with respect to disease modelling, drug screening or neurodevelopmental studies, as the heterogeneity could affect the consistency of phenotypes exhibited, masking true differences between diseased and healthy, or treated and non-treated tissues.

Organoid variability would appear to be partly accountable to a bioreactor-based effect, meaning that a more controlled growth microenvironment would contribute to a better reproducibility (Quadrato et al., 2017).

More recently, polymer microfilaments were implemented as scaffolds to promote a more elongated generation of embryoid bodies, which has been found to enhance neuroectoderm formation and cortical development, and also reduce the issues of reproducibility and variability observed in the regional identities of filament scaffolded organoids (Lancaster et al., 2017).

Contrarily to the "intrinsic" self-patterning protocol, patterning of organoids using inductive signals and optimised bioreactors, as conducted by Qian et al. (2016), led to the development of more consistent region specific organoids which were less influenced by batch variability. Optimal patterning and the relevant reproduction of proper developmental axes requires a spatiotemporally defined gradients of morphogens, which is challenging to achieve in culture; it has been suggested that a way to circumvent this could be through the use of slow-releasing microbeads to establish a morphogen gradient (Lee et al., 2011; Sun et al., 2018). In contrast, a recent study revealed that the removal of inductive factors such as those used for the dual SMAD inhibition during the EB differentiation stage, or refraining from using maturating growth factors in culture medium during the organoid stage (such as BDNF, GDNF and TGF-β), yields more optimal organoids with reduced inter and intra batch variability in terms of reproducibility, size, growth and neural cell composition and maturity (Yakoub and Sadek, 2018). Cerebral organoids generated through this optimised protocol exhibited a robust neuronal zone and positive staining for general neuronal and mature astrocytic markers, and were characterised by a strong upregulation of neurotransmitter receptor genes involved in synaptic functions including the glutamate, α-amino-3-hydroxy-5-methyl-4-isoxazolepropionic acid (AMPA) receptor GluA1, and the *N*-methyl-D-aspartate (NMDA) receptors GluN1, GluN2A and GluN2B, and the γ-amino butyric acid (GABA) receptor GABA-B receptor 1 (Yakoub, 2019).

Potentially, the elevated variability observed in EB preparations may contribute to the heterogeneity observed between organoid preparations (Wilson et al., 2014). Therefore, controlling this heterogeneity, deriving from the spatial disorganisation and asynchronous differentiation of EB aggregates, could further minimise reproducibility issues observed during organoid development (Miranda et al., 2015, 2018a). The use of centrifugal forced-aggregation and silicon micro-textured surfaces improved symmetry, size and synchronised differentiation in EB, increasing consistency between preparations (Ungrin et al., 2008). Another example of a possible bioengineering solution to control aggregate size and size by cellular confinement, could be identified in the use of microfabrication technologies where organoids cultured on a micropillar array exhibited robust brain regionalization and cortical organisation (Zhu et al., 2017b).

Organoids lack some cells of the CNS including endothelial cells composing the cerebral vasculature, the blood–brain barrier (BBB), and microglia, as these do not derive from ectodermal tissues (Di Lullo and Kriegstein, 2017). These cells are found to have a role in CNS development via extrinsic signals that induce maturation and differentiation of neural cells including astrocyte and cortical neurons (Stubbs et al., 2009; Cunningham et al., 2013; Sloan et al., 2017).

The lack of vascularisation has been reported to prevent the delivery of oxygen and small molecules deep inside the tissue, often resulting in necrosis within the centre of the organoids. Most importantly, the lack of vascularisation interferes with certain patterning cues necessary for organoid development and progenitor differentiation. Late developing brains are highly dependent on vascularisation as niches of neural progenitors, such as the SVZ, are generally found in proximity of vessels. The solution to the limitations inherent to vascularisation and stochastic patterning cues can only be sought by refinement of the existing protocols, by either modifying culture conditions to mimic the physiological environment as closely as possible or through bio-engineering innovation to provide a flowing system of nutrients to organoids to reproduce vascularisation (Kelava and Lancaster, 2016a).

Recently, it has been suggested that combining organoid culture with microfluidic technology may circumvent the vascularisation issue, for example, by culturing endothelial cells in microfluidic channels (Auger et al., 2013) to provide a flow system of nutrients and trophic molecules, thus allowing the *in vitro* modelling of organoid angiogenesis (Yin et al., 2016). Having highlighted the lack of vascularisation and BBB as major limitations of cerebral organoids, it has been envisaged that the introduction of further structural complexities may enhance the spectrum of applications of this platform (Kelava and Lancaster, 2016a). Several groups have addressed the lack of the BBB by generating vascularised organoids (Mansour et al., 2018; Nzou et al., 2018; Pham et al., 2018). Pham et al. (2018) generated vascularised cerebral organoids by re-embedding organoids in Matrigel droplets, seeded with iPSC-derived endothelial cells. Mansour et al. (2018), employed a different approach and achieved the vascularisation of human organoids, through engraftment in murine cortices *in vivo*. This demonstrated the feasibility of integration with the host, an improvement in viability and longevity of the tissue, a synaptic connectivity of transplanted organoids and the host, and ultimately, the formation of a microvascular network in the grafted organoids (Mansour et al., 2018). Also, Nzou et al. (2018) generated a six cell type cortical organoid consisting of astrocytes, pericytes, oligodendrocytes, NSCs and vascular endothelial cells, creating a functional BBB expressing tight and adherent junctions to examine barrier permeability using neurotoxic compounds.

The structural complexity of cerebral organoids has its pros and cons. Whereas the high degree of neural cell diversity and complex cross-talks are an advantage, this may also represent a disadvantage when trying to test hypotheses related to the contribution of individual cell types to mechanistic processes. The complementation of a 3-D model with a 2-D cell culture system of purified cells of interest from the organoids would allow the compartmentalisation and investigation of individual neural cell types, enabling molecular mechanisms intrinsic to specific cell types to be teased out.

CONCLUDING REMARKS

Studies of neural development and neurodegenerative diseases present many challenges due to the structural and functional complexity of the CNS, together with the limited possibility of *in vivo* experimental manipulation. Although animal models have contributed to the current knowledge, there are significant structural, cellular and molecular differences in the CNS of animal and humans, making data extrapolation and interpretation a formidable task. The past 100 years have seen the evolution of a number of culture systems for modelling the human CNS. Tissue explants and organotypic cultures were replaced by 2-D cultures thereby permitting investigation in more controlled systems. Issues of tissue availability were addressed by the development of human neural cell lines derived from tumours and more recently, the discovery of NSCs has permitted the generation of neuronal and glial cells in large quantities. Three-dimensional culture systems (organoids) are the most recent technological development in CNS modelling and bridge the gap between native tissue and 2-D cell cultures. Many advancements have been made in CNS organoid development, as evidenced by the ability of culturing for prolonged times, the potential to recapitulate late brain developmental milestones and *in vivo* transplantation. However, ethical and epistemological issues have been raised around organoids questioning their potential for developing consciousness (Lavazza and Massimini, 2018; Shepherd, 2018). At present, organoids can only recapitulate early stages of development and can be used in a relatively narrow spectrum of applications. However, their use is currently not free of hindrances and thus continuous efforts must be made for further improvement to overcome their limitations for a more appropriate and reliable use. One of the major improvements can be found in organoids-on-chip, which as opposed to traditional organoids, are not self-assembled but are rather constructed to produce a more reliable and consistent culture, through the inclusion of engineered elements such as biosensors and microfluidic channels (Tachibana, 2018). At present, the excitement for this technology is driving elegant research worldwide and it holds the potential for promising and revolutionary applications.

AUTHOR CONTRIBUTIONS

DP, RP, and BB contributed to the conception, writing, and review of the manuscript.

FUNDING

This work was supported by the Purine Metabolic Patients Association (Grant No. PUMPA14) and the Medical Research Council (Grant No. MRC: K025406/1).

REFERENCES

Allende, M. L., Cook, E. K., Larman, B. C., Nugent, A., Brady, J. M., Golebiowski, D., et al. (2018). Cerebral organoids derived from Sandhoff disease-induced pluripotent stem cells exhibit impaired neurodifferentiation. *J. Lipid Res.* 59, 550–563. doi: 10.1194/jlr.M081323

Almeida, S., Gascon, E., Tran, H., Chou, H. J., Gendron, T. F., Degroot, S., et al. (2013). Modeling key pathological features of frontotemporal dementia with C9ORF72 repeat expansion in iPSC-derived human neurons. *Acta Neuropathol.* 126, 385–399. doi: 10.1007/s00401-013-1149-y

Amenduni, M., De Filippis, R., Cheung, A. Y., Disciglio, V., Epistolato, M. C., Ariani, F., et al. (2011). iPS cells to model CDKL5-related disorders. *Eur. J. Hum. Genet.* 19, 1246–1255. doi: 10.1038/ejhg.2011.131

Ananiev, G., Williams, E. C., Li, H., and Chang, Q. (2011). Isogenic pairs of wild type and mutant induced pluripotent stem cell (iPSC) lines from Rett syndrome patients as in vitro disease model. *PLoS One* 6:e25255. doi: 10.1371/journal.pone.0025255

Auger, F. A., Gibot, L., and Lacroix, D. (2013). The pivotal role of vascularization in tissue engineering. *Annu. Rev. Biomed. Eng.* 15, 177–200. doi: 10.1146/annurev-bioeng-071812-152428

Avior, Y., Sagi, I., and Benvenisty, N. (2016). Pluripotent stem cells in disease modelling and drug discovery. *Nat. Rev. Mol. Cell Biol.* 17, 170–182. doi: 10.1038/nrm.2015.27

Awad, O., Sarkar, C., Panicker, L. M., Miller, D., Zeng, X., Sgambato, J. A., et al. (2015). Altered TFEB-mediated lysosomal biogenesis in Gaucher disease iPSC-derived neuronal cells. *Hum. Mol. Genet.* 24, 5775–5788. doi: 10.1093/hmg/ddv297

Baarine, M., Khan, M., Singh, A., and Singh, I. (2015). Functional characterization of IPSC-derived brain cells as a model for X-linked adrenoleukodystrophy. *PLoS One* 10:e0143238. doi: 10.1371/journal.pone.0143238

Barral, S., and Kurian, M. A. (2016). Utility of induced pluripotent stem cells for the study and treatment of genetic diseases: focus on childhood neurological disorders. *Front. Mol. Neurosci.* 9:78. doi: 10.3389/fnmol.2016.00078

Basuodan, R., Basu, A. P., and Clowry, G. J. (2018). Human neural stem cells dispersed in artificial ECM form cerebral organoids when grafted *in vivo*. *J. Anat.* 233, 155–166. doi: 10.1111/joa.12827

Bershteyn, M., Nowakowski, T. J., Pollen, A. A., Di Lullo, E., Nene, A., Wynshaw-Boris, A., et al. (2017). Human iPSC-derived cerebral organoids model cellular features of lissencephaly and reveal prolonged mitosis of outer radial glia. *Cell Stem Cell* 20, 435.e434–449.e434. doi: 10.1016/j.stem.2016.12.007

Bhinge, A., Namboori, S. C., Zhang, X., VanDongen, A. M. J., and Stanton, L. W. (2017). Genetic correction of SOD1 mutant iPSCs reveals ERK and JNK activated AP1 as a driver of neurodegeneration in amyotrophic lateral sclerosis. *Stem Cell Rep.* 8, 856–869. doi: 10.1016/j.stemcr.2017.02.019

Biedler, J. L., Helson, L., and Spengler, B. A. (1973). Morphology and growth, tumorigenicity, and cytogenetics of human neuroblastoma cells in continuous culture. *Cancer Res.* 33, 2643–2652.

Biedler, J. L., Roffler-Tarlov, S., Schachner, M., and Freedman, L. S. (1978). Multiple neurotransmitter synthesis by human neuroblastoma cell lines and clones. *Cancer Res.* 38(11 Part 1), 3751–3757.

Bilican, B., Serio, A., Barmada, S. J., Nishimura, A. L., Sullivan, G. J., Carrasco, M., et al. (2012). Mutant induced pluripotent stem cell lines recapitulate aspects of TDP-43 proteinopathies and reveal cell-specific vulnerability. *Proc. Natl. Acad. Sci. U.S.A.* 109, 5803–5808. doi: 10.1073/pnas.1202922109

Bird, M. J., Needham, K., Frazier, A. E., van Rooijen, J., Leung, J., Hough, S., et al. (2014). Functional characterization of Friedreich ataxia iPS-derived neuronal progenitors and their integration in the adult brain. *PLoS One* 9:e101718. doi: 10.1371/journal.pone.0101718

Birey, F., Andersen, J., Makinson, C. D., Islam, S., Wei, W., Huber, N., et al. (2017). Assembly of functional forebrain spheroids from human pluripotent cells. *Nature* 545, 54–59. doi: 10.1038/nature22330

Bousquet, J., and Meunier, J. M. (1962). Organotypic culture, on natural and artificial media, of fragments of the adult rat hypophysis. *C R Seances Soc. Biol. Fil* 156, 65–67.

Boza-Moran, M. G., Martinez-Hernandez, R., Bernal, S., Wanisch, K., Also-Rallo, E., Le Heron, A., et al. (2015). Decay in survival motor neuron and plastin 3 levels during differentiation of iPSC-derived human motor neurons. *Sci. Rep.* 5:11696. doi: 10.1038/srep11696

Brammer, M. (2009). The role of neuroimaging in diagnosis and personalized medicine–current position and likely future directions. *Dial. Clin. Neurosci.* 11, 389–396.

Brawner, A. T., Xu, R., Liu, D., and Jiang, P. (2017). Generating CNS organoids from human induced pluripotent stem cells for modeling neurological disorders. *Int. J. Physiol. Pathophysiol. Pharmacol.* 9, 101–111.

Brewer, G. J. (1995). Serum-free B27/neurobasal medium supports differentiated growth of neurons from the striatum, substantia nigra, septum, cerebral cortex, cerebellum, and dentate gyrus. *J. Neurosci. Res.* 42, 674–683. doi: 10.1002/jnr.490420510

Brodal, P. (2016). *The Central Nervous System*. Oxford: Oxford University Press. doi: 10.1093/med/9780190228958.001.0001

Camp, J. G., Badsha, F., Florio, M., Kanton, S., Gerber, T., Wilsch-Bräuninger, M., et al. (2015). Human cerebral organoids recapitulate gene expression programs of fetal neocortex development. *Proc. Natl. Acad. Sci. U.S.A.* 112, 15672–15677. doi: 10.1073/pnas.1520760112

Carlessi, L., Fusar Poli, E., Bechi, G., Mantegazza, M., Pascucci, B., Narciso, L., et al. (2014). Functional and molecular defects of hiPSC-derived neurons from patients with ATM deficiency. *Cell Death Dis.* 5, e1342. doi: 10.1038/cddis.2014.310

Carpenter, M. K., Cui, X., Hu, Z.-Y., Jackson, J., Sherman, S., Seiger, Å., et al. (1999). In vitro expansion of a multipotent population of human neural progenitor cells. *Exp. Neurol.* 158, 265–278. doi: 10.1006/exnr.1999.7098

Carter, M., and Shieh, J. (2015). "Cell culture techniques," in *Guide to Research Techniques in Neuroscience*, 2nd Edn, ed. N. Farra (San Diego, CA: Academic Press), 295–310. doi: 10.1016/B978-0-12-800511-8.00014-9

Chamberlain, S. J., Chen, P. F., Ng, K. Y., Bourgois-Rocha, F., Lemtiri-Chlieh, F., Levine, E. S., et al. (2010). Induced pluripotent stem cell models of the genomic imprinting disorders Angelman and Prader-Willi syndromes. *Proc. Natl. Acad. Sci. U.S.A.* 107, 17668–17673. doi: 10.1073/pnas.1004487107

Chambers, S. M., Fasano, C. A., Papapetrou, E. P., Tomishima, M., Sadelain, M., and Studer, L. (2009). Highly efficient neural conversion of human ES and iPS cells by dual inhibition of SMAD signaling. *Nat. Biotechnol.* 27, 275–280. doi: 10.1038/nbt.1529

Chandrasekaran, A., Avci, H. X., Leist, M., Kobolák, J., and Dinnyés, A. (2016). Astrocyte differentiation of human pluripotent stem cells: new tools for neurological disorder research. *Front. Cell. Neurosci.* 10:215. doi: 10.3389/fncel.2016.00215

Chang, T., Zheng, W., Tsark, W., Bates, S., Huang, H., Lin, R. J., et al. (2011). Brief report: phenotypic rescue of induced pluripotent stem cell-derived motoneurons of a spinal muscular atrophy patient. *Stem Cells* 29, 2090–2093. doi: 10.1002/stem.749

Chesselet, M.-F., and Carmichael, S. T. (2012). Animal models of neurological disorders. *Neurotherapeutics* 9, 241–244. doi: 10.1007/s13311-012-0118-9

Clevers, H. (2016). Modeling development and disease with organoids. *Cell* 165, 1586–1597. doi: 10.1016/j.cell.2016.05.082

Cohen, J. (2018). Neanderthal brain organoids come to life. *Science* 360, 1284–1284. doi: 10.1126/science.360.6395.1284

Conti, L., and Cattaneo, E. (2010). Neural stem cell systems: physiological players or in vitro entities? *Nat. Rev. Neurosci.* 11, 176–187. doi: 10.1038/nrn2761

Corti, S., Nizzardo, M., Simone, C., Falcone, M., Nardini, M., Ronchi, D., et al. (2012). Genetic correction of human induced pluripotent stem cells from patients with spinal muscular atrophy. *Sci. Transl. Med.* 4:165ra162. doi: 10.1126/scitranslmed.3004108

Costero, I., and Pomerat, C. M. (1951). Cultivation of neurons from the adult human cerebral and cerebellar cortex. *Am. J. Anat.* 89, 405–467. doi: 10.1002/aja.1000890304

Coyle, D. E., Li, J., and Baccei, M. (2011). Regional differentiation of retinoic acid-induced human pluripotent embryonic carcinoma stem cell neurons. *PLoS One* 6:e16174. doi: 10.1371/journal.pone.0016174

Crain, S. M. (1966). Development of "organotypic" bioelectric activities in central nervous tissues during maturation in culture. *Int. Rev. Neurobiol.* 9, 1–43. doi: 10.1016/S0074-7742(08)60135-X

Cugola, F. R., Fernandes, I. R., Russo, F. B., Freitas, B. C., Dias, J. L. M., Guimarães, K. P., et al. (2016). The Brazilian Zika virus strain causes birth defects in experimental models. *Nature* 534:267. doi: 10.1038/nature18296

Cunningham, C. L., Martínez-Cerdeño, V., and Noctor, S. C. (2013). Microglia regulate the number of neural precursor cells in the developing cerebral cortex. *J. Neurosci.* 33, 4216–4233. doi: 10.1523/jneurosci.3441-12.2013

Curchoe, C. L., Russo, J., and Terskikh, A. V. (2012). hESC derived neuro-epithelial rosettes recapitulate early mammalian neurulation events; an in vitro model. *Stem Cell Res.* 8, 239–246. doi: 10.1016/j.scr.2011.11.003

Dang, J., Tiwari, S. K., Lichinchi, G., Qin, Y., Patil, V. S., Eroshkin, A. M., et al. (2016). Zika virus depletes neural progenitors in human cerebral organoids through activation of the innate immune receptor TLR3. *Cell Stem Cell* 19, 258–265. doi: 10.1016/j.stem.2016.04.014

Dawson, T. M., Golde, T. E., and Lagier-Tourenne, C. (2018). Animal models of neurodegenerative diseases. *Nat. Neurosci.* 21, 1370–1379. doi: 10.1038/s41593-018-0236-8

DeFelipe, J., Alonso-Nanclares, L., and Arellano, J. I. (2002). Microstructure of the neocortex: comparative aspects. *J. Neurocytol.* 31, 299–316. doi: 10.1023/A:1024130211265

Denham, M., and Dottori, M. (2011). Neural differentiation of induced pluripotent stem cells. *Methods Mol. Biol.* 793, 99–110. doi: 10.1007/978-1-61779-328-8_7

Denton, K. R., Lei, L., Grenier, J., Rodionov, V., Blackstone, C., and Li, X. J. (2014). Loss of spastin function results in disease-specific axonal defects in human pluripotent stem cell-based models of hereditary spastic paraplegia. *Stem Cells* 32, 414–423. doi: 10.1002/stem.1569

Dezonne, R. S., Sartore, R. C., Nascimento, J. M., Saia-Cereda, V. M., Romão, L. F., Alves-Leon, S. V., et al. (2017). Derivation of functional human astrocytes from cerebral organoids. *Sci. Rep.* 7:45091. doi: 10.1038/srep45091

Di Lullo, E., and Kriegstein, A. R. (2017). The use of brain organoids to investigate neural development and disease. *Nat. Rev. Neurosci.* 18, 573–584. doi: 10.1038/nrn.2017.107

Dickinson, M. E., Selleck, M. A., McMahon, A. P., and Bronner-Fraser, M. (1995). Dorsalization of the neural tube by the non-neural ectoderm. *Development* 121, 2099–2106.

Diez del Corral, R., and Storey, K. G. (2004). Opposing FGF and retinoid pathways: a signalling switch that controls differentiation and patterning onset in the extending vertebrate body axis. *Bioessays* 26, 857–869. doi: 10.1002/bies.20080

Dingle, Y. T., Boutin, M. E., Chirila, A. M., Livi, L. L., Labriola, N. R., Jakubek, L. M., et al. (2015). Three-dimensional neural spheroid culture: an in vitro model for cortical studies. *Tissue Eng. Part C Methods* 21, 1274–1283. doi: 10.1089/ten.TEC.2015.0135

Djuric, U., Cheung, A. Y. L., Zhang, W., Mok, R. S., Lai, W., Piekna, A., et al. (2015). MECP2e1 isoform mutation affects the form and function of neurons derived from Rett syndrome patient iPS cells. *Neurobiol. Dis.* 76, 37–45. doi: 10.1016/j.nbd.2015.01.001

Doerr, J., Bockenhoff, A., Ewald, B., Ladewig, J., Eckhardt, M., Gieselmann, V., et al. (2015). Arylsulfatase A overexpressing human iPSC-derived neural cells reduce CNS sulfatide storage in a mouse model of metachromatic leukodystrophy. *Mol. Ther.* 23, 1519–1531. doi: 10.1038/mt.2015.106

Doers, M. E., Musser, M. T., Nichol, R., Berndt, E. R., Baker, M., Gomez, T. M., et al. (2014). iPSC-derived forebrain neurons from FXS individuals show defects in initial neurite outgrowth. *Stem Cells Dev.* 23, 1777–1787. doi: 10.1089/scd.2014.0030

Dotti, C. G., Sullivan, C. A., and Banker, G. A. (1988). The establishment of polarity by hippocampal neurons in culture. *J. Neurosci.* 8, 1454–1468. doi: 10.1523/JNEUROSCI.08-04-01454.1988

Ebert, A. D., Yu, J., Rose, F. F. Jr., Mattis, V. B., Lorson, C. L., et al. (2009). Induced pluripotent stem cells from a spinal muscular atrophy patient. *Nature* 457, 277–280. doi: 10.1038/nature07677

Edri, R., Yaffe, Y., Ziller, M. J., Mutukula, N., Volkman, R., David, E., et al. (2015). Analysing human neural stem cell ontogeny by consecutive isolation of Notch active neural progenitors. *Nat. Commun.* 6:6500. doi: 10.1038/ncomms7500

Efthymiou, A. G., Steiner, J., Pavan, W. J., Wincovitch, S., Larson, D. M., Porter, F. D., et al. (2015). Rescue of an in vitro neuron phenotype identified in

Niemann-Pick disease, type C1 induced pluripotent stem cell-derived neurons by modulating the WNT pathway and calcium signaling. *Stem Cells Transl. Med.* 4, 230–238. doi: 10.5966/sctm.2014-0127

Egawa, N., Kitaoka, S., Tsukita, K., Naitoh, M., Takahashi, K., Yamamoto, T., et al. (2012). Drug screening for ALS using patient-specific induced pluripotent stem cells. *Sci. Transl. Med.* 4:145ra104. doi: 10.1126/scitranslmed.3004052

Eigentler, A., Boesch, S., Schneider, R., Dechant, G., and Nat, R. (2013). Induced pluripotent stem cells from friedreich ataxia patients fail to upregulate frataxin during in vitro differentiation to peripheral sensory neurons. *Stem Cells Dev.* 22, 3271–3282. doi: 10.1089/scd.2013.0126

Eiraku, M., Takata, N., Ishibashi, H., Kawada, M., Sakakura, E., Okuda, S., et al. (2011). Self-organizing optic-cup morphogenesis in three-dimensional culture. *Nature* 472, 51–56. doi: 10.1038/nature09941

Eiraku, M., Watanabe, K., Matsuo-Takasaki, M., Kawada, M., Yonemura, S., Matsumura, M., et al. (2008). Self-organized formation of polarized cortical tissues from ESCs and its active manipulation by extrinsic signals. *Cell Stem Cell* 3, 519–532. doi: 10.1016/j.stem.2008.09.002

Elston, G. N., Benavides-Piccione, R., and DeFelipe, J. (2001). The pyramidal cell in cognition: a comparative study in human and monkey. *J. Neurosci.* 21, Rc163. doi: 10.1523/JNEUROSCI.21-17-j0002.2001

Eyal, G., Verhoog, M. B., Testa-Silva, G., Deitcher, Y., Lodder, J. C., Benavides-Piccione, R., et al. (2016). Unique membrane properties and enhanced signal processing in human neocortical neurons. *eLife* 5:e16553. doi: 10.7554/eLife.16553

Fernandez-Santiago, R., Carballo-Carbajal, I., Castellano, G., Torrent, R., Richaud, Y., Sanchez-Danes, A., et al. (2015). Aberrant epigenome in iPSC-derived dopaminergic neurons from Parkinson's disease patients. *EMBO Mol. Med.* 7, 1529–1546. doi: 10.15252/emmm.201505439

Fietz, S. A., Kelava, I., Vogt, J., Wilsch-Brauninger, M., Stenzel, D., Fish, J. L., et al. (2010). OSVZ progenitors of human and ferret neocortex are epithelial-like and expand by integrin signaling. *Nat. Neurosci.* 13, 690–699. doi: 10.1038/nn.2553

Filis, A. K., Moon, K., and Cohen, A. R. (2010). The birth and evolution of neuroscience through cadaveric dissection. *Neurosurgery* 67, 799–810. doi: 10.1227/01.neu.0000383135.92953.a3

Foo, L. C., Allen, N. J., Bushong, E. A., Ventura, P. B., Chung, W.-S., Zhou, L., et al. (2011). Development of a novel method for the purification and culture of rodent astrocytes. *Neuron* 71, 799–811. doi: 10.1016/j.neuron.2011.07.022

Franco, S. J., and Müller, U. (2011). ECM functions during neuronal migration and lamination in the mammalian central nervous system. *Dev. Neurobiol.* 71, 889–900. doi: 10.1002/dneu.20946

Frotscher, M. (1998). Cajal—retzius cells, reelin, and the formation of layers. *Curr. Opin. Neurobiol.* 8, 570–575. doi: 10.1016/S0959-4388(98)80082-2

Fuller, H. R., Mandefro, B., Shirran, S. L., Gross, A. R., Kaus, A. S., Botting, C. H., et al. (2015). Spinal muscular atrophy patient iPSC-derived motor neurons have reduced expression of proteins important in neuronal development. *Front. Cell. Neurosci.* 9:506. doi: 10.3389/fncel.2015.00506

Gähwiler, B. H. (1981). Organotypic monolayer cultures of nervous tissue. *J. Neurosci. Methods* 4, 329–342. doi: 10.1016/0165-0270(81)90003-0

Garcez, P. P., Loiola, E. C., Madeiro, da Costa, R., Higa, L. M., Trindade, P., et al. (2016). Zika virus impairs growth in human neurospheres and brain organoids. *Science* 352, 816–818. doi: 10.1126/science.aaf6116

Gaspard, N., Bouschet, T., Hourez, R., Dimidschstein, J., Naeije, G., van den Ameele, J., et al. (2008). An intrinsic mechanism of corticogenesis from embryonic stem cells. *Nature* 455, 351–357. doi: 10.1038/nature07287

Ge, H., Tan, L., Wu, P., Yin, Y., Liu, X., Meng, H., et al. (2015). Poly-L-ornithine promotes preferred differentiation of neural stem/progenitor cells via ERK signalling pathway. *Sci. Rep.* 5:15535. doi: 10.1038/srep15535

Gharib, W. H., and Robinson-Rechavi, M. (2011). When orthologs diverge between human and mouse. *Brief Bioinform.* 12, 436–441. doi: 10.1093/bib/bbr031

Giandomenico, S. L., and Lancaster, M. A. (2017). Probing human brain evolution and development in organoids. *Curr. Opin. Cell Biol.* 44, 36–43. doi: 10.1016/j.ceb.2017.01.001

Giulian, D., and Baker, T. J. (1986). Characterization of ameboid microglia isolated from developing mammalian brain. *J. Neurosci.* 6, 2163–2178. doi: 10.1523/JNEUROSCI.06-08-02163.1986

Goldman, S. (1990). Neuronal development and migration in explant cultures of the adult canary forebrain. *J. Neurosci.* 10, 2931–2939. doi: 10.1523/JNEUROSCI.10-09-02931.1990

Goldstein, M. N., Burdman, J. A., and Journey, L. J. (1964). Long-term tissue culture of neuroblastomas. II. Morphologic evidence for differentiation and maturation. *J. Natl. Cancer Inst.* 32, 165–199.

Golgi, C. (1906). *The Neuron Doctrine-theory and facts. Nobel Lectures*. Stockholm, Sweden: Nobel Foundation.

Gomes, F. C., Spohr, T. C., Martinez, R., and Moura Neto, V. (2001). Cross-talk between neurons and glia: highlights on soluble factors. *Braz. J. Med. Biol. Res.* 34, 611–620. doi: 10.1590/S0100-879X2001000500008

Gonzalez-Cordero, A., Goh, D., Kruczek, K., Naeem, A., Fernando, M., Kleine Holthaus, S. M., et al. (2018). Assessment of AAV vector tropisms for mouse and human pluripotent stem cell-derived RPE and photoreceptor cells. *Hum. Gene Ther.* 29, 1124–1139. doi: 10.1089/hum.2018.027

Gordon, J., Amini, S., and White, M. K. (2013). General overview of neuronal cell culture. *Methods Mol. Biol.* 1078, 1–8. doi: 10.1007/978-1-62703-640-5_1

Gotz, M., and Huttner, W. B. (2005). The cell biology of neurogenesis. *Nat. Rev. Mol. Cell Biol.* 6, 777–788. doi: 10.1038/nrm1739

Greene, L. A., and Tischler, A. S. (1976). Establishment of a noradrenergic clonal line of rat adrenal pheochromocytoma cells which respond to nerve growth factor. *Proc. Natl. Acad. Sci. U.S.A.* 73, 2424–2428. doi: 10.1073/pnas.73.7.2424

Griesi-Oliveira, K., Acab, A., Gupta, A. R., Sunaga, D. Y., Chailangkarn, T., Nicol, X., et al. (2015). Modeling non-syndromic autism and the impact of TRPC6 disruption in human neurons. *Mol. Psychiatry* 20, 1350–1365. doi: 10.1038/mp.2014.141

Halevy, T., Czech, C., and Benvenisty, N. (2015). Molecular mechanisms regulating the defects in fragile X syndrome neurons derived from human pluripotent stem cells. *Stem Cell Rep.* 4, 37–46. doi: 10.1016/j.stemcr.2014.10.015

Hall, P. E., Lathia, J. D., Caldwell, M. A., and ffrench-Constant, C. (2008). Laminin enhances the growth of human neural stem cells in defined culture media. *BMC Neurosci.* 9:71. doi: 10.1186/1471-2202-9-71

Hansen, D. V., Lui, J. H., Parker, P. R., and Kriegstein, A. R. (2010). Neurogenic radial glia in the outer subventricular zone of human neocortex. *Nature* 464, 554–561. doi: 10.1038/nature08845

Harrison, R. G. (1907). Observations on the living developing nerve fiber. *Proc. Natl. Acad. Sci. U.S.A.* 4, 140–143. doi: 10.3181/00379727-4-98

Harrison, R. G. (1910). The outgrowth of the nerve fiber as a mode of protoplasmic movement. *J. Exp. Zool.* 142, 5–73. doi: 10.1002/jez.1401420103

Hartung, T. (2008). Thoughts on limitations of animal models. *Parkinsonism Relat. Disord.* 14, S81–S83. doi: 10.1016/j.parkreldis.2008.04.003

Haubensak, W., Attardo, A., Denk, W., and Huttner, W. B. (2004). Neurons arise in the basal neuroepithelium of the early mammalian telencephalon: a major site of neurogenesis. *Proc. Natl. Acad. Sci. U.S.A.* 101, 3196–3201. doi: 10.1073/pnas.0308600100

Havlicek, S., Kohl, Z., Mishra, H. K., Prots, I., Eberhardt, E., Denguir, N., et al. (2014). Gene dosage-dependent rescue of HSP neurite defects in SPG4 patients' neurons. *Hum. Mol. Genet.* 23, 2527–2541. doi: 10.1093/hmg/ddt644

Herculano-Houzel, S. (2009). The human brain in numbers: a linearly scaled-up primate brain. *Front. Hum. Neurosci.* 3:31. doi: 10.3389/neuro.09.031.2009

Hick, A., Wattenhofer-Donze, M., Chintawar, S., Tropel, P., Simard, J. P., Vaucamps, N., et al. (2013). Neurons and cardiomyocytes derived from induced pluripotent stem cells as a model for mitochondrial defects in Friedreich's ataxia. *Dis. Model Mech.* 6, 608–621. doi: 10.1242/dmm.010900

Higuchi, T., Kawagoe, S., Otsu, M., Shimada, Y., Kobayashi, H., Hirayama, R., et al. (2014). The generation of induced pluripotent stem cells (iPSCs) from patients with infantile and late-onset types of Pompe disease and the effects of treatment with acid-alpha-glucosidase in Pompe's iPSCs. *Mol. Genet. Metab.* 112, 44–48. doi: 10.1016/j.ymgme.2014.02.012

Higurashi, N., Uchida, T., Lossin, C., Misumi, Y., Okada, Y., Akamatsu, W., et al. (2013). A human Dravet syndrome model from patient induced pluripotent stem cells. *Mol. Brain* 6:19. doi: 10.1186/1756-6606-6-19

Hoadley, L. (1924). The independent differentiation of isolated chick Primordia in chorioallantoic grafts. I. The eye, nasal region, otic region, and mesencephalon. *Biol. Bull.* 46, 281–315. doi: 10.2307/1536697

Hogue, M. J. (1946). Tissue cultures of the brain. Intercellular granules. *J. Compar. Neurol.* 85, 519–530. doi: 10.1002/cne.900850308

Hogue, M. J. (1947). Human fetal brain cells in tissue cultures; their identification and motility. *J. Exp. Zool.* 106, 85–107. doi: 10.1002/jez.1401060104

Howard, B. M., Zhicheng, M., Filipovic, R., Moore, A. R., Antic, S. D., and Zecevic, N. (2008). Radial glia cells in the developing human brain. *Neuroscientist* 14, 459–473. doi: 10.1177/1073858407313512

Huang, Y., Williams, J. C., and Johnson, S. M. (2012). Brain slice on a chip: opportunities and challenges of applying microfluidic technology to intact tissues. *Lab Chip* 12, 2103–2117. doi: 10.1039/c2lc21142d

Hughes, C. S., Postovit, L. M., and Lajoie, G. A. (2010). Matrigel: a complex protein mixture required for optimal growth of cell culture. *Proteomics* 10, 1886–1890. doi: 10.1002/pmic.200900758

Iefremova, V., Manikakis, G., Krefft, O., Jabali, A., Weynans, K., Wilkens, R., et al. (2017). An organoid-based model of cortical development identifies non-cell-autonomous defects in Wnt signaling contributing to miller-dieker syndrome. *Cell Rep.* 19, 50–59. doi: 10.1016/j.celrep.2017.03.047

Imura, T., Nakano, I., Kornblum, H. I., and Sofroniew, M. V. (2006). Phenotypic and functional heterogeneity of GFAP-expressing cells in vitro: differential expression of LeX/CD15 by GFAP-expressing multipotent neural stem cells and non-neurogenic astrocytes. *Glia* 53, 277–293. doi: 10.1002/glia.20281

Itskovitz-Eldor, J., Schuldiner, M., Karsenti, D., Eden, A., Yanuka, O., Amit, M., et al. (2000). Differentiation of human embryonic stem cells into embryoid bodies compromising the three embryonic germ layers. *Mol. Med.* 6, 88–95. doi: 10.1007/BF03401776

Jaenisch, R., and Young, R. (2008). Stem cells, the molecular circuitry of pluripotency and nuclear reprogramming. *Cell* 132, 567–582. doi: 10.1016/j.cell.2008.01.015

Jakel, R. J., Schneider, B. L., and Svendsen, C. N. (2004). Using human neural stem cells to model neurological disease. *Nat. Rev. Genet.* 5, 136–144. doi: 10.1038/nrg1268

Janesick, A., Wu, S. C., and Blumberg, B. (2015). Retinoic acid signaling and neuronal differentiation. *Cell Mol. Life Sci.* 72, 1559–1576. doi: 10.1007/s00018-014-1815-9

Jang, J., Kang, H. C., Kim, H. S., Kim, J. Y., Huh, Y. J., Kim, D. S., et al. (2011). Induced pluripotent stem cell models from X-linked adrenoleukodystrophy patients. *Ann. Neurol.* 70, 402–409. doi: 10.1002/ana.22486

Jiang, X., and Nardelli, J. (2016). Cellular and molecular introduction to brain development. *Neurobiol. Dis.* 92(Pt A), 3–17. doi: 10.1016/j.nbd.2015.07.007

Jiao, J., Yang, Y., Shi, Y., Chen, J., Gao, R., Fan, Y., et al. (2013). Modeling dravet syndrome using induced pluripotent stem cells (iPSCs) and directly converted neurons. *Hum. Mol. Genet.* 22, 4241–4252. doi: 10.1093/hmg/ddt275

Jo, J., Xiao, Y., Sun, A. X., Cukuroglu, E., Tran, H. D., Goke, J., et al. (2016). Midbrain-like organoids from human pluripotent stem cells contain functional dopaminergic and neuromelanin-producing neurons. *Cell Stem Cell* 19, 248–257. doi: 10.1016/j.stem.2016.07.005

Johns, P. (2014). *Clinical Neuroscience: An Illustrated Colour Text.* Edinburgh: Churchill Livingstone.

Kadoshima, T., Sakaguchi, H., Nakano, T., Soen, M., Ando, S., Eiraku, M., et al. (2013). Self-organization of axial polarity, inside-out layer pattern, and species-specific progenitor dynamics in human ES cell-derived neocortex. *Proc. Natl. Acad. Sci. U.S.A.* 110, 20284–20289. doi: 10.1073/pnas.1315710110

Kelava, I., and Lancaster, M. A. (2016a). Dishing out mini-brains: current progress and future prospects in brain organoid research. *Dev. Biol.* 420, 199–209. doi: 10.1016/j.ydbio.2016.06.037

Kelava, I., and Lancaster, M. A. (2016b). Stem cell models of human brain development. *Cell Stem Cell* 18, 736–748. doi: 10.1016/j.stem.2016.05.022

Kim, K. Y., Hysolli, E., and Park, I. H. (2011). Neuronal maturation defect in induced pluripotent stem cells from patients with Rett syndrome. *Proc. Natl. Acad. Sci. U.S.A.* 108, 14169–14174. doi: 10.1073/pnas.1018979108

Kirkeby, A., Grealish, S., Wolf, D. A., Nelander, J., Wood, J., Lundblad, M., et al. (2012). Generation of regionally specified neural progenitors and functional neurons from human embryonic stem cells under defined conditions. *Cell Rep.* 1, 703–714. doi: 10.1016/j.celrep.2012.04.009

Kleinman, H. K., and Martin, G. R. (2005). Matrigel: basement membrane matrix with biological activity. *Semin. Cancer Biol.* 15, 378–386. doi: 10.1016/j.semcancer.2005.05.004

Knopfel, T., Rietschin, L., and Gahwiler, B. H. (1989). Organotypic co-cultures of rat locus coeruleus and hippocampus. *Eur. J. Neurosci.* 1, 678–689. doi: 10.1111/j.1460-9568.1989.tb00374.x

Ko, K. R., and Frampton, J. P. (2016). Developments in 3D neural cell culture models: the future of neurotherapeutics testing? *Exp. Rev. Neurother.* 16, 739–741. doi: 10.1586/14737175.2016.1166053

Komssi, S., and Kähkönen, S. (2006). The novelty value of the combined use of electroencephalography and transcranial magnetic stimulation for neuroscience research. *Brain Res. Rev.* 52, 183–192. doi: 10.1016/j.brainresrev.2006.01.008

Kovalevich, J., and Langford, D. (2013). Considerations for the use of SH-SY5Y neuroblastoma cells in neurobiology. *Methods Mol. Biol.* 1078, 9–21. doi: 10.1007/978-1-62703-640-5_2

Kuff, E. L., and Fewell, J. W. (1980). Induction of neural-like cells and acetylcholinesterase activity in cultures of F9 teratocarcinoma treated with retinoic acid and dibutyryl cyclic adenosine monophosphate. *Dev. Biol.* 77, 103–115. doi: 10.1016/0012-1606(80)90459-5

Lancaster, M. A., Corsini, N. S., Wolfinger, S., Gustafson, E. H., Phillips, A. W., Burkard, T. R., et al. (2017). Guided self-organization and cortical plate formation in human brain organoids. *Nat. Biotechnol.* 35:659. doi: 10.1038/nbt.3906

Lancaster, M. A., and Knoblich, J. A. (2012). Spindle orientation in mammalian cerebral cortical development. *Curr. Opin. Neurobiol.* 22, 737–746. doi: 10.1016/j.conb.2012.04.003

Lancaster, M. A., and Knoblich, J. A. (2014). Generation of cerebral organoids from human pluripotent stem cells. *Nat. Protoc.* 9, 2329–2340. doi: 10.1038/nprot.2014.158

Lancaster, M. A., Renner, M., Martin, C. A., Wenzel, D., Bicknell, L. S., Hurles, M. E., et al. (2013). Cerebral organoids model human brain development and microcephaly. *Nature* 501, 373–379. doi: 10.1038/nature12517

Lange, S. C., Bak, L. K., Waagepetersen, H. S., Schousboe, A., and Norenberg, M. D. (2012). Primary cultures of astrocytes: their value in understanding astrocytes in health and disease. *Neurochem. Res.* 37, 2569–2588. doi: 10.1007/s11064-012-0868-0

LaVail, J. H., and Wolf, M. K. (1973). Postnatal development of the mouse dentate gyrus in organotypic cultures of the hippocampal formation. *Am. J. Anat.* 137, 47–65. doi: 10.1002/aja.1001370105

Lavazza, A., and Massimini, M. (2018). Cerebral organoids: ethical issues and consciousness assessment. *J. Med. Ethics* 44, 606–610. doi: 10.1136/medethics-2017-104555

Lee, C.-T., Chen, J., Kindberg, A. A., Bendriem, R. M., Spivak, C. E., Williams, M. P., et al. (2017). CYP3A5 mediates effects of cocaine on human neocorticogenesis: studies using an in vitro 3D self-organized hPSC model with a single cortex-like unit. *Neuropsychopharmacology* 42, 774–784. doi: 10.1038/npp.2016.156

Lee, G., Papapetrou, E. P., Kim, H., Chambers, S. M., Tomishima, M. J., Fasano, C. A., et al. (2009). Modelling pathogenesis and treatment of familial dysautonomia using patient-specific iPSCs. *Nature* 461, 402–406. doi: 10.1038/nature08320

Lee, G., Ramirez, C. N., Kim, H., Zeltner, N., Liu, B., Radu, C., et al. (2012). Large-scale screening using familial dysautonomia induced pluripotent stem cells identifies compounds that rescue IKBKAP expression. *Nat. Biotechnol.* 30, 1244–1248. doi: 10.1038/nbt.2435

Lee, K., Silva, E. A., and Mooney, D. J. (2011). Growth factor delivery-based tissue engineering: general approaches and a review of recent developments. *J. R. Soc. Interface* 8, 153–170. doi: 10.1098/rsif.2010.0223

Lee, S.-W., Lee, H. J., Hwang, H. S., Ko, K., Han, D. W., and Ko, K. (2015). Optimization of matrigel-based culture for expansion of neural stem cells. *Anim. Cells Syst.* 19, 175–180. doi: 10.1080/19768354.2015.1035750

LePage, K. T., Dickey, R. W., Gerwick, W. H., Jester, E. L., and Murray, T. F. (2005). On the use of neuro-2a neuroblastoma cells versus intact neurons in primary culture for neurotoxicity studies. *Crit. Rev. Neurobiol.* 17, 27–50. doi: 10.1615/CritRevNeurobiol.v17.i1.20

Li, Y., Muffat, J., Omer, A., Bosch, I., Lancaster, M. A., Sur, M., et al. (2017). Induction of expansion and folding in human cerebral organoids. *Cell Stem Cell* 20, 385.e383–96.e383. doi: 10.1016/j.stem.2016.11.017

Liddelow, S. A., and Barres, B. A. (2017). Reactive astrocytes: production, function, and therapeutic potential. *Immunity* 46, 957–967. doi: 10.1016/j.immuni.2017.06.006

Lingor, P., Unsicker, K., and Krieglstein, K. (1999). Midbrain dopaminergic neurons are protected from radical induced damage by GDF-5 application, short communication. *J. Neural Transm. (Vienna)* 106, 139–144. doi: 10.1007/s007020050146

Liu, H., Lu, J., Chen, H., Du, Z., Li, X. J., and Zhang, S. C. (2015). Spinal muscular atrophy patient-derived motor neurons exhibit hyperexcitability. *Sci. Rep.* 5:12189. doi: 10.1038/srep12189

Liu, J., Gao, C., Chen, W., Ma, W., Li, X., Shi, Y., et al. (2016). CRISPR/Cas9 facilitates investigation of neural circuit disease using human iPSCs: mechanism of epilepsy caused by an SCN1A loss-of-function mutation. *Transl. Psychiatry* 6:e703. doi: 10.1038/tp.2015.203

Liu, J., Verma, P. J., Evans-Galea, M. V., Delatycki, M. B., Michalska, A., Leung, J., et al. (2011). Generation of induced pluripotent stem cell lines from Friedreich ataxia patients. *Stem Cell Rev.* 7, 703–713. doi: 10.1007/s12015-010-9210-x

Liu, Y., Lopez-Santiago, L. F., Yuan, Y., Jones, J. M., Zhang, H., O'Malley, H. A., et al. (2013). Dravet syndrome patient-derived neurons suggest a novel epilepsy mechanism. *Ann. Neurol.* 74, 128–139. doi: 10.1002/ana.23897

Lohle, M., Hermann, A., Glass, H., Kempe, A., Schwarz, S. C., Kim, J. B., et al. (2012). Differentiation efficiency of induced pluripotent stem cells depends on the number of reprogramming factors. *Stem Cells* 30, 570–579. doi: 10.1002/stem.1016

Lojewski, X., Staropoli, J. F., Biswas-Legrand, S., Simas, A. M., Haliw, L., Selig, M. K., et al. (2014). Human iPSC models of neuronal ceroid lipofuscinosis capture distinct effects of TPP1 and CLN3 mutations on the endocytic pathway. *Hum. Mol. Genet.* 23, 2005–2022. doi: 10.1093/hmg/ddt596

Ma, W., Tavakoli, T., Derby, E., Serebryakova, Y., Rao, M. S., and Mattson, M. P. (2008). Cell-extracellular matrix interactions regulate neural differentiation of human embryonic stem cells. *BMC Dev. Biol.* 8:90. doi: 10.1186/1471-213X-8-90

Maden, M. (2002). Retinoid signalling in the development of the central nervous system. *Nat. Rev. Neurosci.* 3:843. doi: 10.1038/nrn963

Mansour, A. A., Gonçalves, J. T., Bloyd, C. W., Li, H., Fernandes, S., Quang, D., et al. (2018). An in vivo model of functional and vascularized human brain organoids. *Nat. Biotechnol.* 36:432. doi: 10.1038/nbt.4127

Marchetto, M. C., Carromeu, C., Acab, A., Yu, D., Yeo, G. W., Mu, Y., et al. (2010). A model for neural development and treatment of Rett syndrome using human induced pluripotent stem cells. *Cell* 143, 527–539. doi: 10.1016/j.cell.2010.10.016

Mariani, J., Coppola, G., Zhang, P., Abyzov, A., Provini, L., Tomasini, L., et al. (2015). FOXG1-dependent dysregulation of GABA/glutamate neuron differentiation in autism spectrum disorders. *Cell* 162, 375–390. doi: 10.1016/j.cell.2015.06.034

Mariani, J., Simonini, M. V., Palejev, D., Tomasini, L., Coppola, G., Szekely, A. M., et al. (2012). Modeling human cortical development in vitro using induced pluripotent stem cells. *Proc. Natl. Acad. Sci. U.S.A.* 109, 12770–12775. doi: 10.1073/pnas.1202944109

Mastrangelo, L., Kim, J. E., Miyanohara, A., Kang, T. H., and Friedmann, T. (2012). Purinergic signaling in human pluripotent stem cells is regulated by the housekeeping gene encoding hypoxanthine guanine phosphoribosyltransferase. *Proc. Natl. Acad. Sci. U.S.A.* 109, 3377–3382. doi: 10.1073/pnas.1118067109

Matsui, T. K., Matsubayashi, M., Sakaguchi, Y. M., Hayashi, R. K., Zheng, C., Sugie, K., et al. (2018). Six-month cultured cerebral organoids from human ES cells contain matured neural cells. *Neurosci. Lett.* 670, 75–82. doi: 10.1016/j.neulet.2018.01.040

Mattei, C., Alshawaf, A., D'Abaco, G., Nayagam, B., and Dottori, M. (2018). Generation of neural organoids from human embryonic stem cells using the rotary cell culture system: effects of microgravity on neural progenitor cell fate. *Stem Cells Dev.* 27, 848–857. doi: 10.1089/scd.2018.0012

McCarthy, K. D., and de Vellis, J. (1980). Preparation of separate astroglial and oligodendroglial cell cultures from rat cerebral tissue. *J. Cell Biol.* 85, 890–902. doi: 10.1083/jcb.85.3.890

McGivern, J. V., Patitucci, T. N., Nord, J. A., Barabas, M. A., Stucky, C. L., and Ebert, A. D. (2013). Spinal muscular atrophy astrocytes exhibit abnormal calcium regulation and reduced growth factor production. *Glia* 61, 1418–1428. doi: 10.1002/glia.22522

McKinney, C. E. (2017). Using induced pluripotent stem cells derived neurons to model brain diseases. *Neural Regen. Res.* 12, 1062–1067. doi: 10.4103/1673-5374.211180

Mellios, N., Feldman, D. A., Sheridan, S. D., Ip, J. P. K., Kwok, S., Amoah, S. K., et al. (2017). MeCP2-regulated miRNAs control early human neurogenesis through differential effects on ERK and AKT signaling. *Mol. Psychiatry* 23:1051. doi: 10.1038/mp.2017.86

Miranda, C. C., Fernandes, T. G., Diogo, M. M., and Cabral, J. M. S. (2018a). Towards multi-organoid systems for drug screening applications. *Bioeng. (Basel, Switzerland)* 5:49. doi: 10.3390/bioengineering5030049

Miranda, C. C., Fernandes, T. G., Pinto, S. N., Prieto, M., Diogo, M. M., and Cabral, J. M. S. (2018b). A scale out approach towards neural induction of human induced pluripotent stem cells for neurodevelopmental toxicity studies. *Toxicol. Lett.* 294, 51–60. doi: 10.1016/j.toxlet.2018.05.018

Miranda, C. C., Fernandes, T. G., Pascoal, J. F., Haupt, S., Brüstle, O., Cabral, J. M. S., et al. (2015). Spatial and temporal control of cell aggregation efficiently directs human pluripotent stem cells towards neural commitment. *Biotechnol. J.* 10, 1612–1624. doi: 10.1002/biot.201400846

Mishra, H. K., Prots, I., Havlicek, S., Kohl, Z., Perez-Branguli, F., Boerstler, T., et al. (2016). GSK3ss-dependent dysregulation of neurodevelopment in SPG11-patient induced pluripotent stem cell model. *Ann. Neurol.* 79, 826–840. doi: 10.1002/ana.24633

Miyata, T., Kawaguchi, A., Saito, K., Kawano, M., Muto, T., and Ogawa, M. (2004). Asymmetric production of surface-dividing and non-surface-dividing cortical progenitor cells. *Development* 131, 3133–3145. doi: 10.1242/dev.01173

Mohan, H., Verhoog, M. B., Doreswamy, K. K., Eyal, G., Aardse, R., Lodder, B. N., et al. (2015). Dendritic and axonal architecture of individual pyramidal neurons across layers of adult human neocortex. *Cereb. Cortex* 25, 4839–4853. doi: 10.1093/cercor/bhv188

Monzel, A. S., Smits, L. M., Hemmer, K., Hachi, S., Moreno, E. L., van Wuellen, T., et al. (2017). Derivation of human midbrain-specific organoids from neuroepithelial stem cells. *Stem Cell Rep.* 8, 1144–1154. doi: 10.1016/j.stemcr.2017.03.010

Muguruma, K., Nishiyama, A., Kawakami, H., Hashimoto, K., and Sasai, Y. (2015). Self-organization of polarized cerebellar tissue in 3D culture of human pluripotent stem cells. *Cell Rep.* 10, 537–550. doi: 10.1016/j.celrep.2014.12.051

Muotri, A. R., Marchetto, M. C., Coufal, N. G., Oefner, R., Yeo, G., Nakashima, K., et al. (2010). L1 retrotransposition in neurons is modulated by MeCP2. *Nature* 468, 443–446. doi: 10.1038/nature09544

Nayler, S., Gatei, M., Kozlov, S., Gatti, R., Mar, J. C., Wells, C. A., et al. (2012). Induced pluripotent stem cells from ataxia-telangiectasia recapitulate the cellular phenotype. *Stem Cells Transl. Med.* 1, 523–535. doi: 10.5966/sctm.2012-0024

Ng, S. Y., Soh, B. S., Rodriguez-Muela, N., Hendrickson, D. G., Price, F., Rinn, J. L., et al. (2015). Genome-wide RNA-seq of human motor neurons implicates selective er stress activation in spinal muscular atrophy. *Cell Stem Cell* 17, 569–584. doi: 10.1016/j.stem.2015.08.003

Nguyen, H. N., Byers, B., Cord, B., Shcheglovitov, A., Byrne, J., Gujar, P., et al. (2011). LRRK2 mutant iPSC-derived DA neurons demonstrate increased susceptibility to oxidative stress. *Cell Stem Cell* 8, 267–280. doi: 10.1016/j.stem.2011.01.013

Nizzardo, M., Simone, C., Dametti, S., Salani, S., Ulzi, G., Pagliarani, S., et al. (2015). Spinal muscular atrophy phenotype is ameliorated in human motor neurons by SMN increase via different novel RNA therapeutic approaches. *Sci. Rep.* 5:11746. doi: 10.1038/srep11746

Nzou, G., Wicks, R. T., Wicks, E. E., Seale, S. A., Sane, C. H., Chen, A., et al. (2018). Human cortex spheroid with a functional blood brain barrier for high-throughput neurotoxicity screening and disease modeling. *Sci. Rep.* 8:7413. doi: 10.1038/s41598-018-25603-5

Okita, K., Yamakawa, T., Matsumura, Y., Sato, Y., Amano, N., Watanabe, A., et al. (2013). An efficient nonviral method to generate integration-free human-induced pluripotent stem cells from cord blood and peripheral blood cells. *Stem Cells* 31, 458–466. doi: 10.1002/stem.1293

Ostergaard, K., Finsen, B., and Zimmer, J. (1995). Organotypic slice cultures of the rat striatum: an immunocytochemical, histochemical and in situ hybridization study of somatostatin, neuropeptide Y, nicotinamide adenine dinucleotide phosphate-diaphorase, and enkephalin. *Exp. Brain Res.* 103, 70–84. doi: 10.1007/BF00241966

Pacitti, D. (2018). *The Development of An In Vitro Cerebral Organoid Model for Investigating the Pathomolecular Mechanisms Associated with the Central Nervous System of Patients with Mitochondrial Neurogastrointestinal Encephalomyopathy (MNGIE): A Proof of Concept Study*. Doctoral Ph.D. Thesis, St. George's, University of London, London.

Pacitti, D., and Bax, B. (2018). The development of an in vitro cerebral organoid model for investigating the pathomolecular mechanisms associated with the Central Nervous System involvement in Mitochondrial Neurogastrointestinal Encephalomyopathy. *Nucleosides Nucleotides Nucleic Acids* doi: 10.1080/15257770.2018.1492139 [Epub ahead of print].

Pahlman, S., Ruusala, A. I., Abrahamsson, L., Mattsson, M. E., and Esscher, T. (1984). Retinoic acid-induced differentiation of cultured human neuroblastoma cells: a comparison with phorbolester-induced differentiation. *Cell Differ.* 14, 135–144. doi: 10.1016/0045-6039(84)90038-1

Panicker, L. M., Miller, D., Park, T. S., Patel, B., Azevedo, J. L., Awad, O., et al. (2012). Induced pluripotent stem cell model recapitulates pathologic hallmarks of Gaucher disease. *Proc. Natl. Acad. Sci. U.S.A.* 109, 18054–18059. doi: 10.1073/pnas.1207889109

Park, C. Y., Halevy, T., Lee, D. R., Sung, J. J., Lee, J. S., Yanuka, O., et al. (2015). Reversion of FMR1 methylation and silencing by editing the triplet repeats in fragile X iPSC-derived neurons. *Cell Rep.* 13, 234–241. doi: 10.1016/j.celrep.2015.08.084

Park, J., Wetzel, I., Marriott, I., Dréau, D., D'Avanzo, C., Kim, D. Y., et al. (2018). A 3D human triculture system modeling neurodegeneration and neuroinflammation in Alzheimer's disease. *Nat. Neurosci.* 21, 941–951. doi: 10.1038/s41593-018-0175-4

Pasca, A. M., Sloan, S. A., Clarke, L. E., Tian, Y., Makinson, C. D., Huber, N., et al. (2015). Functional cortical neurons and astrocytes from human pluripotent stem cells in 3D culture. *Nat. Methods* 12, 671–678. doi: 10.1038/nmeth.3415

Pasca, S. P., Panagiotakos, G., and Dolmetsch, R. E. (2014). Generating human neurons in vitro and using them to understand neuropsychiatric disease. *Annu. Rev. Neurosci.* 37, 479–501. doi: 10.1146/annurev-neuro-062012-170328

Pasca, S. P., Portmann, T., Voineagu, I., Yazawa, M., Shcheglovitov, A., Pasca, A. M., et al. (2011). Using iPSC-derived neurons to uncover cellular phenotypes associated with Timothy syndrome. *Nat. Med.* 17, 1657–1662. doi: 10.1038/nm.2576

Patitucci, T. N., and Ebert, A. D. (2016). SMN deficiency does not induce oxidative stress in SMA iPSC-derived astrocytes or motor neurons. *Hum. Mol. Genet.* 25, 514–523. doi: 10.1093/hmg/ddv489

Pauklin, S., and Vallier, L. (2015). Activin/Nodal signalling in stem cells. *Development* 142, 607–619. doi: 10.1242/dev.091769

Paşca, S. P. (2018). The rise of three-dimensional human brain cultures. *Nature* 553:437. doi: 10.1038/nature25032

Pekny, M., and Pekna, M. (2014). Astrocyte reactivity and reactive astrogliosis: costs and benefits. *Physiol. Rev.* 94, 1077–1098. doi: 10.1152/physrev.00041.2013

Petros, T. J., Tyson, J. A., and Anderson, S. A. (2011). Pluripotent stem cells for the study of CNS development. *Front. Mol. Neurosci.* 4:30. doi: 10.3389/fnmol.2011.00030

Pham, M. T., Pollock, K. M., Rose, M. D., Cary, W. A., Stewart, H. R., Zhou, P., et al. (2018). Generation of human vascularized brain organoids. *Neuroreport* 29, 588–593. doi: 10.1097/wnr.0000000000001014

Pleasure, S. J., and Lee, V. M. (1993). NTera 2 cells: a human cell line which displays characteristics expected of a human committed neuronal progenitor cell. *J. Neurosci. Res.* 35, 585–602. doi: 10.1002/jnr.490350603

Puschmann, T. B., Zanden, C., De Pablo, Y., Kirchhoff, F., Pekna, M., Liu, J., et al. (2013). Bioactive 3D cell culture system minimizes cellular stress and maintains the in vivo-like morphological complexity of astroglial cells. *Glia* 61, 432–440. doi: 10.1002/glia.22446

Puschmann, T. B., Zanden, C., Lebkuechner, I., Philippot, C., de Pablo, Y., Liu, J., et al. (2014). HB-EGF affects astrocyte morphology, proliferation, differentiation, and the expression of intermediate filament proteins. *J. Neurochem.* 128, 878–889. doi: 10.1111/jnc.12519

Qian, X., Nguyen, Ha, N., Song, Mingxi, M., Hadiono, C., et al. (2016). Brain-region-specific organoids using mini-bioreactors for modeling ZIKV exposure. *Cell* 165, 1238–1254. doi: 10.1016/j.cell.2016.04.032

Quadrato, G., Nguyen, T., Macosko, E. Z., Sherwood, J. L., Min Yang, S., Berger, D. R., et al. (2017). Cell diversity and network dynamics in photosensitive human brain organoids. *Nature* 545, 48–53. doi: 10.1038/nature22047

Raja, W. K., Mungenast, A. E., Lin, Y.-T., Ko, T., Abdurrob, F., Seo, J., et al. (2016). Self-organizing 3D human neural tissue derived from induced pluripotent stem cells recapitulate Alzheimer's disease phenotypes. *PLoS One* 11:e0161969. doi: 10.1371/journal.pone.0161969

Ramón y Cajal, S. (1894). *Les Nouvelles Idées Sur la Structure du Système Nerveux Chez l'homme et Chez les Vertébrés*. Paris: MIT Press. doi: 10.5962/bhl.title.48561

Ramón y Cajal, S. (1904). *Textura del Sistema Nervioso del Hombre y de los Vertebrados, tomo II, primera parte*. Madrid: Imprenta y Libreria de Nicolas Moya *(Reprinted by Graficas Vidal Leuka, Alicante 1992*, 399–402).

Ramón y Cajal, S. (1909). *Histologie du Système Nerveux de l'homme et des Vertébrés (French Edition Reviewed and Updated by the Author, Translated from Spanish by L. Azoulay)*. Paris: Hachette Livre-Bnf.

Ramón y Cajal, S. (1913). *Estudios sobre la Degeneración y Regeneración del Sistema Nerviosa*. Madrid: Imprenta de Hijos de Nicolás Moya.

Renner, M., Lancaster, M. A., Bian, S., Choi, H., Ku, T., Peer, A., et al. (2017). Self-organized developmental patterning and differentiation in cerebral organoids. *EMBO J.* 36, 1316–1329. doi: 10.15252/embj.201694700

Reubinoff, B. E., Itsykson, P., Turetsky, T., Pera, M. F., Reinhartz, E., Itzik, A., et al. (2001). Neural progenitors from human embryonic stem cells. *Nat. Biotechnol.* 19, 1134–1140. doi: 10.1038/nbt1201-1134

Reynolds, B. A., and Weiss, S. (1992). Generation of neurons and astrocytes from isolated cells of the adult mammalian central nervous system. *Science* 255, 1707–1710. doi: 10.1126/science.1553558

Ricciardi, S., Ungaro, F., Hambrock, M., Rademacher, N., Stefanelli, G., Brambilla, D., et al. (2012). CDKL5 ensures excitatory synapse stability by reinforcing NGL-1-PSD95 interaction in the postsynaptic compartment and is impaired in patient iPSC-derived neurons. *Nat. Cell Biol.* 14, 911–923. doi: 10.1038/ncb2566

Ring, K. L., Tong, L. M., Balestra, M. E., Javier, R., Andrews-Zwilling, Y., Li, G., et al. (2012). Direct reprogramming of mouse and human fibroblasts into multipotent neural stem cells with a single factor. *Cell Stem Cell* 11, 100–109. doi: 10.1016/j.stem.2012.05.018

Robertson, R. T., Baratta, J., Kageyama, G. H., Ha, D. H., and Yu, J. (1997). Specificity of attachment and neurite outgrowth of dissociated basal forebrain cholinergic neurons seeded on to organotypic slice cultures of forebrain. *Neuroscience* 80, 741–752. doi: 10.1016/S0306-4522(97)00067-5

Roth, G., and Dicke, U. (2005). Evolution of the brain and intelligence. *Trends Cognit. Sci.* 9, 250–257. doi: 10.1016/j.tics.2005.03.005

Rowitch, D. H., and Kriegstein, A. R. (2010). Developmental genetics of vertebrate glial-cell specification. *Nature* 468, 214–222. doi: 10.1038/nature09611

Sakaguchi, H., Kadoshima, T., Soen, M., Narii, N., Ishida, Y., Ohgushi, M., et al. (2015). Generation of functional hippocampal neurons from self-organizing human embryonic stem cell-derived dorsomedial telencephalic tissue. *Nat. Commun.* 6:8896. doi: 10.1038/ncomms9896

Sanchez-Danes, A., Richaud-Patin, Y., Carballo-Carbajal, I., Jimenez-Delgado, S., Caig, C., Mora, S., et al. (2012). Disease-specific phenotypes in dopamine neurons from human iPS-based models of genetic and sporadic Parkinson's disease. *EMBO Mol. Med.* 4, 380–395. doi: 10.1002/emmm.201200215

Sareen, D., Ebert, A. D., Heins, B. M., McGivern, J. V., Ornelas, L., and Svendsen, C. N. (2012). Inhibition of apoptosis blocks human motor neuron cell death in a stem cell model of spinal muscular atrophy. *PLoS One* 7:e39113. doi: 10.1371/journal.pone.0039113

Schuldiner, M., Eiges, R., Eden, A., Yanuka, O., Itskovitz-Eldor, J., Goldstein, R. S., et al. (2001). Induced neuronal differentiation of human embryonic stem cells. *Brain Res.* 913, 201–205. doi: 10.1016/S0006-8993(01)02776-7

Schwab, A. J., and Ebert, A. D. (2014). Sensory neurons do not induce motor neuron loss in a human stem cell model of spinal muscular atrophy. *PLoS One* 9:e103112. doi: 10.1371/journal.pone.0103112

Schwartz, M. P., Hou, Z., Propson, N. E., Zhang, J., Engstrom, C. J., Santos Costa, V., et al. (2015). Human pluripotent stem cell-derived neural constructs for predicting neural toxicity. *Proc. Natl. Acad. Sci. U.S.A.* 112, 12516–12521. doi: 10.1073/pnas.1516645112

Schwartz, P. H., Brick, D. J., Stover, A. E., Loring, J. F., and Muller, F. J. (2008). Differentiation of neural lineage cells from human pluripotent stem cells. *Methods* 45, 142–158. doi: 10.1016/j.ymeth.2008.03.007

Serio, A., Bilican, B., Barmada, S. J., Ando, D. M., Zhao, C., Siller, R., et al. (2013). Astrocyte pathology and the absence of non-cell autonomy in an induced pluripotent stem cell model of TDP-43 proteinopathy. *Proc. Natl. Acad. Sci. U.S.A.* 110, 4697–4702. doi: 10.1073/pnas.1300398110

Shcheglovitov, A., Shcheglovitova, O., Yazawa, M., Portmann, T., Shu, R., Sebastiano, V., et al. (2013). SHANK3 and IGF1 restore synaptic deficits in neurons from 22q13 deletion syndrome patients. *Nature* 503, 267–271. doi: 10.1038/nature12618

Shepherd, J. (2018). Ethical (and epistemological) issues regarding consciousness in cerebral organoids. *J. Med. Ethics* 44, 611–612. doi: 10.1136/medethics-2018-104778

Shi, Y., Kirwan, P., Smith, J., MacLean, G., Orkin, S. H., and Livesey, F. J. (2012a). A human stem cell model of early Alzheimer's disease pathology in down syndrome. *Sci. Transl. Med.* 4:124ra129. doi: 10.1126/scitranslmed.3003771

Shi, Y., Kirwan, P., Smith, J., Robinson, H. P. C., and Livesey, F. J. (2012b). Human cerebral cortex development from pluripotent stem cells to functional excitatory synapses. *Nat. Neurosci.* 15:477. doi: 10.1038/nn.3041

Shipley, M. M., Mangold, C. A., and Szpara, M. L. (2016). Differentiation of the SH-SY5Y human neuroblastoma cell line. *J. Vis. Exp.* 108, 53193–53193. doi: 10.3791/53193

Siegenthaler, J. A., Ashique, A. M., Zarbalis, K., Patterson, K. P., Hecht, J. H., Kane, M. A., et al. (2009). Retinoic acid from the meninges regulates cortical neuron generation. *Cell* 139, 597–609. doi: 10.1016/j.cell.2009.10.004

Sloan, S. A., Darmanis, S., Huber, N., Khan, T. A., Birey, F., Caneda, C., et al. (2017). Human astrocyte maturation captured in 3D cerebral cortical spheroids derived from pluripotent stem cells. *Neuron* 95, 779.e776–790.e776. doi: 10.1016/j.neuron.2017.07.035

Sneddon, L. U., Halsey, L. G., and Bury, N. R. (2017). Considering aspects of the 3Rs principles within experimental animal biology. *J. Exp. Biol.* 220(Pt 17), 3007–3016. doi: 10.1242/jeb.147058

Soldner, F., Hockemeyer, D., Beard, C., Gao, Q., Bell, G. W., Cook, E. G., et al. (2009). Parkinson's disease patient-derived induced pluripotent stem cells free of viral reprogramming factors. *Cell* 136, 964–977. doi: 10.1016/j.cell.2009.02.013

Stan, A. D., Ghose, S., Gao, X.-M., Roberts, R. C., Lewis-Amezcua, K., Hatanpaa, K. J., et al. (2006). Human postmortem tissue: what quality markers matter? *Brain Res.* 1123, 1–11. doi: 10.1016/j.brainres.2006.09.025

Stubbs, D., DeProto, J., Nie, K., Englund, C., Mahmud, I., Hevner, R., et al. (2009). Neurovascular congruence during cerebral cortical development. *Cereb. Cortex (New York, NY)* 19(Suppl. 1), i32–i41. doi: 10.1093/cercor/bhp040

Suga, H., Kadoshima, T., Minaguchi, M., Ohgushi, M., Soen, M., Nakano, T., et al. (2011). Self-formation of functional adenohypophysis in three-dimensional culture. *Nature* 480, 57–62. doi: 10.1038/nature10637

Sun, A. X., Ng, H. H., and Tan, E. K. (2018). Translational potential of human brain organoids. *Ann. Clin. Transl. Neurol.* 5, 226–235. doi: 10.1002/acn3.505

Sun, Y., Florer, J., Mayhew, C. N., Jia, Z., Zhao, Z., Xu, K., et al. (2015). Properties of neurons derived from induced pluripotent stem cells of Gaucher disease type 2 patient fibroblasts: potential role in neuropathology. *PLoS One* 10:e0118771. doi: 10.1371/journal.pone.0118771

Sun, Y., Pollard, S., Conti, L., Toselli, M., Biella, G., Parkin, G., et al. (2008). Long-term tripotent differentiation capacity of human neural stem (NS) cells in adherent culture. *Mol. Cell. Neurosci.* 38, 245–258. doi: 10.1016/j.mcn.2008.02.014

Sutcliffe, M., and Lancaster, M. A. (2017). A simple method of generating 3D brain organoids using standard laboratory equipment. *Methods Mol. Biol.* doi: 10.1007/7651_2017_2 [Epub ahead of print].

Tachibana, C. Y. (2018). Stem-cell culture moves to the third dimension. *Nature* 558, 329–331. doi: 10.1038/d41586-018-05380-x

Takahashi, K., Tanabe, K., Ohnuki, M., Narita, M., Ichisaka, T., Tomoda, K., et al. (2007). Induction of pluripotent stem cells from adult human fibroblasts by defined factors. *Cell* 131, 861–872. doi: 10.1016/j.cell.2007.11.019

Tang, X., Kim, J., Zhou, L., Wengert, E., Zhang, L., Wu, Z., et al. (2016). KCC2 rescues functional deficits in human neurons derived from patients with Rett syndrome. *Proc. Natl. Acad. Sci. U.S.A.* 113, 751–756. doi: 10.1073/pnas.1524013113

Temple, S. (1989). Division and differentiation of isolated CNS blast cells in microculture. *Nature* 340, 471–473. doi: 10.1038/340471a0

The Hd iPsc Consortium (2012). Induced pluripotent stem cells from patients with huntington's disease show CAG-repeat-expansion-associated phenotypes. *Cell Stem Cell* 11, 264–278. doi: 10.1016/j.stem.2012.04.027

Thomson, J. A., Itskovitz-Eldor, J., Shapiro, S. S., Waknitz, M. A., Swiergiel, J. J., Marshall, V. S., et al. (1998). Embryonic stem cell lines derived from human blastocysts. *Science* 282, 1145–1147. doi: 10.1126/science.282.5391.1145

Tian, Y., Voineagu, I., Pasca, S. P., Won, H., Chandran, V., Horvath, S., et al. (2014). Alteration in basal and depolarization induced transcriptional network in iPSC derived neurons from Timothy syndrome. *Genome Med.* 6:75. doi: 10.1186/s13073-014-0075-5

Tibbitt, M. W., and Anseth, K. S. (2009). Hydrogels as extracellular matrix mimics for 3D cell culture. *Biotechnol. Bioeng.* 103, 655–663. doi: 10.1002/bit.22361

Tiscornia, G., Vivas, E. L., Matalonga, L., Berniakovich, I., Barragan Monasterio, M., Eguizabal, C., et al. (2013). Neuronopathic Gaucher's disease: induced pluripotent stem cells for disease modelling and testing chaperone activity of small compounds. *Hum. Mol. Genet.* 22, 633–645. doi: 10.1093/hmg/dds471

Tonge, P. D., Shigeta, M., Schroeder, T., and Andrews, P. W. (2011). Functionally defined substates within the human embryonic stem cell compartment. *Stem Cell Res.* 7, 145–153. doi: 10.1016/j.scr.2011.04.006

Trilck, M., Hubner, R., Seibler, P., Klein, C., Rolfs, A., and Frech, M. J. (2013). Niemann-pick type C1 patient-specific induced pluripotent stem cells display disease specific hallmarks. *Orphanet. J. Rare Dis.* 8:144. doi: 10.1186/1750-1172-8-144

Ullrich, C., Daschil, N., and Humpel, C. (2011). Organotypic vibrosections: novel whole sagittal brain cultures. *J. Neurosci. Methods* 201, 131–141. doi: 10.1016/j.jneumeth.2011.07.021

Ungrin, M. D., Joshi, C., Nica, A., Bauwens, C., and Zandstra, P. W. (2008). Reproducible, ultra high-throughput formation of multicellular organization from single cell suspension-derived human embryonic stem cell aggregates. *PLoS One* 3:e1565. doi: 10.1371/journal.pone.0001565

Urbach, A., Bar-Nur, O., Daley, G. Q., and Benvenisty, N. (2010). Differential modeling of fragile X syndrome by human embryonic stem cells and induced pluripotent stem cells. *Cell Stem Cell* 6, 407–411. doi: 10.1016/j.stem.2010.04.005

Uusi-Rauva, K., Blom, T., von Schantz-Fant, C., Blom, T., Jalanko, A., and Kyttala, A. (2017). Induced pluripotent stem cells derived from a CLN5 Patient manifest phenotypic characteristics of neuronal ceroid lipofuscinoses. *Int. J. Mol. Sci.* 18:E955. doi: 10.3390/ijms18050955

Velasco, I., Salazar, P., Giorgetti, A., Ramos-Mejía, V., Castaño, J., Romero-Moya, D., et al. (2014). Concise review: generation of neurons from somatic cells of healthy individuals and neurological patients through induced pluripotency or direct conversion. *Stem Cells (Dayton, Ohio)* 32, 2811–2817. doi: 10.1002/stem.1782

Vescovi, A. L., Parati, E. A., Gritti, A., Poulin, P., Ferrario, M., Wanke, E., et al. (1999). Isolation and cloning of multipotential stem cells from the embryonic human CNS and establishment of transplantable human neural stem cell lines by epigenetic stimulation. *Exp. Neurol.* 156, 71–83. doi: 10.1006/exnr.1998.6998

Vessoni, A. T., Herai, R. H., Karpiak, J. V., Leal, A. M. S., Trujillo, C. A., Quinet, A., et al. (2016). Cockayne syndrome-derived neurons display reduced synapse density and altered neural network synchrony. *Hum. Mol. Genet.* 25, 1271–1280. doi: 10.1093/hmg/ddw008

Vierbuchen, T., Ostermeier, A., Pang, Z. P., Kokubu, Y., Südhof, T. C., and Wernig, M. (2010). Direct conversion of fibroblasts to functional neurons by defined factors. *Nature* 463, 1035–1041. doi: 10.1038/nature08797

Villanueva, S., Glavic, A., Ruiz, P., and Mayor, R. (2002). Posteriorization by FGF, Wnt, and retinoic acid is required for neural crest induction. *Dev. Biol.* 241, 289–301. doi: 10.1006/dbio.2001.0485

Waddington, C. H., and Cohen, A. (1936). Experiments on the development of the head of the chick embryo. *J. Exp. Biol.* 13, 219–236.

Waddington, S. N., Privolizzi, R., Karda, R., and O'Neill, H. C. (2016). A broad overview and review of CRISPR-cas technology and stem cells. *Curr. Stem Cell Rep.* 2, 9–20. doi: 10.1007/s40778-016-0037-5

Walsh, K., Megyesi, J., and Hammond, R. (2005). Human central nervous system tissue culture: a historical review and examination of recent advances. *Neurobiol. Dis.* 18, 2–18. doi: 10.1016/j.nbd.2004.09.002

Wang, Y., Wang, L., Zhu, Y., and Qin, J. (2018). Human brain organoid-on-a-chip to model prenatal nicotine exposure. *Lab Chip* 18, 851–860. doi: 10.1039/C7LC01084B

Watanabe, K., Kamiya, D., Nishiyama, A., Katayama, T., Nozaki, S., Kawasaki, H., et al. (2005). Directed differentiation of telencephalic precursors from embryonic stem cells. *Nat. Neurosci.* 8, 288–296. doi: 10.1038/nn1402

Wataya, T., Ando, S., Muguruma, K., Ikeda, H., Watanabe, K., Eiraku, M., et al. (2008). Minimization of exogenous signals in ES cell culture induces rostral hypothalamic differentiation. *Proc. Natl. Acad. Sci. U.S.A.* 105, 11796–11801. doi: 10.1073/pnas.0803078105

Whetsell, W. O. Jr., Mytilineou, C., Shen, J., and Yahr, M. D. (1981). The development of the dog nigrostriatal system in organotypic culture. *J. Neural Transm.* 52, 149–161. doi: 10.1007/BF01249600

Williams, E. C., Zhong, X., Mohamed, A., Li, R., Liu, Y., Dong, Q., et al. (2014). Mutant astrocytes differentiated from Rett syndrome patients-specific iPSCs have adverse effects on wild-type neurons. *Hum. Mol. Genet.* 23, 2968–2980. doi: 10.1093/hmg/ddu008

Wilson, J. L., Suri, S., Singh, A., Rivet, C. A., Lu, H., and McDevitt, T. C. (2014). Single-cell analysis of embryoid body heterogeneity using microfluidic trapping array. *Biomed. Microdev.* 16, 79–90. doi: 10.1007/s10544-013-9807-3

Wood, C., Wolf, C. J., Belair, D. G., Abbott, B. D., Becker, C., and Moorefield, S. D. (2018). A three-dimensional organoid culture model to assess the influence of chemicals on morphogenetic fusion. *Toxicol. Sci.* 166, 394–408. doi: 10.1093/toxsci/kfy207

Workman, M. J., Mahe, M. M., Trisno, S., Poling, H. M., Watson, C. L., Sundaram, N., et al. (2017). Engineered human pluripotent-stem-cell-derived intestinal tissues with a functional enteric nervous system. *Nat. Med.* 23, 49–59. doi: 10.1038/nm.4233

Wu, J. Q., Habegger, L., Noisa, P., Szekely, A., Qiu, C., Hutchison, S., et al. (2010). Dynamic transcriptomes during neural differentiation of human embryonic stem cells revealed by short, long, and paired-end sequencing. *Proc. Natl. Acad. Sci. U.S.A.* 107, 5254–5259. doi: 10.1073/pnas.0914114107

Xu, C. C., Denton, K. R., Wang, Z. B., Zhang, X., and Li, X. J. (2016). Abnormal mitochondrial transport and morphology as early pathological changes in human models of spinal muscular atrophy. *Dis. Model. Mech.* 9, 39–49. doi: 10.1242/dmm.021766

Yakoub, A. (2019). Cerebral organoids exhibit mature neurons and astrocytes and recapitulate electrophysiological activity of the human brain. *Neural Regener. Res.* 14, 757–761. doi: 10.4103/1673-5374.249283

Yakoub, A. M., and Sadek, M. (2018). Development and characterization of human cerebral organoids: an optimized protocol. *Cell Transplant.* 27, 393–406. doi: 10.1177/0963689717752946

Yamashita, S., Chiyonobu, T., Yoshida, M., Maeda, H., Zuiki, M., Kidowaki, S., et al. (2016). Mislocalization of syntaxin-1 and impaired neurite growth observed in a human iPSC model for STXBP1-related epileptic encephalopathy. *Epilepsia* 57, e81–e86. doi: 10.1111/epi.13338

Yang, N., Chanda, S., Marro, S., Ng, Y.-H., Janas, J. A., Haag, D., et al. (2017). Generation of pure GABAergic neurons by transcription factor programming. *Nat. Methods* 14, 621–628. doi: 10.1038/nmeth.4291

Yang, Y. M., Gupta, S. K., Kim, K. J., Powers, B. E., Cerqueira, A., Wainger, B. J., et al. (2013). A small molecule screen in stem-cell-derived motor neurons identifies a kinase inhibitor as a candidate therapeutic for ALS. *Cell Stem Cell* 12, 713–726. doi: 10.1016/j.stem.2013.04.003

Ye, F., Kang, E., Yu, C., Qian, X., Jacob, F., Yu, C., et al. (2017). DISC1 regulates neurogenesis via modulating kinetochore attachment of Ndel1/Nde1 during Mitosis. *Neuron* 96, 1041.e1045–1054.e1045. doi: 10.1016/j.neuron.2017.10.010

Yin, X., Mead, Benjamin, E., Safaee, H., Langer, R., Karp, et al. (2016). Engineering stem cell organoids. *Cell Stem Cell* 18, 25–38. doi: 10.1016/j.stem.2015.12.005

Ying, Q. L., Stavridis, M., Griffiths, D., Li, M., and Smith, A. (2003). Conversion of embryonic stem cells into neuroectodermal precursors in adherent monoculture. *Nat. Biotechnol.* 21, 183–186. doi: 10.1038/nbt780

Yoshida, M., Kitaoka, S., Egawa, N., Yamane, M., Ikeda, R., Tsukita, K., et al. (2015). Modeling the early phenotype at the neuromuscular junction of spinal muscular atrophy using patient-derived iPSCs. *Stem Cell Rep.* 4, 561–568. doi: 10.1016/j.stemcr.2015.02.010

Zhang, S. C., Wernig, M., Duncan, I. D., Brustle, O., and Thomson, J. A. (2001). In vitro differentiation of transplantable neural precursors from human embryonic stem cells. *Nat. Biotechnol.* 19, 1129–1133. doi: 10.1038/nbt1201-1129

Zhang, Y., Pak, C., Han, Y., Ahlenius, H., Zhang, Z., Chanda, S., et al. (2013). Rapid single-step induction of functional neurons from human pluripotent stem cells. *Neuron* 78, 785–798. doi: 10.1016/j.neuron.2013.05.029

Zhang, Y., Schmid, B., Nikolaisen, N. K., Rasmussen, M. A., Aldana, B. I., Agger, M., et al. (2017). Patient iPSC-derived neurons for disease modeling of frontotemporal dementia with mutation in CHMP2B. *Stem Cell Rep.* 8, 648–658. doi: 10.1016/j.stemcr.2017.01.012

Zhu, P. P., Denton, K. R., Pierson, T. M., Li, X. J., and Blackstone, C. (2014). Pharmacologic rescue of axon growth defects in a human iPSC model of hereditary spastic paraplegia SPG3A. *Hum. Mol. Genet.* 23, 5638–5648. doi: 10.1093/hmg/ddu280

Zhu, Y., Wang, L., Yin, F., Yu, Y., Wang, Y., Shepard, M. J., et al. (2017a). Probing impaired neurogenesis in human brain organoids exposed to alcohol. *Integr. Biol. (Camb)* 9, 968–978. doi: 10.1039/c7ib00105c

Zhu, Y., Wang, L., Yu, H., Yin, F., Wang, Y., Liu, H., et al. (2017b). In situ generation of human brain organoids on a micropillar array. *Lab Chip* 17, 2941–2950. doi: 10.1039/C7LC00682A

Conflict of Interest Statement: The authors declare that the research was conducted in the absence of any commercial or financial relationships that could be construed as a potential conflict of interest.

Copyright © 2019 Pacitti, Privolizzi and Bax. This is an open-access article distributed under the terms of the Creative Commons Attribution License (CC BY). The use, distribution or reproduction in other forums is permitted, provided the original author(s) and the copyright owner(s) are credited and that the original publication in this journal is cited, in accordance with accepted academic practice. No use, distribution or reproduction is permitted which does not comply with these terms.

frontiers in Cellular Neuroscience

ORIGINAL RESEARCH
published: 24 April 2019
doi: 10.3389/fncel.2019.00165

Cortical Pain Processing in the Rat Anterior Cingulate Cortex and Primary Somatosensory Cortex

Zhengdong Xiao[1,2], Erik Martinez[2,3], Prathamesh M. Kulkarni[2], Qiaosheng Zhang[3†], Qianning Hou[2,4], David Rosenberg[5], Robert Talay[3], Leor Shalot[3], Haocheng Zhou[3], Jing Wang[3,6] and Zhe Sage Chen[2,6,7]**

[1] Department of Instrument Science and Technology, Zhejiang University, Hangzhou, China, [2] Department of Psychiatry, New York University School of Medicine, New York, NY, United States, [3] Department of Anesthesiology, Perioperative Care and Pain Medicine, New York University School of Medicine, New York, NY, United States, [4] Department of Biophysics, University of Science and Technology of China, Hefei, China, [5] New York University School of Medicine, New York, NY, United States, [6] Department of Neuroscience and Physiology, New York University School of Medicine, New York, NY, United States, [7] Neuroscience Institute, New York University School of Medicine, New York, NY, United States

Pain is a complex multidimensional experience encompassing sensory-discriminative, affective-motivational and cognitive-emotional components mediated by different neural mechanisms. Investigations of neurophysiological signals from simultaneous recordings of two or more cortical circuits may reveal important circuit mechanisms on cortical pain processing. The anterior cingulate cortex (ACC) and primary somatosensory cortex (S1) represent two most important cortical circuits related to sensory and affective processing of pain. Here, we recorded *in vivo* extracellular activity of the ACC and S1 simultaneously from male adult Sprague-Dale rats ($n = 5$), while repetitive noxious laser stimulations were delivered to animalÕs hindpaw during pain experiments. We identified spontaneous pain-like events based on stereotyped pain behaviors in rats. We further conducted systematic analyses of spike and local field potential (LFP) recordings from both ACC and S1 during evoked and spontaneous pain episodes. From LFP recordings, we found stronger phase-amplitude coupling (theta phase vs. gamma amplitude) in the S1 than the ACC ($n = 10$ sessions), in both evoked ($p = 0.058$) and spontaneous pain-like behaviors ($p = 0.017$, paired signed rank test). In addition, pain-modulated ACC and S1 neuronal firing correlated with the amplitude of stimulus-induced event-related potentials (ERPs) during evoked pain episodes. We further designed statistical and machine learning methods to detect pain signals by integrating ACC and S1 ensemble spikes and LFPs. Together, these results reveal differential coding roles between the ACC and S1 in cortical pain processing, as well as point to distinct neural mechanisms between evoked and putative spontaneous pain at both LFP and cellular levels.

Keywords: evoked pain, spontaneous pain, anterior cingulate cortex (ACC), primary somatosensory cortex (S1), phase-amplitude coupling (PAC)

OPEN ACCESS

Edited by:
Marco Martina,
Northwestern University, United States

Reviewed by:
Parisa Gazerani,
Aalborg University, Denmark
Paul Geoffrey Overton,
University of Sheffield,
United Kingdom

***Correspondence:**
Jing Wang
jing.wang2@nyulangone.org
orcid.org/0000-0003-1580-1356
Zhe Sage Chen
zhe.chen@nyulangone.org
orcid.org/0000-0002-6483-6056

†Qiaosheng Zhang
orcid.org/0000-0003-0485-3126

Specialty section:
This article was submitted to Cellular Neurophysiology, a section of the journal Frontiers in Cellular Neuroscience

Received: *22 February 2019*
Accepted: *08 April 2019*
Published: *24 April 2019*

Citation:
Xiao Z, Martinez E, Kulkarni PM, Zhang Q, Hou Q, Rosenberg D, Talay R, Shalot L, Zhou H, Wang J and Chen ZS (2019) Cortical Pain Processing in the Rat Anterior Cingulate Cortex and Primary Somatosensory Cortex. Front. Cell. Neurosci. 13:165. doi: 10.3389/fncel.2019.00165

INTRODUCTION

Pain is a complex sensory experience involving multidimensional components, encoded by distributed cortical pain circuits. For example, the primary somatosensory cortex (S1) is known to represent the sensory-discriminative component of pain (Vierck et al., 2013), whereas the anterior cingulate cortex (ACC) is known to represent the affective-motivational component of pain (Bushnell et al., 2013). Human neuroimaging experiments have suggested that many other neocortical regions, such as the insular, secondary somatosensory cortex, prefrontal cortex, and orbitofrontal cortex, also play important roles in pain processing (Davis et al., 2017). With regards to the duration of pain experiences, pain is often classified as acute and chronic pain. Stimulus-evoked pain is induced by a noxious stimulus, whereas spontaneous pain is detached from an overt external stimulus. It is known that repeated noxious stimulations can elicit spontaneous pain behaviors (Bennett, 2012); however, identification of spontaneous pain remains challenging in animal studies (Tappe-Theodor and Kuner, 2014).

At the single cell level, ACC neurons are known to encode the affective component of pain experiences, and chronic pain may enhance the aversive responses of ACC neurons (Zhang et al., 2017; Zhou et al., 2018). At the mesoscopic and macroscopic levels, intracortical local field potential (LFP) signals provide important physiological signatures for characterizing pain at a fine timescale comparable to that of single neuronal activity (Ploner et al., 2017; Peng et al., 2018; Ploner and May, 2018). The EEG-based *phase-locked* event-related potentials (ERPs) have been suggested for identifying biomarkers for pain (Pinheiro et al., 2016). The ERP amplitude reflects the degree of synchrony within local neuronal populations. A power increase or decrease is referred to as *non-phase-locked* event-related synchronization or desynchronization (ERS or ERD), respectively (Bressler, 2002). ERPs are referred to as "evoked potentials" when occurring soon after a stimulus, and spontaneous in the period without any stimulus presentation. If ERPs are not directly evoked by overt stimuli, they are sometimes called as "induced potentials." While ERP was primarily used in EEG analyses, here we adapted this concept for LFP recordings. In pain experiments, ERPs are often temporally associated with stereotyped pain behaviors (such as the paw withdrawal and licking in rodents) (Cheppudira, 2006; Kawasaki et al., 2012; Whittaker and Howarth, 2014; Murai et al., 2016). Since identifying spontaneous pain in rodent studies is difficult due to the lack of pain report, ERPs may be viewed as a proxy measure of pain (Davis et al., 2017). Throughout the paper, we use the term ERP interchangeably for both evoked pain and spontaneous pain-like episodes, which are referred to as pain-evoked potentials and pain-induced potentials, respectively.

In this report, we focused the investigation on simultaneous ACC and S1 recordings, and examined the differences between evoked pain and spontaneous pain-like episodes. We combined animal behavior, neurophysiology (spikes and LFP), and machine learning to examine the neural codes during identified pain episodes in freely behaving rats. While single neuronal spikes present precise timing information related to sensory coding or representation, it imposes a technical challenge to obtain stable ensembles in chronic recordings over days. In contrast, LFPs represent the aggregate subthreshold activity of neurons in a local localized area, and are relatively stable over time, thereby providing a reliable macroscopic readout from local microcircuits related to pain processing.

MATERIALS AND METHODS

Animals and Protocols

All experimental studies were performed in accordance with the National Institutes of Health (NIH) *Guide for the Care and Use of Laboratory Animals* to ensure minimal animal use and discomfort, and were approved by the New York University School of Medicine (NYUSOM) Institutional Animal Care and Use Committee (IACUC). Male adult Sprague-Dale rats (250–300 g, Taconic Farms, Albany, NY) were used in our current study and kept at the new Science Building at NYUSOM, with controlled humidity, temperature and 12-h (6:30 a.m.–6:30 p.m.) light-dark cycle. Food and water were available *ad libitum*. Animals were given on average 10 days to adjust to the new environment before the initiation of experiments.

Thermal pain stimuli were used for rats freely exploring in a plastic chamber of size $38 \times 20 \times 25$ cm^3 on top of a mesh table. A blue (473 nm diode-pumped solid-state) laser with varying laser intensities was delivered to the animal's hindpaw (**Figure 1A**). The laser stimulation was delivered in repeated trials (25–40) during 30–45 min. During experiments, two video cameras (120 frame per second) were used to continuously monitor the animal's behavior. The rat's evoked pain behavior was characterized by its latency to paw withdrawal (Cheppudira, 2006; Deuis et al., 2017).

Identification of Spontaneous Pain-Like Events Based on Stereotyped Behaviors

Repeated noxious stimulus stimulations to the rat hindpaw could induce spontaneous pain-like behaviors. Between the inter-trial intervals of laser stimulations, we examined the animal's behavior to search for putative spontaneous pain episodes. Specifically, we categorized the spontaneous pain-like behavior into several subtypes: (i) twitch—short and sudden jerking movement that was not associated with locomotion or a pain stimulus; (ii) lifting/flicking—the lift of the foot would not involve movement of the whole leg or bending of the knee; (iii) paw withdrawal and paw licking—taking the foot up and into the body with bending of the knee, which is often accompanied by shaking the foot. Lick is characterized as lifting the foot off of the grating and licking it. The licks mirrored the licking involved immediately after a pain stimulus. None of these behaviors were associated with locomotion or a pain stimulus.

Due to the lack of ground truth, we referred to those events as spontaneous pain-like episodes. Such behaviors could also indicate pain anticipation due to repeated stimulations (Barrot, 2012; Urien et al., 2018).

Electrode Implant and Electrophysiology

We used silicon probes (Buzsaki32, NeuroNexus) with 3D printed drive to record multi-channel (up to 64 channels) neural

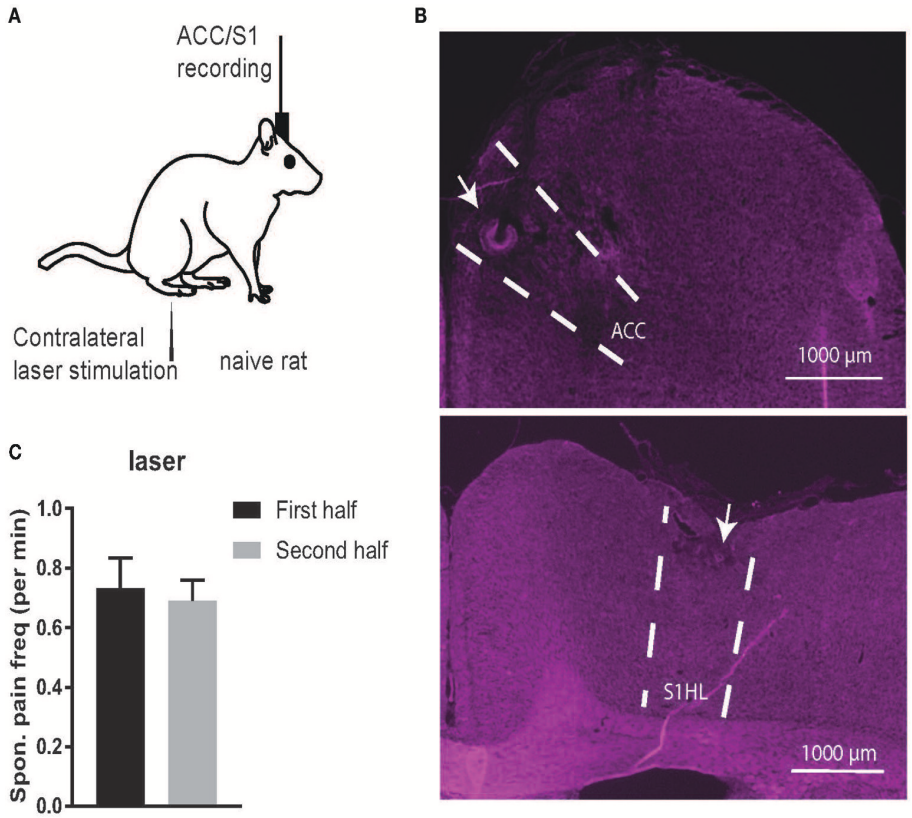


FIGURE 1 | (A) Schematic diagrams of noxious stimulation and recording on naive rats. **(B)** Histology of recording areas in the rat ACC and S1. **(C)** Comparison of the frequency (per minute) of spontaneous pain-like episodes between the first and second half of recording sessions. There was no statistical difference between the first and second half ($p > 0.05$, paired t-test).

activities from the rat ACC and S1 areas simultaneously, at the contralateral side of the paw that received noxious laser stimulation. For surgery, rats were anesthetized with isoflurane (1.5–2%). The skull was exposed and a 3 mm-diameter hole was drilled above the target region. The coordinates for the ACC and S1 implants were: ACC: AP 2.7, ML 1.4–2.0, DV 2.0, with an angle of 20° toward the middle line; S1: AP −1.5, ML 2.5–3.2, DV 1.5. The drive as secured to the skull screws with dental cement.

Using a Plexon (Dallas, TX) data acquisition system, we recorded *in vivo* neurophysiological signals at a 40 kHz sampling rate, and band-pass filtered (0.3 Hz–7.5 kHz). Spikes were thresholded from the high-passed (> 300 Hz) raw signals, and the subsequent band-pass filtered (1–100 Hz) signals produced LFPs. Detected spikes were further sorted offline using commercial software (Offline Sorter, Plexon).

A total of 15 animals were used in the current study: 10 naive rats were used for behavioral analysis only, and another 5 naive rats were used for both behavioral and physiological analyses (**Table 1**). In rats #11-13, we recorded LFP signals from the ACC and S1 simultaneously using silicon probes (**Figure 1B**). In rats #14–15, we obtained both LFP recordings and well-isolated units from the ACC and S1. In total, we have analyzed 81 ACC units and 41 S1 units from these two rats.

Identification of Pain-Modulated Units

Triggered on the stimulus onset, we computed the peri-stimulus time histogram (PSTH) of each neuron (50 ms bin size). From the PSTH, we identified the positively (or negatively) pain-modulated units from the S1 and ACC (Chen et al., 2017; Zhang et al., 2017), which showed significantly increased (or decreased) firing rates compared to the baseline (5 s window before the stimulus onset).

At a finer timescale, we also computed the ERP peak-triggered PSTH for each neuron using a 10 ms bin size. The PSTH was further smoothed using a Gaussian kernel with a bandwidth of 20 ms.

Identification of ERPs

A cortical ERP reflects the coordinated behavior of a large number of neurons in relation to an external or internal event. Traditional ERP analysis is based on trial averaging (Garcia et al., 2002). In contrast, all studies reported here were based on single-trial analyses. From LFP recordings, we identified the induced ERPs during evoked and spontaneous pain episodes. Since the ERP was associated with low-frequency activity, to remove the high-frequency noise, we further applied band-pass filtering (2–15 Hz) to the multi-channel LFP traces, followed by principal component analysis (PCA). We extracted the dominant

TABLE 1 | Summary of experimental data.

Animal	Stimulus	Behavior analysis	LFP analysis	# Unit analysis (ACC + S1)	# Sessions per rat
naive rats #1–5	None	Yes	n/a	n/a	1
naive rats #6–10	blue laser	Yes	n/a	n/a	1
naive rat #11	blue laser	Yes	Yes	0 + 0	2
naive rat #12	blue laser	Yes	Yes	0 + 0	2
naive rat #13	blue laser	Yes	Yes	0 + 0	3
naive rat #14	blue laser	Yes	Yes	33 + 5	2
naive rat #15	blue laser	Yes	Yes	48 + 36	3

principal component that produced an ERP waveform associated with the largest variance, which was used in the subsequent ERP analysis. The duration of the ERP waveform was 200–250 ms, and the signal-to-noise ratio (SNR) varied in each evoked pain or spontaneous pain-like episode. We used a conservative SNR criterion for the ERPs, and sought ERPs around the pain-like behaviors (within a window of $[-5, 5]$ s centered at the event onset).

Spectrum and Time-Frequency Analyses

The coherence measures the amplitude-amplitude coupling between two random signals across a wide range of frequencies. The spike-field coherence (SFC) measures phase synchronization between the LFP and spike times as a function of frequency. The coherence and SFC is scaled between 0 and 1. We assumed trial stationarity and derived trial-averaged coherence and SFC, as well as their jackknife error bars. In single-trial analyses, we computed the spectrogram or SFC in the time-frequency representation by using a moving window.

Multitapered spectral analyses for LFP spectrogram, LFP coherence and SFC were performed using the Chronux toolbox (chronux.org). Specifically, we chose a half-bandwidth parameter W such that the windowing functions were maximally concentrated within $[-W, W]$. We chose $W > 1/T$ (where T denotes the duration) such that the Slepian taper functions were well concentrated in frequency and had bias reducing characteristics. In terms of Chronux function setup, we used the tapers setup $[TW, N]$, where TW is the time-bandwidth product, and $N = 2 \times TW - 1$ is the number of tapers. Since the taper functions are mutually orthogonal, they give independent spectral estimates. In all time-frequency analyses, we used a moving window length of 0.5–1 s and a step size of 1 ms. In the LFP coherence and SFC analyses, a 2 s window was used across all pain episodes. We used $TW = 5$ for LFP spectrogram and coherence, and $TW = 3$ for SFC. From the spectrogram, we computed the Z-scored spectrogram, where the baseline was defined as the 5-s period before the noxious stimulus presentation.

Cross-Frequency Phase-Amplitude Coupling

PAC was used to characterize the coupling between the low-frequency (theta) phase and high-frequency (gamma) amplitude of EEG recordings during nociception (Wang et al., 2011). We adapted the PAC analysis to LFP recordings during pain episodes. Specifically, we band-pass filtered LFP signals into proper frequency (theta or gamma) band and computed their Hilbert transform. From the derived complex-valued signals, we extracted the instantaneous theta phase and gamma amplitude (envelope), and further constructed the phase-amplitude histogram (18 bins within 0–360°). In light of the phase-amplitude distribution, we ran a parametric test based on the generalized linear model (GLM) to assess the PAC. A quantitative scalar statistic $r = \max\{|1 - A_s./A_0|\}$ (where A_s and A_0 denote the predicted amplitude vectors defined at the phase vector $[0, 2\pi]$ using the spline model and the null model, respectively; ./ denotes the dot division operator in MATLAB) along with its confidence intervals was reported (Kramer and Eden, 2013).

Detection of the Onset of Pain Signals

We have previously developed model-based methods for detecting the onset of acute pain signals based on the ACC and/or S1 neural ensemble spike activity (Chen et al., 2017; Hu et al., 2018; Xiao et al., 2018). Assuming that subjective pain signal was latent and evolved dynamically in time, we proposed a Poisson linear dynamical system (PLDS) to link the pain stimulus to neural spiking activity of a population of C Poisson-spiking neurons, as follows:

$$z_t = az_{t-1} + \epsilon_t \tag{1}$$

$$\boldsymbol{y}_t \sim \text{Poisson}\Big(\exp(cz_t + d)\Delta\Big) \tag{2}$$

where $\boldsymbol{y}_t = [y_{1,t}, \ldots, y_{C,t}]^\top$ denotes a C-dimensional population vector, with each element consisting of the neuronal spike count within the time interval $((t-1)\Delta, t\Delta]$ (bin size Δ); the univariate (latent) variable z_t represents the latent common input that drives the neuronal population firing rate. The dynamics of the latent variable is governed by a first-order autoregressive (AR) model $(0 < |a| < 1)$ driven by a zero-mean Gaussian noise process $\epsilon_t \in \mathcal{N}(0, \sigma_\epsilon^2)$. The parameters c and d are unconstrained. During evoked pain episodes, we used an expectation-maximization (EM) algorithm to estimate the unknown state variables $z_{1:T}$ and all unknown parameters $\{a, c, d, \sigma_\epsilon\}$ from the spike count observations $\boldsymbol{y}_{1:T}$ in a single trial.

During spontaneous pain episodes, we assumed that the model parameters were identical to those derived from a previous evoked pain episode, and ran a recursive (forward) filtering algorithm to estimate the latent state variable $\hat{z}_{t|t}$ (Hu et al., 2018)

$$\begin{aligned}
\hat{z}_{t|t-1} &= a\hat{z}_{t-1|t-1} \\
Q_{t|t-1} &= a^2 Q_{t-1|t-1} + \sigma_\epsilon^2 \\
\hat{\boldsymbol{y}}_{t|t-1} &= \exp(c\hat{z}_{t|t-1} + d)\Delta \\
Q_{t|t}^{-1} &= Q_{t|t-1}^{-1} + c^\top diag(\hat{\boldsymbol{y}}_{t|t-1})c \\
\hat{z}_{t|t} &= \hat{z}_{t|t-1} + Q_{t|t}\boldsymbol{c}^\top(\boldsymbol{y}_t - \hat{\boldsymbol{y}}_{t|t-1})
\end{aligned}$$

where $Q_{t|t} = \mathrm{Var}[\hat{z}_{t|t}]$ denotes the filtered state variance. Furthermore, we computed the Z-score with respect to the pre-stimulus baseline: Z-score $= \frac{\hat{z}_t - \text{mean of } z_{\text{baseline}}}{\text{SD of } z_{\text{baseline}}}$ and converted it to probability:

$$P(\text{Z-score} > \theta_0) = 1 - \int_{-\infty}^{\theta_0} \frac{1}{\sqrt{2\pi}} e^{\frac{-u^2}{2}} du \tag{3}$$

The criterion of Z-score change was determined by a statistical threshold θ_0 depending on the significance level. We used $\theta_0 = 1.65$, which is associated with a P-value of 0.05. Finally, we identified the onset of pain signal when the Z-score crossed the significance threshold (Chen et al., 2017).

LFP-Based Classification of Spontaneous Pain-Like Events

For each spontaneous pain-like episode, we constructed a window of $[-5, 5]$ s centered around the behavior onset. Based on the simultaneous LFP recordings from the rat ACC and S1, we computed the LFP power features at five different frequency bands: theta (4–8 Hz), alpha (8–12 Hz), beta (13–30 Hz), lower gamma (30–50 Hz), high gamma (50–80 Hz), for both pre-behavior ($[-5, 0]$ s) and post-behavior ($[0, 5]$ s) periods separately. In total, we used $5 \times 2 \times 2 = 20$ power features. Each power feature was preprocessed with zero mean and unit variance. At each recording session, we also selected the pain-free control baseline prior to the first pain stimulus presentation. In total, we constructed 252 spontaneous pain episodes (positive examples) and 252 negative control examples for training and testing (rats #12-15, $n = 10$ sessions).

We trained these features with a two-class support vector machine (SVM) classifier (Scholkopf and Smola, 2001). The SVM is a discriminative supervised learning model that constructs the classification boundary by a separating hyperplane with maximum margin. Specifically, the SVM maps the input $\boldsymbol{x}$ into a high-dimensional feature space and maximizes the margin from the hyperplane to the origin. The nonlinear decision function can be written as follows

$$y(\boldsymbol{x}_i) = \sum_{i=1}^{n} \alpha_i K(\boldsymbol{x}, \boldsymbol{x}_i) + b$$

where $y_i \in \{-1, +1\}$ denote the class label for the training sample $\boldsymbol{x}_i$ (some of which associated with nonzero α_i are called support vectors), b denotes the bias, and $K(\cdot, \cdot)$ denotes the kernel function. We used a polynomial kernel and trained the nonlinear SVM with a sequential minimal optimization algorithm (MATLAB Machine Learning Toolbox: "`fitcsvm`" function). The decoding accuracy was assessed by 5-fold cross-validation. The chance level of classification accuracy is 50%. We also assessed the sensitivity and specificity of SVM classifier by reporting the AUROC (area under the curve of receiver operating characteristic). The chance level of AUROC is 0.5 (Zhang et al., 2017; Dale et al., 2018).

We have tested both linear and Gaussian kernels in SVM. The nonlinear SVM produced a slightly better classification accuracy, but the feature weights derived from the linear SVM would yield informative assessment or interpretation of each feature.

Statistical Tests

We conducted a paired or unpaired t-test provided that the data normality was satisfied; otherwise, we used a nonparametric signed-rank test or rank-sum test.

RESULTS

Frequency of Spontaneous Pain-Like Behaviors

In animal studies, pain cannot be measured directly; therefore, pain can only be inferred from stereotyped "pain-like" behaviors (Deuis et al., 2017). Evoked pain episodes are uniquely associated with the noxious stimulus presentation and quantitative pain behaviors (e.g., paw withdrawal or lifting) (Cheppudira, 2006); whereas spontaneous pain-like behaviors often involve frequent aberrant movement such as flinching, shaking, paw lifting and paw licking (Kawasaki et al., 2012; Whittaker and Howarth, 2014; Murai et al., 2016).

When splitting the time of each recording session in half, the total spontaneous pain-like behaviors occurred in a similar frequency (per minute) in time during the course of a recording session (**Figure 1C**). As a control, we also examined naive rats (rats #1–5) in a completely pain-free condition (Day 1, without presenting any noxious stimulus) based on the same behavior criterion. The number of identified spontaneous pain-like behaviors was zero in the control condition.

In addition, we computed the number and latency statistics of identified spontaneous pain-like events. The median number of spontaneous pain-like events between two evoked pain episodes was 1 (min: 0; max: 5); and the median latency from the previous evoked pain episode was 26.9 s (min: 5.1 s; max: 4.5 min).

ERPs During Evoked and Spontaneous Pain-Like Behaviors

During evoked pain episodes ($[0, 5]$ s from the stimulus onset 0), ERPs occurred either in the ACC or S1 separately, or in both regions simultaneously; in the latter case, their ERP latencies differed (**Figure 2A**). The mean ± SEM latency from the ERP peak amplitude to the laser stimulus onset was 0.875 ± 0.050 s in the ACC and 0.640 ± 0.038 s in the S1 (**Figure 2H**, $p = 0.0002$, rank-sum test). During spontaneous pain-like episodes ($[-5, 5]$ s centered around the behavior onset), ERPs did not always occur

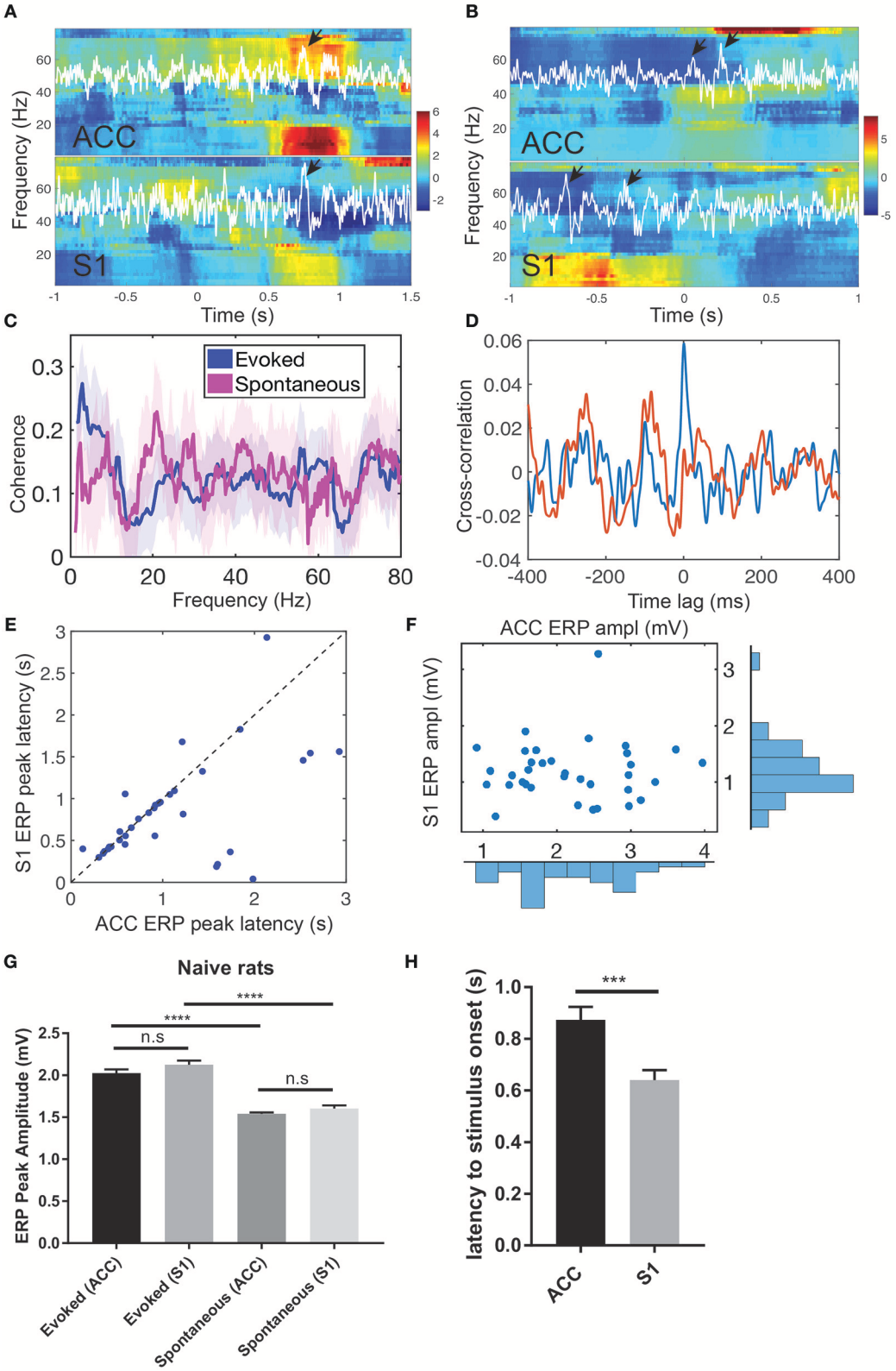


FIGURE 2 | Pain-induced ERPs of the rat ACC and S1. **(A)** Simultaneous recordings of LFPs from the ACC and S1 induced by evoked pain and their Z-scored spectrograms. White LFP traces were the dominant principal component extracted from multi-channel LFP signals. Arrows indicate the identified ERPs. Time 0

(Continued)

FIGURE 2 | indicates the stimulus onset. **(B)** Simultaneous recordings of LFPs from the ACC and S1 induced by spontaneous pain and their Z-scored spectrograms. Arrows indicate the identified ERPs. Using the ACC LFP as a reference, time 0 indicates the onset of identified ERP in the ACC. **(C)** LFP coherence between the ACC and S1 during evoked pain (red) and spontaneous pain-like (blue) episodes. Shaded area denotes the confidence intervals. **(D)** Cross-correlation between the band-pass filtered LFP (4–80 Hz) ACC and S1 from two representative single trials during evoked pain episodes (rat #15). Note that the red trial had a peak at the zero lag, whereas the blue trial showed rhythmic activity at a theta cycle (∼200 ms). **(E)** Latency of ERP peak to the stimulus onset in evoked pain: ACC vs. S1 ($n = 40$ trials). **(F)** Peak-to-trough amplitude of ACC vs. S1 ERP in evoked pain. **(G)** Comparison of ACC and ERP peak amplitudes between evoked and spontaneous pain in naive rats. n.s., nonsignificant; $^{****}p < 0.0001$, unpaired t-test. **(H)** The latency from the ACC and S1 ERP peak amplitude to the laser stimulus onset during evoked pain (rats #12–15). Error bar shows SEM. $^{***}p < 0.001$, unpaired t-test.

synchronously (**Figure 2B** and **Figure S1**; ratio: 367/638 in ACC and 367/497 in S1), and they occurred more frequently in the ACC than in the S1 (63.8 ± 8.36 per session and a total of 638 within 10 sessions in ACC; 49.7 ± 8.17 per session and a total of 497 within 10 sessions in **Figures S1C,D**). In the spectrogram, pain-evoked ERPs were accompanied with an increased theta band (4-8 Hz) power—known as the theta-ERS (**Figures 2A,B**). The ERS was also visible in the gamma band (30–80 Hz). The gamma-ERS was mostly separated in the slow (30–50 Hz) and fast (>50 Hz) gamma bands.

During spontaneous pain-like episodes, ERPs tended not to occur together in the ACC and S1, and the gamma-ERS was more pronounced in the S1. In either of the two regions, we often observed the theta-ERS followed by the gamma-ERS (**Figure 2B** and **Figures S1A,B,E,F**). At the trial-average level, there was enhanced coherence in the theta band between the ACC and S1 during evoked pain episodes (**Figure 2C**), but not in spontaneous pain-like episodes (peak coherence evoked: 0.26 ± 0.08 vs. mean coherence spontaneous: 0.13 ± 0.08).

During evoked pain episodes, the cross-correlation of LFPs between the ACC and S1 varied between single trials—for instance, having a high peak at zero time lag in one trial, or having a rhythmic theta cycle in another trial (e.g., see **Figure 2D**). When ERPs occurred simultaneously in both the ACC and S1 regions, the S1 had shorter ERP latencies to the stimulus onset than the ACC (**Figure 2E**; $p = 0.0113$, paired t-test, rat #12), but had comparable ERP amplitudes (**Figure 2F**; $p > 0.05$, paired t-test). See **Figure S2** for population statistics. As pain behavior was characterized by the paw withdrawal latency (to the stimulus onset at time 0), we correlated the paw withdrawal latency with the evoked ERP latency (**Figure S3A**) and the ERP amplitude (**Figure S3B**), respectively. We found strong positive (or negative) correlations ($p < 10^{-4}$) between the paw withdrawal latency and ERP latency (or amplitude).

Furthermore, we compared the ERP peak amplitude between evoked pain and spontaneous pain-like episodes (**Figure 2G**). There was no statistical difference in evoked ERP amplitude between the ACC and S1 ($p > 0.05$, unpaired t-test). However, the ERP amplitude was significantly greater in evoked pain than spontaneous pain-like episodes, in both the ACC and S1 ($p < 0.0001$).

During spontaneous pain-like episodes, when ERPs occurred together (within a window of ±3 s) in two areas, the S1-ERP tended to appear earlier than the ACC-ERP. The averaged lag was 0.080 ± 0.054 s ($n = 367$, rats #12–15), which shared a similar latency trend as in evoked pain.

Put together, these results suggest that pain-induced ERPs correlate well with pain-like behaviors and can serve as a neural signature readout of evoked pain and spontaneous pain-like episodes. During evoked pain episodes, the ERPs in the ACC and S1 were comparable in latency and amplitude; whereas during spontaneous pain-like episodes, ERPs did not always appear together in the ACC and S1, and appeared more frequently in the ACC.

Phase-Amplitude Coupling

Phase-amplitude coupling (PAC) is useful to characterize nonlinear interactions between two different frequency oscillations (Canolty and Knight, 2010; Tort et al., 2010). Specifically, phase (theta) and amplitude (gamma) coupling has been reported in rat EEG recordings during acute pain experiments (Wang et al., 2011). We extended this analysis to the rat LFP recordings in ACC and S1 areas (**Figure 3A**). We found significant PAC in both ACC and S1 areas, and the strength of coupling was stronger in evoked pain than spontaneous pain-like episodes (**Table 2** and **Figures 3B,C**). In addition, the gamma power showed a significant increase from baseline to evoked pain in both areas; however, during spontaneous pain-like episodes, there was an increase of gamma power in the S1, but not in the ACC (**Figures 3B,C**). This finding supports the notion that the S1 gamma-ERS is indicative of pain perception. In addition, the strength of PAC coupling was different between the ACC and S1, and varied between sub-gamma bands (**Figure S4**). The preferred phases of the ACC and S1 might differ between evoked pain and spontaneous pain-like episodes (**Figure S5A**), whereas the ACC and S1 also had different preferred theta phases (**Figure S5B**).

These PAC results were consistent across all rats (**Figures 3D,E** and **Table 2**). Overall, the strength of PAC in evoked pain was stronger than in baseline ($p = 0.0013$, paired signed-rank test; **Figure 3D**), and showed an increasing trend compared to spontaneous pain-like episodes ($p = 0.079$, **Figure 3E**). Combining all tested rats, we found a stronger coupling strength in the S1 than ACC, during both evoked pain ($p = 0.058$, paired signed-rank test) and spontaneous pain-like episodes ($p = 0.017$; **Figure 3F**).

LFP Power

We computed the trial-averaged LFP power at the theta (4–8 Hz), alpha (8–12 Hz), beta (13–30 Hz), low-gamma (30–50 Hz) and high-gamma (50–80 Hz) frequency bands. There was an increase in high-gamma power from baseline ($[-5, 0]$ s) to evoked pain ($[0, 5]$ s, with 0 being the stimulus onset) in both the ACC and S1 (**Figures 4A,B**). During spontaneous pain-like episodes, we extracted the LFP signals within a window of $[-5, 5]$ s centered

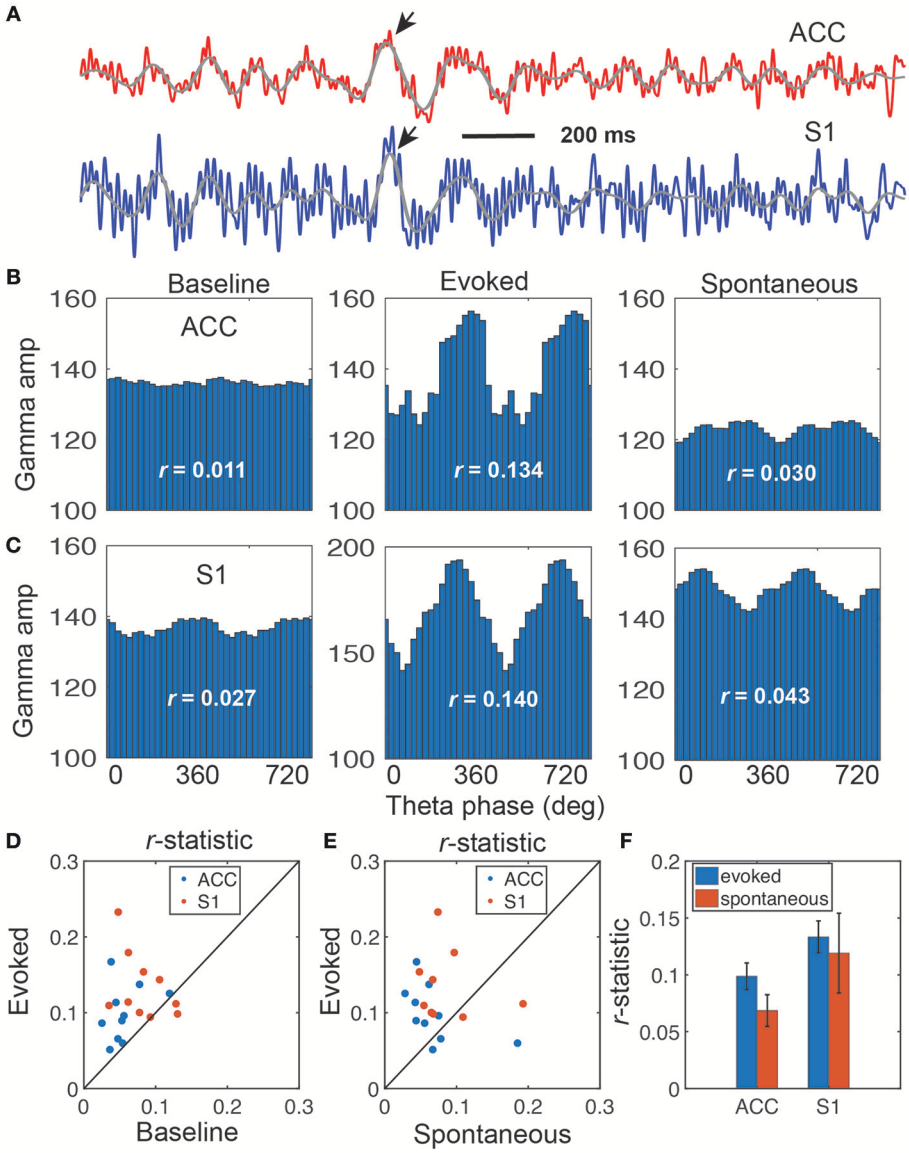


FIGURE 3 | Illustration of coupling between the theta phase and gamma amplitude. **(A)** Representative LFP traces from the rat ACC (red) and S1 (blue), which shows strong coupling between the theta phase and gamma amplitude (rat #15). Two arrows indicate the identified ERPs, and two overlaid gray traces indicate the bandpass filtered (4–11 Hz) LFP traces. **(B,C)** Coupling of gamma amplitude and theta phase (0–720°) in the ACC **(B)** and S1 **(C)**: baseline (left), evoked pain (middle), and spontaneous pain (right). In each panel, the *r*-statistic is shown. **(D)** Scatter plot comparison of *r*-statistic (red: ACC, blue: S1) between evoked pain and baseline ($n = 10$ sessions, rats #12–15). Paired signed-rank test, $p = 0.0013$. **(E)** Scatter plot comparison of *r*-statistic (red: ACC, blue: S1) between evoked pain and spontaneous pain-like episodes ($n = 10$ sessions). Paired signed-rank test, $p = 0.079$. **(F)** Comparison of *r*-statistic in the S1 and ACC. Error bar denotes SEM ($n = 10$ sessions).

around the event onset, and found a reduction in alpha and beta power for both regions. In contrast, gamma power reduced in the ACC but increased in the S1 during spontaneous pain-like episodes (**Figure 4C**).

Spike-LFP Modulation

We further investigated the relationship between the pain-modulated ACC or S1 unit activity and the LFP amplitude. To do so, we varied the intensity of noxious stimulation across trials to produce a wider range of firing rate changes.

We observed a sharp change in the ERP peak-aligned ACC or S1 neuronal spike activity (**Figures 5A,G**), and this abrupt change became less pronounced when neuronal spike trains were aligned with the stimulus onset (**Figure S6**). Notably, these pain-modulated units showed a sharp reduction in firing rates around the ERP peaks. A close examination of the unit's PSTH revealed striking theta oscillations in spike activity (**Figures S7A–C**).

TABLE 2 | Results of phase-amplitude coupling for the *r*-statistic (95% confidence intervals shown in bracket, and the greatest values in each region are shown in bold font).

Rat	ACC			S1		
	Baseline	Evoked	Spontaneous	Baseline	Evoked	Spontaneous
#12	0.030 [0.026, 0.053]	0.084 [0.072, 0.101]	0.056 [0.047, 0.073]	0.028 [0.023, 0.050]	0.154 [0.127, 0.175]	0.075 [0.060, 0.093]
#13	0.053 [0.041, 0.077]	0.105 [0.091, 0.132]	0.031 [0.025, 0.044]	0.072 [0.060, 0.099]	0.108 [0.103, 0.134]	0.069 [0.058, 0.085]
#14	0.042 [0.030, 0.061]	0.064 [0.052, 0.083]	0.050 [0.043, 0.064]	0.057 [0.046, 0.073]	0.083 [0.075, 0.101]	0.065 [0.051, 0.081]
#15	0.052 [0.045, 0.081]	0.113 [0.088, 0.145]	0.076 [0.060, 0.096]	0.069 [0.053, 0.102]	0.138 [0.116, 0.176]	0.110 [0.092, 0.154]

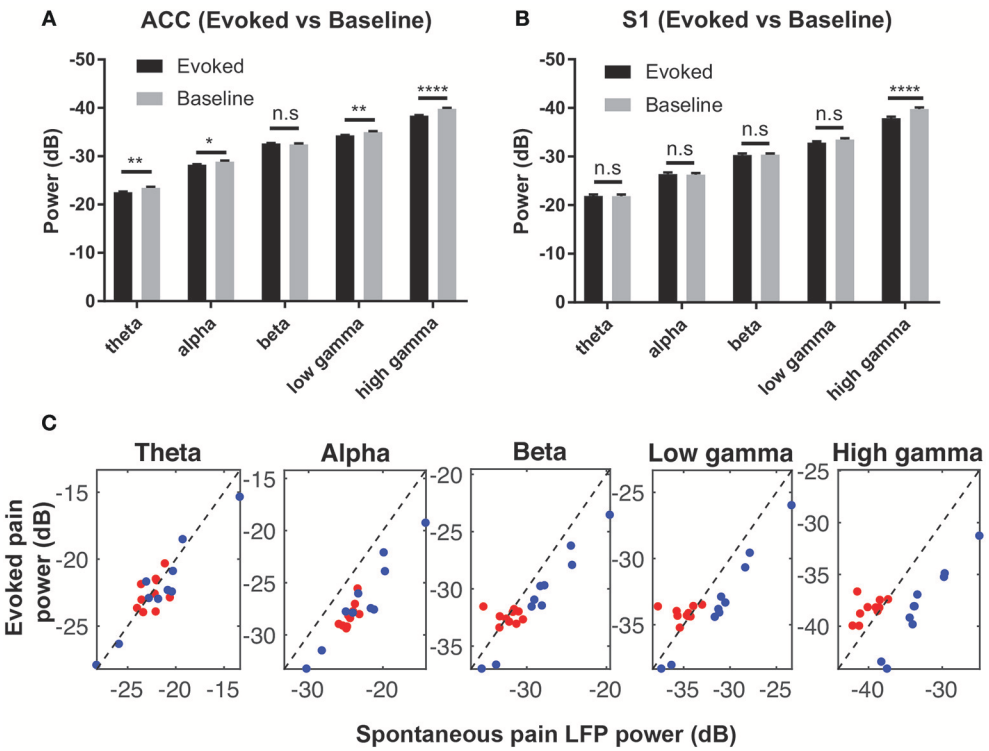


FIGURE 4 | (A) Comparison of the mean LFP power between evoked pain and baseline at various frequency bands in the ACC **(A)** and S1 **(B)** (rats #12–15, $n = 232$ trials). Note that the y-axis shows the negative value in dB. $^{*}p < 0.05$; $^{**}p < 0.01$, $^{****}p < 0.0001$, paired *t*-test. **(C)** Mean LFP power comparison between the evoked and spontaneous pain-like episodes (ACC: red; S1: blue; rats #12–15, $n = 10$ sessions).

During evoked pain episodes, we also observed enhanced trial-averaged SFC in the theta frequency band (**Figure 5B**; see **Figure S7D** for a single-trial analysis). Meanwhile, the SFC also varied between the evoked and spontaneous pain conditions (**Figures 5B** vs. **5E**; **Figures 5H** vs. **5K**). In addition, these pain-modulated ACC or S1 units showed a strong correlation with the evoked ERP amplitude, regardless of their response properties (**Figures 5C,I**).

During spontaneous pain-like episodes, pain-modulated ACC and S1 units showed reduced firing rate modulations (**Figures 5D,J**) and reduced modulations in relation to the ERP amplitudes (**Figures 5F,L**). However, the rhythmic theta spiking was still preserved (**Figures S7E–H**). Overall, the Z-score firing rates of pain-modulated ACC and S1 units and their modulation degree to ERP amplitudes were greater in evoked pain than spontaneous pain-like episodes (**Figures 5M,N**).

Detection of Evoked Pain and Spontaneous Pain-Like Events

During stimulus-evoked pain episodes, the spike activities of pain-modulated ACC and S1 units were temporally coordinated (by increasing or decreasing firing rates synchronously) to signal the pain onset (**Figure 6A**). Using an unsupervised population decoding algorithm (Methods), we identified the onset of evoked pain signals based on the ACC and S1 ensemble spike activity in single trials (**Figure 6B**). Among those successfully detected trials, the onset of detected acute pain signals matched or correlated closely with the ERP peak latency (**Figure 6C**, success ratio: 24/32 trials in session 3 from rat #15). In contrast, the change level in neuronal population spiking during spontaneous pain-like events was consistently lower, and the ERP peak amplitude was also

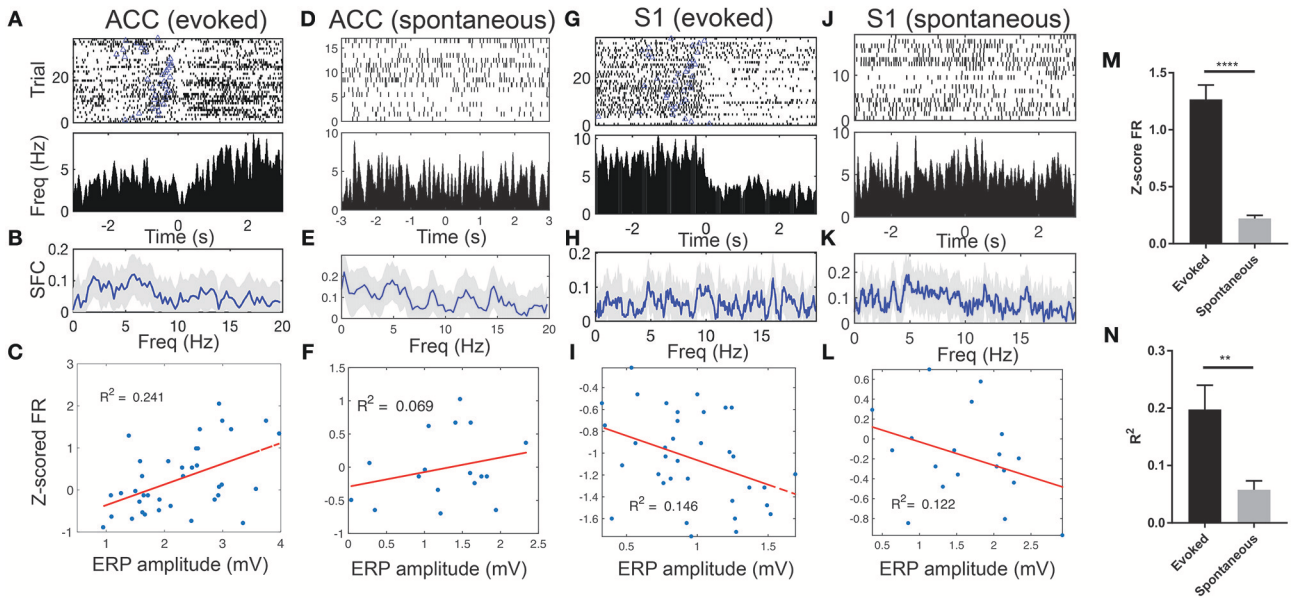


FIGURE 5 | Spike phase locking of one representative ACC units and one representative S1 unit simultaneously recorded during evoked pain and spontaneous pain-like episodes (rat #15). **(A)** Spike raster and ERP-triggered peri-stimulus time histogram (PSTH). Bin size: 10 ms. Time 0 represents the peak of ERP. Blue triangle at each row indicates the onset of laser stimulation at each trial. Note that these two units decreased their firing rates around time 0. **(B)** Spike-field coherence (SFC). Shaded areas denote the jackknife error bar. Note that there was a peak in the theta frequency band. **(C)** Correlation between the Z-scored firing rate (FR) of pain-modulated units and the ERP peak-to-trough amplitude ($p = 0.002$, Pearson's correlation). **(D–F)** Similar to **A–C**, the same ACC unit during spontaneous pain-like episodes. **(G–L)** Similar to **A–F**, except for the S1 unit. In panels **F,I,L**, the *P*-values of Pearson's correlation are 0.307, 0.023, and 0.142, respectively. **(M)** Population statistics of Z-scored mean FR (in absolute value) of pain-modulated ACC and S1 units ($n = 32$) during evoked pain and spontaneous pain-like episodes. **(N)** Population statistics of R^2 values (for regressing the Z-scored FR and the ERP amplitude). $^{**}p < 0.01$, $^{****}p < 0.0001$, unpaired *t*-test.

considerably smaller (**Figure 2G**). Together, this posed a greater challenge for detecting the onset of spontaneous pain signals (**Figures 6D,E**).

To distinguish spontaneous pain-like episodes from pain-free negative control, we further trained a SVM classifier (Methods) using the combined LFP power features from the ACC and S1. Using 5-fold cross-validation on a total of 252 spontaneous pain episodes (rats #12–15, 10 sessions), we obtained a mean classification accuracy of 75% and an AUROC (area under the curve of receiver operating characteristic) of 0.85 (**Figure 6F**). By assessing the contribution of individual LFP power features, we found that the low-gamma and high-gamma power features from both the ACC and S1 were associated with more significant weights (**Figure S8**).

DISCUSSION

To date, most human or animal pain research has focused on stimulus-evoked pain, whereas spontaneous pain has not been fully investigated (Baliki et al., 2007; Bennett, 2012). In neuropathic pain, spontaneous pain is thought to emerge as a consequence of ectopic activity in axons in the injured nerve's action potentials arising spontaneously from hyper excitable membranes; but it remains unclear whether the source of this activity originates in injured neurons or in neighboring intact ones, and in nociceptors or non-nociceptors (Djouhri et al., 2006; Woolf , 2010). In contrast to human pain research (He et al., 2017), the lack of self-report has created a great obstacle for studying spontaneous pain in animal models (Tappe-Theodor and Kuner, 2014). A strong limitation and potential critique of our study is the subjective criterion for identifying spontaneous pain-like events. Although pain is usually inferred from stereotyped pain-like behaviors, other experimental techniques (such as spinal cord post-stimulation and nociceptive recording) can be used to help identify or confirm pain experiences. In the future, integrating behavioral with physiological measures may further help refine pain assessment for rodents (Whittaker and Howarth, 2014; Mouraux and Iannetti, 2018).

Simultaneous recordings of neuronal spikes and LFPs from multiple cortical areas provide a good opportunity to study differential neural mechanisms of evoked and spontaneous pain. In contrast to scalp or intracranial EEG signals, intracortical LFPs provide a more accurate readout from local microcircuits related to pain processing (Wang et al., 2015; Harris and Peng, 2016). Specifically, cortical ERP is a phase-locked signal generated by neuronal networks in relation to an externally or internally generated, yet behaviorally significant event. During evoked or spontaneous pain, ERPs are primarily contributed by the postsynaptic potentials of a large population of simultaneously active pyramidal cells with the same or similar orientation (Bressler, 2002). Our results show that ERPs from the ACC and S1 tend to synchronize during evoked pain episodes, but are highly variable during spontaneous pain-like episodes. While the ERP amplitudes are comparable between the ACC and S1, their amplitudes is greater during

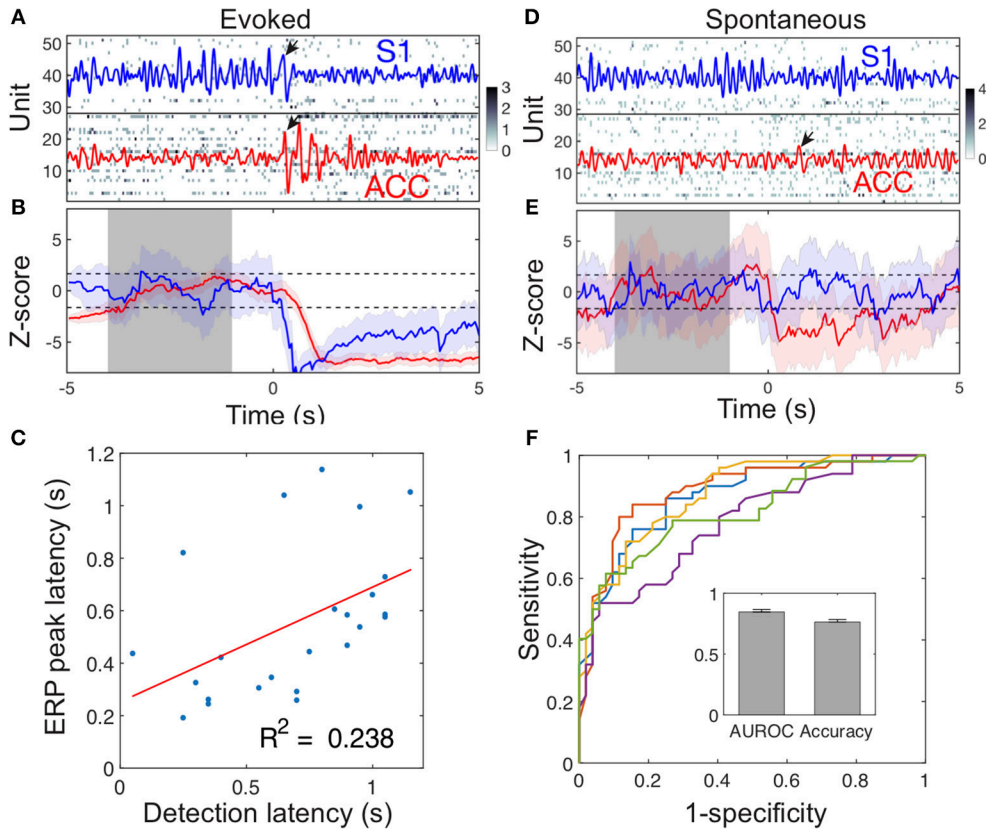


FIGURE 6 | Illustration of detecting acute and spontaneous pain-like events. **(A)** The simultaneous ACC and S1 ensemble spike activity during a laser-evoked pain episode. Dark pixel represents high spike count. Time 0 denotes the onset of 250 mW laser stimulation. The ACC (red) and S1 (blue) LFPs were overlaid in the spike raster. Pain-induced ERPs are marked by arrows. In this example, the S1 ERP peak occurred 30 ms earlier than the ACC ERP peak. **(B)** The evoked pain event was detected based on our previously developed algorithm (Methods). Shaded periods of [−4, −1] s denote the baseline for computing the Z-score (ACC: red; S1: blue). When the upper or lower confidence interval of the Z-score was below or above the significance threshold (horizontal dash lines), the onset of pain signal was detected as a change point. In this example, the detected acute pain onset in the S1 was earlier than the onset in the ACC, whereas the S1 ERP peak latency was also earlier than the ACC ERP peak latency. **(C)** During evoked pain episodes, the ensemble spike-based acute pain detection latency to the stimulus onset positively correlated with the ERP peak latency ($n = 24$ trials; $p = 0.0156$, Pearson's correlation). **(D,E)** Similar to respective panels **A,B**, except for a spontaneous pain-like episode. Time 0 denotes the onset of paw withdrawal. **(F)** Receiver operating characteristic (ROC) curves of 5-fold cross-validated SVM classification for spontaneous pain. The AUROC and accuracy statistics (mean ± SEM) are shown in the inset.

evoked pain than during spontaneous condition. In the frequency domain, the pain-evoked ERPs are directly linked to the low-frequency cortical oscillations (LeBlanc et al., 2014, 2017; Taesler and Rose, 2016; Peng et al., 2018). The theta-ERS has been demonstrated during evoked pain and spontaneous pain-like episodes, in either the ACC or S1, or both. Increased theta oscillations are possibly due to thalamic dysfunction or a decreased inhibition of the thalamus that affects pain processing (Stern et al., 2006). Previous studies have shown that increased theta power may represent a biomarker of chronic neuropathic pain (Pinheiro et al., 2016; Ploner et al., 2017).

The ACC and S1 are the two most important cortical regions related to pain processing. Neuroimaging studies in mice have shown that intra-regional remodeling within the S1 accelerates chronic pain behaviors by modulating the activity of ACC units (Eto et al., 2011). Specifically, the ACC displays cross-frequency coupling and spike-phase locking during pain perception in rats (Wang et al., 2011, 2015). Recent findings in rodent studies from our lab and others have suggested that ACC units are necessary for the "aversiveness" of pain (Johansen et al., 2001; Zhang et al., 2017). In addition, we have demonstrated that pairing auditory tones with repeated noxious stimulation can teach ACC neurons to produce a pain anticipation signal (Urien et al., 2018). Our rat LFP results of the ACC further support these previous findings that the ACC is a key component of an internal aversive network for both evoked and spontaneous pain. On the other hand, gamma oscillations in the human S1 have been shown to correlate with pain perception (Gross et al., 2007; Zhang et al., 2012; Tu et al., 2016), but these studies are limited to evoked pain. In the absence of overt noxious stimuli as in spontaneous pain episodes, the S1 may be involved in both the perception and modulation of various somatosensory sensations (Bushnell

et al., 1999; Vierck et al., 2013). A rat S1 lesion study has implied a significant role of the S1 in pain affect without direct somatosensory processing, challenging the traditional view on the role of S1 in processing the sensory-discriminatory aspect of pain (Uhelski et al., 2012). Our rat S1 results during spontaneous pain-like episodes seem to support the lesion study. Nevertheless, a causal investigation (e.g., optogenetic S1 inactivation) is still required to fully dissect the role of the S1 in spontaneous pain perception. In some identified spontaneous pain-like episodes, we only observed ERPs in the ACC but not in the S1; this could be due to the fact that top-down input or anticipation was the primary driving force. However, further experimental investigation is required to distinguish between "spontaneous pain" and "pain anticipation."

The functional state of cortical circuits may be defined by the amplitude and phase of ongoing frequency-specific oscillations of neuronal populations. LFP-based cross-frequency coupling measures nonlinear functional interactions between neural oscillations at different frequencies (Canolty and Knight, 2010; Tort et al., 2010). Complementary to amplitude-amplitude coupling (i.e., coherence), PAC may provide plausible physiological mechanisms on functional interactions—low-frequency phase reflects the local neuronal excitability, and high-frequency amplitude reflects the change in population synaptic activity or selective activation of a subnetwork in the microcircuit. To date, human pain studies have shown LFP cross-frequency coupling between the low-frequency phase (theta or alpha) and the gamma amplitude in the amygdala and hippocampus (Liu et al., 2015)—both regions are associated with pain and negative moods as a continuum of aversive behavioral learning (Baliki and Apkarian, 2015). Source-localized human EEG recordings have also shown theta phase-gamma amplitude coupling in the dorsal and subgenus ACC (Vanneste et al., 2018). One plausible interpretation of these findings is that theta oscillations reflect negative symptoms, and gamma oscillations obversely reflect positive symptoms. Theta oscillations may act as a traveling wave, communicating information across a large-scale network responsible for declarative or emotional memories (Zhang and Jacobs, 2015). On the other hand, gamma oscillations modulate long-range communication between distributed neuronal assemblies, which may subserve a wide range of cognitive functions including multi-sensory integration (Fries, 2009). Gamma oscillations can be nested on the theta wave for information transmission. While gamma oscillations may correlate with pain perception (Gross et al., 2007; Ploner et al., 2017), the high gamma activity can have a broader role in sensory processing. In addition, mechanisms of gamma sub-bands may have different origins, depending on differential distribution of cell types and cortical layers that receive thalamic or cortical input (Buzsaki and Wang, 2012). Our results have indeed showed that the strengths of PAC coupling vary across different gamma bands for the ACC and S1. A speculative neural coding role of PAC coupling is to segregate sensory (pain) responses into specific temporal windows within different cortical regions. However, circuit mechanisms of pain-associated slow and fast gamma oscillations are still incompletely understood.

Detection and identification of subjective pain signals for humans or animals has been an active research topic (Brown et al., 2011; Huang et al., 2013; Vijayakumar et al., 2017). While this problem has been well studied for evoked pain events in freely behaving rats (Chen et al., 2017; Hu et al., 2018; Xiao et al., 2018; Zhang et al., 2018), the challenge for detecting spontaneous pain events still remains. Our supervised learning results suggest that LFP power features from multiple brain regions may help detect spontaneous pain-like events (**Figure 6**). The future decoding strategy is to consider integrating the information from multi-regional LFP and ensemble spike activity to detect pain signals.

The results derived from our rodent study have important clinical implications. First, the ERP and LFP phenomena observed at the ACC and S1 circuit levels may be examined from human high-density EEG recordings combined with advanced source localization techniques. This would further allow us to investigate both evoked and spontaneous pain episodes in human subjects. Second, our algorithmic development and investigation on pain decoding also provide insight into detecting evoked and spontaneous pain events based on human EEG recordings (Huang et al., 2013).

In conclusion, our report has revealed differential coding roles between the S1 and ACC in pain processing, as well as point to distinct neural mechanisms between evoked pain and putative spontaneous pain at both LFP and cellular levels. These findings may suggest important circuit mechanisms that induce distinct pain perception or behaviors.

DATA AVAILABILITY

All datasets generated for this study are available upon the request of corresponding authors. Software is publicly available at http://www.cn3lab.org/software.html.

ETHICS STATEMENT

All experimental studies were performed in accordance with the National Institutes of Health (NIH) Guide for the Care and Use of Laboratory Animals to ensure minimal animal use and discomfort, and were approved by the New York University School of Medicine (NYUSOM) Institutional Animal Care and Use Committee (IACUC).

AUTHOR CONTRIBUTIONS

ZC and JW designed the research. ZX, EM, QZ, DR, and HZ collected the data. ZX, EM, PK, DR, RT, and LS analyzed the behavioral data. ZX and QH analyzed the neurophysiological data. ZC wrote the paper with contributing input from all other authors.

FUNDING

The work was supported by the NSF-NCS grant CBET-1835000 (ZC and JW), NIH grants R01-NS100065 (ZC and JW), R01-MH118928 (ZC) and R01-GM115384 (JW). DR was supported by the Irene and Eric Simon (IES) Brain Research Foundation Summer Rolf Weil Fellowship. HZ was supported by the China Scholarship Council (201606370208). The work was supported by the China's National Science Foundation No. 31627802 and Fundamental Research Funds for the Central Universities (ZX).

SUPPLEMENTARY MATERIAL

The Supplementary Material for this article can be found online at: https://www.frontiersin.org/articles/10.3389/fncel.2019.00165/full#supplementary-material

REFERENCES

Baliki, M. N., and Apkarian, A. V. (2015). Nociception, pain, negative moods, and behavior selection. *Neuron* 87, 474–491. doi: 10.1016/j.neuron.2015.06.005

Baliki, M. N., Geha, P. Y., and Apkarian, A. V. (2007). Spontaneous pain and brain activity in neuropathic pain: functional MRI and pharmacologic functional MRI studies. *Curr Pain Headache Rep.* 11, 171–177. doi: 10.1007/s11916-007-0187-3

Barrot, M. (2012). Tests and models of nociception and pain in rodents. *Neuroscience* 211, 39–50. doi: 10.1016/j.neuroscience.2011.12.041

Bennett, G. J. (2012). What is spontaneous pain and who has it? *J. Pain* 13, 921–929. doi: 10.1016/j.jpain.2012.05.008

Bressler, S. L. (2002). "Event-related potentials," in *The Handbook of Brain Theory and Neural Networks*, ed M. A. Arbib (Cambridge, MA: MIT Press), 412–415.

Brown, J. E., Chatterjee, N., Younger, J., and Mackey S. (2011). Towards a physiology-based measure of pain: patterns of human brain activity distinguish painful from non-painful thermal stimulation. *PLoS ONE* 6:e24124. doi: 10.1371/journal.pone.0024124

Bushnell, M. C., Ceko, M., and Low, L. A. (2013). Cognitive and emotional control of pain and its disruption in chronic pain. *Nat. Rev. Neurosci.* 14, 502–511. doi: 10.1038/nrn3516

Bushnell, M. C., Duncan, G. H., Hofbauer, R. K., Ha, B., Chen, J. I., and Carrier, B. (1999). Pain perception: is there a role for primary somatosensory cortex? *Proc. Natl. Acad. Sci. U.S.A.* 96, 7705–7709. doi: 10.1073/pnas.96.14.7705

Buzsaki, G., and Wang, X. J. (2012). Mechanisms of gamma oscillations. *Annu. Rev. Neurosci.* 35, 203–225. doi: 10.1146/annurev-neuro-062111-150444

Canolty, R. T., and Knight, R. T. (2010). The functional role of cross-frequency coupling. *Trends Cog. Sci.* 14, 506–515. doi: 10.1016/j.tics.2010.09.001

Chen, Z., Zhang, Q., Tong, A. P. S., Mander, T. R., and Wang, J. (2017). Deciphering neuronal population codes for acute thermal pain. *J. Neural Engr.* 14:036023. doi: 10.1088/1741-2552/aa644d

Cheppudira, B. P. (2006). Characterization of hind paw licking and lifting to noxious radiant heat in the rat with and without chronic inflammation. *J. Neurosci. Methods* 155, 122–125. doi: 10.1016/j.jneumeth.2006.01.001

Dale, J., Zhou, H., Zhang, Q., Martinez, E., Hu, S., Liu, K., et al. (2018). Scaling up cortical control inhibits pain. *Cell Rep.* 23, 1301–1313. doi: 10.1016/j.celrep.2018.03.139

Davis, K. D., Flor, H., Greely, H. T., Iannetti, G. D., Mackey, S., Ploner, M., et al. (2017). Brain imaging tests for chronic pain: medical, legal and ethical issues and recommendations. *Nat. Rev. Neurol.* 13, 624–638. doi: 10.1038/nrneurol.2017.122

Deuis, J. R., Dvorakova, L. S., and Vetter, I. (2017). Methods used to evaluate pain behaviors in rodents. *Front. Molecular Neurosci.* 10:284. doi: 10.3389/fnmol.2017.00284

Djouhri, L., Koutsikou, S., Fang, X., McMullan, S., and Lawson, S. N. (2006). Spontaneous pain, both neuropathic and inflammatory, is related to frequency of spontaneous firing in intact C-fiber nociceptors. *J. Neurosci.* 26, 1281–1292. doi: 10.1523/JNEUROSCI.3388-05.2006

Eto, K., Wake, H., Watanabe, M., Ishibashi, H., Noda, M., Yanagawa, Y., et al. (2011). Inter-regional contribution of enhanced activity of the primary somatosensory cortex to the anterior cingulate cortex accelerates chronic pain behavior. *J. Neurosci.* 31, 7631–7636. doi: 10.1523/JNEUROSCI.0946-11.2011

Fries, P. (2009). Neuronal gamma-band synchronization as a fundamental process in cortical computation. *Annu. Rev. Neurosci.* 32, 209–224. doi: 10.1146/annurev.neuro.051508.135603

Garcia-Larrea, L., Convers, P., Magin, M., Andre-Obadia, N., Peyron, R., Lauren, B., et al. (2002). Laser-evoked potential abnormalities in central pain patients: the influence of spontaneous and provoked pain. *Brain* 125, 2766–2781. doi: 10.1093/brain/awf275

Gross, J., Schnizler, A., Timmermann, L., and Ploner, M. (2007). Gamma oscillations in human primary somatosensory cortex reflect pain perception. *PLoS Biol.* 5:e133. doi: 10.1371/journal.pbio.0050133

Harris-Bozer, A. L., and Peng, Y. B. (2016). Inflammatory pain by carrageenan recruits low-frequency local field potential changes in the anterior cingulate cortex. *Neurosci. Lett.* 632, 8–14. doi: 10.1016/j.neulet.2016.08.016

He, D., Grant, B., Holden, R. R., and Gilron, I. (2017). Methodology for self-report of rest pain (or spontaneous pain) vs evoked pain in chronic neuropathic conditions: a prospective observational pilot study. *Pain Rep.* 2:e587. doi: 10.1097/PR9.0000000000000587

Hu, S., Zhang, Q., Wang, J., and Chen, Z. (2018). Real-time particle filtering and smoothing algorithms for detecting abrupt changes in neural ensemble spike activity. *J. Neurophysiol.* 149, 1394–1410. doi: 10.1152/jn.00684.2017

Huang, G., Xiao, P., Hung, Y. S., Iannetti, G. D., Zhang, Z. G., and Hu, L. (2013). A novel approach to predict subjective pain perception from single-trial laser-evoked potentials. *Neuroimage* 81, 283–293. doi: 10.1016/j.neuroimage.2013.05.017

Johansen, J. P., Fields, H. L., and Manning, B. H. (2001). The affective component of pain in rodents: direct evidence for a contribution of the anterior cingulate cortex. *Proc. Natl. Acad. Sci. U.S.A.* 98, 8077–8082. doi: 10.1073/pnas.141218998

Kawasaki-Yatsugi, S., Nagakura, Y., Ogino, S., Sekizawa, T., Kiso, T., Takahashi, M., et al. (2012). Automated measurement of spontaneous pain-associated limb movement and drug efficacy evaluation in a rat model of neuropathic pain. *Eur. J. Pain* 16, 1426–1436. doi: 10.1002/j.1532-2149.2012.00142.x

Kramer, M. A., and Eden, U. T. (2013). Assessment of cross-frequency coupling with confidence using generalized linear models. *J. Neurosci. Methods* 220, 64–74. doi: 10.1016/j.jneumeth.2013.08.006

LeBlanc, B. W., Cross, B., Smith, K. A., Roach, C., Xia, J., Chao, Y C., et al. (2017). Thalamic bursts down-regulate cortical theta and nociceptive behavior. *Sci. Rep.* 7, 2482. doi: 10.1038/s41598-017-02753-6

LeBlanc, B. W., Lii, T. R., Silverman, A. E., Alleyne, R. T., and Saab, C. Y. (2014). Cortical theta is increased while thalamocortical coherence is decreased in rat models of acute and chronic pain. *PAIN* 155, 773–782. doi: 10.1016/j.pain.2014.01.013

Liu, C. C., Chien, J. H., Kim, J. H., Chuang, Y. F., Cheng, D. T., Anderson, W. S., et al. (2015). Cross-frequency coupling in deep brain structures upon processing the painful sensory inputs. *Neuroscience* 303, 412–421. doi: 10.1016/j.neuroscience.2015.07.010

Mouraux, A., and Iannetti, G. D. (2018). The search for pain biomarkers in the human brain. *Brain* 141, 3290–3307. doi: 10.1093/brain/awy281

Murai, N., Sekizawa, T., Gotoh, T., Watabiki, T., Takahashi, M., Kakimoto, S., et al. (2016). Spontaneous and evoked pain-associated behaviors in a rat model of neuropathic pain respond differently to drugs with different mechanisms of action. *Pharmacol. Biochem. Behav.* 141, 10–17. doi: 10.1016/j.pbb.2015.11.008

Peng, W., Xia, X., Yi, M., Huang, G., Zhang, Z., Iannetti, G., et al. (2018). Brain oscillations reflecting pain-related behavior in freely moving rats. *PAIN* 159, 106–118. doi: 10.1097/j.pain.0000000000001069

Pinheiro, E. S., de Queiros, F. C., Montoya, P., Santos, C. L., do Nascimento, M. A., Ito C. H., et al. (2016). Electroencephalographic patterns in chronic pain: a systematic review on the literature. *PLoS ONE* 11:e0149085. doi: 10.1371/journal.pone.0149085

Ploner, M., and May, E. S. (2018). Electroencephalography and magnetoencephalography in pain research—current state and future perspectives. *PAIN* 159, 206–211. doi: 10.1097/j.pain.0000000000001087

Ploner, M., Sorg, C., and Gross, J. (2017). Brian rhythms of pain. *Trends Cog. Sci.* 21, 100–110. doi: 10.1016/j.tics.2016.12.001

Scholkopf, B., and Smola, A. J. (2001). *Learning with Kernels: Support Vector Machines, Regularization, Optimization, and Beyond.* Cambridge, MA: MIT Press.

Stern, J., Jeanmonod, D., and Sarnthein, J. (2006). Persistent EEG over activation in the cortical pain matrix of neurogenic pain patients. *Neuroimage* 31, 721–731. doi: 10.1016/j.neuroimage.2005.12.042

Taesler, P., and Rose, M. (2016). Prestimulus theta oscillations and connectivity modulate pain perception. *J. Neurosci.* 36, 5026–5033. doi: 10.1523/JNEUROSCI.3325-15.2016

Tappe-Theodor, A., and Kuner, R. (2014). Studying ongoing and spontaneous pain in rodents–challenges and opportunities. *Eur J Neurosci.* 39, 1881–1890. doi: 10.1111/ejn.12643

Tort, A. B. L., Komorowski, R., Eichenbaum, H., and Kopell, N. (2010). Measuring phase-amplitude coupling between neuronal oscillations of different frequency. *J. Neurophysiol.* 104, 1195–1210. doi: 10.1152/jn.00106.2010

Tu, Y., Zhang, Z., Tan, A., Peng, W., Hung, Y. S., Moayedi, M., et al. (2016). Alpha and gamma oscillation amplitudes synergistically predict the perception of forthcoming nociceptive stimuli. *Hum. Brain Mapp.* 37, 501–514. doi: 10.1002/hbm.23048

Uhelski, M. L., Davis, M. A., and Fuchs, P. N. (2012). Pain affect in the absence of pain sensation: evidence of asomaesthesia after somatosensory cortex lesions in the rat. *PAIN* 153, 885–892. doi: 10.1016/j.pain.2012.01.018

Urien, L., Xiao, Z., Bauer, E. P., Chen, Z., and Wang, J. (2018). Rate and temporal coding mechanisms in the anterior cingulate cortex for pain anticipation. *Sci. Rep.* 8, 8298. doi: 10.1038/s41598-018-26518-x

Vanneste, S., Song, J. J., and De Ridder, D. (2018). Thalamocortical dysrhythmia detected by machine learning. *Nat. Commun.* 9, 1103. doi: 10.1038/s41467-018-02820-0

Vierck, C. J., Whitsel, B. L., Favorov, O. V., Brown, A. W., and Tommerdahl, M. (2013). Role of primary somatosensory cortex in the coding of pain. *PAIN* 154, 334–344. doi: 10.1016/j.pain.2012.10.021

Vijayakumar, V., Case, M., Shirinpour, S., and He, B. (2017). Quantifying and characterizing tonic thermal pain across subjects from EEG data using random forest models. *IEEE Trans. Biomed. Eng.* 64, 2988–2966. doi: 10.1109/TBME.2017.2756870

Wang, J., Cao, B., Yu, T. R., Jelfs, B., Yan, J., Chan, R. H., et al. (2015). Theta-frequency phase-locking of single anterior cingulate cortex neurons and synchronization with the medial thalamus are modulated by visceral noxious stimulation in rats. *Neuroscience* 298, 200–210. doi: 10.1016/j.neuroscience.2015.04.024

Wang, J., Li, D., Li, X., Liu, F. Y., Xing, G. G., Cai, J., et al. (2011). Phase-amplitude coupling between theta and gamma oscillations during nociception in rat electroencephalography. *Neurosci. Lett.* 499, 84–87. doi: 10.1016/j.neulet.2011.05.037

Whittaker, A. L., and Howarth, G. S. (2014). Use of spontaneous behavior measures to assess pain in laboratory rats and mice: how are we progressing? *Appl. Anim. Behav. Sci.* 151, 1–12. doi: 10.1016/j.applanim.2013.11.001

Woolf, C. J. (2010). What is this thing called pain? *J. Clin. Invest.* 120, 3742–3744. doi: 10.1172/JCI45178

Xiao, Z., Hu, S., Zhang, Q., Tian, X., Chen, Y., Wang, J., et al. (2018). Ensembles of change-point detectors: implications for real-time BMI applications. *J. Comput. Neurosci.* 46, 107–124. doi: 10.1007/s10827-018-0694-8

Zhang, H., and Jacobs, J. (2015). Traveling theta waves in the human hippocampus. *J. Neurosci.* 35, 12477–12487. doi: 10.1523/JNEUROSCI.5102-14.2015

Zhang, Q., Mander, T. R., Tong, A. P. S., Yang, R., Garg, A., Martinez, E., et al. (2017). Chronic pain induces generalized enhancement of aversion. *eLife* 6:e25302. doi: 10.7554/eLife.25302

Zhang, Q., Xiao, Z., Huang, C., Hu, S., Kulkarni, P., Martinez, E., et al. (2018). Local field potential decoding of the onset and intensity of acute thermal pain in rats. *Sci. Rep.* 8:8299. doi: 10.1038/s41598-018-26527-w

Zhang, Z. G., Hu, L., Hung, Y. S., Mouraux, A., and Iannetti, G. D. (2012). Gamma-band oscillations in the primary somatosensory cortex—a direct and obligatory correlate of subjective pain intensity. *J. Neurosci.* 32, 7429–7438. doi: 10.1523/JNEUROSCI.5877-11.2012

Zhou, H., Zhang, Q., Martinez, E., Hu, S., Liu, K., Dale, J., et al. (2018). Ketamine reduces hyperactivity of the anterior cingulate cortex to provide enduring relief of chronic pain. *Nat. Commun.* 9:3751. doi: 10.1038/s41467-018-06295-x

Conflict of Interest Statement: The authors declare that the research was conducted in the absence of any commercial or financial relationships that could be construed as a potential conflict of interest.

Copyright © 2019 Xiao, Martinez, Kulkarni, Zhang, Hou, Rosenberg, Talay, Shalot, Zhou, Wang and Chen. This is an open-access article distributed under the terms of the Creative Commons Attribution License (CC BY). The use, distribution or reproduction in other forums is permitted, provided the original author(s) and the copyright owner(s) are credited and that the original publication in this journal is cited, in accordance with accepted academic practice. No use, distribution or reproduction is permitted which does not comply with these terms.

frontiers in Cellular Neuroscience

ORIGINAL RESEARCH
published: 26 April 2019
doi: 10.3389/fncel.2019.00163

Diazepam Accelerates $GABA_AR$ Synaptic Exchange and Alters Intracellular Trafficking

*Joshua M. Lorenz-Guertin[1], Matthew J. Bambino[1], Sabyasachi Das[1], Susan T. Weintraub[2] and Tija C. Jacob[1]**

[1] Department of Pharmacology and Chemical Biology, School of Medicine, University of Pittsburgh, Pittsburgh, PA, United States, [2] Department of Biochemistry and Structural Biology, University of Texas Health Science Center at San Antonio, San Antonio, TX, United States

Despite 50+ years of clinical use as anxiolytics, anti-convulsants, and sedative/hypnotic agents, the mechanisms underlying benzodiazepine (BZD) tolerance are poorly understood. BZDs potentiate the actions of gamma-aminobutyric acid (GABA), the primary inhibitory neurotransmitter in the adult brain, through positive allosteric modulation of γ2 subunit containing GABA type A receptors ($GABA_ARs$). Here we define key molecular events impacting γ2 $GABA_AR$ and the inhibitory synapse gephyrin scaffold following initial sustained BZD exposure *in vitro* and *in vivo*. Using immunofluorescence and biochemical experiments, we found that cultured cortical neurons treated with the classical BZD, diazepam (DZP), presented no substantial change in surface or synaptic levels of γ2-$GABA_ARs$. In contrast, both γ2 and the postsynaptic scaffolding protein gephyrin showed diminished total protein levels following a single DZP treatment *in vitro* and in mouse cortical tissue. We further identified DZP treatment enhanced phosphorylation of gephyrin Ser270 and increased generation of gephyrin cleavage products. Selective immunoprecipitation of γ2 from cultured neurons revealed enhanced ubiquitination of this subunit following DZP exposure. To assess novel trafficking responses induced by DZP, we employed a γ2 subunit containing an N terminal fluorogen-activating peptide (FAP) and pH-sensitive green fluorescent protein ($\gamma2^{pH}FAP$). Live-imaging experiments using $\gamma2^{pH}FAP$ $GABA_AR$ expressing neurons identified enhanced lysosomal targeting of surface $GABA_ARs$ and increased overall accumulation in vesicular compartments in response to DZP. Using fluorescence resonance energy transfer (FRET) measurements between α2 and γ2 subunits within a $GABA_AR$ in neurons, we identified reductions in synaptic clusters of this subpopulation of surface BZD sensitive receptor. Additional time-series experiments revealed the gephyrin regulating kinase ERK was inactivated by DZP at multiple time points. Moreover, we found DZP simultaneously enhanced synaptic exchange of both γ2-$GABA_ARs$ and gephyrin using fluorescence recovery after photobleaching (FRAP) techniques. Finally we provide the first proteomic analysis of the BZD sensitive $GABA_AR$ interactome in DZP vs. vehicle treated mice. Collectively, our results indicate DZP exposure elicits down-regulation of gephyrin scaffolding and BZD sensitive $GABA_AR$ synaptic availability via multiple dynamic trafficking processes.

Keywords: $GABA_AR$, benzodiazepine, trafficking, gephyrin, mass spectrometry, diazepam, inhibitory synapse

OPEN ACCESS

Edited by:
Arianna Maffei,
Stony Brook University, United States

Reviewed by:
Angel L. De Blas,
University of Connecticut, United States
Shiva Tyagarajan,
University of Zurich, Switzerland
Hermann Schindelin,
University of Würzburg, Germany
Vikram Kasaragod,
University of Würzburg, Germany,
in collaboration with reviewer HS

***Correspondence:**
Tija C. Jacob
tcj11@pitt.edu

Specialty section:
This article was submitted to Cellular Neurophysiology, a section of the journal Frontiers in Cellular Neuroscience

Received: *17 January 2019*
Accepted: *08 April 2019*
Published: *26 April 2019*

Citation:
Lorenz-Guertin JM, Bambino MJ, Das S, Weintraub ST and Jacob TC (2019) Diazepam Accelerates $GABA_AR$ Synaptic Exchange and Alters Intracellular Trafficking. Front. Cell. Neurosci. 13:163. doi: 10.3389/fncel.2019.00163

INTRODUCTION

$GABA_ARs$ are ligand-gated ionotropic chloride (Cl^-) channels responsible for the majority of fast inhibitory neurotransmission in the adult CNS. The most prevalent synaptic $GABA_AR$ subtype is composed of two α, two β, and a γ2 subunit forming a heteropentamer (Uusi-Oukari and Korpi, 2010). Benzodiazepines (BZDs) are a widely used clinical sedative-hypnotic drug class that selectively bind between the interface of a $GABA_AR$ γ2 subunit and either an α1/2/3/5 subunit (Vinkers and Olivier, 2012). Receptors containing these α subunits are considered to be primarily synaptic, with the exception of α5, which is localized both synaptically and extrasynaptically (Brady and Jacob, 2015). Positive allosteric modulation by BZD enhances $GABA_AR$ inhibition by increasing the binding affinity of GABA and increasing channel opening frequency (Uusi-Oukari and Korpi, 2010). Recent cryo-electron microscopy publications have provided unprecedented structural and pharmacological information about benzodiazepine-sensitive $GABA_ARs$ and the benzodiazepine binding site (Phulera et al., 2018; Zhu et al., 2018; Laverty et al., 2019; Masiulis et al., 2019) reinvigorating interest in the molecular actions of BZD drugs. It is known that the potentiating effect of BZDs are lost after prolonged or high dose acute exposure (Tietz et al., 1989; Holt et al., 1999), characterized first by a loss of sedative/hypnotic activity followed by the anti-convulsant properties behaviorally (Lister and Nutt, 1986; Wong et al., 1986; File et al., 1988; Bateson, 2002). The induction of BZD tolerance occurs in part due to the uncoupling of allosteric actions between GABA and BZD (Gallager et al., 1984; Marley and Gallager, 1989), a process that appears to rely on $GABA_AR$ receptor internalization (Ali and Olsen, 2001; Gutierrez et al., 2014). We have previously shown that 24 h BZD treatment leads to decreased surface and total levels of the α2 subunit in cultured hippocampal neurons that was dependent on lysosomal-mediated degradation (Jacob et al., 2012); however, the process by which the α2 subunit is selectively targeted to lysosomes is still unknown. $GABA_AR$ subunit ubiquitination and subsequent degradation at proteasomes or lysosomes modulates cell surface expression of receptors (Saliba et al., 2007; Arancibia-Carcamo et al., 2009; Crider et al., 2014; Jin et al., 2014; Di et al., 2016). Ubiquitination of the γ2 subunit is the only currently known mechanism identified to target internalized surface $GABA_ARs$ to lysosomes (Arancibia-Carcamo et al., 2009).

Another major regulator of $GABA_AR$ efficacy is postsynaptic scaffolding. Confinement at synaptic sites maintains receptors at GABA axonal release sites for activation. Furthermore, this limits receptor diffusion into the extrasynaptic space where internalization occurs (Bogdanov et al., 2006; Gu et al., 2016). The scaffolding protein gephyrin is the main organizer of $GABA_AR$ synaptic localization and density, as gephyrin knock-down and knock-out models show dramatic reductions in γ2- and α2-$GABA_AR$ clustering (Kneussel et al., 1999; Jacob et al., 2005). Evidence suggests gephyrin interacts directly with $GABA_AR$ α1, α2, α3, α5, β2, and β3 subunits (Tretter et al., 2008; Maric et al., 2011; Mukherjee et al., 2011; Kowalczyk et al., 2013; Tyagarajan and Fritschy, 2014; Brady and Jacob, 2015). Gephyrin recruitment is involved in inhibitory long term potentiation (Petrini et al., 2014; Flores et al., 2015), while its dispersal coincides with $GABA_AR$ diffusion away from synapses (Jacob et al., 2005; Bannai et al., 2009). Extensive post-translational modifications influence gephyrin function (Zacchi et al., 2014; Ghosh et al., 2016). Accordingly, expression of gephyrin phosphorylation site mutants revealed complex effects on $GABA_AR$ diffusion and gephyrin ultrastructure and scaffolding (Ghosh et al., 2016; Battaglia et al., 2018). Phosphorylation at the gephyrin serine 270 (Ser270) site has been particularly characterized to negatively modulate scaffold clustering and density, in part by enhancing calpain-1 protease mediated degradation of gephyrin (Tyagarajan et al., 2013). Given the well-established interdependent relationship between gephyrin and the γ2 subunit in maintaining receptor synaptic integrity (Essrich et al., 1998; Kneussel et al., 1999; Schweizer et al., 2003; Alldred et al., 2005; Jacob et al., 2005; Li et al., 2005), impaired postsynaptic scaffolding should affect both pre-existing and newly inserted $GABA_AR$ clustering and ultimately the efficacy of inhibitory neurotransmission. Thus a central unanswered question is if BZD exposure causes changes in gephyrin phosphorylation or protein levels.

Here we demonstrate that 12–24 h treatment with the BZD diazepam (DZP) leads to a reduction in total γ2 subunit and full-length gephyrin levels *in vitro* and *in vivo*. This reduction occurred coincident with enhanced γ2 subunit ubiquitination, but resulted in no significant change in overall γ2 surface levels. Using our recently published dual fluorescent BZD-sensitive $GABA_AR$ reporter ($\gamma2^{pH}FAP$), we further show that cell surface γ2-$GABA_ARs$ are more frequently targeted to lysosomes after DZP exposure. Forester resonance energy transfer (FRET) experiments further confirmed specific loss of synaptic α2/γ2 $GABA_AR$ levels following DZP treatment. The scaffolding protein gephyrin also demonstrated augmented phosphorylation at Ser270, increased cleavage and was significantly decreased in membrane and cytosolic compartments. Fluorescence recovery after photobleaching (FRAP) assays identified that DZP treatment increased the simultaneous recovery of γ2-$GABA_AR$ and gephyrin at synaptic sites, indicating reduced receptor confinement and accelerated exchange between the synaptic and extrasynaptic $GABA_AR$ pool. This process was reversed by the BZD site antagonist Ro 15-1788. Lastly, co-immunoprecipitation, quantitative mass spectrometry and bioinformatics analysis revealed shifts in the γ2-$GABA_AR$ interactome toward trafficking pathways *in vivo*. Together, these data suggest that DZP exposure causes a compensatory decrease in inhibitory neurotransmission by reducing BZD-sensitive $GABA_AR$ and gephyrin confinement at synapses and via ubiquitination and lysosomal targeting of γ2.

MATERIALS AND METHODS

Cell Culture, Transfection, Expression Constructs and Mice

Cortical neurons were prepared from embryonic day 18 rats and nucleofected with constructs at plating (Amaxa). The $\gamma2^{pH}FAP$ construct was characterized in Lorenz-Guertin et al. (2017) and

RFP-gephyrin was described in Brady and Jacob (2015). The $\gamma2^{RFP}$ construct was generated by PCR cloning and fully sequenced: the red fluorescent protein mCherry replaced pHluorin in the previously published $\gamma2^{pHGFP}$ construct (Jacob et al., 2005). GFP-ubiquitin was a gift from Nico Dantuma (Addgene plasmid # 11928) (Dantuma et al., 2006). 8–10 weeks old male C57BL/6J mice (Jackson Laboratory) were maintained on a reverse 12 h dark/light schedule. Mouse cortical brain tissue was collected and flash frozen 12 h after I.P. injection with either vehicle or diazepam [in 40% PEG, 10% EtOH, 5% Na Benzoate, 1.5% Benzyl alcohol (Hospira)]. All procedures were approved by the University of Pittsburgh Institutional Animal Care and Use Committee.

Reagents, Antibodies, and MG Dye

Diazepam (cell culture, Sigma; injections, Hospira); Ro 15-1788 (Tocris Bioscience); calpain-1 inhibitor MDL-28170 (Santa Cruz); L-glutamic acid (Tocris Bioscience). Primary antibodies: rabbit GAPDH (WB) (14C10, Cell Signaling); guinea pig GAD-65 (IF) (198104, Synaptic Systems); rabbit γ2 $GABA_AR$ subunit (IF, WB, and IP) (224003, Synaptic Systems); rabbit gephyrin (WB) (sc-14003, Santa Cruz); rabbit gephyrin (IF, total) (147002, Synaptic Systems) (antibody validation **Supplementary Figure S1**); mouse gephyrin mAb7a (IF, phospho) (147011, Synaptic Systems); chicken GFP (WB) (GFP-1020, Aves); rabbit (P)ERK (WB) (4370, Cell Signaling); mouse ERK (WB) (9107, Cell Signaling); rabbit (P)GSK3β (WB) (9322, Cell Signaling); rabbit GSK3β (WB) (9315. Cell Signaling); rabbit CDK5 (WB) (2506, Cell Signaling). MG-BTau dye prepared as in Lorenz-Guertin et al. (2017).

Fixed and Live-Imaging

Measurements were made on days *in vitro* (DIV) 15–19 cortical neurons. Live-imaging performed in Hepes-buffered saline (HBS), containing the following (in mM): 135 NaCl, 4.7 KCl, 10 Hepes, 11 glucose, 1.2 $MgCl_2$, and 2.5 $CaCl_2$ (adjusted to pH 7.4 with NaOH). Images were acquired using a Nikon A1 confocal microscope with a 60× oil objective (N.A., 1.49) at 3× zoom. Data were analyzed in NIS Elements software (Nikon, N.Y.). Measurements were taken from whole cell or averaged from three dendritic 10 μm regions of interest (ROI) per cell. For fixed imaging, media was quickly removed and coverslips were washed twice with Dulbecco's Phosphate Buffered Saline (DPBS) and immediately fixed with 4% paraformaldehyde and then blocked in PBS containing 10% fetal bovine serum and 0.5% bovine serum albumin. Surface antibody staining was performed under non-permeabilized conditions overnight at 4°C. Intracellular staining was performed overnight at 4°C following 0.2% Triton-X permeabilization for 10 min in blocking solution. Synaptic sites were determined during analysis by binary thresholds and colocalization with GAD-65. Extrasynaptic intensity was measured by taking the total dendrite ROI sum intensity minus background and synaptic fluorescence intensity. Dendritic fluorescence was measured using binary thresholds. Experimental conditions were blinded during image acquisition and analysis. The ROUT test (Q = 1%) or Grubbs' Test (alpha = 0.05) was used to remove a single outlier from a data set.

Lysosomal Targeting Assay

Neuron surface and lysosomal-association assays utilized MG-BTau dye for surface receptor pulse-labeling. DIV 15–16 neurons were treated with vehicle or DZP for 8–12 h, then pulse labeled with 100 nM MG-BTau for 2 min at room temperature in HBS. Neurons were then washed 5× times with HBS and returned to conditioned media ± DZP for 1 h. To identify lysosomal targeting, 50 nM LysoTracker Blue DND-22 (Life Technologies) and the lysosomal inhibitor, Leupeptin (200 μM Amresco), was added 30 min prior to imaging. Following incubation, neurons were washed and imaged in 4°C HBS. Two–three neurons were immediately imaged per culture dish within 10 min of washing. For image analysis, independent ROIs were drawn to capture the soma, three 10 μm sections of dendrite and the whole cell. Binary thresholds and colocalization measurements were performed to identify MG-BTau, pHGFP synaptic $GABA_AR$ clusters and lysosomes. Total surface pHGFP expression was determined by taking the entire cell surface signal following background subtraction.

NH_4Cl Intracellular Imaging

DIV 15–16 neurons were washed and continuously perfused with HBS + treatment at room temperature. Multiposition acquisition was used to image 2–3 neurons per dish. An initial image was taken to identify surface $\gamma2^{pH}$FAP $GABA_ARs$. Neurons were then perfused with NH_4Cl solution to collapse the cellular pH gradient and were reimaged. NH_4Cl solution (in mM): 50 NH_4Cl, 85 NaCl, 4.7 KCl, 10 Hepes, 11 glucose, 1.2 $MgCl_2$, and 2.5 $CaCl_2$ (adjusted to pH 7.4 with NaOH). pHGFP intensity was measured following background subtraction and smoothing. Surface/total levels were determined by dividing the first image (surface only) from the second image (total). The spot detection tool in Nikon Elements was used to selectively count larger intracellular vesicles positive for $\gamma2^{pH}$FAP. A stringent threshold was set to identify brightly fluorescent circular objects with a circumference of approximately 0.75 μm. Values reflect new vesicle objects that were only seen after NH_4Cl perfusion (second image – first image).

Intermolecular FRET Imaging, Characterization and Analysis

The α2 pHGFP ($\alpha2^{pH}$) construct was previously published (Tretter et al., 2008) and the $\gamma2^{RFP}$ construct was generated by PCR cloning and fully sequenced. DIV 15–16 neurons were treated with Veh or DZP for 20–28 h, then washed and continuously perfused with HBS at room temperature. Images were acquired with a 60× objective at 2× zoom. For each cell, an initial image was acquired containing two channels to identify surface $\alpha2^{pH}$ (excited by 488 laser, emission band pass filter 500–550) and $\gamma2^{RFP}$ participating in FRET (excited 488 FRET, emission band pass filter 575–625 nm, FRET channel). A second, single channel image was taken immediately following with only 561 nm excitation to reveal total $\gamma2^{RFP}$ levels (excited by 561 laser, emission band pass filter 575–625 nm). For synaptic quantifications, binary thresholding based on intensity was applied with smoothing and size exclusion (0–3 μm) factors.

FRET and 561 channel binaries shared identical minimum and maximum binary threshold ranges. Individual synaptic ROIs were created to precisely target and measure synaptic clusters containing both $\alpha2^{pH}$ and $\gamma2^{RFP}$. Manual trimming and single pixel removal were used to remove signal not meeting the criteria of a receptor cluster. Restriction criteria were applied in the following order: (1) at least 15 synapses measured per cell, (2) FRET $\gamma2^{RFP}$: raw $\gamma2^{RFP}$ sum intensity ratio must be less than one, (3) synaptic $\alpha2^{pH}$ mean intensity of at least 500, and (4) $\alpha2^{pH}$ sum intensity limit of 300% of average sum intensity. ROI data was then normalized to vehicle control as percent change. The percentage of RFP participating in FRET was also calculated using FRET RFP:Total RFP ratio.

Fluorescence resonance energy transfer activity was directly assessed by acceptor ($\gamma2^{RFP}$) photobleaching. Photobleaching ROIs were implemented on 2 synapses per cell. Pre-bleaching images were acquired every 5 s, followed by a $\gamma2^{RFP}$ photobleaching event using 80% 561 nm laser power. After photobleaching, image capturing resumed without delay using pre-bleach laser power settings for 2 min. Image analysis incorporated background subtraction and the measurement of percent change in $\alpha2^{pH}$/FRET $\gamma2^{RFP}$ ratio over the time course. FRET efficacy measurements compared directly adjacent $\alpha2^{pH}$ and $\gamma2^{RFP}$ subunits in a $GABA_AR$ complex. Live-imaging with perfusion of pH 6.0 extracellular imaging saline solution (MES) was used to quench the pH-dependent GFP fluorescence from the $\alpha2^{pH}$ donor fluorophores and show the dependence of FRET on surface $\alpha2^{pH}$ fluorescence. Acidic extracellular saline solution, MES solution pH 6.0 (in mM): 10 MES, 135 NaCl, 4.7 KCl, 11 glucose, 1.2 $MgCl_2$, and 2.5 $CaCl_2$ (adjusted to pH 7.4 with NaOH). Images were collected under HBS conditions for 1 min at 20 s intervals, and then followed by a 2 min MES wash with the same imaging interval to quench donor emissions. FRET RFP mean intensity was measured under both conditions and normalized to HBS. Percent or fold change in FRET RFP emissions were reported as indicated.

Synaptic Exchange Rate FRAP Imaging

Neurons were washed and media was replaced with HBS + treatment. Imaging was performed in an enclosed chamber at 37°C. An initial image was taken for baseline standardization. Photobleaching was performed by creating a stimulation ROI box encompassing two or more dendrites. This stimulation region was photobleached using the 488 and 561 lasers at 25% power for 1 min. The same stimulation ROI was used for every cell in an experiment. Immediately following photobleaching, 10 nM MG-Tau dye was added to the cell culture dish to re-identify surface synaptic $GABA_AR$ clusters. Time-lapse imaging was then started every 2 min for 60 min. During image analysis, objects were only considered synaptic if they demonstrated colocalization with $\gamma2^{pH}$FAP pHGFP signal, RFP-gephyrin signal and had obvious surface MG-BTau fluorescence. ROIs were drawn measuring the rate of fluorescence recovery at 4–8 synaptic sites and one extrasynaptic site (10 μm long region; Bezier tool) per cell. For data analysis, synapse post-bleach fluorescence intensity time point data was first normalized to pre-bleach fluorescence intensity (post-bleach/pre-bleach). Normalized synapse post-bleach data was then calculated as percent change from t0 [(tx/t0)*100, where x = min]. Individual synapses were then averaged to calculate fluorescence recovery and statistically significant changes across time points.

Western Blot and Immunoprecipitation

Protein concentration was determined by BCA protein assay for all biochemistry. Neurons were lysed in denaturing buffer for immunoprecipitation: 50 mM Tris HCl, 1 mM EDTA, 1% SDS, 2 mM Na3VO4, 10 mM NaF, 50 mM *N*-ethylmaleimide, protease inhibitor cocktail (Sigma). Lysates were sonicated and heated at 50°C for 20 min, then diluted 1:5 in RIPA buffer (50 mM Tris HCl pH 7.6, 150 mM NaCl, 1% Igepal, 0.5% Sodium deoxycholate, 1 mM EDTA, 2 mM Na3VO4, 10 mM NaF, 50 mM *N*-ethylmaleimide, protease inhibitor cocktail). Standard immunoprecipitation procedures were performed using overnight incubation with γ2 subunit antibody or rabbit IgG (sci2027; Sigma), 1 h incubation with Protein A Sepharose 4B beads (Invitrogen), three RIPA buffer washes, and loading for SDS-PAGE. After electrophoresis and transfer to nitrocellulose membrane, samples were probed with primary antibody overnight followed by the appropriate horseradish peroxide (HRP)-coupled secondary antibody.

Membrane and Subcellular Fractionation

Cultured neurons were lysed using fractionation buffer: 50 mM Tris-HCl, 50 mM NaCl, 1 mM EDTA, 2 mM Na3VO4, 10 mM NaF, 320 mM sucrose, 0.25% igepal, and protease inhibitor cocktail. Lysates were spun at 88,881 *g* for 30 min at 4°C to separate pellet (membrane) from supernatant (cytosol). Fraction integrity was tested by localization specific markers in all experiments (**Supplementary Figure S2** and data not shown).

Co-immunoprecipitation

Mice were intraperitoneally (I.P.) injected with vehicle control or 10 mg/kg DZP and sacrificed 12 h post-injection (n = 4 mice per treatment). Mouse cortical tissue was homogenized in co-IP buffer (50 mM Tris HCl pH 7.6, 50 mM NaCl, 0.25% Igepal, 1 mM EDTA, 2 mM Na3VO4, 10 mM NaF, 50 mM *N*-ethylmaleimide, and Sigma protease inhibitor cocktail) using a Dounce homogenizer. Tissue was solubilized with end-over-end mixing at 4°C for 15 min, and then spun at 1,000 g to remove non-solubilized fractions. Each immunoprecipitation tube contained 375 μg of tissue lysate brought up to 1 ml volume using co-IP buffer. Lysates were precleared using Protein A Sepharose 4B beads (Invitrogen) for 1 h at 4°C. Lysate was then immunoprecipitated overnight with 2.5 μg rabbit γ2 subunit antibody (224003, Synaptic Systems) or 2.5 μg rabbit IgG (2027, Santa Cruz). The next day, 40 μl Protein A Sepharose slurry was added and mixed for 2 h at 4°C on a nutator. Beads were then washed 3× at 4°C on a nutator in 1 ml co-IP buffer. Beads were denatured with SDS-PAGE loading buffer [Laemmli Sample buffer (Bio-Rad) + β-mercaptoethanol] with heat at 70°C for 10 min and intermittent vortexing. Two immunoprecipitation reactions were performed per animal and were pooled into a single tube without beads to be used for downstream in-gel digestion.

Mass Spectrometry and Data Processing

Immunoprecipitated proteins were separated by electrophoresis in Criterion XT MOPS 12% SDS-PAGE reducing gels (Bio-Rad), with subsequent protein visualization by staining with Coomassie blue. Each gel lane was divided into six slices. After de-staining, proteins in the gel slices were reduced with TCEP [tris(2-carboxyethyl)phosphine hydrochloride] and then alkylated with iodoacetamide before digestion with trypsin (Promega). HPLC-electrospray ionization-tandem mass spectrometry (HPLC-ESI-MS/MS) was accomplished by data-dependent acquisition on a Thermo Fisher Orbitrap Fusion Lumos Tribrid mass spectrometer. Mascot (Matrix Science; London, United Kingdom) was used to search the MS files against the mouse subset of the UniProt database combined with a database of common contaminants. Subset searching of the Mascot data, determination of probabilities of peptide assignments and protein identifications, were accomplished by Scaffold (v 4.8.4, Proteome Software). MS data files for each entire gel lane were combined via the "MudPIT" option. Identification criteria were: minimum of two peptides; 96% peptide threshold; 1% FDR; 99% protein threshold. One vehicle- and one DZP-treated animal were removed from analysis due to insufficient γ2 subunit pulldown relative to all other groups. $N = 3$ animals per condition were used for downstream analysis. Protein clustering was applied in Scaffold and weighted spectrum values and exclusive unique peptides were exported for manual excel analysis. Student's *t*-test analysis was performed using relative fold change (ratio) of DZP compared to vehicle group. In some cases peptides were only detected in vehicle or DZP treated groups, resulting in DZP/V ratio values of zero or undefined error (cannot divide by zero). These were annotated as NF-DZP (not found in DZP samples) or NF-V (not found in vehicle samples) in the tables.

Bioinformatics Analysis

Ingenuity Pathways Analysis (IPA) (Ingenuity Systems) was used for cellular pathway analysis. Relative fold levels of DZP proteins compared to vehicle were used for analysis. To be suitable for IPA analysis, proteins NF-DZP were assigned a value of −1E+99, while proteins NF-V were assigned a value of 1E+99. Significant enrichment in protein networks were calculated by right tailed Fisher's exact test. *Z*-score analysis is a statistical measure of an expected relationship direction and observed protein/gene expression to predict pathway activation or inhibition. IPA core analysis was searched to determine direct and indirect relationships within 35 molecules per network and 25 networks per analysis. All data repositories available through IPA were used to determine experimentally observed and highly predicted interactions occurring in mammalian tissue and cell lines. Ratio data were converted to fold change values in IPA, where the negative inverse ($-1/x$) was taken for values between 0 and 1, while ratio values greater than 1 were not affected. Proteins found to be enhanced in their association with γ2 (**Table 1**) were searched in the Mus musculus GO Ontology database (released 2018-10-08) for GO biological process and GO molecular function and analyzed by the PANTHER overrepresentation test; significance was determined using Fisher's Exact with Bonferroni correction for multiple testing.

Statistics

Relevant statistical test information is described in the figure legends or within the individual methods sections. *p*-values are reported in the results section if significance is between 0.01 and <0.05 or if the data is approaching significance.

RESULTS

DZP Exposure Modifies γ2-$GABA_AR$ and Gephyrin Levels

We first examined if DZP exposure reduced surface levels of γ2-$GABA_A$Rs and altered gephyrin Ser270 phosphorylation in cortical neurons by immunofluorescence (**Figure 1A**). Cortical neurons were treated for 24 h with vehicle or 1 μM DZP, then immunostained for surface γ2, followed by permeabilization and immunostaining with GAD65 (glutamic acid decarboxylase 65, a marker for presynaptic GABAergic terminals) and the phospho-Ser270 specific gephyrin mAb7a antibody (Kuhse et al., 2012; Kalbouneh et al., 2014). Image analysis identified no sizable change in surface synaptic (91.6 ± 5.3%) or extrasynaptic (93.3 ± 3.8%) γ2 intensity in DZP treated neurons relative to control, but DZP induced a significant 18.9 ± 7.4% ($p = 0.033$) increase in synaptic phospho-gephyrin (**Figure 1B**). No change in extrasynaptic phosphorylated Ser270 gephyrin was measured. We repeated this DZP treatment and examined total and phospho-gephyrin levels in dendrites (**Figure 1C**). Again DZP significantly enhanced phospho-Ser270 gephyrin compared to vehicle (132 ± 12%; $p = 0.013$), while a decrease in overall gephyrin levels was found (69.7 ± 5.4%) (**Figure 1D**). Accordingly, the mean ratio of phospho/total gephyrin was 78.1 ± 21% higher following DZP (**Figure 1D**). Complimentary biochemical studies using membrane fractionation were used to compare cytosolic, membrane, and total protein pools in cortical neurons. In agreement with immunofluorescence data, membrane levels of γ2 (0.929 ± 0.06) were not reduced after 1 μM DZP, although the total pool of γ2 was diminished (0.793 ± 0.07) (**Figures 2A,B**) compared to vehicle. Cytosolic levels of γ2 (1.03 ± 0.06) were also unchanged. Comparatively, DZP reduced full-length gephyrin in every compartment measured relative to control (cytosol: 0.871 ± 0.03; membrane: 0.722 ± 0.06, total: 0.695 ± 0.05). We confirmed the integrity of our fractions using cytosolic and membrane specific markers (**Supplementary Figure S2**).

Next we assessed if the decrease in gephyrin and γ2 total levels at 24 h was a result of altered gene expression. qRT-PCR experiments revealed no difference in gephyrin ($p = 0.206$), γ2, or control $GABA_AR$ β3 subunit mRNA levels between vehicle and DZP treated neurons (**Figure 2C**). To determine if post-translational modification of γ2 also occurs coincident with decreased γ2 protein levels, we examined ubiquitination of γ2 in response to DZP exposure. We reasoned that changes in

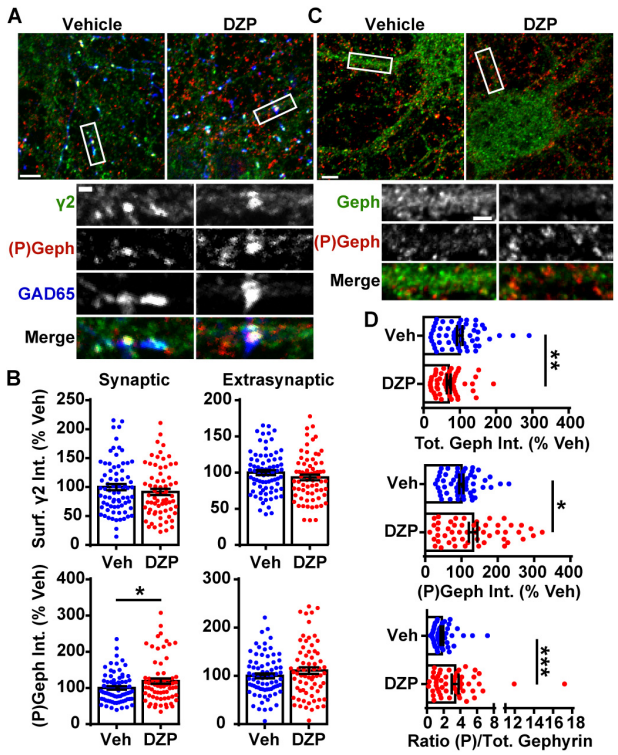


FIGURE 1 | DZP downregulates gephyrin independent of γ2 surface levels. **(A)** Cortical neurons were treated for 24 h with vehicle or 1 μM DZP, then immunostained for surface γ2 GABA$_A$R (green), followed by permeabilization and immunostaining for (P)Ser270 gephyrin (red), and GAD65 (blue). Panels below show enlargements of GABA$_A$R synapses on dendrites. **(B)** Dendrite surface synaptic and extrasynaptic γ2 levels are not significantly altered by DZP. Synaptic phospho-gephyrin was enhanced in response to DZP (n = 69–74 neurons; 4 independent cultures). **(C)** Neurons were treated as in **(A)** followed by antibody staining for total gephyrin (green) and (P)Ser270 gephyrin (red). Panels below show enlargements of dendrite region. **(D)** The dendritic pool of gephyrin was decreased, while (P)Ser270 gephyrin levels were augmented, resulting in a dramatic increase in the ratio of phosphorylated gephyrin to total gephyrin (n = 52–59 neurons; 3 independent cultures). Int., fluorescence intensity. Image scale bars: main panels = 5 μm, enlargements = 1 μm. *$p \leq 0.05$, **$p < 0.01$, ***$p < 0.001$, Student's t-test; error bars ± s.e.m.

ubiquitination of γ2 would likely precede the loss of total γ2 seen at 24 h (**Figures 2A,B**). GFP-ubiquitin transfected cortical neurons were treated with vehicle or 1 μM DZP for 12 h. Neurons were lysed under denaturing conditions to isolate the γ2 subunit from the receptor complex (**Supplementary Figure S3**). Immunoprecipitation of the γ2 subunit revealed a 2.13-fold increase (p = 0.015) in ubiquitination in DZP treated neurons relative to vehicle (**Figures 2D,E**). Furthermore, just as observed with 24 h DZP treatment, a reduced total pool of γ2 was also found at 12 h (p = 0.020) (**Figures 2D,E**). Notably, this is the first demonstration of endogenous γ2 ubiquitination occurring in neurons (previous findings were of recombinant receptors in HEK cells) (Arancibia-Carcamo et al., 2009; Jin et al., 2014). To investigate mechanisms underlying reduced full-length gephyrin levels, we examined gephyrin cleavage. Gephyrin is degraded post-translationally by the protease calpain-1 (Tyagarajan et al., 2013; Costa et al., 2015; Kumar et al., 2017), and gephyrin Ser270 phosphorylation promotes cleavage by calpain-1 (Tyagarajan et al., 2013). Consistent with the enhanced gephyrin Ser270 phosphorylation (**Figure 1**) and reduced full-length levels (**Figures 1**, **2**) we found a significant increase in the ratio of cleaved/full length gephyrin after 24 h DZP *in vitro* (**Figures 2F,G**). We confirmed the identity of the gephyrin cleavage product using a well-characterized glutamate stimulation protocol that induces gephyrin cleavage in cultured neurons (Costa et al., 2015; Kumar et al., 2017), a process blocked by calpain-1 inhibition (**Supplementary Figure S4**).

Finally, we wanted to determine if similar mechanisms occur *in vivo* following DZP treatment. Prior publications show that BZDs and metabolites are not present 24 h post-injection due to rapid drug metabolism in rodents (Yoong et al., 1986; Xie and Tietz, 1992; Van Sickle et al., 2004; Markowitz et al., 2010). Furthermore, BZD uncoupling does not persist 24 h after a single dose (15 mg/kg) or 2 weeks daily DZP treatment, whereas uncoupling can be seen 12 h after a single injection, indicating this is the appropriate time point for measuring *in vivo* loss of γ2-GABA$_A$R function (Holt et al., 1999). Accordingly, mice were given a single intraperitoneal (IP) injection of 10 mg/kg DZP or vehicle control, and cortex tissues were harvested 12 h later. We found DZP significantly reduced the total pool of γ2 (87.3 ± 3.0%) and full-length gephyrin (73.9 ± 9.1%; p = 0.046) relative to vehicle treated mice at 12 h post injection (**Figures 2H,I**). These findings indicate both BZD-sensitive GABA$_A$Rs and full-length gephyrin are downregulated by post-translational mechanisms after initial DZP treatment *in vitro* and *in vivo* to temper potentiation of GABA$_A$R function.

DZP Enhances Intracellular Accumulation and Lysosomal Targeting of γ2-GABA$_A$Rs

We then investigated if surface γ2-containing GABA$_A$Rs are more frequently targeted to lysosomes after DZP exposure by live-imaging. For these experiments we used our recently characterized optical sensor for synaptic GABA$_A$R (γ2^{pH}FAP). This dual reporter is composed of a γ2 subunit tagged with an N terminal pH-sensitive GFP, myc, and the fluorogen-activating peptide DL5 (Lorenz-Guertin et al., 2017). The pH-sensitive GFP tag selectively identifies cell surface GABA$_A$Rs and the DL5 FAP binds malachite green (MG) dye derivatives including MG-BTau (Szent-Gyorgyi et al., 2008, 2013; Pratt et al., 2017). MG-BTau is cell impermeable and non-fluorescent until bound by DL5. Upon binding, MG-BTau fluoresces in the far red spectral region (∼670 nM). This FAP-dye system allows for selective labeling of surface γ2-containing GABA$_A$Rs which can then be tracked through various phases of trafficking (Lorenz-Guertin et al., 2017). As previously shown, γ2^{pH}FAP GABA$_A$Rs are expressed on the neuronal surface, form synaptic clusters, do not perturb neuronal development and show equivalent functional responsiveness to GABA and DZP both in the

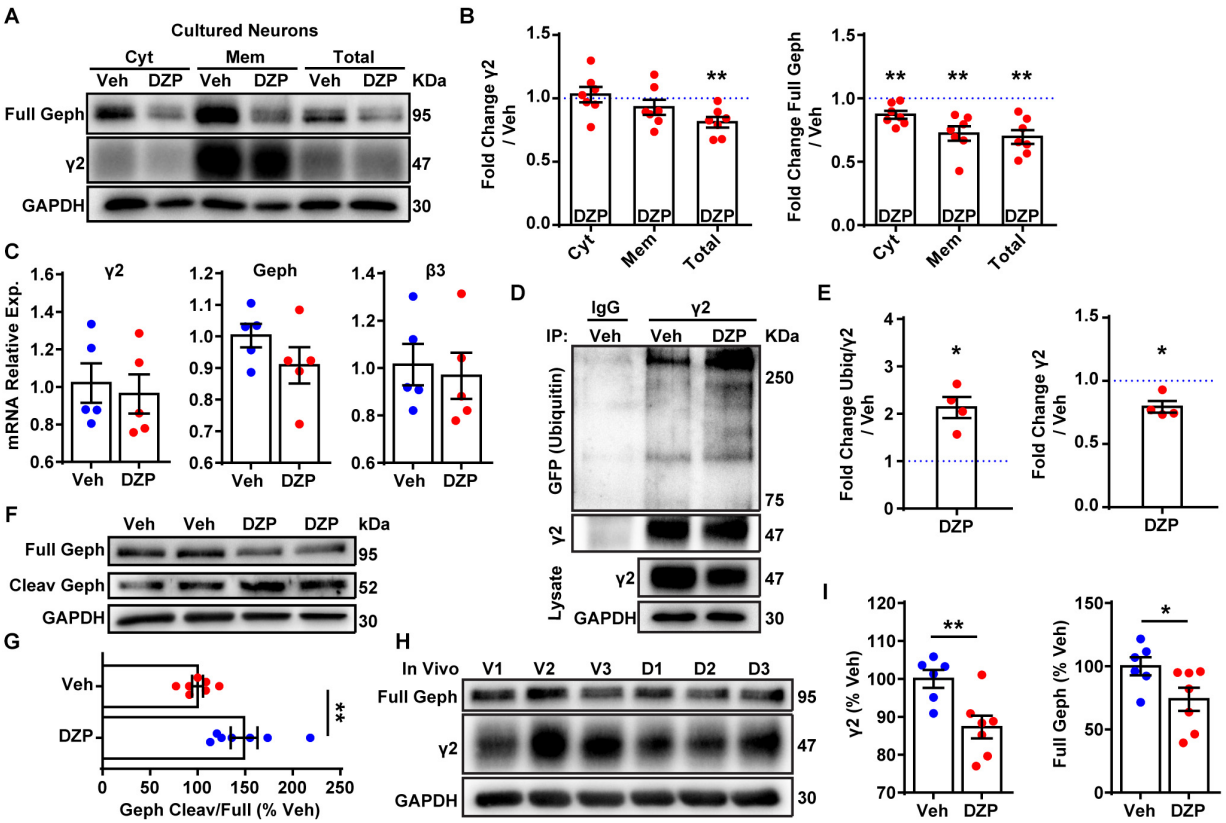


FIGURE 2 | DZP induces degradation of γ2 and gephyrin *in vitro* and *in vivo*. **(A)** Cortical neurons exposed to 1 μM DZP or vehicle for 24 h were subjected to membrane fraction and western blot analysis. Full Geph = full-length gephyrin. **(B)** Total γ2 subunit and cytosolic, membrane, and total gephyrin were significantly reduced after DZP (n = 7 independent cultures). **(C)** Quantitative RT-PCR revealed no change in γ2 subunit, β3 subunit or gephyrin mRNA expression following 24 h DZP *in vitro* (n = 5 independent cultures). **(D)** GFP-ubiquitin transfected neurons were treated with vehicle or DZP for 12 h. Lysates were immunoprecipitated with control IgG or γ2 antibody, followed by blotting with anti-GFP, γ2 and GAPDH. **(E)** DZP treatment increased the levels of γ2 ubiquitin conjugates and decreased γ2 total levels. **(F,G)** DZP treatment enhanced the ratio of cleaved gephyrin fragments/full length gephyrin (n = 7 biological replicates/dishes from 4 independent cultures). Full, full-length gephyrin; Cleav, cleaved gephyrin. **(H)** Western blots of cortical tissue collected from mice 12 h after a single IP injection of 10 mg/kg DZP or vehicle. **(I)** γ2 subunit and full-length gephyrin levels are significantly reduced in DZP-treated animals (6–7 mice per condition). [$^*p \leq 0.05$, $^{**}p < 0.01$, paired t-test **(B,E)**, Student's t-test **(C,G,I)**; error bars ± s.e.m].

absence and presence of MG dyes (Lorenz-Guertin et al., 2017). We transfected neurons with γ2^{pH}FAP and treated them with DZP for 8–16 h. Neurons were then pulse-labeled with 100 nM MG-BTau dye and returned to conditioned media at 37°C ± DZP for 1 h. The lysosomal inhibitor leupeptin (200 μM) and the lysosomal specific dye, Lysotracker (50 nM), were added after 30 min. At the end of the incubation, neurons were washed in 4°C saline to inhibit trafficking and immediately used for live-imaging experiments. Representative images demonstrate MG-BTau labeled γ2^{pH}FAP-GABA$_A$Rs localized on the cell surface (**Figure 3A**) and at synaptic clusters on dendrites (**Figure 3B**) based on colocalization with surface specific pHGFP signal. MG-BTau further reveals internalized receptors at lysosomes (**Figure 3C**). Image quantification showed synaptic γ2-GABA$_A$R intensity remained largely unchanged (**Figure 3D**). Importantly, we found a significant 8.0 ± 2.5% (p = 0.015) enhancement in the mean intensity of GABA$_A$Rs labeled with MG-BTau at lysosomes following DZP (**Figure 3E**). The area of GABA$_A$Rs colocalized at lysosomes trended toward an increase in DZP treated cells (140.2 ± 23.6%; p = 0.144) but did not reach significance.

We complemented these lysosomal targeting studies with an NH_4Cl live-imaging approach that allows us to compare the ratio of cell surface vs. intracellular GABA$_A$Rs in living neurons. γ2^{pH}FAP expressing neurons were treated with vehicle or DZP for 24 h. Additional control groups included the BZD antagonist Ro 15-1788 (1–2 h) to reverse the effects of DZP. Neurons were actively perfused with HEPES buffered saline (HBS) treatment and an initial image was taken of surface pHGFP receptor signal (**Figure 3F**). Neurons were then exposed to pH 7.4 NH_4Cl solution to neutralize the pH gradient of all intracellular membrane compartments, revealing internal pools of γ2 containing GABA$_A$Rs. Analysis revealed no change in surface γ2 levels between treatments (**Figure 3G**) consistent with **Figures 1**, **2**. However, the number of large intracellular vesicles (circular area ∼0.75 μm) containing receptors was significantly enhanced (p = 0.047) (**Figure 3H**),

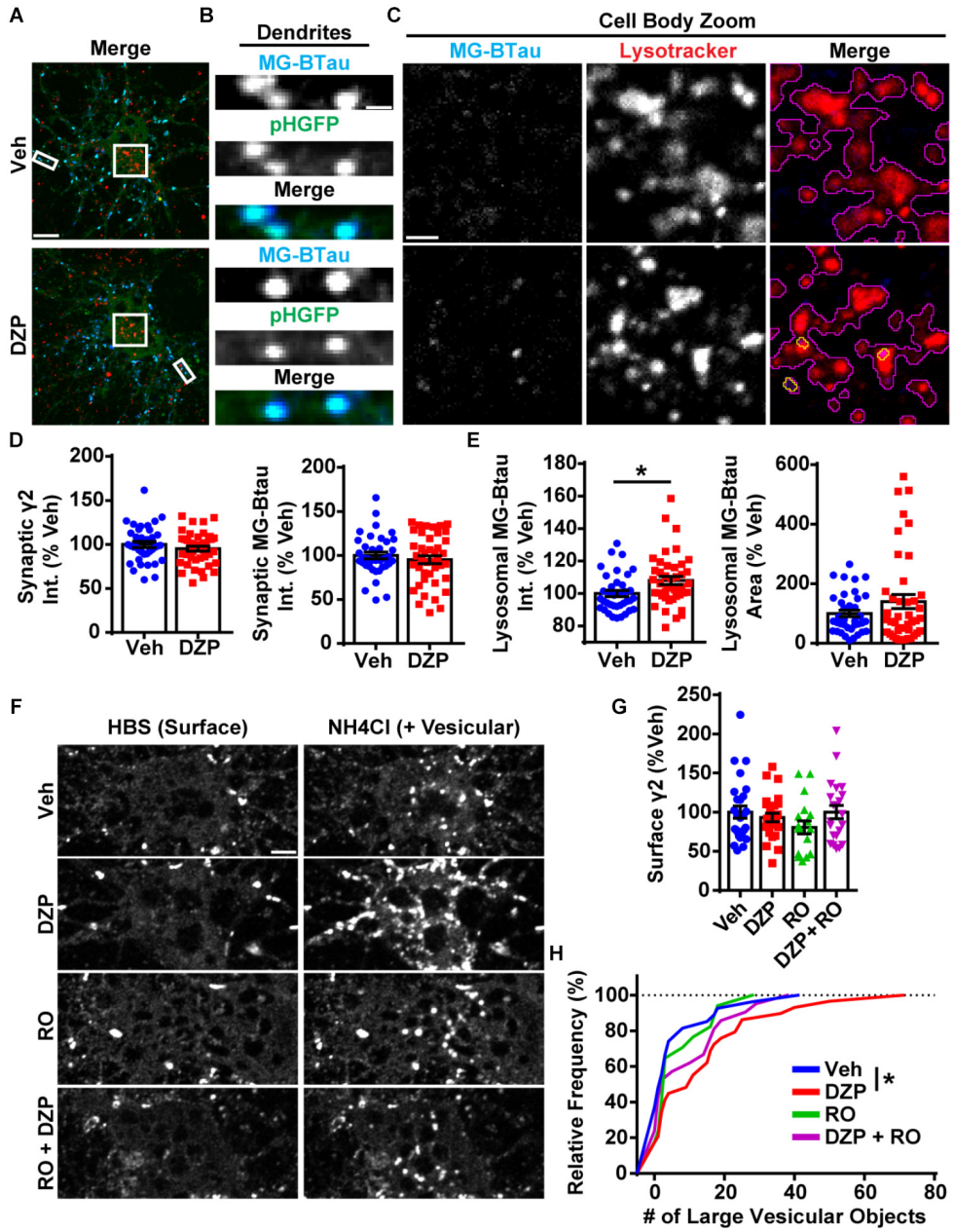


FIGURE 3 | Lysosomal targeting and vesicular accumulation of γ2-GABA$_A$Rs in response to DZP. **(A)** γ2^{pH}FAP neurons were pretreated for 12–18 h with 1 μM DZP, then pulse-labeled with 100 nM MG-BTau dye for 2 min, and returned to conditioned media at 37°C ± DZP for 1 h. 50 nM Lysotracker dye was added at the 30 min mark to identify lysosomes. MG-BTau = blue; pHGFP = green; Lysotracker = red (n = 37–42 neurons; 5 independent cultures). **(B)** Dendrite zoom images show MG-BTau labeling at γ2^{pH}FAP synapses. **(C)** Cell body zoom images highlighting colocalization of MG-BTau labeled GABA$_A$Rs (yellow trace) at lysosomes (purple trace). **(D)** Dendrite pHGFP and MG-BTau measurements reveal surface synaptic γ2-GABA$_A$R levels are not altered by DZP. **(E)** The pool of internalized MG-BTau GABA$_A$Rs colocalized at lysosomes was enhanced in DZP treated neurons as measured by intensity (*$p \leq 0.05$, Student's t-test; error bars ± s.e.m). **(F)** Neurons treated 20–28 h with vehicle or DZP. The DZP site antagonist Ro 15–1788 (5 μM) was added 1–2 h prior to imaging to inhibit DZP binding at GABA$_A$Rs. Neurons were first imaged in HBS, and then perfused with NH_4Cl (pH 7.4) to reveal intracellular γ2^{pH}FAP receptors. DZP treated neurons accumulated more γ2-GABA$_A$Rs in large vesicular structures compared to vehicle (n = 20–27 neurons; 3–4 independent cultures). **(G)** Surface intensity of γ2^{pH}FAP was not different between treatments (one-way ANOVA; error bars ± s.e.m). **(H)** DZP-treated neurons more frequently demonstrated accumulation of γ2^{pH}FAP in large vesicles (*$p \leq 0.05$ Kolmogorov–Smirnov statistical test). Int., fluorescence intensity. Scale bars in μm: **(A)** = 10; **(B)** = 1; **(C)** = 2, **(F)** = 5.

consistent with increased localization in intracellular vesicles. Ro 15-1788 and DZP + Ro 15-1788 treated neurons were not significantly different from vehicle. Overall, these findings suggest γ2-GABA$_A$R ubiquitination, intracellular accumulation, lysosomal targeting and degradation are part of the adaptive response to DZP.

Surface Levels of Synaptic α2/γ2 $GABA_AR$ Are Decreased Following DZP

Despite the increase in ubiquitination and lysosomal targeting of γ2-$GABA_ARs$ after DZP, we did not detect decreased overall surface or synaptically localized γ2 levels. This suggested two possibilities, one being that a slight decrease in surface γ2-$GABA_ARs$ could be challenging to detect with current methods (DZP treated cells total γ2 levels 80% of control in cultured cortical neurons; 85% *in vivo*). Alternatively, there could be an increase in γ2 subunit assembly with BZD-insensitive α subunits (γ2α4β) (Wafford et al., 1996) with a concomitant reduction in surface levels of BZD-sensitive receptors (γ2α1/2/3/5β). Our previous work showed 24 h BZD exposure in hippocampal neurons causes decreased total and surface levels of the α2 $GABA_AR$ subunit via lysosomal mediated degradation, without any changes in receptor insertion or removal rate (Jacob et al., 2012). To determine if α2/γ2 $GABA_ARs$ are specifically decreased by DZP treatment, we developed an intermolecular FRET assay, using pH-sensitive GFP tagged $\alpha2^{pH}$ (Tretter et al., 2008) as a donor fluorophore and a red fluorescent protein (RFP) tagged γ2 subunit ($\gamma2^{RFP}$) as an acceptor. FRET is an accurate measurement of molecular proximity at distances of 10–100 Å and is highly efficient if donor and acceptor are within the Förster radius, typically 30–60 Å (3–6 nm), with the efficiency of FRET being dependent on the inverse sixth power of intermolecular separation (Förster, 1965). Synaptic $GABA_ARs$ exist as five subunits assembled in γ2-α-β-α-β order forming a heteropentameric ion channel (**Figure 4A**). We first expressed $\alpha2^{pH}$ and $\gamma2^{RFP}$ in neurons and examined their ability to participate in intermolecular FRET. Photobleaching of the acceptor $\gamma2^{RFP}$ channel enhanced donor $\alpha2^{pH}$ signal (**Supplementary Figure S5**), confirming energy transfer from $\alpha2^{pH}$ to $\gamma2^{RFP}$. Next, we confirmed measurable FRET only occurs between $\alpha2^{pH}/\gamma2^{RFP}$ in surface $GABA_AR$ at synaptic sites; FRET was blocked with quenching of donor $\alpha2^{pH}$ when the extracellular pH was reduced from 7.4 to 6.0 (**Figures 4A,B**). Following FRET assay validation, $\alpha2^{pH}/\gamma2^{RFP}$ $GABA_AR$ expressing neurons were treated for 24 h with vehicle or DZP and examined for total synaptic $\alpha2^{pH}$ and $\gamma2^{RFP}$ fluorescence as well as the γ2 FRET signal (**Figure 4C**). These studies identified a DZP-induced reduction in synaptic α2 (−12.6%), synaptic γ2 (−14.3%) and diminished association of α2 with γ2 in synaptic $GABA_ARs$ as measured by decreased FRET γ2 signal (−10.6%; $p = 0.024$) (**Figure 4D**). In summary, this sensitive FRET method indicates that cortical neurons show a similar susceptibility for α2 subunit downregulation by BZD treatment as seen in hippocampal neurons (Jacob et al., 2012). Furthermore it identifies a DZP-induced decrease in a specific pool of surface synaptic BZD-sensitive γ2-$GABA_AR$.

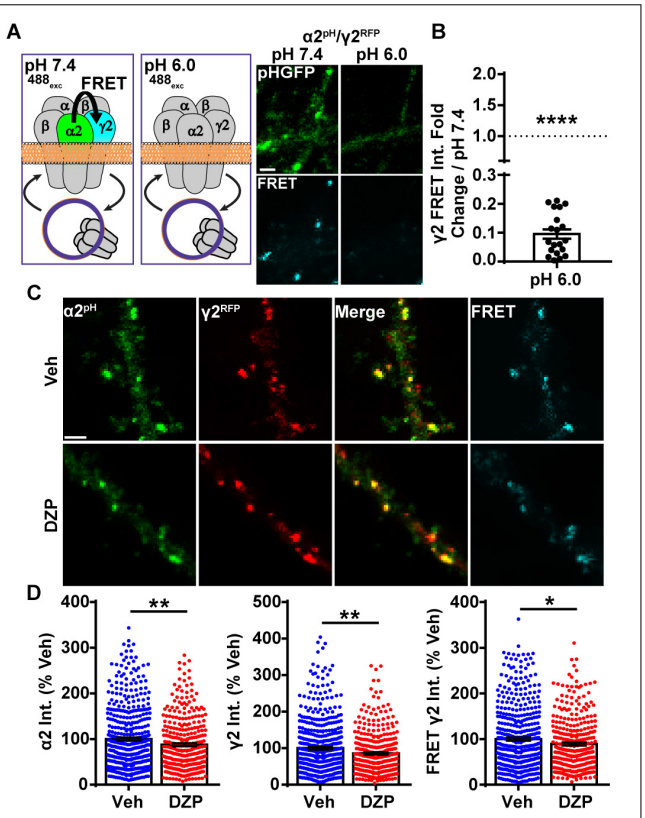


FIGURE 4 | Intermolecular FRET reveals decreased dendritic synaptic α2/γ2 surface $GABA_ARs$ after DZP. **(A)** Diagram and time-series images of cortical neurons expressing donor $\alpha2^{pH}$ (green) and acceptor $\gamma2^{RFP}$ during imaging at pH 7.4 and pH 6.0. Surface $\alpha2^{pH}$ (green) signal and intermolecular FRET (teal) between α2/γ2 subunits occurs at pH 7.4, but is eliminated by brief wash with pH 6.0 extracellular saline and quenching of the $\alpha2^{pH}$ donor pHGFP fluorescence. **(B)** Quantification of relative FRET at pH 7.4 and pH 6.0 ($n = 20$ synapses). **(C)** Neurons $\alpha2^{pH}$ (green) and $\gamma2^{RFP}$ (red) were treated with vehicle or DZP for 20–28 h ± and then subjected to live-imaging. For each cell, an initial image used 488 nm laser excitation to identify surface $\alpha2^{pH}$ and FRET $\gamma2^{RFP}$. A second image was taken immediately afterwards to acquire $\gamma2^{RFP}$ total levels (561 nm laser excitation). Dendritic lengths show multiple synaptic clusters with α2/γ2 surface $GABA_ARs$. **(D)** Synaptic cluster intensity quantification of $\alpha2^{pH}$, $\gamma2^{RFP}$, and FRET $\gamma2^{RFP}$ (at least 15 synapses per cell; $n = 335–483$ synapses; 6 independent cultures). Int., fluorescence intensity. Image scale bars = 2 μm [$^*p \leq 0.05$, $^{**}p < 0.01$, $^{****}p < 0.0001$, paired *t*-test **(B)**, Student's *t*-test **(D)**; error bars ± s.e.m].

Selective ERK Inactivation After DZP Treatment

To gain additional mechanistic insight into the molecular mechanisms controlling phosphorylation and degradation of gephyrin observed in **Figures 1**, **2**, we performed a DZP time series experiment to measure changes in expression or activation of the gephyrin regulating kinases ERK, GSK3β, and CDK5. CDK5 and GSK3β phosphorylate gephyrin at the Ser270 site (Tyagarajan et al., 2011; Kalbouneh et al., 2014), while ERK phosphorylates a neighboring Ser268 residue (Tyagarajan et al., 2013). We first measured ERK activation by examining ERK phosphorylation across time points. DZP treatment caused a significant decrease in ERK phosphorylation at 45 min (−50.2%), 3 h (−44.5%) and 6 h (−51.2%), with a recovery in phosphorylation to vehicle levels occurring around 12 and 24 h (**Figures 5A,B**). Total ERK levels were unchanged after DZP, except for a significant enhancement in expression at the 12 h time point, coinciding with recovery of ERK phosphorylation. We did not detect a change in the

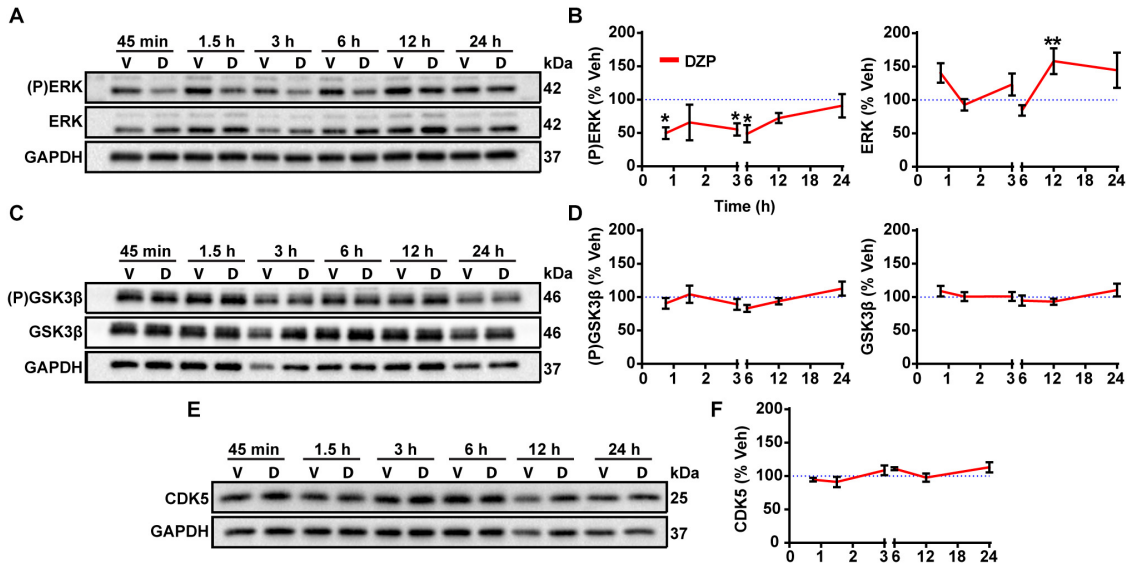


FIGURE 5 | Gephyrin regulating kinases following DZP treatment. DIV 16 cortical neurons were treated with vehicle (V) or DZP (D) at multiple time points. Known kinase regulators of gephyrin synaptic clustering were tested for total protein levels and activation status with phospho-specific antibodies as indicated. (P)ERK and total ERK **(A,B)**, (P)GSK3β and total GSK3β **(C,D)** and CDK5 **(E,F)** western blot and quantification (n = 4 independent cultures). DZP strongly inhibited ERK phosphorylation across multiple time points while GSK3β activation and total levels did not change. CDK5 total levels were also unchanged by DZP treatment. ($^*p \leq 0.05$, $^{**}p < 0.01$, Two-way ANOVA followed by Sidak's multiple comparisons test; error bars ± s.e.m).

phosphorylation or total levels of GSK3β (**Figures 5C,D**) or expression of CDK5 (**Figures 5E,F**). This data indicates that kinases involved in gephyrin phosphorylation at Ser270 do not demonstrate global changes after DZP, suggesting that the kinases may be recruited to gephyrin, or that an unknown phosphatase responsible for dephosphorylating Ser270 is inhibited after DZP exposure. Conversely, ERK inactivation by DZP is predicted to decrease phosphorylation of the functionally relevant Ser268 site of gephyrin, which has also been implicated in gephyrin synaptic remodeling (Tyagarajan et al., 2013). Gephyrin point mutant studies suggest reduced phosphorylation at Ser268 coupled with enhanced Ser270 phosphorylation, or the inverse, promotes calpain-1 degradation and scaffold remodeling (Tyagarajan et al., 2013). This data provides evidence that a known kinase pathway responsible for fine-tuning GABA$_A$R synapse dynamics (Brady et al., 2017) and scaffold (Tyagarajan et al., 2013) is robustly inactivated by DZP.

Synaptic Exchange of γ2-GABA$_A$Rs and Gephyrin Are Accelerated After Prolonged DZP Treatment

We previously found 24 h BZD exposure reduces the amplitude of miniature inhibitory postsynaptic currents (mIPSCs) (Jacob et al., 2012), suggesting changes in synaptic GABA$_A$R function. Having identified both reductions in full-length gephyrin (**Figures 1**, **2**) and BZD sensitive GABA$_A$Rs (**Figures 2**, 4), we next tested if DZP treatment altered the synaptic retention properties of gephyrin and/or GABA$_A$Rs. Neurons expressing γ2^{pH}FAP and RFP-gephyrin were used for live-imaging fluorescence recovery after photobleaching experiments (FRAP) to measure synaptic and extrasynaptic exchange following exposure to vehicle, 1 μm DZP, 5 μm Ro 15-1788, or DZP + Ro 15-1788. After an initial image was taken, dendrites were photobleached, and signal recovery was measured every 2 min over 30 min at synaptic sites and extrasynaptic regions (**Figure 6A** synapses panel; **Figure 6B** larger dendritic region with white arrows denoting extrasynaptic region). MG-BTau dye was added directly after the photobleaching step to immediately re-identify the photobleached surface synaptic GABA$_A$Rs, and improve spatial measurements (**Figure 6B**). These experiments revealed synaptic γ2 turnover rates were nearly doubled in DZP treated neurons, a process reversed by Ro 15-1788 co-treatment (**Figure 6C**). DZP also accelerated gephyrin synaptic exchange rates compared to vehicle, with Ro 15-1788 co-treatment restoring exchange to control levels. No significant correlation was found between cluster area measured and fluorescence recovery rates of γ2 and gephyrin across all conditions, suggesting synaptic exchange rate is independent of cluster size (**Supplementary Figure S6**). Moreover, no statistical difference was found in γ2 or gephyrin extrasynaptic exchange rates (**Figure 6D**). These findings suggest concurrent reduction of gephyrin and GABA$_A$R synaptic confinement is a compensatory response to mitigate prolonged DZP potentiation of GABA$_A$Rs.

Co-immunoprecipitation and Quantitative Proteomics of γ2 GABA$_A$R Following DZP Injection

We sought to observe DZP-induced changes in receptor trafficking *in vivo*. As an orthogonal approach, we utilized label-free quantitative proteomics to measure changes in the quantities

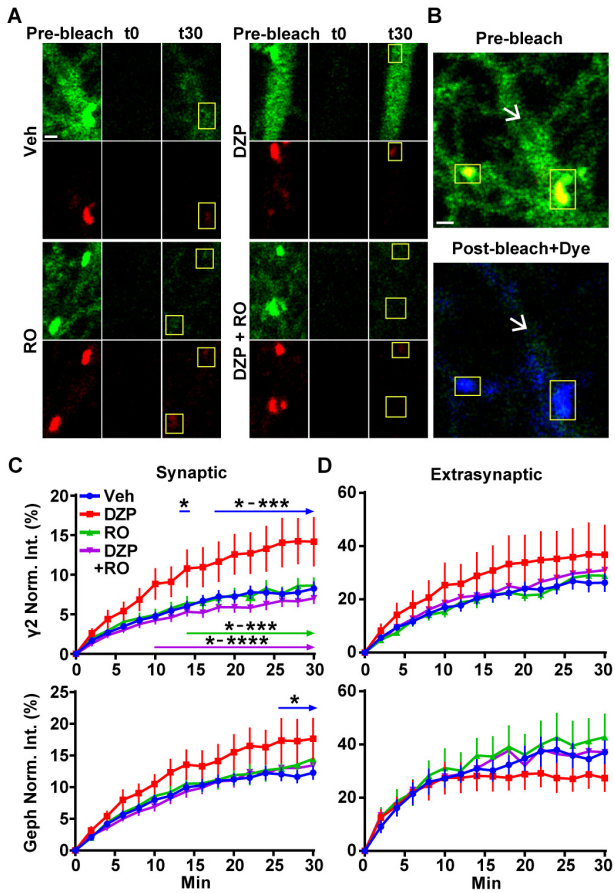


FIGURE 6 | Prolonged DZP exposure accelerates γ2 GABA$_A$R and gephyrin synaptic exchange. **(A)** Neurons expressing γ2^{pH}FAP GABA$_A$R (green) and RFP-gephyrin (red) were treated with vehicle or DZP for 20–28 h ± Ro 15-1788 for the last 1–2 h. Neurons were imaged at 37°C in constant presence of treatment. Initial image of dendrites taken prior to photobleaching (Pre-bleach), then imaged post-bleach (t0) every 2 min for 30 min. Images of dendritic regions show synaptic cluster sites (yellow boxes) and extrasynaptic regions. **(B)** 10 nM MG-BTau dye (blue) was added immediately after bleaching events in **(A)** to resolve bleached γ2^{pH}FAP GABA$_A$Rs and provide spatial accuracy for time series measurements. Panels show enlargement of vehicle dendritic regions identified in **(A)**. Yellow boxes indicate synaptic clusters and arrows indicate extrasynaptic region seen by pHGFP fluorescence in pre-bleach (green) followed by post-bleach labeling with Mg-Btau (blue). **(C,D)** Fluorescence recovery of γ2 GABA$_A$R and gephyrin measured at synaptic sites and extrasynaptic sites from **(A)**. Synapse = γ2^{pH}FAP cluster colocalized with gephyrin cluster. Int., fluorescence intensity. Image scale bars = 1 μm (*$p \leq 0.05$, **$p < 0.01$, ***$p < 0.001$, ****$p < 0.0001$, two-way ANOVA; Tukey's multiple comparisons test; 4–8 synapses and one 10 μm extrasynaptic region per cell; n = 51–56 synapses from 16 neurons per treatment; 4 independent cultures; error bars ± s.e.m).

of proteins associated with γ2-GABA$_A$Rs in the cortex of mice after DZP. Cortical tissue was collected from DZP- or vehicle-treated mice 12 h post injection, lysed, and immunoprecipitated with anti-γ2 subunit antibody or IgG control. Following label-free mass spectrometry analysis, spectrum counts were used to assess relative abundance of γ2-associated proteins. A total of 395 proteins were identified using our inclusion criteria: minimum of two peptides; identified in at least three samples overall or in two of three samples in a specific treatment group; demonstrated at least 3:1 enrichment over IgG control across at least three samples overall (**Supplementary Dataset 1**). The relative abundance of γ2-GABA$_A$R associated proteins in the DZP group compared to vehicle was used to determine which proteins were increased (**Table 1**) or decreased (**Table 2**). As a result we identified 46 proteins with elevated levels of interaction with γ2-GABA$_A$Rs, including 10 proteins that were only found in the DZP treated group (**Table 1**, not found in vehicle samples, NF-V). Notably, we found a significant ($p < 0.05$) increase in γ2 association with 14-3-3 protein family members tyrosine 3-monooxygenase/tryptophan 5-monooxygenase activation protein gamma (also known as 14-3-3γ) and tyrosine 3-monooxygenase/tryptophan 5-monooxygenase activation protein epsilon (also known as 14-3-3ε), the phosphatase protein phosphatase 3 catalytic subunit alpha (also known as calcineurin/PPP3CA) and a near significant increase in the GABA$_A$R α5 subunit ($p = 0.057$), suggesting DZP induced changes in GABA$_A$R surface trafficking (Qian et al., 2012; Nakamura T. et al., 2016), synaptic retention (Bannai et al., 2009, 2015; Muir et al., 2010; Niwa et al., 2012; Eckel et al., 2015), and receptor composition (van Rijnsoever et al., 2004). In contrast, 23 proteins were found to co-immunoprecipitate with γ2 less in DZP animals relative to control, seven of which were only present in the vehicle treatment group (**Table 2**, not found in DZP, NF-DZP). Interestingly, the calcium-sensitive kinase CaMKIIα, which can regulate GABA$_A$R membrane insertion, synaptic retention and drug binding properties (26, 70–72), was found to be significantly decreased in interaction with γ2-GABA$_A$R following DZP injection *in vivo*.

Bioinformatics Analysis of the γ2 GABA$_A$R Interactome

To better understand the consequences of the DZP-induced shift in the γ2-GABA$_A$R protein interaction network, protein fold change data was subjected to core Ingenuity Pathway Analysis (IPA). Top enriched canonical pathways with −log(p-value) > 6.2 are shown in **Figure 7**. Notably, GABA receptor signaling pathways were highly enriched, as expected, although IPA was unable to determine pathway activation status by z-score analysis. γ2-GABA$_A$R association with proteins involved in 14-3-3 mediated signaling and RhoA signaling pathways were greatly increased after DZP (**Figure 7A**, orange), while interaction with proteins involved in EIF2 signaling and sirtuin signaling pathways were reduced (**Figure 7A**, blue) relative to vehicle.

We further examined alterations in functional network association relevant to receptor trafficking by checking the predicted activation status of select pathways when only using proteins which were found to be increased or decreased (**Tables 1**, **2**). **Figure 7B** lists γ2-GABA$_A$R major functional pathways found to be altered by DZP, contributing to processes such as endocytosis (z-score = 2.626), organization of cytoskeleton (z-score = 0.672), and development of neurons (z-score = −0.293). Significant protein changes ($p < 0.05$)

TABLE 1 | Proteins demonstrating increased association with γ2-$GABA_ARs$ after DZP *in vivo* by mass spectrometry.

Ratio DZP/V	*P*-value	UniProtKB	Gene ID	Entrez gene name	Location	Type(s)
9.6	8.9E-02	Q14BI2	GRM2	Glutamate metabotropic receptor 2	Plasma Membrane	G-protein coupled receptor
9.5	4.3E-02	P12960	CNTN1	Contactin 1	Plasma Membrane	Enzyme
7.0	5.9E-02	P11276	FN1	Fibronectin 1	Extracellular Space	Enzyme
5.4	2.7E-02	E9Q4P0	KXD1	KxDL motif containing 1	Cytoplasm	Other
5.4	3.1E-02	Q62277	SYP	Synaptophysin	Cytoplasm	Transporter
5.0	5.0E-03	Q9QXY6	EHD3	EH domain containing 3	Cytoplasm	Other
5.0	7.8E-02	P48774	GSTM3	Glutathione *S*-transferase mu 3	Cytoplasm	Enzyme
4.9	1.9E-05	P38647	HSPA9	Heat shock protein family A (Hsp70) member 9	Cytoplasm	Other
4.7	6.4E-02	Q91V41	RAB14	RAB14, member RAS oncogene family	Cytoplasm	Enzyme
4.2	6.4E-02	P48758	CBR1	Carbonyl reductase 1	Cytoplasm	Enzyme
4.2	7.2E-02	Q8K3F6	KCNQ3	Potassium voltage-gated channel subfamily Q member 3	Plasma Membrane	Ion channel
4.2	3.3E-02	A0A0R4J036	Nefm	Neurofilament, medium polypeptide	Plasma Membrane	Other
4.0	7.9E-02	Q921I1	TF	Transferrin	Extracellular Space	Transporter
3.8	8.6E-02	Q9CYZ2	TPD52L2	Tumor protein D52 like 2	Cytoplasm	Other
3.3	4.2E-02	Q99KI0	ACO2	Aconitase 2	Cytoplasm	Enzyme
2.6	8.0E-02	Q9EQF6	DPYSL5	Dihydropyrimidinase like 5	Cytoplasm	Enzyme
2.4	2.2E-02	P56480	ATP5F1B	ATP synthase F1 subunit beta	Cytoplasm	Transporter
2.4	9.2E-02	P46096	SYT1	Synaptotagmin 1	Cytoplasm	Transporter
2.4	3.7E-02	Q6P1J1	CRMP1	Collapsin response mediator protein 1	Cytoplasm	Enzyme
2.2	3.8E-02	Q9DB20	ATP5PO	ATP synthase peripheral stalk subunit OSCP	Cytoplasm	Transporter
1.9	N.A.	P61027	RAB10	RAB10, member RAS oncogene family	Cytoplasm	Enzyme
1.8	9.6E-02	P63017	HSPA8	Heat shock protein family A (Hsp70) member 8	Cytoplasm	Enzyme
1.8	1.8E-02	P63011	RAB3A	RAB3A, member RAS oncogene family	Cytoplasm	Enzyme
1.8	1.3E-02	P17426-2	AP2A1	Adaptor related protein complex 2 subunit alpha 1	Cytoplasm	Transporter
1.7	9.1E-02	P18760	CFL1	Cofilin 1	Nucleus	Other
1.7	8.2E-02	Q9Z2I9	SUCLA2	Succinate-CoA ligase ADP-forming beta subunit	Cytoplasm	Enzyme
1.7	4.0E-02	P63328	PPP3CA	Protein phosphatase 3 catalytic subunit alpha	Cytoplasm	Phosphatase
1.7	7.1E-02	Q8R191	SYNGR3	Synaptogyrin 3	Plasma Membrane	Other
1.6	5.7E-02	Q8BHJ7	GABRA5	Gamma-aminobutyric acid type A receptor alpha5 subunit	Plasma Membrane	Ion channel
1.6	1.8E-02	O35129	PHB2	Prohibitin 2	Cytoplasm	Transcription regulator
1.6	1.6E-02	P61982	YWHAG	Tyrosine 3-monooxygenase/tryptophan 5-monooxygenase activation protein gamma (14-3-3 gamma)	Cytoplasm	Other
1.5	5.3E-02	P07901	HSP90AA1	Heat shock protein 90 alpha family class A member 1	Cytoplasm	Enzyme
1.5	7.8E-03	P67778	PHB	Prohibitin	Nucleus	Transcription regulator
1.5	8.1E-02	Q3UGC7	EIF3J	Eukaryotic translation initiation factor 3 subunit J	Cytoplasm	Translation regulator
1.5	7.5E-02	Q8VEM8	SLC25A3	Solute carrier family 25 member 3	Cytoplasm	Transporter
1.3	3.3E-02	P60710	ACTB	Actin beta	Cytoplasm	Other
NF-V	7.9E-04	P62259	YWHAE	Tyrosine 3-monooxygenase/tryptophan 5-monooxygenase activation protein epsilon (14-3-3 epsilon)	Cytoplasm	Other
NF-V	1.0E-02	P63044	VAMP2	Vesicle associated membrane protein 2	Plasma Membrane	Other
NF-V	1.6E-02	P46660	INA	Internexin neuronal intermediate filament protein alpha	Cytoplasm	Other
NF-V	3.7E-02	Q9QYM9	TMEFF2	Transmembrane protein with EGF like and two follistatin like domains 2	Cytoplasm	Other
NF-V	4.1E-02	Q6PHN9	RAB35	RAB35, member RAS oncogene family	Cytoplasm	Enzyme
NF-V	6.0E-02	P19246	NEFH	Neurofilament heavy	Cytoplasm	Other
NF-V	6.3E-02	Q9CZ13	UQCRC1	Ubiquinol-cytochrome c reductase core protein 1	Cytoplasm	Enzyme
NF-V	1.2E-06	Q9CQQ7	ATP5PB	ATP synthase peripheral stalk-membrane subunit b	Cytoplasm	Transporter
NF-V	2.8E-06	P80317	CCT6A	Chaperonin containing TCP1 subunit 6A	Cytoplasm	Other
NF-V	2.8E-06	Q9CWS0	DDAH1	Dimethylarginine dimethylaminohydrolase 1	Cytoplasm	Enzyme

Ratio DZP/V is fold change in DZP animals' peptide spectral counts (SC) relative to control vehicle treated animals. NF-V, not found in vehicle samples. N = 3 animals per treatment condition, t-test. Significant results ($p < 0.05$) and near significant results ($p < 0.1$) are shown.

TABLE 2 | Proteins demonstrating decreased association with γ2-$GABA_ARs$ after DZP *in vivo* by mass spectrometry.

Ratio DZP/V	*P*-value	UniProtKB	Gene ID	Entrez gene name	Location	Type(s)
0.2	3.4E-02	P62717	RPL18A	Ribosomal protein L18a	Cytoplasm	Other
0.2	3.9E-02	P62874	GNB1	G protein subunit beta 1	Plasma Membrane	Enzyme
0.2	4.2E-02	Q60900-2	ELAVL3	ELAV like RNA binding protein 3	Nucleus	Other
0.2	5.8E-02	Q920I9	WDR7	WD repeat domain 7	Cytoplasm	Other
0.3	2.0E-02	P53026	RPL10A	Ribosomal protein L10a	Nucleus	Other
0.3	3.4E-02	Q91VM5	Rbmxl1	RNA binding motif protein, X-linked like-1	Nucleus	Other
0.4	6.9E-02	P49312	Hnrnpa1	Heterogeneous nuclear ribonucleoprotein A1	Nucleus	Other
0.4	8.5E-02	Q8BG05	Hnrnpa3	Heterogeneous nuclear ribonucleoprotein A3	Nucleus	Transporter
0.4	7.9E-02	Q922F4	TUBB6	Tubulin beta 6 class V	Cytoplasm	Other
0.5	5.2E-02	P62334	PSMC6	Proteasome 26S subunit, ATPase 6	Nucleus	Peptidase
0.5	2.9E-04	P11798	CAMK2A	Calcium/calmodulin dependent protein kinase II alpha	Cytoplasm	Kinase
0.5	3.6E-02	E9PV14	EPB41L1	Erythrocyte membrane protein band 4.1 like 1	Plasma Membrane	Other
0.7	6.8E-02	P16330	CNP	2′,3′-cyclic nucleotide 3′ phosphodiesterase	Cytoplasm	Enzyme
0.7	7.6E-02	O35643	AP1B1	Adaptor related protein complex 1 subunit beta 1	Cytoplasm	Transporter
0.8	1.4E-02	P68369	TUBA1A	Tubulin alpha 1a	Cytoplasm	Other
0.8	8.0E-02	P52480	PKM	Pyruvate kinase M1/2	Cytoplasm	Kinase
NF-DZP	1.5E-02	P61358	RPL27	Ribosomal protein L27	Cytoplasm	Other
NF-DZP	3.5E-02	Q9Z1X4-3	ILF3	Interleukin enhancer binding factor 3	Nucleus	Transcription regulator
NF-DZP	5.5E-02	Q80UJ0	ELAVL2	ELAV like RNA binding protein 2	Cytoplasm	Other
NF-DZP	2.8E-06	Q3UHB8	CCDC177	Coiled-coil domain containing 177	Other	Other
NF-DZP	2.8E-06	P49615	CDK5	Cyclin dependent kinase 5	Nucleus	Kinase
NF-DZP	2.8E-06	Q6ZWV3	RPL10	Ribosomal protein L10	Cytoplasm	Translation regulator
NF-DZP	2.8E-06	Q9CQ69	UQCRQ	Ubiquinol-cytochrome c reductase complex III subunit VII	Cytoplasm	Enzyme

Ratio DZP/V is fold change in DZP animals' peptide SC relative to control vehicle treated animals. NF-DZP, not found in DZP samples. N = 3 animals per treatment condition, t-test. Significant results ($p < 0.05$) and near significant results ($p < 0.1$) are shown.

conserved between two or more pathways include decreased γ2-$GABA_AR$ association with CAMKIIα and CDK5 and enhanced association with calcineurin/PPP3CA, the intracellular trafficking protein RAB35 and the cytoskeletal protein NEFH (also known as heavy neurofilament protein). As an additional measurement, we performed gene ontology (GO) database analysis of proteins which were found to be increased in DZP treated mice relative to vehicle control (**Table 3**). GO analysis identified enrichment in γ2 association with proteins involved in intracellular trafficking and cellular localization biological pathways after DZP, consistent with IPA analysis findings. Taken together, these results suggest DZP modifies intracellular and surface trafficking of γ2-$GABA_ARs$ both *in vitro* and *in vivo*.

DISCUSSION

This work identifies key trafficking pathways involved in $GABA_AR$ neuroplasticity in response to initial DZP exposure. Using a combination of biochemical and imaging techniques, we identified total γ2 subunit levels are diminished in response to 12–24 h of DZP exposure *in vitro* and *in vivo*. Concurrent with the decrease in the overall γ2 pool, we found DZP treatment enhanced ubiquitination of this subunit. Use of an innovative optical sensor for BZD sensitive $GABA_AR$ ($\gamma2^{pH}FAP$) in combination with MG dye pulse-labeling approaches revealed DZP exposure moderately enhanced targeting of surface γ2-$GABA_ARs$ to lysosomes. Live-imaging experiments with pH 7.4 NH_4Cl revealed increased intracellular receptor pools, providing further evidence that DZP enhances γ2-$GABA_AR$ lysosomal accumulation, a response reversed by BZD antagonist Ro 15-1788 treatment. We used novel intersubunit FRET based live-imaging to identify that surface synaptic α2/γ2 $GABA_ARs$ were specifically decreased after DZP, suggesting these receptor complexes were subjected to ubiquitination, lysosomal targeting, and degradation. In addition to DZP modulation of receptor trafficking, the postsynaptic scaffolding protein gephyrin demonstrated significant plasticity including increased Ser270 phosphorylation and production of gephyrin proteolytic fragments, concurrent with a decrease in total and membrane full-length gephyrin levels and ERK inactivation. Given the fundamental role of gephyrin in scaffolding $GABA_ARs$ and regulating synaptic confinement, we used simultaneous FRAP live-imaging of receptors and scaffold in neurons to monitor inhibitory synaptic dynamics. We found ∼24 h DZP exposure accelerates both the rate of gephyrin and $GABA_AR$ exchange at synapses as shown by enhanced fluorescence recovery rates. Control experiments using the BZD antagonist Ro 15-1788 were able to reverse the DZP induced loss of synaptic confinement, reducing gephyrin and $GABA_AR$ mobility back to vehicle levels. Finally, we used label-free quantitative mass spectrometry and bioinformatics to identify key changes in γ2-$GABA_AR$ protein association *in vivo* suggesting alterations in trafficking at the cell surface and intracellularly. Collectively, this work defines a DZP-induced reduction of gephyrin scaffolding coupled with increased synaptic exchange of gephyrin and $GABA_ARs$.

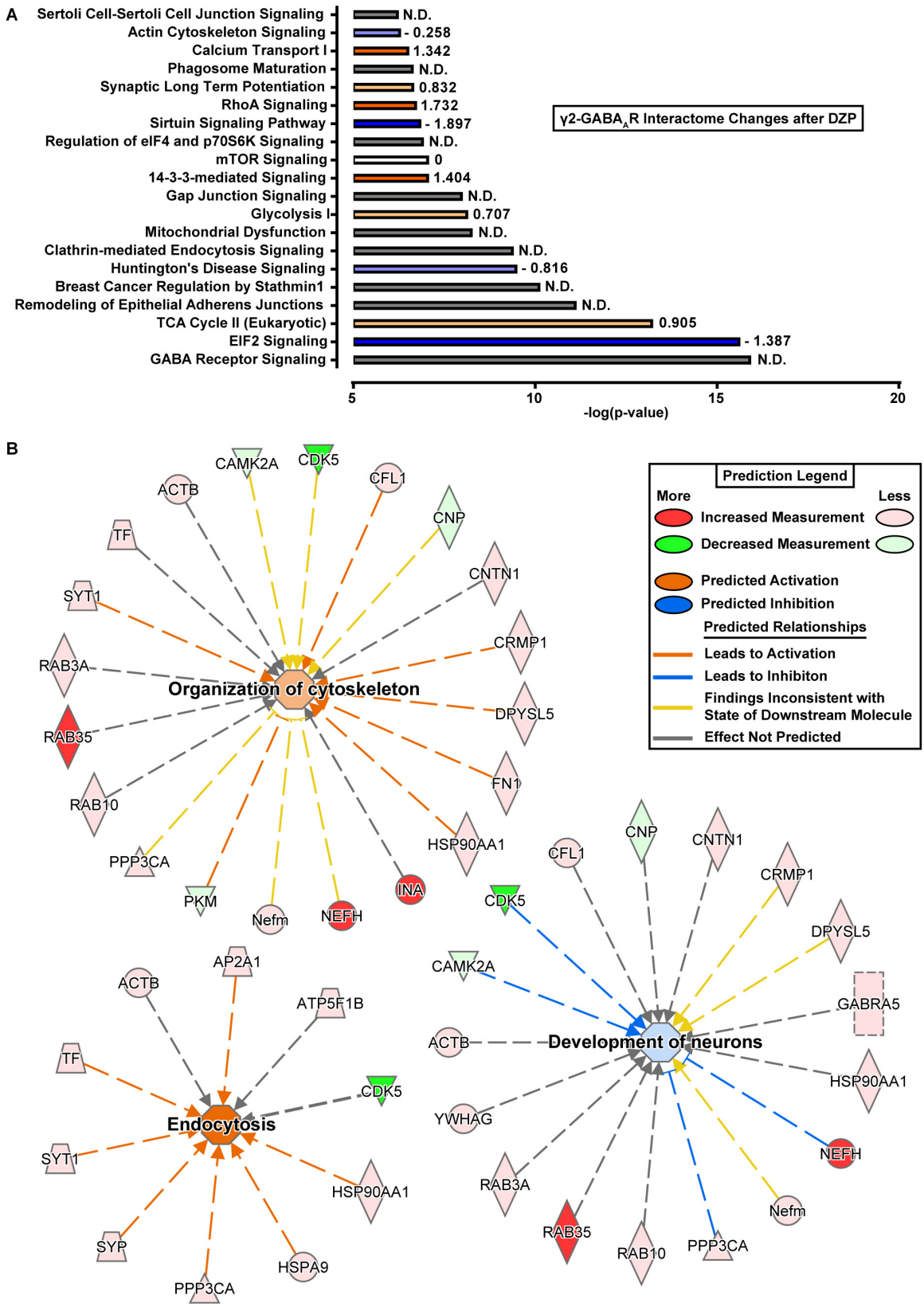


FIGURE 7 | Continued

FIGURE 7 | Ingenuity pathway analysis reveals shifts in protein interaction networks following DZP exposure. **(A)** Canonical pathways found to be enriched with γ2-$GABA_A$Rs and differentially expressed following DZP administration *in vivo*. Enriched pathways with –log(*p*-value) greater than 6.2 were considered as calculated by Fisher's exact test right-tailed. Values to right of bars represent pathway activation *z*-score. Positive *z*-score represents predicted upregulation of a pathway (orange), negative *z*-score predicts inhibition (blue), *z*-score = 0 represents no change in pathway (white), while not determined (N.D.) conveys the analysis program was unable to determine a significant change (gray). Intensity of color represents size of *z*-score value. **(B)** Functional network association of select pathways when using proteins which were found to be increased or decreased with a $p < 0.1$. Major functional pathways altered by DZP include endocytosis (*z*-score = 2.626), organization of cytoskeleton (*z*-score = 0.672), and development of neurons (*z*-score = –0.293). Significant protein changes ($p < 0.05$) conserved between two or more pathways include decreased γ2-$GABA_A$R association with CAMKIIα and CDK5 and enhanced association with calcineurin/PPP3CA, the intracellular trafficking protein RAB35 and the cytoskeletal protein NEFH (also known as heavy neurofilament protein). Red = increased measurement, green = decreased measurement, orange = activation of pathway, blue = inhibition of pathway, yellow = findings inconsistent with state of downstream molecule, gray = effect not predicted.

TABLE 3 | GO analysis reveals enrichment of intracellular trafficking, transport, and protein localization pathways after DZP.

GO biological process	GO term ID	Fold enrichment	*P*-value
Transport	GO:0006810	4.2	9.8E-09
Establishment of localization	GO:0051234	4.0	2.5E-08
Establishment of localization in cell	GO:0051649	6.8	2.0E-07
Localization	GO:0051179	3.3	2.5E-07
Intracellular transport	GO:0046907	7.2	1.6E-06
Regulation of localization	GO:0032879	4.3	3.7E-06
Intracellular protein transport	GO:0006886	9.1	7.8E-06
Regulation of transport	GO:0051049	5.1	2.2E-05
Cellular localization	GO:0051641	4.8	4.8E-05
Protein transport	GO:0015031	6.1	2.2E-04

Proteins found to have enhanced association with γ2-$GABA_A$Rs during Scaffold analysis were searched in the GO Ontology database for biological process pathway enrichments. PANTHER Overrepresentation test and Fisher's Exact test with Bonferroni correction for multiple testing was used to determine significance.

This dynamic flux of $GABA_A$Rs between synapses and the extrasynaptic space was associated with enhanced γ2-$GABA_A$R accumulation in intracellular vesicles and γ2-$GABA_A$R subtype specific lysosomal degradation. We propose DZP treatment alters these key intracellular and surface trafficking pathways ultimately diminishing responsiveness to DZP.

Numerous classical studies have examined gene and protein expression adaptations in $GABA_A$R subunits after BZD exposure with minimal agreement that a specific change occurs (Bateson, 2002; Uusi-Oukari and Korpi, 2010; Vinkers and Olivier, 2012). Here molecular mechanistic insight is provided, through direct measurements of enhanced ubiquitination of the γ2 subunit (**Figure 2**), lysosomal targeting (**Figure 3**), reduced surface synaptic α2/γ2 $GABA_A$R levels (**Figure 4**), and reduced synaptic confinement (**Figure 6**) of DZP-sensitive $GABA_A$Rs. Together this suggests BZD exposure primarily decreases synaptic retention of γ2 containing $GABA_A$R while downregulating surface levels of the α2 subunit. Ubiquitination of the γ2 subunit by the E3 ligase Ring Finger Protein 34 (RNF 34) (Jin et al., 2014) is the only currently known mechanism targeting internalized synaptic $GABA_A$Rs to lysosomes (Arancibia-Carcamo et al., 2009). Due to the requirement of the γ2 subunit in all BZD-sensitive $GABA_A$Rs, it is likely that ubiquitination of the γ2 subunit is a contributing factor for increased lysosomal-mediated degradation in response to DZP. Despite a small decrease in the γ2 total protein, changes in surface levels were not significant by biochemical approaches, consistent with evidence that γ2-$GABA_A$R surface levels are tightly regulated to maintain baseline inhibition and prevent excitotoxicity. For example, in heterozygous γ2 knockout mice a 50% reduction in γ2 levels appears to be compensated by increased cell surface trafficking, resulting in only an approximately 25% reduction in BZD binding sites in the cortex and a limited reduction in synaptic $GABA_A$R clusters (Crestani et al., 1999; Ren et al., 2015). In contrast, homozygous γ2 knockout mice show a complete loss of behavioral drug response to BZD and over 94% of the BZD sites in the brain (GABA binding sites unchanged) and early lethality (Gunther et al., 1995). Similarly, studies have shown that prolonged $GABA_A$R agonist or BZD application increases γ2 $GABA_A$R internalization in cultured neurons, while surface $GABA_A$R levels are variably affected (Chaumont et al., 2013; Nicholson et al., 2018). Importantly, by using high sensitivity surface $GABA_A$R intersubunit FRET measurements we were able to detect a decrease in BZD sensitive α2/γ2 $GABA_A$Rs (**Figure 4**).

The role of inhibitory scaffolding changes in responsiveness to BZD has been largely under investigated. Phosphorylation of gephyrin at Ser270 is mediated by CDK5 and GSK3β, while a partnering and functionally relevant Ser268 site is regulated by ERK (Tyagarajan et al., 2013). DZP time series experiments revealed a global decrease in ERK phosphorylation but not GSK3β, without a change in total kinase levels of ERK, GSK3β, or CDK5 over the course of the assay (except 12 h ERK) (**Figure 5**). A previous model by Tyagarajan et al. (2013) using gephyrin point mutants at Ser268 and Ser270 suggested that enhanced Ser270 phosphorylation coupled with decreased Ser268 phosphorylation by ERK promotes gephyrin remodeling and calpain-1 degradation. This is consistent with the ERK inactivation measured in our data and the increase in gephyrin Ser270 phosphorylation demonstrated by immunofluorescence after DZP (**Figure 1**), enhanced gephyrin degradation and decreased full-length gephyrin levels (**Figures 1**, **2**). Calpain-1 mediated gephyrin cleavage can occur within 1 min in hippocampal membranes (Kawasaki et al., 1997), and cleavage products are increased following *in vitro* ischemia at 30 min and up to 48 h following ischemic events *in vivo* (Costa et al., 2015). Gephyrin cleavage may be occurring at earlier time points than the DZP 24 h mark measured here (**Figures 2F,G**), coinciding with ERK dephosphorylation as early as 45 min (**Figures 5A,B**). One limitation of our results is that measuring total and phospho levels of these kinases does not directly address changes in association or

regulation of gephyrin, although it does provide an additional piece of evidence supporting gephyrin cleavage by calpain-1 and scaffold remodeling. Accordingly, our previous work found 30 min treatment with the $GABA_AR$ agonist muscimol in immature neurons (depolarizing) leads to ERK/BDNF signaling and decreased Ser270 phosphorylated gephyrin levels at synapses and overall (Brady et al., 2017). Thus, ERK activation status negatively correlates with the level of phosphorylation at gephyrin Ser270.

Recent work has demonstrated 12 h DZP treatment of organotypic hippocampal slices expressing eGFP-gephyrin causes enhanced gephyrin mobility at synapses and reduced gephyrin cluster size (Vlachos et al., 2013). Here we found the synaptic exchange rate of γ2 $GABA_ARs$ and gephyrin to be nearly doubled at synapses in cortical neurons after ∼24 h DZP exposure (**Figure 6**). γ2 extrasynaptic fluorescence recovery in DZP treated neurons was variable but also trended toward an increase relative to controls (**Figure 6**), which could be a result of increased diffusion of receptors out of the synaptic space. This effect occurred coincident with the formation of truncated gephyrin cleavage products (**Figure 2**), which has previously been shown to decrease γ2 synaptic levels (Costa et al., 2015). These findings are also consistent with our previous work showing RNAi gephyrin knockdown doubles the rate of γ2-$GABA_AR$ turnover at synaptic sites (Jacob et al., 2005). Later quantum dot single particle tracking studies confirmed γ2 synaptic residency time is linked to gephyrin scaffolding levels (Renner et al., 2012). Importantly, $GABA_AR$ diffusion dynamics also reciprocally regulate gephyrin scaffolding levels (Niwa et al., 2012), suggesting gephyrin and $GABA_ARs$ synaptic residency are often functionally coupled. Accordingly, γ2 subunit and gephyrin levels both decrease in responses to other stimuli including status epilepticus (Gonzalez et al., 2013) or prolonged inhibition of IP_3 receptor-dependent signaling (Bannai et al., 2015). Additionally, chemically induced inhibitory long-term potentiation (iLTP) protocols demonstrate gephyrin accumulation occurs concurrent with the synaptic recruitment of $GABA_ARs$ within 20 min (Petrini et al., 2014). Collectively, these proteins display a high degree of interdependence across different experimental paradigms of inhibitory synapse plasticity occurring over minutes to days.

Increasing receptor synaptic retention enhances synaptic currents, while enhanced receptor diffusion via decreased scaffold interactions reduces synaptic currents. For example, reduction of gephyrin binding by replacement of the α1 $GABA_AR$ subunit gephyrin binding domain with non-gephyrin binding homologous region of the α6 subunit results in faster receptor diffusion rates and a direct reduction in mIPSC amplitude (Mukherjee et al., 2011). Similarly, enhanced diffusion of $GABA_ARs$ following estradiol treatment also reduces mIPSCs in cultured neurons and in hippocampal slices (Mukherjee et al., 2017). In contrast, brief DZP exposure (<1 h) reduces $GABA_AR$ synaptic mobility (Levi et al., 2015) without a change in surface levels (Gouzer et al., 2014), consistent with initial synaptic potentiation of $GABA_AR$ neurotransmission by DZP. Together with our current findings, this suggests post-translational modifications on $GABA_AR$ subunits or gephyrin that enhance receptor diffusion are a likely key step leading to functional tolerance to BZD drugs.

It is a significant technical challenge to examine dynamic alterations in receptor trafficking occurring *in vivo*. To overcome this we examined changes in γ2-$GABA_AR$ protein association following DZP injection in mice using quantitative proteomics and bioinformatics analysis. This work revealed shifts toward γ2-$GABA_AR$ association with protein pathway networks associated with endocytosis and organization of cytoskeleton (**Figure 7B** and **Table 3**), confirming similar fluctuations in membrane and intracellular trafficking occur *in vivo* and *in vitro* after DZP. We also found that shifts in association of proteins involved in the development of neurons (CAMKIIα, CDK5, NEFH, and calcineurin/PPP3CA) suggested an inhibition in this pathway after DZP (**Figure 7B**). When considering all protein hits between vehicle and DZP, γ2-$GABA_AR$ association with proteins involved in 14-3-3 mediated signaling and RhoA signaling pathways were greatly increased after DZP (**Figure 7A**, orange), while interaction with proteins involved in EIF2 signaling and sirtuin signaling pathways were reduced (**Figure 7A**, blue). 14-3-3 proteins are heavily linked in $GABA_AR$ intracellular to surface trafficking (Qian et al., 2012; Nakamura T. et al., 2016), and the RhoA signaling pathway is directly involved in actin cytoskeleton organization (Negishi and Katoh, 2002) and α5-$GABA_AR$ anchoring (Hausrat et al., 2015), providing further evidence of $GABA_AR$ shifts in membrane and cytosolic trafficking after DZP exposure.

Recent inhibitory synapse proteomics studies have identified a number of new protein synaptic constituents or modulators of $GABA_AR$ function (Butko et al., 2013; Kang et al., 2014; Nakamura Y. et al., 2016; Uezu et al., 2016; Ge et al., 2018). We show here that proteins known to have roles in synaptic function and trafficking of membrane receptors show changes in their association with γ2-receptors. For example, the calcium-sensitive kinase CaMKIIα was found to be significantly decreased in interaction with γ2-$GABA_AR$ following DZP, which can regulate $GABA_AR$ membrane insertion, synaptic retention and drug binding properties (Churn et al., 2002; Marsden et al., 2010; Saliba et al., 2012; Petrini et al., 2014) (**Table 2**). Calcineurin/PPP3CA has been recognized as a key regulator of $GABA_AR$ synaptic retention and plasticity (Bannai et al., 2009; Muir et al., 2010; Niwa et al., 2012; Bannai et al., 2015; Eckel et al., 2015) and has been linked to the response to DZP *in vitro* (Nicholson et al., 2018). Here we provide the first evidence that DZP exposure enhances the association of calcineurin with γ2-$GABA_ARs$ *in vivo*. Furthermore, DZP was found to enhance γ2 association with 14-3-3 protein family members (**Table 1**), which are known mediators of $GABA_AR$ surface and intracellular trafficking (Qian et al., 2012; Nakamura T. et al., 2016). γ2 coassembly with the $GABA_AR$ α5 subunit was also elevated post DZP exposure (**Table 1**). Interestingly, the α5 subunit is required for the development of BZD sedative tolerance in mice (van Rijnsoever et al., 2004). It is notable that our proteomic studies are in part limited by the specificity of our antibody used and general downstream effects of reduced neuronal activity.

Future follow up studies using the DZP site antagonist R015-1788 will be needed to dissect the individual roles of proteins found to be significantly altered in their association with $GABA_AR$, and their physiological and pharmacological importance to BZD tolerance and inhibitory neurotransmission.

Through application of novel and highly sensitive fluorescence imaging approaches combined with *in vivo* proteomics, we provide unprecedented resolution of $GABA_AR$ synapse plasticity induced by BZDs at both the level of the single neuron and cortex. Our study reveals that sustained initial DZP treatment diminishes synaptic BZD sensitive $GABA_AR$ availability through multiple fundamental cellular mechanisms: through reduction of the post-synaptic scaffolding protein gephyrin; shifts toward intracellular trafficking pathways and targeting of receptors for lysosomal degradation; and enhanced synaptic exchange of both gephyrin and $GABA_ARs$. Proteomic and bioinformatics studies using DZP-treated mouse brain tissue provide further evidence that altered γ2-$GABA_AR$ surface and intracellular trafficking mechanisms play a critical role to the response to DZP *in vivo*. These results define key events leading to BZD irresponsiveness in initial sustained drug exposure. Future studies utilizing this dual approach will address the neuroadaptations produced by long term BZD use to systematically identify the effects of a critical drug class that has seen a tripling in prescription numbers over the last two decades (Bachhuber et al., 2016).

AUTHOR CONTRIBUTIONS

JL-G and TJ designed the research. JL-G, TJ, and SW wrote and revised the manuscript. JL-G performed the biochemistry, immunoprecipitation, bioinformatics analysis and fixed and live imaging acquisition and analysis in **Figures 1–6**. MB performed the FRET imaging and analysis. JL-G and SD performed the tissue collection. TJ, JL-G, and SW designed the Mass spectrometry experiments. SW and the Weintraub lab performed mass spectrometry and data was analyzed by JL-G, TJ, and SW.

FUNDING

This work was supported by funding from National Institutes of Health Grants R56MH114908-01 (to TJ), T32GM008424 (to JL-G), F31MH117839-01 (to JL-G), University of Pittsburgh Pharmacology and Chemical Biology Fellowship (to JL-G, William C. deGroat Neuropharmacology Departmental Fellowship), NARSAD young investigator grant R01MH114908-01A1 (to TJ) and Pharmacology and Chemical Biology Startup Funds.

ACKNOWLEDGMENTS

We thank Jonathan Beckel for technical advice on qRT-PCR and Katarina Vajn for assistance with neuronal cultures. Mass spectrometry analyses were conducted at the UTHSCSA Institutional Mass Spectrometry Laboratory, supported in part by UTHSCSA and the University of Texas System for purchase of the Orbitrap Fusion Lumos mass spectrometer. The expert technical assistance of Sammy Pardo and Dana Molleur is gratefully acknowledged. This manuscript has been released as a Pre-Print at bioRxiv (Lorenz-Guertin et al., 2019).

SUPPLEMENTARY MATERIAL

The Supplementary Material for this article can be found online at: https://www.frontiersin.org/articles/10.3389/fncel.2019.00163/full#supplementary-material

REFERENCES

Ali, N. J., and Olsen, R. W. (2001). Chronic benzodiazepine treatment of cells expressing recombinant GABA(A) receptors uncouples allosteric binding: studies on possible mechanisms. *J. Neurochem.* 79, 1100–1108. doi: 10.1046/j.1471-4159.2001.00664.x

Alldred, M. J., Mulder-Rosi, J., Lingenfelter, S. E., Chen, G., and Luscher, B. (2005). Distinct gamma2 subunit domains mediate clustering and synaptic function of postsynaptic GABAA receptors and gephyrin. *J. Neurosci.* 25, 594–603. doi: 10.1523/jneurosci.4011-04.2005

Arancibia-Carcamo, I. L., Yuen, E. Y., Muir, J., Lumb, M. J., Michels, G., Saliba, R. S., et al. (2009). Ubiquitin-dependent lysosomal targeting of GABA(A) receptors regulates neuronal inhibition. *Proc. Natl. Acad. Sci. U.S.A.* 106, 17552–17557. doi: 10.1073/pnas.0905502106

Bachhuber, M. A., Hennessy, S., Cunningham, C. O., and Starrels, J. L. (2016). Increasing benzodiazepine prescriptions and overdose mortality in the united states, 1996-2013. *Am. J. Public Health* 106, 686–688. doi: 10.2105/ajph.2016.303061

Bannai, H., Levi, S., Schweizer, C., Inoue, T., Launey, T., Racine, V., et al. (2009). Activity-dependent tuning of inhibitory neurotransmission based on GABAAR diffusion dynamics. *Neuron* 62, 670–682. doi: 10.1016/j.neuron.2009.04.023

Bannai, H., Niwa, F., Sherwood, M. W., Shrivastava, A. N., Arizono, M., Miyamoto, A., et al. (2015). Bidirectional control of synaptic GABAAR clustering by glutamate and calcium. *Cell Rep.* 13, 2768–2780. doi: 10.1016/j.celrep.2015.12.002

Bateson, A. N. (2002). Basic pharmacologic mechanisms involved in benzodiazepine tolerance and withdrawal. *Curr. Pharm. Des.* 8, 5–21. doi: 10.2174/1381612023396681

Battaglia, S., Renner, M., Russeau, M., and Come, E. (2018). Activity-dependent inhibitory synapse scaling is determined by gephyrin phosphorylation and subsequent regulation of GABAA receptor diffusion. *eNeuro* 5:ENEURO.0203-17.2017. doi: 10.1523/eneuro.0203-17.2017

Bogdanov, Y., Michels, G., Armstrong-Gold, C., Haydon, P. G., Lindstrom, J., Pangalos, M., et al. (2006). Synaptic GABAA receptors are directly recruited from their extrasynaptic counterparts. *EMBO J.* 25, 4381–4389. doi: 10.1038/sj.emboj.7601309

Brady, M. L., and Jacob, T. C. (2015). Synaptic localization of alpha5 GABA (A) receptors via gephyrin interaction regulates dendritic outgrowth and spine maturation. *Dev. Neurobiol.* 75, 1241–1251. doi: 10.1002/dneu.22280

Brady, M. L., Pilli, J., Lorenz-Guertin, J. M., Das, S., Moon, C. E., Graff, N., et al. (2017). Depolarizing, inhibitory GABA type A receptor activity regulates GABAergic synapse plasticity via ERK and BDNF signaling. *Neuropharmacology* 128, 324–339. doi: 10.1016/j.neuropharm.2017.10.022

Butko, M. T., Savas, J. N., Friedman, B., Delahunty, C., Ebner, F., Yates, J. R. III, et al. (2013). In vivo quantitative proteomics of somatosensory cortical synapses shows which protein levels are modulated by sensory deprivation. *Proc. Natl. Acad. Sci. U.S.A.* 110, E726–E735. doi: 10.1073/pnas.1300424110

Chaumont, S., Andre, C., Perrais, D., Boue-Grabot, E., Taly, A., and Garret, M. (2013). Agonist-dependent endocytosis of gamma-aminobutyric acid type A (GABAA) receptors revealed by a gamma2(R43Q) epilepsy mutation. *J. Biol. Chem.* 288, 28254–28265. doi: 10.1074/jbc.M113.470807

Churn, S. B., Rana, A., Lee, K., Parsons, J. T., De Blas, A., and Delorenzo, R. J. (2002). Calcium/calmodulin-dependent kinase II phosphorylation of the GABAA receptor alpha1 subunit modulates benzodiazepine binding. *J. Neurochem.* 82, 1065–1076. doi: 10.1046/j.1471-4159.2002.01032.x

Costa, J. T., Mele, M., Baptista, M. S., Gomes, J. R., Ruscher, K., Nobre, R. J., et al. (2015). Gephyrin cleavage in in vitro brain ischemia decreases GABA receptor clustering and contributes to neuronal death. *Mol. Neurobiol.* 53, 3513–3527. doi: 10.1007/s12035-015-9283-2

Crestani, F., Lorez, M., Baer, K., Essrich, C., Benke, D., Laurent, J. P., et al. (1999). Decreased GABAA-receptor clustering results in enhanced anxiety and a bias for threat cues. *Nat. Neurosci.* 2, 833–839. doi: 10.1038/12207

Crider, A., Pandya, C. D., Peter, D., Ahmed, A. O., and Pillai, A. (2014). Ubiquitin-proteasome dependent degradation of GABAAα1 in autism spectrum disorder. *Mol. Autism* 5:45. doi: 10.1186/2040-2392-5-45

Dantuma, N. P., Groothuis, T. A., Salomons, F. A., and Neefjes, J. (2006). A dynamic ubiquitin equilibrium couples proteasomal activity to chromatin remodeling. *J. Cell Biol.* 173, 19–26. doi: 10.1083/jcb.200510071

Di, X. J., Wang, Y. J., Han, D. Y., Fu, Y. L., Duerfeldt, A. S., Blagg, B. S., et al. (2016). Grp94 protein delivers gamma-aminobutyric acid type a (GABAA) receptors to Hrd1 protein-mediated endoplasmic reticulum-associated degradation. *J. Biol. Chem.* 291, 9526–9539. doi: 10.1074/jbc.M115.705004

Eckel, R., Szulc, B., Walker, M. C., and Kittler, J. T. (2015). Activation of calcineurin underlies altered trafficking of alpha2 subunit containing GABAA receptors during prolonged epileptiform activity. *Neuropharmacology* 88, 82–90. doi: 10.1016/j.neuropharm.2014.09.014

Essrich, C., Lorez, M., Benson, J. A., Fritschy, J. M., and Luscher, B. (1998). Postsynaptic clustering of major GABAA receptor subtypes requires the gamma 2 subunit and gephyrin. *Nat. Neurosci.* 1, 563–571. doi: 10.1038/2798

File, S. E., Wilks, L. J., and Mabbutt, P. S. (1988). Withdrawal, tolerance and sensitization after a single dose of lorazepam. *Pharmacol. Biochem. Behav.* 31, 937–940. doi: 10.1016/0091-3057(88)90408-x

Flores, C. E., Nikonenko, I., Mendez, P., Fritschy, J. M., Tyagarajan, S. K., and Muller, D. (2015). Activity-dependent inhibitory synapse remodeling through gephyrin phosphorylation. *Proc. Natl. Acad. Sci. U.S.A.* 112, E65–E72. doi: 10.1073/pnas.1411170112

Förster, T. (1965). *Delocalized Excitation and Excitation Transfer*. New York, NY: Academic Press Inc.

Gallager, D. W., Lakoski, J. M., Gonsalves, S. F., and Rauch, S. L. (1984). Chronic benzodiazepine treatment decreases postsynaptic GABA sensitivity. *Nature* 308, 74–77. doi: 10.1038/308074a0

Ge, Y., Kang, Y., Cassidy, R. M., Moon, K. M., Lewis, R., Wong, R. O. L., et al. (2018). Clptm1 limits forward trafficking of GABAA receptors to scale inhibitory synaptic strength. *Neuron* 97, 596–610.e8. doi: 10.1016/j.neuron.2017.12.038

Ghosh, H., Auguadri, L., Battaglia, S., Simone Thirouin, Z., Zemoura, K., Messner, S., et al. (2016). Several posttranslational modifications act in concert to regulate gephyrin scaffolding and GABAergic transmission. *Nat. Commun.* 7:13365. doi: 10.1038/ncomms13365

Gonzalez, M. I., Cruz Del Angel, Y., and Brooks-Kayal, A. (2013). Down-regulation of gephyrin and GABAA receptor subunits during epileptogenesis in the CA1 region of hippocampus. *Epilepsia* 54, 616–624. doi: 10.1111/epi.12063

Gouzer, G., Specht, C. G., Allain, L., Shinoe, T., and Triller, A. (2014). Benzodiazepine-dependent stabilization of GABA(A) receptors at synapses. *Mol. Cell. Neurosci.* 63, 101–113. doi: 10.1016/j.mcn.2014.10.004

Gu, Y., Chiu, S. L., Liu, B., Wu, P. H., Delannoy, M., Lin, D. T., et al. (2016). Differential vesicular sorting of AMPA and GABAA receptors. *Proc. Natl. Acad. Sci. U.S.A.* 113, E922–E931. doi: 10.1073/pnas.1525726113

Gunther, U., Benson, J., Benke, D., Fritschy, J. M., Reyes, G., Knoflach, F., et al. (1995). Benzodiazepine-insensitive mice generated by targeted disruption of the gamma 2 subunit gene of gamma-aminobutyric acid type A receptors. *Proc. Natl. Acad. Sci. U.S.A.* 92, 7749–7753. doi: 10.1073/pnas.92.17.7749

Gutierrez, M. L., Ferreri, M. C., and Gravielle, M. C. (2014). GABA-induced uncoupling of GABA/benzodiazepine site interactions is mediated by increased GABAA receptor internalization and associated with a change in subunit composition. *Neuroscience* 257, 119–129. doi: 10.1016/j.neuroscience.2013.10.077

Hausrat, T. J., Muhia, M., Gerrow, K., Thomas, P., Hirdes, W., Tsukita, S., et al. (2015). Radixin regulates synaptic GABAA receptor density and is essential for reversal learning and short-term memory. *Nat. Commun.* 6:6872. doi: 10.1038/ncomms7872

Holt, R. A., Bateson, A. N., and Martin, I. L. (1999). Decreased GABA enhancement of benzodiazepine binding after a single dose of diazepam. *J. Neurochem.* 72, 2219–2222. doi: 10.1046/j.1471-4159.1999.0722219.x

Jacob, T. C., Bogdanov, Y. D., Magnus, C., Saliba, R. S., Kittler, J. T., Haydon, P. G., et al. (2005). Gephyrin regulates the cell surface dynamics of synaptic GABAA receptors. *J. Neurosci.* 25, 10469–10478. doi: 10.1523/jneurosci.2267-05.2005

Jacob, T. C., Michels, G., Silayeva, L., Haydon, J., Succol, F., and Moss, S. J. (2012). Benzodiazepine treatment induces subtype-specific changes in GABA(A) receptor trafficking and decreases synaptic inhibition. *Proc. Natl. Acad. Sci. U.S.A.* 109, 18595–18600. doi: 10.1073/pnas.1204994109

Jin, H., Chiou, T. T., Serwanski, D. R., Miralles, C. P., Pinal, N., and De Blas, A. L. (2014). Ring finger protein 34 (RNF34) interacts with and promotes gamma-aminobutyric acid type-A receptor degradation via ubiquitination of the gamma2 subunit. *J. Biol. Chem.* 289, 29420–29436. doi: 10.1074/jbc.M114.603068

Kalbouneh, H., Schlicksupp, A., Kirsch, J., and Kuhse, J. (2014). Cyclin-dependent kinase 5 is involved in the phosphorylation of gephyrin and clustering of GABAA receptors at inhibitory synapses of hippocampal neurons. *PLoS One* 9:e104256. doi: 10.1371/journal.pone.0104256

Kang, Y., Ge, Y., Cassidy, R. M., Lam, V., Luo, L., Moon, K. M., et al. (2014). A combined transgenic proteomic analysis and regulated trafficking of neuroligin-2. *J. Biol. Chem.* 289, 29350–29364. doi: 10.1074/jbc.M114.549279

Kawasaki, B. T., Hoffman, K. B., Yamamoto, R. S., and Bahr, B. A. (1997). Variants of the receptor/channel clustering molecule gephyrin in brain: distinct distribution patterns, developmental profiles, and proteolytic cleavage by calpain. *J. Neurosci. Res.* 49, 381–388. doi: 10.1002/(sici)1097-4547(19970801)49:3<381::aid-jnr13>3.0.co;2-2

Kneussel, M., Brandstatter, J. H., Laube, B., Stahl, S., Muller, U., and Betz, H. (1999). Loss of postsynaptic GABA(A) receptor clustering in gephyrin-deficient mice. *J. Neurosci.* 19, 9289–9297. doi: 10.1523/jneurosci.19-21-09289.1999

Kowalczyk, S., Winkelmann, A., Smolinsky, B., Forstera, B., Neundorf, I., Schwarz, G., et al. (2013). Direct binding of GABAA receptor beta2 and beta3 subunits to gephyrin. *Eur. J. Neurosci.* 37, 544–554. doi: 10.1111/ejn.12078

Kuhse, J., Kalbouneh, H., Schlicksupp, A., Mukusch, S., Nawrotzki, R., and Kirsch, J. (2012). Phosphorylation of gephyrin in hippocampal neurons by cyclin-dependent kinase CDK5 at Ser-270 is dependent on collybistin. *J. Biol. Chem.* 287, 30952–30966. doi: 10.1074/jbc.M112.349597

Kumar, A., Dejanovic, B., Hetsch, F., Semtner, M., Fusca, D., Arjune, S., et al. (2017). S-sulfocysteine/NMDA receptor-dependent signaling underlies neurodegeneration in molybdenum cofactor deficiency. *J. Clin. Invest.* 127, 4365–4378. doi: 10.1172/jci89885

Laverty, D., Desai, R., Uchanski, T., Masiulis, S., Stec, W. J., Malinauskas, T., et al. (2019). Cryo-EM structure of the human alpha1beta3gamma2 GABAA receptor in a lipid bilayer. *Nature* 565, 516–520. doi: 10.1038/s41586-018-0833-4

Levi, S., Le Roux, N., Eugene, E., and Poncer, J. C. (2015). Benzodiazepine ligands rapidly influence GABAA receptor diffusion and clustering at hippocampal inhibitory synapses. *Neuropharmacology* 88, 199–208. doi: 10.1016/j.neuropharm.2014.06.002

Li, R. W., Yu, W., Christie, S., Miralles, C. P., Bai, J., Loturco, J. J., et al. (2005). Disruption of postsynaptic GABA receptor clusters leads to decreased GABAergic innervation of pyramidal neurons. *J. Neurochem.* 95, 756–770. doi: 10.1111/j.1471-4159.2005.03426.x

Lister, R. G., and Nutt, D. J. (1986). Mice and rats are sensitized to the proconvulsant action of a benzodiazepine-receptor inverse agonist (FG 7142) following a single dose of lorazepam. *Brain Res.* 379, 364–366. doi: 10.1016/0006-8993(86)90791-2

Lorenz-Guertin, J. M., Bambino, M. J., Das, S., Weintraub, S. T., and Jacob, T. C. (2019). Diazepam accelerates GABAAR synaptic exchange and alters intracellular trafficking. *bioRxiv* [Preprint]. doi: 10.1101/514133

Lorenz-Guertin, J. M., Wilcox, M. R., Zhang, M., Larsen, M. B., Pilli, J., Schmidt, B. F., et al. (2017). A versatile optical tool for studying synaptic GABAA receptor trafficking. *J. Cell Sci.* 130, 3933–3945. doi: 10.1242/jcs.205286

Maric, H. M., Mukherjee, J., Tretter, V., Moss, S. J., and Schindelin, H. (2011). Gephyrin-mediated gamma-aminobutyric acid type A and glycine receptor clustering relies on a common binding site. *J. Biol. Chem.* 286, 42105–42114. doi: 10.1074/jbc.M111.303412

Markowitz, G. J., Kadam, S. D., Boothe, D. M., Irving, N. D., and Comi, A. M. (2010). The pharmacokinetics of commonly used antiepileptic drugs in immature CD1 mice. *Neuroreport* 21, 452–456. doi: 10.1097/wnr.0b013e328338ba18

Marley, R. J., and Gallager, D. W. (1989). Chronic diazepam treatment produces regionally specific changes in GABA-stimulated chloride influx. *Eur. J. Pharmacol.* 159, 217–223. doi: 10.1016/0014-2999(89)90151-9

Marsden, K. C., Shemesh, A., Bayer, K. U., and Carroll, R. C. (2010). Selective translocation of Ca2+/calmodulin protein kinase IIalpha (CaMKIIalpha) to inhibitory synapses. *Proc. Natl. Acad. Sci. U.S.A.* 107, 20559–20564. doi: 10.1073/pnas.1010346107

Masiulis, S., Desai, R., Uchanski, T., Serna Martin, I., Laverty, D., Karia, D., et al. (2019). GABAA receptor signalling mechanisms revealed by structural pharmacology. *Nature* 565, 454–459. doi: 10.1038/s41586-018-0832-5

Muir, J., Arancibia-Carcamo, I. L., MacAskill, A. F., Smith, K. R., Griffin, L. D., and Kittler, J. T. (2010). NMDA receptors regulate GABAA receptor lateral mobility and clustering at inhibitory synapses through serine 327 on the gamma2 subunit. *Proc. Natl. Acad. Sci. U.S.A.* 107, 16679–16684. doi: 10.1073/pnas.1000589107

Mukherjee, J., Cardarelli, R. A., Cantaut-Belarif, Y., Deeb, T. Z., Srivastava, D. P., Tyagarajan, S. K., et al. (2017). Estradiol modulates the efficacy of synaptic inhibition by decreasing the dwell time of GABAA receptors at inhibitory synapses. *Proc. Natl. Acad. Sci. U.S.A.* 114, 11763–11768. doi: 10.1073/pnas.1705075114

Mukherjee, J., Kretschmannova, K., Gouzer, G., Maric, H. M., Ramsden, S., Tretter, V., et al. (2011). The residence time of GABA(A)Rs at inhibitory synapses is determined by direct binding of the receptor alpha1 subunit to gephyrin. *J. Neurosci.* 31, 14677–14687. doi: 10.1523/jneurosci.2001-11.2011

Nakamura, T., Arima-Yoshida, F., Sakaue, F., Nasu-Nishimura, Y., Takeda, Y., Matsuura, K., et al. (2016). PX-RICS-deficient mice mimic autism spectrum disorder in Jacobsen syndrome through impaired GABAA receptor trafficking. *Nat. Commun.* 7:10861. doi: 10.1038/ncomms10861

Nakamura, Y., Morrow, D. H., Modgil, A., Huyghe, D., Deeb, T. Z., Lumb, M. J., et al. (2016). Proteomic characterization of inhibitory synapses using a novel pHluorin-tagged GABAAR alpha2 subunit knock-in mouse. *J. Biol. Chem.* 291, 12394–12407. doi: 10.1074/jbc.M116.724443

Negishi, M., and Katoh, H. (2002). Rho family GTPases as key regulators for neuronal network formation. *J. Biochem.* 132, 157–166. doi: 10.1093/oxfordjournals.jbchem.a003205

Nicholson, M. W., Sweeney, A., Pekle, E., Alam, S., Ali, A. B., Duchen, M., et al. (2018). Diazepam-induced loss of inhibitory synapses mediated by PLCδ/Ca2+/calcineurin signalling downstream of GABAA receptors. *Mol. Psychiatry* 23, 1851–1867. doi: 10.1038/s41380-018-0100-y

Niwa, F., Bannai, H., Arizono, M., Fukatsu, K., Triller, A., and Mikoshiba, K. (2012). Gephyrin-independent GABA(A)R mobility and clustering during plasticity. *PLoS One* 7:e36148. doi: 10.1371/journal.pone.0036148

Petrini, E. M., Ravasenga, T., Hausrat, T. J., Iurilli, G., Olcese, U., Racine, V., et al. (2014). Synaptic recruitment of gephyrin regulates surface GABAA receptor dynamics for the expression of inhibitory LTP. *Nat. Commun.* 5:3921. doi: 10.1038/ncomms4921

Phulera, S., Zhu, H., Yu, J., Claxton, D. P., Yoder, N., Yoshioka, C., et al. (2018). Cryo-EM structure of the benzodiazepine-sensitive α1β1γ2S tri-heteromeric GABAA receptor in complex with GABA. *eLife* 7:e39383. doi: 10.7554/eLife.39383

Pratt, C. P., Kuljis, D. A., Homanics, G. E., He, J., Kolodieznyi, D., Dudem, S., et al. (2017). Tagging of endogenous BK channels with a fluorogen-activating peptide reveals beta4-mediated control of channel clustering in cerebellum. *Front. Cell. Neurosci.* 11:337. doi: 10.3389/fncel.2017.00337

Qian, Z., Micorescu, M., Yakhnitsa, V., and Barmack, N. H. (2012). Climbing fiber activity reduces 14-3-3-theta regulated GABA(A) receptor phosphorylation in cerebellar Purkinje cells. *Neuroscience* 201, 34–45. doi: 10.1016/j.neuroscience.2011.11.021

Ren, Z., Sahir, N., Murakami, S., Luellen, B. A., Earnheart, J. C., Lal, R., et al. (2015). Defects in dendrite and spine maturation and synaptogenesis associated with an anxious-depressive-like phenotype of GABAA receptor-deficient mice. *Neuropharmacology* 88, 171–179. doi: 10.1016/j.neuropharm.2014.07.019

Renner, M., Schweizer, C., Bannai, H., Triller, A., and Levi, S. (2012). Diffusion barriers constrain receptors at synapses. *PLoS One* 7:e43032. doi: 10.1371/journal.pone.0043032

Saliba, R. S., Kretschmannova, K., and Moss, S. J. (2012). Activity-dependent phosphorylation of GABAA receptors regulates receptor insertion and tonic current. *EMBO J.* 31, 2937–2951. doi: 10.1038/emboj.2012.109

Saliba, R. S., Michels, G., Jacob, T. C., Pangalos, M. N., and Moss, S. J. (2007). Activity-dependent ubiquitination of GABA(A) receptors regulates their accumulation at synaptic sites. *J. Neurosci.* 27, 13341–13351. doi: 10.1523/jneurosci.3277-07.2007

Schweizer, C., Balsiger, S., Bluethmann, H., Mansuy, I. M., Fritschy, J. M., Mohler, H., et al. (2003). The gamma 2 subunit of GABA(A) receptors is required for maintenance of receptors at mature synapses. *Mol. Cell. Neurosci.* 24, 442–450. doi: 10.1016/s1044-7431(03)00202-1

Szent-Gyorgyi, C., Schmidt, B. F., Creeger, Y., Fisher, G. W., Zakel, K. L., Adler, S., et al. (2008). Fluorogen-activating single-chain antibodies for imaging cell surface proteins. *Nat. Biotechnol.* 26, 235–240. doi: 10.1038/nbt1368

Szent-Gyorgyi, C., Stanfield, R. L., Andreko, S., Dempsey, A., Ahmed, M., Capek, S., et al. (2013). Malachite green mediates homodimerization of antibody VL domains to form a fluorescent ternary complex with singular symmetric interfaces. *J. Mol. Biol.* 425, 4595–4613. doi: 10.1016/j.jmb.2013.08.014

Tietz, E. I., Chiu, T. H., and Rosenberg, H. C. (1989). Regional GABA/benzodiazepine receptor/chloride channel coupling after acute and chronic benzodiazepine treatment. *Eur. J. Pharmacol.* 167, 57–65. doi: 10.1016/0014-2999(89)90747-4

Tretter, V., Jacob, T. C., Mukherjee, J., Fritschy, J. M., Pangalos, M. N., and Moss, S. J. (2008). The clustering of GABA(A) receptor subtypes at inhibitory synapses is facilitated via the direct binding of receptor alpha 2 subunits to gephyrin. *J. Neurosci.* 28, 1356–1365. doi: 10.1523/jneurosci.5050-07.2008

Tyagarajan, S. K., and Fritschy, J. M. (2014). Gephyrin: a master regulator of neuronal function? *Nat. Rev. Neurosci.* 15, 141–156. doi: 10.1038/nrn3670

Tyagarajan, S. K., Ghosh, H., Yevenes, G. E., Imanishi, S. Y., Zeilhofer, H. U., Gerrits, B., et al. (2013). Extracellular signal-regulated kinase and glycogen synthase kinase 3beta regulate gephyrin postsynaptic aggregation and GABAergic synaptic function in a calpain-dependent mechanism. *J. Biol. Chem.* 288, 9634–9647. doi: 10.1074/jbc.M112.442616

Tyagarajan, S. K., Ghosh, H., Yevenes, G. E., Nikonenko, I., Ebeling, C., Schwerdel, C., et al. (2011). Regulation of GABAergic synapse formation and plasticity by GSK3beta-dependent phosphorylation of gephyrin. *Proc. Natl. Acad. Sci. U.S.A.* 108, 379–384. doi: 10.1073/pnas.1011824108

Uezu, A., Kanak, D. J., Bradshaw, T. W., Soderblom, E. J., Catavero, C. M., Burette, A. C., et al. (2016). Identification of an elaborate complex mediating postsynaptic inhibition. *Science* 353, 1123–1129. doi: 10.1126/science.aag0821

Uusi-Oukari, M., and Korpi, E. R. (2010). Regulation of GABA(A) receptor subunit expression by pharmacological agents. *Pharmacol. Rev.* 62, 97–135. doi: 10.1124/pr.109.002063

van Rijnsoever, C., Tauber, M., Choulli, M. K., Keist, R., Rudolph, U., Mohler, H., et al. (2004). Requirement of alpha5-GABAA receptors for the development of tolerance to the sedative action of diazepam in mice. *J. Neurosci.* 24, 6785–6790. doi: 10.1523/jneurosci.1067-04.2004

Van Sickle, B. J., Xiang, K., and Tietz, E. I. (2004). Transient plasticity of hippocampal CA1 neuron glutamate receptors contributes to benzodiazepine withdrawal-anxiety. *Neuropsychopharmacology* 29, 1994–2006. doi: 10.1038/sj.npp.1300531

Vinkers, C. H., and Olivier, B. (2012). Mechanisms underlying tolerance after long-term benzodiazepine use: a future for subtype-selective GABA(A) receptor modulators? *Adv. Pharmacol. Sci.* 2012:416864. doi: 10.1155/2012/416864

Vlachos, A., Reddy-Alla, S., Papadopoulos, T., Deller, T., and Betz, H. (2013). Homeostatic regulation of gephyrin scaffolds and synaptic strength at mature hippocampal GABAergic postsynapses. *Cereb. Cortex* 23, 2700–2711. doi: 10.1093/cercor/bhs260

Wafford, K. A., Thompson, S. A., Thomas, D., Sikela, J., Wilcox, A. S., and Whiting, P. J. (1996). Functional characterization of human gamma-aminobutyric acidA receptors containing the alpha 4 subunit. *Mol. Pharmacol.* 50, 670–678.

Wong, P. T., Yoong, Y. L., and Gwee, M. C. (1986). Acute tolerance to diazepam induced by benzodiazepines. *Clin. Exp. Pharmacol. Physiol.* 13, 1–8. doi: 10.1111/j.1440-1681.1986.tb00309.x

Xie, X. H., and Tietz, E. I. (1992). Reduction in potency of selective gamma-aminobutyric acidA agonists and diazepam in CA1 region of in vitro hippocampal slices from chronic flurazepam-treated rats. *J. Pharmacol. Exp. Ther.* 262, 204–211.

Yoong, Y. L., Lee, H. S., Gwee, M. C., and Wong, P. T. (1986). Acute tolerance to diazepam in mice: pharmacokinetic considerations. *Clin. Exp. Pharmacol. Physiol.* 13, 153–158. doi: 10.1111/j.1440-1681.1986.tb00329.x

Zacchi, P., Antonelli, R., and Cherubini, E. (2014). Gephyrin phosphorylation in the functional organization and plasticity of GABAergic synapses. *Front. Cell. Neurosci.* 8:103. doi: 10.3389/fncel.2014.00103

Zhu, S., Noviello, C. M., Teng, J., Walsh, R. M. Jr., Kim, J. J., and Hibbs, R. E. (2018). Structure of a human synaptic GABAA receptor. *Nature* 559, 67–72. doi: 10.1038/s41586-018-0255-3

Conflict of Interest Statement: The authors declare that the research was conducted in the absence of any commercial or financial relationships that could be construed as a potential conflict of interest.

Copyright © 2019 Lorenz-Guertin, Bambino, Das, Weintraub and Jacob. This is an open-access article distributed under the terms of the Creative Commons Attribution License (CC BY). The use, distribution or reproduction in other forums is permitted, provided the original author(s) and the copyright owner(s) are credited and that the original publication in this journal is cited, in accordance with accepted academic practice. No use, distribution or reproduction is permitted which does not comply with these terms.

frontiers in Cellular Neuroscience

ORIGINAL RESEARCH
published: 16 May 2019
doi: 10.3389/fncel.2019.00204

Human Mesenchymal Stem Cells Prevent Neurological Complications of Radiotherapy

Bernat Soria[1,2], Alejandro Martin-Montalvo[1], Yolanda Aguilera[1], Nuria Mellado-Damas[1], Javier López-Beas[1], Isabel Herrera-Herrera[3], Escarlata López[4], Juan A. Barcia[5], Manuel Alvarez-Dolado[1], Abdelkrim Hmadcha[1,2] and Vivian Capilla-González[1]*†*

[1] Department of Regeneration and Cell Therapy, Andalusian Center for Molecular Biology and Regenerative Medicine (CABIMER), University of Pablo de Olavide – University of Seville, CSIC, Seville, Spain, [2] Centro de Investigación Biomédica en Red de Diabetes y Enfermedades Metabólicas Asociadas (CIBERDEM), Madrid, Spain, [3] Department of Neuroradiology, Hospital Universitario Fundación Jiménez Díaz, Madrid, Spain, [4] Department of Radiation Oncology, Hospital Universitario Fundación Jiménez Díaz, Madrid, Spain, [5] Service of Neurosurgery, Hospital Clínico San Carlos, Instituto de Investigación Sanitaria San Carlos (IdISSC), Department of Surgery, Universidad Complutense de Madrid, Madrid, Spain

OPEN ACCESS

Edited by:
Jose Manuel Garcia-Verdugo,
University of Valencia, Spain

Reviewed by:
Munjal M. Acharya,
University of California, Irvine, United States
Rachel Sarabia Estrada,
Mayo Clinic Florida, United States

***Correspondence:**
Abdelkrim Hmadcha
karim.hmadcha@cabimer.es
Vivian Capilla-González
vivian.capilla@cabimer.es

†Lead author

Specialty section:
This article was submitted to Cellular Neurophysiology, a section of the journal Frontiers in Cellular Neuroscience

Received: 31 January 2019
Accepted: 24 April 2019
Published: 16 May 2019

Citation:
Soria B, Martin-Montalvo A, Aguilera Y, Mellado-Damas N, López-Beas J, Herrera-Herrera I, López E, Barcia JA, Alvarez-Dolado M, Hmadcha A and Capilla-González V (2019) Human Mesenchymal Stem Cells Prevent Neurological Complications of Radiotherapy. Front. Cell. Neurosci. 13:204. doi: 10.3389/fncel.2019.00204

Radiotherapy is a highly effective tool for the treatment of brain cancer. However, radiation also causes detrimental effects in the healthy tissue, leading to neurocognitive sequelae that compromise the quality of life of brain cancer patients. Despite the recognition of this serious complication, no satisfactory solutions exist at present. Here we investigated the effects of intranasal administration of human mesenchymal stem cells (hMSCs) as a neuroprotective strategy for cranial radiation in mice. Our results demonstrated that intranasally delivered hMSCs promote radiation-induced brain injury repair, improving neurological function. This intervention confers protection against inflammation, oxidative stress, and neuronal loss. hMSC administration reduces persistent activation of damage-induced c-AMP response element-binding signaling in irradiated brains. Furthermore, hMSC treatment did not compromise the survival of glioma-bearing mice. Our findings encourage the therapeutic use of hMSCs as a non-invasive approach to prevent neurological complications of radiotherapy, improving the quality of life of brain tumor patients.

Keywords: radiotherapy, stem cells, cognition, neuroprotection, intranasal cell delivery, CREB, neurocognitive sequelae, brain cancer

INTRODUCTION

Radiotherapy is one of the most common treatments for cancer. Around 50% of all tumor patients receive radiation at a given time (Delaney et al., 2005). Unfortunately, radiotherapy comes with short and long term side effects. In particular, radiation for brain tumors, the most common cancer in children (Ostrom et al., 2016), causes accelerated aging that is manifested as neurofunctional sequelae, which may be progressive and permanent (Douw et al., 2009; Marazziti et al., 2012; Padovani et al., 2012; Armstrong et al., 2013; Ma et al., 2017). The most frequently described adverse effects of cranial radiation include learning and memory difficulties, problems in executive functions, motor coordination, visual alterations and intellectual decline. These radiation-related sequelae compromise the quality of life of cancer survivors

and represent a serious clinical problem with no satisfactory solutions at present.

Studies in brain cancer patients and rodent evidences that radiation-related neurofunctional sequelae are associated with a variety of anatomical changes that occur in the irradiated non-tumoral tissue (Makale et al., 2017). Immediately after radiation, brain exhibits vascular damages, oligodendrocyte loss, demyelination and neuroinflammation. Radiation-induced brain injury also disrupts the neurogenic niches located at the dentate gyrus (DG) of the hippocampus and the subventricular zone (SVZ) of the lateral ventricles. Moreover, brain injury also affects neuronal dendritic spines and white matter, leading to necrosis of specific areas. The discovery of the negative effects induced by radiation in the non-tumoral tissue has promoted the development of strategies to minimize radiotherapy side effects. In this context, stem cell-based therapy represents a novel alternative to attenuate radiation-induced brain injury (Acharya et al., 2011, 2015; Joo et al., 2012; Piao et al., 2015). In this line, Joo et al. (2012) described the benefits of supplementing whole-brain irradiated mice with fetal mouse neural stem cells (NSCs), which were injected via tail vein 24 h after radiation. The irradiated brain induced homing of the exogenous NSCs, which differentiated along glial and neuronal lineages. Two months after NSC administration, mice showed inhibited radiation-induced hippocampus atrophy and preserved short-term memory. Similarly, human embryonic stem cell-derived oligodendrocyte progenitors (hOPCs) have provided promising results. After bilateral injections into the corpus callosum of rats, hOPCs were able to remyelinate the brain and ameliorate radiation-induced cognitive dysfunction (Piao et al., 2015). However, stem cell-based therapies proposed in current studies present some restrictions that need to be solved if translation to human is sought (Ramos-Zuriga et al., 2012). First, several studies used stem cells with scarce availability and whose isolation procedure is highly invasive (e.g., NSCs). Second, the routes used for administration have limited effectiveness (e.g., systemic transplantation renders reduced concentration of transplanted cells in the brain) or requires invasive techniques that risk host safety (e.g., intracranial injections). Here we explored the non-invasive intranasal delivery of human mesenchymal stem cells (hMSCs) derived from adipose tissue to prevent radiation-induced brain damage in a mouse model of whole-brain radiation. Our results demonstrated that transplanted hMSCs promoted neuroprotection and improved neurological function after irradiation, without compromising survival of glioma-bearing mice.

MATERIALS AND METHODS

Animals

Two-month-old male C57BL/6 mice were purchased from Charles River Laboratories (Barcelona, Spain). For cell transplant, two-month-old male immunodeficient athymic nude mice (Charles River Laboratories) were used to maximize the non-rejection and survival of transplanted cells. Experimental groups were randomly assigned. Mice were housed in a specific pathogen free animal facility. Animals were maintained on a 12-h light/dark cycle, with stable temperature (22°C) and humidity (60%), and with food and water available *ad libitum*.

X-Ray Irradiation

Mice were anesthetized via intraperitoneal injection of a combination of 100 mg/kg ketamine and 10 mg/kg xylazine. Then, animals were positioned in a prone position in the X-ray irradiation device (MBR-1505R; Hitachi, Tokyo, Japan) for head-only irradiation, as described elsewhere (Suarez-Pereira et al., 2015). Animals were irradiated at 160 kV and 6.3 mA with a lead shield covering the entire body, excluding the head. A total dose of 10 Gy in 2 fractions (2×5 Gy) was delivered at a source-to-skin distance of 33 cm. Control animals were littermates handled similarly and did not receive radiation.

hMSC Culture

Human mesenchymal stem cell (ATCC, PCS-500-011™; see **Supplementary Table 1** for cell lines information) were cultured in growth media composed of Dulbecco's Modified Eagle Medium (DMEM; Life Technologies, Carlsbad, CA) supplemented with 10% fetal bovine sera and 1% penicillin-streptomycin, and incubated at 37°C in a 20% O_2 and 5% CO_2 humidified atmosphere. Media were changed every 2–3 days. For all experiments, hMSCs were used at passage 4–7. The ability of hMSCs to generate multiple lineages and express established MSC markers was previously verified (Capilla-Gonzalez et al., 2018).

hMSC Transplantation and Biodistribution

Human mesenchymal stem cell treatment was initiated the day after radiation. Briefly, animals were anesthetized and placed in a supine position to administrate total of 100 U of hyaluronidase as 2 repeated inoculations in each nostril with 5-min intervals (3 μl per inoculation). After 30 min, 5×10^5 of hMSCs in PBS were delivered as 2 repeated inoculations in each nostril with 5-min intervals (3 μl per inoculation). Mice received a dose of cells per week during 4 consecutive weeks. Control mice received hyaluronidase followed by PBS. For evaluation of cell biodistribution, cultured hMSCs were incubated with 400 μg/mL XenoLight DiR fluorescent dye (Perkin Elmer, Inc., Boston, MA) for 30 min at 37°C before transplantation. Transplanted mice were daily monitored using an IVIS Imaging System 200 Series (Caliper Life Science, Hopkinton, MA).

Behavioral Tests

Neurological function was tested between day 33 and day 44 post-radiation using a battery of behavioral tests, following previously described protocols. First, motor coordination was evaluated by *rotarod* performance (Lopez-Noriega et al., 2017) on days 33–34. Second, muscle strength was evaluated by the *wirehang* test (Klein et al., 2012) on day 35. Third,

olfaction was evaluated by measuring odor discrimination capacity in a two-odorants test (*habituation-dishabituation test*) (Capilla-Gonzalez et al., 2012) on day 37. Finally, cognition was assessed by performing the *novel object recognition* task with a long habituation phase, using odorless objects that do not retain any olfactory cues (Leger et al., 2013), on days 40–44.

Microarray

RNA was isolated from the brain lateral ventricle (PLv) and the hippocampus (Hipp) using the RNeasy Mini Kit (Qiagen, Hilden, Germany). 100 ng of RNA was used to obtain the gene expression profile of each sample. All samples showed the characteristics of high-quality RNA and were subjected to subsequent analysis. cDNA was hybridized to the Clariom^{TM} S Assay Mouse Array (Affymetrix, Santa Clara, CA) using manufacturer's protocol (Affymetrix, GeneChip WT PLUS). Microarrays were scanned using the GeneChip Scanner 3000 7G of Affymetrix. Data processing and statistical analysis was performed using Transcriptome Analysis Console (TAC) software from Affymetrix, using default parameters. Canonical pathway analysis was performed using Ingenuity Pathway Analysis (IPA) software from Qiagen. Venn diagrams were generated using the open-source online tool Venny 2.1.0. Microarray data are deposited in Gene Expression Omnibus (GEO) database repository (accession number: GSE115735).

Western Blots

Dissected PLv and Hipp were lysed for protein extraction using RIPA buffer (Sigma-Aldrich, Madrid, Spain), containing 0.5% sodium deoxycholate, 1 mM PMSF, 2 mM EDTA, 1× protease inhibitor (Roche Diagnostics, Mannheim, Germany) and 1× phosphatase inhibitor cocktail (Thermo Fisher Scientific, Madrid, Spain). Proteins from whole tissue lysates (25 μg) were resolved using 10% Tris-Glycine gel electrophoresis, and transferred onto nitrocellulose membranes (Whatman, Dassel, Germany). Membranes were then blocked with 5% non-fat milk and primary antibodies were probed (see **Supplementary Table 1** for antibody information). Detection was done with the appropriate horseradish-peroxidase conjugated secondary antibodies and using the enhanced chemiluminescence reagent (GE Healthcare Life Sciences, Buckinghamshire, United Kingdom). Densitometric analyses for the blots were performed using ImageJ software (version 1.4r; National Institute of Health, Bethesda, MD) and normalized to Ponceau S staining or GAPDH expression.

Brain Tissue Fixation

Mice were anesthetized and subjected to intracardiac perfusion using a peristaltic pump. As a fixative, 2% paraformaldehyde and 2.5% glutaraldehyde was used for electron microscopy, while 4% paraformaldehyde was used for immunohistochemistry. Brains were removed and post-fixed in the same fixative solution overnight.

Transmission Electron Microscopy

Fixed brains were rinsed in 0.1 M phosphate buffer (PB) and cut into 200 μm sections using a VT 1000M vibratome (Leica, Wetzlar, Germany). Sections were postfixed in 2% osmium tetroxide, dehydrated in ethanol, stained in 2% uranyl acetate and embedded in araldite (Durcupan, Fluka BioChemika, Ronkokoma, NY). Ultrathin sections (60–70 nm) were cut with a diamond knife, stained with lead citrate, and examined under a Spirit transmission electron microscope (FEI Tecnai, Hillsboro, OR) (Capilla-Gonzalez et al., 2010).

Immunohistochemistry

Fixed brains were rinsed in 0.1 M phosphate buffer (PB) and cut into serial 10 μm thick sections using a CM 3050S cryostat (Leica, Mannheim, Germany). Sections were incubated in blocking solution for 1 h at room temperature, followed by overnight incubation at 4°C with primary antibodies (see **Supplementary Table 1** for antibody information). Then, sections were washed and incubated with the appropriate secondary antibodies conjugated with fluorophores and examined under a Leica DM6000B microscope or Leica TC5 SP5 confocal microscope and imaged with the Leica Application Suite software. Fluorescence signal was quantified using ImageJ or MetaMorph software (Molecular Devices, San Jose, CA).

Brain Tumor Model

To investigate the side effects effect of transplanting hMSCs into mice bearing a brain tumor, 7-weeks-old male immunodeficient athymic nude mice were stereotactically injected with 0.5×10^6 glioma cells (U87MG; ATCC, HTB-14^{TM}; see **Supplementary Table 1** for cell lines information) into the right striatum (A: 0.5, L: 2.0, D: 3.5). The stereotactic surgery procedure was done as previously described (Capilla-Gonzalez et al., 2014). Prior transplantation, glioma cells were labelled with the XenoLight DiR fluorescent dye, following the same protocol described for hMSCs labeling. The days after cell transplant, mice were imaged using an IVIS Imaging System 200 Series (Caliper Life Science, Hopkinton, MA) to ensure that grafted cells form a tumor. Ten days after tumor cell injection, animals were randomly distributed into three groups: mice bearing a brain tumor (n = 11), mice bearing a brain tumor that received radiation (n = 11), and mice bearing a brain tumor that received radiation and hMSCs (n = 12). Radiation and hMSC transplant were given as described above. Mice were euthanized when the condition of the animal was considered incompatible with continued survival. Survival curves were plotted using the Kaplan–Meier method, which include any animal found dead or euthanized. Histopathological analysis of brains at time of death was performed on cryosections stained with hematoxylin and eosin method.

Statistical Analysis

Data were expressed as mean ± SEM. Data were analyzed using the GraphPad Prism 7 software (GraphPad Software Inc., San Diego, CA) and SigmaPlot 12.0 software (Jandel Scientific, San Rafael, CA). The t-test was performed to compare two means,

while ANOVA was performed to compare more than two means. Repeated-measures ANOVA and Multiple *t*-test were applied when appropriated. Log-rank test was performed to determine differences in survival. All differences were considered significant at a p value <0.05.

RESULTS

Radiation Induces Anatomical Changes in the Mouse Brain

To characterize the impact of radiation in mouse brain, two month-old C57BL/6 mice were subjected to whole-brain radiation (total dose of 10 Gy). The histopathological analysis of mouse brain tissue by electron microscopy revealed frequent necrotic cells and microglia 30 days post-radiation (**Figures 1A–C**). Microglia staining to detect Iba1 expression evidenced bushy microglia (activated cells) in the irradiated brain that manifested an inflammatory state, while the non-irradiated brain displayed more ramified microglia (resting cells) (**Figures 1D–E**). Furthermore, NSCs residing in the irradiated brain frequently presented envelope-limited chromatin sheets (i.e., quiescent NSCs), while NSCs in the non-irradiated brain often displayed condensed chromosomes associated with an early prophase (i.e., active NSCs) (**Figure 1F**). This observation was in line with the reduced proliferation (Ki67 staining) and scarce newly born neurons (DCX, doublecortin staining) in the DG and SVZ after radiation, while the NSC marker nestin showed no evident differences (**Figures 1G–J**).

hMSCs Reached the Brain After Intranasal Administration

To validate that the intranasal route is a feasible via to deliver cells to the brain, XenoLight DiR-labeled hMSCs were administrated into the nostrils of athymic nude mice (a dose of cells per week during 4 consecutive weeks) (**Supplementary Figure 1**). A cohort of animals was injected with PBS as control group. Biodistribution analysis revealed that 2 h after the first dose of cells, fluorescence was restricted to the head, becoming maximal at day 1 and then tending to gradually decrease within the following 6 days (**Figures 2A,B**). However, the repeated doses of cells presented a cumulative effect that allowed to prolong fluorescence signal over time (**Supplementary Figure 1**). Temporary fluorescence signal was observed in the peritoneal region 24 h after cell delivery (**Supplementary Figure 1**). No signal was observed in mice treated with PBS at any time point. In order to demonstrate the presence of hMSCs in the brain, a group of mice was sacrificed the day after cell administration and brains were dissected. Fluorescence signal was detected in the olfactory bulbs and frontal lobes (**Figure 2C**). To analyze whether hMSCs persist into the brain on day 50, immunofluorescence against human-specific mitochondria (hMito) and human-specific nuclei (hNuclei) was performed in brain sections. Immunostaining revealed the presence of some human cells at different levels of the rostrocaudal brain axis (**Supplementary Figure 1**). Necropsies did not reveal any visible

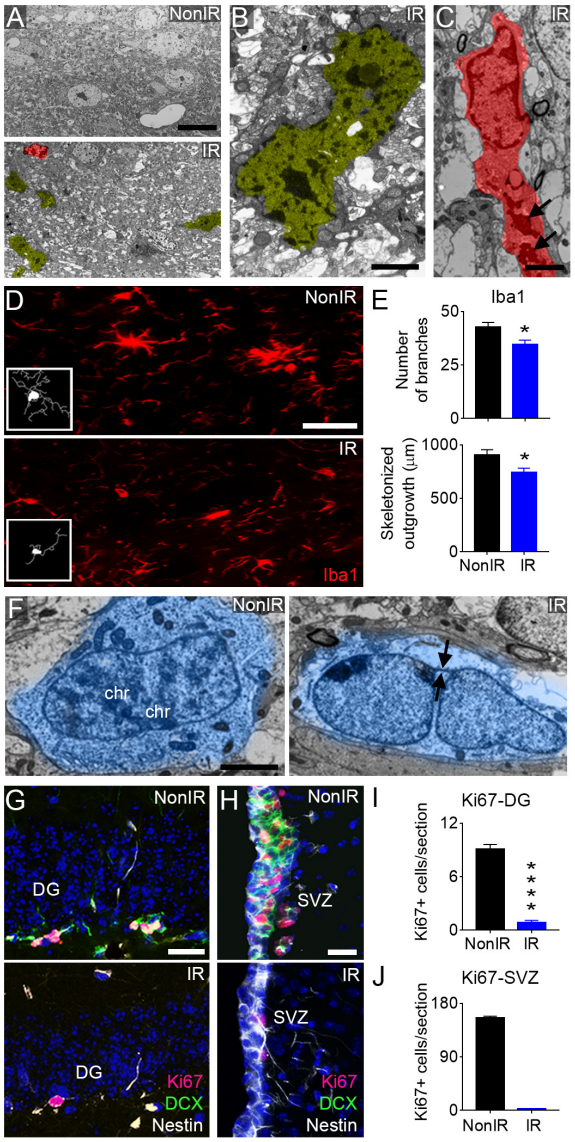


FIGURE 1 | Radiation induces anatomical changes in the mouse brain. Representative images of radiation-induced damages in the mouse brain 30 days post-radiation (total dose of 10 Gy). **(A)** Electron microscopy micrograph showing multiple pyknotic cells (yellow) and microglia (red) in the irradiated brain, compared to non-irradiated mice. **(B)** High magnification of a pyknotic cell in the irradiated brain. **(C)** High magnification of a microglia cell in the irradiated brain displaying round shape and abundant dense bodies (arrows) in the cytoplasm. **(D)** Immunofluorescence against Iba1 reveals the presence of ramified microglia (resting cells) in the non-irradiated brain and bushy microglia (activated cells) in the irradiated brain. **(E)** Quantification of the number of branches and total length of processes (skeletonized outgrowth) in Iba1 expressing cells. **(F)** Representative images showing the presence of a NSC with condensed chromosomes (chr) in the non-irradiated SVZ and a quiescent NSC identified by the presence of envelope-limited chromatin sheets (arrows) in the irradiated SVZ. **(G)** Immunofluorescence against Ki67, Nestin, and DCX in the irradiated DG. **(H)** Immunofluorescence against Ki67, Nestin, and DCX in the irradiated SVZ. **(I)** Quantification of Ki67+ cells in the DG. **(J)** Quantification of Ki67+ cells in the SVZ. IR, irradiated mice; NonIR, non-irradiated mice. Scale bar: **(A)** 10 μm, **(B,C)** 2 μm, **(D)** 50 μm, **(F)** 2 μm, **(G)** 25 μm, **(H)** 200 μm. Data are represented as mean ± SEM. $n = 5$ per group, $^{*}p < 0.05$, $^{****}p < 0.0001$; *t*-test.

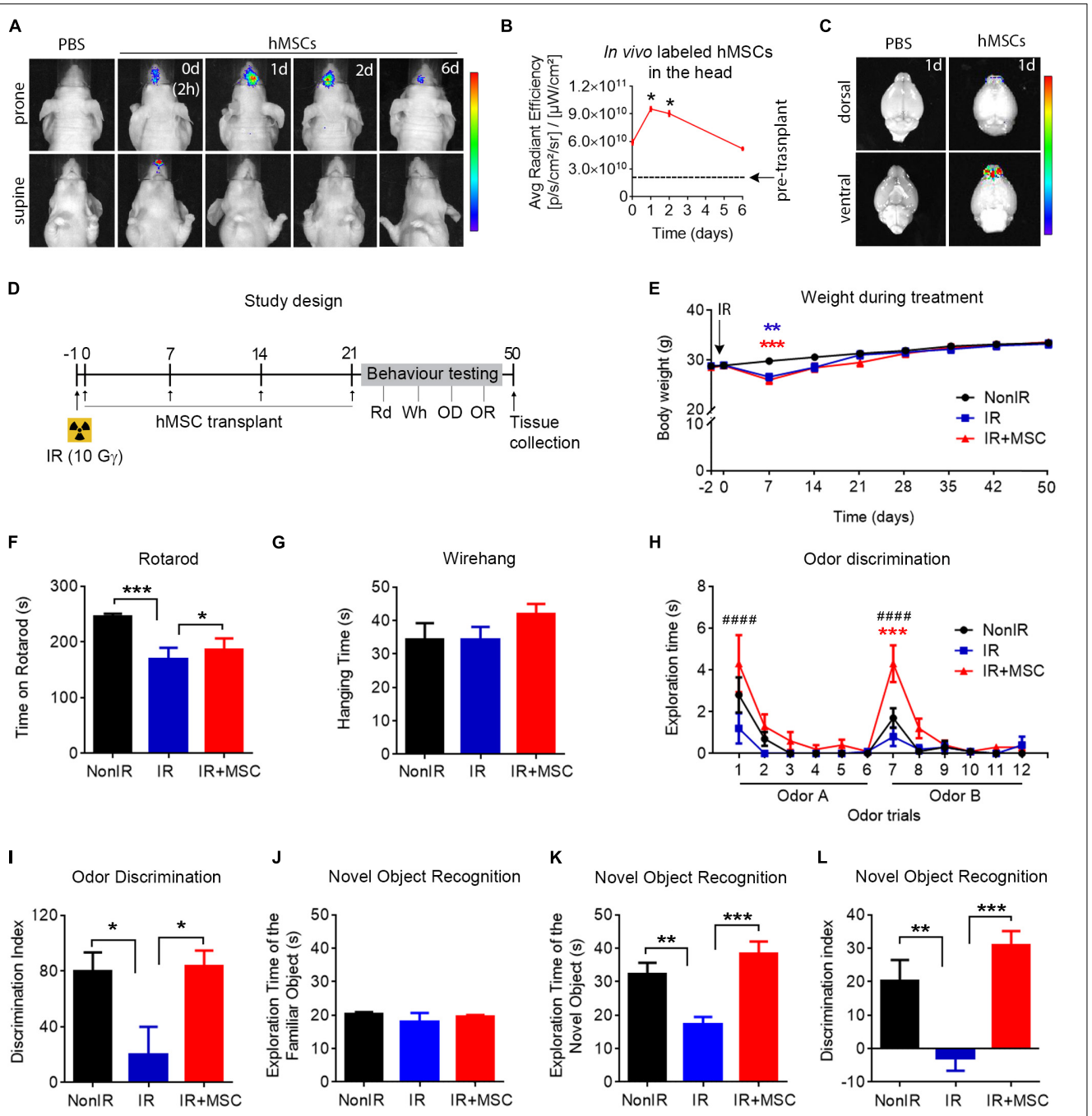


FIGURE 2 | Transplanted hMSCs improved neurological function after whole-brain radiation. **(A)** Representative images showing *in vivo* fluorescence signal in the head at 2 h, 1 day, 2 days, and 6 days after the first intranasal cell delivery (5×10^5 hMSCs). **(B)** Quantification of the *in vivo* fluorescence signal in the head within the first 6 days post transplantation, compared to day 0 (2 h after hMSC delivery). **(C)** *In vivo* fluorescence signal in dissected brains 1 day after intranasal delivery of hMSCs. **(D)** Schematic representation of the study design. Mice received whole-brain radiation (total dose of 10 Gy). Twenty-four hours after radiation, 5×10^5 cells hMSCs were administered intranasally once per week for 4 weeks. Then, mice were tested in a behavioral test battery (Rotarod, Rd on days 33–34; Wirehang, Wh on day 35; Odor discrimination task, OD on day 37; Novel Object Recognition test, OR on days 40–44) before being sacrificed. **(E)** Body weight during the course of the experiment revealing a temporary weight loss in irradiated mice (receiving or not hMSCs) the week after radiation exposure. **(F)** Rotarod test performance showing an improvement in IR+MSC mice, as compared to IR mice. **(G)** Wirehang test performance showing no differences between any experimental group. **(H)** Time spent sniffing the stimuli (Odor A and Odor B) in an odor discrimination task. **(I)** Discrimination index of Odor A and Odor B (presentation 6 vs. presentation 7), showing a rescued OD performance in IR+MSC mice. **(J)** Exploration time of the familiar object in the Novel Object Recognition test. **(K)** Exploration time of the novel object in the Novel Object Recognition test. **(L)** Discrimination index between familiar and novel object, showing a rescued OR performance in IR+MSC mice. Data are represented as mean ± SEM. $n = 3$ per group **(B)**, $n = 10$–15 per group **(E–L)**. Comparisons of IR or IR+MSC versus Non-IR are indicated with *. Comparisons of IR+MSC versus IR are indicated with #. $^{*}p < 0.05$, $^{**}p < 0.01$, $^{***}p < 0.001$, $^{****}p < 0.0001$, $^{\#\#\#\#}p < 0.0001$; One-way ANOVA **(B,F,G,I–L)**, Two-way repeated-measures ANOVA **(E,H)**. Rainbow color scale: red indicates highest fluorescence signal and blue indicates lowest fluorescence signal.

tumor mass in mice transplanted with hMSCs 50 days after the first cell dose. These results indicate that intranasal delivery is a feasible route to administrate cells to the brain.

Transplanted hMSCs Improved Neurological Function After Whole-Brain Radiation

We then examined whether intranasally delivered hMSCs could ameliorate neurological function in whole-brain irradiated mice. For this, animals were randomly assigned to three experimental groups: Non-irradiated mice receiving PBS (NonIR), irradiated mice receiving PBS (IR) and irradiated mice receiving hMSCs (IR+MSC). hMSC treatment (a dose of cells per week during 4 consecutive weeks) was initiated 24 h after radiation (**Figure 2D**). First, body weight was monitored during the course of the experiment (**Figure 2E**) as indicative of animal health status. We found a significant weight loss the week after radiation in IR and IR+MSC mice that was rapidly recovered, reaching the values of NonIR animal by 2-weeks post-irradiation. Then, animals were subjected to serial behavior testing to evaluate motor coordination (rotarod), muscle strength (wirehang), olfaction (odor discrimination task; OD) and cognition (novel object recognition test; OR). The IR group showed poor rotarod performance, as compared to NonIR and IR+MSC mice (**Figure 2F**). Wirehang performance was not different between any experimental group, indicating that results from rotarod were not influenced by muscle strength (**Figure 2G**). Then, mice were subjected to OD test. IR mice showed impaired ability to discriminate between two odorants, as compared to the Non-IR group, while hMSC treatment rescued OD performance (**Figures 2H,I**). Finally, mice were tested to the OR task. Exploration time of the familiar object was not different between any experimental groups, while exploration time of the novel object was reduced in IR mice, as compared to the other groups (**Figures 2J,K**). The discrimination index indicated that both, NonIR and IR+MSC mice exhibited a similar preference for the novel object (**Figure 2L**). These observations demonstrated a robust effect of hMSC treatment on neurofunctional recovery after radiation.

The Gene Expression Profile of the Irradiated Brain Was Modulated by hMSC Transplantation

After behavioral testing (i.e., at day 50 post-radiation; **Figure 2D**), all mice were sacrificed and brain tissue was collected to evaluate the molecular and cellular changes induced by hMSC administration. First, a group of mice was used to characterize genome-wide gene expression modulations in the PLv and Hipp, which contain the neurogenic niches. Principal component analysis (PCA) showed a distinct global transcriptional profile in the PLv and Hipp of IR mice, as compared to NonRx animals, while it was less evident in samples of animals receiving hMSCs (**Figures 3A,B**). Gene-expression profiling revealed that the vast majority of the genes whose expression was significantly up-regulated (∼81.3%) or down-regulated (∼76.8%) by radiation or radiation plus hMSCs in each tissue were specific to the tissue and experimental condition, indicating an overall distinct expression profile (**Figures 3C,D**). The analysis of genes significantly modulated in the comparison IR+MSC versus IR indicated that 1210 genes were differentially expressed in the PLv and 1050 in the Hipp (**Figures 3E,F** and **Supplementary Tables 2**, **3**). Of these, Calretinin (Calb2), a calcium-binding protein that plays a role in neuron excitability, was among the most up-regulated transcripts in the PLv of IR+MSC mice. The T cell specific GTPase 2 (Tgtp2), a member of the immune-related p47 GTPases, and the aldehyde oxidase 1 (Aox1), involved in Phase I metabolism of xenobiotics, were among the most highly over-expressed genes in the Hipp of IR+MSC mice. Several genes were similarly regulated in the PLv and Hipp of IR+MSC mice when compared to IR samples, suggesting that the modulation of these genes might contribute to the aforementioned improvements in neurological function after radiation (**Figure 3G**). Of these, the down-regulation of the formyl peptide receptor 1 (Fpr1) was particularly interesting since this gene is a member of the family of receptors for neutrophil chemotactic factors. Subsequent analysis using IPA indicated that several pathways involved in metabolite degradation were significantly modulated in the PLv of IR+MSC mice when compared to IR mice (**Figure 3H** and **Supplementary Figures 2**, **3**). In the Hipp, the focal adhesion kinase (FAK) signaling, a key regulator of cell movement, was the most significantly modulated pathway (**Figure 3I** and **Supplementary Figures 2**, **3**). Remarkably, several pathways involved in immune-related processes and melatonin degradation were altered in both, the PLv and the Hipp of IR+MSC mice when compared to IR mice (**Figures 3H,I** and **Supplementary Figures 2**, **3**). A modulation of genes involved in immune response and chemotaxis was also found by Gene Ontology (GO) enrichment analysis using Database for Annotation, Visualization and Integrated Discovery (DAVID) (**Supplementary Figure 4**). The overall interpretation of these results is that hMSC transplantation modulates genetic pathways associated with inflammation, immune system and cell motility in mice.

hMSC Administration Attenuates Radiation-Induced Persistent CREB Activation

The protective effect of hMSC administration in the PLv and Hipp 50 days post-radiation (**Figure 2D**) was further evaluated by examining CREB signaling, a key mediator of neuroprotection (**Figures 4A–D**). We observed a persistent activation of the transcription factor cAMP response element-binding (CREB) through phosphorylation at Ser133 in IR mice, which mediates neuroprotection in brain injury. CREB activation was accompanied by increased expression of the CREB-binding protein (CBP), a protein required to initiate transcriptional regulations mediated by CREB. Interestingly, hMSC treatment normalized the increased levels of the active isoform of CREB (PLv: IR+MSC vs. NonIR, p-value = 0.0565; Hipp: IR+MSC vs. NonIR, p-value = 0.0065). Consistently, the PLv of IR+MSC mice exhibited lower levels of phosphorylated

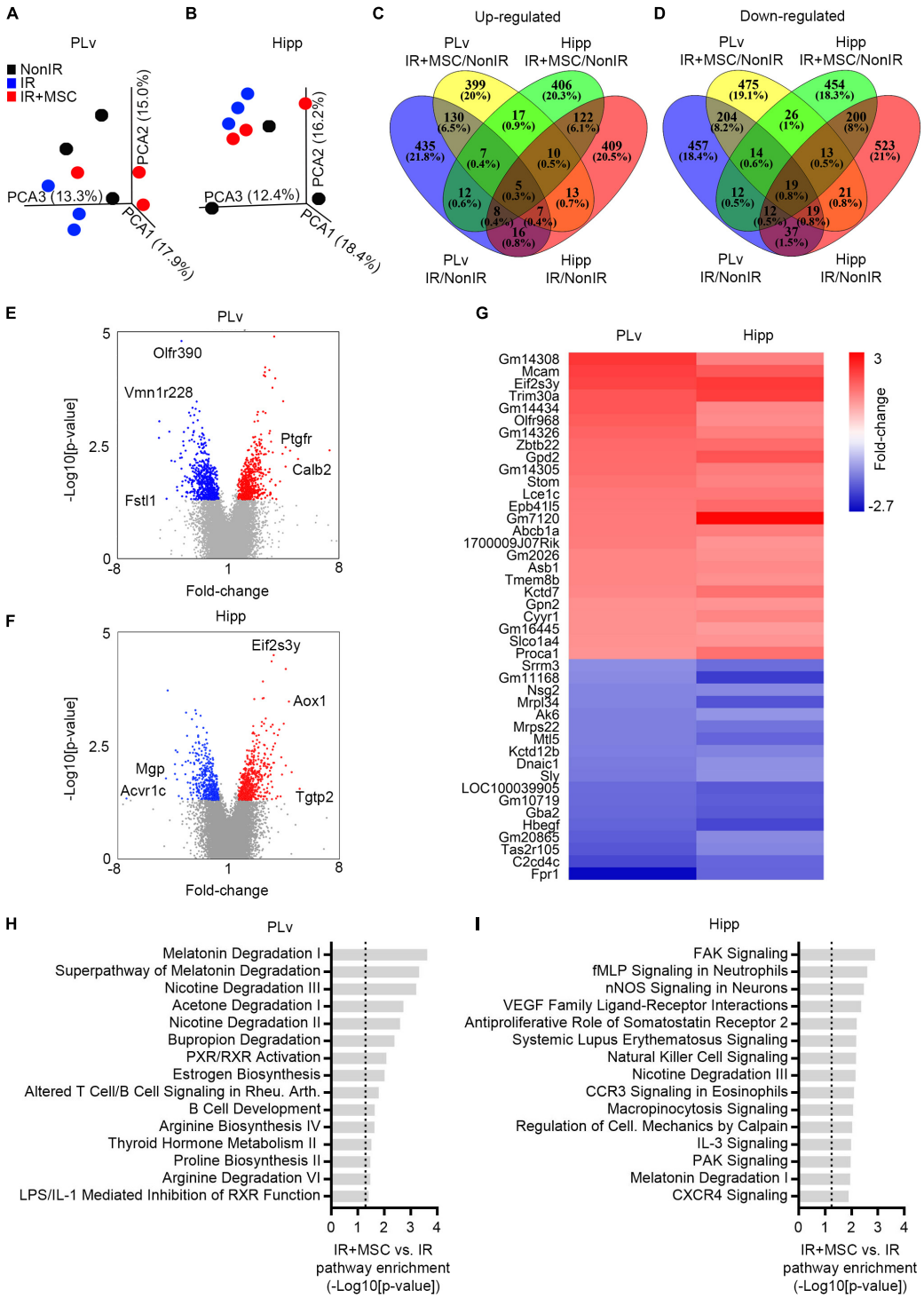


FIGURE 3 | The gene expression profile of the irradiated brains was modulated by hMSC transplantation. **(A)** PCA of genes expressed in the PLv. Plots represent individual samples. **(B)** PCA of genes expressed in the Hipp. Plots represent individual samples. **(C)** Venn diagrams showing the number and percentage of significantly up-regulated genes between the different tissues (PLv and Hipp) and different experimental groups (IR vs. NonIR and IR+MSC vs. NonIR). **(D)** Venn diagrams showing the number and percentage of significantly down-regulated genes between the different tissues (PLv and Hipp) and different experimental groups (IR vs. NonIR and IR+MSC vs. NonIR). **(E)** Volcano plot showing the fold change and statistical significance of genes expressed in the comparison IR+MSC vs. IR in the PLv. **(F)** Volcano plot showing the fold change and statistical significance of genes expressed in the comparison IR+MSC vs. IR in the Hipp. **(G)** Heat map depicting relative expression levels of shared significantly modulated genes in IR+MSC as compared to IR in PLv and Hipp. **(H)** Comparison of canonical pathways significantly altered in the PLv of IR+MSC as compared to IR using the IPA platform. **(I)** Comparison of canonical pathways significantly altered in the Hipp of IR+MSC as compared to IR using the IPA platform. *n* = 3 per group.

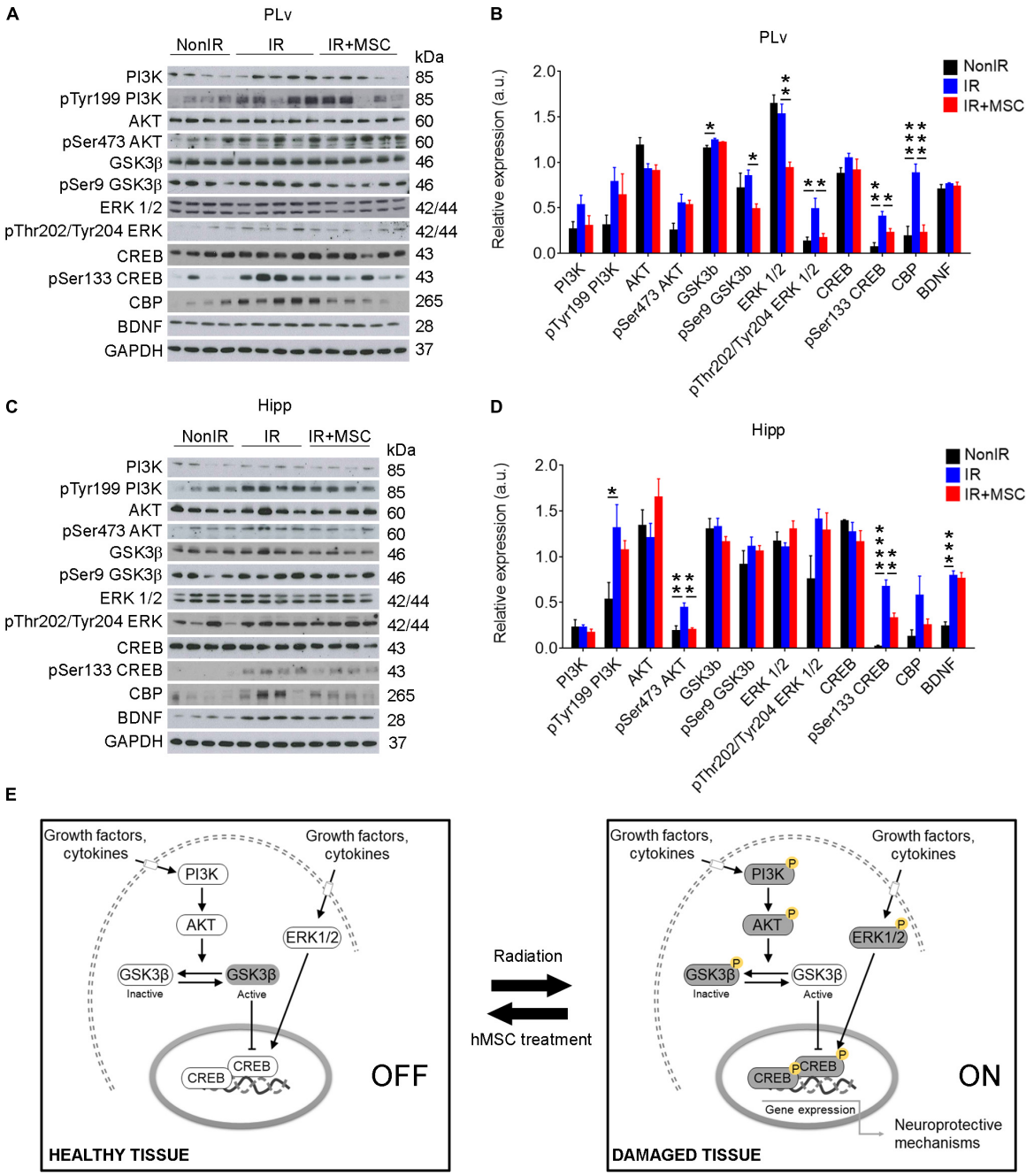


FIGURE 4 | hMSC administration attenuates radiation-induced persistent CREB activation. **(A)** Western blots showing the activation of CREB signaling in the PLv of IR mice and partial normalization of CREB expression in IR+MSC mice. **(B)** Densitometric analysis of the western blots of proteins involved in CREB signaling in the PLv. Values were normalized to the GAPDH. **(C)** Western blots showing the activation of CREB signaling in the Hipp of IR mice and partial normalization of CREB expression in IR+MSC mice. **(D)** Densitometric analysis of the western blots of proteins involved in CREB signaling in the Hipp. Values were normalized to the GAPDH. **(E)** Schematic representation of proteins involved in CREB signaling modulation during radiation and hMSC treatment. Data are represented as mean ± SEM. $n = 4–5$ per group. $^{*}p < 0.05$, $^{**}p < 0.01$, $^{***}p < 0.001$, $^{****}p < 0.0001$; One-way ANOVA.

ERK1/2 at Thr202/Tyr204, a well-known activator of CREB, when compared to IR mice. In contrast, levels of the Ser9 phospho-inactive isoform of GSK3β, an inhibitor of CREB, were reduced in the PLv of IR+MSC mice. Interestingly, phospho-Ser9 GSK3β levels in the Hipp were similar between the different experimental groups, despite the fact that phospho-Ser473 Protein Kinase B (AKT) levels were increased in IR mice, as compared to the other groups. Furthermore, the brain-derived neurotrophic factor (BDNF), a downstream target of CREB, was up-regulated in the Hipp of mice receiving radiation.

However, MSC treatment did not rescue BNDF levels. Together, these results indicate that radiation-induced damage response was down-regulated in IR+MSC mice, suggesting that hMSC administration promotes brain injury repair, as compared to IR mice (**Figure 4E**).

hMSCs Protected From Neural Cell Loss, Inflammation and Oxidative Stress

To further delineate the effects of hMSC treatment in irradiated mice, we performed a brain histopathological analysis (**Figure 5A**). The neurogenic niches (i.e., SVZ and DG) of IR and IR+MSC mice exhibited similar levels of Ki67- and DCX-expressing cells (**Figures 5B,C**). However, we found that hMSC treatment preserved the number of NeuN-expressing cells in the Hipp of irradiated mice (**Figure 5D**). Cranial radiation significantly promoted reactive gliosis, as evidenced by a greater GFAP immunoreactivity, and induced the expression of activated microglia (CD68 marker) in IR mice, while transplanted animals exhibited expression levels near NonIR mice (**Figures 5E,F**). The number of cells immunoreactive for iNOS, a classic glial proinflammatory mediator, was also enhanced in the IR group, while hMSC treatment reverted this effect (**Figure 5G**). Plasma levels of IL-2 and IL-1β also support a normalization of the inflammatory status in transplanted mice (**Supplementary Figure 5**).

Protein extracts from the PLv and the Hipp were further used to evaluate the neuroprotective role of hMSC infusion. We found that hMSC treatment prevented the elevation of radiation-induced Caspase 3 expression in the Hipp by western blot. In contrast, the expression of Caspase 3 in the PLv did not show differences across the experimental groups (**Figures 5H–J**). We determined the oxidative damage by quantifying the levels of lysine-4-hydroxynonenal (Lys-4-HNE), a marker of protein-bound lipid peroxidation. The irradiated PLv displayed increased levels of Lys-4-HNE that were reduced in the PLv of IR+MSC mice. The reduction of Lys-4-HNE levels in the Hipp of IR+MSC was less robust (**Figures 5J,K**). These data suggest that hMSC administration reduces neuroinflammation, oxidative damage and neuronal loss in whole-brain irradiated mice, although it does not prevent neurogenesis decline.

hMSC Administration Does Not Compromise Survival of Glioma-Bearing Mice

Finally, we aimed to evaluate whether intranasal delivery of hMSCs affects life expectancy of brain tumor-bearing mice. For this, U87 glioma cells were intracranially implanted into the right striatum of athymic nude mice. Ten days post-glioma implantation mice received whole-brain radiation and the following day intranasal administration of hMSCs was initiated (a dose of cells per week during 4 consecutive weeks) (**Figures 6A,B**). All mice exposed to radiation lose ∼15–20% of body weight on the week after irradiation. However, body weight loss was rapidly recovered, reaching values of non-irradiated animal (U87 NonIR) by 2-weeks post-irradiation. During the course of the experiment weight loss prior to animal death was also observed in all experimental groups (**Figure 6C**). Irradiated glioma-bearing mice (i.e., U87 IR and U87 IR+MSC) exhibited a ∼40% extended median survival when compared to U87 NonIR mice. Despite median survival showed no significant differences between U87 IR and U87 IR+MSC, maximal longevity was registered in U87 IR+MSC mice (**Figure 6D**). Histopathological analysis of the brain at the time of death suggested no differences in tumor progression between groups, as evidenced by hematoxylin and eosin staining and immunohistochemistry against Ki67 (**Figure 6E**). These findings indicate that hMSC treatment does not compromise survival of mice after oncological radiotherapy.

DISCUSSION

The life expectancy of cancer patients has increased over the past 10 years due to more effective treatments. However, the greater effectiveness of these treatments is commonly associated with a high cost, since patients often face late severe side effects that significantly limit their quality of life. The majority of brain tumor patients that receive cranial radiation exhibit cognitive dysfunction that includes deficits in learning, memory, language, attention, and executive function (Ali et al., 2018). Here we demonstrate that the intranasal delivery of hMSCs prevents late neurofunctional sequelae after radiotherapy in mice. Our results hold promise in the prevention of radiation-induced damages in oncological patients to maximize their quality of life, particularly in pediatric patients whose developing brain is more radiosensitive.

Seminal reports have shown promising results using stem cells to prevent radiation-induced damages, although the cells were intracerebrally or systemically administrated (Acharya et al., 2009, 2011; Joo et al., 2012; Piao et al., 2015). The intranasal delivery proposed here is a clinically relevant strategy due to different aspects. First, the intranasal route is a non-invasive and feasible method of cell delivery that allows the transplantation of multiple doses of cells, as compared to intracranial implantation. Second, therapeutic effectiveness of systemic administration is hampered by the blood–brain barrier (BBB) (Li et al., 2015), while the intranasal delivery provides a practical method that efficiently bypasses the BBB allowing transplanted cells to reach the brain within minutes to rapidly accomplish their therapeutic effects (Danielyan et al., 2009). In addition, nose-to-brain cell delivery uses the olfactory and trigeminal extracellular pathways to distribute the cells throughout the central nervous system, thus eliciting effects at multiple sites within the brain (Thorne et al., 2004; Danielyan et al., 2009). Accordingly, we found that intranasal administration of hMSCs improves motor coordination, olfaction and memory, which are functions coordinated by specific areas located in different parts of the brain. This represents an advantage over intracerebral administration, which requires injections at different sites of the brain to achieve multiple neurofunctional effects. In this regard, a previous study demonstrated that bilateral injections of hOPCs into the corpus callosum of rats prevent memory deficits after radiation, while concomitant transplantation of hOPCs into the

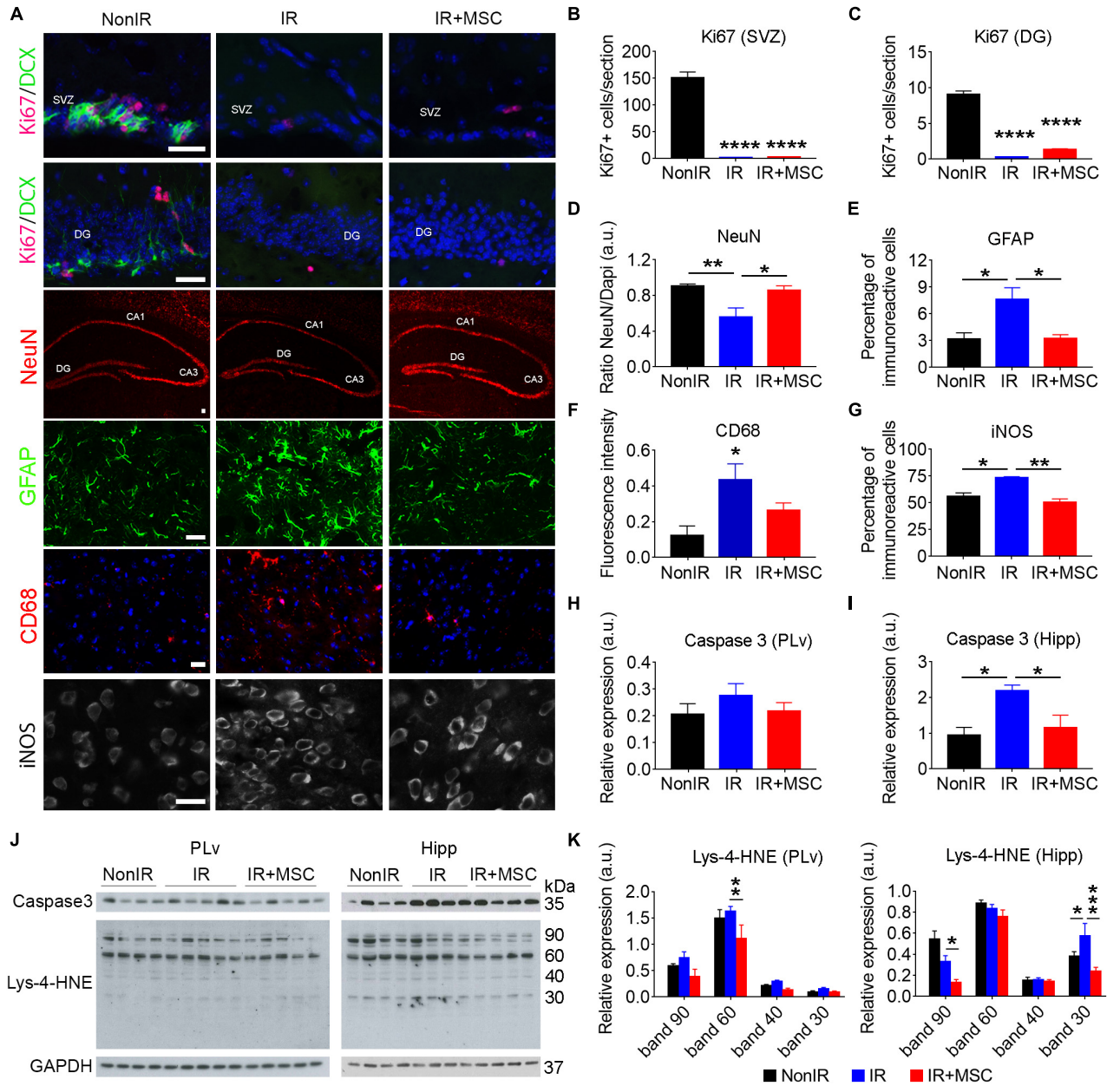


FIGURE 5 | hMSCs protected from neural cell loss, inflammation and oxidative stress. **(A)** Immunofluorescence analysis in the brain of NonIR, IR and IR+MSC mice, using Ki67, DCX, NeuN, GFAP, CD68 and iNOS markers (n = 3–5 per group). **(B)** Quantification of Ki67 positive cells in the SVZ. **(C)** Quantification of Ki67 positive cells in the DG. **(D)** Quantification of NeuN immunoreactive area in the Hipp. **(E)** Quantification of the percentage of GFAP immunoreactivity in the striatum. **(F)** Quantification of the CD68 immunoreactivity in the cortex. **(G)** Quantification of iNOS immunoreactivity in the striatum. **(H)** Densitometric quantification of Caspase 3 expression by western blot in the PLv. Western blot images are shown in panel **(J)**. **(I)** Densitometric quantification of Caspase 3 expression by western blot in the Hipp. Western blot images are shown in panel **(J)**. **(J)** Representative western blots of Caspase 3 and Lys-4-HNE from PLv and Hipp tissue lysates (n = 4–5 per group). **(K)** Densitometric quantification of Lys-4-HNE levels by western blot in PLv and Hipp tissue lysates. Scale bar 25 μm. Data are represented as mean ± SEM. *$p < 0.05$, **$p < 0.01$, ***$p < 0.001$, ****$p < 0.0001$; One-way ANOVA **(B–I)**, Two-way ANOVA **(K)**.

cerebellum was necessary to obtain benefits on motor function (Piao et al., 2015). Finally, our model focuses on the use of hMSCs derived from the adipose tissue, which represents an interesting clinical option due to the ease of obtaining large quantities of cells using a minimally invasive procedure (Lescaudron et al., 2012; Escacena et al., 2015).

Radiation injury has a multifactorial etiology that includes vascular damage (Li et al., 2003; Brown et al., 2005), demyelination (Panagiotakos et al., 2007; Gazdzinski et al., 2012), inflammation (Hwang et al., 2006), neuronal death, and neurogenesis decline (Achanta et al., 2012; Capilla-Gonzalez et al., 2014, 2016). In particular, inflammatory processes

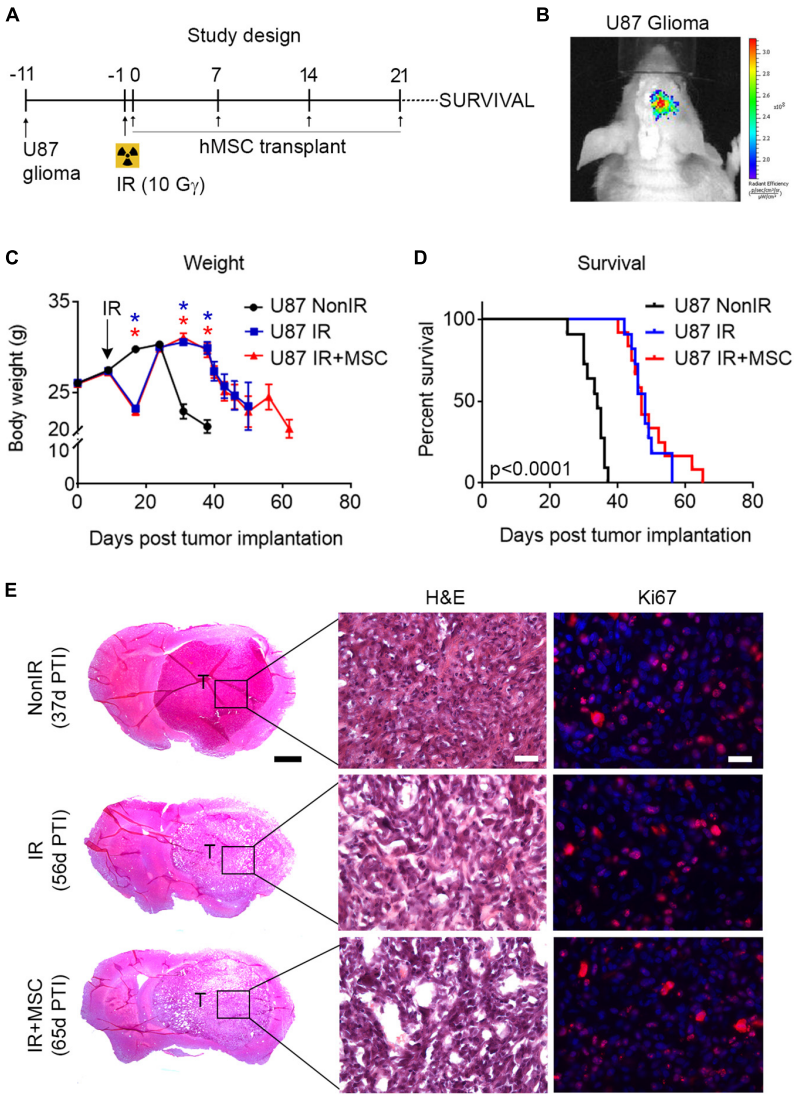


FIGURE 6 | hMSC administration does not compromise survival of glioma-bearing mice. **(A)** Schematic representation of the study design. U87 glioma cells were intracranially transplanted into the striatum of nude mice. After 10 days, mice received whole-brain radiation (total dose of 10 Gy) and the day after, 5×10^5 hMSCs were administered intranasally once per week for 4 weeks and time of death was monitored. **(B)** Xenolight DiR-labeled U87 glioma cells were locally transplanted into the striatum of nude mice. Images show bioluminescence activity in a representative animal 24 h after cell transplantation. **(C)** Animal weight was measured during the course of the experiment. Note the weight loss after radiation exposure. **(D)** Kaplan–Meier curve showing the percentage of survival of glioma-bearing mice. Note that IR and IR+MSC mice exhibited similar response, increasing survival as compared to NonIR mice. **(E)** Histological images of brain tumors at the time of death (indicated as days post tumor implantation, PTI) in the last individual surviving for each experimental group. H&E: Hematoxylin and eosin staining. Scale bar 1 mm (25 μm for details). Data are represented as mean ± SEM. n = 11–12 per group. *$p < 0.0001$ compared to U87 NonIR mice; Multiple t-test **(C)**, Log-rank test **(D)**.

have been proposed as a major triggering factor leading to neuropathology in the irradiated brain (Acharya et al., 2016). In this regard, MSCs are known to exhibit immunomodulatory and anti-inflammatory properties (Hmadcha et al., 2009; Prockop and Oh, 2012; Escacena et al., 2015; Fu et al., 2017). Therefore, MSCs might be the ideal candidate for restoring brain homeostasis in radiation-induced inflammatory milieu. Here, we found that the therapeutic application of hMSCs reduces neuroinflammation and oxidative damage in whole-brain irradiated mice, which may help to prevent the loss of mature neurons. In contrast, newly born neurons were not protected by the hMSC treatment. The study of the neurogenic niche after a longer post-treatment period of time would be of interest to conclusively determine if intranasal hMSC delivery rescues irradiation-induced damages in neurogenesis. Consistently with the histopathological study, gene expression profiling at long-term evidences a modulation of neuroprotective processes, such those induced by melatonin (Mendivil-Perez et al., 2017; Paul et al., 2018), and changes in immune response pathways in the PLv and the Hipp of IR+MSC mice. Remarkably, we found a robust long-term activation of CREB signaling in irradiated mice, which was attenuated in mice receiving hMSC. In response to injury, CREB coordinates

expression of genes encoding neuroprotective processes, such as BDNF that ultimately reduces inflammation, prevents oxidative damage and promotes anti-apoptotic effects (Han et al., 2000; Han and Holtzman, 2000). We also observed that both ERK and GSK3β signaling pathways play an important role in mediating CREB activation. The overall interpretation of our data indicates that hMSC transplantation allows a rapid and efficient repair of radiation-induced damages in mice, which is reflected in the normalization of neuroprotective cellular pathways at long-term post-radiation (i.e., 50 days post-radiation). However, further studies are required to fully understand the specific mechanisms that hMSCs modulate to induce radiation-damages repair. Based on our results and previous studies, we speculate that the beneficial effects of hMSCs are due to their paracrine activity rather than neural differentiation of hMSCs (Li et al., 2005; Wakabayashi et al., 2010; Wu et al., 2018). Extracellular vesicles (EVs) released by hMSCs are one of the main actors involved in the paracrine effects by modulating processes such as immune responses, inflammation, angiogenesis and homeostasis maintenance (Keshtkar et al., 2018). Indeed, latest research on regenerative medicine are moving toward cell-free therapies by employing stem cell-derived EVs due to their reduced immunogenicity (Zhu et al., 2017). However, obtaining sufficient amounts of EVs is still a major challenge toward their clinical application.

The therapeutic application of hMSCs to reduce neurological complications of radiation could be debatable due to their potential implications in tumor progression (Shahar et al., 2017; Whiteside, 2018). However, our pre-clinical study and others demonstrate that hMSC treatment does not compromise the survival of rodents with brain tumors (Balyasnikova et al., 2014; Li et al., 2014; Pacioni et al., 2017). Indeed, beneficial effects of hMSC administration have been reported through inhibition of tumor growth in orthotopic glioblastoma xenografts (Pacioni et al., 2017). Furthermore, the therapeutic effect of hMSCs to ameliorate complications associated with cancer treatments is currently under evaluation in humans. In this line, a Phase I clinical trial is recruiting patients to evaluate the safety and feasibility of delivering hMSCs by intracardiac injections to cancer survivors with cardiomyopathy induced by the chemotherapeutic anthracycline (NCT02509156). Another Phase II clinical study is also evaluating the safety and feasibility of hMSC injections into the submandibular gland to revert radiation-induced xerostomia in head and neck cancer patients (NCT02513238).

In conclusion, we demonstrate that intranasally delivered hMSCs is a non-invasive and effective treatment to promote brain damage repair after radiation and to improve neurological function in mice. These results also hold great promise for other inflammatory disorders, as well as for those diseases involving cognitive deterioration. The robust pre-clinical data presented here encourages the clinical use of hMSCs in cell-based therapy as an attractive option to prevent side effects induced by oncological radiotherapy. Despite the therapeutic window after radiation should be defined in brain tumor patients, hMSC application to reverse normal tissue toxicity could become an essential step in their treatment schedule.

ETHICS STATEMENT

All animal handling procedures were approved by the CABIMER Ethics Committee for Animal Experimentation, and complied with national and European Union legislation (Spanish RD 53/2013 and EU Directive 2010/63) for the protection of animals used for scientific purposes.

AUTHOR CONTRIBUTIONS

BS, AM-M, AH, and VC-G contributed to the conceptualization, methodology and funding acquisition. AM-M, YA, NM-D, JL-B, MA-D, and VC-G performed the investigation. AM-M and VC-G wrote the original draft. BS, AM-M, EL, JAB, AH, and VC-G wrote, reviewed and edited the manuscript. BS, IH-H, EL, JAB, AH, and VC-G provided the resources. VC-G supervised the study.

FUNDING

This work was funded by grants from the non-profit foundation "Fundación Progreso y Salud" of the Andalusian Regional Ministry of Health (VC-G, PI-0109-2014 and PI-0272-2017), the Spanish Ministry of Economy, Industry and Competitiveness, Instituto de Salud Carlos III co-funded by Fondos FEDER (BS, RD16/0011/0034, PI17/02104; AM-M, PI18/01590, PI15/00134; AH, PI16/00259) and the crowdfunding platform PRECIPITA of the Spanish Foundation for Science and Technology (VC-G, 2018-000237). AM-M is a recipient of a Miguel Servet contract (CP14/00105) from the Instituto de Salud Carlos III co-funded by Fondos FEDER whereas VC-G is a recipient of a Sara Borrell contract (CD16/00118) from the Instituto de Salud Carlos III co-funded by Fondos FEDER. CIBERDEM is an initiative of the Instituto de Salud Carlos III.

ACKNOWLEDGMENTS

We would like to thank Modesto Carballo and Olimpia Perez-Morato for their valuable technical help, and Angel M. Carrion for providing the lead shield for animal radiation. We acknowledge Aladina Foundation and Miguel Angel Martín Adan for their support in this project.

SUPPLEMENTARY MATERIAL

The Supplementary Material for this article can be found online at: https://www.frontiersin.org/articles/10.3389/fncel.2019.00204/full#supplementary-material

REFERENCES

Achanta, P., Capilla-Gonzalez, V., Purger, D., Reyes, J., Sailor, K., Song, H., et al. (2012). Subventricular zone localized irradiation affects the generation of proliferating neural precursor cells and the migration of neuroblasts. *Stem Cells* 30, 2548–2560. doi: 10.1002/stem.1214

Acharya, M. M., Christie, L. A., Lan, M. L., Donovan, P. J., Cotman, C. W., Fike, J. R., et al. (2009). Rescue of radiation-induced cognitive impairment through cranial transplantation of human embryonic stem cells. *Proc. Natl. Acad. Sci. U.S.A.* 106, 19150–19155. doi: 10.1073/pnas.0909293106

Acharya, M. M., Christie, L. A., Lan, M. L., Giedzinski, E., Fike, J. R., Rosi, S., et al. (2011). Human neural stem cell transplantation ameliorates radiation-induced cognitive dysfunction. *Cancer Res.* 71, 4834–4845. doi: 10.1158/0008-5472.CAN-11-0027

Acharya, M. M., Green, K. N., Allen, B. D., Najafi, A. R., Syage, A., Minasyan, H., et al. (2016). Elimination of microglia improves cognitive function following cranial irradiation. *Sci Rep*. 6:31545. doi: 10.1038/srep31545

Acharya, M. M., Rosi, S., Jopson, T., and Limoli, C. L. (2015). Human neural stem cell transplantation provides long-term restoration of neuronal plasticity in the irradiated hippocampus. *Cell Transplant.* 24, 691–702. doi: 10.3727/096368914X684600

Ali, F. S., Hussain, M. R., Gutierrez, C., Demireva, P., Ballester, L. Y., Zhu, J. J., et al. (2018). Cognitive disability in adult patients with brain tumors. *Cancer Treat. Rev.* 65, 33–40. doi: 10.1016/j.ctrv.2018.02.007

Armstrong, G. T., Reddick, W. E., Petersen, R. C., Santucci, A., Zhang, N., Srivastava, D., et al. (2013). Evaluation of memory impairment in aging adult survivors of childhood acute lymphoblastic leukemia treated with cranial radiotherapy. *J. Natl. Cancer Inst.* 105, 899–907. doi: 10.1093/jnci/djt089

Balyasnikova, I. V., Prasol, M. S., Ferguson, S. D., Han, Y., Ahmed, A. U., Gutova, M., et al. (2014). Intranasal delivery of mesenchymal stem cells significantly extends survival of irradiated mice with experimental brain tumors. *Mol. Ther.* 22, 140–148. doi: 10.1038/mt.2013.199

Brown, W. R., Thore, C. R., Moody, D. M., Robbins, M. E., and Wheeler, K. T. (2005). Vascular damage after fractionated whole-brain irradiation in rats. *Radiat Res.* 164, 662–668. doi: 10.1667/rr3453.1

Capilla-Gonzalez, V., Bonsu, J. M., Redmond, K. J., Garcia-Verdugo, J. M., and Quinones-Hinojosa, A. (2016). Implications of irradiating the subventricular zone stem cell niche. *Stem Cell Res.* 16, 387–396. doi: 10.1016/j.scr.2016.02.031

Capilla-Gonzalez, V., Gil-Perotin, S., Ferragud, A., Bonet-Ponce, L., Canales, J. J., and Garcia-Verdugo, J. M. (2012). Exposure to N-ethyl-N-nitrosourea in adult mice alters structural and functional integrity of neurogenic sites. *PLoS One* 7:e29891. doi: 10.1371/journal.pone.0029891

Capilla-Gonzalez, V., Gil-Perotin, S., and Garcia-Verdugo, J. M. (2010). Postnatal exposure to N-ethyl-N-nitrosurea disrupts the subventricular zone in adult rodents. *Eur. J. Neurosci.* 32, 1789–1799. doi: 10.1111/j.1460-9568.2010.07450.x

Capilla-Gonzalez, V., Guerrero-Cazares, H., Bonsu, J. M., Gonzalez-Perez, O., Achanta, P., Wong, J., et al. (2014). The subventricular zone is able to respond to a demyelinating lesion after localized radiation. *Stem Cells* 32, 59–69. doi: 10.1002/stem.1519

Capilla-Gonzalez, V., Lopez-Beas, J., Escacena, N., Aguilera, Y., de la Cuesta, A., Ruiz-Salmeron, R., et al. (2018). PDGF restores the defective phenotype of adipose-derived mesenchymal stromal cells from diabetic patients. *Mol. Ther.* 26, 2696–2709. doi: 10.1016/j.ymthe.2018.08.011

Danielyan, L., Schafer, R., von Ameln-Mayerhofer, A., Buadze, M., Geisler, J., Klopfer, T., et al. (2009). Intranasal delivery of cells to the brain. *Eur. J. Cell Biol.* 88, 315–324.

Delaney, G., Jacob, S., Featherstone, C., and Barton, M. (2005). The role of radiotherapy in cancer treatment: estimating optimal utilization from a review of evidence-based clinical guidelines. *Cancer* 104, 1129–1137. doi: 10.1002/cncr.21324

Douw, L., Klein, M., Fagel, S. S., van den Heuvel, J., Taphoorn, M. J., Aaronson, N. K., et al. (2009). Cognitive and radiological effects of radiotherapy in patients with low-grade glioma: long-term follow-up. *Lancet Neurol.* 8, 810–818. doi: 10.1016/S1474-4422(09)70204-2

Escacena, N., Quesada-Hernandez, E., Capilla-Gonzalez, V., Soria, B., and Hmadcha, A. (2015). Bottlenecks in the efficient use of advanced therapy medicinal products based on mesenchymal stromal cells. *Stem Cells Int.* 2015:895714. doi: 10.1155/2015/895714

Fu, Y., Karbaat, L., Wu, L., Leijten, J., Both, S. K., and Karperien, M. (2017). Trophic effects of mesenchymal stem cells in tissue regeneration. *Tissue Eng. Part B Rev.* 23, 515–528. doi: 10.1089/ten.TEB.2016.0365

Gazdzinski, L. M., Cormier, K., Lu, F. G., Lerch, J. P., Wong, C. S., and Nieman, B. J. (2012). Radiation-induced alterations in mouse brain development characterized by magnetic resonance imaging. *Int. J. Radiat. Oncol. Biol. Phys.* 84, e631–e638. doi: 10.1016/j.ijrobp.2012.06.053

Han, B. H., D'Costa, A., Back, S. A., Parsadanian, M., Patel, S., Shah, A. R., et al. (2000). BDNF blocks caspase-3 activation in neonatal hypoxia-ischemia. *Neurobiol. Dis.* 7, 38–53. doi: 10.1006/nbdi.1999.0275

Han, B. H., and Holtzman, D. M. (2000). BDNF protects the neonatal brain from hypoxic-ischemic injury in vivo via the ERK pathway. *J. Neurosci.* 20, 5775–5781. doi: 10.1523/jneurosci.20-15-05775.2000

Hmadcha, A., Dominguez-Bendala, J., Wakeman, J., Arredouani, M., and Soria, B. (2009). The immune boundaries for stem cell based therapies: problems and prospective solutions. *J. Cell Mol. Med.* 13, 1464–1475. doi: 10.1111/j.1582-4934.2009.00837.x

Hwang, S. Y., Jung, J. S., Kim, T. H., Lim, S. J., Oh, E. S., Kim, J. Y., et al. (2006). Ionizing radiation induces astrocyte gliosis through microglia activation. *Neurobiol. Dis.* 21, 457–467. doi: 10.1016/j.nbd.2005.08.006

Joo, K. M., Jin, J., Kang, B. G., Lee, S. J., Kim, K. H., Yang, H., et al. (2012). Trans-differentiation of neural stem cells: a therapeutic mechanism against the radiation induced brain damage. *PLoS One* 7:e25936. doi: 10.1371/journal.pone.0025936

Keshtkar, S., Azarpira, N., and Ghahremani, M. H. (2018). Mesenchymal stem cell-derived extracellular vesicles: novel frontiers in regenerative medicine. *Stem Cell Res. Ther.* 9:63. doi: 10.1186/s13287-018-0791-7

Klein, S. M., Vykoukal, J., Lechler, P., Zeitler, K., Gehmert, S., Schreml, S., et al. (2012). Noninvasive in vivo assessment of muscle impairment in the mdx mouse model–a comparison of two common wire hanging methods with two different results. *J. Neurosci. Methods* 203, 292–297. doi: 10.1016/j.jneumeth.2011.10.001

Leger, M., Quiedeville, A., Bouet, V., Haelewyn, B., Boulouard, M., Schumann-Bard, P., et al. (2013). Object recognition test in mice. *Nat. Protoc.* 8, 2531–2537. doi: 10.1038/nprot.2013.155

Lescaudron, L., Boyer, C., Bonnamain, V., Fink, K. D., Leveque, X., Rossignol, J., et al. (2012). Assessing the potential clinical utility of transplantations of neural and mesenchymal stem cells for treating neurodegenerative diseases. *Methods Mol. Biol.* 879, 147–164. doi: 10.1007/978-1-61779-815-3_10

Li, Q., Wijesekera, O., Salas, S. J., Wang, J. Y., Zhu, M., Aprhys, C., et al. (2014). Mesenchymal stem cells from human fat engineered to secrete BMP4 are nononcogenic, suppress brain cancer, and prolong survival. *Clin. Cancer Res.* 20, 2375–2387. doi: 10.1158/1078-0432.CCR-13-1415

Li, Y., Chen, J., Zhang, C. L., Wang, L., Lu, D., Katakowski, M., et al. (2005). Gliosis and brain remodeling after treatment of stroke in rats with marrow stromal cells. *Glia* 49, 407–417. doi: 10.1002/glia.20126

Li, Y. H., Feng, L., Zhang, G. X., and Ma, C. G. (2015). Intranasal delivery of stem cells as therapy for central nervous system disease. *Exp. Mol. Pathol.* 98, 145–151. doi: 10.1016/j.yexmp.2015.01.016

Li, Y. Q., Chen, P., Haimovitz-Friedman, A., Reilly, R. M., and Wong, C. S. (2003). Endothelial apoptosis initiates acute blood-brain barrier disruption after ionizing radiation. *Cancer Res.* 63, 5950–5956.

Lopez-Noriega, L., Cobo-Vuilleumier, N., Narbona-Perez, A. J., Araujo-Garrido, J. L., Lorenzo, P. I., Mellado-Gil, J. M., et al. (2017). Levothyroxine enhances glucose clearance and blunts the onset of experimental type 1 diabetes mellitus in mice. *Br. J. Pharmacol.* 174, 3795–3810. doi: 10.1111/bph.13975

Ma, T. M., Grimm, J., McIntyre, R., Anderson-Keightly, H., Kleinberg, L. R., Hales, R. K., et al. (2017). A prospective evaluation of hippocampal radiation dose volume effects and memory deficits following cranial irradiation. *Radiother. Oncol.* 125, 234–240. doi: 10.1016/j.radonc.2017.09.035

Makale, M. T., McDonald, C. R., Hattangadi-Gluth, J. A., and Kesari, S. (2017). Mechanisms of radiotherapy-associated cognitive disability in patients with brain tumours. *Nat. Rev. Neurol.* 13, 52–64. doi: 10.1038/nrneurol.2016.185

Marazziti, D., Baroni, S., Catena-Dell'Osso, M., Schiavi, E., Ceresoli, D., Conversano, C., et al. (2012). Cognitive, psychological and psychiatric effects of ionizing radiation exposure. *Curr. Med. Chem.* 19, 1864–1869. doi: 10.2174/092986712800099776

Mendivil-Perez, M., Soto-Mercado, V., Guerra-Librero, A., Fernandez-Gil, B. I., Florido, J., Shen, Y. Q., et al. (2017). Melatonin enhances neural stem cell differentiation and engraftment by increasing mitochondrial function. *J. Pineal Res.* 63:e12415. doi: 10.1111/jpi.12415

Ostrom, Q. T., Gittleman, H., de Blank, P. M., Finlay, J. L., Gurney, J. G., McKean-Cowdin, R., et al. (2016). American brain tumor association adolescent and young adult primary brain and central nervous system tumors diagnosed in the United States in 2008-2012. *Neuro Oncol.* 18, i1–i50. doi: 10.1093/neuonc/nov297

Pacioni, S., D'Alessandris, Q. G., Giannetti, S., Morgante, L., Cocce, V., Bonomi, A., et al. (2017). Human mesenchymal stromal cells inhibit tumor growth in orthotopic glioblastoma xenografts. *Stem Cell Res. Ther.* 8:53. doi: 10.1186/s13287-017-0516-3

Padovani, L., Andre, N., Constine, L. S., and Muracciole, X. (2012). Neurocognitive function after radiotherapy for paediatric brain tumours. *Nat. Rev. Neurol.* 8, 578–588. doi: 10.1038/nrneurol.2012.182

Panagiotakos, G., Alshamy, G., Chan, B., Abrams, R., Greenberg, E., Saxena, A., et al. (2007). Long-term impact of radiation on the stem cell and oligodendrocyte precursors in the brain. *PLoS One* 2:e588. doi: 10.1371/journal.pone.0000588

Paul, R., Phukan, B. C., Justin Thenmozhi, A., Manivasagam, T., Bhattacharya, P., and Borah, A. (2018). Melatonin protects against behavioral deficits, dopamine loss and oxidative stress in homocysteine model of Parkinson's disease. *Life Sci.* 192, 238–245. doi: 10.1016/j.lfs.2017.11.016

Piao, J., Major, T., Auyeung, G., Policarpio, E., Menon, J., Droms, L., et al. (2015). Human embryonic stem cell-derived oligodendrocyte progenitors remyelinate the brain and rescue behavioral deficits following radiation. *Cell Stem Cell.* 16, 198–210. doi: 10.1016/j.stem.2015.01.004

Prockop, D. J., and Oh, J. Y. (2012). Mesenchymal stem/stromal cells (MSCs): role as guardians of inflammation. *Mol. Ther.* 20, 14–20. doi: 10.1038/mt.2011.211

Ramos-Zuriga, R., Gonzalez-Perez, O., Macedas-Ornelas, A., Capilla-Gonzlez, V., and Quiñones-Hinojosa, A. (2012). Ethical implications in the use of embryonic and adult neural stem cells. *Stem Cells Int.* 2012:7.

Shahar, T., Rozovski, U., Hess, K. R., Hossain, A., Gumin, J., Gao, F., et al. (2017). Percentage of mesenchymal stem cells in high-grade glioma tumor samples correlates with patient survival. *Neuro Oncol.* 19, 660–668. doi: 10.1093/neuonc/now239

Suarez-Pereira, I., Canals, S., and Carrion, A. M. (2015). Adult newborn neurons are involved in learning acquisition and long-term memory formation: the distinct demands on temporal neurogenesis of different cognitive tasks. *Hippocampus* 25, 51–61. doi: 10.1002/hipo.22349

Thorne, R. G., Pronk, G. J., Padmanabhan, V., and Frey, W. H. II (2004). Delivery of insulin-like growth factor-I to the rat brain and spinal cord along olfactory and trigeminal pathways following intranasal administration. *Neuroscience* 127, 481–496. doi: 10.1016/j.neuroscience.2004.05.029

Wakabayashi, K., Nagai, A., Sheikh, A. M., Shiota, Y., Narantuya, D., Watanabe, T., et al. (2010). Transplantation of human mesenchymal stem cells promotes functional improvement and increased expression of neurotrophic factors in a rat focal cerebral ischemia model. *J. Neurosci. Res.* 88, 1017–1025. doi: 10.1002/jnr.22279

Whiteside, T. L. (2018). Exosome and mesenchymal stem cell cross-talk in the tumor microenvironment. *Semin. Immunol.* 35, 69–79. doi: 10.1016/j.smim.2017.12.003

Wu, Q., Wang, Q., Li, Z., Li, X., Zang, J., Wang, Z., et al. (2018). Human menstrual blood-derived stem cells promote functional recovery in a rat spinal cord hemisection model. *Cell Death Dis.* 9:882. doi: 10.1038/s41419-018-0847-8

Zhu, X., Badawi, M., Pomeroy, S., Sutaria, D. S., Xie, Z., Baek, A., et al. (2017). Comprehensive toxicity and immunogenicity studies reveal minimal effects in mice following sustained dosing of extracellular vesicles derived from HEK293T cells. *J. Extracell. Vesicles* 6:1324730. doi: 10.1080/20013078.2017.1324730

Conflict of Interest Statement: The authors declare that the research was conducted in the absence of any commercial or financial relationships that could be construed as a potential conflict of interest.

Copyright © 2019 Soria, Martin-Montalvo, Aguilera, Mellado-Damas, López-Beas, Herrera-Herrera, López, Barcia, Alvarez-Dolado, Hmadcha and Capilla-González. This is an open-access article distributed under the terms of the Creative Commons Attribution License (CC BY). The use, distribution or reproduction in other forums is permitted, provided the original author(s) and the copyright owner(s) are credited and that the original publication in this journal is cited, in accordance with accepted academic practice. No use, distribution or reproduction is permitted which does not comply with these terms.

frontiers in Cellular Neuroscience

REVIEW
published: 19 June 2019
doi: 10.3389/fncel.2019.00271

Human Dorsal Root Ganglia

Rainer Viktor Haberberger[1,2], Christine Barry[1], Nicholas Dominguez[1] and Dusan Matusica[1,2]*

[1] Pain and Pulmonary Neurobiology Laboratory, Centre for Neuroscience, Anatomy and Histology, Flinders University, Adelaide, SA, Australia, [2] Órama Institute, Flinders University, Adelaide, SA, Australia

Sensory neurons with cell bodies situated in dorsal root ganglia convey information from external or internal sites of the body such as actual or potential harm, temperature or muscle length to the central nervous system. In recent years, large investigative efforts have worked toward an understanding of different types of DRG neurons at transcriptional, translational, and functional levels. These studies most commonly rely on data obtained from laboratory animals. Human DRG, however, have received far less investigative focus over the last 30 years. Nevertheless, knowledge about human sensory neurons is critical for a translational research approach and future therapeutic development. This review aims to summarize both historical and emerging information about the size and location of human DRG, and highlight advances in the understanding of the neurochemical characteristics of human DRG neurons, in particular nociceptive neurons.

Keywords: DRG, satellite cells, immunohistochemistry, nociceptor, MRI

OPEN ACCESS

Edited by:
Marco Martina,
Northwestern University,
United States

Reviewed by:
Michelino Puopolo,
Stony Brook University, United States
Kalyana Srinivas Vadduri,
Independent Researcher,
New York, United States

****Correspondence:***
Rainer Viktor Haberberger
rainer.haberberger@flinders.edu.au

Specialty section:
This article was submitted to Cellular Neurophysiology, a section of the journal Frontiers in Cellular Neuroscience

Received: *11 April 2019*
Accepted: *04 June 2019*
Published: *19 June 2019*

Citation:
Haberberger RV, Barry C, Dominguez N and Matusica D (2019) Human Dorsal Root Ganglia. Front. Cell. Neurosci. 13:271. doi: 10.3389/fncel.2019.00271

INTRODUCTION

Sensory neurons relay information about a variety of intrinsic and environmental cues such as temperature, touch, muscle length, organ volume or actual or potential harm to the body. They also contribute to regulation of blood supply and change neuronal sensitivity and other functions by ortho- and antidromic release of molecules. The cell bodies of sensory neurons are located primarily in dorsal root ganglia (DRG) or trigeminal ganglia (TG; see reviews Belmonte and Viana, 2008; Pope et al., 2013; Krames, 2015; Nascimento et al., 2018). The last three decades have seen significant advances in understanding the electrochemical, cellular and molecular characteristics of sensory neurons found in DRG, primarily stemming from animal studies. These studies have focused heavily on understanding mechanisms underlying the development and pathophysiology of chronic and/or neuropathic pain. Far less, however, is known about the cellular and molecular characteristics of human DRG. The emergence of recent comparative genetic and proteomic studies between animal and human models has highlighted critical differences and similarities in molecular and cellular characteristics of DRG. These may have profound implications for translating data from rodent models to human pathologies, and subsequent therapeutic developments. In view of the large-scale failure of clinical trials based on animal models, the success of new drugs to treat pain in the clinic will likely require studies of human cells and tissues. The emergence of researchers with the capacity to acquire and study native human sensory neurons in the DRG through organ-donor networks, in conjunction with data gained from clinical trials of DRG stimulation for treatment of chronic neuropathic pain, will be critical to validate important pain mechanisms discovered in animal models. There are numerous comprehensive reviews summarizing advances in the understanding of rodent DRG, however, to our knowledge, no reviews focused on collating

information on human DRG have been published to date. This review aims to encapsulate existing information about human DRG neurons in relation to their size, location, blood supply, and neurochemical content under non-pathological conditions.

Dorsal root ganglia do not only contain the cell bodies of primary sensory neurons but also a variety of other cell types such as a specific form of glia, called satellite cells, that form a layer (envelope) around neuronal cell bodies (Pannese, 1981; Hanani, 2005, 2010a,b; Takeda et al., 2009). Neurons and satellite cells form a functionally close relationship (**Figure 1**). Studies on cat DRG demonstrate the presence of microvilli as extensions of the neuronal cell surface, in close contact with surrounding satellite cells (Pannese, 1981). Satellite cells express a characteristic pattern of surface receptors (Hanani, 2005), transporters, and enzymes. Glutamine synthetase and proteins of the S100 family can be used to neurochemically identify these cells (Hanani, 2005). Satellite cells are able to modify the microenvironment of neurons by uptake and release of molecules, but interestingly seem not to have a barrier function (Hanani, 2005). In addition to neurons and satellite cells, DRG contain small blood vessels, thus endothelial and smooth muscle cells, delivering blood to satisfy the extensive energy and therefore oxygen demand of sensory neurons. With neuronal processes as long as a meter, ongoing synthesis and transport of proteins over hundreds of millimeters is critical for normal neuronal function. The blood vessels build an extensive network of arterioles and capillaries within DRG (Kutcher et al., 2004; Kubicek et al., 2010). The interface between accumulations of sensory neurons and blood vessels in DRG is unique. Capillaries in DRG are fenestrated and in the absence of a blood–brain barrier, many blood borne molecules can directly enter the DRG and interact with neuronal and non-neuronal cells (Arvidson, 1979; Kiernan, 1996). Non-neuronal target cells include a group of immune cells contained within DRG that consist mainly of macrophages and T-lymphocytes and a lower number of B-lymphocytes (Schmid et al., 2013; Lakritz et al., 2015; Makker et al., 2017) (**Figure 2**).

Compared to rodents, human DRG are larger and contain more cells with different proportions of sensory neuron subtypes and substantially more connective tissue between neurons. Recent studies have showed that compared to classical laboratory animals, human sensory neurons contain similar sets of receptor and channel proteins but their expression levels and function of key components relevant to mechanisms underlying chronic pain, such as sodium channels, can differ (Han et al., 2015; Castro et al., 2017; Zhang et al., 2017, 2019). Given that sodium channel blockers are currently in clinical trials for analgesic drug development (Levinson et al., 2012; Thomas and Atkinson, 2018), this further demonstrates the importance of comparative human data. Additional differences are demonstrated by functional studies examining non-neuronal cells in the DRG. Recent animal studies suggest an important function for satellite glia and immune cells in the development of pain. However, only one publication to date addresses the presence of immune cells such as macrophages and lymphocytes in human DRG under non-pathological conditions (Graus et al., 1990a). Shifting focus to the functional characteristics of mast cells in the DRG, there are no human studies. Considering that a small number of recent comparative studies have demonstrated critical rodent and human inter-species differences between the cellular machinery associated with the development of pathological pain conditions, it is fundamentally important to investigate the cellular and molecular components of human DRG to advance our understanding of these diseases. As a first step toward the objective of investigating human DRG, we believe it is pivotal to summarize current existing knowledge in this field. Here, we focus on describing the location and structure of human DRG, and neurochemical characteristics of satellite glia cells (SGCs) and DRG neurons with emphasis on the nociceptor-related neurochemistry.

HUMAN DORSAL ROOT GANGLIA: MACRO-ANATOMY

Information about the location and size of human DRG is mainly based on investigations using cadaveric material or studies using magnetic resonance imaging (MRI).

Humans possess 31 pairs of spinal nerves containing, inter alia, sensory nerve fibers with cell bodies in DRG. The number of DRG often equals the number of spinal nerves. Nevertheless, the first cervical (C1) DRG has been shown to be smaller compared to DRG at other vertebral levels, in addition to being present in only about a quarter of investigated bodies (28.5%) (Tubbs et al., 2007). The size of human DRG depends on the vertebral level. Even though there might be size differences between ganglia in individuals, on average, no differences exist between ganglia on the left and right side of the body and no age-dependent differences have been reported (Hasegawa et al., 1996; West et al., 2012; Reinhold et al., 2015; Godel et al., 2017). In the cervical region, DRG size increases from the very small and sometimes absent DRG at the level C1 to larger DRG at the C8 level. The C8 DRG also has a larger volume (177 ± 27.5 mm^3) than the adjacent T1 DRG (144 ± 30.8 mm^3) (West et al., 2012). No studies to date have measured human thoracic DRG at lower levels (T3–T12), whereas several studies provide data for DRG at lumbar and sacral levels. **Table 1** summarizes studies that have identified various human DRG dimensions: width; width and length; or volume. The size of lumbar DRG increases from vertebral levels L1 to L5, from approximately 3–5 mm × 4–5 mm at L1 to 5–6 mm × 9–11 mm at L5. Conversely, the size of sacral DRG decreases from S1 to S4 with a very large ganglion at level S1 (6–7 mm × 11–12 mm) (Hasegawa et al., 1996; Ebraheim and Lu, 1998) (**Table 1**). The correlation between DRG size and the number of neurons contained within has also been demonstrated (West et al., 2012).

Considering that human DRG are susceptible to damage by compression, e.g., by disc herniation (Weinstein, 1986), the location of DRG in relation to adjacent structures is important. Compared to other DRG, the second cervical (C2) DRG has an unusual relationship to unique adjacent structures such as atlas and axis or the non-bony posterior border created by the ligamentum flavum (Lu and Ebraheim, 1998; Bilge, 2004). Substantial mobility at

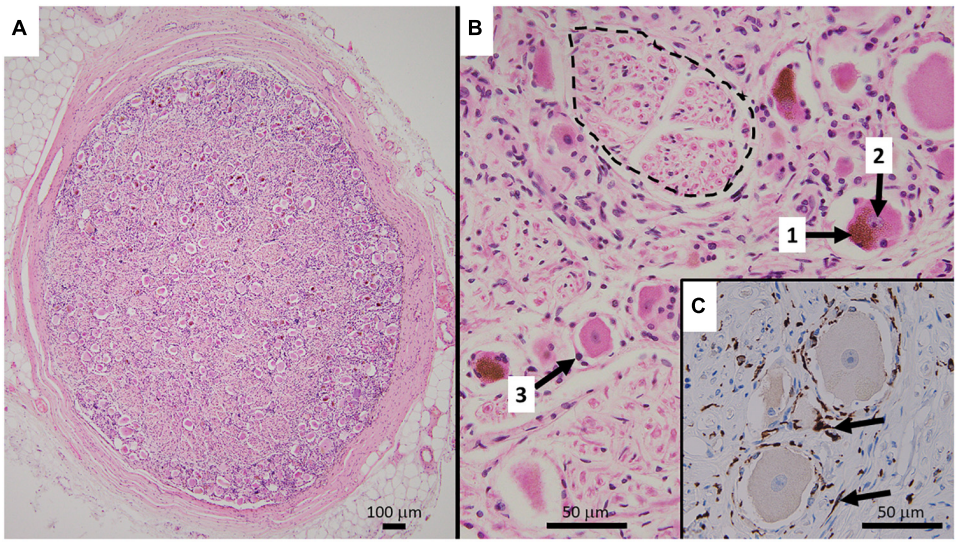


FIGURE 1 | (A) Representative HE stained micrograph section of a thoracic human DRG (medical dissection course, ethics approval obtained from The Southern Adelaide Clinical Human Research Ethics Committee, OFR no.: 55.17) with a thick protective layer of connective tissue demonstrating the predominant localization of cell bodies in the periphery of the ovoid DRG cross-section. **(B)** Cell bodies of sensory neurons containing lipofuszin (1) and a nucleus with a prominent nucleolus (2), surrounded by satellite cells (3). Bundles of nerve fibers (dashed line) are predominantly present in the center of the ganglion. The HE staining method results in shrinkage of the cell bodies which disconnects them from the layer of satellite cells. **(C)** Immunohistochemistry micrograph for CD163 with counterstaining for hematoxylin shows the presence and distribution of macrophages (arrows) in DRG.

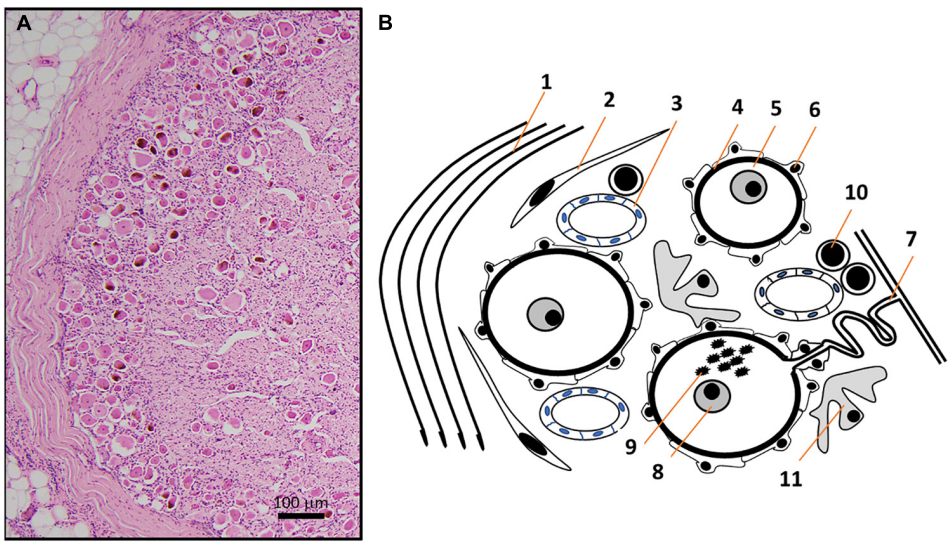


FIGURE 2 | (A) HE micrograph section of a thoracic human DRG in higher magnification shows a high number of neuronal somata of different sizes in the periphery of DRG, next to the thick connective tissue covering. **(B)** Schematic representation of the HE micrograph figure highlighting the variety of different structures and cell types in human DRG. Connective tissue layers (Reina et al., 1996) (1), fibroblasts (2), capillaries (Kutcher et al., 2004) (3), basement membrane (Johnson, 1983) (4) between nerve cells (5) and satellite cells (Hanani, 2005) (6). The pseudo-unipolar process (Rudomin, 2002) (7) originates from sensory neurons with prominent nuclei containing a singular nucleolus (Berciano et al., 2007) (8) and sometimes lipofuszin (Moreno-Garcia et al., 2018) (9). Non-neuronal cells in DRG include T- and B-lymphocytes (10) and macrophages (11) (Graus et al., 1990a).

this intervertebral level might contribute to vulnerability of the ganglion. Besides mobility, the location of blood vessels can also influence DRG function. Alleyne et al. (1998) described the close location to and compression of the C5 cervical ganglion and ventral roots via the vertebral artery which normally lie anterior or lateral to the cervical DRG (Turnbull et al., 1966).

Dorsal root ganglia are normally localized within, or close to, intervertebral foramina, the openings between the pedicles of vertebrae that allow peripheral structures to connect with

TABLE 1 | Summary table for sizes of human DRGs.

Dorsal root ganglia (mm^3)			**Cervical**		**Thoracic**	**Lumbar**			**Sacral**	
References	**Method**	**Participants (*n*)**	**C7**	**C8**	**T1**	**L3**	**L4**	**L5**	**S1**	**S2**
West et al., 2012	MRI	19 (14 m and 5 f)	182 ± 16.2	177 ± 27.5	144 ± 30.8					
Godel et al., 2016	MRI	46 (24 m and 22 f)								
Godel et al., 2017	MRI	13 (13 m)				149.26 ± 45.41	182.58 ± 65.78	239.47 ± 74.96	269.90 ± 70.58	163.42 ± 57.49
Godel et al., 2018	MRI	26 (13 m and 13 f)				124.1 ± 51.7	158.0 ± 59.7	225.2 ± 61.6	230.3 ± 72.8	134.7 ± 57.5

Dorsal root ganglia, length/width (mm)			**Lumbar**					**Sacral**			
References	**Method**	**Participants (*n*)**	**L1**	**L2**	**L3**	**L4**	**L5**	**S1**	**S2**	**S3**	**S4**
Hasegawa et al., 1996	MRI	20 (20 m)	4.3 ± 0.8	5.7 ± 1.2	7.1 ± 1.3	8.1 ± 1.1	9.4 ± 1.4	11.2 ± 1.7			
			3.7 ± 0.7	4.6 ± 0.7	5.7 ± 0.7	6.2 ± 0.7	5.9 ± 0.7	6.2 ± 0.4			
Shen et al., 2006	MRI	115 (54 m and 61 f)	4.35 ± 0.89	5.85 ± 1.11	7.20 ± 1.36	8.64 ± 1.49	11.58 ± 2.25				
			3.38 ± 0.77	4.51 ± 0.88	5.37 ± 0.96	5.83 ± 0.94	6.40 ± 0.91				
Ebraheim and Lu, 1998	Dissection	20 (9 m and 11 f)						12.8 ± 1.8	10.1 ± 1.5	8.0 ± 1.4	5.1 ± 1.6
								6.3 ± 1.3	5.1 ± 0.9	4.1 ± 0.8	2.9 ± 0.9
Silav et al., 2016	Dissection	15 (gender unspecified)	5.39	5.83	7.24	7.97	10.83				
			4.36	4.56	4.99	5.22	5.82				
Reinhold et al., 2015	MRI T1.5/T3	20 (10 m and 10 f)	7	7.3	7.9	7.9	8	8.9			
			4.6	4.9	5.2	4.8	4.8	5.4			
Reinhold et al., 2015	MRI T1.5/T3	20 (10 m and 10 f)	6.6	7.4	8	7.8	7.9	8.1			
			4.5	5.1	5.4	5.1	5	5.3			
Silverstein et al., 2015	MRI and dissect.	16 (10 m and 6 f)	No data	No data	No data	No data	No data				
			3.2 ± 0.7	4.3 ± 0.4	4.9 ± 0.3	6.1 ± 0.4	6.5 ± 0.5				

Dorsal root ganglia height (mm)			**Lumbar**				
References	**Method**	**Participants (*n*)**	**L1**	**L2**	**L3**	**L4**	**L5**
Hasegawa et al., 1996	MRI	20 (20 m)	4.3 ± 0.9	5.6 ± 1.2	7.3 ± 1.4	8.2 ± 0.9	

Dorsal root ganglia diameter (mm)			**Lumbar**				**Cervical**
References	**Method**	**Participants (*n*)**	**L4 left**	**L4 right**	**L5 left**	**L5 right**	**C2**
Zhao et al., 2018	3D CT	23 (15 m and 8 f)	5.8 ± 0.3	5.5 ± 0.4	5.7 ± 0.4	6.1 ± 0.5	
Koeppen et al., 2017	Dissection	12					4.6-4.97

Dorsal root ganglia area (mm^2)		**Lumbar**	**Sacral**
References	**Method**	**Participants (*n*)**	**L5**	**S1**
Beom et al., 2018	MRI	10 (8 m and 2 f)	66.6 ± 13.7	79.5 ± 14.3

m, male; f, female.

the vertebral canal. Within the intervertebral foramen, DRG are normally localized superolaterally, but at lower vertebral levels they tend to be positioned more centrally within the foramen. Kikuchi et al. (1994) classified DRG location as intraspinal (in the vertebral canal, proximal to the vertebral foramina), intraforaminal (in the intervertebral foramina) or extraforaminal (distal to the intervertebral foramina). A study investigating C6 and C7 DRG showed that about half were situated extraforaminally (Yabuki and Kikuchi, 1996). Lumbar DRG are predominantly intraforaminal. Sacral DRG are localized more centrally, with DRG at levels S1 and S2 localized intraforaminal and S3 and S4 in the vertebral canal (intraspinal) (Sato and Kikuchi, 1993; Kikuchi et al., 1994; Hasegawa et al., 1996; Ebraheim and Lu, 1998; Moon et al., 2010). No differences have been observed in the location of DRG with respect to gender, age, height, and weight (Moon et al., 2010).

HUMAN DORSAL ROOT GANGLIA: MICRO-ANATOMY

Interestingly in humans, individual DRG can occasionally consist of one, two or three smaller and distinctly sheathed ganglia (Kikuchi et al., 1994; Shen et al., 2006). DRG containing two or even three ganglia are predominantly present at vertebral levels L3 and L4 (Shen et al., 2006). Whether this is of functional significance remains unknown.

Human DRG normally consist of a peripheral region that contains the somata of primary sensory neurons and a central region that predominantly contains bundles of nerve fibers (Jimenez-Andrade et al., 2008; Godel et al., 2016) (**Figure 1**). They are encased by meninges including a thick layer of dura mater, comprised of collagenous connective tissue (Reina et al., 1996). Based on light microscopy and routine hematoxylin and eosin (HE) staining, neuronal cell bodies can be subdivided into small phase-dark neurons and large phase-light neurons, with distinct types of neurons already present at gestational week 6 (Marti et al., 1987). Fluorescence and light microscopy show human DRG neurons often contain highly autofluorescent accumulations of material (fluorescence microscopy) or accumulations of brownish material. This is the pigment lipofuscin which consists of a mixture of lipids, misfolded proteins and sugar molecules (Moreno-Garcia et al., 2018) (**Figures 1**, **2**). Human DRG neurons show age-dependent inclusions of lipofuscin, which are accompanied by accumulations of melanin (Scharf and Blumenthal, 1967). The nuclei of human DRG neurons normally contain one nucleolus that is relative in size to the cell body, and possess Cajal bodies, suborganelles that are in involved in RNA processing (Berciano et al., 2007) (**Figures 1**, **2**).

It is difficult to determine the exact number of primary sensory neurons within DRG as the ganglia are not round but rather ovoid and elongated. Furthermore, DRG contain not only neurons but also non-neuronal cells, connective tissue, blood vessels and bundles of nerve fibers. Stereological quantification was used to determine the number of DRG neurons that project with the brachial plexus to peripheral targets. The study determined that about 60,000 neurons are present in DRG at the level of C5 and about 100,000 at the C7 level (West et al., 2012).

Developmentally, all DRG neurons are initially similar in size, and differences in cell size start to appear from week 6 of gestation on Marti et al. (1987). The size of human DRG neurons identified in cryostat sections ranges from approximately 20 to 100 μm in diameter. Human neurons are larger compared to rodent DRG but the distribution of small and large neurons is similar (Josephson et al., 2001; Zhang et al., 2017). Small to medium sized human neurons are considered those with somata of <60 μm (Davidson et al., 2014; Han et al., 2015; Chang et al., 2018). In contrast to human DRG neurons *in situ*, neurons of small to medium sizes dominate in neuronal cultures of dissociated ganglia [36 ± 2.6 μm in diameter (Anand et al., 2016)] as the conditions of isolation probably destroy larger neurons, similar to laboratory animals. In cultured, dissociated human DRG neurons ranged from 28 to 56 μm in diameter (Davidson et al., 2014).

Neurons in DRG possess a T-shaped pseudo-unipolar process that originates from the cell body via an initial segment (**Figure 2**). Animal studies have shown that it extends with a shorter "axonal" central process connected to and arborizing within the spinal cord dorsal horn (see review, Rudomin, 2002) and a peripheral "axonal" process innervating target tissues. Data in relation to the central sensory fiber arborization in human spinal cord do not exist. Peripheral processes have been described in different human tissues. Some processes are only one micrometer in diameter but travel large distances. The peripheral process from a lumbar DRG neuron that innervates for example the big toe, can exceed 1 m = 1,000,000 μm. This presents a massive extension of the cell, restricting only 1–2% of the cytosol to the cell body with the majority of cytosol and cytoskeletal elements present in pseudo-unipolar processes (see review, Devor, 1999).

The initial segment of the pseudo-unipolar process of human DRG neurons is elongated and it forms a glomerulus-like structure (**Figure 2**). With age, the structure is increasingly surrounded by glial fibrillary acidic protein (GFAP)-positive SGCs (Murayama et al., 1991) but neurons and satellite glia are still separated by a basement membrane approximately 100 nm thick (Johnson, 1983).

HUMAN DORSAL ROOT GANGLIA: BLOOD SUPPLY

Dorsal root ganglia are situated outside of the blood brain barrier and animal studies clearly show the presence of fenestrated capillaries (**Figure 2**). Hence, molecules circulating in the vascular system can directly access to the DRG. This vascular organization provides the human DRG with a robust blood supply, serving neurons that have long processes with the required high-energy demand critical for maintaining the production and transport of receptors, ion channels, cytoskeletal and transport proteins. Two interconnected

arterial plexuses, situated superficially and deep, supply human DRG. These plexuses originate from arteries that derive from the radiculomedullary branches of segmental arteries (Yoshizawa et al., 1991; Gilchrist et al., 2002; Parke and Whalen, 2002). Peri-ganglionic venous plexuses drain predominantly from the dorsal side of DRG into intervertebral veins (Takano et al., 1998; Parke and Whalen, 2002). Recently, Godel et al. (2016, 2017) used dynamic-contrast-enhanced MRI perfusion to investigate the dynamics of blood supply of human DRG. The blood supply *in vivo*, expressed as perfusion of DRG determined by blood-tissue permeability and interstitial leakage fraction, was higher in DRG compared to spinal nerves. Interestingly the perfusion of DRG was significantly higher in women compared to men (Godel et al., 2016, 2017).

SATELLITE GLIAL CELLS (SGCs)

This specialized group of DRG and TG-specific glia cells (Hanani, 2005, 2010a,b) not only surround the initial segment, but build an envelope around the somata of nerve cells (**Figures 1**, **2**) and are able to modulate neuronal function (Pannese, 1981; Hanani, 2005, 2010a,b). Animal studies to date have revealed a substantial amount of receptors, transporters and ion channels are expressed in SGC (see review, Hanani, 2005). Unfortunately, only a small number of studies have investigated the neurochemical characteristic of human SGC (**Table 2**). Those studies show that, similar to those of laboratory animals, human glia cells exhibit characteristic immunoreactivities for S100 beta protein and glutamine synthetase (Pan et al., 2012; Koeppen et al., 2016). Koeppen et al. (2016) performed a carefully controlled immunohistochemical analysis of characteristic molecules in human SGCs, and showed the presence of the metabotropic glutamate receptor 2/3, (mGlu2/3), the ATP-sensitive inward rectifying potassium channel 1.4 (Kir 1.4) and the excitatory amino acid transporter 1 (EAAT1) in human SGCs (Koeppen et al., 2016) (**Table 2**). Since the primary transmitter of nociceptive DRG neurons is glutamate, the presence of mGlu2/3 and EAAT1 suggest active involvement of SGC in the glutamate turnover of human DRG neurons. Animal studies showing inter-SGC connections and the presence of connexin 43, a major component of gap-junctions (Koeppen et al., 2016), suggest SGC involvement in cells-to-cell communication. Recently, Li et al. (2018) demonstrated immunoreactivity for $Na_V1.7$ in GFAP-positive putative SGCs within DRG removed from patients with cancer-related neuropathic pain. It remains unknown if this "nociceptive" ion channel is present in SGC under normal conditions. Nevertheless, immunoreactivity for glial-derived neurotrophic factor (GDNF), another molecule relevant for both DRG development and pain signaling, is present in SGC (Bar et al., 1998).

Evidence indicates satellite cells recognize foreign molecules and participate in immune-mediated processes. Earlier studies showed that SGC in human DRG express class I and II Major Histocompatibility Complex (Graus et al., 1990a,b). More recently, studies in human SGC obtained from TG have

TABLE 2 | Molecules described in human satellite glial cells using immunohistochemistry.

Antigen	Host, supplier	References	Specificity control	Number	Source
S100	Mouse; Santa Cruz	Koeppen et al., 2016	Preabsorption	12 (gender unspecified)	Autopsy
Glutamate synthetase	Mouse; Santa Cruz	Koeppen et al., 2016	Preabsorption	12 (gender unspecified)	Autopsy
Metabotropic glutamate receptor 2/3 (mGluR2/3)	Rabbit; Novus	Koeppen et al., 2016	Preabsorption	12 (gender unspecified)	Autopsy
ATP-sensitive potassium channel 1.4 (Kir 1.4)	Rabbit; Alomone	Koeppen et al., 2016	Preabsorption	12 (gender unspecified)	Autopsy
Excitatory amino acid transporter 1 (EAAT1)	Goat; Santa Cruz	Koeppen et al., 2016	Validated via MIDAS	12 (gender unspecified)	Autopsy
Connexin 43	Mouse; Abcam	Koeppen et al., 2016	Validated via MIDAS	12 (gender unspecified)	Autopsy
Voltage-gated sodium channel 1.7 ($Na_V1.7$)	Rabbit; Alomone	Li et al., 2018	Preabsorption	6 DRG, 3 donors (2 m and 1 f)	Spinal surgery
Glial-derived neurotrophic factor (GDNF)	Not specified; Santa Cruz	Bar et al., 1998	Preabsorption	5 DRG, 5 donors (gender unspecified)	Autopsy

Specificity control: Accepted as evidence supporting the specificity of the primary antiserum/antibody were preabsorption with the corresponding antigen and Western blot showing the complete blot with a single band at the correct molecular weight. Evidence considered not specific for immunoreactivity in human DRG included absence of immunoreactivity in antigen-deficient (knock-out) cells or positive staining in target tissues in animals.

demonstrated a class of pathogen- and damage-associated pattern recognition receptors, the Toll-like receptors (Mitterreiter et al., 2017). Studies characterizing subpopulations of DRG neurons through the differential expression of surface carbohydrate antigens discovered that SGC express gangliosides such as the GD1b ganglioside and fucosyl GM1 (Kusunoki et al., 1989, 1991, 1997). Similarly, interest in expression of molecules in DRG neurons demonstrated the expression of a variety of molecules in SGC, such as the EGF receptor and the Bcl-2 homologous antagonist Bak (Huerta et al., 1996; Krajewski et al., 1996). SGCs also express the olfactory receptor 6B2 protein (Flegel et al., 2015). In summary, human SGCs share many features with SGCs of small laboratory animals, such as the expression of glia- and neuron-related molecules. But compared to results of animal experiments human data is limited and taking into account the established close relationship between sensory neurons and DRG-specific glia, a lot of work needs to be done to further characterize this important cell type in human DRGs.

NEUROCHEMICAL CHARACTERISTICS OF HUMAN DRG NEURONS

Dorsal root ganglia contain a complex array of sensory neuron cell bodies that have different functions and innervate different targets. Many proteins such as channel proteins are highly related to neuron function. The method capable of identifying protein localization in complex tissues with high resolution is immunohistochemistry. This section aims to provide data for normal, uninjured human DRG immunohistochemistry, and does not focus on molecules related to any form of pathology. Only data obtained from studies of normal human DRG and from studies using normal human DRG as control tissues are discussed in this segment.

As noted previously, human DRG neurons measure between about 20 and 100 μm in diameter (Holford et al., 1994; Coward et al., 2000; Anand et al., 2006; Li et al., 2018) and occupy areas between 1,500 and 5,000 μm^2 (Koeppen et al., 2011). There are no reliable and distinct morphological characteristics that allow the functional subdivision of sensory neuron subpopulations based on neuronal soma size or shape. However, neurochemical characteristics represent the most commonly used method to describe aspects of neuronal function and classification in the DRG. The emergence of genomic and transcriptomic studies has recently opened a window for researchers to re-evaluate the classification of DRG neuron subtypes based on mRNA expression patterns in individual rodent neurons (Usoskin et al., 2015). However, further validation of these groundbreaking studies will be required before a more advanced classification systems is established and widely accepted. This section will focus on neurochemical characteristics of human DRG neurons, starting with the description of common neuronal markers with an overarching focus on neurochemical characteristics associated with nociceptive function. Given the relative wealth of data included in this section, **Supplementary Table 1** provides an appended overview of critical variables, including the number of participants or DRG donors, and more importantly the presence or absence of controls used for the specificity of the primary antisera/antibodies (Saper, 2009).

Common Neuronal Markers

Neurofilaments (NFs)

Neurofilaments (NFs) are cytoskeletal intermediate filaments of varying molecular weights ranging from ∼56 to 200 kDa. They provide structural support and regulate axonal diameter, and are present in all neurons, including the DRG. In rodents, NF200, a neurofilament of 200 kDa, labels a population of larger, myelinated A-fiber neurons. Human studies have shown the presence of neurofilaments in DRG neurons early in development. Immunoreactivity for a neurofilament 150 kDa was present in fetal DRG neurons at week 6 (Marti et al., 1987). Neurofilament 200 immunoreactivity was detected in few cells in week 10 but in all neurons at weeks 17–18 of gestation (Suburo et al., 1992). This is also true for adult human DRG where, in contrast to rodents, NF200 immunoreactivity is not restricted to larger neurons but present in virtually all DRG neurons (Suburo et al., 1992; Naves et al., 1996; Rostock et al., 2017; Chang et al., 2018). Similarly, most or all adult human DRG neurons show immunoreactivity for other cytoskeletal molecules such as α- and β-tubulin, microtubule-associated proteins 1 and 5, and neurofilaments 68 and 160 (Naves et al., 1996).

PGP9.5 (UCHL1)

PGP9.5 (UCHL1), a ubiquitin C-terminal hydrolase is present in all neurons and is a pan-neuronal marker. This protein has emerged as one of the key neuronal markers in rodents and humans, and is used to differentiate between neuronal and non-neuronal structures in DRG (Coward et al., 2000; Anand et al., 2018; Desormeaux et al., 2018).

Tuj1 (Beta3 Tubulin, TUBB3)

Tuj1 (beta3 tubulin, TUBB3) is part of microtubule element within the tubulin family found predominantly in neurons and testes in healthy tissues. Detection of this protein is widely used as a pan-neuronal marker in immunohistochemical studies, as it readily differentiates neuronal from glial cells, which do not express beta3 tubulin. It is primarily detected in somata and processes of human DRG neurons *in situ* and under culture conditions (Naves et al., 1996; Robinson et al., 2007; Enright et al., 2016; Rostock et al., 2017; Anand et al., 2018).

Peripherin (PRPH)

Peripherin (PRPH) is an intermediate filament protein that is expressed in neurons of the peripheral nervous system such as small DRG neurons and in central neurons that innervate peripheral targets such as motor neurons (Bae et al., 2015).

Brn3a (Pou4f1)

Brn3a (Pou4f1), a sensory neuron marker, is a POU homeodomain transcription factor that regulates gene expression and differentiation of sensory neurons. In animal studies it has been shown to be expressed from nearly all sensory DRG neurons

(Badea et al., 2012). It has been found present in all human DRG neurons of adults (Rostock et al., 2017) and gestational weeks 9–11 (Schonemann et al., 2012), and has been found colocalized with NF200 (Rostock et al., 2017).

NeuN (RBFOX3)

NeuN (RBFOX3) is a RNA binding protein found predominantly in the neuronal nuclei, and another common neuronal biomarker found in the vast majority of postmitotic (mature) neurons (Duan et al., 2016). In the limited studies performed to date, NeuN is expressed in all adult human DRG neurons but was not detected at gestational week 10 (Schonemann et al., 2012).

Molecules Characteristic of Nociceptors

Ion Channels

Ion channels are essential for the regulation of neuronal excitability leading to the generation and conduction of action potentials and are therefore critical to sensory neuron function. Important channel proteins for the generation of inward membrane currents in nociceptors belong to the groups of voltage-gated sodium (Na_V) and calcium (Ca_V) channels as well as transient receptor potential (TRP) channels (Waxman and Zamponi, 2014). Given the sensory nature of the DRG, and their role in the development of chronic pain conditions, it's not surprising that in relation to the detection of channel proteins in individual neurons, human DRG studies have predominantly focused on channels related to nociception.

Voltage-activated sodium channels

Voltage-activated sodium channels are key components of action potential generation in DRG neurons. Out of the nine Na_V subtypes, the Na_V 1.7, 1.8, and 1.9 are of particular interest as they have established roles as key components of pain signaling events (Waxman and Zamponi, 2014; Namer et al., 2015; Dib-Hajj et al., 2017). Studies using multiple labeling immunohistochemistry (Coward et al., 2000, 2001; Li et al., 2018) have demonstrated that immunoreactivity for the voltage-gated sodium channel $Na_V1.7$ is present in about half of all DRG neurons. In contrast to animal studies, in humans the $Na_V1.7$ immunoreactivity is not restricted to small neurons but present in neurons of all sizes (Li et al., 2018). Immunoreactivities for $Na_V1.7$ (PN1), $Na_V1.8$ (SNS/PN3) and Na_V 1.9 (NaN/SNS2) have been detected in all small (<30 μm), medium-sized (<50–55 μm) and large (>55 μm) neurons (Coward et al., 2000, 2001), which also suggests the presence of voltage-gated sodium channels Na_V 1.7, 1.8, and 1.9 in neurons of all sizes. Nevertheless, the strongest immunoreactivity was detected in small neurons (Coward et al., 2000, 2001).

A recent study investigating the presence of Na_V 1.6, 1.7, 1.8, and 1.9 in human DRG using *in situ* hybridization (Rostock et al., 2017), has shown that all Na_V channels were present in human DRG and expressed in presumably nerve growth factor-dependent, TrkA expressing neurons. The Na_V 1.9 showed the lowest level of colocalization with TrkA (present in about 25% of neurons), the $Na_V1.8$ the highest (about 70% of neurons). Interestingly, the study directly compared proportions of positive cells in human and mouse DRG and showed significant differences between mouse and humans for $Na_V1.8$ and $Na_V1.9$ (Rostock et al., 2017).

These findings are supported by RT-PCR and RNAseq studies that demonstrated the expression of mRNA for Na_V subunits in human DRG explants (Dib-Hajj et al., 1999; Jeong et al., 2000; Chang et al., 2018; Ray et al., 2018). Interestingly, qRT-PCR showed that the expression levels and proportions of Na_V channel subtypes were different between humans and mice (Chang et al., 2018). The expression of the Na_V 1.8 channel subtype gene SCN10A, was much lower in human DRG, when compared to gene expression levels reported in mouse studies. In contrast, the expression of the $Na_V1.7$ channel subtype gene SCN9A, was much higher in human than mouse samples (Chang et al., 2018). These findings are supported by an RNAseq study (Ray et al., 2018) that found channel subunit SCN9A expression levels are more abundant in human DRG compared to mouse data. The sequencing data support qRT-PCR data and show differences in expression levels between mice and human DRG.

In addition to transcriptional and translational data, electrophysiological studies confirm the functional presence of $Na_V1.7$ and $Na_V1.8$ channels in human DRG neurons. Sensitivity to the puffer fish toxin tetrodotoxin (TTX) selectively differentiates between channel subtypes, where $Na_V1.8$ and 1.9 are TTX-resistant, $Na_V1.1$, 1.2, 1.3, 1.6, and 1.7 are TTX-sensitive (Waxman and Zamponi, 2014). Human DRG neurons possess TTX-sensitive and TTX-resistant channels, but in contrast to rodents, where TTX-resistant currents are mainly restricted to small diameter neurons, in humans they are present in small and large diameter neurons (Han et al., 2015; Zhang et al., 2017). Nevertheless, the $Na_V1.7$ channel is the major TTX-sensitive sodium channel in DRGs in both humans and mice (Alexandrou et al., 2016). However, in humans, $Na_V1.8$ channels exhibit different functional properties and the density of TTX-sensitive and -resistant channels is much higher than that detected in animal studies (Han et al., 2015; Zhang et al., 2017).

Voltage-gated calcium channels (Ca_V)

Voltage-gated calcium channels (Ca_V) are essential components of sensory neuron function (Park and Luo, 2010) as activation of these channels contributes to exocytosis of transmitter-filled vesicles at synaptic endings. The channels can be subdivided based on different criteria such as high-voltage activated and low voltage activated (HVA, LVA), similarity of the α1-subunit (Ca_V1, Ca_V2, Ca_V3) or sensitivity to pharmacological inhibitors (L, N, P/Q, R, T) (Lacinova, 2005; Park and Luo, 2010). To date no studies have reported the cellular location of Ca_V proteins in human DRG neurons, however, the expression of Ca_V-mRNA has been confirmed by RT-PCR as well as single cell PCR. Interestingly, the $Ca_V2.2$ channel was expressed in 56.4% of cultured human DRG neurons whereas the $Ca_V2.3$ was found to be expressed only in 5% of neurons (Castro et al., 2017).

Calcium-activated potassium channels (K_{Ca})

Calcium-activated potassium channels (K_{Ca}) are important contributors to the after hyper-polarization of neurons which can be modulated by NMDA-type glutamate receptor activation and

nerve ligation, and therefore contribute to nociceptive signaling (Li et al., 2007; Pagadala et al., 2013). Immunoreactivities for voltage-independent human $K_{Ca}2.1$ (SK1) and $K_{Ca}3.1$ (IK1) channels were shown in almost all (between 87% and 95%) sensory DRG neurons independent of size (Boettger et al., 2002).

Purinergic receptor (P_2X)

Purinergic receptor (P_2X) subunits, P_2X_2 and P_2X_3, can build homo- or heterotrimeric ligand-gated ion channels that are activated by ATP. The channels are part of a variety of neuronal signaling pathways including nociception. Studies in rodents have established that P_2X_2 and P_2X_3 channels are expressed in DRG neurons with the P_2X_3 subunit predominantly expressed in non-peptidergic, GDNF-dependent but NGF-independent nociceptors (Mo et al., 2009).

Interestingly, mRNA for the P_2X_2 subunit was reported to be absent in human DRG (Serrano et al., 2012) whereas P_2X_3 mRNA and protein were clearly detected in human DRG (Yiangou et al., 2000; Pan et al., 2012; Serrano et al., 2012). Using a carefully tested antiserum, Pan et al. (2012) confirmed the presence of P_2X_3-immunoreactivity in virtually all DRG neurons, independent of size. Pan et al. (2012) and Yiangou et al. (2000) demonstrated the presence of strong P_2X_3-immunoreactivity only in small to medium sized neurons which, similar to rodents, usually do not express the nociceptor subtype-defining NGF receptor TrkA.

The functional validation of P_2X channels in human DRG neurons was also supported by electrophysiological studies and Ca^{2+}-imaging. However, in this instance only a subgroup of small-sized (30–60 μm in diameter) isolated human DRG neurons responded to ATP with action potential discharges, and increase in intracellular Ca^{2+} levels (Davidson et al., 2014; Enright et al., 2016).

Transient receptor potential cation channel subfamily V member 1 (TRPV1)

Transient receptor potential cation channel subfamily V member 1 (TRPV1) is a channel protein that is activated by the vanilloid capsaicin, an ingredient of hot chili peppers, by low pH and noxious heat. Endogenous agonists are endocannabinoids such as anandamide and *N*-arachidonoyl-dopamine (Suh and Oh, 2005). TRPV1 is a non-selective cation channel that has been shown to be an important component of nociceptive signaling (Suh and Oh, 2005). Capsaicin induces pain in humans (Simone et al., 1989), but also induces desensitization of TRPV1 channels and modulates nociceptor function. Consequently, topical capsaicin is currently being successfully used in treatment of pain conditions such as postherpetic neuralgia (Anand and Bley, 2011).

As has been done in animal studies, immunohistochemical studies have confirmed the presence of the TRPV1 protein in human DRG neurons. Interestingly, most studies describe the presence of immunoreactivity not only in small-sized neurons but also in medium and some studies in large-sized somata (Lauria et al., 2006; Facer et al., 2007; Li et al., 2015, 2018; Anand et al., 2016; Chang et al., 2018). The average diameter of TRPV1-immunoreactive neurons was reported as 44 ± 7 μm (Chang et al., 2018). TRPV1 expression was also validated in cultured human DRG neurons (Anand et al., 2008; Enright et al., 2016; Valtcheva et al., 2016), with a high proportion of neurons showing TRPV1-immunoreactivity (Anand et al., 2008).

TRPV1 mRNA expression was detected in human DRG explants (Cortright et al., 2001; Flegel et al., 2015; Ray et al., 2018; Sheahan et al., 2018; Snyder et al., 2018) and cultured human DRG (Han et al., 2016). Functional evidence for the presence of TRPV1 channels in human DRG neurons has been provided using capsaicin, a TRPV1 agonist. Capsaicin activation of cultured human DRG neurons induced action potential discharge and increased intracellular Ca^{2+} levels (Baumann et al., 1996; Li et al., 2015; Anand et al., 2016; Han et al., 2016; Valtcheva et al., 2016; Sheahan et al., 2018).

Transient receptor potential cation channel ankyrin 1 (TRPA1)

Transient receptor potential cation channel ankyrin 1 (TRPA1) is a channel protein activated by mustard oil and cinnamaldehyde, and plays an important role as an irritant sensor of a vast amount of compounds in nociceptive signaling, with its expression confirmed in animal DRG neurons (Chen and Hackos, 2015). Immunohistochemistry showed the presence of TRPA1 immunoreactivity in 20% of human DRG neurons, predominantly in small-medium sized (<50 μm) neurons with some staining in larger neurons. Most of the TRPA1 positive cells were also immunoreactive for TRPV1 (Anand et al., 2008). Cultured human DRG neurons obtained from patients with avulsion injury, responded to cinnamaldehyde with an increase in intracellular Ca^{2+} levels (Anand et al., 2008). Additionally, the TRPA1 channel has also been detected in human DRG via *in situ* hybridization, which demonstrated that TRPA1 mRNA expressing cells also express TRPV1 mRNA (Rostock et al., 2017).

Peptides

Neuropeptides such as CGRP, SP and galanin are neuromodulators that are co-released with transmitters at the central and peripheral terminals of sensory neurons. In addition to being important cellular markers used in identifying subpopulations of sensory neurons, they are also fundamental contributors to nociceptor function.

Calcitonin-gene-related-peptide (CGRP)

Calcitonin-gene-related-peptide (CGRP) is a neuropeptide composed of 37 amino acids. Two isoforms of the peptide exist (α-CGRP and β-CGRP) encoded from two separate genes. CGRP interacts with heteromeric receptors consisting of the calcitonin-receptor-like-receptor (CRLR) and receptor activity-modifying proteins (RAMPs). Although the peptide is a strong arterial vasodilator, it also plays a major role in nociception (Marti et al., 1987; Suburo et al., 1992; Nordlind et al., 2000; Shi et al., 2008, 2012; Patil et al., 2010; Yarwood et al., 2017; Li et al., 2018). Furthermore, CGRP is widely used to define a subpopulation of nociceptive DRG neurons.

Immunoreactivity for CGRP is present in human DRG neurons from early fetal life (Marti et al., 1987; Suburo et al., 1992; Nordlind et al., 2000; Shi et al., 2008, 2012; Patil et al., 2010; Yarwood et al., 2017; Li et al., 2018), initially appearing at weeks 14–16, with staining intensity in DRG

neurons increasing between 5 months and adulthood (Pan et al., 2012). Subpopulations of CGRP-containing neurons possess immunoreactivity for other peptides such as substance P or signaling molecules such as TRPV1 and phospholipase C beta 3 (PLCβ3) (Shi et al., 2008) or angiotensin II (Patil et al., 2010).

In situ hybridization confirmed the presence of CGRP mRNA in 50–70% of DRG neurons (Giaid et al., 1989; Landry et al., 2003), predominantly but not exclusively in small-medium sized neurons. Some studies have identified only about 20% of DRG neurons showing CGRP-immunoreactivity (Giaid et al., 1989), although others placed the reported proportion as high as 60% (Nordlind et al., 2000).

Substance P (SP)

Substance P (SP) is a neuropeptide composed of 11 amino acids. It is synthesized by alternative splicing from a larger precursor mRNA, preprotachykinin-A, coded by the TAC1 gene. It selectively binds to the neurokinin 1 receptor present on nociceptive projection neurons in the rat spinal cord dorsal horn and causes enhanced synaptic activity (Gautam et al., 2016). Animal studies demonstrate a clear involvement of SP in nociceptive signaling, however, in humans, the evidence to date is not as convincing (Babenko et al., 1999; Hill, 2000). SP is present in human DRG, with pre-protachykinin mRNA detected in small-sized neurons representing 10% of all DRG, whereas the proportion of human DRG neurons reported to show immunoreactivity for the peptide varies from 5 to 60% (Giaid et al., 1989; Nagao et al., 1994; Nordlind et al., 2000; Landry et al., 2003). Similarly, SP immunoreactivity is present early in development in neuronal cell bodies of fetal DRG but reports vary. Marti et al. (1987) detected immunoreactivity from week 24 onward, whereas Suburo et al. (1992) reported the presence of SP immunoreactivity from week 11 onward (Marti et al., 1987; Suburo et al., 1992). Despite the apparent similarities between humans and rodents, with both having a subpopulation of nociceptive DRG neurons containing SP, blockade of the action of SP via inhibition of neurokinin 1 receptors is effective in relieving pain in mice (Laird et al., 2000; Borbely et al., 2013), but has failed to generate analgesia in human clinical trials (Hill, 2000).

Galanin

Galanin is a peptide consisting of 29/30 amino acids (Lang et al., 2015). Galanin modulates the excitability of dorsal horn neurons and the presynaptic release of glutamate from primary afferents (see review, Lang et al., 2015). It is present in DRG of laboratory animals (Ch'ng et al., 1985; Lang et al., 2015). Galanin mRNA has been detected in human DRG via *in situ* hybridization in a small subpopulation (12.5% ± 1.4) of small-sized ($<$1550 μm^2) neurons. The majority of galanin mRNA-expressing neurons also contained CGRP-mRNA (Landry et al., 2003).

Somatostatin and its receptors

Somatostatin is a neuropeptide of either 14 or 28 amino acids in length, generated from a precursor peptide and is involved in pain processing via interaction with its cognate receptors producing inhibitory, analgesic effects (Mollenholt et al., 1994). More recent studies suggest that somatostatin is also involved in the signaling of itch (Huang et al., 2018).

Dorsal root ganglia neurons with immunoreactivity for somatostatin are present by gestational weeks 9 and 10, and a small population of immunoreactive cells are detectable throughout all fetal stages, with enduring expression within cells present in DRG of 4-month-old infants (Charnay et al., 1987; Marti et al., 1987). Furthermore, somatostatin immunoreactivity is also present in a subpopulation (17%) of adult human DRG neurons (Nagao et al., 1994; Shi et al., 2014) whereas the somatostatin$_{2A}$ receptor is present only in few neurons in human DRG (Shi et al., 2014).

Endothelin-1 (ET1)

Endothelin-1 (ET1) is one of three peptide isoforms, 21 amino acids in length, which act as vasoconstrictors but also induce pruritus and pain (Smith et al., 2014). The ET1 peptide is elevated in patients suffering from sickle cell disease, which is associated with episodes of severe pain and animal studies showed that absence of the ET_A receptor subtype blocked sickle cells disease-related pain behavior (Lutz et al., 2018).

In human DRG 30% of neurons show ET1 immunoreactivity (Giaid et al., 1989). *In situ* hybridization shows the presence of ET1 in 75% of large and small DRG neurons. The mRNA for ET1 has been reported to be often colocalized with mRNAs for preprotachykinin or CGRP, where all preprotachykinin mRNA expressing DRG neurons contained mRNA for ET1 (Giaid et al., 1989).

Angiotensin II and its receptors

The eight amino acids long peptide angiotensin II is part of the renin–angiotensin–aldosterone system (RAAS) that controls water and electrolyte balance and therefore blood pressure. This peptide also contributes to the regulation of nociception. Animal studies show intrathecally applied angiotensin II elicits nociceptive behavioral responses (Cridland and Henry, 1988; Nemoto et al., 2013), suggesting that angiotensin II released by central projections of DRG neurons may contribute to nociception. In human DRG, the presence of angiotensin II has to date been demonstrated by radio-immuno-assay, HPLC and immunolabeling (Patil et al., 2010; Anand et al., 2013). Angiotensin II immunoreactivity was observed in 75% of small and medium-sized human DRG neurons (Anand et al., 2015). Double-labeling of human DRG showed angiotensin II in neurons expressing CGRP, synaptophysin and cathepsin D (Patil et al., 2010).

There is also evidence that human DRG neurons themselves respond to angiotensin II. The angiotensin II type 2 receptor (AT_2R) has been identified in cultured human DRG and in 60% of small and medium diameter neurons in immunolabeled sections of human DRG (Anand et al., 2013). Multiple labeling studies affirm the expression of angiotensin II, AT_2R and TRPV1 in the same neurons (Anand et al., 2015), where over 40% of TRPV1-positive neurons expressed AT_2R (Anand et al., 2013). Direct involvement of angiotensin II in pain signaling pathways, was supported by experiments where angiotensin II treatment of cultured human DRG neurons increased their response

to capsaicin, whereas treatment with an AT_2R antagonist reduced capsaicin responses (Anand et al., 2013). However, more recently the presence of AT_2R in human and rodent DRG has been disputed, by studies finding no evidence of mRNA for AT_2R genes in mouse DRG (Shepherd et al., 2018). Instead, these reports that mechanical pain hypersensitivity induced by angiotensin II is mediated by macrophage AT_2R, leading to production of reactive nitrogen/oxygen species that in turn activate neuronal TRPA1 (Shepherd et al., 2018). Whether this occurs via a direct action on neurons, or via effects on immune cell-neuron interactions remains to be determined. Despite the uncertainty surrounding their mechanism of action, AT_2R antagonists are being used as effective analgesics in humans and laboratory animals (Rice et al., 2014; Bessaguet et al., 2016; Shepherd et al., 2018).

Other Markers of Sensory and Nociceptive Neurons

Isolectin B4 (I-B4)

Isolectin B4 (I-B4) is a plant lectin isolated from *Griffonia simplicifolia*, which labels a subpopulation of nociceptive DRG neurons. In mice, these neurons have been shown represent the group of GDNF-dependent, non-peptidergic nociceptors (Bogen et al., 2015). Although Davidson et al. (2014) noted that they could not detect I-B4 staining in cultured human DRG neurons, others have readily demonstrated I-B4 staining in sections of human DRG (Shi et al., 2008, 2014; Pan et al., 2012). However, it is known that control for the specificity of lectin binding in human sections is difficult, and this is further highlighted in these studies reporting varying detection between membrane and cytosolic I-B4 staining identified by different research groups. On the other hand, mRNA for the gene of the binding partner of I-B4, versican (Bogen et al., 2005, 2015), is expressed in human DRG explants (Ray et al., 2018), but whether the versican V2 isoform that binds I-B4 is produced in human DRG remains to be confirmed.

Neurotrophins

Neurotrophins are a family of neurotrophic factors that includes nerve growth factor (NGF), brain-derived neurotrophic factor (BDNF), neurotrophin-3 (NT-3), and neurotrophin-4/5 (NT-4/5). Receptors for these factors include the tropomyosin receptor kinases (Trk) A, B, and C, and the low affinity receptor p75 (Lewin and Nykjaer, 2014). NGF and the activation of its cognate receptor TrkA, is a key factor in the development of DRG neurons, but also critical for the induction of hyperalgesia and pain via modulation of signaling events in adult DRG neurons. Neurotrophin receptors are present in DRG from early in development through to adulthood, however, the dynamics of receptor expression patterns from development to adulthood remain to be studied. Immunoreactivity for TrkB and TrkC is present in human fetal DRG at gestational weeks 9–11 (Schonemann et al., 2012), however, the confirmation of immunoreactivity for their respective ligands BDNF and NT-3 is still lacking.

Glial-derived neurotrophic factor is another neurotrophic factor which, after interaction with its receptors RET proto-oncogene tyrosine kinase (RET) and co-receptor GFRalpha1, modulates a subpopulation of nociceptive, I-B4 binding neurons. The effect of GDNF is complex. Similar to NGF, GDNF is a key factor in the development of DRG neurons, in particular nociceptive neurons but it also impacts adult DRG neurons. In neuropathic pain animal models, intrathecal GDNF reversed pain behavior (Boucher et al., 2000), but GDNF injected into rat muscle induced prolonged hyperalgesia (Alvarez et al., 2012).

Nerve growth factor and its receptors have been described in human DRG (Vega et al., 1994; Anand et al., 1997; Widenfalk et al., 1999; Rostock et al., 2017). Immunohistochemistry shows NGF-like immunoreactivity in small cells, whereas TrkA was present in 65% of DRG neurons with the expression of the receptor distributed between both small and medium-sized cells. More recently, the presence of TrkA, B, and C proteins in human DRG has been described, with almost no overlap of immunoreactivities between TrkA and TrkB, or between TrkA and TrkC-positive cells. TrkA immunoreactivity was localized to small cells with cell bodies measuring between 400 and 800 μm^2, whereas TrkB and TrkC immunoreactivity was detected in cells with areas much larger cell bodies (the majority around 1,400 and 1,600 μm^2). As with animal studies, a substantial proportion (about 50%) of human TrkA positive cells express TRPV1 (Rostock et al., 2017). In addition to NGF and its receptors, immunoreactivity for both GDNF protein and one of its receptors, RET, has been detected at 25% and 37% respectively in cell bodies of all sizes (Bar et al., 1998).

The validation of protein expression is further supported by the detection of mRNA in numerous studies reporting high levels of mRNAs for neurotrophins and their receptors, with NGF, BDNF, NT-3 and GDNF, p75 and TrkA, TrkB and TrkC having been validated to date (Yamamoto et al., 1996; Widenfalk et al., 1999; Josephson et al., 2001). Detection of mRNA via *in situ* hybridization for the GDNF receptors RET and GFRalpha 1–3 in human DRG neurons has been also reported in multiple studies (Josephson et al., 2001; Rostock et al., 2017) with RET present in about 70% of investigated neurons (Josephson et al., 2001).

The size of DRG neurons immunoreactive for NGF and GDNF receptors, compared to BDNF receptors was not different (Josephson et al., 2001). The response to NGF and GDNF determines the fate of nociceptors, at least in laboratory animals, where neurons develop into NGF- or GDNF-dependent subtypes with different neuropeptide expression patterns (Molliver et al., 1997). Therefore, it is of fundamental interest to determine factors that drive neurotrophin receptor mRNA expression in development. To date, receptor mRNAs for p75, TrkA-C, as well as the GDNF receptors RET and GFRalpha3 have been validated in fetal DRG at gestational age weeks 9–11 with additional presence of TrkA and TrkB (Widenfalk et al., 1999; Josephson et al., 2001). In contrast to

adult DRG, BDNF and neurotrophin-3 (NT-3) mRNAs were detected in fetal DRG.

The roles of NGF and GDNF in rodent DRG neurons have become more clearly defined, especially in driving cell differentiation, survival and target innervation. However, in humans, NGF and GDNF appear to also modulate the size of cultured human DRG neurons obtained from patients with brachial plexus avulsion. Presence of these growth factors increased the mean diameter of cultured human cervical DRG neurons significantly from 42 ± 4 μm to 62 ± 5 μm and, in line with animal studies, the presence of NGF and GDNF also increased the percentage of TRPV1 immunoreactive neurons coupled with an increased response to the TRPV1 agonist capsaicin (Anand et al., 2006).

Nitric oxide synthase (NOS)

Nitric oxide synthase (NOS) isoforms 1–3 are present in DRG and its product nitric oxide (NO) is involved in nociceptive signaling with evidence supporting analgesic and algesic actions. In particular NOS1 (neuronal NOS) has been shown to be upregulated in DRG neurons in animal models of neuropathic and inflammatory pain (Cury et al., 2011). NOS1 has been described in small-medium sized human DRG neurons and was present in 40–50% of all neurons in the investigated ganglia (Terenghi et al., 1993).

Gamma amino butyric acid (GABA)

Gamma amino butyric acid (GABA) and its receptors are the main inhibitors in the nervous system. $GABA_A$-receptors are ligand-gated chloride channels whereas $GABA_B$ receptors are G-protein coupled receptors. Both are expressed in DRG neurons. Activation of $GABA_A$ leads to conformational change in $GABA_B$, inhibiting the excitability of neurons via blockade of Ca_V channels (Huang et al., 2015; Zhang et al., 2015). Animal models showed that $GABA_A$-receptors have a role in the pathophysiology of neuropathic pain (Wang et al., 2017).

Pharmacological evidence for the presence of $GABA_A$ receptors in human DRG neurons, has been provided by experiments that completely blocked GABA-induced currents by the $GABA_A$ receptor antagonists, bicuculline and picrotoxin. Interestingly, electrophysiological properties of $GABA_A$-mediated current were different between human and mouse DRG neurons (Zhang et al., 2015).

Additional evidence for the presence and involvement of $GABA_B$ receptors in the excitability of human DRG neurons has been provided from experiments investigating the inhibitory action of a cone-snail venom $V_C1.1$. Those experiments showed the expression of $GABA_B$ and demonstrated the absence of an inhibitory effect $V_C1.1$ when $GABA_B$ could not be activated (Castro et al., 2017).

Phospholipase β3

Phospholipases (PLC) are present in DRG neurons and participate in pain signaling (Joseph et al., 2007). Phospolipases β, γ, δ, and ε are part of a magnitude of different signaling pathways with the PLC β3 isoform implicated in nociceptive signaling. This isoform is present in small human DRG neurons and colocalises with CGRP immunoreactive and I-B4 positive neurons (Shi et al., 2008).

SUMMARY AND CONCLUSION

In summary, only a small population of molecules that have been described to be involved in the function of DRG neurons in laboratory animals have so far been investigated in humans. It is evident from existing studies that expression patterns and functions of molecules in DRG do not perfectly match between human and laboratory animal. Important differences exist between human DRG compared to laboratory animals and careful conducted future studies will be essential to reconcile and validate these to appropriately translate animal data into human context. At the physiological level, the longer peripheral processes and associated soma size of human DRG is likely to account for some of these differences, such as immunoreactivity for neurofilament 200 in all human DRG neurons including those classified as large. Similarly, many molecules characteristic of nociceptors including TRPV1, CGRP and P_2X_3 and voltage-gated sodium channels are restricted to small and medium sized neurons in mice but in not in humans where nociception-related proteins (immunohistochemistry) and mRNAs (*in situ* hybridization) are present in neurons of all sizes. Furthermore, ion channel proteins such as TRPV1, $Na_V1.8$, $Na_V1.9$, and nicotinic receptor subtypes seem to be expressed in larger proportions of human DRG nociceptors compared to mice (Rostock et al., 2017; Zhang et al., 2019). In addition, the separation of nociceptive DRG neurons into NGF- and GDNF-dependent populations might also be questioned in relation to human DRG as the GDNF receptor protein RET is present in neurons that express the receptor for NGF, TrkA (Rostock et al., 2017).

By all means, these discrepancies do not completely invalidate results from animal studies in a human translational context. Indeed, most human DRG neurons show remarkably similar patterns in respect to immunoreactivities for pain-related molecules being detected in smaller sized neurons characteristic for nociceptors. But the diversity across sizes combined with differences in electrophysiological properties (Zhang et al., 2015, 2017, 2019) suggests a more complex array of human DRG neuronal subtypes, that may differ in detecting and conveying nociceptive information when compared to laboratory animals such as rats and mice.

Regardless of species, DRG contain multiple types of neurons and multiple types of other cells including satellite cells and cells associated with immune and vascular function. Dissociation of ganglia and culture of primary sensory neurons is useful to identify neuronal characteristics, but inferences from these studies must recognize that some types of neurons, specifically those with larger size, will likely not survive mechanical isolation and subsequent culture conditions. More importantly, critical issues related to antibody specificity highlight challenges relevant to data collections from both human and animal tissues, including the ability to compare neuronal subpopulations across species.

An emerging and clinically significant area for further investigation is the interaction of neuronal and non-neuronal

cells within DRG, and certain neuron-immune cell interactions involved in pain sensitivity have been shown to be consistent in humans and in laboratory animals. Sensory neuron-immune cell interactions are increasingly recognized as important mechanisms that contribute to chronic pain, yet there is surprisingly sparse investigative reporting of cells such as macrophages and satellite cells in human DRG. In the next few decades, researchers will hopefully find increasing opportunities to investigate and validate molecular and cellular characteristics of human DRG tissues. The failure of swathes of clinical trials based on animal model data in the past few decades reinforces the importance of human studies in clinical translation and therapeutic development, especially in very complex conditions such as chronic pain. Early insights from a handful of comparative studies suggest fundamental differences in molecular characteristics of rodent and human DRG nociceptive neurons, as well as other cell types in the DRG, and may provide key pieces of information to select optimal targets and aid more effective drug design strategies.

AUTHOR CONTRIBUTIONS

RH planned the manuscript. RH, DM, CB, and ND wrote the manuscript.

ACKNOWLEDGMENTS

We thank Assoc. Prof. Sonja Klebe for her expertise in the use of the CD163 antiserum and Patricia Vilimas for her support in the staining procedure.

SUPPLEMENTARY MATERIAL

The Supplementary Material for this article can be found online at: https://www.frontiersin.org/articles/10.3389/fncel.2019.00271/full#supplementary-material

REFERENCES

Alexandrou, A. J., Brown, A. R., Chapman, M. L., Estacion, M., Turner, J., and Mis, M. A. (2016). Subtype-selective small molecule inhibitors reveal a fundamental role for Nav1.7 in nociceptor electrogenesis, axonal conduction and presynaptic release. *PLoS One* 11:e0152405. doi: 10.1371/journal.pone.0152405

Alleyne, C. H. Jr., Cawley, C. M., Barrow, D. L., and Bonner, G. D. (1998). Microsurgical anatomy of the dorsal cervical nerve roots and the cervical dorsal root ganglion/ventral root complexes. *Surg. Neurol.* 50, 213–218. doi: 10.1016/s0090-3019(97)00315-7

Alvarez, P., Chen, X., Bogen, O., Green, P. G., and Levine, J. D. (2012). IB4(+) nociceptors mediate persistent muscle pain induced by GDNF. *J. Neurophysiol.* 108, 2545–2553. doi: 10.1152/jn.00576.2012

Anand, P., and Bley, K. (2011). Topical capsaicin for pain management: therapeutic potential and mechanisms of action of the new high-concentration capsaicin 8% patch. *Br. J. Anaesth.* 107, 490–502. doi: 10.1093/bja/aer260

Anand, P., Terenghi, G., Birch, R., Wellmer, A., Cedarbaum, J. M., Lindsay, R. M., et al. (1997). Endogenous NGF and CNTF levels in human peripheral nerve injury. *Neuroreport* 8, 1935–1938. doi: 10.1097/00001756-199705260-00028

Anand, U., Facer, P., Yiangou, Y., Sinisi, M., Fox, M., McCarthy, T., et al. (2013). Angiotensin II type 2 receptor (AT2 R) localization and antagonist-mediated inhibition of capsaicin responses and neurite outgrowth in human and rat sensory neurons. *Eur. J. Pain* 17, 1012–1026. doi: 10.1002/j.1532-2149.2012.00269.x

Anand, U., Otto, W. R., Bountra, C., Chessell, I., Sinisi, M., Birch, R., et al. (2008). Cytosine arabinoside affects the heat and capsaicin receptor TRPV1 localisation and sensitivity in human sensory neurons. *J. Neurooncol.* 89, 1–7. doi: 10.1007/s11060-008-9585-6

Anand, U., Otto, W. R., Casula, M. A., Day, N. C., Davis, J. B., Bountra, C., et al. (2006). The effect of neurotrophic factors on morphology, TRPV1 expression and capsaicin responses of cultured human DRG sensory neurons. *Neurosci. Lett.* 399, 51–56. doi: 10.1016/j.neulet.2006.01.046

Anand, U., Otto, W. R., Facer, P., Zebda, N., Selmer, I., Gunthorpe, M. J., et al. (2008). TRPA1 receptor localisation in the human peripheral nervous system and functional studies in cultured human and rat sensory neurons. *Neurosci. Lett.* 438, 221–227. doi: 10.1016/j.neulet.2008.04.007

Anand, U., Sinisi, M., Fox, M., MacQuillan, A., Quick, T., Korchev, Y., et al. (2016). Mycolactone-mediated neurite degeneration and functional effects in cultured human and rat DRG neurons: mechanisms underlying hypoalgesia in Buruli ulcer. *Mol. Pain* 12:1744806916654144.

Anand, U., Yiangou, Y., Akbar, A., Quick, T., MacQuillan, A., Fox, M., et al. (2018). Glucagon-like peptide 1 receptor (GLP-1R) expression by nerve fibres in inflammatory bowel disease and functional effects in cultured neurons. *PLoS One* 13:e0198024. doi: 10.1371/journal.pone.0198024

Anand, U., Yiangou, Y., Sinisi, M., Fox, M., MacQuillan, A., Quick, T., et al. (2015). Mechanisms underlying clinical efficacy of Angiotensin II type 2 receptor (AT2R) antagonist EMA401 in neuropathic pain: clinical tissue and in vitro studies. *Mol. Pain* 11:38.

Arvidson, B. (1979). Distribution of intravenously injected protein tracers in peripheral ganglia of adult mice. *Exp. Neurol.* 63, 388–410. doi: 10.1016/0014-4886(79)90134-1

Babenko, V. V., Graven-Nielsen, T., Svensson, P., Drewes, A. M., Jensen, T. S., and Arendt-Nielsen, L. (1999). Experimental human muscle pain induced by intramuscular injections of bradykinin, serotonin, and substance P. *Eur. J. Pain* 3, 93–102. doi: 10.1053/eujp.1998.0103

Badea, T. C., Williams, J., Smallwood, P., Shi, M., Motajo, O., and Nathans, J. (2012). Combinatorial expression of Brn3 transcription factors in somatosensory neurons: genetic and morphologic analysis. *J. Neurosci.* 32, 995–1007. doi: 10.1523/jneurosci.4755-11.2012

Bae, J. Y., Kim, J. H., Cho, Y. S., Mah, W., and Bae, Y. C. (2015). Quantitative analysis of afferents expressing substance P, calcitonin gene-related peptide, isolectin B4, neurofilament 200, and Peripherin in the sensory root of the rat trigeminal ganglion. *J. Comp. Neurol.* 523, 126–138. doi: 10.1002/cne.23672

Bar, K. J., Saldanha, G. J., Kennedy, A. J., Facer, P., Birch, R., Carlstedt, T., et al. (1998). GDNF and its receptor component Ret in injured human nerves and dorsal root ganglia. *Neuroreport* 9, 43–47. doi: 10.1097/00001756-199801050-00009

Baumann, T. K., Burchiel, K. J., Ingram, S. L., and Martenson, M. E. (1996). Responses of adult human dorsal root ganglion neurons in culture to capsaicin and low pH. *Pain* 65, 31–38. doi: 10.1016/0304-3959(95)00145-x

Belmonte, C., and Viana, F. (2008). Molecular and cellular limits to somatosensory specificity. *Mol. Pain* 4:14.

Beom, J., Kim, S., Suh, H. C., Kim, D. K., Kang, S. H., Lee, S. U., et al. (2018). Association between sensory nerve action potential and lumbar dorsal root ganglion area. *J. Clin. Neurosci.* 59, 37–40. doi: 10.1016/j.jocn.2018.11.019

Berciano, M. T., Novell, M., Villagra, N. T., Casafont, I., Bengoechea, R., Val-Bernal, J. F., et al. (2007). Cajal body number and nucleolar size correlate with the cell body mass in human sensory ganglia neurons. *J. Struct. Biol.* 158, 410–420. doi: 10.1016/j.jsb.2006.12.008

Bessaguet, F., Magy, L., Desmouliere, A., and Demiot, C. (2016). The therapeutic potential of renin angiotensin aldosterone system (RAAS) in chronic pain: from preclinical studies to clinical trials. *Expert Rev. Neurother.* 16, 331–339. doi: 10.1586/14737175.2016.1150179

Bilge, O. (2004). An anatomic and morphometric study of C2 nerve root ganglion and its corresponding foramen. *Spine (Phila Pa 1976)* 29, 495–499. doi: 10.1097/01.brs.0000113872.18219.7b

Boettger, M. K., Till, S., Chen, M. X., Anand, U., Otto, W. R., Plumpton, C., et al. (2002). Calcium-activated potassium channel SK1- and IK1-like immunoreactivity in injured human sensory neurones and its regulation by neurotrophic factors. *Brain* 125(Pt 2), 252–263. doi: 10.1093/brain/awf026

Bogen, O., Bender, O., Lowe, J., Blenau, W., Thevis, B., Schroder, W., et al. (2015). Neuronally produced versican V2 renders C-fiber nociceptors IB4 -positive. *J. Neurochem.* 134, 147–155. doi: 10.1111/jnc.13113

Bogen, O., Dreger, M., Gillen, C., Schroder, W., and Hucho, F. (2005). Identification of versican as an isolectin B4-binding glycoprotein from mammalian spinal cord tissue. *FEBS J.* 272, 1090–1102. doi: 10.1111/j.1742-4658.2005.04543.x

Borbely, E., Hajna, Z., Sandor, K., Kereskai, L., Toth, I., Pinter, E., et al. (2013). Role of tachykinin 1 and 4 gene-derived neuropeptides and the neurokinin 1 receptor in adjuvant-induced chronic arthritis of the mouse. *PLoS One* 8:e61684. doi: 10.1371/journal.pone.0061684

Boucher, T. J., Okuse, K., Bennett, D. L., Munson, J. B., Wood, J. N., and McMahon, S. B. (2000). Potent analgesic effects of GDNF in neuropathic pain states. *Science* 290, 124–127. doi: 10.1126/science.290.5489.124

Castro, J., Harrington, A. M., Garcia-Caraballo, S., Maddern, J., Grundy, L., Zhang, J., et al. (2017). alpha-Conotoxin Vc1.1 inhibits human dorsal root ganglion neuroexcitability and mouse colonic nociception via GABAB receptors. *Gut* 66, 1083–1094. doi: 10.1136/gutjnl-2015-310971

Chang, W., Berta, T., Kim, Y. H., Lee, S., Lee, S. Y., and Ji, R. R. (2018). Expression and role of voltage-gated sodium channels in human dorsal root ganglion neurons with special focus on Nav1.7, species differences, and regulation by paclitaxel. *Neurosci. Bull.* 34, 4–12. doi: 10.1007/s12264-017-0132-3

Charnay, Y., Chayvialle, J. A., Pradayrol, L., Bouvier, R., Paulin, C., and Dubois, P. M. (1987). Ontogeny of somatostatin-like immunoreactivity in the human fetus and infant spinal cord. *Brain Res.* 433, 63–73. doi: 10.1016/0165-3806(87)90065-4

Chen, J., and Hackos, D. H. (2015). TRPA1 as a drug target–promise and challenges. *Naunyn Schmiedebergs Arch. Pharmacol.* 388, 451–463. doi: 10.1007/s00210-015-1088-3

Ch'ng, J. L., Christofides, N. D., Anand, P., Gibson, S. J., Allen, Y. S., Su, H. C., et al. (1985). Distribution of galanin immunoreactivity in the central nervous system and the responses of galanin-containing neuronal pathways to injury. *Neuroscience* 16, 343–354. doi: 10.1016/0306-4522(85)90007-7

Cortright, D. N., Crandall, M., Sanchez, J. F., Zou, T., Krause, J. E., and White, G. (2001). The tissue distribution and functional characterization of human VR1. *Biochem. Biophys. Res. Commun.* 281, 1183–1189. doi: 10.1006/bbrc.2001.4482

Coward, K., Aitken, A., Powell, A., Plumpton, C., Birch, R., Tate, S., et al. (2001). Plasticity of TTX-sensitive sodium channels PN1 and brain III in injured human nerves. *Neuroreport* 12, 495–500. doi: 10.1097/00001756-200103050-00014

Coward, K., Plumpton, C., Facer, P., Birch, R., Carlstedt, T., Tate, S., et al. (2000). Immunolocalization of SNS/PN3 and NaN/SNS2 sodium channels in human pain states. *Pain* 85, 41–50. doi: 10.1016/s0304-3959(99)00251-1

Cridland, R. A., and Henry, J. L. (1988). Effects of intrathecal administration of neuropeptides on a spinal nociceptive reflex in the rat: VIP, galanin, CGRP, TRH, somatostatin and angiotensin II. *Neuropeptides* 11, 23–32. doi: 10.1016/0143-4179(88)90024-8

Cury, Y., Picolo, G., Gutierrez, V. P., and Ferreira, S. H. (2011). Pain and analgesia: the dual effect of nitric oxide in the nociceptive system. *Nitric Oxide* 25, 243–254. doi: 10.1016/j.niox.2011.06.004

Davidson, S., Copits, B. A., Zhang, J., Page, G., Ghetti, A., and Gereau, R. W. (2014). Human sensory neurons: membrane properties and sensitization by inflammatory mediators. *Pain* 155, 1861–1870. doi: 10.1016/j.pain.2014.06.017

Desormeaux, C., Bautzova, T., Garcia-Caraballo, S., Rolland, C., Barbaro, M. R., Brierley, S. M., et al. (2018). Protease-activated receptor 1 is implicated in irritable bowel syndrome mediators-induced signalling to thoracic human sensory neurons. *Pain* 159, 1257–1267. doi: 10.1097/j.pain.0000000000001208

Devor, M. (1999). Unexplained peculiarities of the dorsal root ganglion. *Pain Suppl.* 6, S27–S35.

Dib-Hajj, S. D., Geha, P., and Waxman, S. G. (2017). Sodium channels in pain disorders: pathophysiology and prospects for treatment. *Pain* 158(Suppl. 1), S97–S107.

Dib-Hajj, S. D., Tyrrell, L., Cummins, T. R., Black, J. A., Wood, P. M., and Waxman, S. G. (1999). Two tetrodotoxin-resistant sodium channels in human dorsal root ganglion neurons. *FEBS Lett.* 462, 117–120. doi: 10.1016/s0014-5793(99)01519-7

Duan, W., Zhang, Y. P., Hou, Z., Huang, C., Zhu, H., Zhang, C. Q., et al. (2016). Novel insights into NeuN: from neuronal marker to splicing regulator. *Mol. Neurobiol.* 53, 1637–1647. doi: 10.1007/s12035-015-9122-5

Ebraheim, N. A., and Lu, J. (1998). Morphometric evaluation of the sacral dorsal root ganglia: a cadaveric study. *Surg. Radiol. Anat.* 20, 105–108. doi: 10.1007/s00276-998-0105-3

Enright, H. A., Felix, S. H., Fischer, N. O., Mukerjee, E. V., Soscia, D., McNerney, M., et al. (2016). Long-term non-invasive interrogation of human dorsal root ganglion neuronal cultures on an integrated microfluidic multielectrode array platform. *Analyst* 141, 5346–5357. doi: 10.1039/c5an01728a

Facer, P., Casula, M. A., Smith, G. D., Benham, C. D., Chessell, I. P., Bountra, C., et al. (2007). Differential expression of the capsaicin receptor TRPV1 and related novel receptors TRPV3, TRPV4 and TRPM8 in normal human tissues and changes in traumatic and diabetic neuropathy. *BMC Neurol.* 7:11. doi: 10.1186/1471-2377-7-11

Flegel, C., Schobel, N., Altmuller, J., Becker, C., Tannapfel, A., Hatt, H., et al. (2015). RNA-Seq analysis of human trigeminal and dorsal root ganglia with a focus on chemoreceptors. *PLoS One* 10:e0128951. doi: 10.1371/journal.pone.0128951

Gautam, M., Prasoon, P., Kumar, R., Reeta, K. H., Kaler, S., and Ray, S. B. (2016). Role of neurokinin type 1 receptor in nociception at the periphery and the spinal level in the rat. *Spinal Cord* 54, 172–182. doi: 10.1038/sc.2015.206

Giaid, A., Gibson, S. J., Ibrahim, B. N., Legon, S., Bloom, S. R., Yanagisawa, M., et al. (1989). Endothelin 1, an endothelium-derived peptide, is expressed in neurons of the human spinal cord and dorsal root ganglia. *Proc. Natl. Acad. Sci. U.S.A.* 86, 7634–7638. doi: 10.1073/pnas.86.19.7634

Gilchrist, R. V., Slipman, C. W., and Bhagia, S. M. (2002). Anatomy of the intervertebral foramen. *Pain Phys.* 5, 372–378.

Godel, T., Baumer, P., Pham, M., Kohn, A., Muschol, N., Kronlage, M., et al. (2017). Human dorsal root ganglion in vivo morphometry and perfusion in Fabry painful neuropathy. *Neurology* 89, 1274–1282. doi: 10.1212/wnl.0000000000004396

Godel, T., Mautner, V. F., Farschtschi, S., Pham, M., Schwarz, D., Kronlage, M., et al. (2018). Dorsal root ganglia volume differentiates schwannomatosis and neurofibromatosis 2. *Ann. Neurol.* 83, 854–857. doi: 10.1002/ana.25191

Godel, T., Pham, M., Heiland, S., Bendszus, M., and Baumer, P. (2016). Human dorsal-root-ganglion perfusion measured in-vivo by MRI. *Neuroimage* 141, 81–87. doi: 10.1016/j.neuroimage.2016.07.030

Graus, F., Campo, E., Cruz-Sanchez, F., Ribalta, T., and Palacin, A. (1990a). Expression of lymphocyte, macrophage and class I and II major histocompatibility complex antigens in normal human dorsal root ganglia. *J. Neurol. Sci.* 98, 203–211. doi: 10.1016/0022-510x(90)90261-k

Graus, F., Ribalta, T., Campo, E., Monforte, R., Urbano, A., and Rozman, C. (1990b). Immunohistochemical analysis of the immune reaction in the nervous system in paraneoplastic encephalomyelitis. *Neurology* 40, 219–222.

Han, C., Estacion, M., Huang, J., Vasylyev, D., Zhao, P., Dib-Hajj, S. D., et al. (2015). Human Na(v)1.8: enhanced persistent and ramp currents contribute to distinct firing properties of human DRG neurons. *J. Neurophysiol.* 113, 3172–3185. doi: 10.1152/jn.00113.2015

Han, Q., Kim, Y. H., Wang, X., Liu, D., Zhang, Z. J., Bey, A. L., et al. (2016). SHANK3 deficiency impairs heat hyperalgesia and TRPV1 signaling in primary sensory neurons. *Neuron* 92, 1279–1293. doi: 10.1016/j.neuron.2016.11.007

Hanani, M. (2005). Satellite glial cells in sensory ganglia: from form to function. *Brain Res. Brain Res. Rev.* 48, 457–476. doi: 10.1016/j.brainresrev.2004.09.001

Hanani, M. (2010a). Satellite glial cells in sympathetic and parasympathetic ganglia: in search of function. *Brain Res. Rev.* 64, 304–327. doi: 10.1016/j.brainresrev.2010.04.009

Hanani, M. (2010b). Satellite glial cells: more than just 'rings around the neuron'. *Neuron Glia Biol.* 6, 1–2. doi: 10.1017/s1740925x10000104

Hasegawa, T., Mikawa, Y., Watanabe, R., and An, H. S. (1996). Morphometric analysis of the lumbosacral nerve roots and dorsal root ganglia by magnetic

resonance imaging. *Spine (Phila Pa 1976)* 21, 1005–1009. doi: 10.1097/00007632-199605010-00001

Hill, R. (2000). NK1 (substance P) receptor antagonists–why are they not analgesic in humans? *Trends Pharmacol. Sci.* 21, 244–246. doi: 10.1016/s0165-6147(00)01502-9

Holford, L. C., Case, P., and Lawson, S. N. (1994). Substance P, neurofilament, peripherin and SSEA4 immunocytochemistry of human dorsal root ganglion neurons obtained from post-mortem tissue: a quantitative morphometric analysis. *J. Neurocytol.* 23, 577–589. doi: 10.1007/bf01262058

Huang, D., Huang, S., Peers, C., Du, X., Zhang, H., and Gamper, N. (2015). GABAB receptors inhibit low-voltage activated and high-voltage activated Ca(2+) channels in sensory neurons via distinct mechanisms. *Biochem. Biophys. Res. Commun.* 465, 188–193. doi: 10.1016/j.bbrc.2015.07.137

Huang, J., Polgar, E., Solinski, H. J., Mishra, S. K., Tseng, P. Y., Iwagaki, N., et al. (2018). Circuit dissection of the role of somatostatin in itch and pain. *Nat. Neurosci.* 21, 707–716. doi: 10.1038/s41593-018-0119-z

Huerta, J. J., Diaz-Trelles, R., Naves, F. J., Llamosas, M. M., Del Valle, M. E., and Vega, J. A. (1996). Epidermal growth factor receptor in adult human dorsal root ganglia. *Anat. Embryol. (Berl.)* 194, 253–257.

Jeong, S. Y., Goto, J., Hashida, H., Suzuki, T., Ogata, K., Masuda, N., et al. (2000). Identification of a novel human voltage-gated sodium channel alpha subunit gene, SCN12A. *Biochem. Biophys. Res. Commun.* 267, 262–270. doi: 10.1006/bbrc.1999.1916

Jimenez-Andrade, J. M., Herrera, M. B., Ghilardi, J. R., Vardanyan, M., Melemedjian, O. K., and Mantyh, P. W. (2008). Vascularization of the dorsal root ganglia and peripheral nerve of the mouse: implications for chemical-induced peripheral sensory neuropathies. *Mol. Pain* 4:10.

Johnson, P. C. (1983). Thickening of the human dorsal root ganglion perineurial cell basement membrane in diabetes mellitus. *Muscle Nerve* 6, 561–565. doi: 10.1002/mus.880060805

Joseph, E. K., Bogen, O., Alessandri-Haber, N., and Levine, J. D. (2007). PLC-beta 3 signals upstream of PKC epsilon in acute and chronic inflammatory hyperalgesia. *Pain* 132, 67–73. doi: 10.1016/j.pain.2007.01.027

Josephson, A., Widenfalk, J., Trifunovski, A., Widmer, H. R., Olson, L., and Spenger, C. (2001). GDNF and NGF family members and receptors in human fetal and adult spinal cord and dorsal root ganglia. *J. Comp. Neurol.* 440, 204–217. doi: 10.1002/cne.1380

Kiernan, J. A. (1996). Vascular permeability in the peripheral autonomic and somatic nervous systems: controversial aspects and comparisons with the blood-brain barrier. *Microsc. Res. Tech.* 35, 122–136. doi: 10.1002/(sici)1097-0029(19961001)35:2<122::aid-jemt3>3.0.co;2-s

Kikuchi, S., Sato, K., Konno, S., and Hasue, M. (1994). Anatomic and radiographic study of dorsal root ganglia. *Spine (Phila Pa 1976)* 19, 6–11. doi: 10.1097/00007632-199401000-00002

Koeppen, A. H., Becker, A. B., Qian, J., and Feustel, P. J. (2017). Friedreich Ataxia: hypoplasia of spinal cord and dorsal root ganglia. *J. Neuropathol. Exp. Neurol.* 76, 101–108. doi: 10.1093/jnen/nlw111

Koeppen, A. H., Morral, J. A., McComb, R. D., and Feustel, P. J. (2011). The neuropathology of late-onset Friedreich's ataxia. *Cerebellum* 10, 96–103.

Koeppen, A. H., Ramirez, R. L., Becker, A. B., and Mazurkiewicz, J. E. (2016). Dorsal root ganglia in Friedreich ataxia: satellite cell proliferation and inflammation. *Acta Neuropathol. Commun.* 4:46.

Krajewski, S., Krajewska, M., and Reed, J. C. (1996). Immunohistochemical analysis of in vivo patterns of Bak expression, a proapoptotic member of the Bcl-2 protein family. *Cancer Res.* 56, 2849–2855.

Krames, E. S. (2015). The dorsal root ganglion in chronic pain and as a target for neuromodulation: a review. *Neuromodulation* 18, 24–32; discussion 32.

Kubicek, L., Kopacik, R., Klusakova, I., and Dubovy, P. (2010). Alterations in the vascular architecture of the dorsal root ganglia in a rat neuropathic pain model. *Ann. Anat.* 192, 101–106. doi: 10.1016/j.aanat.2010.01.005

Kusunoki, S., Inoue, K., Iwamori, M., Nagai, Y., and Mannen, T. (1989). Discrimination of human dorsal root ganglion cells by anti-fucosyl GM1 antibody. *Brain Res.* 494, 391–395. doi: 10.1016/0006-8993(89)90611-2

Kusunoki, S., Inoue, K., Iwamori, M., Nagai, Y., and Mannen, T. (1991). Fucosylated glycoconjugates in human dorsal root ganglion cells with unmyelinated axons. *Neurosci. Lett.* 126, 159–162. doi: 10.1016/0304-3940(91)90543-3

Kusunoki, S., Mashiko, H., Mochizuki, N., Chiba, A., Arita, M., Hitoshi, S., et al. (1997). Binding of antibodies against GM1 and GD1b in human peripheral nerve. *Muscle Nerve* 20, 840–845. doi: 10.1002/(sici)1097-4598(199707)20:7<840::aid-mus8>3.0.co;2-7

Kutcher, M. E., Klagsbrun, M., and Mamluk, R. (2004). VEGF is required for the maintenance of dorsal root ganglia blood vessels but not neurons during development. *FASEB J.* 18, 1952–1954. doi: 10.1096/fj.04-2320fje

Lacinova, L. (2005). Voltage-dependent calcium channels. *Gen. Physiol. Biophys.* 24(Suppl. 1), 1–78.

Laird, J. M., Olivar, T., Roza, C., De, Felipe, C., Hunt, S. P., et al. (2000). Deficits in visceral pain and hyperalgesia of mice with a disruption of the tachykinin NK1 receptor gene. *Neuroscience* 98, 345–352. doi: 10.1016/s0306-4522(00)00148-2

Lakritz, J. R., Bodair, A., Shah, N., O'Donnell, R., Polydefkis, M. J., Miller, A. D., et al. (2015). Monocyte traffic, dorsal root ganglion histopathology, and loss of intraepidermal nerve fiber density in SIV peripheral neuropathy. *Am. J. Pathol.* 185, 1912–1923. doi: 10.1016/j.ajpath.2015.03.007

Landry, M., Aman, K., Dostrovsky, J., Lozano, A. M., Carlstedt, T., Spenger, C., et al. (2003). Galanin expression in adult human dorsal root ganglion neurons: initial observations. *Neuroscience* 117, 795–809. doi: 10.1016/s0306-4522(02)00965-x

Lang, R., Gundlach, A. L., Holmes, F. E., Hobson, S. A., Wynick, D., Hokfelt, T., et al. (2015). Physiology, signaling, and pharmacology of galanin peptides and receptors: three decades of emerging diversity. *Pharmacol. Rev.* 67, 118–175. doi: 10.1124/pr.112.006536

Lauria, G., Morbin, M., Lombardi, R., Capobianco, R., Camozzi, F., Pareyson, D., et al. (2006). Expression of capsaicin receptor immunoreactivity in human peripheral nervous system and in painful neuropathies. *J. Peripher. Nerv. Syst.* 11, 262–271. doi: 10.1111/j.1529-8027.2006.0097.x

Levinson, S. R., Luo, S., and Henry, M. A. (2012). The role of sodium channels in chronic pain. *Muscle Nerve* 46, 155–165. doi: 10.1002/mus.23314

Lewin, G. R., and Nykjaer, A. (2014). Pro-neurotrophins, sortilin, and nociception. *Eur. J. Neurosci.* 39, 363–374. doi: 10.1111/ejn.12466

Li, W., Gao, S. B., Lv, C. X., Wu, Y., Guo, Z. H., Ding, J. P., et al. (2007). Characterization of voltage-and Ca2+-activated K+ channels in rat dorsal root ganglion neurons. *J. Cell. Physiol.* 212, 348–357. doi: 10.1002/jcp.21007

Li, Y., Adamek, P., Zhang, H., Tatsui, C. E., Rhines, L. D., and Mrozkova, P. (2015). The cancer chemotherapeutic paclitaxel increases human and rodent sensory neuron responses to TRPV1 by activation of TLR4. *J. Neurosci.* 35, 13487–13500. doi: 10.1523/jneurosci.1956-15.2015

Li, Y., North, R. Y., Rhines, L. D., Tatsui, C. E., Rao, G., Edwards, D. D., et al. (2018). DRG voltage-gated sodium channel 1.7 is upregulated in paclitaxel-induced neuropathy in rats and in humans with neuropathic pain. *J. Neurosci.* 38, 1124–1136. doi: 10.1523/jneurosci.0899-17.2017

Lu, J., and Ebraheim, N. A. (1998). Anatomic considerations of C2 nerve root ganglion. *Spine (Phila Pa 1976)* 23, 649–652. doi: 10.1097/00007632-199803150-00001

Lutz, B. M., Wu, S., Gu, X., Atianjoh, F. E., Li, Z., Fox, B. M., et al. (2018). Endothelin type A receptors mediate pain in a mouse model of sickle cell disease. *Haematologica* 103, 1124–1135. doi: 10.3324/haematol.2017.187013

Makker, P. G., Duffy, S. S., Lees, J. G., Perera, C. J., Tonkin, R. S., Butovsky, O., et al. (2017). Characterisation of immune and neuroinflammatory changes associated with chemotherapy-induced peripheral neuropathy. *PLoS One* 12:e0170814. doi: 10.1371/journal.pone.0170814

Marti, E., Gibson, S. J., Polak, J. M., Facer, P., Springall, D. R., Van Aswegen, G., et al. (1987). Ontogeny of peptide- and amine-containing neurones in motor, sensory, and autonomic regions of rat and human spinal cord, dorsal root ganglia, and rat skin. *J. Comp. Neurol.* 266, 332–359. doi: 10.1002/cne.902660304

Mitterreiter, J. G., Ouwendijk, W. J. D., van Velzen, M., van Nierop, G. P., Osterhaus, A., and Verjans, G. (2017). Satellite glial cells in human trigeminal ganglia have a broad expression of functional Toll-like receptors. *Eur. J. Immunol.* 47, 1181–1187. doi: 10.1002/eji.201746989

Mo, G., Bernier, L. P., Zhao, Q., Chabot, Dore, A. J., Ase, A. R., et al. (2009). Subtype-specific regulation of P2X3 and P2X2/3 receptors by phosphoinositides in peripheral nociceptors. *Mol. Pain* 5:47.

Mollenholt, P., Rawal, N., Gordh, T. Jr., and Olsson, Y. (1994). Intrathecal and epidural somatostatin for patients with cancer. Analgesic effects and postmortem neuropathologic investigations of spinal cord and nerve roots. *Anesthesiology* 81, 534–542. doi: 10.1097/00000542-199409000-00004

Molliver, D. C., Wright, D. E., Leitner, M. L., Parsadanian, A. S., Doster, K., Wen, D., et al. (1997). IB4-binding DRG neurons switch from NGF to GDNF dependence in early postnatal life. *Neuron* 19, 849–861. doi: 10.1016/s0896-6273(00)80966-6

Moon, H. S., Kim, Y. D., Song, B. H., Cha, Y. D., Song, J. H., and Lee, M. H. (2010). Position of dorsal root ganglia in the lumbosacral region in patients with radiculopathy. *Korean J. Anesthesiol.* 59, 398–402.

Moreno-Garcia, A., Kun, A., Calero, O., Medina, M., and Calero, M. (2018). An overview of the role of lipofuscin in age-related neurodegeneration. *Front. Neurosci.* 12:464. doi: 10.3389/fnins.2018.00464

Murayama, S., Bouldin, T. W., and Suzuki, K. (1991). Onion bulb formation in the initial complex of neurons in human dorsal root ganglion: their significance and alterations in amyotrophic lateral sclerosis. *Acta Neuropathol.* 82, 462–470. doi: 10.1007/bf00293380

Nagao, M., Oka, N., Kamo, H., Akiguchi, I., and Kimura, J. (1994). Differential localization of lectin binding sites and neuropeptides in human dorsal root ganglia. *Histochemistry* 102, 279–286. doi: 10.1007/bf00269164

Namer, B., Orstavik, K., Schmidt, R., Kleggetveit, I. P., Weidner, C., Mork, C., et al. (2015). Specific changes in conduction velocity recovery cycles of single nociceptors in a patient with erythromelalgia with the I848T gain-of-function mutation of Nav1.7. *Pain* 156, 1637–1646. doi: 10.1097/j.pain.0000000000000229

Nascimento, A. I., Mar, F. M., and Sousa, M. M. (2018). The intriguing nature of dorsal root ganglion neurons: linking structure with polarity and function. *Prog. Neurobiol.* 168, 86–103. doi: 10.1016/j.pneurobio.2018.05.002

Naves, F. J., Huerta, J. J., Garcia-Suarez, O., Urdangaray, N., Esteban, I., Del Valle, M. E., et al. (1996). Distribution of immunoreactivity for cytoskeletal (microtubule, microtubule-associated, and neurofilament) proteins in adult human dorsal root ganglia. *Anat. Rec.* 244, 246–256. doi: 10.1002/(sici)1097-0185(199602)244:2<246::aid-ar12>3.0.co;2-p

Nemoto, W., Nakagawasai, O., Yaoita, F., Kanno, S., Yomogida, S., Ishikawa, M., et al. (2013). Angiotensin II produces nociceptive behavior through spinal AT1 receptor-mediated p38 mitogen-activated protein kinase activation in mice. *Mol. Pain* 9:38.

Nordlind, K., Eriksson, L., Seiger, A., and Bakhiet, M. (2000). Expression of interleukin-6 in human dorsal root ganglion cells. *Neurosci. Lett.* 280, 139–142. doi: 10.1016/s0304-3940(00)00772-2

Pagadala, P., Park, C. K., Bang, S., Xu, Z. Z., Xie, R. G., Liu, T., et al. (2013). Loss of NR1 subunit of NMDARs in primary sensory neurons leads to hyperexcitability and pain hypersensitivity: involvement of Ca(2+)-activated small conductance potassium channels. *J. Neurosci.* 33, 13425–13430. doi: 10.1523/jneurosci.0454-13.2013

Pan, A., Wu, H., Li, M., Lu, D., He, X., Yi, X., et al. (2012). Prenatal expression of purinergic receptor P2X3 in human dorsal root ganglion. *Purinergic Signal.* 8, 245–254. doi: 10.1007/s11302-011-9277-0

Pannese, E. (1981). The satellite cells of the sensory ganglia. *Adv. Anat. Embryol. Cell Biol.* 65, 1–111.

Park, J., and Luo, Z. D. (2010). Calcium channel functions in pain processing. *Channels (Austin)* 4, 510–517. doi: 10.4161/chan.4.6.12869

Parke, W. W., and Whalen, J. L. (2002). The vascular pattern of the human dorsal root ganglion and its probable bearing on a compartment syndrome. *Spine (Phila Pa 1976)* 27, 347–352. doi: 10.1097/00007632-200202150-00004

Patil, J., Schwab, A., Nussberger, J., Schaffner, T., Saavedra, J. M., and Imboden, H. (2010). Intraneuronal angiotensinergic system in rat and human dorsal root ganglia. *Regul. Pept.* 162, 90–98. doi: 10.1016/j.regpep.2010.03.004

Pope, J. E., Deer, T. R., and Kramer, J. (2013). A systematic review: current and future directions of dorsal root ganglion therapeutics to treat chronic pain. *Pain. Med.* 14, 1477–1496. doi: 10.1111/pme.12171

Ray, P., Torck, A., Quigley, L., Wangzhou, A., Neiman, M., Rao, C., et al. (2018). Comparative transcriptome profiling of the human and mouse dorsal root ganglia: an RNA-seq-based resource for pain and sensory neuroscience research. *Pain* 159, 1325–1345. doi: 10.1097/j.pain.0000000000001217

Reina, M. A., Lopez-Garcia, A., Dittmann, M., and de Andres, J. A. (1996). [Structural analysis of the thickness of human dura mater with scanning electron microscopy]. *Rev. Esp Anestesiol. Reanim.* 43, 135–137.

Reinhold, M., Ederer, C., Henninger, B., Eberwein, A., and Kremser, C. (2015). Diffusion-weighted magnetic resonance imaging for the diagnosis of patients with lumbar nerve root entrapment syndromes: results from a pilot study. *Eur. Spine J.* 24, 319–326. doi: 10.1007/s00586-014-3602-6

Rice, A. S. C., Dworkin, R. H., McCarthy, T. D., Anand, P., Bountra, C., and McCloud, P. I. (2014). EMA401, an orally administered highly selective angiotensin II type 2 receptor antagonist, as a novel treatment for postherpetic neuralgia: a randomised, double-blind, placebo-controlled phase 2 clinical trial. *Lancet* 383, 1637–1647. doi: 10.1016/s0140-6736(13)62337-5

Robinson, B., Li, Z., and Nath, A. (2007). Nucleoside reverse transcriptase inhibitors and human immunodeficiency virus proteins cause axonal injury in human dorsal root ganglia cultures. *J. Neurovirol.* 13, 160–167. doi: 10.1080/13550280701200102

Rostock, C., Schrenk-Siemens, K., Pohle, J., and Siemens, J. (2017). Human vs. Mouse nociceptors – Similarities and differences. *Neuroscience* 387, 13–27. doi: 10.1016/j.neuroscience.2017.11.047

Rudomin, P. (2002). Selectivity of the central control of sensory information in the mammalian spinal cord. *Adv. Exp. Med. Biol.* 508, 157–170. doi: 10.1007/978-1-4615-0713-0_19

Saper, C. B. (2009). A guide to the perplexed on the specificity of antibodies. *J. Histochem. Cytochem.* 57, 1–5. doi: 10.1369/jhc.2008.952770

Sato, K., and Kikuchi, S. (1993). An anatomic study of foraminal nerve root lesions in the lumbar spine. *Spine (Phila Pa 1976)* 18, 2246–2251. doi: 10.1097/00007632-199311000-00017

Scharf, J. H., and Blumenthal, H. J. (1967). Current aspects on the age-dependent involution of the sensory peripheral nervous system. *Z. Zellforsch Mikrosk Anat.* 78, 280–302.

Schmid, A. B., Coppieters, M. W., Ruitenberg, M. J., and McLachlan, E. M. (2013). Local and remote immune-mediated inflammation after mild peripheral nerve compression in rats. *J. Neuropathol. Exp. Neurol.* 72, 662–680. doi: 10.1097/nen.0b013e318298de5b

Schonemann, M. D., Muench, M. O., Tee, M. K., Miller, W. L., and Mellon, S. H. (2012). Expression of P450c17 in the human fetal nervous system. *Endocrinology* 153, 2494–2505. doi: 10.1210/en.2011-1545

Serrano, A., Mo, G., Grant, R., Pare, M., O'Donnell, D., Yu, X. H., et al. (2012). Differential expression and pharmacology of native P2X receptors in rat and primate sensory neurons. *J. Neurosci.* 32, 11890–11896. doi: 10.1523/jneurosci.0698-12.2012

Sheahan, T. D., Valtcheva, M. V., McIlvried, L. A., Pullen, M. Y., Baranger, D. A. A., and Gereau, R. W. (2018). Metabotropic glutamate receptor 2/3 (mGluR2/3) activation suppresses TRPV1 sensitization in mouse, but not human, sensory neurons. *eNeuro* 5:ENEURO.412–ENEURO.417.

Shen, J., Wang, H. Y., Chen, J. Y., and Liang, B. L. (2006). Morphologic analysis of normal human lumbar dorsal root ganglion by 3D MR imaging. *AJNR Am. J. Neuroradiol.* 27, 2098–2103.

Shepherd, A. J., Mickle, A. D., Golden, J. P., Mack, M. R., Halabi, C. M., de, et al. (2018). Macrophage angiotensin II type 2 receptor triggers neuropathic pain. *Proc. Natl. Acad. Sci. U.S.A.* 115, E8057–E8066.

Shi, T. J., Liu, S. X., Hammarberg, H., Watanabe, M., Xu, Z. Q., and Hokfelt, T. (2008). Phospholipase C{beta}3 in mouse and human dorsal root ganglia and spinal cord is a possible target for treatment of neuropathic pain. *Proc. Natl. Acad. Sci. U.S.A.* 105, 20004–20008. doi: 10.1073/pnas.0810899105

Shi, T. J., Xiang, Q., Zhang, M. D., Barde, S., Kai-Larsen, Y., Fried, K., et al. (2014). Somatostatin and its 2A receptor in dorsal root ganglia and dorsal horn of mouse and human: expression, trafficking and possible role in pain. *Mol. Pain* 10:12.

Shi, T. J., Xiang, Q., Zhang, M. D., Tortoriello, G., Hammarberg, H., Mulder, J., et al. (2012). Secretagogin is expressed in sensory CGRP neurons and in spinal cord of mouse and complements other calcium-binding proteins, with a note on rat and human. *Mol. Pain* 8:80.

Silav, G., Arslan, M., Comert, A., Acar, H. I., Kahilogullari, G., Dolgun, H., et al. (2016). Relationship of dorsal root ganglion to intervertebral foramen in lumbar

region: an anatomical study and review of literature. *J. Neurosurg. Sci.* 60, 339–344.

Silverstein, M. P., Romrell, L. J., Benzel, E. C., Thompson, N., Griffith, S., and Lieberman, I. H. (2015). Lumbar dorsal root Ganglia location: an anatomic and MRI assessment. *Int. J. Spine Surg.* 9, 1–10. doi: 10.14444/2003

Simone, D. A., Baumann, T. K., and LaMotte, R. H. (1989). Dose-dependent pain and mechanical hyperalgesia in humans after intradermal injection of capsaicin. *Pain* 38, 99–107. doi: 10.1016/0304-3959(89)90079-1

Smith, T. P., Haymond, T., Smith, S. N., and Sweitzer, S. M. (2014). Evidence for the endothelin system as an emerging therapeutic target for the treatment of chronic pain. *J. Pain Res.* 7, 531–545.

Snyder, L. M., Chiang, M. C., Loeza-Alcocer, E., Omori, Y., Hachisuka, J., Sheahan, T. D., et al. (2018). Kappa opioid receptor distribution and function in primary afferents. *Neuron* 99, 1274.e1276–1288.e1276.

Suburo, A. M., Gu, X. H., Moscoso, G., Ross, A., Terenghi, G., and Polak, J. M. (1992). Developmental pattern and distribution of nerve growth factor low-affinity receptor immunoreactivity in human spinal cord and dorsal root ganglia: comparison with synaptophysin, neurofilament and neuropeptide immunoreactivities. *Neuroscience* 50, 467–482. doi: 10.1016/0306-4522(92)90438-8

Suh, Y. G., and Oh, U. (2005). Activation and activators of TRPV1 and their pharmaceutical implication. *Curr. Pharm. Des.* 11, 2687–2698. doi: 10.2174/1381612054546789

Takano, M., Tanuma, K., Ito, H., and Shirai, Y. (1998). Veins of the lumbar spinal ganglia in human adults and fetuses. *Nihon Ika Daigaku Zasshi* 65, 298–306. doi: 10.1272/jnms1923.65.298

Takeda, M., Takahashi, M., and Matsumoto, S. (2009). Contribution of the activation of satellite glia in sensory ganglia to pathological pain. *Neurosci. Biobehav. Rev.* 33, 784–792. doi: 10.1016/j.neubiorev.2008.12.005

Terenghi, G., Riveros-Moreno, V., Hudson, L. D., Ibrahim, N. B., and Polak, J. M. (1993). Immunohistochemistry of nitric oxide synthase demonstrates immunoreactive neurons in spinal cord and dorsal root ganglia of man and rat. *J. Neurol. Sci.* 118, 34–37. doi: 10.1016/0022-510x(93)90242-q

Thomas, A. M., and Atkinson, T. J. (2018). Old friends with new faces: are sodium channel blockers the future of adjunct pain medication management? *J. Pain* 19, 1–9. doi: 10.1016/j.jpain.2017.08.001

Tubbs, R. S., Loukas, M., Slappey, J. B., Shoja, M. M., Oakes, W. J., and Salter, E. G. (2007). Clinical anatomy of the C1 dorsal root, ganglion, and ramus: a review and anatomical study. *Clin. Anat.* 20, 624–627. doi: 10.1002/ca.20472

Turnbull, I. M., Brieg, A., and Hassler, O. (1966). Blood supply of cervical spinal cord in man. A microangiographic cadaver study. *J. Neurosurg.* 24, 951–965. doi: 10.3171/jns.1966.24.6.0951

Usoskin, D., Furlan, A., Islam, S., Abdo, H., Lonnerberg, P., Lou, D., et al. (2015). Unbiased classification of sensory neuron types by large-scale single-cell RNA sequencing. *Nat. Neurosci.* 18, 145–153. doi: 10.1038/nn.3881

Valtcheva, M. V., Copits, B. A., Davidson, S., Sheahan, T. D., Pullen, M. Y., McCall, J. G., et al. (2016). Surgical extraction of human dorsal root ganglia from organ donors and preparation of primary sensory neuron cultures. *Nat. Protoc.* 11, 1877–1888. doi: 10.1038/nprot.2016.111

Vega, J. A., Vazquez, E., Naves, F. J., Del Valle, M. E., Calzada, B., and Represa, J. J. (1994). Immunohistochemical localization of the high-affinity NGF receptor (gp140-trkA) in the adult human dorsal root and sympathetic ganglia and in the nerves and sensory corpuscles supplying digital skin. *Anat. Rec.* 240, 579–588. doi: 10.1002/ar.1092400415

Wang, L. J., Wang, Y., Chen, M. J., Tian, Z. P., Lu, B. H., Mao, K. T., et al. (2017). Effects of niflumic acid on gamma-aminobutyric acid-induced currents in isolated dorsal root ganglion neurons of neuropathic pain rats. *Exp. Ther. Med.* 14, 1373–1380. doi: 10.3892/etm.2017.4666

Waxman, S. G., and Zamponi, G. W. (2014). Regulating excitability of peripheral afferents: emerging ion channel targets. *Nat. Neurosci.* 17, 153–163. doi: 10.1038/nn.3602

Weinstein, J. (1986). Report of the 1985 ISSLS Traveling Fellowship. Mechanisms of spinal pain. The dorsal root ganglion and its role as a mediator of low-back pain. *Spine (Phila Pa 1976)* 11, 999–1001. doi: 10.1097/00007632-198612000-00005

West, C. A., McKay, Hart, A., Terenghi, G., and Wiberg, M. (2012). Sensory neurons of the human brachial plexus: a quantitative study employing optical fractionation and in vivo volumetric magnetic resonance imaging. *Neurosurgery* 70, 1183–1194; discussion 1194. doi: 10.1227/neu.0b013e318241ace1

Widenfalk, J., Widmer, H. R., and Spenger, C. (1999). GDNF, RET and GFRalpha-1-3 mRNA expression in the developing human spinal cord and ganglia. *Neuroreport* 10, 1433–1439. doi: 10.1097/00001756-199905140-00009

Yabuki, S., and Kikuchi, S. (1996). Positions of dorsal root ganglia in the cervical spine. An anatomic and clinical study. *Spine (Phila Pa 1976)* 21, 1513–1517. doi: 10.1097/00007632-199607010-00004

Yamamoto, M., Sobue, G., Yamamoto, K., Terao, S., and Mitsuma, T. (1996). Expression of mRNAs for neurotrophic factors (NGF, BDNF, NT-3, and GDNF) and their receptors (p75NGFR, trkA, trkB, and trkC) in the adult human peripheral nervous system and nonneural tissues. *Neurochem. Res.* 21, 929–938. doi: 10.1007/bf02532343

Yarwood, R. E., Imlach, W. L., Lieu, T., Veldhuis, N. A., Jensen, D. D., Klein Herenbrink, C., et al. (2017). Endosomal signaling of the receptor for calcitonin gene-related peptide mediates pain transmission. *Proc. Natl. Acad. Sci. U.S.A.* 114, 12309–12314. doi: 10.1073/pnas.1706656114

Yiangou, Y., Facer, P., Birch, R., Sangameswaran, L., Eglen, R., and Anand, P. (2000). P2X3 receptor in injured human sensory neurons. *Neuroreport* 11, 993–996. doi: 10.1097/00001756-200004070-00019

Yoshizawa, H., Kobayashi, S., and Hachiya, Y. (1991). Blood supply of nerve roots and dorsal root ganglia. *Orthop. Clin. North Am.* 22, 195–211.

Zhang, X., Hartung, J. E., Friedman, R. L., Koerber, H. R., Belfer, I., and Gold, M. S. (2019). Nicotine Evoked Currents in Human Primary Sensory Neurons. *J. Pain* doi: 10.1016/j.jpain.2019.01.005 [Epub ahead of print].

Zhang, X., Priest, B. T., Belfer, I., and Gold, M. S. (2017). Voltage-gated Na(+) currents in human dorsal root ganglion neurons. *Elife* 6:e23235.

Zhang, X. L., Lee, K. Y., Priest, B. T., Belfer, I., and Gold, M. S. (2015). Inflammatory mediator-induced modulation of GABAA currents in human sensory neurons. *Neuroscience* 310, 401–409. doi: 10.1016/j.neuroscience.2015.09.048

Zhao, X., Zhao, J., Guan, J., Zeng, J., Han, C., He, Y., et al. (2018). Measurement of the nerve root of the lower lumbar region using digital images. *Medicine* 97:e9848. doi: 10.1097/MD.0000000000009848

Conflict of Interest Statement: The authors declare that the research was conducted in the absence of any commercial or financial relationships that could be construed as a potential conflict of interest.

Copyright © 2019 Haberberger, Barry, Dominguez and Matusica. This is an open-access article distributed under the terms of the Creative Commons Attribution License (CC BY). The use, distribution or reproduction in other forums is permitted, provided the original author(s) and the copyright owner(s) are credited and that the original publication in this journal is cited, in accordance with accepted academic practice. No use, distribution or reproduction is permitted which does not comply with these terms.

frontiers in Cellular Neuroscience

ORIGINAL RESEARCH
published: 05 July 2019
doi: 10.3389/fncel.2019.00297

PARK2 Mutation Causes Metabolic Disturbances and Impaired Survival of Human iPSC-Derived Neurons

*Helle Bogetofte[1,2], Pia Jensen[3], Matias Ryding[1], Sissel I. Schmidt[1], Justyna Okarmus[1], Louise Ritter[1], Christina S. Worm[1], Michaela C. Hohnholt[4], Carla Azevedo[5], Laurent Roybon[5], Lasse K. Bak[4], Helle Waagepetersen[4], Brent J. Ryan[2], Richard Wade-Martins[2], Martin R. Larsen[3] and Morten Meyer[1,6]**

[1] Department of Neurobiology Research, Institute of Molecular Medicine, University of Southern Denmark, Odense, Denmark, [2] Oxford Parkinson's Disease Centre, Medical Sciences Division, Department of Physiology, Anatomy and Genetics, University of Oxford, Oxford, United Kingdom, [3] Department of Biochemistry and Molecular Biology, University of Southern Denmark, Odense, Denmark, [4] Department of Drug Design and Pharmacology, Faculty of Health and Medical Sciences, University of Copenhagen, Copenhagen, Denmark, [5] Department of Experimental Medical Science, Wallenberg Neuroscience Center, Lund University, Lund, Sweden, [6] Brain Research – Inter-Disciplinary Guided Excellence, University of Southern Denmark, Odense, Denmark

OPEN ACCESS

Edited by:
Dirk Schubert,
Radboud University, Netherlands

Reviewed by:
Kah-Leong Lim,
National University of Singapore, Singapore
Philip Seibler,
Universität zu Lübeck, Germany

***Correspondence:**
Morten Meyer
mmeyer@health.sdu.dk

Specialty section:
This article was submitted to Cellular Neurophysiology, a section of the journal Frontiers in Cellular Neuroscience

Received: 14 January 2019
Accepted: 18 June 2019
Published: 05 July 2019

Citation:
Bogetofte H, Jensen P, Ryding M, Schmidt SI, Okarmus J, Ritter L, Worm CS, Hohnholt MC, Azevedo C, Roybon L, Bak LK, Waagepetersen H, Ryan BJ, Wade-Martins R, Larsen MR and Meyer M (2019) PARK2 Mutation Causes Metabolic Disturbances and Impaired Survival of Human iPSC-Derived Neurons. Front. Cell. Neurosci. 13:297. doi: 10.3389/fncel.2019.00297

The protein parkin, encoded by the *PARK2* gene, is vital for mitochondrial homeostasis, and although it has been implicated in Parkinson's disease (PD), the disease mechanisms remain unclear. We have applied mass spectrometry-based proteomics to investigate the effects of parkin dysfunction on the mitochondrial proteome in human isogenic induced pluripotent stem cell-derived neurons with and without *PARK2* knockout (KO). The proteomic analysis quantified nearly 60% of all mitochondrial proteins, 119 of which were dysregulated in neurons with *PARK2* KO. The protein changes indicated disturbances in oxidative stress defense, mitochondrial respiration and morphology, cell cycle control, and cell viability. Structural and functional analyses revealed an increase in mitochondrial area and the presence of elongated mitochondria as well as impaired glycolysis and lactate-supported respiration, leading to an impaired cell survival in PARK2 KO neurons. This adds valuable insight into the effect of parkin dysfunction in human neurons and provides knowledge of disease-related pathways that can potentially be targeted for therapeutic intervention.

Keywords: Parkinson's, proteomics, oxidative stress, metabolism, survival, mitochondria

INTRODUCTION

Parkinson's disease (PD) is an incurable neurodegenerative disorder characterized by the progressive loss of midbrain dopaminergic neurons and subsequent striatal dopamine depletion. Key contributions to the pathogenesis of both sporadic and familial PD come from mitochondrial dysfunction and oxidative stress (Abou-Sleiman et al., 2006; Ryan et al., 2015). This is supported by studies demonstrating that toxins inhibiting the mitochondrial respiratory chain complex I produce PD pathogenesis in both humans and animal models by elevating the production of reactive

oxygen species (ROS) and causing dopaminergic cell death (Langston et al., 1983; Langston, 1996). Importantly, decreased activity of complex I and increased oxidative damage have been detected in substantia nigra of sporadic PD patients (Dexter et al., 1989; Parker et al., 1989; Schapira et al., 1990; Alam et al., 1997).

Mutations in the genes *PARK2* (parkin), *PARK6* (PINK1), and *PARK7* (DJ-1), which are all important for mitochondrial function, cause autosomal recessive familial PD, with *PARK2* mutations being the most common (Abou-Sleiman et al., 2006). *PARK2* encodes the ubiquitin E3 ligase, parkin, which is recruited to damage mitochondria by PINK1. Phosphorylation of ubiquitin and parkin by PINK1 is required for parkin recruitment and activity (Kazlauskaite et al., 2014). When activated, parkin ubiquitinates target mitochondrial proteins, marking them and the mitochondria for degradation through the autophagy–lysosome pathway (ALP), a process known as mitophagy (Clark et al., 2006; Narendra et al., 2008). Besides its role in mitochondrial quality control, parkin appears to be involved in numerous other functions, including cytoskeletal stability, cell mitosis, and cell survival, where its role is less well described (Moore, 2006). The study of parkin dysfunction in PD pathogenesis is, however, impeded by the fact that genetic parkin knockout (KO) rodents show only minor disease phenotypes and limited pathology (Kitada et al., 2009; Oliveras-Salvá et al., 2011).

Instead induced pluripotent stem cells (iPSCs) derived from patients with familial PD or cells with *PARK2* mutations introduced by genome editing have enabled investigations of parkin dysfunction in human dopaminergic neurons *in vitro*. PD patient iPSC-derived neurons with *PARK2* mutations show increased oxidative stress, α-synuclein accumulation, and disturbances in mitochondrial morphology and function (Imaizumi et al., 2012; Jiang et al., 2012; Chung et al., 2016). However, the cellular changes and sequence of events leading from disruption of parkin function to disease development remain largely unknown.

Mass spectrometry-based proteomics enable the unbiased characterization of changes in large numbers of proteins simultaneously. Such methods have been applied to cell and animal models of parkin and PINK1 dysfunction revealing changes in proteins involved in oxidative stress, synaptic plasticity, protein folding, and energy metabolism (Ozgul et al., 2015; Triplett et al., 2015). In addition, several proteomics studies have specifically aimed at identifying and quantifying changes in mitochondrial proteins in various PD models, however, with limited commonality in their findings, perhaps due to variability between the different models (Aroso et al., 2016).

We report for the first time the investigation of mitochondria-specific proteomic and phospho-proteomic changes caused by parkin dysfunction in human iPSC-derived neurons. Our analysis identified and quantified more than half of all reported mitochondrial proteins and determined large numbers of dysregulated proteins in *PARK2* KO neurons compared to healthy isogenic controls. Among the affected mitochondrial proteins were key components in the cellular defense against oxidative stress as well as in glycolysis and lactate–pyruvate metabolism, which was confirmed by a functional impairment of glycolysis and lactate-supported respiration. Such changes may lead to mitochondrial energy deficits, increased susceptibility to oxidative stress, and cell death, which was seen for neurons with PARK2 KO in the present study.

MATERIALS AND METHODS

Ethics Statement

All use of human stem cells was performed in accordance with the Danish national regulations, the ethical guidelines issued by the Network of European CNS Transplantation and Restoration (NECTAR) and the International Society for Stem Cell Research (ISSCR).

NSCs Culture and Differentiation

The control and *PARK2* KO iPSC lines and corresponding NSC derivatives were obtained from XCell Science Inc. (Novato, CA, United States) (Shaltouki et al., 2015). iPSCs and NSCs were characterized and propagated according to standard protocols. iPSC differentiation to NSCs was performed by XCell Science Inc. using a 14-day protocol (Swistowski et al., 2009). Dopaminergic differentiation was achieved by culturing NSCs in DOPA Induction and Maturation Medium (XCell Science Inc., Novato, CA, United States) according to manufacturer instructions for at least 25 days from NSC stage (39 days from iPSC stage). See the **Supplementary Information** for detailed procedures.

Mitochondrial Enrichment

Mitochondria were purified from day 25 *PARK2* KO and control neuronal cultures from three independent differentiations (39 days differentiation from iPSC stage). Briefly, the cells were collected on ice in phosphate-buffered saline (PBS, ThermoFisher) with protease (Complete Tablets, Roche) and phosphatase inhibitors (PhosSTOP Tablets, Roche) and stored at −20°C. The QProteome Mitochondria Isolation Kit (Qiagen #37612) was used according to the manufacturer's instruction for standard preparation.

Lysis, Reduction, and Enzymatic Digestion

Samples were incubated for 2 h in 10 μl lysis buffer consisting of 6 M urea, 2 M thiourea, and 10 mM DTT (all Sigma). Thereafter, samples were dilutes 10 times in 20 mM triethylammonium bicarbonate buffer (TEAB, Sigma), pH 7.5, and sonicated two times 10 s on ice followed by alkylation with 20 mM Iodacetamide (Sigma) for 30 min in the dark. Protein concentration was measured by Qubit® according to the manufacturer's instruction. Samples were digested with 1 μg trypsin (Sigma) per 50 μg protein at room temperature (RT).

Tandem Mass Tag Labeling and Enrichment of Phosphorylated Peptides

Forty-five micrograms of each sample were labeled with tandem mass tag (TMT) Sixplex Isobaric label Reagents (ThermoFisher) according to the manufacturer's instructions. Efficient labeling

was confirmed by MALDI, the ratios adjusted, and the labeled peptides mixed 1:1:1:1:1:1 and dried by vacuum centrifugation.

Phospho-peptide enrichment was essentially performed as earlier described (Engholm-Keller et al., 2012). See the **Supplementary Information** for detailed procedure.

Hydrophobic Interaction Liquid Chromatography (HILIC) and High pH Fractionation

Mono-phosphorylated and non-modified peptides were fractionated to reduce sample complexity by HILIC as described previously (Engholm-Keller et al., 2012). Detailed description can be found in the **Supplementary Information**. To increase the coverage, high pH fractionation was also performed using approximately 50 μg peptide of the non-modified peptide sample. Briefly, the sample was dissolved in 1% ammonium (NH_3, Sigma), pH 11, and loaded on a R2/R3 column equilibrated with 0.1% NH_3. The peptides were eluted in a stepwise fashion using a gradient of 5–60% ACN/0.1% NH_3. All fractions were dried by vacuum centrifugation.

Reversed-Phase NanoLC–ESI–MS/MS

The samples were resuspended in 0.1% formic acid (FA) and loaded onto a two-column EASY-nLC System (Thermo Scientific). The pre-column was a 3 cm long fused silica capillary (100 μM inner diameter) with a fritted end and in-house packed with ReproSil-Pur C18 AQ 5 μm (Dr. Maisch GmbH) whereas the analytical column was a 17 cm long fused silica capillary (75 μm inner diameter) and packed with ReproSil-Pur C18 AQ 3 μm reversed-phase material (Dr. Maisch GmbH).

The peptides were eluted with an organic solvent gradient from 100% phase A (0.1% FA) to 34% phase B (95% ACN, 0.1% FA) at a constant flow-rate of 250 nl/min. Depending on the samples based on the HILIC, the gradient was from 1 to 30% solvent B in 60 or 90 min, 30–50% solvent B in 10 min, 50–100% solvent B in 5 min and 8 min at 100% solvent B.

The nLC was online connected to a QExactive HF Mass Spectrometer (Thermo Scientific) operated at positive ion mode with data-dependent acquisition. The Orbitrap acquired the full MS scan with an automatic gain control (AGC) target value of 3×10^6 ions and a maximum fill time of 100 ms. Each MS scan was acquired at high-resolution [120,000 full width half maximum (FWHM)] at m/z 200 in the Orbitrap with a mass range of 400–1400 Da. The 12 most abundant peptide ions were selected from the MS for higher energy collision-induced dissociation (HCD) fragmentation (collision energy: 34 V). Fragmentation was performed at high resolution (60,000 FWHM) for a target of 1×10^5 and a maximum injection time of 60 ms using an isolation window of 1.2 m/z and a dynamic exclusion. All raw data were viewed in Thermo Xcalibur v3.0.

Mass Spectrometry Data Analysis

The raw data were processed using Proteome Discoverer (v2.1, ThermoFisher) and searched against the Swissprot human database using an in-house Mascot server (v2.3, Matrix Science Ltd.) and the Sequest HT search engine.

Database searches were performed with the following parameters: precursor mass tolerance of 10 ppm, fragment mass tolerance of 0.02 Da (HCD fragmentation), TMT 6-plex (Lys and N-terminal) as fixed modifications, and a maximum of two missed cleavages for trypsin. Variable modifications were carbamidomethylation of alkylated Cys and N-terminal acetylation along with phosphorylation of Ser/Thr/Tyr for the phosphorylated group. Only peptides with up to a q-value of 0.01 (Percolator), Mascot rank 1, and cut-off value of Mascot score >15 were considered for further analysis. Only proteins with more than one unique peptide were considered for further analysis in the non-modified group.

The mass spectrometry proteomics data have been deposited to the ProteomeXchange Consortium via the PRIDE partner repository with the dataset identifier PXD008894 (Vizcaíno et al., 2016).

Pathway analysis on proteomics data was performed using String 10.0, ProteinCenter (ThermoFisher) and the ingenuity pathway analysis (IPA) software (QIAGEN).

Immunofluorescence and Western Blotting

Immunofluorescence and Western blotting were performed using standard methods. Detailed descriptions can be found in the **Supplementary Information**. Primary antibodies were used in the following concentrations:

For immunofluorescence: rabbit anti-tyrosine hydroxylase (TH, Millipore #AB152) 1:600, mouse anti-TH (Millipore #AB5280) 1:600, mouse anti-microtubule-associated protein 2a+b (MAP2, Sigma #M1406) 1:2000, mouse anti-Ki67 (BD Pharmingen #550609) 1:500, goat anti-Annexin V (GeneCopoeia #A037) 1:200, mouse anti-synaptophysin (Sigma # S5768) 1:200, and rabbit anti-TOM20 (Santa Cruz #SC-11415) 1:1000.

For Western blotting: Mouse anti-β-actin-HRP (Abcam #49900) 1:50,000, rabbit anti-BAX (Cell Signaling #5023) 1:1000, rabbit anti-COXIV (Abcam #16056) 1:2000, rabbit anti-DJ-1 (Abcam #18257) 1:1000, mouse anti-lactate dehydrogenase (LDH) (Santa Cruz #133123) 1:100, rabbit anti-MIEF1 (Abcam #89944) 1:1000, mouse anti-Parkin (Cell Signaling #4211) 1:1000, rabbit anti-SOD1 (Abcam #16831) 1:2000, mouse anti-TH (Millipore #AB5280) 1:600, anti-TOM20 (Santa Cruz #11415) 1:1000, rabbit anti-voltage-dependent anion-selective channel 1 (VDAC1) (Abcam #154856) 1:1000, and rabbit anti-14-3-3ε (Cell Signaling #9635) 1:1000.

Fluorescence images were acquired on an FV1000MPE confocal microscope (Olympus). Analysis of mitochondrial morphology and numbers was performed in ImageJ by converting TOM20 images to binary format and using the "analyse particles" function. For mitochondrial morphology the following criteria were applied after calculating the ratio of pixels^2 to μm^2: Large, elongated: size = 0.71–3.50 μm^2, circularity = 0.01–0.50. Large, round: size = 0.71–3.50 μm^2, circularity = 0.50–1.00. Small, elongated: size = 0.15–0.70 μm^2,

circularity = 0.01–0.50. Small, round: size = 0.15–0.70 μm^2, circularity = 0.50–1.00. **Supplementary Figure S4** shows an example of the analysis and the four categories of mitochondria.

Area and numbers of mitochondria were normalized to total cell numbers as quantified by CellProfiler analysis for DAPI+ nuclei (Carpenter et al., 2006; Schneider et al., 2012).

Oxygen Consumption Rate Analysis

On differentiation day 18 (32 from iPSC stage), cells were replated onto poly-L-ornithine (Sigma) and laminin (Life Tech) coated Seahorse 96-well plates (Agilent Tech.) at a density of 200,000 cells/well. Four wells with no cells were used as background control in the OCR and extracellular acidification rate (ECAR) analysis. Oxygen consumption rate **(OCR)** and ECAR were measured on differentiation day 25 (from the NSC stage) on the Seahorse XFe 96 analyzer using the Seahorse XF Mito Stress Test Kit (Agilent Tech.) according to the manufacturer's instructions. Briefly, the cells were washed once and incubated in XF Base Medium (Agilent Tech.) supplemented with either 2.5 mM glucose (Sigma) or 2.5 mM lactate (Sigma) 37°C for 5 min in a non-CO_2 incubator prior to analysis. After equilibration in the XFe 96 analyzer the following measurements were acquired: three baseline readings, two following 2 μM oligomycin treatment, two following 2 μM FCCP treatment, and three following 0.5 μM rotenone/antimycin treatment. The background corrected OCR and ECAR readings were normalized to protein levels per well as measured by Pierce Bicinchoninic Acid (BCA) Protein Assay (ThermoFisher) and these values were normalized to the average basal level of the control in each independent experiment.

Cell Viability and Death

Cell viability was measured by Trypan blue staining of cells in suspension following 5 min accutase treatment at differentiation days 0, 5, 10, and 25 from the NSC stage.

The nuclear morphology was quantified by counting the number of fragmented and pyknotic nuclei on DAPI-stained neuronal cultures as a proportion of total cells per field of view.

Lactate dehydrogenase release was quantified at differentiation day 25 as a measure of cell death applying the CytoTox 96 Non-Radioactive Cytotoxicity Assay (Promega) according to manufacture instructions with a cell density of 20,000 per well plated at day 18. Values were normalized to protein concentrations to account for differences in cell numbers per well.

Statistical Analysis

An in house R-tool was applied to perform paired Limma test (moderated *t*-test) with correction for multiple testing to allow for the detection of significant protein and PTM level changes in the proteomic dataset (Storey, 2002; Schwämmle et al., 2013). Analyses of functional assays were performed in Graphpad Prism version 5.0 (GraphPad Software, United States) using two-tailed Student's *T*-tests or one-way ANOVA with Tukey's *post hoc* test where appropriate. Results are expressed as mean ± SEM, and *P*-values < 0.05 were considered statistically significant.

RESULTS

Mitochondrial-Enriched Proteomics Quantify More Than Half of Known Mitochondrial Proteins in Control and *PARK2* KO Neurons

To explore the effects of parkin dysfunction, we utilized two isogenic iPSC lines created from a healthy control iPSC line, where deletions have been introduced in exon 2 on both alleles of the *PARK2* gene by genome editing (Shaltouki et al., 2015). The *PARK2* KO was confirmed by Western blotting for parkin protein (**Figure 1A**). We have previously demonstrated that the *PARK2* KO and isogenic control NSCs equally can be differentiated into neuronal cultures with a high proportion of midbrain dopaminergic neurons (manuscript in resubmission) (**Figures 1B,C**). These results were supported by qRT-PCR analysis showing a down-regulation of the pluripotency marker OCT4 and an up-regulation of the midbrain dopaminergic markers EN1, LMX1A, and GIRK2 (**Supplementary Figures S1A–D**). Calcium-imaging recordings indicated that the neurons were functionally matured as they displayed spontaneous activity and could be depolarized by potassium chloride (data not shown). This finding was further supported by immunocytochemistry showing a significant expression of the presynaptic marker synaptophysin in polarized neurons (**Figure 1D**).

Using the reported differentiation protocol, *PARK2* KO and isogenic control neurons from three independent differentiations were collected and subjected to mitochondrial enrichment prior to the proteomic analysis (**Figure 1E**), leading to the identification of a total of 5747 proteins (**Figure 1F**). Data are available via ProteomeXchange with identifier PXD008894. Based on the proteins identified with high confidence (more than or equal to two unique peptides), our analysis quantified levels of 945 out of 1564 mitochondrial proteins (60%) listed in the Gene Ontology (GO) Database (GO term: mitochondrion, organism: *Homo sapiens*, type: protein), giving us a comprehensive description of mitochondrial protein changes in human neurons in response to parkin dysfunction (**Figures 1F,G**). The average abundances of mitochondrial proteins were identical in the six samples, indicating that the enrichment procedure had resulted in similar amounts of mitochondria in each sample (**Figure 1H**). The average abundances of the neuronal markers TUJ1, MAP2, and synaptophysin were similar in control and *PARK2* KO samples (**Figure 1I**). Levels of 1064 proteins were significantly altered in the *PARK2* KO neurons, and 119 of these were connected to mitochondria (**Figures 1F,G** and **Supplementary Tables S1A,B**). In addition, we quantified levels of 4585 phosphorylated peptides of which 296 were mitochondrial. However, none of these were significantly altered, indicating that parkin dysfunction did not consistently change the mitochondrial phospho-proteome in this model (**Supplementary Table S1C**).

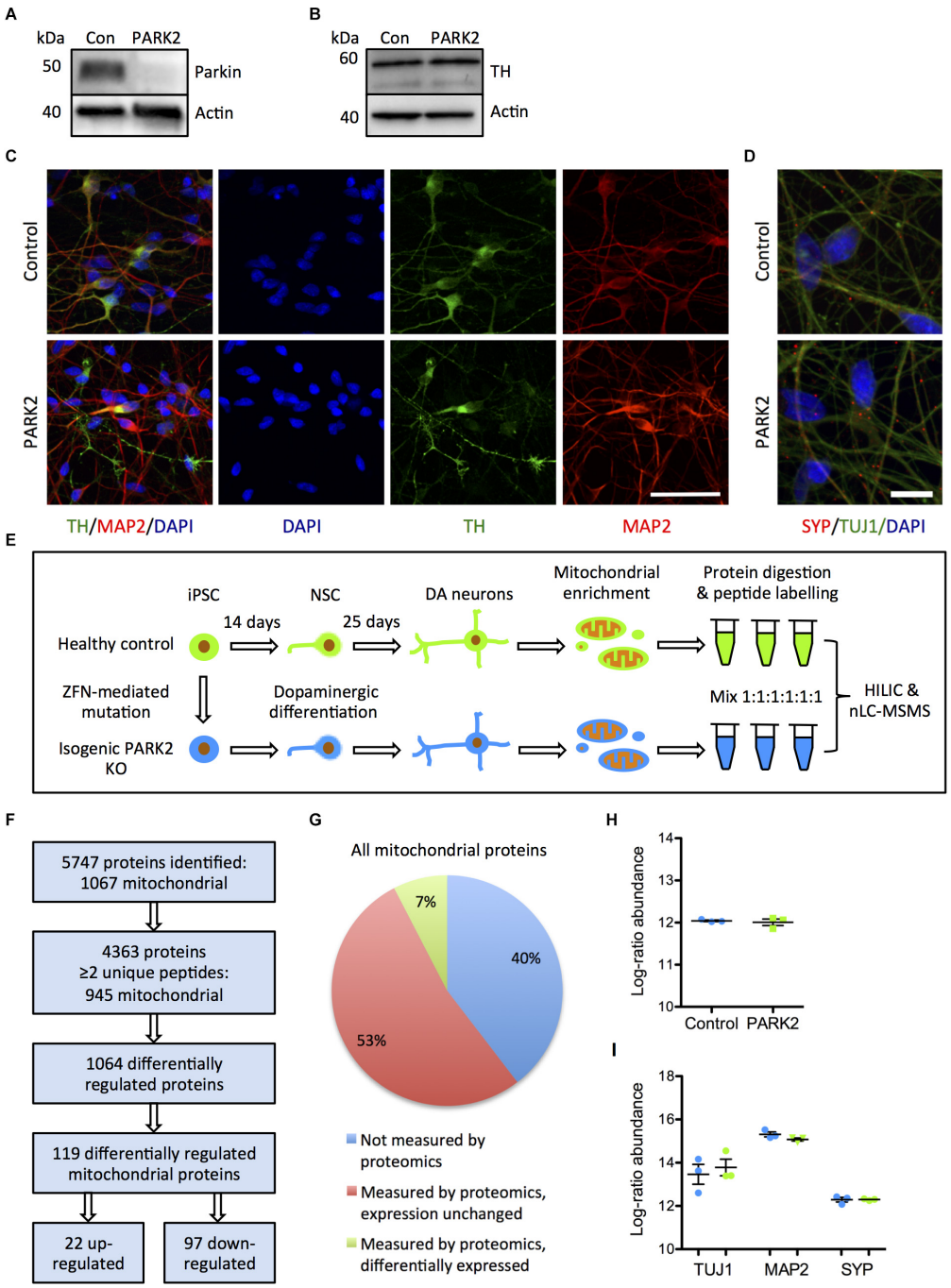


FIGURE 1 | Proteomic analysis of mitochondrial changes in PARK2 knockout (KO)-induced pluripotent stem cell (iPSC)-derived neurons. **(A,B)** Western blotting for **(A)** parkin protein verifying the *PARK2* KO and **(B)** tyrosine hydroxylase (TH) indicating comparable dopaminergic (DA) differentiation. **(C)** Immunofluorescence staining of control and *PARK2* KO neurons on differentiation day 25 showed no differences in levels of TH (green) and microtubule-associated protein 2 (MAP2, red) positive neurons. Scale bar = 50 μm. **(D)** Immunofluorescence staining for synaptophysin (SYP) and β-III-tubulin (TUJ1) confirmed the presence of mature *PARK2* KO and control neurons. Scale bar = 25 μm. **(E)** Schematic illustration of the experimental set-up: *PARK2* KO iPSCs created by zinc finger nucleases (ZFNs) and the isogenic healthy control iPSC line were differentiated to neural stem cells (NSCs) and onward to DA neurons. Mitochondrial enrichment was performed on cell lysates from three independent differentiations. Proteins were digested to peptides, which were labeled and mixed in 1:1:1:1:1:1:1 ratio prior to hydrophilic interaction liquid chromatography (HILIC) and nano-liquid chromatography tandem mass spectrometry analysis (nLC-MSMS). **(F)** Overview of the identified proteins: 945 mitochondrial proteins were identified by two or more peptides and levels of 119 of these were significantly altered in *PARK2* KO neurons. **(G)** The analysis identified 60% of all mitochondrial proteins listed in the Gene Ontology (GO) Database (GO term: mitochondrion, organism: homo sapiens, type: protein), 7% of these were differentially expressed in *PARK2* KO neurons. **(H,I)** The average proteomics-identified abundances (log ratio) of **(H)** all mitochondrial proteins as well as **(I)** the neuronal markers TUJ1, MAP2, and SYP were similar between control and *PARK2* KO neurons. Mean ± SEM, $n = 3$ independent differentiations.

Pathway Analysis of Proteomic Changes Reveals Disturbances in Cell Cycle Regulation, Oxidative Stress, and Energy Metabolism in *PARK2* KO Neurons

A large proportion of the differentially regulated mitochondrial proteins were related to oxidative stress defense, energy metabolism, and cell cycle regulation. This was demonstrated by STRING analysis, which revealed a cluster of 14-3-3 (YWHA-) proteins involved in cell cycle regulation and apoptosis signaling and two clusters containing proteins involved in defense against oxidative stress and energy metabolism, respectively (**Figure 2A**). Pathway analysis, based on differences in protein profiles, revealed that the central toxicity-related pathways included cell cycle check points for DNA damage and processes related to mitochondrial dysfunction including oxidative stress, decreasing respiration, and mitochondrial swelling among others (**Figure 2B**). The decreased level of 14-3-3ε (YWHAE) was confirmed by Western blotting (**Figure 2C**), as were the lower level of BAX although with a large degree of variation in total BAX expression between differentiations (**Supplementary Figure S2A**).

The reduced levels of antioxidant enzymes in *PARK2* KO neurons were surprising, but could be confirmed, as the significant down-regulation of the PD-related protein DJ-1 as well as SOD1 was documented by Western blotting (**Figures 3A–C**). In addition we have earlier confirmed that significantly decreased levels of catalase are present in *PARK2* KO neurons, overall indicating that impairment in the defense against oxidative stress is apparent (manuscript in resubmission).

Perturbations in Mitochondrial Area and Morphology in *PARK2* KO Neurons

The *PARK2* KO did not significantly affect the total number of mitochondria as measured by TOM20 immunofluorescence staining (**Figures 4A,B**). However, the *PARK2* KO neurons contained a significantly increased area of TOM20 immunoreactivity, indicating an overall larger mitochondrial area per cell (**Figures 4A,C**). To examine the mitochondrial morphology, we divided the mitochondria into four categories based on shape and size (**Supplementary Figure S4**). This demonstrated a significant increase in the numbers of elongated mitochondria (both large and small) in the *PARK2* KO cells, whereas numbers of round mitochondria were unchanged (**Figure 4D**). The proteomic data revealed identical levels of TOM20 (*PARK2* KO/control ratio = 0.99) and the mitochondrial marker, VDAC1 (*PARK2* KO/control ratio = 1.06) between the lines (**Figure 4E**). Western blotting for TOM20 and VDAC1 levels confirmed no difference between the lines (**Figures 4F,G**). This supported that the observed changes might be related to mitochondrial morphology rather than changes in numbers. Interestingly, levels of the mitochondrial dynamics protein MIEF1 and the dynamin-1-like protein (Drp1) were significantly decreased as shown by the proteomic analysis whereas levels of other key mitochondrial fission-fusion proteins were unaffected (**Figure 4H**). By Western blotting the decrease in the MIEF1 level was validated (**Figure 4I**), but no change in Drp1 levels was detected (**Supplementary Figure S2B**).

PARK2 KO Neurons Are Deficient in Glycolysis and Lactate Metabolism

The proteomic analysis quantified large numbers of electron transport chain (ETC) proteins. Interestingly, cytochrome c oxidase (COX) IV levels were, as measured by Western blotting, significantly reduced in *PARK2* KO neurons (**Figure 4J**), which was in agreement with the proteomic data showing decreased levels of 3 complex IV-related proteins [COX copper chaperone (COX17), COX assembly factor 6 and 7 (COA6/7)] out of 21 identified (**Supplementary Table S2**). Forty-one complex I subunits or related proteins as well as 12 complex III proteins were identified (**Supplementary Tables S3**, **S4**), but none of these were significantly affected, indicating that the changes were specific for complex IV.

In addition, a number of the mitochondrial proteins dysregulated in *PARK2* KO neurons were of importance for energy metabolism and the pathway analysis pointed to a decrease in mitochondrial respiration. The proteins related to energy metabolism were almost exclusively down-regulated with LDH B, pyruvate kinase PKM (PKM), and monocarboxylate transporter 1 displaying the most significantly decreased levels (**Figure 5A**). Significantly decreased levels of LDH were confirmed by Western blotting (**Figure 5B**). These observations correlated with a significantly decreased ability of *PARK2* KO neurons to respire using lactate as a substrate. This was demonstrated by measuring OCRs of control and *PARK2* KO neurons in medium with either glucose or lactate as the only energy source (**Figures 5C,D**). Both the basal OCR and ATP production was significantly reduced in *PARK2* KO neurons respiring on lactate, confirming a disturbance in lactate metabolism (**Figure 5D** and **Supplementary Figure S3**). With glucose no difference in OCR between control and *PARK2* KO neurons was observed despite the decreased COXIV levels (**Figure 4J**). However, the basal ECAR with glucose was significantly decreased, indicating an impairment of glycolysis in *PARK2* KO neurons (**Figures 5E,F**).

Decreased Proliferation and Survival of *PARK2* KO Cells

Pathway analysis based on the 119 dysregulated proteins indicated that cell cycle regulation, cell viability, and neuronal cell death were affected in *PARK2* KO neurons (**Figure 6A**). We therefore sought to first determine proliferation rates during the differentiation. At the early time points similar numbers of cells gave rise to much fewer *PARK2* KO cells 5 days later (**Figure 6B**). This correlated with a significantly lower percentage of Ki67+ proliferative cells in the *PARK2* KO cultures at day 0 (control: 95.9 ± 0.2%, *PARK2*: 93.0 ± 0.8%, $P < 0.01$) (**Figures 6C,E**) while similar numbers were found at day 25 from the NSC stage (control: 6.1 ± 1.4%, *PARK2*: 5.6 ± 1.6%) (**Figures 6D,F**). To investigate cell viability, we examined the number of Annexin V+ apoptotic cells, which was very low for both cell lines at days 0 and 25 (**Figures 6G,H**). This indicated low levels of apoptotic

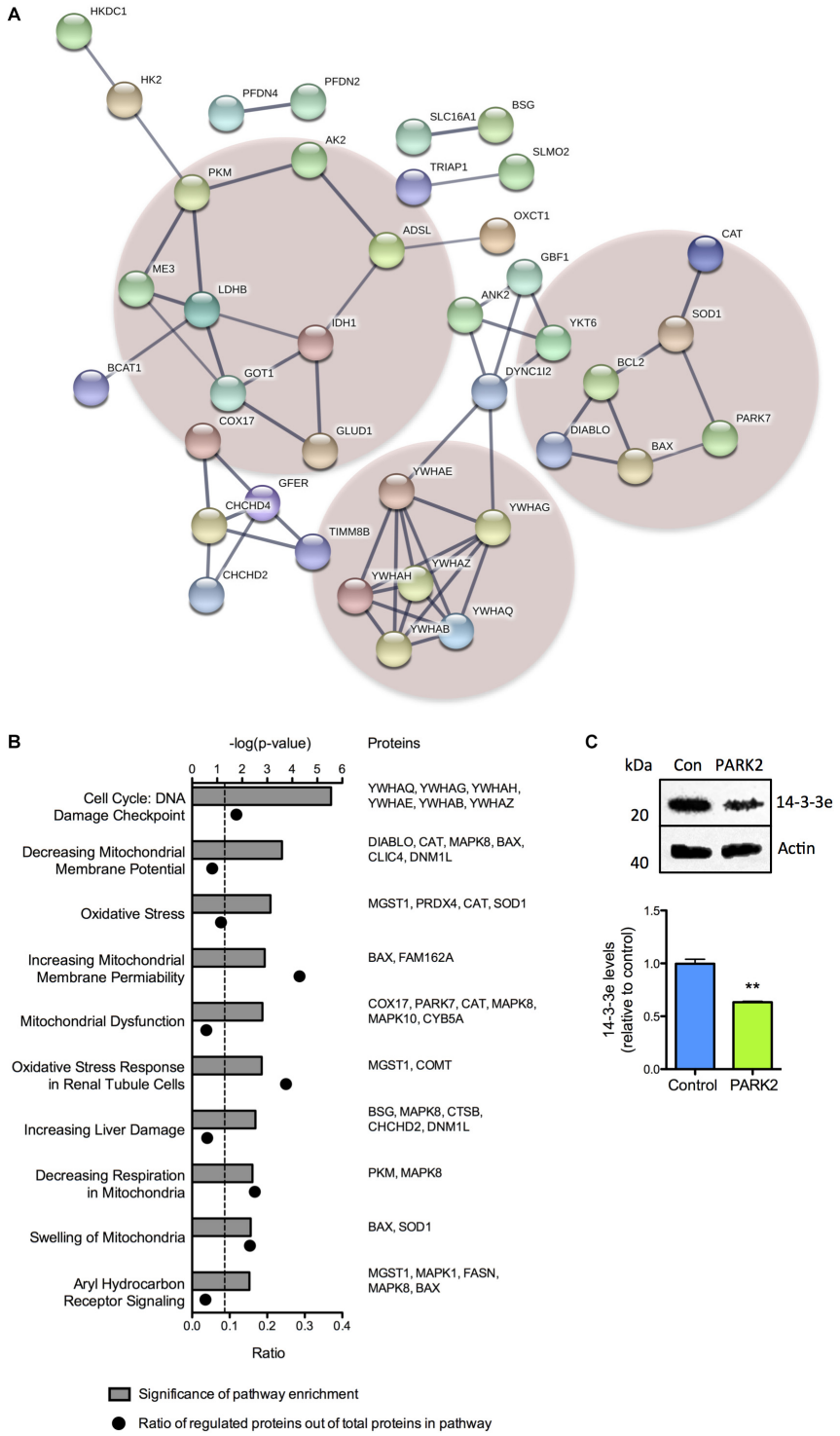


FIGURE 2 | Cluster and pathway analysis of proteomic changes in *PARK2* KO neurons. **(A)** STRING analysis on the 119 significantly dysregulated mitochondrial proteins identified by the proteomic analysis, revealed three clusters of proteins related to lactate–pyruvate metabolism (left cluster), oxidative stress (right cluster), and cell cycle regulation and cell death (lower cluster), respectively. Only connected nodes are shown. The line thickness indicates the strength of the supporting data. **(B)** Top toxicity-related pathways identified by ingenuity pathway analysis (IPA) of the significantly dysregulated mitochondrial proteins. Bar graphs indicate the enrichment level of each pathway shown as –log(*P*-value). The corresponding dots indicate the ratio of identified proteins out of the total number of proteins in the pathway. **(C)** Western blotting confirming a significant decrease in the level of 14-3-3ε in *PARK2* KO neurons. Protein expression levels were normalized to β-actin and shown relative to control neurons. Mean ± SEM, $n = 3$ technical replicates, data from three independent differentiations. $^{**}P < 0.01$, Student's *T*-test.

A

Accession	Gene name	Description	PARK2 / Control	q-value	Unique Peptides
P10620	MGST1	Microsomal glutathione S-transferase 1	1.32	0.023	4
Q13162	PRDX4	Peroxiredoxin-4	1.20	0.033	9
Q5VUM1	SDHAF4	Succinate dehydrogenase assembly factor 4	0.86	0.040	2
Q99497	PARK7	Protein deglycase DJ-1	0.82	0.022	12
Q86X76	NIT1	Deaminated glutathione amidase	0.80	0.032	3
O75874	IDH1	Isocitrate dehydrogenase	0.79	0.017	17
Q07812	BAX	Apoptosis regulator BAX	0.77	0.014	6
Q8IWL3	HSCB	Iron-sulfur cluster co-chaperone HSCB	0.79	0.015	3
P32119	PRDX2	Peroxiredoxin-2	0.73	0.013	10
P00441	SOD1	Superoxide dismutase	0.64	0.033	7
P04040	CAT	Catalase	0.34	0.000	18

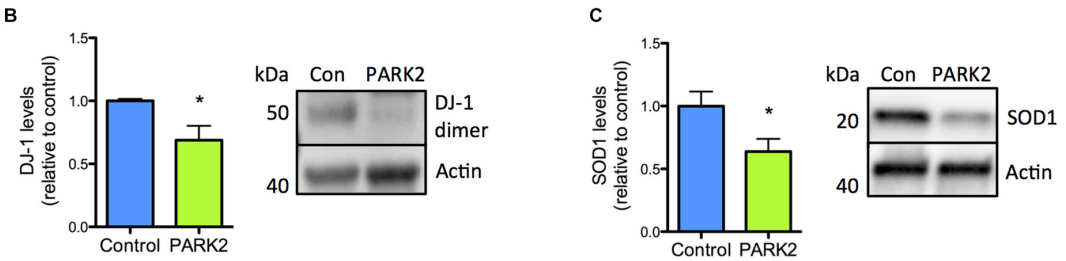


FIGURE 3 | Confirmation of down-regulation of oxidative stress defense proteins identified by the proteomic analysis. **(A)** Table listing the proteins related to oxidative stress defense identified by the mitochondrial proteomic analysis with the ratio of protein levels in *PARK2* KO neurons compared to controls; *q*-value (FDR-adjusted *P*-value) and number of unique peptides, $n = 3$ independent differentiations. **(B,C)** Western blotting confirmed a significant decrease in levels of **(B)** DJ-1 and **(C)** superoxide dismutase 1 (SOD1) in *PARK2* KO neurons. Expression levels were normalized to β-actin and shown relative to control neurons. Mean ± SEM, $n = 6$ technical replicates, data from three independent differentiations. $^*P < 0.05$, Student's *T*-test.

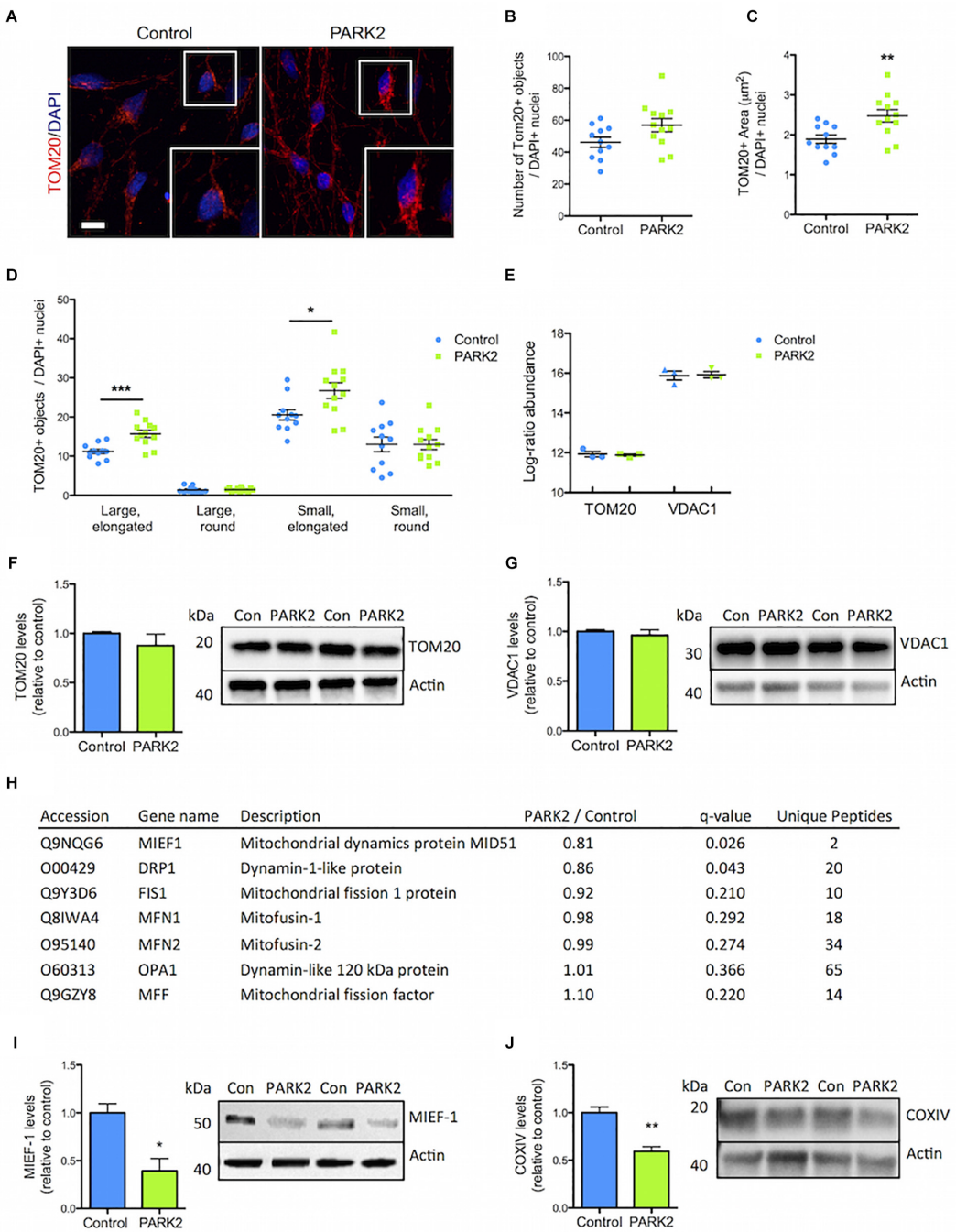
cell death in general. However, Trypan blue staining of cells in suspension after accutase treatment revealed a significantly lower viability of the *PARK2* KO neurons at day 25 (control: 84.1 ± 1.2%, *PARK2*: 77.7 ± 2.3%, $P < 0.05$) (**Figure 6I**), which was confirmed by a significantly higher LDH release from the *PARK2* KO cultures at day 25, indicating increased necrosis (**Figure 6J**). Analysis of the nuclear morphologies at days 25, 35, and 45 revealed significantly increased percentages of fragmented and pyknotic nuclei for *PARK2* KO neurons relative to controls at the later time points, indicating higher levels of cell death over time (**Figures 6K,L**). In conclusion, both cell proliferation and neuronal cell survival was altered for *PARK2* KO cells.

DISCUSSION

The importance of mitochondrial dysfunction in sporadic and certain forms of familial PD is well established, but the specific mechanisms and pathways are not well understood (Abou-Sleiman et al., 2006). Human iPSC-derived neurons with *PARK2* KO allow for the study of chronic mitochondrial dysfunction in PD without toxic insults or other stressors (Imaizumi et al., 2012; Jiang et al., 2012; Chung et al., 2016). By applying isogenic iPSC-derived neurons and large-scale mass spectrometry-based proteomics, we have been able to investigate the effect of parkin dysfunction on large numbers of proteins. Using this approach we have identified 60% of the known mitochondrial proteins of which 119 were significantly dysregulated in *PARK2* KO neurons.

Several proteins of importance for the cellular defense against oxidative stress were reduced in *PARK2* KO neurons, rendering them more susceptible to oxidative damage. An earlier study on patient fibroblasts with *PARK2* mutation has similarly reported decreased levels and/or activity of catalase and superoxide dismutase (SOD) 2 (Pacelli et al., 2011). Palacino et al. (2004) identified 15 proteins, with altered levels in *PARK2* KO mice, of which 4 involved in protection against oxidative stress displayed decreased levels. One of these, peroxiredoxin-2, was significantly reduced in the *PARK2* KO neurons (Palacino et al., 2004). As the mitochondrial dysfunction caused by parkin deficiency can independently increase oxidative stress levels, a compensatory increase in proteins such as DJ-1, catalase, and SOD1/2 could have been expected (Abou-Sleiman et al., 2006). These results, however, indicate that *PARK2* KO has direct negative impact on antioxidant enzyme levels.

Earlier proteomic studies applying mitochondrial enrichment to toxin-based animal and cell models have shown limited commonality in the identified regulated proteins (Aroso et al., 2016). However, two proteins that have been consistently changed across different studies, including in post-mortem PD patient brain tissue, are PKM and 14-3-3 epsilon, which were among the most significantly down-regulated proteins in our *PARK2* KO neurons (Periquet et al., 2005; Jin et al., 2006; Aroso et al., 2016). PKM is the last enzyme in the glycolysis pathway and



H

Accession	Gene name	Description	PARK2 / Control	q-value	Unique Peptides
Q9NQG6	MIEF1	Mitochondrial dynamics protein MID51	0.81	0.026	2
O00429	DRP1	Dynamin-1-like protein	0.86	0.043	20
Q9Y3D6	FIS1	Mitochondrial fission 1 protein	0.92	0.210	10
Q8IWA4	MFN1	Mitofusin-1	0.98	0.292	18
O95140	MFN2	Mitofusin-2	0.99	0.274	34
O60313	OPA1	Dynamin-like 120 kDa protein	1.01	0.366	65
Q9GZY8	MFF	Mitochondrial fission factor	1.10	0.220	14

FIGURE 4 | Perturbed mitochondrial morphology in *PARK2* KO neurons. **(A)** TOM20 (red) immunofluorescence staining and **(B,C)** quantification in control and *PARK2* KO neurons showed **(B)** unchanged numbers of TOM20+ objects and **(C)** significantly increased area of TOM20 staining when normalized to number of DAPI+ nuclei (blue). **(D)** The number of elongated mitochondria was significantly increased in *PARK2* KO cells, whereas the number of round mitochondria was unchanged, when separating TOM20+ objects depending on size (small vs. large) and shape (round vs. elongated). Scale bar = 10 µm. Mean ± SEM, n = 11–12 technical replicates, data from four independent differentiations. **(E)** The average proteomics-identified abundance (log ratio) of TOM20 and VDAC1 was similar between control and *PARK2* KO neurons. Mean ± SEM, n = 3 independent differentiations. **(F,G)** Western blotting showed no changes in **(F)** TOM20 and **(G)** VDAC1 levels. Protein expression levels were normalized to β-actin and shown relative to control neurons. Mean ± SEM, n = 4–10 technical replicates, data from three independent differentiations. **(H)** Table listing the proteins related to mitochondrial dynamics identified by the mitochondrial proteomic analysis with the ratio of protein levels in *PARK2* KO neurons compared to controls; q-value (FDR-adjusted P-value) and number of unique peptides, n = 3 independent differentiations. **(I,J)** Western blotting showed a significant decrease in the levels of **(I)** MIEF1 and **(J)** COXIV in *PARK2* KO neurons. Protein expression levels were normalized to β-actin and shown relative to control neurons. Mean ± SEM, n = 3–4 technical replicates, data from three independent differentiations. *$P < 0.05$, **$P < 0.01$, ***$P < 0.005$, Student's T-test.

A

Accession	Gene name	Description	PARK2 / Control	q-value	Unique Peptides
P00367	GLUD1	Glutamate dehydrogenase 1	1.55	0.022	35
Q5VUM1	SDHAF4	Succinate dehydrogenase assembly factor 4	0.86	0.040	2
O15294	OGT	O-GlcNAc transferase subunit p110	0.85	0.041	6
P09972	ALDOC	Fructose-bisphosphate aldolase C	0.81	0.040	3
O75874	IDH1	Isocitrate dehydrogenase cytoplasmic	0.79	0.017	17
P54819	AK2	Adenylate kinase	0.74	0.013	15
Q16798	ME3	NADP-dependent malic enzyme	0.73	0.017	5
P07195	LDHB	L-lactate dehydrogenase B	0.66	0.004	14
P53985	SLC16A1	Monocarboxylate transporter 1 (MCT1)	0.63	0.013	2
P14618	PKM	Pyruvate kinase PKM	0.62	0.004	40

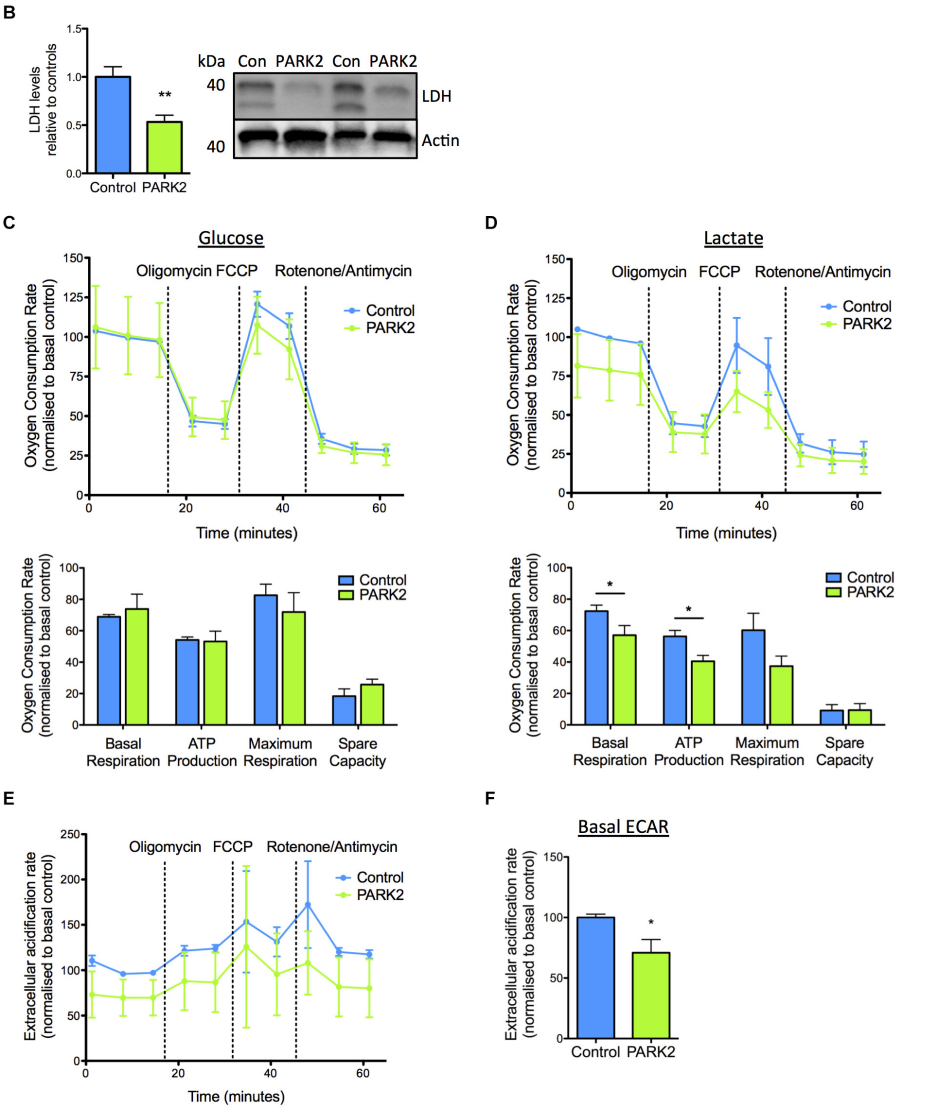


FIGURE 5 | Functional changes in lactate metabolism in *PARK2* KO neurons support protein changes revealed by proteomic analysis. **(A)** Table listing the mitochondrial proteins related to lactate–pyruvate metabolism identified by the proteomic analysis with the ratio of protein levels in *PARK2* KO neurons compared to controls; *q*-value (FDR-adjusted *P*-value) and number of unique peptides, $n = 3$ independent differentiations. **(B)** Western blotting confirmed a significant decrease in levels of lactate dehydrogenase (LDH) in *PARK2* KO neurons. Expression levels were normalized to β-actin and shown relative to control neurons. Mean ± SEM, $n = 6$ technical replicates, data from three independent differentiations. **(C–F)** Oxygen consumption rates (OCRs) and extracellular acidification rates (ECARs) of *PARK2* KO and control neurons normalized to protein content illustrating basal respiration, the respiration coupled to mitochondrial ATP production after oligomycin treatment, maximal respiration after FCCP treatment, and non-mitochondrial respiration after rotenone/antimycin treatment. The spare respiratory activity is defined as the difference between the baseline and FCCP-induced maximal respiration. **(C)** *PARK2* KO neurons had similar OCR when incubated in medium with 2.5 mM glucose and **(D)** significantly decreased basal respiration and ATP production in medium with 2.5 mM lactate. **(E,F)** Basal ECAR was significantly decreased in *PARK2* KO neurons. Mean ± SEM, $n = 3$–9 technical replicates, data from three independent differentiations. $^*P < 0.05$, $^{**}P < 0.01$, Student's *T*-test.

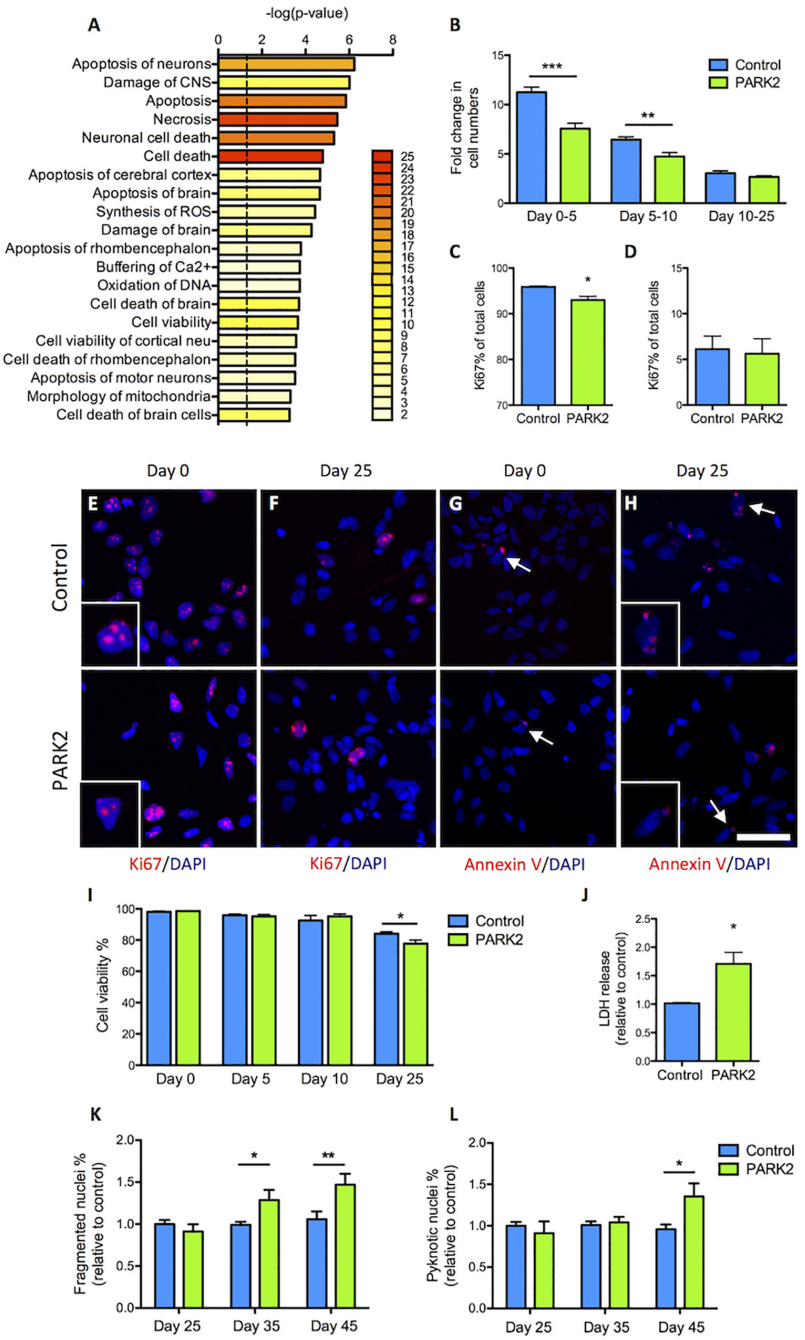


FIGURE 6 | Cell proliferation and survival is impeded in *PARK2* KO neurons. **(A)** Pathway analysis on the differentially expressed proteins showing with bar graphs the enrichment score –log 10(*P*-value) and with color labeling the number of identified proteins belonging to each pathway. Only pathways with two or more proteins are shown. **(B)** Cell counts on differentiation days 0, 5, 10, and 25 from the NSC stage indicated that the fold change in cell numbers from days 0–5 and 5–10 was significantly lower in *PARK2* KO cells compared to isogenic controls, whereas from days 10 to 25 there was no such difference between the lines. Mean ± SEM, n = 5–10 independent differentiations. **(C,E)** Quantification of immunofluorescence staining for Ki67+ (red) cells at differentiation day 0 revealed significantly lower levels of proliferation in *PARK2* KO cultures. **(D,F)** At differentiation day 25, no difference in the relative content of Ki67+ cells was observed between *PARK2* KO and control neurons. Mean ± SEM, N = 2 independent differentiations. **(G,H)** Immunofluorescence staining for Annexin V (red) on control and *PARK2* KO cells on differentiation day 0 and day 25 identified very few apoptotic cells in both cell lines. Cell nuclei were stained with DAPI (blue). Scale bar = 50 μm. **(I)** Cell viability as measured by Trypan blue staining of cells in suspension at differentiation days 0, 5, 10, and 25 showed significantly decreased survival of *PARK2* KO neurons at day 25. Mean ± SEM, N = 4 independent differentiations. **(J)** LDH release to the medium was increased in *PARK2* KO cultures compared to isogenic controls at day 25. Data presented relative to average controls. Mean ± SEM, n = 3 independent differentiations. **(K,L)** Analysis of nuclear morphologies at differentiation days 25, 35, and 45 indicating the percentage of fragmented and pyknotic nuclei as a proportion of total cells per field of view. Mean ± SEM, N = 15–36 fields of view, data from two independent differentiations. $^{*}P < 0.05$, $^{**}P < 0.01$, $^{***}P < 0.001$, Student's T-test.

corresponding with this, decreased ECAR, an indirect measure of glycolysis, was present in *PARK2* KO neurons metabolizing glucose. Periquet et al. (2005) in their study of proteomic changes in *PARK2* KO mice found decreased levels of both PKM, LDH, fructose-bisphosphate aldolase C (ALDOC), agreeing with our results, and also of pyruvate dehydrogenase, which converts pyruvate to acetyl CoA. Out of the 15 dysregulated proteins identified in Palacino et al. (2004), pyruvate dehydrogenase was the one showing the highest reduction in *PARK2* KO mice. A proteomic study on PINK1 KO rat brain similarly documented changes in levels of glycolysis-related proteins, including LDH, which were increased, and PKM, which was reduced (Villeneuve et al., 2016). Overall this indicates that changes in glycolytic flux could be generally present in PD. A study on human cancer cell lines identified PKM2, the PKM splice form present in cancer cells, as a parkin substrate and demonstrated that parkin KO caused increased activity of PKM2 and glycolysis in general (Liu et al., 2016). Although these results appear conflicting they do point to a link between parkin dysfunction and glycolysis.

Functionally, *PARK2* KO neurons incubated without glucose supplementation and having only lactate as a substrate exhibited significantly decreased basal respiration and ATP production, confirming that in addition to glycolysis, lactate metabolism is also perturbed in *PARK2* KO neurons.

Accumulating evidence indicates that astrocyte-derived lactate is an important energy source for neurons and neuroprotective in pathological situations (Wyss et al., 2011; Jourdain et al., 2016). However, in mice an age-dependent increase in brain lactate levels happens as a result of mitochondrial dysfunction promoting pyruvate to lactate conversion (Ross et al., 2010; Quistorff and Grunnet, 2011). In our *PARK2* KO neurons, the observed reduction in LDH and monocarboxylase transporter 1 may explain the decreased capacity of the cells to utilize lactate (**Supplementary Figure S3**). Combined with a reduction in glycolytic capacity, such metabolic changes may lead to harmful energy deficits.

A significant decrease in complex IV levels was also documented in the *PARK2* KO neurons. As important components of complex IV are encoded by mitochondrial DNA (mtDNA), mitochondrial dysfunction and oxidative stress causing damage to mtDNA could potentially explain this (Ross et al., 2010). Earlier studies have linked mtDNA damage and complex IV dysfunction (Bender et al., 2006; Kraytsberg et al., 2006). It remains to be determined whether higher levels of mtDNA damage are present in our *PARK2* KO neurons; however, a recent study has documented this in *PARK2* KO neurons from mice (Pinto et al., 2018).

Despite the decrease in complex IV levels, no effect on OCR was observed when glucose was present in the medium. However, the lower complex IV level could perhaps be a rate-limiting factor when lactate is the substrate. Palacino et al. (2004) found a reduction of proteins from both complexes I and IV, correlating with a decreased respiratory capacity of mitochondria in *PARK2* KO mice. Other studies, addressing OCR in the context of parkin dysfunction, have examined fibroblasts from *PARK2* PD patients and reported contradictory results of decreased or increased basal and maximum OCR (Pacelli et al., 2011; Zanellati et al., 2015). The discrepancy between these studies and also the present study remains unclear, but perhaps differences in energy metabolism between fibroblasts and neurons play a role.

The proteomic analysis revealed that known parkin substrates such as TOM20, VDAC1, Drp1, and MFN1/2 are not accumulating in this model. Earlier studies of proteomic changes in *PARK2* KO mice show similar results (Palacino et al., 2004; Periquet et al., 2005).

The TOM20 IF staining for mitochondria revealed increased overall area of immunoreactivity and enhanced numbers of elongated mitochondria in the *PARK2* KO neurons, whereas the levels of TOM20 and VDAC1 protein were unchanged. This indicates that the total mitochondrial content is not affected in the *PARK2* KO neurons, but that mitochondrial morphology is perturbed in the direction of larger, more elongated mitochondria (Zanellati et al., 2015; Pinto et al., 2018). This corroborates earlier results indicating increased swelling of mitochondria in *PARK2* KO neurons (Shaltouki et al., 2015). This may be explained by the role of parkin in promoting mitochondrial fission through Drp1 and is supported by reports of decreased fission and mitochondrial swelling observed for other parkin dysfunction models (Poole et al., 2008; Buhlman et al., 2014; Chung et al., 2016). However, others have reported increased mitochondrial fragmentation as a result of acute down-regulation of parkin (Lutz et al., 2009). The mitochondrial enlargement observed in the present model may reflect a compensatory response, given that mitochondrial swelling, as a result of altered fission-fusion processes, has been reported to occur to maintain oxidative phosphorylation and increase respiratory activity under stress (MacVicar and Lane, 2014; Mishra et al., 2014). Interestingly, Drp1 and MIEF1, which promotes mitochondrial fusion and inhibits fission, were found to be significantly decreased in *PARK2* KO neurons by proteomic analysis, which for MIEF1 was confirmed by Western blotting. Although no significant phosphorylation changes were detected in the *PARK2* KO neurons, MIEF1 was among the proteins with high levels of phosphorylation on several known phospho-sites and could potentially be involved in the observed morphological changes (Zhao et al., 2011).

The above-mentioned changes in oxidative stress defense and energy metabolism could be a cause of the documented impairment of proliferation and survival of *PARK2* KO cells. Although *PARK2* mutations cause early-onset PD, they are not known to affect neurodevelopment and proliferation of NSCs *in vivo*. The increased oxidative stress related to *in vitro* conditions could explain this discrepancy as resulting DNA damage could negatively impact proliferation (Jagannathan et al., 2016). In relation to this, six out of seven of the 14-3-3 proteins, which are known to regulate the cell cycle and promote cell survival by inhibiting apoptosis (Xing et al., 2000), were decreased in our *PARK2* KO neurons, which for 14-3-3ε was confirmed by Western blotting. 14-3-3 proteins can interact with both α-synuclein and parkin and their overexpression has neuroprotective effects in PD cell and animal models (Xing et al., 2000; Yacoubian et al., 2010). As earlier mentioned, 14-3-3ε is one out of two proteins consistently found decreased in proteomics studies of PD (Aroso et al., 2016). Interestingly, the

decrease in survival was not evident until the final stages of the differentiation where MAP2+ neurons were present, indicating perhaps an increased vulnerability of the post-mitotic neurons.

In conclusion, we have applied advanced mass spectrometry-based proteomics to obtain a comprehensive characterization of mitochondrial protein changes in response to *PARK2* KO in isogenic human iPSC-derived neurons with perturbed mitochondrial morphology. This resulted in the identification of dysfunctions in oxidative stress defense, glycolysis, and lactate–pyruvate metabolism as well as impaired cell survival, adding valuable new insight into the role of parkin dysfunction in PD pathogenesis.

AUTHOR CONTRIBUTIONS

HB, PJ, ML, and MM designed the research. HB, PJ, MR, SS, JO, MH, LR, CW, and CA performed the research. LR, LB, HW, and RW-M contributed new reagents or analytic tools. HB, PJ, MR, SS, JO, BR, MH, and CA analyzed the data. HB, LB, BR, and MM wrote the manuscript.

FUNDING

This work was supported by the Innovation Fund Denmark (BrainStem: www.brainstem.dk, 4108-00008A), the Lundbeck Foundation (R167-2013-15778), the Danish Parkinson Foundation, the Jascha Foundation (3687, 5611), IMK Almene Fond, the A. P. Møller Foundation for the Advancement of Medical Science (15-396, 14-427), Knud og Edith Eriksens Mindefond, Frimodt-Heineke Fonden, and Carl og Ellen Hertz Legat, and the Faculty of Health Sciences, University of Southern Denmark.

ACKNOWLEDGMENTS

The bioimaging experiments reported in this manuscript were performed at DaMBIC, a bioimaging research core facility, at the University of Southern Denmark. DaMBIC was established by an equipment grant from the Danish Agency for Science Technology and Innovation and by internal funding from the University of Southern Denmark. The authors would like to thank Dorte Lyholmer, Ulla Melchior Hansen, and Taewook Kang for technical assistance.

SUPPLEMENTARY MATERIAL

The Supplementary Material for this article can be found online at: https://www.frontiersin.org/articles/10.3389/fncel.2019.00297/full#supplementary-material

REFERENCES

Abou-Sleiman, P. M., Muqit, M. M. K., and Wood, N. W. (2006). Expanding insights of mitochondrial dysfunction in Parkinson's disease. *Nat. Rev. Neurosci.* 7, 207–219. doi: 10.1038/nrn1868

Alam, Z. I., Daniel, S. E., Lees, A. J., Marsden, D. C., Jenner, P., and Halliwell, B. (1997). A generalised increase in protein carbonyls in the brain in Parkinson's but not incidental Lewy body disease. *J. Neurochem.* 69, 1326–1329. doi: 10.1046/j.1471-4159.1997.69031326.x

Aroso, M., Ferreira, R., Freitas, A., Vitorino, R., and Gomez-Lazaro, M. (2016). New insights on the mitochondrial proteome plasticity in Parkinson's disease. *Proteomics Clin. Appl.* 10, 416–429. doi: 10.1002/prca.201500092

Bender, A., Krishnan, K. J., Morris, C. M., Taylor, G. A., Reeve, A. K., Perry, R. H., et al. (2006). High levels of mitochondrial DNA deletions in substantia nigra neurons in aging and Parkinson disease. *Nat. Genet.* 38, 515–517. doi: 10.1038/ng1769

Buhlman, L., Damiano, M., Bertolin, G., Ferrando-Miguel, R., Lombès, A., Brice, A., et al. (2014). Functional interplay between Parkin and Drp1 in mitochondrial fission and clearance. *Biochim. Biophys. Acta* 1843, 2012–2026. doi: 10.1016/j.bbamcr.2014.05.012

Carpenter, A. E., Jones, T. R., Lamprecht, M. R., Clarke, C., Kang, I. H., Friman, O., et al. (2006). CellProfiler: image analysis software for identifying and quantifying cell phenotypes. *Genome Biol.* 7:R100. doi: 10.1186/gb-2006-7-10-r100

Chung, S. Y., Kishinevsky, S., Mazzulli, J. R., Graziotto, J., Mrejeru, A., Mosharov, E. V., et al. (2016). Parkin and PINK1 patient iPSC-derived midbrain dopamine neurons exhibit mitochondrial dysfunction and α-synuclein accumulation. *Stem Cell Rep.* 7, 664–677. doi: 10.1016/j.stemcr.2016.08.012

Clark, I. E., Dodson, M. W., Jiang, C., Cao, J. H., Huh, J. R., Seol, J. H., et al. (2006). Drosophila pink1 is required for mitochondrial function and interacts genetically with parkin. *Nature* 441, 1162–1166. doi: 10.1038/nature04779

Dexter, D. T., Carter, C. J., Wells, F. R., Javoy-Agid, F., Agid, Y., Lees, A., et al. (1989). Basal lipid peroxidation in substantia nigra is increased in Parkinson's disease. *J. Neurochem.* 52, 381–389. doi: 10.1111/j.1471-4159.1989.tb09133.x

Engholm-Keller, K., Birck, P., Størling, J., Pociot, F., Mandrup-Poulsen, T., and Larsen, M. R. (2012). TiSH–a robust and sensitive global phosphoproteomics strategy employing a combination of TiO2, SIMAC, and HILIC. *J. Proteomics* 75, 5749–5761. doi: 10.1016/j.jprot.2012.08.007

Imaizumi, Y., Okada, Y., Akamatsu, W., Koike, M., Kuzumaki, N., Hayakawa, H., et al. (2012). Mitochondrial dysfunction associated with increased oxidative stress and α-synuclein accumulation in PARK2 iPSC-derived neurons and postmortem brain tissue. *Mol. Brain* 5:35. doi: 10.1186/1756-6606-5-35

Jagannathan, L., Cuddapah, S., and Costa, M. (2016). Oxidative stress under ambient and physiological oxygen tension in tissue culture. *Curr. Pharmacol. Rep.* 2, 64–72. doi: 10.1007/s40495-016-0050-5

Jiang, H., Ren, Y., Yuen, E. Y., Zhong, P., Ghaedi, M., Hu, Z., et al. (2012). Parkin controls dopamine utilization in human midbrain dopaminergic neurons derived from induced pluripotent stem cells. *Nat. Commun.* 3:668. doi: 10.1038/ncomms1669

Jin, J., Hulette, C., Wang, Y., Zhang, T., Pan, C., Wadhwa, R., et al. (2006). Proteomic identification of a stress protein, mortalin/mthsp70/GRP75: relevance to Parkinson disease. *Mol. Cell. Proteomics MCP* 5, 1193–1204. doi: 10.1074/mcp.M500382-MCP200

Jourdain, P., Allaman, I., Rothenfusser, K., Fiumelli, H., Marquet, P., and Magistretti, P. J. (2016). L-Lactate protects neurons against excitotoxicity: implication of an ATP-mediated signaling cascade. *Sci. Rep.* 6:21250. doi: 10.1038/srep21250

Kazlauskaite, A., Kondapalli, C., Gourlay, R., Campbell, D. G., Ritorto, M. S., Hofmann, K., et al. (2014). Parkin is activated by PINK1-dependent phosphorylation of ubiquitin at Ser65. *Biochem. J.* 460, 127–139. doi: 10.1042/BJ20140334

Kitada, T., Tong, Y., Gautier, C. A., and Shen, J. (2009). Absence of nigral degeneration in aged parkin/DJ-1/PINK1 triple knockout mice. *J. Neurochem.* 111, 696–702. doi: 10.1111/j.1471-4159.2009.06350.x

Kraytsberg, Y., Kudryavtseva, E., McKee, A. C., Geula, C., Kowall, N. W., and Khrapko, K. (2006). Mitochondrial DNA deletions are abundant and cause functional impairment in aged human substantia nigra neurons. *Nat. Genet.* 38, 518–520. doi: 10.1038/ng1778

Langston, J. W. (1996). The etiology of Parkinson's disease with emphasis on the MPTP story. *Neurology* 47, S153–S160.

Langston, J. W., Ballard, P., Tetrud, J. W., and Irwin, I. (1983). Chronic Parkinsonism in humans due to a product of meperidine-analog synthesis. *Science* 219, 979–980. doi: 10.1126/science.6823561

Liu, K., Li, F., Han, H., Chen, Y., Mao, Z., Luo, J., et al. (2016). Parkin regulates the activity of pyruvate kinase M2. *J. Biol. Chem.* 291, 10307–10317. doi: 10.1074/jbc.M115.703066

Lutz, A. K., Exner, N., Fett, M. E., Schlehe, J. S., Kloos, K., Lämmermann, K., et al. (2009). Loss of parkin or PINK1 function increases Drp1-dependent mitochondrial fragmentation. *J. Biol. Chem.* 284, 22938–22951. doi: 10.1074/jbc.M109.035774

MacVicar, T. D. B., and Lane, J. D. (2014). Impaired OMA1-dependent cleavage of OPA1 and reduced DRP1 fission activity combine to prevent mitophagy in cells that are dependent on oxidative phosphorylation. *J. Cell Sci.* 127, 2313–2325. doi: 10.1242/jcs.144337

Mishra, P., Carelli, V., Manfredi, G., and Chan, D. C. (2014). Proteolytic cleavage of Opa1 stimulates mitochondrial inner membrane fusion and couples fusion to oxidative phosphorylation. *Cell Metab.* 19, 630–641. doi: 10.1016/j.cmet.2014.03.011

Moore, D. J. (2006). Parkin: a multifaceted ubiquitin ligase. *Biochem. Soc. Trans.* 34, 749–753. doi: 10.1042/BST0340749

Narendra, D., Tanaka, A., Suen, D.-F., and Youle, R. J. (2008). Parkin is recruited selectively to impaired mitochondria and promotes their autophagy. *J. Cell Biol.* 183, 795–803. doi: 10.1083/jcb.200809125

Oliveras-Salvá, M., Van Rompuy, A.-S., Heeman, B., Van den Haute, C., and Baekelandt, V. (2011). Loss-of-function rodent models for parkin and PINK1. *J. Park. Dis.* 1, 229–251. doi: 10.3233/JPD-2011-11041

Ozgul, S., Kasap, M., Akpinar, G., Kanli, A., Güzel, N., Karaosmanoglu, K., et al. (2015). Linking a compound-heterozygous Parkin mutant (Q311R and A371T) to Parkinson's disease by using proteomic and molecular approaches. *Neurochem. Int.* 85–86, 1–13. doi: 10.1016/j.neuint.2015.03.007

Pacelli, C., De Rasmo, D., Signorile, A., Grattagliano, I., di Tullio, G., D'Orazio, A., et al. (2011). Mitochondrial defect and PGC-1α dysfunction in parkin-associated familial Parkinson's disease. *Biochim. Biophys. Acta* 1812, 1041–1053. doi: 10.1016/j.bbadis.2010.12.022

Palacino, J. J., Sagi, D., Goldberg, M. S., Krauss, S., Motz, C., Wacker, M., et al. (2004). Mitochondrial dysfunction and oxidative damage in parkin-deficient mice. *J. Biol. Chem.* 279, 18614–18622. doi: 10.1074/jbc.M401135200

Parker, W. D., Boyson, S. J., and Parks, J. K. (1989). Abnormalities of the electron transport chain in idiopathic Parkinson's disease. *Ann. Neurol.* 26, 719–723. doi: 10.1002/ana.410260606

Periquet, M., Corti, O., Jacquier, S., and Brice, A. (2005). Proteomic analysis of parkin knockout mice: alterations in energy metabolism, protein handling and synaptic function. *J. Neurochem.* 95, 1259–1276. doi: 10.1111/j.1471-4159.2005.03442.x

Pinto, M., Nissanka, N., and Moraes, C. T. (2018). Lack of parkin anticipates the phenotype and affects mitochondrial morphology and mtDNA levels in a mouse model of parkinson's disease. *J. Neurosci.* 38, 1042–1053. doi: 10.1523/JNEUROSCI.1384-17.2017

Poole, A. C., Thomas, R. E., Andrews, L. A., McBride, H. M., Whitworth, A. J., and Pallanck, L. J. (2008). The PINK1/Parkin pathway regulates mitochondrial morphology. *Proc. Natl. Acad. Sci. U.S.A.* 105, 1638–1643. doi: 10.1073/pnas.0709336105

Quistorff, B., and Grunnet, N. (2011). High brain lactate is not caused by a shift in the lactate dehydrogenase A/B ratio. *Proc. Natl. Acad. Sci. U.S.A.* 108:E21. doi: 10.1073/pnas.1017750108

Ross, J. M., Öberg, J., Brené, S., Coppotelli, G., Terzioglu, M., Pernold, K., et al. (2010). High brain lactate is a hallmark of aging and caused by a shift in the lactate dehydrogenase A/B ratio. *Proc. Natl. Acad. Sci. U.S.A.* 107, 20087–20092. doi: 10.1073/pnas.1008189107

Ryan, B. J., Hoek, S., Fon, E. A., and Wade-Martins, R. (2015). Mitochondrial dysfunction and mitophagy in Parkinson's: from familial to sporadic disease. *Trends Biochem. Sci.* 40, 200–210. doi: 10.1016/j.tibs.2015.02.003

Schapira, A. H., Cooper, J. M., Dexter, D., Clark, J. B., Jenner, P., and Marsden, C. D. (1990). Mitochondrial complex I deficiency in Parkinson's disease. *J. Neurochem.* 54, 823–827. doi: 10.1016/j.ymgme.2011.11.193

Schneider, C. A., Rasband, W. S., and Eliceiri, K. W. (2012). NIH Image to ImageJ: 25 years of image analysis. *Nat. Methods* 9, 671–675. doi: 10.1038/nmeth.2089

Schwämmle, V., León, I. R., and Jensen, O. N. (2013). Assessment and improvement of statistical tools for comparative proteomics analysis of sparse data sets with few experimental replicates. *J. Proteome Res.* 12, 3874–3883. doi: 10.1021/pr400045u

Shaltouki, A., Sivapatham, R., Pei, Y., Gerencser, A. A., Momčilović, O., Rao, M. S., et al. (2015). Mitochondrial alterations by PARKIN in dopaminergic neurons using PARK2 patient-specific and PARK2 knockout isogenic iPSC lines. *Stem Cell Rep.* 4, 847–859. doi: 10.1016/j.stemcr.2015.02.019

Storey, J. D. (2002). A direct approach to false discovery rates. *J. R. Stat. Soc. Ser. B Stat. Methodol.* 64, 479–498. doi: 10.1111/1467-9868.00346

Swistowski, A., Peng, J., Han, Y., Swistowska, A. M., Rao, M. S., and Zeng, X. (2009). Xeno-free defined conditions for culture of human embryonic stem cells, neural stem cells and dopaminergic neurons derived from them. *PLoS One* 4:e6233. doi: 10.1371/journal.pone.0006233

Triplett, J. C., Zhang, Z., Sultana, R., Cai, J., Klein, J. B., Büeler, H., et al. (2015). Quantitative expression proteomics and phosphoproteomics profile of brain from PINK1 knockout mice: insights into mechanisms of familial Parkinson's disease. *J. Neurochem.* 133, 750–765. doi: 10.1111/jnc.13039

Villeneuve, L. M., Purnell, P. R., Boska, M. D., and Fox, H. S. (2016). Early expression of parkinson's disease-related mitochondrial abnormalities in PINK1 knockout rats. *Mol. Neurobiol.* 53, 171–186. doi: 10.1007/s12035-014-8927-y

Vizcaíno, J. A., Csordas, A., del-Toro, N., Dianes, J. A., Griss, J., Lavidas, I., et al. (2016). 2016 update of the PRIDE database and its related tools. *Nucleic Acids Res.* 44, D447–D456. doi: 10.1093/nar/gkv1145

Wyss, M. T., Jolivet, R., Buck, A., Magistretti, P. J., and Weber, B. (2011). *In Vivo* evidence for lactate as a neuronal energy source. *J. Neurosci.* 31, 7477–7485. doi: 10.1523/JNEUROSCI.0415-11.2011

Xing, H., Zhang, S., Weinheimer, C., Kovacs, A., and Muslin, A. J. (2000). 14-3-3 proteins block apoptosis and differentially regulate MAPK cascades. *EMBO J.* 19, 349–358. doi: 10.1093/emboj/19.3.349

Yacoubian, T. A., Slone, S. R., Harrington, A. J., Hamamichi, S., Schieltz, J. M., Caldwell, K. A., et al. (2010). Differential neuroprotective effects of 14-3-3 proteins in models of Parkinson's disease. *Cell Death Dis.* 1:e2. doi: 10.1038/cddis.2009.4

Zanellati, M. C., Monti, V., Barzaghi, C., Reale, C., Nardocci, N., Albanese, A., et al. (2015). Mitochondrial dysfunction in Parkinson disease: evidence in mutant PARK2 fibroblasts. *Front. Genet.* 6:78. doi: 10.3389/fgene.2015.00078

Zhao, J., Liu, T., Jin, S., Wang, X., Qu, M., Uhlén, P., et al. (2011). Human MIEF1 recruits Drp1 to mitochondrial outer membranes and promotes mitochondrial fusion rather than fission. *EMBO J.* 30, 2762–2778. doi: 10.1038/emboj.2011.198

Conflict of Interest Statement: The authors declare that the research was conducted in the absence of any commercial or financial relationships that could be construed as a potential conflict of interest.

Copyright © 2019 Bogetofte, Jensen, Ryding, Schmidt, Okarmus, Ritter, Worm, Hohnholt, Azevedo, Roybon, Bak, Waagepetersen, Ryan, Wade-Martins, Larsen and Meyer. This is an open-access article distributed under the terms of the Creative Commons Attribution License (CC BY). The use, distribution or reproduction in other forums is permitted, provided the original author(s) and the copyright owner(s) are credited and that the original publication in this journal is cited, in accordance with accepted academic practice. No use, distribution or reproduction is permitted which does not comply with these terms.

frontiers in Cellular Neuroscience

ORIGINAL RESEARCH
published: 10 July 2019
doi: 10.3389/fncel.2019.00316

Mitochondria Are Dynamically Transferring Between Human Neural Cells and Alexander Disease-Associated GFAP Mutations Impair the Astrocytic Transfer

*Longfei Gao[1], Zhen Zhang[1], Jing Lu[1] and Gang Pei[1,2,3]**

[1] State Key Laboratory of Cell Biology, CAS Center for Excellence in Molecular Cell Science, Shanghai Institute of Biochemistry and Cell Biology, Chinese Academy of Sciences, University of Chinese Academy of Sciences, Shanghai, China, [2] Shanghai Key Laboratory of Signaling and Disease Research, Collaborative Innovation Center for Brain Science, School of Life Sciences and Technology, Tongji University, Shanghai, China, [3] Institute for Stem Cell and Regeneration, Chinese Academy of Sciences, Beijing, China

Mitochondria are the critical organelles for energy metabolism and cell survival in eukaryotic cells. Recent studies demonstrated that mitochondria can intercellularly transfer between mammalian cells. In neural cells, astrocytes transfer mitochondria into neurons in a CD38-dependent manner. Here, using co-culture system of neural cell lines, primary neural cells, and human pluripotent stem cell (hPSC)-derived neural cells, we further revealed that mitochondria dynamically transferred between astrocytes and also from neuronal cells into astrocytes, to which CD38/cyclic ADP-ribose signaling and mitochondrial Rho GTPases (MIRO1 and MIRO2) contributed. The transfer consequently elevated mitochondrial membrane potential in the recipient cells. By introducing Alexander disease (AxD)-associated hotspot mutations (R79C, R239C) into GFAP gene of hPSCs and subsequently inducing astrocyte differentiation, we found that GFAP mutations impaired mitochondrial transfer from astrocytes and reduced astrocytic CD38 expression. Thus, our study suggested that mitochondria dynamically transferred between neural cells and revealed that AxD-associated mutations in GFAP gene disrupted the astrocytic transfer, providing a potential pathogenic mechanism in AxD.

Keywords: mitochondria, transfer, astrocytes, neuronal cells, GFAP mutation, Alexander disease

OPEN ACCESS

Edited by:
Lang Wang,
Zhejiang University, China

Reviewed by:
Albee Messing,
University of Wisconsin–Madison, United States
Yu-Feng Wang,
Harbin Medical University, China

****Correspondence:***
Gang Pei
gpei@sibs.ac.cn

Specialty section:
This article was submitted to Cellular Neurophysiology, a section of the journal Frontiers in Cellular Neuroscience

Received: *04 May 2019*
Accepted: *27 June 2019*
Published: *10 July 2019*

Citation:
Gao L, Zhang Z, Lu J and Pei G (2019) Mitochondria Are Dynamically Transferring Between Human Neural Cells and Alexander Disease-Associated GFAP Mutations Impair the Astrocytic Transfer. Front. Cell. Neurosci. 13:316. doi: 10.3389/fncel.2019.00316

INTRODUCTION

Mitochondria are critical organelles in eukaryotic cells. They are not only the major providers of cellular ATP and some macromolecules, but also important participants in calcium signaling, apoptosis, and other signaling pathways. Mitochondria were previously considered to be inherited from maternal lineage. However, this concept is challenged by increasing amounts of studies revealing that mitochondria can intercellularly transfer between mammalian cells, such as from stromal cells to damaged cells and from host cells to tumor cells (Islam et al., 2012; Tan et al., 2015). The functional consequences of the transfer range from promoting survival and recovery of

damaged cells to enhancing metastasis and chemoresistance of tumor cells (Griessinger et al., 2017; Torralba et al., 2016). In the brain, one of the organs with high requirements of mitochondria-derived energy, mitochondria can transfer from astrocytes into neurons and contribute to the neuroprotection and neurorecovery after stroke (Hayakawa et al., 2016). Here, using *in vitro* co-culture system of astrocytes and neurons, the two most abundant brain cells, we further revealed intercellular mitochondrial transfer between astrocytes and from neuronal cells into astrocytes, suggesting that intercellular mitochondrial transfer might prevalently occur between neural cells.

Alexander disease (AxD) is a rare but fatal neurological disorder. It is mainly caused by the mutation of astrocyte specific intermediate filament GFAP (Olabarria and Goldman, 2017). However, how GFAP mutation leads to astrocyte disorder and AxD pathology has not been clearly elucidated. Recent study reveals that the distribution and function of endoplasmic reticulum and lysosome are disrupted in astrocytes with GFAP mutations (Jones et al., 2018). Several reports indicate that mitochondrial function may also be compromised in AxD (Caceres-Marzal et al., 2006; Nobuhara et al., 2004), though it has not been strictly examined with isogenic cell pairs. In this study, we introduced AxD-associated hotspot mutations into GFAP gene of human pluripotent stem cells (hPSCs) and subsequently induced astrocyte differentiation to generate astrocytes with GFAP mutations as previously reported (Canals et al., 2018). By comparing the mitochondrial transfer capacity between wildtype (WT) and GFAP-mutated astrocytes, we found that GFAP mutations impaired intercellular mitochondrial transfer from astrocytes, providing a perspective to dissect a potential pathogenic mechanism of the complicated neurological disorders.

MATERIALS AND METHODS

Cell Culture

Human astrocyte cell line (HA) was purchased from ScienCell (#1800) and maintained in DMEM medium with 10% FBS. Human neuronal cell line SK-N-SH (SK) was purchased from ATCC and cultured in MEM medium with 10% FBS. H1 ESC was kindly provided by Dr. Duanqing Pei and cultured with mTeSR^{TM}1 (StemCell, #85850) and Matrigel Matrix (Corning, #354277) following manufacturer's instructions. The use of animals was approved by the Institutional Animal Care and Use Committee (IACUC) of Shanghai Institute of Biochemistry and Cell Biology, Chinese Academy of Sciences. C57BL/6 mouse of postnatal day 1 and both gender were used and purchased from Shanghai SLAC Laboratory Animal Co., Ltd. (Shanghai, China). Primary mouse astrocytes and neurons were isolated as previously described (Cheng et al., 2015). Astrocytes were maintained in DMEM/F12 medium supplemented with 2% B27 and 10% FBS and neurons were maintained in Neurobasal medium supplemented with 2% B27 and 1% glutamax. The medium was changed every 2 days. Brightfield images were captured with Zeiss Observer. Z1 microscope. Time lapse images were captured with Olympus FV10i microscope. Cells for time lapse live imaging were plated into Matrigel-pretreated Lab-Tek II Chambered Coverglass (Thermo Fisher Scientific, #155409PK). Images were captured at a 5 min interval after the cells were attached. The chamber of the microscope was maintained at 37℃ and constantly bubbled with 5% CO_2 / 20% O_2 / 75% N_2 mixture. For cADPR and CD38 inhibitors treatment, the chemicals were added 1 h after the co-cultured cells attached. The following final concentration were used: 2 mM cADPR (Sigma, #C7344), 30 μM quercetin (Selleck, #S2391), and 30 μM apigenin (Selleck, #2262). Cell cultures were routinely tested by PCR and confirmed to be free of mycoplasma contamination.

Plasmids Construction and shRNA Sequences

The GFP-expressing lentiviral vector FuGW and NGN2 vector were used in previously studies (Gao et al., 2017). pLV-mitodsred vector was purchased from Addgene (#44386). SOX9 and NFIB vector were constructed by replacing the GFP with SOX9 cDNA (purchased from Sino Biological Inc.) and NFIB cDNA (kindly provided by Dr. Jiahuai Han) in FuGW vector. mitoBFP vector was constructed by (1) replacing dsred sequence with BFP sequence, which was derived from pCAG mito-mTagBFP2 plasmid (Addgene, #105011), in pLV-mitodsred plasmid; (2) replacing GFP with mitoBFP in FuGW. hGFAP::GFP vector was constructed by replacing the hUbC promoter in FuGW with human GFAP promoter (Cheng et al., 2015; Guo et al., 2014). hSYN1::mitoBFP vector was constructed by replacing the hUbC promoter in mitoBFP with human SYN1 promoter (kindly provided by Dr. Jiawei Zhou) (Zhu et al., 2015). CD38 overexpression vector was constructed by replacing GFP sequence in FuGW with CD38 cDNA (purchased from Kelei biological Technology, Shanghai). shRNA targeting CD38, MIRO1, or MIRO2 was inserted into pLKO.1 puro vector (Addgene, #8453) following the provider's instructions. The shRNA sense sequences were as follows:

scramble, AGATCATGCGCTCTTAGTGCT;
shCD38-1, CCAAAGTGTATGGGATGCTTT;
shCD38-2, CCAGAGAAGGTTCAGACACTA;
shMIRO1-1, GTGGACGCTCACGACTTATTT;
shMIRO1-2, ATGATCCTTTGGGTTCTATAA;
shMIRO2-1, CGTCTACAAGCACCATTACAT;
shMIRO2-2, GCGTCTACAAGCACCATTACA.

Lentivirus Preparation and Infection

Lentivirus was produced with HEK 293T cells as previously described (Gao et al., 2017). Briefly, the day before transfection, 8 million cells were seeded into a 10 cm dish in DMEM (with 10% FBS) medium. On the next day, lentiviral vectors was co-transfected into 293T cells with Vsv-g and Pax2 plasmids using calcium phosphate transfection. Medium was refreshed 6 h after transfection. The supernatant was collected and filtered with a 0.45 μm filter at 48 and 72 h after transfection. Lentivirus was concentrated with Lenti-concentin virus precipitation solution (Excellbio) following the manufacturer's instructions. For the

infection of H1 ESC, cells were dissociated into single cells with accutase and replated onto Matrigel pretreated plates with 2 μM Thiazovivin (MedChemExpress, #HY-13257). On the next day, concentrated lentivirus was diluted with fresh mTeSR medium and added to the cells. 4 μg/ml polybrene was also added to improve the infection efficiency. After incubated in the incubator for 1 h, the cells were washed with fresh DMEM/F12 medium for three times and maintained with fresh mTeSR medium. For infection of other cells in this study, concentrated lentivirus diluted in fresh medium containing 8 μg/ml polybrene was added. After incubated in the incubator for 6 h, the cells were washed with fresh DMEM/F12 medium for three times and maintained with fresh medium.

Astrocyte and Neuron Differentiation From H1 ESCs

Astrocyte differentiation was induced as previously described (Canals et al., 2018). Briefly, H1 ESC were dissociated into single cells with Accutase (Gibco, #A1110501) and seeded into 6-well plates at a density of 1×10^5 cells per well in mTeSR containing 2 μM Thiazovivin. The next day (day 0), cells were infected with lentivirus expressing NFIB and SOX9. On days 1 and 2, the medium was changed into expansion medium (DMEM/F12, 10% FBS, 1% N2 supplement, and 1% glutamax). Day 3, the medium was changed into 75% expansion medium and 25% FGF medium (Neurobasal, 2% B27 supplement, 1% non-essential amino acid, 1% glutamax, 10% FBS, 5 ng/ml CNTF, 10 ng/ml FGF, 10 ng/ml BMP4). Day 4, cells were maintained in 50% expansion medium and 50% FGF medium. Day 5, medium was changed into 75% expansion medium and 25% FGF medium. Day 6, cells were maintained in FGF medium. Cells were dissociated and replated on day 7 and maintained in FGF medium. From day 10, cells were maintained with maturation medium (DMEM/F12:Neurobasal = 1:1, 1% N2, 1% sodium pyruvate, 1% glutamax, 5 μg/ml N-acetyl-cysteine, 10 ng/ml CNTF, 10 ng/ml BMP4, 5 ng/ml heparin-binding EGF-like growth factor, 500 μg/ml dbcAMP) and cluture medium was half changed every 2 days. Astrocytes differentiated more than 1 week, when most cells were double positive for GFAP and S100B, were used for experiments.

Neuron differentiation was also performed as previously described (Zhang et al., 2013). Briefly, H1 ESC was seeded into 6-well plates at a density of 2×10^5 cells per well in mTeSR containing 2 μM Thiazovivin. On the next (day 0), lentivirus expressing NGN2 was added to infect cells. On days 1 and 2, culture medium was changed into DMEM/F12 medium containing 1% N2, 1% non-essential amino acid, 10 ng/ml BDNF, 10 ng/ml GDNF, 10 ng/ml IGF, and 0.2 μg/ml laminin. On day 3, the medium was further changed into Neurobasal medium supplemented with 2% B27, 1% glutamax, 10 ng/ml BDNF, 10 ng/ml GDNF, 10 ng/ml IGF, and 0.2 μg/ml laminin. From day 4, the medium was half-changed every 2 days. Neurons differentiated for more than 7 days, when most cells exhibited a neuronal morphology and were positive for neuronal markers, were used for experiments.

Immunofluorescence Staining

Immunostaining was performed as previously described (Gao et al., 2017). Briefly, cells for immunostaining were seeded onto Matrigel pretreated coverslips. After aspiration of medium, cells were fixed with 4% PFA for 15 min at room temperature. Then cells were treated with permeabilization and blocking buffer (1% BSA and 0.5% Triton-X 100 in PBS) for 1 h at room temperature. Primary antibodies were incubated overnight at 4℃. The next day, fluorescent-dye conjugated secondary antibodies were incubated for 1 h at room temperature. Slides were mounted and images were captured with Leica SP8 microscope. The following antibodies were used in this study: TOM20 (Santa Cruz, #sc-17764), ATP5A1 (Abclonal, #5884), LAMP1 (Abcam, #24170), OCT4 (Santa Cruz, #sc-9081), NANOG (Santa Cruz, #sc-33760), SOX2 (Santa Cruz, #sc-17320), S100B (Sigma, #S2532), GFAP (Dako, #Z033401; Thermo Fisher, #13-0300), CRYAB (Santa Cruz, #sc-137143), TUJ1 (Biolegend, #801202), DCX (Santa Cruz, #sc-8066), MAP2 (Millipore, #AB5622), NEUN (Millipore, #ABN78), and SYN1 (Millipore, #Ab1543).

Flow Cytometry, Fluorescence Activated Cell Sorting, and TMRE Staining

Cells for flow cytometry analysis were dissociated into single cells by TrypLE (Thermo Fisher Scientific, #12604021) and resuspended with cold PBS buffer. BD LSRII or Beckman CytoFlex LX was used for flow cytometry analysis. Flowjo or CytExpert software were used for data analysis. Fluorescence activated cell sorting (FACS) was performed with BD Influx. For separation of GFP^+dsred^+ and GFP^+dsred^- cells in **Supplementary Figure S4**, HA-GFP and HA-mitodsred cells were co-cultured for 48 h before FACS.

For TMRE staining, cells were washed with 0.2% FBS-containing DMEM/F12 for twice. Then cells were incubated with 500 nM TMRE (Thermo Fisher Scientific, #T669), which was diluted in 0.2% FBS-containing DMEM/F12, in the incubator for 30 min. After the incubation, cells were washed with 0.2% FBS-containing DMEM/F12 for twice and then dissociated into single cells with TrypLE. Beckman CytoFlex LX and CytExpert software were used to read and analysis TMRE intensity.

Quantification of RNA and Mitochondrial DNA

RNA extraction and reverse transcription were performed with Trizol reagent (Sigma) and PrimeScript^{TM}RT Master Mix (Takara, #RR036A) following manufacturer's instructions. Quantitative real-time PCR was performed with HotStart SYBR Green qPCR Master Mix (Excell, #MB000-3013) and MX3000P Stratagene PCR machine. The gene expression levels were normalized to the internal control (HPRT). Total DNA was extracted from indicated cells with DNA extraction kit (Tiangen, #DP304). Quantitative PCR was performed as above-mentioned with specific primers. Mitochondrial copy number was calculated as the ratio of mitochondrial DNA to nuclear DNA. The following primers were used:

MIRO1-Forward, AAGGTAACAAGTCGATGGATTCC;
MIRO1-Reverse, TCAGGTTTTTCGCTGAACACT;
MIRO2-Forward, CCACAAGGCAAACGTGGTG;
MIRO2-Reverse, AGGTCTCAATCTCGGGAAACT;
CD38-Forward, AGACTGCCAAAGTGTATGGGA;
CD38-Reverse, GCAAGGTACGGTCTGAGTTCC;
COX1-Forward, CTTCGTCTGATCCGTCCTAATC;
COX1-Reverse, TTGAGGTTGCGGTCTGTTAG;
CYTB-Forward, AGACAGTCCCACCCTCACAC;
CYTB-Reverse, AAGAGAAGTAAGCCGAGGGC;
PGC1a-Forward, CCTGTGGATGAAGACGGATT;
PGC1a-Reverse, TAGCTGAGTGTTGGCTGGTG;
PPARa-Forward, GCTTTGGCTTTACGGAATA;
PPARa-Reverse, TCCCGACAGAAAGGCACT;
TFAM-Forward, GATGCTTATAGGGCGGAG;
TFAM-Reverse, GCTGAACGAGGTCTTTTTGG;
NRF1-Forward, GATCGTCTTGTCTGGGGAAA;
NRF1-Reverse, GGTGACTGCGCTGTCTGATA;
NRF2a-Forward, TAGACCTCACCACACTCAAC;
NRF2a-Reverse, GTGACCAAACGGTTCAACTC;
HPRT-Forward, CCTGGCGTCGTGATTAGTGAT;
HPRT-Reverse, AGACGTTCAGTCCTGTCCATAA;
Human mtDNA-F, CCTTCTTACGAGCCAAAA;
Human mtDNA-R, CTGGTTGAACATTGTTTG (Sokolova et al., 2004);
Human nDNA-F, GAGTGGGAATCAGAGCTTCACGGGT;
Human nDNA-R, CCACGTCATTTACAGCATTTCAATG (Hobbs et al., 1992).

Western Blot

Western blot was performed as previously described (Hu et al., 2015). Cells were washed with cold PBS and lysed with RIPA lysis buffer (Beyotime). Protein concentration was measured with Pierce^{TM} BCA Protein Assay Kit (Thermo Fisher Scientific, #23227) and adjusted with Laemmli's sample buffer. Proteins were denatured at 95℃ for 5 min. Cell samples were separated on SDS-PAGE and transferred onto nitrocellulose membrane. Primary antibodies include rabbit anti-MIRO1 (1: 500, Abclonal, #A5838), rabbit anti-MIRO2 (1:300, Cell Signaling Technology, #14016), rabbit anti-CD38 (1:500, Abclonal, #A13611), and rabbit anti-actin (1:1000, sigma, #A2066). HRP-conjugated secondary antibody and Clarity^{TM} Western ECL Substrate were used to detect the membrane with MiniChemi^{TM} Chemiluminescence imager (Sagecreation).

CRISPR/Cas9 Gene Editing

H1 ESCs were dissociated into single cells with accutase and re-plated onto Matrigel pretreated 6-well plate with 2 μM Thiazovivin. On the next day, 1 μg px330-mcherry (Addgene, #98750, kindly provided by Dr. Jinsong Li) inserted with sgRNA and 2.5 μg donor vector (T vectors with mutations and recombination homologous arms) were transfected into each well with 8 μl FuGene (Promega, #2311) following the manufacturer's instructions. 24 h after transfection, mcherry-positive H1 cells were purified by FSCS (BD Influx) and plated onto Matrigel pretreated 10-cm plate with 2 μM Thiazovivin. Single colony was picked about 10 days after sorting. The mutations were validated with PCR and sequencing. The following oligonucleotides were used:

R79C-sgRNA1, TCTCGATGTAGCTGGCAAAG;
R79C-sgRNA2, CATCGAGAAGGTTCGCTTCC;
R79C-sgRNA3, GCGAACCTTCTCGATGTAGC;
R79C-Forward, CTCAGCCCTTTCCTTCCTTT;
R79C-Reverse, CGCTTCCAACTCCTCCTTTAT;
R79C_Mutation-Forward, ATGACTGCTTTGCCAGC;
R79C_Mutation-Reverse, GCTGGCAAAGCAGTCAT;
R239C-sgRNA1, ACTGCGTGCGGATCTCTTTC (Canals et al., 2018);
R239C-sgRNA2, ACATGCATGAAGCCGAAGAG (Canals et al., 2018);
R239C-sgRNA3, CTGCGTGCGGATCTCTTTCA;
R239C-Forward, CTTAATCCTCCTGCTGCTCTAC;
R239C-Reverse, GTTCTCTACGGGCACTATGTT;
R239C_Mutation-Forward, AGATCTGCACGCAGTATG;
R239C_Mutation-Reverse, CATACTGCGTGCAGATCT.

Statistical Analysis

All quantified data were presented as mean ± SEM and statistically analyzed. Two-tailed student *t* test was used to calculate the statistical significance with *p* values between two groups. One-way ANOVA followed Dunnett's multiple comparison test was applied to calculate the statistical significance with *p* values among three or more groups. The statistical values and used methods were specified in the figure legends. A *p* value less than 0.05 was considered as significant different. *, $p < 0.05$; **, $p < 0.01$; ***, $p < 0.001$.

RESULTS

Intercellular Mitochondrial Transfer Between Astrocytes

To label mitochondria, we infected human astrocyte (HA) cell line with lentivirus expressing mitochondria-localized dsred (mitodsred) (**Figure 1A**), which specifically labeled mitochondria as shown by co-staining of MitoTracker and TOM20, a mitochondrial marker (**Supplementary Figures S1A,B**). Then the mitodsred-labeled HA (HA-mitodsred) were co-cultured with another group of HA, which were labeled with GFP, at a ratio of 1:1 (**Figure 1A**). Within 24 h, mitochondria from HA-mitodsred were dynamically transferred into GFP-labeled HA (HA-GFP) as showed by time lapse live imaging and confocal images (**Figures 1B,C**). The transferred mitochondria were inside of HA-GFP, but not merely associated with the surface of HA-GFP, as showed by confocal z-stack images (**Figure 1C**). Moreover, transferred mitochondria were positive for TOM20 and ATP5A1, another mitochondrial marker (**Figures 1D,E**). The mitochondrial transfer efficiency (percentage of GFP^+dsred^+ cells in the co-culture system) was about 5% after co-cultured for 24 h (**Figure 1F**). These data suggested that intercellular mitochondrial transfer occurred between HA.

To further explore whether mitochondria transferred between other types of astrocytes, we differentiated H1

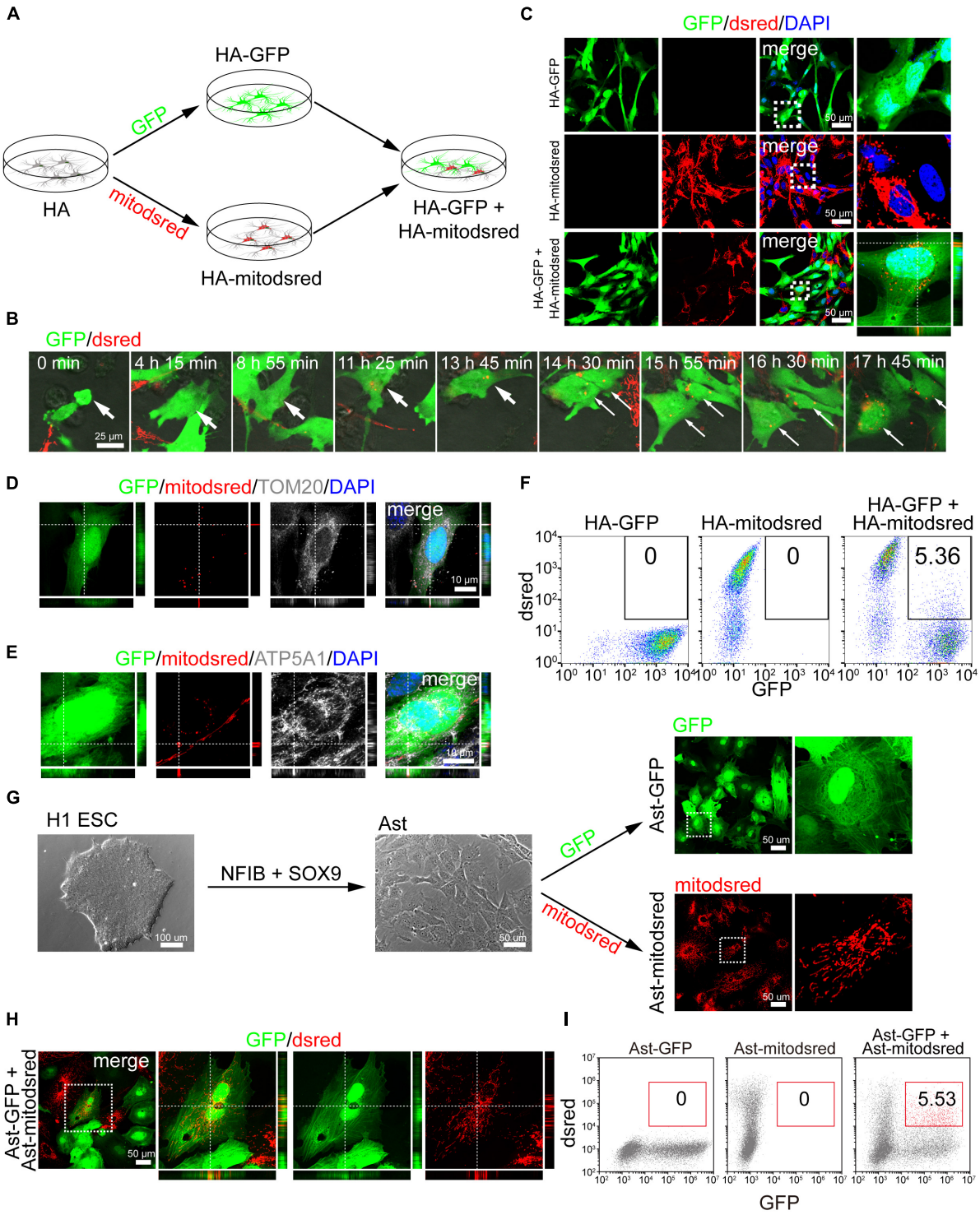


FIGURE 1 | Intercellular mitochondrial transfer between astrocytes. **(A)** Schematic showing that human astrocytes (HA) were labeled with GFP or mitodsred and then co-cultured at a ratio of 1:1. **(B)** Time-lapse live images showing mitochondria from HA-mitodsred dynamically transferring into HA-GFP. **(C)** Confocal images showing dsred-labeled mitochondria in HA-GFP after co-cultured for 24 h. **(D,E)** Immunostaining of TOM20 **(D)** and ATP5A1 **(E)** on transferred mitochondria in HA after co-cultured for 24 h. **(F)** Flow cytometry analyzing mitochondrial transfer efficiency between HA after co-cultured for 24 h. **(G)** Astrocytes (Ast) were derived from H1 ESCs with NFIB and SOX9 and then labeled with GFP or mitodsred lentivirus. **(H)** Confocal images showing that mitochondria from Ast-mitodsred were observed in Ast-GFP after co-cultured for 24 h. **(I)** Flow cytometry analyzing mitochondrial transfer efficiency between Ast after co-cultured for 24 h.

ESCs, which were confirmed to be positive for pluripotency markers OCT4, NANOG, and SOX2 by immunostaining (**Supplementary Figures S1C–E**), into astrocytes with NFIB and SOX9 as previously described (Canals et al., 2018). The percentage of $GFAP^+S100B^+$ cells in differentiated astrocytes (Ast) were about 80% (**Supplementary Figures S1F,G**, **5C**). GFP or mitodsred virus was used to label Ast as mentioned above (**Figure 1G**) and then the differentially labeled cells were co-cultured at a ratio of 1:1. Mitochondria from Ast-mitodsred were detected in Ast-GFP and the transfer efficiency was about 5% after co-cultured for 24 h (**Figures 1H,I**).

We also isolated primary astrocytes from the cortex of postnatal mouse (**Supplementary Figure S1H**) and confirmed that nearly all the cells were positive for astrocyte marker S100B (**Supplementary Figure S1I**). Then we labeled mouse astrocytes (mAst) with mitodsred or GFP and co-cultured the distinctly labeled mAst as above-mentioned (**Supplementary Figure S1H**). Mitochondria from mAst-mitodsred were detected in mAst-GFP after co-cultured for 24 h (**Supplementary Figures S1J,K**). When HAs and mouse astrocytes were co-cultured at 1:1, mitochondrial transfer from mouse astrocytes into HAs (**Supplementary Figure S1L**) and from HAs into mouse astrocytes (**Supplementary Figure S1M**) were also observed after co-cultured for 24 h. Collectively, these data demonstrated that mitochondria were dynamically transferring between astrocytes.

Mitochondrial Transfer From Neuronal Cells Into Astrocytes

HA-GFP were co-cultured with mitodsred-labeled human neuronal cell line SK (SK-mitodsred) at a ratio of 1:1 (**Figure 2A**). Within 24 h of co-culture, dsred-labeled mitochondria were transferring into HA-GFP (**Figure 2B**) and confirmed to be inside of HA-GFP by confocal z-stack images (**Figure 2C**). Transferred mitochondria were positive for TOM20 and ATP5A1 (**Figures 2D,E**), but negative for lysosomal marker LAMP1 (**Figure 2F**), which suggested that unlike previous report (Davis et al., 2014), the transferred mitochondria here might not be degraded. Flow cytometry showed that about 5% cells were double positive for GFP and dsred in the co-culture system (**Figure 2G**).

Besides aforementioned Ast, we also generated neuronal cells from H1 ESCs by NGN2 (Zhang et al., 2013; **Figure 2H**). Immunostaining performed on day 7 cells showed that differentiated neurons (hN) were positive for TUJ1, MAP2, NEUN, and SYN1 (**Supplementary Figures S2A–D**). hSYN1::mitoBFP lentivirus was used to label mitochondria in hN and hGFAP::GFP to label Ast (**Figure 2H**). Immunostaining showed that BFP-labeled neurons (hN-mitoBFP) were positive for TUJ1, MAP2, and NEUN (**Supplementary Figures S2E,F**) and GFP-labeled astrocytes (Ast-GFP) were positive for GFAP and S100B (**Supplementary Figure S2G**). Then Ast-GFP were dissociated and re-plated onto hN-mitoBFP at a ratio of approximately 1:1. After co-cultured for 48 h, BFP^+ mitochondria were observed inside of the Ast-GFP (**Figure 2I**). The transfer efficiency was about 1%, lower than that on cell lines (**Figure 2J**).

We also isolated primary neurons (mNeuron) from the cortex of postnatal mouse (**Supplementary Figure S2H**). Judging from cell morphology and TUJ1 staining, the purity of mNeuron was above 90% (**Supplementary Figure S2I**). Then we used GFP or mitodsred to label above-mentioned mAst or mitochondria in mNeuron, respectively (**Supplementary Figure S2H**). When dissociated mAst-GFP were re-plated onto mNeuron-mitodsred, mitochondrial transfer from mNeuron into mAst was detected after 48 h of co-culture (**Supplementary Figure S2J**). Taken together, our data suggested that neuronal mitochondria were also dynamically transferring into astrocytes.

Contribution of CD38/Cyclic ADP-Ribose (cADPR) Signaling and Mitochondrial Rho GTPases to the Transfer

Previous study demonstrates that transfer of mitochondria from astrocytes into neurons and from bone marrow stromal cells into multiple myeloma cells is mediated by CD38, a transmembrane glycoprotein catalyzing the production of cADPR (Hayakawa et al., 2016; Marlein et al., 2019). To explore whether CD38/cADPR signaling involved here, we treated co-cultured HA-GFP and HA-mitodsred with cADPR or CD38 inhibitor (quercetin or apigenin) (Escande et al., 2013; Kellenberger et al., 2011; **Figure 3A**). The treatment of cADPR, quercetin, or apigenin for 24 h did not reduce cell viability as indicated by cellular ATP levels (**Figure 3B**). However, mitochondrial transfer efficiency was significantly inhibited by quercetin or apigenin (**Figure 3C** and **Supplementary Figure S3A**). Similarly, we also found that quercetin and apigenin significantly inhibited mitochondrial transfer from SK into HA without affecting cell viability (**Figures 3D–F** and **Supplementary Figure S3B**). The addition of cADPR slightly, but not significantly, promoted the transfer efficiency (**Figures 3C,F**). We also constructed CD38-targeting shRNA to genetically inhibit the expression of CD38 in HA-mitodsred cells (**Figures 3G–I** and **Supplementary Figure S6**), and found that consistent with the effect of pharmacological inhibition, genetic inhibition of CD38 also reduced the transfer efficiency (**Figure 3J** and **Supplementary Figure S3C**). However, overexpression of CD38 did not promote the transfer (**Figures 3K–N** and **Supplementary Figure S3D**). Similar results were observed when the expression level of CD38 was genetically inhibited or increased in SK-mitodsred and then the SK-mitodsred were co-cultured with HA-GFP (**Figures 3O–V** and **Supplementary Figures S3E,F**). These data collectively indicated that CD38/cADPR might be necessary, but not sufficient, for the mitochondrial transfer between neural cells.

Aside from CD38, MIRO1, one of the two mitochondrial Rho GTPases, also regulates mitochondrial transfer from mesenchymal stem cells into epithelial cells and cardiomyocytes (Ahmad et al., 2014; Zhang et al., 2016). To assess whether mitochondrial Rho GTPase affected the mitochondrial transfer here, we constructed shRNAs targeting MIRO1 or MIRO2, another mitochondrial Rho GTPase. Compared to scramble shRNA, MIRO1- or MIRO2-targeting shRNA reduced the expression level of MIRO1 or MIRO2 in HA (**Figures 4A–C**

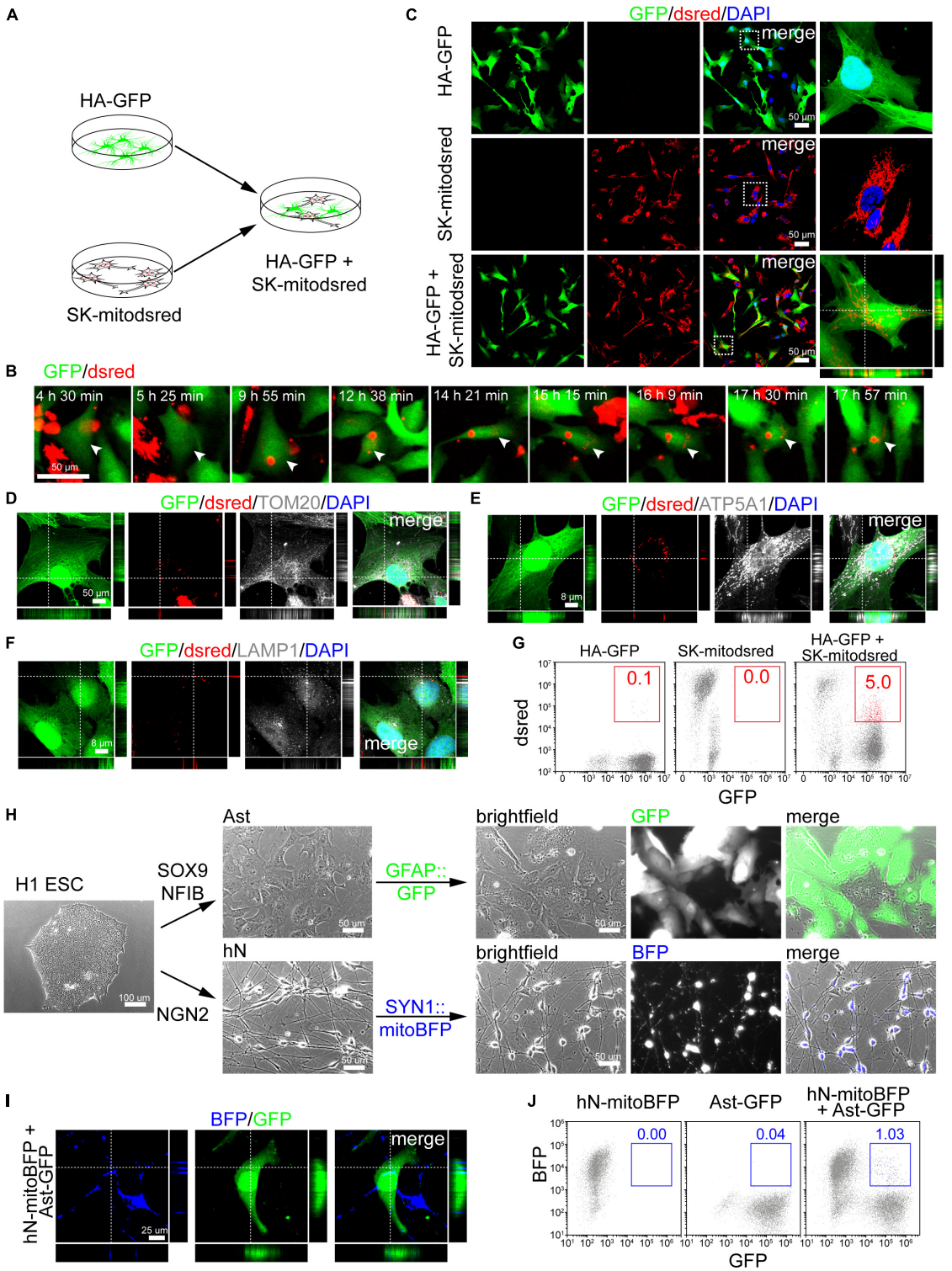


FIGURE 2 | Mitochondrial transfer from neuronal cells into astrocytes. **(A)** Schematic showing that HA-GFP were co-cultured with SK-mitodsred at a ratio of 1:1. **(B)** Time-lapse live images showing mitochondria from SK-mitodsred dynamically transferring into HA-GFP. **(C)** Confocal images showing mitochondria from SK-mitodsred in HA-GFP after co-cultured for 24 h. **(D–F)** Immunostaining of TOM20 **(D)**, ATP5A1 **(E)**, and LAMP1 **(F)** after co-cultured for 24 h. **(G)** Flow cytometry analyzing mitochondrial transfer efficiency from SK into HA after co-cultured for 24 h. **(H)** H1 ESC-derived astrocytes (Ast) or neurons (hN) were labeled with GFAP::GFP or SYN1::mitoBFP. **(I)** Confocal images showing that mitochondria from hN-mitoBFP were observed in Ast-GFP after co-cultured for 48 h. **(J)** Flow cytometry analyzing mitochondrial transfer efficiency from hN cells into Ast after co-cultured for 48 h.

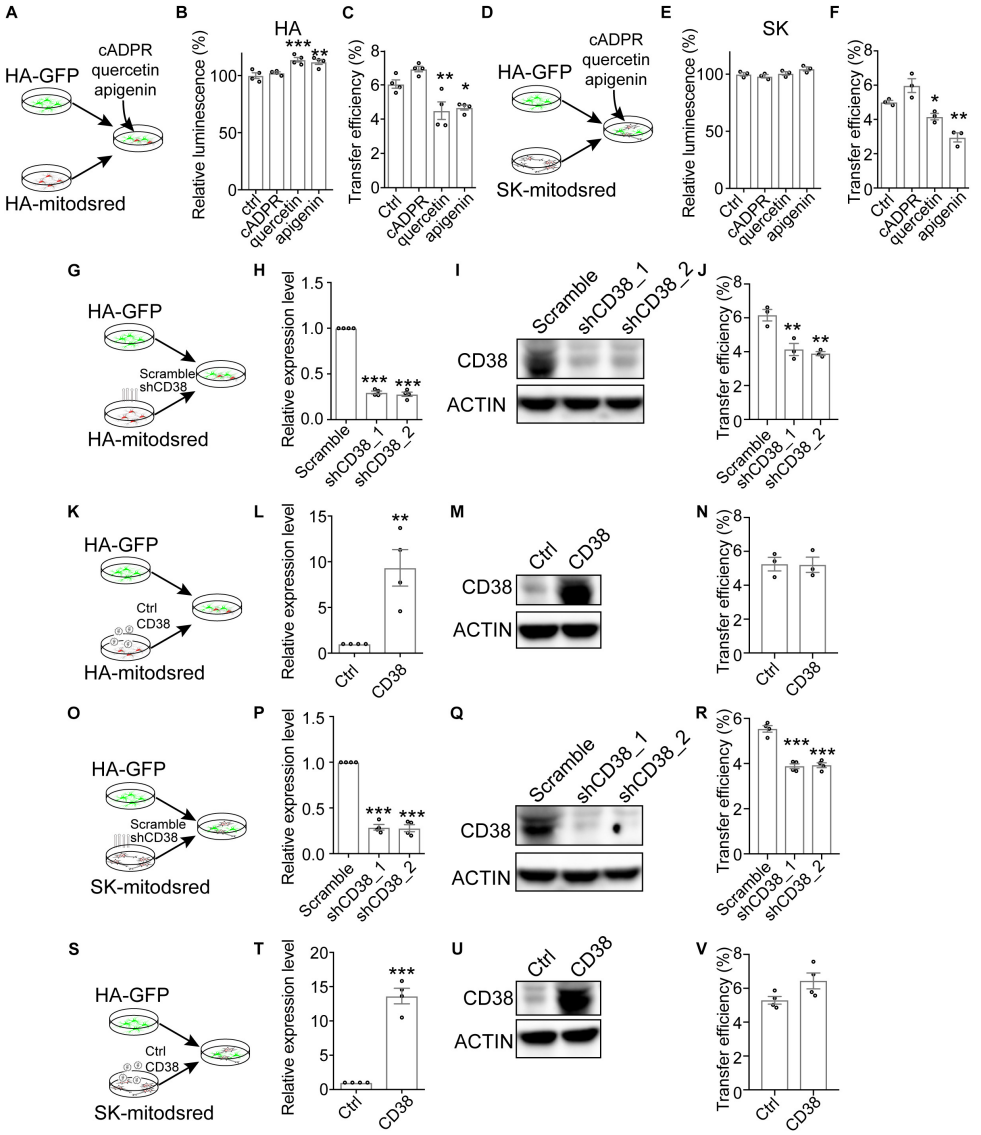


FIGURE 3 | Contribution of CD38/cADPR signaling to the transfer **(A–F)**. Effects of cADPR or CD38 inhibitors (quercetin, apigenin) on mitochondrial transfer between neural cells. **(A)** Schematic showing that co-cultured HA-GFP and HA-mitodsred cells were treated with cADPR, quercetin, or apigenin. **(B)** Analysis of cell viability on HA with indicated treatment for 24 h by CellTiter Glo. (Adjusted *p* values: ctrl vs. cADPR, 0.7403; ctrl vs. quercetin, 0.0009; and ctrl vs. apigenin, 0.0029). **(C)** Flow cytometry analyzing mitochondrial transfer efficiency between HA with indicated chemical treatment for 24 h. (Adjusted *p* values: ctrl vs. cADPR, 0.1478; ctrl vs. quercetin, 0.0091; and ctrl vs. apigenin, 0.0194). **(D)** Schematic showing that co-cultured HA-GFP and SK-mitodsred cells were treated with cADPR, quercetin, or apigenin. **(E)** Analysis of cell viability on SK with indicated treatment for 24 h by CellTiter Glo. (Adjusted *p* values: ctrl vs. cADPR, 0.7573; ctrl vs. quercetin, 0.9783; and ctrl vs. apigenin, 0.1579). **(F)** Flow cytometry analyzing mitochondrial transfer efficiency from SK into HA with indicated chemical treatment for 24 h. (Adjusted *p* values: ctrl vs. cADPR, 0.0775; ctrl vs. quercetin, 0.01263; and ctrl vs. apigenin, 0.0015). **(G–N)** Effects of CD38 in HA-mitodsred on mitochondrial transfer between HA. **(G)** Schematic showing that HA-GFP were co-cultured with indicated HA-mitodsred. **(H,I)**. RT-qPCR **(H)** and western blot **(I)** analysis of CD38 expression on HA-mitodsred with indicated shRNA transduction. (Adjusted *p* values in H: Scramble vs. shCD38_1, <0.001; Scramble vs. shCD38_2, <0.001). **(J)** Flow cytometry analyzing mitochondrial transfer efficiency from indicated HA-mitodsred into HA-GFP after co-cultured for 24 h. (Adjusted *p* values: Scramble vs. shCD38_1, 0.0048; Scramble vs. shCD38_2, 0.0027). **(K)** Schematic showing that HA-GFP were co-cultured with indicated HA-mitodsred. **(L,M)** RT-qPCR **(L)** and western blot **(M)** analysis of CD38 expression on HA-mitodsred with indicated lentiviral infection. ($p = 0.0059$ in **M**). **(N)** Flow cytometry analyzing mitochondrial transfer efficiency from indicated HA-mitodsred into HA-GFP after co-cultured for 24 h. ($p = 0.9483$). **(O–V)** Effects of CD38 in SK-mitodsred on mitochondrial transfer from SK into HA. **(O)** Schematic showing that HA-GFP were co-cultured with indicated SK-mitodsred. **(P,Q)** RT-qPCR **(P)** and western blot **(Q)** analysis of CD38 expression on SK-mitodsred with indicated shRNA transduction. (Adjusted *p* values in P: Scramble vs. shCD38_1, <0.001; Scramble vs. shCD38_2, <0.001). **(R)** Flow cytometry analyzing mitochondrial transfer efficiency from indicated SK-mitodsred into HA-GFP after co-cultured for 24 h. (Adjusted *p* values: Scramble vs. shCD38_1, $p < 0.001$; Scramble vs. shCD38_2, $p < 0.001$). **(S)** Schematic showing that HA-GFP were co-cultured with indicated SK-mitodsred. **(T,U)** RT-qPCR **(T)** and western blot **(U)** analysis of CD38 expression on SK-mitodsred with indicated lentiviral infection. ($p < 0.001$) **(V)** Flow cytometry analyzing mitochondrial transfer efficiency from indicated SK-mitodsred into HA-GFP after co-cultured for 24 h. ($p = 0.0697$) Data are represented as mean ± SEM. One-way ANOVA followed Dunnett's multiple comparisons test was applied in **B, C, E, F, H, J, P, R**; Two-tailed student *t* test was used in **L, N, T, V**. $^*p < 0.05$, $^{**}p < 0.01$, and $^{***}p < 0.001$.

and **Supplementary Figure S6**). When HA-mitodsred were infected with MIRO1- or MIRO2-targeting shRNAs and then co-cultured with HA-GFP for 24 h (**Figure 4A**), mitochondrial transfer efficiency was reduced by MIRO1- or MIRO2-targeting shRNAs (**Figure 4D** and **Supplementary Figure S3G**). On the contrast, when MIRO1 was overexpressed in HA-mitodsred, mitochondrial transfer efficiency from HA-mitodsred into HA-GFP increased (**Figures 4E–H** and **Supplementary Figure S3H**). However, when MIRO1 or MIRO2 was down-regulated or up-regulated in HA-GFP, the transfer efficiency from HA-mitodsred into HA-GFP was not altered (**Supplementary Figures S3I–L**). We also assessed the effects of MIRO1 and MIRO2 on transfer of neuronal mitochondria into astrocytes. When shRNAs targeting MIRO1 or MIRO2 were transduced on SK-mitodsred, the expression level of MIRO1 or MIRO2 in SK-mitodsred was also reduced (**Figures 4J,K**). These SK-mitodsred were then co-cultured with HA-GFP (**Figure 4I**) and the transfer efficiency from SK into HA was reduced by MIRO1 or MIRO2 knockdown (**Figure 4L** and **Supplementary Figure S3M**). On the other hand, the efficiency was increased when MIRO1 or MIRO2 was overexpressed in SK-mitodsred (**Figures 4M–P** and **Supplementary Figure S3N**). Taken together, these data suggested that CD38/cADPR signaling and the two mitochondria-localized Rho GTPases contributed to the intercellular mitochondrial transfer between neural cells.

Elevation of Mitochondrial Membrane Potential (MMP) in Cells With Transferred Mitochondria

To assess the effects of mitochondrial transfer on recipient cells, we measured MMP by tetramethylrhodamine ethyl ester perchlorate (TMRE) staining (Crowley et al., 2016). HA transduced with mitoBFP (HA-mitoBFP) were co-cultured with HA-GFP for 24 h and then TMRE staining was performed on co-cultured cells. The results showed that HA-GFP with transferred mitochondria (GFP^+BFP^+) had a relative higher TRME signal than HA-GFP without transferred mitochondria (GFP^+BFP^-) (**Figure 5A**). Similarly, mitochondrial transfer from SK or hNeuron also elevated the TMRE signal of recipient HA-GFP or Ast-GFP, respectively (**Figures 5B,C**). HA-GFP with transferred mitochondria (GFP^+dsred^+) and HA-GFP without transferred mitochondria (GFP^+dsred^-) were further separated from HA-GFP and HA-mitodsred co-cultured cells by FACS (**Supplementary Figure S4B**) and the expression levels of mitochondrial biogenesis and metabolism markers in GFP^+dsred^+ and GFP^+dsred^- cells were analyzed. The results showed that except that *NRF1* was significantly, though slightly, upregulated in GFP^+dsred^+, there were no significant differences in the expression levels of other markers between GFP^+dsred^+ and GFP^+dsred^- cells (**Supplementary Figure S4C**). These data collectively demonstrated that mitochondrial transfer might not impair, but instead slightly enhance, mitochondrial function of the recipient cells.

To assess the effects of mitochondrial transfer on cell cycle of the recipient cells, we performed time lapse live imaging on co-cultured HA-GFP and HA-mitodsred. These cells were co-cultured for 48 h to accumulate enough mitochondrial transfer. Then they were dissociated and re-plated and live imaging was performed once the cells attached. During the imaging periods, HA-GFP went through cell division and the transferred mitochondria distributed into the daughter cells during the division (**Figure 5D**). There was no significant difference in cell cycle duration between GFP^+dsred^+ and GFP^+dsred^- cells (**Supplementary Figure S4A**). Similarly, HA-GFP with mitochondria transferred from SK-mitodsred also went through cell division normally and the transferred mitochondria also distributed into the daughter cells during the division (**Figure 5E**). These data indicated that mitochondrial transfer might not affect normal cell cycle progression of the recipient cells.

Impaired Mitochondrial Transfer From Astrocytes With AxD-Associated GFAP Mutations

AxD is a severe leukodystrophy and mainly caused by GFAP mutation (Olabarria and Goldman, 2017). Of all the GFAP mutations identified in AxD patients, R79C and R239C are the most frequently observed mutations (Hagemann et al., 2006). We therefore introduced R79C or R239C mutation into GFAP gene in H1 ESCs using CRISPR/Cas9 and validated the mutations by sanger sequencing (**Figure 6A** and **Supplementary Figure S5J**). Then GFAP-mutated, as well as WT, H1 ESCs were differentiated into astrocytes with SOX9 and NFIB as mentioned above. We found that the differentiated astrocytes were positive for S100B and GFAP (**Figure 6B**), and there was no difference in differentiation efficiency among WT, R79C, or R239C cells (**Figure 6C**). The notable hallmark of AxD is the presence of Rosenthal fibers, which contain GFAP, alphaB-crystallin (CRYAB), and other components, in astrocytes (Olabarria and Goldman, 2017). Notably, GFAP and CRYAB aggregates were observed in R79C or R239C astrocytes, as well as in R239C heterozygous astrocytes, but rarely detected in WT astrocytes (**Figures 6D,E** and **Supplementary Figures S5K,L**), suggesting that astrocytes with GFAP mutations here recapitulated phenocopied the core pathology of AxD.

Then, we examined the mitochondrial properties on WT, R79C, and R239C astrocytes. The mitochondrial copy number calculated as the ratio of mitochondrial DNA (mtDNA) to nuclear DNA (nDNA) (Tarrago et al., 2018) was not altered in astrocytes with GFAP mutation (**Supplementary Figure S5A**). R79C or R239C mutation in GFAP slightly, but not significantly, increased the MMP as measured by TMRE staining (**Supplementary Figure S5B**). We did not observe significant difference in mitochondrial morphology or expression of mitochondrial biogenesis and metabolism markers between WT and GFAP-mutated astrocytes, either (**Supplementary Figures S5C,D**).

Next, we analyzed whether intercellular transfer of astrocytic mitochondria was affected by GFAP mutation. WT or GFAP-mutated astrocytes were divided into two parts and each part was labeled with GFP or mitodsred as above-described (**Figure 6F**

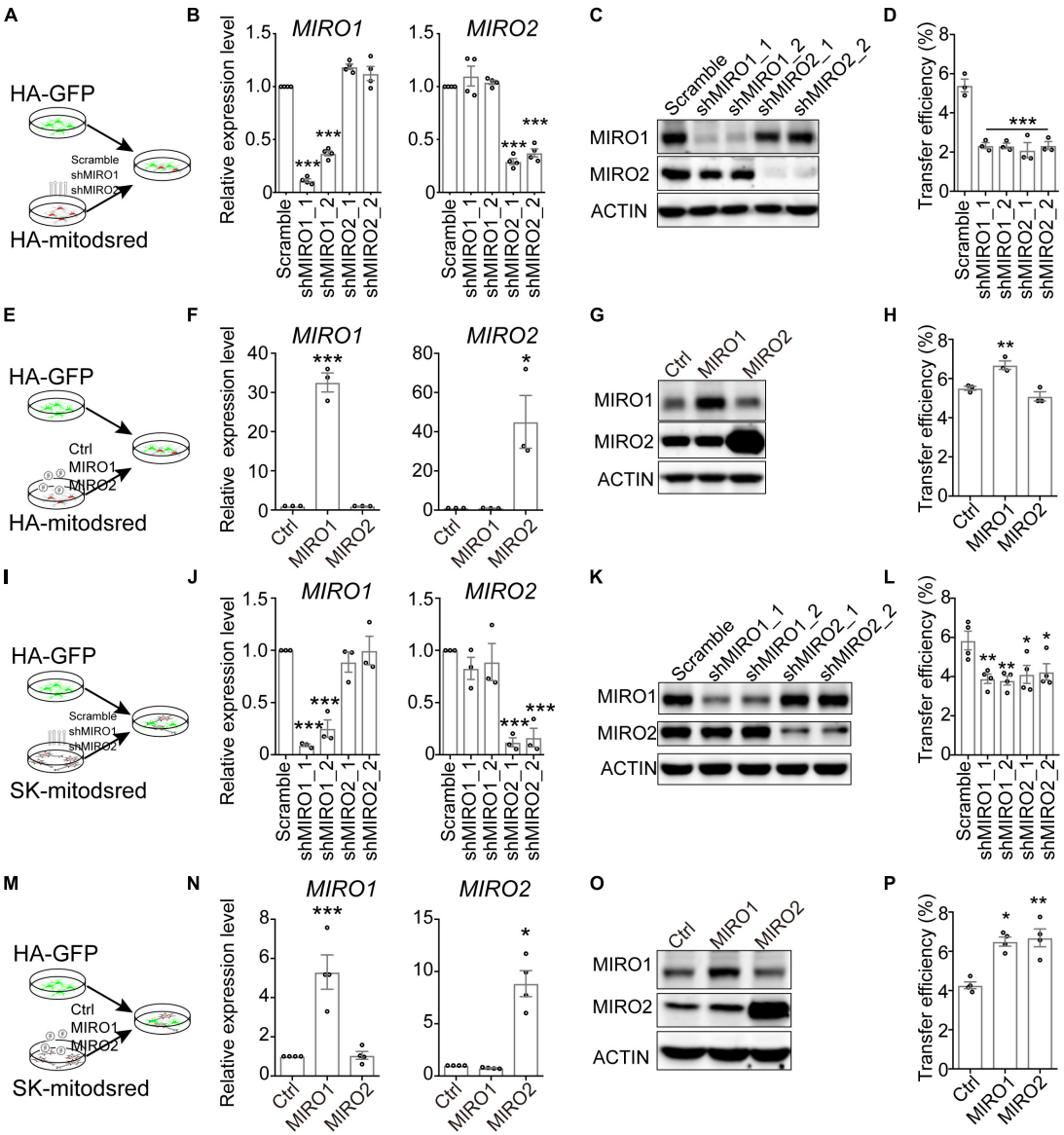


FIGURE 4 | Contribution of mitochondrial Rho GTPases to the transfer. **(A–H)** Effects of MIRO1 and MIRO2 in HA-mitodsred on mitochondrial transfer between HA. **(A)** Schematic showing that HA-GFP were co-cultured with indicated HA-mitodsred. **(B,C)** RT-qPCR **(B)** and western blot **(C)** analysis of MIRO1 and MIRO2 expression on HA-mitodsred with indicated shRNA transduction. (Adjusted *p* values in B: *MIRO1*, Scramble vs. shMIRO1_1, <0.001; Scramble vs. shMIRO1_2, <0.001; Scramble vs. shMIRO2_1, 0.056; Scramble vs. shMIRO2_2, 0.0721. *MIRO2*, Scramble vs. shMIRO1_1, 0.4154; Scramble vs. shMIRO1_2, 0.9288; Scramble vs. shMIRO2_1, <0.001; Scramble vs. shMIRO2_2, <0.001). **(D)** Flow cytometry analyzing mitochondrial transfer efficiency from indicated HA-mitodsred into HA-GFP after co-cultured for 24 h. (Adjusted *p* values vs. Scramble <0.001) **(E)** Schematic showing that HA-GFP were co-cultured with indicated HA-mitodsred. **(F,G)** RT-qPCR **(F)** and western blot **(G)** analysis of MIRO1 and MIRO2 expression on HA-mitodsred with indicated lentiviral infection. (Adjusted *p* values in F: *MIRO1*, Ctrl vs. MIRO1, <0.001; ctrl vs. MIRO2, >0.999; *MIRO2* Ctrl vs. MIRO1, >0.999; ctrl vs. MIRO2, 0.0127). **(H)** Flow cytometry analyzing mitochondrial transfer efficiency from indicated HA-mitodsred into HA-GFP after co-cultured for 24 h. (Adjusted *p* values: Ctrl vs. MIRO1, 0.009; ctrl vs. MIRO2, 0.2953). **(I–P)** Effects of MIRO1 or MIRO2 in SK-mitodsred on mitochondrial transfer from SK into HA. **(I)** Schematic showing that HA-GFP were co-cultured with indicated SK-mitodsred. **(J,K)** RT-qPCR **(J)** and western blot **(K)** analysis of MIRO1 and MIRO2 expression on SK-mitodsred with indicated shRNA transduction. (Adjusted *p* values in J: *MIRO1*, Scramble vs. shMIRO1_1, <0.001; Scramble vs. shMIRO1_2, <0.001; Scramble vs. shMIRO2_1, 0.7474; Scramble vs. shMIRO2_2, >0.999. *MIRO2*, Scramble vs. shMIRO1_1, 0.5991; Scramble vs. shMIRO1_2, 0.8561; Scramble vs. shMIRO2_1, <0.001; Scramble vs. shMIRO2_2, <0.001). **(L)** Flow cytometry analyzing mitochondrial transfer efficiency from indicated SK-mitodsred into HA-GFP after co-cultured for 24 h. (Adjusted *p* values: Scramble vs. shMIRO1_1, 0.0084; Scramble vs. shMIRO1_2, 0.006; Scramble vs. shMIRO2_1, 0.0189; Scramble vs. shMIRO2_2, 0.0302). **(M)** Schematic showing that HA-GFP were co-cultured with indicated SK-mitodsred. **(N,O)** RT-qPCR **(N)** and western blot **(O)** analysis of MIRO1 and MIRO2 expression on SK-mitodsred with indicated lentiviral infection. (Adjusted *p* values in N: *MIRO1*, Ctrl vs. MIRO1, <0.001; ctrl vs. MIRO2, 0.9969; *MIRO2* Ctrl vs. MIRO1, 0.9599; ctrl vs. MIRO2, 0.0127). **(P)** Flow cytometry analyzing mitochondrial transfer efficiency from indicated SK-mitodsred into HA-GFP after co-cultured for 24 h. (Adjusted *p* values: Ctrl vs. MIRO1, 0.0119; ctrl vs. MIRO2, 0.005). Data are represented as mean ± SEM. One-way ANOVA followed Dunnett's multiple comparisons test was applied in **B**, **D**, **F**, **H**, **J**, **L**, **N**, **P**. $^{*}p < 0.05$, $^{**}p < 0.01$, and $^{***}p < 0.001$.

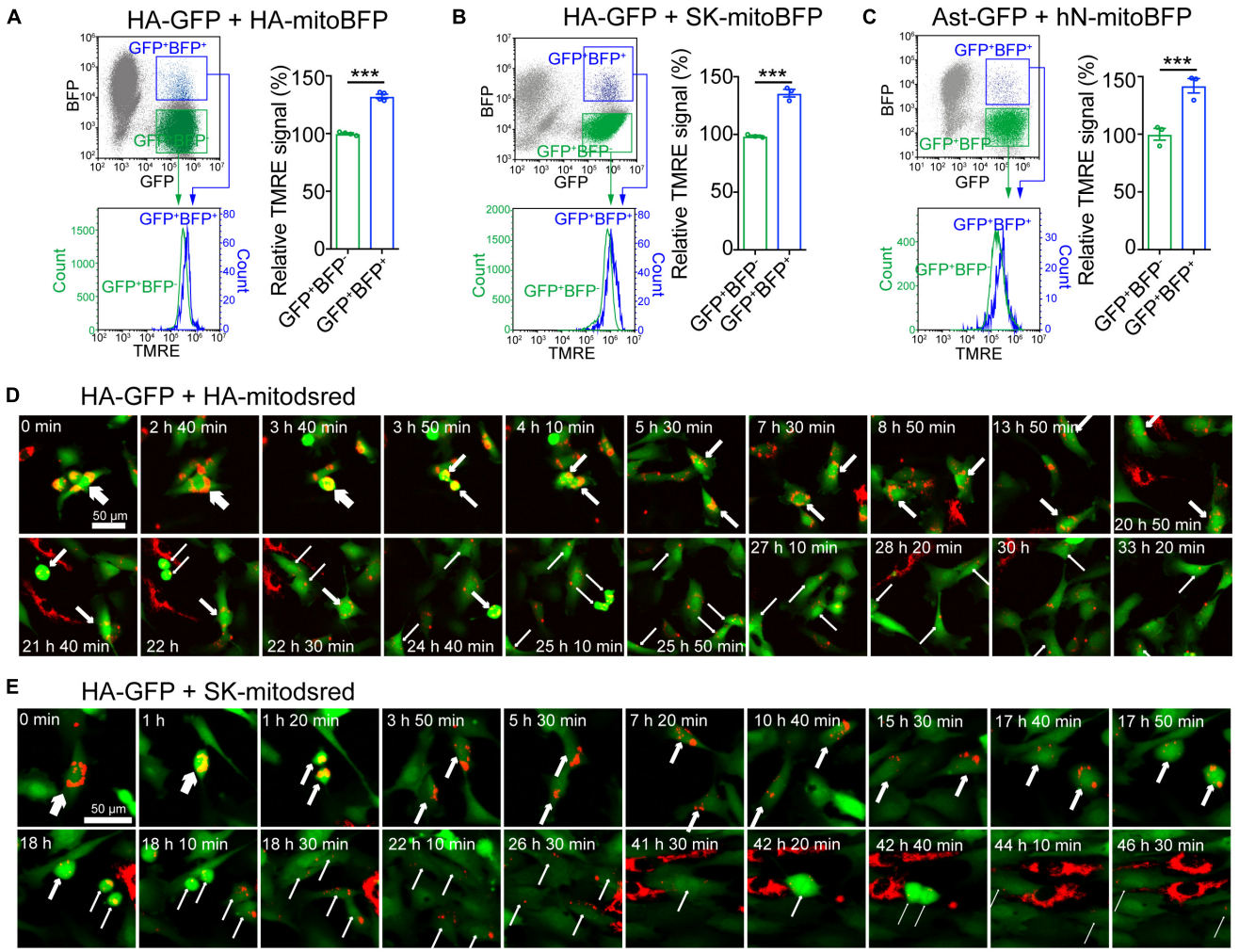


FIGURE 5 | Elevation of mitochondrial membrane potential (MMP) in cells with transferred mitochondria **(A–C)** Measurement of MMP on co-cultured HA-GFP and HA-mitoBFP **(A)**, HA-GFP and SK-mitoBFP **(B)**, and Ast-GFP and hN-mitoBFP **(C)** by TMRE staining. TMRE signal intensity was compared between gated GFP^+BFP^+ and GFP^+BFP^- cells. **(D,E)** Time-lapse live images showing the dynamics of mitochondria transferred from HA-mitodsred **(D)** or from SK-mitodsred **(E)** into HA-GFP along cell division. Data are represented as mean ± SEM. *P* values in **A, B, C** calculated with two-tailed student *t* test were <0.001. ***$p < 0.001$.

and **Supplementary Figure S5M**). Then the distinctly labeled astrocytes were co-cultured at a ratio of 1:1. After 24 h, we found that astrocytes with R79C or R239C mutation had a significantly lower transfer efficiency than WT astrocytes (**Figure 6F** and **Supplementary Figure S5E**), indicating an impairment of mitochondrial transfer by GFAP mutation. As the lower efficiency might be attributed to impairment in giving or receiving mitochondria, we analyzed mitochondrial transfer from WT or GFAP-mutated astrocytes into SK cells. Astrocytes were labeled with mitodsred and then co-cultured with SK-GFP. After co-cultured for 24 h, mitochondrial transfer into SK from astrocytes with R79C or R239C mutation was less efficient than that from WT astrocytes (**Figure 6G** and **Supplementary Figure S5F**). On the contrast, when WT or GFAP-mutated astrocytes were labeled with GFP and then co-cultured with SK-mitodsred, the efficiency of mitochondrial transferred from SK into astrocytes was not significantly different (**Figure 6H** and **Supplementary Figure S5G**). Similar results were observed when mouse primary neurons, instead of SK, were used to compare the capacity of WT and GFAP-mutated astrocytes to give (**Figure 6I** and **Supplementary Figure S5H**) or receive (**Figure 6J** and **Supplementary Figure S5I**) mitochondria. Similarly, R239C heterozygous mutation in GFAP gene also led to a reduced mitochondrial transfer efficiency between astrocytes (**Supplementary Figure S5M**) and from astrocytes into SK cells (**Supplementary Figure S5N**), but did not significantly alter the transfer from SK into astrocytes (**Supplementary Figure S5O**). Taken together, these data indicated that astrocytes with GFAP mutations failed to intercellularly transfer mitochondria as efficient as WT astrocytes, but might normally receive transferred mitochondria.

To explore the mechanism underlying the impaired transfer, we compared the expression levels of *CD38*, *MIRO1*, and *MIRO2* between WT and GFAP-mutated astrocytes. We found

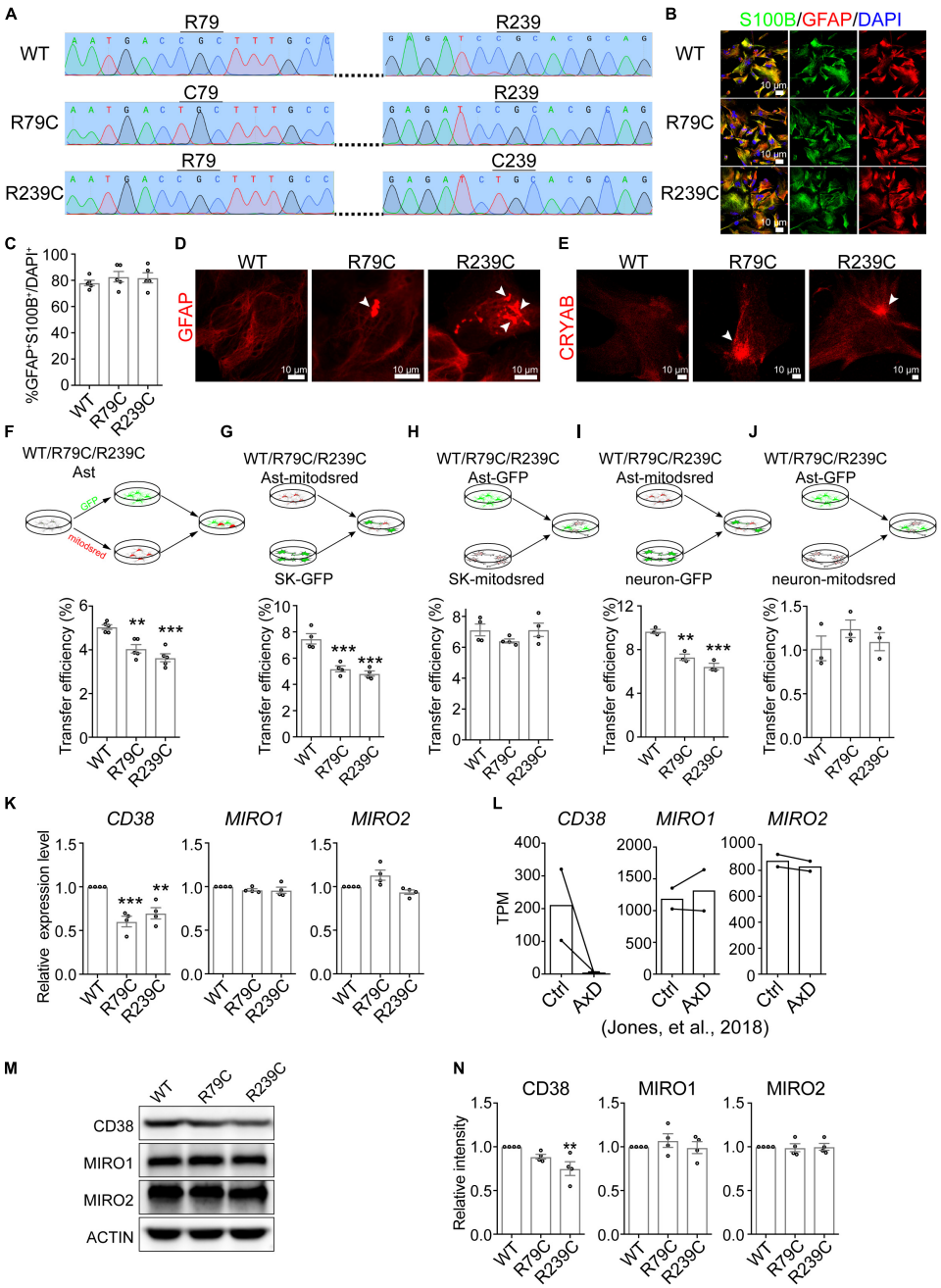


FIGURE 6 | Impaired mitochondrial transfer from astrocytes with GFAP mutation. **(A)** Sanger sequencing validating R79C or R239C mutation in GFAP gene in H1 ESCs. **(B)** Immunostaining of S100B and GFAP on astrocytes derived from WT or GFAP-mutated ESCs. **(C)** Quantification of the percentage of $GFAP^{+}S100B^{+}$ cells in astrocytes derived from WT or GFAP-mutated ESCs. (Adjusted *p* values: WT vs. R79C, 0.5332; WT vs. R239C, 0.6487). **(D,E)** Representative images showing that GFAP aggregates **(D)** and CRYAB **(E)** (indicated by white arrowheads) were observed in R79C or R239C astrocytes, but rarely detected in WT astrocytes. **(F–J)** Flow cytometry analyzing mitochondrial transfer efficiency between indicated hESC-derived astrocytes **(F)**, from indicated hESC-derived astrocytes into SK cells **(G)**, from SK cells into indicated hESC-derived astrocytes **(H)**, from indicated hESC-derived astrocytes into neurons **(I)**, and from neurons into indicated hESC-derived astrocytes **(J)**. Cells co-cultured for 24 h were analyzed. (Adjusted *p* values in F: WT vs. R79C, 0.002; WT vs. R239C, <0.001. in G: WT vs. R79C, <0.001; WT vs. R239C, <0.001. in H: WT vs. R79C, 0.2924; WT vs. R239C, 0.9998. in I: WT vs. R79C, 0.0013; WT vs. R239C, <0.001. in J: WT vs. R79C, 0.3566; WT vs. R239C, 0.8587). **(K)** RT-qPCR analyzing the expression levels of *CD38*, *MIRO1*, and *MIRO2* on WT, R79C, or R239C astrocytes. (Adjusted *p* values: *CD38*, WT vs. R79C, <0.001; WT vs. R239C, 0.0041. *MIRO1*, WT vs. R79C, 0.3915; WT vs. R239C, 0.3568. *MIRO2*, WT vs. R79C, 0.0565; WT vs. R239C,0.4048). **(L)** TPM values of *CD38*, *MIRO1*, and *MIRO2* in control or AxD astrocytes. The data were derived from Jones et al., Cell Reports, 2018. **(M,N)** Western blotting detecting CD38, MIRO1, and MIRO2 on WT, R79C, or R239C astrocytes. (Adjusted *p* values in N: *CD38*, WT vs. R79C, 0.2153; WT vs. R239C, 0.0094. *MIRO1*, WT vs. R79C, 0.635; WT vs. R239C, 0.9902. *MIRO2*, WT vs. R79C, 9647; WT vs. R239C,0.9998). Representative results were shown in **M** and the quantification of band intensity was shown in **N**. Data are represented as mean ± SEM. One-way ANOVA followed Dunnett's multiple comparisons test was applied in **C, F, G, H, I, J, K, N**. $^{**}p < 0.01$ and $^{***}p < 0.001$.

that the mRNA expression levels of *CD38* in R79C or R239C astrocytes were significantly lower than that in WT astrocytes, while *MIRO1* or *MIRO2* had a similar expression level between WT and GFAP-mutated astrocytes (**Figure 6K**). These data were consistent with previously published RNA-sequencing data showing that *CD38* had a lower TPM value in astrocytes differentiated from AxD patient-derived iPSCs, while *MIRO1* and *MIRO2* were not significantly altered (**Figure 6L**; Jones et al., 2018). Using immunoblotting to detect the protein levels of CD38, MIRO1, and MIRO2, we found that MIRO1 or MIRO2 was not significantly altered by GFAP mutation, while CD38 was significantly lower in R239C astrocytes and slightly, but not significantly, lower in R79C astrocytes (**Figures 6M,N** and **Supplementary Figure S6**). Overexpression of CD38 in GFAP-mutated astrocytes failed to rescue the defect in mitochondrial transfer efficiency (**Supplementary Figures S5P,Q**), which was consistent with the potential necessary, but not sufficient, role of CD38 (**Figure 3**), and also suggested that some other mediators might be compromised in GFAP-mutated astrocytes.

DISCUSSION

Previous study demonstrated transfer of mitochondria from astrocytes into neurons (Hayakawa et al., 2016). Here, we further revealed intercellular mitochondrial transfer between astrocytes and from neuronal cells into astrocytes, suggesting that intercellular mitochondrial transfer might prevalently occur. Technically, lentivirus-mediated fluorescent proteins were used here to specifically label mitochondria, avoiding the possibility of cytotoxicity and leakage of fluorescent dyes (Berridge et al., 2018; Berridge et al., 2016). Furthermore, the lentivirus was prepared with the third-generation packaging system, which uses three plasmids consisting of packaging, envelope, and vector constructs separately, thus excluding the possibility of generating replication- or mobilizing-competent virus in the transduced cells (Miyoshi et al., 1998; Tiscornia et al., 2006; Zufferey et al., 1998). Thus, it seemed unlikely that the appearance of dsred-positive mitochondria in GFP-positive cells was because of cross infection of mitodsred lentivirus to the GFP cells during co-culture. Indeed, no GFP signal was detected in the mitodsred-labeled cells, further demonstrating that the cross infection of lentivirus during co-culture might not occur. We found that MMP was elevated in the recipient cells, suggesting that mitochondrial transfer might alter mitochondrial function in the receipt cells. However, transfer of astrocytic mitochondrial into neurons occurs *in vivo* and promotes neuronal survival after stroke (Hayakawa et al., 2016). Whether mitochondrial transfer between astrocytes and from neuronal cells into astrocytes also occurs *in vivo* and more detailed cellular functions of the transfer need further investigation.

CD38 catalyzes the production of cADPR, which mobilizes Ca^{2+} to elicit diverse cellular responses (Wei et al., 2014). Previous studies showed that CD38/cADPR signaling mediated mitochondrial transfer from astrocytes into neurons and from bone marrow stromal cells into multiple myeloma cells (Hayakawa et al., 2016; Marlein et al., 2019). We found that CD38/cADPR signaling also contributed to mitochondrial transfer between astrocytes and from neuronal cells into astrocytes here. MIRO1, one of the two mitochondrial localized Rho GTPases, also regulates mitochondrial transfer from mesenchymal stem cells into airway epithelial cells and cardiomyocytes (Ahmad et al., 2014; Zhang et al., 2016). We found that MIRO1, as well as MIRO2, the other mitochondrial Rho GTPase, also played a role in mitochondrial transfer here, which seems reasonable considering the involvement of the two GTPases in intracellular mitochondrial transport and trafficking (Fransson et al., 2006; Lee and Lu, 2014). Interestingly, both MIRO1 and MIRO2 have two EF-hand Ca^{2+}-binding domains (Fransson et al., 2006; Fransson et al., 2003), whether they cross-talked with CD38/cADPR signaling awaits to be explored. Our study, together with previous studies, indicate that there may exist universal mediators for intercellular mitochondrial transfer between different cells. Therefore, it is possible that previously reported mechanisms such as extracellular vesicles, tunneling nanotubes, and gap junctions (Griessinger et al., 2017; Hayakawa et al., 2016; Islam et al., 2012) may also participate in the transfer here.

Using cellular model of AxD, recent studies reveal that GFAP mutations in astrocytes inhibit oligodendrocyte progenitor cell (OPC) proliferation and myelination by secreting CHI3L1 (Li et al., 2018) and disrupt intracellular vesicle regulation and ATP secretion (Jones et al., 2018), taking a step forward to understand how GFAP mutations in astrocytes affect intercellular communication and lead to AxD (Sofroniew, 2018). By introducing R79C or R239C, two hotspot AxD-causative mutations, into the GFAP gene of hPSCs and then inducing astrocyte differentiation, we also generated astrocytes with GFAP mutations as previously described (Canals et al., 2018). We found that intercellular mitochondrial transfer from GFAP-mutated astrocytes was significantly impaired, which might lead to the failure of satisfying the material and energy demands of other neural cells and might also represent the disrupted intercellular communication under pathological conditions. The expression level of CD38 in GFAP-mutated astrocytes tended to be lower than that in WT astrocytes. It is reported that CD38 expression is regulated by TNF-α through NF-κB (Kang et al., 2006; Sun et al., 2006; Tirumurugaan et al., 2008) and TNF-α secretion is increased in AxD astrocytes (Kondo et al., 2016), which appears to contradict our observation. However, even though we are not aware of it, we speculate that except TNF-α and NF-κB, there might also exist some other unrevealed, especially GFAP- related, mechanisms regulating CD38 expression in astrocytes. We found that the restoration of CD38 expression in GFAP-mutated astrocytes failed to rescue the impaired mitochondrial transfer, indicating that some downstream mediators might also be compromised. Besides CD38, the plasticity and dynamics of GFAP filament itself would affect the translocation of functional molecules (such as glutamine synthase, and AQP4) and cellular organelles (such as intracellular vesicles, endoplasmic reticulum, and lysosome) and therefore regulates the activity of adjacent

neurons (Jones et al., 2018; Middeldorp and Hol, 2011; Wang and Parpura, 2018). Thus it is also possible that the impaired mitochondrial transfer results from the deficiency in guiding mitochondrial movement of abnormal GFAP filament, during which the CD38/cADPR signaling and MIRO1/MIRO2 might involve and even act as an upstream regulator.

In AxD, the pathological astrocytes lead to the dysfunction of other cell types in central nervous system, including neurons and oligodendrocytes (Olabarria and Goldman, 2017). However, the underlying mechanisms are not fully elucidated. Previous studies indicate that the upregulation of N-cadherin and impairment in ATP release in AxD astrocytes might lead to altered intercellular interaction between astrocytes and other neural cells including neurons and oligodendrocytes (Jones et al., 2018; Kondo et al., 2016). Besides, the decreased ability to buffer glutamate and potassium, as well as elevated levels of cytokines and chemokines, of AxD astrocytes could also result in neuronal dysfunction (such as more sensitive to glutamate-generated death and more depolarized) and oligodendrocyte degeneration (such as toxicity and loss of myelin) (Deng et al., 2006; Olabarria and Goldman, 2017). Meanwhile, AxD-associated GFAP mutations would inhibit the proliferation and terminal differentiation of OPCs (Gomez-Pinedo et al., 2017; Li et al., 2018). Our study here suggested an impairment in intercellular mitochondrial transfer between GFAP-mutated astrocytes and from these astrocytes into neurons. It seems reasonable to speculate that mitochondrial transfer from GFAP-mutated astrocytes into OPCs and mature oligodendrocytes might also be compromised, which needs future investigation. Moreover, it would be interesting to further explore whether the impaired mitochondrial transfer also involves in disrupted proliferation and differentiation of OPCs and demyelination and dysfunction of mature oligodendrocytes. Though we are currently not fully aware of the underlying mechanisms and the functional consequence, the impaired mitochondrial transfer from GFAP-mutated astrocytes might provide a perspective to dissect the pathogenic mechanism in AxD.

DATA AVAILABILITY

Publicly available datasets were analyzed in this study. This data can be found here: https://www.cell.com/cell-reports/pdf/S2211-1247(18)31543-2.pdf.

ETHICS STATEMENT

The use of animals was approved by the Institutional Animal Care and Use Committee (IACUC) of the Shanghai Institute of Biochemistry and Cell Biology, Chinese Academy of Sciences. C57BL/6 mouse of postnatal day 1 and both genders were used and purchased from the Shanghai SLAC Laboratory Animal Co., Ltd. (Shanghai, China).

AUTHOR CONTRIBUTIONS

GP supervised and controlled the research conception and design, interpreted the data, and revised the manuscript. LG organized the figures and drafted the manuscript. JL revised the manuscript. LG, ZZ, and JL conducted the experiments and analyzed the data. All authors contributed to manuscript preparation and approved the submitted manuscript.

FUNDING

This work was supported by the National Key Research and Development Program of China (2018YFA0108000 and 2018YFA0108003), the "Strategic Priority Research Program" of the Chinese Academy of Sciences (XDA16010309), and the National Key Research and Development Program of China Stem Cell and Translational Research (2016YFA0101200 and 2016YFA0101202).

ACKNOWLEDGMENTS

We thank Dr. Jiawei Zhou for sharing hSYN1 promoter plasmid and CRYAB antibody, Dr. Jiahuai Han for sharing human NFIB cDNA, and Dr. Jinsong Li for sharing px330-mcherry vector. We are also thankful for Yan Wang and Yanke Wang from the National Center for Protein Science Shanghai for technical support and all the members of the lab for sharing advice and reagents.

SUPPLEMENTARY MATERIAL

The Supplementary Material for this article can be found online at: https://www.frontiersin.org/articles/10.3389/fncel.2019.00316/full#supplementary-material

REFERENCES

Ahmad, T., Mukherjee, S., Pattnaik, B., Kumar, M., Singh, S., Kumar, M., et al. (2014). Miro1 regulates intercellular mitochondrial transport & enhances mesenchymal stem cell rescue efficacy. *EMBO J.* 33, 994–1010. doi: 10.1002/embj.201386030

Berridge, M. V., Herst, P. M., Rowe, M. R., Schneider, R., and McConnell, M. J. (2018). Mitochondrial transfer between cells: methodological constraints in cell culture and animal models. *Anal. Biochem.* 552, 75–80. doi: 10.1016/j.ab.2017.11.008

Berridge, M. V., Schneider, R. T., and McConnell, M. J. (2016). Mitochondrial transfer from astrocytes to neurons following ischemic insult: guilt by association? *Cell Metab.* 24, 376–378. doi: 10.1016/j.cmet.2016.08.023

Caceres-Marzal, C., Vaquerizo, J., Galan, E., and Fernandez, S. (2006). Early mitochondrial dysfunction in an infant with Alexander disease. *Pediatr. Neurol.* 35, 293–296. doi: 10.1016/j.pediatrneurol.2006.03.010

Canals, I., Ginisty, A., Quist, E., Timmerman, R., Fritze, J., Miskinyte, G., et al. (2018). Rapid and efficient induction of functional astrocytes from human pluripotent stem cells. *Nat. Methods* 15, 693–696. doi: 10.1038/s41592-018-0103-2

Cheng, L., Gao, L., Guan, W., Mao, J., Hu, W., Qiu, B., et al. (2015). Direct conversion of astrocytes into neuronal cells by drug cocktail. *Cell Res.* 25, 1269–1272. doi: 10.1038/cr.2015.120

Crowley, L. C., Christensen, M. E., and Waterhouse, N. J. (2016). Measuring mitochondrial transmembrane potential by TMRE staining. *Cold Spring Harb. Protoc.* 2016, doi: 10.1101/pdb.prot087361

Davis, C.-H., Kim, K.-Y., Bushong, E. A., Mills, E. A., Boassa, D., Shih, T., et al. (2014). Transcellular degradation of axonal mitochondria. *Proc. Natl. Acad. Sci. U.S.A.* 111, 9633–9638. doi: 10.1073/pnas.1404651111

Deng, W., Yue, Q., Rosenberg, P. A., Volpe, J. J., and Jensen, F. E. (2006). Oligodendrocyte excitotoxicity determined by local glutamate accumulation and mitochondrial function. *J. Neurochem.* 98, 213–222. doi: 10.1111/j.1471-4159.2006.03861.x

Escande, C., Nin, V., Price, N. L., Capellini, V., Gomes, A. P., Barbosa, M. T., et al. (2013). Flavonoid apigenin is an inhibitor of the NAD(+)ase CD38 implications for cellular NAD(+) metabolism, protein acetylation, and treatment of metabolic syndrome. *Diabetes* 62, 1084–1093. doi: 10.2337/db12-1139

Fransson, A., Ruusala, A., and Aspenstom, P. (2006). The atypical Rho GTPases Miro-1 and Miro-2 have essential roles in mitochondrial trafficking. *Biochem. Biophys. Res. Commun.* 344, 500–510. doi: 10.1016/j.bbrc.2006.03.163

Fransson, A., Ruusala, A., and Aspenstrom, P. (2003). Atypical Rho GTPases have roles in mitochondrial homeostasis and apoptosis. *J. Biol. Chem.* 278, 6495–6502. doi: 10.1074/jbc.m208609200

Gao, L., Guan, W., Wang, M., Wang, H., Yu, J., Liu, Q., et al. (2017). Direct generation of human neuronal cells from adult astrocytes by small molecules. *Stem Cell Rep.* 8, 538–547. doi: 10.1016/j.stemcr.2017.01.014

Gomez-Pinedo, U., Sirerol-Piquer, M. S., Duran-Moreno, M., Garcia-Verdugo, J. M., and Matias-Guiu, J. (2017). Alexander disease mutations produce cells with coexpression of glial fibrillary acidic protein and NG2 in neurosphere cultures and inhibit differentiation into mature oligodendrocytes. *Front. Neurol.* 8:255. doi: 10.3389/fneur.2017.00255

Griessinger, E., Moschoi, R., Biondani, G., and Peyron, J. F. (2017). Mitochondrial transfer in the leukemia microenvironment. *Trends Cancer* 3, 828–839. doi: 10.1016/j.trecan.2017.10.003

Guo, Z., Zhang, L., Wu, Z., Chen, Y., Wang, F., and Chen, G. (2014). In vivo direct reprogramming of reactive glial cells into functional neurons after brain injury and in an alzheimer's disease model. *Cell Stem Cell* 14, 188–202. doi: 10.1016/j.stem.2013.12.001

Hagemann, T. L., Connor, J. X., and Messing, A. (2006). Alexander disease-associated glial fibrillary acidic protein mutations in mice induce rosenthal fiber formation and a white matter stress response. *J. Neurosci.* 26, 11162–11173. doi: 10.1523/jneurosci.3260-06.2006

Hayakawa, K., Esposito, E., Wang, X., Terasaki, Y., Liu, Y., Xing, C., et al. (2016). Transfer of mitochondria from astrocytes to neurons after stroke. *Nature* 535, 551–555. doi: 10.1038/nature18928

Hobbs, H. H., Brown, M. S., and Goldstein, J. L. (1992). Molecular genetics of the LDL receptor gene in familial hypercholesterolemia. *Hum. Mutat.* 1, 445–466. doi: 10.1002/humu.1380010602

Hu, W., Qiu, B., Guan, W., Wang, Q., Wang, M., Li, W., et al. (2015). Direct conversion of normal and alzheimer's disease human fibroblasts into neuronal cells by small molecules. *Cell Stem Cell* 17, 204–212. doi: 10.1016/j.stem.2015.07.006

Islam, M. N., Das, S. R., Emin, M. T., Wei, M., Sun, L., Westphalen, K., et al. (2012). Mitochondrial transfer from bone-marrow–derived stromal cells to pulmonary alveoli protects against acute lung injury. *Nat. Med.* 18, 759–765. doi: 10.1038/nm.2736

Jones, J. R., Kong, L., Hanna, M. G., Hoffman, B., Krencik, R., Bradley, R., et al. (2018). Mutations in GFAP disrupt the distribution and function of organelles in human astrocytes. *Cell Rep.* 25, 947–958. doi: 10.1016/j.celrep.2018.09.083

Kang, B. N., Tirumurugaan, K. G., Deshpande, D. A., Amrani, Y., Panettieri, R. A., Walseth, T. F., et al. (2006). Transcriptional regulation of CD38 expression by tumor necrosis factor-alpha in human airway smooth muscle cells: role of NF-kappaB and sensitivity to glucocorticoids. *FASEB J.* 20, 1000–1002. doi: 10.1096/fj.05-4585fje

Kellenberger, E., Kuhn, I., Schuber, F., and Muller-Steffner, H. (2011). Flavonoids as inhibitors of human CD38. *Bioorg. Med. Chem. Lett.* 21, 3939–3942. doi: 10.1016/j.bmcl.2011.05.022

Kondo, T., Funayama, M., Miyake, M., Tsukita, K., Era, T., Osaka, H., et al. (2016). Modeling Alexander disease with patient iPSCs reveals cellular and molecular pathology of astrocytes. *Acta Neuropathol. Commun.* 4:69.

Lee, K. S., and Lu, B. (2014). The myriad roles of Miro in the nervous system: axonal transport of mitochondria and beyond. *Front. Cell. Neurosci.* 8:330. doi: 10.3389/fncel.2014.00330

Li, L., Tian, E., Chen, X., Chao, J., Klein, J., Qu, Q., et al. (2018). GFAP mutations in astrocytes impair oligodendrocyte progenitor proliferation and myelination in an hiPSC model of alexander disease. *Cell Stem Cell* 23, 239.e6–251.e6. doi: 10.1016/j.stem.2018.07.009

Marlein, C. R., Piddock, R. E., Mistry, J. J., Zaitseva, L., Hellmich, C., Horton, R. H., et al. (2019). CD38-driven mitochondrial trafficking promotes bioenergetic plasticity in multiple myeloma. *Cancer Res.* 79, 2285–2297. doi: 10.1158/0008-5472.CAN-1118-0773

Middeldorp, J., and Hol, E. M. (2011). GFAP in health and disease. *Prog. Neurobiol.* 93, 421–443. doi: 10.1016/j.pneurobio.2011.01.005

Miyoshi, H., Blomer, U., Takahashi, M., Gage, F. H., and Verma, I. M. (1998). Development of a self-inactivating lentivirus vector. *J. Virol.* 72, 8150–8157.

Nobuhara, Y., Nakahara, K., Higuchi, I., Yoshida, T., Fushiki, S., Osame, M., et al. (2004). Juvenile form of Alexander disease with GFAP mutation and mitochondrial abnormality. *Neurology* 63, 1302–1304. doi: 10.1212/01.wnl.0000140695.90497.e2

Olabarria, M., and Goldman, J. E. (2017). Disorders of astrocytes: alexander disease as a model. *Annu. Rev. Pathol. Mech.* 12, 131–152. doi: 10.1146/annurev-pathol-052016-100218

Sofroniew, M. V. (2018). Stem-cell-derived astrocytes divulge secrets of mutant GFAP. *Cell Stem Cell* 23, 630–631. doi: 10.1016/j.stem.2018.10.020

Sokolova, V. A., Kustova, M. E., Arbuzova, N. I., Sorokin, A. V., Moskaliova, O. S., Bass, M. G., et al. (2004). Obtaining mice that carry human mitochondrial DNA transmitted to the progeny. *Mol. Reprod. Dev.* 68, 299–307. doi: 10.1002/mrd.20075

Sun, L., Iqbal, J., Zaidi, S., Zhu, L. L., Zhang, X., Peng, Y., et al. (2006). Structure and functional regulation of the CD38 promoter. *Biochem. Biophys. Res. Commun.* 341, 804–809. doi: 10.1016/j.bbrc.2006.01.033

Tan, A. S., Baty, J. W., Dong, L. F., Bezawork-Geleta, A., Endaya, B., Goodwin, J., et al. (2015). Mitochondrial genome acquisition restores respiratory function and tumorigenic potential of cancer cells without mitochondrial DNA. *Cell Metab.* 21, 81–94. doi: 10.1016/j.cmet.2014.12.003

Tarrago, M. G., Chini, C. C. S., Kanamori, K. S., Warner, G. M., Caride, A., de Oliveira, G. C., et al. (2018). A potent and specific CD38 inhibitor ameliorates age-related metabolic dysfunction by reversing tissue NAD(+) decline. *Cell Metab.* 27, 1081–1095. doi: 10.1016/j.cmet.2018.03.016

Tirumurugaan, K. G., Kang, B. N., Panettieri, R. A., Foster, D. N., Walseth, T. F., and Kannan, M. S. (2008). Regulation of the cd38 promoter in human airway smooth muscle cells by TNF-alpha and dexamethasone. *Respir. Res.* 9:26. doi: 10.1186/1465-9921-9-26

Tiscornia, G., Singer, O., and Verma, I. M. (2006). Production and purification of lentiviral vectors. *Nat. Protoc.* 1, 241–245. doi: 10.1038/nprot.2006.37

Torralba, D., Baixauli, F., and Sanchez-Madrid, F. (2016). Mitochondria know no boundaries: mechanisms and functions of intercellular mitochondrial transfer. *Front. Cell Dev. Biol.* 4:107. doi: 10.3389/fcell.2016.00107

Wang, Y. F., and Parpura, V. (2018). Astroglial modulation of hydromineral balance and cerebral edema. *Front. Mol. Neurosci.* 11:204. doi: 10.3389/fnmol.2018.00204

Wei, W., Graeff, R., and Yue, J. (2014). Roles and mechanisms of the CD38/cyclic adenosine diphosphate ribose/Ca(2+) signaling pathway. *World J. Biol. Chem.* 5, 58–67. doi: 10.4331/wjbc.v5.i1.58

Zhang, Y., Pak, C., Han, Y., Ahlenius, H., Zhang, Z., Chanda, S., et al. (2013). Rapid single-step induction of functional neurons from human pluripotent stem cells. *Neuron* 78, 785–798. doi: 10.1016/j.neuron.2013.05.029

Zhang, Y., Yu, Z., Jiang, D., Liang, X., Liao, S., Zhang, Z., et al. (2016). iPSC-MSCs with high intrinsic MIRO1 and sensitivity to TNF-alpha yield efficacious mitochondrial transfer to rescue anthracycline-induced cardiomyopathy. *Stem Cell Rep.* 7, 749–763. doi: 10.1016/j.stemcr.2016.08.009

Zhu, S., Zhao, C., Wu, Y., Yang, Q., Shao, A., Wang, T., et al. (2015). Identification of a Vav2-dependent mechanism for GDNF/Ret control of mesolimbic DAT trafficking. *Nat. Neurosci.* 18, 1084–1093. doi: 10.1038/nn.4060

Zufferey, R., Dull, T., Mandel, R. J., Bukovsky, A., Quiroz, D., Naldini, L., et al. (1998). Self-inactivating lentivirus vector for safe and efficient in vivo gene delivery. *J. Virol.* 72, 9873–9880.

Conflict of Interest Statement: The authors declare that the research was conducted in the absence of any commercial or financial relationships that could be construed as a potential conflict of interest.

Copyright © 2019 Gao, Zhang, Lu and Pei. This is an open-access article distributed under the terms of the Creative Commons Attribution License (CC BY). The use, distribution or reproduction in other forums is permitted, provided the original author(s) and the copyright owner(s) are credited and that the original publication in this journal is cited, in accordance with accepted academic practice. No use, distribution or reproduction is permitted which does not comply with these terms.

frontiers in Cellular Neuroscience

ORIGINAL RESEARCH
published: 13 August 2019
doi: 10.3389/fncel.2019.00374

Lack of Neuronal Glycogen Impairs Memory Formation and Learning-Dependent Synaptic Plasticity in Mice

Jordi Duran[1,2], Agnès Gruart[3], Olga Varea[1], Iliana López-Soldado[1,2], José M. Delgado-García[3] and Joan J. Guinovart[1,2,4]**

[1] Institute for Research in Biomedicine (IRB Barcelona), The Barcelona Institute of Science and Technology, Barcelona, Spain, [2] Centro de Investigación Biomédica en Red de Diabetes y Enfermedades Metabólicas Asociadas (CIBERDEM), Madrid, Spain, [3] Division of Neurosciences, Pablo de Olavide University, Seville, Spain, [4] Department of Biochemistry and Molecular Biomedicine, University of Barcelona, Barcelona, Spain

OPEN ACCESS

Edited by:
Enrico Cherubini,
European Brain Research Institute,
Italy

Reviewed by:
Hajime Hirase,
University of Copenhagen, Denmark
Marco Fuenzalida,
University of Valparaíso, Chile

***Correspondence:**
José M. Delgado-García
jmdelgar@upo.es
Joan J. Guinovart
guinovart@irbbarcelona.org

Specialty section:
This article was submitted to Cellular Neurophysiology, a section of the journal Frontiers in Cellular Neuroscience

Received: 20 June 2019
Accepted: 30 July 2019
Published: 13 August 2019

Citation:
Duran J, Gruart A, Varea O, López-Soldado I, Delgado-García JM and Guinovart JJ (2019) Lack of Neuronal Glycogen Impairs Memory Formation and Learning-Dependent Synaptic Plasticity in Mice. Front. Cell. Neurosci. 13:374. doi: 10.3389/fncel.2019.00374

Since brain glycogen is stored mainly in astrocytes, the role of this polysaccharide in neurons has been largely overlooked. To study the existence and relevance of an active neuronal glycogen metabolism *in vivo*, we generated a mouse model lacking glycogen synthase specifically in the Camk2a-expressing postnatal forebrain pyramidal neurons (GYS1$^{Camk2a-KO}$), which include the prefrontal cortex and the CA3 and CA1 cell layers of the hippocampus. The latter are involved in memory and learning processes and participate in the hippocampal CA3-CA1 synapse, the function of which can be analyzed electrophysiologically. Long-term potentiation evoked in the hippocampal CA3-CA1 synapse was decreased in alert behaving GYS1$^{Camk2a-KO}$ mice. They also showed a significant deficiency in the acquisition of an instrumental learning task – a type of associative learning involving prefrontal and hippocampal circuits. Interestingly, GYS1$^{Camk2a-KO}$ animals did not show the greater susceptibility to hippocampal seizures and myoclonus observed in animals completely depleted of glycogen in the whole CNS. These results unequivocally demonstrate the presence of an active glycogen metabolism in neurons *in vivo* and reveal a key role of neuronal glycogen in the proper acquisition of new motor and cognitive abilities, and in the changes in synaptic strength underlying such acquisition.

Keywords: glycogen, learning, LTP, memory, metabolism

INTRODUCTION

Glycogen is a polymer of glucose that is synthesized by glycogen synthase (GS), and it acts as an energy reservoir. In the brain, it is present at concentrations much lower than those found in muscle or liver. It has traditionally been accepted that brain glycogen is stored exclusively in astrocytes. However, an increasing number of observations reveal the presence of an active glycogen metabolism in neurons. Indirect evidence comes from conditions such as Lafora disease and Pompe disease, in which glycogen abnormally accumulates in this cell population (Sidman et al., 2008;

Duran et al., 2014). Furthermore, we previously demonstrated that primary cultured neurons have an active glycogen metabolism that protects them from hypoxia-induced death (Saez et al., 2014).

The use of genetically modified animals has allowed the study of the normal and pathological aspects of brain glycogen. The capacity to delete specific genes only in the brain ensures that the results reflect the effects of brain glycogen, without the influence of the manipulation of glycogen metabolism in other organs. In this regard, we generated a mouse model devoid of GS (and thus of glycogen) in the CNS ($GYS1^{Nestin-KO}$) (Duran et al., 2013). These animals showed a significant deficit in learning capacity, which unequivocally demonstrated the key role of brain glycogen in the proper acquisition of relatively difficult learning tasks, in accordance with previous results obtained using inhibitors of glycogen degradation (Gibbs et al., 2006; Suzuki et al., 2011). We also described changes in synaptic strength at the electrophysiological level that correlate with this deficit in learning capacity. Furthermore, $GYS1^{Nestin-KO}$ mice showed greater susceptibility to hippocampal seizures and myoclonus following the administration of kainate and/or a brief train stimulation of Schaffer collaterals. Thus, these observations indicate that brain glycogen plays a protective role in the prevention of brain seizures (Lopez-Ramos et al., 2015).

However, since GS was ablated from both astrocytes and neurons in these animals, it was not possible to dissect whether these abnormalities were due to the lack of astrocytic or neuronal glycogen. Therefore, to address the existence and relevance of an active glycogen metabolism in neurons *in vivo*, we generated a new mouse model lacking GS specifically in the Camk2a-positive neurons of the forebrain, including the prefrontal cortex and hippocampal pyramidal cells involved in CA3-CA1 synapses ($GYS1^{Camk2a-KO}$).

These animals showed decreased long-term potentiation (LTP) evoked in the hippocampal CA3-CA1 synapse and a significant deficiency in the acquisition of an instrumental learning task – a type of associative learning involving both prefrontal and hippocampal circuits. In contrast, they did not show differences in a fear-conditioning task, which involves medial prefrontal-amygdala circuits. Furthermore, these mice did not present the greater susceptibility to hippocampal seizures and myoclonus observed in the $GYS1^{Nestin-KO}$ model.

These results unequivocally demonstrate the presence of an active glycogen metabolism in neurons *in vivo* and its fundamental role in the proper acquisition of new motor and cognitive abilities and in the changes in synaptic strength underlying such acquisition.

MATERIALS AND METHODS

Animals

Experiments were carried out in C57BL/6 male mice aged 5.4 ± 1.3 months ($GYS1^{Camk2a-KO}$) and 5.1 ± 1.7 months (control littermates) (n = 15 for each group). All experiments were carried out following Spanish (BOE 34/11370-421, 2013) and European Union (2010/63/EU) regulations on the use of laboratory animals. All experimental protocols were approved by the Ethics Committee of the Pablo de Olavide University. Animals were kept in collective cages (up to five animals per cage) on a 12-h light/dark cycle with constant temperature (21 ± 1°C) and humidity (50 ± 5%) until the beginning of the experiments. Afterward, they were kept in individual cages until the end of the study. Unless otherwise indicated, animals were allowed access *ad libitum* to commercial mouse chow and water.

Biochemical Analyses

Animals were anesthetized, perfused intracardiacally with saline, and killed by decapitation. Brains were removed and cortexes, hippocampi and cerebella were dissected under a loupe, frozen on liquid nitrogen and stored at −80°C until use. For western blot analyses, protein homogenates of the different regions were obtained using the following buffer: 25 mM Tris–HCl (pH 7.4), 25 mM NaCl, 1% Triton X-100, 0.1% SDS, 0.5 mM EGTA, 10 mM sodium pyrophosphate, 1 mM sodium orthovanadate, 10 mM NaF, 25 nM okadaic acid and a protease inhibitor cocktail tablet (Roche). Homogenates were loaded in 10% acrylamide gels for SDS-PAGE and transferred to Immobilon membranes (Millipore). The antibody against GYS1 used was ref. 3886 from Cell Signaling. Proteins were detected by the ECL method (Immobilon Western Chemiluminescent HRP Substrate, Millipore) and loading control of the western blot membrane was performed using the REVERT total protein stain. For quantitative (q)PCR, total RNA was isolated from frozen brain region samples using Trizol reagent (Life Technologies, Carlsbad, CA, United States), purified with an RNeasy Mini Kit (Qiagen, Hilden, Germany) and treated with DNase I (Qiagen) to degrade genomic DNA. Reverse transcription was performed using qScript cDNA Synthesis Kit (Quanta Biosciences, Beverly, MA, United States). qPCR was performed using a Quantstudio 6 Flex (Applied Biosystems, Foster City, CA, United States). The following mouse-specific SYBRgreen set of primers (Sigma, Madrid, Spain) was used: Gys1 (forward: 5′-CAGAGCAAAGCACGAATCCA-3′; reverse: 5′-CATAGCG GCCAGCGATAAAG-3′); Gys2 (forward: 5′-ACCAAGGCC AAAACGACAG-3′; reverse: 5′-GGGCTCACATTGTTCTACT TGA-3′) and beta-2 microglobulin (b2M), used as a housekeeping gene (forward: 5′-ATGCACGCAGAAAG AAATAGCAA-3′; reverse: 5′-AGCTATCTAGGATATTTCC AATTTTTGAA-3′). All the samples were run as triplicates. For representation of the results: dCt was calculated as: Ct (b2M)-Ct (gene of interest), and average dCt from control hippocampus was used to calculate ddCT. Results are expressed as 2^ddCt in relative units for each brain region and genotype analyzed.

Operant Conditioning

Following previous descriptions by some of the authors of this paper (Madronal et al., 2010; Jurado-Parras et al., 2012), training and testing was done in three Skinner box operant chambers (12.5 × 13.5 × 18.5 cm) (MED Associates, St. Albans, VT, United States). Each module was housed within a sound-attenuating chamber (90 × 55 × 60 cm), which was constantly lit (19 W lamp) and exposed to 45-dB white noise (Cibertec, S.A., Madrid, Spain). Each Skinner box was equipped with a food

dispenser from which pellets (MLabRodent Tablet, 20 mg; Test Diet, Richmond, IN, United States) were released by pressing a lever. Before training, mice were handled daily for 5–7 days and food-deprived to 90% of their free-feeding weight. Training took place for 20 min on successive days, in which mice were trained to press the lever to receive pellets from the food dispenser using a fixed-ratio (1:1) schedule. The start and end of each session was indicated by a tone (2 kHz, 200 ms, 70 dB) provided by a loudspeaker located in the recording chamber. Animals were maintained on this fixed-ratio (1:1) schedule until they reached the selected criterion, namely until they obtained $\geq$ 20 pellets in two successive sessions. The mean number of pellets received by each animal during these two sessions was calculated.

In the following experimental step, conditioning was carried out for 10 days using a light/dark protocol. In this protocol, only lever presses performed by the animal during the light period (20 s), in which a small light bulb located over the lever was switched on, were reinforced with a pellet. Lever presses performed during the dark period (20 $\pm$ 10 s) were not rewarded. In addition, lever presses during the dark period restarted the dark protocol for an additional random (1–10 s) time. The number of lever presses carried out during the light and dark periods were counted. The light/dark coefficient was calculated as follows: (number of lever presses during the light period − number of lever presses during the dark period)/total number of lever presses. As we previously described, control mice never obtain positive coefficients > 0.2 in this task (Hasan et al., 2013). Conditioning programs, lever presses, and pellets rewarded were monitored and recorded by a computer, using a MED-PC program (MED Associates, St. Albans, VT, United States). All operant sessions were filmed with a synchronized video capture system (Sony HDR-SR12E, Tokyo, Japan).

Surgery

A minimum of a week after the end of operant conditioning experiments, animals were anesthetized with 0.8–3% halothane delivered from a calibrated Fluotec 5 (Fluotec-Ohmeda, Tewksbury, MA, United States) vaporizer at a flow rate of 1–2 L/min oxygen. Animals were implanted with bipolar stimulating electrodes at the right Schaffer collateral-commissural pathway of the dorsal hippocampus (2 mm lateral and 1.5 mm posterior to bregma; depth from brain surface, 1.3 mm) (Paxinos and Franklin, 2001) and with two recording electrodes in the ipsilateral CA1 area (1.2 mm lateral and 2.2 mm posterior to bregma; depth from brain surface, 1.3 mm). They were also implanted bilaterally with two pairs of recording electrodes in the prelimbic cortex (0.3 mm lateral, 1.75 mm anterior to bregma, and 1.8 from brain surface) (Paxinos and Franklin, 2001). Electrodes were made of 50 μm Teflon-coated tungsten wire (Advent Research Materials Ltd., Eynsham, England). The final location of the CA1 recording electrode was determined using as a guide the field potential depth profile evoked by paired (40 ms of interval) pulses presented at the Schaffer collateral pathway. Two bare silver wires (0.1 mm) were affixed to the skull as ground. The 10 wires were connected to a 4-pin and a 6-pin socket. Sockets were fixed to the skull with the help of small screws and dental cement (see Gruart et al., 2006 for details).

Fear Conditioning

Fear conditioning was carried out as previously described (Ortiz et al., 2010; Madronal et al., 2016). A week after surgery, animals were subjected to a fear conditioning test. On the first training day, they were subjected to a three-shock acquisition protocol in a fear-conditioning box (25 × 25 × 35 cm; TSE Systems GmbH, Bad Homburg, Germany) provided with a metallic grid floor, transparent Plexiglas wall, 70% ethanol smell, and 800 lux illumination (context A). Mice were allowed to explore the box for 3 min, after which a 30-s, 80-dB, 7.5-kHz tone was given as a conditioning stimulus (CS). The last 2 s of the tone overlapped with a 0.4-mA foot shock as unconditioned stimulus (US). The CS-US pairing was repeated two more times with 2-min intervals between each presentation and following the last one. Therefore, the fear conditioning acquisition test lasted for 10.5 min. Two days after the test session, animals were placed in the same box for 6 min but no CS or US was given. Finally, the cued fear test was repeated 3 days later in the same fear-conditioning box but this time with different floor (opaque gray plastic) and walls (black plastic), including acetic acid smell and 400 lux illumination (context B). Mice were allowed to explore the box for 3 min, after which the CS was presented continuously for another 3 min (total duration 6 min).

Input/Output Curves, Paired Pulse Facilitation, and LTP in Behaving Mice

Local field potentials (LFPs) were recorded with the animal located in a small (5 × 5 × 5 cm) box, aimed to avoid overwalking (Gruart et al., 2006). For input/output curves, mice were stimulated at the CA3-CA1 synapse with single pulses at increasing intensities (0.02–0.4 mA). We also checked the effects of paired pulses at various (10, 20, 40, 100, 200, and 500 ms) inter-pulse intervals, using intensities corresponding to ∼ 40% of the amount necessary to evoke a saturating response. In all cases, pulses of a given intensity and/or interval were repeated 10 times at a rate of 3/min, to avoid interferences with slower short-term potentiation (augmentation) or depression processes (Zucker and Regehr, 2002); moreover, to avoid any cumulative effect, intensities and/or intervals were presented at random.

To evoke LTP in behaving mice, we followed procedures described previously (Gruart et al., 2006). Baseline field excitatory postsynaptic potential (fEPSP) values evoked at the CA3-CA1 synapse were collected 15 min prior to LTP induction using single 100 μs, square, biphasic pulses. Pulse intensity was set at ∼40% of the amount necessary to evoke a maximum fEPSP response (0.15–0.25 mA) – i.e., well below the threshold for causing a population spike. For LTP induction, animals were presented with a high-frequency stimulus (HFS) protocol consisting of five 200 Hz, 100-ms trains of pulses at a rate of 1/s, repeated six times, at intervals of 1 min. Thus, a total of

600 pulses were presented during the HFS session. To avoid evoking large population spikes and/or electroencephalographic seizures, the stimulus intensity during HFS was set at the same value as that used for generating baseline recordings. After each HFS session, the same stimuli were presented individually every 20 s for 60 additional min and for 30 min on the following 4 days.

Hippocampal Seizures Evoked by Kainate Injection

In order to determine the propensity of control and $GYS1^{Camk2a-KO}$ mice to generate convulsive seizures, animals were injected (i.p.) with the AMPA/kainate receptor agonist kainic acid (8 mg/kg; Sigma, St. Louis, MO, United States) dissolved in 0.1 M phosphate buffered saline (PBS) pH = 7.4. LFPs were recorded in the hippocampal CA1 area from 5 min before to 60 min after kainate injections (see Valles-Ortega et al., 2011 for details).

Histology

Once the experiments had ended, mice were deeply re-anesthetized (sodium pentobarbital, 50 mg/kg) and perfused transcardially with saline and 4% phosphate-buffered paraformaldehyde. Their brains were removed, postfixed overnight at 4°C, and cryoprotected in 30% sucrose in PBS. Sections were obtained in a microtome (Leica, Wetzlar, Germany) at 50 μm. Selected sections, including the dorsal hippocampus and the prefrontal cortex, were mounted on gelatinized glass slides and stained with 0.1% toluidine blue to determine the location of stimulating and recording electrodes.

Experimental Design and Statistical Analysis

fEPSPs, 1-V rectangular pulses corresponding to lever presses, pellet delivery, tone and shock presentations, and brain stimulation were stored digitally on a computer through an analog/digital converter (CED 1401 Plus, CED, Cambridge, England). Recorded videos were synchronized to the CED recording system. Data were analyzed off-line for quantification of each animal's performance in the Skinner box, in the fear conditioning test, and for fEPSP recordings with the Spike 2 (CED) program. The slope of evoked fEPSPs was computed as the first derivative (V/s) of fEPSP recordings (volts). Five successive fEPSPs were averaged, and the mean value of the slope during the rise-time (i.e., the period of the slope between the initial 10% and the final 10% of the fEPSP) was determined. The power spectrum of recorded LFPs activity was computed with the help of the Mat Lab 7.4.0 software (MathWorks, Natick, MA, United States), using the fast Fourier transform with a Hanning window, expressed as relative power and averaged across each recording session (Munera et al., 2000). Computed results were processed for statistical analysis using the IBM SPSS Statistics 18.0 (IBM, Armonk, NY, United States). Data are represented as the mean ± SEM. Statistical significance of differences between groups was inferred by one-way ANOVA and ANOVA for repeated measures (data by groups), with a contrast analysis (Dunnett's posttest) for a further study of significant differences. Statistical significance was set at $p < 0.05$.

RESULTS

Generation of Neuron-Specific $GYS1^{Camk2a-KO}$ Animals

$GYS1^{Camk2a-KO}$ animals were generated by crossing GYS1 conditional knockout, based on the Cre/lox technology (Duran et al., 2013), with Camk2a Cre animals, which express Cre recombinase specifically in Camk2a-positive neurons of the forebrain (Tsien et al., 1996). Homozygous conditional non-expressing Cre littermates were used as controls. To corroborate the efficiency of the deletion, we analyzed the expression of GYS1 by qPCR and western blot in three regions of the brain, namely the hippocampus, cortex and cerebellum. qPCR results showed a significantly lower expression of GYS1 in hippocampus and cortex of $GYS1^{Camk2a-KO}$ mice. As expected, no differences in GYS1 expression were found between the cerebella of the two genotypes, since the Camk2a-cre mouse line does not have a significant Cre recombinase expression in this region (Tsien et al., 1996) (**Figure 1A**). The difference between control and $GYS1^{Camk2a-KO}$ mice was greater in the cortex than in the hippocampus, probably due to the higher ratio of astrocytes to neurons present in the latter (Keller et al., 2018), which would dilute the difference in GYS1 expression that results from knocking out only Camk2a neurons. To discard a compensatory upregulation, GYS2 expression levels were also measured. However, no significant expression in any of the regions in either genotype was detected (data not shown). At the protein level, western blot analyses also showed a significant difference in GYS1 in the cortex and hippocampus, but not in the cerebellum (**Figure 1B**).

Differences in the Electrophysiological Properties of the CA3-CA1 Synapse in Control and $GYS1^{Camk2a-KO}$ Mice

To determine functional differences in the electrophysiological properties of hippocampal circuits, we studied input/output curves, paired-pulse facilitation, and LTP evoked at the CA3-CA1 synapse in behaving control and $GYS1^{Camk2a-KO}$ mice (**Figure 2**). First, we examined the response of CA1 pyramidal neurons to paired-pulses (40 ms of inter-pulse intervals) of increasing intensity (0.02–04 mA) presented to the ipsilateral Schaffer collaterals (**Figure 2A**). Control and $GYS1^{Camk2a-KO}$ mice presented similar increases in the slope of fEPSP evoked at the CA3-CA1 synapse by the stimuli presented to the CA3 area (**Figure 2B**). These two relationships were best fitted by sigmoid curves ($r \geq 0.99$; $p < 0.0001$; not illustrated), thereby suggesting the normal functioning of the CA3-CA1 synapse in both groups.

The paired-pulse facilitation evoked in control and $GYS1^{Camk2a-KO}$ mice was then analyzed with increasing inter-pulse intervals (10, 20, 40, 100, 200, 500 ms), but presenting a fix stimulus intensity (40% of asymptotic values).

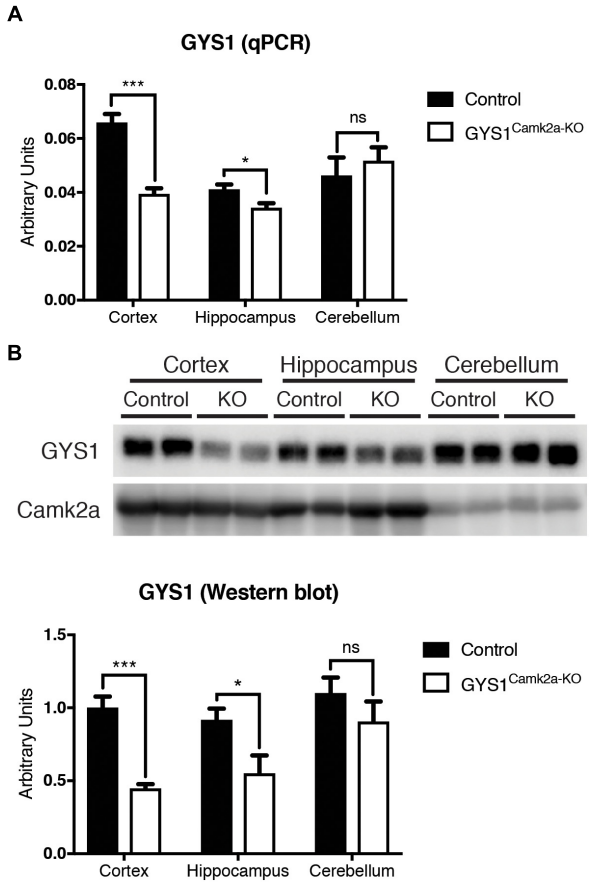


FIGURE 1 | Analysis of GYS1 expression in brain regions of control and $GYS1^{Camk2a-KO}$ mice. **(A)** qPCR analysis of GYS1 gene expression. The expression of GYS1 was measured in the cortex, hippocampus and cerebellum of control ($n = 4$) and $GYS1^{Camk2a-KO}$ mice ($n = 5$). The data shown are mean ± SEM of 2^ddCt in relative units for each genotype analyzed. Significant differences between groups were found in the cortex ($p < 0.0001$) and hippocampus ($p = 0.0383$), but not in cerebellum. **(B)** Western blot analyses of GYS1 protein and quantification of the results. Protein homogenates of the same regions were analyzed by western blot with an antibody specific for GYS1 protein ($n = 4$ per region and genotype). Again significant differences between groups were found in the cortex ($p = 0.0006$) and hippocampus ($p = 0.0474$), but not in the cerebellum. Statistics were calculated using unpaired *t*-test, statistical values. $^*p < 0.05$, $^{***}p < 0.001$.

Both groups of mice presented a paired pulse facilitation at short (20 and 40 ms) inter-pulse intervals (**Figure 2C**). Although control mice presented slightly larger facilitation to paired pulses than $GYS1^{Camk2a-KO}$ animals, no significant differences were observed.

We next studied LTP in the two groups of behaving mice as a reflection of synaptic plasticity. The CA3-CA1 synapse is involved in the acquisition of various kinds of associative learning tasks and is usually selected for evoking LTP in behaving mice (Gruart et al., 2006). For baseline values, animals were stimulated every 20 s for ≥15 min at the implanted Schaffer collaterals (**Figure 2D**). Afterward, they were presented with the high frequency stimulation (HFS) protocol. Following HFS, the same single stimulus used to generate baseline records was presented at the initial rate (3/min) for another 60 min. Recording sessions were repeated for four additional days (30 min each; **Figure 2D**). Both groups of mice presented a significant increase in fEPSP slopes following the HFS session. However, the control group presented a larger and longer lasting LTP than the $GYS1^{Camk2a-KO}$ group. The point to point comparison between LTPs evoked in the two groups of mice indicated that WT animals presented larger LTP values for the five recording sessions and that these values were significantly different during the first two sessions ($p \leq 0.05$) (**Figure 2D**).

In summary, at the electrophysiological level, $GYS1^{Camk2a-KO}$ mice presented similar input/output curves and paired-pulse potentiation but less LTP than their littermate controls.

$GYS1^{Camk2a-KO}$ Mice Presented a Deficit in the Acquisition of an Instrumental Conditioning Task

The acquisition of operant conditioning tasks involves many cortical (medial prefrontal and motor cortices, hippocampus) and subcortical (dorsal and ventral striatum) structures (Jurado-Parras et al., 2012, 2013). The capacity of the two groups of mice to acquire these complex associative learning tasks was examined. Animals were trained in Skinner box modules to obtain a food pellet every time they pressed a lever located near the feeder (**Figure 3A**). In a first series of experiments, we checked the time (days) animals needed to learn this operant task, using a fixed-ratio (1:1) schedule. The criterion was to press the lever a minimum of 20 times/session for two successive 20-min sessions (**Figure 3B**, top diagram). A total of 13 controls (out of 15) and 15 $GYS1^{Camk2a-KO}$ (out of 15) mice reached the criterion for the fixed-ratio (1:1) schedule task in ≤10 days (8.8 ± 0.5 days for controls and 6.7 ± 0.7 days for KO; $t = 239.000$; $p = 0.017$; Shapiro–Wilk *t* test; **Figure 3C**). $GYS1^{Camk2a-KO}$ mice seemed to press the lever more frequently than controls (**Figure 3D**), which was suggestive of a sort of compulsive behavior in $GYS1^{Camk2a-KO}$. Animals from the two groups that reached the criterion for the fixed-ratio (1:1) schedule task in ≤10 days were further trained in a more complex task. In this case, they were rewarded [again in a fixed-ratio (1:1) schedule] only during the period in which a small light bulb, located over the lever, was switched on (**Figure 3B**, bottom diagram). Periods with light lasted for 20 s and were followed by dark periods during which the animal was not rewarded. Pressing the lever during the dark period punished the animal by delaying the reappearance of the light period by ≤10 additional seconds (see Jurado-Parras et al., 2012; Hasan et al., 2013). Control mice acquired this complex task earlier than $GYS1^{Camk2a-KO}$ mice, reaching significant differences during the first three training sessions (**Figure 3E**). Indeed, $GYS1^{Camk2a-KO}$ mice took longer (up to 5 sessions) to understand that pressing the lever during the dark period did not provide any reinforcement and, in addition, delayed the reappearance of light. In conclusion, the deficit in neuronal glycogen caused a significant impairment of the

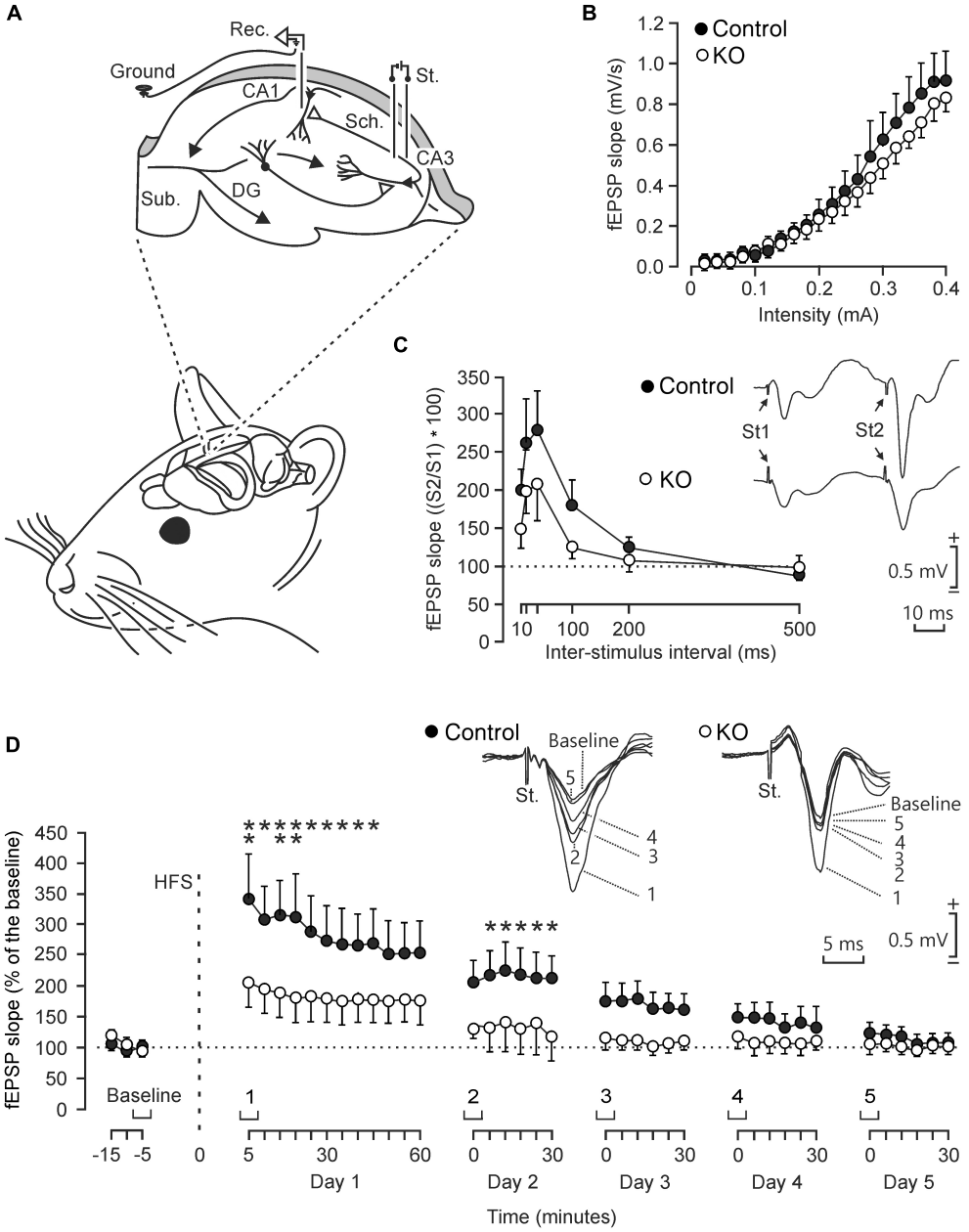


FIGURE 2 | Electrophysiological properties of hippocampal synapses in alert behaving control and GYS1$^{Camk2a-KO}$ mice. **(A)** Experimental design. Animals were chronically implanted with stimulating electrodes in CA3 Schaffer collaterals and with a recording electrode in the ipsilateral CA1 area. An extra wire was attached to the bone as ground. DG, dentate gyrus; Sub., subiculum. Adapted from Duran et al. (2013). **(B)** Input/output curves of fEPSPs evoked at the CA3-CA1 synapse by paired (40 ms of inter-pulse interval) pulses of increasing intensities (0.02–0.4 mA) in control (n = 8; black circles) and GYS1$^{Camk2a-KO}$ (n = 8; white circles) mice. Data are represented as mean ± SEM. No significant differences [$F_{(19,266)}$ = 0.579; p = 0.92] were observed between groups. **(C)** In addition, no significant [$F_{(5,110)}$ = 0.753; p = 0.586] differences in paired-pulse facilitation between control (n = 12; black circles) and GYS1$^{Camk2a-KO}$ (n = 12; white circles) mice were detected. The data shown are mean ± SEM slopes of the 2nd fEPSP expressed as a percentage of the first of six (10, 20, 40, 100, 200, 500) inter-pulse intervals. Selected fEPSP paired traces (40 ms of inter-pulse interval) collected from representative control and GYS1$^{Camk2a-KO}$ mice are shown at the top right. **(D)** The two graphs illustrate the time course of LTP evoked in the CA3-CA1 synapse (fEPSP mean ± SEM) of control (n = 14; black circles) and GYS1$^{Camk2a-KO}$ (n = 14; white circles) mice following a HFS session. The HFS was presented after 15 min of baseline recordings, at the time marked by the dashed line. LTP evolution was monitored over 5 days. At the top, illustrated representative examples of fEPSPs from representative control and GYS1$^{Camk2a-KO}$ mice collected at the times indicated in the bottom graphs. fEPSP slopes are given as a percentage of fEPSP values collected during baseline recordings (100%). Although the two groups presented significant ($p < 0.001$) increases (ANOVA, two-tailed) in fEPSP slopes after HFS when compared with baseline recordings, the control group showed a larger and longer lasting LTP [$F_{(38,988)}$ = 2.049; $p < 0.001$] than GYS1$^{Camk2a-KO}$ mice. fEPSP slopes collected from control animals were significantly larger than those from GYS1$^{Camk2a-KO}$ mice at the indicated times (*$p < 0.05$; **$p < 0.01$).

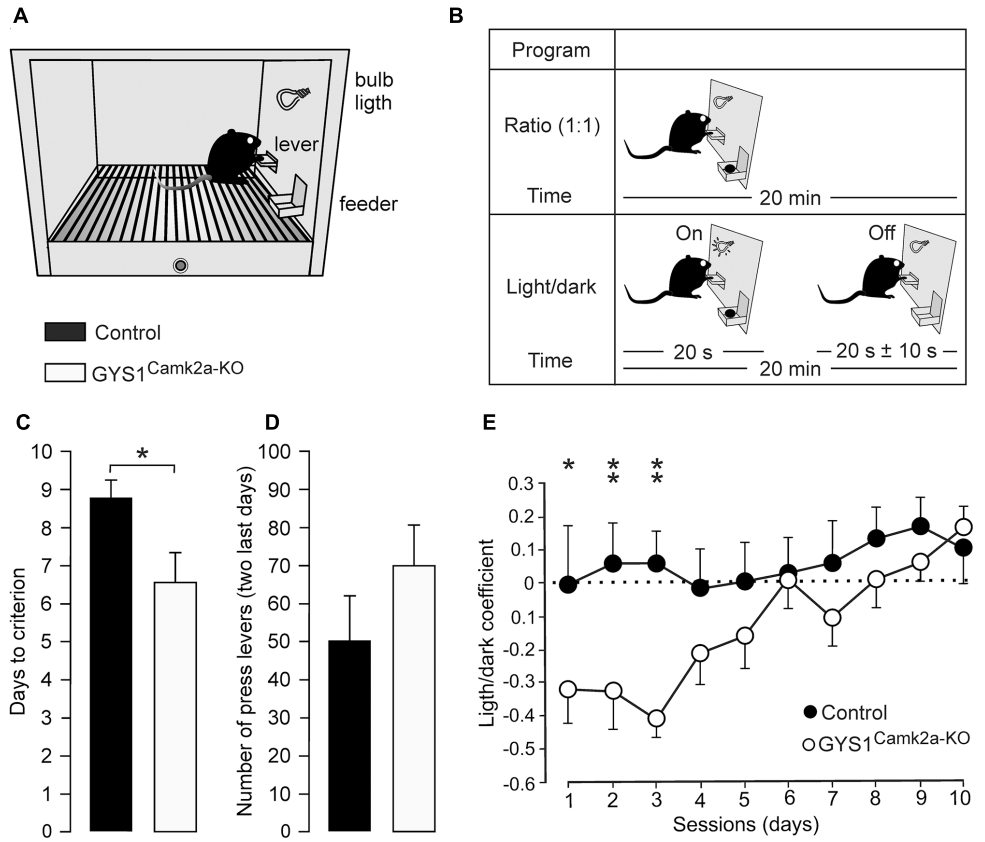


FIGURE 3 | Performance of control and GYS1$^{Camk2a-KO}$ mice in an operant conditioning task. **(A)** Experimental setup. Mice were trained in a Skinner box to press a lever to obtain a food pellet, with a fixed-ratio (1:1) schedule. Adapted from Duran et al. (2013). **(B)** Animals were trained with two programs of increasing difficulty. As illustrated in the top diagram, they were first trained to acquire a fixed-ratio (1:1) schedule until obtaining 20 pellets/20 min session on two successive days (criterion). Afterward, lever presses were rewarded only when a light bulb was switched on (see bottom diagram). **(C)** Time to reach the selected criterion for control (n = 13) and GYS1$^{Camk2a-KO}$ (n = 15) mice (t = 239.000; p = 0.017; Shapiro–Wilk t test). **(D)** Data collected from the first 2 days after reaching the criterion with the fixed-ratio (1:1) schedule. Illustrated data correspond to the mean ± SEM collected from control (n = 13) and GYS1$^{Camk2a-KO}$ (n = 15) animals. Note that although GYS1$^{Camk2a-KO}$ mice pressed the lever more frequently than the control group, there were no significant differences between groups (U = 58.5; p = 0.13; Mann–Whitney U statistic test). **(E)** Performance of control (n = 13) and GYS1$^{Camk2a-KO}$ (n = 14) mice during the light/dark test. Note that although both groups showed an improvement in performance across sessions [$F_{(1,225)}$ = 10.49; p < 0.01], control mice outperformed GYS1$^{Camk2a-KO}$ mice [$F_{(9,225)}$ = 2.82; p = 0.01]. The light/dark coefficient was calculated as follows: (number of lever presses during the light period – number of lever presses during the dark period)/total number of lever presses. For individual sessions *p = 0.05; **p = 0.01.

learning capacity of GYS1$^{Camk2a-KO}$ mice, which was probably aggravated by deficient control of compulsive behaviors.

GYS1$^{Camk2a-KO}$ Mice Showed a Similar Performance to Control Animals in a Fear Conditioning Task

Medial prefrontal-amygdala circuits are actively involved in the control of fear conditioning (Dejean et al., 2016). In particular, it has been shown that delta oscillations synchronize these circuits during fear conditioning (Karalis et al., 2016). Given these observations, we carried out a fear conditioning test in control (n = 14) and GYS1$^{Camk2a-KO}$ (n = 15) mice (**Figures 4A,B**). Freezing time during the context test was similar for the two groups (control, 190.5 ± 9.0 s; GYS1$^{Camk2a-KO}$, 182.5 ± 10.0 s). In addition, the total freezing time during the cued fear test was also similar for both groups (control, 136.7 ± 17.2 s; GYS1$^{Camk2a-KO}$, 136.5 ± 22.7 s) (**Figure 4C**). According to these results, amygdala control of fear behavior (Dejean et al., 2016) was not altered in GYS1$^{Camk2a-KO}$ mice.

Susceptibility to Kainate-Induced Epilepsy in Control and GYS1$^{Camk2a-KO}$ Mice

Local field potentials recorded in the hippocampus of control (n = 12) and GYS1$^{Camk2a-KO}$ (n = 12) mice presented no significant differences in their respective spectral powers (**Figures 5A,B**). In addition, we checked the susceptibility of the two groups to a single and low dose (8 mg/kg) i.p. injection of kainate (**Figures 5C–E**). Both control (6 out of 13; 43.2%) and GYS1$^{Camk2a-KO}$ (10 out of 15; 66.7%) mice presented spontaneous hippocampal seizures after kainate injection, with no significant differences between groups (Chi-square = 0.506

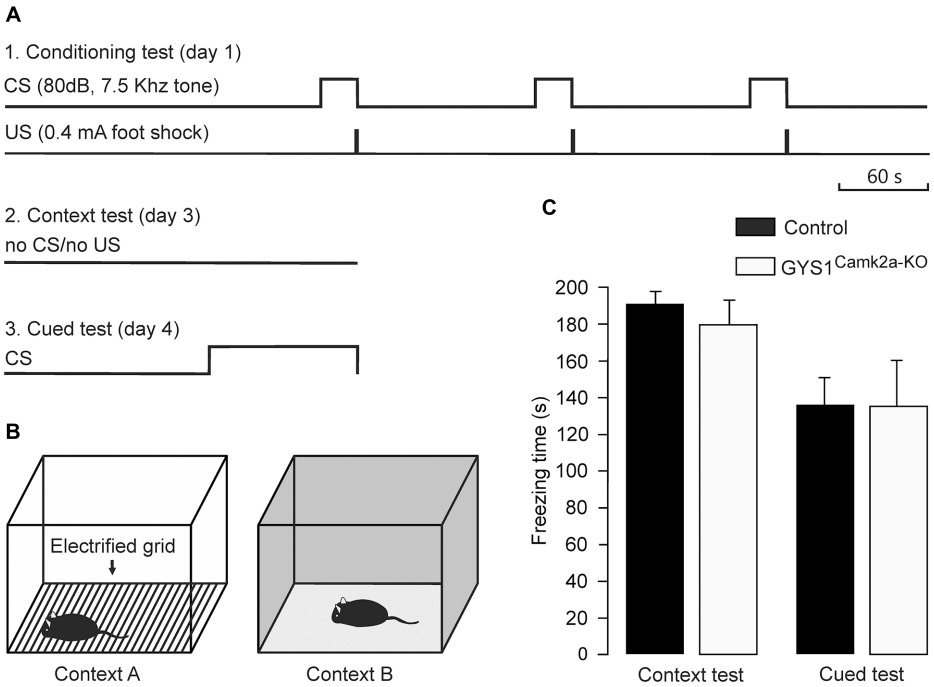


FIGURE 4 | Performance of control and GYS1$^{Camk2a-KO}$ mice in a fear conditioning task. **(A)** Experimental design. During the conditioning test (1), animals were allowed to explore context A for 3 min, after which they were presented with a conditioning tone for 30 s (CS). The tone co-terminated with a foot shock (0.4 mA, 2 s). As illustrated, the CS-US pairing was repeated two more times. For the context test (2), the animal was located in the same box for 6 min in absence of CS or US presentations. Finally, for the cued test (3), the animal was located in context B for a control period of 3 min, followed by 3 min with a CS presentation. **(B)** Diagrammatic representation of contexts A (left) and B (right). **(C)** No significant differences between the two groups (n = 14 control and n = 15 GYS1$^{Camk2a-KO}$ mice) were observed for either of context (t = 0.595; 27 degrees of freedom; p = 0.557) or the cued tests (t = 0.0166; 27 degrees of freedom; p = 0.987).

with 1 degree of freedom; p = 0.477) (**Figure 5D**). The mean duration of kainate-evoked seizures was also similar between groups (control: 214 ± 111 s; GYS1$^{Camk2a-KO}$: 242 ± 57 s; $F_{(1,14)}$ = 0.0604; p = 0.809; ANOVA and Shapiro–Wilk test) (**Figure 5E**). These results indicate that susceptibility to kainate-induced epilepsy is not significantly altered in GYS1$^{Camk2a-KO}$ mice with respect to littermate controls.

DISCUSSION

Brain glycogen is involved in multiple functions, including learning and memory. In this regard, in a previous study we showed that GYS1$^{Nestin-KO}$ mice, which are devoid of glycogen in the brain, show a significant impairment of learning capacity and in the concomitant activity-dependent changes in synaptic strength (Duran et al., 2013). In a subsequent report with the same mouse model, we demonstrated the importance of brain glycogen in resistance to epileptic seizures (Lopez-Ramos et al., 2015). However, since the GYS1 gene is knocked out in both astrocytes and neurons in these animals, it was not possible to determine the contribution of each cell type to these abnormalities.

Studying glycogen in the brain is challenging due to the rapid degradation of this polysaccharide after the interruption of brain circulation, which inevitably results in the loss of glycogen during histologic preparation of tissue even when perfusion of fixatives is used. Traditionally, it has been considered that brain glycogen is present only in astrocytes, where it is easy to identify thanks to its relatively high concentration (Cataldo and Broadwell, 1986; Hertz and Chen, 2018). However, the presence of the polysaccharide in specific subsets of neurons (e.g., motoneurons) has also been reported (Cammermeyer and Fenton, 1981; Borke and Nau, 1984). The most thorough analysis performed to date of the localization of brain glycogen in microwave-fixed brains (which stops enzymatic activity immediately and thus preserves the metabolic state) indicates that neurons may also contain glycogen, although at much lower concentrations than astrocytes (Oe et al., 2016). The notion of an active glycogen metabolism in neurons is supported by a key observation, namely the accumulation of glycogen in several pathological conditions like Lafora disease and Pompe disease (Sidman et al., 2008; Duran et al., 2014). However, this observation does not shed any light on the physiological role of the polysaccharide in these cells. In this regard, we previously demonstrated that primary cultured neurons have an active glycogen metabolism that protects them from hypoxia (Saez et al., 2014). However, since primary cultured neurons have embryonic features, the importance of neuronal glycogen in adult brains could differ to that in *in vitro* conditions.

To address the physiological role of neuronal glycogen, we generated a novel mouse model depleted of glycogen only in

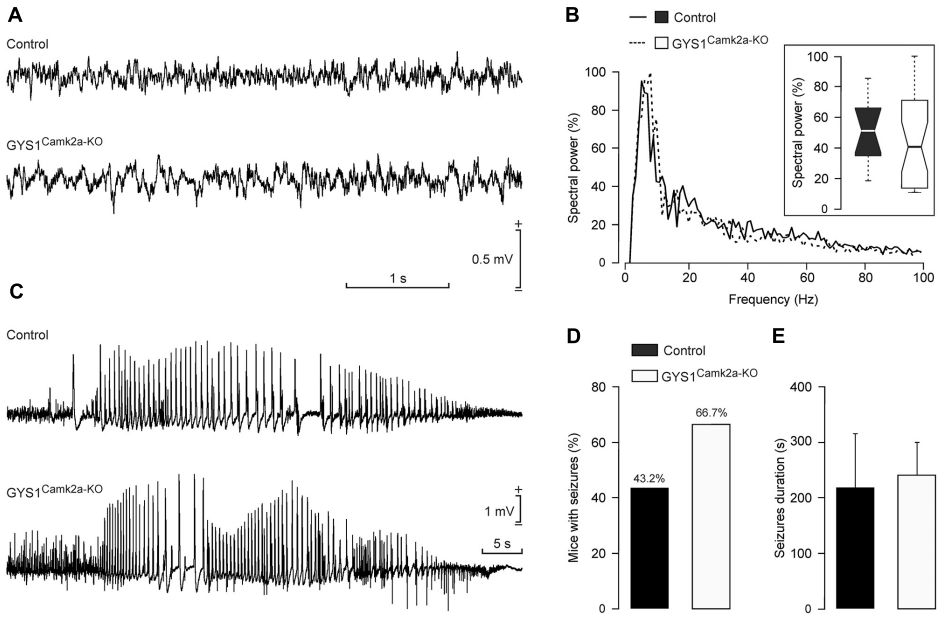


FIGURE 5 | Susceptibility of control and GYS1$^{Camk2a-KO}$ mice to kainate. **(A)** RLFPs recorded in the CA1 area of representative control and GYS1$^{Camk2a-KO}$ mice. **(B)** Spectral power of LFPs (60-s segments collected from n = 12 control and n = 12 GYS1$^{Camk2a-KO}$ mice). The inset illustrates the global boxplot of peak spectral powers [$F_{(1,22)}$ = 0.07; p = 0.7908]. **(C)** Representative examples of hippocampal seizures evoked in control and GYS1$^{Camk2a-KO}$ mice following the administration of 8 mg/kg i.p. of kainate. **(D)** Percentage of control (n = 13) and GYS1$^{Camk2a-KO}$ (n = 15) mice presenting spontaneous seizures at the CA1 area during the recording period (60 min). No significant differences between groups (Chi-square = 0.506 with 1 degree of freedom; p = 0.477) were observed. **(E)** Mean duration of kainate-evoked seizures in control and GYS1$^{Camk2a-KO}$ mice. No significant differences between groups were observed [$F_{(1,14)}$ = 0.0604; p = 0.809; ANOVA and Shapiro–Wilk test].

neurons. To this end, we used Camk2a Cre to delete GYS1 specifically in Camk2a neurons of the forebrain, including those of the CA1 pyramidal cell layer of the hippocampus, thus generating GYS1$^{Camk2a-KO}$ mice. We selected these neurons since they are involved in memory and learning processes and participate in the hippocampal CA3-CA1 synapse, whose function can be analyzed electrophysiologically (Gruart et al., 2006). Although initially reported to occur exclusively in CA1 pyramidal neurons (Tsien et al., 1996), Cre recombinase-driven gene edition in Camk2A-Cre mice takes place in other pyramidal neurons of the forebrain and cortex (Victoria et al., 2016), which could thus contribute to the electrophysiological and learning deficits observed in GYS1$^{Camk2a-KO}$ animals – these mostly related to prefrontal functions related to the acquisition of instrumental tasks (Jurado-Parras et al., 2012; Hasan et al., 2013) and to LTP induction in the intrinsic hippocampal circuit (Gruart et al., 2006).

Synaptic changes evoked by the presentation of a pair of pulses are commonly accepted as an indication of presynaptic short-term plasticity of hippocampal synapses, related to the process of neurotransmitter release (Zucker and Regehr, 2002). Thus, paired-pulse stimulation is used as an indirect measure of changes in the probability of neurotransmitter release at the presynaptic terminal (Fernandez De Sevilla et al., 2002; Zucker and Regehr, 2002; Lauri et al., 2007). Unlike GYS1$^{Nestin-KO}$ mice (Duran et al., 2013), GYS1$^{Camk2a-KO}$ animals did not show significant differences in paired-pulse facilitation with respect to their littermate controls. However, the trend may indicate a lower probability of neurotransmitter release. In contrast, postsynaptic LTP responses, a type of long-term synaptic plasticity, were significantly smaller in GYS1$^{Camk2a-KO}$ mice. These results resemble those obtained in GYS1$^{Nestin-KO}$ mice and indicate that neuronal glycogen participates in the correct establishment of LTP.

LTP has been proposed to be the mechanism underlying the acquisition of cognitive abilities at the cellular level. GYS1$^{Camk2a-KO}$ animals showed a deficit in the acquisition of a complex associative task requiring inhibition of spontaneous exploratory activities. Again, although of a smaller magnitude, these results resemble those found in GYS1$^{Nestin-KO}$ mice. Interestingly, fear conditioning was not affected in the neuron-specific KO mice, thereby indicating that other brain regions and circuits are not affected by the lack of glycogen in Camk2a neurons. Furthermore, and in contrast to GYS1$^{Nestin-KO}$ mice, neuron-specific KO mice did not show greater susceptibility to hippocampal seizures or myoclonus induced by kainate administration or train stimulation. These results suggest that this alteration in GYS1$^{Nestin-KO}$ mice is caused by the absence of astrocytic glycogen.

Interestingly, results collected during the operant conditioning task indicated that GYS1$^{Camk2a-KO}$ mice reached the selected criterion for the fixed ratio (1:1) before control animals. We assumed that this was the result of hyperactive behavior, which was confirmed by the light/dark

test. The light/dark test was designed to detect hyperactive or compulsive behaviors, and it has been successfully used in mice (Jurado-Parras et al., 2012; Hasan et al., 2013) and rats (Berger et al., 2017).

If glycogen in neurons is present at such low levels that make it very difficult to detect, then why is it important for brain function? Glycogen is mobilized very quickly and thus provides a faster way to obtain energy than through importing extracellular glucose. Furthermore, the product of glycogen breakdown is glucose-1P, which does not need the initial ATP required for glucose phosphorylation. Since the activity (and thus the energetic requirements) of neurons is pulsatile, a small amount of glycogen would be sufficient to cover this transient increase in energy needs. Furthermore, glycogen may be located in regions of high energetic demand, for example in synaptic boutons. If this were the case, the overall concentration of glycogen in neurons would still be low. In this regard, it is worth noting that glycogen molecules are small enough to fit into narrow processes in which mitochondria cannot. Furthermore, the activation of GS and consequent synthesis of glycogen during LTP induction could represent one of the mechanisms of synaptic plasticity.

In previous reports we showed that glycogen accumulation over a modest concentration is deleterious for neurons (Duran et al., 2012, 2014), thus raising the question as to why neurons have indeed maintained GS expression throughout evolution if its activation and the consequent deposition of glycogen cause the death of this cell population. This paradox led Magistretti and Allaman to refer to GS as a neuronal Trojan horse (Magistretti and Allaman, 2007). The observations described here clearly indicate that neurons do need an active glycogen metabolism to ensure proper functioning. Therefore, the challenge faced by neurons is how to maintain functionally active GS without allowing glycogen deposits to damage them.

In the light of the results presented here, we propose that neuronal glycogen is responsible for some of the roles previously attributed exclusively to astrocytic glycogen (e.g., experiments using glycogen degradation inhibitors to study the importance of brain glycogen in learning) (Hertz and Chen, 2018). Therefore, the relevance of neuronal glycogen for brain function should be reconsidered.

DATA AVAILABILITY

All datasets generated for this study are included in the manuscript/supplementary files.

AUTHOR CONTRIBUTIONS

JD, JG, and JD-G conceived and designed the study. JD generated and bred the animal models. JD, OV, and IL-S performed the biochemical experiments and analyzed the data. AG and JD-G performed the electrophysiological and behavioral experiments, and analyzed the data. JD and JG wrote the first version of the manuscript. JD, OV, AG, and JD-G prepared the figures. All authors contributed to the improvement of the project and reviewed the final version of the manuscript.

FUNDING

IRB Barcelona is the recipient of a Severo Ochoa Award of Excellence from MINECO (Government of Spain). This study was supported by grants from the MINECO (BFU2017-82375-R to AG and JD-G and BFU2017-84345-P to JD and JG), the Junta de Andalucía (BIO122) to AG and JD-G, the CIBER de Diabetes y Enfermedades Metabólicas Asociadas (ISCIII, Ministerio de Ciencia e Innovación), and a grant from the National Institutes of Health (NIH-NINDS) (P01NS097197) to JG.

ACKNOWLEDGMENTS

The authors thank José María Gonzalez Martín, María Sánchez-Enciso, Anna Adrover, Emma Veza and Laura Alcaide for technical assistance.

REFERENCES

Berger, S. M., Fernandez-Lamo, I., Schonig, K., Fernandez Moya, S. M., Ehses, J., Schieweck, R., et al. (2017). Forebrain-specific, conditional silencing of staufen2 alters synaptic plasticity, learning, and memory in rats. *Genome Biol.* 18:222. doi: 10.1186/s13059-017-1350-8

Borke, R. C., and Nau, M. E. (1984). Glycogen, its transient occurrence in neurons of the rat CNS during normal postnatal development. *Brain Res.* 318, 277–284. doi: 10.1016/0165-3806(84)90032-4

Cammermeyer, J., and Fenton, I. M. (1981). Improved preservation of neuronal glycogen by fixation with iodoacetic acid-containing solutions. *Exp. Neurol.* 72, 429–445. doi: 10.1016/0014-4886(81)90234-x

Cataldo, A. M., and Broadwell, R. D. (1986). Cytochemical identification of cerebral glycogen and glucose-6-phosphatase activity under normal and experimental conditions. II. Choroid plexus and ependymal epithelia, endothelia and pericytes. *J. Neurocytol.* 15, 511–524. doi: 10.1007/bf01611733

Dejean, C., Courtin, J., Karalis, N., Chaudun, F., Wurtz, H., Bienvenu, T. C., et al. (2016). Prefrontal neuronal assemblies temporally control fear behaviour. *Nature* 535, 420–424. doi: 10.1038/nature18630

Duran, J., Gruart, A., Garcia-Rocha, M., Delgado-Garcia, J. M., and Guinovart, J. J. (2014). Glycogen accumulation underlies neurodegeneration and autophagy impairment in Lafora disease. *Hum. Mol. Genet.* 23, 3147–3156. doi: 10.1093/hmg/ddu024

Duran, J., Saez, I., Gruart, A., Guinovart, J. J., and Delgado-Garcia, J. M. (2013). Impairment in long-term memory formation and learning-dependent synaptic plasticity in mice lacking glycogen synthase in the brain. *J. Cereb. Blood Flow Metab.* 33, 550–556. doi: 10.1038/jcbfm.2012.200

Duran, J., Tevy, M. F., Garcia-Rocha, M., Calbo, J., Milan, M., and Guinovart, J. J. (2012). Deleterious effects of neuronal accumulation of glycogen in flies and mice. *EMBO Mol. Med.* 4, 719–729. doi: 10.1002/emmm.201200241

Fernandez De Sevilla, D., Cabezas, C., De Prada, A. N., Sanchez-Jimenez, A., and Buno, W. (2002). Selective muscarinic regulation of functional glutamatergic schaffer collateral synapses in rat CA1 pyramidal neurons. *J. Physiol.* 545, 51–63. doi: 10.1113/jphysiol.2002.029165

Gibbs, M. E., Anderson, D. G., and Hertz, L. (2006). Inhibition of glycogenolysis in astrocytes interrupts memory consolidation in young chickens. *Glia* 54, 214–222. doi: 10.1002/glia.20377

Gruart, A., Munoz, M. D., and Delgado-Garcia, J. M. (2006). Involvement of the CA3-CA1 synapse in the acquisition of associative learning in behaving mice. *J. Neurosci.* 26, 1077–1087. doi: 10.1523/jneurosci.2834-05.2006

Hasan, M. T., Hernandez-Gonzalez, S., Dogbevia, G., Trevino, M., Bertocchi, I., Gruart, A., et al. (2013). Role of motor cortex NMDA receptors in learning-dependent synaptic plasticity of behaving mice. *Nat. Commun.* 4:2258. doi: 10.1038/ncomms3258

Hertz, L., and Chen, Y. (2018). Glycogenolysis, an astrocyte-specific reaction, is essential for both astrocytic and neuronal activities involved in learning. *Neuroscience* 370, 27–36. doi: 10.1016/j.neuroscience.2017.06.025

Jurado-Parras, M. T., Gruart, A., and Delgado-Garcia, J. M. (2012). Observational learning in mice can be prevented by medial prefrontal cortex stimulation and enhanced by nucleus accumbens stimulation. *Learn. Mem.* 19, 99–106. doi: 10.1101/lm.024760.111

Jurado-Parras, M. T., Sanchez-Campusano, R., Castellanos, N. P., Del-Pozo, F., Gruart, A., and Delgado-Garcia, J. M. (2013). Differential contribution of hippocampal circuits to appetitive and consummatory behaviors during operant conditioning of behaving mice. *J. Neurosci.* 33, 2293–2304. doi: 10.1523/JNEUROSCI.1013-12.2013

Karalis, N., Dejean, C., Chaudun, F., Khoder, S., Rozeske, R. R., Wurtz, H., et al. (2016). 4-Hz oscillations synchronize prefrontal-amygdala circuits during fear behavior. *Nat. Neurosci.* 19, 605–612. doi: 10.1038/nn.4251

Keller, D., Ero, C., and Markram, H. (2018). Cell densities in the mouse brain: a systematic review. *Front. Neuroanat.* 12:83. doi: 10.3389/fnana.2018.00083

Lauri, S. E., Palmer, M., Segerstrale, M., Vesikansa, A., Taira, T., and Collingridge, G. L. (2007). Presynaptic mechanisms involved in the expression of STP and LTP at CA1 synapses in the hippocampus. *Neuropharmacology* 52, 1–11. doi: 10.1016/j.neuropharm.2006.06.017

Lopez-Ramos, J. C., Duran, J., Gruart, A., Guinovart, J. J., and Delgado-Garcia, J. M. (2015). Role of brain glycogen in the response to hypoxia and in susceptibility to epilepsy. *Front. Cell Neurosci.* 9:431. doi: 10.3389/fncel.2015.00431

Madronal, N., Delgado-Garcia, J. M., Fernandez-Guizan, A., Chatterjee, J., Kohn, M., Mattucci, C., et al. (2016). Rapid erasure of hippocampal memory following inhibition of dentate gyrus granule cells. *Nat. Commun.* 7:10923. doi: 10.1038/ncomms10923

Madronal, N., Lopez-Aracil, C., Rangel, A., Del Rio, J. A., Delgado-Garcia, J. M., and Gruart, A. (2010). Effects of enriched physical and social environments on motor performance, associative learning, and hippocampal neurogenesis in mice. *PLoS One* 5:e11130. doi: 10.1371/journal.pone.0011130

Magistretti, P. J., and Allaman, I. (2007). Glycogen: a trojan horse for neurons. *Nat. Neurosci.* 10, 1341–1342. doi: 10.1038/nn1107-1341

Munera, A., Gruart, A., Munoz, M. D., and Delgado-Garcia, J. M. (2000). Scopolamine impairs information processing in the hippocampus and performance of a learned eyeblink response in alert cats. *Neurosci. Lett.* 292, 33–36. doi: 10.1016/s0304-3940(00)01430-0

Oe, Y., Baba, O., Ashida, H., Nakamura, K. C., and Hirase, H. (2016). Glycogen distribution in the microwave-fixed mouse brain reveals heterogeneous astrocytic patterns. *Glia* 64, 1532–1545. doi: 10.1002/glia.23020

Ortiz, O., Delgado-Garcia, J. M., Espadas, I., Bahi, A., Trullas, R., Dreyer, J. L., et al. (2010). Associative learning and CA3-CA1 synaptic plasticity are impaired in D1R null, Drd1a-/- mice and in hippocampal siRNA silenced Drd1a mice. *J. Neurosci.* 30, 12288–12300. doi: 10.1523/JNEUROSCI.2655-10.2010

Paxinos, G., and Franklin, K. B. J. (2001). *The Mouse Brain in Stereotaxic Coordinates*. San Diego: Academic Press.

Saez, I., Duran, J., Sinadinos, C., Beltran, A., Yanes, O., Tevy, M. F., et al. (2014). Neurons have an active glycogen metabolism that contributes to tolerance to hypoxia. *J. Cereb. Blood Flow Metab.* 34, 945–955. doi: 10.1038/jcbfm.2014.33

Sidman, R. L., Taksir, T., Fidler, J., Zhao, M., Dodge, J. C., Passini, M. A., et al. (2008). Temporal neuropathologic and behavioral phenotype of 6neo/6neo Pompe disease mice. *J. Neuropathol. Exp. Neurol.* 67, 803–818. doi: 10.1097/NEN.0b013e3181815994

Suzuki, A., Stern, S. A., Bozdagi, O., Huntley, G. W., Walker, R. H., Magistretti, P. J., et al. (2011). Astrocyte-neuron lactate transport is required for long-term memory formation. *Cell* 144, 810–823. doi: 10.1016/j.cell.2011.02.018

Tsien, J. Z., Chen, D. F., Gerber, D., Tom, C., Mercer, E. H., Anderson, D. J., et al. (1996). Subregion- and cell type-restricted gene knockout in mouse brain. *Cell* 87, 1317–1326. doi: 10.1016/s0092-8674(00)81826-7

Valles-Ortega, J., Duran, J., Garcia-Rocha, M., Bosch, C., Saez, I., Pujadas, L., et al. (2011). Neurodegeneration and functional impairments associated with glycogen synthase accumulation in a mouse model of Lafora disease. *EMBO Mol. Med.* 3, 667–681. doi: 10.1002/emmm.201100174

Victoria, N. C., Marron Fernandez De Velasco, E., Ostrovskaya, O., Metzger, S., Xia, Z., Kotecki, L., et al. (2016). G protein-gated K(+) channel ablation in forebrain pyramidal neurons selectively impairs fear learning. *Biol. Psychiatry* 80, 796–806. doi: 10.1016/j.biopsych.2015.10.004

Zucker, R. S., and Regehr, W. G. (2002). Short-term synaptic plasticity. *Annu. Rev. Physiol.* 64, 355–405.

Conflict of Interest Statement: The authors declare that the research was conducted in the absence of any commercial or financial relationships that could be construed as a potential conflict of interest.

Copyright © 2019 Duran, Gruart, Varea, López-Soldado, Delgado-García and Guinovart. This is an open-access article distributed under the terms of the Creative Commons Attribution License (CC BY). The use, distribution or reproduction in other forums is permitted, provided the original author(s) and the copyright owner(s) are credited and that the original publication in this journal is cited, in accordance with accepted academic practice. No use, distribution or reproduction is permitted which does not comply with these terms.

frontiers in Cellular Neuroscience

ORIGINAL RESEARCH
published: 20 August 2019
doi: 10.3389/fncel.2019.00358

A Kinetic Map of the Homomeric Voltage-Gated Potassium Channel (Kv) Family

Rajnish Ranjan[1†‡], Emmanuelle Logette[1,2†], Michela Marani[2], Mirjia Herzog[1,2], Valérie Tâche[1], Enrico Scantamburlo[1], Valérie Buchillier[1] and Henry Markram[1,2*]*

[1] Blue Brain Project, Ecole Polytechnique Fédérale de Lausanne, Geneva, Switzerland, [2] Laboratory of Neural Microcircuitry, Brain Mind Institute, Ecole Polytechnique Fédérale de Lausanne, Lausanne, Switzerland

OPEN ACCESS

Edited by:
Maria Cristina D'Adamo,
University of Malta, Malta

Reviewed by:
Pietro Balbi,
IRCCS Scientific Clinical Institutes Maugeri (ICS Maugeri), Italy
Robert Brenner,
The University of Texas Health Science Center at San Antonio, United States

***Correspondence:**
Rajnish Ranjan
ranjan.rajnish@epfl.ch
Henry Markram
henry.markram@epfl.ch

[†]These authors have contributed equally to this work

[‡]Lead contact

Specialty section:
This article was submitted to Cellular Neurophysiology, a section of the journal Frontiers in Cellular Neuroscience

Received: 28 January 2019
Accepted: 19 July 2019
Published: 20 August 2019

Citation:
Ranjan R, Logette E, Marani M, Herzog M, Tâche V, Scantamburlo E, Buchillier V and Markram H (2019) A Kinetic Map of the Homomeric Voltage-Gated Potassium Channel (Kv) Family. Front. Cell. Neurosci. 13:358. doi: 10.3389/fncel.2019.00358

The voltage-gated potassium (Kv) channels, encoded by 40 genes, repolarize all electrically excitable cells, including plant, cardiac, and neuronal cells. Although these genes were fully sequenced decades ago, a comprehensive kinetic characterization of all Kv channels is still missing, especially near physiological temperature. Here, we present a standardized kinetic map of the 40 homomeric Kv channels systematically characterized at 15, 25, and 35°C. Importantly, the Kv kinetics at 35°C differ significantly from commonly reported kinetics, usually performed at room temperature. We observed voltage-dependent Q_{10} for all active Kv channels and inherent heterogeneity in kinetics for some of them. Kinetic properties are consistent across different host cell lines and conserved across mouse, rat, and human. All electrophysiology data from all Kv channels are made available through a public website (Channelpedia). This dataset provides a solid foundation for exploring kinetics of heteromeric channels, roles of auxiliary subunits, kinetic modulation, and for building accurate Kv models.

Keywords: Kv channel, electrophysiology, automated patch clamp, kinetics, temperature, Q_{10}, modeling, database

HIGHLIGHTS

- A reference map of kinetics of all 40 homomeric Kv channels at 15, 25, and 35°C.
- Kv kinetics are consistent across cell lines and conserved across species.
- Some Kv channels exhibit inherent heterogeneity in kinetics.
- A public resource of over a million current traces from Kv channel kinetics.

INTRODUCTION

Ion channels (ICs) are proteins that selectively allow ions to diffuse through the cell membrane, creating an electrical potential across the membrane. They are classified in terms of which ion passes through the channel (sodium, potassium, chloride, calcium etc.) and by gating activity (voltage gating, ligand gating, other forms of gating; Hille, 2001; Alberts et al., 2008).

The **∼350** IC types expressed in the mammalian brain include **145** voltage-gated channels, of which **40** are voltage-gated potassium (Kv) channels, divided into **12** sub-families, Kv1-Kv12 (**Figure 1A**). The Kv channels are expressed in many different tissues/organs, including muscle, heart, and brain (Post et al., 1992; Lai and Jan, 2006; Li and Dong, 2010; Southan et al., 2016),

and also exhibit specific expression patterns at the subcellular level (Rasband, 2010; Jensen et al., 2011; Trimmer, 2015). In all these tissues, Kv channels are activated by variations in the voltage across the cell membrane. These changes regulate the return of the membrane to a resting state (hyperpolarization) after depolarization, thus controlling the excitability of different cell types (neurons, cardiomyocytes, skeletal muscle cells, etc.).

Functionally, Kv channels are known to regulate the threshold potential for firing, the duration of action potentials and, the firing rates (Storm, 1988; Gabel and Nisenbaum, 1998; Glazebrook et al., 2002; Begum et al., 2016). They are also involved in cell proliferation, and play a significant role in neurotoxicity, neuroprotection, and neuroregulation (Kaczmarek, 2006; Shah and Aizenman, 2014). Hence, malfunction in Kv channels are implicated in a range of neurological diseases known as channelopathies (Graves and Hanna, 2005; Kullmann and Waxman, 2010).

Structurally, mammalian Kv channels as homotetramers, consist of four identical alpha (α)-subunits arranged around a central axis that forms a pore (Coetzee et al., 1999). Each α-subunit is made up of six α-helical transmembrane spanning segments (S1-S6), five loops connecting successive segments, and cytoplasmic regions at the N and C terminal ends. The first four segments (S1–S4) form the voltage sensor domain (VSD). Within VSD, the fourth segment, S4, which contains a positively charged amino acid (arginine or lysine) at every third position (Bezanilla, 2000), is considered the main voltage sensor. The pore is formed by the S5–S6 segments and the corresponding connecting loop, which contains a conserved sequence (glycine-tyrosine-glycine or glycine-phenylalanine-glycine) that acts as a K^+ ion selectivity filter (Heginbotham et al., 1994).

In mammalian genomes, the Kv channels are encoded by 40 genes. Each Kv gene encodes a corresponding protein (α-subunit) with a unique structure (**Figure 1B**). While all Kv channels share a similar core structure, differences in their connecting loops, and in the length and sequence of their N and C terminals, make each one of them unique. The genes coding for the Kv channels have been cloned and studied in cell lines for many decades. However, a comprehensive and standardized kinetic characterization of all homomeric Kv channels is still missing. The literature focuses on just a few Kv channels (e.g., Kv7.1, Kv11.1, Kv1.5, Kv1.1, Kv1.3, Kv1.2, Kv2.1, etc.), and neglects many others (e.g., Kv1.7, Kv1.8, Kv6.x, Kv9.x, Kv12.x; **Table 1**). Moreover, different studies have used different species, cloning procedures, host cell lines, cell culture conditions, intracellular and extracellular solutions, and stimulation protocols, making it difficult to compare and integrate their data and sometimes producing discrepant results. In addition, the raw electrophysiology data needed to build realistic IC models are not publicly available; available data are only in the form of figures or extracted features. Eventually, the majority of previous studies on Kv channels has been conducted at room temperature (RT), which can vary from 18°C (Heinemann et al., 1996) to 28°C (Hatton et al., 2001) that could produce inconsistencies in results.

The thermal sensitivity of any biological process can be described by its temperature coefficient (Q_{10}). Classically, it is defined as the ratio of a reaction rate (α) measured at two temperatures 10 degrees apart (Bělehrádek, 1935). In ion channel research, instead of reaction rates, current amplitudes or time constants are often used to calculate Q_{10} value. A single value of Q_{10} is typically reported to indicate the temperature dependence of a channel. However, it is important to note that the Q_{10} for an IC can be different for different temperature ranges (Beam and Donaldson, 1983). Moreover, the kinetic properties (activation, inactivation, deactivation, recovery from inactivation) of an IC can have different temperature dependence (Q_{10} value; Lee and Deutsch, 1990). These additional complexities have often been overlooked especially in IC modeling, where a single approximate Q_{10} value between 1 and 5 is used to account for temperature dependence. This approximation is used mainly because of the limited number of studies conducted near physiological temperature (last column of **Table 2**).

Taken together, the non-standardized experimental conditions, the lack of studies near physiological temperature and the unavailability of the electrophysiological traces, prevent reaching a consensus on Kv channel's kinetic properties. We have therefore developed a standardized method to systematically characterize the electrophysiology of the homomeric Kv channels at different temperatures: 15 and 25°C to compare against the literature, and 35°C to provide data on the behavior of these channels near physiological temperature. Briefly, we cloned the Kv genes from the rat brain and generated a library of isogenic cell lines over-expressing single homomeric Kv channels, in an inducible manner. We then used automated patch clamping to characterize the biophysics of each channel. This allowed us to construct comprehensive maps of the kinetics of the homomeric Kv channels at 15, 25, and at 35°C—a temperature close to physiological conditions.

The large amount of data produced using automated patch clamping, especially near physiological temperature, allowed us to observe unexpected qualitative changes for specific Kv channels, beside quantitative changes in kinetics associated with changes in temperature. We found that the Q_{10} is non-linear not only with temperature but also with voltage. Furthermore, the systematic kinetic characterization revealed that some ICs exhibit inherent kinetic variability (heterogeneity), which might have been overlooked as artifacts. We illustrate how these data on temperature and voltage dependencies in IC kinetics can also be used to build more accurate temperature-dependent models of Kv channels, using the data for the Kv1.1 channel as an example. Contrarily to previous reports (Petersen and Nerbonne, 1999; Fernandez et al., 2003) that show that host cell lines affect Kv kinetic properties, we show that, under standardized conditions and with large sample sizes, the kinetic properties of the homomeric Kv channels are largely consistent across host cell lines (CHO, HEK, CV1). We also show that kinetics is well-conserved across mouse, rat, and human species. The raw and processed data from our study have been made publicly

Abbreviations: AP, Action potential; APC, Automated patch clamp; CHO, Chinese hamster ovary; CV1, *Cercopithecus aethiops* kidney; FT, Flp-In™T-Rex™; HEK, Human embryonic kidney; HSP, Heat shock proteins; IC, ion channel; Kv, Voltage-gated potassium channel; RT, Room temperature.

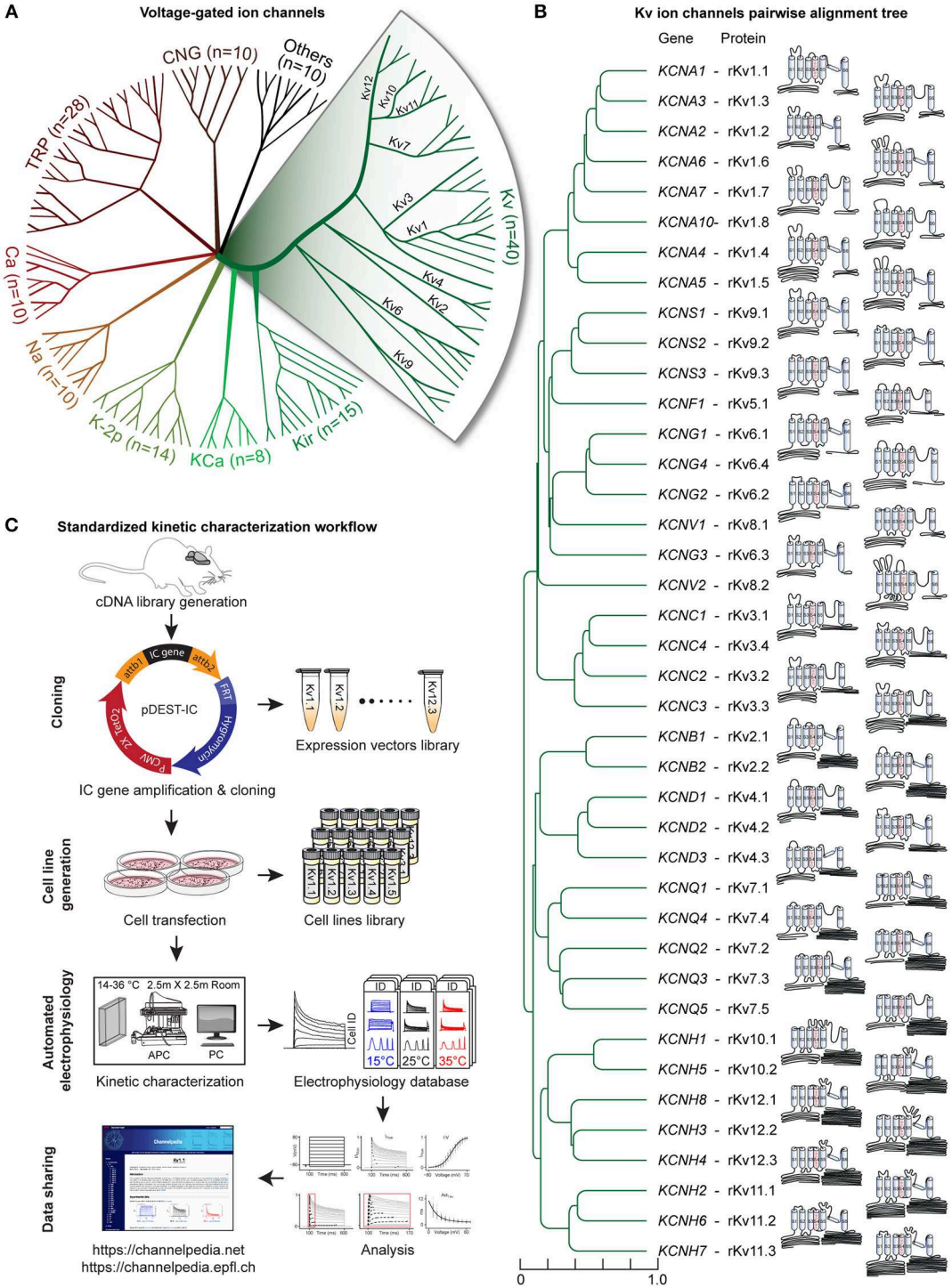


FIGURE 1 | Voltage-gated potassium channels, kinetic characterization workflow. **(A)** Radial phylogenetic tree of the 145 known voltage-gated ion channel genes, where half are potassium channels (in green). Our study focuses on the 40 voltage-gated potassium (Kv) channels, divided into 12 subfamilies (expanded area). **(B)** Phylogenetic tree obtained from pairwise alignment of the coding sequences of isoform1 of all rat Kv channel genes; scale represents normalized phylogenetic distance; the corresponding Kv protein names are indicated (prefix r stands for rat). The schematic and scaled depiction of the protein structure of each Kv channel is based on the amino acid length of each domain. **(C)** Standardized workflow for Kv channels kinetic characterization. Each Kv gene is amplified from a rat brain cDNA library and cloned in a mammalian-expression vector **(Table S6)**, building a library of expression vectors. A library of stable cell lines is generated after transfection of each expression vector in host cell lines (CHO, HEK, or CV1; See also **Figures S1, S2** and **Table S7**). The kinetics of each cell line is characterized using an automated patch clamp setup (APC) in a dedicated temperature-controlled room (14–36°C; **Table S8**). Each recorded cell is assigned a unique ID (Cell ID). Electrophysiology data are analyzed, stored and shared through the "Channelpedia" website.

TABLE 1 | Number of publications on Kv channels in PubMed as of January 2019 (after search by gene names and/or protein names).

S.No	Search on gene name		Search on protein name		Search on gene or protein name
	Gene	Count	Protein	Count	Total Count
1	*KCNQ1*	1,978	Kv7.1	168	2,026
2	*KCNH2*	1,662	Kv11.1	169	1,745
3	*KCNA5*	322	Kv1.5	925	963
4	*KCNA1*	344	Kv1.1	899	967
5	*KCNA3*	201	Kv1.3	1,023	1,037
6	*KCNA2*	174	Kv1.2	855	878
7	*KCNB1*	265	Kv2.1	672	739
8	*KCNQ2*	692	Kv7.2	134	740
9	*KCND2*	166	Kv4.2	609	651
10	*KCND3*	166	Kv4.3	555	618
11	*KCNA4*	142	Kv1.4	561	577
12	*KCNH6*	546	Kv11.2	3	549
13	*KCNQ3*	407	Kv7.3	87	446
14	*KCNH1*	285	Kv10.1	52	309
15	*KCNC1*	79	Kv3.1	239	281
16	*KCNQ4*	247	Kv7.4	74	284
17	*KCNQ5*	141	Kv7.5	63	172
18	*KCNC4*	38	Kv3.4	138	150
19	*KCNA6*	30	Kv1.6	145	161
20	*KCNC3*	76	Kv3.3	89	118
21	*KCNB2*	28	Kv2.2	75	91
22	*KCNC2*	22	Kv3.2	74	85
23	*KCND1*	22	Kv4.1	67	72
24	*KCNV2*	56	Kv8.2	8	56
25	*KCNS3*	14	Kv9.3	38	49
26	*KCNH7*	40	Kv11.3	9	46
27	*KCNH5*	34	Kv10.2	5	37
28	*KCNA7*	12	Kv1.7	24	31
29	*KCNS1*	26	Kv9.1	7	28
30	*KCNF1*	13	Kv5.1	13	25
31	*KCNG3*	15	Kv6.3	9	19
32	*KCNH3*	17	Kv12.2	5	19
33	*KCNV1*	13	Kv8.1	8	16
34	*KCNH4*	16	Kv12.3	2	18
35	*KCNG1*	7	Kv6.1	10	17
36	*KCNG4*	6	Kv6.4	12	17
37	*KCNA10*	12	Kv1.8	3	15
38	*KCNH8*	10	Kv12.1	5	15
39	*KCNG2*	8	Kv6.2	4	12
40	*KCNS2*	3	Kv9.2	7	7

available through Channelpedia (https://channelpedia.net or https://channelpedia.epfl.ch)—a web-based wiki-like resource.

RESULTS

Standardized Kinetic Characterization of Kv Channels

To establish a standardized kinetic map of the Kv family, we developed a screening workflow for the kinetic characterization of Kv channels. The workflow consists of four main steps: cloning, cell line generation, automated electrophysiology, and data sharing (**Figure 1C**).

Heterologous over-expression of ICs in host cell lines is commonly used to characterize IC kinetics. Previous studies have used many different host cell lines (e.g., CHO, COS7, CV1, HEK, LTK, ND7-23, NG108, NIH3T3; Lalik et al., 1993; Stephens et al., 1997; John et al., 2004). We chose CHO cells as they meet a broad range of criteria for successful IC experiments (Gamper et al., 2005), in particular: an efficient exogenous expression of recombinant proteins, very low endogenous ionic current and a good compatibility with planar automated patch clamp method. To ensure highly standardized conditions, we produced isogenic cell lines using the Flp-In™ system (O'Gorman et al., 1991), which provides reproducible conditions within and across different cell lines. We combined the Flp-In system with the tetracycline induction system T-Rex™, that enables expression of IC on demand, avoiding possible side effects of constitutive expression (Yao et al., 1998).

We generated a cDNA library from rat brain tissue, and attempted to amplify the 40 known Kv coding genes using the corresponding RefSeqs from the GenBank database (NCBI, Resource Coordinators, 2013; **Figure S1**). Thirty-five out of **40** Kv genes were successfully amplified from rat brain tissue. The remaining five channels (Kv1.8, Kv6.2, Kv7.4, Kv11.3, and Kv12.1), which we did not succeed to amplify, were obtained by commercial synthesis (see Methods "IC gene cloning"). All the amplified genes were fully sequenced and verified against the original RefSeqs. With minor exceptions, all cloned sequences were identical to the RefSeqs or contained synonymous variations (**Table S1**). The amplification process also revealed several new splicing variants (**Table S2**). As we only focused on the main isoforms (commonly known as isoform 1), these new variants are not included in this study.

We then cloned each amplified Kv gene in a customized mammalian expression vector and transfected them in CHO Flp-In™ T-Rex™ cells to construct a library of isogenic tetracycline-inducible CHO-Kv stable cell lines (**Figure S1**). Each Kv cell line was validated before kinetic characterization, as shown for the CHO rKv1.1 cell line as an example (**Figure S2**). Gene expression screening of the entire library confirmed that each cell line over-expressed a single target Kv gene (**Figure S3** and **Table S4**).

Electrophysiology experiments were performed with an automated patch clamp (APC) robot in a dedicated temperature-controlled room, ensuring temperature stability of the environment (see Methods "Electrophysiology environment"). Different voltage protocols were applied at three different temperatures (15, 25, and 35°C) to probe the kinetic properties of each Kv channel. To allow comparisons across all Kv channels, we used the same ion concentrations in intracellular and extracellular solutions and the same voltage protocols for all Kv channels. Each recorded cell has been assigned a unique ID (Cell ID) for ease of data management. Overall, we recorded from more than **18,700** cells, extracting kinetic features from each recording. **13,401** of these recordings met quality assurance criteria for qualitative analysis and **6,540** met criteria for quantitative analysis (see Methods "QA-QC electrophysiology data"). The raw traces of all cells are publicly available for

TABLE 2 | Summary of reported inactivation patterns at room temperature or at higher temperature for each Kv channel, with references (detailed references are listed in supplementary document).

IC		RT (18–28°C)	High T° (30–39°C)
Kv1.1	Non-inactivating (18–22°C, 24–28°C)	Mourre et al., 1999; Hatton et al., 2001; Sankaranarayanan et al., 2005; Al-Sabi et al., 2013; D'Adamo et al., 2014; García-Fernández et al., 2016; Mestre et al., 2016	**No data**
	Slow inactivating/inactivating (19–22°C)	Stühmer et al., 1989; Bertoli et al., 1994; Elinder et al., 1996; Gòmez-Hernandez et al., 1997	
	Fast inactivating when co-expressed with Kvβ1.1 or with Kvβ3 (RT, 17–18°C)	Heinemann et al., 1996; Bähring et al., 2004	
Kv1.2	Non-inactivating (RT, 20°C)	Heinemann et al., 1996; Sprunger et al., 1996; Mourre et al., 1999; Akhtar et al., 2002; Ferber et al., 2004	Activation and Inactivation time constants decrease with increase in temperature **(23 vs. 32°C;** Russell et al., 1994
	Slow inactivating (RT)	Po et al., 1993; Xie et al., 2010; Lee et al., 2011; Syrbe et al., 2015	
	Variable (22–23°C)	Rezazadeh et al., 2007	
	Fast inactivating when co-expressed with Kvβ1.1 or with Kvβ3 (RT, 17–18°C)	Heinemann et al., 1996; Bähring et al., 2004	
Kv1.3	Slow inactivating (RT)	Mourre et al., 1999; Rangaraju et al., 2010; Lee et al., 2011; Zhu et al., 2011; Kinoshita et al., 2012	**No data**
	Fast Inactivating (20–24°C)	Nicolaou et al., 2007; Hou et al., 2014; Yan et al., 2015	
	Become non-inactivating at higher expression (UKN)	Honoré et al., 1992	
Kv1.4	Fast inactivating (20–25°C)	Bertoli et al., 1994; Akhtar et al., 1999; Sankaranarayanan et al., 2005; Xie et al., 2014; Chen et al., 2016	**No data**
Kv1.5	Non-inactivating (20–24°C)	Po et al., 1993; Wible et al., 1998; Kuryshev et al., 2001; Remillard et al., 2007; Tipparaju et al., 2012; Wang et al., 2016	Inactivation time constant decreases with increase in temperature. Wettwer and Terlau, 2014 **(24 vs. 37°C)**, Rich and Snyders, 1998; **22 vs. 34°C).**
	Slow inactivating (22–24°C)	Yang et al., 1997; Jeong et al., 2012; Lee et al., 2016; Wang et al., 2016	
	Fast inactivating when co-expressed with Kvβ1.1, Kvβ3 or Kvβ1.3 (RT, 17–18°C)	Heinemann et al., 1996; Bähring et al., 2004; Tipparaju et al., 2012	
Kv1.6	Non-inactivating (18–22°C)	Roeper et al., 1998; Ferber et al., 2004; Aguilar et al., 2010; Rangaraju et al., 2010; Zhu et al., 2011; García-Fernández et al., 2016	Channel inactivates near physiological temperature **(35°C;** Guihard et al., 2003
	Slow inactivating (UKN)	Bertoli et al., 1994; Guihard et al., 2003	
	Inactivating when co-expressed with Kvβ3 (RT)	Bähring et al., 2004	
Kv1.7	Slow or fast inactivating depending on the isoform or species (20–22°C)	Kalman et al., 1998; Bardien-Kruger et al., 2002; Finol-Urdaneta et al., 2006	**No data**
Kv1.8	Non-inactivating (UKN)	Lang et al., 2000; Tian et al., 2002	**No data**
Kv2.1	Non-inactivating (20–26°C)	Wible et al., 1997; Blaine and Ribera, 1998; Malin and Nerbonne, 2002; Kihira et al., 2010	Activation and Inactivation time constant decrease with increase in temperature **(32–35°C)** MacDonald et al., 2003; Zhong et al., 2010; Yang and Zheng, 2014
	Slow inactivating (20-22 °C)	Kerschensteiner et al., 2003, 2005; Aréchiga-Figueroa et al., 2015	
Kv2.2	Non-inactivating (22–26°C)	Blaine and Ribera, 1998; Malin and Nerbonne, 2002; Kihira et al., 2010; Dong et al., 2013	**No data**

(Continued)

TABLE 2 | Continued

IC		RT (18–28°C)	High T° (30–39°C)
Kv3.1	Slow inactivating (22–23°C)	Diochot et al., 1998; Sung et al., 2009	Inactivation time constant decreases with increase in temperature **(27, 36, 39°C)** Oliver et al., 2017
	Non-inactivating (RT)	Weiser et al., 1994; Moreno et al., 1995; Rudy et al., 1999	
	Non-inactivating with sharp inactivation peak at start (RT, 22–25°C)	Kanemasa et al., 1995; Macica et al., 2003; Lewis et al., 2004; Kanda et al., 2011; Brown et al., 2016	
Kv3.2	Non-inactivating (RT, 21–23°C)	Weiser et al., 1994; Moreno et al., 1995; Hernández-Pineda et al., 1999; Rudy et al., 1999	**No data**
	Non-inactivating with sharp inactivation peak at start (RT)	Lewis et al., 2004	
Kv3.3	Non-inactivating (UKN)	Rudy et al., 1999	**No data**
	Non-inactivating with sharp inactivation peak at start (RT)	Rashid et al., 2001	
	Slow inactivating (RT)	Kanda et al., 2011; Zhang et al., 2016	
	Fast inactivating (20–22°C)	Weiser et al., 1994; Diochot et al., 1998; Mock et al., 2010	
	Non-or slow inactivating depending on the cell line (UKN)	Fernandez et al., 2003	
Kv3.4	Fast inactivating (20–24°C)	Weiser et al., 1994; Elinder et al., 1996; Diochot et al., 1998; Rudy et al., 1999; Baranauskas et al., 2003; Yeung et al., 2005; Kanda et al., 2011	**No data**
Kv4.1	Fast inactivating outward A-type current (20–23°C)	Jerng et al., 1999; Beck et al., 2002; Yunoki et al., 2014	**No data**
Kv4.2	Fast inactivating outward A-type current (RT, 20–23°C)	Pérez-García et al., 1999; Jerng et al., 2004; Yunoki et al., 2014; Abbott, 2016	**No data**
	Low current (RT)	Zhou et al., 2004	
Kv4.3	Fast inactivating outward A-type current (20–24°C)	Beck et al., 2002; Jeong et al., 2011; Yunoki et al., 2014	Activation and Inactivation rates increase with increase in temperature **(23–39°C)** Yang and Zheng, 2014
Kv7.1	Non-inactivating (22–24°C)	Gamper et al., 2003; Zaika et al., 2008; Oliveras et al., 2014	Increasing the temperature decreases the half-activation time **(20 vs. 37°C)** Unsöld et al., 2000
	Non-inactivating with inactivation peak at start (RT)	Tinel et al., 2000; Yang et al., 2004	
Kv7.2	Non-inactivating (UKN)	Gamper et al., 2003; Li et al., 2004; Peretz et al., 2010; Orhan et al., 2014	**No data**
	Silent or low current becomes more active as heteromers with Kv7.3 (RT, 25°C)	Wang et al., 1998; Jentsch, 2000; Nakajo and Kubo, 2008; Zaika et al., 2008; Choveau et al., 2012a	
	Active or silent depending on the isoform (20–22°C)	Smith et al., 2001	
Kv7.3	Non-inactivating (RT)	Gamper et al., 2003; Zaika et al., 2008; Choveau et al., 2012a	**No data**
	Silent or low current; becomes more active as heteromers with Kv7.2 (RT)	Wang et al., 1998; Jentsch, 2000; Miceli et al., 2009; Choveau et al., 2012a	
Kv7.4	Non-inactivating	Schrøder et al., 2001; Li et al., 2004; Choveau et al., 2012b; Blom et al., 2014	**No data**
Kv7.5	Non-inactivating, low current (RT, 22–25°C)	Gamper et al., 2003; Li et al., 2004; Bentzen et al., 2006; Blom et al., 2009	**No data**
	More active as heteromers with Kv7.3 (RT)	Gilling et al., 2013; Kim et al., 2016	
Kv10.1	Non-inactivating (20–22°C)	Ju and Wray, 2002; Schönherr et al., 2002; Hsu et al., 2012; Chuang et al., 2014	Activation time constant decreases with increase in temperature **(25 vs. 30°C)** Mortensen et al., 2015
Kv10.2	Non-inactivating (20–22°C)	Ju and Wray, 2002; Schönherr et al., 2002; Hsu et al., 2012; Yang et al., 2013; Chuang et al., 2014	**No data**

(Continued)

TABLE 2 | Continued

IC		RT (18–28°C)	High T° (30–39°C)
Kv11	This family requires special 2 pulse protocol for kinetic characterization		
Kv12.1	Non-inactivating (22–24°C)	Zou et al., 2003; Zhang et al., 2009; Kazmierczak et al., 2013	**No data**
Kv12.2	Low-current, non-inactivating with inactivation peak at start (21–25°C)	Trudeau et al., 1999; Clancy et al., 2009; Noma et al., 2009	**No data**
Kv12.3	Non-inactivating (25°C)	Miyake et al., 1999	**No data**

Temperature is indicated when known (RT, room temperature; UKN, unknown temperature).

download from Channelpedia (https://channelpedia.net or https://channelpedia.epfl.ch; **Figure 1C**).

Kinetic Characterization of the Rat Kv1.1 Channel

To illustrate our method, we describe the detailed kinetic characterization of Kv1.1 at 25°C (**Figure 2**), a well-studied ion channel that has been implicated in several diseases including episodic ataxia, malignant hyperthermia, and hypomagnesaemia (Rajakulendran et al., 2007; van der Wijst et al., 2010; D'Adamo et al., 2014).

Activation properties were analyzed in terms of their I-V relation, time constant for activation (Act_τ), and activation voltage (Act_Volt) (**Figure 2A**). Normalized peak currents against command voltage (I-V) curves were fitted to a Boltzmann function, yielding $V_{1/2}$ = **4.54** ± 5.87 mV, and slope k = **19.84** ± 1.72 mV. Act_τ was measured by fitting a single exponential curve to the recorded current trace from start of stimulus to peak current. For voltages from −10 to +80 mV, the value of Act_τ decreased from **4.68** ± 1.76 to **0.71** ± 0.15 ms. The median activation voltage (Act_Volt)—defined as the voltage where the channel current exceeds 10% of the peak current—was **−31.0** mV (IQR = −34.2 to −27.38).

Deactivation properties were characterized by measuring the tail currents evoked by 200 ms hyperpolarizing stimuli at voltages increasing from −80 to +50 mV in 10 mV steps (**Figure 2B**). For voltages between −60 and +10 mV, the deactivation time constant ($Deact_\tau$) increased from **14.96** ± 7.32 ms to **120.68** ± 64.9 ms.

Inactivation properties were analyzed in terms of their I-V relation, time constant ($Inact_\tau$) and inactivation factor (**Figure 2C**), yielding a $V_{1/2}$ value of **–35.26** ± 4.0 mV and slope k = **5.62** ± 2.01 mV. For voltages from −20 mV to +70 mV, $Inact_\tau$ from the peak to the end of the first pulse decreased from **313.25** ± 81.7 ms to **166** ± 48.38 ms. Kv1.1 has been reported to be a non-inactivating or slowly inactivating IC which becomes rapidly inactivating in presence of Kvβ1 subunits (Heinemann et al., 1996; Jow et al., 2004). Our characterization study shows that at +70 mV, this channel inactivates as much as **57.4** ± 10%. However, targeted PCR and full transcriptome screening showed no significant Kvβ1 expression in CHO cells (**Figure S4**). This led us to conclude that Kv1.1 is indeed an inactivating IC, and that Kvβ1 is not essential for its inactivation.

Recovery from inactivation was analyzed at a recovery potential of −80 mV using 1.5 s conditioning pulse (+50 mV) to induce inactivation, followed by 150 ms test pulses at varying intervals (**Figure 2D**). The time constant for recovery from inactivation (Rec_τ) was measured by fitting a single exponential curve to the maximum current values during the test pulse, yielding median Rec_τ = **0.85** s (IQR = 0.72 to 0.95).

To gain more insight into the behavior of Kv1.1, we used two *in vivo*-like stimuli: a slow voltage ramp and a train of 27 action potentials (APs). With the slow ramp we observed maximum conductance at **+12.03** mV (IQR = 1.40 to 18.71; **Figure 2E**). The response to the train of APs displayed median inactivation of **39**% (IQR = 29 to 47), providing further evidence that Kv1.1 is indeed inactivating (**Figure 2F**).

Kinetic Characterization of All Rat Kv Channels at 25 and 15°C

Each of the Kv cell lines was characterized using the method described above for Kv1.1. **Figure 3A** shows typical behavior of all the 40 Kv channels in response to the activation protocol. This map provides the first comparative overview of all rat Kv channels kinetics obtained in standardized condition.

As a first analysis, in order to differentiate between active and silent channels we measured voltage-dependent activity with activity index (AI) for each cell. AI is calculated by combining signal to noise ratio (SNR) and non-linearity factor (NLF) (**Figure S5**). An AI value close to 0 for a cell indicates low voltage dependence denoting an electrically silent channel. Whereas, an AI value close to 1 represents a highly active channel. We produced box plot of AI values for all cells of a Kv cell line and assigned a cut-off value of 0.3 for third quartile (i.e., 75% of the population) to distinguish between active and silent channel. Below this cut-off channels are considered as silent. The remaining channels are considered as active, with a wide range of activity levels. We further used the median values of AI to divide active channels in highly active (median value above 0.3) and low active channels (median value below 0.3).

According to this criterion, at 25°C all members of the Kv5, Kv6, Kv8, and Kv9 families were classified as silent (**Figure 3B**), which is consistent with the literature; these channels are known to have regulatory effects on active channels (Salinas et al., 1997; Kramer et al., 1998; Bocksteins et al., 2014). Several other channels were silent according to the AI criterion: Kv1.8, Kv7.2, Kv7.3, Kv7.4, Kv7.5, Kv11.2, and Kv12.2. Previous studies reported Kv7.2, Kv7.3, Kv7.4, and Kv7.5 channels as active, showing however that the homomeric channels conduct relatively small current, becoming substantially more active as

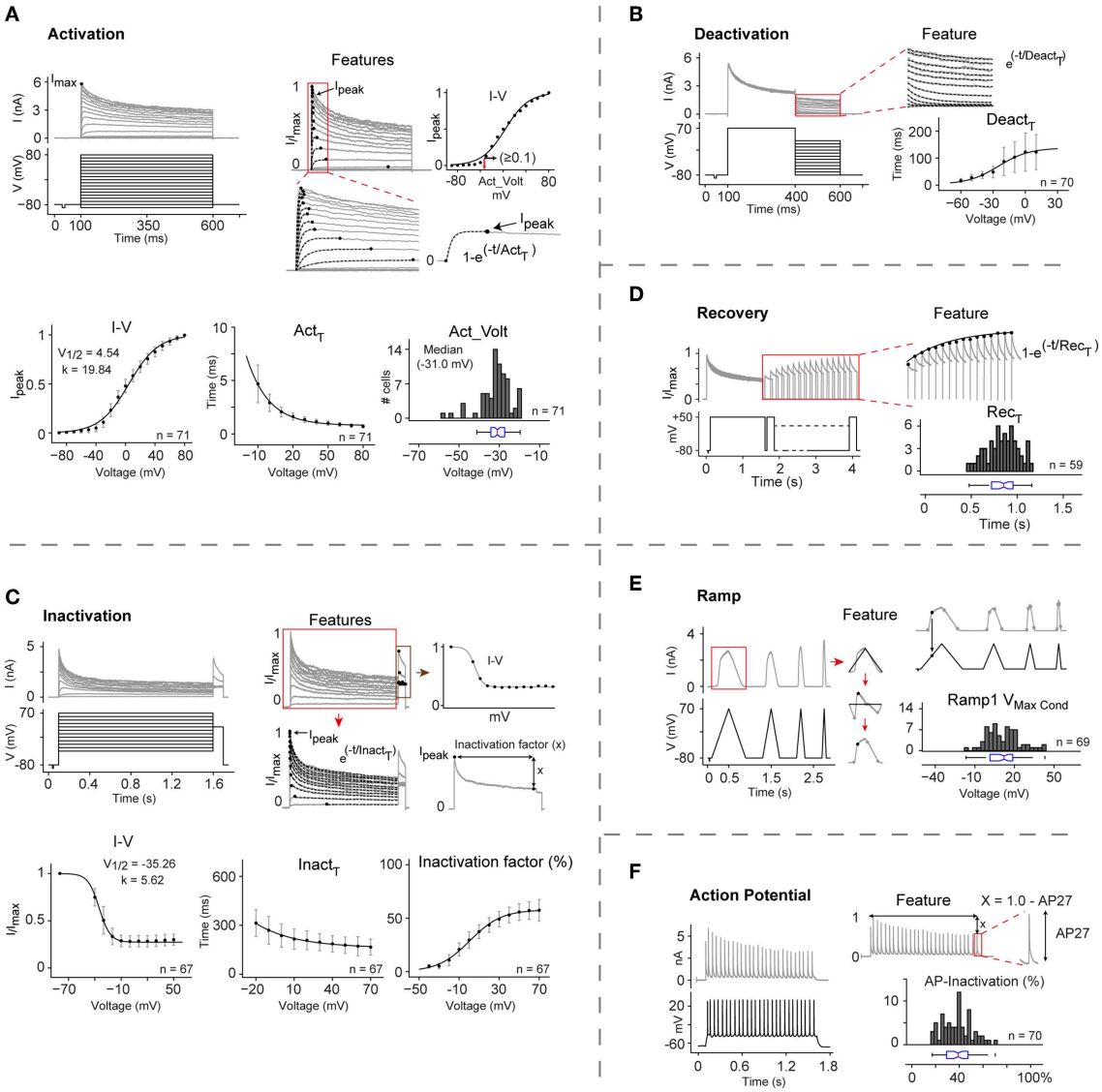


FIGURE 2 | Automated kinetic characterization of CHO rKv1.1 at 25°C. **(A–F)** The kinetic properties of rat Kv1.1 channel in CHO cells are extracted from the current response of six different voltage protocols: Activation, Deactivation, Inactivation, Inactivation recovery, and two *in vivo*-like stimuli, Ramp, and Action potential. Each panel shows the applied voltage stimulus (black traces), representative traces of the current responses (gray traces), region of interest for analysis (red box), and extracted features. For all analysis, current traces are first normalized to overall maximum current (I_{max}). All data are presented as means ± S.D. **(A)** I-V curve, activation voltage (Act_Volt), and activation time constant (Act_τ) are extracted for all cells ($n = 71$). Peak current (I_{peak}) for each trace is identified and plotted against command voltage to get I-V curve (top right panel). For each cell the voltage where normalized current (I_{peak}) exceeds 0.1 in I-V curve is considered as the activation voltage (red arrow). Act_τ is calculated by fitting single exponential curve from 0 to I_{peak} for each current trace. I_{peak} and Act_τ from each cell are plotted and fitted with Boltzmann and single exponential function, respectively to get mean I-V curve and mean Act_τ. **(B)** Deactivation time constant ($Deact_\tau$) for each trace is calculated by fitting a single exponential to current response during the second stimulus pulse (400–600 ms) and then plotted against command voltage ($n = 70$). **(C)** Inactivation curve, time constant ($Inact_\tau$), and inactivation factor are features extracted for all cells ($n = 67$). I_{peak} from the second stimulus pulse (red box) are plotted against command voltage to get Inactivation curve. $Inact_\tau$ is calculated by fitting a single exponential to each current trace from I_{peak} to the end of the first stimulus pulse. Inactivation factor (x) is the difference from I_{peak} to the end of the first stimulus pulse. Inactivation I-V, $Inact_\tau$, and Inactivation factors from all cells are averaged and plotted against command voltage and fitted with Boltzmann, single exponential, and Boltzmann function, respectively. **(D)** Inactivation recovery time constant (Rec_τ) is obtained by fitting a single exponential function to the peak current values of the responses to recovery pulses (red box) ($n = 59$). **(E)** Maximum conductance (V_{max_Cond}) is calculated on the rising phase of the first Ramp ($n = 69$). **(F)** AP-Inactivation is measured by subtracting last AP (AP27) amplitude from normalized maximum value (1) ($n = 70$). Act_Volt, Rec_τ, V_{max_Cond}, and AP-inactivation values for cell population are reported with histograms and box plots.

heteromers (Wang et al., 1998; Nakajo and Kubo, 2008; Gilling et al., 2013), or in association with their accessory subunits KCNE (Barhanin et al., 1996). According to transcriptomic data, KCNE subunits are not expressed in CHO cells (**Table S3**), that could explain why these channels are silent in this system. Kv11.2 and Kv12.2 have not been formally considered as silent

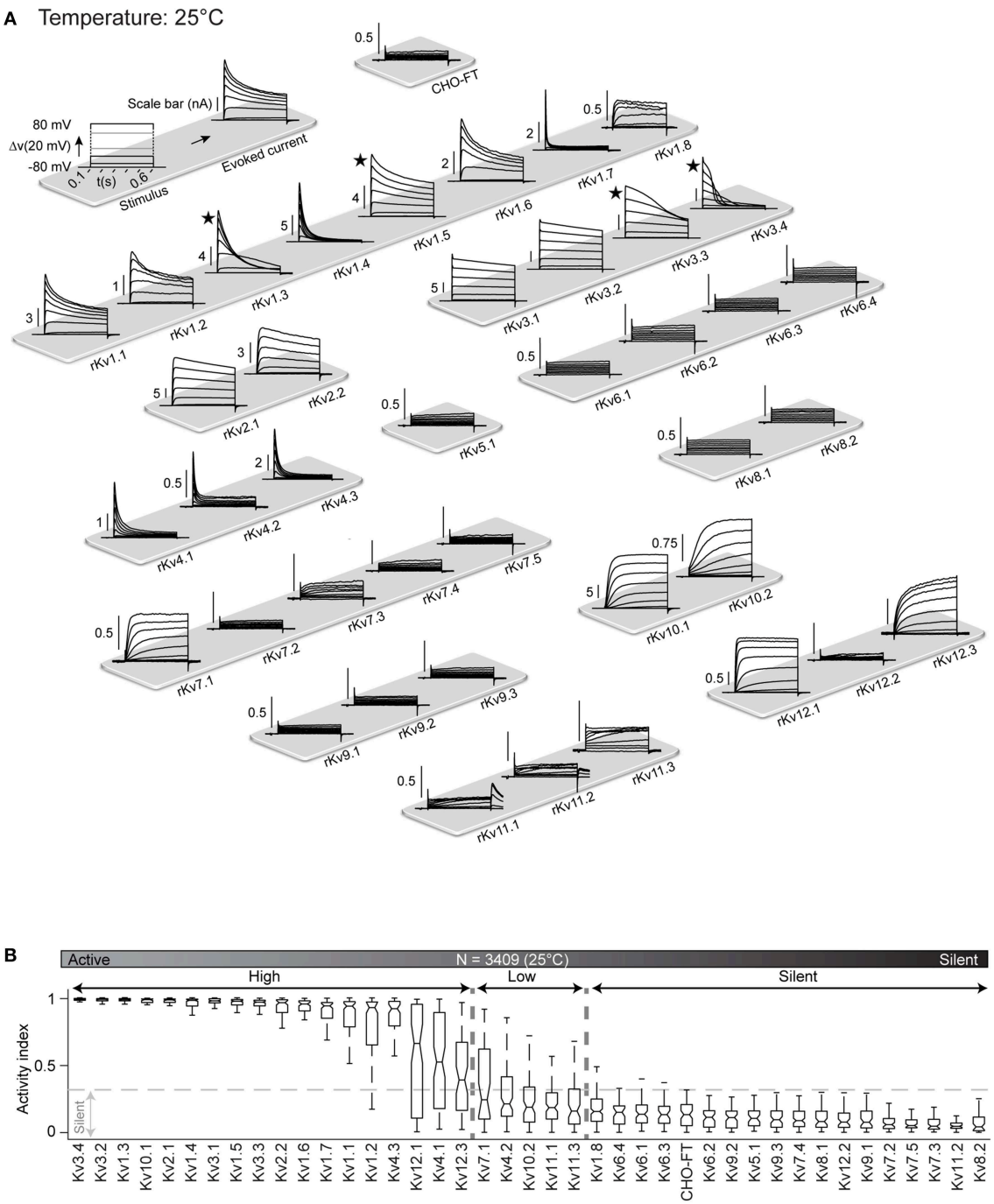


FIGURE 3 | Kv channels kinetic map at 25°C. **(A)** Illustration of activation stimulus with 20 mV steps and evoked current response are shown (top left panel). The amplitude is indicated in nA with scale bar. The non-transfected CHO-FT cell line is shown as control for the background current (top right panel). Representative traces of the typical response to activation stimulus for each Kv channel, recorded at 25°C, is shown. Current traces are sorted by Kv subfamily. ★ indicates a channel with inherent kinetic heterogeneity (see also **Figure 6**); for these channels, only one from a range of recorded responses is shown. **(B)** Box plots of AI values for each Kv channel at 25°C; ion channels are ordered by their median AI values and categorized as active or silent based on the 0.3 cut-off value for the 3rd quartile of the box plot ($N = 3,409$ cells). Active channels are further divided into highly active or low active based on 0.3 cut-off value for the median value of the box plot.

channels but have been shown to have very low conductance (Engeland et al., 1998; Wimmers et al., 2002; Sturm et al., 2005), that is consistent with our data. The remaining 23 Kv channels (Kv1.1-Kv1.7, Kv2.x, Kv3.x, Kv4.x, Kv7.1, Kv10.x, Kv11.1, Kv11.3, Kv12.1, Kv12.3) are all electrically active at 25°C, with wide range of activity levels (**Figure 3B**). As control, screening for

mRNA expression confirmed that all cell lines, for both active and silent channels, correctly expressed the target gene (**Figure S3** and **Table S4**). In addition, analysis of membrane fraction by western-blot on a sample of two active and two silent channels further showed that they had been correctly translocated to the membrane (**Figure S6**).

The kinetics of all active channels have been already reported (**Table 2**), but mainly at room temperature which can vary between 18 and 28°C from one study to another. These reports contain many inconsistencies, with agreement only for a few channels (Kv1.4, Kv2.2, Kv4.1-4.3, Kv10.1, Kv10.2). The largest inconsistencies concern Kv1.3, Kv1.5, and Kv3.3 (sometimes described as non-inactivating and sometimes as fast inactivating channels), that could be due to differences in experimental conditions across studies (species, host cell lines, method of expression, temperature, intracellular/extracellular solutions, patch clamp technique etc.). The standardized workflow used in our study makes it possible to compare the kinetic properties for all Kv channels, potentially reconciling these inconsistencies.

In our study at 25°C, most of the active ICs shows more inactivation than previously reported; for example, Kv1.1, Kv1.6, Kv2.1, and Kv2.2, mainly reported as non-inactivating (**Table 2**), show a consistent inactivating pattern at 25°C (**Figure 3A**). One possible reason could be that the data reported in literature were acquired at temperatures below 25°C (**Table 2**). To assess this possible effect of lower temperature, we re-characterized the complete Kv cell line library at 15°C. Indeed, all cell lines show less inactivation at 15°C than at 25°C (**Figures S7A, S8A**); for example, Kv1.1, Kv1.6, Kv2.1, and Kv2.2 are almost non-inactivating at 15°C providing a closer match to the results in literature (**Table 2**). This substantial temperature sensitivity points out that measurements of IC kinetics around room temperature do not necessarily reflect their behavior at physiological temperature.

Kinetic Characterization of All Kv Channels at 35°C

Like other biological processes, Kv channel kinetics is known to become faster with increase in temperature (**Table 3**). However, there are very few studies on Kv kinetics near physiological temperature (**Table 2**, right column), and moreover temperature varies between 30 and 39°C depending on the study. To obtain detailed kinetic behavior for all Kv channels near physiological temperature, we screened the complete Kv cell line library at 35°C (**Figure 4**), close to the maximum limit of the temperature controller in our setup. From a technical perspective, it is more difficult to patch cells at 35°C than at lower temperatures: cell membrane becomes less stable, making it more difficult to achieve and maintain a good seal—likely the reason why so few studies are conducted at higher temperature. In our case, for example, the success rate at 35°C could be as low as ∼**15**% compared to ∼**80**% at 25 and 15°C. However, the automated patch clamp robot used in our study produced a sufficient number of recordings to compensate for this high failure rate. The map in **Figure 4A**, provides the first comparative overview of the Kv channel kinetics near physiological temperature (35°C). The kinetics is qualitatively very different from 15, to 25 to 35°C (especially for inactivation; see **Figure S7** and **Figures 3**, **4**). Quantitatively, Kv channels activate and inactivate faster at 35°C than at 25°C (**Figures S8B,C**). In addition, the comparison of AI values of all channels at 15, 25, and 35°C (**Figure S9**) shows a surprising temperature-dependent effect on the overall level of activity of specific Kv channels. With increases in temperature, Kv10.2, Kv11.1, and Kv11.3 become significantly more active, while Kv4.1 becomes significantly less active (**Figure 4C**). At 35°C, Kv7.1 becomes even completely silent; all these specific temperature-dependent effects would require further investigations. The voltage-dependent activity of the other Kv channels is not affected by the temperature; as shown in **Figure S9**, the channels with high activity stay highly active at all three temperatures. In addition, Kv5, Kv6, Kv8, and Kv9 families stay silent at all temperatures. This observation is consistent with the literature where these channels are described to have regulatory effects on active channels (Salinas et al., 1997; Kramer et al., 1998; Bocksteins et al., 2014). As mentioned before, Kv7.2-Kv7.5, Kv11.2, and Kv12.2 homomeric channels are reported in literature to have low conductance at room temperature; our study shows that they remain silent also at 35°C in CHO cells. These channels might require heteromerization or modulatory subunits to be active at physiological temperature.

Comparative Kinetic Properties of Kv Channels at 35°C

Our standardized kinetic characterization of active ICs at 35°C enables us to provide the first comparative analysis of the kinetic properties of the Kv channels near physiological temperature (**Figure 5**).

The activation protocol used in our characterization captures the opening of an IC in response to a given voltage stimulus. As illustrated in **Figure 5A**, at 35°C, all active Kv channels show a range of current responses from **0.67** to **18.35** nA (median values). The ICs with the largest current responses (mainly Kv3 family) activate at the highest voltages (**Figure 5B**) and have the fastest activation rate (**Figure 5C**, see also **Figure S10** in blue). This is consistent with reports of neuronal AP repolarization by currents mediated by Kv3 family (Rudy and McBain, 2001; Labro et al., 2015). In contrast, ICs of the Kv11 and Kv12 families, that show low current responses, activate at lower voltages and have the slowest activation rate (**Figures 5A–C** and **Figure S10** in red). These ICs may play a role in repolarizing the cell membrane at sub-threshold voltages and during sub-threshold oscillations. The behavior of the other Kv ICs lies between these extremes. In general, we observe that channels with high current responses tend to be activated by high voltages and vice-versa (**Figure S10** in black).

The Kv4 family is an exception, with all members activating at high voltage but having a low current response (**Figure S10** in green).

Deactivation refers to the closing of a channel when a stimulus is removed. The lowest deactivation time constants at 35°C are found for the Kv3 and Kv10 families. The ICs with the highest

TABLE 3 | Summary of literature reports on the effect of temperature on Kv kinetics, indicating temperatures and reported effects (brief descriptions) with references (detailed references are listed in supplementary document).

IC	Temperatures	Reported kinetics	References
Kv1.1	16,3 vs. 26.6°C	Activation time constant decreases with increase in temperature	Moran and Conti, 1995
Shaker B (Kv1.3)	Range of T° (9.9–30.7°C)	N-type inactivation is accelerated with increase in temperature	Meyer and Heinemann, 1997
Kv7.2-7.5	28 vs. 18°C	Faster activation and deactivation kinetics with increase in temperature	Miceli et al., 2009
Kv11.1, Kv11.3	21, 30, and 35°C	Faster activation and inactivation at higher temperature	Mauerhöfer and Bauer, 2016
Kv	Range of T°	Faster activation and inactivation at higher temperature	Pahapill and Schlichter, 1990; Yang and Zheng, 2014

deactivation time constants (up to **60** ms) belong to Kv11 and Kv12 families (**Figure 5D**).

Inactivation refers to the closing of a channel during stimulation. Inactivation is an important property of most of the Kv channels, determining how long the channel affects the cell, under suitable activation conditions. There are several conflicting reports about the inactivation properties of Kv channels (**Table 2**). Our study shows that their kinetic behavior span from highly inactivating (e.g., Kv1.4, Kv1.3, Kv3.4, Kv1.7) to non-inactivating (e.g., Kv12.1, Kv10.1, Kv12.3; **Figure 5E**). In some cases, we confirm previous reports. For example, we confirm that Kv1.3, Kv1.4, and Kv.4.3 inactivates more than **80**% at 35°C. We also confirm that Kv10.1, Kv10.2, Kv12.1 are truly non-inactivating ICs, maintaining this characteristic at 35°C (**Figure 5E**). However, in other cases, the extrapolation from 25 to 35°C does not hold. For example, at 35°C, Kv1.6, Kv1.1, and Kv1.2, which are non-inactivating at 15°C, and slowly inactivating at 25°C, actually inactivate by **83**, **74**, and **70**%, respectively at 35°C. Other Kv channels show similar trends. For example, Kv2.1 and Kv2.2, which have been reported in literature to be less inactivating, actually inactivate by **65**% and **75**% respectively, at 35°C.

Apart from conventional inactivation (N, C, P, and U-types), we also observed delayed inactivation for three channels (Kv1.3, Kv3.3, Kv3.4), which is a new type of inactivation recently reported for Kv3.1 (Oliver et al., 2017). This observation is further discussed below. At 35°C, a few Kv channels, particularly Kv1.7, show slow inactivation recovery time (**1.9, 1.18, 0.91**, and **0.81 s** for Kv1.7, Kv1.4, Kv1.3, and Kv3.1, respectively; **Figure 5F**). All other inactivating ICs require <**0.6 s** (median values) to recover from inactivation.

We also observed inactivation in response to AP-like physiological stimuli. When applying a train of APs, inactivating channels like Kv1.4 and Kv1.7 show up to **80**% inactivation, whereas non-inactivating channels like Kv10.1 and Kv12.1 show no inactivation at all (**Figure 5G**).

Inherent Kinetic Heterogeneity and Delayed Inactivation

The effect of temperature on inactivation explains some inconsistencies in ion channel literature. For example, Kv1.1, Kv1.6, and Kv2.1 are reported as non-inactivating or slow-inactivating depending on the study (**Table 2**); that we show is a temperature-dependent effect as these channels are all non-inactivating at 15°C but become inactivating at 25°C (**Figure S7** and **Figure 3**). This systematic characterization led to an additional observation: in our study, the majority of the Kv cell lines shows responses that are consistent across different cells from the same cell line. However, in some cases, different cells from the same cell line systematically show different responses (kinetic heterogeneity), despite the fact that they are isogenic (**Figures 6A,B**). To quantify this kinetic heterogeneity, we have measured the variance in current response for all cells of each cell line, in response to +80 mV command stimulus from activation protocol (**Figure 6C**). This analysis shows that at 25°C, four ICs, namely Kv1.3, Kv1.5, Kv3.3, Kv3.4, exhibit particularly high kinetic heterogeneity. This phenomenon was observed independently of the temperature or the host cell line (data not shown).

We have verified that the heterogeneity observed is not due to gene mutations (**Table S1**), cell contamination (**Figure S3**), recording artifacts (series resistance, intracellular/extracellular composition, extracellular K^+ accumulation, etc.), cell handling or cell environment. Since the methods used were highly consistent (standardized workflow, isogenic cell lines, recording of ∼100 cells for each of these channels), we conclude that the kinetic heterogeneity is an inherent property of specific Kv channels. The underlying mechanism may include transcriptional, post-translational and/or translocational factors and requires further investigation. Except for one previous report about two distinct phenotypes for Kv1.2 cells (Rezazadeh et al., 2007), this is the first report of inherent kinetic heterogeneity in Kv channels. The inherent heterogeneity of Kv1.3, Kv1.5, and Kv3.3 could also explain inconsistencies in previously reported kinetics for these channels. However, the high heterogeneity we observed in the kinetics of Kv3.4, contradicts all previous reports, which describe this channel as a fast inactivating channel (**Table 2**).

Three of the abovementioned channels (Kv1.3, Kv3.3, Kv3.4) also show striking delayed inactivation, with inactivation starting after a delay that varies from cell to cell—a behavior that differs from classical inactivation patterns (slow, intermediate, or fast inactivation; **Figures S11A,B**). With longer stimuli, delayed inactivation also appears in two further channels (Kv3.1, Kv3.2) (data not shown). The delayed inactivation was observed at all three temperatures (**Figure S11C**). To assess if the delayed inactivation is linked with extracellular potassium accumulation, we performed control experiment on Kv3.4 cells. A single voltage pulse of +70 mV was applied to evoke delayed inactivation and then extracellular space was washed with extracellular

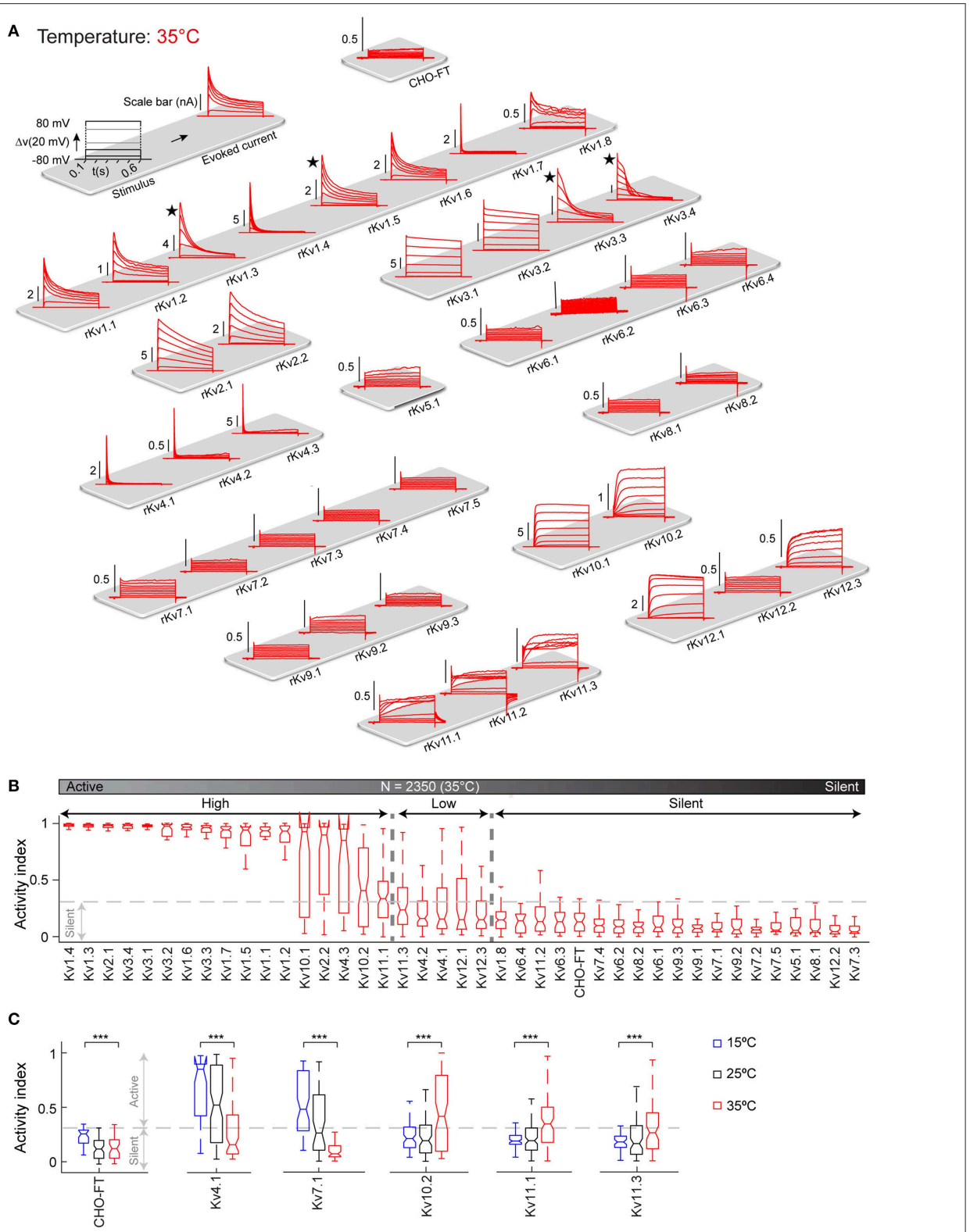


FIGURE 4 | Kv channels kinetic map at 35°C. **(A)** Illustration of activation stimulus with 20 mV steps and evoked current response are shown (top left panel). The amplitude is indicated in nA with scale bar. The non-transfected CHO-FT cell line is shown as control for the background current (top right panel). Representative traces of the typical response to activation stimulus for each Kv channel, recorded at 35°C is shown. Current traces are sorted by Kv subfamily. ★Indicates a channel

(Continued)

FIGURE 4 | with inherent kinetic heterogeneity (see also **Figure 6**); for these channels only one response from the range of recorded responses is shown. **(B)** Box plots of AI values for each ion channel at 35°C; ion channels are ordered by their median AI values and categorized as active or silent based on the 0.3 cut-off value for the 3rd quartile of the box plot (N = 2,350 cells). Active channels are further divided into highly active or low active based on 0.3 cut-off value for the median value of the box plot. **(C)** AI values at 15°C (blue), 25°C (black), and 35°C (red) are plotted for Kv channels that show significant change in activity over temperature. AI values for the non-transfected CHO-FT cell line is plotted as a control (see also **Figure S9**). ***$p < 0.001$, Student's t-test.

solution for 90 s to remove potassium accumulation. The delayed inactivation was observed even after multiple washes with extracellular solution (**Figure S12A**). Moreover, for Kv3.4 cells, Person's linear correlation coefficient between maximum current amplitude and delay in inactivation resulted in a value of 0.12, indicating that the delayed inactivation is not correlated with outward potassium current amplitude (**Figures S12B1–B3**). Full transcriptome analysis showed no significant expression of Ih, Ca or Na voltage-gated channels, indicating that this delay was not caused by inward current (**Figure S12C** and **Table S3**). The mechanism behind this delayed inactivation requires further investigations.

Voltage-Dependent Q_{10}

The Q_{10} has been widely used in biology as a convenient measure of temperature effects. For ion channel modeling, Hodgkin and Huxley (1952) used a constant value of $Q_{10} = 3$ to model Na^+ and K^+ conductances in the squid axon. Since then, other authors have used a fixed Q_{10} value between 1 and 5 in models to estimate the kinetic rates for Kv channels at different temperatures. Our experiments at 15, 25, and 35°C, allowed us to measure empirical Q_{10} values for all kinetic parameters, using Van't Hoff's equation:

$$\tau\,(T1) = \tau\,(T)^{*}\,Q_{10}^{\left(\frac{T-T1}{10}\right)} \tag{1}$$

where T and $T1$ are the temperatures (in °C) at which experiments were carried out, and $\tau\,(T)$ and $\tau\,(T1)$ are the time constants.

As an example, **Figure 7** shows Q_{10} for Act_τ for selected Kv channels with very different activation profiles. Act_τ was obtained by fitting the current traces to a single exponential and plotted against command voltage (**Figure 7A**). Q_{10} for 15 and 35°C were calculated considering 25°C as the base temperature, the usual temperature used for ion channel studies:

$$Q_{10_{15c}} = \frac{\tau\,(15^{\circ}C)}{\tau\,(25^{\circ}C)}\; and\; Q_{10_{35c}} = \frac{\tau\,(25^{\circ}C)}{\tau\,(35^{\circ}C)} \tag{2}$$

Applying Equation (2) to our empirical data for all active Kv channels yields values that vary not only as a function of temperature but also of voltage (**Figure 7B**). For example, Kv1.1 has a $Q_{10_{15c}}$ value around 5 and a $Q_{10_{35c}}$ value between 3 and 4, varying with voltages. Data for other IC show that Q_{10} can be lower than 2 (ex: Kv7.1 at 15°C) or as high as 8 (e.g., Kv2.1 at 15°C) depending on voltages and temperature range. Our detailed kinetic characterization of all Kv channels provides data to calculate accurate temperature and voltage-dependent Q_{10} for all kinetic parameters.

Voltage-Dependent Q_{10} Hodgkin-Huxley Model

One case where extrapolating across temperatures may lead to inaccurate results is the implementation of IC kinetics in computational models. Neuronal models often use the Hodgkin-Huxley (H-H) formalism to describe IC conductances. In this section, we describe a revised model-fitting procedure, which accurately incorporates voltage dependence in temperature sensitivity. We use Kv1.1 as an example.

Briefly, current traces from individual cells were fitted to single activation and inactivation gates in the H-H formulation, and model parameters were extracted for each cell. The medians of these parameters were fitted with Q_{10} functions.

The net transmembrane current flow, $I_{Kv1.1}$, and the conductance $g_{Kv1.1}$ were computed using Equations (3) and (4):

$$I_{Kv1.1} = g_{Kv1.1}\,(V_m - E_k) \tag{3}$$

$$g_{Kv1.1} = \frac{I_{Kv1.1}}{(V_m - E_k)} = \bar{g} m^p h^q \tag{4}$$

Where V_m is the membrane potential, and E_k denotes the Nernst potential. Variable $\bar{g}$ scales for maximum channel conductance. m and h represent the proportion of open activation and inactivation gates, respectively; p and q are the numbers of independent gates required to account for the observed time course of activation and inactivation. Since single gates are used both for activation and for inactivation, $p = q = 1$. Gating variables are modeled as a first-order kinetic process

$$\frac{dm}{dt} = \frac{m_\infty - m}{m_\tau} \tag{5}$$

$$\frac{dh}{dt} = \frac{h_\infty - h}{h_\tau} \tag{6}$$

Where m_∞, h_∞ represent the voltage-dependent steady state and m_τ, h_τ are the voltage-dependent time constants for activation and inactivation gates.

The free parameters in Equations (3)–(6) were fitted to the normalized conductance for each cell (**Figure 8A** for a sample fit). The fitted parameter values for all cells were plotted and median parameter values for each temperature were calculated (**Figure 8B**).

The m_∞ function was considered temperature independent, thus a single Boltzmann function was used for all three temperatures. The remaining three parameters, h_∞, m_τ *and* h_τ, were fitted with three different Q_{10} functions. For the steady state inactivation function h_∞, we used a temperature-dependent linear function $h_\infty Q_{10}$. m_τ curves were fitted using a double exponential function of voltage and temperature, $m\tau Q_{10}$. The $h\tau Q_{10}$ function was represented by a constant value of

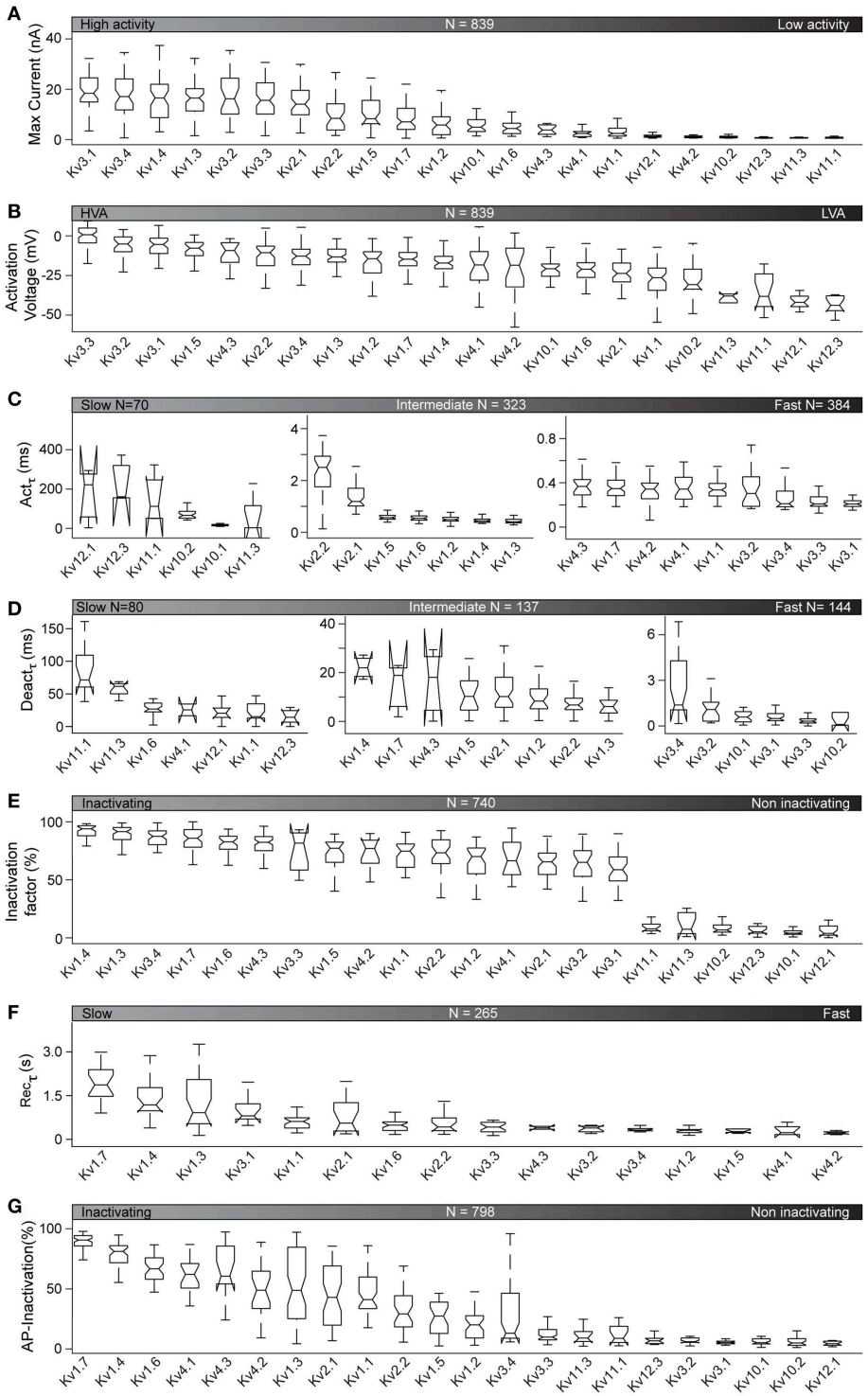


FIGURE 5 | Kinetic properties of active Kv channels at 35°C. Kinetic features, analyzed as illustrated in **Figure 2**, are plotted for the 22 active Kv channels at 35°C (see **Figure 4B**). Features are represented as box plots for each ion channel and sorted by their median values. *N* is the total number of cells used for the analysis of each feature (see also **Table S5** for detailed cell counts of each group). **(A–G)** Kv responses to the activation stimulus are analyzed to get maximum current response **(A)**, activation voltage (HVA = high voltage activation, LVA = low voltage activation) **(B)**, and activation time constant for V = +50 mV **(C)** (see also **Figure S10**). Kv responses to the deactivation protocol are analyzed for deactivation time constant for V = −30 mV **(D)**. Responses to the inactivation protocol are analyzed to calculate inactivation factor values at V = +70 mV **(E)**. The 16 inactivating Kv channels (Kv1.4 to Kv3.1) from **(E)** are further analyzed to compare time constants for recovery after inactivation **(F)**. Responses to AP-like stimuli are analyzed for AP-inactivation **(G)**.

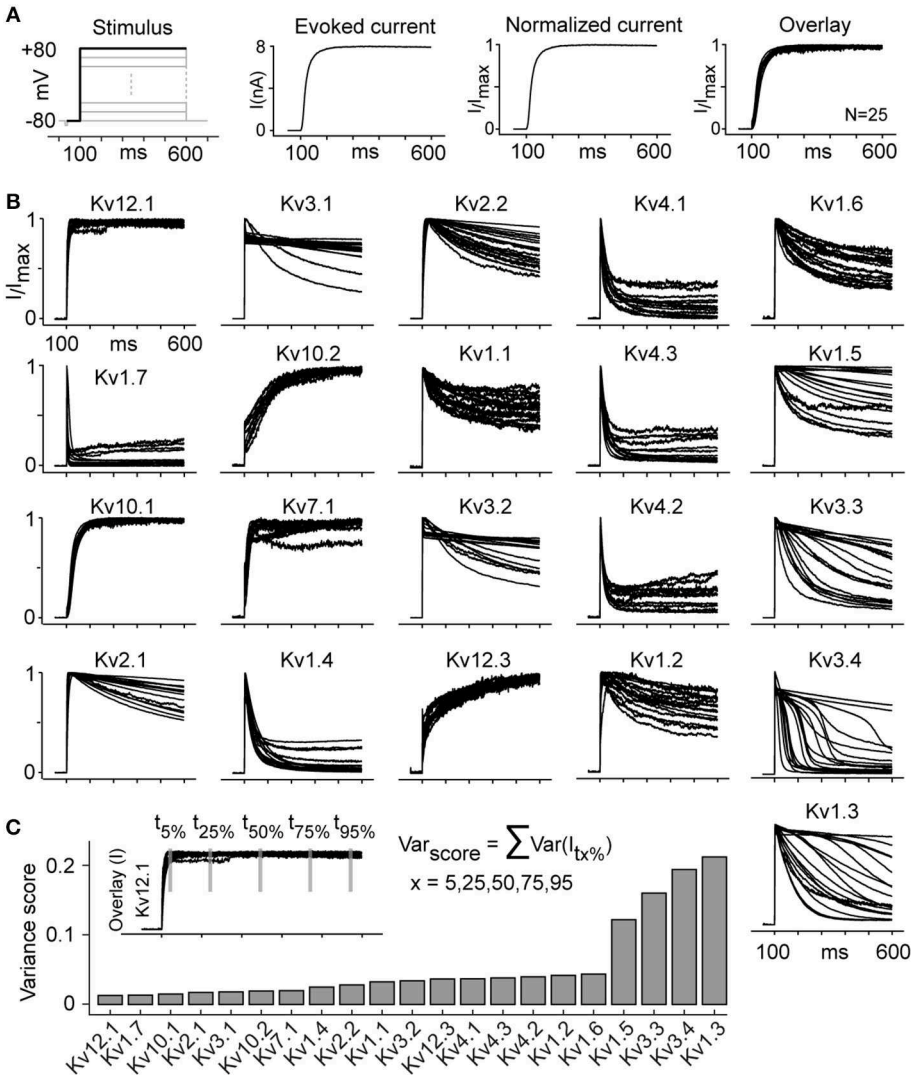


FIGURE 6 | Kv channels kinetic heterogeneity (see also **Figure S11**). **(A)** The evoked current trace corresponding to the activation stimulus at +80 mV is normalized to maximum current for each cell. The overlay plot presents the normalized currents from 25 cells that statistically represent the whole group (same variance). **(B)** Overlay plots as described in panel A are shown for all active channels at 25°C (Kv11.1 and Kv11.3 are not included due to low current and high noise). The overlay plots visually represent the kinetic heterogeneity. **(C)** Kinetic heterogeneity is quantified by calculating Var_{score}, obtained by summing five variances of normalized currents evaluated at five time points for all cells of a given cell line, as shown for Kv12.1 as an example. The channels that show the highest heterogeneity (highest Var_{score}) are Kv1.3, Kv1.5, Kv3.3, and Kv3.4. The number of cells (*N*) for each group is listed in **Table S5**.

2.7 (**Figure 8D**). **Figure 8C** shows the final plots for each gating variable, and the normalized conductance plot for each temperature.

The main difference between our approach and regular H-H modeling was that, instead of using a constant value for Q_{10} (usually between 2 and 3), we used a voltage and temperature-dependent function for m_τ and a temperature-dependent linear function for h_∞. With these changes, we were able to fit the temperature sensitivity of Kv1.1 to the experimental data, which was not possible with the standard model. The resulting revised H-H model can thus be used to extrapolate kinetics from the temperature at which the channel was studied to physiological temperatures.

Kv Channel Kinetics Across Host Cell Lines and Species

Previous studies of IC kinetics used many different host cell lines, with different origins, morphologies, intracellular environments, cell handling etc. These differences may also have contributed to all those conflicting reports on the kinetics of specific ICs. To verify possible dependencies on the specific cell line (i.e., CHO) used in our study, we used our standardized workflow to characterize the kinetics of five significantly different active Kv channels (Kv1.1, Kv1.4, Kv1.5, Kv1.6, and Kv2.1) in two additional cell lines (CV1 and HEK). The three cell lines are all adherents and have different morphologies (**Figure 9A**). In contrast with CHO cells, CV1 and HEK

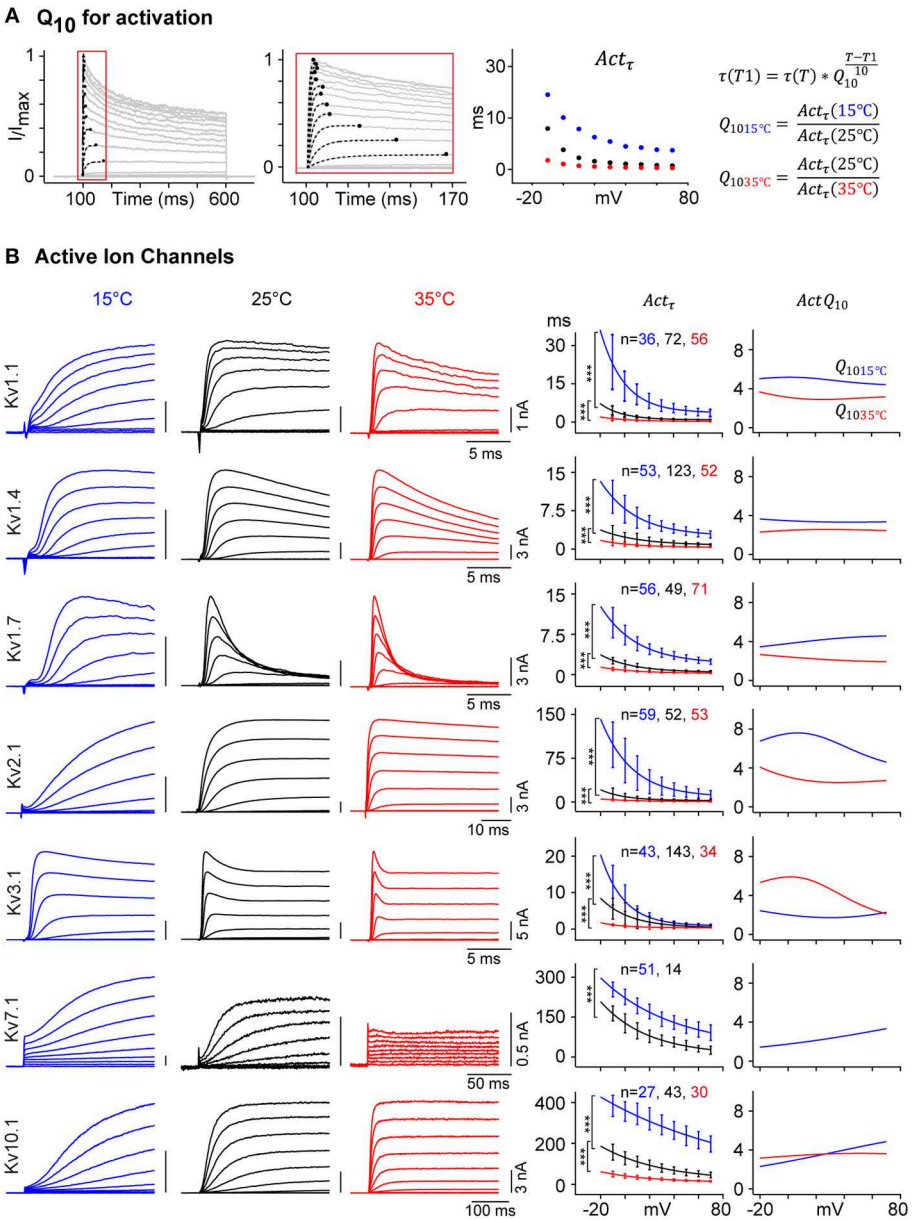


FIGURE 7 | Temperature dependence of Kv channel kinetics. **(A)** Voltage-dependent Act_τ is measured as shown in **Figure 2**. Q_{10} of Act_τ is calculated for 15 and 35°C, with 25°C as a reference. **(B)** Representative current traces for selected Kv channels in response to activation protocol at 15°C (blue), 25°C (black), and 35°C (red) are shown (left panels), the amplitude in nA and time in ms are indicated with scale bars. Single exponential curve is fitted to the median value of Act_τ for each of the three temperatures (middle panel, solid line; ***p-value < 1e-5, Student's t-test). For each selected Kv channel, Q_{10} values for 15°C (blue) and 35°C (red) are plotted against command voltage (right panel). For a given Kv channel, Q_{10} value is different for different temperature range and vary between 2 and 8 across different voltages. For Kv7.1, which becomes electrically silent at 35°C, Act_τ and Q_{10} values for 35°C are not plotted. Error bars are ± S.D.

cells both generate small outward currents, possibly due to higher levels of endogenous IC expression (**Table S3**). Our analysis of three kinetic features (I-V, Act_τ, Inactivation factor) shows that, except for Kv1.5's inactivation factor, the kinetic behaviors of the ICs are largely consistent across the three cell lines at 25°C (**Figures 9B,C**). Furthermore, the kinetics are comparable also at 35°C for Kv1.1, Kv1.4, and Kv2.1 (**Figures S13A,B**).

IC genes are highly conserved across species (Siepel et al., 2005); 36 out of 40 rat Kv channels have >**97%** homology with mouse orthologs (**Table 4**) and even the least homologous channels (Kv6.4, Kv8.2) share >**95%** homology in their protein sequence. Similarly, 23 out of 40 rat Kv channels show >**95%** homology with human orthologs, and 36 out of 40 share >**90%** homology. However, some channels do show differences in the length of their N-terminus and/or C-terminus regions (**Table 4**).

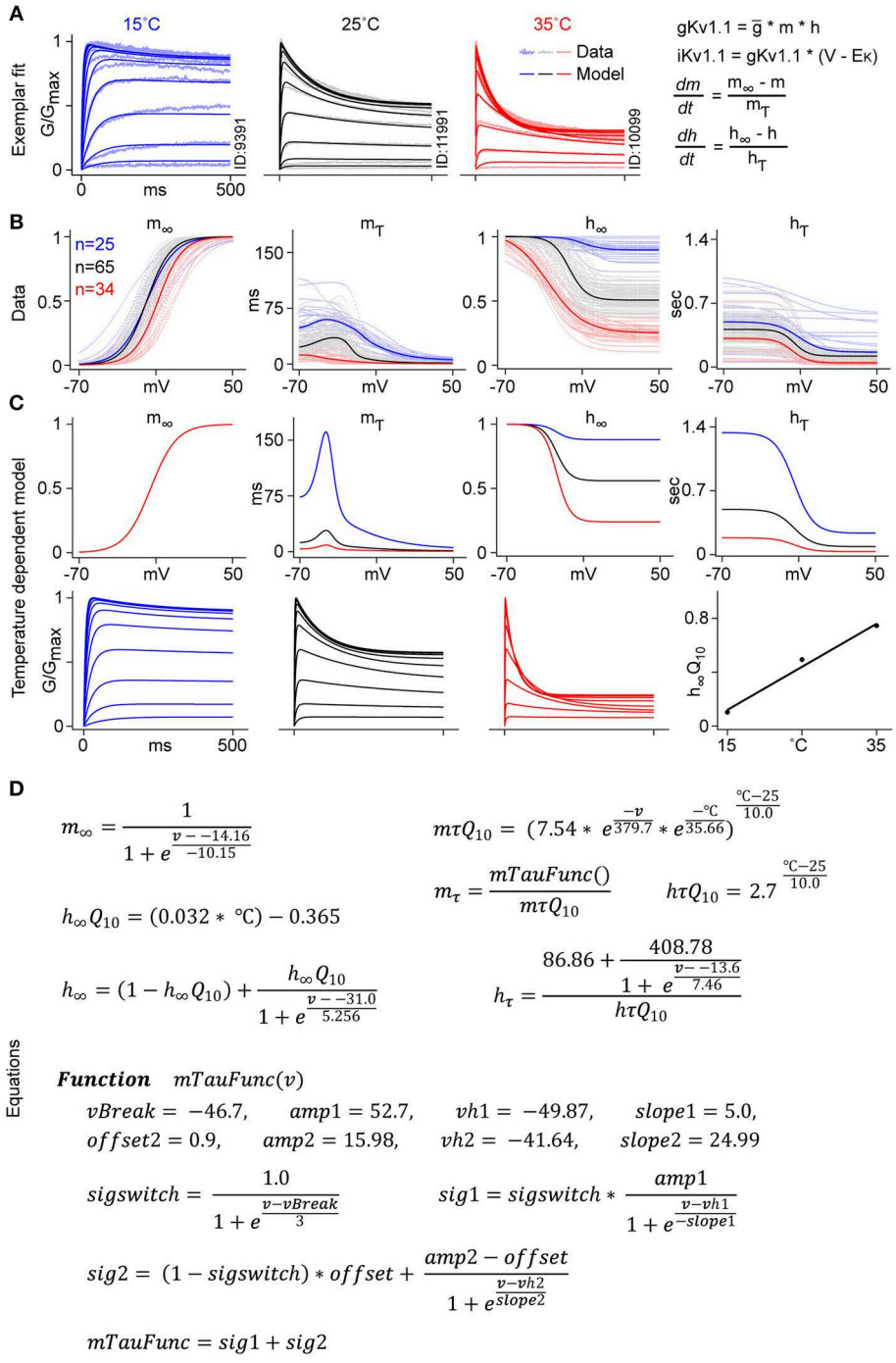


FIGURE 8 | Kv1.1 temperature-dependent H-H modeling. **(A)** Kv1.1 CHO cells recorded from three different temperatures are used for H-H model fitting. An example of the fit to normalized conductance for cells recorded at three different temperatures, 15°C (blue), 25°C (black), and 35°C (red) is shown (see Methods "H-H model fitting"). **(B)** Voltage-dependent $m_\infty, h_\infty, m_\tau$, h_τ parameters are plotted (in dots) for all fitted cells. Median values, fitted with a smooth function, are represented with solid lines. **(C)** Voltage dependence of the m_∞ parameter is approximated with a single Boltzmann function for all three temperatures. m_τ is fitted with voltage and temperature-dependent Q_{10}. The steady state value of h_∞ is computed using the temperature-dependent linear function $h_\infty Q_{10}$. h_τ is fitted to a Boltzmann curve with a constant Q_{10} value of 2.7. **(D)** Equations used to fit the temperature-dependent Kv1.1 model.

What is not known is whether and how these small differences in sequences translate into a difference in Kv channels kinetics. To address this question, we cloned the mouse and human versions of the same five active channels previously used for host cells comparison, and we characterized them in CHO cells at 25°C (**Figures 9D,E**) and at 35°C for Kv1.1, Kv1.4, and Kv2.1

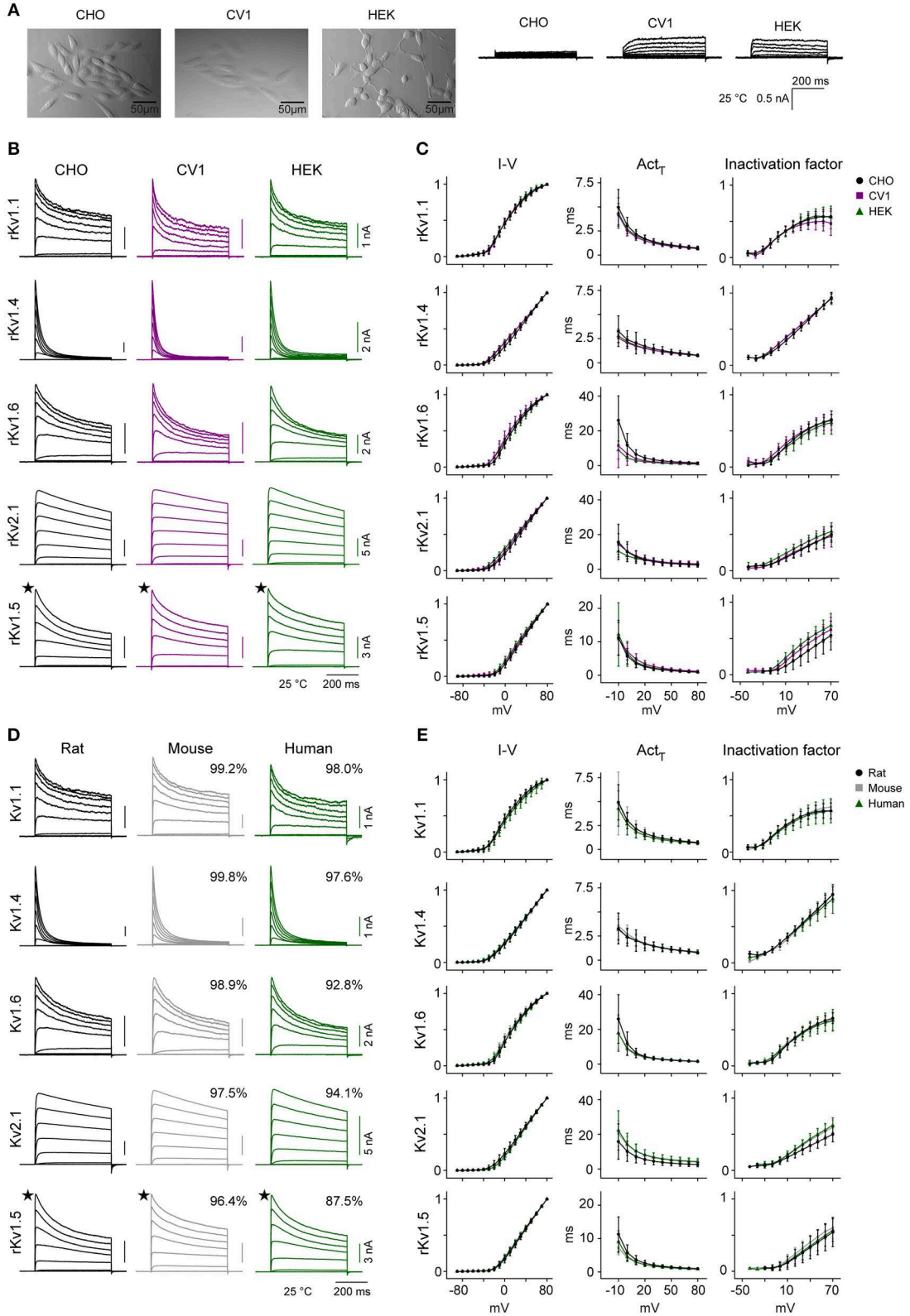


FIGURE 9 | Kv channel kinetics across host cell lines and species at 25°C. **(A–C)** Comparison of Kv kinetics across three mammalian host cell lines. **(A)** Pictures showing the morphology of the three adherent host cell lines (CHO, HEK, and CV1) used in the study, with their corresponding endogenous outward currents in response to the activation protocol at 25°C. **(B)** Representative current traces from rat Kv1.1, Kv1.4, Kv1.6, Kv2.1, and Kv1.5 expressed in the three different cell

(Continued)

FIGURE 9 | lines, in response to activation protocol at 25°C. **(C)** Median values for three kinetic features (I-V curve, activation time constant, and inactivation factor calculated as explained in **Figure 2**) obtained from CHO, CV1, and HEK host cell lines for each Kv channel, overlaid for comparison. **(D,E)** Comparison of Kv kinetics across three species. **(D)** Representative current traces for rat, mouse, and human Kv1.1, Kv1.4, Kv1.6, Kv2.1, and Kv1.5 expressed in CHO cells, in response to activation protocol at 25°C. The percentage of homology compared to rat are shown in box above current traces (see also **Table 4**). **(E)** Median values for three kinetic features (I-V curve, activation time constant, and inactivation factor calculated as explained in **Figure 2**) obtained from rat, mouse, and human genes of each Kv channel, overlaid for comparison. Error bars are ± S.D. The amplitude in nA and time in ms are indicated with scale bars. ★: For Kv1.5, only one representative trace from a range of responses is shown. The number of cells (*N*) for each group is listed in **Table S5**.

(**Figures S13C,D**). Among these five characterized channels, Kv1.1, Kv1.4, Kv1.6, and Kv2.1 have high homology between species, whereas Kv1.5 was chosen as an example of an active channel with one of the lowest homology across species. We detected only subtle quantitative differences in some kinetic parameters across species both at 25 and 35°C (**Figures 9D,E** and **Figures S13C,D**). For example at 25°C, we measured a slightly slower activation time constant for human Kv2.1 compared to rat Kv2.1, as previously reported (Ju et al., 2003; **Figure 9E**); however, the difference no longer remains significant at 35°C (**Figure S13D**). We conclude that the behavior of these five Kv channels is relatively conserved across the three species.

A Data Resource of Ion Channel Kinetics

To facilitate sharing and further validation of our results, we have published all raw and processed data from our study as a wiki-like web resource (https://channelpedia.net or https://channelpedia.epfl.ch), freely available for academic use. Each cell has been assigned a unique cell ID, which is appended to the data file name. The raw data file provides the recorded currents for each repetition of the voltage protocols and a description of the stimuli applied. The analyzed data file contains features extracted from recordings of each repetition of each protocol. The experimental and analyzed data for each Kv IC are made available in Neurodata without Borders (NWB) format under "Experimental Data" section on the Channelpedia website. NWB is a new format designed to promote data standardization and sharing (Teeters et al., 2015). NWB is based on the HDF5 file format, thus can be viewed with any HDF5 viewer. The raw data, stimulus and metadata are stored under "acquisition/timeseries," "stimulus/presentation," and "general," respectively. The data can be accessed via a web interface or a REST API. Over 1 million recording traces from over **18,700** cells are available and can be downloaded for academic use.

DISCUSSION

In this study, we produced a standardized map of the kinetics of the homomeric form of all members of the Kv family, at 15, 25, and 35°C. The map includes all the channels, also those not previously studied or underrepresented in the literature (**Table 1**). The data we provide near physiological temperature were not available for most of the Kv family members. We show that under controlled conditions, these channels kinetics is reproducible and mostly conserved across host cell lines and species. We find that for many Kv channels, the kinetics near physiological temperature not only differ quantitatively as expected from temperature-dependent effects, but also qualitatively. We find that for all Kv channels, Q_{10} is not only temperature-dependent, but also voltage-dependent. To allow extrapolation from the large number of low temperature kinetics available in the literature to kinetics at physiological temperatures, we provide the data on the voltage-dependent Q_{10} for each channel and a revised Hodgkin-Huxley model to capture the channel kinetics accurately. We found a novel form of delayed inactivation and inherent heterogeneity in kinetics for some Kv members, behavior that was likely interpreted as artifacts in previous studies. We suggest that different experimental conditions, non-trivial temperature dependencies and inherent heterogeneity can account for most of the inconsistencies in kinetics reported in the ion channel literature. The full dataset of over one million traces is available as a publicly accessible resource (https://channelpedia.net or https://channelpedia.epfl.ch).

Reference Kinetic Dataset for Kv Channels

A vast amount of data on Kv channel kinetics is available in the literature. The lack of consistency limits the value of these data and prevents a consensus on ion channel kinetics. The reference dataset we provide was generated using a standardized heterologous system with isogenic cell lines and an inducible-expression system to achieve a high level of reproducibility and reliability.

Our system, however, does have limitations. In particular, levels of expression are probably much higher than *in vivo,* and it is not possible to control levels of expression across cells. We also cannot account for possible effects of transcriptional regulation in different cells of the body at different stages of development.

The need of special recording solutions for APC experiments is another limitation of this study. Specific fluoride-based intracellular solution (ICS) (50 mM KCl, 10 mM NaCl, 20 mM EGTA, 60 mM KF, 10 mM Hepes), extracellular solution (ECS) (140 mM NaCl, 4 mM KCl, 1 mM $MgCl_2$, 2 mM $CaCl_2$, 5 mM D-glucose monohydrate, 10 mM Hepes) and seal enhancer solution (SES) (80 mM NaCl, 3 mM KCl, 10 mM $MgCl_2$, 35 mM $CaCl_2$, 10 mM Hepes) were used for APC experiments. In ICS, instead of usual 2–10 mM, 20 mM EGTA was used as per specifications of APC robot to keep cells longer in whole cell configuration and to maintain constant access resistance. However, we verified that reducing EGTA to 10 or 0 mM did not affect the kinetics of the selected Kv ion channels (data not shown). Inclusion of fluoride in ICS has been shown to improve patch clamp seal quality and to stabilize the cell membrane, resulting in longer and more stable patch clamp recordings (Kostyuk et al., 1975). While the effect of internal fluoride on Kv channel kinetics has been reported, directly (Adams and Oxford, 1983) or through PIP2 (Rodriguez-Menchaca et al., 2012), there are other reports claiming a lack of side effects on Kv channel kinetics (Clay,

TABLE 4 | Protein sequences of rat, mouse, and human Kv channels were aligned and analyzed for homology using the ClustalW method alignment function in the DNAstar software.

Ion channel	% Homology with rat		Main inter-species size differences
	Mouse	Human	
Kv1.1	99.2	98	
Kv1.2	100	99.4	
Kv1.3	99.6	97.3	Human, 52 aa longer N-tail
Kv1.4	99.8	97.6	
Kv1.5	96.4	87.5*	Human, 11 aa insertion in N-ter region
Kv1.6	98.9	92.8	
Kv1.7	98.4	93.6	Human, 32 aa shorter N-tail
Kv1.8	98	92.4	
Kv2.1	97.5	94.1	
Kv2.2	97.7	93.7	
Kv3.1	100	99.7	
Kv3.2	96.4	97.4	Mouse, different, and 22 aa longer N-tail
Kv3.3	97.7	91.4	Human, different, and 11 aa shorter N-tail
Kv3.4	99.4	95	Human, different, and 11 aa longer N-tail
Kv4.1	98.2	95.2	
Kv4.2	99.7	99	
Kv4.3iso2	99.5	99.4	Mouse, 19 aa insertion in C-ter region
Kv5.1	99.2	96.6	Human, 12 aa shorter N-tail
Kv6.1	98.6	92.6	
Kv6.2	97.3	90	Human, different, and 14 aa shorter N-tail
Kv6.3	99.1	96.8	
Kv6.4	95.9	81.1*	Human, 11 aa insertion in C-ter region
Kv7.1	97.5	90.3	Human, 6 aa insertion in C-ter region
Kv7.2	99.3	95.5	
Kv7.3	99.7	95.3	
Kv7.4	99.3	96.7	
Kv7.5	98.4	95.3	Human, 19 aa deletion in N-ter region
Kv8.1	99.2	95.6	
Kv8.2	95	83.5*	Human, shorter N-ter region, and S3-S4 loop
Kv9.1	97.8	90.9	Human, 31 aa longer N-tail
Kv9.2	99.6	98.1	
Kv9.3	98.8	95.5	
Kv10.1	98.7	97.6	
Kv10.2	99.4	98.3	
Kv11.1	99	95.9	
Kv11.2	97	90.2	Human, 44 aa insertion in C-ter region
Kv11.3	98.2	94.7	
Kv12.1	97.6	92.6	
Kv12.2	98.7	95.9	Difference in length of the S5–S6 region
Kv12.3	97.1	89.9*	

*Homology of the mouse and human sequences with respect to the rat sequence are indicated as a percentage, along with other significant interspecies differences in sequence length. *Indicates sequences with <90% homology.*

1988; López-López et al., 1993; Zeng et al., 2013). Along with fluoride in ICS, SES with high Ca^{2+} and Mg^{2+} was also applied extracellularly to achieve the giga seal. In our experience, without fluoride in ICS and high Ca^{2+} extracellularly, the APC robot could not form the giga seal. The SES was washed out with ECS after reaching whole cell configuration as well as between each repetition of voltage protocols. We observed that high Ca^{2+} and Mg^{2+} in SES did cause membrane potential oscillation artifacts for Kv11.1 and Kv11.3 cell lines, but it disappeared after washing with ECS solution (**Figure S14**). In conclusion, fluoride in ICS and high Ca^{2+} in SES were necessary to achieve giga seal in our APC experiments. Previous studies have found no significant differences in channel kinetics between manual and automated patch clamp system (Li et al., 2017). In addition, we did not find any difference in Kv2.1 kinetics when comparing with data obtained with another automated patch clamp robot (Fejtl et al., 2007) that worked with physiological ICS, ECS, and without the need of SES solution (data not shown). Despite these limitations, the solutions used in this study still contain physiological levels of sodium and potassium concentration to better reflect *in vivo* ion composition, and not bi-ionic high potassium (K^+) solution as used in many previous studies on potassium channels.

Currently, the reference dataset we provide, contains the main isoform of each Kv channel and does not include other known splicing variants. It is known that Kv channel genes, such as those involved in the immune system, are highly prone to alternative splicing (Lipscombe, 2005) that substantially increases the repertoire of Kv channels proteins. For example, the 40 known human Kv genes have 73 validated, and 113 predicted splicing isoforms. Our study additionally identified several unreported splicing variants (**Table S2**), showing that the full repertoire is yet to be mapped. The investigation of the kinetic activity of the different variants using our standardized system would also be of high value.

Kv Kinetics Near Physiological Temperature

Data on Kv kinetics near physiological temperature were not available for most of the Kv members (**Table 2**). This is the first complete map of Kv channels kinetics at 35°C. The qualitative differences we found at 35°C clearly suggests the need of a reassessment of previous functional characterizations of ICs. For example, Kv1.1 is generally considered to be a non-inactivating channel, which only inactivates in presence of Kvß1 or Kvß3 subunits (**Table 2**). We show that Kv1.1 actually inactivates strongly at 35°C, even in absence of these subunits in CHO cells (**Figure S4**). Similarly, Kv1.2 and Kv1.6, reported to become fast inactivating in presence of Kvß1 or Kvß3 subunits (Heinemann et al., 1996; Bähring et al., 2004), actually are strongly inactivating at 35°C even in absence of these subunits. As another example, we show that Kv7.1, one of the most studied ion channel, reported as active at room temperature and also at 35°C (Loussouarn et al., 1997), is actually only active at low temperatures and becomes silent at 35°C in CHO cells. Furthermore, it is generally accepted that KCNE1 subunit (mink) is required for proper functioning of Kv7.1 (Sanguinetti et al.,

1996; Aromolaran et al., 2014); the KCNE1 subunit might make Kv7.1 more active, but it is not required to form a functional channel, at least at low temperature. These examples illustrate how understanding the homomeric channel kinetics across temperatures is essential to correctly interpreting the effects of the several levels of regulation, such as heteromerization, accessory subunit associations or effects of post translational modifications (e.g., phosphorylation, glycosylation).

Implications for Ion Channel Modeling

The biophysical map and the reference dataset provide data for both improving the accuracy of genetically specified ion channel models and for cellular models (e.g., neurons and heart cells) which often use generic conductances (e.g., A-type channels, delayed rectifier channels) that do not capture the diversity of kinetics present within these generic classes. For example, Kv1.1 and Kv1.7 both belong to the Kv1 family but have completely different time constants for activation and inactivation. Generic IC models are unable to exploit the growing volume of data from single cell transcriptomics, which makes it possible to identify the full spectrum of IC genes expressed by specific cell types.

The data we publish will enable researchers to develop improved models for all the Kv channels. Particularly important is the availability of temperature and voltage-dependent Q_{10} for all kinetic parameters of Kv channels. Patch clamp experiments on cell lines at physiological temperature are difficult and hence majority of the experiments in the future might continue to be performed at lower temperatures. The availability of Q_{10} values from our data makes it possible to interpret those data in the context of physiological temperature. This prospect is very important for ongoing brain modeling programs such as the Blue Brain Project and the Allen Institute for Brain Sciences as well as for initiatives which develop on their work, such as the Human Brain Project. In addition, since specific receptors affect different subsets of ICs in different cells, the new data open the prospect of modeling the effects of neuromodulators on specific neuron types (Nicoll, 1988; Khorkova and Golowasch, 2007).

Inherent Heterogeneity and Delayed Inactivation

Our standardized kinetic characterization has revealed inherent kinetic heterogeneity in four Kv channels, namely Kv1.3, Kv1.5, Kv3.3, and Kv3.4, three of which also show a novel form of delayed inactivation. This inherent heterogeneity is present in isogenic cell lines that have not been manipulated in any way. The large number of recordings in standardized condition and screening of all Kv channels, allowed us to conclude that it is a truly inherent property. To our knowledge, the only previous study that mentions inherent heterogeneity is a report of two distinct phenotypes for rat Kv1.2 expressed in CHO cells after transient transfection (Rezazadeh et al., 2007). Specifically, the authors describe two gating phenotypes (fast and slow) influenced by a cytoplasmic regulator. Modulation in IC kinetics have been reported to occur upon glycosylation (Brooks et al., 2006; Noma et al., 2009), phosphorylation (Desai et al., 2008; Ritter et al., 2012), oxidation (Hoshi and Heinemann, 2001), or by co-expression of beta-subunits (Heinemann et al., 1996; Bähring et al., 2004) or other binding proteins (Pongs and Schwarz, 2010). We suggest that especially these four channels (Kv1.3, Kv1.5, Kv3.3, and Kv3.4) are susceptible to abovementioned modifications. The inherent heterogeneity we described may also explain some of the conflicting reports present in the literature (**Table 2**).

The delayed inactivation has been observed only for human Kv3.1, and only at high (>35°C) temperatures (Oliver et al., 2017). The mechanism underlying this novel form of delayed inactivation is unknown and would require further investigation.

Conserved Kinetics Across Species

Using a sample set of five Kv channels with different kinetics and different degree of homology, we found only subtle differences in some kinetics parameters between mouse, rat and human channel kinetics. Compared to the strong temperature-dependent effect on ion channel kinetics, the inter-species differences we observed are minor. According to these data on a sample set and the high degree of homology of ion channels (**Table 4**), we postulate that data on ion channels kinetics could be generalized over species. However, this has to be done with caution as even subtle differences observed in kinetics for a single ion channel type could have a strong impact over a neuronal network.

Our observation is consistent with the fact that transmembrane regions S4 to S6, believed to be primarily responsible for channel kinetics, are structurally almost identical across the three species. Nearly all the interspecies differences in the Kv channels sequences concern the N-terminus and C-terminus regions and the S1–S2 loop. The N and C-terminus contain protein binding motifs that are involved in the distribution of IC through the cell (Lai and Jan, 2006; Vacher et al., 2008; Duménieu et al., 2017). The N-terminus region is also involved in tetramerization and N-type inactivation via the "ball and chain" mechanism (Bezanilla and Armstrong, 1977). Hence significant differences in the length of N-terminus or C-terminus regions could affect channels kinetics between different species. For example, human Kv1.7, that has a 32 amino acids shorter N-terminus, has been reported as slow-inactivating while the longer versions in mouse and rat are reported as fast inactivating (Finol-Urdaneta et al., 2006, 2012). Such channels with significant difference in the length of their N-terminus and/or C-terminus regions (**Table 4**) would require separate studies to clarify the effect of such possible interspecies differences on their kinetics.

Implications for Drug Discovery

The methods we have established to create the kinetic map of Kv channels can be used to systematically screen drug candidates for potentially positive or deleterious effects on their kinetics. They can also be used to test the effects of targeted mutations and the ability of drugs to reverse their effects. Such studies have the potential to improve our understanding of disease mechanisms, and have obvious applications in drug discovery. In a longer-term perspective, detailed neuron models incorporating genetically specified ion channels could allow simulation of channelopathies at the cellular and network level.

Future Outlook

For the first time in ion channel research, electrophysiology data from a complete family of ICs have been obtained and made publicly available. We have developed Channelpedia as an online tool for data sharing and we believe that the availability and the ease of data access on this website may encourage other researchers to make their electrophysiology data available through Channelpedia or similar platforms. The availability of the new dataset allows us to investigate links between IC genetics, structure, and biophysics. For example, preliminary results from pairwise alignment of the sequences for the S1–S2 loops, reveal a genetic basis for at least two big groups—inactivating and non-inactivating ICs (data not shown). Large-scale bioinformatics studies aimed at establishing genotype-phenotype correlations are now possible. A key issue for future works is to unravel the mechanism for inherent heterogeneity of IC kinetics.

Homotetrameric Kv channels consist of four identical alpha (α)-subunits, but additional diversity is introduced when different α-subunits combine to form heterotetramers (Dodson et al., 2002; Hadley et al., 2003; Zhang et al., 2016). The function of homotetramers and heterotetramers is further modulated by a broad range of auxiliary (signaling/scaffolding) proteins (Levitan, 2006; Li et al., 2006), including Kvβ-subunits (Pongs and Schwarz, 2010), chaperone proteins (HSP90, HSP70) (Ficker et al., 2003), and other regulatory protein families like K^+ channel-Interacting proteins (KChIPs), K^+ channel-associated proteins (KChAP), 14-3-3 proteins, A-kinase-anchoring proteins (AKAP) (Zhang et al., 2016), Dipeptidyl aminopeptidase-like protein (DPP), and KCNE-encoded proteins (Coetzee et al., 1999). Among all possible combinations for heterotetramers and auxiliary subunits, some have been shown to have modulatory effects on kinetic properties, trafficking, permeation, and stability of Kv channels. However, there are also contradictory results on the role of auxiliary subunits; for example on the role of Kvβ3 on Kv1.1 activity ((Bähring et al., 2004) shows that co-expression of Kvβ3 modulates the inactivation of Kv1.1 whereas (Majumder et al., 1995) shows no effect of Kvβ3 on Kv1.1 kinetics) or on the effect of KCNE1(Mink) on Kv7.1 activity ((Bett et al., 2006) shows that Mink modulates KCNQ1 kinetic whereas (Sanguinetti et al., 1996) shows that Mink is necessary for KCNQ1 to be active). The next layers of the kinetic map for the Kv family are the heterotetramers map (kinetics of viable combinations of α-subunits), the β-subunits map (kinetics when bound to β-subunits), and the neuromodulatory map (kinetics for all forms of modulation). The biggest challenge in building these maps is to identify principles for biologically viable combinations of subunits and modulation since all theoretical combinations cannot be mapped. Knowledge of the detailed kinetics of the homotetrameric channels with their structural and genetic correlates, combined with transcriptomics data on the expression of channels in single cells or cell types, will provide a starting point for investigation of this vast, as yet unexplored, combinatorial space.

ETHICS STATEMENT

All procedures were conducted in conformity with the Swiss Welfare Act and the Swiss National Institutional Guidelines on Animal Experimentation for the ethical use of animals.

AUTHOR CONTRIBUTIONS

RR, EL, and HM: conceptualization, writing, and supervision. RR, EL, and MM: methodology and data curation. RR: data analysis. RR and ES: coding and channelpedia. RR, EL, MM, MH, VT and VB: investigation.

FUNDING

This work was funded by the EPFL Blue Brain Project Fund, ETH board funding to the Blue Brain Project and the funding from the EPFL to the Laboratory of Neural Microcircuitry (LNMC).

ACKNOWLEDGMENTS

We thank C. Pernet and S. Petitprez for their contribution at the initial phase of the study, A. Nojku for cell lines images, D. Jovandic for his contribution to Channelpedia web application, G. Zouein for NWB data conversion, B-J. Zandt for his help in H-H modeling, N. Khanna for Literature review, D. LaMendola, and J. Meystre for technical support, O. Hagens, G. Khazen, R. Perin, and J. Ryge for helpful discussions, K. Harshman for Nanostring screening, Nanion team for technical support, BBP infrastructure team for providing help to host Channelpedia web server and storage, E. Muller and F. Schuermann for their help in project management. Special thanks to R. Walker, K. Holm for editing of the manuscript.

SUPPLEMENTARY MATERIAL

The Supplementary Material for this article can be found online at: https://www.frontiersin.org/articles/10.3389/fncel.2019.00358/full#supplementary-material

REFERENCES

Adams, D. J., and Oxford, G. S. (1983). Interaction of internal anions with potassium channels of the squid giant axon. *J. Gen. Physiol.* 82, 429–448. doi: 10.1085/jgp.82.4.429

Alberts, B., Wilson, J. H., and Hunt, T. (eds.). (2008). *Molecular Biology of the Cell, 5th Edn*. New York, NY: Garland Science.

Aromolaran, A. S., Subramanyam, P., Chang, D. D., Kobertz, W. R., and Colecraft, H. M. (2014). LQT1 mutations in KCNQ1 C-terminus assembly domain suppress IKs using different mechanisms. *Cardiovasc. Res.* 104, 501–511. doi: 10.1093/cvr/cvu231

Bähring, R., Vardanyan, V., and Pongs, O. (2004). Differential modulation of Kv1 channel-mediated currents by co-expression of Kvbeta3 subunit in a mammalian cell-line.

Mol. Membr. Biol. 21, 19–25. doi: 10.1080/096876803100015 97749

Barhanin, J., Lesage, F., Guillemare, E., Fink, M., Lazdunski, M., and Romey, G. (1996). K(V)LQT1 and lsK (minK) proteins associate to form the I(Ks) cardiac potassium current. *Nature* 384, 78–80. doi: 10.1038/384078a0

Beam, K. G., and Donaldson, P. L. (1983). A quantitative study of potassium channel kinetics in rat skeletal muscle from 1 to 37 degrees C. *J. Gen. Physiol.* 81, 485–512. doi: 10.1085/jgp.81.4.485

Begum, R., Bakiri, Y., Volynski, K. E., and Kullmann, D. M. (2016). Action potential broadening in a presynaptic channelopathy. *Nat. Commun.* 7:12102. doi: 10.1038/ncomms12102

Bělehrádek, J. (1935). *Temperature and Living Matter*. Berlin: Gebrüder Borntraeger.

Bett, G. C. L., Morales, M. J., Beahm, D. L., Duffey, M. E., and Rasmusson, R. L. (2006). Ancillary subunits and stimulation frequency determine the potency of chromanol 293B block of the KCNQ1 potassium channel. *J. Physiol.* 576, 755–767. doi: 10.1113/jphysiol.2006.116012

Bezanilla, F. (2000). The voltage sensor in voltage-dependent ion channels. *Physiol. Rev.* 80, 555–592. doi: 10.1152/physrev.2000.80.2.555

Bezanilla, F., and Armstrong, C. M. (1977). Inactivation of the sodium channel. I. Sodium current experiments. *J. Gen. Physiol.* 70, 549–566. doi: 10.1085/jgp.70.5.549

Bocksteins, E., Mayeur, E., Van Tilborg, A., Regnier, G., Timmermans, J.-P., and Snyders, D. J. (2014). The subfamily-specific interaction between Kv2.1 and Kv6.4 subunits is determined by interactions between the N- and C-termini. *PLoS ONE* 9:e98960. doi: 10.1371/journal.pone.0098960

Brooks, N. L., Corey, M. J., and Schwalbe, R. A. (2006). Characterization of N-glycosylation consensus sequences in the Kv3.1 channel. *FEBS J.* 273, 3287–3300. doi: 10.1111/j.1742-4658.2006.05339.x

Clay, J. R. (1988). Lack of effect of internal fluoride ions on potassium channels in squid axons. *Biophys. J.* 53, 647–648. doi: 10.1016/S0006-3495(88)83144-8

Coetzee, W. A., Amarillo, Y., Chiu, J., Chow, A., Lau, D., McCormack, T., et al. (1999). Molecular diversity of K^+ channels. *Ann. N. Y. Acad. Sci.* 868, 233–285. doi: 10.1111/j.1749-6632.1999.tb11293.x

D'Adamo, M. C., Gallenmüller, C., Servettini, I., Hartl, E., Tucker, S. J., Arning, L., et al. (2014). Novel phenotype associated with a mutation in the KCNA1(Kv1.1) gene. *Front. Physiol.* 5:525. doi: 10.3389/fphys.2014.00525

Desai, R., Kronengold, J., Mei, J., Forman, S. A., and Kaczmarek, L. K. (2008). Protein kinase C modulates inactivation of Kv3.3 channels. *J. Biol. Chem.* 283, 22283–22294. doi: 10.1074/jbc.M801663200

Dodson, P. D., Barker, M. C., and Forsythe, I. D. (2002). Two heteromeric Kv1 potassium channels differentially regulate action potential firing. *J. Neurosci. Off. J. Soc. Neurosci.* 22, 6953–6961. doi: 10.1523/JNEUROSCI.22-16-06953.2002

Duménieu, M., Oulé, M., Kreutz, M. R., and Lopez-Rojas, J. (2017). The segregated expression of voltage-gated potassium and sodium channels in neuronal membranes: functional implications and regulatory mechanisms. *Front. Cell. Neurosci.* 11:115. doi: 10.3389/fncel.2017.00115

Engeland, B., Neu, A., Ludwig, J., Roeper, J., and Pongs, O. (1998). Cloning and functional expression of rat ether-à-go-go-like K^+ channel genes. *J. Physiol.* 513 (Pt 3), 647–654. doi: 10.1111/j.1469-7793.1998.647ba.x

Fejtl, M., Czubayko, U., Hümmer, A., Krauter, T., and Lepple-Wienhues, A. (2007). Flip-the-tip: automated patch clamping based on glass electrodes. *Methods Mol. Biol.* 403, 71–85. doi: 10.1007/978-1-59745-529-9_5

Fernandez, F. R., Morales, E., Rashid, A. J., Dunn, R. J., and Turner, R. W. (2003). Inactivation of Kv3.3 potassium channels in heterologous expression systems. *J. Biol. Chem.* 278, 40890–40898. doi: 10.1074/jbc.M304235200

Ficker, E., Dennis, A. T., Wang, L., and Brown, A. M. (2003). Role of the cytosolic chaperones Hsp70 and Hsp90 in maturation of the cardiac potassium channel HERG. *Circ. Res.* 92, e87–100. doi: 10.1161/01.RES.0000079028.31393.15

Finol-Urdaneta, R. K., Remedi, M. S., Raasch, W., Becker, S., Clark, R. B., Strüver, N., et al. (2012). Block of Kv1.7 potassium currents increases glucose-stimulated insulin secretion. *EMBO Mol. Med.* 4, 424–434. doi: 10.1002/emmm.201200218

Finol-Urdaneta, R. K., Strüver, N., and Terlau, H. (2006). Molecular and functional differences between heart mKv1.7 channel isoforms. *J. Gen. Physiol.* 128, 133–145. doi: 10.1085/jgp.200609498

Gabel, L. A., and Nisenbaum, E. S. (1998). Biophysical characterization and functional consequences of a slowly inactivating potassium current in neostriatal neurons. *J. Neurophysiol.* 79, 1989–2002. doi: 10.1152/jn.1998.79.4.1989

Gamper, N., Stockand, J. D., and Shapiro, M. S. (2005). The use of Chinese hamster ovary (CHO) cells in the study of ion channels. *J. Pharmacol. Toxicol. Methods* 51, 177–185. doi: 10.1016/j.vascn.2004.08.008

Gilling, M., Rasmussen, H. B., Calloe, K., Sequeira, A. F., Baretto, M., Oliveira, G., et al. (2013). Dysfunction of the heteromeric KV7.3/KV7.5 potassium channel is associated with autism spectrum disorders. *Front. Genet.* 4:54. doi: 10.3389/fgene.2013.00054

Glazebrook, P. A., Ramirez, A. N., Schild, J. H., Shieh, C.-C., Doan, T., Wible, B. A., et al. (2002). Potassium channels Kv1.1, Kv1.2 and Kv1.6 influence excitability of rat visceral sensory neurons. *J. Physiol.* 541, 467–482. doi: 10.1113/jphysiol.2001.018333

Graves, T. D., and Hanna, M. G. (2005). Neurological channelopathies. *Postgrad. Med. J.* 81, 20–32. doi: 10.1136/pgmj.2004.022012

Hadley, J. K., Passmore, G. M., Tatulian, L., Al-Qatari, M., Ye, F., Wickenden, A. D., et al. (2003). Stoichiometry of expressed KCNQ2/KCNQ3 potassium channels and subunit composition of native ganglionic M channels deduced from block by tetraethylammonium. *J. Neurosci. Off. J. Soc. Neurosci.* 23, 5012–5019. doi: 10.1523/JNEUROSCI.23-12-05012.2003

Hatton, W. J., Mason, H. S., Carl, A., Doherty, P., Latten, M. J., Kenyon, J. L., et al. (2001). Functional and molecular expression of a voltage-dependent K^+ channel (Kv1.1) in interstitial cells of Cajal. *J. Physiol.* 533, 315–327. doi: 10.1111/j.1469-7793.2001.0315a.x

Heginbotham, L., Lu, Z., Abramson, T., and MacKinnon, R. (1994). Mutations in the K^+ channel signature sequence. *Biophys. J.* 66, 1061–1067. doi: 10.1016/S0006-3495(94)80887-2

Heinemann, S. H., Rettig, J., Graack, H. R., and Pongs, O. (1996). Functional characterization of Kv channel beta-subunits from rat brain. *J. Physiol.* 493, 625–633. doi: 10.1113/jphysiol.1996.sp021409

Hille, B. (2001). *Ion Channels of Excitable Membranes*. Sunderland: Mass Sinauer.

Hodgkin, A. L., and Huxley, A. F. (1952). A quantitative description of membrane current and its application to conduction and excitation in nerve. *J. Physiol.* 117, 500–544. doi: 10.1113/jphysiol.1952.sp004764

Hoshi, T., and Heinemann, S. (2001). Regulation of cell function by methionine oxidation and reduction. *J. Physiol.* 531, 1–11. doi: 10.1111/j.1469-7793.2001.0001j.x

Jensen, C. S., Rasmussen, H. B., and Misonou, H. (2011). Neuronal trafficking of voltage-gated potassium channels. *Mol. Cell. Neurosci.* 48, 288–297. doi: 10.1016/j.mcn.2011.05.007

John, V. H., Main, M. J., Powell, A. J., Gladwell, Z. M., Hick, C., Sidhu, H. S., et al. (2004). Heterologous expression and functional analysis of rat Nav1.8 (SNS) voltage-gated sodium channels in the dorsal root ganglion neuroblastoma cell line ND7-23. *Neuropharmacology* 46, 425–438. doi: 10.1016/j.neuropharm.2003.09.018

Jow, F., Zhang, Z.-H., Kopsco, D. C., Carroll, K. C., and Wang, K. (2004). Functional coupling of intracellular calcium and inactivation of voltage-gated Kv1.1/Kvbeta1.1 A-type K^+ channels. *Proc. Natl. Acad. Sci. U.S.A.* 101, 15535–15540. doi: 10.1073/pnas.0402081101

Ju, M., Stevens, L., Leadbitter, E., and Wray, D. (2003). The Roles of N- and C-terminal determinants in the activation of the Kv2.1 potassium channel. *J. Biol. Chem.* 278, 12769–12778. doi: 10.1074/jbc.M212973200

Kaczmarek, L. K. (2006). Non-conducting functions of voltage-gated ion channels. *Nat. Rev. Neurosci.* 7, 761–771. doi: 10.1038/nrn1988

Khorkova, O., and Golowasch, J. (2007). Neuromodulators, not activity, control coordinated expression of ionic currents. *J. Neurosci. Off. J. Soc. Neurosci.* 27, 8709–8718. doi: 10.1523/JNEUROSCI.1274-07.2007

Kostyuk, P. G., Krishtal, O. A., and Pidoplichko, V. I. (1975). Effect of internal fluoride and phosphate on membrane currents during intracellular dialysis of nerve cells. *Nature* 257, 691–693. doi: 10.1038/257691a0

Kramer, J. W., Post, M. A., Brown, A. M., and Kirsch, G. E. (1998). Modulation of potassium channel gating by coexpression of Kv2.1 with regulatory Kv5.1 or Kv6.1 alpha-subunits. *Am. J. Physiol.* 274, C1501–1510. doi: 10.1152/ajpcell.1998.274.6.C1501

Kullmann, D. M., and Waxman, S. G. (2010). Neurological channelopathies: new insights into disease mechanisms and ion channel function. *J. Physiol.* 588, 1823–1827. doi: 10.1113/jphysiol.2010.190652

Labro, A. J., Priest, M. F., Lacroix, J. J., Snyders, D. J., and Bezanilla, F. (2015). Kv3.1 uses a timely resurgent K^+ current to secure action potential repolarization. *Nat. Commun*. 6:10173. doi: 10.1038/ncomms10173

Lai, H. C., and Jan, L. Y. (2006). The distribution and targeting of neuronal voltage-gated ion channels. *Nat. Rev. Neurosci*. 7, 548–562. doi: 10.1038/nrn1938

Lalik, P. H., Krafte, D. S., Volberg, W. A., and Ciccarelli, R. B. (1993). Characterization of endogenous sodium channel gene expressed in Chinese hamster ovary cells. *Am. J. Physiol.* 264, C803–809. doi: 10.1152/ajpcell.1993.264.4.C803

Lee, S. C., and Deutsch, C. (1990). Temperature dependence of K^+-channel properties in human T lymphocytes. *Biophys. J.* 57, 49–62. doi: 10.1016/S0006-3495(90)82506-6

Levitan, I. B. (2006). Signaling protein complexes associated with neuronal ion channels. *Nat. Neurosci*. 9, 305–310. doi: 10.1038/nn1647

Li, G.-R., and Dong, M.-Q. (2010). Pharmacology of cardiac potassium channels. *Adv. Pharmacol.* 59, 93–134. doi: 10.1016/S1054-3589(10)59004-5

Li, T., Lu, G., Chiang, E. Y., Chernov-Rogan, T., Grogan, J. L., and Chen, J. (2017). High-throughput electrophysiological assays for voltage gated ion channels using SyncroPatch 768PE. *PLoS ONE*. 12:e0180154. doi: 10.1371/journal.pone.0180154

Li, Y., Um, S. Y., and McDonald, T. V. (2006). Voltage-gated potassium channels: regulation by accessory subunits. *Neurosci. Rev. J. Bringing Neurobiol. Neurol. Psychiatry* 12, 199–210. doi: 10.1177/1073858406287717

Lipscombe, D. (2005). Neuronal proteins custom designed by alternative splicing. *Curr. Opin. Neurobiol*. 15, 358–363. doi: 10.1016/j.conb.2005.04.002

López-López, J. R., De Luis, D. A., and Gonzalez, C. (1993). Properties of a transient K^+ current in chemoreceptor cells of rabbit carotid body. *J. Physiol.* 460, 15–32. doi: 10.1113/jphysiol.1993.sp019456

Loussouarn, G., Charpentier, F., Mohammad-Panah, R., Kunzelmann, K., Baró, I., and Escande, D. (1997). KvLQT1 potassium channel but not IsK is the molecular target for trans-6-cyano-4-(N-ethylsulfonyl-N-methylamino)-3-hydroxy-2,2-dimethyl- chromane. *Mol. Pharmacol.* 52, 1131–1136. doi: 10.1124/mol.52.6.1131

Majumder, K., De Biasi, M., Wang, Z., and Wible, B. A. (1995). Molecular cloning and functional expression of a novel potassium channel beta-subunit from human atrium. *FEBS Lett*. 361, 13–16. doi: 10.1016/0014-5793(95)00120-X

Nakajo, K., and Kubo, Y. (2008). Second coiled-coil domain of KCNQ channel controls current expression and subfamily specific heteromultimerization by salt bridge networks. *J. Physiol.* 586, 2827–2840. doi: 10.1113/jphysiol.2007.148601

NCBI, Resource Coordinators (2013). Database resources of the National Center for Biotechnology Information. *Nucleic Acids Res.* 41, D8–D20. doi: 10.1093/nar/gks1189

Nicoll, R. A. (1988). The coupling of neurotransmitter receptors to ion channels in the brain. *Science* 241, 545–551. doi: 10.1126/science.2456612

Noma, K., Kimura, K., Minatohara, K., Nakashima, H., Nagao, Y., Mizoguchi, A., et al. (2009). Triple N-glycosylation in the long S5-P loop regulates the activation and trafficking of the Kv12.2 potassium channel. *J. Biol. Chem*. 284, 33139–33150. doi: 10.1074/jbc.M109.021519

O'Gorman, S., Fox, D. T., and Wahl, G. M. (1991). Recombinase-mediated gene activation and site-specific integration in mammalian cells. *Science* 251, 1351–1355. doi: 10.1126/science.1900642

Oliver, K. L., Franceschetti, S., Milligan, C. J., Muona, M., Mandelstam, S. A., Canafoglia, L., et al. (2017). Myoclonus epilepsy and ataxia due to KCNC1 mutation: Analysis of 20 cases and K^+ channel properties. *Ann. Neurol.* 81, 677–689. doi: 10.1002/ana.24929

Petersen, K. R., and Nerbonne, J. M. (1999). Expression environment determines K^+ current properties: Kv1 and Kv4 alpha-subunit-induced K^+ currents in mammalian cell lines and cardiac myocytes. *Pflugers Arch*. 437, 381–392. doi: 10.1007/s004240050792

Pongs, O., and Schwarz, J. R. (2010). Ancillary subunits associated with voltage-dependent K^+ channels. *Physiol. Rev*. 90, 755–796. doi: 10.1152/physrev.00020.2009

Post, J. M., Hume, J. R., Archer, S. L., and Weir, E. K. (1992). Direct role for potassium channel inhibition in hypoxic pulmonary vasoconstriction. *Am. J. Physiol.* 262, C882–890. doi: 10.1152/ajpcell.1992.262.4.C882

Rajakulendran, S., Schorge, S., Kullmann, D. M., and Hanna, M. G. (2007). Episodic ataxia type 1: a neuronal potassium channelopathy. *Neurother. J. Am. Soc. Exp. Neurother*. 4, 258–266. doi: 10.1016/j.nurt.2007.01.010

Rasband, M. N. (2010). Clustered K^+ channel complexes in axons. *Neurosci. Lett.* 486, 101–106. doi: 10.1016/j.neulet.2010.08.081

Rezazadeh, S., Kurata, H. T., Claydon, T. W., Kehl, S. J., and Fedida, D. (2007). An activation gating switch in Kv1.2 is localized to a threonine residue in the S2-S3 linker. *Biophys. J.* 93, 4173–4186. doi: 10.1529/biophysj.107.116160

Ritter, D. M., Ho, C., O'Leary, M. E., and Covarrubias, M. (2012). Modulation of Kv3.4 channel N-type inactivation by protein kinase C shapes the action potential in dorsal root ganglion neurons. *J. Physiol.* 590, 145–161. doi: 10.1113/jphysiol.2011.218560

Rodriguez-Menchaca, A. A., Adney, S. K., Tang, Q.-Y., Meng, X.-Y., Rosenhouse-Dantsker, A., Cui, M., et al. (2012). PIP2 controls voltage-sensor movement and pore opening of Kv channels through the S4-S5 linker. *Proc. Natl. Acad. Sci. U.S. A*. 109, E2399–2408. doi: 10.1073/pnas.1207901109

Rudy, B., and McBain, C. J. (2001). Kv3 channels: voltage-gated K^+ channels designed for high-frequency repetitive firing. *Trends Neurosci.* 24, 517–526. doi: 10.1016/S0166-2236(00)01892-0

Salinas, M., Duprat, F., Heurteaux, C., Hugnot, J. P., and Lazdunski, M. (1997). New modulatory alpha subunits for mammalian Shab K^+ channels. *J. Biol. Chem*. 272, 24371–24379. doi: 10.1074/jbc.272.39.24371

Sanguinetti, M. C., Curran, M. E., Zou, A., Shen, J., Spector, P. S., Atkinson, D. L., et al. (1996). Coassembly of K(V)LQT1 and minK (IsK) proteins to form cardiac I(Ks) potassium channel. *Nature* 384, 80–83. doi: 10.1038/384080a0

Shah, N. H., and Aizenman, E. (2014). Voltage-gated potassium channels at the crossroads of neuronal function, ischemic tolerance, and neurodegeneration. Transl. *Stroke Res.* 5, 38–58. doi: 10.1007/s12975-013-0297-7

Siepel, A., Bejerano, G., Pedersen, J. S., Hinrichs, A. S., Hou, M., Rosenbloom, K., et al. (2005). Evolutionarily conserved elements in vertebrate, insect, worm, and yeast genomes. *Genome Res.* 15, 1034–1050. doi: 10.1101/gr.3715005

Southan, C., Sharman, J. L., Benson, H. E., Faccenda, E., Pawson, A. J., Alexander, S. P. H., et al. (2016). The IUPHAR/BPS Guide to PHARMACOLOGY in 2016: towards curated quantitative interactions between 1300 protein targets and 6000 ligands. *Nucleic Acids Res*. 44, D1054–1068. doi: 10.1093/nar/gkv1037

Stephens, G. J., Page, K. M., Burley, J. R., Berrow, N. S., and Dolphin, A. C. (1997). Functional expression of rat brain cloned alpha1E calcium channels in COS-7 cells. Pflüg. *Arch. Eur. J. Physiol.* 433, 523–532. doi: 10.1007/s004240050308

Storm, J. F. (1988). Temporal integration by a slowly inactivating K^+ current in hippocampal neurons. *Nature* 336, 379–381. doi: 10.1038/336379a0

Sturm, P., Wimmers, S., Schwarz, J. R., and Bauer, C. K. (2005). Extracellular potassium effects are conserved within the rat erg K^+ channel family. *J. Physiol.* 564, 329–345. doi: 10.1113/jphysiol.2004.078840

Teeters, J. L., Godfrey, K., Young, R., Dang, C., Friedsam, C., Wark, B., et al. (2015). Neurodata without borders: creating a common data format for neurophysiology. *Neuron* 88, 629–634. doi: 10.1016/j.neuron.2015.10.025

Trimmer, J. S. (2015). Subcellular localization of K^+ channels in mammalian brain neurons: remarkable precision in the midst of extraordinary complexity. *Neuron* 85, 238–256. doi: 10.1016/j.neuron.2014.12.042

Vacher, H., Mohapatra, D. P., and Trimmer, J. S. (2008). Localization and targeting of voltage-dependent ion channels in mammalian central neurons. *Physiol. Rev.* 88, 1407–1447. doi: 10.1152/physrev.00002.2008

van der Wijst, J., Glaudemans, B., Venselaar, H., Nair, A. V., Forst, A.-L., Hoenderop, J. G. J., et al. (2010). Functional analysis of the Kv1.1 N255D mutation associated with autosomal dominant hypomagnesemia. *J. Biol. Chem.* 285, 171–178. doi: 10.1074/jbc.M109.041517

Wang, H. S., Pan, Z., Shi, W., Brown, B. S., Wymore, R. S., Cohen, I. S., et al. (1998). KCNQ2 and KCNQ3 potassium channel subunits: molecular correlates of the M-channel. *Science* 282, 1890–1893. doi: 10.1126/science.282.5395.1890

Wimmers, S., Bauer, C. K., and Schwarz, J. R. (2002). Biophysical properties of heteromultimeric erg K^+ channels. *Pflugers Arch*. 445, 423–430. doi: 10.1007/s00424-002-0936-4

Yao, F., Svensjö, T., Winkler, T., Lu, M., Eriksson, C., and Eriksson, E. (1998). Tetracycline repressor, tetR, rather than the tetR-mammalian cell transcription factor fusion derivatives, regulates inducible gene expression in mammalian cells. *Hum. Gene Ther.* 9, 1939–1950. doi: 10.1089/hum.1998.9.13-1939

Zeng, H., Balasubramanian, B., Penniman, J. R., Kinose, F., Salata, J. J., and Lagrutta, A. (2013). Halide ion effects on human Ether-à-go-go related gene potassium channel properties. *Assay Drug Dev. Technol.* 11, 544–550. doi: 10.1089/adt.2013.531

Zhang, J., Carver, C. M., Choveau, F. S., and Shapiro, M. S. (2016). Clustering and functional coupling of diverse ion channels and signaling proteins revealed by super-resolution STORM microscopy in neurons. *Neuron* 92, 461–478. doi: 10.1016/j.neuron.2016.09.014

Conflict of Interest Statement: The authors declare that the research was conducted in the absence of any commercial or financial relationships that could be construed as a potential conflict of interest.

Copyright © 2019 Ranjan, Logette, Marani, Herzog, Tâche, Scantamburlo, Buchillier and Markram. This is an open-access article distributed under the terms of the Creative Commons Attribution License (CC BY). The use, distribution or reproduction in other forums is permitted, provided the original author(s) and the copyright owner(s) are credited and that the original publication in this journal is cited, in accordance with accepted academic practice. No use, distribution or reproduction is permitted which does not comply with these terms.

frontiers in Cellular Neuroscience

ORIGINAL RESEARCH
published: 12 November 2019
doi: 10.3389/fncel.2019.00509

High-Fat Diet Induces Neuroinflammation and Mitochondrial Impairment in Mice Cerebral Cortex and Synaptic Fraction

Gina Cavaliere[1†], Giovanna Trinchese[1†], Eduardo Penna[1], Fabiano Cimmino[1], Claudio Pirozzi[2], Adriano Lama[2], Chiara Annunziata[2], Angela Catapano[1,2], Giuseppina Mattace Raso[2], Rosaria Meli[2], Marcellino Monda[3], Giovanni Messina[4], Christian Zammit[5], Marianna Crispino[1] and Maria Pina Mollica[1]*

[1]Department of Biology, University of Naples Federico II, Naples, Italy, [2]Department of Pharmacy, University of Naples Federico II, Naples, Italy, [3]Unit of Dietetics and Sports Medicine, Section of Human Physiology, Department of Experimental Medicine, University of Campania Luigi Vanvitelli, Naples, Italy, [4]Department of Clinical and Experimental Medicine, University of Foggia, Foggia, Italy, [5]Department of Anatomy, Faculty of Medicine and Surgery, University of Malta, Msida, Malta

OPEN ACCESS

Edited by:
Francesco Moccia, University of Pavia, Italy

Reviewed by:
Carmine Rocca, University of Calabria, Italy
Hermona Soreq, Hebrew University of Jerusalem, Israel

***Correspondence:**
Marianna Crispino
crispino@unina.it

[†]These authors have contributed equally to this work and share first authorship

Received: *26 June 2019*
Accepted: *29 October 2019*
Published: *12 November 2019*

Citation:
Cavaliere G, Trinchese G, Penna E, Cimmino F, Pirozzi C, Lama A, Annunziata C, Catapano A, Mattace Raso G, Meli R, Monda M, Messina G, Zammit C, Crispino M and Mollica MP (2019) High-Fat Diet Induces Neuroinflammation and Mitochondrial Impairment in Mice Cerebral Cortex and Synaptic Fraction. Front. Cell. Neurosci. 13:509. doi: 10.3389/fncel.2019.00509

Brain mitochondrial dysfunction is involved in the development of neurological and neurodegenerative diseases. Mitochondria specifically located at synapses play a key role in providing energy to support synaptic functions and plasticity, thus their defects may lead to synaptic failure, which is a common hallmark of neurodegenerative diseases. High-Fat Diet (HFD) consumption increases brain oxidative stress and impairs brain mitochondrial functions, although the underlying mechanisms are not completely understood. The aim of our study is to analyze neuroinflammation and mitochondrial dysfunctions in brain cortex and synaptosomal fraction isolated from a mouse model of diet-induced obesity. Male C57Bl/6 mice were divided into two groups fed a standard diet or HFD for 18 weeks. At the end of the treatment, inflammation (detected by ELISA), antioxidant state (measured by enzymatic activity), mitochondrial functions and efficiency (detected by oxidative capacity and Seahorse analysis), and brain-derived neurotrophic factor (BDNF) pathway (analyzed by western blot) were determined in brain cortex and synaptosomal fraction. In HFD animals, we observed an increase in inflammatory parameters and oxidative stress and a decrease in mitochondrial oxidative capacity both in the brain cortex and synaptosomal fraction. These alterations parallel with modulation of BDNF, a brain key signaling molecule that is linking synaptic plasticity and energy metabolism. Neuroinflammation HFD-dependent negatively affects BDNF pathway and mitochondrial activity in the brain cortex. The effect is even more pronounced in the synaptic region, where the impaired energy supply may have a negative impact on neuronal plasticity.

Keywords: high-fat diet, neuroinflammation, mitochondria, synaptic plasticity, BDNF

INTRODUCTION

High-Fat diet (HFD) consumption induces obesity-related metabolic disorders characterized by low-grade inflammation (Mollica et al., 2011). Inflammation is a response to stress designed for adaptation and recovery from insults (Hernández-Aguilera et al., 2013). When an inflammatory state is prolonged, it can compromise cell functions, leading to altered metabolism and associated pathological conditions (Hernández-Aguilera et al., 2013). Mitochondria, the primary cellular energy-generating system, produce key factors during inflammation and oxidation and constitute the main source of reactive oxygen species (ROS). Therefore, mitochondrial dysfunction is related to inflammation and other energy-dependent disturbances, where the generation of ROS exceeds the physiological antioxidant protective activity, causing cellular oxidative damage (Chan, 2006). In the brain, neuroinflammation is an important risk factor for neurodegenerative disorders, characterized by learning and cognitive decline that depends on altered neuronal connectivity and atypical synaptic plasticity (Kumar, 2018). Numerous data indicate that HFD may activate signaling pathways with deleterious effects in several brain regions such as the hippocampus and brain cortex (Dutheil et al., 2016; Chen et al., 2019). The non-coding RNAs are assuming escalating importance in the regulation of metabolic disease at RNA levels, linking nutritional influence, neuroinflammation and brain-derived neurotrophic factor (BDNF) pathway (Hanin et al., 2018; Haviv et al., 2018; Meydan et al., 2018). BDNF is a neurotrophin playing a key role in the physiology and pathology of the brain (Lima Giacobbo et al., 2019). In particular, neuroinflammation HFD-induced is known to affect BDNF-related pathways in several brain regions (Mi et al., 2017; Zhao et al., 2019). The brain requires high amounts of energy for numerous processes, including neurotransmitter production and synaptic activity. Thus, the brain utilizes about 20% of the body's total ATP, although it weighs only 2% of the entire body (Jain et al., 2010). Since mitochondrial energy demand is higher in the brain compared to other tissues, subtle changes in mitochondrial energy production have a strong impact on the brain (Joshi and Mochly-Rosen, 2018). In particular, the impaired neurotransmission and cognitive failure associated to neurodegenerative diseases may be related to the dysfunctional synaptic mitochondria that do not satisfy the high energy demands required at the synapses (Reddy and Beal, 2008). At pre-synaptic terminals, mitochondria produce most of the ATP required for exocytosis and neurotransmitter reuptake into synaptic vesicles, while at postsynaptic level, a high amount of energy is required mainly for plasma membrane excitability and receptor and ion channel functioning (Lores-Arnaiz et al., 2016). To study the bioenergetics and mitochondrial functions in the synaptic regions, synaptosomal fraction from the mammalian brain is a very useful tool. Here, we evaluate the mitochondrial function and efficiency, oxidative stress, inflammation, and BDNF pathway both in the brain cortex and in the corresponding synaptosomal fraction of HFD-induced obese mice.

MATERIALS AND METHODS

Materials

The analytical-grade chemicals used were purchased from Sigma (St. Louis, MO, USA).

Animal and Diet

Male C57Bl/6J mice (Charles River Laboratories, Calco, Lecco, Italy) were caged in a temperature-controlled room and exposed to daily 12 h light-12 h dark cycle with free access to water and food. Young animals (average 27 $\pm$ 0.8 *g*) were used. A group (n = 7) was sacrificed at the beginning of the study to establish baseline measurements. The remaining mice were divided into two experimental groups (n = 7 each): the first group received a standard diet (control diet, CD; 10.6% fat J/J; Mucedola 4RF21; Settimo Milanese, Milan, Italy) for 18 weeks; the second group received the HFD (50% fat J/J; Teklad# 93075) for 18 weeks. The last week of the treatment, the respiratory quotients (RQs) were measured in live animals using indirect open-circuit calorimeter. At the end of the experimental period, the animals were anesthetized by injection of chloral hydrate (40 mg/100 *g* body weight) and were killed by decapitation. Blood was taken from the inferior cava and serum was obtained by centrifuging at 1,000$\times$ *g* for 10 min and stored at $-80°$C for subsequent biochemical analyses. The cerebral cortex was removed and subdivided; samples not immediately used for synaptosomes and mitochondria preparation were frozen and stored at $-80°$C for subsequent determinations.

Measurement of Oxygen Consumption, Carbon Dioxide Production, and Respiratory Quotient

Following an adaption period to the experimental environment, oxygen consumption (VO_2) and carbon dioxide production (VCO_2) were recorded by a monitoring system (Panlab s.r.l., Cornella, Barcelona, Spain) that is composed of a four-chambered indirect open-circuit calorimeter, designed for continuous and simultaneous monitoring. VO_2 and VCO_2 were measured every 15 min (for 3 min) in each chamber for a total of 6 h. The mean VO_2, VCO_2 and RQ values were calculated by the "Metabolism H" software (Dominguez et al., 2009).

Body Composition and Energy Balance

During treatments, body weight and food intake were monitored daily to obtain body weight gain and gross energy intake. Energy balance assessments were conducted during the 18 weeks of feeding by comparative carcass evaluation (Mollica et al., 2017). The gross energy density for CD or HFD (15.8 or 21.9 kJ/g, respectively) and the energy density of the feces and the carcasses were determined by bomb calorimetric (Parr adiabatic calorimetric; Parr Instrument Company, Moline, IL, USA). Metabolizable energy (ME) intake was determined by subtracting the energy measured in feces and urine from the gross energy intake, which was determined from the daily food consumption and gross energy density. Evaluation of the energy, fat, and protein content in animal carcasses was conducted according to a published protocol (Mollica et al., 2017). Energy

efficiency was calculated as the percentage of body energy gain per ME intake, and energy expenditure was determined as the difference between ME intake and body energy gain. Body energy gain was calculated as the difference between the body energy content at the end of the treatment and the energy content of the mice sacrificed at the beginning of the experiment (baseline measurements).

Serum Parameters

The serum levels of triglycerides and cholesterol were measured by the colorimetric enzymatic method using commercial kits (SGM Italia, Rome, Italy, and Randox Laboratories Limited, Crumlin, UK). Glucose levels were determined by glucometer (Contour next, Ascensia, Switzerland). The serum levels of interleukin (IL)-1β, tumor necrosis factor-α (TNF-α; BioVendor, Brno, Czechia), insulin (Mercodia AB, Uppsala, Sweden), adiponectin and leptin (B-Bridge International, Mountain View, CA, USA) were measured using commercially available kits. As an index of insulin resistance (IR), HOmeostasis Model Assessment (HOMA)-IR was calculated using formula [HOMA = fasting glucose (mmol/L^{-1}) × fasting insulin ($\mu U/mL^{-1}$)/22.5].

Brain and Synaptosomes Parameters

To determine the lipid peroxidation in cerebral cortex homogenate and synaptosomal fraction, the level of malondialdehyde (MDA) was measured using the thiobarbituric acid (TBAR) method. MDA reacts with thiobarbituric acid (TBA) to form a pink chromogen that is detected at the wavelength of 532 nm. MDA values were expressed as micromoles per milligram of protein (Lu et al., 2009). The levels of TNF-α and IL-1β in the cerebral cortex homogenate and in synaptosomal fraction were determined as previously reported (Cavaliere et al., 2018). Reduced GSH and oxidized glutathione (GSSG) concentration in the cerebral cortex homogenate and in the synaptosomal fraction were measured with the dithionitrobenzoic acid-GSSG reductase recycling assay; the GSH to GSSG ratio was used as an oxidative stress marker (Viggiano et al., 2016).

Preparation of Mitochondria and Synaptosomes From the Cerebral Cortex

Synaptosomes were prepared using the standard procedure (Rao and Steward, 1991) yielding a well-characterized synaptosomal fraction (Eyman et al., 2007, 2013; Ferrara et al., 2009; Cefaliello et al., 2014; Penna et al., 2019). In brief, the cerebral cortex was quickly dissected and homogenized in a Dounce homogenizer with nine volumes of cold isotonic medium (HM) containing 0.32 M sucrose and 10 mM Tris-Cl, pH 7.4. To prepare subcellular fractions, following centrifugation of the homogenate (2,200 *g*, 1 min, 4°C), the sediment was resuspended in the same volume of HM and centrifuged under the same conditions to yield a sediment containing nuclei, cell debris and large synaptosomes (P1). The mixed supernatant fractions were centrifuged at higher speed (23,000 *g*, 4 min, 4°C) to yield a sediment that was resuspended in HM and centrifuged under the same conditions to yield a second sediment containing free mitochondria, synaptosomes and myelin fragments (P2) that was resuspended in HM. Differential centrifugation of P2 aliquots was used to prepare isolated synaptosomes and mitochondria. Further purification of synaptosomes was achieved by fractionating an aliquot of the P2 fraction on a discontinuous Ficoll gradient. One milliliter of the P2 fraction, brought to a final protein concentration of 3.5 mg/ml, was layered over a discontinuous gradient of 5% and 13% Ficoll dissolved in HM (2 ml each), and centrifuged at 45,000 *g*, for 45 min, 4°C. The purified synaptosomal fraction was recovered at the interface between the two Ficoll layers, diluted with nine volumes HM, and sedimented by centrifugation (23,000 *g*, 20 min, 4°C). The sediment was homogenized in HM and protein concentration was determined by Bradford colorimetric assay (Biorad) using bovine serum albumin (BSA) as standard. To obtain mitochondrial fraction the P2 fraction was resuspended in a medium containing 80 mM LiCl, 50 mM HEPES, 5 mM Tris-PO_4, 1 mM EGTA and 0.1% (w/v) fatty-acid-free BSA, pH 7.0, and centrifuged at 500 *g*, 10 min, 4°C. The supernatant was centrifuged at 10,000 *g* for 10 min at 4°C, the pellet was washed once and resuspended in a medium containing 80 mM LiCl, 50 mM HEPES, 5 mM Tris-PO_4, 1 mM EGTA and 0.1% (w/v) fatty-acid-free BSA, pH 7.0. The protein content of the mitochondrial fraction was determined by Bradford colorimetric assay (Biorad) using BSA as standard. The quality of isolated mitochondria was assured by checking that contamination of mitochondria by other ATPase-containing membranes was lower than 10%, and that addition of cytochrome c (3 nmol/mg protein) enhanced only state 3 respiration by approximately 10% (Cavaliere et al., 2016).

Measurements of Mitochondrial Oxidative Capacities and Degree of Coupling

Oxygen consumption in isolated mitochondria was measured with high-resolution respirometry Hansatech oxygraph (Yellow Spring Instruments, Yellow Springs, OH, USA) at a temperature of 30°C. Isolated mitochondria were incubated in a medium (pH 7.0) containing 80 mM KCl, 50 mM HEPES, 5 mM KH_2PO_4, 1 mM EGTA and 0.1% (w/v) fatty-acid-free BSA to oxidize their endogenous substrates for a few minutes. Substrates were then added at the following concentrations: 10 mM succinate plus 3.75 mM rotenone; 10 mM pyruvate plus 2.5 mM malate. State 4 oxygen consumption was obtained in the absence of ADP, and State 3 oxygen consumption was measured in the presence of 0.3 mM ADP. The respiratory control ratio (RCR) was calculated as the ratio between states 3 and 4 according to Estabrook (1967). The degree of coupling was determined in the brain by applying equation by Cairns et al. (1998):

$$\text{degree of coupling } = \sqrt{1 - (\text{Jo})_{\text{sh}}/(\text{Jo})_{\text{unc}}}$$

where (Jo)sh represents the oxygen consumption rate (OCR) in the presence of oligomycin that inhibits ATP synthase, and (Jo)unc is the uncoupled rate of oxygen consumption induced by carbonyl cyanide-p-trifluoromethoxyphenylhydrazone (FCCP), which dissipates the transmitochondrial proton gradient. (Jo)sh and (Jo)unc were measured as above using succinate

(10 mmol/L) and rotenone (3.75 μmol/L) in the presence of oligomycin (2 μg/ml) or FCCP (1 μmol/L), respectively. Aconitase and superoxide dismutase (SOD) specific activity were measured spectrophotometrically as previously reported (Flohè and Otting, 1984; Cavaliere et al., 2016).

Seahorse XFp Analyzer Cell Mito Stress Test

Oxygen consumption (OCR) and extracellular acidification rate (ECAR) measurements in synaptosomal fraction from mice cortex were performed by Seahorse XFp (Seahorse Biosciences, North Billerica, MA, USA), by using Cell Mito Stress Test kit (Seahorse Bioscience, 101706-100). XFp cartridges (Seahorse Bioscience) were hydrated by incubation with 200 μl calibrant (Seahorse Bioscience) per well at 37°C overnight. Before loading a cartridge onto the XFp analyzer, 20 μl of 30 μM oligomycin, 22 μl of 40 μM FCCP, 24 μl of 20 μM rotenone/antimycin A were added onto the cartridges (final concentrations of oligomycin, FCCP, and rotenone injected during the assay were 3 μM, 4 μM, and 2.0 μM, respectively). The cartridge was loaded onto the XFp analyzer for calibration. In each well of Seahorse XFp plate (Seahorse Bioscience, North Bilerica, MA, USA), precoated with poly-D-lysine, we seeded 10 μg of synaptosomal protein in a final volume of 100 μl ionic medium (20 mM HEPES, 10 mM D-Glucose, 1.2 mM Na_2HPO_4, 1 mM $MgCl_2$, 5 mM $NaHCO_3$, 5 mM KCl, 140 mM NaCl, pH 7.4 at 4°C). The plate was centrifuged at 2,000 *g* for 1 h at 4°C in swinging bucket rotor (Thermo Scientific 75003624) in a Thermo Fisher Scientific 3000R centrifuge. Before cell mito stress analyses, the medium was replaced with 180 μl of incubation medium (3.5 mM KCl, 120 mM NaCl, 1.3 mM $CaCl_2$, 0.4 mM KH_2PO_4, 1.2 mM Na_2SO_4, 2 mM $MgSO_4$, 4 mg/ml BSA, 15 mM D-glucose, 5 mM pyruvate, 2.5 mM malate, pH 7.4 at 37°C). The basal OCR was determined in the presence of the incubation medium. The proton leak was determined after inhibition of mitochondrial ATP production by oligomycin, as an inhibitor of the F0 F1 ATPase. Furthermore, the measurement of the ATP production in the basal state was obtained from the decrease in respiration by inhibition of the ATP synthase with oligomycin. Afterward, the mitochondrial electron transport chain was stimulated maximally by the addition of the uncoupler FCCP. Finally, the extra-mitochondrial respiration was estimated after the addition of the antimycin A and rotenone inhibitors of the complexes III and I, respectively. Coupling efficiency is the proportion of the oxygen consumed to drive ATP synthesis compared with that driving proton leak and was calculated as the fraction of basal mitochondrial OCR used for ATP synthesis (ATP-linked OCR/basal OCR). Spare capacity is the capacity of the cell to respond to an energetic demand and was calculated as the difference between the maximal respiration and basal respiration.

Western Blot Analysis

The cerebral cortex and synaptosomal fraction were homogenized in lysis buffer (20 mM MOPS pH 7.4, 2 mM EGTA pH 8, 5 mM EDTA pH 8, 30 mM NaF, 60 mM β-Glycerophosphate, 1 mM Sodium orthovanadate, 1% Triton X-100, 1 mM DTT) with a cocktail of protease inhibitors (Sigma-Aldrich). Western blot analyses were performed as previously described (Chun et al., 2004). Briefly, proteins (20 or 40 μg/lane) were separated on 12% SDS-PAGE and transferred to nitrocellulose membranes. The blots were incubated with anti-BDNF polyclonal antibody (Santa Cruz Biotechnology, 1:200), anti-phospho-CREB, and anti-CREB, mouse and rabbit monoclonal antibodies, respectively, anti-TrkB (80E3) rabbit monoclonal antibody (Cell Signaling Technology; 1:1,000), and anti-GAPDH rabbit antibody (Sigma-Aldrich; 1:8,000) overnight at 4°C, and then with secondary antibody against mouse or rabbit IgG (Sigma-Aldrich; 1:1,000–2,000) for 1 h at RT. The signals were visualized with the ECL system (Pierce). The same membrane was used to test all reported markers and the expression level of GAPDH was used to normalize the data.

Statistical Analysis

All data are presented as means ± SEM. Differences among groups were compared by unpaired *t*-test. Differences were considered statistically significant at $p < 0.05$. All analyses were performed using GraphPad Prism (GraphPad Software, San Diego, CA, USA).

Ethics Statement

This study was carried out in strict accordance with the Institutional Guidelines and complied with the Italian D.L. no. 116 of January 27, 1992, of Ministero Della Salute and associated guidelines in the European Communities Council Directive of November 24, 1986 (86/609/ECC). All animal procedures reported herein were approved by the Institutional Animal Care and Use Committee (CSV) of the University of Naples Federico II.

RESULTS

Oxygen Consumption, Carbon Dioxide Production, and Respiratory Quotient

O_2 consumption (ml/min/$Kg^{0.75}$ bw) of HDF mice was not significantly different from control animals (15.82 ± 0.55 vs. 17.06 ± 0.46), while CO_2 production (ml/min/$Kg^{0.75}$ bw; 12.22 ± 0.58 vs. 15.69 ± 0.48; $p < 0.05$) and RQ (0.77 ± 0.02 vs. 0.92 ± 0.01; $p < 0.05$) were significantly decreased compared to control mice. RQ index reflects the ratio of carbohydrate/fatty acid oxidation, therefore the decreased RQ index in HFD-fed animals demonstrates that these animals used fatty acid as a preferential fuel source compared to control animals.

Body Composition and Energy Balance

HFD consumption produced a significant increase in body weight, body lipids percentage, lipid gain, and body energy compared to the control diet. HFD mice exhibited a decrease in body water and body protein percentage compared to control mice, while protein gain did not change between groups. In addition, HFD animals exhibited a higher ME intake, energy expenditure and energy efficiency compared to control mice

TABLE 1 | Body composition and energy balance in control and high-fat diet (HFD) mice.

	CD	HFD
Body weight gain, g	11.1 ± 1.56	18.65 ± 1.44*
Lipid, %	9.6 ± 0.8	31.9 ± 4.2*
Protein, %	21.6 ± 0.8	17.0 ± 1.1*
H_2O, %	63.7 ± 1.96	46.0 ± 2.1*
Body energy content, kJ/g	8.45 ± 0.43	16.9 ± 1.91*
Body weight gain, kJ	94.0 ± 12.8	411.2 ± 50.7*
Metabolizable energy intake, kJ	4828.0 ± 152.6	5516.0 ± 163.8*
Energy expenditure, kJ	4734.0 ± 81.8	5104.8 ± 106.8*
Energy efficiency	0.02 ± 0.002	0.07 ± 0.008*
Protein gain, kJ	57.2 ± 6.6	66.1 ± 21.7
Lipid gain, kJ	59.0 ± 13.7	414.0 ± 50.4*

*Data are presented as means ± SEM from n = 7 animals/group. *p < 0.05 compared to CD group. CD, control diet; HFD, high-fat diet.*

(**Table 1**). These data are in agreement with our previous results (Mollica et al., 2017).

Serum Metabolites and Inflammatory Parameters

HFD mice exhibited increased serum levels of triglycerides and cholesterol compared to control animals (**Figures 1A,B**), in agreement with our previous results (Mollica et al., 2017). Leptin concentration significantly increased in HFD mice compared to controls, while adiponectin concentration decreased in HFD animals compared to the control group (**Figures 1C,D**). Serum levels of TNF-α, and IL-1β, significantly increased in the HFD group compared to controls (**Figures 1E,F**). Compared with the control group, HFD mice showed a marked increase in glucose and insulin level and HOMA-IR (**Figures 1G–I**).

Inflammation and Oxidative Stress in Brain Cortex

In the brain cortex of HFD group TNF-α, IL-1β, and MDA content was significantly higher than control mice (**Figures 2A–C**). GSH content significantly decreased in the HFD animals compared to controls (**Figure 2D**), while no difference was observed in GSSG content between groups (**Figure 2E**). Consistently, the HFD mice exhibited a lower GSH/GSSG ratio compared to controls (**Figure 2F**), indicating that HFD affected the oxidant state of the brain cortex.

Inflammation and Oxidative Stress in Synaptosomes From Brain Cortex

In synaptosomes from the HFD group, the inflammatory state was more pronounced than in the brain cortex homogenate. Indeed, the TNF-α, IL-1β and MDA content were about 140%, 240%, and 220% higher than control mice (**Figures 3A–C**). GSH content significantly decreased in HFD animals compared to controls (**Figure 3D**), while no difference was observed in GSSG content between groups (**Figure 3E**). Moreover, HFD mice exhibited a lower GSH/GSSG ratio compared to controls (**Figure 3F**).

Mitochondrial Function, Efficiency and Oxidative Stress in Brain Cortex

Mitochondrial state 3 respiration, evaluated using succinate or pyruvate as substrates, significantly decreased in the HFD mice compared to control, while no variation in state 4 was detected between groups (**Figures 4A,B**). Oligomycin state 4 respiration showed a trend of reduction in the HFD mice, and maximal FCCP-stimulated respiration was significantly reduced in in the HFD mice compared to control (**Figure 4C**). Consequently, brain mitochondria energetic efficiency, evaluated as degree of coupling, was increased in the HFD mice (**Figure 4D**). SOD and aconitase activities were significantly lower in HFD than in control mice (**Figures 4E,F**).

Mitochondrial Function in the Synaptosomal Fraction

The mitochondrial function of the synaptosomal fraction was examined using the Seahorse XFp cell mito stress kit (Seahorse Bioscience, North Billerica, MA, USA). It was performed in real-time at basal level and following a sequential addition of mitochondrial respiration inhibitors: oligomycin, FCCP, and a combination of antimycin A and rotenone. Oligomycin, an inhibitor of ATP synthase, was used to distinguish between oxygen consumption that cells use to synthesize ATP (ATP-linked respiration) and oxygen consumption that is used to overcome the proton leak across the mitochondrial membrane. FCCP treatment collapses the proton gradient and disrupts the mitochondrial membrane potential, which allows measurement of the maximal uncoupled respiration (maximal respiration). A combination treatment of rotenone, a complex I inhibitor, and antimycin A, a complex III inhibitor, was used to shut down mitochondrial respiration, which enables differentiation between the mitochondrial (basal respiration) and non-mitochondrial respiration contribution to total respiration. The difference between maximal and basal respiration constitutes the spare capacity.

The results from the Cell Mito Stress Test on synaptosomal fractions showed a decrease in the basal respiration in the HFD mice compared to controls (**Figure 5A**). These results are consistent with the decreased maximal rate of respiration and ATP production in HFD animals compared to controls (**Figures 5B,C**). Spare respiratory capacity, i.e., the capacity of the cells to respond to an energetic demand by generating ATP *via* oxidative phosphorylation (OXPHOS), was not different between groups (**Figure 5D**). Proton leak significantly decreased and, as a consequence, coupling efficiency increased in the HFD mice compared to control (**Figures 5E,F**).

Effect of HFD on the BDNF Pathway in Brain Cortex and Synaptosomal Fraction

The modulation of the BDNF pathway by HFD was evaluated by western blot analysis. We demonstrated that in both brain cortex and synaptosomal fraction from HFD mice the expression level of BDNF was significantly decreased compared to CD animals. Notably, the decrease was more pronounced in the synaptosomal fraction than in the homogenate (80% vs. 50%; **Figures 6A,B**).

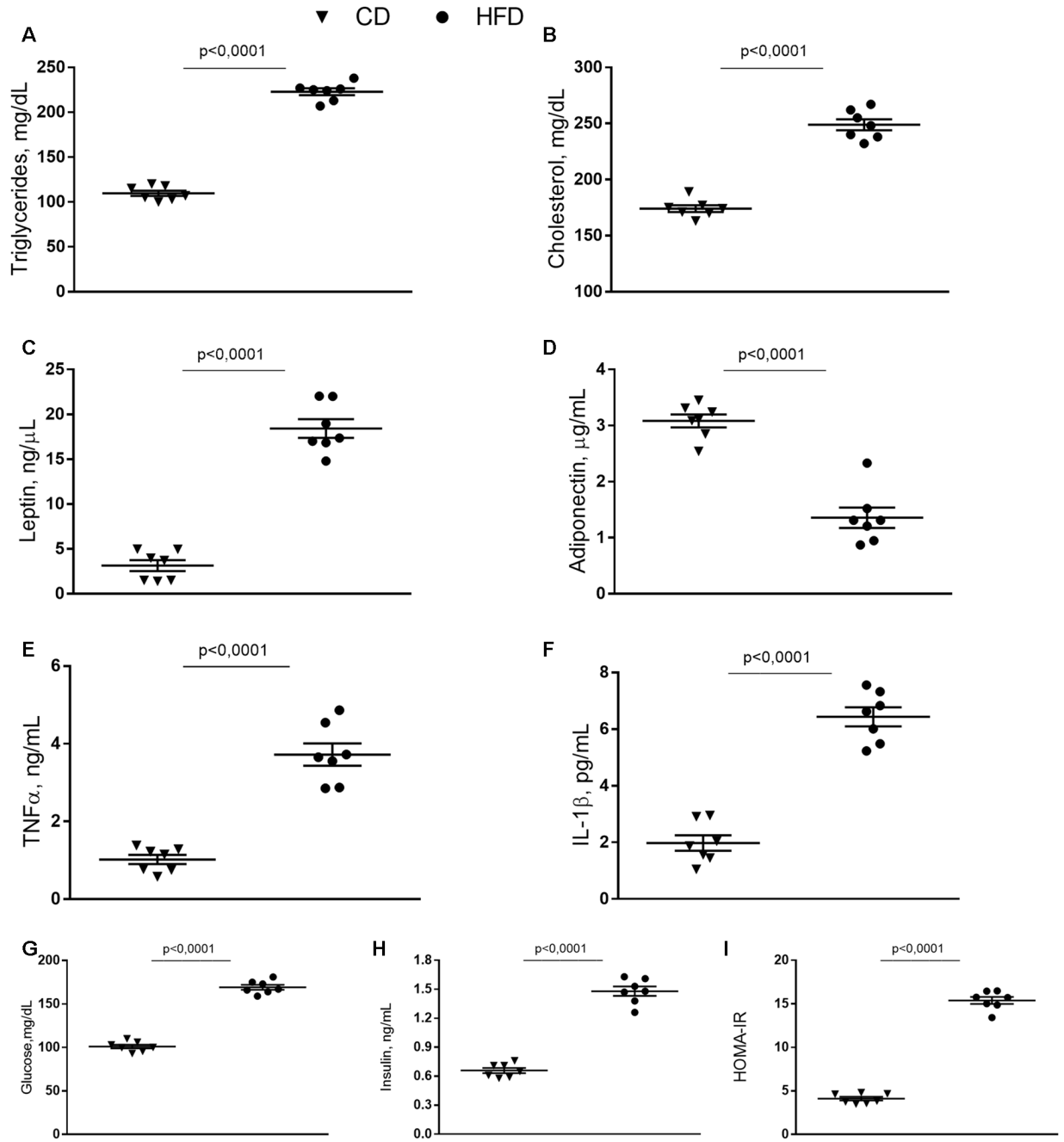


FIGURE 1 | Effect of high-fat diet (HFD) on serum metabolic parameters and proinflammatory markers. Triglycerides **(A)**, cholesterol **(B)**, leptin **(C)**, adiponectin **(D)**, tumor necrosis factor α (TNF-α, **E**), interleukin 1β (IL-1β, **F**), glucose **(G)**, insulin **(H)** serum levels, and homeostasis model assessment of insulin resistance (HOMA-IR, **I)** are reported. Data are presented as means ± SEM from $n = 7$ animals/group. Triangle: control diet (CD), circle: high-fat diet (HFD). Differences have been evaluated by unpaired *t*-test.

In addition, we also observed that the HFD decreased the CREB phosphorylation level both in homogenate and synaptosomes, although the effect was significant only in synaptosomal fraction (**Figures 6A–C**). No difference was observed in the TrkB expression level between the HFD and the CD group (**Figures 6A–D**).

DISCUSSION

The main finding of this study is that HFD consumption in mouse has a detrimental influence on brain cortex bioenergetic, altering mitochondrial function, efficiency and oxidative stress. Notably, these alterations were observed also in mitochondria

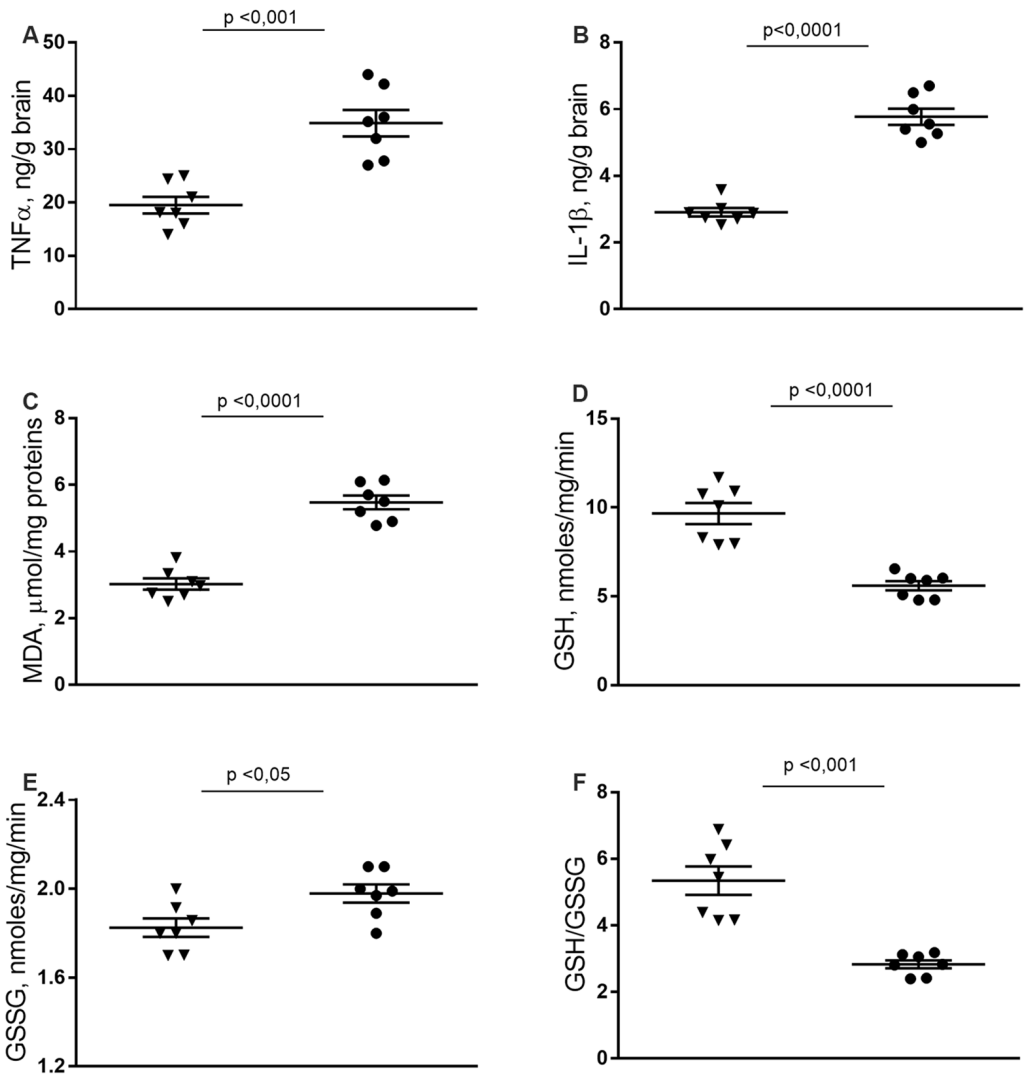


FIGURE 2 | Effect of HFD on redox status and pro-inflammatory parameters in cerebral cortex tissue. Tissue levels of TNF-α **(A)**, IL-1β **(B)**, malondialdehyde (MDA, **C**), glutathione (GSH, **D**), oxidized glutathione (GSSG, **E**) and GSH/GSSG ratio **(F)** are reported. Data are presented as means ± SEM from $n = 7$ animals/group. Triangle: control diet (CD), circle: high-fat diet (HFD). Differences have been evaluated by unpaired *t*-test.

from synaptosomal fractions. It is noteworthy that the dysfunctions of presynaptic mitochondria may be one of the underlying mechanisms contributing to cognitive decline in neurodegenerative diseases (Devine and Kittler, 2018). As known, HFD increases ME intake, metabolic efficiency, weight gain, and body lipid levels, leading to metabolic alterations, such as dyslipidemia, associated with low-grade inflammation. The effects on body weight and lipids can be explained by a decrease in energy expenditure and an increase in energy efficiency. The impaired ability to use fat as a metabolic fuel of HFD animals, suggests that the large part of the higher energy intake is stored as fat, confirming previous reports (Mollica et al., 2017; Cavaliere et al., 2018). In addition, in HFD the discrepancy between fatty acid uptake and utilization leads to the accumulation of toxic lipid species resulting in overproduction of ROS, IR, and inflammation. Our data, showing dysregulation of leptin and adiponectin serum levels in the HFD animals, confirm the link between these adipokines, obesity-related metabolic disorders, and inflammation. In particular, decreased adiponectin levels in the HFD group is associated with increased serum levels of TNF-α and oxidative stress (Chakraborti, 2015). Interestingly, we observed increased levels of TNF-α and oxidative stress also in brain cortex of the HFD mice, confirming that neuroinflammation observed in the diet-induced obesity animal model may be linked to increase in TNF-α secretion. It is noteworthy that the inflammation and

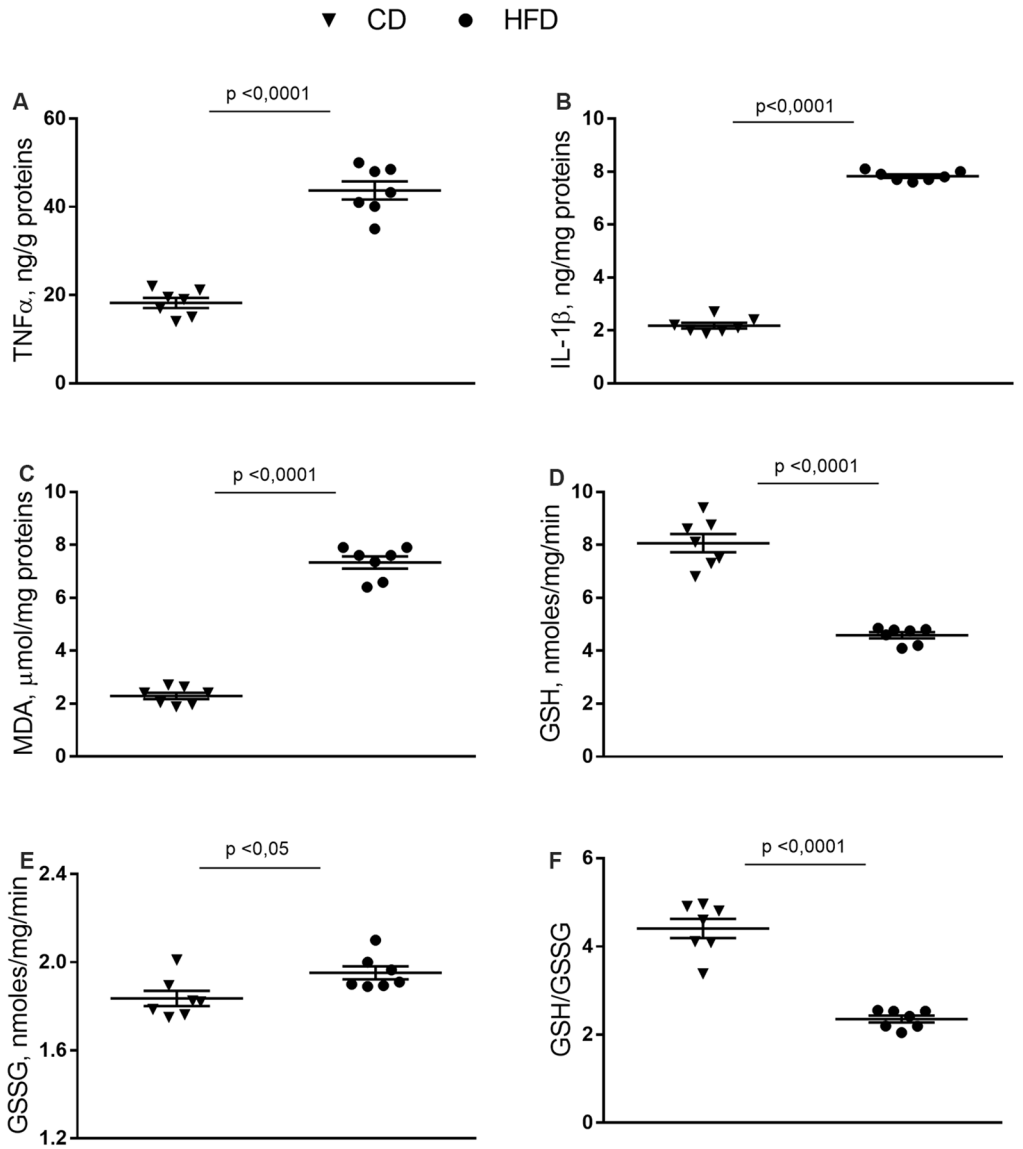


FIGURE 3 | Effect of HFD on redox status and pro-inflammatory parameters in synaptosomal fraction. Synaptosomal levels of TNF-α **(A)**, IL-1β **(B)**, MDA **(C)**, GSH **(D)**, GSSG **(E)** and GSH/GSSG ratio **(F)** are reported. Data are presented as means ± SEM from $n = 7$ animals/group. Triangle: control diet (CD), circle: high-fat diet (HFD). Differences have been evaluated by unpaired *t*-test.

oxidative stress is even more pronounced in the synaptosomal fraction from the brain cortex. The synaptosomes are vescicles produced *in vitro*, during homogenization of nervous tissue, that contain all the components of synaptic regions *in vivo* (Eyman et al., 2007; Crispino et al., 2009, 2014). Therefore, the synaptosomal fraction is a good model to study the modulation occurring at the synaptic level. Neuronal plasticity reflects the ability of synapses to be modified in number and strength in response to physiological and pathological stimuli. As a consequence, analyzing the dynamics of the synaptic region of brain areas opened a new perspective in the investigation of the molecular mechanisms underlying the physiological and pathological responses of the nervous system. Our data, indicating that inflammation and oxidative stress in the synaptic area is even higher than in the brain cortex homogenate, are particularly relevant; indeed, since impaired synaptic plasticity has been associated to neurodegeneration (Merlo et al., 2016), the HFD-induced inflammation may be indicated as a possible risk factor for the development of these diseases. Interestingly, recent data showed that acetylcholine plays an anti-inflammatory role in inhibiting NF-kB activity and suppressed the production of TNF-α and other proinflammatory cytokines (Chavan et al., 2017). We also demonstrated that the altered inflammatory state of the HFD animals can be linked to mitochondria dysfunctions. In the central nervous system, mitochondria have a crucial role in controlling energy homeostasis, which is essential for

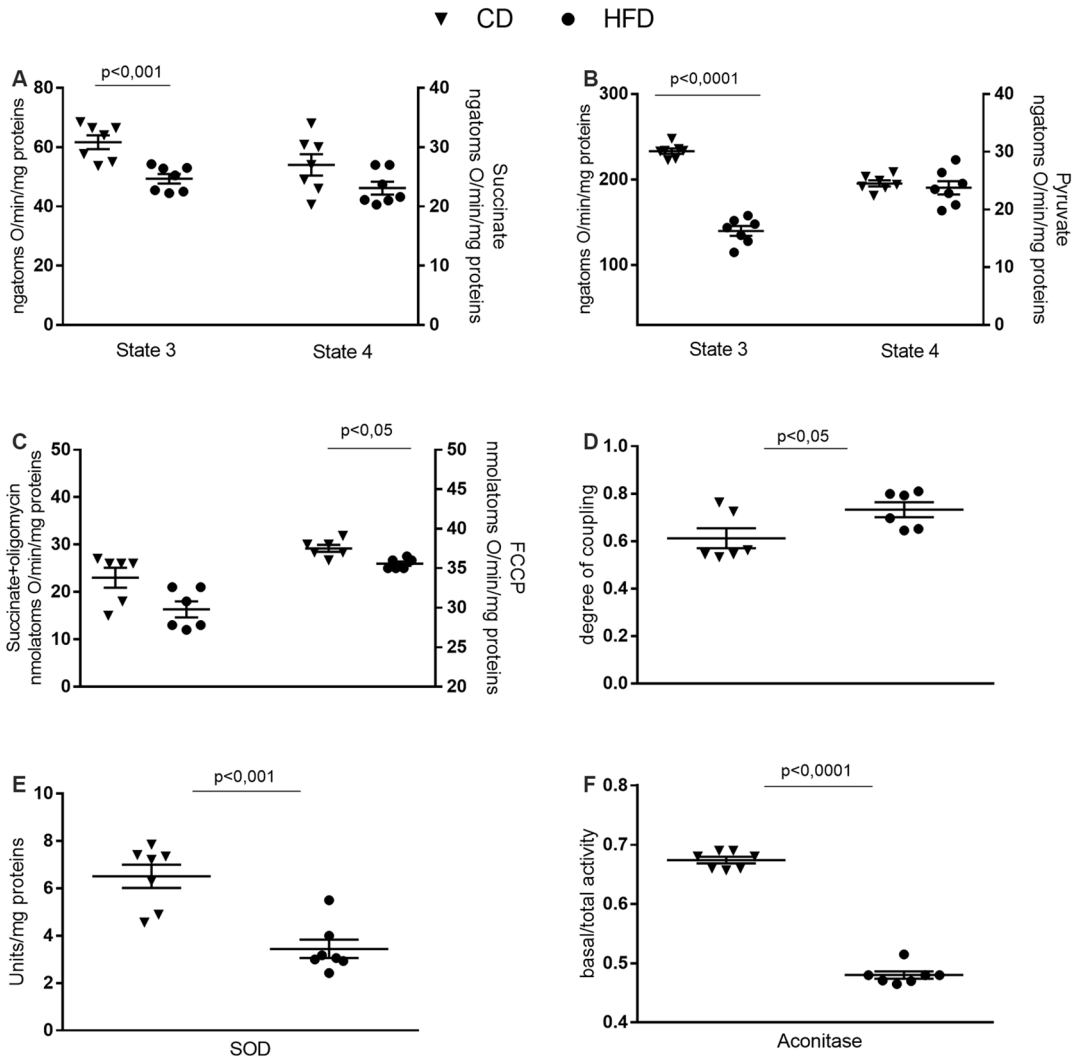


FIGURE 4 | Effect of HFD on mitochondrial respiration parameters in the cerebral cortex. Mitochondrial respiration rates measured in the presence of succinate **(A)**, pyruvate **(B)** as substrates, oxygen consumption in the presence of oligomycin or uncoupled by carbonyl cyanide 4-(trifluoromethoxy) phenylhydrazone (FCCP, **C**), degree of coupling **(D)**, superoxide dismutase (SOD, **E**) and aconitase activities **(F)** are reported. Data are presented as means ± SEM from $n = 6$ or 7 animals/group. Triangle: control diet (CD), circle: high-fat diet (HFD). Differences have been evaluated by unpaired t-test.

cognitive functions. In particular, mitochondria specifically located at synapses play a key role in providing energy to support synaptic functions and plasticity, thus their defects may lead to the synaptic failure responsible for neurodegenerative disease (Reddy and Beal, 2008). Therefore, we analyzed the effect of HFD on mitochondria isolated from the brain cortex and from cerebral cortex synaptosomes. Our data demonstrated that HFD induced alterations in the brain cortex and synaptic mitochondria. Mitochondria from the brain cortex of HFD mice exhibited a reduced respiratory capacity. Indeed, state 3 respiration significantly decreased both in presence of NADH-linked (pyruvate) and FADH-linked (succinate) substrate. A decrease in succinate State 3 respiration may be due to defects in the activity of substrate oxidation reactions (complex II, complex III, complex IV, and dicarboxylate carrier) and/or in the activity of the phosphorylation reactions (ANT, ATP synthase and phosphate carrier). In the presence of succinate plus FCCP, we also observed a decreased oxygen consumption in the HFD mice. These results suggest that the HFD-induced impairment of mitochondrial functions is not related to phosphorylating reactions but depends on altered substrate oxidation reactions. Indeed, when respiration is measured in the presence of succinate plus FCCP, the phosphorylation reactions do not exert control over respiration. Moreover, HFD mice showed an increased degree of coupling and, as a consequence, an increased mitochondrial efficiency. Mitochondria generate ATP by oxidizing nutrients, and the energy generated by the electron transport is utilized to phosphorylate ADP to ATP. Electron transport and ATP synthesis are tightly coupled, but some of the energy generated by electron transport is uncoupled from

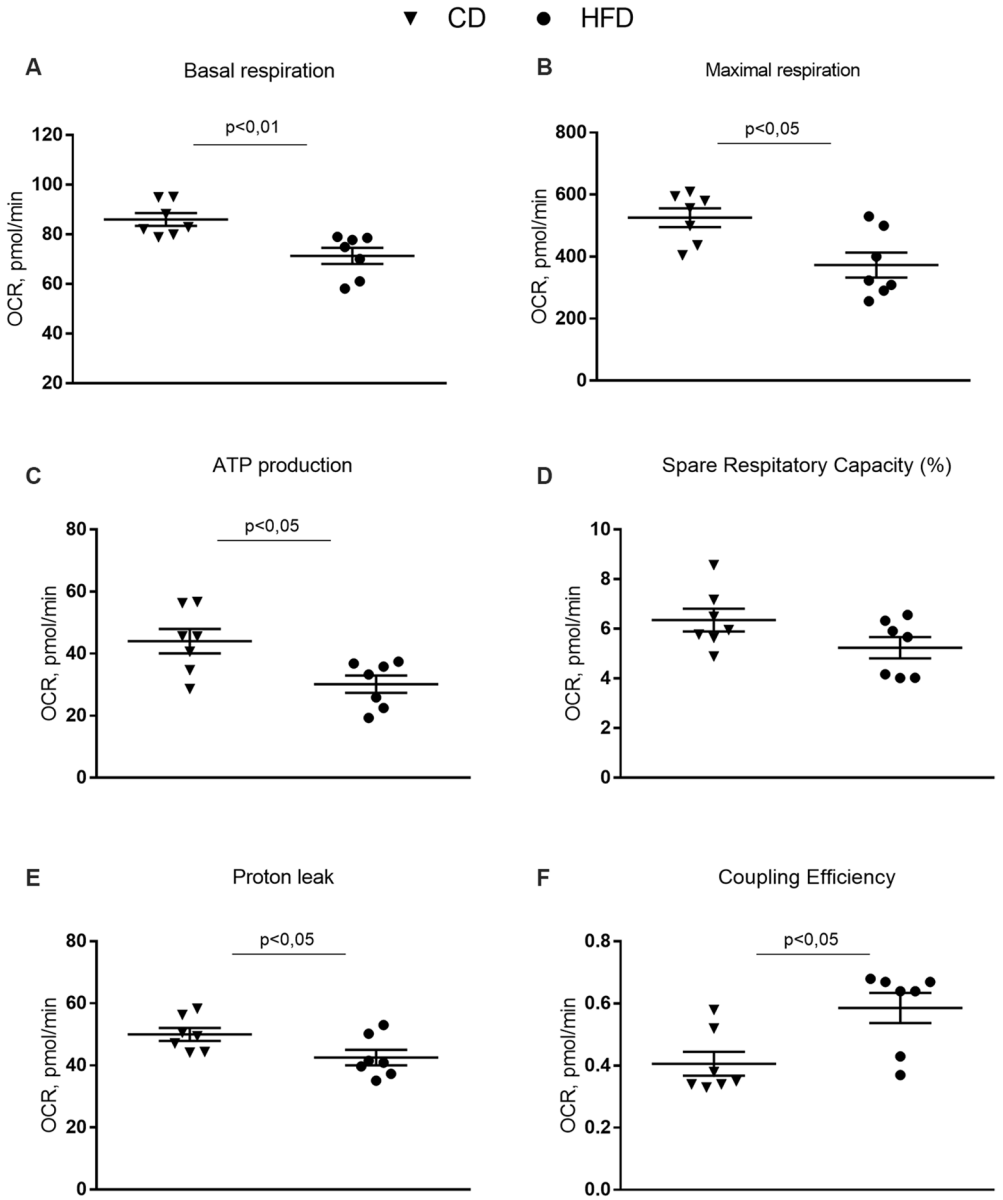


FIGURE 5 | Effect of HFD on mitochondrial respiration parameters in synaptosomal fraction. Basal respiration **(A)**, maximal respiration **(B)**, ATP production **(C)**, spare respiratory capacity percentage **(D)**, proton leak **(E)** and coupling efficiency **(F)** are reported. Data are presented as means ± SEM from $n = 7$ animals/group. Triangle: control diet (CD), circle: high-fat diet (HFD). Differences have been evaluated by unpaired *t*-test.

ATP synthesis. This mitochondrial uncoupling dissipates part of the proton gradient across the inner membrane without generating ATP (Nedergaard et al., 2005; Tseng et al., 2010). Increased mitochondrial energy efficiency implies that less substrate needs to be burned to obtain the same amount of ATP. As a consequence, the excess of unburned substrate favors lipid deposition. The partial block of electron flow within the respiratory chain, due to respiratory chain impairment, and the decrease in mitochondrial uncoupling both contribute to the enhanced oxidative stress (MDA, aconitase activity) observed in the HFD mice. In fact, the uncoupling is a major mechanism for the adjustment of the membrane potential to control mitochondrial ROS emission. By mildly uncoupling, the mitochondria can avoid the oversupply of electrons/reducing equivalents into the respiratory complexes and minimize the likelihood of electron interaction with oxygen (Skulachev, 1998). In addition, the HFD animals also showed a decrease in SOD enzyme activity, the first line of defense against oxidative stress (Lu et al., 2009), contributing to the increased oxidative stress of these animals. Accordingly, HFD induces an imbalance of ratio GSH/GSSG, a clear sign of altered redox state in cells. HFD also induced impairment of synaptic mitochondrial functions.

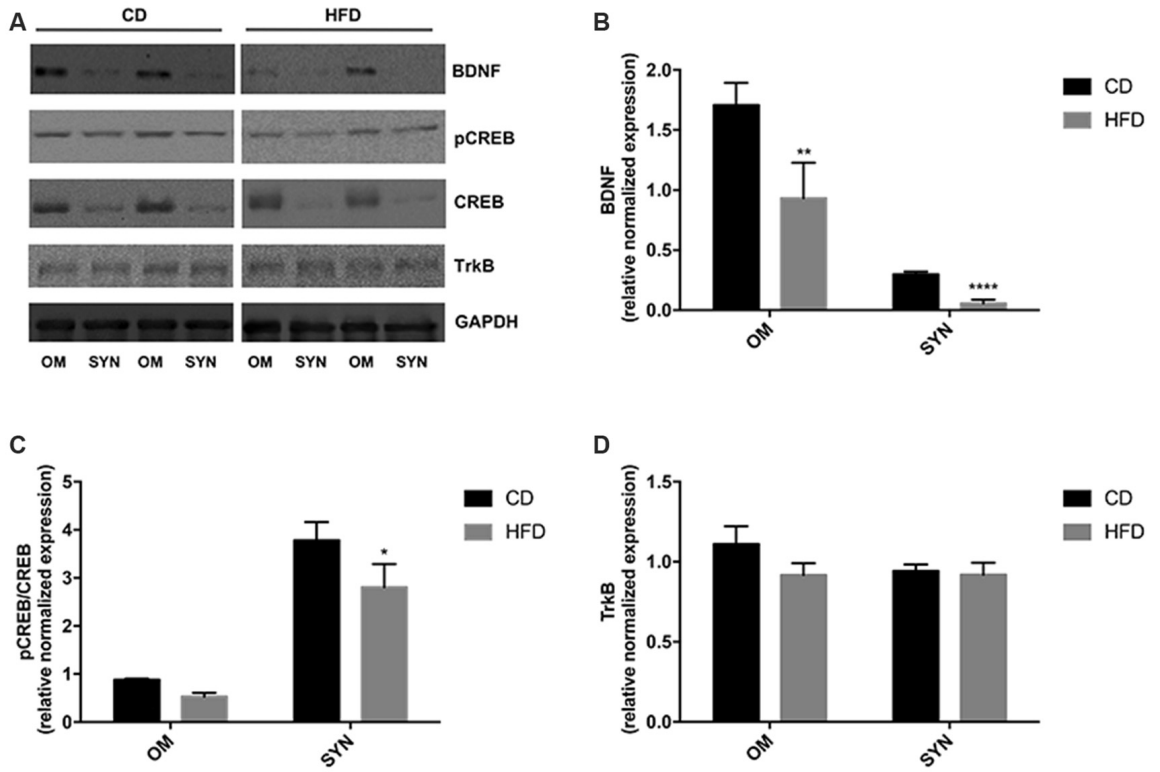


FIGURE 6 | Effect of HFD on the BDNF pathway in the brain cortex homogenate and synaptosomal fraction. Expression levels of BDNF **(B)**, pCREB/CREB **(C)**, and TrkB **(D)** were normalized with that of GADPH in the brain cortex homogenate (OM) and synaptosomes (SYN) from control diet (CD) and high-fat diet (HFD) group. Panel **(A)** shows representative immunoreactive signals. Data are presented as means ± SEM from $n = 4$ animals/group. $^{*}p < 0.05$, $^{**}p < 0.01$, and $^{****}p < 0.0001$ compared to control mice. CD, control diet; HFD, high-fat diet.

Indeed, in the HFD mice, we observed a reduced basal and maximal respiration, and a reduced ATP production. Moreover, these animals also showed an increased coupling efficiency linked to a decreased proton leak. These features can be responsible for the increased oxidative stress and the inflammatory state that was observed in synaptic regions of the HFD mice. Since neuroinflammation is known to affect BDNF signaling in the brain (Lima Giacobbo et al., 2019), we investigate the BDNF and CREB expression levels in brain cortex and synaptosomal fraction from the same region. BDNF is a neurotrophin that plays an important role in plasticity of the central nervous system and is also involved in the pathogenesis of neurological diseases (Autry and Monteggia, 2012). In particular, BDNF has a short-term effect in synaptic plasticity influencing post-translation modification of proteins already available at the synapse, but also long-term effects including the modulation of the synaptic system of protein synthesis (Leal et al., 2014). Our results indicate a significant decrease in BDNF expression in both HFD homogenate and synaptosomal fractions. Therefore, it is possible to hypothesize that, in HFD animals, the decreased synaptosomal level of BDNF results in a decrease of the synaptic protein synthesis, affecting in turn mitochondria activity. Indeed, recent data demonstrated that axonal protein synthesis is crucial for local mitochondrial maintenance, and its alteration may lead to neuropathologies (Cioni et al., 2019). It has been also shown that the mitochondria located at the synaptic level fuel the local protein synthesis necessary for synaptic plasticity (Rangaraju et al., 2019). Thus, this two-way crosstalk between local translation and mitochondria function in synapse may represent an innovative mechanism to guide neuronal plasticity (Rossoll and Bassell, 2019). The modulation of BDNF that we observed in the HFD animals was accompanied by a decreased phosphorylation of its upstream factor CREB in the synaptosomal fraction, confirming that HFD has a relevant effect on molecular plasticity pathways located at the synaptic level. Moreover, BDNF in the brain is one of the key proteins in food intake regulation and body weight control (Lapchak and Hefti, 1992), playing a critical role in regulating feeding and energy balance (Noble et al., 2011; Rios, 2013). BDNF inversely correlates with fasting plasma glucose and homeostasis model assessment of insulin resistance score (HOMA-IR), which is an indirect measure of IR (Eyileten et al., 2017). In line with these findings, our results related to altered food intake, energy balance, body weight and HOMA index of HFD group correlate with the reduced levels of BDNF that we observed in the same group of animals. We performed our experiments selectively on male animals that are free from estrous-related hormonal changes affecting brain physiology. Nonetheless, it will be of

interest to extend these analyses to female animals to investigate a possible gender difference in the response of the brain to HFD.

CONCLUSION

Our data provided evidence regarding the link between HFD and low-grade systemic inflammation, but also inflammation and oxidative stress in the brain cortex. The effect is even more pronounced in the synaptic regions indicating the strong impact of the diet on neuronal plasticity. The oxidative stress depends on the overproduction of free radicals that is partially due to the impaired mitochondrial functions. Indeed, HFD induces in brain mitochondria a decrease in mild uncoupling, that has the role to maintain mitochondrial membrane potential below the critical threshold for ROS production. Therefore, our data indicate that improving mitochondria functions may be used as a strategy to counteracts neuroinflammation and brain oxidative stress.

DATA AVAILABILITY STATEMENT

The datasets generated for this study are available on request to the corresponding author.

ETHICS STATEMENT

The animal study was reviewed and approved by Institutional Animal Care and Use Committee (CSV) of University of Naples Federico II.

AUTHOR CONTRIBUTIONS

MPM and MC conceived and designed the experiments, analyzed the data, and wrote the manuscript. GC, GT, EP, FC, CP, AL, CA, and AC performed the experiments, collected the data, and performed the data analyses. GMR, RM, MM, GM, and CZ contributed to the discussion and to the editing of the manuscript. MC was the guarantor of this work and, as such, had full access to all the data in the study and takes responsibility for the integrity of the data and the accuracy of the data analysis.

ACKNOWLEDGMENTS

We thank Dr. Roberta Scognamiglio, Dr. Aurora Bracale, Dr. Fabiana Alfieri, and Dr. Ornella Smith for technical assistance.

REFERENCES

Autry, A. E., and Monteggia, L. M. (2012). Brain-derived neurotrophic factor and neuropsychiatric disorders. *Pharmacol. Rev.* 64, 238–258. doi: 10.1124/pr.111.005108

Cairns, C. B., Walther, J., Harken, A. H., and Banerjee, A. (1998). Mitochondrial oxidative phosphorylation thermodynamic efficiencies reflect physiological organ roles. *Am. J. Physiol.* 274, R1376–R1383. doi: 10.1152/ajpregu.1998.274.5.r1376

Cavaliere, G., Trinchese, G., Bergamo, P., De Filippo, C., Mattace Raso, G., Gifuni, G., et al. (2016). Polyunsaturated fatty acids attenuate diet induced obesity and insulin resistance, modulating mitochondrial respiratory uncoupling in rat skeletal muscle. *PLoS One* 11:e0149033. doi: 10.1371/journal.pone.0149033

Cavaliere, G., Viggiano, E., Trinchese, G., De Filippo, C., Messina, A., Monda, V., et al. (2018). Long feeding high-fat diet induces hypothalamic oxidative stress and inflammation, and prolonged hypothalamic AMPK activation in rat animal model. *Front. Physiol.* 9:818. doi: 10.3389/fphys.2018.00818

Cefaliello, C., Eyman, M., Melck, D., De Stefano, R., Ferrara, E., Crispino, M., et al. (2014). Brain synaptosomes harbor more than one cytoplasmic system of protein synthesis. *J. Neurosci. Res.* 92, 1573–1580. doi: 10.1002/jnr.23435

Chakraborti, C. K. (2015). Role of adiponectin and some other factors linking type 2 diabetes mellitus and obesity. *World J. Diabetes* 6, 1296–1308. doi: 10.4239/wjd.v6.i15.1296

Chan, D. C. (2006). Mitochondria: dynamic organelles in disease, aging, and development. *Cell* 125, 1241–1252. doi: 10.1016/j.cell.2006.06.010

Chavan, S. S., Pavlov, V. A., and Tracey, K. J. (2017). Mechanisms and therapeutic relevance of neuro-immune communication. *Immunity* 46, 927–942. doi: 10.1016/j.immuni.2017.06.008

Chen, T. J., Chen, S. S., Wang, D. C., and Hung, H. S. (2019). High-fat diet reduces novelty-induced expression of activity-regulated cytoskeleton-associated protein. *J. Cell. Physiol.* doi: 10.1002/jcp.29021

Chun, J. T., Crispino, M., and Tocco, G. (2004). The dual response of protein kinase Fyn to neural trauma: early induction in neurons and delayed induction in reactive astrocytes. *Exp. Neurol.* 185, 109–119. doi: 10.1016/j.expneurol.2003.09.019

Cioni, J. M., Lin, J. Q., Holtermann, A. V., Koppers, M., Jakobs, M. A. H., Azizi, A., et al. (2019). Late endosomes act as mRNA translation platforms and sustain mitochondria in axons. *Cell* 176, 56.e15–72.e15. doi: 10.1016/j.cell.2018.11.030

Crispino, M., Cefaliello, C., Kaplan, B., and Giuditta, A. (2009). Protein synthesis in nerve terminals and the glia-neuron unit. *Results Probl. Cell Differ.* 48, 243–267. doi: 10.1007/400_2009_9

Crispino, M., Chun, J. T., Cefaliello, C., Perrone Capano, C., and Giuditta, A. (2014). Local gene expression in nerve endings. *Dev. Neurobiol.* 74, 279–291. doi: 10.1002/dneu.22109

Devine, M. J., and Kittler, J. T. (2018). Mitochondria at the neuronal presynapse in health and disease. *Nat. Rev. Neurosci.* 19, 63–80. doi: 10.1038/nrn.2017.170

Dominguez, J. F., Guo, L., Carrasco Molnar, M. A., Ballester Escobedo, A., Dunphy, T., Lund, T. D., et al. (2009). Novel indirect calorimetry technology to analyze metabolism in individual neonatal rodent pups. *PLoS One* 4:e6790. doi: 10.1371/journal.pone.0006790

Dutheil, S., Ota, K. T., Wohleb, E. S., Rasmussen, K., and Duman, R. S. (2016). High-fat diet induced anxiety and anhedonia: impact on brain homeostasis and inflammation. *Neuropsychopharmacology* 41, 1874–1887. doi: 10.1038/npp.2015.357

Estabrook, R. W. (1967). Mitochondrial respiratory control and the polarographic measurement of ADP:O ratios. *Methods Enzymol.* 10, 41–47. doi: 10.1016/0076-6879(67)10010-4

Eyileten, C., Kaplon-Cieslicka, A., Mirowska-Guzel, D., Malek, L., and Postula, M. (2017). Antidiabetic effect of brain-derived neurotrophic factor and its association with inflammation in type 2 diabetes mellitus. *J. Diabetes Res.* 2017:2823671. doi: 10.1155/2017/2823671

Eyman, M., Cefaliello, C., Ferrara, E., De Stefano, R., Crispino, M., and Giuditta, A. (2007). Synaptosomal protein synthesis is selectively modulated by learning. *Brain Res.* 1132, 148–157. doi: 10.1016/j.brainres.2006.11.025

Eyman, M., Cefaliello, C., Mandile, P., Piscopo, S., Crispino, M., and Giuditta, A. (2013). Training old rats selectively modulates synaptosomal protein synthesis. *J. Neurosci. Res.* 91, 20–29. doi: 10.1002/jnr.23133

Ferrara, E., Cefaliello, C., Eyman, M., De Stefano, R., Giuditta, A., and Crispino, M. (2009). Synaptic mRNAs are modulated by learning. *J. Neurosci. Res.* 87, 1960–1968. doi: 10.1002/jnr.22037

Flohè, L., and Otting, F. (1984). Superoxide dismutase assay. *Methods Enzymol.* 105, 93–104. doi: 10.1016/s0076-6879(84)05013-8

Hanin, G., Yayon, N., Tzur, Y., Haviv, R., Bennett, E. R., Udi, S., et al. (2018). miRNA-132 induces hepatic steatosis and hyperlipidaemia by synergistic multitarget suppression. *Gut* 67, 1124–1134. doi: 10.1136/gutjnl-2016-312869

Haviv, R., Oz, E., and Soreq, H. (2018). The stress-responding miR-132–3p shows evolutionarily conserved pathway interactions. *Cell. Mol. Neurobiol.* 38, 141–153. doi: 10.1007/s10571-017-0515-z

Hernández-Aguilera, A., Rull, A., Rodríguez-Gallego, E., Riera-Borrull, M., Luciano-Mateo, F., Camps, J., et al. (2013). Mitochondrial dysfunction: a basic mechanism in inflammation-related non-communicable diseases and therapeutic opportunities. *Mediators Inflamm.* 2013:135698. doi: 10.1155/2013/135698

Jain, V., Langham, M. C., and Wehrli, F. W. (2010). MRI estimation of global brain oxygen consumption rate. *J. Cereb. Blood Flow Metab.* 30, 1598–1607. doi: 10.1038/jcbfm.2010.49

Joshi, A. U., and Mochly-Rosen, D. (2018). Mortal engines: mitochondrial bioenergetics and dysfunction in neurodegenerative diseases. *Pharmacol. Res.* 138, 2–15. doi: 10.1016/j.phrs.2018.08.010

Kumar, A. (2018). Editorial: neuroinflammation and cognition. *Front. Aging Neurosci.* 10:413. doi: 10.3389/fnagi.2018.00413

Lapchak, P. A., and Hefti, F. (1992). BDNF and NGF treatment in lesioned rats: effects on cholinergic function and weight gain. *Neuroreport* 3, 405–408. doi: 10.1097/00001756-199205000-00007

Leal, G., Comprido, D., and Duarte, C. B. (2014). BDNF-induced local protein synthesis and synaptic plasticity. *Neuropharmacology* 76, 639–656. doi: 10.1016/j.neuropharm.2013.04.005

Lima Giacobbo, B., Doorduin, J., Klein, H. C., Dierckx, R. A. J. O., Bromberg, E., and de Vries, E. F. J. (2019). Brain-derived neurotrophic factor in brain disorders: focus on neuroinflammation. *Mol. Neurobiol.* 56, 3295–3312. doi: 10.1007/s12035-018-1283-6

Lores-Arnaiz, S., Lombardi, P., Karadayian, A. G., Orgambide, F., Cicerchia, D., and Bustamante, J. (2016). Brain cortex mitochondrial bioenergetics in synaptosomes and non-synaptic mitochondria during aging. *Neurochem. Res.* 41, 353–363. doi: 10.1007/s11064-015-1817-5

Lu, H., Zhang, D. M., Chen, H. L., Lin, Y. X., Hang, C. H., Yin, H. X., et al. (2009). N-acetylcysteine suppresses oxidative stress in experimental rats with subarachnoid hemorrhage. *J. Clin. Neurosci.* 16, 684–688. doi: 10.1016/j.jocn.2008.04.021

Merlo, D., Cuchillo-Ibañez, I., Parlato, R., and Rammes, G. (2016). DNA damage, neurodegeneration, and synaptic plasticity. *Neural Plast.* 2016:1206840. doi: 10.1155/2016/1206840

Meydan, C., Bekenstein, U., and Soreq, H. (2018). Molecular regulatory pathways link sepsis with metabolic syndrome: non-coding RNA elements underlying the sepsis/metabolic cross-talk. *Front. Mol. Neurosci.* 11:189. doi: 10.3389/fnmol.2018.00189

Mi, Y., Qi, G., Fan, R., Qiao, Q., Sun, Y., Gao, Y., et al. (2017). EGCG ameliorates high-fat- and high-fructose-induced cognitive defects by regulating the IRS/AKT and ERK/CREB/BDNF signaling pathways in the CNS. *FASEB J.* 31, 4998–5011. doi: 10.1096/fj.201700400rr

Mollica, M. P., Lionetti, L., Putti, R., Cavaliere, G., Gaita, M., and Barletta, A. (2011). From chronic overfeeding to hepatic injury: role of endoplasmic reticulum stress and inflammation. *Nutr. Metab. Cardiovasc. Dis.* 21, 222–230. doi: 10.1016/j.numecd.2010.10.012

Mollica, M. P., Mattace Raso, G., Cavaliere, G., Trinchese, G., De Filippo, C., Aceto, S., et al. (2017). Butyrate regulates liver mitochondrial function, efficiency, and dynamics in insulin-resistant obese mice. *Diabetes* 66, 1405–1418. doi: 10.2337/db16-0924

Nedergaard, J., Ricquier, D., and Kozak, L. P. (2005). Uncoupling proteins: current status and therapeutic prospects. *EMBO Rep.* 6, 917–921. doi: 10.1038/sj.embor.7400532

Noble, E. E., Billington, C. J., Kotz, C. M., and Wang, C. (2011). The lighter side of BDNF. *Am. J. Physiol. Regul. Integr. Comp. Physiol.* 300, R1053–R1069. doi: 10.1152/ajpregu.00776.2010

Penna, E., Cerciello, A., Chambery, A., Russo, R., Cernilogar, F. M., Pedone, E. M., et al. (2019). Cystatin B involvement in synapse physiology of rodent brains and human cerebral organoids. *Front. Mol. Neurosci.* 12:195. doi: 10.3389/fnmol.2019.00195

Rangaraju, V., Lauterbach, M., and Schuman, E. M. (2019). Spatially stable mitochondrial compartments fuel local translation during plasticity. *Cell* 176, 73.e15–84.e15. doi: 10.1016/j.cell.2018.12.013

Rao, A., and Steward, O. (1991). Evidence that protein constituents of postsynaptic membrane specializations are locally synthesized: analysis of proteins synthesized within synaptosomes. *J. Neurosci.* 11, 2881–2895. doi: 10.1523/jneurosci.11-09-02881.1991

Reddy, P. H., and Beal, M. F. (2008). Amyloidβ, mitochondrial dysfunction and synaptic damage: implications for cognitive decline in aging and Alzheimer's disease. *Trends Mol. Med.* 14, 45–53. doi: 10.1016/j.molmed.2007.12.002

Rios, M. (2013). BDNF and the central control of feeding: accidental bystander or essential player? *Trends Neurosci.* 36, 83–90. doi: 10.1016/j.tins.2012.12.009

Rossoll, W., and Bassell, G. J. (2019). Crosstalk of local translation and mitochondria: powering plasticity in axons and dendrites. *Neuron* 101, 204–206. doi: 10.1016/j.neuron.2018.12.027

Skulachev, V. P. (1998). Uncoupling: new approaches to an old problem of bioenergetics. *Biochim. Biophys. Acta* 1363, 100–124. doi: 10.1016/s0005-2728(97)00091-1

Tseng, Y. H., Cypess, A. M., and Kahn, C. R. (2010). Cellular bioenergetics as a target for obesity therapy. *Nat. Rev. Drug Discov.* 9, 465–482. doi: 10.1038/nrd3138

Viggiano, E., Mollica, M. P., Lionetti, L., Cavaliere, G., Trinchese, G., De Filippo, C., et al. (2016). Effects of an high-fat diet enriched in lard or in fish oil on the hypothalamic amp-activated protein kinase and inflammatory mediators. *Front. Cell. Neurosci.* 10:150. doi: 10.3389/fncel.2016.00150

Zhao, Z., Yao, M., Wei, L., and Ge, S. (2019). Obesity caused by a high-fat diet regulates the Sirt1/PGC-1α/FNDC5/BDNF pathway to exacerbate isoflurane-induced postoperative cognitive dysfunction in older mice. *Nutr. Neurosci.* 22, 1–12. doi: 10.1080/1028415X.2019.1581460

Conflict of Interest: The authors declare that the research was conducted in the absence of any commercial or financial relationships that could be construed as a potential conflict of interest.

Copyright © 2019 Cavaliere, Trinchese, Penna, Cimmino, Pirozzi, Lama, Annunziata, Catapano, Mattace Raso, Meli, Monda, Messina, Zammit, Crispino and Mollica. This is an open-access article distributed under the terms of the Creative Commons Attribution License (CC BY). The use, distribution or reproduction in other forums is permitted, provided the original author(s) and the copyright owner(s) are credited and that the original publication in this journal is cited, in accordance with accepted academic practice. No use, distribution or reproduction is permitted which does not comply with these terms.

frontiers in Cellular Neuroscience

ORIGINAL RESEARCH
published: 27 February 2020
doi: 10.3389/fncel.2020.00030

Bi-Directional Communication Between Neurons and Astrocytes Modulates Spinal Motor Circuits

*Matthew J. Broadhead and Gareth B. Miles**

School of Psychology and Neuroscience, University of St Andrews, St Andrews, United Kingdom

Evidence suggests that astrocytes are not merely supportive cells in the nervous system but may actively participate in the control of neural circuits underlying cognition and behavior. In this study, we examined the role of astrocytes within the motor circuitry of the mammalian spinal cord. Pharmacogenetic manipulation of astrocytic activity in isolated spinal cord preparations obtained from neonatal mice revealed astrocyte-derived, adenosinergic modulation of the frequency of rhythmic output generated by the locomotor central pattern generator (CPG) network. Live Ca^{2+} imaging demonstrated increased activity in astrocytes during locomotor-related output and in response to the direct stimulation of spinal neurons. Finally, astrocytes were found to respond to neuronally-derived glutamate in a metabotropic glutamate receptor 5 (mGluR5) dependent manner, which in turn drives astrocytic modulation of the locomotor network. Our work identifies bi-directional signaling mechanisms between neurons and astrocytes underlying modulatory feedback control of motor circuits, which may act to constrain network output within optimal ranges for movement.

Keywords: astrocyte, spinal cord, locomotion, neuromodulation, mGlu receptor5

OPEN ACCESS

Edited by:
Jonathan Mapelli,
University of Modena and Reggio Emilia, Italy

Reviewed by:
Rita Bardoni,
University of Modena and Reggio Emilia, Italy
Patrick John Whelan,
University of Calgary, Canada

****Correspondence:***
Gareth B. Miles
gbm4@st-andrews.ac.uk

Received: *01 November 2019*
Accepted: *03 February 2020*
Published: *27 February 2020*

Citation:
Broadhead MJ and Miles GB (2020) Bi-Directional Communication Between Neurons and Astrocytes Modulates Spinal Motor Circuits. Front. Cell. Neurosci. 14:30. doi: 10.3389/fncel.2020.00030

LAY SUMMARY

We have investigated how astrocytes, a type of supportive cell within the nervous system, may be directly involved in the control of movements, such as walking (locomotion). We found that astrocytes are active participants in the neural circuits of the mammalian spinal cord that control locomotion. The function of astrocytes within these networks appears to relate to the modulation of locomotor speed. We also identify the chemical signaling pathways involved in a modulatory feedback loop between astrocytes and neurons. Our findings suggest that this bi-directional communication between astrocytes and neurons may act to constrain spinal motor circuits within operational ranges for desired movements.

INTRODUCTION

Astrocytes, one of the predominant forms of glial cells in the nervous system, are a diverse and multifunctional group of cells with the capacity to integrate numerous neuronal-derived signals and modulate neuronal activity at a network level (Verkhratsky and Butt, 2013). There is growing evidence that astrocytes play a role in a wide range of basic central nervous

system (CNS) functions (Gibbs et al., 2008; Robertson, 2018). Within motor systems, astrocytes are implicated in the control of rhythmic behaviors, such as respiration (Gourine et al., 2010; Huxtable et al., 2010; Sheikhbahaei et al., 2018), mastication (Morquette et al., 2015), feeding (Yang et al., 2015; Sweeney et al., 2016) and locomotion (Acton and Miles, 2015, 2017; Witts et al., 2015; Acton et al., 2018). These rhythmic motor behaviors are generated by a dedicated central pattern generator (CPG) networks. For example, the lumbar spinal cord contains a CPG network that consists of interneurons, which generate rhythmic activity, and motor neurons, which convey the network's output to coordinate alternating left-right and flexor-extensor muscle activation as required for the generation of locomotor behavior (Grillner, 2003, 2006; Selverston, 2005; Kiehn, 2016). CPGs underlying behaviors such as locomotion, respiration, chewing and gut motility, require various modulatory mechanisms to fine-tune the speed, pattern and power of behavior in accordance with the requirements of the animal at any given time (Harris-Warrick, 2011; Miles and Sillar, 2011). Although neurons have traditionally been considered the primary, if not sole, source of such modulation, a growing body of evidence supports important roles for astrocytes in the modulation of CPG networks (Gourine et al., 2010; Acton and Miles, 2015; Morquette et al., 2015; Yang et al., 2015).

Previous research suggests that pharmacological activation or ablation of spinal cord astrocytes alters the synaptic activity of interneurons and modulates the frequency of locomotor output (Witts et al., 2012, 2015; Carlsen and Perrier, 2014; Acton and Miles, 2015; Acton et al., 2018). These effects are thought to be dependent on the astrocytic release of ATP with subsequent conversion to adenosine, which acts *via* neuronal A1 adenosine receptors. Although these findings support that astrocytes are active participants within locomotor circuitry, further analyses utilizing additional methods for activating and, importantly, inhibiting endogenous astrocytic activity are required to provide a greater understanding of their functional roles. Furthermore, if spinal cord astrocytes are indeed active participants in the locomotor CPG, then it is likely their role is driven by neuronally-derived signals, which remain to be identified. Given growing evidence that astrocytes play a role in a host of neurological and neurodegenerative diseases, including chronic pain (Ji et al., 2006; Gao and Ji, 2010), spinal cord injury (Okada et al., 2006) and Amyotrophic Lateral Sclerosis (ALS; Phatnani et al., 2013; Pehar et al., 2018), identifying the physiological roles of astrocytes within spinal circuits, and the signaling mechanisms involved, could pave the way for the development of novel therapeutic strategies.

In this study, we aimed to further our investigation into whether spinal cord astrocytes are active participants within mammalian locomotor circuits and identify the signaling mechanisms between spinal neurons and astrocytes. To address these aims, we have used transgenic mouse lines to both visualize and manipulate astrocytic activity in the isolated mammalian spinal cord *in vitro*. We reveal neuron-astrocyte and astrocyte-neuron signaling mechanisms that underlie modulatory, inhibitory feedback control of motor circuit output.

MATERIALS AND METHODS

Animals

All procedures performed on animals were conducted in accordance with the UK Animals (Scientific Procedures) Act 1986 and were approved by the University of St Andrews Animal Welfare and Ethics Committee. Mice were euthanized *via* cervical dislocation and decapitation. All lines of mice were obtained from Jackson Laboratories and are listed in **Table 1**.

To induce expression of genes in astrocytes, heterozygous GFAP::Cre transgenic mice were injected with 100 μg/g mouse weight of Tamoxifen (Sigma) starting from neonatal day 5 (P5) with subsequent injections every 24 h until sacrificed for the experiment. Experiments requiring ventral root recordings of fictive locomotion in whole isolated spinal cords and hemisected spinal cords of transgenic mice were performed at P6–8. Ca^{2+} imaging experiments were performed on neonates at P6–10. Where transgenic mice were not required for fictive locomotor experiments (with the exception of the non-transgenic controls for DREADD experiments), mice aged P1–5 were used as obtaining fictive locomotion is more reliable in younger mice.

Tissue Preparation

For ventral root recordings from whole isolated spinal cords or hemisected spinal cords, animals were sacrificed by cervical dislocation, decapitated and eviscerated before being transferred to a dissection chamber containing artificial cerebrospinal fluid (aCSF, equilibrated with 95% O_2, 5% CO_2, ∼4°C). Spinal cords were isolated between the midthoracic and upper sacral segments, and the dorsal roots trimmed, leaving ventral roots intact. For hemisected spinal cords, the pia was carefully removed and the two halves cleaved gradually with a dissecting pin. For preparing acute spinal cord slices, neonatal mice were sacrificed as described above, and the spinal cord dissected in aCSF. Slices were made at 300 μm thickness from the lumbar segments using a vibratome (VT1200, Leica) and transferred to recovery aCSF maintained at ∼34°C (equilibrated with 95% O_2, and 5% CO_2) for 30–60 min. Slices were subsequently transferred to recording aCSF.

Drugs and Solutions

Recording aCSF contained the following (in mM): 127 NaCl, 3 KCl, 1.25 NaH_2PO_4, 1 $MgCl_2$, 2 CaCl, 26 $NaHCO_3$, and 10 glucose. The dissecting aCSF contained the following (in mM): 25 NaCl, 188 sucrose, 1.9 KCl, 1.2 NaH_2PO_4, 10 $MgSO_4$, 1 CaCl, 26 $NaHCO_3$, 25 glucose, and 1.5 kynurenic acid. The recovery aCSF contained the following (in mM): 119 NaCl, 1.9 KCl, 1.2 NaH_2PO_4, 10 $MgSO_4$, 1 CaCl, 26 $NaHCO_3$, 20 glucose, and 1.5 kynurenic acid. Intracellular solution used for single-cell recordings contained the following (in mM): 140 $KMeSO_4$, 10 NaCl, 1 CaCl, 10 HEPES, 1 EGTA, 3 Mg-ATP, and 0.4 GTP-Na_2 (pH 7.2–7.3, adjusted with KOH).

The following drugs were purchased from Sigma: Glutamate, γ-aminobutyric acid (GABA), N-methyl-D-aspartate (NMDA) and Dopamine (DA). The following drugs were purchased from Tocris: 8-Cyclopentyl-1,3-dipropylxanthine (DPCPX), 2-Methyl-6-(phenylethynyl)pyridine hydrochloride

TABLE 1 | Details of the transgenic mouse lines used for the study.

Jackson laboratories stock number	Full name	Abbreviated name	Purpose
012849	*hGFAP::CRE/ERT2*	*GFAP::Cre*	Tamoxifen inducible cre expression in astrocytes
024106	*Ai96(RCL-GCaMP6s)*	*GCAMP6s*	Fluorescent Ca^{2+} indication
026220	*R26-LSL-hM3Dq-DREADD*	*hM3Dq*	Excitatory DREADD receptor
026219	*R26-LSL-hM4Di-DREADD*	*hM4Di*	Inhibitory DREADD receptor
007905	*Gt(ROSA)26Sor*$^{tm9(CAG-tdTomato)Hze}$	*TdTomato*	Fluorescence reporter line

(MPEP), 5-hydroxytryptamine (5-HT) and (RS)-2-Chloro-5-hydroxyphenylglycine (CHPG). Tetrodotoxin (TTX) and CNO were purchased from HelloBio. With the exception of Glutamate, CHPG, MPEP and DPCPX, all drugs were made up in deionized H_2O. Glutamate and CHPG were made up in 1 M NaOH, while MPEP and DPCPX were made up in dimethyl sulfoxide (DMSO). CNO and DPCPX were prepared fresh on a weekly basis. Drug concentrations were chosen based on previous publications (Bowman and Kimelberg, 1984; Queiroz et al., 1999; Parri et al., 2010; Iwagaki and Miles, 2011; Takeuchi et al., 2014; Acton and Miles, 2015; Mariotti et al., 2016; Jennings et al., 2017).

Ca^{2+} Imaging

Ca^{2+} imaging of spinal cord slices was performed in aCSF (equilibrated with 95% O_2, 5% CO_2) warmed to ∼34°C with an inline heater (Warner Instruments). Imaging of hemisected spinal cords was performed at 20–24°C in order to ensure robust fictive locomotor output. Images were captured as described in Acton et al. (2018). Briefly, images were acquired using a Zyla 4.2 scientific CMOS camera (Andor, Oxford Instruments) using a 40× water immersion objective lens (0.9 numerical aperture), controlled using Micro-Manager 2 software. Data were acquired with a rolling shutter at 1 fps with a 200 ms exposure time. Illumination was provided by a 470-nm CoolLED system. Analysis of Ca^{2+} imaging was performed with FIJI software. Data were first converted to eight bit and processed with background subtraction, 3D smoothing and histogram-based bleach correction. If required, manual drift correction was performed. Active cells were selected and delineated from the images, guided by a maximum intensity projected image to highlight high-intensity structures. Intensity measurements were normalized as ΔF/F0, calculated as:

100 × (fluorescence value − baseline fluorescence ÷ baseline fluorescence).

Baseline fluorescence was calculated as the mean intensity from 30 frames during a control period of recording. Ca^{2+} transients from astrocytes in hemisected spinal cords were detected in a semi-automated manner using Hill-Valley analysis through Dataview software (courtesy of Dr. W. J. Heitler, University of St Andrews). Events were detected using a slope height filter of 10% of the valley-to-peak height. Due to variation in Ca^{2+} event intensity and duration, false-positive events were excluded manually and some false negative events were selected manually. In hemisect experiments where events were analyzed with Dataview, Ca^{2+} event intensity was calculated from the normalized intensity, averaged across all the events within a time window for a cell and across cells of each experiment. The maximum intensity of cells is taken as the maximum normalized intensity for a cell within a time frame. Ca^{2+} images are displayed in figures as maximum projections from across 120 frames following initial processing steps.

Whole-Cell Patch-Clamp

Whole-cell patch-clamp recordings were performed from ventral horn interneurons using glass microelectrodes (2.5–5 MΩ) filled with intracellular solution. Signals were amplified and filtered (4 kHz low-pass Bessel filter) with a Multi-Clamp 700B amplifier (Molecular Devices) and acquired at 10 kHz using a Digidata 1440A A/D board and pClamp software (Molecular Devices). Gigaseals (∼2 GΩ) were obtained before the establishment of whole-cell mode and neurons with resting membrane potentials between −40 mV and −70 mV were used for experiments. All recordings were performed in current-clamp mode. Cells were given a 10 s pulse of 200 pA to induce trains of action potentials (eliciting ∼100 action potentials). All experiments were conducted at ∼34°C.

Ventral Root Recording

For whole spinal cord preparations in which locomotor-related activity was induced pharmacologically, glass suction electrodes were attached to the upper lumbar segment roots (L1–3) on both the left and right side of the isolated spinal cords to assess left-right alternation and flexor-related activity. Fictive locomotion was induced with 5-HT (10 μM), NMDA (5 μM) and DA (50 μM). Preparations displaying stable fictive locomotion for ∼20 min during control periods were used for full experiments with the addition of additional drugs. Data were amplified and filtered (band-pass filter 10–5,000 Hz, A-M Systems Model 1700) and acquired at a sampling frequency of 6 kHz with a Digidata 1440A analog-digital converter and Axoscope software (Molecular Devices, Sunnyvale, CA, USA). For hemisected spinal cord experiments with simultaneous Ca^{2+} imaging, only one root was attached (L1–L3). Data were amplified and filtered (30–3,000 Hz; Qjin Design) and then acquired at a sampling frequency of 6 kHz using a Digidata 1440A A/D board and AxoScope software.

Immunohistochemistry and Fluorescence Microscopy

Spinal cords from wild type, non-transgenic C57Bl/6J mice (P6) were harvested in ice-cold recording aCSF and subsequently fixed in paraformaldehyde (4%) for 4 h at 4°C. Cords were then sunk in a 33% sucrose solution overnight and cryo-embedded for cryosectioning at 20 μm thickness. Frozen sections were washed in 0.1 M phosphate-buffered saline (PBS) and then blocked and permeabilized in 5% Bovine serum albumin (BSA) and 0.2%

Triton X100 for 90 min at room temperature. Sections were incubated for 48 h at 4°C with a primary antibody solution of 2.5% BSA and 0.1% Triton X100 with rabbit polyclonal anti-mGluR5 (Abcam) and mouse monoclonal anti-glutamine synthetase (Abcam), both at 1:200 dilution. Sections were then washed five times with PBS before a secondary antibody incubation in 0.1% Triton X100 for 60 min at room temperature. Following another five washes in PBS, sections were washed once briefly in DI-H_2O and incubated in DAPI (diluted 1:5,000 in deionized-H_2O) for 5 min before mounting in vectashield. Fixed, stained samples were imaged at 63× with a Zeiss Axio Imager M2 microscope equipped with an Apotome.2. Illumination was provided by an HXP120 lamp, and images acquired using an MRm digital camera. Three-channel images of glutamine synthetase, mGluR5 and DAPI were captured with exposure times of 500, 100 and 30 ms, respectively. Z-stacks were acquired with all channels per slice and an optimal z-step of 0.28 μm. Images were processed and visualized in FIJI (ImageJ).

Data Handling and Statistics

All data were stored using a 20 TB NAS drive, with hot-swappable hard drives and a back-up NAS drive (QNAP Turbo). Data files and graphs were handled and produced in Excel (Microsoft). Statistics were performed with SPSS v24 and SPSS v25 (IBM). Shapiro Wilks tests were performed to assess normality. Fictive locomotor experiments were analyzed using repeated-measures ANOVAs with a *post hoc* Bonferroni test for pairwise comparisons. Where appropriate, sphericity was assessed with Mauchly's test and Greenhouse-Giesser corrections were applied. For Ca^{2+} imaging data where two or more groups were compared, one-way ANOVAs with *post hoc* Tukey's test for pairwise comparisons were performed. For Ca^{2+} imaging with two groups, two-sample *T*-tests were performed. Significance is given as $^{*}p < 0.05$, $^{**}p < 0.01$, $^{***}p < 0.001$ and not significant (ns). Ca^{2+} traces from astrocytes are displayed with a mean smoothing over five frames. Bar charts display mean with standard error bars. Samples sizes (*n*) are stated in the results where appropriate.

RESULTS

Spinal Cord Astrocytes Respond to Neuronal Activity

We first asked whether spinal astrocytes were active during fictive locomotion. Hemisected spinal cords were prepared from neonatal (P6–8) GFAP::Cre;GCAMP6s mice to enable the visualization of gray matter astrocytes, broadly in laminae VII, VIII and X, whilst simultaneously recording fictive locomotor output *via* lumbar segment roots (L1–3; depicted in the schematic of **Figure 1A**).

Across all experiments (108 astrocytes from $n = 6$ hemisected spinal cords), the average density of astrocytes displaying Ca^{2+} transients, as indicated by changes in fluorescence, was 400 cells per mm^2 (ranging from 80 to 690 cells per mm^2 between experiments). Astrocytes showed little to no activity during the "control" phase of recording, with an average frequency of 0.1 transients per minute (**Figure 1B**). After 3–4 min of control recording, DA (50 μM), 5-HT (10 μM) and NMDA (5 μM) were perfused to evoke fictive locomotion. Within 1–2 min of drug perfusion, a tonic increase in motor neuron activity was observed, as evidenced by an increase in the baseline of ventral root recordings, which lasted approximately 5 min. This tonic activity was followed by rhythmic locomotor-related bursts which first appeared 6–10 min after the perfusion of the locomotor drugs. Astrocytic Ca^{2+} transients showed no significant change in their duration (**Figure 1C**; $F_{(3)} = 0.63$; $p = 0.602$) or intensity (**Figure 1D**; $F_{(3)} = 2.1$; $p = 0.133$) during these different phases of ventral root output. There was also no significant change in the frequency of astrocytic Ca^{2+} transients immediately following the addition of the locomotor drugs nor during the induction phase when tonic ventral root activity was recorded. However, the frequency of astrocytic Ca^{2+} transients significantly increased above baseline levels during the period when rhythmic, locomotor-related bursting was present (**Figure 1E**; $F_{(3)} = 3.6$; $p = 0.032$). There was no specific coupling between individual astrocytic Ca^{2+} transients and single fictive locomotor bursts, perhaps due to the fact that the locomotor bursts recorded from ventral roots averaged 4 s in duration, while astrocytic Ca^{2+} transients averaged 25 s in duration. Nevertheless, there was a significant increase in the occurrence of astrocytic Ca^{2+} transients when fictive locomotor network activity was established.

We next confirmed that elevations in astrocytic activity were due to locomotor network activity, rather than a direct astrocytic response to the drugs used to induce locomotor-related output. We performed a series of hemisected spinal cord experiments in the presence of (TTX, 0.5 μM) to block neuronal activity (**Figure 1F**). As expected, no motor output was evoked when DA, 5-HT, and NMDA were applied in the presence of TTX. Analysis of astrocytic activity in these experiments (89 astrocytes from $n = 6$ hemisected spinal cords), revealed no significant change in the duration ($F_{(3)} = 1.2$; $p = 0.326$), intensity ($F_{(3)} = 1.3$; $p = 0.291$) or the frequency (**Figure 1F**; $F_{(3)} = 0.78$; $p = 0.516$) of Ca^{2+} transients after the addition of the locomotion-inducing drugs. These results suggest that spinal cord astrocytes are responsive to neuronal activity in the spinal cord, rather than any direct actions of the drugs used to induce locomotor-related activity.

We next asked whether spinal cord astrocytes could respond directly to interneurons within the spinal cord. To test this, we used whole-cell patch-clamp electrophysiology to evoke trains of action potentials in individual interneurons in spinal cord slices from GFAP::Cre;GCAMP6s mice (**Figure 1G**). A total of nine neurons were patched and stimulated. In eight out the nine experiments, we observed Ca^{2+} responses in astrocyte somas following neural stimulation (measurements from 53 astrocytes from $n = 8$ slice experiments; **Figures 1H,I**). The maximum intensity (ΔF/F0), averaged from responsive astrocytes within individual experiments, rose by 19.4 ± 15.3% following neuronal stimulation (**Figure 1J**; $F_{(2)} = 4.4$; $p = 0.024$).

Astrocytic mGluR5 Receptors Mediate Neuron-to-Astrocyte Signaling

Next, we sought to address how neurons were signaling to astrocytes in the spinal cord. Spinal cord slices were

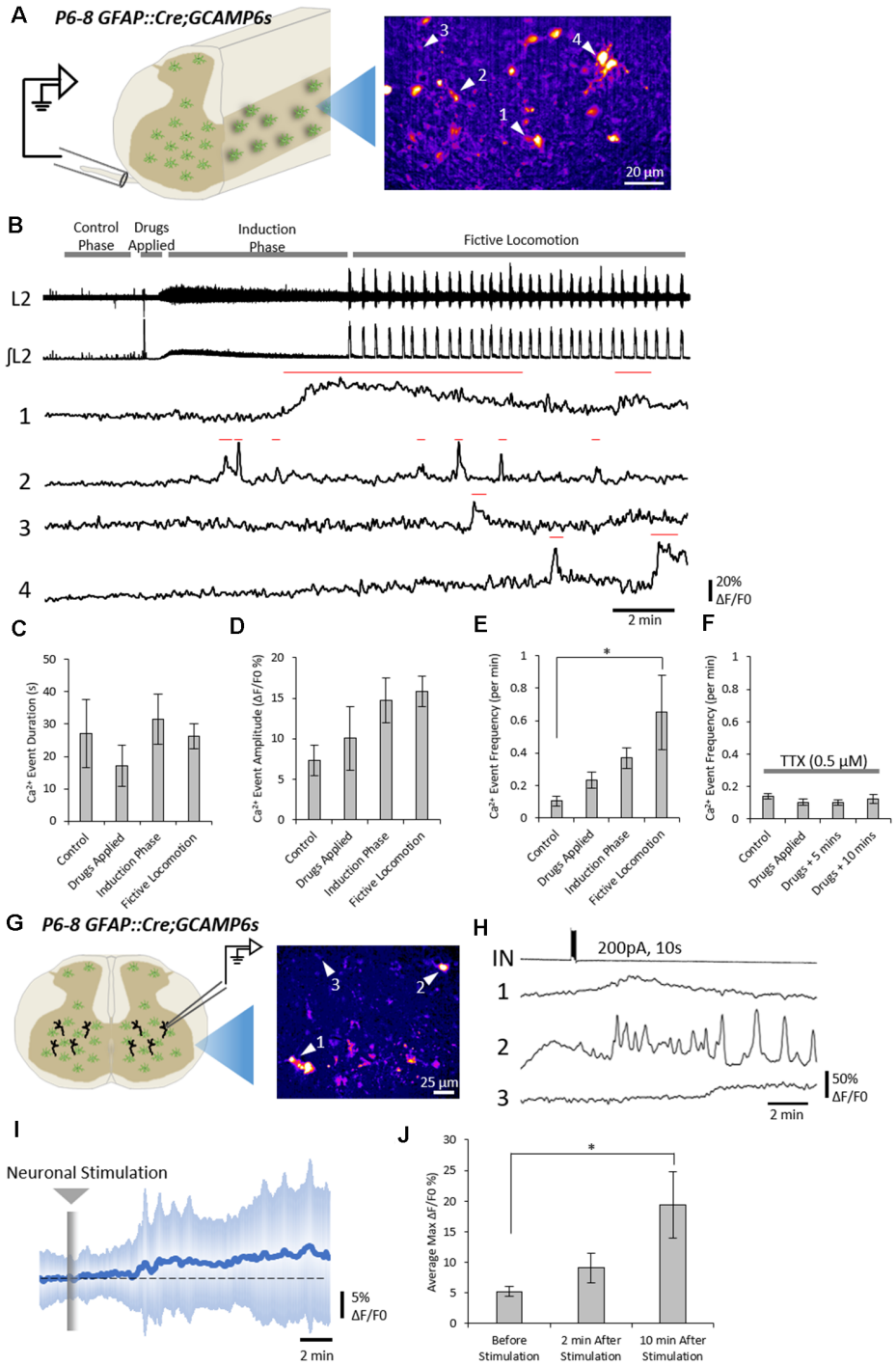


FIGURE 1 | Neuronal activity evokes Ca^{2+} responses in spinal astrocytes. **(A)** Schematic of hemisected spinal cord preparations in which simultaneous ventral root recording and Ca^{2+} imaging of astrocytic activity were performed. **(B)** Example data from one experiment showing ventral root activity from baseline to the induction of fictive locomotion and Ca^{2+} imaging traces from four astrocytes (denoted in panel **A**). Red lines above traces indicate the Ca^{2+} events detected for analysis. **(C)** Bar chart showing the duration of astrocytic Ca^{2+} transients during different phases of the experiment. **(D)** Bar chart showing the intensity of astrocytic Ca^{2+} transients during different phases of the experiment. **(E)** Bar chart showing the frequency of astrocytic Ca^{2+} transients during different phases of the experiment. **(F)** Bar chart showing the frequency of astrocytic Ca^{2+} transients during different phases of the experiment when the hemisected cord was perfused with tetrodotoxin (TTX). **(G)** Schematic of a spinal cord slice with a simultaneous whole-cell patch-clamp recording from a ventral horn interneuron and Ca^{2+} imaging of astrocytic activity. **(H)** Example data from one experiment showing the activation of a spinal cord interneuron (IN), and the Ca^{2+} transients from three astrocytes (denoted in panel **G**). **(I)** Averaged Ca^{2+} imaging trace from 52 astrocytes from eight separate experiments in response to neuronal stimulation. **(J)** Bar chart showing the maximum intensity of Ca^{2+} transients in astrocytes before and after neuronal stimulation. $^*p < 0.05$.

prepared from neonatal (P6–10) GFAP::Cre;GCAMP6s mice and astrocytic activity was visualized while receptor agonists were locally applied to the recording chamber to evoke responses from astrocytes (**Figure 2A**). Experiments were conducted in the presence of TTX (1 μM) to block neuronal activity. Positive responses from astrocytes within an experiment were defined as an increase in normalized fluorescence intensity (ΔF/F0) of at least 5% occurring within 2 min of agonist application (**Figures 2A,B**).

Glutamate and the metabotropic glutamate receptor 5 (mGluR5) agonist, CHPG, both elicited strong Ca^{2+} responses from large numbers of astrocytes, significantly more so than the vehicle control (aCSF; CHPG: $p = 0.003$; Glutamate: $p = 0.0002$), 5-HT (CHPG: $p = 0.007$; Glutamate: $p = 0.001$) and NMDA (CHPG: $p = 0.04$; Glutamate: $p = 0.029$). GABA and DA also evoked moderate responses from astrocytes, though the number of astrocytes that responded was far less than the number that responded to Glutamatergic signaling, and not significantly greater than control. Based on cell density measurements from a TdTomato fluorescence reporter ($n = 12$ slices from two individual GFAP::Cre;TdTomato mice aged P8–9; **Supplementary Figure S1**), we estimate that approximately 70–100% of astrocytes are activated by Glutamate and CHPG. From these results, we conclude that glutamatergic signaling *via* metabotropic receptors is the most probable mechanism by which spinal neurons communicate with astrocytes.

Next, we sought to confirm whether spinal astrocytes express the mGluR5 receptor. Immunolabeling experiments revealed widespread expression of the mGluR5 receptor in the neonatal spinal cord (**Figures 2C,D**). Co-labeling with the astrocytic marker, Glutamine Synthetase, confirmed that mGluR5 is expressed on the soma, primary branches and smaller branchlets of astrocytes (**Figures 2C,D**, arrows).

Finally, we examined whether the mGluR5 antagonist, MPEP, could reduce neuron-to-astrocyte communication. Having previously shown that astrocytes do not respond to NMDA directly in the presence of TTX, we applied NMDA to spinal cord slices for 5 min to evoke neuronal activity while visualizing astrocyte Ca^{2+} activity (221 astrocytes from $n = 7$ slice experiments). Any astrocytic responses were, therefore, the indirect result of enhanced neuronal activity induced by NMDA (**Figure 2E**). In a second condition (124 astrocytes from $n = 6$ slice experiments), slices were incubated in MPEP (50 μM) 15–20 min prior to, and during, NMDA application (**Figure 2F**). Analysis of Ca^{2+} imaging data revealed that MPEP reduced both the degree of astrocytic activation, as determined by the maximum intensity (**Figure 2G**; $t = 2.4$; $p = 0.038$), and the number of activated astrocytes (**Figure 2H**; $t = 3.2$; $p = 0.008$).

Pharmacogenetic Manipulation of Astrocytic Activity Modulates Fictive Locomotion

Finally, we wanted to determine whether manipulating neuronal-astrocyte interactions would modulate the locomotor CPG output. In previous studies, we have used pharmacological methods to excite spinal astrocytes (Acton and Miles, 2015; Acton et al., 2018). Here we decided to employ pharmacogenetics to more specifically excite and inhibit astrocytes, an approach that has been used by others to manipulate astrocytic activity (Yang et al., 2015). Transgenic DREADD (Designer Receptor Exclusively Activated by Designer Drug) mice were crossed with GFAP::Cre mice to produce GFAP::Cre;hM3Dq and GFAP::Cre;hM4Di offspring. In spinal cords or spinal slices from GFAP::Cre;hM3Dq and GFAP::Cre;hM4Di neonates, perfusion with the specific DREADD agonist Clozapine-N-Oxide (CNO) should excite (hM3Dq) or inhibit (hM4Di) astrocytes.

To first validate the ability of the DREADD receptors to excite or inhibit astrocytes in hM3Dq and hM4Di mice respectively, Ca^{2+} imaging was performed in triple transgenic mice expressing GFAP::Cre;GCAMP6s;hM3Dq or GFAP::Cre;GCAMP6s;hM4Di (**Figures 3A–C**). Perfusion of CNO (1 μM) to spinal cord slices evoked robust Ca^{2+} responses in astrocytes expressing hM3Dq (**Figure 3A**) but had no clear effect on non-transgenic control astrocytes (**Figure 3B**) or astrocytes expressing hM4Di (**Figure 3C**). We then confirmed that activation of the inhibitory hM4Di receptor with CNO (2 μM) diminished the responses of astrocytes to applications of glutamate, as compared with hM4Di-expressing astrocytes that were not incubated in CNO (**Figures 3D–H**; $n = 4$ slices; $t = 4.0$; $p < 0.007$). Similarly, we demonstrated that 26 astrocytes from the same GFAP::Cre;GCAMP6s;hM4Di spinal cord slice showed little response to glutamate in the presence of CNO (2 μM), but showed more typical responses to glutamate after the CNO was washed off (**Supplementary Figure S2**). These results suggest that pharmacogenetics can be used to either excite or inhibit spinal cord astrocytes using Cre-driven hM3Dq and hM4Di receptor activation respectively.

We next addressed whether activation or inhibition of astrocytes using DREADDs could modulate fictive locomotion recorded from isolated spinal cord preparations. Fictive locomotion was recorded from the upper lumbar roots (L1–3) of isolated spinal cords from control ($n = 9$), GFAP::Cre;hM3Dq (hM3Dq; $n = 10$) and GFAP::Cre;hM4Di (hM4Di; $n = 11$) mice (**Figures 4A–C**). There was no significant difference in the baseline amplitude, duration or frequency of locomotor bursts between control, hM3Dq and hM4Di cords (**SupplementaryFigures S3A,B**), confirming that the expression of the DREADD receptors in astrocytes alone had no significant effect on spinal motor circuits. The application of CNO (2 μM) had no effect on the frequency of fictive locomotion in control spinal cords (**Figure 4D**; $F_{(2,18)} = 1.5$; $p = 0.256$). However, CNO caused a significant reduction in burst frequency in hM3Dq cords (**Figure 4E**; $F_{(2,18)} = 4.0$; $p < 0.05$). In contrast, CNO elicited an increase in burst frequency in hM4Di cords (**Figure 4F**; $F_{(2,20)} = 9.5$; $p < 0.01$). CNO had no significant effect on burst duration (**Supplementary Figures S3C–E**) or amplitude (**Supplementary Figures S3F–H**) in control, hM3Dq or hM4Di cords.

It has previously been suggested that pharmacologically stimulated astrocytes modulate fictive locomotion through adenosine signaling (Acton and Miles, 2015; Witts et al., 2015; Acton et al., 2018), which can be inhibited by the A1 adenosine receptor antagonist, DPCPX at 50 μM (Witts et al., 2012;

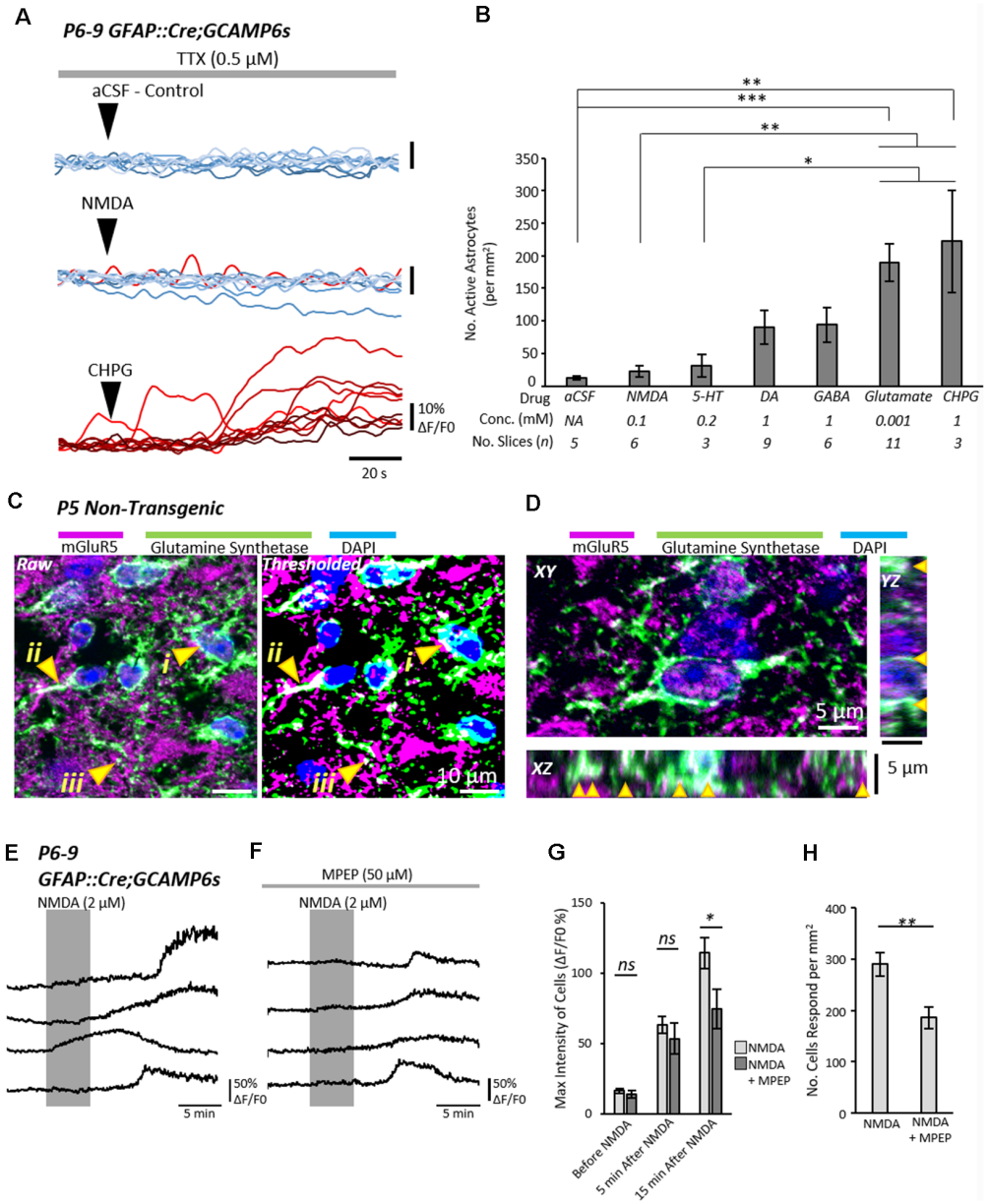


FIGURE 2 | Astrocytic metabotropic glutamate receptor 5 (mGluR5) receptors mediate neuronal-to-astrocyte signaling in the mammalian spinal cord. **(A)** Example traces from Ca^{2+} imaging of astrocytes during local applications of vehicle control artificial cerebrospinal fluid (aCSF), N-methyl-D-aspartate (NMDA) and (RS)-2-Chloro-5-hydroxyphenylglycine (CHPG) in the presence of TTX (1 µM). Traces from 10 cells from within the same experiment are shown for each agonist overlayed. Traces are displayed in a red-hue if responsive to the drug, and blue if non-responsive. **(B)** Bar chart displaying the density of astrocytes that responded to a given pharmacological stimulus. The agonist concentrations and the number of slices (*n* number) for each agent are listed below the graph. **(C)** Visualization of mGluR5 receptor expression in glutamine synthetase-labeled astrocytic cell bodies (i), primary leaflet/processes (ii) and finer processes (iii). **(D)** 3D visualization of mGluR5 localization on astrocytes with orthogonal views of XY, XZ and YZ. Arrows denote cases of colocalization between mGluR5 and glutamine synthetase observed in 3D. **(E)** Application of NMDA in spinal cord slices from GFAP::Cre;GCAMP6s mice enables the visualization of astrocyte activity in response to neuronal activation. NMDA does not activate astrocytes directly (see **Figure 3**). **(F)** Application of NMDA in the presence of mGluR5 antagonist Methyl-6-(phenylethynyl)pyridine hydrochloride (MPEP) shows attenuated responses from astrocytes. **(G)** Bar chart showing that the degree of astrocytic activation 15 min after NMDA application was significantly reduced when slices were incubated in the mGluR5 antagonist, MPEP. **(H)** Bar chart showing the number of astrocytes that responded to neuronal activity induced by NMDA was reduced in the presence of MPEP. $^{*}p < 0.05$, $^{**}p < 0.01$, $^{***}p < 0.001$; ns, not significant.

Acton and Miles, 2015). We, therefore, utilized DPCPX to assess whether modulation of fictive locomotion following pharmacogenetic manipulation of astrocytic activity involves adenosine signaling. We found that there was no change in locomotor frequency when astrocytes in hM3Dq ($n = 10$) and hM4Di ($n = 11$) cords were stimulated with CNO in the presence

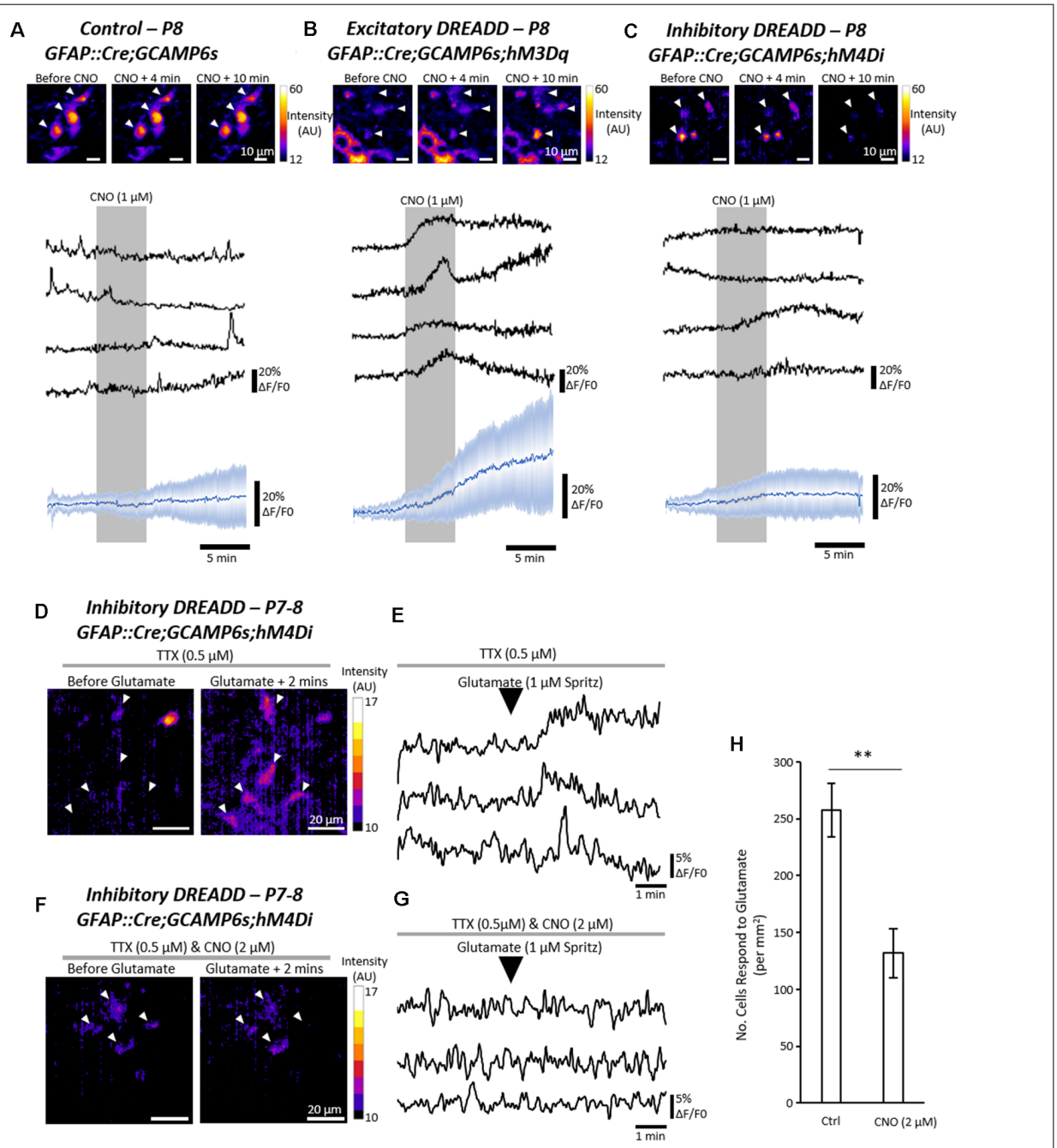


FIGURE 3 | Pharmacogenetic techniques can manipulate astrocytic Ca^{2+} activity in the mammalian spinal cord. **(A)** Ca^{2+} imaging of GFAP::cre;GCAMP6s astrocytes in response to Clozapine-N-Oxide (CNO). Example (top), and averaged (bottom) traces of Ca^{2+} imaging from astrocytes during applications of CNO (19 cells for averaged trace). **(B)** Ca^{2+} imaging of GFAP::cre;GCAMP6s;hM3Dq astrocytes in response to CNO. Example (top), and averaged (bottom) traces of Ca^{2+} imaging from astrocytes during applications of CNO (25 cells for averaged trace). **(C)** Ca^{2+} imaging of GFAP::cre;GCAMP6s;hM4Di astrocytes in response to CNO. Example (top), and averaged (bottom) traces of Ca^{2+} imaging from astrocytes during applications of CNO (30 cells for averaged trace). **(D)** Ca^{2+} responses in GFAP::cre;GCAMP6s;hM4Di astrocytes in response to glutamate, perfused in TTX to prevent neuronal-mediated responses. **(E)** Example traces of Ca^{2+} responses in GFAP::cre;GCAMP6s;hM4Di astrocytes in response to glutamate. **(F)** Ca^{2+} responses in GFAP::cre;GCAMP6s;hM4Di astrocytes in response to glutamate, perfused in both TTX and CNO to inhibit astrocyte activity. **(G)** Example traces of Ca^{2+} responses in GFAP::cre;GCAMP6s;hM4Di astrocytes showing no response to glutamate due to pharmacogenetic inhibition with CNO. **(H)** Bar chart displaying the number of astrocytes responding to glutamate in GFAP::cre;GCAMP6s;hM4Di spinal cord slices under control conditions and when perfused with CNO to inhibit astrocytes. $^{**}p < 0.01$.

of DPCPX (50 µM; hM3Dq: $F_{(1.28,11.5)} = 0.23$; $p = 0.702$; hM4Di: $F_{(2,20)} = 1.0$; $p = 0.414$; **Figures 4G,H**).

Finally, we interrogated the neuron-astrocyte signaling mechanism responsible for driving astrocyte-derived purinergic

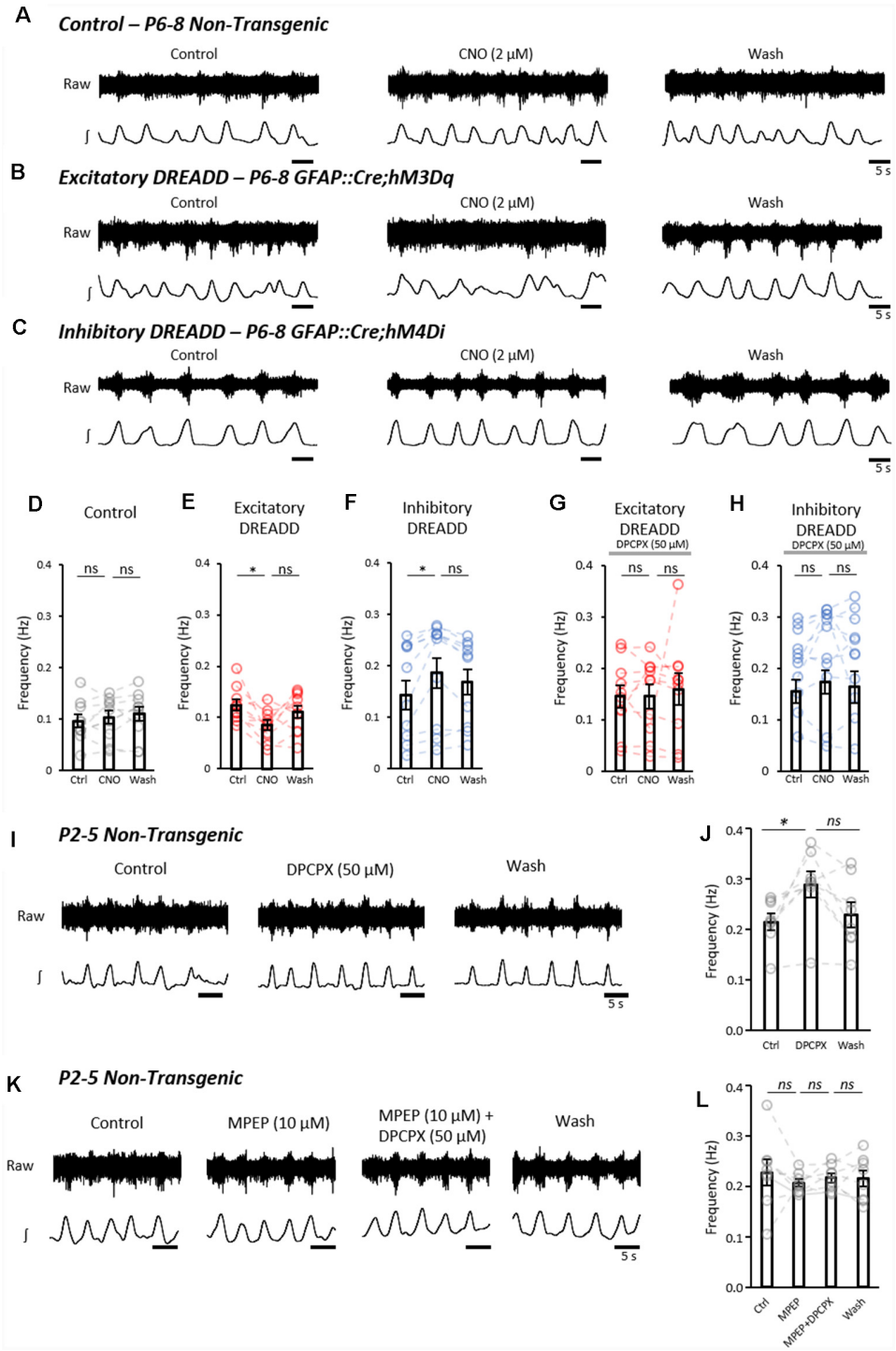


FIGURE 4 | Astrocytes exert purinergic modulation of locomotion in response to mGluR5 dependent activation. **(A)** Example raw (top) and rectified/integrated (bottom) traces of pharmacologically induced fictive locomotor bursts recorded from *in vitro* spinal cord preparations from control non-transgenic neonatal mice. The burst frequency, duration and amplitude were analyzed in control conditions, in the presence of CNO and following the washout of CNO. **(B)** Pharmacologically induced fictive locomotor bursts recorded from a GFAP::cre;hM3Dq (excitatory DREADD) neonatal mouse spinal cord *in vitro* during control conditions, in the presence of CNO and following the washout of CNO. **(C)** Pharmacologically induced fictive locomotor bursts recorded from a GFAP::cre;hM4Di (inhibitory DREADD) neonatal mouse spinal cord *in vitro* during control conditions, in the presence of CNO and following the washout of CNO. **(D)** Bar chart displaying the frequency of fictive locomotor bursts in control, non-transgenic mouse spinal cords in response to CNO. **(E)** Bar chart displaying the frequency of fictive locomotor bursts in excitatory DREADD mouse spinal cords in response to CNO. **(F)** Bar chart displaying the frequency of fictive locomotor bursts in inhibitory

(*Continued*)

FIGURE 4 | Continued
DREADD mouse spinal cords in response to CNO. **(G)** Bar chart displaying the frequency of fictive locomotor bursts in excitatory DREADD mouse spinal cords in response to CNO when perfused with 8-Cyclopentyl-1,3-dipropylxanthine (DPCPX) throughout to block the adenosine A1 receptor. **(H)** Bar chart displaying the frequency of fictive locomotor bursts in inhibitory DREADD mouse spinal cords in response to CNO when perfused with DPCPX throughout to block the adenosine A1 receptor. **(I)** Example traces of fictive locomotion recorded from *in vitro* spinal cord preparations from control non-transgenic neonatal mouse spinal cords, showing the effects of a 20 min application of the A1 receptor antagonist, DPCPX. **(J)** Bar chart showing that the frequency of fictive locomotion is significantly increased with the application of DPCPX. **(K)** Example traces of fictive locomotion recorded from *in vitro* spinal cord preparations, showing blockade of the effects of the application of DPCPX when in the presence of MPEP. **(L)** Bar chart showing that DPCPX has no effect on the frequency of fictive locomotion when spinal cords are also incubated in MPEP. $^*p < 0.05$; ns, not significant.

modulation of the locomotor CPG. Having shown that glutamate and the mGluR5 agonist, CHPG, evoked robust Ca^{2+} responses in a high proportion of spinal astrocytes, we hypothesized that glutamatergic signaling, acting *via* mGluR5, represents the physiological activator of astrocyte-derived adenosine-dependent modulation. We, therefore, assessed whether blocking the mGluR5 receptor could reduce astrocytic adenosine-mediated modulation of the locomotor CPG. In isolated spinal cords from control non-transgenic mice (P1–5; $n = 8$), fictive locomotion was induced pharmacologically, and DPCPX (50 μM) was applied for 20 min to block astrocyte-derived adenosine (**Figure 4I**). Consistent with the pharmacogenetic inhibition of astrocytes, A1-receptor inhibition with DPCPX significantly increased the frequency of fictive locomotion (**Figure 4J**; $F_{(2,14)} = 5.9$; $p < 0.05$). DPCPX showed no effect on burst duration (data not shown, $F_{(2,14)} = 1.9$; $p = 0.19$) or amplitude (data not shown, $F_{(2,14)} = 0.9$; $p = 0.44$). In separate experiments, fictive locomotion was initiated in spinal cords ($n = 8$) which were then subsequently perfused with the mGluR5 antagonist MPEP (10 μM) for 20 min, followed by MPEP and DPCPX together, after-which both MPEP and DPCPX were washed out (**Figure 4K**). No significant differences in the frequency of locomotion were observed between Control, MPEP, MPEP+DPCPX and Washout conditions (**Figure 4L**; $F_{(1.53,10.73)} = 0.35$; $p = 0.657$). From this final experiment, we conclude that inhibiting mGluR5-mediated activation of astrocytes reduces the astrocytic release of purines and thus the degree of adenosine-dependent neuromodulation of the locomotor CPG.

DISCUSSION

In this study, we have used pharmacogenetic manipulation of astrocytes to show that astrocytes actively modulate spinal cord motor circuitry. Furthermore, live imaging of astrocytic activity in the isolated spinal cord suggests they respond to the activity of ventral interneurons that may form part of the spinal cord locomotor CPG. The evidence we present here suggests a modulatory feedback loop between astrocytes and neurons that depends on bi-directional communication between these two cell groups. In our proposed model, locomotor CPG activity, and associated increases in glutamatergic signaling between CPG neurons, activates astrocytes through the mGluR5 receptor. Astrocytic activation evokes the release of ATP which is metabolized extracellularly to adenosine. Adenosine acts at A1 receptors to inhibit interneurons within the CPG, which in turn affects the frequency of motor output.

Previous research has focussed on the astrocyte-to-neuron communication mechanisms that may impact motor circuits (Witts et al., 2012, 2015; Acton and Miles, 2015, 2017; Acevedo et al., 2016; Acton et al., 2018; Rivera-Oliver et al., 2018). In this study, we have identified previously unexplored neuron-to-astrocyte signaling mechanisms which may drive astrocyte-dependent modulation of the spinal cord locomotor CPG. We reveal that astrocytes are active during fictive locomotion in the isolated hemisected spinal cord, supporting observations from *in vivo* imaging of glia in the awake and moving adult mouse (Sekiguchi et al., 2016). The results from our experiments utilizing pharmacologically-induced fictive locomotion in the hemisected spinal cord do not definitively distinguish whether astrocytic activity gradually increases following the pharmacological stimulation of the neurons or whether astrocytic activity is specifically enhanced when rhythmic neural activity emerges. However, we also observed astrocytic responses to direct stimulation of ventral horn interneurons, and given that astrocyte manipulation using DREADDs only affected the frequency of locomotor output, these results offer compelling evidence that astrocytic activity is functionally linked to the locomotor CPG interneurons.

We provide compelling evidence that mGluR5 is necessary for the neuron-astrocyte signaling pathway that drives astrocytic modulation within the spinal cord. There is considerable literature on the expression of mGluRs by astrocytes and the role of mGluR5 at the tripartite synapse as a mechanism for astrocytes to detect synaptic activity (Ota et al., 2013; Panatier and Robitaille, 2016). Our data supports this theory, as spinal astrocytes express mGluR5 and responded robustly to the mGluR5 agonist, CHPG. Blocking the mGluR5 receptor reduced astrocytic activity and blocked the modulatory effects of astrocyte-derived adenosine on fictive locomotion, suggesting that mGluR5 signaling could be the "driving force" behind astrocytic modulation of motor output.

We have previously shown that astrocyte activation in P1–4 neonatal mouse spinal cords using a PAR1 agonist reduces the frequency of fictive locomotion (Acton and Miles, 2015), which matches our current findings here that DREADD-based activation of astrocytes in P6–8 spinal cords leads to reduced locomotor frequency. This suggests that the neuronal-astrocytic interactions underlying this modulatory feedback mechanism are preserved throughout early developmental stages. Whether this bi-directional signaling mechanism exists in adult mice remains to be explored. On the one hand, there is evidence that spinal astrocytes respond to walking-like behavior in the awake adult mouse (Sekiguchi et al., 2016), in a manner that is comparable to the effects we observe in our study. On the other hand, mGluR5 expression in astrocytes may not exist past adolescence (Sun et al., 2013), suggesting there could be developmentally

regulated alterations in this bi-directional signaling pathway controlling the locomotor CPG.

Interestingly, mGluR5 antagonism did not completely abolish the Ca^{2+} transients we observed in astrocytes in response to neuronal activity. This suggests that multiple, parallel pathways of neuron-to-astrocyte signaling may occur in the spinal cord. Several other neurotransmitters and neuromodulators evoked Ca^{2+} transients in small numbers of spinal astrocytes. Although these responses were not significantly greater than those observed after applications of aCSF, we cannot exclude the possibility that non-mGluR5 mediated neural-glial transmission may occur. The inhibitory neurotransmitters GABA and Glycine may be the most likely candidates for low-level neuron-to-astrocyte signaling, given the increasing body of literature on inhibitory tripartite synapse interactions (Garrett and Weiner, 2009; Matos et al., 2018; Allen, 2019; Nagai et al., 2019), the expression of inhibitory neurotransmitter receptors by spinal glial cells (Kirchhoff et al., 1996), and evidence that spinal astrocytes may modulate inhibitory synaptic release probability (Witts et al., 2015). While there is some evidence that astrocytes may express 5-HT and DA receptors, activation of these receptors may not lead to Ca^{2+} transients, and may instead hyperpolarize astrocytes (Hösli et al., 1987; Miyazaki et al., 2013). Although DA evoked Ca^{2+} responses in a small number of astrocytes, we believe that DA is unlikely to be a key activator of spinal astrocytes. The mammalian spinal cord lacks dopaminergic neurons; all dopaminergic input to the spinal cord is derived from descending systems. Thus, DA could not mediate the responses we observed in astrocytes following the direct stimulation of interneurons within isolated spinal cord tissue. Furthermore, astrocytes only showed elevated activity in hemisected spinal cord preparations once clear locomotor activity was established, with no significant response to the application of DA along with 5-HT and NMDA in the presence of TTX. These findings, therefore, indicate that astrocytes are responsive to intrinsic spinal neurotransmitters released during physiological network activity.

In addition to classic transmitter-based signaling, changes in the extracellular environment induced by neuronal activity may also stimulate astrocytic activity. For example, rises in extracellular K+ concentration, which occurs during neuronal activity including that of the locomotor CPG (Brocard et al., 2013), represents an alternative mechanism by which astrocytes may be activated (Scemes and Spray, 2012; Bellot-Saez et al., 2017). Given the number of different neurotransmitter receptors that are reported to be expressed by astrocytes throughout the nervous system (Verkhratsky and Butt, 2013) and the ability of spinal astrocytes to respond to multiple neuronally-derived signals, it is possible that astrocytes act as global integrators of neuronal activity and contribute to a wide range of spinal neuromodulatory systems.

There is converging evidence that stimulating astrocytes pharmacologically, or ablating astrocytes with gliotoxins, reveals purinergic-dependent, glial-derived modulation of the spinal cord locomotor CPG (Dale and Gilday, 1996; Dale, 1998; Brown and Dale, 2000; Witts et al., 2012, 2015; Acton and Miles, 2015; Acevedo et al., 2016; Acton and Miles, 2017; Acton et al., 2018; Rivera-Oliver et al., 2018). Although astrocytes in other CNS regions demonstrate the ability to utilize other transmitters, such as glutamate or GABA (Malarkey and Parpura, 2008; Christensen et al., 2018); there is a paucity of evidence to suggest that other gliotransmitters are involved in the astrocytic control of the locomotor CPG. In previous studies, antagonists of purinergic signaling were sufficient to block all the astrocytic effects on the locomotor network (Acton and Miles, 2015; Witts et al., 2015; Acton and Miles, 2017; Acton et al., 2018). In this study, we have employed the pharmacogenetic DREADD approach to specifically target astrocytes and allow us to both excite and inhibit astrocytes. The hM3Dq-based activation of astrocytes elicits a strong response comparable with the use of the PAR1 agonist, TFLLR, which has been used to excite astrocytes in previous similar studies (Acton and Miles, 2015; Acton et al., 2018). While these high levels of stimulation may invoke non-physiological responses from cells, it is important to note that the hM4Di-based inhibition of astrocytes results in a complementary, opposing effect on fictive locomotion as compared to stimulating astrocytes. Furthermore, the effects of stimulating and inhibiting astrocytes were both nullified by blocking A1 adenosine receptors. Our data, therefore, support previously proposed mechanisms of glial-mediated modulation of the spinal locomotor CPG. The theory stands that astrocytes release ATP, which is subsequently converted to adenosine, which then acts at heteromeric dimers comprised of A1 adenosine and D1 dopaminergic receptors on CPG interneurons to reduce neuronal activity (Witts et al., 2015; Acton and Miles, 2017; Acton et al., 2018; Rivera-Oliver et al., 2018).

There remains debate as to whether gliotransmission occurs under physiological conditions, or whether reported incidences of glia-to-neuron signaling are merely artifacts of *in vitro* studies or the stimulation method employed (Fiacco and McCarthy, 2018; Savtchouk and Volterra, 2018). As demonstrated by our study, the locomotor circuitry of the spinal cord represents a useful model in which to interrogate these questions. The spinal cord can be isolated for experimentation while still conserving the essential sensory inputs and motor outputs for reflex responses and locomotor activity. The outputs generated by spinal circuits are measurable and directly correlative to the *in vivo* behaviors they serve. Thus, spinal circuits may provide a practical solution to the gliotransmission debate by avoiding the caveats of other approaches such as *in vitro* cell culture studies.

Our results strongly imply a physiological role for the astrocytic release of purines in modulating a basic, neuronally-mediated behavior. What remains to be investigated is the precise gliotransmitter release mechanism in spinal astrocytes; i.e., whether transmission utilizes vesicular release machinery or occurs *via* hemichannel pores formed by connexins. This could be addressed by using mutant mice with perturbed Vesicle-Associated Membrane Proteins (VAMPs) or mutated Connexin-43 which forms hemichannel pores. Recent findings suggest reactive astrocytes in ALS display enhanced expression of Connexin 43, contributing to motor neuron toxicity (Almad et al., 2016). Therefore, understanding the precise signaling

machinery between both astrocytes and neurons may reveal therapeutic targets for treating neurodegenerative diseases, such as ALS.

The locomotor CPG is just one of several rhythmic neural circuits of the CNS in which gliotransmission has been interrogated. Astrocytes have been shown to be active in the respiratory control networks of the brainstem (Guyenet et al., 2009; Gourine et al., 2010; Okada et al., 2012; Sheikhbahaei et al., 2018). Chemosensitive astrocytes in the retrotrapezoid nucleus respond to circulating CO_2 and consequently release ATP to initiate respiration (Gourine et al., 2010; Huxtable et al., 2010; Sheikhbahaei et al., 2018). Meanwhile, the ATP metabolite, adenosine, has been shown to exhibit an inhibitory effect on the respiratory CPG (Huxtable et al., 2010). Studies into mastication have revealed an entirely different astrocytic modulatory mechanism. In the rat trigeminal sensorimotor circuit, astrocytes release the Ca^{2+} binding protein S100β, which sequesters extracellular Ca^{2+} and reduces NMDA-induced bursting of rhythmogenic neurons that lead to chewing behavior (Morquette et al., 2015). It is conceivable that this mechanism is also present in other networks such as those controlling respiration or locomotion.

Feeding behavior is also regarded as rhythmic, though not strictly under the control of a CPG but rather orchestrated by an "entrained oscillator" in the medial basal hypothalamus (Mieda et al., 2006). Here in the hypothalamus, astrocytes also act as a source of adenosine to modulate feeding behavior (Yang et al., 2015). In this instance, pharmacogenetic manipulation of astrocytes demonstrated their ability to bi-directionally modulate food intake in mice, helping to maintain feeding within a constrained range to prevent energy deficit or surfeit.

Glial cells have also been implicated in the control of rhythmic CPGs in the periphery, for example, within networks of the enteric nervous system that regulate gut motility patterns (Smith and Koh, 2017). Here it has been shown that enteric glia (likened to CNS astrocytes) are responsive to neural-mediated motor events that aid in colonic transport of fecal matter (MacEachern et al., 2011; Broadhead et al., 2012; McClain et al., 2014, 2015). Genetic manipulations that perturb astrocytic gliotransmitter release mechanisms significantly affected colonic fecal transit in mice (Grubišić and Parpura, 2017). The nature of the enteric glial transmitter involved remains unknown, but both ATP and NO are implicated (Gulbransen and Sharkey, 2012).

There are clearly diverse roles for astrocytes and other glial cells throughout the nervous system. A growing body of evidence indicates that astrocytes play active roles within many neural circuits, as they are able to respond to neuronal signaling and release chemical messengers *via* gliotransmission. While it remains to be determined whether there is any conserved logic to the role of astrocytes within neural circuits, our study on the locomotor CPG indicates a purinergic-dependent modulation of rhythmogenic neural network activity, which is driven by glutamate derived from the neural network itself. Based on previous literature (Yang et al., 2015; Cinelli et al., 2017; Sheikhbahaei et al., 2018), it is conceivable that astrocyte-derived purinergic modulation is a key mechanism within rhythmic circuits, which helps to constrain network output in order to control rhythmic behaviors. Further advances in our knowledge of the roles of glial cells within neural circuits will pave the way for a greater understanding of how the nervous system coordinates behavior.

DATA AVAILABILITY STATEMENT

The datasets generated for this study are available on request to the corresponding author.

ETHICS STATEMENT

The animal study was reviewed and approved by the University of St Andrews Animal Welfare and Ethics Committee and conducted in accordance with the UK Animals (Scientific Procedures) Act 1986.

AUTHOR CONTRIBUTIONS

MB designed and performed the experiments, data analysis and wrote the manuscript. GM designed the experiments, wrote the manuscript and supervised the project.

FUNDING

Funding was provided by the Biotechnology and Biological Science Research Grant (BB/M021793/1), the Motor Neurone Disease (MND) Association UK and the RS MacDonald Charitable Trust.

ACKNOWLEDGMENTS

We would also like to acknowledge Stefan Pulver for his assistance in establishing the data management and Ca^{2+} imaging techniques employed.

SUPPLEMENTARY MATERIAL

The Supplementary Material for this article can be found online at: https://www.frontiersin.org/articles/10.3389/fncel.2020.00030/full#supplementary-material.

FIGURE S1 | Astrocyte cell density using a fluorescence reporter line. **(A)** Spinal cord slices were prepared from GFAP::Cre;TdTomato neonatal mice and images of the ventral horn were captured. Red fluorescent cells were counted to estimate the total density of astrocytes (n = 12 spinal cord slices from two mice, P8–9). **(B)** Box and whisker plot showing the average number of TdTomato +ve astrocytes in neonatal spinal cord slices per mm^2.

FIGURE S2 | Inhibition of spinal astrocytes using hM4Di DREADD receptor activation. **(A)** Spinal cord slice prepared from a neonatal P8 GFAP::Cre;GCAMP6s;hM4Di mouse. Astrocytes from the same slice were visualized using Ca^{2+} imaging to investigate their responses to Glutamate with and without the presence of CNO to inhibit them (n = 26). **(B)** Astrocytes were first visualized in the presence of TTX and CNO, to block neurons and hM4Di-expressing astrocytes respectively. Three example traces are shown of three astrocytes, and an averaged trace of the ΔF/F0 with standard deviation from a total of 26 astrocytes. **(C)** After the first recording, CNO was washed off for 15 min leaving only TTX to inhibit the neurons. The three traces depict the ΔF/F0 from the same three cells as in panels **(A,B)**. A greater number of cells

responded to glutamate, typically showing a more sustained ΔF/F0 elevation, when CNO was absent.

FIGURE S3 | Additional fictive locomotor bursting parameters for control (non-transgenic), GFAP::cre;hM3Dq and GFAP::cre;hM4Di neonatal spinal cords. **(A)** Bar chart showing the duration of fictive locomotor bursts in each of the three genotypes of mice used. **(B)** Bar chart showing the frequency of fictive locomotor bursts in each of the three genotypes of mice used. **(C)** Bar charts displaying the burst duration under control, CNO and wash conditions for control (non-transgenic) spinal cords. **(D)** Bar charts displaying the burst duration under control, CNO and wash conditions for GFAP::Cre;hM3Dq spinal cords. **(E)** Bar charts displaying the burst duration under control, CNO and wash conditions for GFAP::Cre;hM4Di spinal cords. **(F)** Bar charts displaying the burst amplitude under control, CNO and wash conditions for control (non-transgenic) spinal cords. **(G)** Bar charts displaying the burst amplitude under control, CNO and wash conditions for GFAP::Cre;hM3Dq spinal cords. **(H)** Bar charts displaying the burst amplitude under control, CNO and wash conditions for GFAP::Cre;hM4Di spinal cords. ns, not significant.

REFERENCES

Acevedo, J., Santana-Almansa, A., Matos-Vergara, N., Marrero-Cordero, L. R., Cabezas-Bou, E., and Díaz-Ríos, M. (2016). Caffeine stimulates locomotor activity in the mammalian spinal cord *via* adenosine A1 receptor-dopamine D1 receptor interaction and PKA-dependent mechanisms. *Neuropharmacology* 101, 490–505. doi: 10.1016/j.neuropharm.2015.10.020

Acton, D., Broadhead, M. J., and Miles, G. B. (2018). Modulation of spinal motor networks by astrocyte-derived adenosine is dependent on D_1-like dopamine receptor signaling. *J. Neurophysiol.* 120, 998–1009. doi: 10.1152/jn.00783.2017

Acton, D., and Miles, G. B. (2015). Stimulation of glia reveals modulation of mammalian spinal motor networks by adenosine. *PLoS One* 10:e0134488. doi: 10.1371/journal.pone.0134488

Acton, D., and Miles, G. B. (2017). Gliotransmission and adenosinergic modulation: insights from mammalian spinal motor networks. *J. Neurophysiol.* 118, 3311–3327. doi: 10.1152/jn.00230.2017

Allen, N. J. (2019). Star power: astrocytes regulate behavior. *Cell* 177, 1091–1093. doi: 10.1016/j.cell.2019.04.042

Almad, A. A., Doreswamy, A., Gross, S. K., Richard, J., Huo, Y., Haughey, N., et al. (2016). Connexin 43 in astrocytes contributes to motor neuron toxicity in amyotrophic lateral sclerosis. *Glia* 64, 1154–1169. doi: 10.1002/glia.22989

Bellot-Saez, A., Kékesi, O., Morley, J. W., and Buskila, Y. (2017). Astrocytic modulation of neuronal excitability through K^+ spatial buffering. *Neurosci. Biobehav. Rev.* 77, 87–97. doi: 10.1016/j.neubiorev.2017.03.002

Bowman, C. L., and Kimelberg, H. K. (1984). Excitatory amino acids directly depolarize rat brain astrocytes in primary culture. *Nature* 311, 656–659. doi: 10.1038/311656a0

Broadhead, M. J., Bayguinov, P. O., Okamoto, T., Heredia, D. J., and Smith, T. K. (2012). Ca^{2+} transients in myenteric glial cells during the colonic migrating motor complex in the isolated murine large intestine. *J. Physiol.* 590, 335–350. doi: 10.1113/jphysiol.2011.219519

Brocard, F., Shevtsova, N. A., Bouhadfane, M., Tazerart, S., Heinemann, U., Rybak, I. A., et al. (2013). Activity-dependent changes in extracellular Ca^{2+} and K^+ reveal pacemakers in the spinal locomotor-related network. *Neuron* 77, 1047–1054. doi: 10.1016/j.neuron.2013.01.026

Brown, P., and Dale, N. (2000). Adenosine A_1 receptors modulate high voltage-activated Ca^{2+} currents and motor pattern generation in the *Xenopus* embryo. *J. Physiol.* 525, 655–667. doi: 10.1111/j.1469-7793.2000.00655.x

Carlsen, E. M., and Perrier, J.-F. (2014). Purines released from astrocytes inhibit excitatory synaptic transmission in the ventral horn of the spinal cord. *Front. Neural Circuits* 8:60. doi: 10.3389/fncir.2014.00060

Christensen, R. K., Delgado-Lezama, R., Russo, R. E., Lind, B. L., Alcocer, E. L., Rath, M. F., et al. (2018). Spinal dorsal horn astrocytes release GABA in response to synaptic activation. *J. Physiol.* 596, 4983–4994. doi: 10.1113/jp276562

Cinelli, E., Iovino, L., and Mutolo, D. (2017). ATP and astrocytes play a prominent role in the control of the respiratory pattern generator in the lamprey. *J. Physiol.* 595, 7063–7079. doi: 10.1113/jp274749

Dale, N. (1998). Delayed production of adenosine underlies temporal modulation of swimming in frog embryo. *J. Physiol.* 511, 265–272. doi: 10.1111/j.1469-7793.1998.265bi.x

Dale, N., and Gilday, D. (1996). Regulation of rhythmic movements by purinergic neurotransmitters in frog embryos. *Nature* 383, 259–263. doi: 10.1038/383259a0

Fiacco, T. A., and McCarthy, K. D. (2018). Multiple lines of evidence indicate that gliotransmission does not occur under physiological conditions. *J. Neurosci.* 38, 3–13. doi: 10.1523/JNEUROSCI.0016-17.2017

Gao, Y.-J., and Ji, R.-R. (2010). Targeting astrocyte signaling for chronic pain. *Neurotherapeutics* 7, 482–493. doi: 10.1016/j.nurt.2010.05.016

Garrett, A. M., and Weiner, J. A. (2009). Control of CNS synapse development by γ-protocadherin-mediated astrocyte-neuron contact. *J. Neurosci.* 29, 11723–11731. doi: 10.1523/JNEUROSCI.2818-09.2009

Gibbs, M. E., Hutchinson, D., and Hertz, L. (2008). Astrocytic involvement in learning and memory consolidation. *Neurosci. Biobehav. Rev.* 32, 927–944. doi: 10.1016/j.neubiorev.2008.02.001

Gourine, A., Kasymov, V., Marina, N., Tang, F., Figueiredo, M. F., Lane, S., et al. (2010). Astrocytes control breathing through pH-dependent release of ATP. *Science* 329, 571–575. doi: 10.1126/science.1190721

Grillner, S. (2003). The motor infrastructure: from ion channels to neuronal networks. *Nat. Rev. Neurosci.* 4, 573–586. doi: 10.1038/nrn1137

Grillner, S. (2006). Biological pattern generation: the cellular and computational logic of networks in motion. *Neuron* 52, 751–766. doi: 10.1016/j.neuron.2006.11.008

Grubišić, V., and Parpura, V. (2017). Two modes of enteric gliotransmission differentially affect gut physiology. *Glia* 65, 699–711. doi: 10.1002/glia.23121

Gulbransen, B. D., and Sharkey, K. A. (2012). Novel functional roles for enteric glia in the gastrointestinal tract. *Nat. Rev. Gastroenterol. Hepatol.* 9, 625–632. doi: 10.1038/nrgastro.2012.138

Guyenet, P. G., Bayliss, D. A., Stornetta, R. L., Fortuna, M. G., Abbott, S. B. G., and DePuy, S. D. (2009). Retrotrapezoid nucleus, respiratory chemosensitivity and breathing automaticity. *Respir. Physiol. Neurobiol.* 168, 59–68. doi: 10.1016/j.resp.2009.02.001

Hösli, L., Hösli, E., Baggi, M., Bassetti, C., and Uhr, M. (1987). Action of dopamine and serotonin on the membrane potential of cultured astrocytes. *Exp. Brain Res.* 65, 482–485. doi: 10.1007/bf00236323

Harris-Warrick, R. M. (2011). Neuromodulation and flexibility in central pattern generator networks. *Curr. Opin. Neurobiol.* 21, 685–692. doi: 10.1016/j.conb.2011.05.011

Huxtable, A. G., Zwicker, J. D., Alvares, T. S., Ruangkittisakul, A., Fang, X., Hahn, L. B., et al. (2010). Glia contribute to the purinergic modulation of inspiratory rhythm-generating networks. *J. Neurosci.* 30, 3947–3958. doi: 10.1523/JNEUROSCI.6027-09.2010

Iwagaki, N., and Miles, G. B. (2011). Activation of group I metabotropic glutamate receptors modulates locomotor-related motoneuron output in mice. *J. Neurophysiol.* 105, 2108–2120. doi: 10.1152/jn.01037.2010

Jennings, A., Tyurikova, O., Bard, L., Zheng, K., Semyanov, A., Henneberger, C., et al. (2017). Dopamine elevates and lowers astroglial Ca^{2+} through distinct pathways depending on local synaptic circuitry. *Glia* 65, 447–459. doi: 10.1002/glia.23103

Ji, R.-R., Kawasaki, Y., Zhuang, Z.-Y., Wen, Y.-R., and Decosterd, I. (2006). Possible role of spinal astrocytes in maintaining chronic pain sensitization: review of current evidence with focus on bFGF/JNK pathway. *Neuron Glia Biol.* 2, 259–269. doi: 10.1017/s1740925x07000403

Kiehn, O. (2016). Decoding the organization of spinal circuits that control locomotion. *Nat. Rev. Neurosci.* 17, 224–238. doi: 10.1038/nrn.2016.9

Kirchhoff, F., Mülhardt, C., Pastor, A., Becker, C. M., and Kettenmann, H. (1996). Expression of glycine receptor subunits in glial cells of the rat spinal cord. *J. Neurochem.* 66, 1383–1390. doi: 10.1046/j.1471-4159.1996.66041383.x

MacEachern, S. J., Patel, B. A., McKay, D. M., and Sharkey, K. A. (2011). Nitric oxide regulation of colonic epithelial ion transport: a novel role for enteric glia in the myenteric plexus. *J. Physiol.* 589, 3333–3348. doi: 10.1113/jphysiol.2011.207902

Malarkey, E. B., and Parpura, V. (2008). Mechanisms of glutamate release from astrocytes. *Neurochem. Int.* 52, 142–154. doi: 10.1016/j.neuint.2007.06.005

Mariotti, L., Losi, G., Sessolo, M., Marcon, I., and Carmignoto, G. (2016). The inhibitory neurotransmitter GABA evokes long-lasting Ca^{2+} oscillations in cortical astrocytes. *Glia* 64, 363–373. doi: 10.1002/glia.22933

Matos, M., Bosson, A., Riebe, I., Reynell, C., Vallée, J., Laplante, I., et al. (2018). Astrocytes detect and upregulate transmission at inhibitory synapses of somatostatin interneurons onto pyramidal cells. *Nat. Commun.* 9:4254. doi: 10.1038/s41467-018-06731-y

McClain, J. L., Fried, D. E., and Gulbransen, B. D. (2015). Agonist-evoked Ca^{2+} signaling in enteric glia drives neural programs that regulate intestinal motility in mice. *Cell. Mol. Gastroenterol. Hepatol.* 1, 631–645. doi: 10.1016/j.jcmgh.2015.08.004

McClain, J., Grubišić, V., Fried, D., Gomez-Suarez, R. A., Leinninger, G. M., Sévigny, J., et al. (2014). Ca^{2+} responses in enteric glia are mediated by connexin-43 hemichannels and modulate colonic transit in mice. *Gastroenterology* 146, 497.e1–507.e1. doi: 10.1053/j.gastro.2013.10.061

Mieda, M., Williams, S. C., Richardson, J. A., Tanaka, K., and Yanagisawa, M. (2006). The dorsomedial hypothalamic nucleus as a putative food-entrainable circadian pacemaker. *Proc. Natl. Acad. Sci. U S A* 103, 12150–12155. doi: 10.1073/pnas.0604189103

Miles, G. B., and Sillar, K. T. (2011). Neuromodulation of vertebrate locomotor control networks. *Physiology* 26, 393–411. doi: 10.1152/physiol.00013.2011

Miyazaki, I., Asanuma, M., Murakami, S., Takeshima, M., Torigoe, N., Kitamura, Y., et al. (2013). Targeting 5-HT_{1A} receptors in astrocytes to protect dopaminergic neurons in parkinsonian models. *Neurobiol. Dis.* 59, 244–256. doi: 10.1016/j.nbd.2013.08.003

Morquette, P., Verdier, D., Kadala, A., Féthière, J., Philippe, A. G., Robitaille, R., et al. (2015). An astrocyte-dependent mechanism for neuronal rhythmogenesis. *Nat. Neurosci.* 18, 844–854. doi: 10.1038/nn.4013

Nagai, J., Rajbhandari, A. K., Gangwani, M. R., Masmanidis, S. C., Fanselow, M. S., and Khakh, B. S. (2019). Hyperactivity with disrupted attention by activation of an astrocyte synaptogenic cue. *Cell* 177, 1280.e20–1292.e20. doi: 10.1016/j.cell.2019.03.019

Okada, S., Nakamura, M., Katoh, H., Miyao, T., Shimazaki, T., Ishii, K., et al. (2006). Conditional ablation of Stat3 or Socs3 discloses a dual role for reactive astrocytes after spinal cord injury. *Nat. Med.* 12, 829–834. doi: 10.1038/nm1425

Okada, Y., Sasaki, T., Oku, Y., Takahashi, N., Seki, M., and Ujita, S. (2012). Preinspiratory calcium rise in putative pre-Botzinger complex astrocytes. *J. Physiol.* 590, 4933–4944. doi: 10.1113/jphysiol.2012.231464

Ota, Y., Zanetti, A. T., and Hallock, R. M. (2013). The role of astrocytes in the regulation of synaptic plasticity and memory formation. *Neural Plast.* 2013:185463. doi: 10.1155/2013/185463

Panatier, A., and Robitaille, R. (2016). Astrocytic mGluR5 and the tripartite synapse. *Neuroscience* 323, 29–34. doi: 10.1016/j.neuroscience.2015.03.063

Parri, H. R., Gould, T. M., and Crunelli, V. (2010). Sensory and cortical activation of distinct glial cell subtypes in the somatosensory thalamus of young rats. *Eur. J. Neurosci.* 32, 29–40. doi: 10.1111/j.1460-9568.2010.07281.x

Pehar, M., Harlan, B. A., Killoy, K. M., and Vargas, M. R. (2018). Role and therapeutic potential of astrocytes in amyotrophic lateral sclerosis. *Curr. Pharm. Des.* 23, 5010–5021. doi: 10.2174/1381612823666170622095802

Phatnani, H. P., Guarnieri, P., Friedman, B. A., Carrasco, M. A., Muratet, M., O'Keeffe, S., et al. (2013). Intricate interplay between astrocytes and motor neurons in ALS. *Proc. Natl. Acad. Sci. U S A* 110, E756–E765. doi: 10.1073/pnas.1222361110

Queiroz, G., Meyer, D. K., Meyer, A., Starke, K., and von Kügelgen, I. (1999). A study of the mechanism of the release of ATP from rat cortical astroglial cells evoked by activation of glutamate receptors. *Neuroscience* 91, 1171–1181. doi: 10.1016/s0306-4522(98)00644-7

Rivera-Oliver, M., Moreno, E., Álvarez-Bagnarol, Y., Ayala-Santiago, C., Cruz-Reyes, N., Molina-Castro, G. C., et al. (2018). Adenosine A_1-dopamine D_1 receptor heteromers control the excitability of the spinal motoneuron. *Mol. Neurobiol.* 56, 797–811. doi: 10.1007/s12035-018-1120-y

Robertson, J. M. (2018). The gliocentric brain. *Int. J. Mol. Sci.* 19:E3033. doi: 10.3390/ijms19103033

Savtchouk, I., and Volterra, A. (2018). Gliotransmission: beyond black-and-white. *J. Neurosci.* 38, 14–25. doi: 10.1523/jneurosci.0017-17.2017

Scemes, E., and Spray, D. C. (2012). Extracellular K^+ and astrocyte signaling *via* connexin and pannexin channels. *Neurochem. Res.* 37, 2310–2316. doi: 10.1007/s11064-012-0759-4

Sekiguchi, K. J., Shekhtmeyster, P., Merten, K., Arena, A., Cook, D., Hoffman, E., et al. (2016). Imaging large-scale cellular activity in spinal cord of freely behaving mice. *Nat. Commun.* 7:11450. doi: 10.1038/ncomms11450

Selverston, A. I. (2005). A neural infrastructure for rhythmic motor patterns. *Cell. Mol. Neurobiol.* 25, 223–244. doi: 10.1007/s10571-005-3154-8

Sheikhbahaei, S., Turovsky, E. A., Hosford, P. S., Hadjihambi, A., Theparambil, S. M., Liu, B., et al. (2018). Astrocytes modulate brainstem respiratory rhythm-generating circuits and determine exercise capacity. *Nat. Commun.* 9:370. doi: 10.1038/s41467-017-02723-6

Smith, T. K., and Koh, S. D. (2017). A model of the enteric neural circuitry underlying the generation of rhythmic motor patterns in the colon: the role of serotonin. *Am. J. Physiol. Gastrointest. Liver Physiol.* 312, G1–G14. doi: 10.1152/ajpgi.00337.2016

Sun, W., McConnell, E., Pare, J. F., Xu, Q., Chen, M., Peng, W., et al. (2013). Glutamate-dependent neuroglial calcium signaling differs between young and adult brain. *Science* 339, 197–200. doi: 10.1126/science.1226740

Sweeney, P., Qi, Y., Xu, Z., and Yang, Y. (2016). Activation of hypothalamic astrocytes suppresses feeding without altering emotional states. *Glia* 64, 2263–2273. doi: 10.1002/glia.23073

Takeuchi, K., Mohammad, S., Ozaki, T., Morioka, E., Kawaguchi, K., Kim, J., et al. (2014). Serotonin-2C receptor involved serotonin-induced Ca^{2+} mobilisations in neuronal progenitors and neurons in rat suprachiasmatic nucleus. *Sci. Rep.* 4:4106. doi: 10.1038/srep04106

Verkhratsky, A., and Butt, A. M. (2013). *Glial Physiology and Pathophysiology: A Handbook.* Chichester: John Wiley and Sons.

Witts, E. C., Nascimento, F., and Miles, G. B. (2015). Adenosine-mediated modulation of ventral horn interneurons and spinal motoneurons in neonatal mice. *J. Neurophysiol.* 114, 2305–2315. doi: 10.1152/jn.00574.2014

Witts, E. C., Panetta, K. M., and Miles, G. B. (2012). Glial-derived adenosine modulates spinal motor networks in mice. *J. Neurophysiol.* 107, 1925–1934. doi: 10.1152/jn.00513.2011

Yang, L., Qi, Y., and Yang, Y. (2015). Astrocytes control food intake by inhibiting agrp neuron activity *via* adenosine A1 receptors. *Cell Rep.* 11, 798–807. doi: 10.1016/j.celrep.2015.04.002

Conflict of Interest: The authors declare that the research was conducted in the absence of any commercial or financial relationships that could be construed as a potential conflict of interest.

Copyright © 2020 Broadhead and Miles. This is an open-access article distributed under the terms of the Creative Commons Attribution License (CC BY). The use, distribution or reproduction in other forums is permitted, provided the original author(s) and the copyright owner(s) are credited and that the original publication in this journal is cited, in accordance with accepted academic practice. No use, distribution or reproduction is permitted which does not comply with these terms.

frontiers in Cellular Neuroscience

METHODS
published: 19 March 2020
doi: 10.3389/fncel.2020.00063

Advantages of Acute Brain Slices Prepared at Physiological Temperature in the Characterization of Synaptic Functions

Kohgaku Eguchi[1], Philipp Velicky[1], Elena Hollergschwandtner[1], Makoto Itakura[2], Yugo Fukazawa[3], Johann Georg Danzl[1] and Ryuichi Shigemoto[1]**

[1]*Institute of Science and Technology Austria (IST Austria), Klosterneuburg, Austria,* [2]*Department of Biochemistry, Kitasato University School of Medicine, Sagamihara-shi, Japan,* [3]*Department of Brain Structure and Function, Research Center for Child Mental Development, Faculty of Medical Sciences, University of Fukui, Fukui, Japan*

Acute brain slice preparation is a powerful experimental model for investigating the characteristics of synaptic function in the brain. Although brain tissue is usually cut at ice-cold temperature (CT) to facilitate slicing and avoid neuronal damage, exposure to CT causes molecular and architectural changes of synapses. To address these issues, we investigated ultrastructural and electrophysiological features of synapses in mouse acute cerebellar slices prepared at ice-cold and physiological temperature (PT). In the slices prepared at CT, we found significant spine loss and reconstruction, synaptic vesicle rearrangement and decrease in synaptic proteins, all of which were not detected in slices prepared at PT. Consistent with these structural findings, slices prepared at PT showed higher release probability. Furthermore, preparation at PT allows electrophysiological recording immediately after slicing resulting in higher detectability of long-term depression (LTD) after motor learning compared with that at CT. These results indicate substantial advantages of the slice preparation at PT for investigating synaptic functions in different physiological conditions.

Keywords: acute brain slices, synaptic transmission, synaptic plasticity, cerebellum, super-resolution microscopy, electron microscopy, patch-clamp recording

OPEN ACCESS

Edited by:
Rustem Khazipov, Institut National de la Santé et de la Recherche Médicale (INSERM), France

Reviewed by:
Atsuo Fukuda, Hamamatsu University School of Medicine, Japan
Valentin Nägerl, UMR5297 Institut Interdisciplinaire de Neurosciences (IINS), France

****Correspondence:***
Kohgaku Eguchi
kohgaku.eguchi@ist.ac.at
Ryuichi Shigemoto
ryuichi.shigemoto@ist.ac.at

Received: *28 November 2019*
Accepted: *02 March 2020*
Published: *19 March 2020*

Citation:
Eguchi K, Velicky P, Hollergschwandtner E, Itakura M, Fukazawa Y, Danzl JG and Shigemoto R (2020) Advantages of Acute Brain Slices Prepared at Physiological Temperature in the Characterization of Synaptic Functions. Front. Cell. Neurosci. 14:63. doi: 10.3389/fncel.2020.00063

INTRODUCTION

The living acute brain slice preparation has been developed and extensively used as a powerful experimental model for investigating the structural and functional characteristics of synaptic connectivity of neuronal circuits in the brain (Li and McIlwain, 1957; Yamamoto and McIlwain, 1966; Yamamoto, 1975; Takahashi, 1978; Llinás and Sugimori, 1980). The acute slice preparation is readily accessible for electrophysiological and optical recording and expected to retain the cytoarchitecture and synaptic circuits *in vivo* except for the long-range projections. In general, to prepare acute brain slices, a whole-brain is dissected out from an animal and quickly immersed into ice-cold (<4°C) cutting solution to slow down the metabolic activity in tissue blocks, which are sliced by a microtome at ice-cold temperature (CT). The slices are then pre-incubated in artificial cerebrospinal fluid (ACSF) warmed at physiological temperature (PT, 35–37°C) for up to 1 h to recover the neuronal activities prior to electrophysiological or optic recordings (Llinás and Sugimori, 1980; Bischofberger et al., 2006).

The preparation method of acute brain slices at CT, however, causes alterations of molecular and cellular components of neurons. For example, exposure of hippocampal slices to CT induces disassembly of microtubules and eliminates dendritic spines in neurons (Fiala et al., 2003; Kirov et al., 2004). Although re-warming of the hippocampal slices revives microtubule structures in neurons, excessive proliferation of the dendritic spines results in a higher density of synapses than that observed before cooling. Slicing at CT and subsequent incubation at 37°C also reduces the protein level of α-amino-3-hydroxy-5-methyl-4-isoxazolepropionic acid-type glutamate receptors (AMPARs), which mediate synaptic transmission and plasticity, in lysates of the acute hippocampal slices of rats (Taubenfeld et al., 2002). These artificial modifications may cause disadvantages of brain slicing at CT for investigating synaptic features.

Recently, a method for acute slice preparation at PT has been developed to improve the quality of cerebellar slices in aged rodents (Huang and Uusisaari, 2013). In the cerebellar slices from aged rat (>2 months-old) prepared at PT, Purkinje cells (PCs) survived better than those in slices prepared at CT without altered intrinsic excitability of the cells. Another study reported that the slice preparation at PT enhanced the cellular viability and mitochondrial activities in rat hindbrain slices compared with the preparation at CT (Fried et al., 2014). Although these reports suggest some advantages of the acute slice preparation at PT (warm-cutting method), quantitative differences in electrophysiological, molecular biological and ultrastructural properties of synapses in the brain slices prepared at CT and PT have not been examined.

To clarify which parameters of synaptic architecture and functions are affected in slices prepared at CT and PT, we investigated various ultrastructural and electrophysiological features of synapses in acute cerebellar slices prepared at CT and PT using electron microscopic (EM), super-resolution microscopic and electrophysiological techniques in acute cerebellar slices. We show that the conventional cold-cutting method causes loss and reemergence of dendritic spines, rearrangement of synaptic vesicles (SVs) in nerve terminals and decrease in both pre- and postsynaptic proteins such as AMPARs and P/Q-type voltage-gated Ca^{2+} channels ($Ca_V2.1$). In contrast, the acute cerebellar slices prepared at PT showed no significant changes in these features during the recovery time, and also less difference from perfusion-fixed tissue, indicating that the warm-cutting method can preserve the synaptic functions through the preparation process better than the cold-cutting method. We also demonstrate that long-term depression (LTD) in mouse cerebellum caused by adaptation of horizontal optokinetic response (HOKR) is better preserved in slices prepared at PT and recorded immediately after slicing than slices prepared at CT and recorded after the recovery time. Altogether, our quantitative analysis suggests strong advantages of the warm-cutting method over the conventional cold-cutting method for investigating synaptic functions. This method facilitates a wide range of neuroscience research, especially for synaptic plasticity induced *in vivo*.

MATERIALS AND METHODS

Animals

Animal experiments were conducted in accordance with the guideline of the Institute of Science and Technology Austria (IST Austria; Animal license number: BMWFW-66.018/0012-WF/V/3b/2016). Mice were bred and maintained in the Preclinical Facility of IST Austria. Unless otherwise noted, C57BL/6J mice of either sex at postnatal (P) 4–6 weeks were used in this study.

Acute Brain Slice Preparation

Mice were decapitated under isoflurane anesthesia and their brains were quickly removed from the skull and immersed into cutting solution containing (in mM): 300 sucrose, 2.5 KCl, 10 glucose, 1.25 NaH_2PO_4, 2 sodium Pyruvate, 3 *myo*-inositol, 0.5 sodium ascorbate, 26 $NaHCO_3$, 0.1 $CaCl_2$, 6 $MgCl_2$ (pH 7.4 when gassed with 95% O_2/5% CO_2) at ice-cold temperature (CT, <4°C) or physiological temperature (PT, 35–37°C). The cerebellum was dissected from the whole brain and immediately glued on a cutting stage of a tissue slicer (Linear Slicer Pro7, Dosaka EM, Kyoto, Japan). The parameters of the slicer were optimized for slicing at each temperature (CT: amplitude = 4.5, frequency = 84–86 Hz, speed = 2.0–2.5, PT: amplitude = 5.5, frequency = 84–86 Hz, speed = 2.0). Bath temperature was kept within the desired range (below 4°C for CT, 35–37°C for PT) by adding cold water with crushed ice or warm water into the bath of the slicer and was monitored throughout the cutting procedure with a thermometer. Slices were then maintained in the standard ACSF containing (in mM): 125 NaCl, 2.5 KCl, 10 glucose, 1.25 NaH_2PO_4, 2 sodium pyruvate, 3 *myo*-inositol, 0.5 sodium ascorbate, 26 $NaHCO_3$, 2 $CaCl_2$, 1 $MgCl_2$ (pH 7.4 when gassed with 95% O_2/5% CO_2) at 37°C for 1 h and subsequently at room temperature (RT) until use.

Fixations

We used three types of fixative solutions; 2.5% glutaraldehyde and 2% paraformaldehyde (PFA) in 0.1 M HEPES buffer (pH 7.4 adjusted with NaOH) for serial ultrathin sectioning with EM analysis, 2% PFA and 15% picric acid in 0.1 M sodium phosphate buffer (s-PB, pH 7.4) for SDS-FRL, and 4% PFA and 0.05% glutaraldehyde in 0.1 M s-PB for immunofluorescence imaging with a STED microscope.

For the perfusion-fixation of brains, the mice were anesthetized with ketamine/xylazine mixture *via* intraperitoneal injection and perfused transcardially with 0.1 M HEPES buffer (for serial sectioning) or 0.1 M s-PB (for SDS-FRL and STED imaging) for 1 min, followed by the fixative solution for 12 min. The perfusion of the buffers and fixatives was done at RT (23–25°C). The brains were then removed from the skull and post-fixed for 1–2 h at RT and then kept in the fixative solution overnight at 4°C. Sagittal slices of the cerebellum were cut using a tissue slicer (Linear Slicer Pro7, Dosaka, Kyoto, Japan) in 0.1 M HEPES buffer or 0.1 M s-PB. The acute cerebellar slices were immersion-fixed in the fixative solution for each purpose at RT for 1–2 h on a shaker (160 rpm) and then kept in the fixative solution overnight at 4°C.

3D Super-Resolved STED Microscopy

For super-resolution imaging with stimulated emission deletion (STED) microscopy, we used Mosaic Analysis of Double Marker (MADM-11) mice crossed with ubiquitous Cre driver (Hprt-cre) mice (Hippenmeyer et al., 2013). The fixed cerebellar slices (parasagittal, 200 μm thick) of MADM-11 mice (P5–7w, males) were washed three times with PBS and blocked in blocking buffer (3% BSA + 0.1% Triton X-100 in PBS) for 1–2 h at RT. The slices were then incubated with the monoclonal mouse IgG antibody against GFP (1 μg/ml, Abcam) dissolved in the blocking buffer overnight at 4°C. The slices were washed three times with PBS and incubated with the secondary antibody against mouse IgG conjugated with STAR RED fluorescent dye (1:100, goat IgG, Abberior) dissolved in the blocking buffer overnight at 4°C. The slices were washed three times with PBS, transferred on the slide, covered with mounting medium (Abberior Mount Liquid Antifade) using coverslip (#1.5) and sealed with nail polish.

STED microscopy of tissue volumes with resolution increase in all three spatial dimension was performed on a commercial inverted STED microscope (Expert Line, Abberior Instruments, Germany) with pulsed excitation and STED lasers. A 640 nm laser was used for excitation and a 775 nm laser for stimulated emission. A silicone oil immersion objective with a numerical aperture 1.35 (UPLSAPO 100XS, Olympus, Japan) and a correction collar was used for image acquisition. The fluorescence signal was collected in a confocal arrangement with a pinhole size of 0.8 Airy units using a photon-counting avalanche photodiode with a 685/70 nm bandpass filter for STAR RED detection. The pulse repetition rate was 40 MHz and fluorescence detection was time-gated. The imaging parameters used were 20 μs pixel dwell time and two line accumulations. Laser powers at the sample were 2–3 μW (640 nm) excitation and 20–30 mW STED laser power, the power ratio in the xy-STED "doughnut" beam and the beam providing additional resolution increase in the axial (z)-direction ("z-doughnut") was between 40/60 and 60/40. The voxel size was 30 × 30 × 90 nm. Stacks typically spanned 5 μm in the z-direction, covering the full dendrite. We observed the stained dendrites within tens of micrometers from the surface of the tissues. Individual dendritic spines of PCs were manually counted by a blinded experimenter using FIJI software (distributed under the General Public License).

Serial Ultrathin Sectioning With Electron Microscopy

The fixed cerebellar slices (parasagittal, 200 μm thick) were washed three times with 0.1 M HEPES buffer and then treated with 1% osmium tetroxide (30 min at RT) and 1% uranyl acetate (30 min at RT) to provide adequate contrast for EM analysis. Following the dehydration with a series concentration of ethanol (50, 70, 90, 96 and 100%) and acetone, the slices were infiltrated with and embedded in Durcupan resin at 60°C for 3 days. The cerebellar cortex including the molecular layer at lobule V-VI was trimmed and exposed, and serial sections of 40-nm thickness were obtained (within a few microns from the surface of tissues) using an ultramicrotome (UC7, Leica). The serial sections were picked on the grid coated with pioloform and counterstained with 1% uranyl acetate (7 min at RT) and 0.3% lead citrate (4 min at RT). Serial images were taken from the samples under a transmission electron microscope (TEM, Tecnai 10, FEI) with iTEM (OSIS) or RADIUS (EMSIS). The images were analyzed using Reconstruct (SynapseWeb, Kristen M. Harris, PI) and FIJI software. The thickness of the ultrathin sections measured by the minimal folds method (Fiala and Harris, 2001) was 40.3 nm (35.6–46.8 nm, n = 8). Active zones (AZs) are defined as the membrane facing postsynaptic density (PSD) which is clearly identified as an electron-dense thickening in dendritic spines. Docked synaptic vesicles (dSVs) were defined by the distance from AZ membranes (<5 nm; **Figure 3B**).

Antibodies

Rabbit polyclonal antibodies against AMPA receptor subunits were raised against synthetic peptides with the following sequences: anti-GluA1–3, (C)VNLAVLKLSEQGVLDKLK SKWWYDKGE (residues 760–786 of mouse GluA1), anti-GluA1, (C)SMSHSSGMPLGATGL (residues 893–907 in the C-terminal intracellular region of rat GluA1), anti-GluA3, (C)NEYERFVPFSDQQIS (residues 394–408 in the N-terminal extracellular region of rat GluA3), and anti-GluA4, (C)GTAIRQSSGLAVIASDLP (residues 885–902 in the C-terminal intracellular region of rat GluA4). Mouse monoclonal anti-GluA2 was raised against the synthetic peptide (C)YKEGYNVYGIESVKI (residues 869–883 in the C-terminal intracellular region of rat GluA2). Affinity-purified antibodies were obtained from antisera using respective antigen peptides. Mouse anti-actin antibody was obtained from BD Biosciences.

Plasmids

Full-length rat GluA1 and GluA2 cDNAs were subcloned into pcDNA3 (plasmid vector, Invitrogen) to generate pc3-GluA1 and pc3-GluA2. In addition, full-length murine GluA3 and GluA4 cDNAs were subcloned into pRK5 (plasmid vector) to generate pRK5-GluA3 and pRK5-GluA4.

Transfection and Immunoblot Analysis

COS-7 cells were maintained in Dulbecco's modified Eagle's medium (DMEM) with 10% fetal bovine serum (FBS) and were transiently transfected with GluA1–4 expression plasmids using Lipofectamine 2000 (Invitrogen). After 48 h of transfection, the cultured cells were harvested and lysed in 1× SDS sample buffer. Cell lysates were separated by SDS-PAGE, followed by electrotransfer into the PDVF membrane and incubated with respective antibodies. Protein bands were developed by the enhanced chemiluminescence method using a commercially available kit (Nacalai Chemicals).

SDS-Digested Freeze-Fracture Replica Labeling (SDS-FRL)

The fixed cerebellar slices (parasagittal, 150 μm thick) were washed three times with 0.1 M PB and then immersed in graded glycerol of 10–20% in 0.1 M PB at RT for 10 min and then 30%

glycerol in 0.1 M PB at 4°C overnight for the cryoprotection. The molecular layer of the cerebellum at lobule IV-VI was trimmed from the slices and frozen by a high pressure freezing machine (HPM010, BAL-TEC). The frozen samples were fractured into two parts at −130°C and replicated by carbon deposition (5 nm thick), carbon-platinum (uni-direction from 60°, 2 nm) and carbon (20–25 nm) in a freeze-fracture machine (JFD-V, JOEL, Tokyo, Japan). The samples were digested with 2.5% SDS solution containing 20 mM sucrose and 15 mM Tris-HCl (pH 8.3) at 80°C for 17 h. The replicas were washed in the SDS solution, 2.5% bovine serum albumin (BSA) contained SDS solution and then 50-mM Tris-buffered saline (TBS, pH 7.4) containing 5%, 2.5% and 0.1% BSA at RT for 10 min for each. To avoid non-specific binding of antibodies, the replicas were blocked with 5% BSA in TBS for 1–2 h at RT. The replicas were then incubated with the primary antibodies dissolved in TBS with 2% BSA at 15°C overnight. For the labeling of AMPARs, the rabbit polyclonal antibody for GluA1–3 (4.3 μg/ml) was used with guinea pig polyclonal antibody for GluD2 (0.61 μg/ml, provided by Masahiko Watanabe) used as a marker of PF-PC synapses (Nusser et al., 1998; Masugi-Tokita et al., 2007; Wang et al., 2014). The specificity of the GluA1–3 antibody was checked by Western-blotting (**Supplementary Figure S1**). For GluD2 labeling, polyclonal guinea pig antibody for GluD2 (4.1 μg/ml) was used (Masugi-Tokita et al., 2007; Wang et al., 2014). For the labeling of RIM1/2 and $Ca_V2.1$ subunit of voltage-gated calcium channel, rabbit polyclonal antibody for RIM1/2 (5.0 μg/ml, Synaptic Systems) and guinea pig polyclonal antibody for $Ca_V2.1$ (4.1 μg/ml, provided by Masahiko Watanabe; Holderith et al., 2012; Nakamura et al., 2015) were used respectively, with mouse monoclonal antibody for VGluT1 (5.0 μg/ml, NeuroMab) as a marker of PF boutons (Miyazaki et al., 2003). The replicas were then washed three times with TBS with 0.1% BSA and incubated with the secondary antibodies conjugated with gold particles (5 or 15 nm diameter, goat IgG, BBI) dissolved in TBS with 2% BSA (1:30) overnight at 15°C. After immunogold labeling, the replicas were washed with TBS with 0.1% BSA (twice) and distilled water (twice) and picked up onto a grid coated with pioloform. Images (20–25 images per replica) were obtained under TEM (Tecnai 10) with iTEM (OSIS) or RADIUS and analyzed with FIJI software to calculate the density of gold particles defined by the particle number divided by PSD/AZ area. PSD and AZs were indicated with the aggregation of intramembrane particles on the replica at the EM level as described previously (Landis and Reese, 1974; Harris and Landis, 1986; Masugi-Tokita et al., 2007).

Whole-Cell Patch-Clamp Recording

Acute cerebellar slices (lobule IV-V, coronal, 250–300 μm thick) were superfused with oxygenated ACSF in the recording chamber and visualized using an upright microscope (BX51WI, Olympus, Japan) with a 20× water-immersion objective lens. Data were acquired at a sampling rate of 50 kHz using an EPC-10 USB double patch-clamp amplifier controlled by PatchMaster software (HEKA, Germany) after online filtering at 5 kHz. Experiments were performed at RT (26–27°C) within 5 h after slicing at both temperatures. Resistances of patch electrodes were 3–6 MΩ. The series resistances were 6–15 MΩ and compensated for a final value of 5 MΩ.

Throughout the experiments, recordings from Purkinje cells were made in voltage-clamp mode at a holding potential of −70 mV. The recordings were performed up to 1 h after rupturing. The pipette solution contained the following (in mM): 110 Cesium methanesulfonate, 30 CsCl, 10 HEPES, 5 EGTA, 1 $MgCl_2$, and 5 QX314-Cl (pH 7.3, adjusted with CsOH). Cell membrane resistance was estimated from leak current at −70 mV assuming a reversal potential at −15 mV including liquid junction potential between ACSF and pipette solution. EPSCs were evoked by electrical stimulation (0.5–5.0 V, 60 μs) through an ACSF-filled glass pipette electrode placed on the molecular layer of the cerebellar slices using a stimulus isolator (ISO-Flex, A.M.P.I, Israel). The grass pipette for the stimulation was the same size as the one for recording. The distance between the stimulation and recording electrodes was 200–500 μm to avoid the contamination of climbing fiber inputs or the excitation of recording PCs. The EPSC recordings were performed in the presence of bicuculline methiodide (10 μM) to block GABAergic inhibitory synaptic current. Data was off-line analyzed using Igor Pro 6 software (WaveMatrics, Tigard, OR, USA) with Patcher's Power Tools (Max-Planck-Institut für biophysikalische Chemie, Göttingen, Germany).

Mean-variance (M-V) analysis was used to estimate the mean release probability per site (P_r). EPSCs, evoked with a 15-s interval, were recorded in the presence of the low-affinity glutamate receptor antagonist kynurenic acid (2 mM) to reduce possible effects of AMPAR saturation(Foster and Regehr, 2004). Under various extracellular Ca^{2+} concentrations ($[Ca^{2+}]_{out}$, 1.5–6 mM) for altering P_r, 15 successive EPSCs were collected for constructing an M-V plot. To acquire data at the highest P_r, the K^+ channel blocker 4-aminopyridine (10 μM) was added to the ACSF. M-V plots were analyzed by fitting the simple parabola equation:

$$\sigma^2 = qI - \frac{I^2}{N}\left(1 + CV_{II}^2\right) + qI \cdot CV_I^2$$

where I and σ^2 represent the mean amplitude and variance of EPSCs, respectively, q denotes mean quantal size and N denotes the number of release sites. CV_I and CV_{II} mean the coefficients of intrasite and intersite quantal variability respectively, assumed to be 0.3 (Clements and Silver, 2000). In this method, assuming that σ^2 arises entirely from stochastic changes in P_r, q can be estimated from the initial slope of the parabola, Nq from the larger X intercept of the parabola, and P_r can be estimated as I/Nq.

Horizontal Optokinetic Response (HOKR) Training and Miniature EPSC Recording

HOKR was recorded as described previously (Wang et al., 2014). C56BL/6J mice (P8–11w, male) were implanted with a 15-mm-long bolt on the skull with a synthetic resin under isoflurane anesthesia and allowed to recover at least for 24 h. The mouse was mounted on the turntable surrounded by a checked-pattern screen with the head fixed *via* the bolt, and its body was loosely

restrained in a plastic cylinder. The frontal view of the right eye, under the illumination of infrared (wavelength, 860 nm) LED, was captured using a vertically positioned CCD camera (SSC-M350, Sony, Japan) and displayed on a 12-inch TV monitor (magnification, 55×). The area of the pupil was determined from the difference in brightness between the pupil and the iris. The real-time position of the eye was measured by calculating the central position of the left and right margins of the pupil at 50 Hz using a position-analyzing system (C-1170; Hamamatsu Photonics, Japan) and stored on a personal computer. HOKR was evoked with sinusoidal screen oscillation at 17° and 0.25 Hz (maximum screen velocity, 7.9°/s) in the light, and its gain was defined as the averaged amplitudes of eye movements vs. those of screen oscillation. The mice were trained for 1 h with sustained screen oscillation. After the training, mice were sacrificed under isoflurane anesthesia and removed their brains from the skull. The cerebellum was dissected from the brain and mounted in 3% low-melting-point agarose (for ice-cold) or 1% agarose (for PT) in Tyrode's solution contained (mM): 138 NaCl, 3 KCl, 10 HEPES and 7 $MgCl_2$ (pH 7.4, adjusted with NaOH). Acute cerebellar slices containing flocculus/paraflocculus were prepared (coronal, 250–300 μm thick) in cutting solution at CT or PT. The cold-cut slices were pre-incubated in standard ACSF at 37°C before recording. The warm-cut slices were immediately used for patch-clamp recording without the recovery step in ACSF.

Spontaneous miniature EPSC (mEPSC) events were recorded with the same procedure for the evoked EPSC recording as described above. The ACSF during the recordings contained 4 mM $CaCl_2$, 0.5 mM $MgCl_2$ to increase mEPSC frequency, and also 1 μM tetrodotoxin and 10 μM bicuculline methiodide to block firing and inhibitory synaptic currents. Data were analyzed off-line using Python-based software Stimfit (Guzman et al., 2014). Spontaneous mEPSCs were detected using a sliding template method (Jonas et al., 1993) implemented in Stimfit. The templates were made by the averaging of the initial 50–100 mEPSCs selected by the eye. Overlapped events were excluded from analysis by visual inspection. The values of the mean mEPSC amplitude for each cell were calculated from the average of 50–200 (PT) or 100–400 (CT) mEPSC events.

Statistical Analysis

Unless stated otherwise, all data were presented as median [interquartile range (IQR)]. The box plots were drawn with whiskers at the farthest points within 1.5 × IQR. The normality of data was tested with the Kolmogorov–Smirnov test. Normally distributed data were compared with two-tailed Welch's *t*-test or paired *t*-test for two groups. For more than two groups, normally distributed data were compared with ANOVA with *post hoc* Tukey–Kramer test, and others were compared with the Kruskal–Wallis H test with *post hoc* Mann–Whitney *U* test with Bonferroni correction. Comparison is detailed in the respective "Results" section and Figure Legends. Statistical significance was defined as $^{*}p < 0.05$ and $^{**}p < 0.01$. Statistics were performed with Excel (Welch's *t*-test) and R software (other tests). All *P*-values are shown in tables.

RESULTS

Influence of the Temperature During Slice Preparation on Electrophysiological Properties in Synaptic Transmission

We first examined whether different temperatures during slicing affect electrophysiological properties of synaptic transmission in parallel fiber-Purkinje cell (PF-PC) synapses in mouse cerebellum using the whole-cell patch-clamp recording. The cerebellar slices (coronal, 250–300 μm thick) were prepared in ice-cold (<4°C) or warmed (35–37°C) sucrose-based cutting solution to minimize the disruption of the spine structure (Kirov et al., 2004), and then pre-incubated in normal ASCF warmed at 37°C for 1 h as a recovery time. Electrical stimulation applied to the PF in the molecular layer evoked an excitatory postsynaptic current (evoked EPSC) on the recorded PC. The amplitude of the evoked EPSCs increased depending on the stimulation intensity showing no significant difference between the two temperatures (**Figures 1A,B**, **Table 1**). The mean amplitude, 10–90% rise time, or decay time constant of evoked EPSCs also remained unaffected (**Figure 1C**, **Table 1**).

To evaluate cell conditions in acute cerebellar slices, we measured membrane resistance (R_m) of cells at 5 min after whole-cell configuration. R_m of PCs in warm-cut slices was significantly higher than that in cold-cut slices ($P < 0.01$, Welch's *t*-test; **Figure 1D**, **Table 1**). R_m of PCs in both warm- and cold-cut slices were constant for 4–5 h after slicing (**Figure 1D**). These results suggest better conditions of neurons in warm-cut slices compared to cold-cut slices, and stability of the slice quality for at least 5 h after slicing at PT.

We then compared release probability (P_r) of PF-PC synapses between the cold- and warm-cut slices using mean-variance (M-V) analysis (Clements and Silver, 2000; Scheuss et al., 2002). For the parabola fitting, P_r was altered by simply changing extracellular Ca^{2+} concentration ($[Ca^{2+}]_{out}$, 1.5–4 or 6 mM) in ACSF, or by the addition of 4-aminopyridine (10 μM) to attain the highest P_r (**Figures 1D–F**). The M-V analysis revealed significantly higher P_r at 2 mM $[Ca^{2+}]_{out}$ in warm-cut slices compared to cold-cut slices ($P = 0.01$, Welch's *t*-test; **Figure 1G**, **Table 1**). The quantal size of synaptic transmission estimated from the M-V analysis showed no significant differences between them (**Figure 1G**, **Table 1**). These results indicate that the temperature during slice preparations influence the machinery of neurotransmitter release but has little effect on the amplitude and kinetics of postsynaptic events.

Dendritic Spine Density of Purkinje Cells in Cerebellar Slices Prepared at Ice-Cold and Physiological Temperature

It has been reported that the exposure of hippocampal slices to CT causes spine loss and beading of the dendrites, and re-warming of the chilled slices induces proliferation of spine structures (Kirov et al., 2004). Although these structural changes can be minimized by the replacement of NaCl in the cutting solution to sucrose (Kirov et al., 2004), the risk of the ultrastructural reorganization of spines remains.

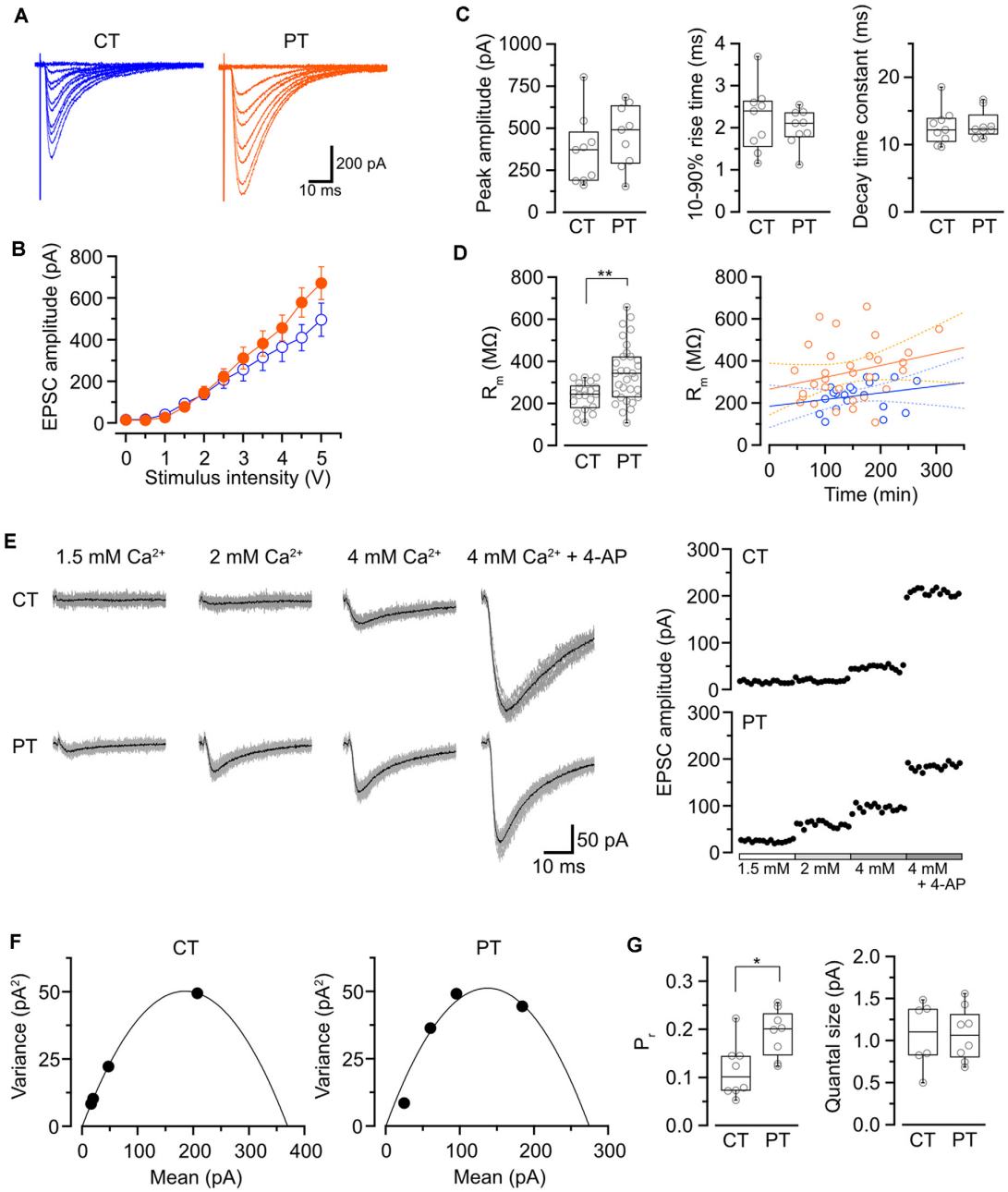


FIGURE 1 | Influence of the temperatures during slicing on synaptic transmission in PC-PF synapses. **(A)** Representative evoked EPSC traces elicited by several stimulus intensities (0–5 V, 0.5 V steps, superimposed) recorded from PCs in the slices prepared at CT (left) and PT (right). **(B)** The relationship of evoked EPSC amplitude and stimulus intensity recorded from PCs in the slices prepared at CT (blue, $n = 9$ cells) and PT (orange, $n = 9$ cells). **(C)** Summary of the peak amplitude (left), 10–90% rise time (middle) and decay time constant (right) of EPSCs (evoked by a 4-V stimulation) in cold- and warm-cut cerebellar slices. Each scatter indicates the mean value obtained from an individual PC ($n = 9$ cells for each). No significant difference was detected between CT and PT (amplitude: $P = 0.34$, rise time: $P = 0.49$, decay time constant: $P = 0.82$, $n = 9$ cells each, Welch's t-test). **(D)** Left, membrane resistance (R_m) of PCs in the slices prepared at CT ($n = 23$) and PT ($n = 33$). The PCs in warm-cut slices showed higher R_m than that in cold-cut slices ($P < 0.01$, Welch's t-test). Right, the relationship between R_m vs. time after slicing (CT: $n = 21$, blue; PT: $n = 30$, orange) with linear fits (solid lines) and 95% confidence interval (dashed lines). Neither slices prepared at CT nor PT showed significance of the correlation coefficient (CT: $r = 0.24$, $P = 0.29$; PT: $r = 0.32$, $P = 0.08$). **(E)** Representative evoked EPSC traces (left) and plots of the amplitude (right) in various $[Ca^{2+}]_{out}$ recorded from a PC in the slice prepared at CT (top) and PT (bottom). In the EPSC traces, gray traces show the individual 15 traces and black traces indicate their averages. **(F)** Mean-variance (M-V) relationship of evoked EPSCs obtained from the amplitudes shown in **(E)**. The plots were fitted by a parabola equation. **(G)** Summary of the release probability at 2 mM $[Ca^{2+}]_{out}$ (P_r, left) and the quantal size (right) of PF-PC synapses in slices prepared at CT or PT estimated by M-V analysis. Each scatter indicates the mean value obtained from an individual PC. P_r recorded from the warm-cut slices ($n = 8$ cells) shows a significantly higher value than that from the cold-cut slices ($n = 8$ cells, $P < 0.05$, Welch's t-test), whereas no significant difference in quantal size was detected between slices prepared at CT and PT (CT: $n = 6$ cells, PT: $n = 8$ cells, $P = 0.96$). Asterisks indicate significant differences (*$P < 0.05$, **$P < 0.01$, Welch's t-test).

TABLE 1 | Electrophysiological properties of parallel fiber-Purkinje cell (PF-PC) synapses in mouse cerebellar slices prepared at CT and PT.

	CT			PT			*P*-value†
	n¶	median	IQR	n¶	median	IQR	
Evoked EPSC kinetics							
amplitude (4-V stim, pA)	9	372.8	190.3–418.2	9	491.8	306.4–619.5	0.344
10–90% rise time (ms)	9	2.4	1.7–2.6	9	2.1	1.9–2.4	0.486
Decay time constant (ms)	9	12.2	10.9–13.7	9	12.3	12.1–12.7	0.822
Mean-variance analysis							
Release probability	8	0.10	0.07–0.15	8	0.20	0.16–0.23	0.011*
quantal size (pA)	6	1.10	0.83–1.37	8	1.06	0.83–1.26	0.963
Cell condition							
Membrane resistance (MΩ)	23	239.1	162.3–275.0	33	343.8	244.4–423.1	<0.001**

†*Welch's t-test*, ¶*Number of cells*, **P* < 0.05, ***P* < 0.01.

Since the loss and proliferation of postsynaptic dendritic spines were prevented by slicing of the hippocampus at room temperature (Bourne et al., 2007), we hypothesized that slicing of the cerebellum at PT may also prevent the potential reorganization of PC spines. To address this point, we examined differences in the density of spines along PC dendrites in acute cerebellar slices prepared at CT and PT. Since the spine density of PC dendrites is too high to measure accurately by conventional confocal microscopy (6–7 spines/μm; Ichikawa et al., 2002; Wang et al., 2014), we examined it by acquiring z-stacks of tissue volumes with resolution increase in all three spatial directions (3D) by stimulated emission depletion (STED) microscopy. To image isolated single PC dendrites for estimating the spine densities, we used the MADM-11 mouse model expressing green fluorescence protein (GFP) in a small subset of PCs (Hippenmeyer et al., 2013). The acute slices (parasagittal, 200 μm thickness) were immersion-fixed immediately after slicing (0 h) or after 1-h recovery time in normal ACSF at 37°C (1 h; **Figure 2A**). PCs were immunolabeled with an anti-GFP antibody and a secondary antibody combined with a dye suitable for 3D-STED imaging (Abberior STAR RED; **Figures 2B,C**). The density of dendritic spines immediately after slicing was significantly lower by 40% in the cold-cut slices than that in the perfusion-fixed tissue ($P < 0.01$; **Figure 2D**, **Table 2**). After 1-h incubation at 37°C for recovery, the spine density increased and reached the same level as observed in the perfusion-fixed tissue. In contrast, the spine density in the warm-cut slices showed no significant difference compared to that in the perfusion-fixed tissue and remained unchanged through the recovery time. These observations suggest substantial reorganization of the dendritic spines during slicing at CT and recovery at 37°C. In contrast, the spine structure remains stable in the warm-cutting method.

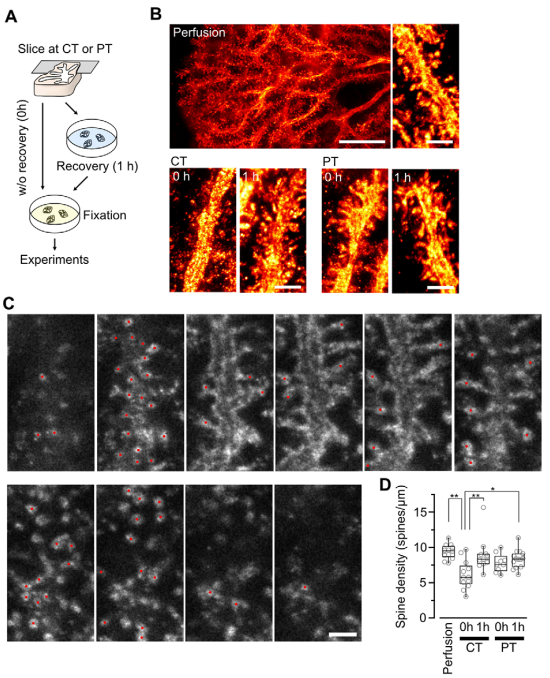


FIGURE 2 | Spine density of Purkinje cells in acute cerebellar slices prepared at CT and physiological temperatures (PT). **(A)** A scheme of the experimental procedure for brain slicing and fixation. Acute cerebellar slices prepared at CT and PT were immersion-fixed in the fixatives immediately after slicing without recovery (0 h) or after recovery in normal ACSF at 37°C for 1 h (1 h). This procedure was common with the other experiments shown in **Figures 3**, **4**. **(B)** Representative super-resolution STED image of PC dendrites and spines in perfusion-fixed cerebellar tissue (top, scale bar = 10 μm for left, 2 μm for right) and in immersion-fixed acute cerebellar slices (bottom, scale bar = 2 μm). The images show maximum projections of 20 z-slices, corresponding to 1.8 μm. **(C)** Counting dendritic spines observed with a 3D STED microscope. Representative z-stack images of a PC dendrite with spines. Red circles indicate individual spines. Scale bar = 1 μm. Optical sections are spaced by 90 nm in the z-direction. **(D)** Summary of the dendritic spine density of PCs in perfusion-fixed, cold-cut and warm-cut slice preparations. Each scatter indicates a value obtained from an individual dendrite (perfusion-fixed: *n* = 12 dendrites, CT/0 h: *n* = 12 dendrites, CT/1 h: *n* = 11 dendrites, PT/0 h: *n* = 9 dendrites, PT/1 h: *n* = 14 dendrites). Asterisks indicate significant differences (**P* < 0.05, ***P* < 0.01, one-way ANOVA with *post hoc* Tukey–Kramer test).

Synaptic Vesicle Distribution in Presynaptic Boutons of Parallel Fibers in Cerebellar Slices

SVs at nerve terminals are accumulated at active zones (AZs) for rapid neurotransmitter release. Cytoskeleton including actin filament and microtubules contributes to SV gathering and mobility (Walker and Agoston, 1987; Hirokawa et al., 2010). The dynamics of the cytoskeleton induced by their polymerization/depolymerization is highly temperature-dependent, and exposure of the cytoskeleton to cold temperature disrupts actin filaments and microtubules (Niranjan et al., 2001). These observations indicate a possibility that exposure

TABLE 2 | Dendritic spine density of Purkinje cells in perfusion-fixed and acute cerebellar slice tissues.

				P-value†				
	n¶	median	IQR	vs Perfusion	vs CT/0 h	vs CT/1 h	vs PT/0 h	vs PT/1 h
Spine density (μm^{-1})								
Perfusion	12	9.55	8.77–10.08	-				
CT/0 h	12	5.78	4.95–7.20	<0.001**	-			
CT/1 h	11	8.33	7.79–9.06	0.968	0.002**	-		
PT/0 h	9	7.60	6.89–8.18	0.217	0.194	0.559	-	
PT/1 h	14	8.36	7.44–9.05	0.520	0.014*	0.904	0.940	-

†*One-way ANOVA with post hoc Tukey–Kramer test,* ¶*Number of dendrites,* $*P < 0.05$, $**P < 0.01$.

of brain slices to cold temperature causes rearrangement of SVs in nerve terminals. To address this, we next observed SV distributions in serial ultrathin sections (40 nm thick) by EM in the presynaptic PF boutons in the acute cerebellar slices (parasagittal, 200 μm thick) prepared at CT or PT (**Figure 3A**). The area of the presynaptic AZs defined as the membrane facing PSD was not significantly different between perfusion-fixed tissues and acute slices prepared at CT and PT, and between slices immersion-fixed immediately after slicing (0 h) and after 1 h-incubation at 37°C (1 h; **Supplementary Figure S2A**). The numbers of docked SVs (dSVs) near AZs membrane within 5 nm (**Figure 3B**) were linearly correlated with the AZ areas in all conditions (**Supplementary Figure S2B**). The total SV numbers were also not significantly different between these preparations (**Figure 3C**, left). In acute slices at 0 h, the number of dSVs showed no significant difference between perfusion-fixed tissues and slices prepared at CT or PT (**Figure 3C**, middle), though their density in slices prepared at PT was significantly higher than that in the perfusion-fixed tissues (**Figure 3C**, right, **Table 3**). At 1 h, the dSV number and density in the cold-cut slices significantly increased and reached higher levels than those in perfusion-fixed tissues (**Figure 3C** middle and right, **Table 3**). The density in the cold-cut slices after 1-h recovery was significantly larger compared to the other preparations (**Table 3**). In contrast, the docked SV number and density in the warm-cut slices showed no significant changes during the incubation at 37°C. These results suggest that the SV distribution in nerve terminals is reorganized in the cold-cutting method, while the warm-cutting method can keep the SV distribution stable during acute slice preparation.

Pre- and Postsynaptic Protein Distribution in PF-PC Synapses

It has been reported that rat hippocampal slices prepared at CT have reduced protein levels for AMPARs, especially GluA1 and GluA3 subunits after incubation at 37°C (Taubenfeld et al., 2002). Besides, the cytoskeleton including actin filaments works as an anchor and/or a trafficking pathway for membrane-associated proteins and regulates the distribution of proteins including AMPARs at the postsynaptic membrane (Hanley, 2014). These reports indicate a possibility that the amount and distribution of membrane-associated proteins at pre- and postsynaptic sites are altered through the brain slice preparation at CT. To investigate the two-dimensional distribution of synaptic proteins contributing synaptic transmission in the AZ and postsynaptic area of PF-PC synapses, we performed SDS-digested freeze-fracture replica labeling (SDS-FRL) for AMPAR (GluA1–3), GluD2, RIM1/2, and $Ca_V2.1$ (**Figure 4**). The cerebellar slices prepared at CT and PT (parasagittal, 200 μm thick) were immersion-fixed immediately after slicing (0 h) or after the 1-h recovery in ACSF at 37°C (1 h) and were frozen using high-pressure freezing machine for fracturing. Postsynaptic areas on the exoplasmic face (E-face) and presynaptic AZs on the protoplasmic face (P-face) in freeze-fracture replica samples were identified with aggregation of intramembrane particles at the EM level as described previously (Landis and Reese, 1974; Harris and Landis, 1986; Masugi-Tokita et al., 2007). To identify PF-PC synapses in replica samples of the molecular layer, labeling for GluD2 or vesicular glutamate transporter 1 (VGluT1) were used as markers (Miyazaki et al., 2003; Masugi-Tokita et al., 2007). Immunogold particles for GluA1–3 were highly concentrated in the postsynaptic areas labeled for GluD2, while those for RIM1/2 and $Ca_V2.1$ were concentrated in the AZs of VGluT1-labeled presynaptic profiles as previously described (Masugi-Tokita et al., 2007; Miki et al., 2017; **Figure 4A**).

For the quantitative analysis of protein distributions on pre-and postsynaptic membranes, we measured the density of immunogold particles for each protein within the synaptic areas (**Figure 4B**, **Table 4**). AT 0 h, labeling for GluA1–3 showed no significant difference between preparations including perfusion-fixed tissues. However, after the recovery time, the GluA1–3 labeling in slices prepared at CT was significantly lower than that in the perfusion-fixed tissue ($P < 0.05$; **Figure 4B**, **Table 4**). In contrast, GluA1–3 labeling in the slices prepared at PT was similar to that in perfusion-fixed tissues both at 0 h and 1 h. The labeling for GluD2 showed no significant differences between these preparations. For RIM1/2 at AZs, the labeling density in the slices prepared at CT temporarily decreased after slicing and recovered during the recovery time. The RIM1/2 labeling in the warm-cut slices was similar to that in perfusion-fixed tissue and kept constant during the recovery. For $Ca_V2.1$ at AZs, the labeling in cold-cut slices was significantly lower than that in the perfusion-fixed tissue (**Figure 4B**, **Table 4**) and only partially recovered after the 1-h recovery time, whereas the warm-cut slices showed no significant differences in $Ca_V2.1$ labeling between these preparations (**Figure 4B**). These results indicate that the exposure of the brains to cold temperature alters synaptic protein distribution at both pre- and postsynaptic sites and some of these changes do not recover by the incubation of slices

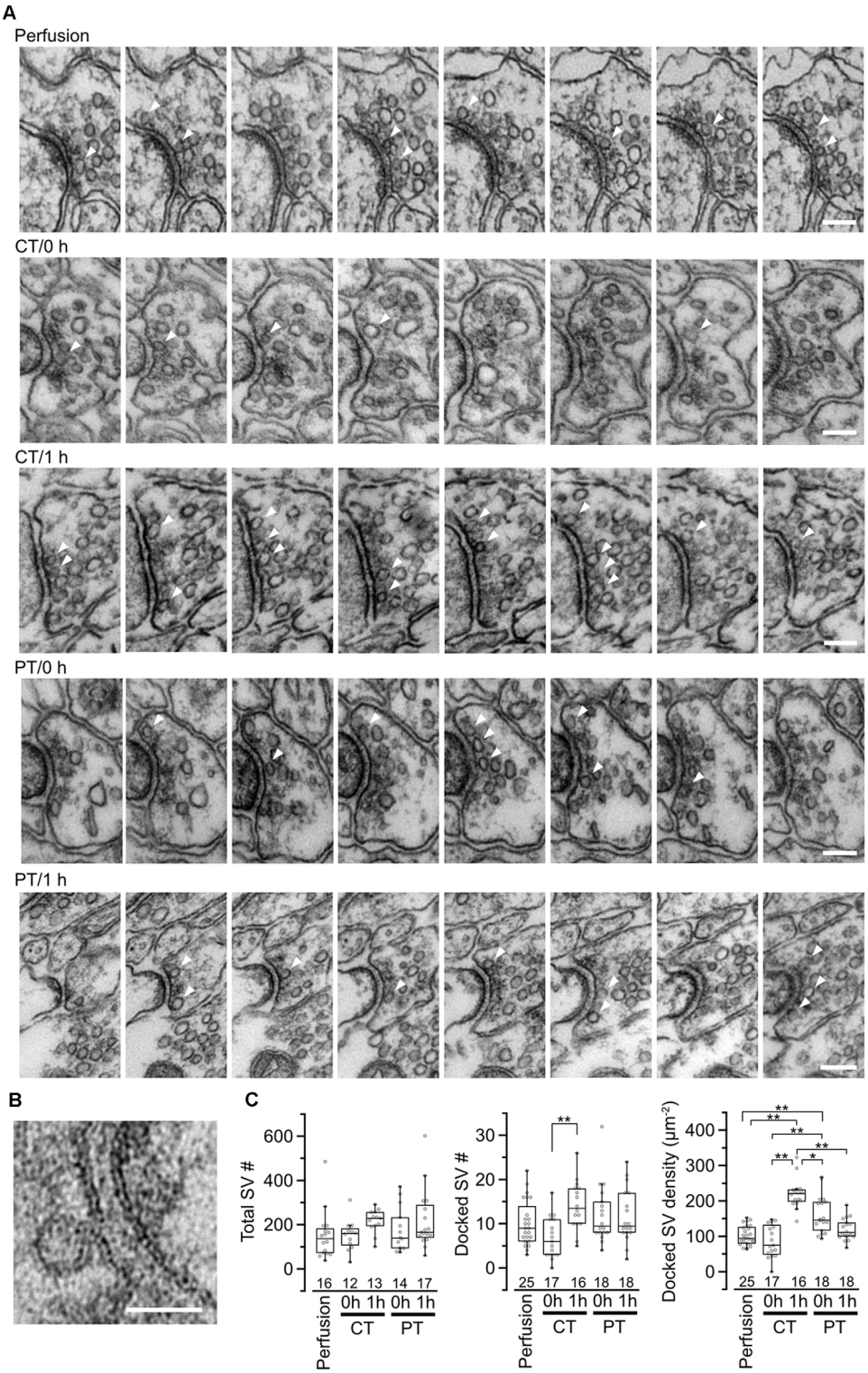


FIGURE 3 | Synaptic vesicle distribution in parallel fiber boutons on PF-PC synapses. **(A)** Example images of serial ultrathin sections (40-nm interval) of PF boutons in perfusion-fixed tissue and immersion-fixed acute cerebellar slices with (1 h) or without (0 h) 1-h recovery time. Arrowheads indicate dSVs. Scale bar = 100 nm. **(B)** An example image of a dSV, which is located within 5 nm from the AZ membrane in the perfusion-fixed tissue. Scale bar = 50 nm. **(C)** Summary of the total SV number in presynaptic boutons (left), the dSV number (middle) and density (right) at AZs. Each scatter indicates a value obtained from an individual bouton. Numerals in the plot indicate the numbers of analyzed boutons for each group. Asterisks indicate significant differences (*$P < 0.05$, **$P < 0.01$, Kruskal–Wallis H test with *post hoc* Mann-Whitney *U*-test with Bonferroni correction).

TABLE 3 | Synaptic vesicle distribution at PF boutons in perfusion-fixed and acute cerebellar slice tissues.

				P-value†				
	n¶	median	IQR	vs. Perfusion	vs. CT/0 h	vs. CT/1 h	vs. PT/0 h	vs. PT/1 h
AZ area (μm^2)								
Perfusion	25	0.085	0.069–0.131	-				
CT/0 h	17	0.068	0.056–0.100	1.000	-			
CT/1 h	16	0.061	0.045–0.080	0.260	1.000	-		
PT/0 h	18	0.071	0.050–0.093	1.000	1.000	1.000	-	
PT/1 h	18	0.087	0.062–0.133	1.000	1.000	0.280	1.000	-
Total SV number								
Perfusion	16	137.0	73.0–177.8	-				
CT/0 h	12	160.0	110.8–177.3	1.000	-			
CT/1 h	13	229.0	196.0–236.0	0.065	0.106	-		
PT/0 h	14	139.5	93.5–224.3	1.000	1.000	0.863	-	
PT/1 h	17	166.0	149.0–272.0	0.838	1.000	1.000	1.000	-
dSV number								
Perfusion	25	9.0	6.0–16.0	-				
CT/0 h	17	6.0	3.0–11.0	0.74	-			
CT/1 h	16	13.5	10.0–17.3	0.15	0.006**	-		
PT/0 h	18	9.5	8.0–14.8	1.000	0.094	1.000	-	
PT/1 h	18	9.5	8.0–17.0	1.000	0.205	1.000	1.000	-
dSV density (μm^{-2})								
Perfusion	25	94.0	80.6–121.9	-				
CT/0 h	17	74.8	52.0–126.6	1.000	-			
CT/1 h	16	221.0	200.1–232.1	<0.001**	<0.001**	-		
PT/0 h	18	146.1	121.0–196.6	0.0012**	0.005**	0.025*	-	
PT/1 h	18	110.9	100.2–138.0	0.631	0.361	<0.001**	0.109	-

†*Kruskal–Wallis H test with post hoc Mann–Whitney U-test with Bonferroni correction,* ¶*Number of boutons,* $^*P < 0.05$, $^{**}P < 0.01$.

at 37°C for 1 h. The warm-cutting method can circumvent these problems.

Long-Term Plasticity Induced by HOKR Adaptation

The changes in synaptic properties during recovery time may affect the measurement of synaptic plasticity that occurred *in vivo*. Thus, we finally tested cold- and warm-cutting methods for detectability of LTD induced *in vivo* using a simple model of cerebellar motor learning. LTD of PF–PC synapses are associated with decreases in the number of synaptic AMPARs (Wang et al., 2014) and reported to be a primary cellular mechanism of adaptation of horizontal optokinetic response (HOKR) in mouse (Kakegawa et al., 2018). One hour HOKR training induced a transient AMPAR reduction by 28% in PF-PC synapses in the flocculus (Wang et al., 2014), which controls horizontal eye movement (Schonewille et al., 2006). This result predicts reduced EPSCs in PF-PC synapses after HOKR adaptation. Indeed, a further study using conventional acute slice preparation showed the decrease in quantal EPSC amplitude of PF-PC synapses in the flocculus of mice after HOKR training, but the reduction was below 10%, much lower than the value expected from the reduction of AMPAR density (Inoshita and Hirano, 2018).

Our study of SDS-FRL showed that the AMPAR density on postsynaptic sites in acute cerebellar slice prepared at CT but not PT was significantly lower after the recovery than that in the perfusion-fixed preparation (**Figure 4B**). This result could indicate a higher sensitivity in warm-cut slices to detect the quantal EPSC amplitude changes in the flocculus induced by the HOKR training. Furthermore, the reduced AMPAR number in PF-PC synapses after HOKR training returns to the control level within 4 h (Aziz et al., 2014), indicating the need to detect changes in the AMPAR-mediated response quickly after the training. Thus, the use of warm-cut slices without a recovery period (1 h) can be advantageous to detect the electrophysiological changes. To examine these possibilities, we recorded spontaneous miniature EPSC (mEPSC) from PCs in the flocculus after 1-h HOKR training (**Figure 5B**). Continuous horizontal optokinetic stimulation enhanced the eye movement of the trained mice, and the gain of HOKR, which was defined as the amplitude of eye movement divided by the screen movement significantly increased by 62% [1 min: 0.54 (0.43–0.56), $n = 10$; 60 min: 0.78 (0.75–0.80), $n = 10$, $P < 0.01$; **Figure 5A**]. We sacrificed the trained mice within 1 min after the training and sliced the cerebellum (coronal, 250–300 μm thick) in the cutting solution at CT or PT within 30 min after the decapitation. To detect maximally the effect of the training on AMPAR density, we used the slices prepared at PT for the recording immediately after slicing. The slices prepared at CT require the recovery period and were used after 1-h incubation at 37°C in ACSF. The mean amplitude of mEPSC in control was not significantly different between the cold-cut and the warm-cut slices, but the amplitude in cold-cut slices varied more than that in warm-cut slices (CV: 0.24 for CT, 0.11 for PT; **Figures 5E,F**). The frequency of spontaneous mEPSCs recorded from PCs in the flocculus showed no significant changes by the HOKR training in both cold- and warm-cut slices (**Figures 5E,F**). The mEPSC frequency in the cold-cut slices was significantly higher than that in the warm-cut slices for both control and trained animals (**Figures 5E,F**, **Table 5**). After the 1-h HOKR training, mEPSC amplitude was significantly decreased by 23.8% in the warm-cut slices (**Figures 5D,F**, **Table 5**), consistent with our previous

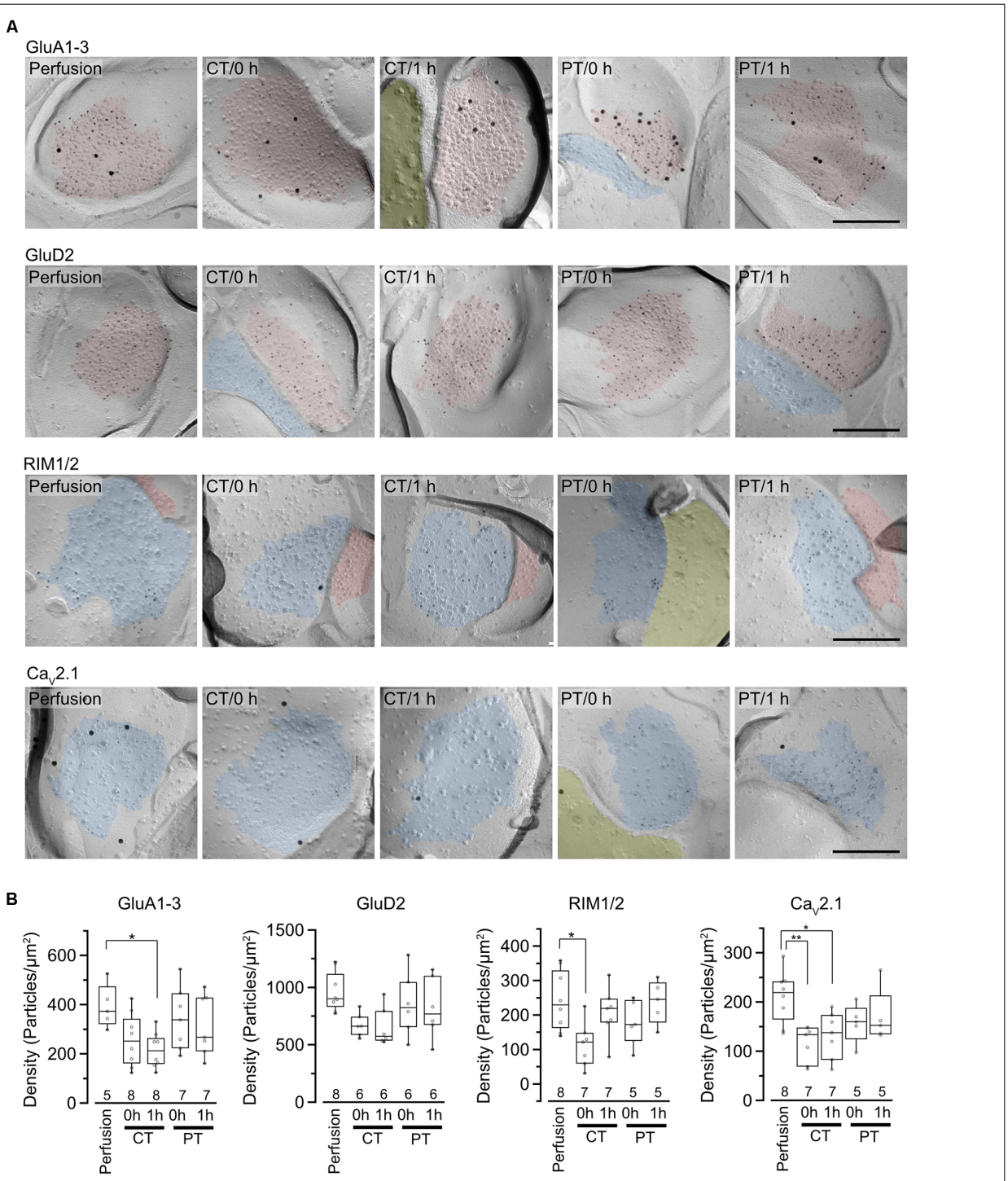


FIGURE 4 | Distribution of synaptic proteins in postsynaptic density (PSD) and AZs. **(A)** Representative images of freeze-fracture replicas of PF-PC synapses labeled for GluA1–3, GluD2, RIM1/2 and $Ca_V2.1$ (5-nm gold) with PF-PC markers (GluD2 for GluA1–3, VGluT1 for RIM1/2 and $Ca_V2.1$, 15-nm gold). PSD on the exoplasmic face (E-face), AZs on the protoplasmic face (P-face) and cross-fractured cytoplasm were indicated with red, blue and yellow, respectively. Scale bar = 200 nm. **(B)** Summary of gold particle density for GluA1–3, GluD2, RIM1/2, and $Ca_V2.1$ on PSD or AZs. Each scatter indicates the mean value obtained from an individual replica. Numerals in the plot indicate the numbers of analyzed replicas for each group. Asterisks indicate significant differences (*$P < 0.05$, **$P < 0.01$, one-way ANOVA with *post hoc* Tukey–Kramer test).

finding of a decrease in AMPARs by 28% (Wang et al., 2014). The amplitude in the cold-cut slices also showed a tendency to decrease but the difference did not reach statistical significance (**Figures 5C,E**, **Table 5**). The higher detectability of LTD in

TABLE 4 | Immunogold particle density on PSD/AZs of PF-PC synapses in perfusion-fixed and acute cerebellar slice tissues.

				P-value†				
	n¶	median	IQR	vs Perfusion	vs CT/0 h	vs CT/1 h	vs PT/0 h	vs PT/1 h
GluA1–3 (μm^{-2})								
Perfusion	5	373.4	344.1–422.6	-				
CT/0 h	8	252.3	170.9–326.2	0.196	-			
CT/1 h	8	213.0	161.6–257.0	0.048*	0.933	-		
PT/0 h	7	338.7	241.1–419.9	0.926	0.545	0.173	-	
PT/1 h	7	268.1	231.9–426.6	0.739	0.818	0.374	0.991	-
GluRD2 (μm^{-2})								
Perfusion	8	902.2	852.9–1072.5	-				
CT/0 h	6	662.4	605.7–724.7	0.104	-			
CT/1 h	6	574.2	541.6–745.0	0.077	1.000	-		
PT/0 h	6	824.3	688.3–1000.5	0.874	0.562	0.478	-	
PT/1 h	6	769.2	682.9–1033.5	0.718	0.735	0.653	0.998	-
RIM1/2 (μm^{-2})								
Perfusion	8	229.7	170.8–318.7	-				
CT/0 h	7	121.6	70.7–139.1	0.017*	-			
CT/1 h	7	219.5	182.3–235.9	0.88	0.15	-		
PT/0 h	5	172.7	167.4–237.0	0.599	0.517	0.976	-	
PT/1 h	5	245.8	207.3–279.1	1.000	0.052	0.948	0.74	-
$Ca_V2.1$ (μm^{-2})								
Perfusion	8	219.3	176.5–241.6	-				
CT/0 h	7	133.8	88.5–143.7	0.005**	-			
CT/1 h	7	137.9	101.4–166.7	0.026*	0.962	-		
PT/0 h	5	160.2	151.4–170.0	0.298	0.569	0.895	-	
PT/1 h	5	152.6	136.3–162.0	0.563	0.309	0.657	0.993	-

†*One-way ANOVA with post hoc Tukey–Kramer test,* ¶*Number of replicas,* $*P < 0.05$, $**P < 0.01$.

the warm-cut slices compared to cold-cut slices indicates an advantage of the warm-cutting method for investigating synaptic plasticity induced by behavior experiments.

DISCUSSION

In this study, we show that brain slice preparation at PT better preserves molecular and ultrastructural properties of synapses compared to the conventional slice preparation at CT (**Figure 6**). These results suggest the strong advantages of the warm-cutting method for investigating synaptic functions.

Acute Brain Slice Preparation at PT

Here we prepared mouse cerebellar slices at CT and PT and compared the synaptic properties in these tissues. The brain in cutting solution at PT was softer than that at CT, so we needed to adjust the parameters of the slicers for the warm-cutting method (see "Material and Methods" section). The parameters may need to be adjusted for each brain region, age and also species of animals.

The first point to verify is whether the warm-cutting method could provide us with brain slices of better or at least comparable quality to those prepared by the conventional cold-cutting method. R_m of PCs higher in warm-cut slices than cold-cut slices (**Figure 1D**) indicates better cell conditions in warm-cut slices since damaged cells usually show low R_m. The stability of the R_m value also indicates the applicability of warm-cut slices for long-term recording. It has been reported that the slice preparation at ice-cold temperature attenuates mitochondrial functions, reducing the cell viability in slices of rat brainstem but not the cerebral cortex (Fried et al., 2014). Although the temperature effect on mitochondrial functions may depend on regions, PCs in cerebellar slices might be affected by ice-cold temperature during slice preparation.

Preservation of Synaptic Properties in Acute Brain Slices Prepared at PT

To investigate synaptic functions in brains, synaptic properties in acute brain slices should be kept as close as possible to those in the intact brain. In the present study, AMPAR and $Ca_V2.1$ in the cold but not warm-cut slices showed significantly lower densities than those in the perfusion-fixed tissue. Although some of the structural parameters of the synapse in perfusion-fixed tissue can be altered by formaldehyde fixation (Siksou et al., 2009; Schrod et al., 2018), we used the same fixative, temperature and time of fixation to compare these properties between perfusion-fixed tissues and immersion-fixed acute slices. Assuming similar effects of chemical fixation between these preparations, our study suggests that the warm-cutting method preserves molecular and structural properties of synapses better than the conventional cold-cutting method. We also found that PF-PC synapses in the cold-cut slices have higher mEPSC frequency than that in warm-cut slices. Although larger P_r may increase the frequency of mEPSCs, P_r measured by M-V analysis in cold-cut slices is significantly smaller than that in warm-cut slices, which is consistent with the reduced $Ca_V2.1$ density at AZs in cold-cut slices. Readily releasable pool (RRP) size of SVs also correlates with mEPSC frequency, and the number of dSVs may indicate RRP size (Schikorski and Stevens, 2001; Kaeser and Regehr, 2017). Thus, the increased number and density of dSVs after the recovery in cold-cut slices could

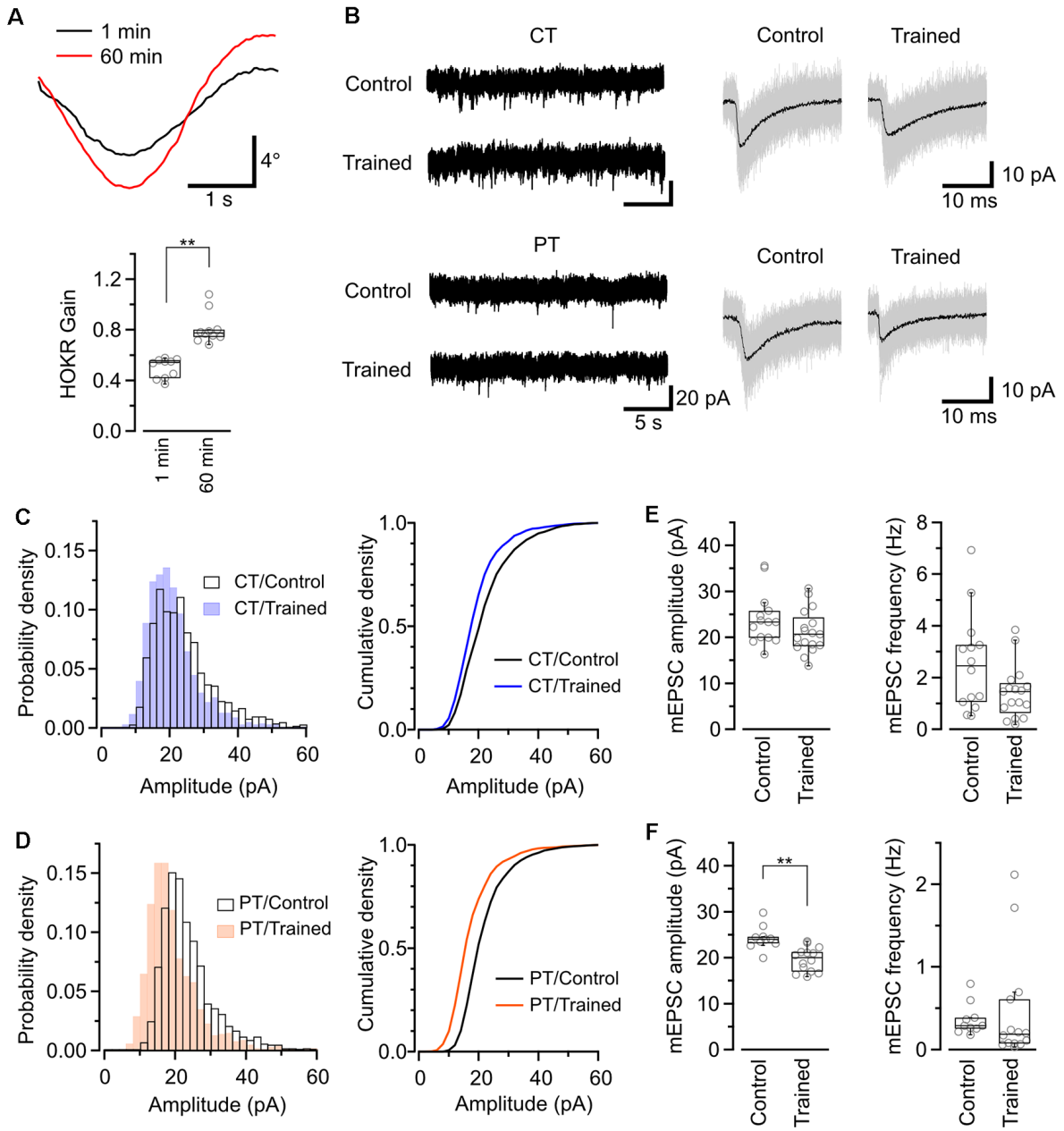


FIGURE 5 | Application of warm-cutting slice preparation method to the detection of long-term depression (LTD) by HOKR training. **(A)** HOKR adaptation. Top, representative eye-movement traces of a mouse before and after 1-h HOKR training. Bottom, HOKR gain changes induced by 1-h HOKR training ($P < 0.01$, paired *t*-test). Each scatter indicates the mean value obtained from individual animals ($n = 10$ animals for each). **(B)** Representative traces of spontaneous mEPSC events recorded from PCs at cerebellar flocculus of untrained (control) and trained mice. Right, superimposed mEPSC traces (50 events, gray). and average of the events (black traces). **(C,D)** Histogram (left) and cumulative curve (right) of mEPSC amplitude distribution recorded from PCs in cold-cut **(C)** and warm-cut **(D)** slices of control and HOKR-trained mice. **(E,F)** Box plot of mEPSC amplitudes (left) and frequency (right) recorded from PCs in cold-cut **(E)** and warm-cut **(F)** slices of control and HOKR-trained mice. Each scatter indicates the mean amplitude and frequency of mEPSCs obtained from an individual PC (CT/control: $n = 14$ cells, CT/trained: $n = 17$ cells, PT/control: $n = 10$ cells, PT/trained: $n = 14$ cells). Asterisks indicate significant differences (**$P < 0.01$, Welch's *t*-test).

contribute to the higher mEPSC frequency. In addition, the resting potential of presynaptic boutons may affect the frequency of mEPSCs. At the calyx of Held synapses, depolarization of presynaptic terminals raised the mEPSC frequency (Sahara and Takahashi, 2001). The lower R_m of the cells (**Figure 1D**) could indicate more positive resting potential of presynaptic boutons in cold-cut slices than that in warm-cut slices, resulting in higher mEPSC frequency. Another possibility is the instability of molecular machinery for neurotransmitter release in cold-cut slices contributing to the higher frequency

TABLE 5 | Long-term depression (LTD) on PF-PC synapses induced by HOKR training.

	Control					HOKR-trained					
	n¶	median	IQR			*n*¶	median	IQR			*P*-value†
mEPSC amplitude (pA)											
CT	14	23.34	19.96	-	25.52	17	20.70	18.29	-	25.59	0.154
PT	10	24.03	23.24	-	24.55	14	19.11	16.70	-	21.06	<0.001**
	P-value†	0.866				*P*-value†	0.278				
mEPSC frequency (Hz)											
CT	14	2.46	1.10	-	3.24	17	1.50	0.96	-	1.66	0.056
PT	10	0.29	0.26	-	0.38	14	0.10	0.07	-	0.51	0.626
	P-value†	<0.001**				*P*-value†	0.005**				

†*Welch's t-test,* ¶*Number of cells,* ***P* < 0.01.*

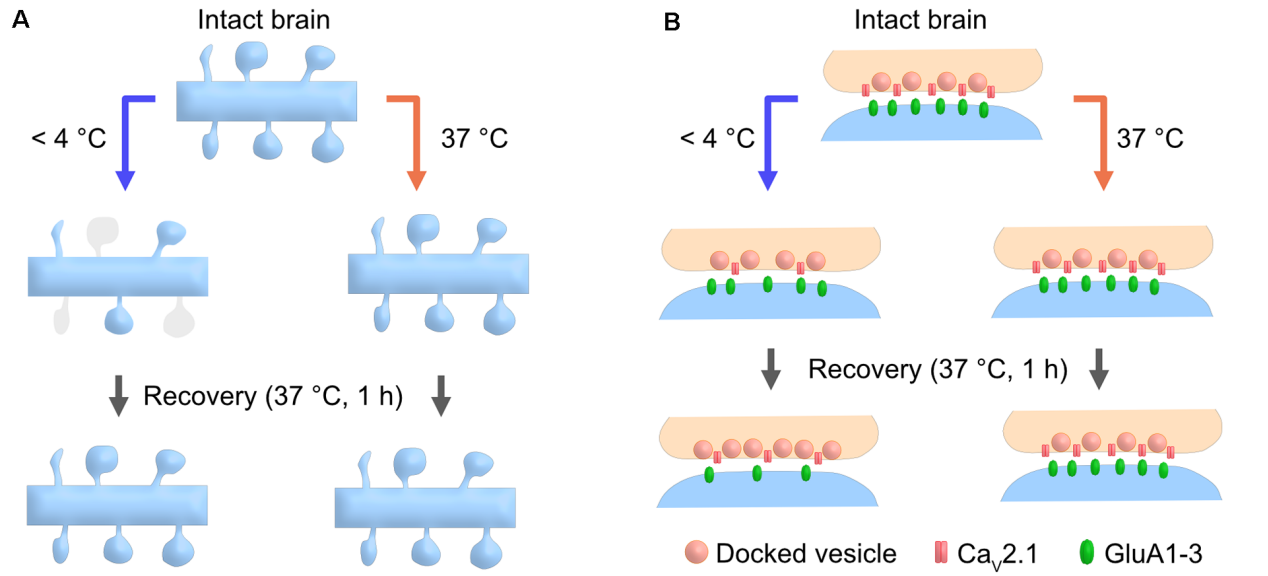


FIGURE 6 | Cartoon schematic demonstrating the advantages of the warm-cutting method compared to the cold-cutting method. **(A)** In cold-cut cerebellar slices, a part of dendritic spines along the PC dendrite transiently disappear by exposure to cold temperature and then recover after 1-h incubation at 37°C, whereas slicing at PT does not cause any changes in spine density. **(B)** In cold-cut cerebellar slices, pre- and postsynaptic components including docked SV density, $Ca_V2.1$ density and AMPAR density change during slicing and/or recovery time, whereas slicing at PT does not cause these changes.

of mESPCs. Although functional properties of synapses in truly intact brains *in vivo* are mostly unknown, our findings indicate that brain slices prepared at PT have an advantage in preserving the synaptic function compared to those prepared at CT.

Changes of Molecular and Structural Properties of Synapses During Recovery Time in Cold-Cut Brain Slices

Another advantage of the warm-cutting method is the stability of synaptic properties during the slice preparation. The PC spine density values obtained with 3D STED microscopy are comparable with those obtained by high-voltage EM (Wang et al., 2014) and 3D EM reconstruction analysis (Ichikawa et al., 2002), indicating the reliability of our data. We found that 40% of spines along PC dendrites disappeared after slicing at CT and then recovered after 1-h recovery time, consistent with previous studies on the spine reorganization in acute hippocampal slices (Fiala et al., 2003; Kirov et al., 2004). Brain slicing at CT also modifies SV distributions in synaptic boutons and the density of RIM1/2, an SV-associated protein at AZs, which recover after 1-h incubation time at 37°C. In contrast, cerebellar slices prepared at PT can keep these post- and presynaptic features stable throughout the slice preparation. Consequently, brain slices prepared at PT can be used immediately after slicing for the electrophysiological experiments as a "ready-to-use" slice preparation. This is a major advantage especially for investigating synaptic plasticity induced in behavioral experiments as discussed below.

Application of the Warm-Cutting Method for Investigating Synaptic Plasticity Induced by Behavior Experiments

In acute slices prepared at PT, the reduction of mEPSC amplitude in PCs induced by HOKR training was larger than that in

the cold-cut slices (**Figure 5**). Why is the difference more detectable in warm-cut slices than in cold-cut slices? One possibility is the difference in variation of mEPSC amplitude. The CV value of mEPSC amplitude in cold-cut slices was larger than in warm-cut slices, which could be due to the high variability of quantal size in the reconstructed spine synapses. Another possibility is that LTD in synapses induced by the training might be partially reset through the spine reconstruction after slicing at CT. AMPAR density is regulated by various proteins including enzymes (e.g., CaMKII and PP2A) and actin (Cingolani and Goda, 2008; Bissen et al., 2019), and exposure to cold temperature reduces metabolic activity of these enzymes and also depolymerizes actin filaments (Niranjan et al., 2001). Cooling and rewarming of brain tissues might reset the activities of these proteins reorganizing AMPAR distribution on the postsynaptic membrane and obscure the plastic changes occurred *in vivo*. Last, earlier timing of measurements with the warm-cut slices after the training *in vivo* could contribute to the better detection of synaptic plasticity lasting less than a few hours. The AMPAR reduction in flocculus induced by HOKR training recovers completely within 4 h (Aziz et al., 2014), indicating that the memory trace, as a form of reduced amplitude of mEPSC is transferred to other forms, such as reduced PF-PC synapses (Wang et al., 2014) or memory traces in the vestibular nucleus (Shutoh et al., 2006), during a few hours after training (Cooke et al., 2004; Okamoto et al., 2011). Even in slice preparation, biochemical, functional and structural changes after training could proceed during the recovery period at 37°C, though we found various parameters stable in warm-cut slices at the basal state. Thus, the recording should be done as soon as possible after the training, and the warm-cutting method makes it possible to shorten the latency by skipping the recovery period, which is necessary for the cold-cutting method. This is a clear advantage of the warm-cutting method for the investigation of synaptic plasticity induced by behavior experiments.

In summary, we demonstrate that the warm-cutting method has substantial advantages over the conventional cold-cutting method, e.g., highly preserved synaptic properties, the stability of synaptic properties through the preparing processes, and "ready-to-use" acute slice preparation, for investigating synaptic functions. These advantages should facilitate a wide range of neuroscience research, especially for synaptic plasticity induced *in vivo*.

DATA AVAILABILITY STATEMENT

The datasets generated for this study are available on request to the corresponding author.

ETHICS STATEMENT

The animal study was reviewed and approved by Ethics committee, IST Austria.

AUTHOR CONTRIBUTIONS

KE and RS initiated the project. KE conducted electrophysiological and electron microscopic experiments. PV and JD designed STED experiments and PV performed STED imaging. EH performed HOKR training for mice. MI and YF generated antibodies against GluA1–3. All authors analyzed data. KE and RS wrote the article with comments from all authors.

FUNDING

This work was financially supported by funding from the Institute of Science and Technology Austria, the European Union's Horizon 2020 research and innovation program under the Marie Skłodowska-Curie grant agreement No. 793482 (to KE) and the European Research Council grant agreement No. 694539 (to RS). JD and PV gratefully acknowledge funding by the Austrian Science Fund (FWF; I3600-B27).

ACKNOWLEDGMENTS

We thank Peter Jonas for critical comments on the manuscript, Simon Hippenmeyer for providing MADM-11 mice, Masahiko Watanabe for providing GluD2 and Cav2.1 antibodies and Peter Koppensteiner for the technical assistance with the experiments. This manuscript has been released as a Preprint at BioRxiv (Eguchi et al., 2019).

SUPPLEMENTARY MATERIAL

The Supplementary Material for this article can be found online at: https://www.frontiersin.org/articles/10.3389/fncel.2020.00063/full#supplementary-material.

REFERENCES

Aziz, W., Wang, W., Kesaf, S., Mohamed, A. A., Fukazawa, Y., and Shigemoto, R. (2014). Distinct kinetics of synaptic structural plasticity, memory formation and memory decay in massed and spaced learning. *Proc. Natl. Acad. Sci. U S A* 111, E194–E202. doi: 10.1073/pnas.1303317110

Bischofberger, J., Engel, D., Li, L., Geiger, J. R. P., and Jonas, P. (2006). Patch-clamp recording from mossy fiber terminals in hippocampal slices. *Nat. Protoc.* 1, 2075–2081. doi: 10.1038/nprot.2006.312

Bissen, D., Foss, F., and Acker-Palmer, A. (2019). AMPA receptors and their minions: auxiliary proteins in AMPA receptor trafficking. *Cell. Mol. Life Sci.* 76, 2133–2169. doi: 10.1007/s00018-019-03068-7

Bourne, J. N., Kirov, S. A., Sorra, K. E., and Harris, K. M. (2007). Warmer preparation of hippocampal slices prevents synapse proliferation that might obscure LTP-related structural plasticity. *Neuropharmacology* 52, 55–59. doi: 10.1016/j.neuropharm.2006.06.020

Cingolani, L. A., and Goda, Y. (2008). Actin in action: the interplay between the actin cytoskeleton and synaptic efficacy. *Nat. Rev. Neurosci.* 9, 344–356. doi: 10.1038/nrn2373

Clements, J. D., and Silver, R. A. (2000). Unveiling synaptic plasticity: a new graphical and analytical approach. *Trends Neurosci.* 23, 105–113. doi: 10.1016/s0166-2236(99)01520-9

Cooke, S. F., Attwell, P. J. E., and Yeo, C. H. (2004). Temporal properties of cerebellar-dependent memory consolidation. *J. Neurosci.* 24, 2934–2941. doi: 10.1523/jneurosci.5505-03.2004

Eguchi, K., Velicky, P., Hollergschwandtner, E., Itakura, M., Fukazawa, Y., Danzl, J. G., et al. (2019). Advantages of acute brain slices prepared at physiological temperature in characterization of synaptic functions. *BioRxiv* [Preprint]. doi: 10.1101/845461

Fiala, J. C., and Harris, K. M. (2001). Cylindrical diameters method for calibrating section thickness in serial electron microscopy. *J. Microsc.* 202, 468–472. doi: 10.1046/j.1365-2818.2001.00926.x

Fiala, J. C., Kirov, S. A., Feinberg, M. D., Petrak, L. J., George, P., Goddard, C. A., et al. (2003). Timing of neuronal and glial ultrastructure disruption during brain slice preparation and recovery *in vitro*. *J. Comp. Neurol.* 465, 90–103. doi: 10.1002/cne.10825

Foster, K. A., and Regehr, W. G. (2004). Variance-mean analysis in the presence of a rapid antagonist indicates vesicle depletion underlies depression at the climbing fiber synapse. *Neuron* 43, 119–131. doi: 10.1016/j.neuron.2004.06.022

Fried, N. T., Moffat, C., Seifert, E. L., and Oshinsky, M. L. (2014). Functional mitochondrial analysis in acute brain sections from adult rats reveals mitochondrial dysfunction in a rat model of migraine. *Am. J. Physiol. Cell Physiol.* 307, C1017–C1030. doi: 10.1152/ajpcell.00332.2013

Guzman, S. J., Schlögl, A., and Schmidt-Hieber, C. (2014). Stimfit: quantifying electrophysiological data with Python. *Front. Neuroinform.* 8:16. doi: 10.3389/fninf.2014.00016

Hanley, J. G. (2014). Actin-dependent mechanisms in AMPA receptor trafficking. *Front. Cell. Neurosci.* 8:381. doi: 10.3389/fncel.2014.00381

Harris, K. M., and Landis, D. M. (1986). Membrane structure at synaptic junctions in area CA1 of the rat hippocampus. *Neuroscience* 19, 857–872. doi: 10.1016/0306-4522(86)90304-0

Hippenmeyer, S., Johnson, R. L., and Luo, L. (2013). Mosaic analysis with double markers reveals cell-type-specific paternal growth dominance. *Cell Rep.* 3, 960–967. doi: 10.1016/j.celrep.2013.02.002

Hirokawa, N., Niwa, S., and Tanaka, Y. (2010). Molecular motors in neurons: transport mechanisms and roles in brain function, development, and disease. *Neuron* 68, 610–638. doi: 10.1016/j.neuron.2010.09.039

Holderith, N., Lorincz, A., Katona, G., Rózsa, B., Kulik, A., Watanabe, M., et al. (2012). Release probability of hippocampal glutamatergic terminals scales with the size of the active zone. *Nat. Neurosci.* 15, 988–997. doi: 10.1038/nn.3137

Huang, S., and Uusisaari, M. Y. (2013). Physiological temperature during brain slicing enhances the quality of acute slice preparations. *Front. Cell. Neurosci.* 7:48. doi: 10.3389/fncel.2013.00048

Ichikawa, R., Miyazaki, T., Kano, M., Hashikawa, T., Tatsumi, H., Sakimura, K., et al. (2002). Distal extension of climbing fiber territory and multiple innervation caused by aberrant wiring to adjacent spiny branchlets in cerebellar purkinje cells lacking glutamate receptor δ2. *J. Neurosci.* 22, 8487–8503. doi: 10.1523/jneurosci.22-19-08487.2002

Inoshita, T., and Hirano, T. (2018). Occurrence of long-term depression in the cerebellar flocculus during adaptation of optokinetic response. *Elife* 7:e36209. doi: 10.7554/elife.36209

Jonas, P., Major, G., and Sakmann, B. (1993). Quantal components of unitary EPSCs at the mossy fibre synapse on CA3 pyramidal cells of rat hippocampus. *J. Physiol.* 472, 615–663. doi: 10.1113/jphysiol.1993.sp019965

Kaeser, P. S., and Regehr, W. G. (2017). The readily releasable pool of synaptic vesicles. *Curr. Opin. Neurobiol.* 43, 63–70. doi: 10.1016/j.conb.2016.12.012

Kakegawa, W., Katoh, A., Narumi, S., Miura, E., Motohashi, J., Takahashi, A., et al. (2018). Optogenetic control of synaptic AMPA receptor endocytosis reveals roles of LTD in motor learning. *Neuron* 99, 985.e6–998.e6. doi: 10.1016/j.neuron.2018.07.034

Kirov, S. A., Petrak, L. J., Fiala, J. C., and Harris, K. M. (2004). Dendritic spines disappear with chilling but proliferate excessively upon rewarming of mature hippocampus. *Neuroscience* 127, 69–80. doi: 10.1016/j.neuroscience.2004.04.053

Landis, D. M., and Reese, T. S. (1974). Differences in membrane structure between excitatory and inhibitory synapses in the cerebellar cortex. *J. Comp. Neurol.* 155, 93–125. doi: 10.1002/cne.901550107

Li, C. L., and McIlwain, H. (1957). Maintenance of resting membrane potentials in slices of mammalian cerebral cortex and other tissues *in vitro*. *J. Physiol.* 139, 178–190. doi: 10.1113/jphysiol.1957.sp005885

Llinás, R., and Sugimori, M. (1980). Electrophysiological properties of *in vitro* Purkinje cell dendrites in mammalian cerebellar slices. *J. Physiol.* 305, 197–213. doi: 10.1113/jphysiol.1980.sp013358

Masugi-Tokita, M., Tarusawa, E., Watanabe, M., Molnár, E., Fujimoto, K., and Shigemoto, R. (2007). Number and density of AMPA receptors in individual synapses in the rat cerebellum as revealed by SDS-digested freeze-fracture replica labeling. *J. Neurosci.* 27, 2135–2144. doi: 10.1523/JNEUROSCI.2861-06.2007

Miki, T., Kaufmann, W. A., Malagon, G., Gomez, L., Tabuchi, K., Watanabe, M., et al. (2017). Numbers of presynaptic Ca^{2+} channel clusters match those of functionally defined vesicular docking sites in single central synapses. *Proc. Natl. Acad. Sci. U S A* 114, E5246–E5255. doi: 10.1073/pnas.1704470114

Miyazaki, T., Fukaya, M., Shimizu, H., and Watanabe, M. (2003). Subtype switching of vesicular glutamate transporters at parallel fibre—Purkinje cell synapses in developing mouse cerebellum. *Eur. J. Neurosci.* 17, 2563–2572. doi: 10.1046/j.1460-9568.2003.02698.x

Nakamura, Y., Harada, H., Kamasawa, N., Matsui, K., Rothman, J. S., Shigemoto, R., et al. (2015). Nanoscale distribution of presynaptic Ca^{2+} channels and its impact on vesicular release during development. *Neuron* 85, 145–159. doi: 10.1016/j.neuron.2014.11.019

Niranjan, P. S., Forbes, J. G., Greer, S. C., Dudowicz, J., Freed, K. F., and Douglas, J. F. (2001). Thermodynamic regulation of actin polymerization. *J. Chem. Phys.* 114, 10573–10576. doi: 10.1063/1.1380693

Nusser, Z., Lujan, R., Laube, G., Roberts, J. D., Molnar, E., and Somogyi, P. (1998). Cell type and pathway dependence of synaptic AMPA receptor number and variability in the hippocampus. *Neuron* 21, 545–559. doi: 10.1016/s0896-6273(00)80565-6

Okamoto, T., Shirao, T., Shutoh, F., Suzuki, T., and Nagao, S. (2011). Post-training cerebellar cortical activity plays an important role for consolidation of memory of cerebellum-dependent motor learning. *Neurosci. Lett.* 504, 53–56. doi: 10.1016/j.neulet.2011.08.056

Sahara, Y., and Takahashi, T. (2001). Quantal components of the excitatory postsynaptic currents at a rat central auditory synapse. *J. Physiol.* 536, 189–197. doi: 10.1111/j.1469-7793.2001.00189.x

Scheuss, V., Schneggenburger, R., and Neher, E. (2002). Separation of presynaptic and postsynaptic contributions to depression by covariance analysis of successive EPSCs at the calyx of Held synapse. *J. Neurosci.* 22, 728–739. doi: 10.1523/JNEUROSCI.22-03-00728.2002

Schikorski, T., and Stevens, C. F. (2001). Morphological correlates of functionally defined synaptic vesicle populations. *Nat. Neurosci.* 4, 391–395. doi: 10.1038/86042

Schonewille, M., Luo, C., Ruigrok, T. J. H., Voogd, J., Schmolesky, M. T., Rutteman, M., et al. (2006). Zonal organization of the mouse flocculus: physiology, input, and output. *J. Comp. Neurol.* 497, 670–682. doi: 10.1002/cne.21036

Schrod, N., Vanhecke, D., Laugks, U., Stein, V., Fukuda, Y., Schaffer, M., et al. (2018). Pleomorphic linkers as ubiquitous structural organizers of vesicles in axons. *PLoS One* 13:e0197886. doi: 10.1371/journal.pone.0197886

Shutoh, F., Ohki, M., Kitazawa, H., Itohara, S., and Nagao, S. (2006). Memory trace of motor learning shifts transsynaptically from cerebellar cortex to nuclei for consolidation. *Neuroscience* 139, 767–777. doi: 10.1016/j.neuroscience.2005.12.035

Siksou, L., Triller, A., and Marty, S. (2009). An emerging view of presynaptic structure from electron microscopic studies. *J. Neurochem.* 108, 1336–1342. doi: 10.1111/j.1471-4159.2009.05888.x

Takahashi, T. (1978). Intracellular recording from visually identified motoneurons in rat spinal cord slices. *Proc. R. Soc. Lond. B Biol. Sci.* 202, 417–421. doi: 10.1098/rspb.1978.0076

Taubenfeld, S. M., Stevens, K. A., Pollonini, G., Ruggiero, J., and Alberini, C. M. (2002). Profound molecular changes following hippocampal slice preparation: loss of AMPA receptor subunits and uncoupled mRNA/protein expression. *J. Neurochem.* 81, 1348–1360. doi: 10.1046/j.1471-4159.2002.00936.x

Walker, J. H., and Agoston, D. V. (1987). The synaptic vesicle and the cytoskeleton. *Biochem. J.* 247, 249–258. doi: 10.1042/bj2470249

Wang, W., Nakadate, K., Masugi-Tokita, M., Shutoh, F., Aziz, W., Tarusawa, E., et al. (2014). Distinct cerebellar engrams in short-term and long-term motor learning. *Proc. Natl. Acad. Sci. U S A* 111, E188–E193. doi: 10.1073/pnas.1315541111

Yamamoto, C. (1975). Recording of electrical activity from microscopically identified neurons of the mammalian brain. *Experientia* 31, 309–311. doi: 10.1007/bf01922555

Yamamoto, C., and McIlwain, H. (1966). Electrical activities in thin sections from the mammalian brain maintained in chemically-defined media *in vitro*. *J. Neurochem.* 13, 1333–1343. doi: 10.1111/j.1471-4159.1966.tb04296.x

Conflict of Interest: The authors declare that the research was conducted in the absence of any commercial or financial relationships that could be construed as a potential conflict of interest.

Copyright © 2020 Eguchi, Velicky, Hollergschwandtner, Itakura, Fukazawa, Danzl and Shigemoto. This is an open-access article distributed under the terms of the Creative Commons Attribution License (CC BY). The use, distribution or reproduction in other forums is permitted, provided the original author(s) and the copyright owner(s) are credited and that the original publication in this journal is cited, in accordance with accepted academic practice. No use, distribution or reproduction is permitted which does not comply with these terms.

frontiers in Cellular Neuroscience

ORIGINAL RESEARCH
published: 30 April 2020
doi: 10.3389/fncel.2020.00095

Glucagon-Like Peptide-1 Secreting L-Cells Coupled to Sensory Nerves Translate Microbial Signals to the Host Rat Nervous System

Maria M. Buckley[1,2], Rebecca O'Brien[1], Eilish Brosnan[1], R. Paul Ross[2,3,4], Catherine Stanton[2,4], Julliette M. Buckley[5,6] and Dervla O'Malley[1,2]†*

[1]*Department of Physiology, University College Cork, Cork, Ireland,* [2]*APC Microbiome Ireland, University College Cork, Cork, Ireland,* [3]*College of Science, Engineering and Food Science, University College Cork, Cork, Ireland,* [4]*Teagasc Food Research Centre, Cork, Ireland,* [5]*Department of Surgery, University College Cork, Cork, Ireland,* [6]*Mater Private Hospital, Cork, Ireland*

An intact gut epithelium preserves the immunological exclusion of "non-self" entities in the external environment of the gut lumen. Nonetheless, information flows continuously across this interface, with the host immune, endocrine, and neural systems all involved in monitoring the luminal environment of the gut. Both pathogenic and commensal gastrointestinal (GI) bacteria can modulate centrally-regulated behaviors and brain neurochemistry and, although the vagus nerve has been implicated in the microbiota-gut-brain signaling axis, the cellular and molecular machinery that facilitates this communication is unclear. Studies were carried out in healthy Sprague–Dawley rats to understand cross-barrier communication in the absence of disease. A novel colonic-nerve electrophysiological technique was used to examine gut-to-brain vagal signaling by bacterial products. Calcium imaging and immunofluorescent labeling were used to explore the activation of colonic submucosal neurons by bacterial products. The findings demonstrate that the neuromodulatory molecule, glucagon-like peptide-1 (GLP-1), secreted by colonic enteroendocrine L-cells in response to the bacterial metabolite, indole, stimulated colonic vagal afferent activity. At a local level indole modified the sensitivity of submucosal neurons to GLP-1. These findings elucidate a cellular mechanism by which sensory L-cells act as cross-barrier signal transducers between microbial products in the gut lumen and the host peripheral nervous system.

Keywords: enteric neurons, indole, GLP-1, microbiota, vagus nerve, tryptophan

OPEN ACCESS

Edited by:
Andrew L. Gundlach,
University of Melbourne, Australia

Reviewed by:
John Bienenstock,
McMaster University, Canada
Richard L. Young,
University of Adelaide, Australia

****Correspondence:***
Dervla O'Malley
d.omalley@ucc.ie

†ORCID:
Dervla O'Malley
orcid.org/0000-0002-7031-4879

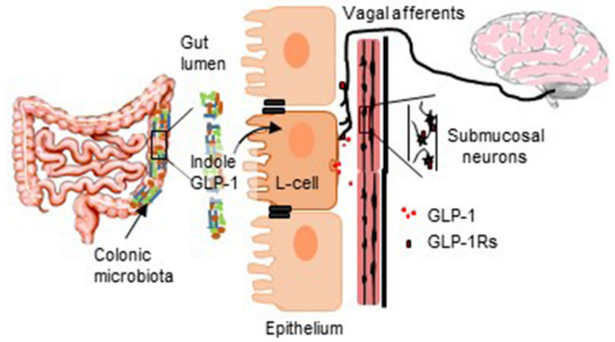
Specialty section:
This article was submitted to Cellular Neurophysiology, a section of the journal Frontiers in Cellular Neuroscience

Received: *14 February 2020*
Accepted: *30 March 2020*
Published: *30 April 2020*

Citation:
Buckley MM, O'Brien R, Brosnan E, Ross RP, Stanton C, Buckley JM and O'Malley D (2020) Glucagon-Like Peptide-1 Secreting L-Cells Coupled to Sensory Nerves Translate Microbial Signals to the Host Rat Nervous System. Front. Cell. Neurosci. 14:95. doi: 10.3389/fncel.2020.00095

INTRODUCTION

The peripheral nervous system innervating the colon has evolved in the continued presence of over a 100 trillion microbial organisms, mostly bacteria. These microbes are predominantly beneficial, scavenging additional calories, secreting vitamins and ensuring normal immune and gastrointestinal (GI) development, but it appears that they may also manipulate host physiology and behavior to their benefit (Stilling et al., 2016). Alterations in the luminal microbiota have been linked with stress-related disorders, Parkinson's disease, autism spectrum disorder and schizophrenia (Dinan and Cryan, 2013, 2017). The vagus nerve has been implicated in the



GRAPHICAL ABSTRACT | The diagram illustrates the proposed role of GLP-1-secreting L-cells in translating bacterially-originating signals to neurostimulatory actions.

modulation of host behavior and altered central expression of neurotransmitters by putative probiotics (Bercik et al., 2011; Bravo et al., 2011; Perez-Burgos et al., 2013). Indeed, stimulation of vagal nerve activity (Perez-Burgos et al., 2013) and activation of intrinsic primary afferent neurons (Mao et al., 2013) in response to the exposure of mouse jejunum mucosa to *Lactobacillus Rhamnosus* JB-1 have been reported. Intrinsic primary afferent neurons may act as a neural starting point of gut-to-brain signaling (Perez-Burgos et al., 2014) and indeed, are less excitable in the absence of gut microbes (McVey Neufeld et al., 2013). However, a mechanistic understanding of how these bacterial signals are interpreted by the host is yet to be established.

Bacteria can infiltrate the gut (Pérez-Berezo et al., 2017; Jaglin et al., 2018) and, this is indeed more likely in disorders associated with increased GI permeability, such as Irritable Bowel Syndrome (IBS). However, given that the healthy gut is immunologically primed to detect and prevent bacterial penetration, it is likely that an integral homeostatic signaling mechanism, which maintains the integrity of the gut barrier, exists to facilitate microbiota-gut-brain signaling. Pathogen associated molecular patterns, which identify and evoke a host response to pathogenic microbes, are well described in the gut epithelium, and Nod-like receptors are implicated in gut-brain signaling (Pusceddu et al., 2019), however, other cells in the epithelium act as chemosensory transducers for non-threating gut stimuli. Serotonin biosynthesis was stimulated by chemical irritants, volatile fatty acid fermentation products and catecholamines (Yano et al., 2015), which subsequently modulated primary afferent nerve fibers *via* synaptic connections (Bellono et al., 2017). Thus, enterochromaffin cells transduce environmental, metabolic, and homeostatic information from the gut lumen to the nervous system. However, L-cells also act as biosensors of the gut lumen.

Electrically-excitable enteroendocrine L-cells are embedded in the epithelium and secrete glucagon-like peptide-1 (GLP-1) from their basolateral face following stimulation (Chimerel et al., 2014). L-cells are found throughout the small and large intestine (Hansen et al., 2013), but function differently depending on their location. For instance, small intestinal L-cells in humans (Sun et al., 2017) and rats (Kuhre et al., 2015) are sensitive to glucose, whereas *in vitro* colonic L-cells express bile receptors and receptors for short-chain fatty acids (Tolhurst et al., 2012). Bacterial metabolites such as indole (Chimerel et al., 2014), S-equol (Harada et al., 2018) and prebiotics (Gibson and Roberfroid, 1995; Cani et al., 2006) induce GLP-1 secretion, but conversely, GLP-1 is also elevated in germ-free mice (Wichmann et al., 2013). Although L-cells are classically described as endocrine cells, like enterochromaffin cells (Bellono et al., 2017), they can synapse directly with peripheral afferent and efferent neurons (Bohórquez et al., 2015), providing a direct neural pathway for bi-directional brain-gut communication (Kaelberer et al., 2018). Despite growing interest in the microbiota-gut-brain axis, relatively little is known about the chemosensory transduction of microbial signals across an intact barrier. In this study, we have investigated the capacity of L-cells to interpret bacterial signals from the gut lumen and activate host colonic afferents and intrinsic neurons by secreting GLP-1.

MATERIALS AND METHODS

Ethical Approval

All animal experiments were in full accordance with the European Community Council Directive (86/609/EEC) and the local University College Cork Animal Experimentation Ethics Committee. Rats were sacrificed by CO_2 overdose and perforation of the diaphragm.

Animals and Tissue Collecting

Sprague–Dawley rats were used to determine if bacterial products could activate enteric neurons and the vagus nerve across an intact, non-leaky colon (Gareau et al., 2007). Male Sprague–Dawley rats (8–12 weeks) purchased from Envigo, Derbyshire, UK, were group-housed five per cage and maintained on a 12/12 h dark-light cycle (08.00–20.00) with a room temperature of 22 ± 1°C. Animals were permitted at least 1 week to acclimatize to their new environment before experimentation. Standard chow diet and water were available *ad libitum*. A section of colon 8 cm proximal to the anus was excised from each rat and maintained in ice-cold Krebs saline containing in mM/L: 117 NaCl, 4.8 KCl, 2.5 $CaCl_2$, 1.2 $MgCl_2$, 25 $NaHCO_3$, 1.2 NaH_2PO_4 and 11 D-glucose (pH 7.4).

Commensal Bacterial Strains

Lactobacillus paracasei NFBC 338 (*L.paracasei*) was transformed to secrete a long-acting analog of GLP-1, confirmed by mass spectrometry and *in vitro* assays of insulinotropic activity (Ryan et al., 2017). The engineered commensal bacteria were cultured at 1% (v/v) in de Man, Rogosa and Sharpe broth (Difco, VWR, Philadelphia, PA, USA) for ∼17 h at 37°C under anerobic conditions [anerobic jars with Anaerocult A Gas Packs (Merck, Darmstadt, Germany)] until stationary phase and centrifuged (16,900× *g* for 15 min, at 4°C; SLA-3000 rotor, Sorvall RC B5-Plus). The cell pellet was washed twice with phosphate-buffered saline (PBS; Sigma Aldrich, UK), re-suspended at ∼2×10^{10} $CFU.ml^{-1}$ in sterile 15% trehalose (Sigma Aldrich), which acted as a cryoprotectant and 1 ml aliquots were dispensed into 2 ml

lyophilization vials. The vials were lyophilized on a 24 h program (freeze temperature −40°C, additional freeze 1 min, condenser set point −60, vacuum setpoint 600 mTorr; VirTis AdVantage Wizard 2.0) and stored at 4 °C. Bacteria were resuspended in distilled water each day to deliver 1×10^{10} CFU.ml^{-1} for each exposure.

Colonic-Afferent Nerve Electrophysiological Recordings

The detailed description of the *ex vivo* dissection technique and recording of distal colonic afferent nerves has been previously reported (Buckley and O'Malley, 2018). In brief, a segment of the esophagus with the attached posterior vagus nerve was excised from an adult Sprague–Dawley rat. Maintaining an intact neural connection to the esophagus, a segment of distal colon (5 cm from the anus) with attached inferior and superior mesenteric ganglia, celiac ganglia and vagus nerve were placed in a recording chamber. Adjacent Sylgard-lined chambers allowed the afferent nerves to be isolated from the distal colon. The colon was opened, mucosal side up and the vagus nerve was carefully threaded through to the adjacent chamber and the gap was sealed with petroleum jelly (**Figure 1B**). Both chambers were superfused with 5% CO_2/95% O_2 bubbled Krebs-buffered saline maintained at 37°C. Multi-unit neural activity was recorded using platinum bipolar recording electrodes (WPI, Sarasota, FL, USA) attached to a Power lab (AD Instruments, Oxford, UK). Reagents [indole (1 mM, Sigma-Aldrich: cat. No. I3408), exendin 3(9–39) amide (10 μM, Tocris; cat. No. 2081), exendin-4 (10 μM, Tocris: cat. No. 1933) or tetrodotoxin (10 nM, Tocris: cat. No. 1078)] were applied to the colonic bath in the superfusate. Nerve activity was viewed and analyzed with Chart 7 (AD Instruments, Oxford, UK). Changes in multi-unit neural activity in the vagal nerve are presented as frequency from raw traces. Both raw and rectified traces are presented.

Immunofluorescence and Confocal Microscopy

Whole-mount colonic submucosal plexus (SMP) preparations were pinned out in Sylgard-lined dishes and fixed in 4% paraformaldehyde (4°C, overnight). The tissues were subsequently permeabilized with 0.1% Triton X-100 and blocked with 1% donkey serum (Sigma Aldrich). SMP tissue was incubated with primary antibodies (1:250 @ 4°C overnight) against GLP-1 [rabbit polyclonal antibody (ab22625), Abcam, Cambridge, UK (Duca et al., 2013)] or goat polyclonal antibody (sc7782; Santa Cruz Biotechnology Inc, TX, USA), GLP-1 receptors [GLP-1R, mouse polyclonal antibody (sc66911), Santa Cruz Biotechnology] and FITC-conjugated anti-rabbit or anti-goat and TRITC-conjugated anti-rabbit or anti-mouse secondary antibodies (1:250, 2 h at room temperature, Jackson Immunoresearch, Westgrove, PA, USA). Images were captured using an FVl0i-Olympus-confocal microscope with Fluoview software (FV10i-SW). No non-specific fluorescence was detected in control experiments where tissues were incubated with primary antibodies or secondary antibodies alone, or where anti-GLP-1R antibodies were neutralized with a blocking peptide before the staining protocol. Changes in the optical density of GLP-1R expression was quantified using ImageJ (National Institute of Health, USA). Membrane expression of GLP-1Rs from three neurons per ganglia in three different tissue preparations were compared when indole was applied to the submucosal neurons or the mucosa.

Calcium Imaging

For calcium imaging studies, whole-mount preparations of SMP neurons were prepared from the distal colon of healthy Sprague–Dawley rats. The colon was mounted on a glass rod, where the outer serosal layer was scored lightly with a blade along the mesenteric border. To prepare an SMP tissue preparation, the serosal and mucosal layers were removed and the colonic tissue (∼2 cm × 2 cm) was pinned out in Sylgard-lined dishes. Submucosal neuronal preparations were loaded with Fura-2AM (7 μM, 1 h, Thermo-Fisher Scientific, UK) or Fluo-8 (8 μM, 1 h, Abcam, UK) in Krebs-buffered saline solution comprised of (in mM l^{-1}): NaCl, 117; KCl, 4.8; $CaCl_2$, 2.5; $MgCl_2$, 1.2; $NaHCO_3$, 25; NaH_2PO_4, 1.2 and D-glucose, 11; prior to imaging. SMP tissue preparations were used to investigate the activation of submucosal neurons in the absence of epithelial and enteroendocrine cells and their secretions. A hemisected colonic tissue preparation (Mao et al., 2013), where the SMP is exposed on one half of the tissue but the mucosa is left intact on the other half (**Figure 3E**), was used to compare calcium responses evoked by neuronal exposure to Ex-4 before and after mucosal application of indole. The presence of the epithelium indicates that mucosally-secreted factors are implicated in the modification of neuronal function. Reagents [indole (1 mM), exendin-4 (10 μM), exendin 3(9–39) amide (10 μM), thapsigargin (100 nM, Tocris: cat. No. 1138), ω-agatoxin IVA (100 nM, Sigma Aldrich: cat. No. A6719), ω-conotoxin GVIA (100 nM, Sigma Aldrich: cat. No. C9915), wortmannin (100 nM, Sigma Aldrich: cat. No. W1628), WP1006 (1 μM, Calbiochem) and PD98059 (1 μM, Sigma Aldrich: cat. No. 513000)] were added to the perfusate. Images were acquired at 1 Hz using a conventional fluorescence imaging system (Cairn Life technologies, UK or Olympus, Melville, NY, USA), and a water-immersion objective (Olympus, 40× magnification, numerical aperture: 0.80) on a fixed stage upright microscope (Olympus BX51WI). Cell R software (Olympus Soft imaging solutions, Munster, Germany) or WinFluor Fluorescence Image Capture and Analysis program (John Dempster, University of Strathclyde, Scotland) was used to record excitation changes in intracellular calcium (O'Malley et al., 2011b).

As previously described (O'Malley et al., 2011a), submucosal neurons were identified based on morphology and responsivity to brief application of 75 mM KCl at the end of the recording protocol. Reagents were applied in a random order to avoid the run-down of calcium stores being a confounding factor. The colonic tissue was continuously superfused with carbogen-bubbled Krebs-buffered saline at room temperature containing the L-type calcium channel blocker, nifedipine (1 μM, Sigma-Aldrich, cat. No.: N7634), to inhibit smooth muscle contraction. Responding neurons were defined as those which exhibited an increase in intracellular calcium ($[Ca^{2+}]_i$) that was greater than two standard deviations from the baseline values in that cell

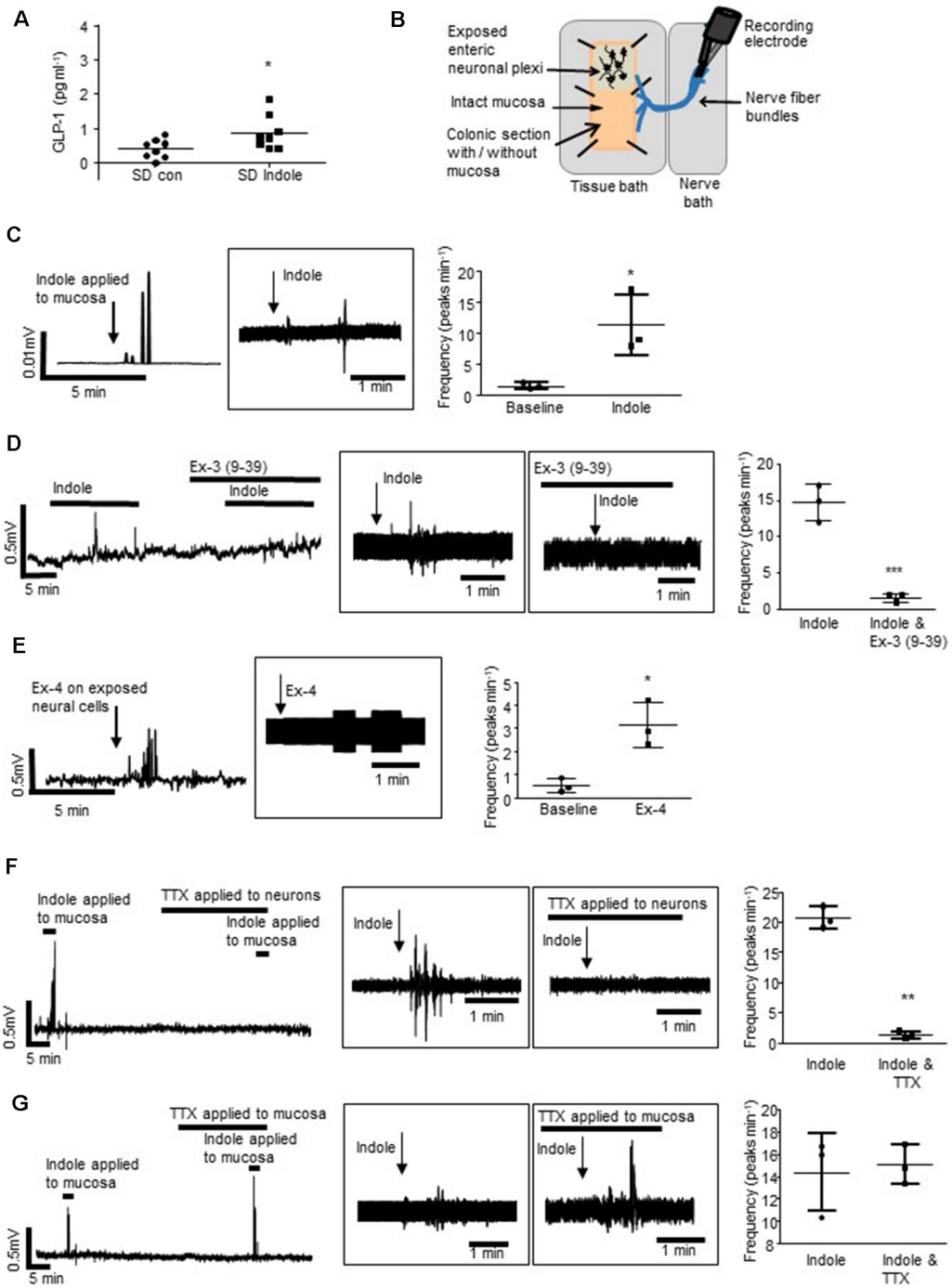


FIGURE 1 | L-cells facilitate indole-evoked activation of vagal afferents. **(A)** The plot illustrates basolateral secretion of Glucagon-like peptide-1 (GLP-1) from colonic tissue apically exposed to indole (1 mM, 30 min) or saline (control). **(B)** The schematic (amended from Buckley and O'Malley, 2018) illustrates the *ex vivo* distal colonic tissue preparation. Recording is made from vagal afferents attached to the esophagus. The mucosa can be left intact, or removed to expose enteric neurons and associated afferent endings. **(C)** The rectified and raw (in boxes) traces show vagal nerve activity in response to stimulation of the distal colonic mucosa. Scatter plots illustrate peak frequency. Indole-evoked vagal nerve activity was attenuated by **(D)** exendin 3(9–39) amide [Ex-3(9–39)]. **(E)** Exendin-4 (Ex-4) stimulated vagal nerve firing when applied to the exposed neurons. **(F)** Tetrodotoxin (TTX) inhibited the indole-evoked response when it is applied to a hemisected piece of colonic tissue but not **(G)** colonic tissue with an intact mucosa. $^{*}p < 0.05$, $^{**}p < 0.01$, $^{***}p < 0.001$.

(calculated during the 150 s preceding stimulus application). Paired analysis of responses within a single neuron were compared to determine the effect of the pharmacological reagent on the control response.

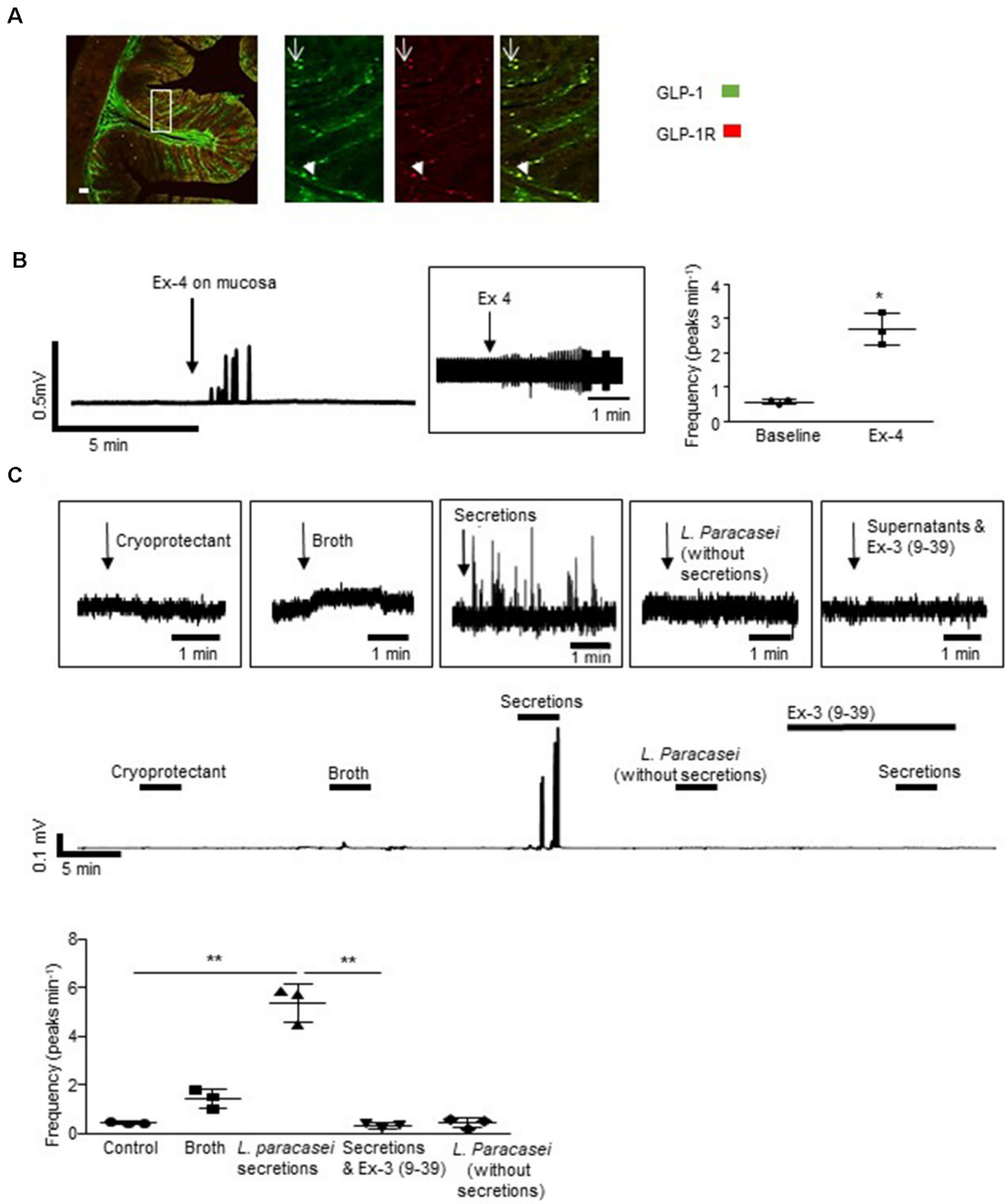


FIGURE 2 | *Lactobacillus paracasei* secretions stimulate host neurons. **(A)** The representative immunofluorescent image of a rat colonic cross-section illustrates that some L-cells expressed GLP-1Rs (arrowhead) but others did not (arrow). **(B)** Mucosal application of exendin-4 (Ex-4) increased vagal activity. **(C)** Increased vagal nerve activity evoked by *L. paracasei* secretions was abolished by Ex-3(9–39). $^{*}p < 0.05$, $^{**}p < 0.01$. Scale bars: 50 μm.

Ussing Chamber Electrophysiology

Mucosa-submucosal preparations of distal colon were mounted in Ussing chambers (exposed area of 0.12cm^2) with 5 mls of Krebs saline solution (95% O_2 / 5% CO_2, 37°C) in the basolateral and luminal reservoirs. Tissues were voltage-clamped at 0 mV using an automatic voltage clamp (EVC 4000, World Precision Instruments, Sarasota, FL, USA) and the short-circuit current (I_{SC}) required to maintain the 0 mV potential was monitored as a recording of the net active ion transport across the epithelium. Experiments were carried out simultaneously in all chambers and connected to a PC equipped with DataTrax II software (WPI). This software was used to measure the peak response and resistance was calculated using Ohms law. Following mounting, tissue was allowed to equilibrate (∼1 h). Reagents [exendin 4

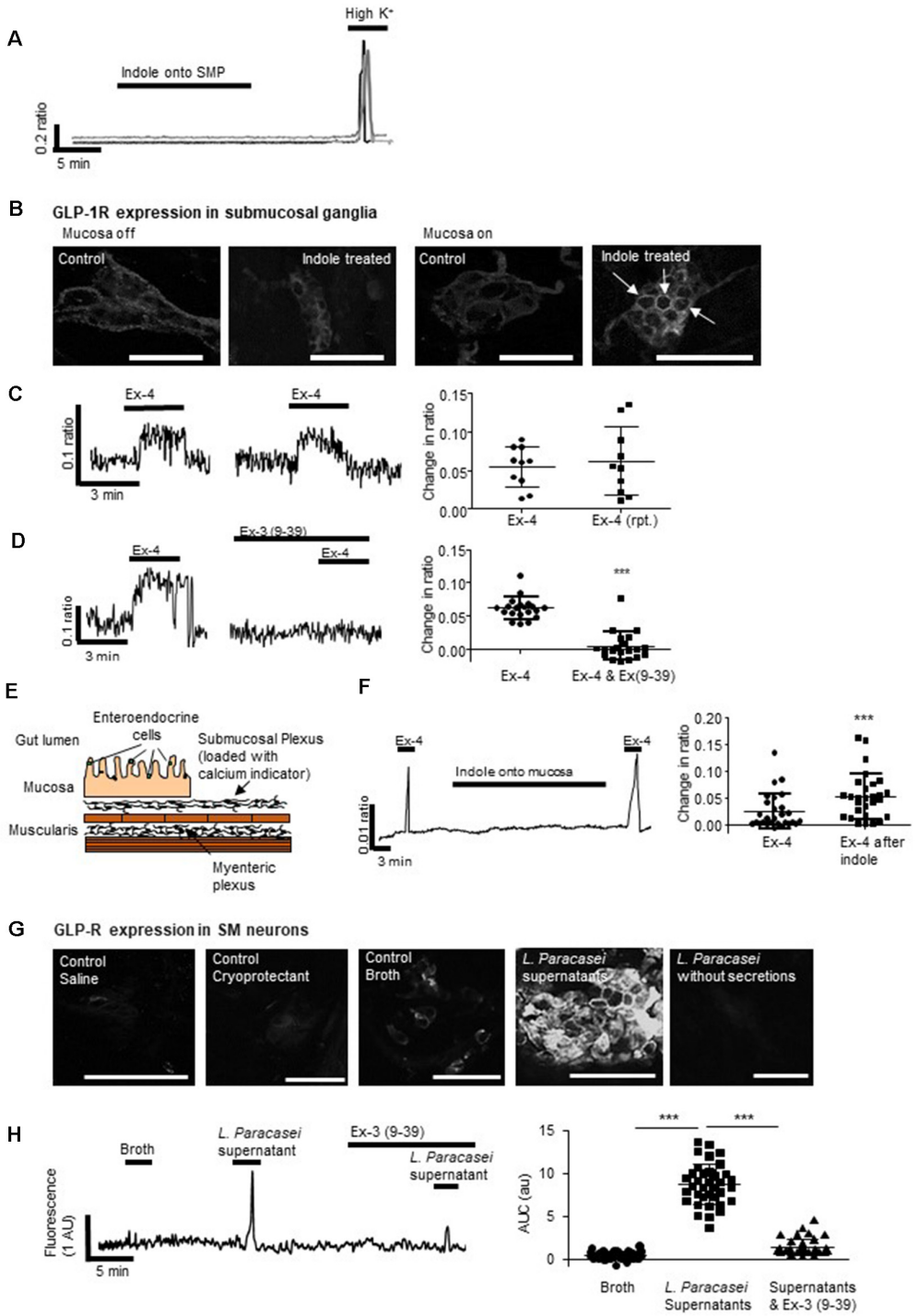


FIGURE 3 | Mucosal L-cells facilitate indole-evoked activation of submucosal neurons. **(A)** Indole did not affect intracellular calcium ($[Ca^{2+}]_i$) levels in submucosal neurons. **(B)** Immunofluorescence images show the GLP-1 receptor (GLP-1R) expression in colonic submucosal neurons following neuronal and mucosal exposure to indole. Arrows indicate increased expression at the neuronal cell membranes. Scalebar: 50 μm. **(C)** The GLP-1R agonist, exendin 4 (Ex-4) stimulated an increase in $[Ca^{2+}]_i$, a reproducible effect that was **(D)** attenuated by the GLP-1R antagonist, exendin 3(9–39) amide [Ex-3(9–39)]. **(E)** The schematic illustrates a cross-section of the hemisected distal colon. By removing half of the mucosa, changes in intracellular calcium can be recorded from submucosal neurons loaded with a calcium indicator dye. By leaving some of the mucosa intact, the role of endocrine hormones secreted by epithelial cells can be investigated. **(F)** In hemisected colonic tissue, the Ex-4-evoked calcium response was enhanced by mucosal indole. **(G)** Immunofluorescent images show GLP-1R expression in colonic submucosal neurons following mucosal stimulation with saline, cryoprotectant, broth, *L. paracasei* secretions, and *L. paracasei* bacteria. Scalebar: 50 μm. **(H)** Mucosal application of *L. paracasei* secretions evoked a calcium response in submucosal neurons which was attenuated by the GLP-1R antagonist, exendin 3(9–39) amide [Ex-3(9–39)]. ***$p < 0.001$.

(10 μM), carbachol (10 μM, Sigma-Aldrich, cat. No.: Y0000113), veratridine (10 μM, Sigma-Aldrich, cat. No.: V5754), capsaicin (1 μM, Sigma-Aldrich, cat. No.: M2028)] were added to the basolateral chamber.

Separation of the basolateral and apical surfaces in the Ussing chambers were exploited to determine if basolateral secretion of GLP-1 by colonic L-cells was induced by indole. Distal colonic tissue was mounted in low-volume (1 ml carbogenated Krebs saline solution) Ussing chambers with an exposed tissue area of 0.64 cm^2. Following mucosal exposure to indole (1 mM, 30 min), secretion of GLP-1 into the basolateral reservoir (1 ml) was ascertained by immunoassay.

Mesoscale Discovery Biomarker Assay

An immunoassay (MesoScale Discovery U-PLEX customized multiplex assay kit I, MesoScale Discovery, Gaithersburg, MD, USA) with a dynamic range for GLP-1 of 0.02–120 pM, was carried out to determine if GLP-1 was secreted in response to indole as compared to saline-treated controls. The assay was run in triplicate and an electrochemiluminescent detection method was used to measure protein levels in each sample. The plates were read using the MesoScale Discovery plate-reader (MESO QuickPlex SQ 120). A calibration curve was generated using standards, and GLP-1 concentrations were determined from the curve.

Statistical Analyses

Data were analyzed using GraphPad prism for windows (version 5, Graphpad Software, San Diego, CA, USA). The data are represented as data plots with mean ± the standard deviation. Paired or unpaired *t*-tests or repeated-measures ANOVA with Tukey multiple comparison *post hoc* test, as appropriate, were used to compare data. $P \leq 0.05$ was considered significant.

RESULTS

Indole Indirectly Stimulates Activity in Colonic Vagal Afferents

Sprague–Dawley rats were used to determine if indole, a bacterial metabolite of tryptophan, which stimulates L-cells (Chimerel et al., 2014), can induce cross-barrier signaling in healthy, non-leaky colons (Gareau et al., 2007). In Ussing chamber experiments, exposure of the intact colonic apical epithelial surface to indole (1 mM, 30 min) resulted in secretion of GLP-1 into the basolateral reservoir as compared to saline-treated control tissues (n = 8 rats, p = 0.0355, **Figure 1A**). To investigate if bacterial products may use L-cells to activate the gut-brain neural signaling axis, an *ex vivo* preparation of rat distal colon with intact colonic afferents was used (**Figure 1B**; Buckley and O'Malley, 2018). Consistent with previous reports (Richards et al., 1996), baseline afferent activity was low. However, mucosal application of indole stimulated a robust increase in vagal nerve activity (n = 3 rats, p = 0.0264, **Figure 1C**). Incubation of the tissue with the GLP-1R antagonist, exendin-3 (9–39) amide [Ex-3 (9–39)], attenuated the indole-evoked response (n = 4, p = 0.001, **Figure 1D**). Given that GLP-1Rs are expressed in the nodose ganglia (Nakagawa et al., 2004), where cell bodies of afferent vagal neurons are located, basolaterally released GLP-1 could activate vagal afferents. Indeed, direct application of Ex-4 to a tissue preparation with exposed colonic submucosal neurons and afferent nerve endings similarly resulted in increased vagal firing (n = 3, p = 0.0219, **Figure 1E**), although in the absence of single-unit recordings it is not possible to determine if the same fibers are activated by both indole and Ex-4. In a hemisected colonic tissue preparation (Mao et al., 2013), where submucosal neurons and afferent and efferent nerve endings are exposed, indole-evoked stimulation of vagal nerves was blocked by the neurotoxin, tetrodotoxin (n = 3, p = 0.0047, **Figure 1F**). Interestingly, in colonic tissue sections where the epithelial layer was left *in situ*, thereby segregating intrinsic and extrinsic neurons from the luminally-applied tetrodotoxin, indole-evoked vagal stimulation was not inhibited (n = 3, p = 0.6821, **Figure 1G**). Thus, action potential generation is crucial for afferent signaling evoked by indole. However, stimulation of neural firing is initiated on the basolateral side of the epithelium. This is consistent with the basolateral secretion of GLP-1 in response to luminal application of indole.

GLP-1 Secreted by *L. paracasei* Stimulates Colonic Afferents

Some, but not all GLP-1 immuno-labeled L-cells in the colonic epithelium of SD rats (n = 4 rats, **Figure 2A**) expressed GLP-1Rs. Thus, GLP-1 originating from sources in the gut lumen could directly or indirectly activate L-cells. Indeed, mucosal application of the GLP-1R agonist, exendin-4 (Ex-4, 10 μM) increased vagal firing (**Figure 2B**, n = 3, p = 0.0124). Although a native GLP-1-secreting microbe has yet to be characterized, a genetically recombineered *Lactobacillus paracasei* NFBC 338 (*L. paracasei*), which secretes a long-lasting analog of GLP-1, has been shown to signal across the gut to modify metabolic physiology (Ryan et al., 2017). To demonstrate that luminal application of a bacterial product can modify neural signaling, *L. paracasei* secretions were applied to the mucosa and similarly evoked vagal activation (p = 0.0074), an effect that was abolished by the GLP-1R antagonist, Ex-3 (9–39; n = 4 rats, p = 0.0095, **Figure 2C**). Application of control solutions (bacterial cryoprotectant, culture broth or the probiotics in the absence of their secretory products) did not affect vagal firing.

Indole Indirectly Stimulates Colonic Submucosal Neurons Through the Activation of GLP-1 Receptors (GLP-1Rs)

Indole can penetrate the gut barrier (Jaglin et al., 2018), however, our studies found that even if this microbial product did cross the epithelium, cytosolic intracellular calcium ($[Ca^{2+}]_i$) in underlying submucosal neurons, important neural regulators of GI absorpto-secretory function, was unchanged in its presence (1 mM, n = 32 neurons from three SMP preparations, **Figure 3A**). Ganglionic expression of GLP-1Rs, which are most evident in neuronal cell membranes and extra-neuronal cells, was unchanged by direct exposure of submucosal neurons to indole (optical density: 11.3 ± 1.0 vs. 10.9 ± 1.2, n = 9 neurons from three tissue preparations, p = 0.804, **Figure 3B**). In contrast,

application of indole to colonic tissue with an intact epithelium resulted in increased GLP-1R expression (optical density: 7.6 ± 0.3 vs. 23.4 ± 3.3, n = 9 neurons from three tissue preparations, p = 0.0002, **Figure 3B**) in submucosal ganglia, which is particularly evident at the cell membranes (indicated by arrows).

To emulate local paracrine actions of basolaterally-secreted GLP-1 on submucosal neurons, a colonic SMP preparation was exposed to Ex-4, a GLP-1 mimetic. Forty-four percentage (n = 14 /34 neurons from three SMP preparations) of neurons responded to Ex-4 with a robust, but variable, increase in $[Ca^{2+}]_i$. The calcium response was reproducible upon second application (n = 10 neurons from three SMP preparations, p = 0.489, **Figure 3C**) and, consistent with previous studies in myenteric neurons (O'Brien et al., 2019), Ex-3 (9–39) abolished this response (n = 22 neurons from three SMP preparations, $p < 0.0001$, **Figure 3D**). In hemisected colonic tissue, where half of the mucosa was retained (**Figure 3E**), the mucosal application of indole did not affect neuronal calcium levels *per se* (**Figure 3F**). However, the neuronal calcium response evoked by Ex-4 (n = 29 from three SMP preparations, **Figure 3F**) was potentiated both in duration and amplitude ($p < 0.0001$) following exposure of the colonic mucosa to indole.

Expression of GLP-1Rs was increased in submucosal neurons following mucosal application of *L. paracasei* secretions but not broth (optical density:14.1 ± 1.4 vs. 29.5 ± 2.0, n = 9 neurons from three tissue preparations, $p < 0.0001$). This was primarily at neuronal cell membranes (**Figure 3G**). Mucosal application of *L. paracasei* secretions to hemisected colonic tissue increased $[Ca^{2+}]_i$ in submucosal neurons ($p < 0.0001$), a response that was attenuated by Ex-3(9–39; n = 38 neurons from three SMP preparations, $p < 0.0001$, **Figure 3H**).

Exendin-4 Induces Calcium Influx From Extracellular Sources in Submucosal Neurons

To understand the cellular mechanisms evoked by activation of neuronal GLP-1Rs after indole-evoked GLP-1 release from colonic L-cells, the neuromodulatory actions of the GLP-1R agonist, Ex-4 (3-min application) was characterized further in the submucosal neurons. Our studies found that the Sarco/endoplasmic reticulum Ca^{2+} ATPase inhibitor, thapsigargin (100 nM, 30 min), reduced but did not abolish calcium responses evoked by Ex-4 (n = 35 neurons from three SMP preparations, $p < 0.0001$, **Figure 4A**), implicating calcium release from intracellular stores in submucosal neurons. However, removal of extracellular calcium also attenuated the Ex-4-evoked response (n = 16 neurons from three SMP preparations, $p < 0.0001$, **Figure 4B**) indicating the importance of the extracellular influx of calcium. Indeed, the P/Q-channel blocker, ω-agatoxin IVA (100 nM, 30 min, n = 9 neurons from three SMP preparations, p = 0.032, **Figure 4C**), and the N-channel blocker, ω-conotoxin GVIA (100 nM, 30 min, n = 14 neurons from three SMP preparations, $p < 0.0001$, **Figure 4D**), attenuated the calcium response evoked by Ex-4. To inhibit smooth muscle contraction, all calcium imaging studies were carried out in the presence of nifedipine (1 μM), an L-type calcium channel blocker, which did not impact on the capacity of Ex-4 to stimulate a calcium response.

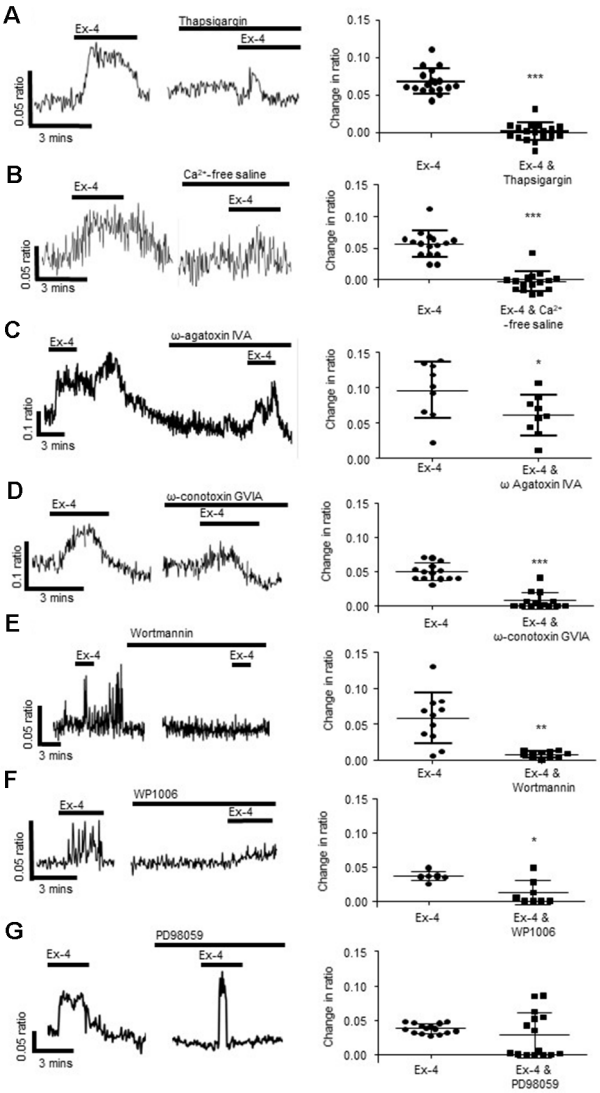


FIGURE 4 | Exendin-4 stimulates calcium release from intracellular stores and influx *via* voltage-gated calcium channels. **(A)** The calcium response evoked by exendin-4 (Ex-4, 10 μM) was attenuated by thapsigargin (100 nM, n = 35) and **(B)** removal of extracellular calcium (n = 17). Specific inhibitors of **(C)** P/Q-(ω agatoxin IVA 100 nM, n = 9) and **(D)** N-(ω-conotoxin GVIA, 100 nM, n = 14) type voltage gated calcium channels inhibited Ex-4-evoked calcium responses. **(E)** The phosphoinositide 3-kinase (PI 3-kinase) inhibitor, wortmannin (100 nM, n = 11), and **(F)** the STAT3 inhibitor, WP1006 (1 μM, n = 8) attenuated Ex-4-evoked calcium responses. **(G)** The ERK-MAPK inhibitor, PD98059 (1 μM, n = 15), had no effect. $^*p < 0.05$, $^{**}p < 0.01$, $^{***}p < 0.001$.

Further studies were carried out to understand the intracellular signaling cascades evoked by Ex-4 in submucosal neurons. The Ex-4-evoked calcium response was attenuated by the phosphoinositide 3-kinase (PI 3-kinase) inhibitor,

wortmannin (100 nM, 30 min; $n = 11$ neurons from three SMP preparations, $p = 0.0013$, **Figure 4E**) and the Signal Transducer and Activator of Transcription (STAT)-3 inhibitor, WP1006 (1 μM, 30 min, $n = 8$ neurons from three SMP preparations, $p = 0.0102$, **Figure 4F**), while the extracellular-signal-regulated kinase, mitogen-activated protein kinase (ERK-MAPK) inhibitor, PD98059 (1 μM, 30 min) had no effect on the Ex-4 evoked increase in $[Ca^{2+}]_i$ ($n = 15$ neurons from three SMP preparations, $p = 0.2295$, **Figure 4G**).

The GLP-1R Agonist, Exendin-4 Modifies Secretory Currents and Gut Permeability

As Ex-4 modifies the excitability of the SMP and this is the neural regulator of gut absorpto-secretory function, Ussing chambers were used to examine the impact of the GLP-1R agonist on colonic absorpto-secretory currents. As GLP-1 is secreted from the basolateral face of L-cells (**Figure 1A**), Ex-4 was added to the basolateral chamber of the Ussing chambers. Incubation with Ex-4 resulted in a small secretory current ($n = 8$ rats, $p = 0.0052$, **Figure 5A**). Whilst, Ex-4 did not modify secretory currents evoked by the cholinergic agonist, carbachol ($n = 6$, $p = 0.0815$, **Figure 5B**), currents evoked by the Na^+ channel agonist, veratridine were potentiated ($n = 8$, $p = 0.0085$, **Figure 5C**). The afferent nerve stimulant, capsaicin evokes a biphasic secretory and anti-secretory response in colonic tissue. Ex-4 enhanced both the initial secretory phase ($n = 6$, $p = 0.0156$) and the anti-secretory response ($p = 0.0462$, **Figure 5D**). Moreover, the relative change in transepithelial resistance (TER), which is a measure of gut leakiness, throughout the experiment (60–90 min), increased in tissues continuously exposed to Ex-4 ($n = 8$, $p < 0.05$) compared to the saline-treated control preparations, which showed no change (**Figure 5E**). This finding suggests that the sustained presence of a GLP-1R agonist reduces colonic permeability.

DISCUSSION

An intact gut epithelium preserves the immunological exclusion of "non-self" entities in the external environment of the gut lumen. However, despite this physiological defense mechanism, information flows continuously across this interface. Enteroendocrine cells sense stimuli such as nutrients, inflammatory products, irritants, and microbial factors and respond by releasing hormones on the basolateral side of the gut barrier to evoke physiological responses (Gribble and Reimann, 2016). Some sensory epithelial cells, such as serotonin-secreting enterochromaffin cells (Bellono et al., 2017) and GLP-1-secreting L-cells (Bohórquez et al., 2015) form direct neural connections with afferent and efferent nerve fibers, meaning they are well equipped to translate luminal signals across an intact gut barrier to the host nervous system. In this study, we have investigated the potential of GLP-1 as a cross-barrier signaling molecule with stimulatory actions both on colonic afferents signaling to the CNS and locally, on submucosal neurons. The neurostimulatory actions of the bacterial metabolite, indole and GLP-1-secreting *L. paracasei* from the luminal side of the colon have been observed. Moreover, we have noted the need for an intact epithelium. Combined with the role of neuronal GLP-1R activation, our data implicates L-cells as cellular transducers that couple microbial signaling molecules with activation of the host peripheral nervous system.

Acute exposure to indole stimulated basolateral secretion of GLP-1 from rat colonic tissue, which is likely to be mediated through direct activation of L-cells by indole (Chimerel et al., 2014) but could also be through indirect mechanisms. Indeed, indole can modify epithelial cells and tight junction proteins (Bansal et al., 2010). Consistent with the importance of the vagus in informing the CNS about changes in the gut microbiome (Bercik et al., 2011; Bravo et al., 2011; Riley et al., 2013), electrophysiological studies demonstrated that application of indole to the mucosa, but not directly onto exposed intrinsic or extrinsic neurons, resulted in GLP-1R-dependent activation of vagal afferents. In terms of gut-brain axis wiring, most innervation of small intestinal epithelial cells is by submucosal neurons (Keast et al., 1984; Ekblad et al., 1987) and intrinsic primary afferent neurons may act as the starting point in gut-brain signaling (Perez-Burgos et al., 2014). Interestingly, longer exposure times suppress GLP-1 release (Chimerel et al., 2014), which may be important in gut-brain signaling regulation.

Mechanistically, inhibition of indole-evoked stimulation of vagal afferents in hemisected SMP tissue with tetrodotoxin indicates the role of action potentials in signal generation. However, when the epithelial layer was left intact, tetrodotoxin did not modify vagal activation by indole. This is consistent with nerve endings terminating below the epithelium and further implicates cells embedded in the epithelium in cross-barrier signaling. We also found that mucosally-applied Ex-4 and GLP-1-secreting *L. paracasei* evoked vagal firing in colonic tissue with an intact epithelium, which may be mediated through activation of GLP-1Rs on L-cells leading to basolateral secretion of GLP-1 and subsequent activation of vagal afferents (Bohórquez et al., 2015). Indeed, the effects of *L. paracasei*, which was applied to colonic sections with intact mucosa, were attenuated by the GLP-1R antagonist.

Application of indole to submucosal neurons, which lie in closest proximity to the mucosal layer and regulate absorpto-secretory function in the gut, had no impact on neuronal calcium levels in the absence of the epithelium. However, in contrast to the indirect mechanism underlying indole-evoked activation of the vagus nerve, submucosal neurons in hemisected tissue preparations were not activated by indole either, although we acknowledge that carrying out these studies at room temperature may have had an impact on temperature-sensitive elements. Nonetheless, the mucosal application of indole did enhance both the amplitude and duration of Ex-4-evoked calcium responses. This change in intracellular calcium levels could reflect slow excitatory postsynaptic potentials, slow inhibitory postsynaptic potentials or inhibitory slow after hyperpolarization seen in intrinsic primary afferent neurons, which are all dependent upon changes in intracellular calcium. Further studies will be needed to specifically determine which neuronal subtypes are affected. GLP-1R expression was increased in submucosal ganglia, which given the brief timeframe is likely to be due to the trafficking of GLP-1Rs to the cell membrane (Jones et al.,

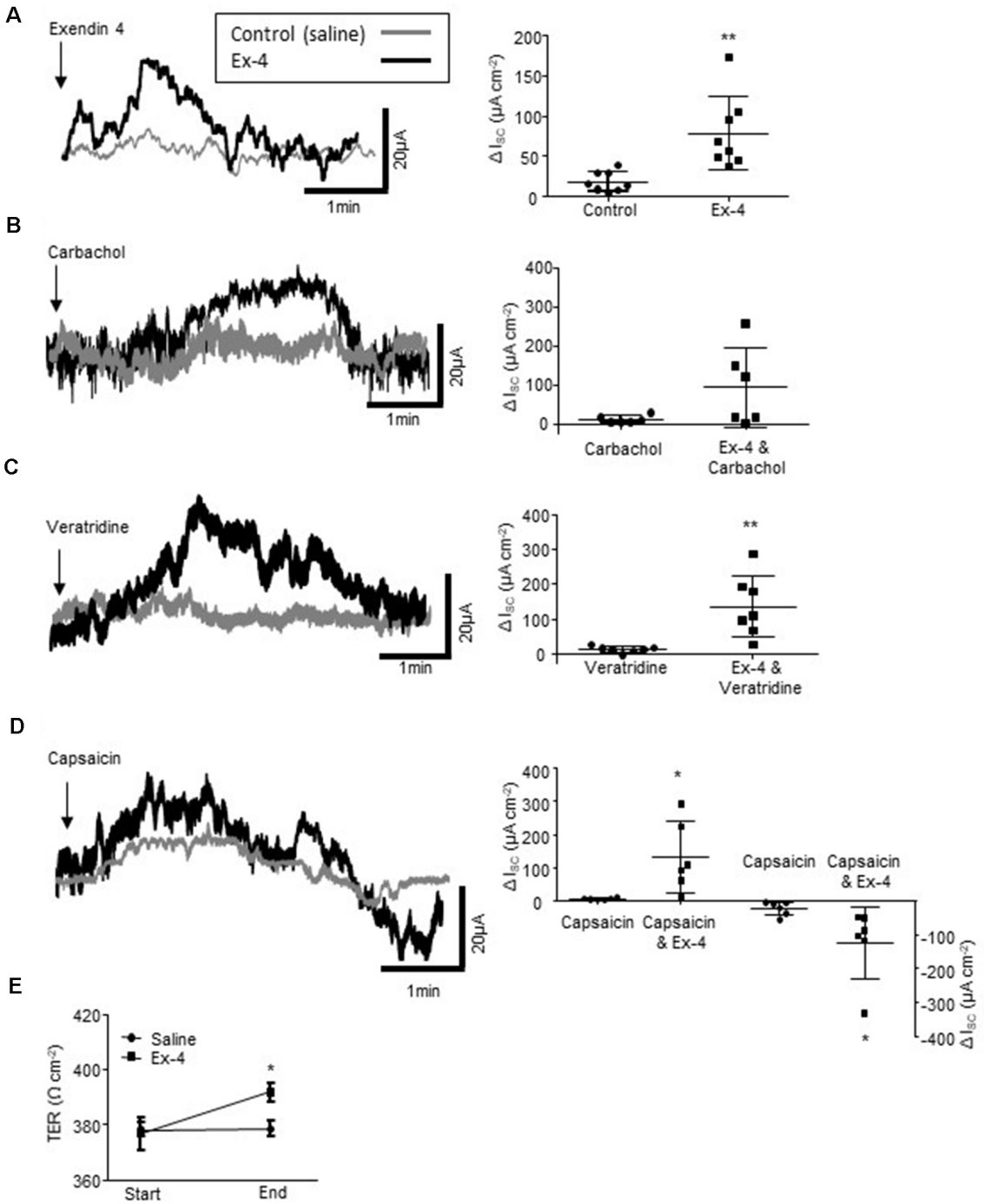


FIGURE 5 | Exendin-4 enhances colonic secretory currents. **(A)** The representative secretory traces from Ussing chamber studies and the associated scatter plots illustrate the secretory current evoked by the GLP-1R agonist, exendin 4 (Ex-4, 10 μM, $n = 8$). **(B)** Ex-4 does not modify the cholinergically-mediated secretory current (I_{SC}) evoked by carbachol (10 μM, $n = 8$) but enhances currents evoked by the **(C)** sodium channel agonist, veratridine (10 μM, $n = 8$) and **(D)** the sensory nerve stimulant, capsaicin (1 μM, $n = 8$). **(E)** Ex-4 also increases transepithelial resistance (TER) throughout an experiment (60–90 min). $^*p < 0.05$, $^{**}p < 0.01$.

2018). Comparable to the neurostimulatory effects of GLP-1 in the nodose ganglia (Kakei et al., 2002) and central neurons (Ma et al., 2007), Ex-4 stimulated a robust increase in $[Ca^{2+}]_i$ in submucosal neurons. This was dependent upon activation of GLP-1Rs, which we and others (Kedees et al., 2013) have detected on submucosal neurons. Mucosal application of the secretory products of GLP-1-secreting *L. paracasei* similarly resulted in increased membrane expression of GLP-1R immunolabeling in

submucosal ganglia, and evoked a GLP-1R-dependent calcium response. Although the ability of this engineered bacteria to modulate host physiology has been reported (Ryan et al., 2017), the mechanisms of action had not previously been elucidated. L-cells are reported to express a variety of receptors (Reimann et al., 2008; Tolhurst et al., 2012) but a study in mice indicated they do not express GLP-1Rs (Grigoryan et al., 2012). By contrast, we detected that some, but not all GLP-1-immuno-labeled L-cells in rat colon expressed GLP-1Rs. Thus, GLP-1 secreted luminally by *L. paracasei* could stimulate the basolateral release of GLP-1 from L-cells in an autocrine manner, which in turn could activate intrinsic and extrinsic neurons. Pharmacological characterization of the Ex-4-evoked calcium response revealed that both, calcium release from intracellular stores and influx from extracellular sources, contributes to the response. The downstream signaling molecule, PI 3-kinase appears to play a role in Ex-4-induced activation of submucosal neurons and the STAT3 inhibitor attenuated, but did not abolish, the calcium response.

In terms of the known consequences of the neurostimulatory actions of the GLP-1 agonist on GI function, GLP-1 suppresses GI contractile activity (Schirra et al., 2006; Hellström et al., 2008), but less was known about the actions of GLP-1 on intestinal secretory activity (Baldassano et al., 2012). Bearing in mind potential confounders of *ex vivo* experiments, including a lack of circulation and the possible deterioration of tissue integrity, we demonstrated that Ex-4 induced a secretory current and enhanced secretion evoked by the voltage-sensitive Na^+ channel agonist, veratridine and capsaicin, which is known to activate vagal afferents (Blackshaw et al., 2000); findings that are consistent with the stimulatory effects of Ex-4 on submucosal neurons. Similar to a previous study (Baldassano et al., 2012), we did not find that GLP-1 impacted on carbachol-evoked secretory responses. However, consistent with our finding that indole enhanced the amplitude and duration of Ex-4-evoked calcium responses in submucosal neurons, microbial-sensing by L-cells may result in enhancement of neurally-regulated colonic secretion. Indeed, acute application of indole prolongs GLP-1 secretion from L-cells (Chimerel et al., 2014). Ex-4 increased colonic TER, indicating that the gut was less permeable. This may reflect a local protective response to prevent penetration of the gut by bacterial products and contribute to the anti-inflammatory actions of Ex-4 in the intestine (Kissow et al., 2013).

CONCLUSION

These studies implicate GLP-1 as a signaling molecule in cross-barrier communication between luminal bacteria and the host peripheral and central nervous systems. Strengths of our experimental design include the ability to record nerve fiber activity signaling to the CNS from the distal colon in real-time, although a lack of pre-planned power calculations for these studies is a design limitation. Understanding this mechanism may be important in appreciating the pathophysiology of several diseases, particularly those associated with microbial dysbiosis. Indeed, in diarrhea-predominant IBS, tryptophan, the precursor of indole is elevated (Christmas et al., 2010). Moreover, increased numbers of afferent neurons expressing GLP-1Rs have been reported in inflammatory bowel disease, which may be important in relaying visceral pain signals in the diseased gut (Anand et al., 2018). Thus, microbial sensing by L-cells and subsequent activation of colonic afferents and local enteric neurons by GLP-1 may play a key role in neural dysregulation of gut function.

DATA AVAILABILITY STATEMENT

The datasets generated for this study are available on request to the corresponding author.

ETHICS STATEMENT

The animal study was reviewed and approved by University College Cork Animal Experimentation Ethics Committee.

AUTHOR CONTRIBUTIONS

MB, RO'B, and EB: generated and analyzed data. RR and CS: provided probiotics. JB: tissue samples. DO'M: generated and analyzed data, supervised study, drafted the manuscript.

FUNDING

This work is supported by SFI-HRB-Wellcome research partnership (108228/Z/15/Z Seed Award), APC MI (12/RC/2273) and the Department of Physiology, University College Cork.

REFERENCES

Anand, U., Yiangou, Y., Akbar, A., Quick, T., MacQuillan, A., Fox, M., et al. (2018). Glucagon-like peptide 1 receptor (GLP-1R) expression by nerve fibres in inflammatory bowel disease and functional effects in cultured neurons. *PLoS One* 13:e0198024. doi: 10.1371/journal.pone.0198024

Baldassano, S., Wang, G. D., Mulè, F., and Wood, J. D. (2012). Glucagon-like peptide-1 modulates neurally-evoked mucosal chloride secretion in guinea pig small intestine *in vitro*. *Am. J. Physiol. Gastrointest. Liver Physiol.* 302, G352–G358. doi: 10.1152/ajpgi.00333.2011

Bansal, T., Alaniz, R. C., Wood, T. K., and Jayaraman, A. (2010). The bacterial signal indole increases epithelial-cell tight-junction resistance and attenuates indicators of inflammation. *Proc. Natl. Acad. Sci. U S A* 107, 228–233. doi: 10.1073/pnas.0906112107

Bellono, N. W., Bayrer, J. R., Leitch, D. B., Castro, J., Zhang, C., O'Donnell, T. A., et al. (2017). Enterochromaffin cells are gut chemosensors that couple to sensory neural pathways. *Cell* 170, 185.e16–198.e16. doi: 10.1016/j.cell.2017.05.034

Bercik, P., Park, A. J., Sinclair, D., Khoshdel, A., Lu, J., Huang, X., et al. (2011). The anxiolytic effect of Bifidobacterium longum NCC3001 involves vagal pathways for gut-brain communication. *Neurogastroenterol. Motil.* 23, 1132–1139. doi: 10.1111/j.1365-2982.2011.01796.x

Blackshaw, L. A., Page, A. J., and Partosoedarso, E. R. (2000). Acute effects of capsaicin on gastrointestinal vagal afferents. *Neuroscience* 96, 407–416. doi: 10.1016/s0306-4522(99)00547-3

Bohórquez, D. V., Shahid, R. A., Erdmann, A., Kreger, A. M., Wang, Y., Calakos, N., et al. (2015). Neuroepithelial circuit formed by innervation of sensory enteroendocrine cells. *J. Clin. Invest.* 125, 782–786. doi: 10.1172/JCI78361

Bravo, J. A., Forsythe, P., Chew, M. V., Escaravage, E., Savignac, H. M., Dinan, T. G., et al. (2011). Ingestion of Lactobacillus strain regulates emotional behavior and central GABA receptor expression in a mouse *via* the vagus nerve. *Proc. Natl. Acad. Sci. U S A* 108, 16050–16055. doi: 10.1073/pnas.1102999108

Buckley, M. M., and O'Malley, D. (2018). Development of an *ex vivo* method for multi-unit recording of microbiota-colonic-neural signaling in real time. *Front. Neurosci.* 12:112. doi: 10.3389/fnins.2018.00112

Cani, P. D., Joly, E., Horsmans, Y., and Delzenne, N. M. (2006). Oligofructose promotes satiety in healthy human: a pilot study. *Eur. J. Clin. Nutr.* 60, 567–572. doi: 10.1038/sj.ejcn.1602350

Chimerel, C., Emery, E., Summers, D. K., Keyser, U., Gribble, F. M., and Reimann, F. (2014). Bacterial metabolite indole modulates incretin secretion from intestinal enteroendocrine L cells. *Cell Rep.* 9, 1202–1208. doi: 10.1016/j.celrep.2014.10.032

Christmas, D. M., Badawy, A. A., Hince, D., Davies, S. J., Probert, C., Creed, T., et al. (2010). Increased serum free tryptophan in patients with diarrhea-predominant irritable bowel syndrome. *Nutr. Res.* 30, 678–688. doi: 10.1016/j.nutres.2010.09.009

Dinan, T. G., and Cryan, J. F. (2013). Melancholic microbes: a link between gut microbiota and depression? *Neurogastroenterol. Motil.* 25, 713–719. doi: 10.1111/nmo.12198

Dinan, T. G., and Cryan, J. F. (2017). Gut instincts: microbiota as a key regulator of brain development, ageing and neurodegeneration. *J. Physiol.* 595, 489–503. doi: 10.1113/JP273106

Duca, F. A., Sakar, Y., and Covasa, M. (2013). Combination of obesity and high-fat feeding diminishes sensitivity to GLP-1R agonist exendin-4. *Diabetes* 62, 2410–2415. doi: 10.2337/db12-1204

Ekblad, E., Winther, C., Ekman, R., Håkanson, R., and Sundler, F. (1987). Projections of peptide-containing neurons in rat small intestine. *Neuroscience* 20, 169–188. doi: 10.1016/0306-4522(87)90010-8

Gareau, M. G., Jury, J., and Perdue, M. H. (2007). Neonatal maternal separation of rat pups results in abnormal cholinergic regulation of epithelial permeability. *Am. J. Physiol. Gastrointest. Liver Physiol.* 293, G198–G203. doi: 10.1152/ajpgi.00392.2006

Gibson, G. R., and Roberfroid, M. B. (1995). Dietary modulation of the human colonic microbiota: introducing the concept of prebiotics. *J. Nutr.* 125, 1401–1412. doi: 10.1093/jn/125.6.1401

Gribble, F. M., and Reimann, F. (2016). Enteroendocrine cells: chemosensors in the intestinal epithelium. *Annu. Rev. Physiol.* 78, 277–299. doi: 10.1146/annurev-physiol-021115-105439

Grigoryan, M., Kedees, M. H., Charron, M. J., Guz, Y., and Teitelman, G. (2012). Regulation of mouse intestinal L cell progenitors proliferation by the glucagon family of peptides. *Endocrinology* 153, 3076–3088. doi: 10.1210/en.2012-1120

Hansen, C. F., Vrang, N., Sangild, P. T., and Jelsing, J. (2013). Novel insight into the distribution of L-cells in the rat intestinal tract. *Am. J. Transl. Res.* 5, 347–358.

Harada, K., Sada, S., Sakaguchi, H., Takizawa, M., Ishida, R., and Tsuboi, T. (2018). Bacterial metabolite S-equol modulates glucagon-like peptide-1 secretion from enteroendocrine L cell line GLUTag cells *via* actin polymerization. *Biochem. Biophys. Res. Commun.* 501, 1009–1015. doi: 10.1016/j.bbrc.2018.05.100

Hellström, P. M., Naslund, E., Edholm, T., Schmidt, P. T., Kristensen, J., Theodorsson, E., et al. (2008). GLP-1 suppresses gastrointestinal motility and inhibits the migrating motor complex in healthy subjects and patients with irritable bowel syndrome. *Neurogastroenterol. Motil.* 20, 649–659. doi: 10.1111/j.1365-2982.2007.01079.x

Jaglin, M., Rhimi, M., Philippe, C., Pons, N., Bruneau, A., Goustard, B., et al. (2018). Indole, a signaling molecule produced by the gut microbiota, negatively impacts emotional behaviors in rats. *Front. Neurosci.* 12:216. doi: 10.3389/fnins.2018.00216

Jones, B., Buenaventura, T., Kanda, N., Chabosseau, P., Owen, B. M., Scott, R., et al. (2018). Targeting GLP-1 receptor trafficking to improve agonist efficacy. *Nat. Commun.* 9:1602. doi: 10.1038/s41467-018-03941-2

Kaelberer, M. M., Buchanan, K. L., Klein, M. E., Barth, B. B., Montoya, M. M., Shen, X., et al. (2018). A gut-brain neural circuit for nutrient sensory transduction. *Science* 361:eaat5236. doi: 10.1126/science.aat5236

Kakei, M., Yada, T., Nakagawa, A., and Nakabayashi, H. (2002). Glucagon-like peptide-1 evokes action potentials and increases cytosolic Ca^{2+} in rat nodose ganglion neurons. *Auton. Neurosci.* 102, 39–44. doi: 10.1016/s1566-0702(02)00182-0

Keast, J. R., Furness, J. B., and Costa, M. (1984). Origins of peptide and norepinephrine nerves in the mucosa of the guinea pig small intestine. *Gastroenterology* 86, 637–644. doi: 10.1016/s0016-5085(84)break80111-0

Kedees, M. H., Guz, Y., Grigoryan, M., and Teitelman, G. (2013). Functional activity of murine intestinal mucosal cells is regulated by the glucagon-like peptide-1 receptor. *Peptides* 48, 36–44. doi: 10.1016/j.peptides.2013.07.022

Kissow, H., Hartmann, B., Holst, J. J., and Poulsen, S. S. (2013). Glucagon-like peptide-1 as a treatment for chemotherapy-induced mucositis. *Gut* 62, 1724–1733. doi: 10.1136/gutjnl-2012-303280

Kuhre, R. E., Frost, C. R., Svendsen, B., and Holst, J. J. (2015). Molecular mechanisms of glucose-stimulated GLP-1 secretion from perfused rat small intestine. *Diabetes* 64, 370–382. doi: 10.2337/db14-0807

Ma, X., Bruning, J., and Ashcroft, F. M. (2007). Glucagon-like peptide 1 stimulates hypothalamic proopiomelanocortin neurons. *J. Neurosci.* 27, 7125–7129. doi: 10.1523/JNEUROSCI.1025-07.2007

Mao, Y. K., Kasper, D. L., Wang, B., Forsythe, P., Bienenstock, J., and Kunze, W. A. (2013). Bacteroides fragilis polysaccharide A is necessary and sufficient for acute activation of intestinal sensory neurons. *Nat. Commun.* 4:1465. doi: 10.1038/ncomms2478

McVey Neufeld, K. A., Mao, Y. K., Bienenstock, J., Foster, J. A., and Kunze, W. A. (2013). The microbiome is essential for normal gut intrinsic primary afferent neuron excitability in the mouse. *Neurogastroenterol. Motil.* 25:183–e88. doi: 10.1111/nmo.12049

Nakagawa, A., Satake, H., Nakabayashi, H., Nishizawa, M., Furuya, K., Nakano, S., et al. (2004). Receptor gene expression of glucagon-like peptide-1, but not glucose-dependent insulinotropic polypeptide, in rat nodose ganglion cells. *Auton. Neurosci.* 110, 36–43. doi: 10.1016/j.autneu.2003.11.001

O'Brien, R., Buckley, M. M., Kelliher, A., and O'Malley, D. (2019). PI 3-kinase- and ERK-MAPK-dependent mechanisms underlie Glucagon-Like Peptide-1-mediated activation of Sprague Dawley colonic myenteric neurons. *Neurogastroenterol. Motil.* 31:e13631. doi: 10.1111/nmo.13631

O'Malley, D., Dinan, T. G., and Cryan, J. F. (2011a). Altered expression and secretion of colonic interleukin-6 in a stress-sensitive animal model of brain-gut axis dysfunction. *J. Neuroimmunol.* 235, 48–55. doi: 10.1016/j.jneuroim.2011.04.003

O'Malley, D., Liston, M., Hyland, N. P., Dinan, T. G., and Cryan, J. F. (2011b). Colonic soluble mediators from the maternal separation model of irritable bowel syndrome activate submucosal neurons *via* an interleukin-6-dependent mechanism. *Am. J. Physiol. Gastrointest. Liver Physiol.* 300, G241–G252. doi: 10.1152/ajpgi.00385.2010

Pérez-Berezo, T., Pujo, J., Martin, P., Le Faouder, P., Galano, J. M., Guy, A., et al. (2017). Identification of an analgesic lipopeptide produced by the probiotic Escherichia coli strain Nissle 1917. *Nat. Commun.* 8:1314. doi: 10.1038/s41467-017-01403-9

Perez-Burgos, A., Mao, Y. K., Bienenstock, J., and Kunze, W. A. (2014). The gut-brain axis rewired: adding a functional vagal nicotinic "sensory synapse". *FASEB J.* 28, 3064–3074. doi: 10.1096/fj.13-245282

Perez-Burgos, A., Wang, B., Mao, Y. K., Mistry, B., McVey Neufeld, K. A., Bienenstock, J., et al. (2013). Psychoactive bacteria Lactobacillus rhamnosus (JB-1) elicits rapid frequency facilitation in vagal afferents. *Am. J. Physiol. Gastrointest. Liver Physiol.* 304, G211–G220. doi: 10.1152/ajpgi.00128.2012

Pusceddu, M. M., Barboza, M., Keogh, C. E., Schneider, M., Stokes, P., Sladek, J. A., et al. (2019). Nod-like receptors are critical for gut-brain axis signalling in mice. *J. Physiol.* 597, 5777–5797. doi: 10.1113/JP278640

Reimann, F., Habib, A. M., Tolhurst, G., Parker, H. E., Rogers, G. J., and Gribble, F. M. (2008). Glucose sensing in L cells: a primary cell study. *Cell Metab.* 8, 532–539. doi: 10.1016/j.cmet.2008.11.002

Richards, W., Hillsley, K., Eastwood, C., and Grundy, D. (1996). Sensitivity of vagal mucosal afferents to cholecystokinin and its role in afferent signal transduction in the rat. *J. Physiol.* 497, 473–481. doi: 10.1113/jphysiol.1996.sp021781

Riley, T. P., Neal-McKinney, J. M., Buelow, D. R., Konkel, M. E., and Simasko, S. M. (2013). Capsaicin-sensitive vagal afferent neurons contribute to the detection of pathogenic bacterial colonization in the gut. *J. Neuroimmunol.* 257, 36–45. doi: 10.1016/j.jneuroim.2013.01.009

Ryan, P. M., Patterson, E., Kent, R. M., Stack, H., O'Connor, P. M., Murphy, K., et al. (2017). Recombinant incretin-secreting microbe improves metabolic dysfunction in high-fat diet fed rodents. *Sci. Rep.* 7:13523. doi: 10.1038/s41598-017-14010-x

Schirra, J., Nicolaus, M., Roggel, R., Katschinski, M., Storr, M., Woerle, H. J., et al. (2006). Endogenous glucagon-like peptide 1 controls endocrine pancreatic secretion and antro-pyloro-duodenal motility in humans. *Gut* 55, 243–251. doi: 10.1136/gut.2004.059741

Stilling, R. M., Dinan, T. G., and Cryan, J. F. (2016). The brain's Geppetto-microbes as puppeteers of neural function and behaviour? *J. Neurovirol.* 22, 14–21. doi: 10.1007/s13365-015-0355-x

Sun, E. W., de Fontgalland, D., Rabbitt, P., Hollington, P., Sposato, L., Due, S. L., et al. (2017). Mechanisms controlling glucose-induced GLP-1 secretion in human small intestine. *Diabetes* 66, 2144–2149. doi: 10.2337/db17-0058

Tolhurst, G., Heffron, H., Lam, Y. S., Parker, H. E., Habib, A. M., Diakogiannaki, E., et al. (2012). Short-chain fatty acids stimulate glucagon-like peptide-1 secretion *via* the G-protein-coupled receptor FFAR2. *Diabetes* 61, 364–371. doi: 10.2337/db11-1019

Wichmann, A., Allahyar, A., Greiner, T. U., Plovier, H., Lunden, G. Ö., Larsson, T., et al. (2013). Microbial modulation of energy availability in the colon regulates intestinal transit. *Cell Host Microbe.* 14, 582–590. doi: 10.1016/j.chom.2013.09.012

Yano, J. M., Yu, K., Donaldson, G. P., Shastri, G. G., Ann, P., Ma, L., et al. (2015). Indigenous bacteria from the gut microbiota regulate host serotonin biosynthesis. *Cell* 161, 264–276. doi: 10.1016/j.cell.2015.02.047

Conflict of Interest: The authors declare that the research was conducted in the absence of any commercial or financial relationships that could be construed as a potential conflict of interest.

Copyright © 2020 Buckley, O'Brien, Brosnan, Ross, Stanton, Buckley and O'Malley. This is an open-access article distributed under the terms of the Creative Commons Attribution License (CC BY). The use, distribution or reproduction in other forums is permitted, provided the original author(s) and the copyright owner(s) are credited and that the original publication in this journal is cited, in accordance with accepted academic practice. No use, distribution or reproduction is permitted which does not comply with these terms.

frontiers in Cellular Neuroscience

ORIGINAL RESEARCH
published: 19 May 2020
doi: 10.3389/fncel.2020.00135

Modeling a Nociceptive Neuro-Immune Synapse Activated by ATP and 5-HT in Meninges: Novel Clues on Transduction of Chemical Signals Into Persistent or Rhythmic Neuronal Firing

*Alina Suleimanova[1], Max Talanov[1], Oleg Gafurov[1], Fail' Gafarov[1], Ksenia Koroleva[1], Anaïs Virenque[2], Francesco M. Noe[2], Nikita Mikhailov[3], Andrea Nistri[4] and Rashid Giniatullin[1,3]**

[1]Laboratory of Neurobiology, Kazan Federal University, Kazan, Russia, [2]Neuroscience Center, Helsinki University, Helsinki, Finland, [3]A.I. Virtanen Institute for Molecular Sciences, University of Eastern Finland, Kuopio, Finland, [4]Department of Neuroscience, International School for Advanced Studies, Trieste, Italy

OPEN ACCESS

Edited by:
Francesco Moccia,
University of Pavia, Italy

Reviewed by:
Yuriy Pankratov,
University of Warwick,
United Kingdom
Elsa Fabbretti,
University of Trieste, Italy

***Correspondence:**
Rashid Giniatullin
rashid.giniatullin@uef.fi

Specialty section:
This article was submitted to Cellular Neurophysiology, a section of the journal Frontiers in Cellular Neuroscience

Received: 02 March 2020
Accepted: 22 April 2020
Published: 19 May 2020

Citation:
Suleimanova A, Talanov M, Gafurov O, Gafarov F, Koroleva K, Virenque A, Noe FM, Mikhailov N, Nistri A and Giniatullin R (2020) Modeling a Nociceptive Neuro-Immune Synapse Activated by ATP and 5-HT in Meninges: Novel Clues on Transduction of Chemical Signals Into Persistent or Rhythmic Neuronal Firing. Front. Cell. Neurosci. 14:135. doi: 10.3389/fncel.2020.00135

Extracellular ATP and serotonin (5-HT) are powerful triggers of nociceptive firing in the meninges, a process supporting headache and whose cellular mechanisms are incompletely understood. The current study aimed to develop, with the neurosimulator NEURON, a novel approach to explore in silico the molecular determinants of the long-lasting, pulsatile nature of migraine attacks. The present model included ATP and 5-HT release, ATP diffusion and hydrolysis, 5-HT uptake, differential activation of ATP P2X or 5-HT3 receptors, and receptor subtype-specific desensitization. The model also tested the role of branched meningeal fibers with multiple release sites. Spike generation and propagation were simulated using variable contribution by potassium and sodium channels in a multi-compartment fiber environment. Multiple factors appeared important to ensure prolonged nociceptive firing potentially relevant to long-lasting pain. Crucial roles were observed in: (i) co-expression of ATP P2X2 and P2X3 receptor subunits; (ii) intrinsic activation/inactivation properties of sodium Nav1.8 channels; and (iii) temporal and spatial distribution of ATP/5-HT release sites along the branches of trigeminal nerve fibers. Based on these factors we could obtain either persistent activation of nociceptive firing or its periodic bursting mimicking the pulsating nature of pain. In summary, our model proposes a novel tool for the exploration of peripheral nociception to test the contribution of clinically relevant factors to headache including migraine pain.

Keywords: model, migraine, trigeminal nerve, mast cells, ATP, 5-HT

INTRODUCTION

The mechanisms responsible for migraine pain, a common and devastating condition, remain poorly understood. Nevertheless, the prevailing opinion suggests that one major component of migraine pain originates from the trigeminal nerve fibers located in meningeal tissues to send nociceptive signals to brainstem nuclei (Messlinger, 2009; Olesen et al., 2009; Pietrobon and Moskowitz, 2013; Zakharov et al., 2015). The meninges harbor a large population of mast cells, which can release various chemicals that activate nearby nerve fibers (Levy et al., 2007; Theoharides et al., 2007; Kilinc et al., 2017). According to the original purinergic hypothesis of migraine (Burnstock, 1981), extracellular ATP (eATP) is one such player for the onset of migraine pathology. In fact, in addition to the effect of eATP on blood vessels (Burnstock, 1981), this endogenous purine can interact with pro-nociceptive P2X3 receptors located almost exclusively on sensory neurons (Cockayne et al., 2000; Souslova et al., 2000), indicating P2X3 receptors as important contributors to pain generation.

Previous studies have described the unique properties of P2X3 receptors including fast activation and desensitization and slow rate of resensitization (Chen et al., 1995; Lewis et al., 1995; Vulchanova et al., 1996; Jin et al., 2004; Burnstock, 2008; Giniatullin and Nistri, 2013). To describe these characteristics, we developed a cyclic model for the function of P2X3 receptors that closely replicates P2X3 mediated responses (Sokolova et al., 2006). However, the original data used for modeling were obtained from cultured sensory neurons and recombinant receptor systems, leaving open the question of their *in vivo* applicability. One paradox (North, 2004) that remains unsolved is how the strong desensitization of P2X3 receptors commonly observed with a patch-clamp recording from cultured neurons is compatible with the well-known role of this ATP-driven receptor in sustained pain signaling (Cockayne et al., 2000; Souslova et al., 2000).

Our recent work has further supported the purinergic hypothesis of migraine by showing the ability of ATP and its chemical analogs to trigger persistent spiking in trigeminal nerve fibers present in the whole-mount rat meninges (Yegutkin et al., 2016). Furthermore, using mast cell-deficient mice, we have shown that eATP could activate trigeminal nerves both directly as well as *via* release of 5-hydroxytryptamine (5-HT) originating from degranulation by immune cells (Koroleva et al., 2019). Interestingly, 5-HT is not only a powerful trigger for prolonged nociceptive firing in meningeal afferents (Kilinc et al., 2017) but also a well-known sensitizing agent (Vaughn and Gold, 2010).

The complex interplay among ATP, 5-HT, and their mast cell release process remains, however, to be elucidated. To address this complex phenomenon, the present study applied a modeling approach to explore the impact of ATP and 5-HT release from immune cells (meningeal mast cells), ATP hydrolysis and diffusion, 5-HT uptake, ATP-activated P2X3 (Sokolova et al., 2006) and P2X2 receptors (Simonetti et al., 2006; Moffatt and Hume, 2007), and of 5-HT-activated 5-HT3 receptors (Corradi et al., 2009). In addition to the standard role of sodium and potassium channels in membrane excitability, former modeling studies have highlighted the importance of certain subtypes of the sodium channel in coding sensory information by nociceptive sensory neurons. Thus, one computational model has described their role in sensory signaling by dorsal DRG neurons innervating the urinary bladder (Mandge and Manchanda, 2018). Zhao et al. (2016) have shown that the density of sodium channels determines the fidelity and precision of neuronal sensory coding. Likewise, the model of C-fibers by Tigerholm et al. (2014) has shown the characteristics of axonal spike propagation in human C-nociceptors. Whereas several subtypes of sodium channel are expressed by nociceptive neurons, the subtypes Nav1.7 and Nav1.8 play are particularly important ones for generation and propagation of action potentials (Choi and Waxman, 2011). For instance, Tanaka et al. (2017) have shown the key role of sodium Nav1.7 channels in several pathological pain syndromes.

The current report provides novel information concerning not only fundamental molecular properties but also strategic topography of neuro-immune crosstalk underlying purinergic and serotonergic signaling and their impact on voltage-gated channels that may contribute to the peripheral mechanisms of migraine pain.

MATERIALS AND METHODS

Model of Meningeal Nociception

To simulate rat meningeal trigeminal fiber activity, we used the NEURON environment version 7.5 (Hines and Carnevale, 2003). The fiber was assumed to be 3 cm long (Messlinger, 2009) with a diameter from 0.25 to 2 μm corresponding to C- and Adelta-fibers, respectively. All A-fibers in the dura belong to the Adelta subtype and are known to be present in the meninges (Strassman et al., 2004). **Figure 1B** shows the basic features of the model with the fiber (green) surrounded by a mast cell containing the secretory vesicles (as sources of eATP or 5-HT; Yegutkin et al., 2016; Kilinc et al., 2017) and forming the neuro-immune synapse (Giniatullin et al., 2019; Koroleva et al., 2019; Nurkhametova et al., 2019). Each segment of the fiber is referred to as a compartment and is indicated as a green rectangle (0.25 μm wide and 250 μm long). In our preliminary tests, we found just one P2X3 receptor in the compartment to be sufficient to depolarize the membrane potential up to the spike threshold (**Figure 1D**). The properties of the following sodium and potassium channels examined in the present report are listed in **Supplementary Table S1**: Nav1.7 (Tigerholm et al., 2014), Nav1.8 (Balbi et al., 2017), Nav1.3 (Cummins et al., 2001), potassium delayed rectifier (K-DR; Tigerholm et al., 2014) and A-type currents (Gasparini et al., 2004).

It has been previously shown that meningeal nerves often branch to make a sort of "neuronal dendritic tree" (Schueler et al., 2014). Thus, we simulated a dendritic tree of the trigeminal nerve fiber with two branches. The tree was 3 cm long and comprised 170 compartments: main dendrite (70 compartments), and each branch with 50 compartments (example in **Figure 6B**). Two branches of the trigeminal nerve were joined at 1.75 cm from the trigeminal ganglion (TG). This is a site that can block the propagation of neuronal signals in the refractory state (Schueler et al., 2014). This property was

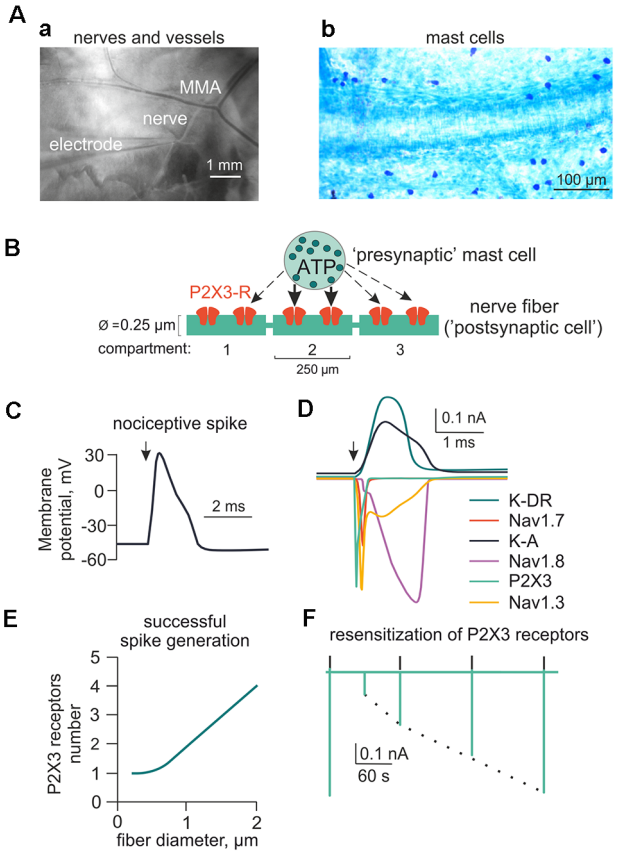


FIGURE 1 | Main components of the model for ATP-induced activation of meningeal afferent (nerve fibers). **(A)** The experimental approach of meningeal spike recording by glass electrode from the local nerve **(Aa)** and the image of meninges with labeled mast cells **(Ab)**. MMA—main meningeal artery. **(B)** Schematic presentation of the model neuroimmune synapse with a mast cell ("presynaptic cell") as the source of the transmitter of ATP (or 5-HT) and meningeal nerve fiber ("postsynaptic cell") consisting of several compartments with ATP-gated P2X3 receptors. **(C)** Changes in the membrane potential of the nerve fiber (spike generation) triggered by activation of the P2X3 receptor. **(D)** Ionic currents through several subtypes of sodium, potassium, and P2X3 receptor channels. **(E)** The graph showing the number of P2X3 receptors required to trigger a spike as a function of nerve fiber diameter. **(F)** The kinetics of P2X3 receptor-induced currents and the recovery time course from desensitization.

further explored in simulation experiments. To implement the ATP induced activation of nerve fibers, we integrated the cyclic scheme of the P2X3 receptor operation (Sokolova et al., 2006) into the model. To simulate ATP release from mast cells, we used the 3D diffusion model described by Saftenku (2005) which is based on the following equation:

$$C(x,y,z,t) = 2\frac{M}{(4\pi Dt)^{3/2}}\exp\left(-kt - \frac{x^2+y^2+z^2}{4Dt}\right)$$

where C is the concentration of ATP, D is the diffusion coefficient (0.8 μm2/ms, Helenius et al., 2002), k is the degradation coefficient (Suleymanov et al., 2015), M is the initial amount of ATP released from mast cells, x, y, z are the space coordinates and t stands for time. The ATP profile in the model was simulated as instant rise and slow decay determined by diffusion.

Experimental Part

The experimental part was performed on 10–12-week-old male WT C57BL/6J mice and adult Wistar rats provided by the Animal Facilities of the University of Eastern Finland (UEF). All procedures were approved by the Committee for the Welfare of Laboratory Animals of the University of Eastern Finland and the Provincial Government of Kuopio. Experiments were conducted according to the European Community Council guidelines (Directives 86/609/EEC). All efforts were made to minimize the number of animals used and their suffering.

Recording of Spikes From Meningeal Afferents

For the aim of validation, model data were compared with experimental results obtained with application of ATP or 5-HT onto meningeal afferents and published by us earlier (Koroleva et al., 2019). For those experiments we used isolated whole-mount mouse hemiskulls as previously described (Zakharov et al., 2015). Hemiskulls were isolated, keeping the dura mater with meningeal nerves and vessels intact. The meningeal branch of the trigeminal nerve was cleaned from surrounding tissue, then cut and placed inside a saline-filled glass electrode. All recordings of electrical activity from trigeminal nerves were performed from hemiskull preparations continuously perfused with ACSF oxygenated with 95% O_2/5% CO_2. Trigeminal nerve spiking activity was recorded using DAM80 amplifier (World Precision Instruments, Sarasota, FL, USA). Electrical signals were digitized using a NI PCI6221 board (National Instruments, USA) and stored on a PC for off-line analysis. Signals were visualized by WinEDR v.3.2.7 software (University of Strathclyde, Glasgow, UK) and analyzed with Matlab-based software (Zakharov et al., 2015).

Mast Cells Labeling

To demonstrate abundance and localization of mast cells in the meninges we used rat hemiskull preparations as described previously (Shelukhina et al., 2017). After decapitation the head was cut mid-sagittally, brain was carefully removed to leave dura mater untouched. Then preparation was fixed in 4% PFA for 4 h, meninges were mounted on microscopy slides and stained in 0.1% Toluidine Blue.

Immunolabeling

For nerve fibers staining (tubilin-beta III positive filaments), dissected meninges (from five *ad hoc* prepared mice) were incubated in a blocking solution containing 2% normal goat serum, 1% BSA, 0, 05% Tween20 and 0.1% Triton X-100 (Sigma Aldrich) for 1 h at room temperature. Meninges were incubated overnight at 4°C, with rabbit anti-tubilin-beta III (1:1,000; Sigma T2200) primary antibody. Meninges were then washed three times in PBS and incubated for 2 h in the dark at room temperature with goat anti-rabbit AF488 (Invitrogen A11008) secondary antibody. After washing three times in PBS, meninges were mounted with Fluoromount-G (Thermo Fisher

Scientific 00-4958-02), and images acquired with a Zeiss LSM 710 confocal microscope.

RESULTS

P2X3 Receptor Probability of Spike Generation

Figure 1Aa shows the two principal components of the meningeal trigeminal system, namely the middle meningeal artery (MMA) and nearby trigeminal nerves with the glass electrode for spike recordings. In **Figure 1Ab** note the abundance of mast cells located in close proximity to meningeal blood vessels, which is a region densely innervated with trigeminal afferents. For modeling the meningeal neuro-immune synapse, we first focused on the pro-nociceptive action of extracellular ATP (eATP; Burnstock, 1981; Yegutkin et al., 2016) and well-known kinetic properties of eATP-gated P2X2 and P2X3 receptors whose kinetics were presented in the earlier models (Skorinkin et al., 2003; Sokolova et al., 2006).

We assumed that meningeal mast cells known to be in close contact with nerve terminals (**Figure 1B**) serve as the main source of the local ATP release ("presynaptic cell"). However, we cannot exclude other sources of local eATP as it is well-known that various cell types can release ATP upon mechanical stress (Bodin and Burnstock, 2001; Sperlágh et al., 2007). Among them, there is release of ATP from endothelial cells during shear stress (John and Barakat, 2001; Boileau et al., 2013). As a first approximation, we did not take into account cellular stress as source of ATP release and modeled just eATP diffusion over time. Segments of the nerve fiber ("postsynaptic cell" in the frame of the hypothesis of neuro-immune synapse) in our first models, express ATP-gated P2X3 receptors (**Figure 1B**). **Figure 1C** shows a simulated nociceptive spike, while **Figure 1D** shows sodium, potassium and P2X3 receptor currents underlying this spike. **Figure 1E** depicts a plot obtained from data modeling to determine the number of receptors necessary for spike generation by a single 250 μm long nerve fiber. We assumed 0.25–2 μm diameter range and observed quadratic dependency of the number of P2X3 receptors for spike generation in one compartment of the nerve fiber. Thus, for the 0.25 × 250 μm compartment, an active P2X3 receptor already effectively generated nociceptive firing. As mentioned earlier, P2X3 receptors possess strong desensitization (Giniatullin and Nistri, 2013). **Figure 1F** shows the model of slow recovery from P2X3 receptor desensitization as the amplitude of the first current response (green deflection) is decreased following closely spaced ATP application and recovers as time lapses. This property was used in subsequent versions of our model (Models 1–14). As low concentration of ATP can produce the inhibitory action on P2X3 receptors *via* high-affinity desensitization (HAD; Sokolova et al., 2006; Khmyz et al., 2008), we also simulated the prolonged action of 1 nM ATP on the stimulatory effect of this purinergic agonist (**Supplementary Figure S2A**). First, we found that, indeed, HAD reduced the probability of spikes generation by low concentrations of ATP. Thus, after HAD, the minimal number of active P2X3 receptors required for spike generation was doubled comparing with model without HAD (**Supplementary Figure S2Ba**). Interestingly, in this test, also the dependance between the number of receptors and the nerve fiber diameter became much steeper. Further, HAD reduced, by half, the amplitude of the P2X3 receptor mediated current induced by 1 μM ATP (**Supplementary Figure S2Bb**). Finally, the probability of repetitive firing *via* P2X3 receptors with HAD was also reduced as now the release of ATP triggered only one spike (**Supplementary Figure S2Cb**), whereas without HAD the same release produced two spikes (**Supplementary Figure S2Ca**).

Because of the large number of tested conditions, **Supplementary Figure S1** shows the hierarchy of models used (see also **Supplementary Table S3**), starting from the simplest model 1 with ATP degradation coefficient = 0, conductance of Nav1.7 = 0.1 S/cm^2 (Tigerholm et al., 2014) and P2X3 receptor function for the receptor potential necessary for spike generation. In model 2, we set the degradation coefficient of ATP to 0.01. Model 3 originates from model 1 with the degradation coefficient of ATP equal to 0.8. Model 5 stemmed from model 2 with the presence of P2X3 and P2X2 receptors in a 50/50 ratio, whereas in model 4 we used only P2X2 receptors (instead of P2X3 receptors) to obtain activation of the nerve fiber. Model 6 was developed from model 2 with a higher Nav1.7 conductivity (0.2 S/cm^2) used also for model 7 with Nav1.7 0.1 S/cm^2 and Nav1.8 0.1 S/cm^2 conductivity, while model 8 with Nav1.8 0.2 S/cm^2 conductivity. The subtype Nav1.3 (Cummins et al., 2001) was present in all models with 0.2 S/cm^2 conductivity. Model 11 is based on model 8 with the fiber topology expressed as a tree, and model 12 was based on the same topology with two ATP release sites.

The Role of Diffusion and ATP Hydrolysis

It is generally accepted that three ATP molecules must occupy three binding sites to activate successfully a single P2X3 receptor (Sokolova et al., 2006). However, in the tissues related to generation of initial migraine pain, such as the meninges, ATP is rapidly degraded by extracellular NTPDases to the less active ADP, and then to AMP and adenosine (Yegutkin et al., 2016). Hence, in our model we introduced the role of ATP diffusion and hydrolysis in the control of trigeminal afferent firing. First, we explored the action of 1 μM ATP, which is close to its EC_{50} on the P2X3 receptor (Sokolova et al., 2006; **Supplementary Table S2**). In this simulation we assumed that P2X3 receptors were homogeneously distributed along the nerve fiber. The ATP concentration profile reaching compartments 1, 2, 3 and 4 of the nerve fiber without hydrolysis (lack of NTPDases) or with partial hydrolysis (active NTPDases) is indicated in **Figure 2A** (compartments 1, 2, 3 were close to the point of ATP release). Compartment 1 was located opposite the release point, whereas the distant compartment 4 was 55 compartments away from the compartment 3 (distance equal to 13.7 mm). The compartment 4, unavailable for ATP, served here only to indicate the propagation of spikes along the fiber. In model 1, in the compartment 1 without hydrolysis (degradation coefficient = 0; **Figure 2Ba**), ATP was as high as 0.9 μM ATP at the nerve fiber. To simulate ATP hydrolysis, we changed the rate of ATP degradation from 0.01 s^{-1} to 0.8 s^{-1}. Thus, model 2 (**Figure 2Bb**) indicates the profile of ATP concentrations in compartments

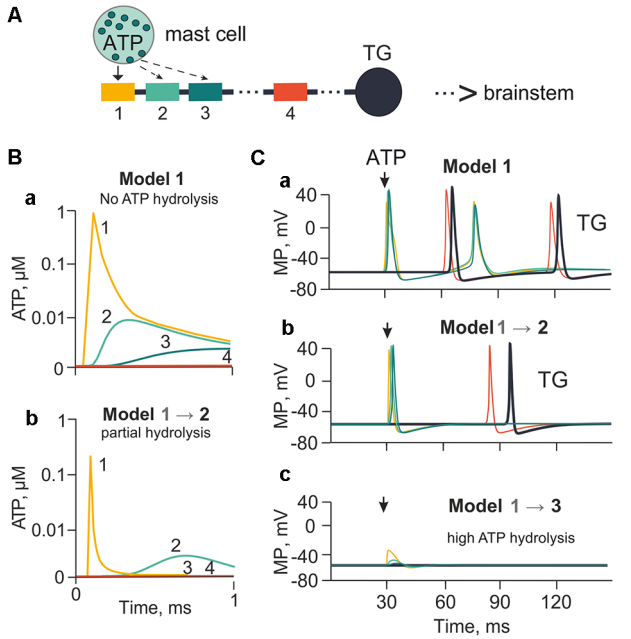


FIGURE 2 | The model of meningeal afferents with different rates of ATP hydrolysis. **(A)** Schematic presentation of the multi-compartment model of neuro-immune synapse with ATP release from mast cells and acting to several neighboring nerve compartments. **(Ba)** ATP concentration *via* diffusion to each (1, 2, 3, 4) nerve compartment without hydrolysis. **(Bb)** ATP concentration at each compartment with partial hydrolysis (degradation coefficient 0.01). **(Ca,b,c)** Spiking activity with no ATP hydrolysis (Model 1), with low ATP hydrolysis (Model 2) and high rate of hydrolysis (degradation coefficient 0.8; Model 3), respectively.

1, 2, 3 and 4 with partial hydrolysis. In this case, the maximal ATP concentration in the compartment 1 (0.06 μM) was over 10 times less than in model 1, and was enough to activate 10% of P2X3 receptors. Strong rate of hydrolysis decreased the concentration of ATP in the compartments 2, 3 and 4 to almost undetectable values because of the exponential character of ATP diffusion (Equation 1). Without ATP hydrolysis, P2X3 receptor activation triggered spiking (two spikes) in compartment 1, which propagated through the compartments 2, 3 and 4 to reach the TG (Model 1; **Figure 2Ca**). In the case of strong hydrolysis (degradation coefficient = 0.01 from maximal 1), there was only one spike produced by 1 μM ATP (Model 2; **Figure 2Cb**). Neuronal activity decreased dramatically when the degradation coefficient was 0.8 (close to the maximal value of 1). In this case, even in compartment 1, the local receptor potential did not reach threshold for spike generation (Model 3; **Figure 2Cc**).

Comparing the Role of P2X2 vs. P2X3 Receptors and Effect of P2X2/3 Heteromers

Although P2X3 receptors are expressed in approximately 80% of trigeminal neurons (Simonetti et al., 2006), sensory neurons also express slowly desensitizing P2X2 receptors which are implicated in pain signaling (Lewis et al., 1995; Fields and Burnstock, 2006). Thus, we next explored the differential ability of P2X2 and P2X3 receptors to support spiking activity in trigeminal fibers (**Figures 3Aa,b**). First, given that cells can release more than 1 μM ATP, we tested the role of higher concentrations of ATP limited by hydrolysis (Model 2; **Figure 3Ba**) in the firing activity triggered by a homogeneous population of P2X3 receptors. Because of slow desensitization (Sokolova et al., 2006), we found that ATP signaling *via* P2X3 receptor provided just one (10 μM ATP) or two (100 μM ATP) spikes propagating to the TG (**Figures 3Bb,c**, respectively).

Next, we simulated the role of P2X2 receptors based on a kinetic model with minimal desensitization state, which is a typical feature of this receptor (Skorinkin et al., 2003; Moffatt and Hume, 2007). Unlike P2X3 receptors, this approach (Model 4) yielded much more prolonged receptor activation (**Figure 3Ca**) and multiple firing in the TG especially in the case of 100 μM ATP (**Figures 3Cb,c**).

Because the potential co-expression of P2X2 and P2X3 receptors with distinct desensitization rates in trigeminal neurons (Simonetti et al., 2006) and because P2X2 receptor subunits can co-assemble with P2X3 ones to form P2X2/P2X3 heteromers (Fields and Burnstock, 2006), we also explored the effect of such co-assembly (comprising 50% P2X3 and 50% P2X2) on meningeal neuronal firing (Model 5). **Figure 3Da** indicated that in such a case, despite hydrolysis, 10 μM ATP produced repeated spikes (**Figure 3Db**), although less intensively than in the case of homogeneous P2X2 receptors (**Figure 3Cb**). Simulating the release of 100 μM ATP led to strong, prolonged TG spiking (Model 5; **Figure 3Dc**). Thus, co-expression of P2X2 and P2X3 receptors appeared to be a powerful process to generate sustained nociceptive activity.

Different Role of Nav1.7 and Nav1.8 Sodium Channels

Among the subtypes of sodium channel expressed by nociceptive neurons, the subtypes Nav1.7 and Nav1.8 play a special role in the onset and propagation of spiking activity (Tigerholm et al., 2014; Balbi et al., 2017). Thus, we explored the impact of Nav1.7 and Nav1.8 channels on ATP-induced firing of trigeminal fibers (**Figures 4Aa,b**). First, we tested the role of Nav1.7 subunit density on fiber activity induced by a single ATP release event (ATP 1 μM) acting on P2X3 receptors in compartment 1 (Model 2; **Figure 4Ba**). When the Nav1.7 conductance was 0.1 S/cm^2, and the P2X3 receptor current depolarized membrane potential to −20 mV, this condition was sufficient to activate sodium channels and trigger limited spiking (**Figure 4Ba**). When the Nav1.7 conductance was doubled to 0.2 S/cm^2, the propagation rate of spikes was slightly increased, yet the number of spikes was unchanged (**Figure 4Bb**).

Similar tests were performed with Nav1.8 channels (co-expressed with Nav1.7) starting from 0.1 S/cm^2 conductance like with Nav1.7 channels. In this case, after a single ATP release event (ATP 1 μM), multiple spiking emerged (**Figure 4Ca**). In contrast to Nav1.7, firing largely increased when the conductance of Nav1.8 channels was doubled (**Figure 4Cb**). During these simulations the activity of potassium channels was not changed, implying that changes in certain sodium channels (especially

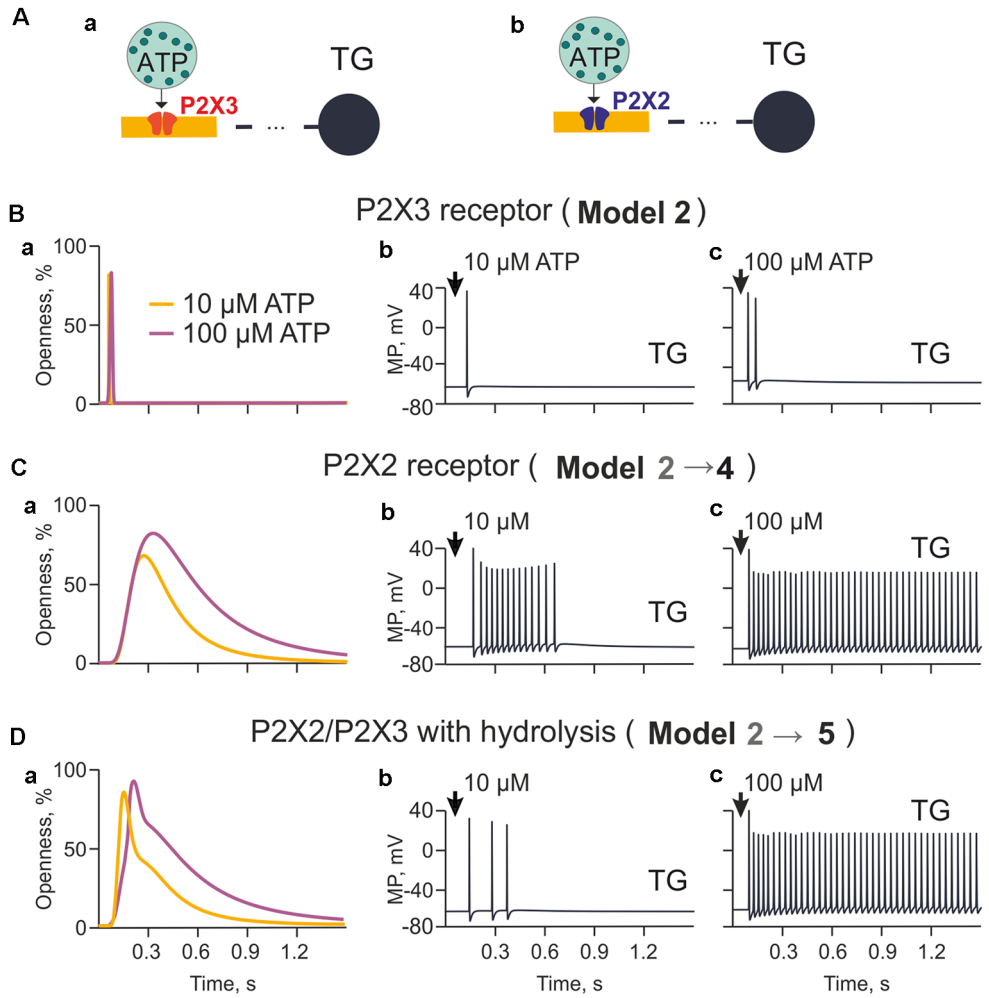


FIGURE 3 | The model of nerve fibers (meningeal afferents) with P2X3 and P2X2 receptors. **(A)** Schematic presentation of the model with P2X3 **(Aa)** or P2X2 receptors **(Ab)**. **(Ba)** The profile of P2X3 receptor responses (openness of receptors) for applications of 10 μM and 100 μM ATP. **(Bb)** Spiking activity induced by activation of P2X3 receptors with 10 μM. **(Bc)** Spiking activity induced by activation of P2X3 receptors with 100 μM. **(Ca)** The profile of P2X2 receptor responses (openness of receptors) for applications of 10 μM and 100 μM ATP. **(Cb)** Spiking activity induced by activation of P2X2 receptors with 10 μM. **(Cc)** Spiking activity induced by activation of P2X2 receptors with 100 μM. **(Da)** The profile of P2X2/3 receptor responses (openness of receptors) with partial hydrolysis for applications of 10 μM and 100 μM ATP. **(Db)** Spiking activity induced by activation of P2X2/3 receptors with 10 μM. **(Dc)** Spiking activity induced by activation of P2X2/3 receptors with 100 μM.

Nav1.8 subtype as indicated in models 7 and 8) were already sufficient to dramatically affect spiking activity of the nerve fiber.

Repetitive ATP Release and Distant Release Sites Along the Nerve Fiber

Because meninges contain an abundance of mast cells along the vessels and the divergent branches of the sensory fibers (Theoharides et al., 2007; **Figure 1Ab**), we next explored the role of repeated ATP release on the probability of repetitive spike generation in this histological arrangement. First, we simulated two release events delivering ATP to same site of the fiber (Model 9). This model consisted of 120 compartments along the nerve fiber, each compartment equipped with Nav1.7, Nav1.3, potassium DR, and potassium A-type conductances. In order to identify factors that can overcome lingering P2X3 desensitization, we again used signaling only *via* P2X3 receptors. This approach provided an initial condition with one ATP-driven spike to facilitate detection of other factors leading to multiple firing.

Using model 9, we set the different timing (Δt) of the two ATP release events in a range of 2–8 min and investigated generation and propagation of spikes from the release point to the TG. As expected, the generation of a second spike in the basal model with a simple one-release point simulation was mostly determined by the slow recovery of P2X3 receptors from desensitization. Thus, we did not observe a second spike with two ATP applications separated by less than 4 min Δt interval. Hence, spikes were generated only when the second release occurred 6 min after

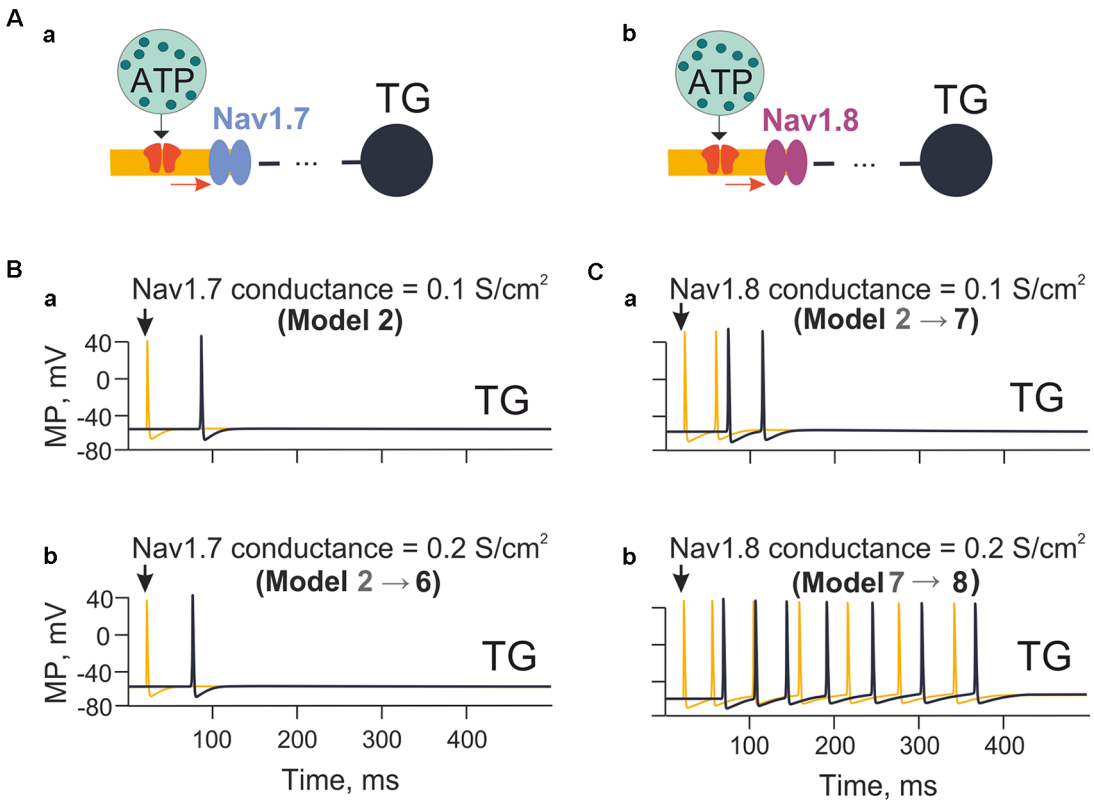


FIGURE 4 | The model with the different contributions of Nav1.7 and Nav1.8 channels. **(Aa)** A model with sodium channels with fast inactivation (Nav1.7). **(Ab)** A model with sodium Nav1.8 channels with slow inactivation. **(Ba)** The spiking activity in the model nerve fiber (Model 2) with Nav1.7 having a conductivity of 0.1 S/cm^2. **(Bb)** The spiking activity (Model 6) with Nav1.7 having a conductivity 0.2 S/cm^2. **(Ca)** The spiking activity (Model 7) with Nav1.8 with a conductivity of 0.1 S/cm^2. **(Cb)** The spiking activity (Model 8) with a conductivity of Nav1.8 equal to 0.2 S/cm^2. Spiking activity is shown either to the first nerve fiber compartment within the neuroimmune synapse (yellow) or in the trigeminal ganglion (TG; black).

the first one (**Figure 5B**). The probability of the second spike firing was nonlinearly dependent on Δt (**Figure 5B**). Thus, at Δt = 5 min the generation of a second spike had 0.5 probability, whereas at Δt ≥ 6 min the function reached saturation with probability 1 for the second spike generation.

We next focused on the effect of the distance (Δl) between two distinct ATP release points (spatial factor) located along the nerve fiber to evoke a second spike and overcome the long-lasting desensitization of P2X3 receptors (**Figure 5A**). The minimal starting distance between two release sites was set at 1 mm to minimize the effect of ATP diffusion from the first release site (**Figure 5B**). Then, we varied the distance (l) and time (t) between two ATP applications (Model 10; **Figure 5C**). **Figure 5Ca** indicates that at Δt = 20 ms and Δl = 5 mm, only one spike emerged despite a dual ATP release, whereas at Δt = 40 ms and Δl = 7 mm two spikes appeared in the same fiber upon the second ATP release (**Figure 5Cb**). **Figure 5C** shows the relation between Δt and Δl for generation of the second spike after two ATP release events. Thus, for triggering more than one spike, the minimal Δt value was 15 ms with 1 mm Δl distance between two ATP release events (**Figure 5C**).

In summary, in the present simplified model with the linear morphology of the nerve fiber and only two mast cells as source of ATP, the probability of the second spike generation was nonlinearly dependent on the timing of the second ATP application (Δt) and was linearly dependent on the distance between ATP release events (Δl).

Complex Architecture of Trigeminal Fibers

We further developed our model to include a simple bifurcation of the single nerve fiber since it has been shown significant branching of trigeminal fibers in meninges (Schueler et al., 2014). The morphology of mouse meningeal innervation with the branched nerve fibers is shown in **Figure 6A**. The schematic presentation of the branched tree is presented in **Figure 6B**. Model 11 shown in **Figure 6B** consists of 170 compartments in two branches, each one with a P2X3 receptor and Nav1.8, Nav1.7, Nav1.3, potassium DR and A-type conductances. The bifurcation point was 70 compartments (1.75 cm) away from the TG, and there were two ATP release points 1 cm apart.

First, we found that a single (first) ATP release (**Figure 6C**, indicated by arrow at simulation time = 50 ms) triggered (after some latency) multiple spiking of the TG branch (eight spikes in the period from 152 up to 485 ms; **Figure 6Ca**). Second, we tested the impact of a second ATP release (40 ms later than the first one) that also triggered repetitive spiking in the other

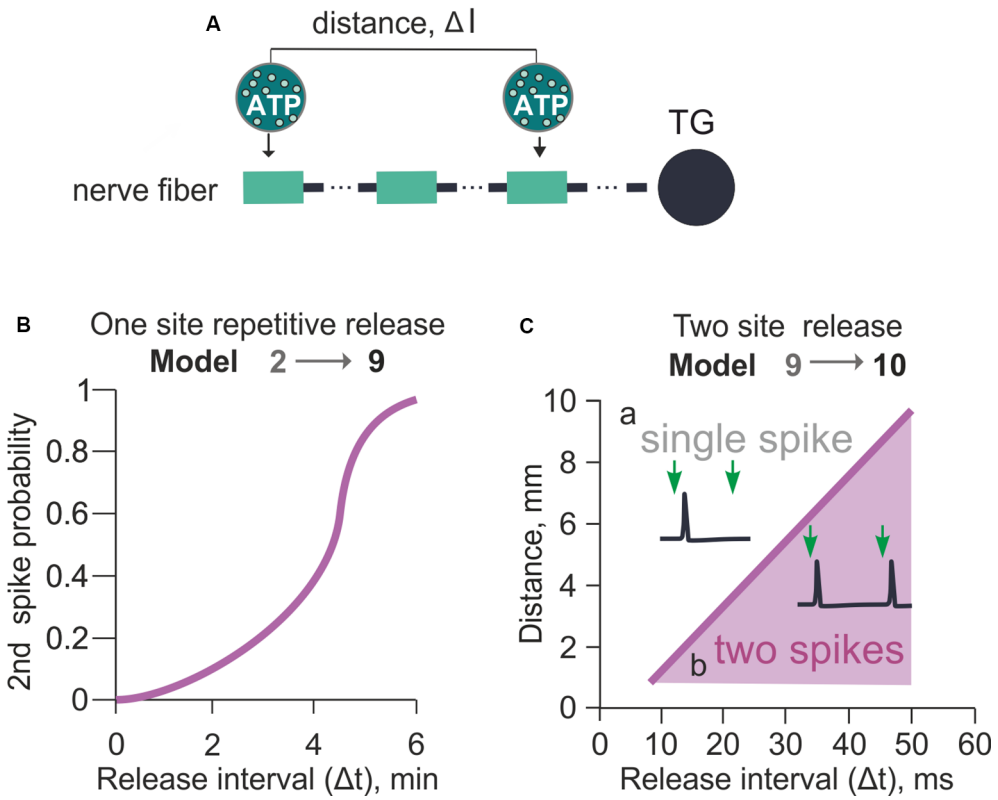


FIGURE 5 | Model of the spiking activity with the repetitive or distant release of ATP from mast cells (variable Δt and Δl between two ATP release events). **(A)** The schematic presentation of the multi-compartment model of a nerve fiber with various distances (Δl) between two ATP applications. **(B)** The probability of successful 2nd spike generation with a variable time (Δt) between two ATP applications. The distance (Δl) between two ATP applications is 0 (Model 9). **(C)** The dependency between the distance (Δl) and time (Δt) between two ATP applications (Model 10). The purple area identifies the conditions for the productive second spike generation (see inset) after two ATP applications whereas white area above—conditions when even a double release of ATP generates only one spike (see inset).

branch of the nerve (eight spikes, activity lasting from 193 ms to 538 ms; **Figure 6Cb**). Then, we explored the firing activity of a whole nerve sequentially activated by ATP released from two (first and second) distinct sites. This resulted in stronger spiking (12 spikes, activity lasting from 152 ms to 538 ms; **Figure 6Cc**) which reached the TG.

Thus, the complex architecture of trigeminal fibers can also contribute to multiple firing.

5-HT Induced Activation of Nerve Fibers

Mast cells containing the principle mediator 5-HT are largely expressed in the meninges (**Figure 1Ab**). We have previously shown the strong pro-nociceptive action of this monoamine on meningeal afferents *via* ligand gated 5-HT3 receptors in rats (Kilinc et al., 2017) and mice (Koroleva et al., 2019). In the present study, we applied the kinetic model of 5-HT3 receptors (Corradi et al., 2009) to our model of C-fibers. The model implied mast cells releasing 2 μM 5-HT acting on 5-HT3 receptors and subjected to 5-HT uptake (**Figure 7A**). For the sake of simplicity, we indicated only two compartments of the trigeminal nerve. **Figure 7Ba** shows the plot of 5-HT concentration with or without 5-HT uptake (Daws et al., 2005; Wood et al., 2014). Unlike the short time profile of ATP (rapidly degraded by ectoenzymes, gray trace), the concentration of 5-HT after single release from mast cells decayed much slower with or without uptake processes (**Figure 7Ba**). In addition, 5-HT3 receptor recovery from desensitization was also faster (**Figure 7Bb**; green) than the one for the ATP-gated P2X3 receptor (**Figure 7Bb**, gray). Comparison of repeated spiking activity triggered by 5-HT3 receptor activation with or without monoamine reuptake and contribution of Nav1.8 channels is shown in **Figures 7Ca, Cb** (Model 13 and 14). Spiking activity was, however, more intense with ATP application and Nav1.8 channel activity (**Figure 4Cb**).

Comparison of Model and Electrophysiological Data

To validate our model, we compared simulated firing with experimentally observed action potentials triggered by ATP and 5-HT on mice meningeal afferents (Koroleva et al., 2019). In this study, we measured the firing of the mouse trigeminal nerve

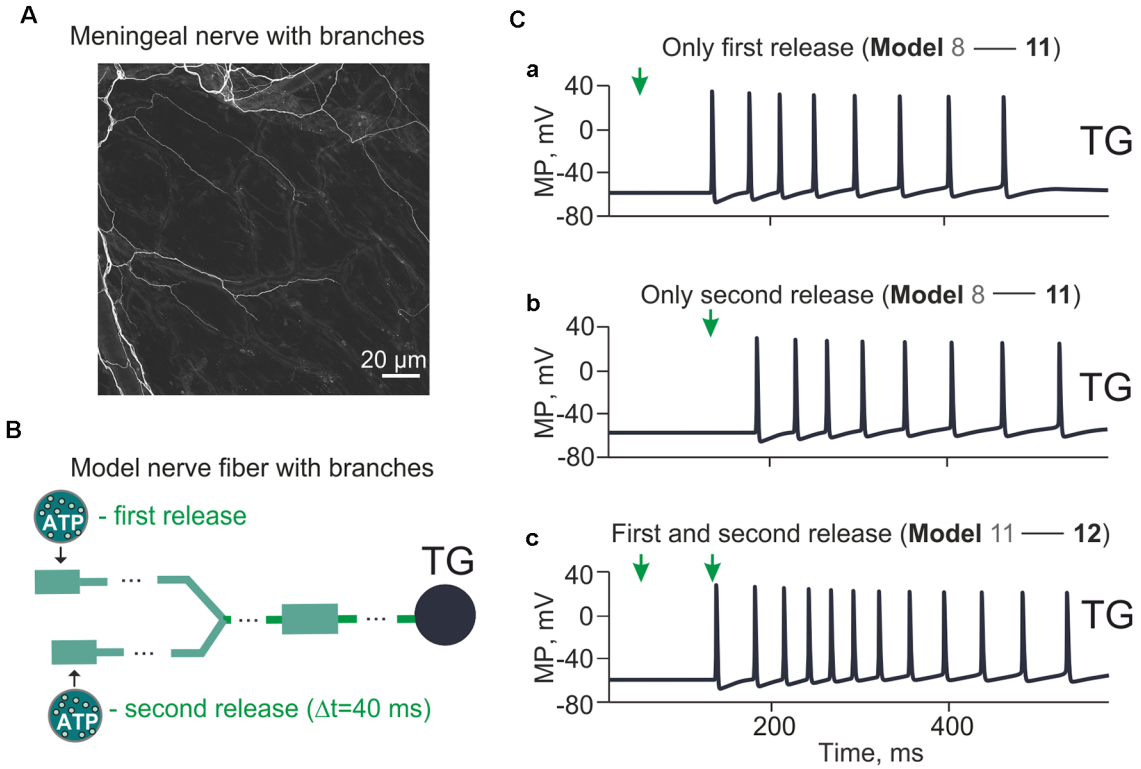


FIGURE 6 | Model with branching meningeal afferents. The spiking activity arriving at the TG from a two-branch structure with Δt = 40 ms between two ATP applications and the distance (Δl) between them 1 cm. **(A)** Image of the nerve fiber with branches. Sections of mouse meninges were stained with the anti-beta-III-tubulin antibody. Single nerves emerging from diffuse bundles of trigeminal fibers are visible throughout the entire section. Bifurcating nerve fibers appear to project directly to meningeal blood vessels (visible from the background staining). **(B)** The "fork" model of the nerve fiber with two separate branches. **(Ca)** The spiking activity induced by a single ATP application at the t = 50 ms (Model 11). **(Cb)** The same after a single ATP application at the t = 90 ms. **(Cc)** The spiking activity with two ATP applications with Δt = 40 ms (Model 12).

activated by application of exogenous ATP. **Figure 8Aa** shows the effect of 100 μM ATP for the 1st and 5th min of its action in meninges.

Next, we compared these experimental results with the simulation of neuronal activity induced by 100 μM ATP (**Figure 8Ab**). **Figure 8A** (inset, left) shows a cross section of the model nerve with several active nerve fibers: either with P2X3 receptors or with a mixture of P2X2 and P2X3 receptors (Models 5 and 8, respectively). The inactive fibers (shown in gray) represent the absence of P2X receptors. Like the experimental approach, our model revealed an intense and prolonged ATP-induced spiking activity in the nerve fiber.

Comparable results were obtained also with experimental and simulated applications of 5-HT. **Figure 8B** shows the structure of the model nerve in which fibers express 5-HT3 receptors or lacking such receptors. In this case, as experimental application of 2 μM 5-HT induced a long-lasting activity in meningeal afferents, a similar phenomenon was also observed with simulated application of 2 μM 5-HT (Model 14; **Figures 8Ba,b**).

Then, we compared the inter-spike intervals (ISI) of experimental and modeling data (**Figures 8C,D**). In experimental ATP application, ISI were 1,213 ± 499 ms, whereas in the model, the median ISI were 502 ms with 50%/50% mixture of P2X2 and P2X3 receptors, 1,704 ms with 75%/25% mixture and 56 ms with 25%/75% mixture (**Figure 8C**). Thus, the 75%/25% ratio of P2X3/P2X2 receptors in the model was the closest combination of P2X2 and P2X3 receptors to the experimental data.

With experimental 5-HT application, the ISI of spiking activity was 4,039 ± 1,134 ms, and the closest model data were obtained with 10% activated fibers which had 5-HT3 receptors with conductances ranging from 0.25 to 0.5 S/cm^2 and 0.1–0.2 S/cm^2 (ISI: 3,041 ms and 6,556 ms, respectively; **Figure 8D**).

Together, these data indicated a high similarity of our model results with experimental ATP- and 5-HT-induced firing.

Modeling Prolonged and Rhythmic Nerve Activity

Migraine pain has a still unexplained pulsating character perhaps due to mechanical fluctuations of meningeal vessels (Mikhailov et al., 2019; Della Pietra et al., 2020) that might interact with nearby nerve fibers and mast cells (**Figures 1Ab**; **6A**). In order to investigate the potential role of pulsating blood flow as a trigger of meningeal nociception and its relation to ATP- and 5-HT-induced firing, we hypothesized that

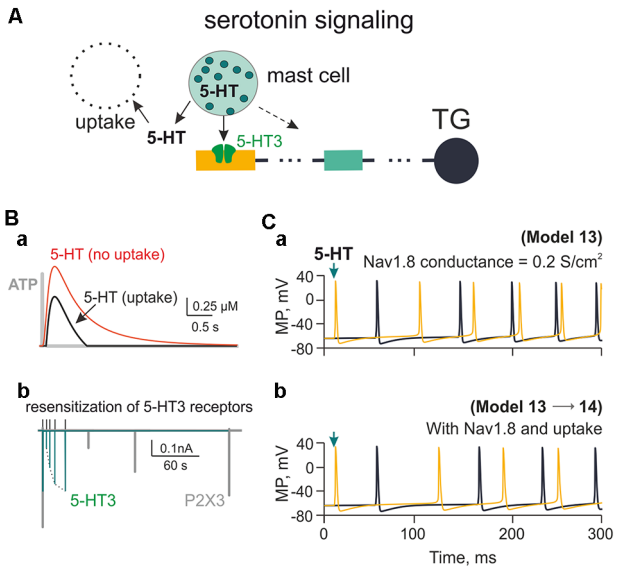


FIGURE 7 | Firing of meningeal afferents induced by 5-HT applications. **(A)** The multi-compartment model of the nerve fiber with 5-HT3 receptors activated by 5-HT released from mast cells and inactivated through uptake mechanism. **(Ba)** The red graph is the time profile of the extracellular concentration of 5-HT without uptake (Model 13), whereas the black graph is 5-HT concentration with uptake (Model 14). For the sake of comparison between the two mediators, the gray graph shows the very short profile of ATP concentration (Model 1). **(Bb)** The green graph shows 5-HT3 receptor recovery from desensitization, whereas the gray graph—the comparative slow desensitization of P2X3 receptor. **(Ca)** The spiking activity of the nerve fiber activated by 5-HT with Nav1.8 having the conductivity of 0.2 S/cm^2 (Model 13). **(Cb)** The same with 5-HT re-uptake (Model 14). Spiking activity is shown either to the first nerve fiber compartment within the neuroimmune synapse (yellow) or in the TG (black).

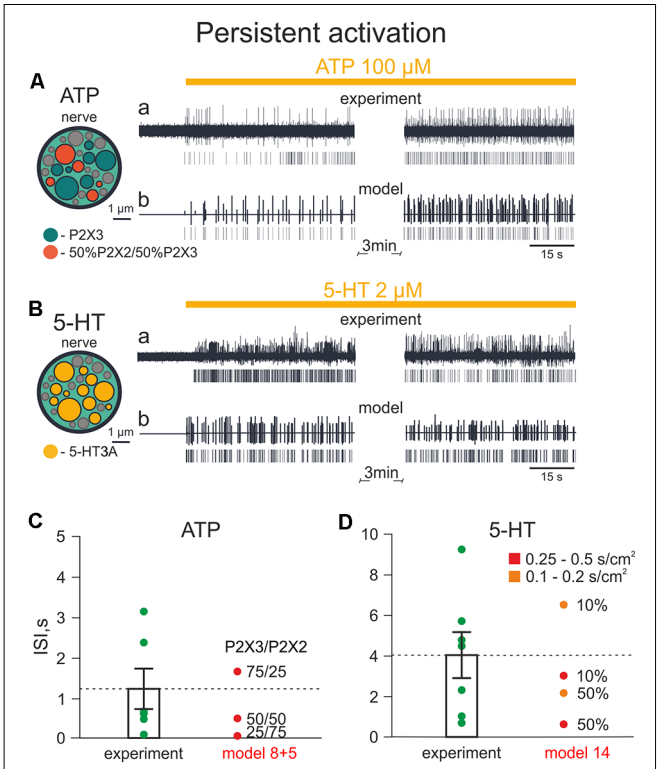


FIGURE 8 | Firing of meningeal afferents induced by *persistent* ATP and 5-HT applications. **(A)** A cross-section of the model nerve with P2X3 receptors and with a mixture of 50% P2X2 + 50% P2X3 receptors. **(Aa)** The spiking activity of fibers with persistent ATP application in a biological experiment. **(Ab)** The same in the model. **(B)** The cross-section of the model nerve with 5 HT3 receptors. **(Ba)** The spiking activity of fibers with persistent 5-HT application in a biological experiment. **(Bb)** The same in the model. **(C)** The inter-spike intervals (ISI) with persistent ATP application. **(D)** The inter-spikes intervals with the persistent 5-HT application.

vasodilation (during migraine attacks) of pulsating meningeal vessels can stimulate release of these two mediators from local mast cells. In addition, we considered that ATP can be released directly from endothelial cells of meningeal vessels (Burnstock, 1981).

Based on the co-assembly of meningeal nerves, mast cells and vessels shown in **Figures 1Aa,b** and on our experimental data obtained from mice lacking mast cells (Koroleva et al., 2019), we hypothesized (**Figure 9A**, shown by arrows) that the pulsatile blood flow can release ATP and 5-HT from mast cells adding more ATP released from the endothelium of meningeal vessels. The extracellular ATP (eATP) can act either directly on nerve fibers or indirectly *via* degranulation of mast cells. These interactions are also shown in the (**Supplementary Movie**).

The structure of modeled nerves for ATP and 5-HT actions in **Figures 9B,C** (insets, left) was the same as shown in **Figure 8**. First, we modeled the neuronal activity in the rat induced by periodic pulsations (assuming an average heart beating rate = 400/min; **Figures 9Ba, Ca**). Thus, we examined the spiking activity assuming that these pulsations released 1 μM eATP (note arrows in **Figure 9Ba**) which, in turn, activated nerve fibers. Interestingly, after the initial continuous spiking induced by ATP, the neuronal discharges (indicated by short vertical lines in **Figure 9Ba**) occurred in short bursts separated by longer silent periods, thus demonstrating a clear periodicity.

Modeling also allows simulating pulse-induced spiking in human afferents. **Figure 9Bb** for ATP and **Figure 9Cb** for 5-HT, show that the assuming human pulsating blood flow (presumed to be 70 beats/min) could produce initial persistent firing, which was quickly transformed into periodic bursts of activity with expected lower rate. In this case, we took into consideration not only the lower human-specific heart rate but also the faster (*circa* two-fold) rate of recovery from desensitization of human P2X3 receptors (Pratt et al., 2005).

DISCUSSION

The main result of the current study is a novel model of meningeal nociception based on the concept of a neuro-immune synapse composed by trigeminal nerve fibers and local mast cells, which may release two mediators, ATP and 5-HT. These two endogenous substances were taken here as chemical triggers of nociception based on their powerful and prolonged stimulatory effect on meningeal afferents experimentally demonstrated with

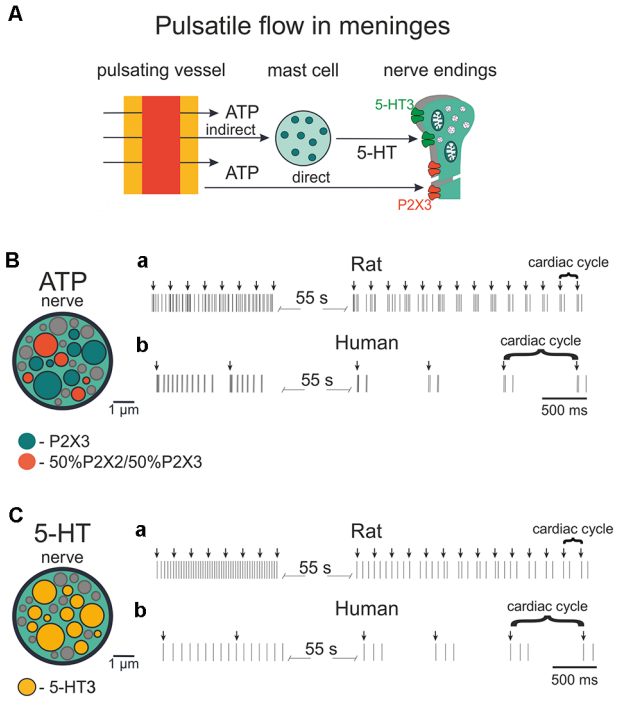


FIGURE 9 | Firing of meningeal afferents induced by *pulsatile* ATP and 5-HT applications. **(A)** The schematic presentation of pulsating vessels inducing transmitter release from mast cells or endothelium. ATP acts either directly on nerve terminals (*via* P2X3 receptors) or by 5-HT released from mast cells and 5HT activates its own neuronal 5-HT3 receptors. **(B)** The cross-section of model nerve with P2X3 receptors and a mixture of 50% P2X2 and 50% P2X3 receptors. **(Ba)** Spiking activity in nerve fibers with ATP release events following at the frequency of the human heart rate (70 beats per minute). **(Bb)** The spiking activity of fibers with ATP action at the frequency of the rat heart rate (400 beats per minute). **(C)** The cross-section of the model nerve with 5-HT3 receptors. **(Ca,Cb)** Spiking activity of nerve fibers with ATP action at the frequency of the human heart rate (70 beats per minute) and rat heart rate (400 beats per minute), respectively.

direct recordings of spikes from trigeminal nerve fibers in rats and mice (Yegutkin et al., 2016; Kilinc et al., 2017; Koroleva et al., 2019).

Role of ATP Receptor Subtypes

To model purinergic (eATP-driven) signaling within the neuro-immune synapse, we first simulated the kinetic properties of eATP-gated P2X2 and P2X3 receptors, which are the major ATP sensitive receptor subtypes in sensory neurons generating pain signals (Burnstock, 2006; Simonetti et al., 2006).

Because of the fast onset of desensitization and slow recovery properties (Sokolova et al., 2006), P2X3 receptors activated by a single pulse of eATP (even without any ATP hydrolysis) evoked only limited activity in meningeal trigeminal nerve fibers (Model 1; **Figure 2Ca**). Assuming moderate ATP hydrolysis to mimic short ATP lifetime in meninges (Yegutkin et al., 2016), repetitive firing of trigeminal fibers was transformed just into a single ATP-driven spike (Model 2; **Figure 2Cb**). Robust ATP hydrolysis left only a small receptor potential unable to trigger nociceptive spikes (Model 3; **Figure 2Cc**).

One crucial factor for the intensity and persistence of firing was the ATP receptor subtype. Unlike P2X3 receptors widely (up to 80%) expressed in the rodent trigeminal neurons (Simonetti et al., 2006), P2X2 receptors are less frequently expressed by sensory neurons, yet they show little desensitization despite relatively fast activation properties (North, 2004). Thus, the current simulations assuming a single release point indicate that the slow desensitization kinetics of P2X2 receptors could ensure high probability of repetitive firing (Model 4; **Figure 3C**).

The relative prevalence of P2X2 and P2X3 receptor subtypes is species and sensory neuron dependent (Simonetti et al., 2006; Viatchenko-Karpinski et al., 2016; Ishchenko et al., 2017). In the human DRG, there is a predominance of the P2X3 subtype (Serrano et al., 2012), whereas in rodents, the P2X2 subtype is significantly present in trigeminal neurons (Simonetti et al., 2006). It should be noted that P2X2 and P2X3 subunits can heteromerize to form P2X2/3 heterotrimers (Burnstock, 2000). It has been proposed that P2X3 homomers are responsible for acute pain, whereas P2X2/3 heterotrimers are involved in chronic pain (Jarvis, 2003). Consistent with this view, our simulations indicated that the co-expression of P2X2/P2X3 receptors supported prolonged firing of fibers activated by eATP (Model 5; **Figure 3D**). Interestingly, unlike homomeric P2X3 or P2X2 receptors, in the case of heteromers, we observed strong increase in neuronal firing after raising the concentration of ATP from 10 μM to 100 μM (Model 5; **Figures 3Db,c**). Thus, co-expression of P2X2 and P2X3 subunits enabled robust firing sensitive to ATP concentration.

The issue of relative contribution of parallel co-expression in the same neurons of homomeric P2X3 and homomeric P2X2 or the co-assembly of P2X2 and P2X3 subunits in the P2X2/3 heteromers is not fully solved in experimental setting. However, the nociceptive action of the P2X3 agonist α,β-meATP in rat meninges was comparable with the action of ATP (Yegutkin et al., 2016), suggesting that the essential fraction of ionotropic ATP receptors in nerve terminals is presented by P2X2/3 heteromers. This issue might have a significant impact for suitability of P2X3 and P2X2/3 inhibitors for treatment of migraine pain. For instance, potent P2X3 and P2X2/3 inhibitors are already under the advanced stage of clinical trials for the treatment of chronic coup (Richards et al., 2019). On the other hand, highly potent P2X3 inhibitors such as various peptide toxins have been reported (Lalo et al., 2001; Grishin et al., 2010). Even emerging migraine treatments such as cannabinoids (Leimuranta et al., 2018) directly inhibited P2X2 and P2X2/3 receptors in sensory neurons (Krishtal et al., 2006) which can provide a dual anti-nociceptive effect. As ATP in living tissues is quickly degrades to ADP, it is also interesting to consider potential action of ADP *via* P2Y receptors, which might be the additional factor shaping the purinergic nociception in meninges. ADP sensitive excitatory receptors are expressed both in trigeminal neurons and in glial cells (Villa et al., 2010). In contrast, the inhibitory action of ADP on P2X3 receptors has been shown in isolated DRG neurons (Gerevich et al., 2007). However, our experimental study (Yegutkin et al., 2016) did not show significant changes

in the nociceptive firing of meningeal afferents after application of ADP suggesting that this type of modulation preferential takes places at the level of neuronal somata in the trigeminal ganglia or DRG. We cannot exclude also the region-specific differences in the relative contribution of P2Y vs. P2X receptors in analogy to the condition detected in the colon where the role of ADP sensitive P2Y receptors is dominating (Hockley et al., 2016).

According to the purinergic hypothesis of migraine (Burnstock, 1981), the powerful algogen eATP is one of key mediators of this disease. In accordance with this notion, we have recently found that, when applied to mouse meninges, 100 μM ATP causes very strong firing (∼25-fold increase) of primary afferents (Koroleva et al., 2019). Our modeling of purinergic mechanisms at the meningeal neuro-immune synapse was facilitated by the known kinetics of P2X3 and P2X2 receptors (Skorinkin et al., 2003; Sokolova et al., 2006). The availability of these input model parameters allowed exploring various factors determining the pattern of nociceptive fiber activity when mast cells were assumed as the source of ATP release. Nonetheless, one should bear in mind that, apart from mast cells, meninges are enriched with other immune cells (McIlvried et al., 2017). Thus, in the natural environment of these tissues, there could be multiple ATP releasing cell types possibly contributing in concert to neuro-immune interactions.

Nociceptive Signaling in Meningeal Afferents *via* 5-HT

Along with eATP, we simulated the action of 5-HT, which is a classical mediator released from mast cells. Recently we showed that 5-HT has a powerful pro-nociceptive action on rat and mouse meningeal afferents mainly *via* ligand-gated 5-HT3 receptors (Kilinc et al., 2017; Koroleva et al., 2019). The selection of 5-HT among other candidate transmitters was further supported by our experimental finding that histamine, also the known as the mast cell mediator, has only little if any excitatory action on nerve terminals (Kilinc et al., 2017). Unlike ATP, the lifespan of extracellular 5-HT in the meninges is expected to be much longer due to relatively slow reuptake (Daws et al., 2005; Wood et al., 2014). Furthermore, 5-HT3 receptors recover from desensitization much more rapidly than P2X3 receptors (**Figure 7Bb**), rendering 5-HT potentially effective to trigger nociception in meninges. Nevertheless, ATP P2X3 receptors possess higher affinity (EC50 1 μM; Sokolova et al., 2006) and widespread expression in the majority of trigeminal neurons (Simonetti et al., 2006). Interestingly, at other non-traditional "synapses," such as taste buds, release of ATP and 5-HT also activates nearby nerve terminals *via* P2X2/3 and 5-HT3 receptors (Larson et al., 2015), indicating that these two transmitters and their receptors may operate in a broader context than the proposed meningeal neuro-immune synapse. It is suggested that the functional outcome of dual activation *via* P2X and 5-HT3 receptors of afferents can multiply the total firing in meningeal nociception as a putative signal of migraine pain. The leading role in such scenario, most likely, belongs to ATP, which, apart from the direct excitation of terminals *via* P2X receptors, can degranulate meningeal mast cells to release serotonin, acting *via* excitatory 5-HT3 receptors (Koroleva et al., 2019).

This novel dual purinergic/serotonergic signaling reveals a new translational aspect of the present study, suggesting pharmacological interventions based on a combination of P2X3 and 5-HT3 antagonism.

Role of Sodium Channels

For effective traffic of nociceptive signals to higher pain centers, sensory neurons must be equipped with a palette of sodium channels, which determine the fidelity and precision of neuronal sensory coding (Zhao et al., 2016). Several subtypes of sodium channel, including Nav1.7, Nav1.8 and Nav1.9 isoforms, are expressed in the peripheral nervous system (Israel et al., 2019). Both the Nav1.7 and Nav1.8 subtypes found in nociceptive neurons can generate depolarizing slow currents with the characteristics to interact with the receptor potential evoked by ATP and 5-HT. In particular, human Nav1.8 channels display slower inactivation kinetics and produce large persistent currents than those observed in other species (Han et al., 2015). In the present model we used the same set of sodium channel data reported by Mandge and Manchanda (2018), and we observed that slow inactivation of Nav1.8 channels is one important determinant of the long-lasting pattern of spiking. Thus, unlike Nav1.7 channels, simulation with high density of Nav1.8 expression largely increased firing activated by ATP *via* P2X3 receptors (**Figure 4**). Thus, Nav1.8 channels could supply an additional mechanism to amplify the initial activation of nerve fibers by P2X3 receptors.

Modeling Multiple Activation Sites

Our modeling with a simple linear structure of the nerve fiber indicated that non-desensitizing P2X2 receptors and Nav1.8 channels could efficiently promote persistent firing after P2X3 receptor activation. We further explored other factors to transform the brief firing evoked by P2X3 receptors into a repetitive discharge. Emphasis on P2X3 receptors as initial condition was based on their wide expression by trigeminal sensory neurons (Simonetti et al., 2006), lack of inflammatory pain in mice genetically ablated for this receptor (Cockayne et al., 2000) and by poor expression of P2X2 subunits by human nociceptive neurons (Serrano et al., 2012).

To this end, we sought to improve our model by approximating its structure to the branching of the nerve fibers recently documented by functional and morphological data in dural afferents (Schueler et al., 2014). One unexpected result was that P2X3 receptors alone were sufficient for repetitive firing when ATP was supposed to act on distinct branches of the trigeminal nerve (Model 12). In Model 12, we also quantified the spatial and temporal requirements, which determined the appearance of the second spike. Thus, our study showed that fiber branching could play a major role to generate repeated firing despite the intrinsic desensitization properties of the P2X3 receptor. Simulations indicated that this phenomenon could occur when ATP was applied to distinct branches with at least 40 ms interval. It seems likely that, in the naturally

more complex structure of meningeal nerves and multiple release sites, repeated firing of trigeminal fibers equipped solely with P2X3 receptors might be even stronger as desensitization of P2X3 receptor represents a local phenomenon maintaining distant sites of the axonal tree sensitive to ATP.

Focusing on the factors promoting repetitive firing we also should consider factors which potentially can prevent it. Thus, the use-dependent inhibition of P2X3 receptor by low nanomolar concentrations of ATP known as HAD (Sokolova et al., 2006; Khmyz et al., 2008) can reduce the operations of ATP *via* P2X3 (but not *via* P2X2) receptors. In our model we confirmed this possibility showing that HAD can reduce but not abolish the activity of homomeric P2X3 receptors. However, HAD was described in isolated neurons and was not previously tested in *ex vivo* preparations like our model of meningeal nociception and it is unknown whether it takes place *in vivo*. Thus, the (patho)physiological significance of HAD remains unclear and its efficiency *in vivo* could be reduced or neutralized by activity of ATP degrading NTPDases expressed in meningeal afferents.

Thus, the present study suggests how, despite their strong desensitization, P2X3 receptors can contribute to nociceptive pain signaling especially when supported by co-expression of P2X2 receptors, Nav1.8 sodium channels, co-release of 5-HT and branching of nerve fibers.

These data are schematically summarized in **Figure 10**, where the efficiency of repetitive firing *via* only P2X3 vs. co-assembly of P2X3 with P2X2 (**Figure 10A**), effect of Nav1.8 for P2X2/3 (**Figure 10B**) and for 5-HT3 receptors (**Figure 10C**) are indicated. **Figure 10D** showed the amplifying firing effect of neuronal branching along with other factors.

These novel results provide the clue to solve the paradox how strong P2X3 desensitization is consistent with *in vivo* evidence on the role of P2X3 in pain behavior (Cockayne et al., 2000; North, 2004).

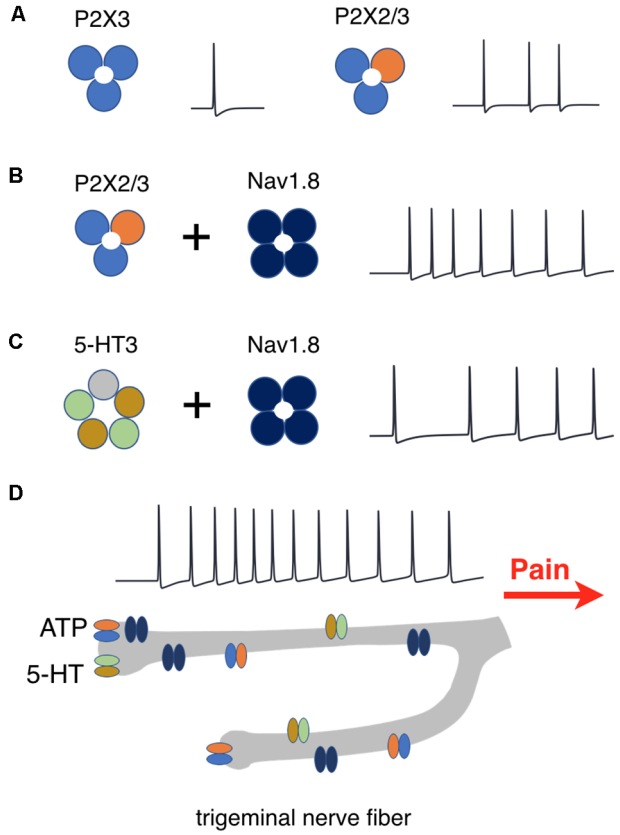


FIGURE 10 | Schematic presentation of factors determining repetitive activation of meningeal afferents. **(A)** P2X3 receptors activation produces one spike whereas activation of P2X2/3 heteromers triggers prolonged activity. **(B)** The co-expression of P2X2/3 or **(C)** 5HT-3 receptors with Nav1.8 channels enhances prolonged spiking activity. **(D)** Nerve branching further increases the duration of spiking activity which signals pain to higher brain centers.

Potential Pathophysiological Implications in Migraine

Our modeling approach together with previously published data provides a functional scenario to account how, during migraine attacks, ATP and 5-HT can persistently excite meningeal afferents. We assumed here the ATP and 5-HT co-release by meningeal immune cells (exemplified as mast cells). Mast cells react to mechanical stimuli (Zhang et al., 2012; Komiyama et al., 2014), which can serve as a signal to release the content of their secretory granules including ATP (Wang et al., 2013) to activate neighboring nerve fibers (Wang et al., 2015). Interestingly, cortical spreading depression (which underlies migraine aura, Charles, 2018), also degranulates mast cells and opens pannexin channels as the pathway for ATP release (Karatas et al., 2013). Further studies are necessary to identify all the endogenous triggers for 5-HT and ATP release during a migraine attack, also taking into account the blood flow-dependent endothelial release of ATP (Wang et al., 2016) due to shear stress or blood vessel pulsations (John and Barakat, 2001).

As migraine pain is not only long-lasting but also pulsating (throbbing), one aim of this project was to elucidate the factors which provide such migraine-typical activation of trigeminal fibers. Hence, to simulate the pulsating character of migraine pain, which is one of the main features of migraine [The International Classification of Headache Disorders 3rd edition (ICHD-3)], we compared the effect of experimental application of ATP or 5-HT to meningeal nerve fibers with similar modeling tests. Then, based on Models 5 and 8, which provided the best match with the experimental approach, we reconstructed pulsatile release of the two mediators ATP and 5-HT to monitor the spiking activity of nerve fibers.

Furthermore, we simulated the effect of rhythmic pulse-induced release of ATP and of 5-HT not only in rodents but in human nerves. In all cases after initial continuous activity, there were short very regular bursts of nociceptive activity, specific for each species. Notably, such a type of activity with high frequency of spikes within the burst should increase the probability of temporal summation and the windup phenomenon to transmit peripheral signals to the second order nociceptive neurons located in the brainstem (Zakharov et al., 2016). Although release of chemical mediators by pulsating blood vessels cannot

per se be the primary process for migraine pain, it is feasible to assume that after the initial stimulation of ATP (and 5-HT) release by certain triggers (whose identity needs further study), pulsatile release might support long-lasting firing. Within this framework, the present basic model of meningeal nociception does not consider the early process of neuronal sensitization. Thus, it has been shown that the main migraine mediator, the neuropeptide CGRP largely increases the activity of P2X3 receptors and reduces their desensitization (Fabbretti et al., 2006; Giniatullin and Nistri, 2013). Notably, mechanical activation of peptidergic nerve fibers containing CGRP can perhaps be achieved through mechanosensitive piezo channels (Mikhailov et al., 2019; Della Pietra et al., 2020; and see **Supplementary Movie**). This effect plus other sensitization mechanisms should enhance the role of ATP in nociceptive firing of meningeal afferents and supply the trigger for resilient firing. In fact, mast cells, apart from 5-HT, release other active substances such as NGF and histamine (Bonini et al., 2003; Borriello et al., 2017). Although histamine may preferentially act on dural vessels (Kilinc et al., 2017), NGF can directly target trigeminal neurons to enhance their responses to ATP *via* P2X3 receptors (D'Arco et al., 2007). Furthermore, for implementation of multiple migraine-related signaling pathways, the model should include G-protein coupled receptors (GPCR), including those for migraine-specific drugs such as triptans and neurotrophins.

In summary, the idea of the meningeal neuro-immune synapse (Giniatullin et al., 2019; Koroleva et al., 2019; Koyuncu Irmak et al., 2019) is supported by the present model, which improves our understanding of the processes underlying peripheral mechanisms generating migraine pain within the concept of trigeminovascular dysfunction (Messlinger, 2009; Edvinsson et al., 2012; Dodick, 2018). The current model can, therefore, serve as a novel tool for further testing the mechanisms of meningeal trigeminal nociception *in silico*.

DATA AVAILABILITY STATEMENT

The raw data supporting the conclusions of this article will be made available by the authors, without undue reservation, to any qualified researcher. Requests to access the datasets should be directed to rashid.giniatullin@uef.fi.

ETHICS STATEMENT

The animal study was reviewed and approved by The Committee for the Welfare of Laboratory Animals of the University of Eastern Finland and the Provincial Government of Kuopio.

AUTHOR CONTRIBUTIONS

AS developed a model. AS, NM, KK, AV, and OG conducted the experiments. AS, RG, FN, MT, and FG analyzed the results. RG, MT, and AN supervised the whole project. All authors reviewed the manuscript.

FUNDING

AS, FG, and MT were supported by Russian Foundation for Basic Research and the Government of the Republic of Tatarstan of the Russian Federation, Grant No. 18-44-160032 and the Program of Competitive Growth of Kazan Federal University. KK, OG, and RG were supported by RFBR KOMFI (Grant No. 17-00-00053). NM and RG are the recipients of the Finnish Academy grant (No. 325392).

SUPPLEMENTARY MATERIAL

The Supplementary Material for this article can be found online at: https://www.frontiersin.org/articles/10.3389/fncel.2020.00135/full#supplementary-material.

REFERENCES

Arnold, M. (2018). Headache classification committee of the international headache society (IHS) the international classification of headache disorders. *Cephalalgia* 38, 1–211. doi: 10.1177/0333102417738202

Balbi, P., Massobrio, P., and Hellgren Kotaleski, J. (2017). A single Markov-type kinetic model accounting for the macroscopic currents of all human voltage-gated sodium channel isoforms. *PLoS Comput. Biol.* 13:e1005737. doi: 10.1371/journal.pcbi.1005737

Bodin, P., and Burnstock, G. (2001). Purinergic signalling: ATP release. *Neurochem. Res.* 26, 959–969. doi: 10.1023/a:1012388618693

Boileau, E., Bevan, R., Sazonov, I., Rees, M., and Nithiarasu, P. (2013). Flow-induced ATP release in patient-specific arterial geometries-a comparative study of computational models. *Int. J. Numer. Methods Biomed. Eng.* 29, 1038–1056. doi: 10.1002/cnm.2581

Bonini, S., Rasi, G., Bracci-Laudiero, M. L., Procoli, A., and Aloe, L. (2003). Nerve growth factor: neurotrophin or cytokine? *Int. Arch. Allergy Immunol.* 131, 80–84. doi: 10.1159/000070922

Borriello, F., Iannone, R., and Marone, G. (2017). Histamine release from mast cells and basophils. *Handb. Exp. Pharmacol.* 241, 121–139. doi: 10.1007/164_2017_18

Burnstock, G. (1981). Pathophysiology of migraine: a new hypothesis. *Lancet* 317, 1397–1399. doi: 10.1016/s0140-6736(81)92572-1

Burnstock, G. (2000). P2X receptors in sensory neurones. *Br. J. Anaesth.* 84, 476–488. doi: 10.1093/oxfordjournals.bja.a013473

Burnstock, G. (2006). Purinergic P_2 receptors as targets for novel analgesics. *Pharmacol. Ther.* 110, 433–454. doi: 10.1016/j.pharmthera.2005.08.013

Burnstock, G. (2008). Purinergic signalling and disorders of the central nervous system. *Nat. Rev. Drug Discov.* 7, 575–590. doi: 10.1038/nrd2605

Charles, A. (2018). The migraine aura. *Continuum* 24, 1009–1022. doi: 10.1212/CON.0000000000000627

Chen, C. C., Akopian, A. N., Sivilottit, L., Colquhoun, D., Burnstock, G., and Wood, J. N. (1995). A P2X purinoceptor expressed by a subset of sensory neurons. *Nature* 377, 428–431. doi: 10.1038/377428a0

Choi, J. S., and Waxman, S. G. (2011). Physiological interactions between Nav1.7 and Nav1.8 sodium channels: a computer simulation study. *J. Neurophysiol.* 106, 3173–3184. doi: 10.1152/jn.00100.2011

Cockayne, D. A., Hamilton, S. G., Zhu, Q. M., Dunn, P. M., Zhong, Y., Novakovic, S., et al. (2000). Urinary bladder hyporeflexia and reduced pain-related behaviour in P2X3-deficient mice. *Nature* 407, 1011–1015. doi: 10.1038/35039519

Corradi, J., Gumilar, F., and Bouzat, C. (2009). Single-channel kinetic analysis for activation and desensitization of homomeric 5-HT3A receptors. *Biophys. J.* 97, 1335–1345. doi: 10.1016/j.bpj.2009.06.018

Cummins, T. R., Aglieco, F., Renganathan, M., Herzog, R. I., Dib-Hajj, S. D., and Waxman, S. G. (2001). Nav1.3 sodium channels: rapid repriming and slow closed-state inactivation display quantitative differences

after expression in a mammalian cell line and in spinal sensory neurons. *J. Neurosci.* 21, 5952–5961. doi: 10.1523/JNEUROSCI.21-16-05952.2001

D'Arco, M., Giniatullin, R., Simonetti, M., Fabbro, A., Nair, A., Nistri, A., et al. (2007). Neutralization of nerve growth factor induces plasticity of ATP-sensitive P2X3 receptors of nociceptive trigeminal ganglion neurons. *J. Neurosci.* 27, 8190–8201. doi: 10.1523/JNEUROSCI.0713-07.2007

Daws, L. C., Montañez, S., Owens, W. A., Gould, G. G., Frazer, A., Toney, G. M., et al. (2005). Transport mechanisms governing serotonin clearance *in vivo* revealed by high-speed chronoamperometry. *J. Neurosci. Methods* 143, 49–62. doi: 10.1016/j.jneumeth.2004.09.011

Dodick, D. W. (2018). A phase-by-phase review of migraine pathophysiology. *Headache* 58, 4–16. doi: 10.1111/head.13300

Della Pietra, A., Mikhailov, N., and Giniatullin, R. (2020). The emerging role of mechanosensitive piezo channels in migraine pain. *Interna. J. Molecu. Sci.* 21, 696. doi: 10.3390/ijms21030696

Edvinsson, L., Villalón, C. M., and MaassenVanDenBrink, A. (2012). Basic mechanisms of migraine and its acute treatment. *Pharmacol. Ther.* 136, 319–333. doi: 10.1016/j.pharmthera.2012.08.011

Fabbretti, E., D'Arco, M., Fabbro, A., Simonetti, M., Nistri, A., and Giniatullin, R. (2006). Delayed upregulation of ATP P2X3 receptors of trigeminal sensory neurons by calcitonin gene-related peptide. *J. Neurosci.* 26, 6163–6171. doi: 10.1523/JNEUROSCI.0647-06.2006

Fields, R. D., and Burnstock, G. (2006). Purinergic signalling in neuron-glia interactions. *Nat. Rev. Neurosci.* 7, 423–436. doi: 10.1038/nrn1928

Gasparini, S., Migliore, M., and Magee, J. C. (2004). On the initiation and propagation of dendritic spikes in CA1 pyramidal neurons. *J. Neurosci.* 24, 11046–11056. doi: 10.1523/JNEUROSCI.2520-04.2004

Gerevich, Z., Zadori, Z., Müller, C., Wirkner, K., Schröder, W., Rubini, P., et al. (2007). Metabotropic P2Y receptors inhibit P2X3 receptor-channels *via* G protein-dependent facilitation of their desensitization. *Br. J. Pharmacol.* 151, 226–236. doi: 10.1038/sj.bjp.0707217

Giniatullin, R., Gupta, K., and Theoharides, T. (2019). Mast cells in itch, pain and neuro-inflammation. *Front. Cell. Neurosci.* 13:521. doi: 10.3389/fncel.2019.00521

Giniatullin, R., and Nistri, A. (2013). Desensitization properties of P2X3 receptors shaping pain signaling. *Front. Cell. Neurosci.* 7:245. doi: 10.3389/fncel.2013.00245

Grishin, E. V., Savchenko, G. A., Vassilevski, A. A., Korolkova, Y. V., Boychuk, Y. A., Viatchenko-Karpinski, V. Y., et al. (2010). Novel peptide from spider venom inhibits P2X3 receptors and inflammatory pain. *Ann. Neurol.* 67, 680–683. doi: 10.1002/ana.21949

Han, C., Estacion, M., Huang, J., Vasylyev, D., Zhao, P., Dib-Hajj, S. D., et al. (2015). Human $Na_v1.8$: enhanced persistent and ramp currents contribute to distinct firing properties of human DRG neurons. *J. Neurophysiol.* 113, 3172–3185. doi: 10.1152/jn.00113.2015

Helenius, J., Soinne, L., Perkiö, J., Salonen, O., Kangasmäki, A., Kaste, M., et al. (2002). Diffusion-weighted MR imaging in normal human brains in various age groups. *AJNR Am. J. Neuroradiol.* 23, 194–199.

Hines, M., and Carnevale, N. (2003). The NEURON simulation environment. *Neural Comput.* 9, 1179–1209. doi: 10.1162/neco.1997.9.6.1179

Hockley, J. R., Tranter, M. M., McGuire, C., Boundouki, G., Cibert-Goton, V., Thaha, M. A., et al. (2016). P2Y receptors sensitize mouse and human colonic nociceptors. *J. Neurosci.* 36, 2364–2376. doi: 10.1523/JNEUROSCI.3369-15.2016

Ishchenko, Y., Shakirzyanova, A., Giniatullina, R., Skorinkin, A., Bart, G., Turhanen, P., et al. (2017). Selective calcium-dependent inhibition of ATP-gated P2X3 receptors by bisphosphonate-induced endogenous ATP analog ApppI. *J. Pharmacol. Exp. Ther.* 361, 472–481. doi: 10.1124/jpet.116.238840

Israel, M. R., Tanaka, B. S., Castro, J., Thongyoo, P., Robinson, S. D., Zhao, P., et al. (2019). Nav1.6 regulates excitability of mechanosensitive sensory neurons. *J. Physiol.* 597, 3751–3768. doi: 10.1113/JP278148

Jarvis, M. F. (2003). Contributions of P2X3 homomeric and heteromeric channels to acute and chronic pain. *Expert Opin. Ther. Targets* 7, 513–522. doi: 10.1517/14728222.7.4.513

Jin, Y. H., Bailey, T. W., Li, B. Y., Schild, J. H., and Andresen, M. C. (2004). Purinergic and vanilloid receptor activation releases glutamate from separate cranial afferent terminals in nucleus tractus solitarius. *J. Neurosci.* 24, 4709–4717. doi: 10.1523/JNEUROSCI.0753-04.2004

John, K., and Barakat, A. I. (2001). Modulation of ATP/ADP concentration at the endothelial surface by shear stress: effect of flow-induced ATP release. *Ann. Biomed. Eng.* 29, 740–751. doi: 10.1114/1.1397792

Karatas, H., Erdener, S. E., Gursoy-Ozdemir, Y., Lule, S., Eren-Koçak, E., Sen, Z. D., et al. (2013). Spreading depression triggers headache by activating neuronal Panx1 channels. *Science* 339, 1092–1095. doi: 10.1126/science.1231897

Khmyz, V., Maximyuk, O., Teslenko, V., Verkhratsky, A., and Krishtal, O. (2008). P2X3 receptor gating near normal body temperature. *Pflugers Arch.* 456, 339–347. doi: 10.1007/s00424-007-0376-2

Kilinc, E., Guerrero-Toro, C., Zakharov, A., Vitale, C., Gubert-Olive, M., Koroleva, K., et al. (2017). Serotonergic mechanisms of trigeminal meningeal nociception: implications for migraine pain. *Neuropharmacology* 116, 160–173. doi: 10.1016/j.neuropharm.2016.12.024

Komiyama, H., Miyake, K., Asai, K., Mizuno, K., and Shimada, T. (2014). Cyclical mechanical stretch enhances degranulation and IL-4 secretion in RBL-2H3 mast cells. *Cell Biochem. Funct.* 32, 70–76. doi: 10.1002/cbf.2973

Koroleva, K., Gafurov, O., Guselnikova, V. V., Nurkhametova, D., Giniatullina, R., Matilla, O., et al. (2019). Meningeal mast cells contribute to ATP-induced nociceptive firing in trigeminal nerve terminals: direct and indirect purinergic mechanisms triggering migraine pain. *Front. Cell. Neurosci.* 13:195. doi: 10.3389/fncel.2019.00195

Koyuncu Irmak, D., Kilinc, E., and Tore, F. (2019). Shared fate of meningeal mast cells and sensory neurons in migraine. *Front. Cell. Neurosci.* 13:136. doi: 10.3389/fncel.2019.00136

Krishtal, O., Lozovaya, N., Fedorenko, A., Savelyev, I., and Chizhmakov, I. (2006). The agonists for nociceptors are ubiquitous, but the modulators are specific: P2X receptors in the sensory neurons are modulated by cannabinoids. *Pflugers Archiv.* 453, 353–360. doi: 10.1007/s00424-006-0094-1

Lalo, U. V., Pankratov, Y. V., Arndts, D., and Krishtal, O. A. (2001). Omega-conotoxin GVIA potently inhibits the currents mediated by P2X receptors in rat DRG neurons. *Brain Res. Bull.* 54, 507–512. doi: 10.1016/s0361-9230(01)00433-6

Larson, E. D., Vandenbeuch, A., Voigt, A., Meyerhof, W., Kinnamon, S. C., and Finger, T. E. (2015). The role of 5-HT_3receptors in signaling from taste buds to nerves. *J. Neurosci.* 35, 15984–15995. doi: 10.1523/JNEUROSCI.1868-15.2015

Leimuranta, P., Khiroug, L., and Giniatullin, R. (2018). Emerging role of (endo)cannabinoids in migraine. *Front. Pharmacol.* 9:420. doi: 10.3389/fphar.2018.00420

Levy, D., Burstein, R., Kainz, V., Jakubowski, M., and Strassman, A. M. (2007). Mast cell degranulation activates a pain pathway underlying migraine headache. *Pain* 130, 166–176. doi: 10.1016/j.pain.2007.03.012

Lewis, C., Neidhart, S., Holy, C., North, R. A., Buell, G., and Surprenant, A. (1995). Coexpression of P2X2 and P2X3 receptor subunits can account for ATP-gated currents in sensory neurons. *Nature* 377, 432–435. doi: 10.1038/377432a0

Mandge, D., and Manchanda, R. (2018). A biophysically detailed computational model of bladder small DRG neuron soma. *PLoS Comput. Biol.* 14:e1006293. doi: 10.1371/journal.pcbi.1006293

McIlvried, L. A., Cruz, J. A., Borghesi, L. A., and Gold, M. S. (2017). Sex-, stress- and sympathetic post-ganglionic- dependent changes in identity and proportions of immune cells in the dura. *Cephalalgia* 37, 36–48. doi: 10.1177/0333102416637832

Messlinger, K. (2009). Migraine: where and how does the pain originate? *Exp. Brain Res.* 196, 179–193. doi: 10.1007/s00221-009-1756-y

Mikhailov, N., Leskinen, J., Fagerlund, I., Poguzhelskaya, E., Giniatullina, R., Gafurov, O., et al. (2019). Mechanosensitive meningeal nociception via piezo channels: implications for pulsatile pain in migraine? *Neuropharmacology* 149, 113–123. doi: 10.1016/j.neuropharm.2019.02.015

Moffatt, L., and Hume, R. I. (2007). Responses of rat P2X2 receptors to ultrashort pulses of ATP provide insights into ATP binding and channel gating. *J. Gen. Physiol.* 130, 183–201. doi: 10.1085/jgp.200709779

North, R. A. (2004). P2X3 receptors and peripheral pain mechanisms. *J. Physiol.* 554, 301–308. doi: 10.1113/jphysiol.2003.048587

Nurkhametova, D., Kudryavtsev, I., Guselnikova, V., Serebryakova, M., Giniatullina, R. R., Wojciechowski, S., et al. (2019). Activation of

P2X7 receptors in peritoneal and meningeal mast cells detected by uptake of organic dyes: possible purinergic triggers of neuroinflammation in meninges. *Front. Cell. Neurosci.* 13:45. doi: 10.3389/fncel.2019.00045

Olesen, J., Burstein, R., Ashina, M., and Tfelt-Hansen, P. (2009). Origin of pain in migraine: evidence for peripheral sensitisation. *Lancet Neurol.* 8, 679–690. doi: 10.1016/s1474-4422(09)70090-0

Pietrobon, D., and Moskowitz, M. A. (2013). Pathophysiology of migraine. *Ann. Rev. Physiol.* 75, 365–391. doi: 10.1146/annurev-physiol-030212-183717

Pratt, E. B., Brink, T. S., Bergson, P., Voigt, M. M., and Cook, S. P. (2005). Use-dependent in- hibition of P2X3 receptors by nanomolar agonist. *J. Neurosci.* 25, 7359–7365. doi: 10.1523/jneurosci.5189-04.2005

Richards, D., Gever, J. R., Ford, A. P., and Fountain, S. J. (2019). Action of MK-7264 (gefapixant) at human P2X3 and P2X2/3 receptors and *in vivo* efficacy in models of sensitisation. *Br. J. Pharmacol.* 176, 2279–2291. doi: 10.1111/bph.14677

Saftenku, E. (2005). Modeling of slow glutamate diffusion and AMPA receptor activation in the cerebellar glomerulus. *J. Theor. Biol.* 234, 363–382. doi: 10.1016/j.jtbi.2004.11.036

Schueler, M., Neuhuber, W. L., De Col, R., and Messlinger, K. (2014). Innervation of rat and human dura mater and pericranial tissues in the parieto-temporal region by meningeal afferents. *Headache* 54, 996–1009. doi: 10.1111/head.12371

Serrano, A., Mo, G., Grant, R., Paré, M., O'Donnell, D., Yu, X. H., et al. (2012). Differential expression and pharmacology of native P2X receptors in rat and primate sensory neurons. *J. Neurosci.* 32, 11890–11896. doi: 10.1523/JNEUROSCI.0698-12.2012

Shelukhina, I., Mikhailov, N., Abushik, P., Nurullin, L., Nikolsky, E. E., and Giniatullin, R. (2017). Cholinergic nociceptive mechanisms in rat meninges and trigeminal ganglia: potential implications for migraine pain. *Front. Neurol.* 8:163. doi: 10.3389/fneur.2017.00163

Simonetti, M., Fabbro, A., D'Arco, M., Zweyer, M., Nistri, A., Giniatullin, R., et al. (2006). Comparison of P2X and TRPV1 receptors in ganglia or primary culture of trigeminal neurons and their modulation by NGF or serotonin. *Mol. Pain* 2:11. doi: 10.1186/1744-8069-2-11

Skorinkin, A., Nistri, A., and Giniatullin, R. (2003). Bimodal action of protons on ATP currents of rat PC12 cells. *J. Gen. Physiol.* 122, 33–44. doi: 10.1085/jgp.200308825

Sokolova, E., Skorinkin, A., Igor, M., Agrachev, A., Nistri, A., and Giniatullin, R. (2006). Experimental and modeling studies of desensitization of P2X3 receptors. *Mol. Pharmacol.* 70, 373–382. doi: 10.1124/mol.106.023564

Souslova, V., Cesare, P., Ding, Y., Akopian, A. N., Stanfa, L., Suzuki, R., et al. (2000). Warm-coding deficits and aberrant inflammatory pain in mice lacking P2X3 receptors. *Nature* 407, 1015–1017. doi: 10.1038/35039526

Sperlágh, B., Heinrich, A., and Csölle, C. (2007). P2 receptor-mediated modulation of neurotransmitter release—an update. *Purinergic Signal.* 3, 269–284. doi: 10.1007/s11302-007-9080-0

Strassman, A. M., Weissner, W., Williams, M., Ali, S., and Levy, D. (2004). Axon diameters and intradural trajectories of the dural innervation in the rat. *J. Comp. Neurol.* 473, 364–376. doi: 10.1002/cne.20106

Suleymanov, Y., Gafarov, F., Khusnutdinov, N., and Yemelyanova, N. (2015). Optimization of calculation of matter concentration in the diffusion equation with a time-dependent source. *Comput. Technol.* 20, 53–62.

Tanaka, B. S., Nguyen, P. T., Zhou, E. Y., Yang, Y., Yarov-Yarovoy, V., Dib-Hajj, S. D., et al. (2017). Gain-of-function mutation of a voltage-gated sodium channel Nav1.7 associated with peripheral pain and impaired limb development. *J. Biol. Chem.* 292, 9262–9272. doi: 10.1074/jbc.m117.778779

Theoharides, T. C., Kempuraj, D., Tagen, M., Conti, P., and Kalogeromitros, D. (2007). Differential release of mast cell mediators and the pathogenesis of inflammation. *Immunol. Rev.* 217, 65–78. doi: 10.1111/j.1600-065x.2007.00519.x

Tigerholm, J., Petersson, M. E., Obreja, O., Lampert, A., Carr, R., Schmelz, M., et al. (2014). Modeling activity-dependent changes of axonal spike conduction in primary afferent C-nociceptors. *J. Neurophysiol.* 111, 1721–1735. doi: 10.1152/jn.00777.2012

Vaughn, A. H., and Gold, M. S. (2010). Ionic mechanisms underlying inflammatory mediator-induced sensitization of dural afferents. *J. Neurosci.* 30, 7878–7888. doi: 10.1523/jneurosci.6053-09.2010

Viatchenko-Karpinski, V., Novosolova, N., Ishchenko, Y., Azhar, M. A., Wright, M., Tsintsadze, V., et al. (2016). Stable, synthetic analogs of diadenosine tetraphosphate inhibit rat and human P2X3 receptors and inflammatory pain. *Mol. Pain* 12:1744806916637704. doi: 10.1177/1744806916637704

Villa, G., Fumagalli, M., Verderio, C., Abbracchio, M. P., and Ceruti, S. (2010). Expression and contribution of satellite glial cells purinoceptors to pain transmission in sensory ganglia: an update. *Neuron Glia Biol.* 6, 31–42. doi: 10.1017/s1740925x10000086

Vulchanova, L., Arvidsson, U., Riedl, M., Wang, J., Buell, G., Surprenant, A., et al. (1996). Differential distribution of two ATP-gated channels (P2X receptors) determined by immunocytochemistry. *Proc. Natl. Acad. Sci. U S A* 93, 8063–8067. doi: 10.1073/pnas.93.15.8063

Wang, S., Chennupati, R., Kaur, H., Iring, A., Wettschureck, N., and Offermanns, S. (2016). Endothelial cation channel PIEZO1 controls blood pressure by mediating flow-induced ATP release. *J. Clin. Invest.* 126, 4527–4536. doi: 10.1172/jci87343

Wang, F., He, Q., Ren, Z., Li, F., Chen, W., Lin, X., et al. (2015). Association of serum levels of intercellular adhesion molecule-1 and interleukin-6 with migraine. *Neurol. Sci.* 36, 535–540. doi: 10.1007/s10072-014-2010-3

Wang, L., Sikora, J., Hu, L., Shen, X., Grygorczyk, R., and Schwarz, W. (2013). ATP release from mast cells by physical stimulation: a putative early step in activation of acupuncture points. *Evid. Based Complement. Alternat. Med.* 2013:350949. doi: 10.1155/2013/350949

Wood, K. M., Zeqja, A., Nijhout, H. F., Reed, M. C., Best, J., and Hashemi, P. (2014). Voltammetric and mathematical evidence for dual transport mediation of serotonin clearance *in vivo*. *J. Neurochem.* 130, 351–359. doi: 10.1111/jnc.12733

Yegutkin, G. G., Guerrero-Toro, C., Kilinc, E., Koroleva, K., Ishchenko, Y., Abushik, P., et al. (2016). Nucleotide homeostasis and purinergic nociceptive signaling in rat meninges in migraine-like conditions. *Purinergic Signal.* 12, 561–574. doi: 10.1007/s11302-016-9521-8

Zakharov, A., Koroleva, K., and Giniatullin, R. (2016). Clustering analysis for sorting ATP-induced nociceptive firing in rat meninges. *BioNanoScience* 6, 508–512. doi: 10.1007/s12668-016-0276-z

Zakharov, A., Vitale, C., Kilinc, E., Koroleva, K., Fayuk, D., Shelukhina, I., et al. (2015). Hunting for origins of migraine pain: cluster analysis of spontaneous and capsaicin-induced firing in meningeal trigeminal nerve fibers. *Front. Cell. Neurosci.* 9:287. doi: 10.3389/fncel.2015.00287

Zhang, D., Spielmann, A., Wang, L., Ding, G., Huang, F., Gu, Q., et al. (2012). Mast-cell degranulation induced by physical stimuli involves the activation of transient-receptor-potential channel TRPV2. *Physiol. Res.* 61, 113–124. doi: 10.33549/physiolres.932053

Zhao, J., Li, Y., Yang, G., Jiang, K., Lin, H., Ade, H., et al. (2016). Efficient organic solar cells processed from hydrocarbon solvents. *Nature Energy* 1:15027. doi: 10.1038/nenergy.2015.27

Conflict of Interest: The authors declare that the research was conducted in the absence of any commercial or financial relationships that could be construed as a potential conflict of interest.

Copyright © 2020 Suleimanova, Talanov, Gafurov, Gafarov, Koroleva, Virenque, Noe, Mikhailov, Nistri and Giniatullin. This is an open-access article distributed under the terms of the Creative Commons Attribution License (CC BY). The use, distribution or reproduction in other forums is permitted, provided the original author(s) and the copyright owner(s) are credited and that the original publication in this journal is cited, in accordance with accepted academic practice. No use, distribution or reproduction is permitted which does not comply with these terms.

Advantages of publishing in Frontiers

OPEN ACCESS
Articles are free to read for greatest visibility and readership

FAST PUBLICATION
Around 90 days from submission to decision

HIGH QUALITY PEER-REVIEW
Rigorous, collaborative, and constructive peer-review

TRANSPARENT PEER-REVIEW
Editors and reviewers acknowledged by name on published articles

Frontiers
Avenue du Tribunal-Fédéral 34
1005 Lausanne | Switzerland

Visit us: www.frontiersin.org
Contact us: frontiersin.org/about/contact

REPRODUCIBILITY OF RESEARCH
Support open data and methods to enhance research reproducibility

DIGITAL PUBLISHING
Articles designed for optimal readership across devices

FOLLOW US
@frontiersin

IMPACT METRICS
Advanced article metrics track visibility across digital media

EXTENSIVE PROMOTION
Marketing and promotion of impactful research

LOOP RESEARCH NETWORK
Our network increases your article's readership